

SERIES IN CONDENSED MATTER PHYSICS

UNDERSTANDING QUANTUM PHASE TRANSITIONS



LINCOLN D. CARR



CRC Press

Taylor & Francis Group

A TAYLOR & FRANCIS BOOK

Understanding Quantum Phase Transitions

Series in Condensed Matter Physics

Series Editor:

D R Vij

Department of Physics, Kurukshetra University, India

Other titles in the series include:

Magnetic Anisotropies in Nanostructured Matter

Peter Weinberger

Aperiodic Structures in Condensed Matter: *Fundamentals and Applications*

Enrique Maciá Barber

Thermodynamics of the Glassy State

Luca Leuzzi, Theo M Nieuwenhuizen

One- and Two-Dimensional Fluids: *Properties of Smectic, Lamellar and*

Columnar Liquid Crystals

A Jákli, A Saupe

Theory of Superconductivity: From Weak to Strong Coupling

A S Alexandrov

The Magnetocaloric Effect and Its Applications

A M Tishin, Y I Spichkin

Field Theories in Condensed Matter Physics

Sumathi Rao

Nonlinear Dynamics and Chaos in Semiconductors

K Aoki

Permanent Magnetism

R Skomski, J M D Coey

Modern Magnetooptics and Magnetooptical Materials

A K Zvezdin, V A Kotov

Series in Condensed Matter Physics

Understanding Quantum Phase Transitions

Lincoln D. Carr



CRC Press

Taylor & Francis Group

Boca Raton London New York

CRC Press is an imprint of the
Taylor & Francis Group, an **informa** business
A TAYLOR & FRANCIS BOOK

CRC Press
Taylor & Francis Group
6000 Broken Sound Parkway NW, Suite 300
Boca Raton, FL 33487-2742

© 2011 by Taylor and Francis Group, LLC
CRC Press is an imprint of Taylor & Francis Group, an Informa business

No claim to original U.S. Government works

Printed in the United States of America on acid-free paper
10 9 8 7 6 5 4 3 2 1

International Standard Book Number: 978-1-4398-0251-9 (Hardback)

This book contains information obtained from authentic and highly regarded sources. Reasonable efforts have been made to publish reliable data and information, but the author and publisher cannot assume responsibility for the validity of all materials or the consequences of their use. The authors and publishers have attempted to trace the copyright holders of all material reproduced in this publication and apologize to copyright holders if permission to publish in this form has not been obtained. If any copyright material has not been acknowledged please write and let us know so we may rectify in any future reprint.

Except as permitted under U.S. Copyright Law, no part of this book may be reprinted, reproduced, transmitted, or utilized in any form by any electronic, mechanical, or other means, now known or hereafter invented, including photocopying, microfilming, and recording, or in any information storage or retrieval system, without written permission from the publishers.

For permission to photocopy or use material electronically from this work, please access www.copyright.com (<http://www.copyright.com/>) or contact the Copyright Clearance Center, Inc. (CCC), 222 Rosewood Drive, Danvers, MA 01923, 978-750-8400. CCC is a not-for-profit organization that provides licenses and registration for a variety of users. For organizations that have been granted a photocopy license by the CCC, a separate system of payment has been arranged.

Trademark Notice: Product or corporate names may be trademarks or registered trademarks, and are used only for identification and explanation without intent to infringe.

Library of Congress Cataloging-in-Publication Data

Understanding quantum phase transitions / [edited by] Lincoln Carr.
p. cm. -- (Condensed matter physics)

Summary: "Exploring a steadily growing field, this book focuses on quantum phase transitions (QPT), frontier area of research. It takes a look back as well as a look forward to the future and the many open problems that remain. The book covers new concepts and directions in QPT and specific models and systems closely tied to particular experimental realization or theoretical methods. Although mainly theoretical, the book includes experimental chapters that make the discussion of QPTs meaningful. The book also presents recent advances in the numerical methods used to study QPTs"-- Provided by publisher.

Includes bibliographical references and index.

ISBN 978-1-4398-0251-9 (hardback)

1. Phase transformations (Statistical physics) 2. Transport theory. 3. Quantum statistics. I. Carr, Lincoln. II. Title. III. Series.

QC175.16.P5U53 2010
530.4'74--dc22

2010034921

Visit the Taylor & Francis Web site at
<http://www.taylorandfrancis.com>

and the CRC Press Web site at
<http://www.crcpress.com>

Dedication

To Badia, Samuel, and Halim
For their patience and love
And to the three magical children
Who appeared in my life as I completed this book
Ahmed, Oumaima, and Yassmina

Contributors

Sami Amasha
Stanford University, U.S.A.

George G. Batrouni
Université de Nice - Sophia
Antipolis, France

Immanuel Bloch
Ludwig-Maximilians-Universität,
Germany

Mark A. Caprio
University of Notre Dame, U.S.A.

Lincoln D. Carr
Colorado School of Mines, U.S.A.

Claudio Castelnovo
Oxford University, U.K.

Sudip Chakravarty
University of California Los Angeles,
U.S.A.

Ignacio Cirac
Max-Planck-Institut für
Quantenoptik, Germany

J.C. Davis
Cornell University, U.S.A.
Brookhaven National Laboratory,
U.S.A.
University of St. Andrews, Scotland

Philipp Gegenwart
University of Göttingen, Germany

Thierry Giamarchi
University of Geneva, Switzerland

David Goldhaber-Gordon
Stanford University, U.S.A.

Andrew D. Greentree
University of Melbourne, Australia

Vladimir Gritsev
University of Fribourg, Switzerland

Sean Hartnoll
Harvard University, U.S.A.

Tetsuo Hatsuda
University of Tokyo, Japan

Lloyd C. L. Hollenberg
University of Melbourne, Australia

Francesco Iachello
Yale University, U.S.A.

Tetsuaki Itou
Kyoto University, Japan

Rina Kanamoto
Ochanomizu University, Japan

Reizo Kato
RIKEN, Japan

Yuki Kawaguchi
University of Tokyo, Japan

Eun-Ah Kim

Cornell University, U.S.A.

Sergey Kravchenko

Northeastern University, U.S.A.

Michael J. Lawler

The State University of New York at
Binghamton, U.S.A.
Cornell University, U.S.A.

Karyn Le Hur

Yale University, U.S.A.

Kenji Maeda

The University of Tokyo, Japan

Andrew J. Millis

Columbia University, U.S.A.

Valentin Murg

Max-Planck-Institut für
Quantenoptik, Germany

Yuval Oreg

Weizmann Institute of Science, Israel

Gerardo Ortiz

Indiana University, U.S.A.

Masaki Oshikawa

University of Tokyo, Japan

Anatoli Polkovnikov

Boston University, U.S.A.

Nikolay Prokof'ev

University of Massachusetts,
Amherst, U.S.A.

Ileana G. Rau

Stanford University, U.S.A.

Subir Sachdev

Harvard University, U.S.A.

Richard T. Scalettar

University of California, Davis,
U.S.A.

Ulrich Schollwöck

University of Munich, Germany

Alexander Shashkin

Institute of Solid State Physics,
Russia

Qimiao Si

Rice University, U.S.A.

Frank Steglich

Max Planck Institute for Chemical
Physics of Solids, Germany

Boris Svistunov

University of Massachusetts,
Amherst, U.S.A.

Simon Trebst

University of California, Santa
Barbara, U.S.A.

Matthias Troyer

ETH Zurich, Switzerland

Masahito Ueda

University of Tokyo, Japan

Frank Verstraete

Universität Wien, Austria

Guifré Vidal

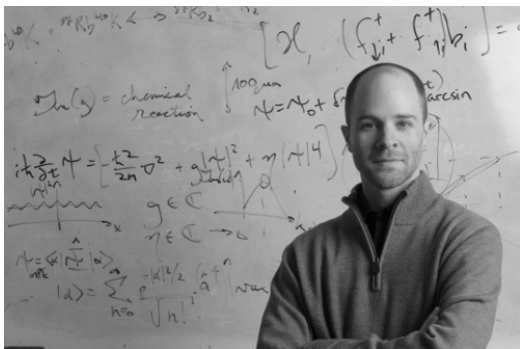
The University of Queensland,
Australia

Philipp Werner

ETH Zurich, Switzerland

Editor

Lincoln D. Carr is a theoretical physicist who works primarily in quantum many-body theory, artificial materials, and nonlinear dynamics. He obtained his B.A. in physics at the University of California, Berkeley in 1994. He attended the University of Washington in Seattle from 1996 to 2001, where he received both his M.S. and Ph.D. in physics. He was a Distinguished International Fellow of the National Science Foundation from 2001-2004 at the Ecole normale supérieure in Paris and a professional research associate at JILA in Boulder, Colorado from 2003-2005. He joined the faculty in the physics department at the Colorado School of Mines in 2005, where he is presently an associate professor. He is an Associate of the National Institute of Standards and Technology and has been a visiting researcher at the Max Planck Institute for the Physics of Complex Systems in Dresden, Germany, the Kavli Institute of Theoretical Physics in Santa Barbara, California, the Institut Henri Poincaré at the Université Pierre et Marie Curie in Paris, and the Kirchhoff Institute for Physics at the University of Heidelberg.



Preface

Phase transitions occur in all fields of the physical sciences and are crucial in engineering as well; abrupt changes from one state of matter to another are apparent everywhere we look, from the freezing of rivers to the steam rising up from the tea kettle. But why should it be only temperature and pressure that drive such abrupt transitions? In fact, quantum fluctuations can replace thermal fluctuations, a phase transition can occur even at zero temperature, and the concept of a phase transition turns out to be a lot more general than it is made out to be in elementary thermodynamics. Over the last twenty or so years the field of *quantum phase transitions* (QPTs) has seen steady growth. This book focuses especially on the latter half of this development. There are now so many experimental examples of QPTs that we hardly have space to include them all in a single volume. New numerical methods have opened up quantum many-body problems thought impossible to solve or understand. We can treat open and closed systems; we begin to understand the role of entanglement; we find or predict QPTs in naturally occurring systems ranging from chunks of matter to neutron stars, as well as engineered ones like quantum dots.

There are now almost five thousand papers devoted to QPTs. This book gives us a chance to pause and look back as well as to look forward to the future and the many open problems that remain. QPTs are a frontier area of research in many-body quantum mechanics, particularly in condensed matter physics. While we emphasize condensed matter, we include an explicit section at the end on QPTs across physics, and connections to other fields appear throughout the text. The book is divided into five parts, each containing from four to seven chapters.

Part I is intended to be somewhat more accessible to advanced graduate students and researchers entering the field. Thus it includes four more pedagogical, slightly longer chapters, covering new concepts and directions in QPTs: finite temperature and transport, dissipation, dynamics, and topological phases. Each of these chapters leads the reader from simpler ideas and concepts to the latest advances in these areas. The last two chapters of Part I cover entanglement, an important new tool for analysis of quantum many-body systems: first from a quantum-information-theoretic perspective, then from a geometrical picture tied to physical observables.

Part II delves into specific models and systems, in seven chapters. These are more closely tied to particular experimental realizations or theoretical methods. The topics include topological order, the Kondo lattice, ultracold

quantum gases, dissipation and cavity quantum electrodynamics (QED), spin systems and group theory, Hubbard models, and metastability and finite-size effects.

Part III covers experiments, in six chapters. Although the book is mainly theoretical, the experimental chapters are key to making our whole discussion of QPTs meaningful; there are many observations now supporting the theories laid out in these pages. We present a selection covering a range of such experiments, including quantum dots, 2D electron systems, high- T_c materials, molecular systems, heavy fermions, and ultracold quantum gases in optical lattices.

Part IV presents recent advances in the key numerical methods used to study QPTS, in five chapters. These include the worm algorithm for quantum Monte Carlo, cluster Monte Carlo for dissipative QPTs, time-dependent density matrix renormalization group methods, new ideas in matrix product state methods, and dynamical mean field theory.

Finally, Part V presents a selection of QPTs in fields besides condensed matter physics, in four chapters. These include neutron stars and the quark-gluon plasma, cavity QED, nuclei, and a new mapping, now used by many string theorists, from classical gravitational theories (anti-de Sitter space) to conformal quantum field theories.

You can read this book by skipping around from topic to topic; that is how I edited it. However, in retrospect, I strongly recommend spending some time in Part I before delving into whichever topics catch your interest in the rest of the book. I also recommend reading thoroughly one or two experimental chapters early on in your perusing of this text, as it puts the rest in perspective.

This book tells its own story, and besides a few words of thanks, I won't delay you further with my remarks.

First and foremost, I thank the authors, who wrote amazing chapters from which I learned a tremendous amount. It is their writing that made the two years of effort I spent taking this book from conception to completion worth every last minute. The layout of the book and topic choices, although ultimately my own choice and my own responsibility, received useful input from many of the authors, for which I am also thankful.

I am grateful to the Aspen Center for Physics, which hosted a number of authors of this book, including myself, while we wrote our respective chapters. I am grateful to the Kirchhoff Institute for Physics and the Graduate School for Fundamental Physics at the University of Heidelberg, for hosting me during an important initial phase of the book.

I thank my post-doc and graduate students who offered a student perspective on these chapters, ensuring the text would be useful for physicists at levels ranging from graduate student to emeritus professor: Dr. Miguel-Ángel García-March, Laith Haddad, Dr. David Larue, Scott Strong, and Michael Wall. I thank Jim McNeil and Chip Durfee for their perspectives on nuclear physics and quantum optics, respectively, which they brought to bear in supplemental reviews for Part V, and Jim Bernard and David Wood for their

overall comments as well. I thank John Navas and Sarah Morris from Taylor & Francis, for doing a spectacular job in bringing the book to a finished product.

My wife and children were very, very patient with me throughout the process. I thank them for their love and support.

Last but not least, I am grateful to Jeff and Jean at Higher Grounds Café, where I did a good part of the detailed work on this book.

This work was supported by the National Science Foundation under Grant PHY-0547845 as part of the NSF CAREER program.

Contents

I New Directions and New Concepts in Quantum Phase Transitions	1
1 Finite Temperature Dissipation and Transport Near Quantum Critical Points	3
<i>Subir Sachdev</i>	
1.1 Model Systems and Their Critical Theories	4
1.1.1 Coupled Dimer Antiferromagnets	4
1.1.2 Deconfined Criticality	6
1.1.3 Graphene	8
1.1.4 Spin Density Waves	9
1.2 Finite Temperature Crossovers	11
1.3 Quantum Critical Transport	15
1.4 Exact Results for Quantum Critical Transport	17
1.5 Hydrodynamic Theory	21
1.5.1 Relativistic Magnetohydrodynamics	21
1.5.2 Dyonic Black Hole	23
1.5.3 Results	23
1.6 The Cuprate Superconductors	25
Bibliography	28
2 Dissipation, Quantum Phase Transitions, and Measurement	31
<i>Sudip Chakravarty</i>	
2.1 Multiplicity of Dynamical Scales and Entropy	32
2.2 Dissipation	35
2.3 Quantum Phase Transitions	36
2.3.1 Infinite Number of Degrees of Freedom	36
2.3.2 Broken Symmetry	38
2.3.2.1 Unitary Inequivalence	38
2.4 Measurement Theory	39
2.4.1 Coleman-Hepp Model	39
2.4.2 Tunneling Versus Coherence	41
2.4.3 Quantum-to-Classical Transition	42
2.5 Von Neumann Entropy	43
2.5.1 A Warmup Exercise: Damped Harmonic Oscillator . .	44
2.5.2 Double Well Coupled to a Dissipative Heat Bath . .	45
2.5.3 Disordered Systems	46

2.5.3.1	Anderson Localization	47
2.5.3.2	Integer Quantum Hall Plateau Transitions	48
2.5.3.3	Infinite Randomness Fixed Point	49
2.6	Disorder and First Order Quantum Phase Transitions	51
2.7	Outlook	53
	Bibliography	55
3	Universal Dynamics Near Quantum Critical Points	59
	<i>Anatoli Polkovnikov and Vladimir Gritsev</i>	
3.1	Brief Review of the Scaling Theory for Second Order Phase Transitions	61
3.2	Scaling Analysis for Dynamics near Quantum Critical Points	65
3.3	Adiabatic Perturbation Theory	73
3.3.1	Sketch of the Derivation	73
3.3.2	Applications to Dynamics near Critical Points	76
3.3.3	Quenches at Finite Temperatures, and the Role of Quasi-particle Statistics	79
3.4	Going Beyond Condensed Matter	81
3.4.1	Adiabaticity in Cosmology	81
3.4.2	Time Evolution in a Singular Space-Time	84
3.5	Summary and Outlook	86
	Bibliography	88
4	Fractionalization and Topological Order	91
	<i>Masaki Oshikawa</i>	
4.1	Quantum Phases and Orders	91
4.2	Conventional Quantum Phase Transitions: Transverse Ising Model	92
4.3	Haldane-Gap Phase and Topological Order	93
4.3.1	Quantum Antiferromagnets	93
4.3.2	Quantum Antiferromagnetic Chains and the Valence Bonds	95
4.3.3	AKLT State and the Haldane Gap	96
4.3.4	Haldane Phase and Topological Order	98
4.3.5	Edge States	99
4.4	RVB Quantum Spin Liquid and Topological Order	100
4.4.1	Introduction to RVB States	100
4.4.2	Quantum Dimer Model	101
4.4.3	Commensurability and Spin Liquids	102
4.4.4	Topological Degeneracy of the RVB Spin Liquid	103
4.4.5	Fractionalization in the RVB Spin Liquid	105
4.5	Fractionalization and Topological Order	106
4.5.1	What is Topological Order?	106
4.5.2	Fractionalization: General Definition	106
4.5.3	Fractionalization Implies Topological Degeneracy	108

4.5.4	Implications	110
4.6	Outlook	111
	Bibliography	113
5	Entanglement Renormalization: An Introduction	115
	<i>Guifré Vidal</i>	
5.1	Coarse Graining and Ground State Entanglement	116
5.1.1	A Real-Space Coarse-Graining Transformation	117
5.1.2	Ground State Entanglement	119
5.1.3	Accumulation of Short-Distance Degrees of Freedom .	121
5.2	Entanglement Renormalization	122
5.2.1	Disentanglers	123
5.2.2	Ascending and Descending Superoperators	123
5.2.3	Multi-scale Entanglement Renormalization Ansatz .	125
5.3	The Renormalization Group Picture	127
5.3.1	A Real-Space Renormalization-Group Map	127
5.3.2	Properties of the Renormalization-Group Map	128
5.3.3	Fixed Points of Entanglement Renormalization	129
5.4	Quantum Criticality	130
5.4.1	Scaling Operators and Critical Exponents	130
5.4.2	Correlators and the Operator Product Expansion . .	132
5.4.3	Surface Critical Phenomena	133
5.5	Summary and Outlook	135
	Bibliography	137
6	The Geometry of Quantum Phase Transitions	139
	<i>Gerardo Ortiz</i>	
6.1	Entanglement and Quantum Phase Transitions	141
6.1.1	Entanglement 101	141
6.1.2	Generalized Entanglement	142
6.1.3	Quantifying Entanglement: Purity	143
6.1.3.1	A Simple Example	144
6.1.4	Statics of Quantum Phase Transitions	145
6.1.5	Dynamics of Quantum Phase Transitions	148
6.2	Topological Quantum Numbers and Quantum Phase Transitions	150
6.2.1	Geometric Phases and Response Functions	151
6.2.2	The Geometry of Response Functions	154
6.2.3	The Geometry of Quantum Information	157
6.2.4	Phase Diagrams and Topological Quantum Numbers .	158
6.3	Outlook	160
6.4	Appendix: Generalized Coherent States	162
	Bibliography	163

II Progress in Model Hamiltonians and in Specific Systems	167
7 Topological Order and Quantum Criticality	169
<i>Claudio Castelnovo, Simon Trebst, and Matthias Troyer</i>	
7.1 Introduction	169
7.1.1 The Toric Code	170
7.2 Quantum Phase Transitions	173
7.2.1 Lorentz-Invariant Transitions	175
7.2.1.1 Other Hamiltonian Deformations	178
7.2.2 Conformal Quantum Critical Points	178
7.2.2.1 Microscopic Model for Wavefunction Deformation	179
7.2.2.2 Dimensionality Reduction and the 2D Ising Model	180
7.2.2.3 Topological Entropy	181
7.2.2.4 Topological Entropy along the Wavefunction Deformation	183
7.3 Thermal Transitions	184
7.3.1 Non-local Order Parameters at Finite Temperature	185
7.3.2 Topological Entropy at Finite Temperature	186
7.3.3 Fragile vs. Robust Behavior: A Matter of (De)confinement	187
7.4 Outlook	188
Bibliography	191
8 Quantum Criticality and the Kondo Lattice	193
<i>Qimiao Si</i>	
8.1 Introduction	194
8.1.1 Quantum Criticality: Competing Interactions in Many-Body Systems	194
8.1.2 Heavy Fermion Metals	196
8.1.3 Quantum Critical Point in Antiferromagnetic Heavy Fermions	198
8.2 Heavy Fermi Liquid of Kondo Lattices	199
8.2.1 Single-Impurity Kondo Model	199
8.2.2 Kondo Lattice and Heavy Fermi Liquid	200
8.3 Quantum Criticality in the Kondo Lattice	203
8.3.1 General Considerations	203
8.3.2 Microscopic Approach Based on the Extended Dynamical Mean-Field Theory	204
8.3.3 Spin-Density-Wave Quantum Critical Point	205
8.3.4 Local Quantum Critical Point	206
8.4 Antiferromagnetism and Fermi Surfaces in Kondo Lattices	207
8.5 Towards a Global Phase Diagram	208

8.5.1	How to Melt a Kondo-Destroyed Antiferromagnet	208
8.5.2	Global Phase Diagram	209
8.6	Experiments	210
8.6.1	Quantum Criticality	210
8.6.2	Global Phase Diagram	211
8.7	Summary and Outlook	212
8.7.1	Kondo Lattice	212
8.7.2	Quantum Criticality	212
8.7.3	Global Phase Diagram	213
8.7.4	Superconductivity	213
	Bibliography	213
9	Quantum Phase Transitions in Spin-Boson Systems: Dissipation and Light Phenomena	217
<i>Karyn Le Hur</i>		
9.1	Dissipative Transitions for the Two-State System	217
9.1.1	Ohmic Case	218
9.1.2	Exact Results	219
9.1.3	Spin Dynamics and Entanglement	221
9.1.4	Sub-ohmic Case	223
9.1.5	Realizations	224
9.2	Dissipative Spin Array	225
9.2.1	Boson-Mediated Magnetic Interaction	225
9.2.2	Solvable Dissipative Model	226
9.2.3	Dissipative ϕ^4 Theory	227
9.2.4	Critical Exponents	227
9.2.5	Realizations	228
9.3	One-Mode Superradiance Model	229
9.3.1	Hamiltonian	229
9.3.2	Normal Phase	230
9.3.3	Superradiant Phase	230
9.3.4	Second-Order Quantum Phase Transition	231
9.3.5	Realizations	232
9.4	Jaynes-Cummings Lattice	232
9.4.1	Hamiltonian	233
9.4.2	Mott Insulator-Superfluid Transition	233
9.4.3	Spin-1/2 Mapping for the Polaritons	235
9.4.4	Field Theory Approach to the Transition	235
9.4.5	Realizations	236
9.5	Conclusion	237
	Bibliography	237

10 Topological Excitations in Superfluids with Internal Degrees of Freedom	241
<i>Yuki Kawaguchi and Masahito Ueda</i>	
10.1 Quantum Phases and Symmetries	242
10.1.1 Group-Theoretic Characterization of the Order Parameter	242
10.1.2 Symmetries and Order Parameters of Spinor BECs	244
10.1.2.1 Spin-1	244
10.1.2.2 Spin-2	245
10.1.3 Order-Parameter Manifold	246
10.2 Homotopy Classification of Defects	247
10.3 Topological Excitations	250
10.3.1 Line Defects	251
10.3.1.1 Nonquantized Circulation	251
10.3.1.2 Fractional Vortices	253
10.3.2 Point Defects	254
10.3.2.1 't Hooft-Polyakov Monopole (Hedgehog)	254
10.3.2.2 Dirac Monopole	254
10.3.3 Particle-like Solitons	255
10.4 Special Topics	257
10.4.1 The Kibble-Zurek Mechanism	257
10.4.2 Knot Soliton	258
10.5 Conclusion and Discussion	261
Bibliography	263
11 Quantum Monte Carlo Studies of the Attractive Hubbard Hamiltonian	265
<i>Richard T. Scalettar and George G. Batrouni</i>	
11.1 Quantum Monte Carlo Methods	267
11.2 Pseudogap Phenomena	269
11.2.1 Chemical Potential and Magnetic Susceptibility	269
11.2.2 Scaling of NMR Relaxation Rate	271
11.3 The Effect of Disorder	272
11.3.1 Real Space Pair Correlation Function	273
11.3.2 Superfluid Stiffness	275
11.3.3 Density of States	276
11.4 Imbalanced Populations	278
11.4.1 FFLO Pairing in 1D	280
11.5 Outlook	280
Bibliography	284
12 Quantum Phase Transitions in Quasi-One-Dimensional Systems	289
<i>Thierry Giamarchi</i>	
12.1 Spins: From Luttinger Liquids to Bose-Einstein Condensates	290

12.1.1 Coupled Spin-1/2 Chains	291
12.1.2 Dimer or Ladder Coupling	292
12.2 Bosons: From Mott Insulators to Superfluids	297
12.2.1 Coupled Superfluid: Dimensional Crossover	298
12.2.2 Coupled Mott Chains: Deconfinement Transition	299
12.3 Fermions: Dimensional Crossover and Deconfinement	300
12.3.1 Dimensional Crossover	302
12.3.2 Deconfinement Transition	304
12.4 Conclusions and Perspectives	306
Bibliography	307
13 Metastable Quantum Phase Transitions in a One-Dimensional Bose Gas	311
<i>Lincoln D. Carr, Rina Kanamoto, and Masahito Ueda</i>	
13.1 Fundamental Considerations	314
13.2 Topological Winding and Unwinding: Mean-Field Theory	317
13.3 Finding the Critical Boundary: Bogoliubov Analysis	319
13.4 Weakly-Interacting Many-Body Theory: Exact Diagonalization	322
13.5 Strongly-Interacting Many-Body Theory: Tonks-Girardeau Limit	327
13.6 Bridging All Regimes: Finite-Size Bethe Ansatz	330
13.7 Conclusions and Outlook	335
Bibliography	336
III Experimental Realizations of Quantum Phases and Quantum Phase Transitions	339
14 Quantum Phase Transitions in Quantum Dots	341
<i>Ileana G. Rau, Sami Amasha, Yuval Oreg, and David Goldhaber-Gordon</i>	
14.1 The Kondo Effect and Quantum Dots: Theory	344
14.1.1 Brief History of the Kondo Effect	344
14.1.2 Theory of Conductance through Quantum Dots	346
14.1.3 Examples of Conductance Scaling Curves	347
14.1.3.1 $G(V, T)$ in the Two-Channel Kondo Case	348
14.1.3.2 $G(V, T)$ in the Single-Channel Kondo Case	348
14.2 Kondo and Quantum Dots: Experiments	349
14.2.1 The Two-Channel Kondo Effect in a Double Quantum Dot	349
14.2.2 The Two-Channel Kondo Effect in Other Quantum Dot Geometries	353
14.2.3 The Two-Channel Kondo Effect in Graphene Sheets	354
14.2.4 The Two-Impurity Kondo Effect in a Double Quantum Dot Geometry	355
14.2.5 The Two-Impurity Kondo Effect in a Quantum Dot at the Singlet-triplet Transition	356

14.3 Looking Forward	358
14.3.1 Influence of Channel Asymmetry and Magnetic Field on the Two-Channel Kondo Effect	359
14.3.2 Multiple Sites	360
14.3.3 Different Types of Reservoirs	361
14.3.3.1 Superconducting Leads and Graphene at the Dirac Point	361
14.3.3.2 The Bose-Fermi Kondo Model in Quantum Dots	362
Bibliography	363
15 Quantum Phase Transitions in Two-Dimensional Electron Systems	369
<i>Alexander Shashkin and Sergey Kravchenko</i>	
15.1 Strongly and Weakly Interacting 2D Electron Systems	369
15.2 Proof of the Existence of Extended States in the Landau Levels	371
15.3 Metal-Insulator Transitions in Perpendicular Magnetic Fields	373
15.3.1 Floating-Up of Extended States	373
15.3.2 Similarity of the Insulating Phase and Quantum Hall Phases	376
15.3.3 Scaling and Thermal Broadening	379
15.4 Zero-Field Metal-Insulator Transition	381
15.5 Possible Ferromagnetic Transition	384
15.6 Outlook	386
Bibliography	387
16 Local Observables for Quantum Phase Transitions in Strongly Correlated Systems	393
<i>Eun-Ah Kim, Michael J. Lawler, and J.C. Davis</i>	
16.1 Why Use Local Probes?	394
16.1.1 Nanoscale Heterogeneity	394
16.1.2 Quenched Impurity as a Tool	395
16.1.3 Interplay between Inhomogeneity and Dynamics	395
16.1.4 Guidance for Suitable Microscopic Models	396
16.2 What are the Challenges?	396
16.3 Searching for Quantum Phase Transitions Using STM	397
16.3.1 STM Hints towards Quantum Phase Transitions	398
16.3.2 Theory of the Nodal Nematic Quantum Critical Point in Homogeneous <i>d</i> -wave Superconductors	402
16.4 Looking Ahead	409
Bibliography	414
17 Molecular Quasi-Triangular Lattice Antiferromagnets	419
<i>Reizo Kato and Tetsuaki Itou</i>	
17.1 Anion Radical Salts of Pd(dmit) ₂	420

17.2	Crystal Structure	420
17.3	Electronic Structure: Molecule, Dimer, and Crystal	422
17.4	Long-Range Antiferromagnetic Order vs. Frustration	424
17.5	Quantum Spin-Liquid State in the EtMe ₃ Sb Salt	425
17.6	Other Ground States: Charge Order and Valence Bond Solid	430
17.6.1	Charge Order Transition in the Et ₂ Me ₂ Sb Salt	430
17.6.2	Valence-Bond Solid State in the EtMe ₃ P Salt	432
17.6.3	Intra- and Inter-Dimer Valence Bond Formations	433
17.7	Pressure-Induced Mott Transition	433
17.7.1	Pressure-Induced Metallic State in the Solid-Crossing Column System	434
17.7.2	Phase Diagram for the EtMe ₃ P Salt: Superconductivity and Valence-Bond Solid	434
17.8	Conclusion	439
	Bibliography	440
18	Probing Quantum Criticality and its Relationship with Superconductivity in Heavy Fermions	445
	<i>Philipp Gegenwart and Frank Steglich</i>	
18.1	Heavy Fermions	445
18.2	Heavy Fermi Liquids and Antiferromagnets	447
18.3	Heavy-Fermion Superconductors	447
18.4	Spin-Density-Wave-Type Quantum Criticality	451
18.5	Quantum Criticality Beyond the Conventional Scenario	453
18.6	Interplay between Quantum Criticality and Unconventional Superconductivity	457
18.7	Conclusions and Open Questions	459
	Bibliography	462
19	Strong Correlation Effects with Ultracold Bosonic Atoms in Optical Lattices	469
	<i>Immanuel Bloch</i>	
19.1	Optical Lattices	469
19.1.1	Optical Potentials	469
19.1.2	Optical Lattices	471
19.1.2.1	Band Structure	473
19.1.3	Time-of-Flight Imaging and Adiabatic Mapping	475
19.1.3.1	Sudden Release	475
19.1.3.2	Adiabatic Mapping	476
19.2	Many-Body Effects in Optical Lattices	477
19.2.1	Bose-Hubbard Model	478
19.2.2	Superfluid-Mott-Insulator Transition	479
19.2.2.1	Superfluid Phase	479
19.2.2.2	Mott-Insulating Phase	480
19.2.2.3	Phase Diagram	481

19.2.2.4	In-Trap Density Distribution	483
19.2.2.5	Phase Coherence Across the SF-MI Transition	484
19.2.2.6	Excitation Spectrum	487
19.2.2.7	Number Statistics	487
19.2.2.8	Dynamics near Quantum Phase Transitions .	488
19.2.2.9	Bose-Hubbard Model with Finite Current .	490
19.3	Outlook	492
	Bibliography	493
IV	Numerical Solution Methods for Quantum Phase Transitions	497
20	Worm Algorithm for Problems of Quantum and Classical Statistics	499
<i>Nikolay Prokof'ev and Boris Svistunov</i>		
20.1	Path-Integrals in Discrete and Continuous Space	499
20.2	Loop Representations for Classical High-Temperature Expansions	502
20.3	Worm Algorithm: The Concept and Realizations	503
20.3.1	Discrete Configuration Space: Classical High-Temperature Expansions	504
20.3.2	Continuous Time: Quantum Lattice Systems	505
20.3.3	Bosons in Continuous Space	508
20.3.4	Momentum Conservation in Feynman Diagrams	509
20.4	Illustrative Applications	510
20.4.1	Optical-Lattice Bosonic Systems	510
20.4.2	Supersolidity of Helium-4	512
20.4.3	The Problem of Deconfined Criticality and the Flowgram Method	516
20.5	Conclusions and Outlook	520
	Bibliography	521
21	Cluster Monte Carlo Algorithms for Dissipative Quantum Phase Transitions	523
<i>Philipp Werner and Matthias Troyer</i>		
21.1	Dissipative Quantum Models	523
21.1.1	The Caldeira-Leggett Model	523
21.1.2	Dissipative Quantum Spin Chains	525
21.1.3	Resistively Shunted Josephson Junction	525
21.1.4	Single Electron Box	527
21.2	Importance Sampling and the Metropolis Algorithm	528
21.3	Cluster Algorithms for Classical Spins	530
21.3.1	The Swendsen-Wang and Wolff Cluster Algorithms .	530
21.3.2	Efficient Treatment of Long-Range Interactions	532
21.4	Cluster Algorithm for Resistively Shunted Josephson Junctions	534

21.4.1 Local Updates in Fourier Space	535
21.4.2 Cluster Updates	535
21.5 Winding Number Sampling	538
21.5.1 Path-Integral Monte Carlo	539
21.5.2 Transition Matrix Monte Carlo	539
21.6 Applications and Open Questions	542
21.6.1 Single Spins Coupled to a Dissipative Bath	542
21.6.2 Dissipative Spin Chains	542
21.6.3 The Single Electron Box	543
21.6.4 Resistively Shunted Josephson Junctions	543
Bibliography	544
22 Current Trends in Density Matrix Renormalization Group Methods	547
<i>Ulrich Schollwöck</i>	
22.1 The Density Matrix Renormalization Group	547
22.1.1 Introduction	547
22.1.2 Infinite-System and Finite-System Algorithms	549
22.2 DMRG and Entanglement	552
22.3 Density Matrix Renormalization Group and Matrix Product States	553
22.3.1 Matrix Product States	553
22.3.2 Density Matrix Renormalization in Matrix Product State Language	555
22.3.3 Matrix Product Operators	555
22.4 Time-Dependent Simulation: Extending the Range	558
22.4.1 Basic Algorithms	558
22.4.1.1 Time Evolution at Finite Temperatures	558
22.4.2 Linear Prediction and Spectral Functions	559
22.5 Density Matrix and Numerical Renormalization Groups	562
22.5.1 Wilson's Numerical Renormalization Group and Matrix Product States	562
22.5.2 Going Beyond the Numerical Renormalization Group	564
Bibliography	566
23 Simulations Based on Matrix Product States and Projected Entangled Pair States	571
<i>Valentin Murg, Ignacio Cirac, and Frank Verstraete</i>	
23.1 Time Evolution using Matrix Product States	572
23.1.1 Variational Formulation of Time Evolution with MPS	572
23.1.2 Time-Evolving Block-Decimation	575
23.1.3 Finding Ground States by Imaginary-Time Evolution	576
23.1.4 Infinite Spin Chains	576
23.2 PEPS and Ground States of 2D Quantum Spin Systems	578
23.2.1 Construction and Calculus of PEPS	579

23.2.2	Calculus of PEPS	581
23.2.3	Variational Method with PEPS	582
23.2.4	Time Evolution with PEPS	584
23.2.5	Examples	587
23.2.6	PEPS and Fermions	591
23.2.7	PEPS on Infinite Lattices	593
23.3	Conclusions	594
	Bibliography	595
24	Continuous-Time Monte Carlo Methods for Quantum Impurity Problems and Dynamical Mean Field Calculations	597
	<i>Philipp Werner and Andrew J. Millis</i>	
24.1	Quantum Impurity Models	597
24.2	Dynamical Mean Field Theory	599
24.3	Continuous-Time Impurity Solvers	600
24.3.1	General Recipe for Diagrammatic Quantum Monte Carlo	601
24.3.2	Weak-Coupling Approach	602
24.3.2.1	Monte Carlo Configurations	602
24.3.2.2	Sampling Procedure and Detailed Balance .	603
24.3.2.3	Determinant Ratios and Fast Matrix Updates	604
24.3.2.4	Measurement of the Green's Function	605
24.3.2.5	Expansion Order and Role of the Parameter K	605
24.3.3	Strong-Coupling Approach: Expansion in the Impurity-Bath Hybridization	606
24.3.3.1	Monte Carlo Configurations	606
24.3.3.2	Sampling Procedure and Detailed Balance .	609
24.3.3.3	Measurement of the Green's Function	609
24.3.3.4	Generalization: Matrix Formalism	610
24.3.4	Comparison Between the Two Approaches	611
24.4	Application: Phase Transitions in Multi-Orbital Systems with Rotationally Invariant Interactions	612
24.4.1	Model	613
24.4.2	Metal-Insulator Phase Diagram of the Three-Orbital Model	613
24.4.3	Spin-Freezing Transition in the Paramagnetic Metallic State	614
24.4.4	Crystal Field Splittings and Orbital Selective Mott Transitions	616
24.4.5	High-Spin to Low-Spin Transition in a Two-Orbital Model	617
24.5	Conclusion	619
	Bibliography	619
V	Quantum Phase Transitions Across Physics	621

25 Quantum Phase Transitions in Dense QCD	623
<i>Tetsuo Hatsuda and Kenji Maeda</i>	
25.1 Introduction to QCD	623
25.1.1 Symmetries in QCD	625
25.1.2 Dynamical Breaking of Chiral Symmetry	627
25.2 QCD Matter at High Temperature	627
25.3 QCD Matter at High Baryon Density	629
25.3.1 Neutron-Star Matter and Hyperonic Matter	630
25.3.2 Quark Matter	631
25.4 Superfluidity in Neutron-Star Matter	632
25.5 Color Superconductivity in Quark Matter	633
25.5.1 The Gap Equation	633
25.5.2 Tightly Bound Cooper Pairs	634
25.6 QCD Phase Structure	635
25.6.1 Ginzburg-Landau Potential for Hot/Dense QCD	637
25.6.2 Possible Phase Structure for Realistic Quark Masses .	639
25.7 Simulating Dense QCD with Ultracold Atoms	640
25.8 Conclusions	644
Bibliography	644
26 Quantum Phase Transitions in Coupled Atom-Cavity Systems	647
<i>Andrew D. Greentree and Lloyd C. L. Hollenberg</i>	
26.1 Introduction	648
26.2 Photon-Photon Interactions in a Single Cavity	649
26.2.1 Jaynes-Cummings Model	650
26.2.2 The Giant Kerr Nonlinearity in Four-State Systems .	653
26.2.3 Many-Atom Schemes	656
26.2.4 Other Atomic Schemes	656
26.3 The Jaynes-Cummings-Hubbard Model	657
26.3.1 The Bose-Hubbard Model	657
26.3.2 Mean-Field Analysis of the JCH Model	658
26.4 Few-Cavity Systems	662
26.5 Potential Physical Implementations	665
26.5.1 Rubidium Microtrap Arrays	665
26.5.2 Diamond Photonic Crystal Structures	666
26.5.3 Superconducting stripline Cavities: Circuit QED .	667
26.6 Outlook	668
Bibliography	669
27 Quantum Phase Transitions in Nuclei	673
<i>Francesco Iachello and Mark A. Caprio</i>	
27.1 QPTs and Excited-State QPTs in s - b Boson Models	674
27.1.1 Algebraic Structure of s - b Boson Models	675
27.1.2 Geometric Structure of s - b Boson Models	676

27.1.3 Phase Diagram and Phase Structure of s - b Boson Models	678
27.2 s - b Models with Pairing Interaction	679
27.3 Two-Level Bosonic and Fermionic Systems with Pairing Interactions	684
27.4 s - b Bosonic Systems with Generic Interactions: The Interacting-Boson Model of Nuclei	687
27.4.1 Algebraic Structure	687
27.4.2 Phase Structure and Phase Diagram	687
27.4.3 Experimental Evidence	691
27.5 Two-Fluid Bosonic Systems	693
27.6 Bosonic Systems with Fermionic Impurities	695
27.6.1 The Interacting Boson-Fermion Model	696
27.7 Conclusions and Outlook	697
Bibliography	698
28 Quantum Critical Dynamics from Black Holes	701
<i>Sean Hartnoll</i>	
28.1 The Holographic Correspondence as a Tool	702
28.1.1 The Basic Dictionary	706
28.1.2 Finite Temperature	709
28.1.3 Spectral Functions and Quasi-normal Modes	711
28.2 Finite Chemical Potential	714
28.2.1 Bosonic Response and Superconductivity	716
28.2.2 Fermionic Response and Non-Fermi Liquids	718
28.3 Current and Future Directions	719
Bibliography	721

Part I

New Directions and New Concepts in Quantum Phase Transitions

1

Finite Temperature Dissipation and Transport Near Quantum Critical Points

Subir Sachdev

Department of Physics, Harvard University, Cambridge, MA 02138, U.S.A.

The author's book [1] on quantum phase transitions has an extensive discussion on the dynamic and transport properties of a variety of systems at non-zero temperatures above a zero temperature quantum critical point. The purpose of this chapter is to briefly review some basic material, and to then update the earlier discussion with a focus on experimental and theoretical developments in the decade since the book was written. We note other recent reviews [2] from which portions of this chapter have been adapted.

We will begin in [Section 1.1](#) by introducing a variety of model systems and their quantum critical points; these are motivated by recent experimental and theoretical developments. We will use these systems to introduce basic ideas on finite temperature crossovers near quantum critical points in [Section 1.2](#). In [Section 1.3](#), we will focus on the important finite temperature *quantum critical region* and present a general discussion of its transport properties. An important recent development has been the complete exact solution of the dynamic and transport properties in the quantum critical region of a variety of (supersymmetric) model systems in two and higher dimensions: this will be described in [Section 1.4](#). The exact solutions are found to agree with the earlier general ideas discussed in [Section 1.3](#). Quite remarkably, the exact solution proceeds via a mapping to the theory of black holes in one higher spatial dimension: we will only briefly mention this mapping here, and refer the reader to Chap. 28 for more information. As has often been the case in the history of physics, the existence of a new class of solvable models leads to new and general insights which apply to a much wider class of systems, almost all of which are not exactly solvable. This has also been the case here, as we will review in [Section 1.5](#): a hydrodynamic theory of the low frequency transport properties has been developed, and has led to new relations between a variety of thermo-electric transport co-efficients. Finally, in [Section 1.6](#) we will turn to the cuprate high temperature superconductors, and present recent proposals on how ideas from the theory of quantum phase transition may help unravel the very complex phase diagram of these important materials.

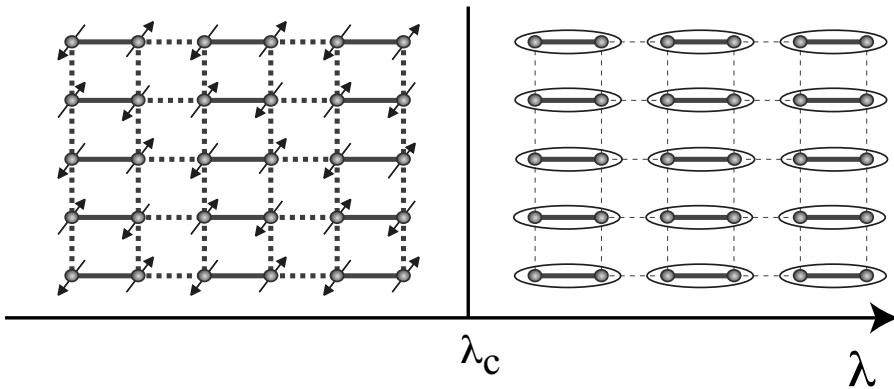


FIGURE 1.1

The coupled dimer antiferromagnet. The full lines represent an exchange interaction J , while the dashed lines have exchange J/λ . The ellipses represent a singlet valence bond of spins $(|\uparrow\downarrow\rangle - |\downarrow\uparrow\rangle)/\sqrt{2}$. The two sides of the figure sketch the Néel and dimerized quantum phases, respectively.

1.1 Model Systems and Their Critical Theories

1.1.1 Coupled Dimer Antiferromagnets

Some of the best studied examples of quantum phase transitions arise in insulators with unpaired $S = 1/2$ electronic spins residing on the sites, i , of a regular lattice. Using S_i^a ($a = x, y, z$) to represent the spin $S = 1/2$ operator on site i , the low energy spin excitations are described by the Heisenberg exchange Hamiltonian

$$H_J = \sum_{i < j} J_{ij} S_i^a \cdot S_j^a + \dots \quad (1.1)$$

where $J_{ij} > 0$ is the antiferromagnetic exchange interaction. We will begin with a simple realization of this model as illustrated in Fig. 1.1. The $S = 1/2$ spins reside on the sites of a square lattice, and have nearest neighbor exchange equal to either J or J/λ . Here $\lambda \geq 1$ is a tuning parameter which induces a quantum phase transition in the ground state of this model.

At $\lambda = 1$, the model has full square lattice symmetry, and this case is known to have a Néel ground state which breaks spin rotation symmetry. This state has a checkerboard polarization of the spins, just as found in the classical ground state, and as illustrated on the left side of Fig. 1.1. It can be characterized by a vector order parameter φ^a which measures the staggered spin polarization

$$\varphi^a = \eta_i S_i^a \quad (1.2)$$

where $\eta_i = \pm 1$ on the two sublattices of the square lattice. In the Néel state we have $\langle \varphi^a \rangle \neq 0$, and we expect that the low energy excitations can be described by long wavelength fluctuations of a field $\varphi^a(x, \tau)$ over space, x , and imaginary time, τ .

On the other hand, for $\lambda \gg 1$ it is evident from Fig. 1.1 that the ground state preserves all symmetries of the Hamiltonian: it has total spin $S = 0$ and can be considered to be a product of nearest neighbor singlet valence bonds on the J links. It is clear that this state cannot be smoothly connected to the Néel state, and so there must be at least one quantum phase transition as a function of λ .

Extensive quantum Monte Carlo simulations [3–5] on this model have shown there is a direct phase transition between these states at a critical λ_c , as in Fig. 1.1. The value of λ_c is known accurately, as are the critical exponents characterizing a second-order quantum phase transition. These critical exponents are in excellent agreement with the simplest proposal for the critical field theory [5], which can be obtained via conventional Landau-Ginzburg arguments. Given the vector order parameter φ^a , we write down the action in d spatial and one time dimension,

$$\mathcal{S}_{\text{LG}} = \int d^d r d\tau \left[\frac{1}{2} [(\partial_\tau \varphi^a)^2 + v^2 (\nabla \varphi^a)^2 + s(\varphi^a)^2] + \frac{u}{4} [(\varphi^a)^2]^2 \right], \quad (1.3)$$

as the simplest action expanded in gradients and powers of φ^a which is consistent with all the symmetries of the lattice antiferromagnet. The transition is now tuned by varying $s \sim (\lambda - \lambda_c)$. Notice that this model is identical to the Landau-Ginzburg theory for the thermal phase transition in a $d + 1$ dimensional ferromagnet, because time appears as just another dimension. As an example of this agreement, the critical exponent of the correlation length, ν , has the same value, $\nu = 0.711 \dots$, to three significant digits in a quantum Monte Carlo study of the coupled dimer antiferromagnet [5] and in a 5-loop analysis [6] of the renormalization group fixed point of \mathcal{S}_{LG} in $d = 2$. Similar excellent agreement is obtained for the double-layer antiferromagnet [7,8] and the coupled-plaquette antiferromagnet [9].

In experiments, the best studied realization of the coupled-dimer antiferromagnet is TlCuCl_3 . In this crystal, the dimers are coupled in all three spatial dimensions, and the transition from the dimerized state to the Néel state can be induced by application of pressure. Neutron scattering experiments by Ruegg and collaborators [10] have clearly observed the transformation in the excitation spectrum across the transition, as is described by a simple fluctuations analysis about the mean field saddle point of \mathcal{S}_{LG} . In the dimerized phase ($s > 0$), a triplet of gapped excitations is observed, corresponding to the three normal modes of φ^a oscillating about $\varphi^a = 0$; as expected, this triplet gap vanishes upon approaching the quantum critical point. In a mean field analysis, valid for $d \geq 3$, the field theory in Eq. (1.3) has a triplet gap of \sqrt{s} . In the Néel phase, the neutron scattering detects two gapless spin waves and one gapped longitudinal mode [11]. This is described by \mathcal{S}_{LG} for $s < 0$,

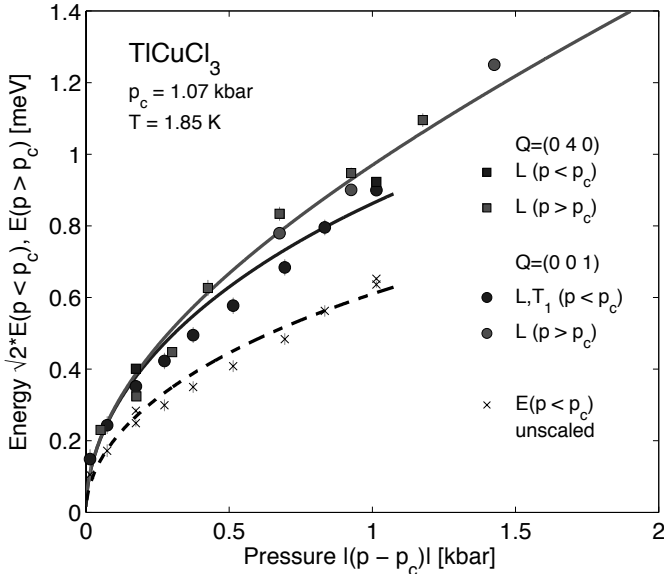


FIGURE 1.2

Energies of the gapped collective modes across the pressure (p) tuned quantum phase transition in $TiCuCl_3$ observed by Ruegg *et al.* [10]. We test the description by the action S_{LG} in Eq. (1.3) with $s \propto (p_c - p)$ by comparing $\sqrt{2}$ times the energy gap for $p < p_c$ with the energy of the longitudinal mode for $p > p_c$. The lines are the fits to a $\sqrt{|p - p_c|}$ dependence, testing the $1/2$ exponent.

where φ^a experiences an inverted ‘Mexican hat’ potential with a minimum at $|\varphi^a| = \sqrt{|s|}/v$. Expanding about this minimum we find that in addition to the gapless spin waves, there is a mode involving amplitude fluctuations of $|\varphi^a|$ which has an energy gap of $\sqrt{2|s|}$. These mean field predictions for the energy of the gapped modes on the two sides of the transition are tested in Fig. 1.2: the observations are in good agreement with the $1/2$ exponent and the predicted $\sqrt{2}$ ratio [12], providing a non-trivial experimental test of the S_{LG} field theory.

1.1.2 Deconfined Criticality

We now consider an analog of the transition discussed in Section 1.1.1, but for a Hamiltonian $H = H_0 + \lambda H_1$ which has full square lattice symmetry at all λ . For H_0 , we choose a form of H_J such that $J_{ij} = J$ for all nearest neighbor links. Thus at $\lambda = 0$ the ground state has Néel order, as in the left panel of Fig. 1.1. We now want to choose H_1 so that increasing λ leads to a spin singlet state with spin rotation symmetry restored. A large number of choices have

been made in the literature, and the resulting ground state invariably [13] has valence bond solid (VBS) order. The VBS state is superficially similar to the dimer singlet state in the right panel of Fig. 1.1: the spins primarily form valence bonds with near-neighbor sites. However, because of the square lattice symmetry of the Hamiltonian, a columnar arrangement of the valence bonds as in Fig. 1.1 breaks the square lattice rotation symmetry; there are 4 equivalent columnar states, with the valence bond columns running along different directions. More generally, a VBS state is a spin singlet state, with a non-zero degeneracy due to a spontaneously broken lattice symmetry. Thus a direct transition between the Néel and VBS states involves two distinct broken symmetries: spin rotation symmetry, which is broken only in the Néel state, and a lattice rotation symmetry, which is broken only in the VBS state. The rules of Landau-Ginzburg-Wilson theory imply that there can be no generic second-order transition between such states.

It has been argued that a second-order Néel-VBS transition can indeed occur [14], but the critical theory is not expressed directly in terms of either order parameter. It involves a fractionalized bosonic spinor z_α ($\alpha = \uparrow, \downarrow$), and an emergent gauge field A_μ . The key step is to express the vector field φ^a in terms of z_α by

$$\varphi^a = z_\alpha^* \sigma_{\alpha\beta}^a z_\beta \quad (1.4)$$

where σ^a are the 2×2 Pauli matrices. Note that this mapping from φ^a to z_α is redundant. We can make a spacetime-dependent change in the phase of the z_α by the field $\theta(x, \tau)$

$$z_\alpha \rightarrow e^{i\theta} z_\alpha \quad (1.5)$$

and leave φ^a unchanged. All physical properties must therefore also be invariant under Eq. (1.5), and so the quantum field theory for z_α has a U(1) gauge invariance, much like that found in quantum electrodynamics. The effective action for the z_α therefore requires introduction of an ‘emergent’ U(1) gauge field A_μ (where $\mu = x, \tau$ is a three-component spacetime index). The field A_μ is unrelated to the electromagnetic field, but is an internal field which conveniently describes the couplings between the spin excitations of the anti-ferromagnet. As we did for \mathcal{S}_{LG} , we can write down the quantum field theory for z_α and A_μ by the constraints of symmetry and gauge invariance, which now yields

$$\mathcal{S}_z = \int d^2r d\tau \left[|(\partial_\mu - iA_\mu)z_\alpha|^2 + s|z_\alpha|^2 + u(|z_\alpha|^2)^2 + \frac{1}{2g^2}(\epsilon_{\mu\nu\lambda}\partial_\nu A_\lambda)^2 \right]. \quad (1.6)$$

For brevity, we have now used a “relativistically” invariant notation, and scaled away the spin-wave velocity v ; the values of the couplings s, u are different from, but related to, those in \mathcal{S}_{LG} . The Maxwell action for A_μ is generated from short distance z_α fluctuations, and it makes A_μ a dynamical field; its coupling g is unrelated to the electron charge. The action \mathcal{S}_z is a valid description of the Néel state for $s < 0$ (the critical upper value of s will have fluctuation corrections away from 0), where the gauge theory enters a

Higgs phase with $\langle z_\alpha \rangle \neq 0$. This description of the Néel state as a Higgs phase has an analogy with the Weinberg–Salam theory of the weak interactions. In the latter case it is hypothesized that the condensation of a Higgs boson gives a mass to the W and Z gauge bosons, whereas here the condensation of z_α quenches the A_μ gauge boson. As written, the $s > 0$ phase of S_z is a ‘spin liquid’ state with an $S = 0$ collective gapless excitation associated with the A_μ photon. Non-perturbative effects [13] associated with the monopoles in A_μ (not discussed here) show that this spin liquid is ultimately unstable to the appearance of VBS order.

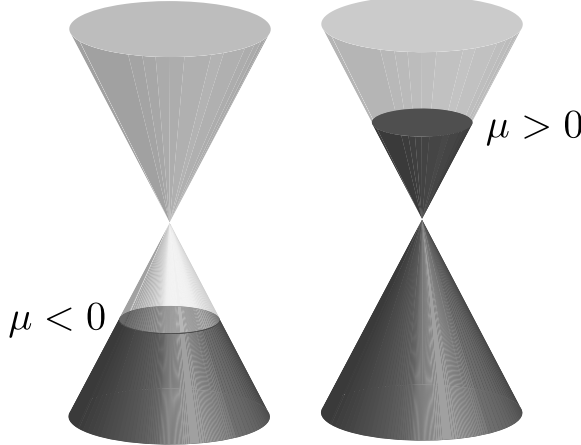
Numerical studies of the Néel–VBS transition have focused on a specific lattice antiferromagnet proposed by Sandvik [15–17]. There is strong evidence for VBS order proximate to the Néel state, along with persuasive evidence of a second-order transition. However, some studies [18, 19] support a very weak first order transition.

1.1.3 Graphene

The last few years have seen an explosion in experimental and theoretical studies [20] of graphene: a single hexagonal layer of carbon atoms. At the currently observed temperatures, there is no evident broken symmetry in the electronic excitations, and so it is not conventional to think of graphene as being in the vicinity of a quantum critical point. However, graphene does indeed undergo a bona fide quantum phase transition, but one without any order parameters or broken symmetry. This transition may be viewed as being ‘topological’ in character, and is associated with a change in the nature of the Fermi surface as a function of carrier density.

Pure, undoped graphene has a conical electronic dispersion spectrum at two points in the Brillouin zone, with the Fermi energy at the particle-hole symmetric point at the apex of the cone. So there is no Fermi surface, just a Fermi point, where the electronic energy vanishes, and pure graphene is a ‘semi-metal.’ By applying a bias voltage, the Fermi energy can move away from this symmetric point, and a circular Fermi surface develops, as illustrated in Fig. 1.3. The Fermi surface is electron-like for one sign of the bias, and hole-like for the other sign. This change from electron to hole character as a function of bias voltage constitutes the quantum phase transition in graphene. As we will see below, with regard to its dynamic properties near zero bias, graphene behaves in almost all respects like a canonical quantum critical system.

The field theory for graphene involves fermionic degrees of freedom. Representing the electronic orbitals near one of the Dirac points by the two-component fermionic spinor Ψ_a , where a is a sublattice index (we suppress

**FIGURE 1.3**

Dirac dispersion spectrum for graphene showing a ‘topological’ quantum phase transition from a hole Fermi surface for $\mu < 0$ to an electron Fermi surface for $\mu > 0$.

spin and ‘valley’ indices), we have the effective electronic action

$$\begin{aligned} \mathcal{S}_\Psi = & \int d^2r \int d\tau \Psi_a^\dagger [(\partial_\tau + iA_\tau - \mu)\delta_{ab} + iv_F \tau_{ab}^x \partial_x + iv_F \tau_{ab}^y \partial_y] \Psi_b \\ & + \frac{1}{2g^2} \int \frac{d^2q}{4\pi^2} \int d\tau \frac{q}{2\pi} |A_\tau(\mathbf{q}, \tau)|^2, \end{aligned} \quad (1.7)$$

where τ_{ab}^i are Pauli matrices in the sublattice space, μ is the chemical potential, v_F is the Fermi velocity, and A_τ is the scalar potential mediating the Coulomb interaction with coupling $g^2 = e^2/\epsilon$ (ϵ is a dielectric constant). This theory undergoes a quantum phase transition as a function of μ , at $\mu = 0$, similar in many ways to that of \mathcal{S}_{LG} as a function of s . The interaction between the fermionic excitations here has coupling g^2 , which is the analog of the non-linearity u in \mathcal{S}_{LG} . However, while u is scaled to a non-zero fixed point value under the renormalization group flow, g flows logarithmically slowly to zero. For many purposes, it is safe to ignore this flow, and to set g equal to a fixed value; this value is characterized by the dimensionless ‘fine structure constant’ $\alpha = g^2/(\hbar v_F)$ which is of order unity in graphene.

1.1.4 Spin Density Waves

Finally, we consider the onset of Néel order, as in Section 1.1.1, but in a metal rather than an insulator. It is conventional to refer to such metallic Néel states as having spin density wave (SDW) order. Our discussion here is motivated by application to the cuprate superconductors: there is good evidence [21, 22]

that the transition we describe below is present in the electron-doped cuprates, and proposals of its application to the hole-doped cuprates will be discussed in [Section 1.6](#).

We begin with the band structure describing the cuprates in the over-doped region, well away from the Mott insulator. Here the electrons $c_{i\alpha}$ are described by the Hamiltonian

$$H_c = - \sum_{i < j} t_{ij} c_{i\alpha}^\dagger c_{i\alpha} \equiv \sum_{\mathbf{k}} \varepsilon_{\mathbf{k}} c_{\mathbf{k}\alpha}^\dagger c_{\mathbf{k}\alpha}$$

with t_{ij} non-zero for first, second, and third neighbors on the square lattice. This leads to the Fermi surface shown in the right-most panel of [Fig. 1.4](#). As in [Section 1.1.3](#), we will consider topological changes to this Fermi surface, but induced here by a conventional SDW (Néel) order parameter φ^a . From the structure of the ordering in [Fig. 1.1](#) we see that φ^a carries momentum $\mathbf{K} = (\pi, \pi)$, and so will transfer momentum \mathbf{K} while scattering the c_α fermions; this leads to the coupling

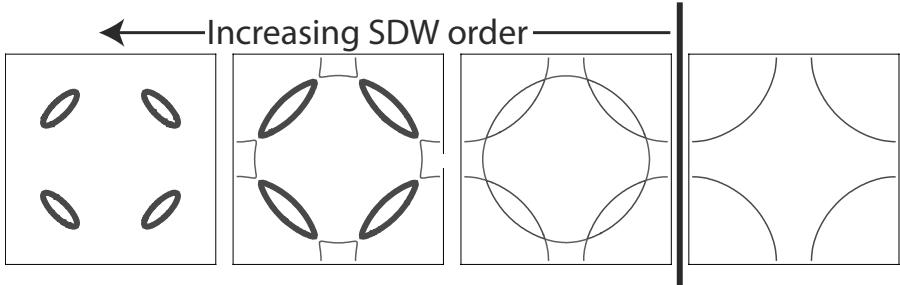
$$H_{\text{sdw}} = \varphi^a \sum_{\mathbf{k}, \alpha, \beta} c_{\mathbf{k}, \alpha}^\dagger \sigma_{\alpha\beta}^a c_{\mathbf{k} + \mathbf{K}, \beta}.$$

We can now follow the evolution of the Fermi surface under the onset of SDW order by diagonalizing $H_c + H_{\text{sdw}}$ for constant φ^a : the results of this [23] are shown in Fig. 1.4. The second panel from the right shows the Fermi surface obtained by translating the original Fermi surface by \mathbf{K} , and the remaining panels show the consequences of mixing between the states at momentum \mathbf{k} and $\mathbf{k} + \mathbf{K}$.

We are now interested in the nature of the quantum critical point at the onset of SDW order, indicated by the vertical line in [Fig. 1.4](#). Note that this transition combines the features of [Sections 1.1.1](#) and [1.1.3](#): it has an order parameter, as in the coupled dimer antiferromagnet, and it has a topological change in the Fermi surface, as in graphene. Thus a complete theory is just the combination of these two features: $\mathcal{S}_{\text{LG}} + H_c + H_{\text{sdw}}$. A common assertion [24, 25] is that we can pay less attention to the Fermi surface change by simply integrating out the c_α fermions and working with the resulting modified action for φ^a . Right at the quantum critical point, the SDW fluctuations, φ^a , connect points on the large Fermi surface, and so can decay into a large density of states of particle-hole excitations. The damping induced by this particle-hole continuum modifies the effective action for φ^a from [Eq. \(1.3\)](#) by adding a relevant dissipative term [24, 25]:

$$\mathcal{S}_H = \mathcal{S}_{\text{LG}} + \int \frac{d^2 k}{4\pi^2} \int \frac{d\omega}{2\pi} |\omega| |\varphi^a(k, \omega)|^2. \quad (1.8)$$

Subsequent analyses [26] have indicated that the procedure of integrating out the fermions is incorrect in two spatial dimensions. A complete theory, which includes the Fermi surface change in a more fundamental manner has been presented recently [27].

**FIGURE 1.4**

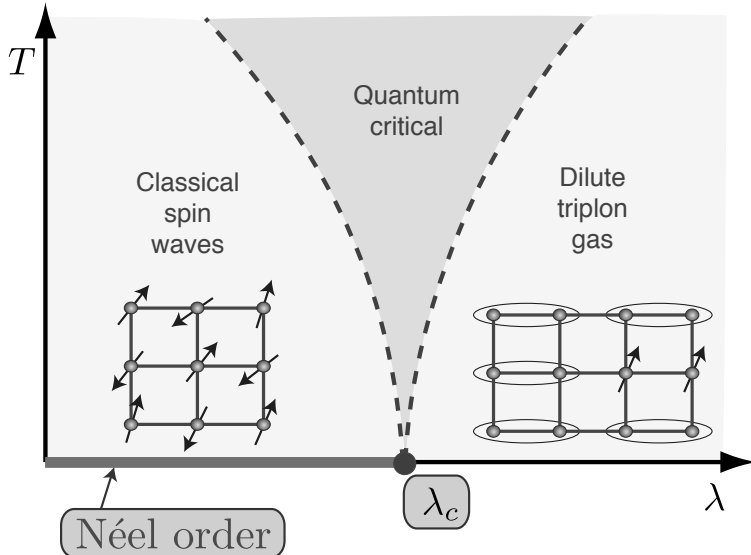
Evolution of the Fermi surface of the hole doped cuprates in a conventional SDW theory [23] as a function of the magnitude of the SDW order $|\varphi^a|$. The right panel is the large Fermi surface state with no SDW order, with states contiguous to $\mathbf{k} = 0$ occupied by electrons. The onset of SDW order induces the formation of electron (thin curves) and hole (thick curves) pockets. With further increase of $|\varphi^a|$, the electron pockets disappear and only hole pockets remain (the converse happens in the last step for the electron-doped cuprates).

1.2 Finite Temperature Crossovers

The previous section has described four model systems at $T = 0$: we examined the change in the nature of the ground state as a function of some tuning parameter, and motivated a quantum field theory which describes the low energy excitations on both sides of the quantum critical point.

We now turn to the important question of the physics at non-zero temperatures. All of the models share some common features, which we will first explore for the coupled dimer antiferromagnet. For $\lambda > \lambda_c$ (or $s > 0$ in \mathcal{S}_{LG}), the excitations consist of a triplet of $S = 1$ particles, or ‘triplons,’ which can be understood perturbatively in the large λ expansion as an excited $S = 1$ state on a dimer, hopping between dimers (see Fig. 1.5). The mean field theory tells us that the excitation energy of this dimer vanishes as \sqrt{s} upon approaching the quantum critical point. Fluctuations beyond mean field, described by \mathcal{S}_{LG} , show that the exponent is modified to $s^{z\nu}$, where $z = 1$ is the dynamic critical exponent, and ν is the correlation length exponent. Now imagine turning on a non-zero temperature. As long as T is smaller than the triplon gap, i.e., $T < s^{z\nu}$, we expect a description in terms of a dilute gas of thermally excited triplon particles. This leads to the behavior shown on the right-hand side of Fig. 1.5, delimited by the crossover indicated by the dashed line. Note that the crossover line approaches $T = 0$ only at the quantum critical point.

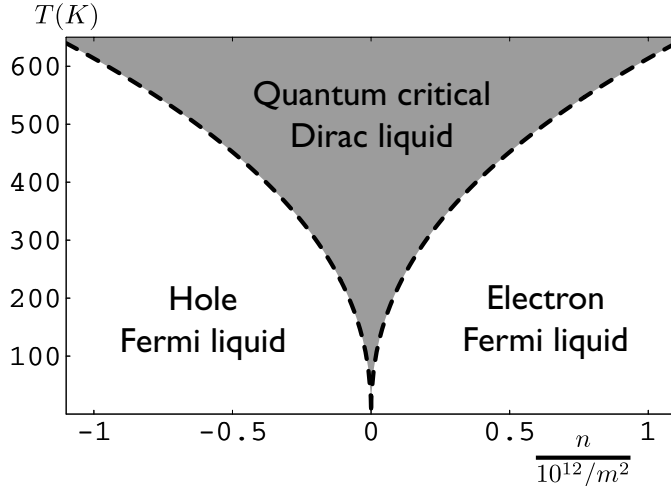
Now let us look at the complementary behavior at $T > 0$ on the Néel-ordered side of the transition, with $s < 0$. In two spatial dimensions, thermal fluctuations prohibit the breaking of a non-Abelian symmetry at all $T > 0$,

**FIGURE 1.5**

Finite temperature crossovers of the coupled dimer antiferromagnet in Fig. 1.1.

and so spin rotation symmetry is immediately restored. Nevertheless, there is an exponentially large spin correlation length, ξ , and at distances shorter than ξ we can use the ordered ground state to understand the nature of the excitations. Along with the spin waves, we also found the longitudinal ‘Higgs’ mode with energy $\sqrt{-2s}$ in mean field theory. Thus, just as was this case for $s > 0$, we expect this spin-wave+Higgs picture to apply at all temperatures lower than the natural energy scale, i.e., for $T < (-s)^{z\nu}$. This leads to the crossover boundary shown on the left-hand side of Fig. 1.5.

Having delineated the physics on the two sides of the transition, we are left with the crucial *quantum critical* region in the center of Fig. 1.5. This is present for $T > |s|^{z\nu}$, i.e., at *higher* temperatures in the vicinity of the quantum critical point. To the left of the quantum critical region, we have a description of the dynamics and transport in terms of an effectively classical model of spin waves: this is the ‘renormalized classical’ regime of Ref. [28]. To the right of the quantum critical region, we again have a regime of classical dynamics, but now in terms of a Boltzmann equation for the triplon particles. A key property of the quantum critical region is that there is no description in terms of either classical particles or classical waves at times on the order of the typical relaxation time τ_r of thermal excitations [29]. Instead, quantum and thermal effects are equally important, and involve the non-trivial dynamics of the fixed-point theory describing the quantum critical point. Note that while the fixed-point theory applies only at a single point ($\lambda = \lambda_c$) at $T = 0$, its influence broadens into the quantum critical region at $T > 0$. Because there

**FIGURE 1.6**

Finite temperature crossovers of graphene as a function of electron density n (tuned) by μ in Eq. (1.7) and temperature T . Adapted from Ref. [30].

is no characteristic energy scale associated with the fixed-point theory, $k_B T$ is the only energy scale available to determine τ_r at non-zero temperatures. Thus, in the quantum critical region [29]

$$\tau_r = \mathcal{C} \frac{\hbar}{k_B T}, \quad (1.9)$$

where \mathcal{C} is a universal constant dependent only upon the universality class of the fixed point theory, i.e., it is a universal number just like the critical exponents. This value of τ_r determines the ‘friction coefficients’ associated with the dissipative relaxation of spin fluctuations in the quantum critical region. It is also important for the transport co-efficients associated with conserved quantities, and this will be discussed in Section 1.3.

Let us now consider the similar $T > 0$ crossovers for the other models of Section 1.1.

The Néel-VBS transition of Section 1.1.2 has crossovers very similar to those in Fig. 1.5, with one important difference. The VBS state breaks a discrete lattice symmetry, and this symmetry remains broken for a finite range of non-zero temperatures. Thus, within the right-hand ‘triplon gas’ regime of Fig. 1.5, there is a phase transition line at a critical temperature T_{VBS} . The value of T_{VBS} vanishes very rapidly as $s \rightarrow 0^+$, and is controlled by the non-perturbative monopole effects which were briefly noted in Section 1.1.2.

For graphene, the discussion above applied to Fig. 1.3 leads to the crossover diagram shown in Fig. 1.6, as noted by Sheehy and Schmalian [30]. We have the Fermi liquid regimes of the electron- and hole-like Fermi surfaces on either side

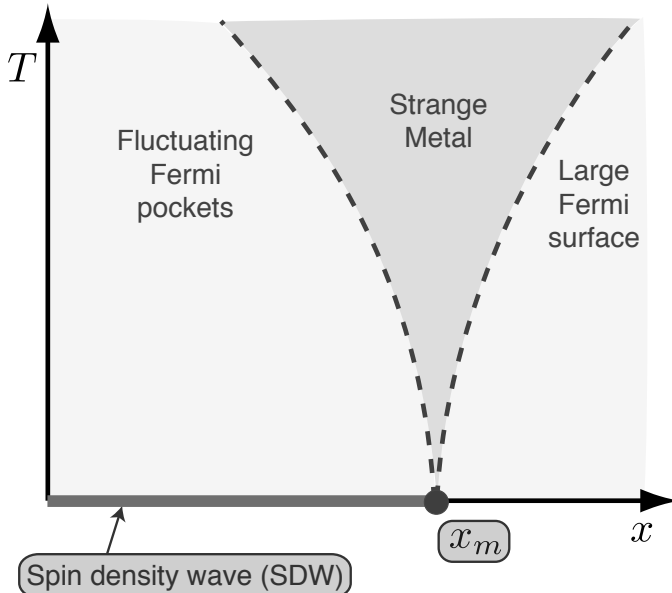


FIGURE 1.7

Finite temperature crossovers near the SDW ordering transition of Fig. 1.4. Here, anticipating application to the cuprates to be discussed in Section 1.6, we have assumed that the carrier density, x , tunes the system across the SDW transition.

of the critical point, along with an intermediate quantum critical Dirac liquid. A new feature here is related to the logarithmic flow of the dimensionless ‘fine structure constant’ α controlling the Coulomb interactions, which was noted in Section 1.1.3. In the quantum critical region, this constant takes the typical value $\alpha \sim 1/\ln(1/T)$. Consequently, for the relaxation time in Eq. (1.9) we have $\mathcal{C} \sim \ln^2(1/T)$. This time determines both the width of the electron spectral functions and also the transport coefficients, as we will see in Section 1.3.

Finally, we turn to the SDW transition of Section 1.1.4. From the evolution in Fig. 1.4 and the discussion above, we have the crossover phase diagram [31] in Fig. 1.7. As in Fig. 1.5, there is no transition at non-zero temperatures, and now the crossover is between the topologically distinct Fermi surface configurations of Fig. 1.4. The Hertz action for the SDW fluctuations in Eq. (1.8) predicts [26,31] logarithmic corrections to the leading scaling behavior, similar to those for graphene. The interplay of such SDW fluctuations with the topological change in the Fermi surface configuration is not fully understood [32], and is labeled as the ‘strange metal’ regime in Fig. 1.7.

1.3 Quantum Critical Transport

We now turn to the ‘transport’ properties in the quantum critical region: we consider the response functions associated with any globally conserved quantity. For the antiferromagnetic systems in Sections 1.1.1 and 1.1.2, this requires consideration of the transport of total spin, and the associated spin conductivities and diffusivities. For graphene, we can consider charge and momentum transport. Our discussion below will also apply to the superfluid-insulator transition: for bosons in a periodic potential, this transition is described [33] by a field theory closely related to that in Eq. (1.3). However, we will primarily use a language appropriate to charge transport in graphene below. We will describe the properties of a generic strongly-coupled quantum critical point and mention, where appropriate, the changes due to the logarithmic flow of the coupling in graphene.

In traditional condensed matter physics, transport is described by identifying the low-lying excitations of the quantum ground state, and writing down ‘transport equations’ for the conserved charges carried by them. Often, these excitations have a particle-like nature, such as the triplon particles of Fig. 1.5 or the electron or hole quasiparticles of the Fermi liquids in Fig. 1.6. In other cases, the low-lying excitations are waves, such as the spin-waves in Fig. 1.5, and their transport is described by a non-linear wave equation (such as the Gross-Pitaevski equation). However, as we have discussed in Section 1.2 neither description is possible in the quantum critical region, because the excitations do not have a particle-like or wave-like character.

Despite the absence of an intuitive description of the quantum critical dynamics, we expect that the transport properties have a universal character determined by the quantum field theory of the quantum critical point. In addition to describing single excitations, this field theory also determines the S -matrix of these excitations by the renormalization group fixed-point value of the couplings, and these should be sufficient to determine transport properties [34]. The transport coefficients and the relaxation time to local equilibrium are not proportional to a mean free scattering time between the excitations, as is the case in the Boltzmann theory of quasiparticles. Such a time would typically depend upon the interaction strength between the particles. Rather, the system behaves like a “perfect fluid” in which the relaxation time is as short as possible, and is determined universally by the absolute temperature, as indicated in Eq. (1.9). Indeed, it was conjectured in Ref. [1] that the relaxation time in Eq. (1.9) is a generic lower bound for interacting quantum systems. Thus the non-quantum-critical regimes of all the phase diagrams in Section 1.2 have relaxation times which are all longer than Eq. (1.9).

The transport coefficients of this quantum-critical perfect fluid also do not depend upon the interaction strength, and can be connected to the fundamental constants of nature. In particular, the electrical conductivity, σ , is given

by (in two spatial dimensions) [34]

$$\sigma_Q = \frac{e^{*2}}{h} \Phi_\sigma, \quad (1.10)$$

where Φ_σ is a universal dimensionless constant of order unity, and we have added the subscript Q to emphasize that this is the conductivity for the case of graphene with the Fermi level at the Dirac point (for the superfluid-insulator transition, this would correspond to bosons at integer filling) with no impurity scattering, and at zero magnetic field. Here e^* is the charge of the carriers: for a superfluid-insulator transition of Cooper pairs, we have $e^* = 2e$, while for graphene we have $e^* = e$. The renormalization group flow of the ‘fine structure constant’ α of graphene to zero at asymptotically low T allows an exact computation in this case [35]: $\Phi_\sigma \approx 0.05 \ln^2(1/T)$. For the superfluid-insulator transition, Φ_σ is T -independent (this is the generic situation with non-zero fixed point values of the interaction¹) but it has only been computed [1,34] to leading order in expansions in $1/N$ and in $3 - d$, where N is the number of order parameter components and d is the spatial dimensionality. However, both expansions are neither straightforward nor rigorous, and require a physically motivated resummation of the bare perturbative expansion to all orders. It would therefore be valuable to have exact solutions of quantum critical transport where the above results can be tested, and we turn to such solutions in Sec. 1.4.

In addition to charge transport, we can also consider momentum transport. This was treated in the context of applications to the quark-gluon plasma [37]; application of the analysis of Ref. [34] shows that the viscosity, η , is given by

$$\frac{\eta}{s} = \frac{\hbar}{k_B} \Phi_\eta, \quad (1.11)$$

where s is the entropy density, and again Φ_η is a universal constant of order unity. The value of Φ_η has recently been computed [40] for graphene, and again has a logarithmic T dependence because of the marginally irrelevant interaction: $\Phi_\eta \approx 0.008 \ln^2(1/T)$.

We conclude this section by discussing some subtle aspects of the physics behind the seemingly simple result in Eq. (1.10). For simplicity, we will consider the case of a “relativistically” invariant quantum critical point in 2+1 dimensions (such as the field theories of Section 1.1.1 and 1.1.2), but marginally violated by graphene, a subtlety we ignore below). Consider the retarded correlation function of the charge density, $\chi(k, \omega)$, where $k = |\mathbf{k}|$ is the wavevector, and ω is frequency; the dynamic conductivity, $\sigma(\omega)$, is related to χ by the Kubo formula,

$$\sigma(\omega) = \lim_{k \rightarrow 0} \frac{-i\omega}{k^2} \chi(k, \omega). \quad (1.12)$$

¹For the case of neutral boson superfluids (but not charged systems like graphene), hydrodynamic ‘long-time tails’ cause the constants D and Θ_2 to acquire a weak logarithmic dependence on $\hbar\omega/k_B T$ at small ω in a sample with perfect momentum conservation [36].

It was argued in Ref. [34] that despite the absence of particle-like excitations of the critical ground state, the central characteristic of the transport is a crossover from collisionless to collision-dominated transport. At high frequencies or low temperatures, the limiting form for χ reduces to that at $T = 0$, which is completely determined by relativistic and scale invariance and current conversion up to an overall constant

$$\chi(k, \omega) = \frac{e^{*2}}{h} K \frac{k^2}{\sqrt{v^2 k^2 - (\omega + i\eta)^2}} , \quad \sigma(\omega) = \frac{e^{*2}}{h} K ; \quad \hbar\omega \gg k_B T, \quad (1.13)$$

where K is a universal number [38]. However, phase-randomizing collisions are intrinsically present in any strongly interacting critical point (above one spatial dimension) and these lead to relaxation of perturbations to local equilibrium and the consequent emergence of hydrodynamic behavior. So at low frequencies, we have instead an Einstein relation which determines the conductivity with

$$\chi(k, \omega) = e^{*2} \chi_c \frac{Dk^2}{Dk^2 - i\omega} , \quad \sigma(\omega) = e^{*2} \chi_c D = \frac{e^{*2}}{h} \Theta_1 \Theta_2 ; \quad \hbar\omega \ll k_B T, \quad (1.14)$$

where χ_c is the compressibility and D is the charge diffusion constant. Quantum critical scaling arguments show that the latter quantities obey

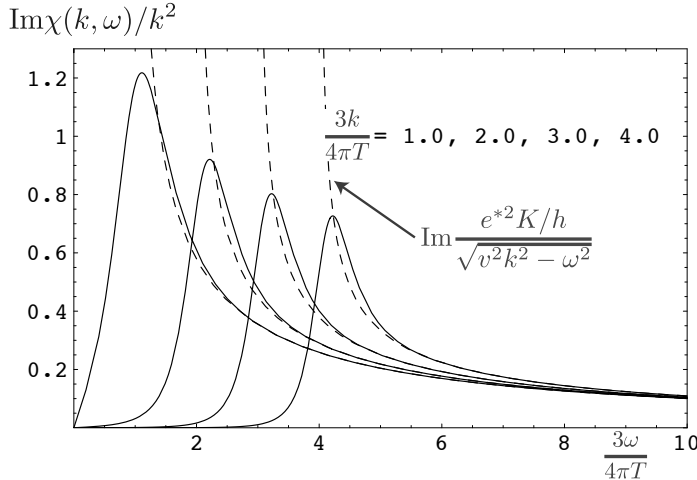
$$\chi_c = \Theta_1 \frac{k_B T}{h^2 v^2} , \quad D = \Theta_2 \frac{h v^2}{k_B T}, \quad (1.15)$$

where $\Theta_{1,2}$ are universal numbers. A large number of papers in the literature, particularly those on critical points in quantum Hall systems, have used the collisionless method of Eq. (1.13) to compute the conductivity. However, the correct d.c. limit is given by Eq. (1.14), and the universal constant in Eq. (1.10) is given by $\Phi_\sigma = \Theta_1 \Theta_2$. Given the distinct physical interpretation of the collisionless and collision-dominated regimes, we expect that $K \neq \Theta_1 \Theta_2$. This has been shown in a resummed perturbation expansion for a number of quantum critical points [1].

1.4 Exact Results for Quantum Critical Transport

The results of Section 1.3 were obtained by using physical arguments to motivate resummations of perturbative expansions. Here we shall support the *ad hoc* assumptions behind these results by examining an exactly solvable model of quantum critical transport.

The solvable model may be viewed as a generalization of the gauge theory in Eq. (1.6) to the maximal possible supersymmetry. In 2+1 dimensions, this is known as $\mathcal{N} = 8$ supersymmetry. Such a theory with the U(1) gauge group

**FIGURE 1.8**

Spectral weight of the density correlation function of the SCFT3 with $\mathcal{N} = 8$ supersymmetry in the collisionless regime.

is free, and so we consider the non-Abelian Yang-Mills theory with an $SU(N)$ gauge group. The resulting supersymmetric Yang-Mills (SYM) theory has only one coupling constant, which is the analog of the electric charge g in Eq. (1.6). The matter content is naturally more complicated than the complex scalar z_α in Eq. (1.6), and also involves relativistic Dirac fermions as in Eq. (1.7). However, all the terms in the action for the matter fields are also uniquely fixed by the single coupling constant g . Under the renormalization group, it is believed that g flows to an attractive fixed point at a non-zero coupling $g = g^*$; the fixed point then defines a supersymmetric conformal field theory in 2+1 dimensions (an SCFT3), and we are interested here in the transport properties of this SCFT3.

A remarkable recent advance has been the exact solution of this SCFT3 in the $N \rightarrow \infty$ limit using the anti-de Sitter space/conformal field theory (AdS/CFT) correspondence [41]. The solution proceeds by a dual formulation as a four-dimensional supergravity theory on a spacetime with uniform negative curvature: anti-de Sitter space, or AdS_4 . Remarkably, the solution is also easily extended to non-zero temperatures, and allows direct computation of the correlators of conserved charges in real time. At $T > 0$ a black hole appears, resulting in an AdS-Schwarzschild spacetime, and T is also the Hawking temperature of the black hole; the real time solutions also extend to $T > 0$.

The results of a full computation [42] of the density correlation function, $\chi(k, \omega)$, are shown in Fig. 1.8 and 1.9. The most important feature of these results is that the expected limiting forms in the collisionless (Eq. (1.13)) and

$$\text{Im}\chi(k, \omega)/k^2$$

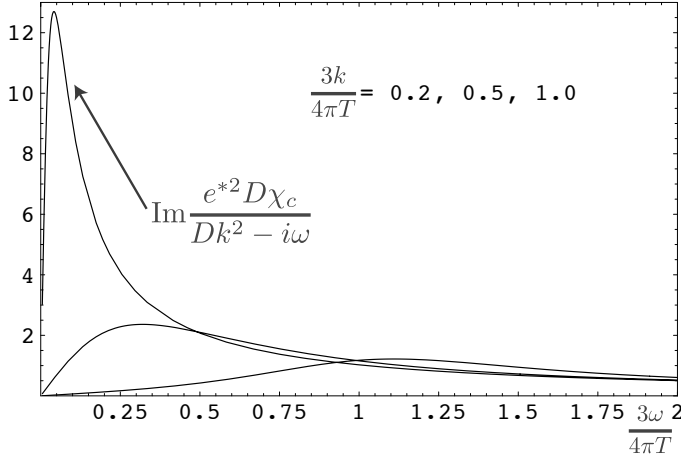


FIGURE 1.9

As in Fig. 1.8, but for the collision-dominated regime.

collision-dominated (Eq. (1.14)) are obeyed. Thus the results do display the collisionless to collision-dominated crossover at a frequency of order $k_B T/\hbar$, as was postulated in Section 1.3.

An additional important feature of the solution is apparent upon describing the full structure of both the density and current correlations. Using spacetime indices ($\mu, \nu = t, x, y$) we can represent these as the tensor $\chi_{\mu\nu}(\mathbf{k}, \omega)$, where the previously considered $\chi \equiv \chi_{tt}$. At $T > 0$, we do not expect $\chi_{\mu\nu}$ to be relativistically covariant, and so can only constrain it by spatial isotropy and density conservation. Introducing a spacetime momentum $p_\mu = (\omega, \mathbf{k})$, and setting the velocity $v = 1$, these two constraints lead to the most general form

$$\chi_{\mu\nu}(\mathbf{k}, \omega) = \frac{e^{*2}}{\hbar} \sqrt{p^2} [P_{\mu\nu}^T K^T(k, \omega) + P_{\mu\nu}^L K^L(k, \omega)] \quad (1.16)$$

where $p^2 = \eta^{\mu\nu} p_\mu p_\nu$ with $\eta_{\mu\nu} = \text{diag}(-1, 1, 1, 1)$, and $P_{\mu\nu}^T$ and $P_{\mu\nu}^L$ are orthogonal projectors defined by

$$P_{00}^T = P_{0i}^T = P_{i0}^T = 0, \quad P_{ij}^T = \delta_{ij} - \frac{k_i k_j}{k^2}, \quad P_{\mu\nu}^L = \left(\eta_{\mu\nu} - \frac{p_\mu p_\nu}{p^2} \right) - P_{\mu\nu}^T, \quad (1.17)$$

with the indices i, j running over the 2 spatial components. The two functions $K^{T,L}(k, \omega)$ define all the correlators of the density and the current, and the results in Eqs. (1.14) and (1.13) are obtained by taking suitable limits of these functions. We will also need below the general identity

$$K^T(0, \omega) = K^L(0, \omega), \quad (1.18)$$

which follows from the analyticity of the $T > 0$ current correlations at $\mathbf{k} = 0$.

The relations of the previous paragraph are completely general and apply to any theory. Specializing to the AdS-Schwarzschild solution of SYM3, the results were found to obey a simple and remarkable identity [42]:

$$K^L(k, \omega)K^T(k, \omega) = \mathcal{K}^2 \quad (1.19)$$

where \mathcal{K} is a known pure number, independent of ω and k . It was also shown that such a relation applies to any theory which is equated to classical gravity on AdS_4 , and is a consequence of the electromagnetic self-duality of its four-dimensional Maxwell sector. The combination of Eqs. (1.18) and (1.19) fully determines the $\chi_{\mu\nu}$ correlators at $\mathbf{k} = 0$: we find $K^L(0, \omega) = K^T(0, \omega) = \mathcal{K}$, from which it follows that the $\mathbf{k} = 0$ conductivity is frequency independent and that $\Phi_\sigma = \Theta_1\Theta_2 = K = \mathcal{K}$. These last features are believed to be special to theories which are equivalent to classical gravity, and not to hold more generally.

We can obtain further insight into the interpretation of Eq. (1.19) by considering the field theory of the superfluid-insulator transition of lattice bosons at integer filling. As we noted earlier, this is given by the field theory in Eq. (1.3) with the field φ^a having 2 components. It is known that this 2-component theory of relativistic bosons is equivalent to a dual relativistic theory, $\tilde{\mathcal{S}}$, of vortices, under the well-known ‘particle-vortex’ duality [43]. Ref. [42] considered the action of this particle-vortex duality on the correlation functions in Eq. (1.16), and found the following interesting relations:

$$K^L(k, \omega)\tilde{K}^T(k, \omega) = 1 \quad , \quad K^T(k, \omega)\tilde{K}^L(k, \omega) = 1 \quad (1.20)$$

where $\tilde{K}^{L,T}$ determine the vortex current correlations in $\tilde{\mathcal{S}}$ as in Eq. (1.16). Unlike Eq. (1.19), Eq. (1.20) does *not* fully determine the correlation functions at $\mathbf{k} = 0$: it only serves to reduce the 4 unknown functions $K^{L,T}$, $\tilde{K}^{L,T}$ to 2 unknown functions. The key property here is that while the theories \mathcal{S}_{LG} and $\tilde{\mathcal{S}}$ are dual to each other, they are not equivalent, and the theory \mathcal{S}_{LG} is not self-dual.

We now see that Eq. (1.19) implies that the classical gravity theory of SYM3 is self-dual under an analog of particle-vortex duality [42]. It is not expected that this self-duality will hold when quantum gravity corrections are included; equivalently, the SYM3 at finite N is expected to have a frequency dependence in its conductivity at $\mathbf{k} = 0$. If we apply the AdS/CFT correspondence to the superfluid-insulator transition, and approximate the latter theory by classical gravity on AdS_4 , we immediately obtain the self-dual prediction for the conductivity, $\Phi_\sigma = 1$. This value is not far from that observed in numerous experiments, and we propose here that the AdS/CFT correspondence offers a rationale for understanding such observations.

1.5 Hydrodynamic Theory

The successful comparison between the general considerations of Section 1.3, and the exact solution using the AdS/CFT correspondence in Section 1.4, emboldens us to seek a more general theory of low frequency ($\hbar\omega \ll k_B T$) transport in the quantum critical regime. We will again present our results for the special case of a relativistic quantum critical point in 2+1 dimensions (a CFT3), but it is clear that similar considerations apply to a wider class of systems. Thus we can envisage applications to the superfluid-insulator transition, and have presented scenarios under which such a framework can be used to interpret measurements of the Nernst effect in the cuprates [39]. We have also described a separate set of applications to graphene [35]: while graphene is strictly not a CFT3, the Dirac spectrum of electrons leads to many similar results, especially in the inelastic collision-dominated regime associated with the quantum critical region. These results on graphene are reviewed in a separate paper [44], where explicit microscopic computations are also discussed.

Our idea is to relax the restricted set of conditions under which the results of Section 1.3 were obtained. We will work within the quantum critical regimes of the phase diagrams of Section 1.2 but now allow a variety of additional perturbations. First, we will move away from the particle-hole symmetric case, allowing a finite density of carriers. For graphene, this means that μ is no longer pinned at zero; for the antiferromagnets, we can apply an external magnetic field; for the superfluid-insulator transition, the number density need not be commensurate with the underlying lattice. For charged systems, such as the superfluid-insulator transition or graphene, we allow application of an external magnetic field. Finally, we also allow a small density of impurities which can act as a sink of the conserved total momentum of the CFT3. In all cases, the energy scale associated with these perturbations is assumed to be smaller than the dominant energy scale of the quantum critical region, which is $k_B T$. The results presented below were obtained in two separate computations, associated with the methods described in Sections 1.3 and 1.4, and are described in the two subsections below.

1.5.1 Relativistic Magnetohydrodynamics

With the picture of relaxation to local equilibrium at frequencies $\hbar\omega \ll k_B T$ developed in Ref. [34], we postulate that the equations of relativistic magnetohydrodynamics should describe the low frequency transport. The basic principles involved in such a hydrodynamic computation go back to the nineteenth century: conservation of energy, momentum, and charge, and the constraint of the positivity of entropy production. Nevertheless, the required results were not obtained until our recent work [39]: the general case of a CFT3 in the presence of a chemical potential, magnetic field, and small density of impurities is

very intricate, and the guidance provided by the dual gravity formulation was very helpful to us. In this approach, we do not have quantitative knowledge of a few transport co-efficients, and this is complementary to our ignorance of the effective couplings in the dual gravity theory to be discussed in [Section 1.5.2](#).

The complete hydrodynamic analysis can be found in Ref. [39]. The analysis is intricate, but is mainly a straightforward adaption of the classic procedure outlined by Kadanoff and Martin [48] to the relativistic field theories which describe quantum critical points. We list the steps:

1. Identify the conserved quantities, which are the energy-momentum tensor, $T^{\mu\nu}$, and the particle number current, J^μ .

2. Obtain the real time equations of motion, which express the conservation laws:

$$\partial_\nu T^{\mu\nu} = F^{\mu\nu} J_\nu \quad , \quad \partial_\mu J^\mu = 0; \quad (1.21)$$

here $F^{\mu\nu}$ represents the externally applied electric and magnetic fields which can change the net momentum or energy of the system, and we have not written a term describing momentum relaxation by impurities.

3. Identify the state variables which characterize the local thermodynamic state—we choose these to be the density, ρ , the temperature T , and an average velocity u^μ .
4. Express $T^{\mu\nu}$ and J^μ in terms of the state variables and their spatial and temporal gradients; here we use the properties of the observables under a boost by the velocity u^μ , and thermodynamic quantities like the energy density, ε , and the pressure, P , which are determined from T and ρ by the equation of state of the CFT. We also introduce transport co-efficients associated with the gradient terms.
5. Express the equations of motion in terms of the state variables, and ensure that the entropy production rate is positive [49]. This is a key step which ensures relaxation to local equilibrium, and leads to important constraints on the transport co-efficients. In $d = 2$, it was found that situations with the velocity u^μ spacetime-independent are characterized by only a *single* independent transport coefficient [39]. This we choose to be the longitudinal conductivity at $B = 0$.
6. Solve the initial value problem for the state variables using the linearized equations of motion.
7. Finally, translate this solution to the linear response functions, as described in Ref. [48].

1.5.2 Dyonic Black Hole

Given the success of the AdS/CFT correspondence for the specific supersymmetric model in [Section 1.4](#), we boldly assume a similar correspondence for a generic CFT3. We assume that each CFT3 is dual to a strongly-coupled theory of gravity on AdS_4 . Furthermore, given the operators associated with the perturbations away from the pure CFT3 we want to study, we can also deduce the corresponding perturbations away from the dual gravity theory. So far, this correspondence is purely formal and not of much practical use to us. However, we now restrict our attention to the hydrodynamic, collision-dominated regime, $\hbar\omega \ll k_B T$, of the CFT3. We would like to know the corresponding low energy effective theory describing the quantum gravity theory on AdS_4 . Here, we make the simplest possible assumption: the effective theory is just the Einstein-Maxwell theory of general relativity and electromagnetism on AdS_4 . As in [Section 1.4](#), the temperature T of CFT3 corresponds to introducing a black hole on AdS_4 whose Hawking temperature is T . The chemical potential, μ , of the CFT3 corresponds to an electric charge on the black hole, and the applied magnetic field maps to a magnetic charge on the black hole. Such a dyonic black hole solution of the Einstein-Maxwell equations is, in fact, known: it is the Reissner-Nordstrom black hole.

We solved the classical Einstein-Maxwell equations for linearized fluctuations about the metric of a dyonic black hole in a space which is asymptotically AdS_4 . The results were used to obtain correlators of a CFT3 using the prescriptions of the AdS/CFT mapping. As we have noted, we have no detailed knowledge of the strongly-coupled quantum gravity theory which is dual to the CFT3 describing the superfluid-insulator transition in condensed matter systems, or of graphene. Nevertheless, given our postulate that its low energy effective field theory is essentially captured by the Einstein-Maxwell theory, we can then obtain a powerful set of results for CFT3s.

1.5.3 Results

In the end, we obtained complete agreement between the two independent computations in [Sections 1.5.1](#) and [1.5.2](#), after allowing for their distinct equations of state. This agreement demonstrates that the assumption of a low energy Einstein-Maxwell effective field theory for a strongly coupled theory of quantum gravity is equivalent to the assumption of hydrodynamic transport for $\hbar\omega \ll k_B T$ in a strongly coupled CFT3.

Finally, we turn to our explicit results for quantum critical transport with $\hbar\omega \ll k_B T$.

First, consider adding a chemical potential, μ , to the CFT3. This will induce a non-zero number density of carriers ρ . The value of ρ is defined so that the total charge density associated with ρ is $e^* \rho$. Then the electrical

conductivity at a frequency ω is

$$\sigma(\omega) = \frac{e^{*2}}{h} \Phi_\sigma + \frac{e^{*2} \rho^2 v^2}{(\varepsilon + P)} \frac{1}{(-i\omega + 1/\tau_{\text{imp}})}. \quad (1.22)$$

In this section, we are again using the symbol v to denote the characteristic velocity of the CFT3 because we will need c for the physical velocity of light below. Here ε is the energy density and P is the pressure of the CFT3. We have assumed a small density of impurities which lead to a momentum relaxation time τ_{imp} [39, 45]. In general, Φ_σ , ρ , ε , P , and $1/\tau_{\text{imp}}$ will be functions of $\mu/k_B T$ which cannot be computed by hydrodynamic considerations alone. However, apart from Φ_σ , these quantities are usually amenable to direct perturbative computations in the CFT3, or by quantum Monte Carlo studies. The physical interpretation of Eq. (1.22) should be evident: adding a charge density ρ leads to an additional Drude-like contribution to the conductivity. This extra current cannot be relaxed by collisions between the unequal density of particle and hole excitations, and so requires an impurity relaxation mechanism to yield a finite conductivity in the d.c. limit.

Now consider thermal transport in a CFT3 with a non-zero μ . The d.c. thermal conductivity, κ , is given by

$$\kappa = \Phi_\sigma \left(\frac{k_B^2 T}{h} \right) \left(\frac{\varepsilon + P}{k_B T \rho} \right)^2, \quad (1.23)$$

in the absence of impurity scattering, $1/\tau_{\text{imp}} \rightarrow 0$. This is a Wiedemann-Franz-like relation, connecting the thermal conductivity to the electrical conductivity in the $\mu = 0$ CFT. Note that κ diverges as $\rho \rightarrow 0$, and so the thermal conductivity of the $\mu = 0$ CFT is infinite.

Next, turn on a small magnetic field B ; we assume that B is small enough that the spacing between the Landau levels is not as large as $k_B T$. The case of large Landau level spacing is also experimentally important, but cannot be addressed by the present analysis. Initially, consider the case $\mu = 0$. In this case, the result Eq. (1.23) for the thermal conductivity is replaced by

$$\kappa = \frac{1}{\Phi_\sigma} \left(\frac{k_B^2 T}{h} \right) \left(\frac{\varepsilon + P}{k_B T B / (hc/e^*)} \right)^2 \quad (1.24)$$

where again $1/\tau_{\text{imp}} \rightarrow 0$. This result relates κ to the electrical *resistance* at criticality, and so can be viewed as a Wiedemann-Franz-like relation for the vortices. A similar $1/B^2$ dependence of κ appeared in the Boltzmann equation analysis of Ref. [46], but our more general analysis applies in a wider and distinct regime [35], and relates the coefficient to other observables.

We have obtained a full set of results for the frequency-dependent thermoelectric response functions at non-zero B and μ . The results are lengthy and we refer the reader to Ref. [39] for explicit expressions. Here we only note that the characteristic feature [39, 47] of these results is a new *hydrodynamic*

cyclotron resonance. The usual cyclotron resonance occurs at the classical cyclotron frequency, which is independent of the particle density and temperature; further, in a Galilean-invariant system this resonance is not broadened by electron-electron interactions alone, and requires impurities for non-zero damping. The situation for our hydrodynamic resonance is very different. It occurs in a collision-dominated regime, and its frequency depends on the density and temperature: the explicit expression for the resonance frequency is

$$\omega_c = \frac{e^* B \rho v^2}{c(\varepsilon + P)}. \quad (1.25)$$

Further, the cyclotron resonance involves particle and hole excitations moving in opposite directions, and collisions between them can damp the resonance even in the absence of impurities. Our expression for this intrinsic damping frequency is [39, 47]

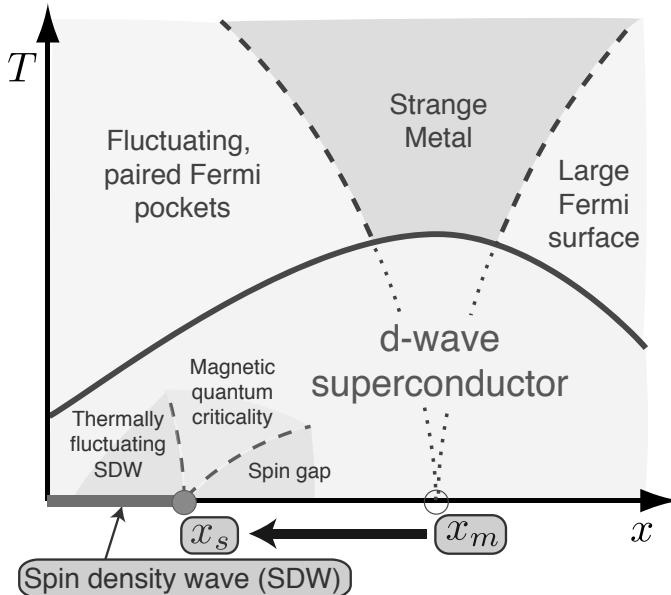
$$\gamma = \frac{e^{*2}}{h} \Phi_\sigma \frac{B^2 v^2}{c^2(\varepsilon + P)}, \quad (1.26)$$

relating it to the quantum-critical conductivity as a measure of collisions between counter-propagating particles and holes. We refer the reader to a separate discussion [35] of the experimental conditions under which this hydrodynamic cyclotron resonance may be observed.

1.6 The Cuprate Superconductors

We close this article by mentioning application to the cuprate superconductors. The phenomenology of these materials is very involved, and they have so far resisted a *global* interpretation in terms of the canonical quantum-critical crossover phase diagrams discussed here. Surely, one of the important complexities is that they involve at least two order parameters: those associated with *d*-wave superconductivity and with SDWs (both commensurate and incommensurate with the underlying lattice). In addition there are also topological changes in the Fermi surface discussed in [Section 1.1.4](#) and [Fig. 1.4](#).

Here we mention recent ideas [50–52] which attempt a synthesis based upon a combination of the crossover phase diagrams we have discussed here. The ideas build upon the results of a number of recent experiments [22, 53, 54] which have explored the phase diagram of both the hole- and electron-doped cuprates in a magnetic field applied perpendicular to the layers. We do not wish to enter into the intricate details of the structure of the phase diagram in the field-doping plane, and refer the reader to a recent review [52]. We will limit ourselves to the assertion that the experiments support the proposal [54] that the underlying metallic state of the cuprates undergoes an SDW transition as in [Fig. 1.7](#) along with the topological change of the Fermi surface, which was illustrated in [Fig. 1.4](#) for the simplest case of commensurate ordering.

**FIGURE 1.10**

Influence of the onset of superconductivity on the crossovers near the SDW ordering transition in Fig. 1.7.

Recent computations [55] and observations [56] of thermoelectric effects have provided additional support for this proposal.

The main ingredient missing from Fig. 1.7 is *d*-wave superconductivity. It is known that the SDW fluctuations can induce *d*-wave pairing for the Fermi surface configuration shown in Fig. 1.4. If we superimpose a superconducting region on Fig. 1.7 we obtain Fig. 1.10. Arguments that this superconducting region will have the dome shape around the quantum critical point were made in Ref. [51]. Here we wish to draw attention to a crucial new feature shown in Fig. 1.10. The onset of superconductivity *shifts* the spin ordering quantum critical point from its apparent position in the underlying metal at $x = x_m$ to its actual position in the superconductor at $x = x_s$. This shift is indicated by the large arrow in Fig. 1.10. We have argued [51, 52] that this shift helps resolve a number of long-standing puzzles in understanding the experimental observations in the cuprates in terms of the quantum-critical crossover phase diagrams.

What is the physical origin of the shift in the position of the quantum critical point? In phenomenological terms, this shift can be understood as a *competition* between the SDW and superconducting order parameters [57]. Once there is an onset of superconductivity, it repels the incipient SDW ordering, and shifts it away from the superconducting to lower carrier

concentration. A microscopic theory has also been presented in Ref. [51, 58]: it requires special attention to the physics of the Fermi surface, and the fact that SDW ordering and superconductivity are ‘eating up’ the same portions of the Fermi surface. Such phenomena are especially pronounced near the Mott insulating state at zero doping.

Once the shift has occurred, the crossovers near the spin-ordering transition within the superconductor are especially simple. There are no longer any Fermi surfaces to contend with, and so we can largely focus on the fluctuations of the order parameter. The latter reduce [59] to those presented in Fig. 1.5, with critical theories like those presented in Sections 1.1.1 and 1.1.2.

So the bottom line is that the proposed cuprate phase diagram in Fig. 1.10 is a combination of the crossovers in Fig. 1.5 and 1.7, along with the all-important shift in the position of the quantum critical point.

It is now interesting to examine the subtle evolution in the physics as the temperature is lowered for $x_s < x < x_m$. Above T_c , we have a metallic state with fluctuating SDW order whose strength increases as T is lowered. Once we cross T_c , the growth in SDW ordering is arrested (because of the competition with superconductivity); the system is now to the *right* of the SDW ordering quantum critical point, and starts to recover aspects of the physics of the large Fermi surface. However, it has been argued [59] that forms of translational symmetry breaking, such as VBS or Ising-nematic ordering, may appear as $T \rightarrow 0$ for $x_s < x < x_m$. In this case, the left crossover line emerging from x_m in Fig. 1.10 would become an actual thermal phase transition at which lattice symmetry is restored.

Exciting new evidence for Ising-nematic ordering along the left line emerging from x_m has emerged in recent experiments [60]; another revealing experimental study of this transition is described in Chap. 16. For future work, a key prediction of the phase diagram in Fig. 1.10 is that the SDW ordering transition in the metal at x_m will reveal itself when superconductivity is suppressed by an applied magnetic field, and that this transition will have a change in Fermi surface similar to that in Fig. 1.4. Such a transition has already been seen recently in electron-doped cuprates in the remarkable experiments of Ref. [22], and many groups are beginning to explore the corresponding regime in the hole-doped cuprates, which requires significantly stronger magnetic fields.

Acknowledgments – This research was supported by the National Science Foundation under grant DMR-0757145, by the FQXi foundation, and by a MURI grant from AFOSR.

Bibliography

- [1] S. Sachdev, *Quantum Phase Transitions*. Cambridge University Press, Cambridge, U.K. (1999).
- [2] S. Sachdev, Nature Physics **4**, 173 (2008); S. Sachdev and M. Müller, Journal of Physics: Condensed Matter **21**, 164216 (2009).
- [3] M. Troyer, M. Imada, and K. Ueda, J. Phys. Soc. Japan **66**, 2957 (1997).
- [4] M. Matsumoto, C. Yasuda, S. Todo, and H. Takayama, Phys. Rev. B **65**, 014407 (2002).
- [5] S. Wenzel and W. Janke, Phys. Rev. B **79**, 014410 (2009).
- [6] M. Campostrini *et al.*, Phys. Rev. B **65**, 144520 (2002).
- [7] A. W. Sandvik and D. J. Scalapino, Phys. Rev. Lett. **72**, 2777 (1994).
- [8] Y. Matsushita, M. P. Gelfand, and C. Ishii, J. Phys. Soc. Jpn **66**, 3648 (1997).
- [9] A. F. Albuquerque, M. Troyer, and J. Oitmaa, Phys. Rev. B **78**, 132402 (2008).
- [10] Ch. Ruegg *et al.*, Phys. Rev. Lett. **100**, 205701 (2008).
- [11] B. Normand and T. M. Rice, Phys. Rev. B **56**, 8760 (1997).
- [12] S. Sachdev, Phys. Rev. B **55**, 142 (1997).
- [13] N. Read and S. Sachdev, Phys. Rev. Lett. **62**, 1694 (1989).
- [14] T. Senthil, A. Vishwanath, L. Balents, S. Sachdev, and M. P. A. Fisher, Science **303**, 1490 (2004).
- [15] A. W. Sandvik, Phys. Rev. Lett. **98**, 227202 (2007).
- [16] J. Lou, A. W. Sandvik, and N Kawashima, Phys. Rev. B **80**, 180414 (2009).
- [17] R. G. Melko and R. K. Kaul, Phys. Rev. Lett. **100**, 017203 (2008); Phys. Rev. B **78**, 014417 (2008).
- [18] F.-J. Jiang, M. Nyfeler, S. Chandrasekharan, and U.-J. Wiese, Stat. Mech. (2008) P02009.
- [19] A. B. Kuklov, M. Matsumoto, N. V. Prokof'ev, B. V. Svistunov, and M. Troyer, Phys. Rev. Lett. **101**, 050405 (2008).

- [20] A. H. Castro Neto, F. Guinea, N. M. Peres, K. S. Novoselov, and A. K. Geim, Rev. Mod. Phys. **81**, 109 (2009).
- [21] N. P. Armitage *et al.*, Phys. Rev. Lett. **88**, 257001 (2002).
- [22] T. Helm *et al.*, Phys. Rev. Lett. **103**, 157002 (2009).
- [23] S. Sachdev, A. V. Chubukov, and A. Sokol, Phys. Rev. B **51**, 14874 (1995).
- [24] M. T. Béal-Monod and K. Maki, Phys. Rev. Lett. **34**, 1461 (1975).
- [25] J. A. Hertz, Phys. Rev. B **14**, 1165 (1976).
- [26] Ar. Abanov and A. Chubukov, Phys. Rev. Lett. **93**, 255702 (2004).
- [27] M. A. Metlitski and S. Sachdev, arXiv:1005.1288 (2010).
- [28] S. Chakravarty, B. I. Halperin, and D. R. Nelson, Phys. Rev. B **39**, 2344 (1989).
- [29] S. Sachdev and J. Ye, Phys. Rev. Lett. **69**, 2411 (1992); A. V. Chubukov, S. Sachdev, and J. Ye, Phys. Rev. B **49**, 11919 (1994).
- [30] D. E. Sheehy and J. Schmalian, Phys. Rev. Lett. **99**, 226803 (2007).
- [31] A. J. Millis, Phys. Rev. B **48**, 7183 (1993).
- [32] H. v. Löhneysen, A. Rosch, M. Vojta, and P. Wölfle, Rev. Mod. Phys. **79**, 1015 (2007).
- [33] M. P. A. Fisher, P. B. Weichman, G. Grinstein, and D. S. Fisher, Phys. Rev. B **40**: 546, 1989.
- [34] K. Damle and S. Sachdev, Phys. Rev. B **56**, 8714 (1997).
- [35] L. Fritz, J. Schmalian, M. Müller, and S. Sachdev, Phys. Rev. B **78**, 085416 (2008); M. Müller and S. Sachdev, Phys. Rev. B **78**, 115419 (2008); M. Müller, L. Fritz, and S. Sachdev, Phys. Rev. B **78**, 115406 (2008).
- [36] P. Kovtun and L. G. Yaffe, Phys. Rev. D **68**, 025007 (2003).
- [37] P. K. Kovtun, D. T. Son, and A. Starinets, Phys. Rev. Lett. **94**, 11601 (2005).
- [38] M. P. A. Fisher, G. Grinstein, and S. M. Girvin, Phys. Rev. Lett. **64**, 587 (1990); M. P. A. Fisher, Phys. Rev. Lett. **65**, 923 (1990).
- [39] S. A. Hartnoll, P. K. Kovtun, M. Müller, and S. Sachdev, Phys. Rev. B **76**, 144502 (2007).

- [40] M. Müller, J. Schmalian, and L. Fritz, Phys. Rev. Lett. **103**, 025301 (2009).
- [41] N. Itzhaki, J. M. Maldacena, J. Sonnenschein, and S. Yankielowicz, Phys. Rev. D **58**, 046004 (1998).
- [42] C. P. Herzog, P. Kovtun, S. Sachdev, and D. T. Son, Phys. Rev. D **75**, 085020 (2007).
- [43] C. Dasgupta and B. I. Halperin, Phys. Rev. Lett. **47**, 1556 (1981).
- [44] M. Müller, L. Fritz, S. Sachdev, and J. Schmalian, Advances in Theoretical Physics: Landau Memorial Conference, Chernogolovka 2008, AIP Conference Proceedings **1134**, 170 (2009).
- [45] S. A. Hartnoll and C. P. Herzog, Phys. Rev. D **77**, 106009 (2008).
- [46] M. J. Bhaseen, A. G. Green, and S. L. Sondhi, Phys. Rev. Lett. **98**, 166801 (2007); Phys. Rev. B **79**, 094502 (2009).
- [47] S. A. Hartnoll and C. P. Herzog, Phys. Rev. D **76**, 106012 (2007).
- [48] L. P. Kadanoff and P. C. Martin, Annals of Physics **24**, 419-469 (1963).
- [49] L. D. Landau and E. M. Lifshitz, *Fluid Mechanics*, Section 127, Butterworth-Heinemann, Oxford, 1987.
- [50] V. Galitski and S. Sachdev, Phys. Rev. B **79**, 134512 (2009).
- [51] E. G. Moon and S. Sachdev, Phys. Rev. B **80**, 035117 (2009).
- [52] S. Sachdev, Physica Status Solidi B **247**, 537 (2010); S. Sachdev, Les Houches lectures, arXiv:1002.3823.
- [53] N. Doiron-Leyraud *et al.*, Nature **447**, 565 (2007); D. LeBoeuf *et al.*, Nature **450**, 533 (2007); S. E. Sebastian *et al.*, Nature **454**, 200 (2008).
- [54] R. Daou *et al.*, Nature Physics **5**, 31 (2009).
- [55] A. Hackl, M. Vojta, and S. Sachdev, Phys. Rev. B **81**, 045102 (2010).
- [56] J. Chang *et al.*, Phys. Rev. Lett. **104**, 057005 (2010).
- [57] E. Demler, S. Sachdev, and Y. Zhang, Phys. Rev. Lett. **87**, 067202 (2001); Y. Zhang, E. Demler, and S. Sachdev, Phys. Rev. B **66**, 094501 (2002).
- [58] E. G. Moon and S. Sachdev, arXiv:1005.3312 (2010).
- [59] R. K. Kaul, M. A. Metlitski, S. Sachdev, and C. Xu, Phys. Rev. B **78**, 045110 (2008).
- [60] R. Daou *et al.*, Nature **463**, 519 (2010).

2

Dissipation, Quantum Phase Transitions, and Measurement

Sudip Chakravarty

*Department of Physics and Astronomy, University of California Los Angeles,
Los Angeles, CA 90095-1547, U.S.A.*

This chapter reflects my subjective choice of topics. My interest falls into three distinct categories. The intense interest in the problem of dissipation in quantum systems began at the time when macroscopic quantum tunneling and coherence in superconducting quantum interference devices (SQUIDs) were proposed. This subject has seen considerable developments over the past three decades both in theory and in experiments [1]. An important problem in this subject is a particle in a double well potential coupled to a bath consisting of an infinite number of harmonic oscillators providing a linear dissipation to the particle, in other words coupled to an Ohmic heat bath in the language of electrical engineering [2]. Yet, it is hardly recognized that this problem constitutes one of the simplest models of quantum criticality [3]. Thus, unsurprisingly, little attention has been paid over the years to experimentally explore this critical phenomenon. It remains equally unrecognized that the same model holds a germ of the quantum-to-classical transition much discussed in measurement theory.¹ Here I have attempted to draw a parallel with an even more elementary model of Coleman and Hepp [4], which actually contains no dissipation. Nonetheless the two problems are united by the dictum that for infinitely many degrees of freedom two distinct states of matter cannot be unitarily related. A particle in a double well coupled to a dissipative environment is indeed a system with an infinite number of degrees of freedom. Of course, the Coleman-Hepp model can be supplemented by dissipation to bring the two models closer, but the basic issue with respect to measurement is clearer in its original form.

Certain aspects of quantum phase transitions (QPTs) have recently been shown to be different from their classical counterparts. A surprise has been that Anderson localization of an electron in a random potential and the plateau-to-plateau transition of the integer quantum Hall effect do not fit the traditional framework [5, 6]. Despite a field theoretical formulation that

¹I have reluctantly succumbed to the trap of using the vague terminology “measurement theory.”

mimics a conventional QPT, there is a glaring issue that is lost in the forest of replica formalism [7] where the number of replicas have to be analytically continued to zero. One finds that the cherished criterion that the ground state energy has to be non-analytic at a QPT is simply not true for these phenomena [6, 8]. Instead, one finds that the von Neumann entropy is beautifully non-analytic and in perfect agreement with the scaling theory of localization [9] and its generalization to integer quantum Hall systems [10]. It is this quantum information theoretical perspective that intrigues me.

Finally, disorder brings some surprises to the subject of quantum phase transitions. It can be argued that a whole class of first order QPTs are rounded by disorder and even converted into continuous phase transitions [11]. Mathematical physicists are beginning to pay some serious attention to this problem [12], which, however, is not a trivial consequence of a similar result for classical first order phase transitions [13]. It makes us wonder how many sightings of quantum critical points are actually first order QPTs in disguise – and, in fact, how one should approach disorder rounded quantum criticality, especially its dynamics. This is a subject that is in its nascent stage, but is likely to become important in the near future.

2.1 Multiplicity of Dynamical Scales and Entropy

A phase transition between two distinct states of matter is characterized by a non-analyticity of the free energy. This is now the dogma, and rightly so, because there are very few cases where this idea could in principle be challenged. In the back of our minds we have the picture of the distribution of zeros of the partition function of the two-dimensional Ising model. Yang and Lee showed that these zeros lie on a unit circle and in the infinite volume limit they become dense and pinch the real axis at a finite temperature, separating two phases [14]. At zero temperature the ground state energy plays the role of free energy.

This dogma was scrutinized a great deal in the context of spin-glass transitions [15] where the interaction between the spins is a quenched random variable distributed according to a probability distribution. But with some tricks involving averaging the free energy (not the partition function) with respect to disorder nothing really changed. Much effort, including those of the present author [16], has been spent in describing the spin-glass transition as an equilibrium phase transition that we have known to love and cherish. When the real world offers us a multiplicity of dynamical scales, equilibrium is difficult to attain within a typical observation time scale. This is nowhere more prominent than in a quantum system where statics and dynamics are intertwined. In fact, the explicit nature of the reservoir to which a system is

coupled can drastically change the nature of a QPT at zero temperature,² and even its very existence can depend upon it.

Before Gibbs, Boltzmann had postulated a famous formula that is perhaps not so practical but conceptually important. It defines entropy, S_B , in terms of the available phase space volume, W :

$$S_B = k_B \ln W, \quad (2.1)$$

where k_B is the Boltzmann constant. But how do we find W ? It appears that in order to find it we must solve the equations of motion and determine the dynamics of the system. The Boltzmann formula can of course be reconciled with the ensemble approach of Gibbs in equilibrium, which is more convenient to use [17]. A system coupled weakly to a reservoir can be described by a canonical ensemble when the total system is described by a microcanonical ensemble in an energy shell, for either a classical phase space distribution or for quantum density matrices. Surprisingly, a stronger result has been obtained [18, 19], that, in the thermodynamic limit, the reduced density matrix of the system is canonical for the overwhelming majority of *wave functions* of the total system, and has been called *canonical typicality*.

We still need to answer when we can assert that the system is in equilibrium and how do we accurately model the very slow dynamical variables, especially if they form a continuum. We also need to know what happens when the system is at exactly $T = 0$, where we can define a geometric entropy [20] by partitioning a system into two parts A and B . In this case we define the von Neumann entropy (vNE) of the subsystem as:

$$S_A^{\text{vN}} = -\text{Tr}_A \rho_A \ln \rho_A; \quad S_B^{\text{vN}} = -\text{Tr}_B \rho_B \ln \rho_B. \quad (2.2)$$

Here, the reduced density matrix ρ_A is obtained by tracing over the degrees of freedom in B : $\rho_A = \text{Tr}_B |\psi_{AB}\rangle\langle\psi_{AB}|$ and similarly for ρ_B . In general, for a pure state $|\psi_{AB}\rangle$ of a composite system, which cannot be factored, the reduced density matrix is a mixture, and the corresponding entropy is a good measure

²A quantum critical point is a point at exactly $T = 0$, where the correlation length diverges as we tune a coupling constant, resulting in a non-analyticity in the ground state energy (sharp avoided level crossing) and/or von Neumann entropy, as in a transverse field Ising model in one spatial dimension for which there is no finite temperature transition. If, on the other hand, we consider a transition, as for example in a transverse field Ising model in two spatial dimensions, there is a finite temperature transition as well. However, the criticality of the finite temperature transition has the Onsager exponents, because at the critical point the correlation length tends to infinity and the criticality is determined by the classical statistical mechanics of the two-dimensional Ising model. Because the energy scales tend to zero as the transition is approached, quantum mechanics is unimportant at such long wavelengths. However, there will be a crossover from quantum-to-classical behavior, as we approach the criticality at non-zero temperature. So the limit $T \rightarrow 0$ can be singular. If we have a first order quantum transition at $T = 0$, where an order parameter develops discontinuously, the story is different, because the correlation length is finite and remains so even if this transition continues to finite temperatures, and in principle quantum mechanics can play an important role even at non-zero temperatures, if the correlation length is sufficiently short.

of entanglement. Therefore the vNE can play an important role for QPTs because correlations build up at the transition. It is also interesting to note that the vNE is analogous in *form* to the classical Gibbs entropy

$$S_G = -k_B \int dX \rho(X) \ln \rho(X), \quad (2.3)$$

where $\rho(X)dX$ is the phase space probability and the integral is over the phase space. If we choose $\rho(X) = 1/W$, uniformly distributed over the available volume, W , of a macrostate, we arrive at the Boltzmann formula. Despite the similarity, the vNE has a different meaning. It can give interesting information even at $T = 0$ for two particles, namely the quantum mechanical entanglement of the particles. More curiously, we can give a useful physical meaning for even a single degree of freedom: for example, for a non-interacting particle in a random potential, we can ask, what is the amplitude of the complete wave function at a given site (a ket in the position basis), that is, how much does it participate at a given site? It can be finite for a localized state and zero for a delocalized state in the limit that the number of sites $N \rightarrow \infty$.

The role of multiplicity of dynamical scales is critical. A simple well known example of two distinct time scales is the problem of ortho- and para-hydrogen. The spins of the nuclei in a hydrogen molecule can be either in a triplet state or a singlet state. The interaction between the nuclei is very small and so is the interaction between the nuclei and the electronic spins which are in a singlet state. Thus, the singlet-triplet conversion takes time, on the order of days, while the momenta of the molecules equilibrate on a microscopic time scale. In this example the number of nuclei in the singlet state and the number of nuclei in the triplet state are separately constants of motion on the time scale of a typical experiment. In considering the statistical mechanics of this system one must take this fact into account, and add the free energies of these two subsystems rather than adding the partition functions. Experimental observations strikingly confirm this fact.

For widely separated scales, it is always clear what the relevant region of the phase space that contributes to the macroscopic property of the system is. When this is not the case, and there is a continuum of time scales, extending from very short microscopic scales to very long macroscopic scales, this is difficult to determine. The common amorphous material, window glass, falls in this category. It is not sufficient to know all the states and sum over all of them; we must examine the actual dynamics of the system. However, the Boltzmann entropy formula is still usable. We could determine the volume of the phase space sampled during the observation time. After all, measurements are carried out on a single system, not on ensembles.

Many models of QPTs consist of a single Hamiltonian, however many flavors of degrees of freedom we may have and however many coupling constants we may have. We are not restricted to a system weakly coupled to a reservoir of a generic character. A particular route to solving the problem may be to calculate the pure state (ground state) of the total system and the correspond-

ing ground state energy. We might find that there is a sharp change of state, a phase transition, at a given value of a coupling constant at which the ground state energy is non-analytic and the states on both sides of this transition are not unitarily related. There are cases where this picture does not hold, however, and we can have a perfectly analytic behavior of the ground state energy but a well defined non-analyticity of the vNE characterizing distinctly different correlations on the two sides of the transition. We do not know if this is a general principle signifying a QPT, but there are cases where we can clearly demonstrate this phenomenon, as we shall see below. Somehow, Boltzmann's notion of entropy continues to play an important role.

2.2 Dissipation

A convenient way to treat dissipative systems in quantum mechanics is to consider a system coupled to a reservoir and to integrate out the reservoir degrees of freedom. In this language dissipation refers to a one-way transfer of energy from a system to its environment, where it can be effectively lost [21]. If the energy levels of the environment are finely spaced,³ there is little chance that energy that leaks out to the environment will ever return to the system in a physically meaningful time. For quantum statistical mechanics, as opposed to its classical cousin, the notion of dissipation is relevant even in equilibrium, because statics and dynamics are intertwined through the complete set of energy eigenvalues of the total Hamiltonian, system plus the environment. A QPT is certainly affected by dissipation, as opposed to a classical phase transition.

If we represent a system plus its environment by a pure-state wave function, there is no dissipation involved at zero temperature. Nonetheless, the internal correlations will still be affected by what we would call the environmental degrees of freedom in an open system, except that we can no longer legitimately characterize them as due to dissipation.⁴ The discussion is not merely semantic, because for many situations we can only measure the observables of the system alone; the environment is important only to the extent that it influences the properties of the system. In such a coarse grained picture it is possible that the environment itself can be classified according to universality classes, and only the overall quantum numbers, such as charge, momentum, angular momentum, etc., are relevant.

Two crisp questions one can address are as follows. (1) Given that we know that the classical system is dissipative and is well characterized by a few ex-

³It is convenient to use the terminology of quantum mechanics.

⁴We can still have a phase transition where the wave function undergoes a sharp change. With infinitely many degrees of freedom, the two Hilbert spaces on the two sides of the transition will generically be unitarily inequivalent.

perimentally determined parameters, how does it behave when it is quantized? (2) Given that a quantum system in the ground state is well characterized by order parameters, how does the environment influence the statics and the dynamics of this order parameter and to what degree? I shall not address these questions further because much has already been said in answer to the first question by Feynman and Vernon [22], Caldeira and Leggett [23], and Mohring and Smilansky [24]. With respect to the second question the pioneering work of John Hertz [25] has triggered a vast literature.

2.3 Quantum Phase Transitions

Classical mechanics is fully described by Newton's laws, a set of differential equations for each degree of freedom. By following the solution, one should be able to predict every single outcome given a set of initial conditions. Yet, in the overwhelmingly majority of cases this is not possible. The outcomes, the emergent states of matter, are strikingly unpredictable, especially when it comes to prediction of a phase transition. Phases of matter are strictly distinct and are not analytic continuations of each other. While Newton's laws are invariant under time-reversal and a given Hamiltonian may also be invariant under the same symmetry, a phase may macroscopically violate this symmetry, for example a ferromagnet. In this respect quantum phases and transitions between them are no different. They emerge from quantum fluctuations of infinitely many degrees of freedom interacting.

2.3.1 Infinite Number of Degrees of Freedom

A mathematically precise solution of a model in two dimensions known as the Ising model by Onsager really clinches any possible doubts one may harbor. The same Hamiltonian, which is invariant under the flip of the Ising spins, can describe both a magnetized and an unmagnetized (disordered) state.⁵ The response to an infinitesimal magnetic field below the phase transition is infinite, while above the transition the response to an infinitesimal field is infinitesimal. Even though both a magnetized and unmagnetized ensemble remain possible mathematical solutions, even a stray physical field can choose one state over the other. It would be difficult to pretend that the actual physical state is a superposition of the two states related by spin flips, hence no magnetization. Experimental observations bear out this conclusion to such a perfection that I can bet my life on it.

⁵Before Onsager's solution there was considerable doubt that this was possible—C. N. Yang, private communication

As is well known, the partition function of the Ising model is a sum,

$$Z = \sum_{\{s_i\}} \prod_{\langle ij \rangle} e^{-\beta S_i S_j}, \quad (2.4)$$

where the product is over nearest-neighbor pairs and I have set the exchange constant to unity. The Ising spins S_i take values ± 1 . As long as the number of spins, N , is finite, Z is a polynomial of finite degree with real coefficients, and the free energy $F = -\frac{1}{\beta} \ln Z$ cannot possibly have any non-analyticity at a real non-zero temperature, hence no phase transitions. But once we entertain the possibility of $N = \infty$, the convergence of the sum is no longer guaranteed, and all bets are off. Now, of course, we are not truly interested in an infinite number of degrees of freedom. This would not be physically meaningful. We are interested in a sufficiently large number of degrees of freedom. How large is large? In a schematic language, given the experimental resolution ϵ , we should choose a $\delta = 1/N$ (or some power, but that is irrelevant), such that $\delta < \epsilon$.

The background of classical statistical mechanics and the role of an infinite number of degrees of freedom is a prelude to helping one understand the quantum-to-classical crossover (transition), which is often ignored in discussions involving foundations of quantum mechanics. That QPTs render the system classical due to dissipation is an important piece of the puzzle. A genuine phase transition involves an infinite number of degrees of freedom.

All we need is a single example where the quantum-to-classical transition can be described in the language of a phase transition of an equivalent classical statistical mechanical problem. However, there is not just one but a whole class of problems where a d -dimensional quantum problem can be mapped onto a $(d+1)$ -dimensional (d refers to the spatial dimension and the remaining dimension is the imaginary time) classical statistical mechanical problem. By analyzing the classical problem, we can learn *some* important aspects of quantum mechanics. One of the simplest examples in this regard is a particle in a symmetric double-well potential.

From standard undergraduate quantum mechanics, we know that the two lowest states are separated by a gap, ΔE , related to the tunneling through the barrier, and a particle initially prepared in one of the wells will exhibit coherent oscillations, so characteristic of quantum mechanics. The same problem can be mapped onto a classical one-dimensional Ising model ($0 \rightarrow 1$) from which we can infer the exact value of ΔE , all correlation functions in imaginary time, and, by analytic continuation to real time, all the traditional aspects of quantum mechanics. We learn that as long as the barrier height is finite, the ground state is a linear superposition of two states separated by ΔE from the first excited state, which is an antisymmetric linear superposition.

This classic example exemplifies all the perplexing aspects of quantum mechanics. Nonetheless, we can derive all its properties from the statistical mechanics of the classical Ising model. Even more shocking is the problem where this symmetric double well is coupled to an infinite number of dissipative degrees of freedom with a special property termed as an Ohmic heat

bath. This time the corresponding $(0 + 1)$ -dimensional classical problem involves special long range interactions, and undergoes a phase transition as a function of the coupling to the environment in the limit that the number of Ising spins $N \rightarrow \infty$. This translates into spontaneous symmetry breaking in the ground state of the quantum system [3]. Parity is broken and one of the states will be selected by an infinitesimal asymmetric perturbation. The correlations within the broken symmetry state have effectively lost all vestige of quantum mechanics and have transformed a quantum problem to a classical problem. Here, then, is a problem that is a tantalizing example of how QPTs can illuminate the foundations of quantum mechanics.

2.3.2 Broken Symmetry

In this subsection the relevance of broken symmetry and quantum criticality will be discussed in the context of quantum measurement theory. The simplest case is that of a ferromagnet (say, the nearest-neighbor Heisenberg model) in its ground state for a Hamiltonian invariant under spin rotation. For simplicity consider spin-1/2. The ground state of a ferromagnet does not respect the spin-rotation symmetry of the Hamiltonian; an infinitesimally weak magnetic field can lock the ferromagnet in a given direction. Another way of expressing the same fact is to note that the two ground states which differ by an arbitrarily small angle are unitarily inequivalent in the limit of an infinite number of spins. The theorems of Wigner, or Stone and von Neumann, regarding unitary equivalence apply only to a finite number of degrees of freedom.

2.3.2.1 Unitary Inequivalence

Let $|0\rangle$ be the ground state of a ferromagnet consisting of N spins. In the S_z representation,

$$|0\rangle = |\uparrow_1\uparrow_2 \dots \uparrow_i \dots \uparrow_N\rangle. \quad (2.5)$$

Consider a new ground state where all spins are rotated by an angle θ , independent of the number of degrees of freedom N , in the $X - Z$ plane:

$$|\theta\rangle = \exp \left[-i \frac{\theta}{2} \sum_{k=1}^N \sigma_2(k) \right] |0\rangle, \quad 0 < \theta \leq \pi. \quad (2.6)$$

The operators σ_α are the standard Pauli matrices. It is trivial to show that the scalar product

$$\langle 0|\theta\rangle = \left(\cos \frac{\theta}{2} \right)^N \rightarrow 0, \text{ as } N \rightarrow \infty, \quad (2.7)$$

however small the non-zero angle θ may be. We can build a Hilbert space by applying operators $\sigma_-(k) = \sigma_1(k) - i\sigma_2(k)$ on $|0\rangle$ and by Cauchy completion. Similarly, we can also start with

$$|\theta\rangle = U(\theta)|0\rangle \quad (2.8)$$

and build up a Hilbert space based on the rotated Pauli matrices

$$\tau_\alpha(k) = U(\theta)\sigma_\alpha(k)U^\dagger(\theta). \quad (2.9)$$

These Hilbert spaces are easily shown to be unitarily inequivalent, as any scalar product of a rotated state and the unrotated state vanishes in the limit $N \rightarrow \infty$.

2.4 Measurement Theory

This is a vast subject with a very long history. In this section we devote ourselves to a very specific neglected aspect, namely the role of broken symmetry and unitary inequivalence.

2.4.1 Coleman-Hepp Model

The above intuition regarding the unitary inequivalence of two degenerate broken-symmetry ground states of a ferromagnet can be used to build a measuring device. In a paper with the title “Quantum Theory of Measurement and Macroscopic Observables,” K. Hepp [4] has discussed how probabilities are generated from probability amplitudes. In one of his examples, the Coleman-Hepp model, a particle, with a kinetic energy linear in momentum, zips along a chain consisting of spin-1/2 objects, flipping their spins. The linearity of the kinetic energy leads to a wave packet that does not diffuse or change its form, which is a useful simplification. Similarly, the model is further simplified by assigning zero energy to the bath of spins; so flipping a spin costs no energy whatsoever. These shortcomings can be easily repaired, but the essential conclusions remain unchanged. Here we focus on implementing the notion of unitary inequivalence discussed above in a pristine form.⁶ It is of course understood that a macroscopic measuring device based on broken symmetry must have the necessary rigidity to be a valid measuring device and must be able to exchange energy with the system, the particle in this case. Nonetheless, we shall see that the interference between the two wave packets of the particle can be destroyed by a dephasing mechanism (a form of decoherence) due to the environment.

The Hamiltonian of the original Coleman-Hepp model is

$$H = vp + \sum_{i=1}^N V(x - x_i)\sigma_1(i), \quad (2.10)$$

where v is the velocity of the particle and $p = \frac{\hbar}{i}\frac{d}{dx}$ is the momentum operator

⁶In *Physics* Aristotle remarks that we should begin by what is clear to us and then proceed to what is clear in itself.

conjugate to the coordinate x , while x_i labels the lattice sites of the environment spins. The interaction $V(x)$ is supposed to have a compact support vanishing beyond a range r , independent of N , that is,

$$V(x) = 0 \text{ for } |x| > r. \quad (2.11)$$

It is useful to parametrize the strength of the interaction by a dimensionless quantity, which will later be interpreted as an angle of rotation of the bath spins:

$$\theta = \frac{1}{\hbar v} \int_{-\infty}^{\infty} dx V(x). \quad (2.12)$$

Then the $S^{[N]}$ matrix is given by

$$S^{[N]} = \lim_{t \rightarrow \infty, t' \rightarrow -\infty} U(t, t') = \prod_{k=1}^N S(k), \quad (2.13)$$

where

$$U(t, t') = e^{ivpt/\hbar} e^{-iH(t-t')/\hbar} e^{-ivpt'/\hbar}, \quad (2.14)$$

and

$$S(k) = \cos \theta - i \sigma_1(k) \sin \theta. \quad (2.15)$$

Consider now a typical interference experiment where the initial state $|I\rangle$ is a direct product of a linear superposition of two wave packet states of the particle, $|\psi_1\rangle$ and $|\psi_2\rangle$ (normalized to unity), and the ground state of the environment $|0\rangle$,

$$|I\rangle = (|\psi_1\rangle + |\psi_2\rangle)|0\rangle. \quad (2.16)$$

Imagine that only $|\psi_2\rangle$ interacts with the environment. Then the final state $|F\rangle$ is

$$|F\rangle = |\psi_1\rangle|0\rangle + S^{[N]}|\psi_2\rangle|0\rangle. \quad (2.17)$$

The probability, P , for the final state after the interaction with the environment has taken place is

$$\begin{aligned} P &= 2 + 2\text{Re}\langle\psi_1|\psi_2\rangle\langle 0|S^{[N]}|0\rangle, \\ &= 2 + 2 \left(\cos \frac{\theta}{2} \right)^N \text{Re}\langle\psi_1|\psi_2\rangle \\ &\rightarrow 2, \text{ as } N \rightarrow \infty. \end{aligned} \quad (2.18)$$

Interference is therefore totally destroyed in the limit $N \rightarrow \infty$. The mechanism, as promised, is the unitary inequivalence of the rotated and unrotated Hilbert spaces in the infinite volume limit. Realistically, this inequivalence arises when the ground state is a ferromagnet with a spontaneously broken symmetry.

The significance of the above result in the context of the quantum measurement problem has been disputed by J. S. Bell [26]. His criticisms are: (1)

the limit $t \rightarrow \infty$, $t' \rightarrow -\infty$ “never comes,” and (2) “While for any given observable one can find a time for which the unwanted interference is as small as you like, for any given time one can find an observable for which it is as big as you do *not* like.” Bell is not entirely justified. To quote from the abstract of Hepp’s paper,

... In several explicitly soluble models, the measurement leads to macroscopically different ‘pointer positions’ and to a rigorous ‘reduction of the wave packet’ with respect to all local observables.

The quotation marks are hints that neither the ‘pointer positions’ nor the ‘reduction of the wave packet’ had a sense of finality in Hepp’s elegant paper. He further remarks

For practical purposes ... one has to establish the existence of the limits $N \rightarrow \infty$ and $t \rightarrow \infty$ and the disjointedness of the resulting states of the system and apparatus, in order to be sure that in the finite approximations the error can be made arbitrarily small for sufficiently large N and t .

It is ironic that Bell, who made popular the playful acronym FAPP (for all practical purposes) [27], seems not to appreciate the strength of Hepp’s argument. However, Bell does provide an example of a complex nonlocal observable for which the unwanted interference can be made as large as you do not like, and he further remarks,

The continuing dispute about quantum measurement theory is not between people ... with different ideas about actual practicality of measuring arbitrarily complicated observables.

In my opinion, physical significance of an arbitrarily complex non-local observable is debatable to say the least. Hepp’s rigorous paper does have an element of truth. He is more right than Bell.

2.4.2 Tunneling Versus Coherence

There is a marvelous semiclassical analysis by Callan and Coleman that is worth revisiting [28]. The tunneling rate from a metastable well in a one-particle quantum mechanics is determined by the bounce formula for the tunneling rate

$$\Gamma = \hbar K e^{-S_0/\hbar}, \quad (2.19)$$

where K is the prefactor and S_0 the Euclidean action for a single bounce. It is easy to show that the bounces form a dilute gas with negligible interactions among them. When the particle in the metastable well is coupled to an Ohmic heat bath, Caldeira and Leggett solved the bounce problem and showed that the quantum tunneling rate is reduced by friction [23, 29]. They were also able to prove that bounces still form a dilute gas, again with negligible interaction.

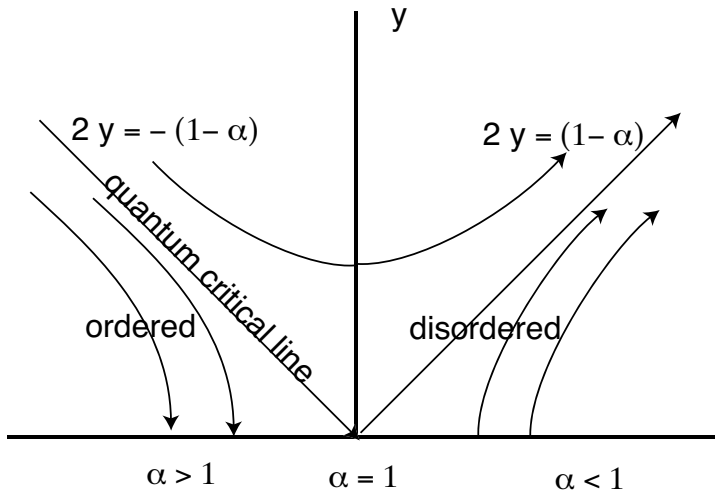
For single particle quantum mechanics in a double well potential, the instanton (analog of bounce) calculation proceeds analogously and once again the dilute gas approximation works accurately. One discovers the familiar splitting between symmetric and antisymmetric states. This calculation can be easily generalized to periodic potential [28]. The instantons are much the same. The only novelty is that when doing the dilute gas sum there is no constraint that instantons and anti-instantons must alternate. We sprinkle them freely along the real axis.

2.4.3 Quantum-to-Classical Transition

The situation changes dramatically in the double well problem, and *inter alia* the periodic potential problem, when we turn on Ohmic dissipation. The instantons now interact logarithmically, or, in the equivalent description in terms of Ising spins, the interaction is an inverse-square interaction in imaginary time. The interactions between the instantons are now scale invariant and the dilute gas approximation fails dramatically, resulting in a phase transition as a function of the dissipation strength (cf. below) $\alpha \sim R_Q/R$ ($R_Q = h/4e^2$ being the quantum of resistance and R the shunt resistance) and the fugacity of the instantons $y = \Delta_{\text{eff}}/2\hbar\omega_c$, where $\hbar\omega_c$ is a high energy cutoff in the dissipative kernel, and Δ_{eff} is the tunneling splitting [3, 30] sans instanton interactions but renormalized by dissipation, as shown in Fig. 2.1.

The continuous QPT for the double well implies that the ground state is two-fold degenerate and the coherence is lost for sufficiently large dissipation due to the environment. This is none other than a quantum-to-classical transition, and as such it should be valuable for a better understanding of the quantum measurement problem (or problems), as was the Coleman-Hepp model. The root of this broken symmetry is the orthogonality catastrophe [31] between the two degenerate states of the double well, which is $\sim (\omega/\omega_c)^\alpha$, vanishing as $\omega \rightarrow 0$, where $1/\omega$ is the observation scale and $(1/\omega_c)$ is a short time cutoff. Morally it is identical to the problem discussed in the context of the Coleman-Hepp model, and the role of the orthogonality catastrophe was also recognized by Hepp in his original paper. It turns out that this orthogonality catastrophe can be cured by a renormalization group analysis [3] for $\alpha < 1$ for small $\Delta_{\text{eff}}/\hbar\omega_c$, but not for $\alpha > 1$. A QPT separates the two regimes and the ensuing criticality has been extensively studied. In a loose sense one might say that an infrared divergent heat bath localizes the particle by repeated measurements (interactions) such that it loses its quantum coherent property. In other words, quantum interference is destroyed, as in the Coleman-Hepp model.

What about a particle in a periodic potential coupled to Ohmic dissipation [32]? A myth has developed in our field that this problem is somehow different. The commonality of the double well and the periodic potential is often not recognized, although it was clearly recognized by Schmid himself [33]. As discussed above in the case of single particle quantum mechanics, the only

**FIGURE 2.1**

The $T = 0$ phase diagram of a two-level system coupled to an Ohmic heat bath and the corresponding renormalization group flows in the regime $|(1 - \alpha)| \ll 1$ and $y \ll 1$. The renormalization group trajectories point along increasing values of the flow parameter $l = \ln(\tau\omega_c)$, where τ is imaginary time. The separatrix $2y = -(1 - \alpha)$ separates a broken symmetry phase with finite magnetization from the disordered phase. At this critical line the magnetization is discontinuous even though the correlation time (imaginary) diverges. At $\alpha = 1/2$ the dynamics of the two-level system changes from an overdamped to an underdamped state, but there is no thermodynamic phase transition at this point.

novelty here is that we can freely sprinkle instantons and anti-instantons without any constraint; the fact that they interact logarithmically leads again to a QPT with details that are a bit different.

2.5 Von Neumann Entropy

Entanglement is a unique feature of a quantum system and the vNE is a widely used measure of entanglement [34].

2.5.1 A Warmup Exercise: Damped Harmonic Oscillator

Consider a single harmonic oscillator (momentum p , position x , mass M , and frequency ω_0) coupled to an environment of harmonic oscillators. We examine the case of Ohmic dissipation, where the spectral function, $J(\omega)$, of the bath is defined by the coupling constants $\{\lambda_n\}$, together with the masses $\{m_n\}$ and the frequencies $\{\omega_n\}$ of the oscillators comprising the bath. In this model $J(\omega)$ defined by

$$J(\omega) = \frac{\pi}{2} \sum_n \frac{\lambda_n^2}{m_n \omega_n} \delta(\omega - \omega_n) \quad (2.20)$$

is taken to be $2\pi\alpha\omega = \eta\omega$ for $\omega < \omega_c$ and zero for $\omega \geq \omega_c$. The ground state expectation values of x^2 and p^2 are [21]

$$\langle x^2 \rangle = \frac{\hbar}{2M\omega_0} f(\kappa) \quad (2.21)$$

$$\langle p^2 \rangle = \frac{\hbar M \omega_0}{2} (1 - 2\kappa^2) f(\kappa) + \frac{2\hbar M \omega_0}{\pi} \kappa \ln\left(\frac{\omega_c}{\omega_0}\right) \quad (2.22)$$

where $\kappa = \eta/2M\omega_0$ is the friction coefficient and

$$f(\kappa) = \frac{1}{\pi\sqrt{\kappa^2 - 1}} \ln\left(\frac{\kappa + \sqrt{\kappa^2 - 1}}{\kappa - \sqrt{\kappa^2 - 1}}\right). \quad (2.23)$$

At $\kappa = 1$ the system crosses over from damped oscillatory to overdamped behavior ($\sqrt{\kappa^2 - 1}$ is to be replaced by $i\sqrt{1 - \kappa^2}$). The function $f(\kappa)$ is real for all $\kappa > 0$ and has an identical power series expansion regardless of the limits $\kappa \rightarrow 1 \pm 0$.

At zero temperature, the normalized reduced density matrix for the damped harmonic oscillator has matrix elements [21]

$$\langle x' | \rho_A | x'' \rangle = \sqrt{4b/\pi} e^{-a(x' - x'')^2 - b(x' + x'')^2} \quad (2.24)$$

where $a = \langle p^2 \rangle / 2\hbar^2$ and $b = 1/8\langle x^2 \rangle$. To compute the von Neumann entropy, we first note [35] that

$$\text{Tr}(\rho_A \ln \rho_A) = \lim_{n \rightarrow 1} \frac{\partial}{\partial n} \int dx' \langle x' | \rho_A^n | x' \rangle. \quad (2.25)$$

The subsequent mathematical manipulations described elsewhere [6] result in the vNE of the damped harmonic oscillator, S ,

$$S = -\frac{1}{2} \ln\left(\frac{4b}{a - b}\right) + \frac{1}{2} \sqrt{\frac{a}{b}} \ln\left(\frac{\sqrt{a} + \sqrt{b}}{\sqrt{a} - \sqrt{b}}\right). \quad (2.26)$$

Note that $S \rightarrow 0$ as $b \rightarrow a$, which corresponds to the minimum uncertainty $\sqrt{\langle x^2 \rangle \langle p^2 \rangle} = \hbar/2$. The uncertainty relation is satisfied only for $b \leq a$. This expression is analytic at $\kappa = 1$ despite the transition from the overdamped to the underdamped behavior because of the analyticity of $f(\kappa)$. The point $\kappa = 1$ is *not* a point of a QPT but a crossover in the dynamics.

2.5.2 Double Well Coupled to a Dissipative Heat Bath

We now return to the double well problem in the specific formulation known as the spin-boson model [2] in which a two-level system is represented by a spin-1/2 degree of freedom and the bath is a collection of harmonic oscillators. The Hamiltonian is

$$H_{\text{sb}} = -\frac{1}{2} \Delta_{\text{eff}} \sigma_1 + H_{\text{osc}} + \frac{1}{2} \sigma_3 \sum_n \lambda_n x_n. \quad (2.27)$$

The last term couples σ_3 to the coordinates $\{x_n\}$ of the oscillators. We shall consider an Ohmic heat bath, as defined above.

At zero temperature, this model has a quantum critical line separating a broken-symmetry phase with $\langle \sigma_3 \rangle = M_0 \neq 0$ from a disordered phase with $\langle \sigma_3 \rangle = 0$ (see Fig. 2.1) [3]. The broken-symmetry state has an effective classical description in which the environmental degrees of freedom are relaxed around a specific state of the qubit. The corresponding uncertainty is zero and so is the von Neumann entropy. In the disordered state, by contrast, an infinitesimal field has only an infinitesimal effect. Right at the quantum critical point the qubit is maximally entangled with the environment, as described below. So the phase transition can be aptly described as a classical-to-quantum transition and was treated by a renormalization group analysis [3].

In the ground state of Eq. 2.27, the reduced density matrix of the spin degree of freedom is determined by the expectation values $\langle \sigma_1 \rangle$ and $\langle \sigma_3 \rangle$:

$$\rho_A = \frac{1}{2} \begin{pmatrix} 1 + \langle \sigma_3 \rangle & \langle \sigma_1 \rangle \\ \langle \sigma_1 \rangle & 1 - \langle \sigma_3 \rangle \end{pmatrix}. \quad (2.28)$$

After diagonalizing ρ_A , we can easily compute the ground state von Neumann entropy. Hence the behavior of the entanglement at the transition follows directly from the behavior of $\langle \sigma_1 \rangle$ and $\langle \sigma_3 \rangle$. Since the order parameter $\langle \sigma_3 \rangle$ is discontinuous at the transition, the von Neumann entropy also jumps by an amount ΔS . It can be shown [6] that the magnitude of this jump is, to leading order in y ,

$$\Delta S = \ln 2 + (y/2) \ln y. \quad (2.29)$$

In the limit of vanishing y , the system goes from being unentangled ($\langle \sigma_1 \rangle = 0$, $\langle \sigma_3 \rangle = 1$) to being maximally entangled ($\langle \sigma_1 \rangle = \langle \sigma_3 \rangle = 0$) as it enters the disordered state. Note that this result depends crucially on a proper treatment of the broken symmetry—without the jump in the order parameter, S would be continuous through the transition. The von Neumann entropy is discontinuous (with a singular derivative) even though the correlation length in imaginary time diverges at the transition. Because this divergence takes the form of an essential singularity, it does not leave a strong signature in other quantities at the critical point.

In addition, the spin-boson model also undergoes a dynamic crossover at $\alpha = 1/2$, from damped oscillations to an overdamped decay. The von Neumann

entropy should be analytic at $\alpha = 1/2$ because no phase transition occurs at this point, similar to the damped harmonic oscillator problem above. This appears to be consistent with the calculations in Ref. [36].

2.5.3 Disordered Systems

We shall give two examples [6, 37] of disordered systems involving non-interacting electrons; probably many more exist. For the Anderson localization transition in three dimensions (3D) and the integer quantum Hall (IQH) plateau transition in two dimensions the ground state energy does not exhibit any non-analyticity [8]. In contrast, the vNE exhibits non-analyticity that can be determined from multifractal scaling [38]. It should be emphasized, however, that because of the single particle and disorder-dominated nature of these QPTs, entanglement as characterized by the vNE and its critical scaling behavior are fundamentally different from those calculated for interacting pure systems.

In a non-interacting electronic system close to a disordered critical point, the wave function intensity at energy E , $|\psi_E(r)|^2$, fluctuates strongly at each spatial point r and exhibits a multiplicity of fractal dimensions. This non-self-averaging nature of the wave function intensity can be expressed by the generalized inverse participation ratios P_q obeying the finite size scaling

$$P_q(E) \equiv \sum_r \overline{|\psi_E(r)|^{2q}} \sim L^{-\tau_q} \mathcal{F}_q[(E - E_C)L^{1/\nu}]. \quad (2.30)$$

Here L is the system size, ν is the localization length exponent given by $\xi_E \sim |E - E_C|^{-\nu}$, and τ_q is the multifractal spectrum. The overbar denotes an average over distinct disorder realizations. $\mathcal{F}_q(x)$ is a scaling function with $\mathcal{F}_q(x \rightarrow 0) = 1$ close to the critical point $E = E_C$. When E is tuned away from E_C , the system either tends towards an ideal metallic state with $P_q(E) \sim L^{-d(q-1)}$ (d being the number of spatial dimensions) or becomes localized with $P_q(E)$ independent of L .

There is no obvious way to define entanglement in the language of particles. Nonetheless, surely the vNE can be defined, and in fact entanglement can also be defined, but in the second-quantized Fock space [39]. A simple analysis shows that the vNE is

$$\begin{aligned} S(E) = & - \sum_{r \in L^d} \left[|\psi_E(r)|^2 \ln |\psi_E(r)|^2 \right. \\ & \left. + (1 - |\psi_E(r)|^2) \ln (1 - |\psi_E(r)|^2) \right]. \end{aligned} \quad (2.31)$$

The second term inside the square bracket in Eq. (2.31) can be dropped, since $|\psi_E(r)|^2 \ll 1$ at all r when the states are close to the critical energy. The disorder averaged (denoted by overbar) entropy using multifractal scaling in

Eq. (2.30) is

$$\overline{S}(E) \approx -\frac{dP_q}{dq} \Big|_{q=1} \approx \frac{d\tau_q}{dq} \Big|_{q=1} \ln L - \frac{\partial \mathcal{F}_q}{\partial q} \Big|_{q=1}. \quad (2.32)$$

The general form of the scaling function \mathcal{F}_q is not known but we can get the approximate L dependence in certain limiting cases. At exact criticality when $\mathcal{F}_q \equiv 1$ for all q , we get

$$\overline{S}(E) \sim \alpha_1 \ln L, \quad (2.33)$$

where $\alpha_1 = d\tau_q/dq|_{q=1}$ is unique for each universality class. From the discussion following Eq. (2.30), the leading scaling behavior of $\overline{S}(E)$ in the ideal metallic and localized states is given by $d \ln L$ and $\alpha_1 \ln \xi_E$ respectively. From the limiting cases, we see that, in general, $\overline{S}(E)$ has the leading scaling form [37]

$$\overline{S}(E) \sim \mathcal{K}[(E - E_C)L^{1/\nu}] \ln L, \quad (2.34)$$

where the coefficient function $\mathcal{K}(x)$ decreases from d in the metallic state to α_1 at criticality and then drops to zero for the localized state.

2.5.3.1 Anderson Localization

Consider the three-dimensional Anderson model [9] on a cubic lattice. The Hamiltonian is

$$H = \sum_i V_i c_i^\dagger c_i - t \sum_{\langle i,j \rangle} (c_i^\dagger c_j + h.c.), \quad (2.35)$$

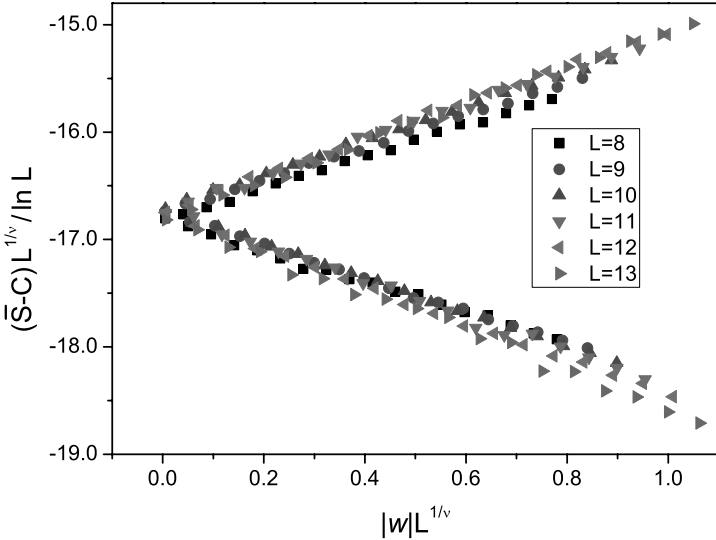
where $c_i^\dagger(c_i)$ is the fermionic creation (annihilation) operator at the site i of the lattice, and the second sum is over all nearest neighbors. We set $t = 1$ and V_i are random variables uniformly distributed in the range $[-W/2, W/2]$. It is known that extended states appear at the band center for W less than $W_c = 16.3$, and the localization length exponent is [40] $\nu = 1.57 \pm 0.03$.

The analysis leading to Eq. (2.34) also holds at a single energy, say $E = 0$, as disorder is tuned through W_c ; the states at $E = 0$ evolve from fully metallic to critical and then to localized behavior. The leading scaling form of the vNE is

$$\overline{S}(E = 0, w, L) \sim \mathcal{C}(wL^{1/\nu}) \ln L, \quad (2.36)$$

where $w = (W - W_c)/W_c$ and $\mathcal{C}(x)$ is a scaling function. As mentioned above, $\mathcal{C}(x) \rightarrow d$ as $w \rightarrow -1$, $\mathcal{C}(x) \rightarrow 0$ as $w \rightarrow \infty$, and $\mathcal{C}(x) = \alpha_1$ when $w = 0$. We can also average Eq. (2.32) over the entire band of energy eigenvalues and construct the vNE,

$$\overline{S}(w, L) = \frac{1}{L^3} \sum_E \overline{S}(E, w, L), \quad (2.37)$$

**FIGURE 2.2**

Scaling curve in the 3D Anderson model. With the choice of $\nu = 1.57$ and $C = 12.96$, all data collapse to universal functions $f_{\pm}(x)$. The two branches correspond to $w < 0$ and $w > 0$, from Ref. [37].

where L^3 is also the total number of states in the band. Then using Eq. (2.34) and Eq. (2.36), one can show that close to $w = 0$,

$$\overline{S}(w, L) \sim C + L^{-1/\nu} f_{\pm}(wL^{1/\nu}) \ln L \quad (2.38)$$

where C is an L independent constant, and $f_{\pm}(x)$ are two universal functions corresponding to the regimes $w > 0$ and $w < 0$.

Numerical results for $\overline{S}(w, L)$ are shown in Figure 2.2. The data collapse is performed with the choice of $\nu = 1.57$, and the non-universal constant $C = 12.96$ is determined by a powerful algorithm described elsewhere [6]. The success of data collapse clearly reflects the non-analyticity of the von Neumann entropy and the validity of the multifractal analysis.

2.5.3.2 Integer Quantum Hall Plateau Transitions

The Hamiltonian for the integer quantum Hall problem in a magnetic field B can be expressed in terms of the matrix elements of the states $|n, k\rangle$, where n is the Landau level index, and k is the wave vector in the y direction. Let us focus on the lowest Landau level $n = 0$, with the impurity distribution $\overline{V(\mathbf{r})V(\mathbf{r}') = V_0^2 \delta(\mathbf{r} - \mathbf{r}')}}$; the elements of the random matrix $\langle 0, k | V | 0, k' \rangle$ can be generated as in Ref. [10].

Consider a square with linear dimension $L = \sqrt{2\pi M l_B}$, where $l_B =$

$(\hbar/eB)^{1/2}$ is the magnetic length and M is an integer with periodic boundary conditions imposed in both directions. Upon discretization with a mesh of size $\sqrt{\pi}l_B/\sqrt{2}M$ the eigenstates $\{|\psi_a\rangle = \sum_k \alpha_{k,a}|0,k\rangle\}_{a=1}^{M^2}$ and the corresponding eigenvalues $\{E_a\}_{a=1}^{M^2}$ are obtained. The energies are measured relative to the center of the lowest Landau band in units of $\Gamma = 2V_0/\sqrt{2\pi}l_B$, and for each eigenstate the wave function in real space is

$$\psi_a(x, y) = \langle x, y | \psi_a \rangle = \sum_k \alpha_{k,a} \psi_{0,k}(x, y) \quad (2.39)$$

where $\psi_{0,k}(x, y)$ is the lowest Landau level wave function. Unfortunately, the dimension of the Hamiltonian matrix, $M^2 \times M^2$, can be very large. Therefore, we compute only those states $|\psi_a\rangle$ whose energies lie in a small window Δ around a preset value of E , i.e., $E_a \in [E - \Delta/2, E + \Delta/2]$. We ensure that Δ is sufficiently small (0.01), containing at the same time enough states within the interval (at least 100 eigenstates).

The next step involves breaking up the $L \times L$ square into non-overlapping squares \mathcal{A}_i of size $l \times l$, where $l = l_B \sqrt{\pi/2}$ is independent of the system size L . We now compute the coarse grained probability $\int_{(x,y) \in \mathcal{A}_i} |\psi_a(x, y)|^2 dx dy$. The computation of the vNE follows the procedure described above. Finally, by averaging over states in the interval Δ , the vNE $\overline{S}(E, L)$ is obtained at the preset energy E . The scaling form of $\overline{S}(E, L)$ given by Eq. (2.34) with $E_C = 0$ is $\overline{S}(E, L) = \mathcal{K}(|E|L^{1/\nu}) \ln L$. Good agreement with the numerical simulations is seen in Fig. 2.3 [37]. Note that there is only one branch, as states at all energies except those at the center of the band are localized. The plateau-to-plateau transition takes place at the band center, and the non-analyticity of this phase transition is correctly captured by the vNE.

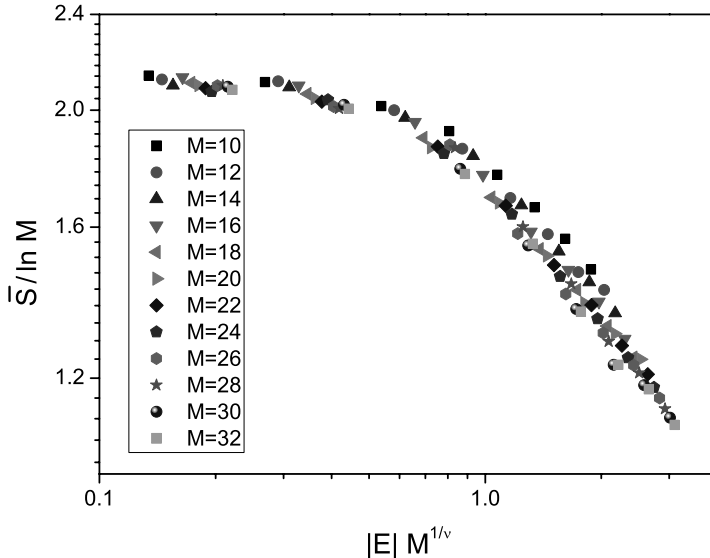
2.5.3.3 Infinite Randomness Fixed Point

Recently an intriguing set of results has been obtained for one-dimensional quantum criticality for strong disorder and has uncovered what is known as an infinite randomness fixed point [41]. There is some work in higher dimensional systems, but much less. The principal defining feature of an infinite randomness fixed point is its scaling properties. In conventional quantum critical points, energy and length satisfy a dynamic scaling relationship defined by $E \sim L^{-z}$, where z is the dynamic scaling exponent. In contrast, for the infinite randomness fixed point the excitation energy behaves as

$$E \sim e^{-L^\psi}, \quad (2.40)$$

where ψ is a universal exponent. The low energy distribution of couplings, $\rho(J)$, obey an unusual distribution,

$$\rho(J) \sim \frac{1}{J^{1-\chi/\Gamma}}, \quad (2.41)$$

**FIGURE 2.3**

Scaling of the von Neumann entropy $\bar{S}(E)$ for the integer quantum Hall effect. M instead of L is used in the data collapse with the accepted value of $\nu = 2.33$, from Ref. [37].

where χ is a universal constant, $\Gamma = \ln(\omega_c/\omega)$, ω is the measurement energy scale, and ω_c is the largest bare coupling.

One-dimensional infinite randomness fixed points are random analogs of pure (1+1)-dimensional conformal field theories whose von Neumann entropies satisfy [35]

$$\lim_{N \rightarrow \infty} S = \frac{c}{3} \log_2 N . \quad (2.42)$$

This entanglement entropy is defined by partitioning the system into A and its complement B , where A is a connected set of N sites in an otherwise infinite system. The parameter c is the universal conformal charge defining the theory. S is bounded away from the critical point as $N \rightarrow \infty$. It is quite remarkable that an equivalent classical theory determines the information entropy of a critical quantum system in a universal manner. Thus it is even more remarkable that the von Neumann entropy corresponding to infinite randomness fixed points satisfy an analogous universal relation [42],

$$\lim_{N \rightarrow \infty} S = \frac{c_{\text{eff}}}{3} \log_2 N . \quad (2.43)$$

One would have intuitively thought this not to be possible because quenched randomness brings along its own probability measure. In either case, note the

TABLE 2.1

Conformal charges of pure and random systems, from Ref. [42].

Model	c	c_{eff}
XXZ -Heisenberg	1	$\ln 2$
Transverse field Ising	$\frac{1}{2}$	$\frac{1}{2} \ln 2$
Spin-1 Heisenberg (breakdown of Haldane phase)	$\frac{3}{2}$	1.232
$SU(2)_3$ (Fibonacci anyons)	$\frac{4}{5}$	0.702

violation of the area law, implying a length scale corresponding to the AB boundary over which entanglement decays. Entanglement becomes infinitely long ranged as the correlations become infinitely long ranged at a quantum critical point. The values of c_{eff} have been calculated in a number of cases. One believes that these are exact results because the real space renormalization group methods in one dimension become asymptotically exact for strong disorder. Table 2.1 summarizes some interesting comparisons of pure and random systems (taken from Ref. [42]).

2.6 Disorder and First Order Quantum Phase Transitions

The effect of disorder on continuous classical phase transitions has been studied over many decades, but less is known about its effect on first order transitions. Imry and Wortis [43] argued that arbitrarily weak disorder can actually round a classical first order transition. Subsequently, Hui and Berker [44] and Aizenman and Wehr [13] have made important contributions to this topic.

Two important questions are as follows. (a) Can disorder convert a first order QPT to a continuous one? (b) If the answer to this question is yes, what are the universality classes, if any? We shall assume that disorder couples to the Hamiltonian in such a way that its symmetry is unchanged, for example, to nearest neighbor bonds, or more generally to energy-like variables. On the other hand, a site-random field breaks symmetry explicitly. Let a tuning parameter g control the relative magnitudes of two non-commuting terms in the Hamiltonian, resulting in a first order transition.

We would like to present an argument [11] that the coexistence of phases is not possible at this transition because of disorder, and the quantum fluc-

tuations do not have a scale. If this is true, and if the state corresponding to $g = 0$ is still a broken symmetry state (this is why we imposed the specific requirement on disorder earlier) and the system for $g = \infty$ is in a quantum-disordered state, the conclusion must be that the transition has been converted to a quantum critical point.

The proof is by contradiction. Assume that there is coexistence of phases at the first order transition at g_c . However, in the presence of disorder there will be local fluctuations of g_c . Thus, within a putative quantum disordered region, randomness can nucleate an ordered region of linear dimension L , with a gain in the volume energy $\propto L^{d/2}$ (assuming the central limit theorem), while the price in the surface energy is $\propto L^{d-1}$ (assuming discrete symmetry). The same is true for a putative ordered region. Therefore, for $d < 2$ (discrete), the picture is that of a “domain within a domain,” and there is no scale. In contrast, for $g < g_c$ nucleation of one broken symmetry phase within another does not gain any energy (disorder does not break the relevant symmetry), but the surface energy is increased. Therefore, by contradiction, coexistence of phases is not possible, and the transition at g_c must be continuous. We have tacitly assumed that the transition involves a broken symmetry. If this is not the case, there is no particular reason for a sharp transition to remain at g_c , and the disorder will simply smear out the transition.

Continuous symmetry leads to a subtlety. While one may be tempted to argue that the domain wall energy is L^{d-2} , as in the Imry-Ma argument [45], this is generally incorrect. If at the domain wall the amplitude of the order parameter vanishes, the domain wall energy is still L^{d-1} , as for discrete symmetry, and the previous result holds. However, if the transition is driven by tuning a “magnetic field” that changes the state from one broken symmetry direction to another, the domain wall energy is indeed L^{d-2} , and the borderline dimensionality is $d = 4$. Since the Mermin-Wagner theorem dictates that there is no long range order in $d = 2$ at any finite temperature, regardless of the order of the transition, for the classical case the question is moot at $d = 2$.

There are no simple arguments known to us for the borderline dimensionalities, but from the rigorous version of the Imry-Ma argument for the random field case, it is safe to conjecture that the above argument should also hold for these cases because of a close connection between the two problems noted by Imry [46]. Note that the dynamic critical exponent z does not enter the above argument — all we need is the extensivity of the ground state energy and its normal fluctuations in the thermodynamic limit. The principal disordering agent that washes out the coexistence is the fluctuation due to impurities and not quantum fluctuations. Quantum fluctuations can only help the process of smoothing the coexistence. Of course the fate of the system in dimensions higher than 2 must depend on the quantum fluctuations. In addition, the actual dynamics of the system must involve these fluctuations as well. The Harris criterion that determines the influence of disorder at a critical point, *inter alia* a quantum critical point, does depend on the exponent z . A nice way to see this is to rephrase the Harris criterion [47] in terms of an argu-

ment by Mott [48]. On one hand, disorder in a domain of linear dimension, ξ , the correlation length of the pure system, will give rise to fluctuations of the quantum critical point g_c of fractional width $\Delta g \sim \xi^{-d/2}$. On the other hand, Δg must be less than the reduced distance from the quantum criticality implied by ξ , that is $\sim \xi^{-1/\nu_{d+z}}$, for the criticality to remain unchanged. Hence, $\nu_{d+z} > 2/d$. Otherwise, the system may be described by a new disorder fixed point for which the same relation will apply with the replacement of the critical exponent of the pure system by the critical exponent of the new fixed point, as in the theorem of Chayes *et al.* [49]. In either case, z appears because the relevant length scale close to the critical point is the *diverging correlation length*, ξ . By contrast, the argument for rounding of a first order transition is restricted by a *finite correlation length*; hence the balance is between the volume energy and the surface energy of a fluctuating domain nucleated by disorder.

In order to substantiate our argument we studied [11], using both a perturbative renormalization group and a real space decimation procedure, the one-dimensional quantum random N -color Ashkin-Teller model in the regime in which the pure model has a first order QPT. The corresponding classical problem in two spatial dimensions has renormalization group flows that curl back to the pure decoupled Ising fixed point at least for weak coupling [50]. In the quantum case the flows are drastically different and are towards the strong coupling regime. It is therefore not possible to reach a definitive conclusion. On the other hand, the strong coupling real space decimation technique shows that for a range of parameters depending on N the flow is to the infinite randomness fixed point. No firm conclusions could be drawn beyond this regime. Recently, rigorous mathematical analysis has been brought to bear on this problem by Greenblatt, Aizenman, and Lebowitz [12]. This proof of rounding of first order QPT is different from the classical proof [13]. Clearly, more work is necessary to fully elucidate this interesting problem, with possibly far-reaching consequences.

2.7 Outlook

One of the simplest QPTs is the dissipative transition in a double well potential in the presence of Ohmic dissipation, which belongs to the same universality class as the transition in the Kondo problem, as the coupling is tuned from ferro to antiferromagnetic, as well as to the inverse square Ising model in one dimension [51, 52]. As of today, there is no direct experimental evidence of this phenomenon, which is a pity. The prediction [53] for $\alpha > 1$ of the finite temperature incoherent tunneling rate between the wells seems to have some

support from experiments [54]. This rate is

$$\frac{1}{\tau} = \frac{\sqrt{\pi}\Delta_{\text{eff}}(\alpha)^2}{2\omega_c} \frac{\Gamma(\alpha)}{\Gamma(\alpha + 1/2)} \left[\frac{\pi k_B T}{\hbar\omega_c} \right]^{2\alpha-1}. \quad (2.44)$$

Instead, the attention has shifted more to reducing dissipation as much as possible in various Josephson devices to observe coherent oscillations of the double well [55, 56]. This is considered to be a miniature prototype for Schrödinger's cat. It can be debated as to the extent to which the phase difference of a Josephson device or equivalently the flux variable in a superconducting interference device can be considered a "macroscopic variable," which appears to be a semantic issue. These are indeed collective degrees of freedom, but the energetics are determined by "microscopic" scales. Very little experimental attention has been paid to exploring the quantum critical dynamics of how one of the basic models of quantum mechanics is influenced by dissipation. As mentioned above, the influence of dissipation in quantum tunneling from a metastable state does not count, because no quantum criticality is involved. Given that convincing experimental demonstrations of quantum criticality are so few and far between and generally so complex (due to complex material issues), it seems hopeless to make further progress without a clear-cut study of the simplest possible example. In any case, as I have argued, this is a well-studied example of a quantum-to-classical transition (FAPP) whose mathematics is firmly grounded at this time.

The second overarching theme of this chapter has been how disorder influences QPTs. While much is understood for classical phase transitions, very few results are available for transitions at zero temperature. This is again a pity because there is considerable theoretical depth to this problem. In fact, practical applications abound as well. Is it possible that many experimental sightings of quantum critical points are in reality first order transitions in disguise, rounded by disorder? If so, how does it enrich our understanding? An interesting question is the uses of von Neumann entropy. There appear to be some QPTs that exhibit no non-analyticity of the ground state energy and yet their existence can be hardly denied, as they signify transition between two distinct states of matter. In this respect, it was quite remarkable that the von Neumann entropy should exhibit the requisite non-analyticity. Perhaps the fundamental criterion should be replaced. So far we have only found such examples in disordered systems involving non-interacting electrons, Anderson localization in three dimensions, and plateau-to-plateau transition in integer quantum Hall systems. Are there more, especially involving interacting systems? Is there a theorem? I conjecture that such results are only possible in disordered systems where the fundamental driving mechanism is fluctuations driven by disorder, belonging to a different class from quantum fluctuations, and triggered by a tuning coupling constant. It will be interesting to tackle the fractional quantum Hall problem from the perspective of the Jain construction [57], as this maps the problem to an essentially non-interacting one.

Another problem involving quantum criticality in disordered systems is

the infinite randomness fixed point. A number of important theoretical calculations involving entanglement entropy have shown that the renormalization group flow is to new fixed points, different from the pure system fixed points, but with universal amplitudes of logarithmic entanglement entropies. Do these fixed points reflect the same properties of conformal invariance of pure systems? Or, are the mathematical underpinnings different? Are there higher dimensional problems that can be solved in a similar manner?

Finally, a more pressing issue is the role of dissipative phase transitions in a number of important fields of current research, to name a few, phase slips in nanowires [58–64], *c*-axis conductivity [65], and local quantum criticality [66] in high temperature superconductors [67]. There is also much interest in low-temperature properties of very thin superconducting wires. The key process of interest is quantum phase slips, a virtual depletion of the superconducting density that allows the system to tunnel to a different value of the supercurrent. The rate of this process depends not only on the bare fugacity of the phase slips, defined by the rate of an individual tunneling event, but also importantly on the interaction between individual quantum phase slips. The backbone of the theoretical work is the logarithmic interaction between the quantum phase slips, which serves almost as a paradigm to a whole class of similar problems [68–70]. Interesting results have been obtained [69]: it has been argued that for a short wire there is no distinction between a superconductor and an insulator. Even an insulator can support a weak Josephson current. Nonetheless, there is a range of parameters for which a short nanowire can act as an insulator down to unobservably low temperatures.

Acknowledgments – I acknowledge a grant from the National Science Foundation (Grant No. DMR-0705092) and discussions with David Garcia-Aldea, Klaus Hepp, Joel Lebowitz, Chetan Nayak, Gil Refael, and David Schwab.

Bibliography

- [1] A. J. Leggett, Journal of Physics-Condensed Matter **14**, R415 (2002).
- [2] A. J. Leggett *et al.*, Rev. Mod. Phys. **59**, 1 (1987).
- [3] S. Chakravarty, Phys. Rev. Lett. **49**, 681 (1982).
- [4] K. Hepp, Helv. Phys. Acta **45**, 237 (1972).
- [5] C. N. Yang and T. D. Lee, Phys. Rev. **87**, 404 (1952).
- [6] A. Kopp, X. Jia, and S. Chakravarty, Ann. Phys. **322**, 1466 (2007).
- [7] D. Belitz and T. R. Kirkpatrick, Rev. Mod. Phys. **66**, 261 (1994).
- [8] J. T. Edwards and D. J. Thouless, J. Phys. C **4**, 453 (1971).

- [9] E. Abrahams, P. W. Anderson, D. C. Licciardello, and T. V. Ramakrishnan, Phys. Rev. Lett. **42**, 673 (1979).
- [10] B. Huckestein, Rev. Mod. Phys. **67**, 357 (1995).
- [11] P. Goswami, D. Schwab, and S. Chakravarty, Phys. Rev. Lett. **100**, 015703 (2008).
- [12] R. L. Greenblatt, M. Aizenman, and J. L. Lebowitz, Phys. Rev. Lett. **103**, 197201 (2009).
- [13] M. Aizenman and J. Wehr, Comm. Math. Phys. **130**, 489 (1990).
- [14] T. D. Lee and C. N. Yang, Phys. Rev. **87**, 410 (1952).
- [15] K. Binder and A. P. Young, Rev. Mod. Phys. **58**, 801 (1986).
- [16] R. R. P. Singh and S. Chakravarty, Phys. Rev. Lett. **57**, 245 (1986).
- [17] J. L. Lebowitz, arXiv:0709.0724 (2007).
- [18] S. Goldstein, J. L. Lebowitz, R. Tumulka, and N. Zanghi, Phys. Rev. Lett. **96**, 050403 (2006).
- [19] J. Gemmer and G. Mahler, The European Physical Journal B - Condensed Matter and Complex Systems **31**, 249 (2003).
- [20] C. Callan and F. Wilczek, Phys. Lett. B **333**, 55 (1994).
- [21] U. Weiss, *Quantum Dissipative Systems* (World Scientific, Singapore, 1999).
- [22] R. P. Feynman and F. L. Vernon, Annals of Physics **24**, 118 (1963).
- [23] A. O. Caldeira and A. J. Leggett, Ann. Phys. **149**, 374 (1983).
- [24] K. Mohring and U. Smilansky, Nucl. Phys. A **338**, 227 (1980).
- [25] J. A. Hertz, Phys. Rev. B **14**, 1165 (1976).
- [26] J. S. Bell, Helv. Phys. Acta **48**, 93 (1975).
- [27] J. Bell, Physics World **3**, 33 (1990).
- [28] S. Coleman, in *The Whys of Subnuclear Physics, International School of Subnuclear Physics "Ettore Majorana,"* edited by A. Zichichi (Plenum, New York, 1977).
- [29] L.-D. Chang and S. Chakravarty, Phys. Rev. B **29**, 130 (1984).
- [30] S. Chakravarty and S. Kivelson, Phys. Rev. B **32**, 76 (1985).
- [31] P. W. Anderson, Phys. Rev. Lett. **18**, 1049 (1967).

- [32] A. Schmid, Phys. Rev. Lett. **51**, 1506 (1983).
- [33] A. Schmid, in *The Art of Measurement*, edited by B. Kramer (VCH-Verlag, Weinheim, 1988), pp. 87–107.
- [34] L. Amico, R. Fazio, A. Osterloh, and V. Vedral, Rev. Mod. Phys. **80**, 517 (2008).
- [35] C. Holzhey, F. Larsen, and F. Wilczek, Nucl. Phys. B **424**, 443 (1994).
- [36] A. Kopp and K. Le Hur, Phys. Rev. Lett. **98**, 220401 (2007).
- [37] X. Jia, A. R. Subramaniam, I. A. Gruzberg, and S. Chakravarty, Phys. Rev. B **77**, 014208 (2008).
- [38] F. Evers and A. D. Mirlin, Rev. Mod. Phys. **80**, 1355 (2008).
- [39] P. Zanardi, Phys. Rev. A **65**, 042101 (2002).
- [40] K. Slevin, P. Markos, and T. Ohtsuki, Phys. Rev. Lett. **86**, 3594 (2001).
- [41] D. S. Fisher, Phys. Rev. B **51**, 6411 (1995).
- [42] G. Refael and J. E. Moore, J. Phys. A **42**, 504010 (2009), see also the references therein.
- [43] Y. Imry and M. Wortis, Phys. Rev. B **19**, 3580 (1979).
- [44] K. Hui and A. N. Berker, Phys. Rev. Lett. **62**, 2507 (1989).
- [45] Y. Imry and S.-k. Ma, Phys. Rev. Lett. **35**, 1399 (1975).
- [46] Y. Imry, Journal of Statistical Physics **34**, 849 (1984).
- [47] A. B. Harris, J. Phys. C **7**, 1671 (1974).
- [48] N. F. Mott, Phil. Mag. Part B **44**, 265 (1981).
- [49] J. T. Chayes, L. Chayes, D. S. Fisher, and T. Spencer, Phys. Rev. Lett. **57**, 2999 (1986).
- [50] J. Cardy, Physica A **263**, 215 (1999).
- [51] S. Chakravarty and J. Rudnick, Phys. Rev. Lett. **75**, 501 (1995).
- [52] K. Völker, Phys. Rev. B **58**, 1862 (1998).
- [53] S. Chakravarty and A. J. Leggett, Phys. Rev. Lett. **52**, 5 (1984).
- [54] S. Han, J. Lapointe, and J. E. Lukens, Phys. Rev. Lett. **66**, 810 (1991).
- [55] J. R. Friedman *et al.*, Nature **406**, 43 (2000).

- [56] I. Chiorescu, Y. Nakamura, C. J. P. M. Harmans, and J. E. Mooij, *Science* **299**, 1869 (2003).
- [57] J. K. Jain, *Composite Fermions* (Cambridge University Press, Cambridge, 2007).
- [58] A. Bezryadin, C. N. Lau, and M. Tinkham, *Nature* **404**, 971 (2000).
- [59] C. N. Lau *et al.*, *Phys. Rev. Lett.* **87**, 217003 (2001).
- [60] A. T. Bollinger, A. Rogachev, and A. Bezryadin, *Europhys. Lett.* **76**, 505 (2006).
- [61] P. Goswami and S. Chakravarty, *Phys. Rev. B* **73**, 094516 (2006).
- [62] G. Refael, E. Demler, Y. Oreg, and D. S. Fisher, *Phys. Rev. B* **75**, 014522 (2007).
- [63] A. T. Bollinger, R. C. Dinsmore, III, A. Rogachev, and A. Bezryadin, *Phys. Rev. Lett.* **101**, 227003 (2008).
- [64] A. Bezryadin, *Journal of Physics: Condensed Matter* **20**, 043202 (2008).
- [65] S. Chakravarty and P. W. Anderson, *Phys. Rev. Lett.* **72**, 3859 (1994).
- [66] S. Chakravarty, G. L. Ingold, S. Kivelson, and G. Zimanyi, *Phys. Rev. B* **37**, 3283 (1988).
- [67] V. Aji and C. M. Varma, *Phys. Rev. Lett.* **99**, 067003 (2007).
- [68] J. E. Mooij and Y. V. Nazarov, *Nature Physics* **2**, 169 (2006).
- [69] S. Khlebnikov, *Phys. Rev. B* **78**, 014512 (2008).
- [70] D. Meidan, Y. Oreg, and G. Refael, *Phys. Rev. Lett.* **98**, 187001 (2007).

3

Universal Dynamics Near Quantum Critical Points

Anatoli Polkovnikov

Department of Physics, Boston University, 590 Commonwealth Ave., Boston, MA 02215, U.S.A.

Vladimir Gritsev

Physics Department, University of Fribourg, Chemin du Musée 3, 1700 Fribourg, Switzerland

Continuous quantum phase transitions (QPTs) have been a subject of intense theoretical research in recent decades (see, e.g., Refs. [1–3] for overview). Unlike usual phase transitions driven by temperature, QPTs are driven entirely by quantum fluctuations. They are believed to occur in many situations as described later in this book. Quite recently a second order QPT was observed in a cold atom system of interacting bosons in an optical lattice. There a system of interacting bosons was driven in real time from the superfluid to the insulating phase [4], confirming an earlier theoretical prediction [5]. Up till now, Ref. [4] has provided probably the cleanest experimental confirmation of a QPT. The unifying property of all continuous (second order) phase transitions is the emergent universality and scale invariance of the long-distance low energy properties of the system near the quantum critical point (QCP) [1]. This universality implies that low-energy properties of the system can be described by very few parameters, like the correlation length or the gap, which typically have power-law scaling with the tuning parameter characterized by critical exponents. These exponents are not sensitive to the microscopic details of the Hamiltonian describing the system, but rather depend only on the *universality class* to which a given phase transition belongs [1].

Recent experimental progress in preparing and manipulating out-of-equilibrium nearly isolated systems has stimulated intense theoretical research on quantum dynamics in closed systems. In particular, such issues as sudden quantum quenches in low dimensional systems [6, 7], adiabatic dynamics near QCPs [8, 9], and connection of dynamics and thermodynamics in quantum systems [10, 11] came to the forefront of theoretical research. A very natural question can be posed about non-equilibrium behavior of systems near QPTs. Since in equilibrium second order phase transitions are characterized by universality, one can expect also universal behavior in driven systems in the vicinity of a QCP. Such universality can be expected, for example, if the

system near the QCP is subject to small amplitude, low frequency modulation of an external field, which couples to the order parameter. Indeed, in the linear response regime QCPs are typically characterized by singular susceptibilities at low frequencies [1, 3]. One can expect that the universality persists even beyond the linear response regime as long as the system remains close to criticality. Another possible situation where one can expect universal behavior is when the system is slowly driven through a QCP. In this case, since the dynamics is nearly adiabatic, one expects that low energy excitations will play the dominant role. Moreover, one can generally expect that non-adiabatic effects will be especially strong near singularities like QPTs, so that the dynamics will be dominated by the universal regime. This is indeed the case at least in sufficiently small dimensions [8, 9, 12]. The third situation where universality of dynamics can be expected is the response to fast small amplitude quenches (sudden changes in the tuning parameter) near the critical point. Analysis of sudden and nearly adiabatic dynamics near QCPs will be the central subject of this chapter.

Typically analysis of slow, nearly adiabatic dynamics is complicated by the fact that the usual perturbative approaches fail. It has been recently realized that adiabatic perturbation theory can become an efficient tool for analyzing the behavior of various thermodynamic quantities like the density of quasi-particles and the non-adiabatic energy (heat) generated during the process [8, 13]. Although to leading order adiabatic perturbation theory often fails to give accurate quantitative analysis of various observables, it does give their correct scaling behavior with the rate of change of the external parameter. The advantage of this method is that it allows one to effectively reduce a dynamical problem to the static one and use the developed machinery for equilibrium quantum phase transitions. In this chapter we will demonstrate how this approach reproduces the correct scaling behavior of the response of the system both to sudden quenches of small amplitude and to slow, nearly adiabatic sweeps through the critical point. We will also discuss the close connection between universal scaling of the density of quasi-particles and the scaling behavior of the fidelity susceptibility near the QCP, the quantity characterizing the overlap of the ground state wave functions corresponding to different coupling constants. In particular, we will show that the Kibble-Zurek scaling [14, 15] can be understood using this concept. We will illustrate some of the results using the transverse-field Ising model. In the end we will briefly discuss connections between adiabatic dynamics near critical points and dynamics associated with space-time singularities in the metrics, which naturally emerge in such areas as cosmology and string theory.

3.1 Brief Review of the Scaling Theory for Second Order Phase Transitions

Continuous quantum phase transitions in many respects are similar to classical second order phase transitions. The main difference is that the quantum transition from one phase to another is driven by quantum rather than by thermal fluctuations, arising from the zero-point motion. So QPTs can happen at zero temperature. Examples of models where QPTs take place include quantum Ising and rotor models, the sine-Gordon model, various transitions from glassy to ordered phases in disordered systems, and many others [1]. Many examples of QPTs will be discussed in consequent chapters in this book. Very often QPTs in d -dimensional systems can be mapped to thermal (classical) transitions in $d+z$ dimensions, where z is the dynamical critical exponent [1]. One of the most important properties of both quantum and classical second order transitions is the universality of the low-energy long-distance properties of the system. This universality implies that the details of underlying microscopic models are not important near critical points. Instead the properties of the system can be well characterized by the parameter describing its proximity to the critical point (tuning parameter) and by universal critical exponents describing the singular behavior of various quantities with this parameter. We note that even though QPTs strictly speaking occur only at zero temperatures, the universality of the scaling governed by QCPs extends well into the finite temperature domain [1]. Recently there has been considerable interest in unconventional phase transitions, the description of which requires deviations from the standard framework. Some of these unconventional transitions will be discussed in other chapters of this book. Here we will not consider them since their dynamics is not yet well understood.

A key quantity characterizing continuous phase transitions is the correlation length $\xi(\lambda)$, which defines the length scale separating the qualitatively different behavior of, e.g., spatial correlation functions of the fluctuations of the order parameter. This length scale diverges with the tuning parameter λ as

$$\xi(\lambda) \sim 1/|\lambda - \lambda_c|^\nu, \quad (3.1)$$

where ν is a critical exponent. Divergence of the length scale is accompanied by divergence of associated time scales. For classical phase transitions the corresponding time scales are associated with relaxational dynamics. In quantum systems, by the uncertainty principle a divergent time scale is also characterized by a vanishing energy scale $\Delta(\lambda)$. The latter is usually associated with a crossover in the quasi-particle spectrum. For example, it can represent a gap, or an energy scale where the dynamical exponent changes. The scaling of Δ defines another dynamical critical exponent z :

$$\Delta(\lambda) \sim 1/\xi(\lambda)^z \sim |\lambda - \lambda_c|^{z\nu}. \quad (3.2)$$

There are many other critical exponents. However, these two will play the most important role in our discussion. Together with critical exponents, one can introduce scaling functions which describe long-distance low-energy properties of the system. For example, if we are talking about a QPT in a spin system then near the critical point we expect the equal-time correlation between the spin s at different positions to scale as

$$\langle s(x)s(0) \rangle \sim |x|^{-2\alpha} F(x/\xi), \quad (3.3)$$

where α is the scaling dimension of the spin s and F is some scaling function which approaches a constant when $x/\xi \ll 1$. Note that the divergence of the correlation functions at very small x will be cut off by non-universal short-distance physics.

Other important quantities characterizing continuous phase transitions are susceptibilities, which describe the response of the system to external perturbations. For example, for a spin system the magnetic susceptibility describes the response of the magnetization to a small modulation of the magnetic field. From standard perturbation theory it is well known that susceptibilities are closely related to correlation functions [1]. Near QCPs static susceptibilities usually have singular non-analytic behavior characterized by their own critical exponents (see, e.g., Ref. [3]). Recently, it was realized that a very useful measure to analyze quantum phase transitions is fidelity susceptibility (FS) χ_f or more generally a quantum geometric tensor [16]. As we will see, this equilibrium concept and its generalizations will be very important for us later when we analyze dynamics near QCPs. Formally in a d -dimensional system FS is defined as

$$\chi_f(\lambda) = \frac{1}{L^d} \langle \partial_\lambda \Psi_0(\lambda) | \partial_\lambda \Psi_0(\lambda) \rangle = \frac{1}{L^d} \sum_{n \neq 0} \frac{|\langle \Psi_0(\lambda) | \partial_\lambda H | \Psi_n(\lambda) \rangle|^2}{|E_n(\lambda) - E_0(\lambda)|^2}, \quad (3.4)$$

where $|\Psi_n(\lambda)\rangle$ denote instantaneous eigenstates of the Hamiltonian $H(\lambda)$ and $E_n(\lambda)$ are the instantaneous energies. In this chapter we are only concerned with a non-degenerate ground state. FS appears in the leading order of expansion of the overlap of the ground state functions $|\langle \Psi_0(\lambda + \delta\lambda) | \Psi_0(\lambda) \rangle|^2$ in the powers of $\delta\lambda$:

$$|\langle \Psi_0(\lambda + \delta\lambda) | \Psi_0(\lambda) \rangle|^2 \approx 1 - \delta\lambda^2 L^d \chi_f(\lambda). \quad (3.5)$$

In the case when the system is translationally invariant and the operator $\partial_\lambda H$ is local, i.e., $\partial_\lambda H = \int d^d x v(x)$, where x is the discrete or continuous coordinate, Eq. (3.4) implies that the scaling dimension of χ_f is $\text{dim}[\chi_f] = 2\Delta_v - 2z - d$, where Δ_v is the scaling dimension of $v(x)$ (i.e., at the critical point $\langle v(x)v(x') \rangle \sim 1/|x - x'|^{2\Delta_v}$). This scaling dimension implies that the singular part of the FS near the critical point behaves as [16, 17]

$$\chi_f(\lambda) \sim |\lambda - \lambda_c|^{2\Delta_v - 2z - d}. \quad (3.6)$$

In finite size systems the singularity of χ_f at the critical point is cut off by the system size so that

$$\chi_f(\lambda_c) \sim L^{-2\Delta_v + 2z + d}. \quad (3.7)$$

The crossover between the scalings (3.6) and (3.7) occurs when the correlation length (3.1) becomes comparable to the system size L . For relevant or marginal perturbations the product $\lambda v(x)$ should have the scaling dimension of the energy density, $d + z$. Because the scaling dimension of λ is by definition $1/\nu$ we find that in this case $\Delta_v = d + z - 1/\nu$ [18, 19]. Then Eqs. (3.6) and (3.7) for the singular part of χ_f reduce to

$$\chi_f(\lambda) \sim \begin{cases} |\lambda - \lambda_c|^{d\nu-2} & \xi(\lambda) \ll L \\ L^{2/\nu-d} & \xi(\lambda) \gg L \end{cases}. \quad (3.8)$$

On top of the singular part there can be a non-singular part, which is generally non-sensitive to the proximity to the critical point. From Eq. (3.8), we see that the singular part of χ_f is dominant near the QCP when $d\nu < 2$. The fidelity susceptibility can be expressed through the imaginary time connected correlation function [16]:

$$\chi_f(\lambda) = \frac{1}{L^d} \int_0^\infty d\tau \tau (\langle \partial_\lambda H(\tau) \partial_\lambda H(0) \rangle - \langle \partial_\lambda H(0) \rangle^2), \quad (3.9)$$

where $\partial_\lambda H(\tau) = \exp[H\tau] \partial_\lambda H \exp[-H\tau]$. The above relation immediately follows from the Lehmann's representation. From Eq. (3.9) it is obvious that the singular scaling of χ_f near the QCP is related to the power-law long-distance asymptotics of the correlation function.

For the reasons which will become clear later, it is very convenient to generalize the fidelity susceptibility (3.4) to the generalized adiabatic susceptibility of order m [19]:

$$\chi_m(\lambda) = \frac{1}{L^d} \sum_{n \neq 0} \frac{|\langle \Psi_0(\lambda) | \partial_\lambda H | \Psi_n(\lambda) \rangle|^2}{|E_n(\lambda) - E_0(\lambda)|^m}. \quad (3.10)$$

For $m = 2$ we recover the fidelity susceptibility: $\chi_2 = \chi_f$. For $m = 1$ the corresponding susceptibility describes the second order correction to the ground state energy. The scaling dimension of χ_m immediately follows from that of χ_f : $\dim[\chi_m] = \dim[\chi_f] - z(m - 2)$. The generalized adiabatic susceptibility can also be expressed through the connected correlation function:

$$\chi_m(\lambda) = \frac{1}{L^d(m-1)!} \int_0^\infty d\tau \tau^{m-1} (\langle \partial_\lambda H(\tau) \partial_\lambda H(0) \rangle - \langle \partial_\lambda H(0) \rangle^2). \quad (3.11)$$

Example: transverse-field Ising model. Let us illustrate some of the generic properties mentioned above using the transverse-field Ising model, which is

perhaps one of the simplest models showing quantum critical behavior. The Hamiltonian describing this model is

$$H_I = -J \sum_i (g\sigma_i^x + \sigma_i^z \sigma_{i+1}^z), \quad (3.12)$$

where σ_i^x and σ_i^z are the Pauli matrices, commuting on different sites, J is the energy scale for spin-spin coupling, and Jg is the energy scale for the transverse field. This model undergoes two QPTs at $g = \pm 1$. At small magnitude of the transverse field g the spins are predominantly magnetized along the z-axis, while at large $|g|$ they are magnetized along the direction of the magnetic field. In both cases there is a finite gap to the lowest energy excitations which vanishes at the critical point [1]. This model can be solved exactly using the Jordan-Wigner transformation to map it to non-interacting fermions.

The Hamiltonian is diagonal in momentum space and can be rewritten as

$$H_I = \sum_k \epsilon_k (\gamma_k^\dagger \gamma_k - 1/2), \quad (3.13)$$

where $\epsilon_k = 2\sqrt{1 + g^2 - 2g \cos k}$ and $\gamma_k, \gamma_k^\dagger$ are the fermionic operators. The ground state of this Hamiltonian, which is the vacuum of γ_k , is written as a direct product:

$$|\Psi_0\rangle = \bigotimes_{k>0} \left[\cos(\theta_k/2) + i \sin(\theta_k/2) c_k^\dagger c_{-k}^\dagger \right] |0\rangle, \quad (3.14)$$

where $|0\rangle$ is the vacuum of original Jordan-Wigner fermions and $\tan \theta_k = \sin(k)/(\cos(k) - g)$. Further details can be found in Sachdev's book [1].

It is convenient to introduce a tuning parameter $\lambda = g - 1$ so that the transition occurs at $\lambda = \lambda_c \equiv 0$. Near the critical point the expressions for θ_k and dispersion simplify: $\tan \theta_k \approx -k/(k^2 + \lambda) \approx -k/\lambda$ and $\epsilon_k \approx 2\sqrt{\lambda^2 + k^2}$. This scaling of energy immediately suggests that the critical exponents here are $z = \nu = 1$. Indeed, according to our general discussion (see Eq. (3.2)) the characteristic energy scale, which is obviously the gap in our case, scales as $\Delta = |\lambda|^{z\nu}$, which implies that $z\nu = 1$. Also, the spectrum clearly has a crossover from a constant to a linear function of momentum at $k^* \sim |\lambda|$, suggesting that there is a characteristic correlation length that scales as $\xi \sim 1/k^* \sim 1/|\lambda|$; this implies that $\nu = 1$. Using the factorization property (3.14) it is easy to check that

$$\chi_f = \frac{1}{L} \langle \partial_\lambda \Psi(0) | \partial_\lambda \Psi(0) \rangle = \frac{1}{4L} \sum_{k>0} \left(\frac{\partial \theta_k}{\partial \lambda} \right)^2 \approx \frac{1}{4} \sum_{k>0} \frac{k^2}{(k^2 + \lambda^2)^2}. \quad (3.15)$$

In the thermodynamic limit for $\lambda \gg 1/L$ we can substitute the sum with the integral and find

$$\chi_f(\lambda) = \int_0^\infty \frac{dk}{2\pi} \frac{k^2}{(k^2 + \lambda^2)^2} = \frac{1}{8\lambda}. \quad (3.16)$$

At the QCP and for finite L , Eq. (3.15) gives $\chi_f(0) \approx L^2/96$. Both asymptotics are consistent with the expected scaling (3.8).

3.2 Scaling Analysis for Dynamics near Quantum Critical Points

Above we gave a brief overview of the universal aspects of the equilibrium ground state properties of quantum critical systems. Our next goal is to see how similar universality emerges in out-of-equilibrium situations where the parameter λ is tuned in time through a QCP. We expect that the dynamics will be universal if it is dominated by the low energy excitations generated near the critical point. In this chapter we will consider two specific situations where such universality is found: (a) instantaneous quench of the small amplitude starting precisely at the critical point; and (b) slow quenches, where the tuning parameter changes gradually across the QCP. We will also allow for slow quenches to start (end) exactly at the QCP. These two situations correspond to two very generic scenarios. The first one is realized when the rate of change of the tuning parameter is fast compared to other relevant time scales. Though starting exactly at the critical point can require fine tuning, the scaling results will remain valid as long as the system is sufficiently close to the critical point both before and after the quench. The second situation is applicable to regimes in which the tuning parameter changes slowly in time. As we will show below these two scenarios can be actually described within the same unifying framework. In this section we will use qualitative arguments based on the scaling of the FS near the critical point. In the next section we will derive these scaling relations more accurately using adiabatic perturbation theory.

We first start from instantaneous quenches. As we mentioned above, we assume the system is initially prepared in the ground state of some Hamiltonian H_0 corresponding precisely to the QCP. We then suddenly apply perturbation λV , where λ is a small parameter and V is some operator independent of λ . We will assume that V is a relevant perturbation which drives the system away from the QCP. Let us discuss the expected scaling of various quantities using ordinary perturbation theory. According to general rules of quantum mechanics, the ground state wave function after the quench will be projected onto the basis of the new (quenched) Hamiltonian. Within ordinary perturbation theory the amplitude $\delta\psi_n$ to occupy the excited state $|n\rangle$ is

$$\delta\psi_n \approx \lambda \frac{\langle n|V|0\rangle}{E_n - E_0}, \quad (3.17)$$

where the matrix elements and the energies are calculated for the unperturbed Hamiltonian. It is clear that quantities which commute with the new Hamiltonian, like the excitation probability or the energy, should scale as a square power of λ . This follows from the fact that such quantities must be quadratic

in $\delta\psi_n$. For example, the probability of exciting the system is

$$P_{\text{ex}} = \sum'_n |\delta\psi_n|^2 = \lambda^2 \sum'_n \frac{|\langle n|V|0\rangle|^2}{|E_n - E_0|^2} = \lambda^2 L^d \chi_f(0), \quad (3.18)$$

where the prime over the sum implies that the ground state is excluded from the summation. The excitation probability is meaningful only for quenches with the amplitude vanishing in the thermodynamic limit such that $\xi(\lambda) \gtrsim L$. For larger amplitude quenches $P_{\text{ex}} \approx 1$. In these situations one needs other quantities to characterize the system's response to the quench. One of these quantities can be the diagonal entropy [20], $S_d = -\sum |\psi_n|^2 \ln |\psi_n|^2$, where $|\psi_n|^2$ are the probabilities to occupy eigenstates of the quenched Hamiltonian. Clearly S_d is a possible measure of the non-adiabatic response of the system, which is well defined for quenches of all amplitudes. Another possible measure characterizing the non-adiabatic response of the system is the energy, or, more precisely, the non-adiabatic part of the energy change due to transitions. This excess energy, or simply heat [21], is the difference between the energy after the quench and the instantaneous ground state energy. Within the perturbation theory we find that the heat density Q is

$$Q(\lambda) = \frac{1}{L^d} \sum_n (E_n - E_0) |\delta\psi_n|^2 = \frac{1}{L^d} \lambda^2 \sum'_n \frac{|\langle n|V|0\rangle|^2}{E_n - E_0} \equiv \lambda^2 \chi_E(0), \quad (3.19)$$

where we introduced the energy susceptibility $\chi_E(\lambda) = \chi_1(\lambda)$. If we additionally assume that excitations in the system are carried by well-defined quasi-particles, i.e., that the energy eigenstates $|n\rangle$ are also the eigenstates of the quasi-particle number operator (which is usually the case only in integrable models), then we can also compute the density of quasi-particles,

$$n_{\text{ex}}(\lambda) = \frac{1}{L^d} \sum_n N_n |\delta\psi_n|^2 = \lambda^2 \chi_n, \quad (3.20)$$

where N_n is the total occupation of each eigenstate n

$$\chi_n = \frac{1}{L^d} \sum'_n N_n \frac{|\langle n|V|0\rangle|^2}{(E_n - E_0)^2}. \quad (3.21)$$

In most systems the number of quasi-particles is actually not conserved due to various collision processes. However, the quasi-particle number can be still a very useful quantity if we are interested in times shorter than the relaxation time, i.e., times in which collisions do not play any significant role. We see that in all these situations we expect $P_{\text{ex}}(\lambda)$, $Q(\lambda)$, and $n_{\text{ex}}(\lambda)$ to scale quadratically in λ to lowest order. The scaling for the d-entropy can acquire additional logarithmic corrections. We will not discuss it here for brevity since it is very similar to that of n_{ex} [19]. We note that this quadratic scaling should

be contrasted with the usual linear response relations where various quantities are proportional to the first power of λ , e.g.,

$$\langle \psi(\lambda) | V | \psi(\lambda) \rangle \approx \text{const} + 2\lambda \sum_n \frac{|\langle n | V | 0 \rangle|^2}{E_n - E_0} = \text{const} + 2L^d \lambda \chi_E. \quad (3.22)$$

To obtain linear dependence it is obviously crucial that the observable of interest does not commute with the Hamiltonian in the excited state. Such situations can also be analyzed. However, we will not consider them.

It is very important to remark that we are dealing with extended systems. As we saw in the simple example of the transverse-field Ising model the FS is extensive in the system size (3.16). This situation is generic if we consider global (spatially-uniform) perturbations. Strictly speaking this implies that the validity of the perturbation theory is restricted to very small perturbations, where $P_{\text{ex}}(\lambda) \ll 1$. However, we know very well that perturbative approaches typically have much larger domains of applicability. It is usually important that only changes of intensive quantities like the energy per unit volume or the density of quasi-particles remain small. Indeed, the probability to produce the next quasi-particle excitation is not affected much by the presence of other quasi-particles if those are very dilute. Thus we expect that Eqs. (3.19) and (3.20) have a much broader domain of applicability than Eq. (3.18) (see also Refs. [12, 19] for additional discussion).

As we discussed earlier, near QCPs susceptibilities may become divergent (see, e.g., Eq. (3.16) for the Ising model) or acquire some other type of singularity. Such divergences can invalidate the quadratic perturbative scaling of various observables and these situations will be the next point of our discussion. Let us look into, e.g., Eq. (3.18) for the probability of exciting the system. Near the critical point, $\chi_f(\lambda)$ may diverge as $\lambda \rightarrow 0$ with the divergence being cut off by the system size (see Eq. 3.8). This results in superextensive scaling of the transition probability:

$$P_{\text{ex}}(\lambda) \sim \lambda^2 L^{2/\nu} \quad (3.23)$$

for $2/\nu > d$. It is clear that P_{ex} should saturate at unity when λ becomes bigger than $\lambda^* \sim 1/L^{1/\nu}$, which is accidentally equivalent to the condition $\xi(\lambda) < L$ where the fidelity susceptibility changes its form (see Eq. 3.8). Likewise, for $2/\nu > d + z$ we find

$$Q(\lambda) \sim \lambda^2 L^{2/\nu - d - z} \quad (3.24)$$

for the heat density for $\lambda < \lambda^*$. However, unlike the probability of excitations, we can extend the perturbative expression for the heat (3.19) to the regime $\lambda > \lambda^*$ by simply evaluating the susceptibility χ_E at the final value of the quench parameter. More accurate derivation based on adiabatic perturbation theory, which we discuss in the next section, shows that one needs to change $\chi_E(0) \rightarrow \int_0^\lambda \chi_E(\lambda') d\lambda'$ in Eq. (3.19). However, the scaling of this integral is

the same as the scaling of $\chi_E(\lambda)$. Then we find that for $\lambda > \lambda^*$,

$$Q(\lambda) \sim |\lambda|^{(d+z)\nu}. \quad (3.25)$$

Finally, if we additionally assume that dominant excitations are coming from isolated quasi-particles (which is often the case) we find that for $\lambda > \lambda^*$,

$$n_{\text{ex}} \sim |\lambda|^{d\nu}, \quad (3.26)$$

while for $\lambda < \lambda^*$ the scaling for n_{ex} is similar to that of P_{ex} given by Eq. (3.23).

Of course, we expect these scalings to remain valid as long as the corresponding exponents do not exceed two. Otherwise, the low-energy singularities associated with the critical point become sub-leading (corresponding susceptibilities do not diverge) and the perturbative quadratic scaling is restored (though the singularities still appear in higher order derivatives with respect to λ).

There is a very simple argument, which reproduces the scalings (3.25) and (3.26). A quench of amplitude λ gives us natural length and energy scales $\xi \sim 1/|\lambda|^\nu$ and $\Delta \sim |\lambda|^{z\nu}$. We thus might expect that the quasi-particle excitations with energies larger than Δ , or equivalently with momenta larger than $1/\xi$, will not be much affected by the quench and can be treated perturbatively, yielding the quadratic scaling. At the same time, for states with energies less than Δ the quench will be effectively very strong, so that they will be excited with the probability of the order of unity. Thus the density of quasi-particles will scale as $1/\xi^d \sim \lambda^{d\nu}$ and we reproduce the scaling (3.26). If $d\nu < 2$ then this contribution to n_{ex} will be dominant over the perturbative contribution coming from high energies (because it is proportional to smaller power of λ). Likewise, we can obtain the scaling of heat (3.25) by noting that the low energy excitations carry energy of the order of Δ . Thus their contribution is $Q \sim n_{\text{ex}}\Delta \sim |\lambda|^{(d+z)\nu}$. When the exponent $(d+z)\nu$ becomes more than two this low energy contribution becomes sub-leading and the perturbative quadratic scaling is restored to leading order in λ (as we mentioned singular non-analytic terms can still persist to higher order in λ). There is a related and very intuitive way of deriving the scaling (3.26) adopting the arguments of Kibble and Zurek [14, 15] to the situation of sudden quenches. Namely, we can interpret the scale ξ as a typical distance between generated quasi-particles. Then the quasi-particle density is $1/\xi^d \sim |\lambda|^{d\nu}$.

It is interesting that Eq. (3.23) can also be understood purely by symmetry arguments. Let us assume that the phase corresponding to finite λ is characterized by some broken symmetry. The symmetry becomes well defined when $\xi(\lambda) \sim 1/|\lambda|^\nu$ becomes less or comparable to the system size: $\xi(\lambda) \lesssim L$. This defines the minimal quench amplitude $\lambda^* \sim 1/L^{1/\nu}$ at which the symmetry is formed. Since the critical point does not correspond to any broken symmetry we anticipate that the overlap between ground state wave-functions $|\psi(0)\rangle$ and $|\psi(\lambda)\rangle$ vanishes for $\lambda \gtrsim \lambda^*$. This implies that

$$\chi_f(0)L^d(\lambda^*)^2 \gtrsim 1 \quad (3.27)$$

or equivalently, $\chi_f(0) \gtrsim L^{2/\nu-d}$, which is actually the correct scaling. In the case, $d\nu > 2$, Eq. (3.27) is satisfied even if $\chi_F(\lambda)$ approaches a constant independent of the system size at the critical point. Note that the argument, in principle, allows $\chi_f(0)$ to vanish at the QCP for $d\nu > 2$ in the thermodynamic limit. However, as we discussed above, generally one can anticipate that $\chi_f(0)$ is non-zero due to high-energy non-universal contributions not sensitive to the presence of the critical point.

Let us now consider a somewhat different setup, where we still start at the critical point but instead of suddenly quenching the parameter λ we assume that it gradually increases over time as a power law $\lambda(t) = (vt^r/r!)\Theta(t)$, where the factor of $1/r!$ is added for convenience. Here $\Theta(t)$ is the step function and v is a real constant, which controls the proximity to the adiabatic limit. For linear quenches ($r = 1$) the parameter v plays the velocity of the quench; for quadratic quenches ($r = 2$) it is the acceleration and so on. It is interesting that in the limit $r \rightarrow 0$ this parameter v becomes the quench amplitude. For simplicity we also assume that for $r > 0$ the final value of λ is sufficiently far from the critical point. As in the case of sudden quenches, it is instructive first to perform analysis of the new state via perturbation in v . Using adiabatic perturbation theory [13, 22], which we will briefly discuss in the next section, one can show that to leading order in v the probability to occupy the state $|n\rangle$ in the instantaneous (co-moving basis) is

$$|\delta\psi_n|^2 \approx v^2 \frac{|\langle n|V|0\rangle|^2}{(E_n - E_0)^{2r+2}}, \quad (3.28)$$

where as before all matrix elements and energies are evaluated at the critical point. We note that the same expression applies to the opposite situation, where one starts far from the critical point and changes the coupling linearly in time until the critical point is reached. This expression can be also generalized to situations when both initial and final couplings are finite [13]. Then the total probability to excite the system reads

$$P_{\text{ex}}(v) \approx v^2 \sum_n \frac{|\langle n|V|0\rangle|^2}{(E_n - E_0)^{2r+2}} = v^2 L^d \chi_{2r+2}(0), \quad (3.29)$$

where $\chi_{2r+2}(\lambda)$ is the generalized adiabatic susceptibility introduced in the previous section (3.10). One can similarly introduce susceptibilities describing the heat density Q and the quasi-particle density n_{ex} for slow quenches. For example, it is easy to see that if the quench ends in the critical point then

$$Q(v) \approx v^2 \chi_{2r+1}(0). \quad (3.30)$$

If, on the other hand, the quench ends far from the critical point, then the energy of the system and the number of quasi-particles are evaluated in the states adiabatically connected to the states $|n\rangle$ at the critical points; thus the expressions for Q and n_{ex} become in general nonuniversal. The situation simplifies in integrable models, where, e.g., the quasi-particle number is conserved

during the adiabatic evolution. The same is true in non-integrable models if the excitations are topological and have very slow relaxation. The ambiguities of choosing the basis also disappear if we consider a cyclic process where coupling first linearly increases in time, then saturates, and then decreases back towards its original value, e.g., $\lambda(t) \propto t^r(t_f - t)^r \Theta(t(t_f - t))$. In this case, the corresponding susceptibilities will essentially have an extra factor of two. Also, there are no complications with choosing the basis if we consider a reverse process where we stop at the critical point.

Now we are in the position of more closely analyzing the scaling of P_{ex} and other quantities. Like in the case of instantaneous quenches, $\chi_{2r+2}(\lambda)$ for $r > 0$ can diverge at the critical point because of low energy contributions to Eq. (3.29). As we discussed earlier, $\dim \chi_{2r+2} = d - 2/\nu - 2zr$; this is indeed the case for $d < 2/\nu + 2zr$. As in the case of sudden quenches this divergence leads to super-extensive scaling for the excitation probability:

$$P_{\text{ex}}(v) \sim |v|^2 L^{2/\nu + 2zr}. \quad (3.31)$$

This probability becomes close to the one at the crossover rate $v^* \sim 1/L^{1/\nu + zr}$. For faster quenches, $v > v^*$, the excitation probability is no longer informative and we need to consider other quantities. If we assume that the quasi-particles are well defined then in the case $|v| > |v^*|$ we can extend Eq. (3.29) as we did for sudden quenches, namely evaluating χ_{2r+2} at some characteristic coupling slightly away from the critical point. Noting also that $\nu^{-1} = \dim[\lambda] = \dim[v] - zr$ we see that the scaling dimension of v is $\dim[v] = zr + 1/\nu$. This means that the characteristic value of λ , which should enter the susceptibility, is related to v via $\lambda \sim v^{(1+z\nu r)}$. Therefore we recover that for $|v| > |v^*|$

$$n_{\text{ex}} \sim |v|^{d\nu/(z\nu r + 1)}, \quad (3.32)$$

which for linear quenches ($r = 1$) is indeed the correct scaling first suggested in Refs. [8, 9], and later generalized to nonlinear quenches in Refs. [23, 24]. If we assume that in the final state the spectrum is gapless and characterized by the exponent z (e.g., if the final state of the evolution corresponds to the critical point), we find the heat is also universal. In particular, for $|v| > |v^*|$:

$$Q \sim |v|^{\frac{(d+z)\nu}{z\nu r + 1}}. \quad (3.33)$$

Equation (3.33) is also the correct scaling first suggested in Ref. [12] for $r = 1$. As in the case of sudden quenches, these scaling results are expected to be valid only if the corresponding exponents in the powers of v are smaller than two. Otherwise the corresponding susceptibilities $\chi_{2r+2}(\lambda)$ or $\chi_{2r+1}(\lambda)$ are not divergent generically, having only cusp singularities at the QCP. In this case the corresponding non-analytic asymptotics of P_{ex} , Q , and n_{ex} become sub-leading.

There is also a very intuitive explanation of the scaling (3.32). As we mentioned in the previous section, critical points are characterized by the quasi-particle energy scale $\Delta \sim |\lambda|^{z\nu} = |vt|^{z\nu}$ (we note that the scale Δ , relevant

to our discussion, is always associated with quasi-particle excitations, even if quasi-particles are ill defined; many-body energy levels are generally exponentially close to each other). If this energy scale changes sufficiently slowly in time then the energy levels have time to adjust to this change and adiabatically evolve. However, if Δ changes sufficiently fast then the adiabaticity breaks down and the states are excited. To find the crossover energy scale separating adiabatic and diabatic states we can use the simple Landau-Zener-Majorana-Stückelberg (LZMS) criterion $d\tilde{\Delta}/dt \sim \tilde{\Delta}^2$. Using the facts that $\Delta \propto |\lambda|^{z\nu}$ and $\lambda \sim vt^r$, we find that $\tilde{\Delta} \sim |v|^{z\nu/(z\nu r+1)}$. This scale corresponds to the characteristic momentum $\tilde{k} \sim |v|^{\nu/(z\nu r+1)}$ and the characteristic length scale $\tilde{\xi} \sim 1/\tilde{k}$. The number of excited quasi-particle states in the spatially uniform system is then $n_{\text{ex}} \sim \tilde{k}^d \sim |v|^{d\nu/(z\nu r+1)}$, which is exactly as in Eq. (3.32). We note that in this form the argument does not require that the initial or final point of the evolution coincides with the critical point. It is only important that the QCP is crossed during the time evolution. In the next section, in which we discuss adiabatic perturbation theory, we will show that this is indeed the case. The crossover to the quadratic scaling is also expected to be generic. In general in the expressions (3.29) and (3.30) one has to evaluate the corresponding susceptibilities in the initial and the final points of the evolution. Away from the phase transitions we expect no singularities in the corresponding susceptibilities and thus the quadratic scaling will hold. This simple scaling argument can be also reformulated in the spirit of Kibble-Zurek mechanism [14, 15]. Namely, one can interpret the length scale $\tilde{\xi}$ as a characteristic distance between generated quasi-particles and the inverse energy scale $\tilde{\Delta}^{-1}$ as a time scale where the process is not adiabatic and the defects are generated.

Example: transverse-field Ising model and multi-dimensional extensions. Let us now illustrate how the scalings we derived apply to the specific example we introduced in Sec. 3.1. We start from sudden quenches. We also focus on the thermodynamic limit $L \rightarrow \infty$, and λ independent of L . Using the explicit structure of the ground state wave function (3.14) it is easy to check that the overlap of two different ground states corresponding to a particular pair of fermions with momenta $k, -k$ is

$$\langle \Psi_0^k(\lambda) | \Psi_0^k(\lambda') \rangle = \cos [(\theta_k - \theta'_k)/2], \quad (3.34)$$

where θ_k and θ'_k correspond to the couplings λ and λ' respectively. This implies that the probability of exciting a pair of quasi-particles with momenta k and $-k$ by quenching the parameter λ' to λ is $p_{\text{ex}}(k) = \sin^2([\theta_k - \theta'_k]/2)$. Noting that we are interested in the limit $\lambda' = 0$ and using low energy expressions for θ_k and θ'_k we find

$$p_{\text{ex}}(k) \approx \frac{1}{2} \left[1 - \frac{|k|}{\sqrt{k^2 + \lambda^2}} \right]. \quad (3.35)$$

The density of quasi-particles excited in the quench is then obviously obtained

by integrating $p_{\text{ex}}(k)$ over different momenta

$$n_{\text{ex}} \approx \int_{-\pi}^{\pi} \frac{dk}{2\pi} p_{\text{ex}}(k) \approx \frac{|\lambda|}{2\pi}. \quad (3.36)$$

This scaling indeed agrees with our general expectation $n_{\text{ex}} \sim |\lambda|^{d\nu}$, noting that $d = \nu = 1$. Similarly we can find heat, noting that each quasi-particle with the momentum k carries energy $\epsilon_k \approx 2\sqrt{\lambda^2 + k^2}$. Then

$$Q \approx 2 \int_{-\pi}^{\pi} \frac{dk}{2\pi} \sqrt{k^2 + \lambda^2} p_{\text{ex}}(k) \approx \frac{1}{2\pi} \lambda^2 \ln \frac{2\pi}{|\lambda|}, \quad (3.37)$$

which also agrees with $Q \sim |\lambda|^{(d+z)\nu}$. However, because in this case the power $(d+z)\nu$ is exactly equal to two, we find an additional logarithmic dependence on both λ and the cutoff π . The logarithmic dependence is natural at the point where we expect crossover from the exponent two at $(d+z)\nu > 2$ to the exponent less than two in the opposite case. Even though the transverse-field Ising model is defined only in 1D, one can extend it to higher dimensions by formally considering the free-fermion Hamiltonian (3.13) in higher dimensional lattices. For example, in 2D a very similar Hamiltonian represents the fermionic sector of the Kitaev model [25], and also describes electrons and holes in graphene [26]. Then it is easy to check that n_{ex} has quadratic scaling with λ in 2D and above with extra logarithmic corrections in 2D where $d\nu = 2$. The heat has quadratic scaling above 1D (see Ref. [19] for additional details).

The transverse-field Ising model can be also solved for slow quenches. For simplicity we will analyze only the linear dependence $\lambda = vt$. Note that the wave function factorizes into a direct product of states corresponding to different momenta with either zero fermions or two fermions in each state. Thus the dynamical problem factorizes into a direct sum of LZMS problems. If the magnetic field linearly crosses the QCP then the transition probability is given by [27]

$$p_{\text{ex}}(k) \approx \exp(-2\pi k^2/v) \quad (3.38)$$

The density of quasi-particles generated in such a process is obtained by integrating $p_{\text{ex}}(k)$ over different momentum states yielding in the slow limit $n_{\text{ex}} \approx \sqrt{v}/(2\pi\sqrt{2})$. This is indeed the expected scaling $n_{\text{ex}} \sim |v|^{d\nu/(z\nu+1)}$ for a particular set of exponents $d = \nu = z = 1$. The problem can be also solved for the linear quench starting at the critical point giving identical scaling with a slightly different prefactor [13]. To see the crossover to the quadratic scaling one needs to consider extension of the Hamiltonian (3.13) to higher dimensions. In this case for each momentum state we are effectively dealing with half LZMS problems, i.e., LZMS problems where the initial coupling corresponds to the minimum gap. Asymptotically, in the slow limit $v \ll \epsilon_k^2$, this probability is found from Eq. (3.28):

$$p_{\text{ex}}(k) \approx (1024)^{-1} v^2/k^4. \quad (3.39)$$

It is clear that above four dimensions the density of quasi-particles $n_{\text{ex}} \sim \int d^d k p_{\text{ex}}$ will be quadratic, dominated by excitations to high energies of the order of the cutoff. Below four dimensions the integral converges at large k so transition probabilities are dominated by small momenta $k \sim \sqrt{v}$ and the scaling $n_{\text{ex}} \sim |v|^{d\nu/(z\nu+1)} = |v|^{d/2}$ is restored.

3.3 Adiabatic Perturbation Theory

3.3.1 Sketch of the Derivation

In this section we will present a more accurate derivation of the scaling of various quantities near the critical point. In particular, our aim is to derive the expression for the transition probability to leading order in v . A very convenient framework to analyze these scaling laws is given by adiabatic perturbation theory. As we will see, this approach will allow us not only to reproduce Eq. (3.28), but also to extend this result to the regime where the corresponding susceptibility $\chi_{2r+2}(\lambda)$ diverges at the QCP and justify Eqs. (3.32) and (3.33). In Ref. [8] this theory was originally applied to derive the scaling of the density of quasi-particles (3.32). In Ref. [12] it was shown that this approach correctly predicts the crossover between analytic and non-analytic regimes of scaling of heat (excess energy) with the rate v for linear quenches. In Refs. [13, 19] this theory was extended to sudden quenches near critical points and also reproduced correct scaling results. While adiabatic perturbation theory is not quantitatively accurate in non-analytic regimes (where the response is not quadratic) [8, 12], i.e., it does not correctly reproduce the prefactor, it predicts correct scaling laws in many different situations. The only known exceptions are in the *non-adiabatic regime*, where the system size or other macroscopic length scale enters the scaling of heat or quasi-particle density [12, 19]. Such regimes can appear, e.g., if we are dealing with low-dimensional systems, which have low energy bosonic excitations, especially at finite temperatures, where the violation of scaling (3.32) comes from the overpopulation of low-energy modes. This regime is quite special and we will not consider it here (we refer the reader interested in more details to Refs. [12, 19]).

In the beginning of the section we will closely follow the discussion of Refs. [13, 28]. We consider a very general setup where the system is described by a Hamiltonian $H(t) = H_0 + \lambda(t)V$, where $\lambda(t)$ monotonically changes in time between initial and final values λ_i and λ_f . For simplicity, in this chapter we will focus only in linear dependence $\lambda(t) = vt$, though this assumption is not important. The limit $v \rightarrow \infty$ corresponds to a sudden quench and $v \rightarrow 0$ to a slow quench. We will always assume that for sudden quenches λ_f is close to λ_i , while for slow quenches this condition is not necessary. In both cases

adiabatic perturbation theory will be justified by the proximity of the system to the ground state after the quench.

Our goal is to approximately solve the Schrödinger equation

$$i\partial_t|\psi\rangle = H(t)|\psi\rangle, \quad (3.40)$$

where $|\psi\rangle$ is the wave function. It is convenient to rewrite Eq. (3.40) in the adiabatic (instantaneous) basis:

$$|\psi(t)\rangle = \sum_n a_n(t)|n(t)\rangle, \quad H(t)|n(t)\rangle = E_n(t)|n(t)\rangle, \quad (3.41)$$

where $E_n(t)$ are the instantaneous eigenvalues. The eigenstates $|n(t)\rangle$ implicitly depend on time through the coupling $\lambda(t)$. Substituting this expansion into the Schrödinger equation and multiplying it by $\langle m|$ (to simplify our notations we drop the time label t in $|n(t)\rangle$) we find:

$$i\partial_t a_n(t) + i \sum_m a_m(t) \langle n | \partial_t | m \rangle = E_n(t) a_n(t). \quad (3.42)$$

Next we will perform a unitary transformation:

$$a_n(t) = \alpha_n(t) \exp[-i\Theta_n(t)], \quad \Theta_n(t) = \int_{t_i}^t E_n(\tau) d\tau. \quad (3.43)$$

The lower limit of integration in the expression for $\Theta_n(t)$ is arbitrary. We chose it to be equal to t_i for convenience. Then the Schrödinger equation becomes

$$\dot{\alpha}_n(t) = - \sum_m \alpha_m(t) \langle n | \partial_t | m \rangle \exp[i(\Theta_n(t) - \Theta_m(t))]. \quad (3.44)$$

In turn this equation can be rewritten as an integral equation

$$\dot{\alpha}_n(t) = - \int_{t_i}^t dt' \sum_m \alpha_m(t') \langle n | \partial_{t'} | m \rangle e^{i(\Theta_n(t') - \Theta_m(t'))}. \quad (3.45)$$

If the energy levels $E_n(t)$ and $E_m(t)$ are not degenerate, the matrix element $\langle n | \partial_t | m \rangle$ can be written as

$$\langle n | \partial_t | m \rangle = - \frac{\langle n | \partial_t H | m \rangle}{E_n(t) - E_m(t)} = - \dot{\lambda}(t) \frac{\langle n | V | m \rangle}{E_n(t) - E_m(t)}. \quad (3.46)$$

If $\lambda(t)$ is a monotonic function of time, like in our case, then in Eq. (3.45) one can change variables from t to $\lambda(t)$ and derive

$$\dot{\alpha}_n(\lambda) = - \int_{\lambda_i}^{\lambda} d\lambda' \sum_m \alpha_m(\lambda') \langle n | \partial_{\lambda'} | m \rangle e^{i(\Theta_n(\lambda') - \Theta_m(\lambda'))}, \quad (3.47)$$

where

$$\Theta_n(\lambda) = \int_{\lambda_i}^{\lambda} d\lambda' E_n(\lambda') (\dot{\lambda}')^{-1}. \quad (3.48)$$

Equations (3.45) and (3.47) suggest a systematic expansion in the transition amplitudes to the excited states. We are interested in either the limit $\dot{\lambda} = v \rightarrow 0$, which suppresses transitions because of the highly oscillating phase

factor, or the limit of small $|\lambda_f - \lambda_i|$, where the transitions are suppressed by the smallness of the integration domain. To leading order in adiabatic perturbation theory only the diagonal terms with $m = n$ should be retained in the sums in Eqs. (3.45) and (3.47). These terms result in the emergence of a Berry phase [29]:

$$\Phi_n(t) = -i \int_{t_i}^t dt' \langle n | \partial_{t'} | n \rangle = -i \int_{\lambda_i}^{\lambda(t)} d\lambda' \langle n | \partial_{\lambda'} | n \rangle, \quad (3.49)$$

so that $a_n(t) \approx a_n(0) \exp[-i\Phi_n(t)]$. In general, the Berry phase can be incorporated into our formalism by performing a unitary transformation $\alpha_n(t) \rightarrow \alpha_n(t) \exp[-i\Phi_n(t)]$ and changing $\Theta_n \rightarrow \Theta_n + \Phi_n$ in Eqs. (3.45) and (3.47).

In many situations, when we deal with real Hamiltonians, the Berry phase is identically equal to zero. However, in some cases when more than one coupling constant changes in time, the contribution of the geometric phases can be important, so that it can change the results for scaling of the physical quantities near the phase transition [30]. Here we only note that since the geometric phase is related to the topology of the phase space, the evolution of physical quantities can depend on the path in the parameter space. The effects of the geometric phase are enhanced near the diabolic points corresponding to the level crossings. Geometric phase effects can be important for open systems, which effectively can be modeled by non-Hermitean (complex) Hamiltonians.

Assuming that the geometric phase is not important, let us compute the first order correction to the wave function assuming that initially the system is in the pure state $n = 0$, so that $\alpha_0(0) = 1$ and $\alpha_n(0) = 0$ for $n \neq 0$. To leading order in $\dot{\lambda}$ we can keep only one term with $m = 0$ in the sums in Eqs. (3.45) and (3.47) and derive

$$\alpha_n(t) \approx - \int_{t_i}^t dt' \langle n | \partial_{t'} | 0 \rangle e^{i[\Theta_n(t') - \Theta_0(t')]} \quad (3.50)$$

or alternatively

$$\alpha_n(\lambda) \approx - \int_{\lambda_i}^{\lambda} d\lambda' \langle n | \partial_{\lambda'} | 0 \rangle e^{i[\Theta_n(\lambda') - \Theta_0(\lambda')]} \quad (3.51)$$

The transition probability from the level $|0\rangle$ to the level $|n\rangle$ as a result of the process is determined by $|\alpha_n(\lambda_f)|^2$. Let us note that in the limit of $\dot{\lambda} = v \rightarrow 0$ one can expect two types of contributions to Eq. (3.51). (i) A non-analytic contribution comes from the saddle points of the phase difference $\Theta_n(\lambda) - \Theta_m(\lambda)$, which in turn correspond to the complex roots of $E_n(\lambda) = E_0(\lambda)$. These terms result in exponential dependence of the transition probability on rate $|\alpha|^2 \sim \exp[-A/|\dot{\lambda}|]$ as in the usual LZMS problem (see Ref. [13] for the additional discussion). (ii) An analytic contribution comes from the moments where we turn on and turn off the process. This second contribution, to leading order in $\dot{\lambda}$, can be obtained by integrating Eq. (3.51) by parts [13, 22]:

$$\alpha_n(\lambda_f) \approx \left[i \dot{\lambda} \frac{\langle n | \partial_\lambda | 0 \rangle}{E_n(\lambda) - E_0(\lambda)} \right] e^{i(\Theta_n(\lambda) - \Theta_0(\lambda))} \Bigg|_{\lambda_i}^{\lambda_f}. \quad (3.52)$$

From this we find the analytic part of the transition probability

$$|\alpha_n(\lambda_f)|^2 \approx v^2 \left[\frac{|\langle n | \partial_{\lambda_i} | 0 \rangle|^2}{(E_n(\lambda_i) - E_0(\lambda_i))^2} + \frac{|\langle n | \partial_{\lambda_f} | 0 \rangle|^2}{(E_n(\lambda_f) - E_0(\lambda_f))^2} \right] - 2v^2 \frac{\langle n | \partial_{\lambda_i} | 0 \rangle}{E_n(\lambda_i) - E_0(\lambda_i)} \frac{\langle n | \partial_{\lambda_f} | 0 \rangle}{E_n(\lambda_f) - E_0(\lambda_f)} \cos[\Delta\Theta_{n0}], \quad (3.53)$$

where $\Delta\Theta_{n0} = \Theta_n(\lambda_f) - \Theta_0(\lambda_f) - \Theta_n(\lambda_i) + \Theta_0(\lambda_i)$. Usually if we deal with many levels the last fast-oscillating term will average out to zero. The remaining first two terms are the transition probabilities associated with turning on and off the coupling λ . If only the first term dominates the scaling (e.g., because the initial state corresponds to a QCP) we recover Eq. (3.28) for $r = 1$. If we deal with nonlinear quenches such that $\lambda = 0$ at the initial and final points of the evolution then we need to continue integrating Eq. (3.51) by parts until we hit the first non-vanishing time-derivative of $\lambda(t)$. It is straightforward to see that in this way we reproduce Eq. (3.28) for any integer power r . The resulting expression can be analytically continued to all positive r . Interestingly, it correctly reproduces the result of ordinary perturbation theory for sudden quenches $r = 0$, where the parameter v plays the role of the quench amplitude.

3.3.2 Applications to Dynamics near Critical Points

Let us now perform the scaling analysis of Eq. (3.51). First we consider the situation of sudden quenches with the initial coupling corresponding to the critical point $\lambda_i = 0$ (or alternatively $\lambda_f = 0$). We will assume that excitations are dominated by quasi-particles created in pairs with opposite momenta $k, -k$. As we saw in the previous section this assumption is well justified for non-interacting models like the transverse-field Ising model. In general, for interacting non-integrable models eigenstates consist of quasi-particles dressed by interactions and the quasi-particles acquire finite life time. If the quasi-particle nature does not qualitatively change because of the interactions we expect that the scaling of the quasi-particle density will remain the same as the scaling of the excitation probability. In fact, the whole scaling analysis can be performed in the spirit of Sec. 3.2, which does not rely on the assumption of having well-defined quasi-particles. However, such an assumption makes all derivations more transparent.

Assuming that $|n\rangle$ corresponds to the quasi-particle pair with momenta $k, -k$ we find¹

$$\alpha_k(\lambda_f) \approx - \int_0^{\lambda_f} d\lambda \frac{\langle k | V | 0 \rangle}{\epsilon_k(\lambda) - \epsilon_0(\lambda)}. \quad (3.54)$$

¹To simplify our notation we denote such pair states by $|k\rangle$ and the corresponding energy of the pair by ϵ_k .

Since the scaling dimension of the operator λV is the same as the scaling dimension of energy we expect the following scaling of the matrix element:

$$\frac{\langle k|V|0\rangle}{\epsilon_k(\lambda) - \epsilon_0(\lambda)} = \frac{1}{\lambda} G(k/|\lambda|^\nu), \quad (3.55)$$

where $G(x)$ is some scaling function. We anticipate that in the limit $x \gg 1$ we have $G(x) \sim x^{-1/\nu}$ so that the matrix element becomes independent of λ at $k \gg \lambda^\nu$. In the opposite limit, $x \ll 1$, the scaling function can either saturate if there is a gap or vanish as some power of x if there is no gap. It is easy to check that for the transverse-field Ising model the scaling assumption is indeed satisfied with $G(x) \propto x/(x^2 + 1)$. This scaling ansatz immediately allows us to analyze the behavior of the quasi-particle density:

$$n_{\text{ex}} \approx \frac{1}{L^d} \sum_k |\alpha_k|^2. \quad (3.56)$$

Then taking the thermodynamic limit where the sum over k becomes an integral and changing variables $\lambda \rightarrow \lambda_f \eta$ and $k \rightarrow |\lambda_f|^\nu \xi$ we immediately find

$$n_{\text{ex}}(\lambda_f) \approx |\lambda_f|^{d\nu} \int \frac{d^d \xi}{(2\pi)^d} \left| \int_0^1 d\eta \frac{1}{\eta} G(\xi/|\eta|^\nu) \right|^2. \quad (3.57)$$

This expression gives the right scaling (3.26) provided that the integral over ξ converges at large ξ . The convergence clearly depends on the large ξ asymptotics of the function $G(\xi/|\eta|^\nu) \sim 1/|\xi|^{1/\nu}$. The integral over ξ clearly converges provided that $d \leq 2/\nu$ or $d\nu \leq 2$. In the opposite case the integral over momenta is dominated by large $k \gg |\lambda_f|^\nu$. In this case Eq. (3.56) reduces to the perturbative quadratic result, e.g., $n_{\text{ex}}(\lambda_f) \approx 2\lambda_f^2 \chi_f(0)$, where the factor of two reflects that each excited state contributes to two quasi-particles. Note that the assumption of scale independence of the transition matrix element is equivalent to the assumption that χ_f does not vanish at the critical point for $d\nu > 2$. As we pointed out earlier, this is generally expected because transitions to the high energy states are insensitive to the proximity to the critical point dominating excitations in the system.² Likewise, one can derive the correct scaling for the heat density (3.25) provided that $(d+z)\nu < 2$; one reproduces the quadratic perturbative result in the opposite case.

In a similar fashion we can derive the results for the adiabatic case, when the coupling constant changes slowly in time. For simplicity we focus again on linear quenches $\lambda(t) = vt$. For now it will not be important whether we start (finish) at the critical point or the initial and final couplings are on different sides of the QCP. The expression for the transition amplitude then becomes

$$\alpha_k(\lambda_f) \approx - \int_{\lambda_i}^{\lambda_f} d\lambda \frac{\langle k|V|0\rangle}{\epsilon_k(\lambda) - \epsilon_0(\lambda)} \exp \left[\frac{i}{v} \int_0^\lambda d\lambda' (\epsilon_k(\lambda') - \epsilon_0(\lambda')) \right]. \quad (3.58)$$

²See detailed discussion in Ref. [19] for a particular sine-Gordon model.

Let us now introduce another scaling function $F(x)$ according to $\epsilon_k(\lambda) - \epsilon_0(\lambda) = |\lambda|^{z\nu} F(k/|\lambda|^\nu)$ with the asymptotic power law $F(x) \sim |x|^z$ for $|x| \gg 1$ (the small x limit depends on whether the system is gapless or not). A convenient change of variables is $k = |v|^{1/(z\nu+1)}\eta$ and $\lambda = |v|^{1/(z\nu+1)}\eta$. Then the expression for the density of quasi-particles becomes

$$n_{\text{ex}} \sim \int \frac{d^d k}{(2\pi)^d} |\alpha_k|^2 = |v|^{\frac{d\nu}{z\nu+1}} \int \frac{d^d \eta}{(2\pi)^d} |\alpha(\eta)|^2, \quad (3.59)$$

where

$$\alpha(\eta) = \int_{\xi_i}^{\xi_f} d\xi \frac{1}{\xi} G\left(\frac{\eta}{\xi^\nu}\right) \exp\left[i \int_{\xi_i}^{\xi} d\xi_1 \xi_1^{z\nu} F(\eta/\xi_1^\nu)\right]. \quad (3.60)$$

An analogous expression is found for heat. If v is small then the limits of integration over ξ can be extended to $(-\infty, \infty)$ if $\lambda_i < 0$ and $\lambda_f > 0$ or to $(0, \infty)$ if $\lambda_i = 0$ and λ_f is finite. Indeed, the integral over ξ is always convergent because of the highly oscillating exponent. If additionally the integral over the rescaled momentum η can be extended to ∞ we get the desired scaling for the quasi-particle density (3.32).

To analyze the convergence (assuming for simplicity that $|\lambda_f| \gg |\lambda_i|$ and λ_i is close to the QCP) we note that at large k the asymptotic expression for the transition amplitude $\alpha(k)$ according to Eq. (3.52) is

$$\alpha(k) \approx iv \frac{\langle k|V|0\rangle}{(E_k - E_0)^2} \sim \frac{v}{k^{z\nu+1/\nu}}, \quad (3.61)$$

where we kept only the term corresponding to the initial coupling $\lambda_i = 0$ because it describes the singularity. We thus immediately infer that the integral over the momentum k (and thus over the rescaled momentum η) can be extended to ∞ (so that the scaling (3.59) is valid) as long as $d \leq 2z\nu + 2/\nu$ or equivalently $d\nu/(z\nu+1) \leq 2$. In the opposite case, the usual adiabatic perturbation theory is restored and we recover the quadratic perturbative result $n_{\text{ex}} \sim v^2 (\chi_f(\lambda_i) + \chi_f(\lambda_f))$. We expect this scaling to be valid even if both λ_i and λ_f are away from the quantum critical region. Indeed, in this case one does not expect any divergences in susceptibilities $\chi_m(\lambda)$ at both λ_i and λ_f so the quadratic scaling should dominate the dynamics over the higher critical power $|v|^{d\nu/(z\nu+1)}$ emerging from the scaling argument. A somewhat special situation emerges if the relevant susceptibilities $\chi_m(\lambda)$ are very small at λ_i and λ_f . Then one might expect that the scaling $|v|^{d\nu/(z\nu+1)}$ will be applicable even when the exponent exceeds two. A similar situation occurs if the initial and final couplings are finite but the time dependence of $\lambda(t)$ is smooth near t_i and t_f and linear only near the critical point. These expectations are well justified only for non-interacting systems like the transverse-field Ising model, where dynamics can be mapped to independent LZMS transitions. In general, interactions lead to dephasing of quasi-particles, which is equivalent to resetting the dynamical process each time the quasi-particle phase is lost.

Then one can expect the quadratic scaling with v will be again restored for $d\nu/(z\nu+1) \geq 2$. At the moment this issue remains an open problem. We note that in the case $d\nu/(z\nu+1)$ one can expect that the non-analytic term coming from low energies will still survive; it will just become sub-leading in the limit of small v .

Another important point is that the susceptibilities $\chi_{2r+2}(\lambda)$ for $r > 0$ can diverge even away from the QCP as long as the system is gapless. Indeed, for bosonic theories gapless phases correspond to $\nu \rightarrow \infty$. Then the susceptibility χ_{2r+2} diverges for $d < 2zr$. This means that even in gapless noncritical phases in low dimensions the quadratic scaling can be violated and replaced by $n_{\text{ex}} \sim |v|^{d/zr}$ and $Q \sim |v|^{(d+z)/zr}$. This is consistent with general prediction of less adiabatic response in low dimensions [12]. It is also interesting to note that in the noncritical case for $d/zr < 2$ the density of quasi-particles, or, for $(d+z)/zr < 2$, the heat density, depend only on the total time of the quench, but not its shape. Indeed, since the total quench time $\tau \sim 1/v^{1/r}$ we see that $n_{\text{ex}} \sim |v|^{d/zr} \sim (1/\tau)^{d/z}$, i.e., is independent of r . On the other hand, for $d/zr > 2$ and in gapped phases in arbitrary dimensions $n_{\text{ex}} \sim (1/\tau)^{2r}$ is very sensitive to the exponent r and thus to the shape of the quench. The existence of these two regimes is true in other situations as well. Thus in Ref. [31] the two regimes of sensitivity of the energy (heating) to the shape pulse were discovered for interacting gapless fermionic systems. In general, relevance of the ramping protocol to the non-adiabatic dynamics in interacting many-body systems remains an open problem, which is likely very important for understanding the problem of dissipation.

3.3.3 Quenches at Finite Temperatures, and the Role of Quasi-particle Statistics

So far, we have exclusively focused on the situation where the system is prepared in the ground state. A natural question arises of how one can extend these results to the finite-temperature domain. It is well established that, in equilibrium near a QPT, influence of the QCP extends into finite temperatures in the *quantum critical region* [1] which can be quite extensive. We can anticipate that a similar situation occurs for non-equilibrium systems. Let us point out that the definition of temperature can be somewhat ambiguous away from equilibrium. One can consider two natural setups where the system is coupled to some external reservoir even during a dynamical process (see, e.g., Ref. [32]). In this situation results are sensitive to the coupling strength to the bath and in this sense are not universal. However, one can imagine a quite different setting, where the system is initially prepared in some thermal state and then the consequent dynamics is purely Hamiltonian, i.e., the effects of the bath are negligible during the time evolution. Such a setup was considered in Refs. [12, 19, 33]. In this setup, no coupling to the environment is assumed during the evolution and one can expect universality of the results. Such setups routinely appear now in the cold-atom context in which systems,

after initial preparation, are essentially isolated from the environment [34]. They also appear generally in thermodynamics when one considers adiabatic or nearly-adiabatic processes (in which changes happen on time scales faster than the time of equilibration with the environment) [35]. Universality can only be expected in this setup if the system is initially prepared close to a QCP. So in this section we restrict our analysis only to such situations.

On general grounds one can expect that at finite temperatures the statistical nature of low energy excitations should play a significant role. Indeed, if we are dealing with bosonic low energy quasi-particles we expect that the initial thermal population enhances the transition probability to the corresponding quasi-particle modes. The reason is that bosonic excitations have a bunching tendency, i.e., a tendency to stimulate transitions to a particular mode if it is already occupied. On the other hand, if quasi-particles are fermionic then Pauli blocking occurs due to already-occupied modes and fewer quasi-particles can be additionally excited. In principle, one can expect situations where low-energy excitations are either described by quasi-particles with fractional statistics like in Kitaev [25] and sine-Gordon models [36], or by many-particle excitations without well defined statistics. There the effect of finite temperature on dynamics is unknown at present and thus will not be discussed here.

If quasi-particles in the quantum critical region are bosonic then it is straightforward to show that the number of excited quasi-particle pairs in the mode with momentum q at initial temperature T is related to the number of quasi-particle pairs created at zero temperature via a very simple expression valid for any dependence of $\lambda(t)$ [12]:

$$n_{\text{ex}}(q, T) = n_{\text{eq}}(q, T) + n_{\text{ex}}^0(q) \coth(\epsilon_q/2T). \quad (3.62)$$

In Eq. (3.62), $n_{\text{eq}}(q, T)$ is the initial equilibrium population of the bosonic mode described by the Bose-Einstein distribution function, ϵ_q is the (initial) energy of the quasi-particle, and $n_{\text{ex}}^0(q)$ is the number of quasi-particles created in the same dynamical process if the initial temperature is zero. At small temperatures $\epsilon_q \gg T$ this expression clearly reduces to the zero temperature limit. In the opposite high temperature limit the transition probability is enhanced by the factor $2T/\epsilon_q \gg 1$. Similarly, in the fermionic case we have [19]

$$n_{\text{ex}}(q, T) = n_{\text{eq}}(q, T) + n_{\text{ex}}^0(q) \tanh(\epsilon_q/2T). \quad (3.63)$$

This expression also reproduces the zero-temperature result for $\epsilon_q \gg T$ while yielding suppression of the transition probability by a factor $\epsilon_q/(2T)$ in the opposite limit. Since the total number of dynamically excited quasi-particles is found by summing $n_{\text{ex}}(q, T) - n_{\text{eq}}(q, T)$ we see that to find the finite temperature scaling we need to change $d \rightarrow d - z$ for bosons and $d \rightarrow d + z$ for fermions in universal expressions (3.26) and (3.32). The same applies to the expression for heat (3.25). For example, for a slow quench starting at the critical point we find, instead of Eq. (3.32),

$$n_{\text{ex}}^{\text{bos}}(T) \sim |v|^{(d-z)\nu/(z\nu r+1)}, \quad n_{\text{ex}}^{\text{ferm}}(T) \sim |v|^{(d+z)\nu/(z\nu r+1)}. \quad (3.64)$$

As before, these scalings are generally valid (to leading order in v) only if the corresponding exponents are less than two; otherwise the scaling of n_{ex} , Q with v becomes quadratic.

There is actually an additional potential issue where the scaling (3.64) can break. This can happen because the integrals over different momentum states q can become divergent at small q . This corresponds to emergence in a new non-adiabatic regime of response of the system where the corresponding intensive observables become system-size-dependent [12]. This situation usually happens in low-dimensional bosonic systems where such infrared divergences correspond to overpopulation of the low energy modes. While there are specific examples of such behavior for slow dynamics in weakly interacting Bose gases [12] and for dynamics in the sine-Gordon model near the massive bosonic limit [19], there is no general understanding of this effect.

3.4 Going Beyond Condensed Matter

Here we focus on some possible extensions of the field of application of slow dynamics to other areas of physics, in particular, to cosmology and field (string) theory. The purpose of this section is to show that there are close similarities appearing between quantum dynamics near various space-time singularities and quantum critical dynamics. We do not intend to give a comprehensive overview of new problems nor present details of derivations. We are not experts in these fields. Our purpose is only to show that the applicability of our previous discussion extends well beyond condensed matter and atomic physics. Our first example will be from cosmology: we consider an early stage of expansion of the universe in d -dimensional space-time and assume that it is described either by a standard de Sitter-type metric or by its simplest generalization, which includes a slow-roll parameter. The second example arises mainly in some recent studies in string theory, where the question is a propagation of strings on some time-dependent background geometries. In particular, these geometries can be singular. This type of singularity is somewhat reminiscent of a phase transition, but it is different, and is of a completely geometrical nature. However, it can have an interpretation in terms of dynamical systems. We consider the simplest illustrative example – quantum evolution in a *Milnes universe*. In both examples the analogue of a QPT is provided by a singularity in the space-time background on which the quantum system is evolved.

3.4.1 Adiabaticity in Cosmology

A beginning of the Universe can also be considered as a (quantum) phase transition. In modern cosmology one usually considers a scalar field (a Higgs field) on some curved background evolving according to the Einstein equation.

A regime of parameters when the potential energy of that field dominates over the kinetic term leads to the rapid blowing up of the Universe, called inflation. Inflation can be modeled by an exponential scale factor in the metric and is called the de Sitter epoch. The velocity of inflation is given by a Hubble parameter which is assumed to be a constant in the de Sitter model. The natural adiabaticity parameter is then given by the ratio of the Hubble constant and the mass of the scalar field. The initial point of the expansion corresponds to the singularity in the metric where the scale factor $a(t)$ (see below) is very small. It is therefore natural to look into the cosmological evolution problem from the point of view of critical dynamics near the phase transition.

We consider a spherically-symmetric metric in $(d + 1)$ -dimensional space-time described by a single time-dependent scale factor

$$ds^2 = -dt^2 + a(t)^2 d\mathbf{x}^2, \quad (3.65)$$

where \mathbf{x} denotes a d -vector. The Hubble parameter is $H = \dot{a}(t)/a(t)$, where the “dot” denotes a time derivative. We consider a massive scalar field $\Phi(\mathbf{x}, t)$ in this geometry, which is minimally coupled to the gravity. The corresponding Klein-Gordon equation is given by [37]

$$\ddot{\Phi}(x, t) + dH\dot{\Phi}(x, t) - \frac{1}{a^2(t)}\nabla^2\Phi(x, t) + m^2\Phi(x, t) = 0. \quad (3.66)$$

Introducing the rescaled field $\phi(x, t) = a^{d/2}\Phi(x, t)$ and making a Fourier transform we obtain

$$\ddot{\phi}_k(t) + \Omega_k^2\phi_k(t) = 0, \quad (3.67)$$

where $\phi_k(t)$ is a Fourier component of $\phi(x, t)$,

$$\Omega_k^2(t) = \omega_k^2(t) - \left[\frac{d}{2} \left(\frac{d}{2} - 1 \right) \left(\frac{\dot{a}}{a} \right)^2 + \frac{d}{2} \frac{\ddot{a}}{a} \right] = \omega_k^2 - H^2 \left[\left(\frac{d}{2} \right)^2 + \frac{d}{2} \epsilon \right], \quad (3.68)$$

$\omega_k^2 = m^2 + k^2/a^2$, and we introduced a slow-roll parameter $\epsilon = \dot{H}/H^2$. This parameter is usually considered to be small during the inflation stage, thus indicating the smallness of the kinetic energy of a scalar field.

To proceed with quantization, we expand the Fourier components into a time-dependent creation and annihilation operator basis, $\phi_k \rightarrow \hat{\phi}_k(t) = \psi_k(t)\hat{a}_k + \psi_k^*(t)\hat{a}_k^\dagger$. The quantization is consistent with the following Klein-Gordon scalar product: $(\phi_1, \phi_2) = i \int d^d x (2\pi)^{-d} [\phi_1^*(x, t)\dot{\phi}_2(x, t) - \dot{\phi}_1^*(x, t)\phi_2(x, t)]$. Because of the time-dependence we have to distinguish $|\text{in}\rangle$ and $|\text{out}\rangle$ vacuum states and corresponding operators $a_k^{\text{in}, \text{out}}$. The linear transformation between these two bases is given by the Bogoliubov coefficients α_k, β_k through $\phi_k^{\text{out}}(t) = \alpha_k(t)\phi_k^{\text{in}}(t) + \beta_k^*\phi_k^{\text{in}*}(t)$, whereas the relation between vacuum states is given by the squeezed states, $|0_{k, \text{in}}\rangle = |\alpha_k|^{-1} \exp(-(\beta_k/\alpha_k^*)a_k^{\text{out}\dagger}a_{-k}^{\text{out}\dagger})|0_{k, \text{out}}\rangle$. The alternative definition of the Bogoliubov coefficients can be then given via the Klein-Gordon scalar product:

$\alpha_k = (\phi_k^{\text{in}}, \phi_k^{\text{out}})$ and $\beta_k^* = -(\phi_k^{\text{in}*}, \phi_k^{\text{out}})$. The number of excitations is now naturally defined as

$$\langle 0_{\text{in}} | a_k^{\text{out}\dagger} a_k^{\text{out}} | 0_{\text{in}} \rangle = |\beta_k|^2. \quad (3.69)$$

The flat de Sitter evolution is defined as a condition that H be a constant, which implies for the scale factor $a(t) = H^{-1} \exp(Ht)$. Apparently, in this case $\epsilon \equiv 0$. The solution for the Klein-Gordon equation is then given by $\phi_k^{\text{in}}(t) = \sqrt{\pi/4H} e^{-\pi\nu/2} \mathcal{H}_{i\nu}^{(1)}(k/[a(t)H])$ where $\mathcal{H}_{i\nu}^{(1)}(z)$ is a Hankel function of the first kind. Here $\nu = \sqrt{(m/H)^2 - (d/2)^2}$. Using the asymptotics of the Hankel function for large $|z|$ we can check that this solution indeed describes an $| \text{in} \rangle$ oscillating state in conformal time $\eta = -\exp(-Ht)$, according to the picture of Ref. [38]. The out solution has the following form:

$$\phi_k^{\text{out}}(t) = \sqrt{\frac{\pi}{2H \sinh(\pi\nu)}} J_{i\nu} \left(\frac{k}{a(t)H} \right), \quad (3.70)$$

where $J_{i\nu}(z)$ is a Bessel function. Now, the small-argument asymptotics corresponds to the $| \text{out} \rangle$ state. Using the relation between the Hankel and Bessel functions,

$$e^{-\pi\nu} \mathcal{H}_{i\nu}^{(1)}(z) = \frac{e^{\pi\nu} J_{i\nu}(z) - e^{-\pi\nu} J_{-i\nu}(z)}{\sinh(\pi\nu)}, \quad (3.71)$$

we obtain the *mode-independent* Bogoliubov coefficients

$$\alpha = \frac{1}{\sqrt{1 - \exp(-2\pi\nu)}}, \quad \beta = \alpha \exp(-\pi\nu). \quad (3.72)$$

We consider now a regime where³

$$v = H/m \ll 1 \quad (3.73)$$

which we identify as an adiabatic regime for reasons which will be clear immediately. In the regime of validity of (3.73), $\nu \approx 1/v$ and one obtains a density distribution of a pair production process at late times ($\eta \rightarrow 0$) in the form of a thermal spectrum

$$n_{\text{ex}} = 1/[\exp(2\pi/v) - 1]. \quad (3.74)$$

The probability of transition between asymptotic in and out vacua is given by the overlap, $P_{\text{in} \rightarrow \text{out}} = \prod_k |\alpha_k|^2$, and therefore in our case, the probability per each mode k is given by

$$P_{\text{in} \rightarrow \text{out}}^{(k)} = 1 - \exp(-2\pi/v), \quad (3.75)$$

³Note that we use dimensionless notations. In physical units the dimensionless combination is $mc^2/(\hbar H)$, and thus establishes a ratio between the Compton wavelength \hbar/mc and the Hubble length c/H . Although H is not a constant, $H \equiv H(t)$, in the present cosmological epoch it is $H = 74.2 \pm 3.6 \text{ (km/s)/Mpc}$. The adiabaticity condition is thus justified sufficiently far from the "phase transition" point, in this case a Big Bang.

which is nothing other than the LZMS transition probability [39]. As we approach the Big Bang singularity the parameter v starts to diverge and we expect that the adiabaticity conditions become violated. We thus expect that the excitations are created at a much higher rate near the singularity, quite similar to what happens in adiabatic dynamics near QCPs. Another possible source of adiabatic/non-adiabatic effects can be found by extending the simple de Sitter solution. In the initial stage of inflation, when the potential energy dominates the kinetic term, their ratio defines a *slow-roll parameter* which is considered to be small; this parameter is strictly zero in the de Sitter case, while it is finite in more general metrics. This slow-roll parameter can play the role of v , which defines the degree of non-adiabaticity in the system.

3.4.2 Time Evolution in a Singular Space-Time

The idea we put forward in this section can be summarized as follows: suppose we have a quantum system which evolves on a curved space with a *time-dependent* metric. Suppose that this metric has singularities in some finite number of points. It is clear intuitively that the presence of these singularities must inevitably appear in the dynamics of the system. In some cases, as we will demonstrate below, nontrivial *geometry* can mimic nontrivial *dynamics*, similar to dynamics across a QCP. A time-dependent metric of the background geometry plays the role of changing the external parameter and thus can induce non-adiabatic effects in quantum dynamics.

Our simple model here is inspired by recent interest in string theory literature on dynamics of quantum fields, mainly of string origin, in time-dependent geometries which contain some singularities. Examples include time-dependent orbifolds, null-branes, pp-wave geometries, Big Crunch, and Big Rip singularities (see Refs. [40–43]). The simplest illustrative example is the *Milne geometry* described by the following metric in 1 + 1 dimensions:

$$ds^2 = -dt^2 + v^2 t^2 dx^2. \quad (3.76)$$

We consider a quantum scalar field propagating in this metric. Its action is given by

$$S = \frac{1}{2} \int dx \int dt |tv| \left[(\partial_t \phi)^2 - \frac{(\partial_x \phi)^2}{t^2 v^2} - m^2 \phi^2 \right], \quad (3.77)$$

where we assume that the evolution starts at $t = -\infty$ and ends at $t = +\infty$. We introduced the scale factor v to emphasize its role as the adiabatic parameter. In principle it can be set to unity by appropriately rescaling space-time units. The quantum Hamiltonian corresponding to this action is therefore

$$H = \frac{1}{2|tv|} \int dx (\Pi^2 + (\partial_x \phi)^2) + \frac{m^2 |tv|}{2} \int dx \phi^2 \quad (3.78)$$

where Π is the canonically conjugate momentum.

Apparently, this type of a system can be given a simple condensed-matter interpretation: a massive scalar field describes a large variety of one-dimensional phenomena. For example, a Luttinger liquid described by the interaction parameter $K \equiv |vt|$ perturbed by some relevant perturbation (which in the strong-coupling regime of corresponding RG can be approximated by a quadratic massive term) could provide a realization of one of the physical models. In our case, both the interaction parameter K and the strength of the perturbation depend explicitly on time. From the flat-space point of view it is therefore a non-equilibrium model.

The equations of motion for the model can be put into the form of time-dependent oscillators describing different momentum modes:

$$\ddot{\varphi}_k + \Omega_k(t)\varphi_k = 0, \quad (3.79)$$

where $\varphi = \sqrt{t}\phi$ and $\Omega_k(t) = m^2 + [(k/v)^2 + 1/4]/t^2$. The solution can be given in terms of the Bessel functions of the order $\nu = ik/v$ of the argument mt .

We note that the situation is rather similar to the previous subsection, except that in the present case the quantum evolution goes across the singularity. The presence of the singularity implies that the wave functions of the system for $t < 0$ and for $t > 0$ must be properly defined and related to each other at the singularity. Several different ways to do so have been suggested in the literature: geometric (by going into covering space), operator-analytic (by properly regularizing the singularity), dimensional, etc. Without discussing this issue in detail (physically relevant quantities should not depend on the regularization prescription anyway) let us simply state the Bogoliubov coefficients, which can be defined again by the matching of in and out states:

$$\alpha_k = -\frac{\cos(A - i\pi k/v)}{\sinh(\pi k/v)}, \quad \beta_k = i\frac{\cos(A)}{\sinh(\pi k/v)} \quad (3.80)$$

where the pure phase factor A plays the role of the reflection coefficient and can be defined from the mode-matching condition at the singularity, $A = \arg[J_{ik/v}(mt)/J_{-ik/v}(-mt)]$.

The number of particles produced is given by $|\beta_k|^2$ and can be characterized as a thermal distribution with some mass-dependent temperature $T(m)$. For large m , $T(m)$ approaches a constant independent of k and therefore $n_{\text{ex}} \sim e^{-\pi m}$ whereas for small m it is independent of m and $n_{\text{ex}} \sim e^{-2\pi k/v}$. Therefore in the latter case the total number of particles $N = \sum_k n_{\text{ex}}(k)$ scales as $|v|$. Correspondingly, the in-out transition probability can be put into the LZMS form with k -dependent effective velocity. For large m , $P \sim 1 - e^{-\pi m}$ independent of k , whereas for small m , $P \sim 1 - e^{-2\pi k/v}$ independent of m .

We therefore conclude that evolution on a singular time-dependent manifold is to some extent equivalent to quantum non-equilibrium dynamical systems evolving across a phase transition. In some cases non-equilibrium dynamics of a quantum system with time-dependent parameters can be modeled by the evolution of a quantum system with time-independent parameters on a

time-dependent background geometry. This geometry can have singularities which then correspond to QCPs in the quantum system.

3.5 Summary and Outlook

In this chapter we gave an overview of different connections between certain universal equilibrium and non-equilibrium properties of continuous quantum phase transitions. It is well known that such transitions are typically characterized by singularities in thermodynamic quantities, in particular, in various susceptibilities. We discussed here that these singularities lead to the universal nonlinear dynamical response of these observables to various dynamical processes near a QCP.

In particular, we analyzed in detail two possibilities: a sudden spatially uniform quench starting at a QCP; and slow passage through a QCP. In the latter case one can also start (end) right at the QCP. In low dimensions such quantities as heat (excess energy) generated in the system or density of generated quasi-particles become universal non-analytic functions of the adiabatic parameter, which is quench amplitude for sudden quenches, quench rate for slow linear quenches, etc. In particular, if the quench $\lambda(t) \sim vt^r$ then the quasi-particle density scales as $n_{\text{ex}} \sim |v|^{d\nu/(z\nu r+1)}$. A similar scaling is valid for heat and for other thermodynamic quantities. These scalings are expected to be generically valid as long as the corresponding exponents of v remain smaller than two. Otherwise, the leading asymptotic behavior becomes quadratic, consistent with standard perturbation theory: $n_{\text{ex}} \sim v^2$. Crossover from non-perturbative to perturbative scaling happens precisely at the point where the scaling dimension of the corresponding generalized adiabatic susceptibility $\chi_{2r+2}(\lambda)$ (see Eq. (3.10)) becomes zero, i.e., when it becomes finite at the QCP. For sudden quenches the relevant susceptibility determines n_{ex} : $\chi_2(\lambda)$ is nothing but the fidelity susceptibility; the latter became recently an interesting new measure of quantum criticality, independent of the choice of the observable. For slow quenches characterized by the exponent r the relevant susceptibilities determining the scaling of the quasi-particle density and the probability of exciting the system $\chi_{2r+2}(\lambda)$ is thus a direct generalization of the fidelity susceptibility. In particular, the scaling for linear quenches $n_{\text{ex}} \sim |v|^{d\nu/(z\nu+1)}$, which can be also explained by the Kibble-Zurek arguments, [9, 14, 15], is associated with the scaling dimension of the susceptibility $\chi_4(\lambda)$. It would be very interesting to analyze situations in the future in which many-body excitations do not directly correspond to a fixed number of quasi-particles. In those situations one still expects that the scaling for the density of defects will deviate from Eq. (3.32). A possible candidate for this scenario is the non-adiabatic regime, where the density of created excitations diverges in the thermodynamic limit [12].

We illustrated how scaling results emerge from adiabatic perturbation theory. This theory has a purely geometric interpretation since time can be dropped completely from the analysis (it only implicitly enters through the rate of change of the coupling). We discussed a somewhat simplistic situation where only one coupling changes in time. One can imagine more general scenarios where several coupling constants change simultaneously. Then the expression for the transition amplitude within adiabatic perturbation theory represents a contour integral in the parameter space. In this case the expectation values of dynamical quantities will be related to the quantum geometric tensors in the Hilbert space of a system. These objects define a structure of the (complex) Riemannian metrics on the space of parameters of a system. Evaluated in the ground state, the real part of this metrics is related to the (generalized) fidelity susceptibilities, whereas its imaginary part is related to the adiabatic Berry curvature. In adiabatic perturbation theory the dynamical phase should then be modified by inclusion of the geometric Berry phase. The Berry curvature can diverge close to QCPs. It is then clear that universal features of evolution close to the phase transition advocated here should be corrected by specifying the path of the quantum evolution in the parameter space. In particular, one can expect additional corrections to the scaling laws coming from the singularities of the Berry phase [30]. We expect an interesting interplay between dynamical and geometrical effects in the scaling dependence of quantities in the linear-quench regime. Such a possibility to reduce critical dynamics to statics quantities, like quantum geometric tensors, looks very intriguing and perhaps requires a closer look beyond adiabatic perturbation theory.

We also showed that the universal dynamical response can be strongly affected by initial thermal fluctuations and that quasi-particle statistics changes the scaling laws. We discussed somewhat simplistic situations where quasi-particles are either non-interacting bosons or fermions. In general, critical dynamics at finite temperatures in the quantum critical region remains an open problem and it is clear that extra input from equilibrium properties to the dynamical response is needed, as compared to the zero temperature case.

In the last section we gave a brief outlook of connections of critical dynamics with other areas of physics like cosmology and string theory. The dynamics near QCPs is qualitatively similar to dynamics near various space-time singularities. In some cases non-equilibrium dynamics of a quantum system with time-dependent parameters can be modeled by the evolution of a quantum system with time-independent parameters. However, the background geometry of space-time is explicitly time-dependent. Quantum dynamics close to singularities of this dynamical geometry may correspond to crossing the phase transition in the static geometry.

There are many other open questions remaining. The main purpose of this chapter was to shed light on some non-equilibrium universal aspects of dynamics near critical points beyond perturbation theory and show their close

connections to static equilibrium properties. We hope that this chapter will partly stimulate further research in this exciting new area.

Acknowledgements – We acknowledge discussions with R. Barankov and C. De Grandi. A.P. was supported through the AFOSR YIP, the National Science Foundation (DMR-0907039), and the Sloan Foundation. V.G. was supported by the Swiss NSF. A.P. also acknowledges the hospitality of the Aspen Center for Physics where part of this work was done.

Bibliography

- [1] S. Sachdev, *Quantum Phase Transitions* (Cambridge University Press, Cambridge, 1999).
- [2] S. L. Sondhi, S. M. Girvin, J. P. Carini, and D. Shahar, Rev. Mod. Phys. **69**, 315 (1997).
- [3] M. Vojta, Rep. Prog. Phys. **66**, 2069 (2003).
- [4] M. Greiner, O. Mandel, T. Esslinger, T. W. Hansch, and I. Bloch, Nature **415**, 39 (2002).
- [5] M. P. A. Fisher, P. B. Weichman, G. Grinstein, and D. S. Fisher, Phys. Rev. B **40**, 546 (1989).
- [6] P. Calabrese and J. Cardy, Phys. Rev. Lett. **96**, 136801 (2006).
- [7] P. Calabrese and J. Cardy, J. Stat. Mech: Th. and Exp. **P06008**, (2007).
- [8] A. Polkovnikov, Phys. Rev. B **72**, R161201 (2005).
- [9] W. H. Zurek, U. Dorner, and P. Zoller, Phys. Rev. Lett. **95**, 105701 (2005).
- [10] P. Reimann, Phys. Rev. Lett. **101**, 190403 (2008).
- [11] M. Rigol, V. Dunjko, and M. Olshanii, Nature **452**, 854 (2008).
- [12] A. Polkovnikov and V. Gritsev, Nat. Phys. **4**, 477 (2008).
- [13] C. De Grandi and A. Polkovnikov, “Adiabatic perturbation theory: from Landau-Zener problem to quenching through a quantum critical point” in *Quantum Quenching, Annealing and Computation*, Eds. A. Das, A. Chandra, and B. K. Chakrabarti, Lect. Notes in Phys., vol. 802 (Springer, Heidelberg 2010), arXiv:0910.2236.
- [14] T. W. B Kibble, J. Phys. A **9**, 1387 (1976).

- [15] W. H. Zurek, Phys. Rep. **276**, 177 (1996).
- [16] L. C. Venuti and P. Zanardi, Phys. Rev. Lett. **99**, 095701 (2007).
- [17] S.-J. Gu and H.-Q. Lin, Europhys. Lett. **87**, 10003 (2009).
- [18] D. Schwandt, F. Alet, and S. Capponi, Phys. Rev. Lett. **103**, 170501 (2009).
- [19] C. De Grandi, V. Gritsev, and A. Polkovnikov Phys. Rev. B **81**, 012303 (2010); *ibid* arXiv:0910.0876.
- [20] A. Polkovnikov, arXiv:0806.2862.
- [21] A. Polkovnikov, Phys. Rev. Lett. **101**, 220402 (2008).
- [22] G. Rigolin, G. Ortiz, and V. H. Ponce, Phys. Rev. A **78**, 052508 (2008).
- [23] D. Sen, K. Sengupta, and S. Mondal, Phys. Rev. Lett. **101**, 016806 (2008).
- [24] R. Barankov and A. Polkovnikov, Phys. Rev. Lett. **101**, 076801 (2008).
- [25] A. Kitaev, Ann. Phys. **321**, 2 (2006).
- [26] A. H. Castro Neto, F. Guinea, N. M. R. Peres, K. S. Novoselov, and A. K. Geim, Rev. Mod. Phys. **81**, 109 (2009).
- [27] J. Dziarmaga, Phys. Rev. Lett. **95**, 245701 (2005).
- [28] G. Rigolin, G. Ortiz, and V. H. Ponce, Phys. Rev. A **78**, 052508 (2008).
- [29] R. Shankar, *Principles of Quantum Mechanics* (Springer, New York, 1994).
- [30] M. Tomka, V. Gritsev, and A. Polkovnikov, Geometric effects in quantum nonequilibrium dynamics, in preparation.
- [31] M. Eckstein and M. Kollar, arXiv:0911.1282.
- [32] D. Rossini, A. Silva, G. Mussardo, and G. E. Santoro, Phys. Rev. Lett. **102**, 127204 (2009).
- [33] S. Sotiriadis, P. Calabrese, and J. Cardy, Europhys. Lett. **87**, 20002 (2009).
- [34] I. Bloch, J. Dalibard, and W. Zwerger, Reviews of Modern Physics **80**, 885 (2008).
- [35] L. D. Landau and E. M. Lifshitz, *Statistical Physics, Third Edition, Part 1: Volume 5* (Butterworth-Heinemann, ADDRESS, 1980).
- [36] S. Lukyanov, Mod. Phys. Lett. **A12**, 2543 (1997).

- [37] A. Linde, Lect. Notes Phys. **738**, 1 (2008).
- [38] T.S. Bunch and P. C. W. Davies, Proc. R. Soc. Lond. Ser. A **360**, 117 (1978).
- [39] L. Landau, Phys. Z. Sovjetunion **1**, 88 (1932); C. Zener, Proc. R. Soc. London, Ser. A **137**, 696 (1932); E. Majorana, Nuovo Cimento **9**, 43 (1932); E. C. G. Stückelberg, Helv. Phys. Acta **5**, 369 (1932).
- [40] B. Craps and O. Evnin, JHEP **0804**, 021 (2008).
- [41] H. Liu, G. Moore, and N. Seiberg, JHEP **0206**, 045 (2002).
- [42] N. A. Nekrasov, Surveys High Energ. Phys. **17**, 115 (2002).
- [43] A. J. Tolley and N. Turok, Phys. Rev. D **66**, 106005 (2002).

4

Fractionalization and Topological Order

Masaki Oshikawa

Institute for Solid State Physics, University of Tokyo, Kashiwa 277-8581, Japan

4.1 Quantum Phases and Orders

States of matter are classified into phases, which are separated by phase transitions. In other words, sharp, well-defined phase transitions make it possible to distinguish different phases unambiguously.

Although the theory of phase transitions was developed initially for classical phase transitions, recently there has been a surge in interest in quantum phase transitions (QPTs) at zero temperature. QPTs are driven by *quantum fluctuations*, instead of thermal fluctuations. Despite this physical difference, there is often a parallel between QPTs and their classical counterpart. In fact, a QPT in d -dimensions is often mathematically equivalent to a classical phase transition in $d + 1$ -dimensions. In particular, a standard phase transition, quantum or classical, can be understood as the border between an ordered phase and a disordered phase; it is characterized by local order parameters and their fluctuations. These transitions fall into the category of the *Landau-Ginzburg-Wilson* type.

On the other hand, there are also QPTs which are outside this paradigm. Indeed, for some QPTs, it is not possible to find any local order parameter. Then we have difficulty in understanding the existence of the transition. As a resolution, the notion of *topological order* was introduced [1]. There must be something different between the phases which are separated by a QPT. When we cannot identify that something in terms of conventional local order parameter, we call it topological order.

In this chapter, I will try to illustrate the notion of topological order through a few examples and demonstrate its usefulness in understanding QPTs. I do not attempt to describe technical details of calculations. Instead, I intend to provide a perspective connecting various issues, to motivate study of this intriguing subject.

4.2 Conventional Quantum Phase Transitions: Transverse Ising Model

Before discussing the issue of topological order, it is instructive to review conventional order and associated QPTs.

One of the most fundamental models describing QPTs is the quantum Ising model. We consider spin 1/2's on a lattice, say, the linear chain in 1 dimension or the square lattice in 2 dimensions. The Hamiltonian of the model is given by

$$\mathcal{H} = -J \sum_{\langle j,k \rangle} \sigma_j^z \sigma_k^z - \Gamma \sum_j \sigma_j^x, \quad (4.1)$$

where σ_j^α is the spin operator (Pauli matrices) at site j , and $\langle j, k \rangle$ refer to the nearest neighbor pairs of lattice sites. This model is called the transverse Ising model, as the second term corresponds to transverse magnetic field applied perpendicular to the axis of the Ising interaction.

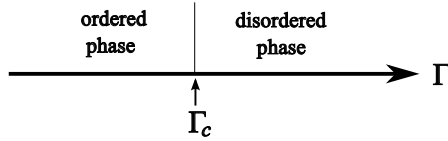
In the following, we assume the ferromagnetic coupling $J \geq 0$, and $\Gamma \geq 0$. The first term is the usual Ising interaction, which favors parallel alignment between the neighboring spins. If $\Gamma = 0$ and $J > 0$, the ground state is given by the ferromagnetic states in which all the spins take the same value $\sigma_j^z = 1$ or $\sigma_j^z = -1$. Correspondingly, the ground state is doubly degenerate.

As the transverse field Γ is increased from zero, it flips each spin between $\sigma_j^z = 1$ and $\sigma_j^z = -1$. This introduces quantum fluctuations. In the limit of $\Gamma/J = \infty$, or equivalently $J = 0$ and $\Gamma > 0$, all the spins are aligned in x -direction: $\sigma^x = 1$ in the ground state. The ground state in this case is unique. Although the spins are completely “ordered” in terms of σ^x , the ground-state spin configuration appears disordered in the σ^z -basis.

Thus we find that the nature of the ground state is very different between the two limits $\Gamma/J = 0$ and $\Gamma/J = \infty$. Do these two limits correspond to different phases? As discussed above, the question is whether there is a sharp QPT between the two limits; if there is, we can distinguish two phases.

In fact, the transverse Ising model in one dimension is exactly solvable via the Jordan-Wigner transformation [2, 3]. The exact solution indeed shows a second-order phase transition at a critical transverse field $\Gamma = \Gamma_c = J$. With this solution, we can define the ordered phase $\Gamma < \Gamma_c$ and the disordered phase $\Gamma > \Gamma_c$. There is no exact analytical solution in higher dimensions. Nevertheless, there is still a sharp phase transition between the ordered and disordered phases.

The presence of the QPT is expected, without an elaborate analysis, on general grounds as follows. In both limits, the system is gapful, i.e., there is a nonzero gap above the ground state(s). However, the ground state is unique at $\Gamma/J \rightarrow \infty$, while it is doubly degenerate at $\Gamma/J = 0$. Thus, between the two limits, there must be a closing of the gap in some way. This should give a QPT. The double degeneracy in the ordered phase actually reflects

**FIGURE 4.1**

Ground state phase diagram of the transverse Ising model (4.1). For a small transverse field Γ , there is a long-range order of σ_j^z , and there are two degenerate ground states. A large transverse field destroys the long-range order, and the ground state is unique. There is a critical point $\Gamma = \Gamma_c$ separating the two phases.

spontaneous breaking of the Z_2 symmetry $\sigma_j^z \rightarrow -\sigma_j^z$ of the model. Namely, the symmetry is spontaneously broken in the ordered phase but unbroken in the disordered phase. This also implies the existence of two distinct phases and a QPT separating them.

The quantum phase diagram of the transverse Ising model is quite similar to that of classical Ising model at finite temperature, where the temperature introduces thermal fluctuations instead of the quantum fluctuations brought on by the transverse field. In fact, the correspondence is not just an analogy, but can be shown to be a mathematical equivalence between the two: the transverse Ising model in d dimensions is equivalent to the classical Ising model in $d + 1$ dimensions.

In both classical and quantum transverse Ising models, if a nonzero magnetic field in the z -direction is introduced, the phase transition is smeared into a smooth crossover. Then the two phases are no longer distinct. This is natural, since the magnetic field destroys the Z_2 symmetry and thus spontaneous symmetry breaking does not occur.

4.3 Haldane-Gap Phase and Topological Order

4.3.1 Quantum Antiferromagnets

The antiferromagnetic Heisenberg model

$$\mathcal{H} = J \sum_{\langle j,k \rangle} \vec{S}_j \cdot \vec{S}_k \quad (4.2)$$

is a fundamental model in magnetism. If the model is defined on a bipartite lattice, the ground state of the classical model is the Néel state. The Néel ground state for the Heisenberg model is infinitely degenerate, as the direction

of one spin can be taken arbitrarily. One of the degenerate Néel ground states is given by spins alternately pointing up ($+z$) and down ($-z$).

Let us consider the quantum case with $S = 1/2$. We can also consider the Néel state, with spins parallel to z -axis, in the quantum model,

$$|\uparrow\downarrow\uparrow\downarrow\dots\rangle. \quad (4.3)$$

However, in the quantum model, the action of the xy components

$$S_j^x S_k^x + S_j^y S_k^y = \frac{1}{2}(S_j^+ S_k^- + S_j^- S_k^+) \quad (4.4)$$

flips spins on neighboring sites. Thus the Néel state cannot be an exact eigenstate of the Hamiltonian and hence cannot be the ground state. This can be regarded as a destruction of Néel order by quantum fluctuations. A major problem in quantum magnetism is to identify the ground state of the quantum antiferromagnet, in which quantum fluctuations are important. In general, this is a highly nontrivial problem of quantum many-body theory.

On the other hand, some aspects of quantum antiferromagnets can be seen in systems with small number of spins. In particular, a pair of $S = 1/2$ spins coupled antiferromagnetically can be solved exactly. The ground state is the unique singlet state

$$\frac{1}{\sqrt{2}}(|\uparrow\downarrow\rangle - |\downarrow\uparrow\rangle). \quad (4.5)$$

The singlet state of the spin pair is invariant under rotation; this is in contrast to the classical Néel state, which does change under rotation.

The singlet state is also a typical state representing quantum entanglement; the state cannot be written as a single direct product of states for two spins. The singlet state of a pair of $S = 1/2$ spins, which is also referred to as *valence bond*, will be very important in many applications. Graphically, it is often represented by a bond connecting two circles, each circle denoting $S = 1/2$. The circle is sometimes omitted, so that the bond represents the singlet.

There are several approaches to understand the ground state of a quantum antiferromagnet. The traditional approach, spin-wave theory, is formally based on a $1/S$ expansion [4]. Physically speaking, it starts from the Néel ordered ground state in the classical limit, and includes quantum fluctuations, usually to leading order in the $1/S$ -expansion. Although it might appear to be a poor method for $S = 1/2$, which is the case in many magnetic materials, spin-wave theory works remarkably well even for the $S = 1/2$ antiferromagnetic Heisenberg model on the square lattice (two dimensions).

However, it is possible that the quantum fluctuations completely destroy Néel order even in the ground state. In such a case, the framework of the spin-wave theory becomes invalid. The ground state of a quantum antiferromagnet without Néel (or any other conventional) order is often called a *quantum spin liquid*. In this chapter, I will discuss a few examples of quantum spin liquids. We may distinguish two classes of quantum spin liquids: gapful and gapless.

If there is a nonzero excitation gap above the ground state (which may be degenerate), the system is said to be gapful. On the contrary, if there is a continuum of excited states just above the ground state(s) without a finite gap, the system is said to be gapless. When the system is gapful, the ground state is stable against various small perturbations, unless the gap is closed. When the system is gapless, the ground state is susceptible to perturbations, which would generically open the gap. Recalling the transverse Ising model example, A gapful state generally belongs to a phase, and a gapless state may be regarded as a quantum critical point (QCP) separating distinct phases. Correlation functions, such as the spin-spin correlation function, often decay algebraically in a gapless state.

In order to describe quantum spin liquids, we need to develop an approach different from the traditional spin-wave theory. One of the useful starting points to deal with quantum spin liquids is the singlet pair of $S = 1/2$ spins, or valence bonds. Namely, we can consider the ground state of quantum spin systems in terms of valence bonds. As we discussed above, the antiferromagnetic Heisenberg exchange energy between two neighboring spins, say at sites j and k , is minimized if these two sites belong to the same valence bond, namely if the two spins form a singlet. However, in this case, the spin j cannot form a singlet with the other neighboring spins and the interaction energy is not minimized for corresponding bonds. Although the Heisenberg antiferromagnet on a bipartite lattice is not frustrated in the classical sense, there is still a certain kind of frustration in the quantum Heisenberg antiferromagnet.

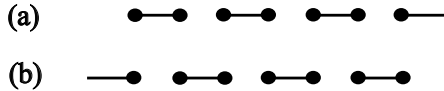
It is useful to introduce *valence-bond basis states*, each of which has a fixed valence-bond configuration covering all the spins. We can introduce more general states, as superpositions of valence-bond basis states. In fact, allowing all the valence-bond configurations, including those with long-ranged valence bonds connecting distant sites, the valence-bond basis is overcomplete in the total spin-singlet sector. Thus, any state which is a total spin singlet can be written as a superposition of the valence-bond basis states [5]. In other words, just being a superposition of valence-bond basis states does not imply anything beyond being a total-spin singlet. The superposition of valence-bond basis states can have long-range order, such as Néel order.

4.3.2 Quantum Antiferromagnetic Chains and the Valence Bonds

Let us consider the one-dimensional version of the Heisenberg antiferromagnet. The Hamiltonian is given as

$$\mathcal{H} = J \sum_j \vec{S}_j \cdot \vec{S}_{j+1}, \quad (4.6)$$

where $J > 0$. This model does not exhibit Néel order even in the ground state, and provides an example of a quantum spin liquid. The destruction of Néel order can be seen within the framework of spin-wave theory; the reduction

**FIGURE 4.2**

Nearest-neighbor valence-bond state of the $S = 1/2$ chain. There are two such states, (a) and (b), which correspond to dimerized states.

of the magnetization to leading order of the $1/S$ expansion actually diverges in one dimension [4]. In fact, Néel order is absent in one dimension, owing to strong quantum fluctuations. Furthermore, there is an interesting dependence on the spin quantum number.

First we discuss the model for $S = 1/2$. If we only allow valence bonds connecting the nearest-neighbor pairs, there are only two valence-bond basis states, as shown in Fig. 4.2. They represent dimerized states, which break the translation symmetry.

On the other hand, the $S = 1/2$ model can be solved exactly via the Bethe Ansatz, and its long-distance asymptotic properties are precisely described by the field-theory method of bosonization. The ground state is unique and does not break the translation symmetry. The system is gapless, and the correlation functions also exhibit critical behavior, power-law decay.

The critical behavior of the $S = 1/2$ Heisenberg antiferromagnetic chain may be understood by considering the following generalized model with a bond-alternation parameter δ :

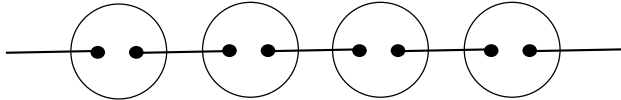
$$\mathcal{H} = J \sum_j [1 + \delta(-1)^j] \vec{S}_j \cdot \vec{S}_{j+1}. \quad (4.7)$$

For $\delta \neq 0$, the translation symmetry of the Hamiltonian is explicitly broken, reduced to the invariance under translation by two sites. In particular, for $\delta = \pm 1$, the system consists of isolated dimers, and one of the completely dimerized states in Fig. 4.2 is the ground state. As δ is changed from the limiting case ± 1 , the valence-bond basis state is no longer the exact ground state. Nevertheless, we can expect that the ground state keeps the same dimerized structure. The standard Heisenberg antiferromagnetic chain (4.6) can be regarded as the QCP separating the dimerized phases with the opposite dimerizations.

In terms of the valence-bond basis states, the ground state is a superposition of valence-bond basis states including long-range valence bonds. The distribution of the range of the valence bonds obeys a power law, reflecting the critical nature [6].

4.3.3 AKLT State and the Haldane Gap

The construction of a candidate ground state in terms of valence bonds turns out to be quite different for the $S = 1$ case.

**FIGURE 4.3**

Construction of the $S = 1$ AKLT state. Each dot is an $S = 1/2$ spin, and the two $S = 1/2$ spins connected by a straight line represent a singlet. Each circle denotes symmetrization of the wavefunction; symmetrization of two $S = 1/2$ spins gives an $S = 1$ state.

Of course, we can also construct completely dimerized states similarly to the $S = 1/2$ case. However, for the $S = 1$ chain, we can construct a translation-invariant state in terms of valence bonds, as given by Affleck, Kennedy, Lieb, and Tasaki (AKLT) [7]. The construction starts from a completely dimerized state of an $S = 1/2$ chain, shown in Fig. 4.2. Then, the wavefunction of every neighboring pair of $S = 1/2$ spins that does not form a singlet is symmetrized. The resulting state is a legitimate quantum state of the $S = 1$ chain, and is invariant under lattice translation. This construction is illustrated in Fig. 4.3. This AKLT state represents a quantum liquid. In fact, correlation functions of local observables, such as the spin-spin correlation function, decay exponentially.

The AKLT state is not the exact ground state of the standard $S = 1$ Heisenberg antiferromagnetic chain (4.6). However, it is the exact ground state of the modified Hamiltonian (AKLT model)

$$\mathcal{H}_{\text{AKLT}} = J \sum_j [\vec{S}_j \cdot \vec{S}_{j+1} + \frac{1}{3}(\vec{S}_j \cdot \vec{S}_{j+1})^2]. \quad (4.8)$$

It is easy to see that the AKLT state is an exact ground state of this model, as follows. The interaction at each bond in the AKLT model can be written as

$$\vec{S}_j \cdot \vec{S}_{j+1} + \frac{1}{3}(\vec{S}_j \cdot \vec{S}_{j+1})^2 = 2P_2^{(j,j+1)} - \frac{2}{3}, \quad (4.9)$$

where $P_2^{(j,j+1)}$ is the projection operator onto the states in which $\vec{S}_j + \vec{S}_{j+1}$ has total spin 2.

By quantum mechanical addition of spin, the total spin for the two sites can take on the values 0, 1, or 2. In the AKLT state, because two $S = 1/2$ spins form a singlet, the total spin is given by the addition of the two remaining $S = 1/2$ spins. Thus the total spin for the two sites j and $j + 1$ can be either 0 or 1, but cannot be 2. It follows that the AKLT state is a ground state with respect to the interaction at every bond simultaneously, and therefore is a ground state of the entire Hamiltonian (4.8). Although it is not straightforward to prove, it was also shown that the ground state is separated from the excited states by a nonzero gap [7].

While the AKLT model is different from the standard Heisenberg chain (4.6), we may expect that their properties are similar. In fact, many theoretical, experimental, and numerical studies of the standard model (4.6) with $S = 1$ confirmed that it shares several characteristics of the AKLT model, including the exponentially decaying correlation functions. I will discuss more about the common characteristics of these models later.

Generalizing this construction, it is easy to see that a similar translation-invariant AKLT state exists for any integer spin S . On the other hand, for a half-integer S , states with various degree of dimerization can be constructed in a similar manner, but not a translation-invariant state. This suggests that the standard Heisenberg antiferromagnetic chain (4.6) is gapped for an integer S , like the corresponding AKLT model, but is gapless at the QCP for a half-integer S . This intriguing difference between integer and half-integer S was originally predicted by Haldane [8] based on the nonlinear sigma model. The excitation gap, characteristic of integer-spin antiferromagnetic chains, is now called the *Haldane gap*.

4.3.4 Haldane Phase and Topological Order

The AKLT state was named the *valence-bond solid* (VBS) phase by the original authors, reflecting the apparently static configuration of valence bonds in the AKLT construction. However, the AKLT state has no long-range order in the conventional sense, and would be better regarded as a quantum spin liquid than a solid. The absence of local order parameter seems to imply that the AKLT state is just disordered. However, it is not that simple.

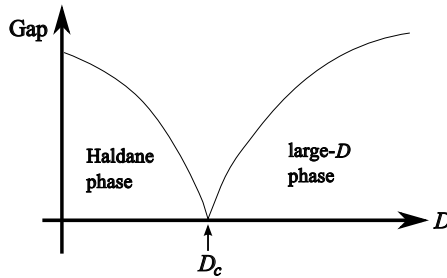
First, numerical studies show that there is no QPT between the standard Heisenberg chain (4.6) and the AKLT model when the coefficient of the bi-quadratic term is changed from 0 to 1/3. This supports our expectation that the two models are similar; we can regard them as belonging to the same phase.

Let us consider the anisotropic generalization of the standard Heisenberg chain (4.6):

$$\mathcal{H} = \sum_j J(S_j^x S_{j+1}^x + S_j^y S_{j+1}^y) + \lambda S_j^z S_{j+1}^z + D(S_j^z)^2. \quad (4.10)$$

In the large- D limit ($D \rightarrow \infty$), all the spins are restricted to the $S_j^z = 0$ state. There is no long-range order in this state. Thus, concerning the local order parameters, there is no distinction between the large- D limit and the Heisenberg point $\lambda = 1, D = 0$.

Nevertheless, numerical study shows that there is a gapless QCP between the Heisenberg point and the large- D limit [9]. This is not accidental, and the QCP cannot be avoided, for example by changing λ . Thus there is a critical line in the λ - D plane. This implies that the Heisenberg point and the large- D limit belongs to two different phases, the *Haldane phase* and the

**FIGURE 4.4**

Schematic diagram of the excitation gap as a function of the uniaxial anisotropy D , in the model (4.10), with $\lambda = 1$ fixed. There is a quantum critical point $D = D_c \sim J$ where the gap closes. Although both sides are apparently disordered and cannot be distinguished by any local order parameter, they can be regarded as distinct phases separated by the QCP.

large- D phase, respectively. This is the case, even though both phases cannot be distinguished by any local order parameter.

This example suggests that we have to generalize the concept of order. We say that the Haldane phase has topological order, which makes this phase distinct from the trivial large- D phase.

In general, when we find a phase separated from other phases by QPTs which cannot be identified with any local order parameter, we consider the phase as characterized by topological order. One might wonder if the introduction of this new jargon is just a tautology. However, as we will discuss in the following, topological order is often accompanied by various peculiar features that make our new terminology important for physical understanding.

4.3.5 Edge States

One of the peculiar characteristics of the Haldane phase is the appearance of free spin degrees of freedom at open ends. This can be understood naturally, in terms of the AKLT state.

Let us consider the $S = 1$ AKLT state on an open chain. At the leftmost site, one of the $S = 1/2$ spins forms a valence bond with an $S = 1/2$ spin in the neighboring site. However, the remaining $S = 1/2$ spin has no partner to form a valence bond, and remains free. That is, the AKLT state is the ground state whether the remaining $S = 1/2$ spin takes either an up or down state. Since the same applies to the right end, the ground state is 4-fold degenerate.

The free spin $1/2$ at each end is often called an *edge state*, in analogy with the gapless mode at open boundaries of quantum Hall systems. Trivial disordered states, such as the large- D state, do not have such edge states. The

existence of the edge state can also be regarded as a signature of topological order, although not every topologically ordered phase has an edge state.

4.4 RVB Quantum Spin Liquid and Topological Order

4.4.1 Introduction to RVB States

As another example of topologically ordered state, here we discuss the *resonating-valence-bond* (RVB) spin liquid state. This problem also has an interesting history.

Let us come back to the problem of $S = 1/2$ Heisenberg antiferromagnets. As we have discussed previously, its ground state is nontrivial due to quantum fluctuations. For the two-spin problem, the ground state is exactly obtained as the singlet valence-bond state.

For more than two spins, a fixed configuration of valence bonds gives a valence-bond crystal state, which breaks the translation symmetry of the system. However, the ground state might still be given by a superposition of the valence-bond basis states. In fact, the ground state for the 4-spin system on a single square is exactly solvable and given by

$$|\Psi_0\rangle = \frac{1}{\sqrt{2}} (| \! || \rangle + | = \rangle), \quad (4.11)$$

i.e., the superposition of two states with parallel valence-bond configurations on the square. Each state given by the parallel valence-bond configuration is not an eigenstate of the Hamiltonian, and thus not the ground state. An application of the Hamiltonian flips the valence bonds on the square between horizontal and vertical configurations of two parallel valence bonds. The ground state is hence given by the superposition as in Eq. (4.11).

Now let us consider a two-dimensional lattice of infinite size. Even if we only allow nearest-neighbor valence bonds, which we call dimers, there are many possible dimer coverings of the entire lattice. For each dimer covering of the lattice, there is a valence-bond basis state. The Hamiltonian flips a pair of vertical valence bonds on a plaquette to a pair of horizontal valence bonds and vice versa. Thus, generalizing the exact result for the 4-spin problem, we might expect that the ground state is given by a superposition of many possible valence-bond states.

If this was actually the case, the resulting ground state would not have long-range magnetic order. Such a hypothetical state is called the resonating-valence-bond (RVB) state. The RVB state was proposed by Anderson as a possible ground state of the Heisenberg antiferromagnetic model [10]. Interest in the RVB state was revived after the discovery of high- T_c superconductivity in 1986. It was conjectured that the ground state of the Heisenberg antiferro-

magnet on a square lattice is an RVB state, and superconductivity might be understood by hole-doping of the RVB state.

4.4.2 Quantum Dimer Model

While it was a very stimulating proposal, there were many obstacles in pursuing the idea further. First, it turned out that the ground state of the standard $S = 1/2$ Heisenberg antiferromagnet on the square lattice has nonvanishing Néel order [11]. Of course Néel order is reduced by quantum fluctuations, but it still remains positive. Nevertheless, we can still hope that, in the presence of frustration, for example by considering a triangular lattice or a square lattice with diagonal interaction, the ground state might become an RVB state.

However, there are several technical difficulties in analyzing quantum spin systems in terms of the valence-bond basis. If we include all elements of the valence-bond basis with arbitrarily long valence bonds, it is overcomplete. Thus any state which is a singlet under a global $SU(2)$ transformation can be written as a superposition of valence-bond basis states. This includes states with long-range magnetic order. If so, the RVB would be a rather meaningless concept. Thus we usually restrict the valence-bond basis to exclude valence bonds that are too long-range. In the most restrictive choice, only the valence bonds between nearest neighbors are allowed. In two and higher dimensions, this still gives a number of basis states that grows exponentially as a function of the system size. However, in the context of the quantum spin system, there is not much justification for the restriction to the nearest-neighbor valence bond.

As another problem, the valence-bond basis is nonorthogonal: the overlap between two valence-bond states corresponding to different dimer coverings does not vanish.

The *quantum-dimer model* is introduced as a simplified version of the problem. The model is described in terms of nearest-neighbor dimer states. We define two dimer states to be orthogonal if their dimer configurations are not completely identical. While the relation to the quantum antiferromagnet, which was our original interest, is not completely clear, the quantum dimer model does represent a nontrivial and interesting quantum many-body problem. The Hamiltonian of the quantum dimer model on a square lattice, for example, is given as

$$\mathcal{H} = \sum_{\square} J(|\square\rangle\langle=| + |=\rangle\langle|\square|) + V(|\square\rangle\langle|\square| + |=\rangle\langle=|). \quad (4.12)$$

Here the sum is taken for every plaquette in which $|\square\rangle$ and $|=\rangle$, representing the states with two parallel dimers covering the plaquette vertically and horizontally, respectively. The second term is a potential energy suppressing (or favoring, for $V < 0$) parallel dimer pairs on each plaquette, while the first term is a kinetic term which flips the orientation of parallel dimer pairs on the plaquette.

By definition, the quantum dimer model excludes the possibility of Néel ordering, which is often dominant in quantum spin systems. Thus we might hope that an RVB liquid phase can be more easily realized in the quantum dimer model. On the other hand, in the quantum dimer model, the configuration of dimers can still be ordered. For example, in the model (4.12), all the plaquettes are occupied by parallel pairs of dimers in the limit $V \rightarrow -\infty$. Such ordered phases are generally called *valence-bond-crystal* (VBC) phases.

Rokhsar and Kivelson [12] have shown that, at the special point $J = V$, the ground state can be written exactly as the superposition of all possible valence-bond states, corresponding to dimer coverings. This appears to be a realization of the RVB liquid scenario, in terms of the quantum dimer model.

However, it turned out that the Rokhsar-Kivelson point for the square lattice corresponds to a QCP between two VBC phases, and does not represent a stable liquid phase with a gap as expected.

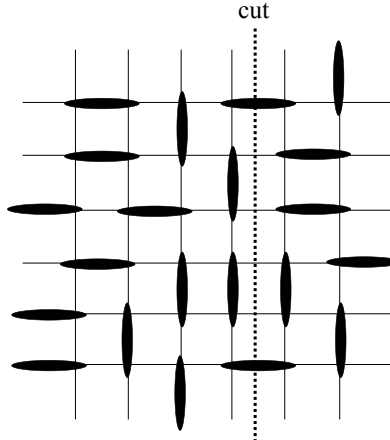
4.4.3 Commensurability and Spin Liquids

One of the reasons why it was difficult to find the RVB liquid phase may be the following. A quantum spin model can be mapped to a quantum many-particle system, for example, for $S = 1/2$ by identifying $S^z = -1/2$ with an empty and $S^z = 1/2$ with an occupied site. The corresponding mapping of a quantum dimer model is less straightforward, but it can still be mapped to a certain quantum many “particle” model. The general feature of an antiferromagnet at zero field, and the corresponding quantum dimer model, is that the quantum many-particle model after the mapping is at half-filling; namely the particle number per unit cell is $1/2$ (modulo integer).

A stable ground state with a nonzero gap would correspond to an insulator, in terms of a quantum many-particle system. If the system is a conductor, there should be gapless excitations. In order to realize an insulator ground state with a gap, we expect, at least naively, that the particles must be locked by the lattice to become immobile. If that is the case, the ground state must break the translation symmetry spontaneously, so that the unit cell of the ground state contains an integer number of particles. In fact, well-known stable ground states with a gap do break the translation symmetry spontaneously, and consistent with the above expectation. Those ground states include the Néel ground state for an easy-axis XXZ antiferromagnet, and various VBC phases.

The expectation that an insulator ground state with a gap requires spontaneous symmetry-breaking of translation symmetry is supported by more than just hand-waving. Namely, for a wide class of models, the generalized Lieb-Schultz-Mattis (LSM) theorem holds [13]. It corresponds roughly to the following statement.

Consider a quantum many-particle system on a finite but large system with periodic boundary conditions. When the particle den-

**FIGURE 4.5**

An example of the valence-bond basis (dimer covering) on the square lattice. Black ellipses represent dimers. A cut (dotted line) is introduced in vertical direction, and the number of dimers crossing the cut is counted, 2 in this example. Although the number itself is not conserved by the application of the kinetic term (dimer flipping), its parity is conserved.

sity is at half-filling, and if the system is gapped, there must be at least two nearly-degenerate ground states below the gap.

4.4.4 Topological Degeneracy of the RVB Spin Liquid

“Nearly degenerate” means that the difference in energy goes to zero as the system size is increased. The generalized LSM theorem apparently implies that the ground state exhibits spontaneous symmetry breaking. If this is the case, it would exclude the possibility of realizing an RVB quantum liquid which should not break any symmetry; this might be related to the difficulty in finding an RVB spin liquid state. However, there can be a loophole: if the degenerate ground states cannot be distinguished by any local order parameter then the degeneracy of the ground states does not correspond to spontaneous symmetry breaking. Such a case of ground state degeneracy is said to reflect topological order.

In fact, it was pointed out that, if the RVB spin liquid state is realized, the ground state must be nearly degenerate under periodic boundary conditions [14]. For the sake of illustration, we consider again the quantum dimer model on the square lattice.¹ We assume that the RVB liquid phase is real-

¹Note that the gapped RVB liquid phase is not actually realized on the square lattice.

ized, and the ground state is given by a superposition of many valence-bond states with different dimer covering. Let us consider a line which cuts the system along one of the lattice axes, as in Fig. 4.5. We choose the line so that it cuts through the middle of bonds. For a given valence-bond state, we can count the number of valence bonds crossing the cut. The number itself is not conserved because of the dimer kinetic term in the Hamiltonian. Nevertheless, the parity of the number of the crossing valence bonds is conserved, because flipping changes the number by 0 or ± 2 .

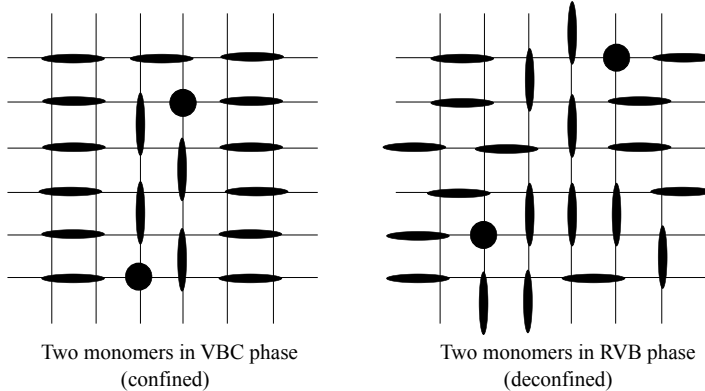
Thus, all the valence-bond states can be classified into even and odd sectors, with respect to the number of the valence bonds crossing the cut. The Hamiltonian does not mix states in the even sector with those in the odd sector; it can be diagonalized separately in each sector. When the RVB liquid phase is realized, the lack of long-range order implies that the ground state energy should become insensitive to the parity, in the thermodynamic limit. Thus the ground states in the two sectors must be degenerate. This degeneracy would satisfy the general statement, without spontaneous symmetry breaking.

This derivation of degeneracy requires periodic boundary conditions in the direction orthogonal to that of the cut. Otherwise, in one of the sectors, there is no allowed valence-bond basis state. Actually, the ground state would be unique under open boundary conditions, even in the RVB liquid phase. The ground state would be two-fold degenerate on a cylinder, in which periodic boundary conditions are imposed in only one direction. On a torus, where periodic boundary conditions are imposed in both directions, the ground state degeneracy is $2 \times 2 = 4$ fold because the cut can be taken in either direction.

The ground-state degeneracy depending on the topology of the space on which the model is defined is referred to as *topological degeneracy*. It cannot be a consequence of standard spontaneous symmetry breaking, which would lead to ground-state degeneracy independent of the topology. The topological degeneracy signals the existence of topological order. The topological degeneracy is unphysical in the sense that it is not distinguished by any local order parameter. Nevertheless, topological degeneracy characterizes distinct topological phases. For example, let us consider a trivial disordered phase with a unique ground state. As long as the system is adiabatically connected to this phase, the ground state must remain unique in any topology. Thus, if the system exhibits topological degeneracy in some parameter regime, there must be a QPT between this regime and the trivial phase. The QPT itself should be independent of topology; once the existence of the transition is inferred, the phase transition should be observed even in a topology, such as an open disk, for which there is no change in degeneracy between the both sides.

Thus, the generalized LSM theorem allows a system at half-filling to have a nonzero excitation gap, if there is spontaneous symmetry breaking or topological order. The RVB spin liquid state with a gap is possible, as it is expected to have topological order.

In fact, many years after the original RVB proposal, it was demonstrated by Moessner and Sondhi [15] that the quantum-dimer model on the triangular

**FIGURE 4.6**

Two monomers (filled circles) created in the VBC (left panel) and RVB spin liquid (right panel) phases. Separating the monomers in the VBC phase creates dislocation, which costs energy proportional to the distance between the monomers. This leads to confinement of monomers in the VBC phase, but in the RVB phase monomers are deconfined.

lattice has a gapped RVB spin liquid phase. Interestingly, an exactly solvable model which shows essentially the same phase as the RVB spin liquid was given independently by Kitaev [16], with a quite different motivation related to quantum computation.

4.4.5 Fractionalization in the RVB Spin Liquid

Here I discuss an intriguing physical property of the RVB spin liquid, given the existence of such a phase. Let us consider the RVB liquid phase in the quantum dimer model. In the quantum dimer model, by definition, each site belongs to a dimer. However, we can generalize the quantum dimer model so that it allows monomer sites, i.e., those not covered by any dimer.

If we regard the quantum dimer as the basic building block or particle of the quantum dimer model, the monomer corresponds to a half of the particle. If the monomer behaves as a quasi-particle, it would be a fractionalized excitation.

However, just the generalization of the quantum dimer model to allow a monomer does not imply the existence of a fractionalized excitation. In order to illustrate the point, let us discuss a VBC phase, in which the dimers are regularly ordered. Suppose we remove one dimer from the ground state, to create two monomers. They can be separated apart by shifting dimers. However, this creates a string of dimers which has a mismatch with the surrounding crystal of the valence bonds, as shown in Fig. 4.6. This implies an energy increase

proportional to the distance between the two monomers. Thus the monomers are confined in the VBC phase, and do not behave as elementary excitations. The confinement of monomers is quite similar to confinement in gauge theory; in fact the quantum dimer model may be related to Z_2 gauge theory.

On the other hand, in the RVB liquid phase, separation of two monomers should not lead to a similar increase of energy linear with the distance, because no order is disturbed by the motion of monomers. Thus the monomers are expected to move freely. Again, this is quite analogous, and in fact related, to deconfinement in gauge theory. Therefore, we expect the RVB liquid phase to exhibit fractionalized elementary excitations. If we assign unit charge to a dimer, the fractionalized monomer carries $1/2$ charge.

4.5 Fractionalization and Topological Order

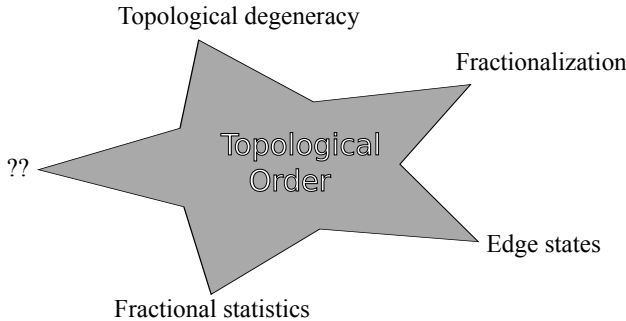
4.5.1 What is Topological Order?

We have seen a few examples of topologically ordered states. However, the reader might still ask the question, “What is topological order, after all?” Actually, I do not know a clear-cut answer to this question. Perhaps we are still looking for an ultimate definition of topological order. Even if there is no clear definition, I believe that topological order is a useful working hypothesis. I think it might be analogous to the concept of M-theory in string theory. M-theory seeks to unify the five known self-consistent string theories in a single description. Although M-theory remains an open problem, its existence is inferred from various pieces of circumstantial evidence, such as the astonishing dualities found between apparently quite different theories. Such dualities suggest that, behind the known theories, there is a yet unknown theory which unifies them. This is called M-theory.

In the quantum many-body problem, some systems exhibit peculiar features which cannot be understood with the conventional notion of order. We have discussed some of these features in this chapter: the existence of QPTs without a local order parameter, edge states, fractionalization, and topological degeneracy. Topological order was introduced as a hypothetical concept which is behind these peculiar features, as illustrated in Fig. 4.7. This is not the final answer, but perhaps is just a starting point for the question, “What is topological order?”

4.5.2 Fractionalization: General Definition

In order to understand topological order better, it would be helpful to see relations between the apparently very different peculiar features which are thought to be related to it.

**FIGURE 4.7**

An illustration: topological order is introduced as an underlying concept to unify various peculiar features.

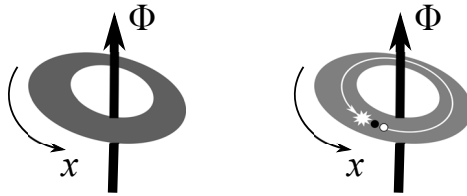
Here I will discuss the relation between two such features, fractionalization and topological degeneracy. Although at a first glance they might seem unrelated, fractionalization implies topological degeneracy under certain assumptions.

First, let us review the definition of fractionalization. In general, in the quantum many-body problem, a model is defined in terms of elementary, constituent particles. The particle can be an elementary particle in the usual sense, such as electron, but need not be. The quantum dimer in the previous section is such an example. We can then assign unit charge to each particle. We assume that the total charge is a conserved quantity.

When many particles are interacting, the ground state is generally nontrivial. On the other hand, the low-energy excited states of the system can often be described in terms of elementary excitations which behave as nearly free particles. Such particle-like elementary excitations are called quasi-particles. The ground state can be regarded as a vacuum in terms of the quasi-particles.

The quasi-particle may be adiabatically connected, when the interaction is introduced adiabatically, to the original particle; Landau's Fermi liquid is an example. In such a case, the quasi-particle has the same charge as the original particle. However, in general, quasi-particles are not necessarily adiabatically connected to the original particle. Then the quasi-particle may have a different charge from the original particle. When the quasi-particle has a fractional charge, in comparison to the unit charge of the original particle, we say fractionalization takes place.

We emphasize that fractionalization in this context does not mean splitting the original particle into its components, like splitting a proton into three quarks; such microscopic processes are simply absent in the model. Fractionalization is still possible because the quasi-particle represents a collective excitation involving many particles. An example of fractionalization is discussed in the context of the RVB spin-liquid phase of the quantum dimer model.

**FIGURE 4.8**

Two unitary operators \mathcal{F}_x and \mathcal{T}_x are introduced as time evolution operators corresponding to *gedanken* experiments. Left: The insertion of flux Φ through the hole of the torus. The adiabatic increase of Φ from 0 to unit-flux quantum (2π) is represented by \mathcal{F}_x . Right: Pair creation of a quasi-particle/hole, followed by the quasi-particle going around the system in x direction. After the quasi-particle completes a circle, it is pair-annihilated with the quasi-hole and the system goes back to the ground state, i.e., the vacuum with respect to quasi-particles. This process is denoted by \mathcal{T}_x .

There are other cases of fractionalization. In particular, fractionalization in the fractional quantum Hall effect was confirmed experimentally.

4.5.3 Fractionalization Implies Topological Degeneracy

I have argued that topological order is a useful working hypothesis to understand several peculiar features, such as fractionalization and topological ground state degeneracy, exhibited by quantum many-body systems, in a unified way. But why should we think these features are related? At a glance, they appear rather independent of each other. If they are unrelated, there would be little point in introducing topological order.

However, empirically, those features often appear together. For example, the RVB spin liquid phase and the fractional quantum Hall state exhibit fractionalization and topological degeneracy at the same time. These examples suggest that they are in fact related, and are consequences of something which we call topological order.

In fact, we can demonstrate a direct relation between apparently independent features. Here, let us demonstrate that fractionalization generally implies topological degeneracy, under certain assumptions [17]. Let us assume that the system is gapful, and that the quasi-particle carries a fractional charge p/q , where p and q are mutually prime integers. (Charges are defined so that the original particle in the microscopic model is unity.) The existence of a quasi-hole, which is the antiparticle of the quasi-particle, is also assumed. Let us first consider a two-dimensional system defined on a rectangle of size $L_x \times L_y$ with periodic boundary conditions, namely on a torus geometry.

Now I introduce two kinds of processes in *gedanken* experiments, as in

Fig. 4.8. The first of them is adiabatic insertion of a unit-flux quantum through the hole of the torus. For simplicity we set $\hbar = c = 1$, so the unit-flux quantum is 2π . The adiabatic insertion of flux is equivalent to adiabatic switching-on of vector potential. Let \mathcal{F}_x be the time-evolution operator representing such a process corresponding to an adiabatic increase of the vector potential in x direction:

$$A_x = 0 \rightarrow \frac{2\pi}{L_x}. \quad (4.13)$$

We can define \mathcal{F}_y similarly for the vector potential A_y in the y direction.

The second type of processes is creation of a quasi-particle–quasi-hole pair and moving the created quasi-particle in the x direction to make a circle back to the original location, followed by pair annihilation.

Both \mathcal{F}_x and \mathcal{T}_x are unitary operators, representing time evolutions. Let us consider the commutation relation between the two operators. Although the flux through the hole of the torus should not change the system at all classically, it affects the system quantum mechanically, through the Aharonov-Bohm (AB) effect. A unit-flux quantum in the hole introduced by \mathcal{F}_x induces a 2π phase, which is equivalent to zero, for the original particle encircling the hole of the torus. That is, the AB effect is absent for the original particle, in the case of unit-flux quantum. However, in the process \mathcal{T}_x , it is the quasi-particle of fractional charge p/q that encircles the flux; it acquires a nontrivial phase $2\pi p/q$ in the presence of a unit-flux quantum.

The nontrivial AB phase appearing after the insertion of unit-flux quantum implies the commutation relation²

$$\mathcal{T}_x \mathcal{F}_x = e^{2\pi i p/q} \mathcal{F}_x \mathcal{T}_x. \quad (4.14)$$

We expect that both \mathcal{F}_x and \mathcal{T}_x map a ground state to a ground state. Then, the commutation relation (4.14), which has the same structure as the magnetic translation group, requires q -fold degeneracy of the ground states as follows.

Since the insertion of a unit-flux quantum does not affect the original particles, \mathcal{F}_x commutes with the Hamiltonian. Thus we can always choose a ground state $|f_x\rangle$, which is also an eigenstate of \mathcal{F}_x :

$$\mathcal{F}_x |f_x\rangle = f_x |f_x\rangle, \quad (4.15)$$

where f_x is the eigenvalue. The commutation relation (4.14) implies that

$$\mathcal{F}_x (\mathcal{T}_x |f_x\rangle) = e^{-2\pi i p/q} \mathcal{T}_x (\mathcal{F}_x |f_x\rangle) = e^{-2\pi i p/q} f_x (\mathcal{T}_x |f_x\rangle). \quad (4.16)$$

Namely, the state $\mathcal{T}_x |f_x\rangle$, which is not a null state because \mathcal{T}_x is unitary, is an eigenstate of \mathcal{F}_x with the eigenvalue $e^{-2\pi i p/q} f_x$. Since the eigenvalue is different from the original one, f_x , the new state $\mathcal{T}_x |f_x\rangle$ must be orthogonal

²Precisely speaking, more careful discussion of gauge invariance is needed. However, the above commutation relation turns out to be valid [17].

to the original ground state $|f_x\rangle$. Since $\mathcal{T}_x|f_x\rangle$ should be a ground state as discussed above, it is degenerate with the original ground state $|f_x\rangle$.

We can repeat the same construction, to obtain other ground states by applying \mathcal{T}_x successively. However, $\mathcal{T}_x^q|f_x\rangle$ has the eigenvalue $e^{2\pi i p} = 1$, and cannot be distinguished from the original ground state $|f_x\rangle$ in terms of the eigenvalue of \mathcal{F}_x . Thus, the present construction gives q degenerate ground states, including the original one, on the torus:

$$|f_x\rangle, \mathcal{T}_x|f_x\rangle, \mathcal{T}_x^2|f_x\rangle, \dots, \mathcal{T}_x^{q-1}|f_x\rangle. \quad (4.17)$$

We can generalize this argument to other topologies. Two-dimensional orientable surfaces can be topologically classified by genus g , which is equal to the number of holes when embedded into 3 dimensions. For a genus- g surface, we can consider adiabatic insertion of a unit-flux quantum similar to \mathcal{F}_x , and quasi-particle–quasi-hole pair creation and annihilation after the quasi-particle encircles the hole similarly to \mathcal{T}_x , for each of the g holes. Each pair of \mathcal{F} and \mathcal{T} operators satisfies the same commutation relation as Eq. (4.14). Thus we can generate q^g degenerate ground states distinguished by different eigenvalues of \mathcal{F} -operators.

We conclude that fractionalization, in units of p/q , requires at least q^g -fold degeneracy of ground states on a genus- g surface. The ground-state degeneracy depending on the topology is nothing but topological degeneracy.

The q^g -fold ground state degeneracy is actually the minimum ground state degeneracy required by fractionalization. Depending on the quantum statistics of the particle, larger ground-state degeneracy may be deduced. For example, if the quasi-particle is either a boson or a fermion (not an anyon), the required ground state degeneracy is q^{2g} . This is consistent with the RVB spin liquid which corresponds to $p/q = 1/2$. The reader is referred to Refs. [17, 18] for details.

4.5.4 Implications

The derivation of topological ground state degeneracy from fractionalization demonstrates a hidden but general link between two apparently independent features. It also has general implications for the phase diagram.

Suppose that a system of interacting many-particles exhibits fractionalization for a set of parameters, but does not fractionalize for another. We would expect that these two points belong to different phases, but at this point cannot be sure if there is a QPT between them. Fractionalization is defined with respect to excited states; excited states might change their nature without a gap closing.

However, the present result implies that the topological ground state degeneracy changes between the two sets of parameters. Thus there must be a gap closing (or a level crossing of the ground state), i.e., a QPT. Therefore, systems with different fractionalization patterns should belong to different phases separated by a QPT.

As discussed before, this supports the existence of an underlying structure, which we call topological order, characterizing a quantum phase with peculiar features.

4.6 Outlook

In this chapter, I have emphasized topological ground state degeneracy as a characteristic of topological order. In fact, as I have discussed, topological degeneracy cannot be a consequence of conventional order, and clearly signals a quantum phase of an unconventional kind, which we now call a topologically ordered phase.

However, this is not to claim that topological degeneracy is the ultimate definition of topological order. As I have emphasized in Sec. 4.5.1, we are still looking for the answer to the question, “What is topological order?”

An interesting new direction pursued recently is the characterization of topological order in terms of quantum entanglement in the ground state. To study bipartite entanglement, we divide the system into two regions, A and its complement \bar{A} . In general, the ground state $|\Psi\rangle$ cannot be written as a single product $|\phi\rangle_A |\phi'\rangle_{\bar{A}}$, but only as a superposition of the product states as

$$|\Psi\rangle = \sum_{\mu} \Lambda_{\mu} |\phi_{\mu}\rangle_A |\phi'_{\mu}\rangle_{\bar{A}}, \quad (4.18)$$

where $\{\Lambda_{\mu}\}$ is real. This nonseparability implies quantum entanglement between A and \bar{A} for a pure state of the system, as can occur at zero temperature. Here we can choose Λ_{μ} nonnegative real numbers in descending order: $\Lambda_1 \geq \Lambda_2 \geq \Lambda_3 \geq \dots \geq 0$. The degree of the entanglement is often measured by the (von Neumann) entanglement entropy

$$S_{\text{vN}} = - \sum_{\mu} \Lambda_{\mu}^2 \log \Lambda_{\mu}^2. \quad (4.19)$$

In general, the entanglement entropy contains a term proportional to the area of the boundary between A and \bar{A} . This “area-law” contribution reflects the short-range correlations and has a non-universal coefficient. Kitaev and Preskill, and Levin and Wen [19] argued that, in addition to the area-law term, there is a universal constant term which reflects topological order. Although this constant contribution is generally a small part of the total entanglement entropy, it can be extracted by a careful analysis.

However, the entanglement entropy is not the only characterization of the entanglement. Recently, degeneracy in the entanglement spectrum has been found in some topologically ordered systems. This might be another important characterization of topological order.

For example, in the Haldane gap phase with odd spin quantum number, the entire entanglement spectrum is doubly degenerate [20]. Namely, $\Lambda_1 = \Lambda_2, \Lambda_3 = \Lambda_4, \dots$. This degeneracy is protected by any one of the following three symmetries: (i) time reversal, (ii) set of π -rotations about x, y , and z axes, and (iii) lattice inversion symmetry about a bond center (a.k.a. bond parity). The protection of the degeneracy indeed implies the protection of the Haldane phase as a distinct phase, separated from a trivial phase, say, the large- D phase, by a QPT. We can also say that topological order of the Haldane phase is protected by the symmetry. When all the symmetries are broken, the Haldane phase can be connected to a trivial phase adiabatically, and is no longer a distinct phase.

On the other hand, in the presence of (iii), the Haldane phase is still separated from a trivial phase by a QPT even when the other two symmetries are broken. This case is of particular interest, since the previously known characterizations of the Haldane phase, namely, the string order parameter and the edge states, do not work. Roughly speaking, the Haldane phase belongs to odd parity eigenvalue with respect to the lattice inversion. This is easy to understand for the representative AKLT state. Since the valence bond at the inversion center is a singlet pair of $S = 1/2$ spins, it is odd under inversion. The other valence bonds are flipped in pairs; so they are even under the inversion. As a whole, the $S = 1$ AKLT state has odd parity with respect to the inversion. As long as the Hamiltonian has inversion symmetry, the ground state belongs to a definite parity, odd or even. A trivial state, which is given as a simple product of local states, has even parity. Thus the Haldane phase (AKLT state) and the trivial state must be separated by a QPT.

The degeneracy of the entanglement spectrum is also related to the entanglement entropy. In fact, the double degeneracy of the entire spectrum implies the minimum entanglement entropy $\log 2$. On the other hand, the entanglement entropy does not necessarily imply degeneracy or other nontrivial structures in the entanglement spectrum. It might be that the degeneracy of the entanglement spectrum is quite fundamental for topological order.³

In any case, we need more investigation of possible characterizations in order to better understand topological order and associated QPTs.

Acknowledgments – I would like to thank many colleagues with whom I have had stimulating discussions on the subject. While it is impossible to list all those people here, I would like to thank particularly Erez Berg, Frank Pollmann, T. Senthil, and Ari M. Turner, as this chapter is partly based on collaborations with them.

This work is supported in part by Grants-in-Aid for Scientific Research (KAKENHI) grant Nos. 20654030 and 20102008.

³See Ref. [21] for other examples exhibiting this degeneracy.

Bibliography

- [1] X.-G. Wen, Int. J. Mod. Phys. **B4**, 239 (1990).
- [2] T. D. Schultz, D. C. Mattis, and E. H. Lieb, Rev. Mod. Phys. **36**, 856 (1964).
- [3] J. B. Kogut, Rev. Mod. Phys. **36**, 856 (1964).
- [4] See, for example, A. Auerbach, *Interacting Electrons and Quantum Magnetism* (Springer-Verlag, 1994).
- [5] M. Mambrini, Phys. Rev. B **77**, 134430 (2008) and references therein.
- [6] K. S. D. Beach, Phys. Rev. B **79**, 224431 (2009).
- [7] I. Affleck, T. Kennedy, E. H. Lieb, and H. Tasaki, Phys. Rev. Lett. **59**, 799 (1987); Commun. Math. Phys. **115**, 477 (1988).
- [8] F. D. M. Haldane, Phys. Rev. Lett. **50**, 1153 (1983).
- [9] U. Glaus and T. Schneider, Phys. Rev. B **30**, 215 (1984).
- [10] P. W. Anderson, Mat. Res. Bull. **8**, 153 (1973).
- [11] E. Manousakis, Rev. Mod. Phys. **63**, 1 (1991).
- [12] D. S. Rokhsar and S. A. Kivelson, Phys. Rev. Lett. **61**, 2376 (1988).
- [13] E. Lieb, T. Schultz, and D. Mattis, Ann. Phys. (N.Y.) **16**, 407 (1961); M. Oshikawa, Phys. Rev. Lett. **84**, 1535 (2000); M. B. Hastings, Phys. Rev. B **69**, 104431 (2004).
- [14] N. E. Bonesteel, Phys. Rev. B **40**, 8954 (1989).
- [15] R. Moessner and S. L. Sondhi, Phys. Rev. Lett. **86**, 1881 (2001).
- [16] A. Yu. Kitaev, Ann. Phys. (N. Y.), **303**, 2 (2003) [arXiv: quant-ph/9707021].
- [17] M. Oshikawa and T. Senthil, Phys. Rev. Lett. **96**, 060601 (2006).
- [18] M. Sato, M. Kohmoto, and Y.-S. Wu, Phys. Rev. Lett. **97**, 010601 (2006).
- [19] A. Kitaev and J. Preskill, Phys. Rev. Lett. **96**, 110404 (2006); M. Levin and X.-G. Wen, Phys. Rev. Lett. **96**, 110405 (2006).
- [20] F. Pollmann, E. Berg, A. M. Turner, and M. Oshikawa, arXiv:0909.4059; Phys. Rev. B **81**, 064439 (2010).
- [21] L. Fidkowski, Phys. Rev. Lett. **104**, 130502 (2010); A. M. Turner, Y. Zhang, and A. Vishwanath, arXiv:0909.3119.

5

Entanglement Renormalization: An Introduction

Guifré Vidal

The University of Queensland, Brisbane, QLD 4067, Australia

One of the main goals of physics is to identify and characterize the possible phases of matter, as well as the transitions between these phases. In this chapter we are concerned with theoretical and computational aspects of quantum phases and quantum phase transitions involving extended quantum many-body systems at zero temperature.

Specifically, we consider the problem of constructing a real-space *coarse-graining transformation* for quantum lattice systems at zero temperature. Such a transformation should dispose of the degrees of freedom corresponding to small distances while preserving the low energy properties of the system. Obtaining an effective description of a system in terms of less degrees of freedom is obviously very convenient for numerical calculations. However, our priority here is to explore the use of the coarse-graining transformation within the context of the *renormalization group* (RG) [1–4]. Accordingly, we aim to define an RG flow in the space of local Hamiltonians, and to study quantum phases and quantum phase transitions by characterizing the fixed points of this flow.

The coarse-graining scheme that we will describe is known as *entanglement renormalization*. Entanglement renormalization has been shown to be suitable to address the emergence of different types of order in systems of quantum spins in one and two spatial dimensions, including symmetry-breaking order and topological order, as well as to characterize quantum critical points. In addition, the formalism can be generalized to study models where the basic degrees of freedom are fermionic or, more generally, anyonic. We will introduce the approach step by step throughout the chapter, and then apply it to the characterization of quantum critical points.

The content is organized in sections as follows. Sec. 5.1 discusses a coarse-graining transformation, based on *isometries*, that is capable of preserving ground state properties, but that fails to remove some of the short-distance degrees of freedom which accumulate over successive iterations. These degrees of freedom are associated with short-range entanglement in the ground state of the system. Failure to properly get rid of short-range entanglement has

important numerical implications, and precludes the use of RG ideas within this first coarse-graining scheme.

Sec. 5.2 explains how to remove short-range entanglement from the lattice. This is achieved by introducing *disentanglers* that act across the boundary of blocks of sites before the coarse-graining step. In this way *all* short-distance degrees of freedom are removed from the system. Local operators are seen to be mapped into local operators by the *ascending superoperator* \mathcal{A} , while its dual, the *descending superoperator* \mathcal{D} , allows us to recover a fine-grained reduced density matrix from a coarse-grained one. We also describe the class of states that can be exactly represented using the entanglement renormalization scheme, known as the *multi-scale entanglement renormalization ansatz* (MERA).

Sec. 5.3 connects the present approach with the RG formalism. An RG map $\mathcal{R}(h)$ in the space of two-site interactions h is defined in terms of the ascending superoperator \mathcal{A} . Each fixed point of the resulting (discrete) RG flow corresponds to a ground state that is invariant under the coarse-graining transformation and is described by a *scale invariant* MERA. The entanglement of scale-invariant ground states allows to distinguish between different types of fixed points. At the fixed point, the ascending superoperator, now independent of the length scale, is known as the scaling superoperator \mathcal{S} .

Sec. 5.4 applies entanglement renormalization to the study of quantum phase transitions. Many universal properties of a quantum critical point, including critical exponents and the conformal data characterizing the pertinent conformal field theory, can be extracted from the scaling superoperator \mathcal{S} . We also address surface critical phenomena by adding a boundary to the scale-invariant MERA.

The formalism of the entanglement renormalization and the MERA were introduced in Refs. [5, 6]. Algorithms to approximate ground states have been described in Refs. [7–9]. Two-dimensional systems have been explored in Refs. [10–13], including scalable simulations in interacting systems [12] and analytical results for systems with topological order [13]. Scale-invariant systems, including non-critical and critical fixed points of the RG flow, have been studied in Refs. [5, 6, 9, 10, 13–16]. Extensions to two-dimensional systems with fermionic and anyonic degrees of freedom have been proposed in Refs. [17, 18].

5.1 Coarse Graining and Ground State Entanglement

Let us consider a system, such as a quantum spin model, that can be described by a lattice \mathcal{L} in D spatial dimensions. For simplicity, most of the present derivations will involve a lattice in one spatial dimension. However, one of the highlights of entanglement renormalization is that it also applies to higher-dimensional cases, to which we will refer occasionally throughout the chapter.

The microscopic degrees of freedom are placed on the N sites of \mathcal{L} , with each site being described by a vector space \mathbb{V} of finite dimension d . The model is further characterized by a Hamiltonian H that decomposes as the sum of local terms, that is, of terms that act on a small number of neighboring sites. Except for the discussion of surface critical phenomena in Sec. 5.4, we assume that the model is invariant under translations.

Our ultimate goal is to be able to compute low energy properties of the system, which we will assume to be in the ground state $|\Psi_{\text{GS}}\rangle \in \mathbb{V}^{\otimes N}$ of H . Let o_1, o_2, \dots, o_k be arbitrary local operators acting on different parts of the lattice. Then we would like to compute quantities such as

$$\langle o_1 o_2 \cdots o_k \rangle_{\Psi_{\text{GS}}} \equiv \langle \Psi_{\text{GS}} | o_1 o_2 \cdots o_k | \Psi_{\text{GS}} \rangle, \quad (5.1)$$

since from these expected values one can predict how the system reacts to arbitrary external probes.¹ However, due to the exponential growth in N of the dimension of $\mathbb{V}^{\otimes N}$, computing $|\Psi_{\text{GS}}\rangle$ by diagonalizing H is only affordable for very small systems. In order to address larger systems, we need a better plan. The strategy that we will pursue here is to build a transformation that removes short-distance degrees of freedom from the lattice model (\mathcal{L}, H) , which is mapped into an effective lattice model (\mathcal{L}', H') such that

$$\langle o'_1 o'_2 \cdots o'_k \rangle_{\Psi'_{\text{GS}}} = \langle o_1 o_2 \cdots o_k \rangle_{\Psi_{\text{GS}}}, \quad (5.2)$$

where $|\Psi'_{\text{GS}}\rangle$ is the ground state of H' and the operators o'_1, o'_2, \dots, o'_k result from transforming o_1, o_2, \dots, o_k .

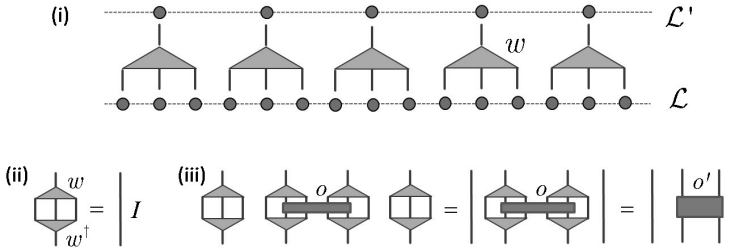
Building an effective description can be helpful in several ways. On the one hand, in the case of a finite system, where the model (\mathcal{L}', H') has a smaller Hilbert space dimension than the original model, diagonalizing H' is computationally more affordable than diagonalizing H . As a result, larger models can often be addressed. In conjunction with finite-size-scaling techniques, this already constitutes a powerful numerical route to study, e.g., quantum critical phenomena. On the other hand, and closer to the goals of this chapter, a coarse-graining transformation that properly removes short-distance degrees of freedom could be used to investigate how H changes under scale transformations. Then, with the help of powerful RG ideas, we might be able to evaluate Eq. (5.1) directly in the thermodynamic limit.

5.1.1 A Real-Space Coarse-Graining Transformation

Following the seminal works of Migdal, Kadanoff and Wilson in real space RG [1–3], we will proceed by coarse-graining blocks of sites of \mathcal{L} into single sites of \mathcal{L}' . For concreteness, we divide \mathcal{L} in blocks of three sites and, as in Wilson's numerical renormalization group (NRG) approach, we implement the coarse-graining by means of an isometry w ,

$$w : \mathbb{V}' \longmapsto \mathbb{V}^{\otimes 3}, \quad w^\dagger w = I_{\mathbb{V}'}, \quad w w^\dagger \equiv P, \quad P^2 = P, \quad (5.3)$$

¹We will only consider equal-time correlators.

**FIGURE 5.1**

(i) Coarse-graining transformations characterized by an isometry w that maps blocks of three sites of lattice \mathcal{L} into single sites of a coarse-grained lattice \mathcal{L}' . (ii) Graphical representation of $w^{\dagger}w = I_{\mathbb{V}'}$. (iii) An operator o supported on, e.g., two blocks of sites of \mathcal{L} becomes a two-site operator o' , cf. Eq. (5.5).

where $\mathbb{V}^{\otimes 3}$ is the vector space of the three sites, \mathbb{V}' is the vector space of the effective site, $I_{\mathbb{V}'}$ is the identity operator in \mathbb{V}' and P is a projector onto the subspace of $\mathbb{V}^{\otimes 3}$ that is preserved by the coarse-graining. Fig. 5.1 illustrates this transformation, which defines an effective lattice \mathcal{L}' made of $N' = N/3$ sites, as well as an effective Hamiltonian H' given by

$$H' = W^{\dagger}HW, \quad W \equiv w^{\otimes N/3}. \quad (5.4)$$

A local operator o with support on r blocks of \mathcal{L} becomes a local operator o' supported on r sites of \mathcal{L}' given by

$$o \rightarrow o' = (w^{\dagger \otimes r}) o (w^{\otimes r}), \quad (5.5)$$

where the isometries act on the relevant sites of \mathcal{L} . Notice that the support of local operators may shrink under coarse-graining, but it never expands. In particular, if H can be expressed as a sum of interactions between pairs of nearest neighbor sites, then H' will also contain at most nearest neighbor interactions.

The above transformation may not preserve the properties of the original ground state, in the sense of Eq. (5.2). As explained by White as part of his density matrix renormalization group (DMRG) [19], in order to preserve ground state properties, the isometry w must retain the whole support of the ground state reduced density matrix ρ on the three-site block,

$$\rho \equiv \text{tr}_E |\Psi_{\text{GS}}\rangle\langle\Psi_{\text{GS}}|, \quad (5.6)$$

where E denotes all the sites of \mathcal{L} not contained in the block. Let

$$\rho = \sum_{\alpha=1}^{\chi} p_{\alpha} |\Psi_{\alpha}\rangle\langle\Psi_{\alpha}|, \quad \sum_{\alpha=1}^{\chi} p_{\alpha} = 1, \quad p_1 \geq p_2 \geq \dots \geq p_{\chi} > 0, \quad (5.7)$$

be the eigenvalue decomposition of ρ . Then *White's rule* consists in choosing w such that the projector P in Eq. (5.3) corresponds to the support of ρ ,

$$P = ww^\dagger = \sum_{\alpha=1}^{\chi} |\Psi_\alpha\rangle\langle\Psi_\alpha|. \quad \text{White's rule} \quad (5.8)$$

In particular, the dimension of \mathbb{V}' is the number χ of non-zero eigenvalues² of ρ . If Eq. (5.8) holds, then it can be seen that the ground state $|\Psi'_{\text{GS}}\rangle$ of H' is given by $|\Psi'_{\text{GS}}\rangle = W^\dagger|\Psi_{\text{GS}}\rangle$, whereas $WW^\dagger|\Psi_{\text{GS}}\rangle = |\Psi_{\text{GS}}\rangle$. It follows that³

$$\langle\Psi_{\text{GS}}|o_1 o_2 \cdots o_k|\Psi_{\text{GS}}\rangle = \langle\Psi_{\text{GS}}|(WW^\dagger)o_1 o_2 \cdots o_k(WW^\dagger)|\Psi_{\text{GS}}\rangle \quad (5.9)$$

$$= (\langle\Psi_{\text{GS}}|W)(W^\dagger o_1 o_2 \cdots o_k W)(W^\dagger|\Psi_{\text{GS}}\rangle) = \langle\Psi'_{\text{GS}}|o'_1 o'_2 \cdots o'_k|\Psi'_{\text{GS}}\rangle, \quad (5.10)$$

which indeed amounts to Eq. (5.2).

By iteration, from the original model $(\mathcal{L}^{(0)}, H^{(0)}) \equiv (\mathcal{L}, H)$ we can now build a sequence of increasingly coarse-grained lattice models

$$(\mathcal{L}^{(0)}, H^{(0)}) \xrightarrow{w^{(1)}} (\mathcal{L}^{(1)}, H^{(1)}) \xrightarrow{w^{(2)}} (\mathcal{L}^{(2)}, H^{(2)}) \rightarrow \dots . \quad (5.11)$$

where lattice $\mathcal{L}^{(\tau+1)}$ results from coarse-graining lattice $\mathcal{L}^{(\tau)}$, such that ground state properties are preserved at each step,

$$\langle o_1^{(\tau+1)} o_2^{(\tau+1)} \cdots o_k^{(\tau+1)} \rangle_{\Psi_{\text{GS}}^{(\tau+1)}} = \langle o_1^{(\tau)} o_2^{(\tau)} \cdots o_k^{(\tau)} \rangle_{\Psi_{\text{GS}}^{(\tau)}}. \quad (5.12)$$

How well does this coarse-graining scheme remove short-distance degrees of freedom? Is it viable in practice? To answer these questions, it is useful to consider the sequence of ground state reduced density matrices $\{\varrho^{(0)}, \varrho^{(1)}, \varrho^{(2)}, \dots\}$ corresponding to increasingly large blocks of sites of \mathcal{L} , where $\varrho^{(\tau)}$ corresponds to 3^τ sites. White's rule, which guarantees that ground state properties are preserved, also implies that the vector space dimension $\chi^{(\tau)}$ of a site of lattice $\mathcal{L}^{(\tau)}$ must be given by the rank of $\varrho^{(\tau)}$. Thus, our next step is to characterize the sequence of effective dimensions $\{\chi^{(0)}, \chi^{(1)}, \chi^{(2)}, \dots\}$.

5.1.2 Ground State Entanglement

The rank χ of the ground state reduced density matrix ρ of a block of sites depends on the amount of entanglement between that block of sites and the

²In practical calculations, one often neglects contributions from the eigenvectors $|\Psi_\alpha\rangle$ with smallest weights p_α , at the price of introducing small errors in Eq. (5.2). Most of the subsequent discussions also apply in the case of approximate coarse-graining transformations.

³For simplicity, we assume that the local operators o'_1, o'_2, \dots, o'_k are supported on different sites of \mathcal{L}' , so that $W^\dagger o_1 o_2 \cdots o_k W = o'_1 o'_2 \cdots o'_k$. If, e.g., operators o'_1 and o'_2 had overlapping support, then they would be fused into a single local operator $o' = (w^{\dagger \otimes r}) o_1 o_2 (w^{\otimes r})$ supported on some larger number r of sites.

rest of the lattice, as can be seen from the so-called Schmidt decomposition, which expands the ground state $|\Psi_{\text{GS}}\rangle$ in terms of the eigenvectors $|\Psi_\alpha\rangle$ of ρ (Eq. (5.7)) and some orthonormal set of states $|\Phi_\alpha\rangle$ for the rest of the lattice,

$$|\Psi_{\text{GS}}\rangle = \sum_{\alpha=1}^{\chi} \sqrt{p_\alpha} |\Psi_\alpha\rangle \otimes |\Phi_\alpha\rangle. \quad (5.13)$$

When $\chi = 1$, corresponding to a reduced density matrix $\rho = |\Psi_1\rangle\langle\Psi_1|$ in a pure state, the ground state $|\Psi_{\text{GS}}\rangle = |\Psi_1\rangle \otimes |\Phi_1\rangle$ factorizes into the product of individual states for the block and for the rest of the lattice. Instead, if $\chi > 1$, the block and the rest of the lattice are entangled. The amount of entanglement between these two parts can be measured with the *entanglement entropy*, namely the von Neumann entropy of the reduced density matrix ρ ,

$$S(\rho) \equiv -\text{tr}(\rho \log(\rho)) = -\sum_{\alpha=1}^{\chi} p_\alpha \log(p_\alpha). \quad (5.14)$$

This measure vanishes for a product state and its maximum occurs for the flat probability distribution $p_\alpha = 1/\chi$, where $S = -\sum_\alpha(1/\chi)\log(1/\chi) = \log(\chi)$. Therefore we always have $\chi \geq \exp(S)$. In subsequent discussions we will assume for simplicity that

$$\chi \approx \exp(S). \quad (5.15)$$

In one spatial dimension, the entanglement entropy of a block of l contiguous sites typically increases with l until l becomes of the order of the correlation length ξ in the system, at which point it saturates to some value S_{max} , whereas it diverges logarithmically at a quantum critical point:

$$S(l) \leq S_{\text{max}}, \quad \text{1D non-critical} \quad (5.16)$$

$$S(l) \approx \frac{c}{6} \log l, \quad \text{1D critical} \quad (5.17)$$

where c is the central charge of the CFT that describes the infrared limit of the quantum phase transition. In two spatial dimensions, the entanglement entropy of a square block of $l \times l$ sites typically grows in proportion to the size of the boundary of the block,

$$S(l) \approx \alpha l, \quad \text{2D} \quad (5.18)$$

where α is some constant that depends on the model and grows with ξ , and where there might be logarithmic multiplicative corrections in some systems with quasi-long range correlations. More generally, in the ground state of a D dimensional model, the entanglement between a block of l^D sites and the rest of the system scales according to the so-called area law $S(l) \approx \alpha l^{D-1}$, that is, as the size of the boundary of the block, with Eqs. (5.16) and (5.18) being particular cases of this expression [20].

The area law translates into an approximate expression for the effective dimension $\chi^{(\tau)}$. Recall that one site of $\mathcal{L}^{(\tau)}$ accommodates $l = 3^\tau$ sites of \mathcal{L} (or $l^2 = 3^{2\tau}$ sites if we had chosen to coarse-grain blocks of 3×3 sites in two spatial dimensions). Eqs. (5.16)-(5.18) combined with Eq. (5.15) lead to

$$\chi^{(\tau)} \leq \chi_{\max} \approx e^{S_{\max}} \quad \text{1D non-critical} \quad (5.19)$$

$$\chi^{(\tau)} \approx l^{c/6} \approx e^\tau \quad \text{1D critical} \quad (5.20)$$

$$\chi^{(\tau)} \approx e^{\alpha l} \approx e^{e^{\sqrt{\tau}}} \quad \text{2D} \quad (5.21)$$

Now that we have an expression for the scaling of $\chi^{(\tau)}$, we can analyze both its origin and its implications.

5.1.3 Accumulation of Short-Distance Degrees of Freedom

From a conceptual viewpoint, the growth of $\chi^{(\tau)}$ reveals an important flaw of the present coarse-graining scheme. Namely, it fails to remove some of the short-distance degrees of freedom, which remain (and even accumulate) over successive iterations.

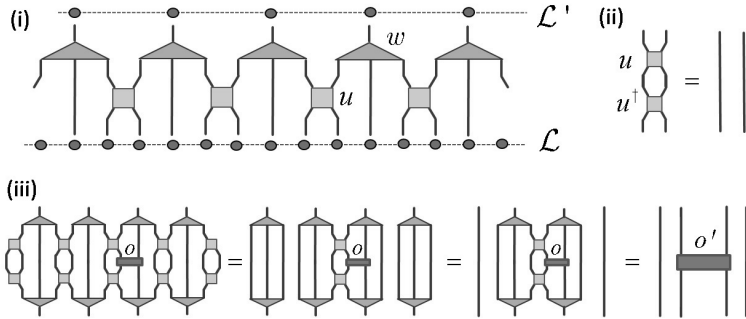
To understand this point, let us assume that two contiguous sites $r, s \in \mathcal{L}$ are in an entangled state, say $(|1_r 1_s\rangle + |2_r 2_s\rangle)/\sqrt{2}$. We compare two situations, depending on how the blocking in Fig. 5.1 affects these sites:

(i) If sites r and s belong to the same block, then they do not contribute to the entanglement between the block and the rest of the lattice, or equivalently, to the spectrum of the reduced density matrix ρ of the block, and are therefore removed during the coarse-graining.

(ii) If sites r and s belong to two adjacent blocks, then they are entangled across the boundary of the blocks, contribute to the spectrum of ρ for each block, and thus will be preserved by the coarse-graining; see Fig. 5.3.

In other words, short-distance degrees of freedom, entangled at scales smaller than the size of a block, are treated differently depending on whether they are entangled within a block or across the boundary between blocks. In the last case, the coarse-graining transformation fails to remove them. As a result, the approach cannot generate a proper RG flow. For instance, two Hamiltonians H_1 and H_2 describing the same phase but differing in short-distance details will remain different under successive iterations of the coarse-graining: some of the short-distance details that distinguish the two models will persist, and two different fixed points of the RG flow will be reached.

In spite of this shortcoming, is the scheme useful for practical computations? The answer strongly depends on the class of problems under consideration. It is a definitive ‘yes’ for systems in one spatial dimension. White’s DMRG [19] (to which this scheme is closely related) revolutionized the computational scene in the early 90’s by providing numerical access, with unprecedented accuracy, to ground state energies, local observables and correlators. The immense success of DMRG can be understood from the saturation of $\chi^{(\tau)}$ for non-critical systems, Eq. (5.19), since the computational cost is a small

**FIGURE 5.2**

(i) Coarse-graining transformation with disentanglers u , acting on two contiguous sites of \mathcal{L} across the boundary of two blocks, followed by isometries w , which map a block of three sites into a single site of the coarse-grained lattice \mathcal{L}' . (ii) Graphical representation of $uu^\dagger = I_{V \otimes 2}$. (iii) A local operator o supported on two contiguous sites of \mathcal{L} is mapped into an effective operator o' on two contiguous sites of \mathcal{L}' . The linear transformation $o \rightarrow o' = \mathcal{A}(o)$ is described by a superoperator (i.e., a linear map in the space of operators) referred to as the ascending superoperator \mathcal{A} .

power of $\chi^{(\tau)}$. Even critical systems can be studied, in spite of Eq. (5.20), by considering reasonably large chains, of up to thousands of sites, and applying finite-size scaling techniques. Instead, the situation is much grimmer in two spatial dimensions. There the double exponential growth of $\chi^{(\tau)}$ in Eq. (5.21) implies that only small systems can be addressed (see, e.g., the discussion in Ref. [21]) and there is a real need for alternative approaches.

5.2 Entanglement Renormalization

Entanglement renormalization was proposed as a means to consistently remove all short-distance degrees of freedom during coarse-graining. It leads to a significant reduction in computational costs, making scalable calculations feasible even in two dimensions. More important to us, it produces an RG flow with the expected properties.

5.2.1 Disentanglers

Let us modify the previous coarse-graining scheme as follows. First we apply a unitary transformation u , a *disentangler*, on pairs of contiguous sites of \mathcal{L} ,

$$u : \mathbb{V}^{\otimes 2} \longmapsto \mathbb{V}^{\otimes 2}, \quad u^\dagger u = uu^\dagger = I_{\mathbb{V}^{\otimes 2}}, \quad (5.22)$$

where each site belongs to one of two adjacent blocks, so that u acts across the boundary of the two blocks; see Fig. 5.2. Then, as before, we use isometries w to map the blocks of 3 sites of \mathcal{L} into single sites of the lattice \mathcal{L}'^4 . Let $U \equiv u^{\otimes N/3}$ be a unitary transformation that contains disentanglers u acting on the boundaries of all the blocks. Then the effective Hamiltonian in \mathcal{L}' reads

$$H' = (W^\dagger U^\dagger) H (UW). \quad (5.23)$$

In order to guarantee the preservation of ground state properties, the isometries w are chosen according to White's rule, namely such that they retain the support of the reduced density matrix $\tilde{\rho}$ on the block,

$$\tilde{\rho} = \text{tr}_{\mathcal{L}/\text{block}} (U^\dagger |\Psi_{\text{GS}}\rangle \langle \Psi_{\text{GS}}| U). \quad (5.24)$$

Notice, however, that $|\Psi_{\text{GS}}\rangle$ has been transformed according to the disentanglers before the density matrix $\tilde{\rho}$ is computed. By properly choosing the disentanglers u , the modified ground state $|\tilde{\Psi}_{\text{GS}}\rangle = U|\Psi_{\text{GS}}\rangle$ will have less entanglement than $|\Psi_{\text{GS}}\rangle$. Specifically, the disentanglers are capable of removing short-range entanglement across the boundary of the blocks; see Fig. 5.3.

By iterating the transformation we can once more build a sequence of increasingly coarse-grained models (Fig. 5.4)

$$(\mathcal{L}^{(0)}, H^{(0)}) \longrightarrow (\mathcal{L}^{(1)}, H^{(1)}) \longrightarrow (\mathcal{L}^{(2)}, H^{(2)}) \longrightarrow \dots, \quad (5.25)$$

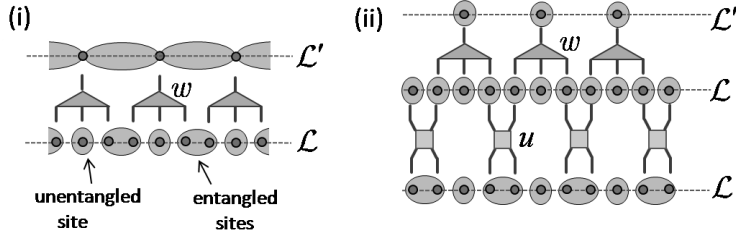
As evidenced by abundant numerical and analytical results (Refs. [5]-[18]), an important consequence of the use of disentanglers is that the dimension $\chi^{(\tau)}$ of the effective sites no longer needs to increase with τ in order to (approximately, but accurately) fulfill White's rule. This is the case in one spatial dimension, both for critical and non-critical systems, cf. Eqs. (5.16)-(5.17), as well as in two spatial dimensions, provided the area law of Eq. (5.18) does not have logarithmic corrections.

5.2.2 Ascending and Descending Superoperators

An operator o supported on two contiguous sites of \mathcal{L} is now mapped into an operator o' supported on two contiguous sites of \mathcal{L}' by means of the ascending superoperator \mathcal{A} (Fig. 5.2),

$$o \rightarrow o' = ((w^{\dagger \otimes 2})(u^\dagger)) o (u(w^{\otimes 2})) \equiv \mathcal{A}(\rho). \quad (5.26)$$

⁴The distinction between disentanglers u and isometries w is useful for pedagogical purposes. However, more generally one can consider isometric transformations $v : \mathbb{V}^{\otimes n_1} \mapsto \mathbb{V}^{\otimes n_2}$, with $v^\dagger v = I_{\mathbb{V}^{\otimes n_1}}$, $n_1 \leq n_2$, that both disentangle the ground state and coarse-grain the lattice.

**FIGURE 5.3**

To illustrate the role of disentanglers u , a simple example is considered where the ground state $|\Psi_{\text{GS}}\rangle$ of a one-dimensional lattice \mathcal{L} factorizes into the product of entangled states $(|1_r 1_s\rangle + |2_r 2_s\rangle)/\sqrt{2}$ involving only two nearest neighbor sites $r, s \in \mathcal{L}$ (on both sides of the boundaries between blocks) and states of single sites (in the interior of each block). (i) When only isometries are used, entanglement across the boundary of the blocks is preserved in \mathcal{L}' . (ii) By using disentanglers u that transform the state $(|1_r 1_s\rangle + |2_r 2_s\rangle)/\sqrt{2}$ of the two boundary sites $r, s \in \mathcal{L}$ into an unentangled state, e.g., $|1_r 1_s\rangle$, entanglement across the boundary of the blocks can be removed before the isometries are applied, and the ground state of \mathcal{L}' has no entanglement.

Notice that locality is again preserved under the coarse-graining transformation, but in this case it results from a compromise between two opposing forces: disentanglers u expand the support of local operators, while isometries w compress it. The balance corresponds to two-site supports, to which both smaller and larger supports tend under coarse-graining. This is why two-site supports play a dominant role in the present discussions. In the case of a sequence of coarse-graining transformations (Fig. 5.4) we can investigate how the two-site operator $o^{(0)} \equiv o$ changes as we increase the scale of observation:

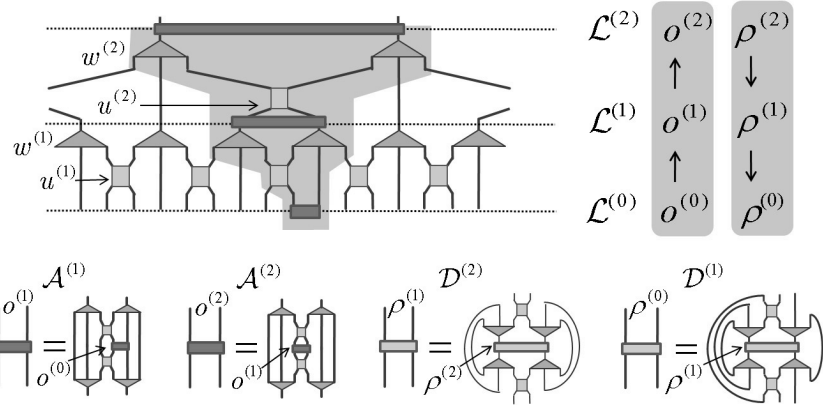
$$o^{(0)} \xrightarrow{\mathcal{A}^{(1)}} o^{(1)} \xrightarrow{\mathcal{A}^{(2)}} o^{(2)} \longrightarrow \dots \quad (5.27)$$

On the other hand, the descending superoperator \mathcal{D} ,

$$\rho' \rightarrow \rho = \text{tr}_{s_1 s_2} ((w^{\otimes 2}) u) \rho' ((w^{\dagger \otimes 2})(u^\dagger)), \quad (5.28)$$

where ρ and ρ' are supported on the same two sites as o and o' in Eq. (5.26) and the partial trace eliminates two superfluous sites $s_1, s_2 \in \mathcal{L}$, produces a fine-grained reduced density matrix ρ from a coarse-grained reduced density matrix ρ' , such that

$$\text{tr}(\rho o) = \text{tr}(\rho' o'), \quad (5.29)$$

**FIGURE 5.4**

Diagrammatic representation of two iterations of the coarse-graining transformation, producing a sequence of increasingly coarse-grained lattices $\mathcal{L}^{(0)}$, $\mathcal{L}^{(1)}$, and $\mathcal{L}^{(2)}$. At each iteration $u^{(\tau)}$ is chosen as to remove short-range entanglement and $w^{(\tau)}$ follows White's rule. The ascending superoperator \mathcal{A} maps $o^{(\tau)}$ into $o^{(\tau+1)}$ while the descending superoperator \mathcal{D} maps $\rho^{(\tau+1)}$ into $\rho^{(\tau)}$.

for all possible two-site operators⁵ o . By iteration, the descending superoperator allows us to obtain a sequence of two-site density matrices

$$\dots \longrightarrow \rho^{(2)} \xrightarrow{\mathcal{D}^{(2)}} \rho^{(1)} \xrightarrow{\mathcal{D}^{(1)}} \rho^{(0)} \quad (5.30)$$

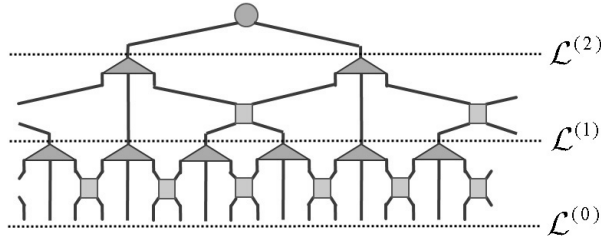
flowing from coarser to finer lattices and therefore monitor how the ground state two-site density matrix changes with the observation scale.

5.2.3 Multi-scale Entanglement Renormalization Ansatz

The *multi-scale entanglement renormalization ansatz* (MERA) is a variational ansatz for pure states $|\Psi\rangle \in \mathbb{V}^{\otimes N}$ of \mathcal{L} that results in a natural way from the above coarse-graining transformation. It consists of a tensor network that collects all the disentanglers and isometries used to produce the sequence of coarse-grained lattices in Eq. (5.25); see Fig. 5.5.

In the case of a translation-invariant system, we need to specify one disentangler $u^{(\tau)}$ and one isometry $w^{(\tau)}$ per layer, and these depend on $O(\chi^q)$ parameters, where $q = 4$ in the one-dimensional scheme discussed here. Since there are $O(\log(N))$ layers of tensors, the MERA depends on $O(\chi^q \log(N))$ parameters, a result valid also in two spatial dimensions for an appropriate value of q .

⁵In other words, the descending superoperator \mathcal{D} is dual to the ascending superoperator \mathcal{A} , and $\text{tr}(\rho' \mathcal{A}(o)) = \text{tr}(\mathcal{D}(\rho')o)$ for all ρ' and o .

**FIGURE 5.5**

Multi-scale entanglement renormalization ansatz (MERA) made of disentanglers and isometries corresponding to two iterations of the coarse-graining transformation in Fig. 5.2. Notice the periodic boundary conditions.

Therefore, the MERA is an efficient representation of certain states of lattice \mathcal{L} . The interest in this ansatz resides in abundant numerical and analytical results demonstrating that it can be used to accurately approximate the ground state $|\Psi_{\text{GS}}\rangle$ of a local Hamiltonian H in large (and even infinite) lattice systems in one and two spatial dimensions. Even at criticality, the error in ground state expected values, Eq. (5.1), decays exponentially with the refinement parameter χ . While it is still unclear exactly what Hamiltonians have ground states that can be well approximated, a MERA with a fixed value of χ naturally reproduces a scaling of entanglement compatible with Eqs. (5.16)-(5.18), suggesting that it might be able to accurately approximate ground states whose block entanglement fulfills the area law.

Given the ground state $|\Psi_{\text{GS}}\rangle$ of a local Hamiltonian H , we have provided an intuitive description of the role played by the tensors that form the MERA. Namely, a disentangler u ‘removes short-range entanglement from $|\Psi_{\text{GS}}\rangle$,’ while an isometry w ‘coarse-grains a block of sites so as to preserve the support of the ground state reduced density matrix.’ These descriptions could perhaps allow us to compute all u ’s and w ’s of the MERA for $|\Psi_{\text{GS}}\rangle$ if we already knew $|\Psi_{\text{GS}}\rangle$. Algorithmically, of course, it is absurd to assume that we already know $|\Psi_{\text{GS}}\rangle$ if our goal is to compute $|\Psi_{\text{GS}}\rangle$. In practical MERA calculations, an approximation to $|\Psi_{\text{GS}}\rangle$ is obtained by minimizing the expected value $\langle \Psi | H | \Psi \rangle$, where $|\Psi\rangle$ is constrained to be a MERA. This is done starting with random u ’s and w ’s and iteratively optimizing them so as to reduce the energy, with a cost that scales as $O(\chi^{q'} \log(N))$ per optimization step ($q' = 7$ in the present scheme). We refer to the literature for further details.

5.3 The Renormalization Group Picture

From now on we consider an infinite lattice \mathcal{L} and a Hamiltonian H that is the sum of nearest neighbor terms,

$$H = \sum_s h(s, s+1), \quad h(s, s+1) \equiv h, \quad (5.31)$$

where the two-site operator h is the same on all pairs of nearest neighbor sites, and thus h completely characterizes H . We assume that disentanglers and isometries have been properly optimized, e.g., by minimizing the expected value $\langle \Psi | H | \Psi \rangle$, and concentrate on analyzing the properties of the resulting coarse-graining from the perspective of the renormalization group.

5.3.1 A Real-Space Renormalization-Group Map

Let us introduce the average ascending superoperator $\bar{\mathcal{A}}^h$,

$$o' = \bar{\mathcal{A}}^h(o) \equiv \frac{\mathcal{A}_L^h(o) + \mathcal{A}_C^h(o) + \mathcal{A}_R^h(o)}{3}, \quad (5.32)$$

that averages over the three inequivalent ways (left, center and right) in which o can be coarse-grained, and where the superscript h highlights the dependence on the Hamiltonian H – recall that the ascending superoperator is built with the disentanglers and isometries corresponding to the ground state $|\Psi_{\text{GS}}\rangle$ of H . Under coarse-graining, H is mapped into an effective Hamiltonian H' ,

$$H' = 3 \sum_s h'(s, s+1), \quad h'(s, s+1) \equiv h', \quad (5.33)$$

where the constant two-site operator h' is obtained from h by the RG map \mathcal{R} ,

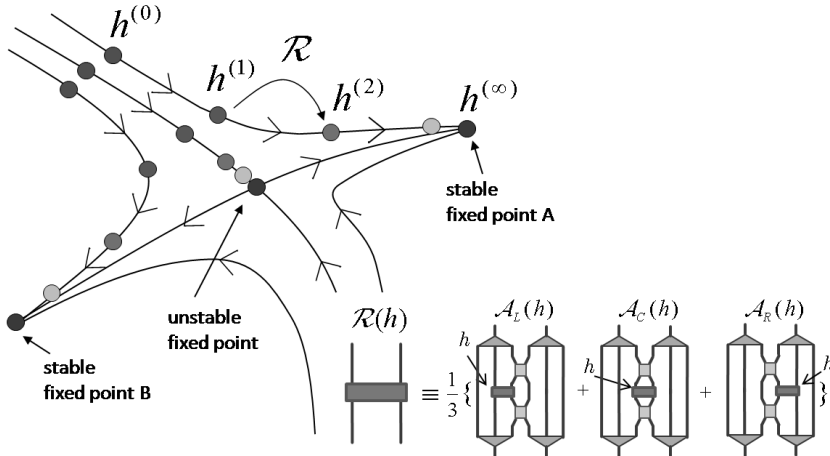
$$h' = \mathcal{R}(h) \equiv \bar{\mathcal{A}}^h(h). \quad (5.34)$$

Notice that, by construction, $\mathcal{R}(h)$ is a non-linear function of h .

Given the two-site interaction term $h^{(0)} \equiv h$ of the initial Hamiltonian $H^{(0)} \equiv H$, we can now build a sequence of two-site interactions

$$h^{(0)} \xrightarrow{\mathcal{R}} h^{(1)} \xrightarrow{\mathcal{R}} h^{(2)} \xrightarrow{\mathcal{R}} \dots \quad (5.35)$$

where $h^{(\tau)}$ characterizes the Hamiltonian $H^{(\tau)} = 3^\tau \sum_s h^{(\tau)}(s, s+1)$ of the coarse-grained lattice $\mathcal{L}^{(\tau)}$. This defines a *discrete* RG flow in the (χ^4 -dimensional) space of possible two-site interactions. We can thus study how the Hamiltonian of the system changes with the observation scale.

**FIGURE 5.6**

The RG map $\mathcal{R}(h)$ defines an RG flow in the space of two-site interactions h . The scaling superoperator $\mathcal{S}(o)$, Eq. (5.41), transforms two-site operators o at the fixed points of this RG flow.

5.3.2 Properties of the Renormalization-Group Map

Let us briefly discuss a few properties of the RG map $\mathcal{R}(h)$:

(i) *Proper RG flow.* Abundant numerical evidence suggests that properly chosen disentanglers indeed succeed at removing *all* short-distance degrees of freedom. As a result, if two Hamiltonians H_1 and H_2 correspond to the same phase, multiple applications of the RG map take $h_1^{(0)}$ and $h_2^{(0)}$ into the same fixed-point interaction $h^* \equiv h^{(\infty)}$, that is, $h_1^* = h_2^*$ (up to trivial changes of local basis).

(ii) *Nearest neighbor interactions.* As mentioned earlier, the present coarse-graining transformation does not generate long-range interactions starting from a short-ranged Hamiltonian (in contrast, e.g., with momentum-space RG methods). In addition, a Hamiltonian containing arbitrary short-range interactions (well beyond nearest neighbors) can be reduced, after a few iterations, to a Hamiltonian with only nearest neighbor interactions.⁶ Therefore the two-site RG map $\mathcal{R}(h)$ can be used to study arbitrary phases with short-range interactions. In two spatial dimensions, the analogous construction leads to an RG flow for four-site Hamiltonians.

(iii) *Unbiased RG map.* Notice that the space \mathbb{V}' for an effective site of \mathcal{L}' is not chosen *a priori* on the basis of heuristic arguments, nor is some specific form of the effective Hamiltonian H' imposed (with a few free parameters

⁶A coarse-graining step with trivial disentanglers is required (once) in order to eliminate some of the next-to-nearest neighbor interactions.

to be fixed). The approach simply searches, through an energy minimization, the subspace $\mathbb{V}'^{\otimes N/3}$ of the total Hilbert space $\mathbb{V}^{\otimes N}$ that best approximates the low energy subspace of H . The only hypothesis that is made concerns the structure of the subspace $\mathbb{V}'^{\otimes N/3}$, assumed to factorize as a tensor product of spaces \mathbb{V}' that are related to the original factorization $\mathbb{V}^{\otimes N}$ through the disentanglers u and isometries w . Numerical evidence (provided, e.g., by the study of critical phenomena in the next section) suggests that the low energy subspace of many local Hamiltonians of interest indeed has this structure.

5.3.3 Fixed Points of Entanglement Renormalization

Following the RG program, our next step is to study the fixed points of the flow generated by the RG map \mathcal{R} , corresponding to Hamiltonians that do not change when we modify the scale of observation. That is, we are interested in models with two-site interactions h^* such that

$$\mathcal{R}(h^*) = \lambda h^* \quad \text{scale invariance} \quad (5.36)$$

where $\lambda \equiv 3^{-\Delta_{h^*}}$ is a proportionality constant to be discussed later on.

A fixed point is characterized by one disentangler u and one isometry w that are repeated at all length scales, i.e., $u^{(\tau)} = u$ and $w^{(\tau)} = w$ for all τ . Thus, the *scale invariant* MERA, specified by this pair (u, w) , depends on just $O(\chi^4)$ parameters and offers an extremely compact description of fixed-point ground states of an infinite lattice. It can be obtained with an algorithm whose cost formally scales as $O(\chi^7)$ [15].

Since a finite correlation length ξ shrinks under coarse-graining, scale invariance requires that $\xi = 0$ or $\xi = \infty$, corresponding to non-critical and critical fixed points respectively. The present approach leads to a natural characterization of RG fixed points in terms of the entanglement of their ground states and the MERA representation:

(i) Non-critical fixed-point ground states ($\xi = 0$) may be unentangled or entangled. Symmetry-breaking phases usually have an unentangled (or product) fixed-point ground state, represented with a trivial scale invariant MERA with $\chi = 1$, whereas the fixed-point ground state in topologically ordered phases is entangled. The results of [13] strongly suggest that a scale invariant MERA with finite χ can exactly represent such entangled ground states.

(ii) Critical fixed-point ground states ($\xi = \infty$) are always highly entangled. An exact MERA representation requires an infinite dimension χ , as will be discussed in Sec. 5.4, but we will also see that accurate estimates of critical properties can be obtained from a scale invariant MERA with finite χ .

In order to further characterize a fixed point, one usually linearizes \mathcal{R} at $h = h^*$ by considering its derivative with respect to a small perturbation ϵo ,

$$\lim_{\epsilon \rightarrow 0} \frac{\mathcal{R}(h^* + \epsilon o) - \mathcal{R}(h^*)}{\epsilon} = \lim_{\epsilon \rightarrow 0} \frac{\bar{\mathcal{A}}^{h^* + \epsilon o}(h^* + \epsilon o) - \bar{\mathcal{A}}^{h^*}(h^*)}{\epsilon}. \quad (5.37)$$

We conjecture⁷ that this derivative is given by $\bar{\mathcal{A}}^{h^*}(o)$, which dictates how two-site operators o transform under coarse-graining at the fixed point $h = h^*$, and which we will call *scaling superoperator* \mathcal{S} ,

$$\mathcal{S}(o) \equiv \bar{\mathcal{A}}^{h^*}(o). \quad (5.38)$$

Recall that one can distinguish between stable fixed points, where *any* perturbed interaction $h^* + \epsilon o$ will flow back to h^* , and unstable fixed points, where relevant perturbations o exist such that $h^* + \epsilon o$ will flow away from h^* . It may also be worth recalling that the notion of stability is relative to what perturbations o are available, and thus may depend on symmetry considerations. As illustrated in the next section for critical fixed points, from the scaling superoperator \mathcal{S} one can identify all relevant perturbations of a fixed point and therefore analyze its stability.

5.4 Quantum Criticality

In this section we apply the scale invariant MERA to the study of critical fixed points of the RG flow, that is, to quantum critical points. In this way we describe an important application of entanglement renormalization, while also demonstrating the validity of the approach. For concreteness, we analyze the quantum Ising chain with critical transverse magnetic field,

$$H = \sum_s \sigma_x(s) \otimes \sigma_x(s+1) + \sum_s \sigma_z(s), \quad (5.39)$$

whose well-known critical properties are described by a (1+1) conformal field theory (CFT) [22].

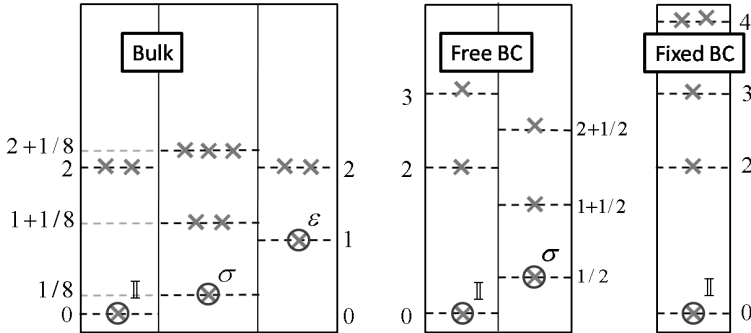
5.4.1 Scaling Operators and Critical Exponents

Most properties of a quantum critical point can be extracted from the spectral decomposition of the (linearized) RG map at the corresponding fixed point of the RG flow; see, e.g., [4]. In the present case, the spectral decomposition of the scaling superoperator \mathcal{S} [14, 15],

$$\mathcal{S}(\bullet) = \sum_{\alpha} \lambda_{\alpha} \phi_{\alpha} \text{Tr}(\hat{\phi}_{\alpha} \bullet), \quad \text{tr}(\hat{\phi}_{\alpha} \phi_{\beta}) = \delta_{\alpha\beta}, \quad (5.40)$$

readily provides us with the scaling operators of the lattice model, namely those operators ϕ_{α} on two contiguous sites that transform into themselves

⁷This conjecture would be true if $\lim_{\epsilon \rightarrow 0} (\bar{\mathcal{A}}^{h^*+\epsilon o}(h^*) - \bar{\mathcal{A}}^{h^*}(h^*))/\epsilon = 0$, which at a critical point is both plausible and compatible with numerical tests.

**FIGURE 5.7**

Scaling dimensions of the quantum critical Ising model extracted from the bulk and surface scaling superoperators of a $\chi = 16$ MERA.

Δ^{CFT}	$\Delta_{\chi=16}^{\text{MERA}}$	error	Δ^{CFT}	$\Delta_{\chi=16}^{\text{MERA}}$	error
(\mathbb{I}) 0	0	—	2	1.99956	0.022%
(σ) 0.125	0.124997	0.003%	2	1.99985	0.007%
(ϵ) 1	0.99993	0.007%	2	1.99994	0.003%
1.125	1.12495	0.005%	2	2.00057	0.03%
1.125	1.12499	0.001%			

TABLE 5.1

Scaling dimensions of the critical quantum Ising chain.

under the coarse-graining transformation,

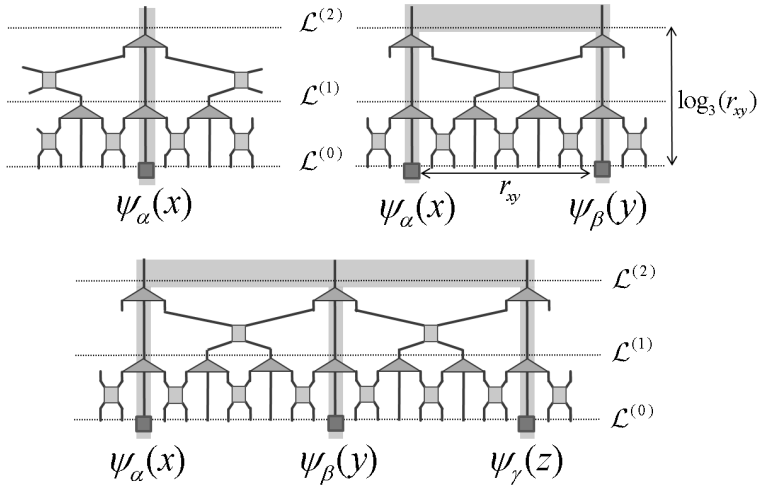
$$\mathcal{S}(\phi_\alpha) = \lambda_\alpha \phi_\alpha, \quad \lambda_\alpha \equiv 3^{-\Delta_\alpha}, \quad (5.41)$$

as well as their scaling dimensions $\Delta_\alpha = -\log_3(\lambda_\alpha)$. An example of a scaling operator is the identity operator $\phi_{\mathbb{I}} \equiv \mathbb{I}$,

$$\mathcal{S}(\mathbb{I}) = \mathbb{I}, \quad \Delta_{\mathbb{I}} = 0, \quad (5.42)$$

as can be seen by using $u^\dagger u = I$ and $w^\dagger w = I$ in Eq. (5.26). Its dual operator $\hat{\phi}_{\mathbb{I}}$ in Eq. (5.40) is the ground state reduced density matrix $\hat{\rho}_{\mathbb{I}} \equiv \hat{\rho}$ for a block of two contiguous sites. A second example of a scaling operator is of course the two-site fixed-point interaction h^* , see Eq. (5.36), with scaling dimension $\Delta_{h^*} = 2$.

Fig. 5.7 shows the 12 smallest scaling dimensions for the Ising model, obtained with a scale invariant MERA with $\chi = 16$. As expected, they appear organized in *conformal towers* of three scaling operators known as the *identity* \mathbb{I} , the *spin* σ , and the *energy* ϵ , which correspond to the *primary fields* of the Ising CFT [22]. Recall that all critical exponents of a model can be obtained

**FIGURE 5.8**

One-point, two-point and three-point correlators for one-site scaling operators. After $\log_3(r_{xy})$ iterations of the coarse-graining transformation, two operators separated by r_{xy} sites become nearest neighbors. Hence the polynomial decay of correlations.

from the scaling dimensions of its primary fields. For instance, for the Ising model the exponents ν and η are $\nu = 2\Delta_\sigma$ and $\eta = \frac{1}{2-\Delta_\epsilon}$, and the *scaling laws* express the critical exponents $\alpha, \beta, \gamma, \delta$ in terms of ν and η . We can also identify, e.g., all the relevant perturbations of the model, corresponding to scaling dimension $\Delta < 2$, as well as its marginal perturbations, with $\Delta = 2$, which are listed in Table 5.1.

5.4.2 Correlators and the Operator Product Expansion

Extracting correlators from a scale invariant MERA is also relatively easy. In terms of the one-site scaling operators ψ_α (see [15] for details), one-point, two-point and three-point correlators read

$$\langle \psi_\alpha(x) \rangle = C_\alpha, \quad \langle \psi_\alpha(x) \psi_\beta(y) \rangle = \frac{C_{\alpha\beta}}{r_{xy}^{\Delta_\alpha + \Delta_\beta}}, \quad (5.43)$$

$$\langle \psi_\alpha(x) \psi_\beta(y) \psi_\gamma(z) \rangle = \frac{C_{\alpha\beta\gamma}}{r_{xy}^{\Delta_\alpha + \Delta_\beta - \Delta_\gamma} r_{yz}^{\Delta_\beta + \Delta_\gamma - \Delta_\alpha} r_{zx}^{\Delta_\gamma + \Delta_\alpha - \Delta_\beta}}, \quad (5.44)$$

where the sites x, y, z have been chosen conveniently and $r_{xy} \equiv |x - y|$, $r_{yz} \equiv |y - z|$ and $r_{xz} \equiv |x - z|$. The coefficients C_α , $C_{\alpha\beta}$ and $C_{\alpha\beta\gamma}$ are given by

$$C_\alpha \equiv \text{tr}(\psi_\alpha \hat{\rho}) = \delta_{\alpha\mathbb{I}}, \quad C_{\alpha\beta} \equiv \text{tr}((\psi_\alpha \otimes \psi_\beta) \hat{\rho}), \quad (5.45)$$

$$C_{\alpha\beta\gamma} \equiv 2^{\Delta_\alpha + \Delta_\gamma - \Delta_\beta} \text{tr}((\psi_\alpha \otimes \psi_\beta \otimes \psi_\gamma) \hat{\rho}), \quad (5.46)$$

where $\hat{\rho}$ simultaneously denotes the reduced density matrix on one, two and three sites respectively. Thus, as expected in a critical system, the scale invariant MERA produces polynomial correlators. How this occurs is very intuitive. Consider for instance the two-point correlator $\langle \psi_\alpha(x) \psi_\beta(y) \rangle$ for $r_{xy} = 3^\tau$. As illustrated in Fig. 5.8, operators ψ_α and ψ_β become nearest neighbors after $\tau = \log_3(r_{xy})$ iterations of the coarse-graining transformation. Since this transformation maps ψ_α into $\psi'_\alpha = 3^{-\Delta_\alpha} \psi_\alpha$, each iteration contributes a factor $3^{-\Delta_\alpha - \Delta_\beta}$ to the correlator, with

$$(3^{-\Delta_\alpha - \Delta_\beta})^\tau = (3^{-\Delta_\alpha - \Delta_\beta})^{\log_3(r_{xy})} = 3^{\log_3(r_{xy})^{-\Delta_\alpha - \Delta_\beta}} = \frac{1}{r_{xy}^{\Delta_\alpha + \Delta_\beta}}, \quad (5.47)$$

which explains its scaling. Finally, in order for the correlator $\langle \psi_\alpha(x) \psi_\beta(y) \rangle$ to be non-zero, the tensor product of the scaling operators $\psi_\alpha \otimes \psi_\beta$ must fuse into the two-site identity operator \mathbb{I} , which occurs with amplitude $C_{\alpha\beta}$.

The coefficients of Eqs. (5.45)-(5.46) are analogous to those that appear in CFT. A proper choice of normalization of the fields leads to $C_{\alpha\beta} = \delta_{\alpha\beta}$, whereas coefficients $C_{\alpha\beta\gamma}$ define the operator product expansion (OPE), which for the primary fields of the Ising CFT reads

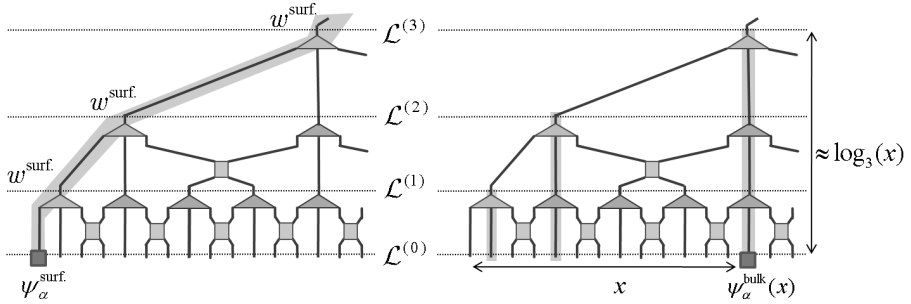
$$C_{\alpha\beta\mathbb{I}}^{\text{CFT}} = \delta_{\alpha\beta}, \quad C_{\sigma\sigma\epsilon}^{\text{CFT}} = \frac{1}{2}, \quad C_{\sigma\sigma\sigma}^{\text{CFT}} = C_{\epsilon\epsilon\epsilon}^{\text{CFT}} = C_{\epsilon\epsilon\sigma}^{\text{CFT}} = 0. \quad (5.48)$$

A MERA with $\chi = 16$ reproduces all these OPE coefficients with errors smaller than 3×10^{-4} .

The above comparisons with exact results from CFT allow us to conclude that entanglement renormalization produces accurate estimates of the critical properties of a system. Once this has been established, the present approach can be used to actually identify which CFT describes a given quantum critical point by estimating the conformal data (central charge, conformal dimensions and OPE of primary fields) that completely characterize it [15]. The present discussion also indicates that the scale invariant MERA can be regarded as approximately realizing an infinite dimensional representation of the Virasoro algebra [22]. The finite value of χ implies that only a finite number of the quasi-primary fields of the theory can be included in the description. Fields with small scaling dimension, such as primary fields, are retained foremost. However, an exact description requires χ to be infinite.

5.4.3 Surface Critical Phenomena

So far we have restricted our attention to translation invariant systems. Critical systems with a boundary can also be described by adding a boundary to

**FIGURE 5.9**

Scale invariant MERA with a boundary made of copies of the same surface isometry w^{surf} and the tensors (u, w) of the bulk.

the scale invariant MERA [16]. This is done by introducing a surface isometry w^{surf} at the boundary, while the pair (u, w) corresponding to the translation invariant case still represents the bulk; see Fig. 5.9.

$\Delta_{\text{BCFT}}^{\text{free}}$	$\Delta_{x=16}^{\text{MERA}}$	error	$\Delta_{\text{BCFT}}^{\text{fixed}}$	$\Delta_{x=16}^{\text{MERA}}$	error
(I) 0	0	—	(I) 0	0	—
(σ) 0.5	0.499	0.2%	2	1.984	0.8%
1.5	1.503	0.18%	3	2.998	0.07%
2	2.001	0.07%	4	4.005	0.12%
2.5	2.553	2.1%	4	4.010	2.5%

TABLE 5.2

Scaling dimensions for free and fixed boundary conditions.

The presence of a boundary modifies the bulk correlators of Eqs. (5.43)-(5.44). For instance, the expected value $\langle \psi_\alpha(x) \rangle$ becomes non-trivial:

$$\langle \psi_\alpha(x) \rangle_{\text{surf}} \approx \frac{C_{0\alpha}^{\text{surf}}}{x^{\Delta_\alpha}}, \quad (5.49)$$

where x is the distance to the boundary (in number of sites) and $C_{0\alpha}^{\text{surf}}$ is some constant. Again, this result is very intuitive. Consider $x = (3^{\tau+1} - 1)/2$. As illustrated in Fig. 5.9, after $\tau = \log_3(\frac{2x+1}{3}) \approx \log_3(x)$ iterations of the coarse-graining transformation the bulk scaling operator $\psi_\alpha^{\text{bulk}}$ has reached the boundary, into which it fuses with $C_{0\alpha}^{\text{surf}}$. In addition, by diagonalizing the *surface scaling superoperator* S^{surf} that maps the boundary into itself at different length scales, we can extract the surface scaling operators $\psi_\alpha^{\text{surf}}$ and their scaling dimensions, as well as the fusion rules between bulk and surface operators. Fig. 5.7 and Table 5.2 show the surface scaling dimensions for *free* and *fixed* boundary conditions. One can see that the number of conformal

towers is smaller than in the bulk: for free boundary conditions, the primary fields left are the identity \mathbb{I} and the spin σ , whereas for fixed boundary conditions only the identity \mathbb{I} remains. Once more, the results compare well with the exact solution provided by (boundary) CFT [22].

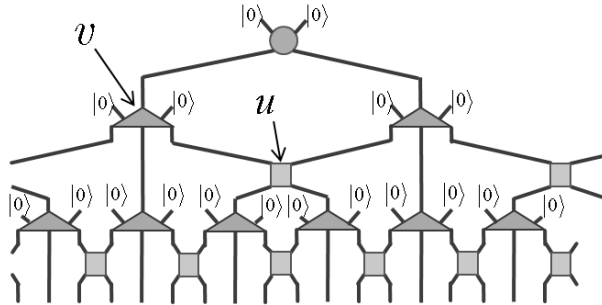
5.5 Summary and Outlook

In this chapter we have reviewed, step by step, the construction of a coarse-graining transformation for quantum many-body systems on a lattice that fulfills two natural requirements: it disposes of all short-distance degrees of freedom while it retains the properties of the ground state of a local Hamiltonian. This is achieved by using disentanglers u , that remove short-range entanglement across the boundary of a block of sites, and isometries w , that coarse-grain these blocks of sites according to White's rule and thus preserve the support of the ground state reduced density matrix.

This transformation can be used to compute ground state expected values of the form $\langle o_1 o_2 \cdots o_k \rangle$ both in finite and infinite systems. In a finite system, we simply coarse-grain the lattice until the effective Hamiltonian can be numerically diagonalized. In an infinite system, we iterate the coarse-graining transformation until we become sufficiently close to a fixed point of the RG flow – that is, until we have eliminated all irrelevant perturbations in the original Hamiltonian. Then we expand local operators in terms of the scaling operators of the theory, whose expected values can also be determined. In a symmetry-breaking phase, the fixed point corresponds to an unentangled ground state, and local operators can be trivially evaluated. In a critical phase, the fixed point corresponds to a highly entangled ground state, but a scale invariant MERA can still be used to approximately compute the scaling operators and evaluate their expected values.

Notice that the scale invariant MERA allows us to make precise the notion of scale invariance in a lattice system. In order to get rid of the dependence on the original lattice spacing, one typically invokes the continuum limit. Here, instead, we have considered a coarse-graining such that all short-distance degrees of freedom are consistently discarded. The ground state of the lattice is then invariant under changes of scale if its effective description is locally identical to the original one. We envisage that this lattice version of scale invariance will become a useful testing ground for ideas and problems that are harder to analyze in the continuum limit. Recent work on the holographic principle might be a first step in this direction [23].

We conclude this chapter with a suggestive interpretation of the MERA. Notice that an isometry $w : \mathbb{V} \rightarrow \mathbb{V}^{\otimes 3}$ can be regarded as a unitary transformation $v : \mathbb{V}^{\otimes 3} \rightarrow \mathbb{V}^{\otimes 3}$ on three sites where two of these sites are initially in some fixed state $|0\rangle$, that is $w = v(|0\rangle \otimes |0\rangle)$. The MERA can thus also

**FIGURE 5.10**

The MERA seen as a unitary transformation V such that $|\Psi_{\text{GS}}\rangle = V|0\rangle^{\otimes N}$.

be understood as a quantum circuit, made of gates v and u , that implements a unitary transformation V such that an unentangled state $|0\rangle^{\otimes N}$ becomes the ground state $|\Psi_{\text{GS}}\rangle$ of a local Hamiltonian H ; see Fig. 5.10. Thus, ground states of local Hamiltonians can be regarded as the result of a quantum computation that flows from the largest available length scales (i.e., the size of the system) to the smallest length scales (distance between sites of \mathcal{L}). At each length scale, unentangled wires in state $|0\rangle$ are added and subsequently entangled with the rest of the system by means of the gates v and u .

The quantum circuit interpretation is quite insightful. For instance, it provides an explicit recipe to experimentally prepare the state $|\Psi_{\text{GS}}\rangle$ by entangling quantum systems, and it has been instrumental in generalizing the MERA to deal with fermionic and anyonic degrees of freedom [17, 18]. It also highlights the *reversible* character of the coarse-graining transformation. During coarse-graining, short-distance degrees of freedom are not actually ‘thrown away,’ but rather ‘stored’ in disentanglers and isometries, and can be re-incorporated in the picture later on. Indeed, as we have seen, from the reduced density matrix describing the state of the system at a given length scale, we can recover the state at a smaller length scale by using the descending superoperator \mathcal{D} . Finally, this viewpoint emphasizes the astonishing *structural similarities* shared by most ground states of local Hamiltonians. Consider two systems in two completely different symmetry-breaking phases but with the same correlation length ξ . Both ground states become essentially disentangled after $O(\log(\xi))$ iterations of the coarse-graining. Therefore, the two ground states can be prepared from the same unentangled state by using the same quantum circuit, made of $O(\log(\xi))$ rows of identically wired gates, just by modifying the specific gates v and u applied in each case.

Acknowledgments – Supported by the Australian Research Council (FF0668731, DP0878830).

Bibliography

- [1] L.P. Kadanoff, Rev. Mod. Phys. 39, 395 (1967).
- [2] K.G. Wilson, Rev. Mod. Phys. 47, 773 (1975).
- [3] M.E. Fisher, Rev. Mod. Phys. 70, 653 (1998).
- [4] *Scaling and Renormalization in Statistical Physics*, J. Cardy (Cambridge University Press, 1996).
- [5] G. Vidal, Phys. Rev. Lett. 99, 220405 (2007).
- [6] G. Vidal, Phys. Rev. Lett. 101, 110501 (2008).
- [7] C.M. Dawson, J. Eisert, and T.J. Osborne, Phys. Rev. Lett. 100, 130501 (2008).
- [8] M. Rizzi, S. Montangero, and G. Vidal, Phys. Rev. A 77, 052328 (2008).
- [9] G. Evenbly and G. Vidal, Phys. Rev. B 79, 144108 (2009).
- [10] G. Evenbly and G. Vidal, Phys. Rev. B 81, 235102 (2010). G. Evenbly and G. Vidal, New J. Phys. 12, 025007 (2010).
- [11] L. Cincio, J. Dziarmaga, and M.M. Rams, Phys. Rev. Lett. 100, 240603 (2008).
- [12] G. Evenbly and G. Vidal, Phys. Rev. Lett. 102, 180406 (2009). G. Evenbly and G. Vidal, Phys. Rev. Lett. 104, 187203 (2010).
- [13] M. Aguado, G. Vidal, Phys. Rev. Lett. 100, 070404 (2008). R. Koenig, B.W. Reichardt, and G. Vidal, Phys. Rev. B 79, 195123 (2009).
- [14] V. Giovannetti, S. Montangero, and R. Fazio, Phys. Rev. Lett. 101, 180503 (2008). S. Montangero, M. Rizzi, V. Giovannetti, and R. Fazio, Phys. Rev. B 80, 113103 (2009). V. Giovannetti, S. Montangero, M. Rizzi, and R. Fazio, Phys. Rev. A 79, 052314 (2009).
- [15] R.N.C. Pfeifer, G. Evenbly, and G. Vidal, Phys. Rev. A 79(4), 040301(R) (2009).
- [16] G. Evenbly et al., arXiv:0912.1642. G. Evenbly et al., arXiv:0912.2166.
- [17] P. Corboz, G. Evenbly, F. Verstraete, and G. Vidal, Phys. Rev. A 81, 010303(R) (2010). C. Pineda, T. Barthel, J. Eisert, Phys. Rev. A 81, 050303(R) (2010). P. Corboz and G. Vidal, Phys. Rev. B 80, 165129 (2009).

- [18] R. Koenig and E. Bilgin, arXiv:1006.2478 (2010); R.N.C. Pfeifer *et al.*, arXiv:1006.3532 (2010).
- [19] S.R. White, Phys. Rev. Lett. **69**, 2863 (1992).
- [20] J. Eisert, M. Cramer, and M.B. Plenio, Rev. Mod. Phys. 82, 277 (2010).
- [21] L. Tagliacozzo and G. Vidal, Phys. Rev. B 80, 235127 (2009).
- [22] *Conformal Invariance and Critical Phenomena*, M. Henkel, (Springer, 1999).
- [23] B. Swingle, arXiv:0905.1317.

6

The Geometry of Quantum Phase Transitions

Gerardo Ortiz

Department of Physics, Indiana University, Bloomington, Indiana 47405, U.S.A.

Quantum matter often displays complex phase diagrams as a result of competing interactions, with orderings (states of matter) which are believed to be influenced by being in proximity to quantum critical points, e.g., high- T_c materials, heavy fermion compounds, and frustrated magnets. Each quantum phase is characterized by different behaviors of appropriate correlation functions, such as long-range order, or algebraic or exponential decay. Since entanglement is a property inherent in quantum states and is strongly related to quantum correlations, one would expect that the entanglement present in the ground state (GS) of the system changes substantially at a quantum phase transition (QPT), i.e., when there is a qualitative change in the behavior of the correlations between constituents. Obviously, the identification and quantification of those changes become issues of utmost relevance.

Achieving a complete characterization of quantum correlations is hindered by the complexity of those many-body states and dynamical evolutions. Motivated by the fact that quantum information (QI) science provides, first and foremost, an organizing framework for addressing and quantifying different aspects of “complexity” in quantum systems, it is natural to ask the following. Can QI concepts and tools contribute to advance our understanding of many-body quantum systems? In recent years, *entanglement theory* has emerged as a powerful bridging test bed for tackling this broad question from an information-physics perspective. On one hand, entanglement is intimately tied to the inherent complexity of QI, by constituting, in particular, a *necessary* resource for computational speed-up in pure-state quantum algorithms [1]. On the other hand, critically reassessing traditional many-body settings in the light of entanglement theory has already resulted in a number of conceptual, computational, and information-theoretic developments. Notable advances include efficient representations of quantum states based on so-called *projected entangled pair states* [2], improved renormalization-group methods for both static 2D and time-dependent 1D lattice systems [3], as well as rigorous results on the computational complexity of such methods and the solvability properties of a class of generalized mean-field Hamiltonians [4, 5].

From a broader perspective, it is interesting to note that the cross-fertilization between geometry, topology, and physics has generated simple ideas that allow one to clarify many subtle issues in condensed matter and quantum field theories.¹ Several problems in distinct areas of physics can be phrased in geometrical and topological terms, resulting in a clearer understanding of their structures and a more elegant expression of their solutions. It is in this spirit that we have identified and used these mathematical concepts to characterize the geometry and topology of stable phases, represented by entangled states, of models of interacting quantum systems. Indeed, a central purpose of this chapter is to show that the field of QPTs may benefit from this interchange of ideas. In particular, two fundamental concepts will prove useful to characterize QPTs and the phases involved, one being the notion of *Generalized Entanglement* (GE), and the other the use of topological quantum numbers, sharp indicators of phase transitions. The first, presented in Sec. 6.1, represents a unifying algebraic approach to study QPTs. The second, presented in Sec. 6.2, constitutes a purely geometric and topological method to determine quantum phase diagrams. Each topological quantum number, related to a Berry phase [7], labels a thermodynamic state, and transitions between them determine the boundaries of the quantum phase diagram.

Our ultimate goal is to understand the geometric content of the set of quantum states of matter, i.e., the *geometry of entanglement*, and its relation to physical behavior, or response to external probes. For instance, what physically distinguishes an insulator from a metal, or superconductor, is the way the system responds to external electromagnetic probes, e.g., in an insulator a steady current cannot flow at zero temperature [8]. This macroscopic characterization of matter translates microscopically into a study of the localization properties of their quantum states, which differ in a fundamental way. What are the topological differences between the states defining a conductor and an insulator? Moreover, we want to understand when and how the geometry and topology of states changes through a QPT.

¹From a mathematical standpoint, the terms geometry and topology of a manifold refer to different concepts. In physics these terms are often used loosely. Imagine a surface made of rubber which you are allowed to deform in various ways. Geometry encompasses all those properties of the surface that do change under such deformation, e.g., the curvature. On the other hand, topology comprises those aspects of the surface which remain unchanged by the deformation, e.g., the number of holes on the surface. Most of the mathematical concepts specifically needed to understand this chapter are introduced along the way. Others, such as fiber bundles, anholonomy, topological invariants, homotopy theory, etc., are not developed because of the lack of space. The reader may consult, e.g., Ref. [6].

6.1 Entanglement and Quantum Phase Transitions

In this Section we introduce the conventional concept of entanglement and its generalizations to include all possible physical settings. We focus, in particular, on the problem of characterizing quantum critical models from a GE perspective [9, 10]. It becomes natural to look for a good measure of entanglement as a way to characterize the QPT. Thus, a relevant question is whether GE may be able to characterize the QPT, and to what extent.

We have a twofold objective: first, to further test the usefulness of GE-based criticality indicators in characterizing static quantum phase diagrams with a higher degree of complexity than considered so far, in particular, multiple competing phases; second, to start analyzing time-dependent, non-equilibrium QPTs, for which a number of outstanding physics questions remain. In this context, special emphasis will be devoted to establish the emergence and validity of *universal scaling laws for non-equilibrium observables*.

6.1.1 Entanglement 101

The *conventional* notion of entanglement defines how quantum correlations of a number of *distinguishable* subsystems differ from classical correlations. Typically these studies focus on two subsystems (the bipartite or “Alice and Bob” setting). Basically, given a quantum system with state space \mathcal{H} , it can *a priori* support inequivalent tensor product structures; for instance, $\mathcal{H} = \mathcal{H}_1 \otimes \mathcal{H}_2 \otimes \cdots \otimes \mathcal{H}_N$, or, for even N , $\mathcal{H} = \mathcal{H}_{12} \otimes \mathcal{H}_{34} \otimes \cdots \otimes \mathcal{H}_{(N-1)N}$, where $\mathcal{H}_{ij} = \mathcal{H}_i \otimes \mathcal{H}_j$. The entanglement of states in \mathcal{H} is unambiguously defined only once a *preferred subsystem decomposition* is chosen: $\mathcal{H} = \bigotimes_j \mathcal{H}_j$. Relative to the selected multipartite structure, a pure state $|\Psi\rangle$ is entangled iff $|\Psi\rangle$ induces at least some mixed subsystem states. For example, if $\mathcal{H} = \mathcal{H}_A \otimes \mathcal{H}_B$, where the Hilbert spaces for Alice and Bob, $\mathcal{H}_A, \mathcal{H}_B$, are two-dimensional, i.e., $|\psi\rangle_{A,B} = a_0^{A,B}|0\rangle_{A,B} + a_1^{A,B}|1\rangle_{A,B}$, and

$$|\Psi\rangle = \frac{|0\rangle_A \otimes |1\rangle_B + |1\rangle_A \otimes |0\rangle_B}{\sqrt{2}}, \text{ then } \begin{cases} \rho_A = \text{Tr}_B |\Psi\rangle \langle \Psi| \\ \rho_B = \text{Tr}_A |\Psi\rangle \langle \Psi| \end{cases} \text{ are mixed. (6.1)}$$

In contrast, if

$$|\Psi\rangle = |0\rangle_A \otimes |1\rangle_B, \text{ then } \rho_A \text{ and } \rho_B \text{ are pure. (6.2)}$$

Thus, in the conventional approach, entangled pure states look *mixed* to at least some *local* observers, while unentangled pure states still look pure. In standard QI settings the choice of preferred subsystem is usually not problematic, as there is a notion of locality in *real space*. Indeed, spatially separated local parties are often taken as synonymous with distinguishable quantum subsystems.

It is clear that not only the assumption of distinguishability, which is natural for spin systems, but also the few-subsystem scenario (*Alice* and *Bob*) are too narrow to embrace all possible physical settings. In particular, the need to go beyond this subsystem-based framework becomes manifest when one tries to apply the conventional concept of entanglement to the physics of matter, since the constituents of a quantum many-body system are *indistinguishable* particles. We therefore pose the following three questions.

First, what does entanglement mean for indistinguishable particles? It has been known since the early days of quantum mechanics that particles in nature are either bosons or fermions in 3 or more spatial dimensions. Indistinguishability places an additional constraint on the space of admissible states which manifests itself in their symmetry properties. The physically accessible state space is the symmetric/antisymmetric, bosonic/fermionic subspace of the full tensor product state space. For example, consider the free electron gas, or Fermi liquid, in the real-space x -representation described by the totally anti-symmetric wave function

$$\langle x_1, x_2, \dots | \Psi \rangle \sim \text{Det} \begin{pmatrix} e^{ik_1 x_1} & e^{ik_1 x_2} & \dots \\ e^{ik_2 x_1} & e^{ik_2 x_2} & \dots \\ \vdots & \vdots & \dots \end{pmatrix}, \quad (6.3)$$

where k_j is a label of momentum. Exchange correlations are present but are not, in principle, a usable resource in the usual QI sense.

Second, what about particle vs. mode entanglement? The state $\langle x_1, x_2, \dots | \Psi \rangle$ in Eq. (6.3) exhibits mode entanglement with respect to the set of momentum modes; yet, the electrons are non-interacting. A set of modes provides a factorization into a distinguishable-subsystem structure, but in principle inequivalent factorizations, e.g., position modes and momentum modes, may occur on the same footing for a given system.

Third, what is the most appropriate operator language? The algebraic language (fermions, bosons, anyons, gauge fields, etc.) used to describe a quantum system may be intentionally changed by mappings such as the Jordan-Wigner transformation and its generalizations [11].

The bottom line is that non-trivial quantum statistics, or other physical superselection rules, can make the choice of preferred subsystem problematic. Our generalized approach can overcome such difficulties, by removing the need for a subsystem decomposition from the start. Even when a subsystem partition exists, we would like to emphasize that from the viewpoint of GE, ordinary separable pure states, i.e., states that can be written as a tensor product of normalized subsystem states, $|\Psi\rangle = |\psi\rangle_1 \otimes |\phi\rangle_2 \otimes \dots \otimes |\varphi\rangle_N$, are not necessarily equivalent to generalized unentangled states.

6.1.2 Generalized Entanglement

GE provides an entanglement framework which is uniquely positioned to answer the three questions above and more. Physically, GE rests on the idea

that entanglement is an *observer-dependent* concept, whose properties are determined by the expectation values of a *subspace of observables*, i.e., the physically relevant point of view, without reference to a preferred decomposition of the overall system into subsystems. The notion of GE can be applied to any operator language (fermions, bosons, spins, etc.) used to describe a physical system and includes the conventional entanglement settings introduced to date in a unified fashion. In other words, GE is a context-dependent concept, i.e., independent of the operator language but dependent upon the way we can access information, on the set of observables used to extract information from the system. The formal development of GE may be found in [9]. Here we will simply recall the key concepts and further illustrate them by example.

As mentioned above, our notion of GE is relative to a subspace of observables \mathcal{A} of the quantum system. The basic idea is to generalize the observation that standard entangled pure states are those that look mixed to local observers. Given a pure state of a system, we remind the reader that the associated *reduced state*, or \mathcal{A} -state, is obtained by only considering the expectation values of the distinguished observables \mathcal{A} . In other words, an \mathcal{A} -state is a linear and positive functional ω on the operators of \mathcal{A} induced by a density matrix ρ according to $\omega(x) = \text{tr}(\rho x)$. The set of reduced states is convex. We then have the following.

Definition : A pure state $|\Psi\rangle$ is generalized unentangled relative to the distinguished set of observables \mathcal{A} , if its reduced state is pure (extremal), and generalized entangled otherwise. Similarly, a mixed state is generalized unentangled relative to \mathcal{A} , if it can be written as a convex combination of generalized unentangled pure states.

While the assumption of a Lie-algebraic structure (see Appendix for a gentle introduction to Lie algebras and *Generalized Coherent States* (GCSs)) is not necessary for the GE framework to be applicable [9], it has the advantage of both suggesting simple GE measures and allowing a complete characterization of generalized unentangled states. When \mathcal{A} is an irreducibly represented Lie algebra $\mathcal{A} = \mathfrak{h}$, the set of unentangled pure states is identical to the set of GCSs. Another, more physically transparent, characterization of generalized-unentangled states is as the set of states that are unique GSs of a distinguished observable (e.g., a Hamiltonian H).

6.1.3 Quantifying Entanglement: Purity

One would like to have a way to quantify how entangled a given state is. In our theory of GE (as well as in conventional entanglement theory), no single measure is able to uniquely characterize the entanglement properties of a state. Indeed, a hierarchy of characterizations of quantum correlations is necessary. In order to connect the notions of generalized unentanglement and coherence, a natural way is to introduce the quadratic purity $P_{\mathfrak{h}}$ relative to the distinguished subspace of observables \mathfrak{h} .

Definition : Let $\{x_i\}$ be a Hermitian ($x_i^\dagger = x_i$) and commonly normalized

orthogonal basis for \mathfrak{h} ($\text{tr}(x_i x_j) \propto \delta_{ij}$). For any $|\Psi\rangle \in \mathcal{H}$, the purity of $|\Psi\rangle$ relative to \mathfrak{h} , \mathfrak{h} -purity, is

$$P_{\mathfrak{h}}(|\Psi\rangle) = K \sum_i |\langle \Psi | x_i | \Psi \rangle|^2 , \quad (6.4)$$

where K is a global normalization factor chosen so that $0 \leq P_{\mathfrak{h}} \leq 1$.

Notice that if \mathfrak{h} is a Lie algebra, it is invariant under group transformations, $\tilde{x}_i = \mathfrak{g}^\dagger x_i \mathfrak{g}$, where $\mathfrak{g} \in e^{i\mathfrak{h}}$. The following characterizations of unentangled states, proven in Ref. [9], demonstrate the power of the Lie-algebraic setting.

Theorem : The following statements are equivalent for an irreducible representation of a Lie algebra \mathfrak{h} on \mathcal{H} and state ρ

- (1) ρ is generalized unentangled relative to \mathfrak{h} .
- (2) $\rho = |\Psi\rangle\langle\Psi|$ with $|\Psi\rangle$ the unique GS of some H in \mathfrak{h} .
- (3) $\rho = |\Psi\rangle\langle\Psi|$ with $|\Psi\rangle$ a lowest-weight vector of \mathfrak{h} .
- (4) ρ has maximum \mathfrak{h} -purity.

6.1.3.1 A Simple Example

Consider a bipartite situation with preferred distinguishable subsystems A and B . The total Hilbert space $\mathcal{H} = \mathcal{H}_A \otimes \mathcal{H}_B$, such that $\dim \mathcal{H}_A = m$ and $\dim \mathcal{H}_B = n$. Physical access is restricted to *local* observables acting on one subsystem, i.e., observables in the set $\mathcal{A}_{\text{loc}} = \{\hat{A} \otimes \mathbf{1} \oplus \mathbf{1} \otimes \hat{B}\}$, with \hat{A} and \hat{B} Hermitian and traceless. For each pure state $|\Psi\rangle \in \mathcal{H}$, the reduced state ρ_{red} is then determined by the pair of reduced density operators ρ_A and ρ_B .

Theorem: An \mathcal{A}_{loc} -state is pure iff it is induced by a pure product state, meaning that *conventional* bipartite entanglement is equivalent to GE relative to \mathcal{A}_{loc} .

For the particular case of two spin-1/2 parties (i.e., two qubits $m = n = 2$), with $\mathcal{A} = \mathfrak{h} = \mathfrak{su}(2) \oplus \mathfrak{su}(2) = \{S_x^j, S_y^j, S_z^j \mid j = 1, 2\}$, where the three generators of $\mathfrak{su}(2)$, $S_\alpha^j = \frac{1}{2}\sigma_\alpha^j$, can be written in terms of Pauli matrices $\sigma_j \equiv (\sigma_x^j, \sigma_y^j, \sigma_z^j)$ with $\hbar = 1$, and a generic normalized state $|\Psi\rangle = a_1|\uparrow\uparrow\rangle + a_2|\uparrow\downarrow\rangle + a_3|\downarrow\uparrow\rangle + a_4|\downarrow\downarrow\rangle$, the purity relative to \mathfrak{h} is

$$P_{\mathfrak{h}}(|\Psi\rangle) = 2 \sum_{j,\alpha} \langle \Psi | S_\alpha^j | \Psi \rangle^2 , \begin{cases} P_{\mathfrak{h}} = 1 & \text{product states} \\ \vdots & \vdots \\ P_{\mathfrak{h}} = 0 & \text{Bell states} \end{cases} . \quad (6.5)$$

When physical access is unrestricted (such as $\mathcal{A} = \mathfrak{su}(4)$), *all* pure states have maximal purity, meaning that all of them are generalized unentangled.

To understand the relevance of the operator language used to describe our physical system, let us consider a maximally entangled Bell state

$$|\text{Bell}\rangle = \frac{|\uparrow\downarrow\rangle - |\downarrow\uparrow\rangle}{\sqrt{2}} = \frac{S_+^1 - S_+^2}{\sqrt{2}} |\downarrow\downarrow\rangle , \quad (6.6)$$

where $S_\pm^j = S_x^j \pm iS_y^j$, and change our spin into a fermionic description. After

a Jordan-Wigner isomorphic mapping between two spins and two fermionic modes,

$$\begin{cases} S_+^1 = c_1^\dagger \\ S_+^2 = (1 - 2n_1)c_2^\dagger \end{cases} \quad \text{and } |\text{Bell}\rangle = \frac{c_1^\dagger - c_2^\dagger}{\sqrt{2}}|0\rangle_F , \quad (6.7)$$

where $|0\rangle_F$ is the fermionic vacuum. Written in the fermionic language this is a single-particle state which can only display *mode* entanglement relative to the local spin algebra \mathfrak{h} . However, had we asked whether $|\text{Bell}\rangle$ is entangled relative to the algebra $\mathfrak{h}'' = \mathfrak{u}(2) = \{(c_1^\dagger c_2 + c_2^\dagger c_1)/\sqrt{2}, i(c_1^\dagger c_2 - c_2^\dagger c_1)/\sqrt{2}, n_1 - \frac{1}{2}, n_2 - \frac{1}{2}\} = \{(S_x^1 S_x^2 + S_y^1 S_y^2)/\sqrt{2}, (S_x^1 S_y^2 - S_y^1 S_x^2)/\sqrt{2}, S_z^1, S_z^2\}$, the answer would be no. The message is that the property of entanglement is independent of the operator language used to describe a state, and only dependent on the observer.

6.1.4 Statics of Quantum Phase Transitions

All these interesting features make the quadratic purity measure of GE a physically appealing measure to characterize a QPT. Consider the class of exactly solvable spin-1/2 one-dimensional models described by the following Hamiltonian (an expanded discussion is given in [12]):

$$H = - \sum_{i=1}^N \left[\frac{(1+\gamma)}{2} \sigma_x^i \sigma_x^{i+1} + \frac{(1-\gamma)}{2} \sigma_y^i \sigma_y^{i+1} \right] + \sum_{i=1}^N (h - (-1)^i \delta) \sigma_z^i , \quad (6.8)$$

where periodic boundary conditions are assumed, that is, $\sigma_\alpha^i \equiv \sigma_\alpha^{i+N}$. Here, $\gamma \in [0, 1]$, $h \in [-\infty, \infty]$, and $\delta \in [-\infty, \infty]$ are the anisotropy in the XY plane, the uniform magnetic field strength, and the alternating magnetic field strength, respectively. For $\delta = 0$, the above Hamiltonian recovers the anisotropic XY model in a transverse field studied in Ref. [10], whereas $\delta > 0$, $\gamma = 1$ corresponds to the Ising model in an alternating transverse field recently analyzed in Ref. [13].

An exact solution for the energy spectrum of the above Hamiltonian may be obtained by generalizing the basic steps used in the standard Ising case [10, 14], to account for the existence of a two-site primitive cell introduced by the alternation. By first separately applying the Jordan-Wigner mapping [11] to even and odd lattice sites [15], and then using a Fourier transformation to momentum space, Hamiltonian (6.8) may be rewritten as

$$H = \sum_{k \in K_+} H_k = \sum_{k \in K_+} \hat{A}_k^\dagger \hat{H}_k \hat{A}_k , \quad K_+ = \left\{ \frac{\pi}{N}, \frac{3\pi}{N}, \dots, \left(\frac{\pi}{2} - \frac{\pi}{N} \right) \right\} . \quad (6.9)$$

In Eq. (6.9), \hat{H}_k is a four-dimensional Hermitian matrix, $\hat{A}_k^\dagger = (a_k^\dagger, a_{-k}^\dagger, b_k^\dagger, b_{-k})$ is a vector operator, and a_k^\dagger (b_k^\dagger) denote canonical fermionic operators that create a spinless fermion with momentum k for even (odd)

sites. Thus, the problem reduces to diagonalizing each of matrices \hat{H}_k , for $k \in K_+$. If $\epsilon_{k,1}, \epsilon_{k,2}, \epsilon_{k,3}, \epsilon_{k,4}$, with $\epsilon_{k,1} \leq \epsilon_{k,2} \leq 0 \leq \epsilon_{k,3} \leq \epsilon_{k,4}$ denoting the energy eigenvalues of \hat{H}_k , then

$$H_k = \sum_{n=1,\dots,4} \epsilon_{k,n} \gamma_{k,n}^\dagger \gamma_{k,n}, \quad (6.10)$$

where $\gamma_{k,n}^\dagger, \gamma_{k,n}$ are quasi-particle excitation operators for mode k in the n th band. At zero temperature, the $\epsilon_{k,1}$ and $\epsilon_{k,2}$ bands are occupied, whereas $\epsilon_{k,3}$ and $\epsilon_{k,4}$ are empty; thus the GS energy $E_{\text{GS}} = \sum_{k \in K_+} (\epsilon_{k,1} + \epsilon_{k,2})$, with $\epsilon_{k,1} < 0, \epsilon_{k,2} \leq 0$.

By denoting $|\text{vac}\rangle$ the fermionic vacuum, and by exploiting the symmetry properties of the Hamiltonian, the many-body GS may be expressed in the form $|\Psi\rangle_{\text{GS}} = \prod_{k \in K^+} |\Psi_k\rangle$, with

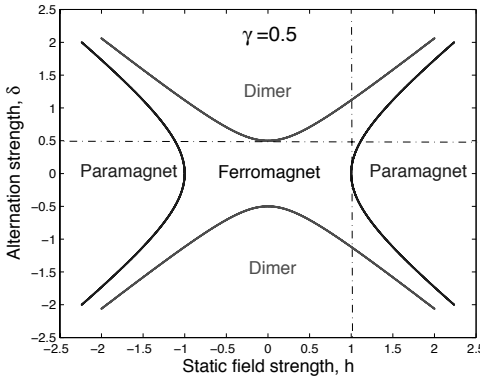
$$|\Psi_k\rangle = \left(u_k^{(1)} + u_k^{(2)} a_k^\dagger a_{-k}^\dagger + u_k^{(3)} b_k^\dagger b_{-k}^\dagger + u_k^{(4)} a_k^\dagger b_{-k}^\dagger + u_k^{(5)} a_{-k}^\dagger b_k^\dagger + u_k^{(6)} a_k^\dagger a_{-k}^\dagger b_k^\dagger b_{-k}^\dagger \right) |\text{vac}\rangle, \quad (6.11)$$

for complex coefficients determined by diagonalizing H_k , and with normalization condition $\sum_{a=1}^6 |u_k^{(a)}|^2 = 1$. Since QPTs are caused by the non-analytical behavior of E_{GS} , QCPs correspond to zeros (h_c, δ_c, γ_c) of $\epsilon_{k,2}$. The quantum phase boundaries are determined by the following pair of equations: $h^2 = \delta^2 + 1$; $\delta^2 = h^2 + \gamma^2$. The resulting anisotropic quantum phase diagram is shown in Fig. 6.1 where, without loss of generality, we set $\gamma = 0.5$. Quantum phases corresponding to disordered (paramagnetic, PM) behavior, dimer order (DM), and ferromagnetic long-range order (FM) emerge as depicted. In the general case, the boundaries between FM and PM phases, as well as between FM and DM phases, are characterized by second-order broken-symmetry QPTs. Interestingly, however, E_{GS} develops singularities at

$$(h_c, \delta_c, \gamma_c) = (0, \delta = \pm\gamma), \quad (h_c, \delta_c, \gamma_c) = (\pm 1, \delta = 0), \quad (6.12)$$

where fourth-order broken-symmetry QPTs occur along the paths approaching the QCPs (Fig. 6.1, dashed-dotted lines). In the isotropic limit ($\gamma = 0$), an insulator-metal Lifshitz QPT occurs, with no broken-symmetry order parameter. For simplicity, we shall restrict ourselves to broken-symmetry QPTs in what follows; thus $\gamma > 0$. Standard finite-size scaling analysis reveals that new quantum critical behavior emerges in connection with the alternating fourth-order QCPs in Eq. (6.12) [13]. Thus, in addition to the usual Ising universality class, characterized by critical exponents $\nu = 1, z = 1$, an alternating universality class occurs, with critical exponents $\nu = 2, z = 1$, where z is the dynamic critical exponent [16].

The key step toward applying GE as a QPT indicator is to identify an algebra of observables whose expectations reflect the changes in the GS as a function of the control parameters. One immediately realizes that Hamiltonian

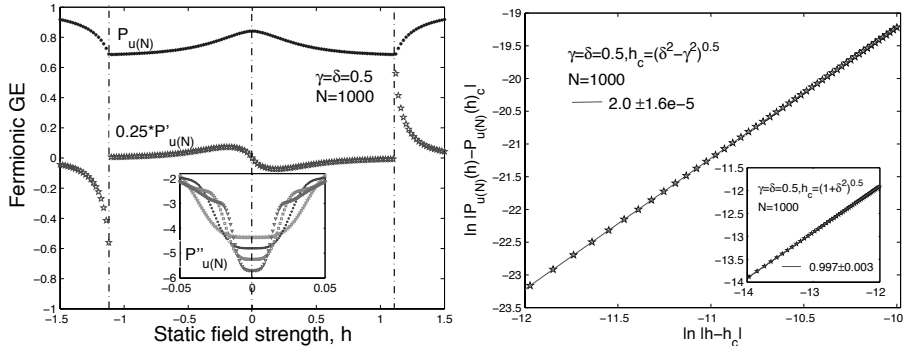
**FIGURE 6.1**

Phase diagram of the spin-1/2 XY alternating Hamiltonian given in Eq. (6.8) with $\gamma = 0.5$.

Eq. (6.8), once written in fermionic language, is an element of the Lie algebra $\mathfrak{so}(2N)$, which includes *arbitrary* bilinear fermionic operators. As a result, the GS is always a GCS of $\mathfrak{so}(2N)$, and GE relative to $\mathfrak{so}(2N)$ carries no information about QCPs. However, the GS becomes a GCS of the number-conserving sub-algebra $\mathfrak{u}(N)$ in both the fully PM and DM limit. This motivates the choice of the fermionic $\mathfrak{u}(N)$ -algebra as a natural candidate for this class of systems [10]. Taking advantage of the symmetries of this Hamiltonian, the fermionic purity becomes:

$$\begin{aligned} P_{\mathfrak{u}(N)} &= \frac{8}{N} \sum_{k \in K_+} \left\{ \left[|\langle a_k^\dagger b_k \rangle|^2 + |\langle a_{-k}^\dagger b_{-k} \rangle|^2 \right] \right. \\ &\quad + \frac{1}{2} \left[\langle a_k^\dagger a_k - 1/2 \rangle^2 + \langle a_{-k}^\dagger a_{-k} - 1/2 \rangle^2 \right. \\ &\quad \left. \left. + \langle b_k^\dagger b_k - 1/2 \rangle^2 + \langle b_{-k}^\dagger b_{-k} - 1/2 \rangle^2 \right] \right\}. \end{aligned} \quad (6.13)$$

Analytical results for $P_{\mathfrak{u}(N)}$ are only available for $\delta = 0$, where GE sharply detects the PM-FM QPT in the XY model [10]. Remarkably, GS fermionic GE still faithfully portrays the full quantum phase diagram with alternation. First, derivatives of $P_{\mathfrak{u}(N)}$ develop singular behavior only at QCPs; see Fig. 6.2 (left). Furthermore, GE exhibits the correct scaling properties near QCPs [10]. By taking a Taylor expansion, $P_{\mathfrak{u}(N)}(h) - P_{\mathfrak{u}(N)}(h_c) \sim \xi^{-1} \sim (h - h_c)^\nu$, where ξ is the correlation length, the static critical exponent ν may be extracted from a log-log plot of $P_{\mathfrak{u}(N)}$ for both the Ising and the alternating universality class, as demonstrated in Fig. 6.2 (right).

**FIGURE 6.2**

$P_{u(N)}$ as a static QPT indicator. Left panel: Purity and rescaled purity derivative vs magnetic field strength. Inset: second derivative for $N = 1000, 2000, 4000, 8000$ (top to bottom). Right panel: Determination of ν for both the alternating and Ising (inset) universality class.

6.1.5 Dynamics of Quantum Phase Transitions

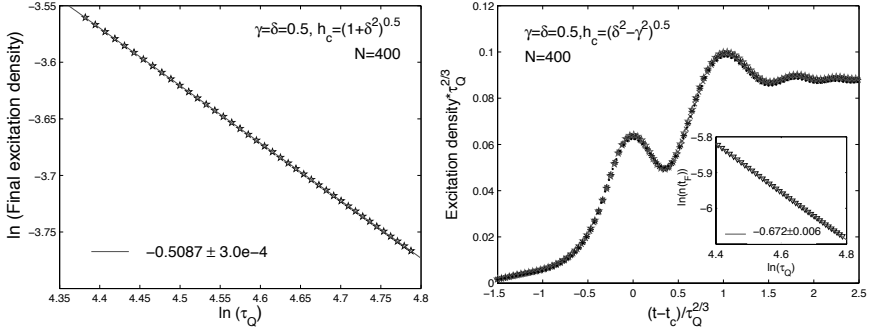
While the above studies provide a satisfactory understanding of *equilibrium* quantum critical properties, *dynamical* aspects of QPTs present a wealth of additional challenges. To what extent can non-equilibrium properties be predicted by using equilibrium critical exponents? The simplest dynamical scenario one may envision arises when a single control parameter is slowly changed in time with constant rate $\tau_Q^{-1} > 0$, that is, $g(t) - g_c = (t - t_c)/\tau_Q$, so that a QCP is crossed at $t = t_c$ ($t_c = 0$ without loss of generality). The typical time scale characterizing the response of the system is the *relaxation time* $\tau = \hbar/\Delta \sim |g(t) - g_c|^{-z\nu}$, Δ being the gap between the GS and first accessible excited state. Since the gap closes at QCPs in the thermodynamic limit (TL), τ diverges even for an arbitrarily slow quench, resulting in a *critical slowing-down*. According to the Kibble-Zurek mechanism (KZM) [17], discussed in Chap. 3, a crossover between an (approximately) adiabatic regime and an (approximately) impulse regime occurs at a freeze-out time $-\hat{t}$, whereby the system's instantaneous relaxation time matches the transition rate,

$$\tau(\hat{t}) = |(g(\hat{t}) - g_c)/(dg/dt)_{t=\hat{t}}|, \quad \hat{t} \sim \tau_Q^{\nu z / (\nu z + 1)}, \quad (6.14)$$

resulting in a predicted scaling of the final density of excitations as

$$n(t_F) \sim \tau_Q^{-\nu / (\nu z + 1)}. \quad (6.15)$$

While agreement with the above prediction has been verified for different quantum systems [18], several key points remain to be addressed: What are the required physical ingredients for the KZM to hold? What features of the

**FIGURE 6.3**

Dynamical scaling of the excitation density. Left panel: log-log plot for Ising universality class. Right panel: alternating universality class, with log-log scaling plot in the inset.

initial (final) quantum phase are relevant? How is dynamical scaling reflected in entanglement?

In our model, the time-evolved many-body state at instant time t , $|\Phi(t)\rangle = \prod_{k \in K_+} |\Phi_k(t)\rangle$, may still be expressed in the form of Eq. (6.11) for time-dependent coefficients $u_k^{(a)}(t)$, $a = 1, \dots, 6$, computed from the solution of the Schrödinger equation. The final excitation density is then obtained from the expectation value of the appropriate quasi-particle number operator over the final time,

$$n(t_F) = \frac{1}{N} \langle \Phi(t_F) | \sum_{k \in K_+} (\gamma_{k,3}^\dagger \gamma_{k,3} + \gamma_{k,4}^\dagger \gamma_{k,4}) | \Phi(t_F) \rangle. \quad (6.16)$$

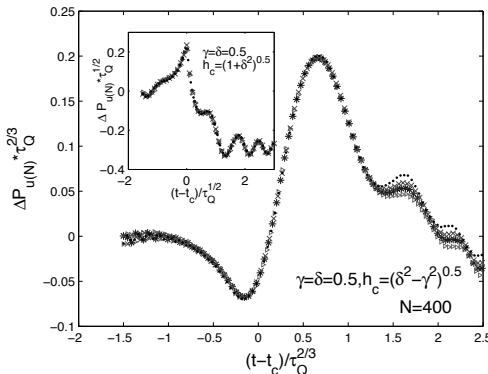
As shown in Fig. 6.3 (left), the resulting value agrees with Eq. (6.15) over an appropriate τ_Q -range *irrespective of the details of the QCP and the initial (final) quantum phase*:

$$n(t_F)^{\text{Ising}} \sim \tau_Q^{-1/2}, \quad n(t_F)^{\text{Alternating}} \sim \tau_Q^{-2/3}. \quad (6.17)$$

More remarkably, our results indicate that *scaling behavior holds throughout the entire time evolution* (see Fig. 6.3, right panel), implying the possibility of expressing the time-dependent excitation density as

$$n(t) = \tau_Q^{-\nu/(\nu z + 1)} F\left(\frac{t - t_c}{\hat{t}}\right), \quad (6.18)$$

where F is a universal scaling function. Numerical results support the conjecture that similar *universal dynamical scaling* may hold for arbitrary observables [12]. In particular, fermionic GE obeys scaling behavior across the entire dynamics provided that the amount relative to the instantaneous GS $|\Psi(t)\rangle_{\text{GS}}$

**FIGURE 6.4**

Dynamical scaling of $P_{u(N)}$ for the alternating and the Ising (inset) universality class.

is considered:

$$\Delta P_{u(N)}(t) \equiv P_{u(N)}(|\Phi(t)\rangle) - P_{u(N)}(|\Psi(t)\rangle_{GS}) = \tau_Q^{-\nu/(\nu z+1)} G\left(\frac{t-t_c}{\hat{\tau}}\right), \quad (6.19)$$

for an appropriate scaling function G , as illustrated in Fig. 6.4.

6.2 Topological Quantum Numbers and Quantum Phase Transitions

In this Section we expand on the concepts of topological quantum number (related to a Berry phase [7]) and *localization* indicator. We show how these ideas can be implemented in practice and emphasize their value as a technique to determine quantum phase diagrams. It turns out that a set of topological quantum numbers labels a thermodynamic state, and transitions between them determine the boundaries of the quantum phase diagram [19].

The Berry phase is an example of a general geometric concept which finds realization in several physical problems [7]. It is the anholonomy associated with the parallel transport of a vector state in a certain parameter space. Anholonomy is a geometric concept related to the failure of certain variables to return to their original values after others, driving them, are cyclically changed. In condensed matter, for instance, the charge Berry phase γ^c is a measure of the macroscopic electric polarization in band or Mott insulators [20, 21] while the spin Berry phase γ^s represents the difference between the

electric polarization per spin up and down [22, 23]. In systems with inversion symmetry, γ^c and γ^s can attain only two values, 0 or π (modulo(2π)). Thus, if two thermodynamic phases differ in the topological vector $\vec{\gamma} = (\gamma^c, \gamma^s)$ this sharp difference allows us to unambiguously identify the transition point even in finite systems. This topological *order parameter* was used by us to detect metallic (superconductor), insulator, and conductor-insulator transitions in lattice fermion models [19].

6.2.1 Geometric Phases and Response Functions

We start by introducing the general framework that allows us to connect certain macroscopic observables to quantum geometric phases. In particular, we present the geometric characterization of the ferrotoroidic moment in terms of a set of Abelian Berry phases [24]. Without loss of generality we will work with a system of N interacting electrons of mass m and charge e enclosed in a d -dimensional box of linear dimension L_μ and volume Ω ($\mu = x, y, \dots$). These ideas can be easily generalized to lattice systems as shown in Refs. [21, 24]. Particle j is labeled by the coordinates r_j^μ and spin $S_j^\nu = \frac{1}{2}\sigma^\nu$ (σ^ν are Pauli matrices with $\nu = x, y, z$). The Hamiltonian of the system is

$$H^\lambda = \sum_{i=1}^N \frac{\Pi_i^2}{2m} + \sum_{i < j} V_{\text{int}}(|\mathbf{r}_i - \mathbf{r}_j|) + \sum_{i=1}^N v_{\text{ext}}(\mathbf{r}_i, \lambda(t)), \quad (6.20)$$

where $\Pi_i = \mathbf{p}_i + \mathbf{A}^\nu$ is the canonical momentum ($p_\mu = -i\partial_\mu$) with gauge field $\mathbf{A}^\nu = (\phi_{\mu\nu}/L_\mu)\sigma^\nu \hat{\mathbf{e}}_\mu$, and $\hat{\mathbf{e}}_\mu$ is a unit vector along the μ direction. The last term in Eq. (6.20) corresponds to the *external* potential, which depends parametrically on $\lambda(t)$, assumed to change adiabatically in time t from $\lambda(0) = 0$ to $\lambda(T) = 1$. V_{int} represents the interaction between electrons.

The flux variable $\phi_{\mu\nu}$ is the twist in spin space at the boundary of the box: $\Psi_\alpha(\mathbf{r}_i + L_\mu \hat{\mathbf{e}}_\mu) = \sum_\beta [e^{i\phi_{\mu\nu}\sigma^\nu}]_{\alpha\beta} \Psi_\beta(\mathbf{r}_i)$, and it induces a spin current of component ν along the spatial direction μ . These generalized boundary conditions provide the system's configuration space with a non-simply connected structure whose topological features relate to the physical properties of the system. The crux of the matter is that the sensitivity of the physical system to appropriate *twists* provides information about the stiffness of the system to that particular perturbation. Note that the transformation defined by $\mathbf{U}(\phi_{\mu\nu}) = \exp(i\phi_{\mu\nu}\sigma^\nu \sum_j r_j^\mu/L_\mu)$ is such that the eigenstates of H^λ satisfy periodic boundary conditions.

The second quantized form of H^λ is $\mathbb{H}^\lambda = \int_\Omega d^3r \mathcal{H}^\lambda(\mathbf{r})$, with Hamiltonian density

$$\mathcal{H}^\lambda(\mathbf{r}) = \Psi^\dagger(\mathbf{r}) \frac{\Pi^2}{2m} \Psi(\mathbf{r}) + \mathcal{H}_{\text{int}}(\mathbf{r}) + \mathcal{H}_{\text{ext}}^\lambda(\mathbf{r}), \quad (6.21)$$

written in terms of the fermionic spinor fields $\Psi^\dagger(\mathbf{r}) = (\psi_+^\dagger(\mathbf{r}), \psi_-^\dagger(\mathbf{r}))$, where

$\psi_\alpha^\dagger(\mathbf{r})$ ($\psi_\beta(\mathbf{r})$) creates (annihilates) an electron with spin $\alpha(\beta) = \{\uparrow, \downarrow\}$ at position \mathbf{r} .

Magnetoelectric materials have the interesting property that an applied electric field produces a magnetization while an applied magnetic field leads to a macroscopic electric polarization. The linear magnetoelectric response is characterized by the magnetoelectric tensor, and the ferrotoroidic moment is an antisymmetric component of that tensor. Ferrotoroidicity is an ordering of matter that combines features of both ferromagnetism, which breaks time-reversal symmetry and displays magnetic moments, and ferroelectricity, which breaks inversion symmetry and shows dipole moments. Thus, ferrotoroidic order breaks both time and inversion symmetries. The spin contribution to the ferrotoroidic moment τ_ν is defined as the antisymmetric component of the tensor $t_{\mu\nu}$. The $t_{\mu\nu}$ -density field is defined by the local condition $\sum_\mu \partial_\mu T_{\mu\nu}(\mathbf{r}) = -2S_\nu(\mathbf{r})$. For a finite system with open boundary conditions (surfaces), the following relation holds as long as $T_{\mu\nu}(\mathbf{r})$ vanishes outside the system:

$$t_{\mu\nu} = \frac{T_{\mu\nu}}{\Omega} = \frac{2}{\Omega} \int_{\Omega} d^3r r_\mu S_\nu(\mathbf{r}) = \frac{1}{\Omega} \int_{\Omega} d^3r T_{\mu\nu}(\mathbf{r}), \quad (6.22)$$

written in terms of the spin density field

$$S_\nu(\mathbf{r}) = \sum_{\alpha\beta} S_{\alpha\beta}^\nu(\mathbf{r}), \quad S_{\alpha\beta}^\nu(\mathbf{r}) = \frac{1}{2} \psi_\alpha^\dagger(\mathbf{r}) \sigma_{\alpha\beta}^\nu \psi_\beta(\mathbf{r}), \quad (6.23)$$

where $\int_{\Omega} d^3r S_\nu(\mathbf{r}) = 0$ is required in order to have $t_{\mu\nu}$ independent of the origin of coordinates.² More specifically, $\tau_\eta = \frac{\mu_B}{4} \sum_{\mu\nu} \epsilon_{\eta\mu\nu} t_{\mu\nu}$, with $\epsilon_{\eta\mu\nu}$ the Levi-Civita tensor. Like for the electric polarization [20, 21], the third member of Eq. (6.22) is not well defined for a system with periodic boundary conditions because the position operator is not well defined [25]. However, the fourth and last member of Eq. (6.22) is still well defined. Starting from such an expression for $t_{\mu\nu}$, we will demonstrate that the change $\langle \Delta t_{\mu\nu} \rangle$ between two different physical states can be obtained from a set of Abelian Berry phases.

Since the GS of H^λ evolves continuously between $\lambda(0) = 0$ and $\lambda(T) = 1$, the change is given by

$$\langle \Delta t_{\mu\nu} \rangle = \frac{1}{\Omega} \int_0^1 d\lambda \int_{\Omega} d^3r \partial_\lambda \langle \Phi_0^\lambda | T_{\mu\nu}(\mathbf{r}) | \Phi_0^\lambda \rangle, \quad (6.24)$$

where $|\Phi_0^\lambda\rangle$ is the GS of \mathbb{H}^λ with flux $\phi_{\mu\nu}$, and $\langle \Delta t_{\mu\nu} \rangle = \langle \Phi_0^{\lambda(T)} | t_{\mu\nu} | \Phi_0^{\lambda(T)} \rangle - \langle \Phi_0^{\lambda(0)} | t_{\mu\nu} | \Phi_0^{\lambda(0)} \rangle$. By using adiabatic perturbation theory [20, 26, 27] up to first

²Since we are interested in changes of the ferrotoroidic spin moment, the formalism can be extended to evolutions with constant non-zero magnetization per unit cell $m_0 = 2 \int_{\Omega_0} d^3r S_\nu(\mathbf{r})$. If $m_0 = m/\ell$ is an irreducible fraction (m, ℓ are integers), symmetry arguments [23, 25] show that the integrals in $\phi_{\mu\nu}$ should be extended to $2\pi\ell$ and $\varphi_{\mu\nu} = 2\pi\ell/L_\mu$ in $z_{\mu\nu}$ [Eq. (6.29)].

order in the time derivative we obtain

$$\begin{aligned} \frac{1}{\Omega} \int_{\Omega} d^3r \partial_{\lambda} \langle \Phi_0^{\lambda} | T_{\mu\nu}(\mathbf{r}) | \Phi_0^{\lambda} \rangle = \\ -\frac{iL_{\mu}}{\Omega} \sum_{m \neq 0} \frac{\langle \Phi_0^{\lambda} | \partial_{\phi_{\mu\nu}} \mathbb{H}^{\lambda} | \Phi_m^{\lambda} \rangle \langle \Phi_m^{\lambda} | \partial_{\lambda} \mathbb{H}^{\lambda} | \Phi_0^{\lambda} \rangle}{[E_0^{\lambda} - E_m^{\lambda}]^2} + \text{c.c.}, \end{aligned} \quad (6.25)$$

where we have used that $\mathbb{H}^{\lambda} | \Phi_m^{\lambda} \rangle = E_m^{\lambda} | \Phi_m^{\lambda} \rangle$ ($\langle \Phi_m^{\lambda} | \Phi_{m'}^{\lambda} \rangle = \delta_{m,m'}$) and

$$i[\mathbb{H}^{\lambda}, T_{\mu\nu}(\mathbf{r})] = \partial_t T_{\mu\nu} = L_{\mu} \partial_{\phi_{\mu\nu}} \mathcal{H}^{\lambda}(\mathbf{r}). \quad (6.26)$$

In the absence of spin-orbit interaction, $\partial_t T_{\mu\nu} = 2\mathcal{J}_{\mu\nu}^s(\mathbf{r})$ with $\mathcal{J}_{\mu\nu}^s(\mathbf{r})$ the density of spin current³ satisfying the continuity equation $\sum_{\mu} \partial_{\mu} \mathcal{J}_{\mu\nu}^s(\mathbf{r}) + \partial_t \mathcal{S}_{\nu}(\mathbf{r}) = 0$. By using the relations $\langle \Phi_m^{\lambda} | \partial_{\lambda} \mathbb{H}^{\lambda} | \Phi_0^{\lambda} \rangle = \langle \Phi_m^{\lambda} | [\partial_{\lambda}, \mathbb{H}^{\lambda}] | \Phi_0^{\lambda} \rangle$, and $\langle \Phi_0^{\lambda} | \partial_{\phi_{\mu\nu}} \mathbb{H}^{\lambda} | \Phi_m^{\lambda} \rangle = \langle \Phi_0^{\lambda} | [\partial_{\phi_{\mu\nu}}, \mathbb{H}^{\lambda}] | \Phi_m^{\lambda} \rangle$, we obtain from Eqs. (6.24) and (6.25)

$$\begin{aligned} \langle \Delta t_{\mu\nu} \rangle &= -\frac{iL_{\mu}}{\Omega} \int_0^1 d\lambda \sum_{m \neq 0} \langle \partial_{\phi_{\mu\nu}} \Phi_0^{\lambda} | \Phi_m^{\lambda} \rangle \langle \Phi_m^{\lambda} | \partial_{\lambda} \Phi_0^{\lambda} \rangle + \text{c.c} \\ &= \frac{L_{\mu}}{\Omega} \int_0^1 d\lambda \mathcal{B}(\xi), \quad \xi = (\phi_{\mu\nu}, \lambda), \end{aligned} \quad (6.27)$$

with $\mathcal{B}(\xi) = i(\langle \partial_{\lambda} \Phi_0^{\lambda} | \partial_{\phi_{\mu\nu}} \Phi_0^{\lambda} \rangle - \langle \partial_{\phi_{\mu\nu}} \Phi_0^{\lambda} | \partial_{\lambda} \Phi_0^{\lambda} \rangle)$. Since $t_{\mu\nu}$ is a bulk property, and we assumed that there is no level crossing for the GS as a function of $\phi_{\mu\nu}$, its value should not depend on the boundary conditions when we take the TL. Thus,

$$\langle \Delta t_{\mu\nu} \rangle = \frac{L_{\mu}}{2\pi\Omega} \int_0^1 d\lambda \int_0^{2\pi} d\phi_{\mu\nu} \mathcal{B}(\xi) = \frac{L_{\mu}}{2\pi\Omega} \oint_{\Gamma} \mathcal{A}(\xi) \cdot d\xi$$

with the line integral performed along the contour Γ of $[0, 2\pi] \times [0, 1]$ in the plane $(\phi_{\mu\nu}, \lambda)$, and $\mathcal{A}(\xi) = i\langle \Phi_0^{\lambda} | \nabla_{\xi} \Phi_0^{\lambda} \rangle$ is a connection. Assuming a path-independent gauge [20],

$$\begin{aligned} \langle \Delta t_{\mu\nu} \rangle &= \frac{L_{\mu}}{2\pi\Omega} [\gamma_{\mu\nu}^s(1) - \gamma_{\mu\nu}^s(0)], \\ \text{with } \gamma_{\mu\nu}^s(\lambda) &= i \int_0^{2\pi} d\phi_{\mu\nu} \langle \Phi_0^{\lambda} | \partial_{\phi_{\mu\nu}} \Phi_0^{\lambda} \rangle. \end{aligned} \quad (6.28)$$

One can also introduce fluxes along space directions other than μ and, as long as the gap does not close, average over these additional fluxes. The Berry

³From the local relation $\sum_{\mu} \partial_{\mu} T_{\mu\nu}(\mathbf{r}) = -2\mathcal{S}_{\nu}(\mathbf{r})$ and the continuity equation, it becomes clear that the spin current $\mathcal{J}_{\mu\nu}^s(\mathbf{r})$ is defined up to the addition of a solenoidal field $\nabla \times \mathbf{f}(\mathbf{r})$ where the vector field $\mathbf{f}(\mathbf{r})$ satisfies the gauge condition $\nabla \cdot \mathbf{f}(\mathbf{r}) = 0$. This additional term represents zero-divergence spin currents (closed loops), such as the edge currents existing in certain insulators, and does not contribute to Eq. (6.25) [20].

phases $\gamma_{\mu\nu}^s$ are anholonomies associated with the parallel transport of a vector state (GS) in the parameter space determined by the fluxes. Equation (6.28) shows that the *quantum of uncertainty*, related to the lack of history in the adiabatic evolution, is at least the inverse of the total transverse section L_μ/Ω . In a periodic system with primitive unit cell volume $\Omega_0 < \Omega$, the quantum is larger and equal to L_μ^0/Ω_0 , where L_μ^0 is the length of the unit cell along the μ -direction [20].

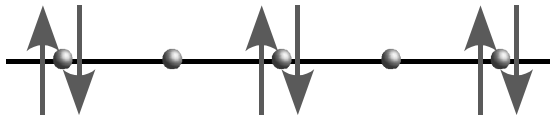
6.2.2 The Geometry of Response Functions

We have so far shown how to relate certain macroscopic observables, e.g., the ferrotoroidic moment, to quantum geometric phases. The physical idea behind this is that different twists in the boundary conditions probe different properties of the system. The next step consists in relating the topological properties of the generated fiber-bundle to physical behavior. To this end we need to introduce the concept of *localization* indicators. We will see that this approach leads to a *geometric fluctuation-dissipation* relation. More specifically, the response of the system to *external geometric twists* is fundamentally related to fluctuations (correlations) of the system.

The seminal work of Kohn on the nature of the insulating state is a landmark in the quantum theory of matter [28]. Kohn was apparently the first to point out that the sensitivity of the GS energy, E_0 , to changes in the boundary conditions is a measure of the static electric conductivity of the system, i.e., its Drude weight D_c . In fact, in the TL, he argued that D_c is finite for a non-disordered conductor (metal or superconductor), while it vanishes for an insulator. Physically, this last result is a consequence of the localization properties of the many-electron wave function, which is exponentially localized in the insulating case. Later on, a complex quantity z_L^c that allows discrimination between conducting and non-conducting thermodynamic phases was introduced in Refs. [25, 29]: $|z_L^c| \rightarrow 0$ or 1 in the TL, for a conductor or insulator, respectively. The heart of the matter is that z_L^c has an enlightening physical interpretation [30, 31]: its phase is related to the macroscopic electric polarization of matter (Berry phase [20]) while its modulus provides information on the polarization fluctuations. Note that there is a mathematical relation between D_c and z_L^c [30]. Likewise, one can define a complex quantity for the spin response z_L^s with similar physical interpretation. For example, in the TL, in the gapless Heisenberg antiferromagnetic chain $z_L^s \rightarrow 0$, while in the gapped AKLT [32] model, $|z_L^s| \rightarrow 1$.

The point we want to emphasize is that there is a formal mathematical link between the geometric phases (γ^c, γ^s) and the localization indicators (z_L^c, z_L^s) [19, 25, 29, 30]. The phase of the localization number z_L^κ (with $\kappa = c, s$) is connected to the Berry phase γ^κ through the relation $\gamma^\kappa = \text{Im} \ln z_L^\kappa$, as illustrated in Fig. 6.5. It is important to stress that different indicators provide complementary information. They may display different convergence properties to the TL, and most importantly, some indicators are more akin to

- CDW:



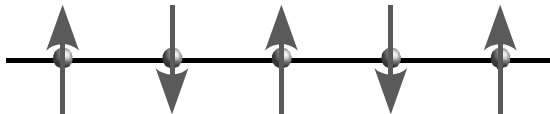
$$\gamma^c = \text{Im} \ln \langle \Psi_0 | e^{i \frac{2\pi}{L} \sum_j j(\hat{n}_{j\uparrow} + \hat{n}_{j\downarrow})} | \Psi_0 \rangle = 0 \text{ [mod } (2\pi)]$$

$$\gamma^s = \text{Im} \ln \langle \Psi_0 | e^{i \frac{2\pi}{L} \sum_j j(\hat{n}_{j\uparrow} - \hat{n}_{j\downarrow})} | \Psi_0 \rangle = 0 \text{ [mod } (2\pi)]$$

- Néel:

$$\gamma^c = \pi \text{ [mod } (2\pi)]$$

$$\gamma^s = \pi \text{ [mod } (2\pi)]$$



- Ferromagnet:

$$\gamma^c = \pi \text{ [mod } (2\pi)]$$

$$\gamma^s = \pi \text{ [mod } (2\pi)]$$

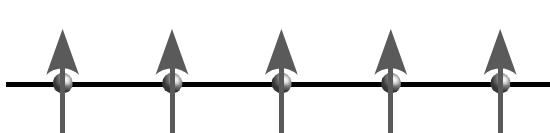


FIGURE 6.5

Examples of topological quantum numbers for representative states of matter in the extreme case where particles are localized ($L \in \text{even}$).

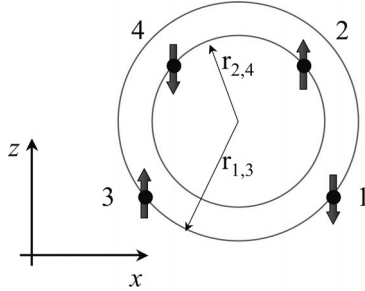
Monte Carlo methods while others are geared towards numerical renormalization group approaches. The localization parameters z_L^κ and their related Berry phases γ^κ have also been used as *sharp* topological indicators (*order parameters*) for establishing quantum phase diagrams of interacting systems [19, 21, 33–36].

Let us introduce the concept of a *generalized localization* indicator. To simplify matters and be consistent with our presentation, we will consider the case of the ferrotoroidic moment. Define the localization indicators

$$z_{\mu\nu}[\varphi_{\mu\nu}] = \langle \Psi_0 | \Psi_0(\varphi_{\mu\nu}) \rangle, \quad |\Psi_0(\varphi_{\mu\nu})\rangle = e^{i\varphi_{\mu\nu} T_{\mu\nu}} |\Psi_0(0)\rangle, \quad (6.29)$$

where $\varphi_{\mu\nu} = 2\pi/L_\mu$ and $|\Psi_0\rangle$ is the GS. z_L^c is obtained by replacing $\varphi_{\mu\nu} \sigma^\nu$ with a scalar coupling φ_μ^c . For a one-dimensional system along the x direction and spin quantization axis z , z_L^s corresponds to the component z_{xz} of the tensor defined by Eq. (6.29). The operator $e^{i\varphi_{\mu\nu} T_{\mu\nu}}$ represents a generalized twist operator whose expectation value measures the character of the spectrum of low-energy excitations. Clearly, more general twists (fiber-bundles) probing other quantum correlations are possible.

Considered as a continuous function of $\varphi_{\mu\nu}$, $z_{\mu\nu}$ plays the role of a characteristic function generating all moments of the $T_{\mu\nu}$ tensor, and trivially satisfies $z_{\mu\nu}[0] = 1$, $|z_{\mu\nu}[\varphi_{\mu\nu}]| \leq 1$, $z_{\mu\nu}[\varphi_{\mu\nu}] = z_{\mu\nu}^*[-\varphi_{\mu\nu}]$. Note, however, that the operator $T_{\mu\nu}$ is not a genuine operator in the Hilbert space bundle defined above, although its exponential is a legitimate one. Therefore, expectation values of arbitrary powers of $T_{\mu\nu}$ only have meaning in terms of $z_{\mu\nu}$ (i.e., there is a *quantum of uncertainty* [20]). Assuming analyticity in the neighborhood

**FIGURE 6.6**

Unit cell with net ferrotoroidic moment. Arrows represent spins with $\sigma^z = \pm 1$.

of $\varphi_{\mu\nu} = 0$, i.e., the system has a gap in the TL, $z_{\mu\nu}$ can be written in terms of cumulants $C_k(T_{\mu\nu})$

$$z_{\mu\nu} = \exp \left[\sum_{k=1}^{\infty} \frac{(i\varphi_{\mu\nu})^k}{k!} C_k(T_{\mu\nu}) \right]. \quad (6.30)$$

This results in

$$\varphi_{\mu\nu}^{-1} \operatorname{Im} \ln z_{\mu\nu} = \langle T_{\mu\nu} \rangle + \mathcal{O}(\varphi_{\mu\nu}^2), \quad (6.31)$$

$$-\varphi_{\mu\nu}^{-2} \ln |z_{\mu\nu}|^2 = \langle T_{\mu\nu}^2 \rangle - \langle T_{\mu\nu} \rangle^2 + \mathcal{O}(\varphi_{\mu\nu}^2), \quad (6.32)$$

so that the phase of $z_{\mu\nu}$ is related to the tensor $T_{\mu\nu}$ while its modulus provides information on its quantum fluctuations (it vanishes in the TL for systems with gapless excitations that have a non-zero spin current).

To illustrate an elementary application of Eq. (6.31), assume that $|\Psi_0\rangle$ is the GS of a periodic system with the primitive unit cell of volume Ω_0 (see Fig. 6.6), consisting of two spin up and two down in the direction z , and displaced in the direction x so that the contribution to T_{xz} from each unit cell $\tilde{t}_{xz} = 2 \sum_{j=1}^4 x_j S_j^z \neq 0$, with $\tilde{t}_{\mu\nu} \equiv \Omega_0 \langle t_{\mu\nu} \rangle$. Thus, the first member of Eq. (6.31) should give $N_u \tilde{t}_{\mu\nu}$ where N_u is the number of unit cells. This equation is invariant if any coordinate r_j^μ is replaced by $r_j^\mu + nL_\mu$ with n integer. Equation (6.29) gives $z_{\mu\nu} = \exp(2\pi i N_u \tilde{t}_{\mu\nu} / L_\mu)$, and replacing into Eq. (6.31), $\langle T_{\mu\nu} \rangle = N_u \tilde{t}_{\mu\nu}$ as expected. Note that the same result is obtained if $\tilde{t}_{\mu\nu}$ is replaced by $\tilde{t}_{\mu\nu} + nq$, where n is integer and $q = L_\mu / N_u$ is the quantum of uncertainty in $\tilde{t}_{\mu\nu}$. However, for translationally invariant systems one can calculate $z_{\mu\nu}$ in the effective one-dimensional problem with fixed total transversal wave vector, (K_y, K_z) , for which $q = L_\mu^0$.

To understand the geometric content of the magnetoelectric response, we need to understand the Riemannian structure of our Hilbert space bundle. Consider a set of normalized states $\{|\Psi_0(\varphi)\rangle\}$, where φ represents $3d$ real numbers $\varphi_{\mu\nu}$. Let's assume that this manifold of quantum states is generated

by the action of the group of transformations $|\Psi_0(\varphi)\rangle = e^{i\varphi \cdot \mathbf{T}} |\Psi_0(0)\rangle$, where $\varphi \cdot \mathbf{T} = \sum_{\mu\nu} \varphi_{\mu\nu} T_{\mu\nu}$. The expectation value of the generalized *twist* operator $e^{i\varphi \cdot \mathbf{T}}$ measures the character of the spectrum of low-energy $T_{\mu\nu}$ -excitations. Can we find a measure of the *distance* between two of these quantum states?

Provost and Vallee addressed the problem of establishing a Riemannian structure on an arbitrary differentiable manifold of quantum states [37]. Their work led to the introduction of a (gauge invariant) metric tensor in such a manifold. We now introduce a general quantum geometric tensor

$$G_{\mu\nu;\alpha\beta}[\varphi] = \langle \partial_{\varphi_{\mu\nu}} \Psi_0 | \hat{P}_0[\varphi] | \partial_{\varphi_{\alpha\beta}} \Psi_0 \rangle, \quad (6.33)$$

whose real and imaginary parts $G_{\mu\nu;\alpha\beta}[\varphi] = g_{\mu\nu;\alpha\beta}[\varphi] + i \Omega_{\mu\nu;\alpha\beta}[\varphi]$ can be written

$$\begin{cases} g_{\mu\nu;\alpha\beta}[\varphi] = \text{Re} \langle \partial_{\varphi_{\mu\nu}} \Psi_0 | \partial_{\varphi_{\alpha\beta}} \Psi_0 \rangle - \gamma_{\mu\nu}[\varphi] \gamma_{\alpha\beta}[\varphi], \\ \Omega_{\mu\nu;\alpha\beta}[\varphi] = \text{Im} \langle \partial_{\varphi_{\mu\nu}} \Psi_0 | \partial_{\varphi_{\alpha\beta}} \Psi_0 \rangle, \end{cases} \quad (6.34)$$

with $\hat{P}_0[\varphi] = \mathbf{1} - |\Psi_0(\varphi)\rangle\langle\Psi_0(\varphi)|$, and $\gamma_{\mu\nu}[\varphi] = i \langle \Psi_0 | \partial_{\varphi_{\mu\nu}} \Psi_0 \rangle$ the Berry connection [20]. The real part of $G_{\mu\nu;\alpha\beta}[\varphi]$ is a symmetric and positive definite tensor representing a generalization of the metric introduced in Ref. [37]. Moreover, it is interesting to remark that the infinitesimal distance is related to the quantum fluctuations of the $T_{\mu\nu}$ tensor, i.e., $g_{\mu\nu;\alpha\beta}(\varphi \rightarrow \mathbf{0}) = \langle T_{\mu\nu} T_{\alpha\beta} \rangle - \langle T_{\mu\nu} \rangle \langle T_{\alpha\beta} \rangle$, with expectation values evaluated over $|\Psi_0(\mathbf{0})\rangle \equiv |\Psi_0\rangle$. In a sense, the metric structure on the manifold is fixed by the quantum fluctuations which determine the modulus of $z_{\mu\nu}$ in the TL. On the other hand, the antisymmetric tensor $\Omega_{\mu\nu;\alpha\beta}[\varphi] = -\Omega_{\alpha\beta;\mu\nu}[\varphi]$ plays the role of a curvature, and is a quantity connected to the non-dissipative part of the spin conductance in adiabatic transport.

6.2.3 The Geometry of Quantum Information

What is the information content of those geometric quantities? Consider the quantum geometric tensor $G_{\mu\nu;\alpha\beta}[\varphi]$. Actually, this tensor is the Fubini-Study metric, which is the natural Hermitian product in the projective Hilbert space of pure quantum states [6]. The Fubini-Study metric is naturally gauge invariant since it is defined in the projective space. On the other hand, the Fisher metric is the expectation value of the square of the symmetric logarithmic derivative [38]. The latter is defined as the Hermitian operator Λ_μ which solves the equation

$$\partial_{\varphi_{\mu\nu}} \rho = \frac{1}{2} (\Lambda_{\varphi_{\mu\nu}} \rho + \rho \Lambda_{\varphi_{\mu\nu}}). \quad (6.35)$$

If ρ is a pure state, then $\rho^2 = \rho$ and $\partial_{\varphi_{\mu\nu}} \rho = \partial_{\varphi_{\mu\nu}} \rho^2 = (\partial_{\varphi_{\mu\nu}} \rho) \rho + \rho (\partial_{\varphi_{\mu\nu}} \rho)$, which implies

$$\Lambda_{\varphi_{\mu\nu}} = 2 \partial_{\varphi_{\mu\nu}} \rho = 2 (|\partial_{\varphi_{\mu\nu}} \Psi\rangle\langle\Psi| + |\Psi\rangle\langle\partial_{\varphi_{\mu\nu}} \Psi|). \quad (6.36)$$

On the other hand, the Helstrom matrix is defined as

$$H_{\mu\nu;\alpha\beta}[\varphi] = \text{Tr} [\rho \Lambda_{\varphi_{\mu\nu}} \Lambda_{\varphi_{\alpha\beta}}]. \quad (6.37)$$

Using the fact that $\langle \Psi | \partial_{\varphi_{\mu\nu}} (\varphi_{\alpha\beta}) \Psi \rangle$ is purely imaginary, it leads to

$$\frac{1}{4} H_{\mu\nu;\alpha\beta}[\varphi] = \langle \partial_{\varphi_{\mu\nu}} \Psi | \partial_{\varphi_{\alpha\beta}} \Psi \rangle - \langle \partial_{\varphi_{\mu\nu}} \Psi | \Psi \rangle \langle \Psi | \partial_{\varphi_{\alpha\beta}} \Psi \rangle \quad (6.38)$$

$$= \langle \partial_{\varphi_{\mu\nu}} \Psi | (1 - |\Psi\rangle\langle\Psi|) | \partial_{\varphi_{\alpha\beta}} \Psi \rangle \\ = G_{\mu\nu;\alpha\beta}[\varphi]. \quad (6.39)$$

Therefore, the quantum geometric tensor $G_{\mu\nu;\alpha\beta}[\varphi]$ is simply the Helstrom matrix or, equivalently, the Fubini-Study metric.

6.2.4 Phase Diagrams and Topological Quantum Numbers

To illustrate the concepts developed in previous Sections, we will determine the quantum phase diagram of the Hubbard chain with correlated hopping at half-filling using topological transitions. A complete analysis can be found in Ref. [19]. The phase diagram is very rich, showing two metallic and two insulating thermodynamic phases, each characterized by one of the four possible values of the topological vector $\vec{\gamma} = (\gamma^c, \gamma^s)$. One of the metallic phases corresponds to a Tomonaga-Luttinger liquid with dominant triplet superconducting (TS), or p-wave correlations at large distances. This is interesting since there is experimental evidence indicating that the Bechgaard salts $(\text{TMTSF})_2\text{ClO}_4$ and $(\text{TMTSF})\text{PF}_6$ under pressure are TS. Furthermore, the insulating spin-density wave (SDW) and spin gapped spin-Peierls phases observed in $(\text{TMTSF})\text{PF}_6$ as the pressure is lowered are also present in the model phase diagram. The effective model Hamiltonian is

$$H = \sum_{\langle i,j \rangle, \sigma} (c_{i\sigma}^\dagger c_{j\sigma} + \text{h.c.}) \{ t_{AA} (1 - n_{i\bar{\sigma}}) (1 - n_{j\bar{\sigma}}) + t_{BB} n_{i\bar{\sigma}} n_{j\bar{\sigma}} \\ + t_{AB} [n_{i\bar{\sigma}} (1 - n_{j\bar{\sigma}}) + n_{j\bar{\sigma}} (1 - n_{i\bar{\sigma}})] \} + U \sum_i (n_{i\uparrow} - \frac{1}{2})(n_{i\downarrow} - \frac{1}{2}), \quad (6.40)$$

where $\bar{\sigma}$ is the σ spin flipped, e.g., if $\sigma = \uparrow$ then $\bar{\sigma} = \downarrow$. H contains the most general form of hopping term describing the low energy physics of a broad class of system Hamiltonians in which four states per effective site are retained. In particular, the Hamiltonian H in Eq. (1) has been derived and studied for transition metals, organic molecules and compounds, intermediate valence systems, cuprates, and other superconductors. In the continuum limit, the only relevant interactions at half-filling are U and $t_{AA} + t_{BB} - 2t_{AB}$ [39]. Therefore, we restrict the present study to the electron-hole symmetric case ($t_{AA} = t_{BB} = 1$) which has spin and pseudospin SU(2) group symmetries, the latter with generators $\eta^+ = \sum_i (-1)^i c_{i\uparrow}^\dagger c_{i\downarrow}^\dagger$, $\eta^- = (\eta^+)^\dagger$, and $\eta^z = \frac{1}{2} \sum_i (\sum_\sigma n_{i\sigma} - 1)$.

The canonical transformation (CT) $\tilde{c}_{i\uparrow} = c_{i\uparrow}$, $\tilde{c}_{i\downarrow} = (-1)^i c_{i\downarrow}^\dagger$ changes the sign of U in H , and interchanges the total spin and pseudospin operators ($\eta^\alpha \longleftrightarrow S^\alpha$). For $t_{AB} = 0$, the model has been solved exactly [40] with the result that the GS is highly degenerate. For $t_{AB} \neq 0$ the physics of the model is still unclear and constitutes our main concern.

For the present case $\gamma^{c,s}$ are defined as

$$\gamma^{c,s} = i \int_0^{2\pi} d\phi \langle g_K(\phi, \pm\phi) | \partial_\phi g_K(\phi, \pm\phi) \rangle, \quad (6.41)$$

where $|g_K(\phi_\uparrow, \phi_\downarrow)\rangle$ is the GS in the subspace with total wave vector K and other quantum numbers kept fixed, with fluxes ϕ_σ for spin σ . Changes in macroscopic polarization with spin σ , P_σ are related to the corresponding changes in the Berry phase by $\Delta P_\uparrow \pm \Delta P_\downarrow = e\Delta\gamma^{c,s}/2\pi, \text{ mod}(e)$ [20, 22, 23]. Thus, a phase transition will be detected by a jump in π of γ^c (γ^s) if and only if both thermodynamic phases differ in $P_\uparrow + P_\downarrow$ ($P_\uparrow - P_\downarrow$) by $e/2, \text{ mod}(e)$. For example, if one of the phases is a charge-density wave (CDW) with maximum order parameter (CDWM) and the other a Néel state (N), one is transformed into the other by translating half of the charges, i.e., those with a given spin, by one lattice spacing. In addition, in the present model topological transitions in γ^c and γ^s indicate the opening of the charge and spin gap Δ_c, Δ_s .

In the case where all particles are localized one can easily determine the value of $\vec{\gamma}$ as $\gamma^{c,s} = \text{Im} \ln z_L^{c,s}$, where

$$z_L^{c,s} = \langle g | e^{i \frac{2\pi}{L} \sum_j j(n_{j\uparrow} \pm n_{j\downarrow})} | g \rangle. \quad (6.42)$$

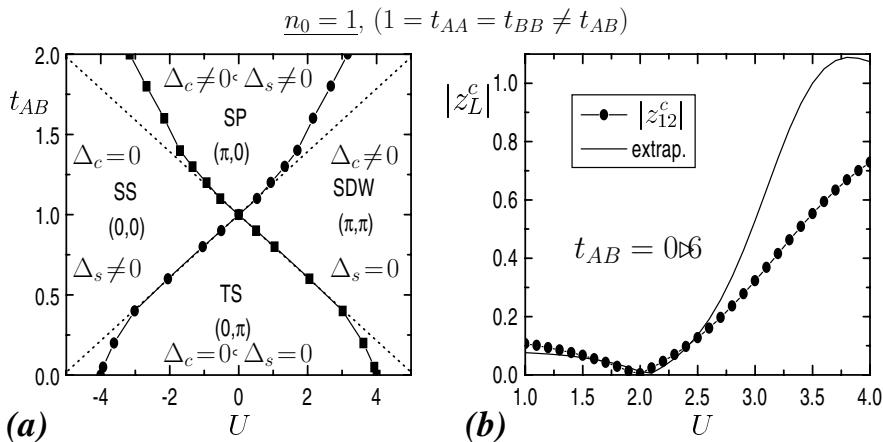
Clearly, $\vec{\gamma}(\text{CDWM}) = (0, 0)$, while $\vec{\gamma}(\text{N}) = (\pi, \pi)$, and by continuity $\vec{\gamma}(\text{CDW}) = (0, 0)$ and $\vec{\gamma}(\text{SDW}) = (\pi, \pi)$. Also, a fully polarized FM state and SDW (GS of a Heisenberg antiferromagnet) have $\vec{\gamma} = (\pi, \pi)$. On the other hand, it is not easy to predict the values of $\vec{\gamma}$ in conducting phases. However, for $U = 0$, the model is invariant under CT. Therefore $\vec{\gamma} = (\pi, 0)$, or $\vec{\gamma} = (0, \pi)$, indicating a topological difference with the above mentioned CDW and SDW states.

While the topological quantum numbers (Berry phases) provide a sharp signal of the transition, their location is size dependent. This is also the case with the localization indicators. We can indeed use both to determine not only the boundaries but also the nature of the phases. The resulting quantum phase diagram is depicted in Fig. 6.7. A summary for each non-equivalent topological region is the following:

a) $\vec{\gamma} = (\pi, 0), \Delta_c \neq 0, \Delta_s \neq 0$. All correlation functions decay exponentially.

b) $\vec{\gamma} = (\pi, \pi), \Delta_c \neq 0, \Delta_s = 0$. As in the ordinary positive U Hubbard model, the GS is an insulating SDW.

c) $\vec{\gamma} = (0, 0), \Delta_c = 0, \Delta_s \neq 0$. The system forms a Luther-Emery liquid with singlet-superconducting and charge correlation functions decaying as $1/x$ (neglecting logarithmic corrections).

**FIGURE 6.7**

(a) Quantum phase diagram of the correlated hopping Hubbard chain. The vector Berry phase $\vec{\gamma} = (\gamma^c, \gamma^s)$ and the nature of each stable phase is indicated: Luther-Emery liquid with equally decaying singlet superconductor and CDW correlations (SS-CDW), Tomonaga-Luttinger liquid with triplet superconducting and bond SDW correlations dominating at large distances (TS-BSDW), SDW insulator (SDW), and spin and pseudospin dimerization (S,P). (b) Localization indicator z_L^c as a function of U for $L = 12$. The solid curve is a polynomial extrapolation in $1/L$.

d) $\vec{\gamma} = (0, \pi), \Delta_c = 0, \Delta_s = 0$. Because of symmetry arguments, for $U = 0$, all correlation functions except the triplet superconducting one show the same $1/x^2$ decay (apparently without logarithmic corrections). Renormalization group arguments show that when $\Delta_s = 0$ TS correlations should decay more slowly than singlet, and therefore dominate for small $|U|$.

Our general approach can be extended to spatial dimensions higher than one [20,21], and applied to arbitrary models of interacting quantum particles.

6.3 Outlook

Generically, the character of the entanglement present in the thermodynamic state of a quantum system changes qualitatively through a quantum phase transition. Almost any quantitative measure of entanglement (for example, entanglement entropy, von Neumann entropy, geometric entanglement, concurrence) will encode that qualitative change. This is not surprising since those measures contain information about *some* quantum correlations. As empha-

sized a long time ago [9, 10], no single measure of entanglement can fully capture the panoply of correlations present in a quantum system. A point we would like to stress, though, is that unless there is a systematic way to *classify* and understand the physical origin of those correlations, these entanglement measures by themselves are of relatively little value. Sometimes the use of a particular measure of entanglement is merely an issue of computational convenience.

The main goal of our work is precisely to provide a systematic and unifying entanglement framework to understand and hierarchically classify quantum correlations in interacting many-body systems. We are providing a new set of tools to understand quantum correlations and identify phase transitions. We have accomplished this by two seemingly different characterizations of the *geometry of entanglement*: one purely algebraic and rooted in convexity (GE), and the other topological. Our measures are not simply convenient computational tools but, most importantly, provide understanding of the physical origin of those quantum correlations. For example, over forty years ago, Kohn [28] recognized that the essential microscopic property that distinguishes the insulating state of matter is the *disconnectedness* of its GS wave function. We have shown that one can quantify this property, by using concepts borrowed from topology, in terms of quantum geometric tensors. Moreover, we have given physical meaning to these geometrical and topological propositions. In this way, we have seen that the phase of z_L^c , a Berry phase, provides information on the macroscopic electric polarization of matter [20, 25], while its modulus, connected to a quantum metric, measures the degree of localization in terms of the electric polarization fluctuations. We have generalized these ideas to other physical properties, such as ferrotoroidicity, and developed a *geometric fluctuation-dissipation* relation that characterizes the response of a system to *external geometric twists*.

What advantage do measures of entanglement have over the more standard correlation function measures as an indicator of quantum phase transitions? First of all, standard correlation function measures can be considered particular instances of more general measures of entanglement. In other words, the generalized entanglement theory is an attempt to have an overarching theory of quantum correlations. Perhaps the most successful instance of a systematic approach that makes no apparent use of the theory of entanglement is Landau's theory of phase transitions, where the important concept of the *order parameter* is associated with the concept of broken symmetry. Correlation functions of the order parameter characterize the phase transition. However, Landau's approach gives no procedure for finding the order parameter [41]. In particular, this problem is manifested if the symmetries of the system are hidden and "veil" the nature of the order. So, in those cases where Landau's order parameter cannot be easily identified other measures of entanglement can provide the tools necessary to understand the nature of the quantum phase transition. It is also important to take into consideration the way experimental probes couple to the degrees of freedom of our physical system. One can

imagine situations where the experiment does not probe the order parameter correlations and other measures of entanglement become more relevant or even more natural. This happens, for instance, in cases where the order parameter does not couple to an external physical field. Another successful example of a systematic approach to study phase transitions, that allows for classification, is conformal field theory in two dimensions and the useful concept of central charge; however, its generalizations to higher dimensions have not been so effective.

Of course, many open questions remain. Perhaps one of the most immediate ones is the detection and characterization of topological quantum order [42], although we suspect that with the help of duality mappings [43] and the concept of gauge-like symmetry [42] we could answer that question. Another important question is the full characterization and classification of quantum critical behavior in two and three spatial dimensions. It would be interesting to better understand the deep connection between the algebraic and topological characterizations, and their logical extensions to finite temperature, or mixed states.

Acknowledgments – It is a pleasure to thank all the collaborators that have contributed to the ideas and results presented in this chapter. I would also like to thank Leonid Isaev for a careful reading of the manuscript.

6.4 Appendix: Generalized Coherent States

The notions of Hilbert space and linear maps or operators are central to the formulation of quantum mechanics. Pure states are elements of a Hilbert space and physical observables are associated to Hermitian (self-adjoint) operators which act on that space, and whose eigenvalues are selected by a measuring apparatus. The role of linear operators in quantum mechanics is not restricted to the representation of physical observables. Non-Hermitian operators are very often used as well, for instance in the context of describing non-unitary quantum dynamics. Linear operators form a complex vector space under the sum and the multiplication by a scalar over the field of complex numbers. If we augment this vector space with a bilinear operation, the set forms an *algebra*. Quantum mechanics also requires that this operation be non-commutative and associative. A *Lie algebra* \mathfrak{h} is a vector space endowed with a bilinear map $[\cdot, \cdot]$ satisfying antisymmetry and the Jacobi identity

$$[x, x] = 0, \quad [x, [y, z]] + [y, [z, x]] + [z, [x, y]] = 0, \quad \forall x, y, z \in \mathfrak{h}. \quad (6.43)$$

An ideal I in a Lie algebra is a subalgebra fixed by the commutator map: for $x \in I$ and arbitrary $h \in \mathfrak{h}$, $[h, x] \in I$. A simple Lie algebra is one with no proper ideals. \mathfrak{h} is said to be semisimple iff it is the direct sum of simple Lie algebras. A Cartan subalgebra (CSA) \mathfrak{c} of a semisimple Lie algebra \mathfrak{h} is a

maximal commutative subalgebra. A vector space carrying a representation of \mathfrak{h} decomposes into orthogonal joint eigenspaces V_λ of the operators in \mathfrak{c} . That is, each V_λ consists of the set of states $|\psi\rangle$ such that for $x \in \mathfrak{c}$, $x|\psi\rangle = \lambda(x)|\psi\rangle$. The label λ is therefore a linear functional on \mathfrak{c} , called the weight of V_λ . The subspace of operators in \mathfrak{h} orthogonal in trace inner product to \mathfrak{c} can be organized into orthogonal *raising* (ϵ_μ) and *lowering* ($\epsilon_{-\mu}$) operators, which connect different weight spaces. For a fixed CSA, the weights form a convex polytope; a lowest (or highest) weight is an extremal point of such a polytope, and the one-dimensional weight-spaces having those weights are known as *lowest-weight states*. The set of lowest-weight states for all CSAs is the orbit of any one such state under the Lie group generated by \mathfrak{h} . These are the group-theoretic generalized coherent states [44], which may be formally represented as

$$|GCS\rangle = e^{\sum_\mu (\eta_\mu \epsilon_\mu - \bar{\eta}_\mu \epsilon_{-\mu})} |\text{ext}\rangle , \quad (6.44)$$

where $|\text{ext}\rangle$ is an extremal state. The GCSs attain *minimum uncertainty* in an appropriate invariant sense [45, 46], thus providing a natural generalization of the familiar harmonic-oscillator coherent states.

Bibliography

- [1] R. Jozsa and N. Linden, Proc. Roy. Soc. London A **459**, 2001 (2003); G. Vidal, Phys. Rev. Lett. **91**, 147902 (2003).
- [2] F. Verstraete and J. I. Cirac, Phys. Rev. A **70**, 060302(R) (2004).
- [3] D. Porras, F. Verstraete, and J. I. Cirac, Phys. Rev. B **73**, 014410 (2006); G. Vidal, Phys. Rev. Lett. **93**, 040502 (2004).
- [4] R. Somma, H. Barnum, G. Ortiz, and E. Knill, Phys. Rev. Lett. **97**, 190501 (2006).
- [5] Z. Nussinov and G. Ortiz, Phys. Rev. B **79**, 214440 (2009).
- [6] M. Nakahara, *Geometry, Topology, and Physics* (IOP Publishing Ltd., Bristol, 1990).
- [7] *Geometric Phases in Physics*, edited by A. Shapere and F. Wilczek (World Scientific, Singapore, 1989).
- [8] L. D. Landau, E. M. Lifshitz, and L. P. Pitaevskii, *Electrodynamics of Continuous Media*, Vol. 8 (Butterworth-Heinemann, Oxford, 1996).
- [9] H. Barnum, E. Knill, G. Ortiz, and L. Viola, Phys. Rev. A **68**, 032308 (2003); H. Barnum, E. Knill, G. Ortiz, R. Somma, and L. Viola, Phys. Rev. Lett. **92**, 107902 (2004).

- [10] R. Somma, G. Ortiz, H. Barnum, E. Knill, and L. Viola, Phys. Rev. A **70**, 042311 (2004); R. Somma, H. Barnum, E. Knill, G. Ortiz, and L. Viola, Int. J. Mod. Phys. B **20**, 2760 (2006).
- [11] C. D. Batista and G. Ortiz, Phys. Rev. Lett. **86**, 1082 (2001); Adv. Phys. **53**, 1 (2004); G. Ortiz and C. D. Batista in *Recent Progress in Many-Body Theories*, Eds. R. F. Bishop, T. Brandes, K. A. Gernoth, N. R. Walet, and Y. Xian (World Scientific, Singapore, 2002), 425.
- [12] S. Deng, G. Ortiz, and L. Viola, Europhys. Lett. **84**, 67008 (2008); Phys. Rev. B **80**, 241109 (2009).
- [13] O. Derzhko and T. Krokhmalskii, Czech. J. Phys. **55**, 605 (2005); O. Derzhko, J. Richter, and T. Krokhmalskii, Phys. Rev. E **69**, 066112 (2004).
- [14] P. Pfeuty, Ann. Phys. **57**, 79 (1970); E. Barouch, B. M. McCoy, and M. Dresden, Phys. Rev. A **2**, 1075 (1970).
- [15] K. Okamoto and K. Yasumura, J. Phys. Soc. Japan **59**, 993 (1990).
- [16] S. Sachdev, *Quantum Phase Transitions* (Cambridge UP, Cambridge, 1999).
- [17] W. H. Zurek, U. Dorner, and P. Zoller, Phys. Rev. Lett. **95**, 105701 (2005).
- [18] J. Dziarmaga, Phys. Rev. Lett. **95**, 245701 (2005); F. M. Cucchietti, B. Damski, J. Dziarmaga, and W. H. Zurek, Phys. Rev. A **75**, 023603 (2007).
- [19] A. A. Aligia, K. Hallberg, C. D. Batista, and G. Ortiz, J. Low Temp. Phys. **117**, 1747 (1999); *ibid* Phys. Rev. B **61**, 7883 (2000).
- [20] G. Ortiz and R. M. Martin, Phys. Rev. B **49**, 14202 (1994).
- [21] G. Ortiz, P. Ordejón, R.M. Martin, and G. Chiappe, Phys. Rev. B **54**, 13515 (1996).
- [22] A. A. Aligia and E.R. Gagliano, Physica C **304**, 29 (1998).
- [23] A. A. Aligia, Europhys. Lett. **45**, 411 (1999).
- [24] C. D. Batista, G. Ortiz, and A. A. Aligia, Phys. Rev. Lett. **101**, 077203 (2008).
- [25] A.A. Aligia and G. Ortiz, Phys. Rev. Lett. **82**, 2560 (1999).
- [26] G. Rigolin, G. Ortiz, and V. H. Ponce, Phys. Rev. A **78**, 052508 (2008).
- [27] D. J. Thouless, Phys. Rev. B **27**, 6083 (1983).
- [28] W. Kohn, Phys. Rev. **133**, A171 (1964).

- [29] R. Resta, Phys. Rev. Lett. **80**, 1800 (1998).
- [30] G. Ortiz and A. A. Aligia, Phys. Stat. Solidi **220**, 737 (2000).
- [31] I. Souza, T. Wilkens, and R. M. Martin, Phys. Rev. B **62**, 1666 (2000).
- [32] I. Affleck, T. Kennedy, E. H. Lieb, and H. Tasaki, Phys. Rev. Lett. **59**, 799 (1987).
- [33] A. A. Aligia *et al.*, Phys. Rev. Lett. **99**, 206401 (2007).
- [34] C. D. Batista and A. A. Aligia, Phys. Rev. Lett. **92**, 246405 (2004); *ibid*, Phys. Rev. B **71**, 125110 (2005).
- [35] M. E. Torio *et al.*, Phys. Rev. B **73**, 115109 (2006).
- [36] M. Nakamura and S. Todo, Phys. Rev. Lett. **89**, 077204 (2002).
- [37] J.P. Provost and G. Vallee, Commun. Math. Phys. **76**, 289 (1980).
- [38] M. Hayashi, *Quantum Information: An Introduction*, (Springer-Verlag, Berlin, 2006).
- [39] G. Japaridze and A.P. Kampf, Phys. Rev. B **59**, 12822 (1999).
- [40] L. Arrachea, A.A. Aligia, and E.R. Gagliano, Phys. Rev. Lett. **76**, 4396 (1996).
- [41] C. D. Batista, G. Ortiz, and J. E. Gubernatis, Phys. Rev. B **65**, 180402 (2002).
- [42] Z. Nussinov and G. Ortiz, Ann. Phys. (NY) **324**, 977 (2009).
- [43] E. Cobanera, G. Ortiz, and Z. Nussinov, Phys. Rev. Lett. **104**, 020402 (2010).
- [44] A. Perelomov, *Generalized Coherent States and their Applications*, (Springer-Verlag, Berlin, 1986).
- [45] R. Delbourgo and J. R. Fox, J. Phys. A, **10** L233 (1977); R. Delbourgo, J. Phys. A **10**, 1837 (1977).
- [46] S. Boixo, L. Viola, and G. Ortiz, Europhys. Lett. **79**, 40003 (2007).
79 40003

Part II

Progress in Model Hamiltonians and in Specific Systems

Topological Order and Quantum Criticality

Claudio Castelnovo

Rudolf Peierls Centre for Theoretical Physics and Worcester College, Oxford University, Oxford OX1 3NP, UK

Simon Trebst

Microsoft Research, Station Q, University of California, Santa Barbara, California 93106, U.S.A.

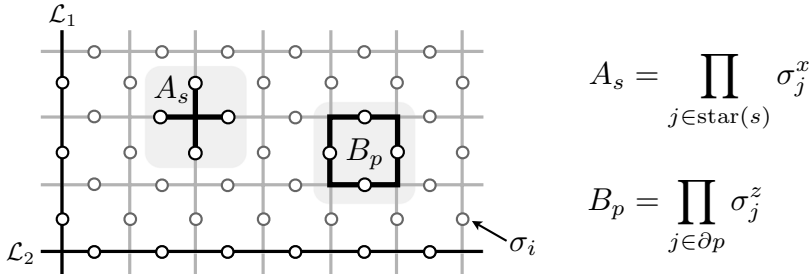
Matthias Troyer

Theoretische Physik, Eidgenössische Technische Hochschule Zurich, 8093 Zurich, Switzerland

In this chapter we discuss aspects of the quantum critical behavior that occurs at a quantum phase transition (QPT) separating a topological phase from a conventional one. We concentrate on a family of quantum lattice models, namely certain deformations of the toric code model, that exhibit continuous QPTs. One such deformation leads to a Lorentz-invariant transition in the 3D Ising universality class. An alternative deformation gives rise to a so-called conformal quantum critical point (QCP) where equal-time correlations become conformally invariant and can be related to those of the 2D Ising model. We study the behavior of several physical observables, such as non-local operators and entanglement entropies, that can be used to characterize these QPTs. Finally, we briefly consider the role of thermal fluctuations and related phase transitions, before closing with a short overview of field theoretical descriptions of these QCPs.

7.1 Introduction

Topological phases are distinct both from high-temperature disordered phases and conventional ordered ones: they exhibit order, albeit of a type which cannot be defined locally [1]. They are often described by an emergent symmetry that is captured by a new set of quantum numbers such as a ground-state degeneracy and fractional quasiparticle statistics. The archetypal physical realizations of topologically ordered states are fractional quantum Hall states.

**FIGURE 7.1**

The toric code model: The elementary degrees of freedom are SU(2) spin-1/2's on the bonds of a square lattice. The star operator A_s acts on the spins surrounding a vertex and the plaquette operator B_p acts on the spins surrounding a plaquette.

This chapter is concerned with topological order and quantum critical behavior in the context of microscopic lattice models. Most of our discussion will concentrate on *time-reversal invariant* systems which in more general terms can be described by so-called quantum double models and are thus quite distinct from fractional quantum Hall states. We start by shortly reviewing the *toric code* model, a particularly simple and exactly solvable spin-1/2 model that exhibits an Abelian topological phase. Our subsequent discussion of QPTs involving topologically ordered phases of matter is structured around two types of deformations of the toric code which we dub *Hamiltonian deformation* and *wavefunction deformation*, respectively, and that give rise to distinct QCPs. We then turn to finite-temperature phase transitions and discuss under which circumstances topological order is robust with regard to thermal fluctuations.

7.1.1 The Toric Code

The toric code (TC) [2] is an exactly solvable model of SU(2) spin-1/2 degrees of freedom, which is typically defined on a square lattice, but can be adapted to other two-dimensional lattice geometries (and even higher-dimensional lattices). The Hamiltonian is generally defined as a sum of vertex and plaquette terms,

$$\mathcal{H}_{\text{TC}} = -J_e \sum_s A_s - J_m \sum_p B_p, \quad (7.1)$$

where the star operator A_s acts on all spins adjacent to a vertex s by coupling their σ^x spin components, $A_s = \prod_{j \in \text{star}(s)} \sigma_j^x$, and the plaquette operator B_p acts on all spins surrounding a plaquette p by coupling their σ^z spin components, $B_p = \prod_{j \in \partial p} \sigma_j^z$. We typically consider the case $J_e, J_m > 0$. In

the case of the square lattice, the star and plaquette operators are both 4-spin operators which are Hermitian and have eigenvalues ± 1 .

The toric code model can be solved exactly, since all terms in the Hamiltonian commute with one another. Indeed, $A_s B_p = B_p A_s$, $\forall s, p$ since any given pair of vertex and plaquette operators either share 0 or 2 bonds, and thus all minus signs arising from the commutation of σ^x and σ^z on those bonds cancel. This allows us to construct eigenstates $|\xi\rangle$ of the toric code as common eigenstates of all terms in the Hamiltonian. For a ground state the minimization of the energy then gives the stabilizer conditions $A_s |\xi\rangle = B_p |\xi\rangle = |\xi\rangle$ for each vertex/plaquette term, and an overall ground-state energy $E_0 = -N(J_e + J_m)$, where N is the number of sites on the lattice.

For a square lattice with periodic boundary conditions in both space directions (thus forming a torus) the sign of the vertex (plaquette) terms can only be flipped on an *even* number of vertices (plaquettes). This implies that there are two overall constraints,

$$\prod_s A_s = \prod_p B_p = +1. \quad (7.2)$$

This in turn lets us estimate the ground-state degeneracy on a torus: The total Hilbert space has 2^{2N} states. With the above constraint there are only $2N - 2$ independent choices of the A_s and B_p operators, thus imposing 2^{2N-2} conditions. As a consequence, we have $2^{2N}/2^{2N-2} = 4$ ground states on the torus.

Another way to see how this ground-state degeneracy arises is by explicitly constructing the ground-state wavefunctions. In doing so we solve the toric code Hamiltonian in the σ^z basis and introduce classical variables $z_j = \pm 1$ to label the σ^z basis states. This allows us to define a plaquette flux

$$\phi_p(\mathbf{s}) = \prod_{j \in \partial p} z_j \quad (7.3)$$

for each classical spin configuration $\mathbf{s} = \{z_j\}_{j=1}^{2N}$. If $\phi_p = -1$, we say there is a vortex on plaquette p . For a ground state $|\psi\rangle$ of the toric code we need to maximize each plaquette term $B_p |\psi\rangle = |\psi\rangle$ and thus find that a ground state contains no vortices:

$$|\psi\rangle = \sum_{\{\mathbf{s}: \phi_p(\mathbf{s})=+1 \forall p\}} c_{\mathbf{s}} |\mathbf{s}\rangle. \quad (7.4)$$

To maximize the vertex operator, e.g., $A_s |\psi\rangle = |\psi\rangle$, all coefficients $c_{\mathbf{s}}$ are then required to be equal (for each orbit of the action of the star operators). A ground state of the toric code is thus an equal-weight superposition of vortex-free spin configurations.

On the square lattice there are four distinct ways to construct such equal-weight superpositions, giving rise to a four-fold ground-state degeneracy. This can be seen by considering the following function measuring the flux through

an extended loop \mathcal{L} (similar to a Wilson loop), as indicated in Fig. 7.1:

$$\Phi_{\mathcal{L}}(\mathbf{s}) = \prod_{j \in \mathcal{L}} z_j. \quad (7.5)$$

If the loop \mathcal{L} is a contractible loop, then the flux $\Phi_{\mathcal{L}}$ is simply the product of the plaquette fluxes ϕ_p within the loop (reminiscent of Stokes' theorem), and for each ground state $\Phi_{\mathcal{L}} = +1$. If on the other hand the loop \mathcal{L} is an essential loop on the torus (which cannot be contracted), then the flux $\Phi_{\mathcal{L}} = \pm 1$ defines a conserved quantity, since an arbitrary star operator A_s overlaps with the loop \mathcal{L} in either 0 or 2 bonds and thus preserves $\Phi_{\mathcal{L}}$. For the torus there are two independent essential loops $\mathcal{L}_1, \mathcal{L}_2$ wrapping the torus as illustrated in Fig. 7.1. The ground states of the toric code can then be labeled by two conserved quantities $\Phi_{\mathcal{L}_1} = \pm 1$ and $\Phi_{\mathcal{L}_2} = \pm 1$. The resulting degeneracy originates from the four distinct *topological sectors* defined by the essential loops. Embedding the toric code onto the surface of a more general manifold, one finds that the ground-state degeneracy increases as 4^g with the genus g of the underlying surface.

We note in passing that one can find another description of the eigenstates of the toric code by solving the Hamiltonian in the σ^x basis. Labeling the basis states by classical variables $x_j = \pm 1$ and identifying the $x_j = +1$ states with loop segments on the corresponding bonds, one finds that the ground states of the toric code form a *quantum loop gas* with fugacity $d = 1$. The four topological sectors then correspond to loop configurations with an even or odd number of loops wrapping the torus across two independent, non-contractible cuts.

The toric code Hamiltonian can also be viewed as a particular lattice regularization of an Ising gauge theory [3]. In this language the spins residing on the bonds correspond to Z_2 -valued gauge potentials, the star operators A_s become gauge transformations, and their commutation with the plaquette flux operators B_p implies an overall gauge invariance. Owing to this equivalence to an Ising gauge theory, the two distinct excitations of the toric code that arise from violating one of the stabilizer conditions of the ground states, $A_s|\psi\rangle = |\psi\rangle$ and $B_p|\psi\rangle = |\psi\rangle$, are commonly identified as *electric charges* and *magnetic vortices*, respectively.

For a given ground state a pair of electric charges is created by applying the σ^z -operator to a spin, which leads to a violation of the stabilizer condition $A_s|\psi\rangle = |\psi\rangle$ on the two adjacent vertices. Therefore, the energy cost to create two electric charges is $4J_e$. While a pair of electric charges does not need to reside on neighboring vertices, it remains connected for any separation by an electric path operator $\prod_{j \in \ell} \sigma_j^z$, where ℓ is a path connecting the two vertices. A similar result holds for a pair of magnetic vortices, upon replacing ℓ with a path on the dual lattice.

Both types of excitations are massive quasiparticles, and for the unperturbed toric code Hamiltonian (7.1) they are static excitations which do not disperse. While single electric charges or magnetic vortices are bosons (consid-

ering the exchange with the same particle type), the composite quasiparticle of an electric charge plus a magnetic vortex constitutes a fermion. Moreover, electric charges and magnetic vortices exhibit an unusual *mutual* exchange statistics in that they are mutual *semions*.¹ This can best be seen when considering a wavefunction $|\xi\rangle$ of a state containing a single vortex at a plaquette \tilde{p} , e.g., $B_{\tilde{p}}|\xi\rangle = -|\xi\rangle$. If we move an electric charge along a contractible loop \mathcal{L} around this plaquette \tilde{p} , the wavefunction transforms as

$$|\xi\rangle \rightarrow \prod_{j \in \mathcal{L}} \sigma_j^z |\xi\rangle = \prod_{p \text{ inside } \mathcal{L}} B_p |\xi\rangle = -|\xi\rangle, \quad (7.6)$$

which reveals the mutual semionic statistics.

In summary, the toric code is one of the simplest and most accessible quantum lattice models that gives rise to a quantum state with *topological order*. This exotic quantum order reveals itself in a (robust) ground-state degeneracy and massive, deconfined quasi-particles with mutual anyonic statistics.

7.2 Quantum Phase Transitions

While conventional ordered phases arise from the spontaneous breaking of a symmetry, the converse is true for topological phases which exhibit an enhanced symmetry at low energies. It is this emerging topological invariance which isolates the low-energy degrees of freedom from local perturbations and gives rise to stable topological phases. However, even a local perturbation, if sufficiently strong, can eventually destabilize a topological phase and give rise to a QPT.

To elucidate the quantum critical behavior at such a transition we consider the pedagogical example of the toric code in a magnetic field. A sufficiently large magnetic field aligns all the spins with the field, resulting in a paramagnetically ordered state, and thus destroys any topological order. The QPT that connects these two phases can be either first-order or continuous depending on the way we couple the magnetic field to the local spin degrees of freedom in the toric code Hamiltonian. We mostly focus on the latter case of a continuous transition and discuss two distinct types of QCPs that can occur.

First, we consider a magnetic field term $\vec{h} \cdot \vec{\sigma}$, where the magnetic field \vec{h} has no transverse h_y component [4–6], i.e., $\vec{h} \cdot \vec{\sigma} = h_x \sigma^x + h_z \sigma^z$. This Hamiltonian deformation gives rise to a QCP at which the system becomes scale invariant and *local* two-point correlation functions show a divergent behavior. This not only allows us to define a dynamical critical exponent, which is found to be $z = 1$, but also enables us to characterize this Lorentz-invariant transition out

¹Semions are the simplest incarnation of Abelian anyons: when moving an electric charge around a magnetic vortex the wavefunction picks up a phase of $e^{i\pi} = -1$.

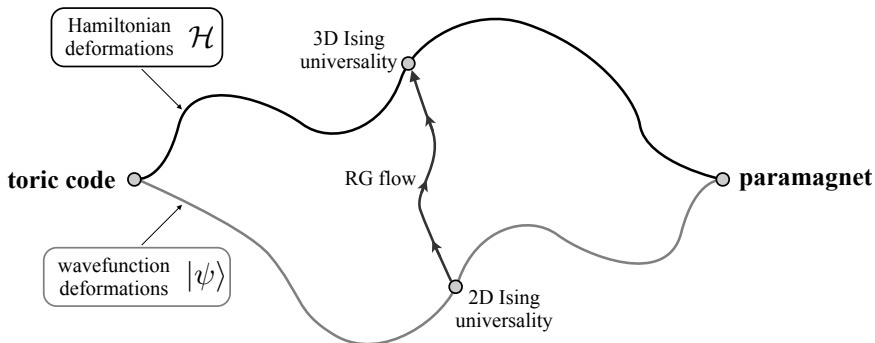


FIGURE 7.2

Toric code deformations. Two distinct types of QCPs are observed in phase space depending on the way the magnetic field is coupled to the local spin degrees of freedom in the toric code.

of the topological phase in terms of a conventional universality class, which for this transition turns out to be the classical 3D Ising model.

Second, we consider a magnetic field term $\exp(-h_z\sigma^z)$, which for large field strength projects onto the fully polarized state, while allowing us to keep track of the ground-state wavefunction for all field strengths [7, 8]. We call this second scenario a wavefunction deformation. It gives rise to a so-called *conformal QCP* [9], where a peculiar type of dimensionality reduction is at play which allows us to describe the equal-time correlations of the ground state by a 2+0 dimensional conformal field theory which at this QCP turns out to be the 2D Ising theory. In contrast to the Hamiltonian deformation, the dynamical critical exponent is $z \neq 1$ for this second QCP. Despite the obvious differences in the intermediate quantum critical behavior both deformations connect the same extremal ground states, namely those of the toric code with a fully polarized, paramagnetic state.

We note in passing that (in the continuum limit) these two QCPs are connected by a renormalization group flow from the conformal QCP to the Lorentz-invariant QCP. A schematic overview of these two types of deformations and their respective QCPs is given in Fig. 7.2.

Finally, we close by discussing the role of thermal fluctuations at the quantum critical points of the deformed toric code models. This also allows us to shed some light on the question whether topological order can survive up to a finite temperature.

7.2.1 Lorentz-Invariant Transitions

We first turn to the case of Lorentz-invariant QCPs which can be observed when adding a longitudinal magnetic field to the toric code

$$\mathcal{H}_{\text{TC+LMF}} = -J_e \sum_s A_s - J_m \sum_p B_p + \sum_i (h_x \sigma_i^x + h_z \sigma_i^z) . \quad (7.7)$$

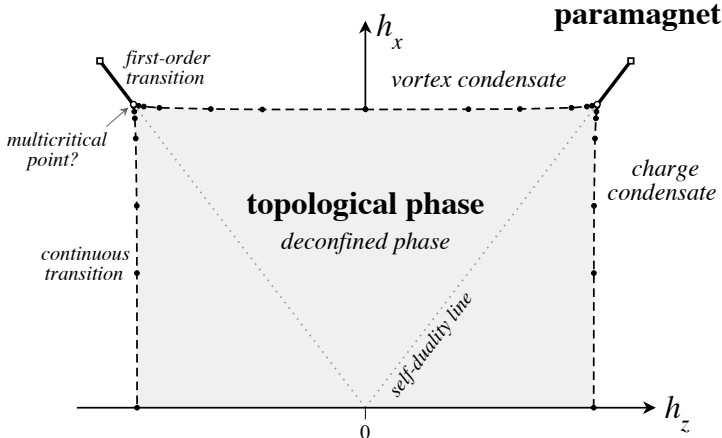
Whereas the model is no longer exactly solvable, we can readily understand the extremal cases of weak and strong magnetic fields.

For $h_z = 0$ the effect of a small field $h_x \ll J_e, J_m$ is the virtual creation and annihilation of pairs of magnetic vortices as discussed in the previous section, or the hopping of a vortex excitation by one plaquette which allows the vortices to acquire a dispersion. In first-order perturbation theory this gives the usual tight-binding form in momentum space,

$$E(q_x, q_y) = 2J_m - 2h_x (\cos q_x + \cos q_y) + O(h_x^2) , \quad (7.8)$$

which can be further expanded to higher orders [6]. A similar observation holds for the dual charge excitations.

With increasing magnetic field strength the quasi-particle gap eventually closes and the transition into the paramagnetic state can be understood as the Bose condensation of these quasi-particles. In the language of Ising gauge theory this leaves us with two seemingly distinct possibilities, as first discussed by Fradkin and Shenker [10]: a Higgs transition into a charge condensate with concurrent vortex confinement for $h_x \ll h_z \approx J_e, J_m$; or, by duality, a confinement transition of the electric charges with the concurrent formation of a vortex condensate for $h_z \ll h_x \approx J_e, J_m$. Both transitions give rise to a *line of continuous transitions*, as illustrated schematically in Fig. 7.3, where fluctuations of the system can be described in terms of two complimentary Z_2 order parameters, namely the amplitudes of the corresponding charge and vortex condensates. As such the two transitions are clearly distinct and owing to the non-trivial mutual statistics of charges and vortices, these two lines of continuous transitions are not expected to join smoothly in the phase diagram. On the basis of extensive numerical simulations it has recently been conjectured [5, 6] that they meet at a *multicritical* point where they join with a first-order line separating the charge and vortex condensates for intermediate $h_x = h_z \approx J_e, J_m$. This first-order transition is accompanied by a sudden change in the density of charges/vortices, similar to a liquid-gas transition. However, if we consider the paramagnetic phase in the large magnetic field limit of the original spin model, then we can continuously rotate the magnetic field in the (h_x, h_z) -plane without inducing a phase transition. As a consequence, the charge and vortex condensates are actually the same phase, and they are connected in the large magnetic field limit. Indeed, the first-order line has a critical endpoint whose location was recently determined by numerical simulations [5, 6].

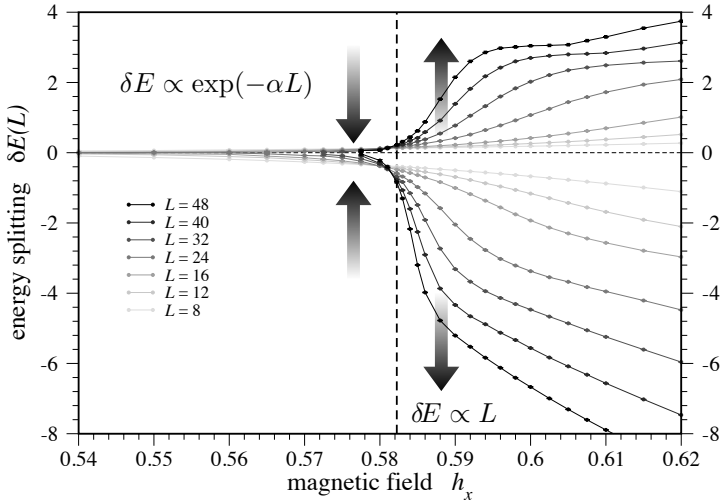
**FIGURE 7.3**

Phase diagram of the toric code in a longitudinal magnetic field. The dashed lines indicate continuous QPTs from the topological phase (shaded area) to a paramagnetically ordered state. The solid lines indicate first-order transitions. The figure has been adapted from the numerical data of Ref. [5] for the closely related classical, anisotropic Z_2 gauge Higgs model on a cubic lattice.

To discuss the quantum critical behavior at one of the continuous transitions in the phase diagram of Fig. 7.3 in more detail, we consider the case of a single-component magnetic field in the x -direction, $h_x \neq 0$ and $h_{y,z} = 0$. As discussed above, such a magnetic field will create/annihilate virtual vortex pairs that can hop through the lattice, while charge excitations remain gapped and static. To describe the vortex dynamics in this limit we introduce a plaquette spin operator μ_p with eigenvalues $\mu_p^z = \pm 1/2$ depending on the eigenvalue of the plaquette operator B_p on the respective plaquette, e.g., $B_p = 2\mu_p^z$. We can then rewrite the spin operators σ^x in terms of these plaquette operators as $\sigma_i^x = \mu_p^x \mu_q^x$, where p and q are the plaquettes separated by the bond i . With these transformations in place, we can now recast the charge-free low-energy sector of the toric code in a single-component magnetic field in the form

$$\tilde{\mathcal{H}}_{\text{TC+LMF}} = -2J_m \sum_p \mu_p^z + h_x \sum_{\langle p,q \rangle} \mu_p^x \mu_q^x \quad (7.9)$$

of a transverse field Ising model. Its well-known QPT thus describes the transition from the topological phase of the toric code into a paramagnetic state, or vortex condensate in the language of the Ising gauge theory. This continuous transition in the 3D Ising universality class occurs for coupling strength $(h_x/J_m)_c \approx 0.65692(2)$ [11], indicating that the topological phase is remarkably stable. It takes an $O(1)$ perturbation, in terms of the coupling strengths,

**FIGURE 7.4**

Splitting of the topological degeneracy. The finite-size splitting of the ground-state degeneracy changes from exponential suppression in the topological phase to linear splitting in the paramagnetic phase². Data for different linear system sizes L are plotted.

to destroy the topologically ordered state, similar to the case of many conventionally ordered states.

The mapping to the transverse field Ising model also allows us to perform extensive Monte Carlo simulations of this transition and to keep track of the ground-state degeneracy across the QPT [4]. As shown in Fig. 7.4 the finite-size splitting of the degeneracy changes from exponentially small in the topological phase to power-law in the paramagnetic phase,² as a function of the linear system size L .

Returning to the full Hamiltonian (7.7) we can ask what effect a small magnetic field h_z has on the QPT discussed above. Since such a field primarily induces dynamics in the gapped charge sector, the transition into the vortex condensate remains largely untouched, and we expect to observe a *line* of continuous transitions emanating from the single-component field limit discussed above. In fact, one can map out the full phase diagram of the two-component case as shown in Fig. 7.3. This is done through a sequence of transformations that allow us to recast the toric code in a two-component magnetic field onto a classical, anisotropic Z_2 gauge Higgs model on a 3D cubic lattice, as described in detail in Ref. [5].

²The critical coupling is slightly lower in the figure than in the text, as the numerical simulations were done for discretized imaginary time and isotropic couplings in space-time. This does not change the long-distance physics.

7.2.1.1 Other Hamiltonian Deformations

A number of other Hamiltonian deformations of the toric code have been considered in the literature. Of particular interest is the case of a transverse field $h_y\sigma^y$. Contrary to the longitudinal case, it is found to drive a first-order phase transition into a paramagnetic state [12].

The effect of dissipation was also studied [4] by coupling the toric code to an Ohmic heat bath. A Berezinsky-Kosterlitz-Thouless-type transition was found when the bath couples to the plaquette spins μ_p^z such that it stabilizes the “classical” state of the system.

7.2.2 Conformal Quantum Critical Points

We now turn to the second scenario of perturbing the toric code model via a *wavefunction deformation* that again connects the ground states of the toric code with a fully polarized, paramagnetic state [7, 8]. Along this wavefunction deformation the system goes through a continuous QPT which is distinct from the one we encountered for the Hamiltonian deformations of the previous section. It belongs in fact to the family of *conformal QCPs*, first discussed by Ardonne, Fendley, and Fradkin [9], where it is the ground-state wavefunction that becomes *scale invariant*, in a peculiar instance of dimensionality reduction. This in turn allows us to describe the *equal-time* correlations in the ground-state wavefunction of a 2D quantum system by those of the related, conformally invariant, *classical* system in 2 dimensions; this is in contrast to the usual correspondence of a D -dimensional quantum system to a $D + 1$ dimensional classical system. This dimensionality reduction at a conformal QCP is reminiscent of the well-known Rokhsar-Kivelson point of the 2D quantum dimer model [13, 14], where in a similar fashion equal-time correlations are captured by a ground-state wavefunction that is the equal-weight superposition of all classical 2D dimer configurations. Following earlier work by Henley [15], Ardonne *et al.* further argued that at a continuous transition the conformal invariance of the ground state wave function enforces a quantum Lifshitz field theory description, with a characteristic $z = 2$ dynamical exponent [9].

To study wavefunction deformations of the toric code we employ a constructive technique dubbed *stochastic matrix form* decomposition [16] that allows us to obtain generalized Rokhsar-Kivelson type Hamiltonians. With this approach we can derive an explicit expression for the ground state wavefunction along the deformation, and we can analyze the intervening conformal QCP in great detail. In particular, we show that the quantum critical behavior is associated with a divergent local length scale, despite the fact that there is no concomitant symmetry-breaking phase transition described by a local order parameter. Finally, we turn to entanglement measures and, after a short introduction, we discuss the behavior of the topological entropy across the phase transition.

7.2.2.1 Microscopic Model for Wavefunction Deformation

To implement the wavefunction deformation we construct a family of quantum Hamiltonians whose ground states interpolate between the toric code wavefunction (7.4) and the fully polarized state $|\psi_p\rangle = \bigotimes_i |\sigma_i^z = +1\rangle$. This can be accomplished by using *stochastic matrix form* (SMF) decompositions [16] for a generic wavefunction of the form

$$|\psi\rangle \propto \sum_{\{\mathbf{s} : \phi_p(\mathbf{s})=+1 \forall p\}} \exp\left(\frac{h}{2} E_{\mathbf{s}}\right) c_{\mathbf{s}} |\mathbf{s}\rangle. \quad (7.10)$$

For $h = 0$ this is the toric code ground state, while for $h \rightarrow \infty$ the polarized state is exponentially selected, provided that $E_{\mathbf{s}}$ is sufficiently peaked at $\mathbf{s} = \{z_j = +1\}$. The corresponding SMF Hamiltonian can simply be expressed as a sum of projectors that annihilate (7.10). So long as the function(al) $E_{\mathbf{s}}$ can be written as a sum of local terms in the variables $\{z_j\}$, then the Hamiltonian can be constructed as a sum of local operators expressed in terms of the Pauli matrices $\sigma_j^{x,y,z}$.

The simplest example is given by the choice $E_{\mathbf{s}} = \sum_j z_j$. It is straightforward to verify that

$$H = -J_e \sum_s A_s + J_e \sum_s \exp\left(-h \sum_{i \in s} \sigma_i^z\right) \quad (7.11)$$

is a sum of projectors, each of which annihilates (7.10) [7, 16].³ However, this remains true if the summation in (7.10) is generalized from $\{\mathbf{s} : \phi_p(\mathbf{s}) = +1 \forall p\}$ to $\{\mathbf{s} : \phi_p(\mathbf{s}) = \bar{\phi}_p \forall p\}$, for any configuration $\{\bar{\phi}_p\}$ of the plaquette eigenvalues. In order to arrive at the desired result, we need to add an appropriate energy cost $-J_m \sum_p B_p$ to the unwanted ground states [7],

$$H = -J_m \sum_p B_p - J_e \sum_s A_s + J_e \sum_s \exp\left(-h \sum_{i \in s} \sigma_i^z\right). \quad (7.12)$$

Not surprisingly, for $h = 0$, the system reduces to the toric code Hamiltonian (7.1), up to a trivial constant shift in energy. Moreover, in the limit $|h| \ll 1$ one can expand the exponential in Eq. (7.12), and to first order one obtains precisely the Hamiltonian deformation studied in the previous section with a longitudinal field $h_z = 2hJ_e$. This equivalence is eventually lost for larger values of h . By construction, both models favor the same fully polarized, paramagnetic state for large fields $h \gg 1$.

For convenience of notation, in the following we shall replace the sum over $\{\mathbf{s} : \phi_p(\mathbf{s}) = +1 \forall p\}$ in Eq. (7.10) by the sum over the Abelian group G of

³A generic construction scheme for SMF Hamiltonians given arbitrary $E_{\mathbf{s}}$ functionals is provided in Ref. [16].

all spin flip operations obtained as products of star operators A_s [2, 17]. Then the ground state wavefunction of model (7.12) reads

$$|\psi_0^{(\alpha)}\rangle = \frac{1}{\sqrt{Z_\alpha}} \sum_{g \in G} \exp \left(\frac{h}{2} \sum_i \sigma_i^z(g, \alpha) \right) g |\Psi_\alpha\rangle, \quad (7.13)$$

$$\text{with } Z_\alpha = \sum_{g \in G} \exp \left(h \sum_i \sigma_i^z(g, \alpha) \right) \quad \text{and} \quad \sigma_i^z(g, \alpha) \equiv \langle \Psi_\alpha | g \sigma_i^z g | \Psi_\alpha \rangle.$$

Here the index α labels the 4 topological sectors, i.e., the orbits of the action of the star operators. The eigenstate $|\Psi_\alpha\rangle$ can be chosen arbitrarily amongst the elements of the orbit α , since the action of the group G on any such state generates the entire orbit.

7.2.2.2 Dimensionality Reduction and the 2D Ising Model

For convenience, we study the QPT to the paramagnetic state in the topological sector containing the fully polarized state $|\psi_p\rangle = \bigotimes_i |\sigma_i^z = +1\rangle$. The explicit form of the wavefunction reduces to

$$|\psi_0\rangle = \frac{1}{\sqrt{Z}} \sum_{g \in G} e^{h \sum_i \sigma_i^z(g)/2} g |\psi_p\rangle \quad \text{with} \quad \sigma_i^z(g) \equiv \langle \psi_p | g \sigma_i^z g | \psi_p \rangle. \quad (7.14)$$

A generic configuration $g|\psi_p\rangle$ is uniquely specified by the set of star operators acting on the reference configuration $|\psi_p\rangle$, modulo the action of the product of all the star operators (which is equal to the identity). Thus, there is a 1-to-2 mapping between $G = \{g\}$ and the configuration space $\Theta = \{\boldsymbol{\theta}\}$ of an Ising model with classical degrees of freedom θ_s living on the sites s of the square lattice, where for example $\theta_s = -1$ (+1) means that the corresponding star operator is (not) acting in the associated g . Since each σ -spin can be flipped only by its two neighboring θ -spins, then $\sigma_i \equiv \theta_s \theta_{s'}$, where i labels the bond between the two neighboring sites $\langle s, s' \rangle$. Using this mapping, the ground state wavefunction of the model, Eq. (7.14), can be rewritten as

$$|\psi_0\rangle = \frac{1}{\sqrt{Z}} \sum_{\boldsymbol{\theta} \in \Theta} \exp \left(\frac{h}{2} \sum_{\langle s, s' \rangle} \theta_s \theta_{s'} \right) g(\boldsymbol{\theta}) |\psi_p\rangle, \quad (7.15)$$

where $Z = \sum_{\boldsymbol{\theta} \in \Theta} \exp(h \sum_{\langle s, s' \rangle} \theta_s \theta_{s'})$.

All equal-time correlation functions of the ground state that can be expressed in terms of the classical θ -spins can thus be computed as correlation functions of a 2D classical Ising model with reduced nearest-neighbor coupling $J/T = h$ [16]. For small values of the field h , we can identify the equal-time correlation functions of the quantum model in the topological phase with the correlation functions of the high-temperature disordered phase of the 2D Ising model. Vice versa, the large field paramagnetic state of the quantum model

exhibits equal-time correlators that match those of the low-temperature Ising ferromagnetically ordered state. For an intermediate magnetic field strength h_c the ground-state wavefunction of the quantum system becomes critical and scale invariant, precisely when the corresponding classical spin system undergoes its thermal phase transition at $h_c = (1/2) \ln(\sqrt{2} + 1) \simeq 0.441$.

While the thermal phase transition in the 2D Ising model can be described in terms of a local order parameter, e.g., its magnetization, we note that this is not the case for the original quantum model. For instance, the magnetization in the original σ -spin language translates into the nearest-neighbor spin-spin correlation, i.e., the energy, in the θ -spin language,

$$m(h) = \frac{1}{N} \sum_i \langle \psi_0 | \sigma_i^z | \psi_0 \rangle = \sum_{\theta \in \Theta} \frac{e^{h \sum_{\langle s, s' \rangle} \theta_s \theta_{s'}}}{Z} \left[\frac{1}{N} \sum_{\langle s, s' \rangle} \theta_s \theta_{s'} \right] = \frac{1}{N} E_{\text{Ising}}(h), \quad (7.16)$$

and one concludes that $m(h)$ does not vanish on either side of the transition. It is continuous across the transition but there is a singularity in its first derivative

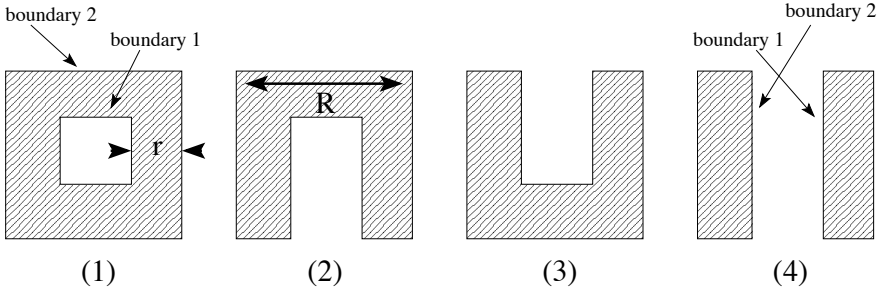
$$\frac{\partial m}{\partial h} = \frac{1}{N} \frac{\partial E_{\text{Ising}}}{\partial h} = -h^2 \frac{1}{N} C_{\text{Ising}}(h), \quad (7.17)$$

as the heat capacity $C_{\text{Ising}}(h)$ of the classical Ising model diverges logarithmically at h_c . While the original quantum model does not allow us to define a local order parameter for the phase transition, there is nevertheless a signature of this transition in terms of a singularity in the derivative of a local observable.

7.2.2.3 Topological Entropy

We have seen that the unusual properties of topologically ordered phases are inherently linked to non-local properties and a peculiar type of long-range entanglement. With all local correlations being short ranged and non-local correlation functions being tedious to define in more general examples, it is helpful to turn to entanglement measures and to define a *topological entropy* that allows us to detect and characterize topological phases [18, 19].

A common measure of quantum entanglement is given by the von Neumann entropy, $S_{\text{vN}} = -\text{Tr}[\rho \ln \rho]$, where ρ is the density matrix of the system. Typically one considers a (smooth) bipartition $(\mathcal{A}, \mathcal{B})$ of the system $\mathcal{S} = \mathcal{A} \cup \mathcal{B}$, with boundary size L , which in 2D is simply its length, and computes the reduced density matrix $\rho_{\mathcal{A}} = \text{Tr}_{\mathcal{B}}(\rho)$. The von Neumann entropy $S_{\text{vN}}(\mathcal{A}) = -\text{Tr}[\rho_{\mathcal{A}} \ln \rho_{\mathcal{A}}]$ is also known as the (bipartite) entanglement entropy, and reflects the amount of information shared between the two subsystems across the boundary. In ordinary short-range correlated phases, the nature of subsystem \mathcal{B} influences subsystem \mathcal{A} only up to some finite distance (of the order of the correlation length) away from the boundary, and vice versa. To leading order in L the von Neumann entropy thus takes a form $S_{\text{vN}}(\mathcal{A}) = \alpha L + \dots$, where the coefficient α is non-universal.

**FIGURE 7.5**

Bipartition scheme for the topological entropy. Illustration of the four distinct bipartitions $\mathcal{S} = \mathcal{A}_i \cup \mathcal{B}_i$ used to compute the topological entropy in Ref. [18]. The shaded area represents subsystem \mathcal{A}_i , with $i = 1, 2, 3, 4$.

If, on the other hand, non-local information is stored across a boundary as in the case of a topologically ordered state, it must show up as a further contribution to the entanglement between the two bipartitions \mathcal{A} and \mathcal{B} . It was argued in Refs. [17–19] that this contribution assumes the form of a correction of order one to the previous scaling form, e.g.,

$$S_{\text{vN}}(\mathcal{A}) = \alpha L - \gamma + O(1/L), \quad (7.18)$$

with all other sub-leading terms vanishing in the limit $L \rightarrow \infty$. This correction $\gamma \geq 0$ is found to be *universal*, and it is related to the *total quantum dimension* of the underlying topological phase [18, 19]. An elegant way to calculate γ is to choose an appropriate set of different bipartitions, such that a linear combination of the respective entanglement entropies cancels out all non-universal terms, at least in the limit of the correlation length being much smaller than the size of the bipartitions. Adopting the scheme proposed in Ref. [18] and illustrated in Fig. 7.5, we define the topological entropy as

$$S_{\text{topo}} = \lim_{r, R \rightarrow \infty} \left[-S_{\text{vN}}(\mathcal{A}_1) + S_{\text{vN}}(\mathcal{A}_2) + S_{\text{vN}}(\mathcal{A}_3) - S_{\text{vN}}(\mathcal{A}_4) \right], \quad (7.19)$$

where the indices $i = 1, \dots, 4$ label the four different bipartitions $\mathcal{S} = \mathcal{A}_i \cup \mathcal{B}_i$. Note that bipartitions $(\mathcal{A}_1, \mathcal{B}_1)$ and $(\mathcal{A}_4, \mathcal{B}_4)$ combined have the same total boundary, with the same number and type of corners, as bipartitions $(\mathcal{A}_2, \mathcal{B}_2)$ and $(\mathcal{A}_3, \mathcal{B}_3)$ combined. As a result, the non-universal part of the entanglement entropy due to local correlations cancels out in Eq. (7.19). However, only bipartitions $(\mathcal{A}_1, \mathcal{B}_1)$ and $(\mathcal{A}_4, \mathcal{B}_4)$ are topologically non-trivial and the universal correction to the corresponding entanglement entropies is doubled. This definition of S_{topo} therefore measures twice the value of γ , i.e., $S_{\text{topo}} = 2\gamma$.

Any approach to compute the topological entropy faces the challenge of isolating a sub-leading term of order one in a quantity, the entanglement en-

tropy, that scales with the size L of the bipartition.⁴ Perturbative techniques can be used only if the achieved accuracy is greater than $O(1/L)$. Likewise, it is rather difficult to obtain reliable numerical estimates [20]. On the other hand, at zero temperature the density matrix of the system becomes the projector onto the ground state $|\psi_0\rangle$, namely $\rho = |\psi_0\rangle\langle\psi_0|$, and one can attempt to calculate S_{vN} and S_{topo} directly whenever an explicit expression for the ground state wavefunction is available. Hereafter, we follow this approach and compute the topological entropy for the wavefunction deformation of the toric code presented in Sec. 7.2.2.1.

7.2.2.4 Topological Entropy along the Wavefunction Deformation

To calculate the topological entropy along the wavefunction deformation we consider a smooth bipartition $(\mathcal{A}, \mathcal{B})$ of the system. Let us define the subgroup $G_{\mathcal{A}} \subset G$ that acts solely on \mathcal{A} and leaves \mathcal{B} invariant: $G_{\mathcal{A}} = \{g = g_{\mathcal{A}} \otimes g_{\mathcal{B}} \in G \mid g_{\mathcal{B}} = I_{\mathcal{B}}\}$. Likewise, we define $G_{\mathcal{B}}$. Following Ref. [7] the von Neumann entropy $S_{vN}(\mathcal{A})$ from the ground state wavefunction in Eq. (7.14) can be expressed as

$$S_{vN}(A) = -\frac{1}{Z} \sum_{g \in G} e^{-hE_g} \ln \left(\frac{1}{Z} \sum_{f \in G_A, k \in G_B} e^{-hE_{fgk}} \right), \quad (7.20)$$

where $E_g = -\sum_i \sigma_i^z(g)$. This is the lattice equivalent of the von Neumann entropy obtained by Fradkin and Moore for quantum Lifshitz field theories [21]. Note that this expression for the von Neumann entropy can also be interpreted as the entropy of mixing (or configurational entropy) of the allowed boundary configurations in G . This was first shown in Ref. [7], and later investigated in more detail in Ref. [22].

Employing the change of variables to classical Ising degrees of freedom $\{\theta_s\}$ (see Sec. 7.2.2.2), and omitting the technical details [7] required to deal with configurations of the form fgk ($f \in G_A$ and $k \in G_B$), one can use Eq. (7.20) to obtain the topological entropy of the system as a function of h , with the bipartition scheme illustrated in Fig. 7.5:

$$S_{topo} = \lim_{r, R \rightarrow \infty} \left\{ \frac{\sum_{g \in G} e^{-hE_g}}{Z} \times \ln \frac{\left[Z_1^\partial(g) + Z_1^{\partial, \text{twisted}}(g) \right] \left[Z_4^\partial(g) + Z_4^{\partial, \text{twisted}}(g) \right]}{Z_2^\partial(g) Z_3^\partial(g)} \right\}. \quad (7.21)$$

Here $Z_2^\partial(g)$ and $Z_3^\partial(g)$ represent the partition functions of an Ising model with nearest-neighbor interactions of reduced strength $J/T = h$, and with

⁴This raises the question of whether there are better measures of the long-range entanglement of topological phases.

fixed spins along the boundary of bipartitions 2 and 3, respectively. Likewise, $Z_{1,4}^\partial(g)$ are analogous partition functions for bipartitions 1 and 4, respectively. Note that the boundaries in bipartitions 1 and 4 have two disconnected components, labeled ‘boundary 1’ and ‘boundary 2’ in Fig. 7.5. The partition functions $Z_{1,4}^{\partial,\text{twisted}}(g)$ differ from $Z_{1,4}^\partial(g)$ in that all the (fixed) spins belonging to boundary 2 in bipartitions 1 and 4 have been flipped, respectively.

The sum over g in Eq. (7.21) acts as a weighed average of the logarithmic term over all possible values of the spins at the boundary. Notice that the partitions with two boundaries, and hence with non-trivial topology, are those that appear with two contributions (bipartitions 1 and 4), corresponding to the sum of each boundary condition with its twisted counterpart.

In the topological phase (i.e., in the disordered phase of the corresponding Ising model), where correlations are short ranged, the choice of boundary conditions affects the partition function of the system only with exponentially small corrections. Thus, we can expect to have $Z_1^\partial(g)Z_4^\partial(g) \simeq Z_1^{\partial,\text{twisted}}(g)Z_4^\partial(g) \simeq \dots \simeq Z_2^\partial(g)Z_3^\partial(g)$ and the topological entropy becomes $S_{\text{topo}} = \ln 4$. On the other hand, in the polarized paramagnetic phase (i.e., in the ferromagnetically ordered phase of the Ising model) the partition function of a system with twisted boundary conditions is exponentially suppressed with respect to the one without the twist. Thus, $Z_1^\partial(g) \gg Z_1^{\partial,\text{twisted}}(g)$, $Z_4^\partial(g) \gg Z_4^{\partial,\text{twisted}}(g)$, while $Z_1^\partial(g)Z_4^\partial(g) \simeq Z_2^\partial(g)Z_3^\partial(g)$ still holds. This leads to $S_{\text{topo}} = 0$.

Using a high-temperature expansion for $h < h_c$, and appropriate Ising duality relations for $h > h_c$, one can show that the behavior of the topological entropy across the transition is *discontinuous*, with a sudden jump from $S_{\text{topo}} = \ln 4$ to $S_{\text{topo}} = 0$ at h_c , in spite of the otherwise continuous nature of the transition [7]. This discontinuity of the topological entropy is probably less surprising if one keeps in mind that the topological entropy is inherently linked to the quantum dimensions of the elementary excitations of a phase [18, 19], and thus it must remain constant for the full extent of the phase.⁵

7.3 Thermal Transitions

Our discussion so far was from a purely zero temperature perspective of phase transitions involving topologically ordered phases. In conventional QPTs, where a local order parameter acquires a non-vanishing expectation value, the zero-temperature QCP controls an extended portion of the finite temperature phase diagram, called the *quantum critical region* or quantum critical fan. One thus wonders to what extent a similar behavior can be expected to hold

⁵ A similar behavior of the topological entropy has been found in numerical simulations [23] of the Hamiltonian deformation discussed in Sec. 7.2.1.

for QPTs involving topological phases of matter. To address this question, we first discuss a framework to measure and characterize topological order at finite temperature, using both non-local correlators and a generalization of the topological entropy. This will further allow us to discuss when topological order survives in the presence of thermal fluctuations, and under what conditions one can expect to observe a *finite-temperature* phase transition.

7.3.1 Non-local Order Parameters at Finite Temperature

At zero temperature we can typically characterize topological order by non-local order parameters, for instance the winding loop operators in the toric code [2]. If we want to use the same order parameters at *finite* temperature, one needs to carefully consider the role of defects, e.g., a flipped spin occurring along the path of a winding loop operator, which changes its expectation value. In a topological phase with excitation gap Δ , a finite temperature T induces a finite density $\rho \sim e^{-\Delta/T}$ of defects. Our ability to detect the topological phase using loop operators relies on the ability to find loops that do not encounter any thermal defects along their path. However, the probability for the occurrence of such unaffected loops scales as $(1 - \rho)^\ell$, where ℓ is the total length of the loop. For winding loops with $\ell \geq L$, where L is the linear size of the system, this probability vanishes exponentially fast in the thermodynamic limit – irrespective of how low the temperature is. This phenomenon was first discussed in the context of topological phases in Ref. [24] and termed *thermal fragility*.⁶ This is quite distinct from conventionally ordered phases, where the thermal uncertainty in the expectation value of a local order parameter scales with the density of defects and becomes negligibly small at low temperature.

Note that this thermal fragility of non-local order parameters cannot directly be equated to a thermal instability of the topological phase. The latter is determined by the nature of the anyonic defects and stable topological phases at finite temperature are indeed possible [26], as captured by the behavior of the topological entropy of the system [27].

For a *finite* system one can nevertheless define a *crossover temperature* T^* . The free energy of a pair of defects, each with gap Δ , is $F = 2\Delta - T \ln N(N-1) \sim 2\Delta - 2T \ln N$. Above a temperature $T^* = \Delta / \ln N$ we always encounter excitations, but for $T \ll T^* \sim 1 / \ln N$ the system is protected. This logarithmic reduction of the gap scale is not a major technological problem for potential devices built on such phases that might operate on system sizes $N \sim 100$. However, it is an interesting and important aspect when discussing topological stability.

⁶The reader familiar with the connection between toric code and \mathbb{Z}_2 lattice gauge theory may recognize that this statement follows from the property that the expectation value of Wilson loop operators always vanishes in the limit of infinite loop size [25].

7.3.2 Topological Entropy at Finite Temperature

To characterize the stability of a topological phase at finite temperature we now turn to topological entropy. While entanglement entropies are often considered zero-temperature quantities, we can readily generalize their definition in terms of the density matrix to finite temperature by simply considering $\rho(T) = \exp(-\beta H)/\text{Tr}[\exp(-\beta H)]$, where H is the Hamiltonian and $\beta = 1/k_B T$.

Computing the so-generalized topological entropy S_{topo} at finite temperature often turns out to be a significant challenge, even for state of the art numerical techniques [20]. On the other hand, some instances such as the toric code model are simple enough to allow for a rigorous calculation as a function of both system size and temperature [27–29], as we briefly discuss in the following.

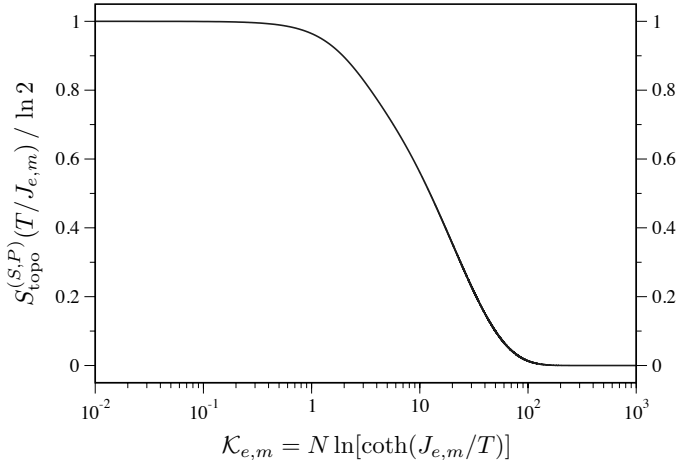
In the toric code Hamiltonian (7.1) we have seen that plaquette (P) and star (S) operators commute with one another. When calculating the finite-temperature generalizations of the entanglement and topological entropies, the resulting expressions are additive in these two contributions:

$$S(\mathcal{A}; T) = S^{(P)}(\mathcal{A}; T/J_m) + S^{(S)}(\mathcal{A}; T/J_e). \quad (7.22)$$

Therefore, vortex defects, i.e., plaquette operators with negative eigenvalues, are immaterial to the star contribution and vice versa. As a consequence, one can conveniently consider the two contributions separately. Moreover, the system is symmetric upon exchanging x with z spin components, and plaquettes with stars. The two contributions $S^{(P)}$ and $S^{(S)}$ can thus be cast in the exact same analytical form.

Deriving the explicit expressions for $S_{\text{topo}}^{(P)}(T/J_m)$ and $S_{\text{topo}}^{(S)}(T/J_e)$ as a function of temperature and system size N is a rather cumbersome exercise and we refer to Ref. [28] for a detailed description. In both cases temperature and system size enter these expressions through the product $\mathcal{K}_{e,m} = N \ln[\coth(J_{e,m}/T)]$, respectively. Hence, the thermodynamic limit, $N \rightarrow \infty$, and the zero temperature limit, $T \rightarrow 0$, do not commute. The zero-temperature value of the topological entropy, $S_{\text{topo}} = \ln 4$, is recovered *only* if the temperature is lowered to zero whilst keeping the system size finite. Vice versa, in the thermodynamic limit the topological entropy vanishes at any finite T , no matter how small.

In Fig. 7.6 we plot the analytical expressions for the topological entropies $S_{\text{topo}}^{(P)}(T/J_m)$ and $S_{\text{topo}}^{(S)}(T/J_e)$ as a function of $\mathcal{K}_{e,m}$. For a fixed system size N , the plotted behavior indicates that the topological entropy decays to zero at a finite temperature. With $T \ll J_{e,m}$ we can expand $N \ln[\coth(J_{e,m}/T)] \sim 2N \exp(-2J_{e,m}/T)$, where the exponential corresponds to the Boltzmann weight for a single spin flip to occur in the ground state of the system, i.e., the density of defects. The decay in Fig. 7.6 occurs when $N \exp(-2J_{e,m}/T) \sim 1$, that is when the average *number* of defect pairs in the system is of order unity. This translates into a crossover temperature

**FIGURE 7.6**

Finite-temperature topological entropy of the toric code. $S_{\text{topo}}^{(S,P)}(T/J_{e,m})$ as a function of $K_{e,m} = N \ln[\coth(J_{e,m}/T)]$.

$T^* \sim 2J_{e,m}/\ln N$, in agreement with the behavior of the non-local order parameters discussed earlier.

7.3.3 Fragile vs. Robust Behavior: A Matter of (De)confinement

The results in Secs. 7.3.1 and 7.3.2 show that the topological order in the 2D toric code is truly fragile to thermal fluctuations, in the sense that it is destroyed by a finite number of defects. In the thermodynamic limit there is no finite-temperature phase transition.

From the behavior of the non-local operators one might mistakenly conclude that this fragility to thermal fluctuations is intrinsic to topological order [24]. On the other hand, we can compare this to the well-known example of a classical Z_2 lattice gauge theory in three dimensions [3, 30], which also lacks a local order parameter in the zero temperature limit. There, the $T = 0$ state does not subside immediately to thermal fluctuations, and a finite temperature phase transition exists between a low-temperature phase with confined defects, and a high-temperature phase where the defects are deconfined (see also Sec. 7.2.1). Whereas non-local operators, such as Wilson loops around the whole system, vanish in both phases in the thermodynamic limit, the finite temperature phase transition is ultimately captured by the way that the winding loop expectation values vanish as the system size is increased. This is the area vs. perimeter law [25].

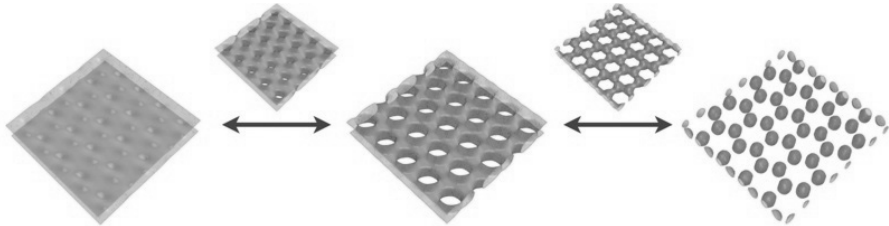
Key to the existence of a finite-temperature phase transition in the Z_2

lattice gauge theory is the confined nature of the thermal excitations in the low-temperature phase. Consistently, the deconfined nature of the defects in the topological phase of the toric code in two dimensions leads to the observed fragile behavior at finite temperature. If, on the other hand, we can devise a model where the excitations are confined, then we might expect a qualitatively different behavior. One example of the latter is the 3D generalization of the toric code [31]. In this model, plaquette and star operators are no longer dual to each other. While the star defects give rise to point-like excitations, much like in the 2D case, plaquette defects become objects which define closed loops, through plaquettes where the stabilizer condition of the ground states is violated. The energy cost of such loops scales with their length. As a consequence, plaquette defects do not fractionalize, but rather form confined structures whose characteristic size is controlled by temperature [26]. This low-temperature phase with confined plaquette excitations is therefore stable to thermal fluctuations resulting in a finite-temperature continuous phase transition at $T_c/J_{m,e} \simeq 1.313346(3)$ [27]. While the star contribution to the topological entropy exhibits a fragile behavior, just as in the 2D case, the plaquette contribution survives unaltered up to the finite-temperature phase transition [27].

These results illustrate that the robustness of a zero-temperature topological phase depends crucially on the confined versus deconfined nature of the thermal excitations. Only if *all* excitations are confined, we expect quantum topological order to survive up to a finite temperature phase transition [26].

7.4 Outlook

In this chapter we discussed phase transitions involving topologically ordered phases of matter in deformations of the toric code model. We focused on continuous QCPs where appropriate local correlators exhibit a divergent behavior. We showed that the growing correlations characterizing the critical region can be understood in terms of dual degrees of freedom. In this dual language, the system undergoes a conventional QPT between a disordered phase, corresponding to the topologically ordered one in the original system, and an ordered phase characterized by a local order parameter in the dual degrees of freedom. While the underlying topological order is typically invisible in the dual picture, the topological degeneracy can be mapped out by the many-to-one correspondence in the definition of the dual degrees of freedom (see in particular the discussion in Sec. 7.2.2.2 and Ref. [32]). Indeed, while the disruption of topological order across the transition occurs because of the conventional phase transition in the underlying dual system, topological order survives unaffected up to the critical point, as witnessed for instance by the step-function behavior of the topological entropy, irrespective of the

**FIGURE 7.7**

Topology driven QPT. Two-dimensional surfaces with different topologies that are populated by anyonic quantum liquids. A QPT driven by fluctuations of the surface topology connects the anyonic liquid with topological order on two separated sheets (on the left) and the anyonic liquid without topological order on decoupled spheres (on the right).

continuous vs first-order nature of the transition (see Sec. 7.2.1.1). The two phenomena – the change in topological properties and the underlying conventional phase transition – appear to be essentially unrelated in nature.

One is then left to wonder whether it would be possible for a perturbation to cause topological order to subside or change without a signature in any local correlators. Such transitions could take place either between topologically ordered phases, or between a topologically ordered phase and a conventional paramagnet, somewhat akin to a glass transition in classical systems. Contrary to the examples considered in this chapter, these transitions would be detected *exclusively* by non-local observables. Or, is it the case that even when there is no local order parameter on either side of the transition, whether in the original or dual degrees of freedom, there must generically be a detectable singularity in sufficiently high order derivatives of some local observables? One approach that does not require any *a priori* knowledge of an order parameter, and which has been argued to detect any singularities in local observables, has recently been proposed by Zanardi *et al.* based on the information theoretic concept of fidelity [33].⁷ However, it remains to be seen whether fidelity-based techniques can be applied in systems where more conventional approaches fail.

Another open question is whether the usual picture of a fan-like quantum critical region in the finite temperature phase diagram above a QCP [35] also applies to QPTs involving topological order. Does such a fan exist only in the presence of local order parameters, either in the system at hand or a dual description, as was the case for the toric code and its dual description in terms of an Ising model? Or does a similar phenomenon appear at all continuous QPTs out of topological phases? A first attempt at addressing this question

⁷Examples of fidelity-based approaches to characterize QPTs involving topologically ordered phases of matter can be found for instance in Refs. [23, 34].

was recently made by Chung *et al.* in Ref. [36], where a QPT separating an Abelian from a non-Abelian topological phase was investigated in the context of an exactly solvable chiral spin liquid model. What Chung *et al.* showed is how non-local order parameters can be used to define a crossover temperature T^* – akin to the one discussed in Sec. 7.3.1 – which thereby allows us to define a temperature region reminiscent of the quantum critical fan in systems with local order parameters. However, the precise nature of this region, and whether its physics is as rich as for conventional QPTs, remains an open question.

More generally, we still need to identify a unifying theoretical framework that allows us to describe topological phases and their phase transitions, akin to the Landau-Ginzburg-Wilson theory for conventional QPTs. A step towards such a general description was taken in Ref. [37], where the field-driven QPT in the toric code model was described in terms of a mutual Chern-Simons Landau-Ginzburg theory. However, a generalization of this approach to non-Abelian phases is non-trivial.

A unifying framework to describe QPTs for both Abelian and non-Abelian topological phases has recently been proposed by some of us by considering a general description in terms of quantum double models [38]. An Abelian or non-Abelian topological phase in a time-reversal invariant quantum lattice model, such as the toric code or the Levin-Wen model [39], can be constructed from *chiral* topological quantum liquids populating the closed surface geometry obtained by fattening the edges of the lattice model, as illustrated for a honeycomb lattice in the middle panel of Fig. 7.7. In this picture the QPT going from a topologically ordered phase to a topologically trivial paramagnetic state corresponds to the transition between different surface topologies as shown in Fig. 7.7. The topological phase corresponds to the limit of two sheets illustrated on the left, while the paramagnet corresponds to the limit of decoupled spheres illustrated on the right. Plaquette flux excitations in the lattice model correspond to wormholes in the quantum double model connecting the two sheets. Independent of their braiding statistics, it is the proliferation of these wormholes that drives a QPT between the two extremal states. The critical point between the topological and trivial phases is then described by a quantum foam where the *surface topology fluctuates* on all length scales. This concept of a topology-driven QPT thereby provides a general framework that describes the quantum critical behavior of time-reversal invariant systems exhibiting topological order.

Acknowledgments – S.T. and M.T. thank the Aspen Center for Physics for hospitality. C.C.’s work was supported by the EPSRC Grant No. GR/R83712/01 and by the EPSRC Postdoctoral Research Fellowship EP/G049394/1. We thank E. Ardonne, C. Chamon, E.-A. Kim, and A. W. W. Ludwig for carefully reading the manuscript. C.C. is particularly grateful to C. Chamon for stimulating discussions which led to some of the ideas presented in the Outlook section.

Bibliography

- [1] X.-G. Wen, Phys. Rev. B **40**, 7387 (1989).
- [2] A. Y. Kitaev, Ann. Phys. (N.Y.) **303**, 2 (2003).
- [3] J. B. Kogut, Rev. Mod. Phys. **51**, 659 (1979).
- [4] S. Trebst, P. Werner, M. Troyer, K. Shtengel, and C. Nayak, Phys. Rev. Lett. **98**, 070602 (2007).
- [5] I. S. Tupitsyn, A. Kitaev, N. V. Prokof'ev, P. C. E. Stamp, arXiv:0804.3175 (2008).
- [6] J. Vidal, S. Dusuel, K. P. Schmidt, Phys. Rev. B **79**, 033109 (2009).
- [7] C. Castelnovo and C. Chamon, Phys. Rev. B **77**, 054433 (2008).
- [8] S. Papanikolaou, K. S. Raman, and E. Fradkin, Phys. Rev. B **76**, 224421 (2007).
- [9] E. Ardonne, P. Fendley, and E. Fradkin, Ann. Phys. (N.Y.) **310**, 493 (2004).
- [10] E. Fradkin and S. Shenker, Phys. Rev. D **19**, 3682 (1979).
- [11] H. W. J. Blöte and Y. Deng, Phys. Rev. E **66**, 066110 (2002).
- [12] J. Vidal, R. Thomale, K. P. Schmidt, S. Dusuel, Phys. Rev. B **80**, 081104 (2009).
- [13] D. Rokhsar and S. Kivelson, Phys. Rev. Lett. **61**, 2376 (1988).
- [14] C. L. Henley, J. Phys.: Condens. Matter **16**, S891 (2004).
- [15] C. L. Henley, J. Stat. Phys. **89**, 483 (1997).
- [16] C. Castelnovo, C. Chamon, C. Mudry, and P. Pujol, Ann. Phys. (N.Y.) **318**, 316 (2005).
- [17] A. Hamma, R. Ionicioiu, and P. Zanardi, Phys. Rev. A **71**, 022315 (2005); Phys. Lett. A **337**, 22 (2005).
- [18] M. Levin and X.-G. Wen, Phys. Rev. Lett. **96**, 110405 (2006).
- [19] A. Y. Kitaev, and J. Preskill, Phys. Rev. Lett. **96**, 110404 (2006).
- [20] S. Furukawa and G. Misguich, Phys. Rev. B **75**, 214407 (2007).
- [21] E. Fradkin and J. E. Moore, Phys. Rev. Lett. **97**, 050404 (2006).

- [22] J.-M. Stéphan, S. Furukawa, G. Misguich, and V. Pasquier, Phys. Rev. B **80**, 184421 (2009).
- [23] A. Hamma, W. Zhang, S. Haas, and D. A. Lidar, Phys. Rev. B **77**, 155111 (2008).
- [24] Z. Nussinov and G. Ortiz, PNAS **106**, 16944 (2009); Ann. Phys. (N.Y.) **324**, 977 (2009).
- [25] F. J. Wegner, J. Math. Phys. **12**, 2259 (1971).
- [26] E. Dennis, A. Kitaev, A. Landahl, and J. Preskill, J. Math. Phys. **43**, 4452 (2002).
- [27] C. Castelnovo and C. Chamon, Phys. Rev. B **78**, 155120 (2008).
- [28] C. Castelnovo and C. Chamon, Phys. Rev. B **76**, 184442 (2007).
- [29] C. Castelnovo and C. Chamon, Phys. Rev. B **76**, 174416 (2007).
- [30] K. G. Wilson, Phys. Rev. D **10**, 2445 (1974); R. Balian, J. M. Drouffe, and C. Itzykson, Phys. Rev. D **11**, 2098 (1975); E. Fradkin and L. Susskind, Phys. Rev. D **17**, 2637 (1978); E. Fradkin and S. Raby, Phys. Rev. D **20**, 2566 (1979); L. Susskind, Phys. Rev. D **20**, 2610 (1979).
- [31] A. Hamma, P. Zanardi, and X.-G. Wen, Phys. Rev. B **72**, 035307 (2005).
- [32] X-Y. Feng, G.-M. Zhang, and T. Xiang, Phys. Rev. Lett. **98**, 087204 (2007).
- [33] P. Zanardi, L. Campos Venuti, and P. Giorda, Phys. Rev. A **76**, 062318 (2007), and references therein.
- [34] E. Eriksson and H. Johannesson, Phys. Rev. A. **79**, 060301(R) (2009).
- [35] S. Chakravarty, B. I. Halperin, and D. R. Nelson, Phys. Rev. B **39**, 2344 (1989).
- [36] S. B. Chung, H. Yao, T. L. Hughes, and E.-A. Kim, Phys. Rev. B **81**, 060403(R) (2010).
- [37] S. P. Kou, J. Yu, and X.G. Wen, Phys. Rev. B **80**, 125101 (2009).
- [38] C. Gils, S. Trebst, A. Kitaev, A. W. W. Ludwig, M. Troyer, and Z. Wang, Nature Physics **5**, 834, (2009).
- [39] M. Levin and X.-G. Wen, Phys. Rev. B **71**, 045110 (2005).

8

Quantum Criticality and the Kondo Lattice

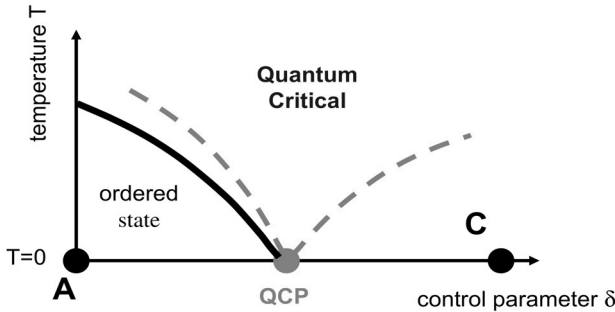
Qimiao Si

*Department of Physics & Astronomy, Rice University, Houston, TX 77005,
U.S.A.*

Quantum phase transitions (QPTs) arise as a result of competing interactions in a quantum many-body system. Kondo lattice models, containing a lattice of localized magnetic moments and a band of conduction electrons, naturally feature such competing interactions. A Ruderman-Kittel-Kasuya-Yosida (RKKY) exchange interaction among the local moments promotes magnetic ordering.¹ However, a Kondo exchange interaction between the local moments and conduction electrons favors the Kondo-screened singlet ground state.

This chapter summarizes the basic physics of QPTs in antiferromagnetic Kondo lattice systems. Two types of quantum critical points (QCPs) are considered. Spin-density-wave quantum criticality occurs at a conventional type of QCP, which invokes only the fluctuations of the antiferromagnetic order parameter. Local quantum criticality describes a new type of QCP, which goes beyond the Landau paradigm and involves a breakdown of the Kondo effect. This critical Kondo breakdown effect leads to non-Fermi liquid electronic excitations, which are part of the critical excitation spectrum and are in addition to the fluctuations of the magnetic order parameter. Across such a QCP, there is a sudden collapse of the Fermi surface from large to small. I close with a brief summary of relevant experiments, and outline a number of outstanding issues, including the global phase diagram.

¹An RKKY exchange interaction between two local moments originates from the interaction each local moment has with a same conduction-electron band. It is generated through the propagation of the conduction electrons.

**FIGURE 8.1**

Phase diagram of the transverse-field Ising model. δ is a non-thermal control parameter, which tunes quantum fluctuations. The solid curve denotes phase transitions into the ordered state, and the corresponding transition temperature approaches zero as δ is tuned towards the QCP. At non-zero temperatures, a quantum-critical regime arises; the dashed curves describe the crossovers into and out of this regime.

8.1 Introduction

8.1.1 Quantum Criticality: Competing Interactions in Many-Body Systems

Quantum criticality describes the collective fluctuations associated with a second order phase transition at zero temperature. It occurs in many-body systems as a result of competing interactions that foster different ground states. An example is the transverse-field Ising model:

$$H = -I \sum_{\langle ij \rangle} \sigma_i^z \sigma_j^z - h_t \sum_i \sigma_i^x - h \sum_i \sigma_i^z. \quad (8.1)$$

Here σ_i^z and σ_i^x denote the z - and x -components of a localized spin-1/2 magnetic moment at site i , I is the Ising exchange interaction between the z -components of nearest-neighbor spins, and h_t is an external magnetic field applied along the transverse x -direction with $g\mu_B$ set to 1. In order to probe the spontaneous symmetry breaking, a longitudinal field h is also introduced which will be set to 0^+ at the end of calculation. In one spatial dimension, this model can be exactly solved through a Jordan-Wigner transformation [1].

The I and h_t terms represent competing interactions of the system. Their competition can be parametrized in terms of a dimensionless quantity, $\delta \equiv h_t/I$. We consider the model in the $T - \delta$ phase diagram, Fig. 8.1, starting from the readily solvable points A and C . Point A corresponds to $T = 0$ and a vanishing transverse field, $\delta = 0$, where we want to minimize the exchange

energy. The ground state is $\Pi_i |\uparrow\rangle_i$, with all the spins lined up along the positive z direction. It spontaneously breaks a global Z_2 symmetry: under the operation $\sigma_i^z \rightarrow -\sigma_i^z$, for every site i , the ground state is changed even though the Hamiltonian is invariant for $h = 0$. The macroscopic order is described by Landau's order parameter, defined as

$$\phi \equiv \lim_{h \rightarrow 0^+} \lim_{N_{\text{site}} \rightarrow \infty} M/N_{\text{site}}, \quad (8.2)$$

where $M = \langle \sum_i \sigma_i^z \rangle$ and $N_{\text{site}} = \sum_i$. We reach an important conclusion that

$$\phi = 1, \quad \text{at point A.} \quad (8.3)$$

Point C is also at $T = 0$ but has $\delta \gg 1$. Since the transverse field is the largest coupling ($h_t \gg I$), the system minimizes the internal energy by lining up all the spins along the positive x direction. The ground state is $\Pi_i |\rightarrow\rangle_i$. At each site, $|\rightarrow\rangle = (|\uparrow\rangle + |\downarrow\rangle)/\sqrt{2}$ maximizes the tunneling between the spin up and spin down states. These two spin states have an equal probability, and the order parameter vanishes:

$$\phi = 0, \quad \text{at point C.} \quad (8.4)$$

When we tune the non-thermal control parameter δ from point A to point C, we can expect at least one phase transition separating the magnetically ordered ($\phi \neq 0$) and disordered ($\phi = 0$) states.

In the absence of the transverse field, the Hamiltonian involves only σ_i^z , which all commute with each other. In the presence of the transverse field, σ_i^x also appears in the Hamiltonian, which now contains variables that do not commute with each other; the system becomes quantum-mechanical. Varying δ amounts to tuning the degree of quantum tunneling or, equivalently, the degree to which the zero-point motion is manifested in the many-body properties. This is referred to as tuning the degree of *quantum fluctuations*.

[Fig. 8.1](#) illustrates the $T - \delta$ phase diagram of the model in dimensions higher than one. In one dimension, the line of the finite-temperature phase transitions collapses to the zero-temperature line, in accordance with the Mermin-Wagner theorem. Importantly, the zero-temperature transition is continuous, with the $T = 0$ order parameter ϕ smoothly going to zero as the control parameter δ is increased to δ_c , the QCP. In common with its classical counterpart at non-zero temperatures, a QCP features critical fluctuations. These collective fluctuations are responsible for non-analyticities in the free energy as a function of δ and other parameters.

Historically, the first example in which such QCPs were formulated in the modern language of critical phenomenon is the case of metallic paramagnets undergoing a second-order phase transition at zero temperature into a Stoner ferromagnet or spin-density-wave (SDW) antiferromagnet. Microscopically, Hertz [2] modeled this transition with a one-band Hubbard model. The Coulomb repulsion among the electrons favors magnetic ordering, and

the electrons' kinetic energy induces paramagnetism. The result is an itinerant magnetic QCP or, in the case of antiferromagnetic (AF) order, an SDW QCP. Hertz constructed an effective field theory for the fluctuations of the order parameter, ϕ , in both space (\mathbf{x}) and imaginary time (τ). The result is a quantum Ginzburg-Landau action,

$$\mathcal{S} = \int d\mathbf{q} \frac{1}{\beta} \sum_{i\omega_n} (r + c\mathbf{q}^2 + |\omega_n|/\Gamma_{\mathbf{q}}) \phi^2 + \int u \phi^4 + \dots \quad (8.5)$$

The effective dimension of the fluctuations is $d + z$, where d is the spatial dimension and z , the dynamic exponent, counts the effective number of extra spatial dimensions that the temporal fluctuations correspond to. In Eq. (8.5), the quadratic part is expressed in terms of wavevector \mathbf{q} and Matsubara frequency ω_n , which are reciprocal to \mathbf{x} and τ , respectively. At non-zero temperatures, this action gives rise to a quantum-critical regime [3–6], whose physical properties are controlled by the many-body excitations of the system's ground state at the QCP.

What underlies the Hertz description is the Landau notion that fluctuations of the order parameter are the only critical degrees of freedom. Order parameters, as we encounter here, are classical variables. However, theoretical developments on QCPs of heavy fermion metals [7,8] and insulating quantum magnets [9] have shown that this is not the only possibility. Instead, inherent quantum modes can emerge as part of the critical degrees of freedom. Identifying these additional modes is nontrivial, as the Landau paradigm of doing so using symmetry-breaking patterns can no longer be used. This task must be completed before the critical field theory can be constructed.

8.1.2 Heavy Fermion Metals

Heavy fermion metals refer to rare-earth- or actinide-based intermetallic compounds in which the effective mass of the electronic excitations is hundreds of times the bare electron mass. They typically arise in compounds including Ce, Yb, and U that contain partially-filled $4f$ or $5f$ orbitals. The large effective mass originates from strong electron correlation, i.e., a large ratio of the on-site Coulomb repulsive interaction to the kinetic energy. Among the outer-shell orbitals of a rare-earth or actinide ion, the f -orbitals are closer to the origin. Correspondingly, the average distance among the f -electrons occupying the same site is relatively short, leading to the enhanced Coulomb interaction.

Microscopically, we have a narrow f -electron band coupled to some wider conduction-electron bands through a finite hybridization matrix [10]. In many compounds, the f -electrons are so strongly correlated that their valence occupation stays at an integer value. This would be one $4f$ -electron for Ce-based compounds, and thirteen $4f$ -electrons, or, equivalently, one $4f$ -hole, for Yb-based compounds. This integer-valency can be thought of in terms of the f -electron band being in its Mott-insulating state, representing an example of

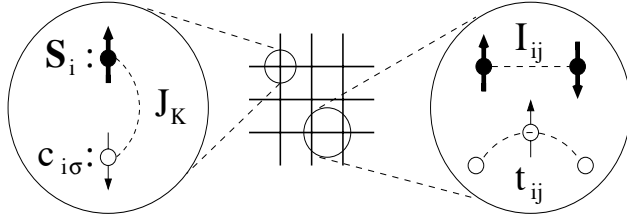


FIGURE 8.2

The Kondo lattice model. At each site of the lattice, there are two types of microscopic degrees of freedom: a spin-1/2 local moment \mathbf{S}_i and a conduction electron $c_{i\sigma}$, which are coupled to each other through an antiferromagnetic Kondo exchange interaction, J_K . The local moments interact with each other through a pair-wise exchange interaction I_{ij} . The conduction electrons have a tight-binding hopping matrix t_{ij} .

the *orbitally-selective Mott insulator*. At energies much smaller than the gap of this orbitally-selective Mott insulator, the f -electrons no longer possess charge fluctuations and behave as localized magnetic moments.

What results is a Kondo lattice Hamiltonian, illustrated in Fig. 8.2. It contains a lattice of local moments and, for simplicity, band of conduction electrons. The local moments interact with each other through the RKKY exchange coupling, and they interact with the conduction electrons via an AF Kondo exchange coupling. The fact that these interactions are much smaller than the orbitally-selective Mott insulating gap is an important feature of the Kondo lattice model. This separation of energy scales allows the local moments to be easily observable, as it gives rise to an extended temperature window over which the local moments are manifested in a Curie-Weiss form for the bulk spin susceptibility.

The central microscopic question is how these local moments interplay with the conduction-electron bands. The early 1980s saw extensive studies of this problem, which were built upon the historical work on the single-impurity Kondo effect. These studies showed how Kondo singlets are formed in the ground state, and how such Kondo screening gives rise to Kondo resonances in the excitation spectrum. The resonances are spin-1/2 and charge excitations, and they combine with conduction electrons to form the heavy quasi-particles. This is the picture of the *heavy Fermi liquid* [10]. Because of the large effective mass, Fermi-liquid effects become amplified. The sentiment was that heavy fermion metals represent a prototype system for Landau's Fermi liquid theory of charged fermions in the presence of a lattice.

That RKKY interactions and Kondo interactions compete against each other was already recognized early on [11, 12]. However, the Fermi liquid theory of the paramagnetic heavy-fermion systems was considered to be so successful that the magnetic order was mostly considered as a descendant of a

heavy Fermi liquid. In this picture, an antiferromagnetically ordered heavy fermion metal arises from an RKKY-interaction-induced SDW instability of the heavy quasi-particles near their Fermi surface. Likewise, heavy-fermion superconductors are considered in terms of the Cooper-pairing instability of the same quasi-particles.

8.1.3 Quantum Critical Point in Antiferromagnetic Heavy Fermions

The field of heavy fermions was interrupted by the discovery and extensive studies of high temperature cuprate superconductivity. When the field re-emerged in full force, the focus was changed in an important way. It was recognized that heavy fermion metals represent an important testing ground for the breakdown of Fermi liquid theory in general [13], and the nature of QCPs in particular.

Over the past decade, magnetic heavy fermion metals have become a prototype setting to realize and explore QCPs. The list of quantum critical heavy fermion metals is by now relatively long, and the readers are referred to some more comprehensive reviews [14,15] and Chap. 18 for a more extensive discussion on the materials and experimental aspects. The most prominent examples are $\text{CeCu}_{6-x}\text{Au}_x$, YbRh_2Si_2 , CePd_2Si_2 , and CeRhIn_5 . Quantum criticality is being explored in many condensed matter systems. Arguably, heavy fermion QCPs have been the most systematically studied, because such QCPs have been explicitly identified in a number of available materials.

One of the first hints about the failure of the order-parameter-fluctuation picture for quantum criticality came from inelastic neutron-scattering measurements [16] in $\text{CeCu}_{6-x}\text{Au}_x$. The inelastic neutron scattering cross section measures the dynamical spin susceptibility, $\chi(\mathbf{q}, \omega, T)$. For $\mathbf{q} = \mathbf{Q}$, $\chi(\mathbf{Q}, \omega, T) \propto 1/(-i\omega)^\alpha$ at $\omega \gg T$, with a non-mean-field exponent $\alpha \approx 0.75$. The static susceptibility goes as $\chi(\mathbf{q}, \omega = 0) \propto 1/(\Theta_{\mathbf{q}} + aT^\alpha)$, with the same exponent α as seen in $\chi''(\mathbf{Q}, \omega, T)$, and with a Weiss temperature $\Theta_{\mathbf{q}}$ which goes to zero as \mathbf{q} approaches \mathbf{Q} . Finally, $\chi(\mathbf{Q}, \omega)$ satisfies ω/T scaling. In contrast, the SDW QCP has a dynamic exponent $z = 2$, and an effective dimensionality of the order-parameter fluctuations $d + z \geq 4$ for $d=2,3$. The critical theory, Eq. (8.5), describes a Gaussian fixed point. The critical exponents are expected to take the mean-field value $\alpha = 1$. Moreover, the non-linear interactions that give rise to spin damping must vanish. In other words, the effective interaction $u(T) \sim T^\theta$, with $\theta > 0$, and hence the damping rate scale as $\Gamma(T) \sim T^{1+\theta}$. Frequency appears with temperature in the combination $\omega/\Gamma(T)$, resulting in a violation of ω/T scaling.²

To search for new kinds of QCPs, the question is what types of new quantum critical modes emerge. For heavy fermion metals, these modes are charac-

²This persists even when the effect of non-analytic corrections, which arise in the process of integrating out the fermions [17,18], is taken into account.

terized by a critical Kondo breakdown [7,8]. The notion is that, at the boundary of the AF order, the amplitude of the Kondo entanglement³ is severely reduced or even completely suppressed. A critical suppression of this singlet amplitude yields new types of critical modes, which drastically modify the critical behavior of the spin dynamics, among other physical properties.

The remainder of the chapter is organized as follows. In Sec. 8.2, we describe the paramagnetic heavy Fermi liquid state of the Kondo lattice. Our emphasis is the Kondo singlet formation, and the ensuing development of a large Fermi surface. Section 8.3 is devoted to the nature of QCPs, with an emphasis on the Kondo breakdown as it appears in the local quantum criticality. In Sec. 8.4, we will study the antiferromagnetically ordered part of the phase diagram, showing that antiferromagnetism can destroy the Kondo effect and yield a small Fermi surface. Section 8.5 considers the global phase diagram. In Sec. 8.6, we briefly summarize the relevant experiments. Some directions for future work are outlined in Section 8.7. The second half of the chapter in part overlaps with Ref. [19], to which I refer for a more complete set of references.

8.2 Heavy Fermi Liquid of Kondo Lattices

8.2.1 Single-Impurity Kondo Model

To introduce the Kondo effect, we follow the historical route and first consider the single-impurity Kondo model. It describes a local moment, \mathbf{S} , interacting with a band of conduction electrons, $c_{\mathbf{k}\sigma}$:

$$H_{\text{Kondo}} = \sum_{\mathbf{k}} \varepsilon_{\mathbf{k}} c_{\mathbf{k}\sigma}^\dagger c_{\mathbf{k}\sigma} + J_K \mathbf{S} \cdot \mathbf{s}_{c,0}. \quad (8.6)$$

Here, $\mathbf{s}_{c,0} = (1/2)c_0^\dagger \vec{\sigma} c_0$ is the spin of the conduction electrons at the impurity site, $\mathbf{x} = 0$, where $\vec{\sigma}$ denote the Pauli matrices and $\varepsilon_{\mathbf{k}}$ is the energy dispersion of the conduction electrons. It is important that the Kondo coupling, $J_K > 0$, is antiferromagnetic.

To address the effect of Kondo coupling, J_K , we ask what its scaling dimension is. This is in the spirit of perturbatively treating the J_K coupling, and the reference point of our analysis corresponds to a free spin and a free band of conduction electrons. Recognizing that the autocorrelator of a free spin is a constant, we have the scaling dimension $[\mathbf{S}] = 0$. Also, for free conduction electrons, the autocorrelator of $\mathbf{s}_{0,c}$ go as $1/\tau^2$, so $[\mathbf{s}_{0,c}] = [1/\tau]$. Correspondingly, $\int d\tau \mathbf{S}(\tau) \cdot \mathbf{s}_{0,c}(\tau)$ has a scaling dimension 0, and J_K is marginal in the renormalization group (RG) sense. A well-known loop-correction calculation [10]

³That is, the strength of the spin singlet formed between the local moments and conduction electrons; see also Eq.(8.8) below.

shows that, at the one loop order, the RG beta function is

$$\beta(J_K) = J_K^2. \quad (8.7)$$

In other words, the AF Kondo coupling is marginally relevant.

The Kondo coupling renormalizes towards strong coupling as the energy is lowered. We interpret this as implying that the effective Kondo coupling is infinite at the fixed point. This interpretation is verified by a host of studies using a variety of methods, including the exact solution based on the Bethe Ansatz and the analysis using conformal invariance. The infinite coupling at the fixed point describes the physics that the local moment and the spin of the conduction electrons are locked into a singlet:

$$|\text{Kondo singlet}\rangle = \frac{1}{2}(|\uparrow\rangle_f|\downarrow\rangle_{c,FS} - |\downarrow\rangle_f|\uparrow\rangle_{c,FS}), \quad (8.8)$$

where $|\sigma\rangle_{c,FS}$ is a linear superposition of the conduction-electron states near the Fermi energy.

Eq. (8.8) is an entangled state between the local moment and the spins of the conduction electrons. As a result of this entanglement, the local moment is converted into a Kondo resonance in the excitation spectrum. The latter possesses the quantum number of a bare electron, spin 1/2, and charge e . The system is a Fermi liquid, in the sense that low-lying excitations are Landau quasi-particles. The Kondo resonance occurs below a crossover temperature scale, the Kondo temperature

$$T_K^0 \approx \rho_0^{-1} \exp(-1/\rho_0 J_K). \quad (8.9)$$

8.2.2 Kondo Lattice and Heavy Fermi Liquid

The microscopic model for heavy fermion materials is the Kondo lattice Hamiltonian (Fig. 8.2):

$$H_{KL} = \sum_{ij} t_{ij} c_{i\sigma}^\dagger c_{j\sigma} + \sum_{ij} I_{ij} \mathbf{S}_i \cdot \mathbf{S}_j + \sum_i J_K \mathbf{S}_i \cdot c_i^\dagger \frac{\vec{\sigma}}{2} c_i. \quad (8.10)$$

The model contains one conduction-electron band, $c_{i\sigma}$, with hopping matrix t_{ij} , and, correspondingly, band dispersion $\varepsilon_{\mathbf{k}}$. At each site i , the spin of the conduction electrons, $\mathbf{s}_{c,i} = (1/2)c_i^\dagger \vec{\sigma} c_i$, is coupled to the spin of the local moment, \mathbf{S}_i , via an AF Kondo exchange interaction J_K .

The Kondo effect is one primary mechanism in the Kondo lattice Hamiltonian to suppress the tendency of the local moments to develop AF order. In the RG sense, the Kondo coupling still renormalizes towards strong coupling, leading to the formation of Kondo singlets. Like in the single-impurity Kondo problem, this Kondo entanglement in the ground state supports Kondo resonances in the excitation spectrum. However, in contrast to the single-impurity

case, the number of the Kondo resonances, being one per site, is thermodynamically finite, and this will influence the electronic structure in a drastic way.

For concreteness, consider that the conduction electron band is filled with x electrons per site, or, equivalently, per unit cell; without loss of generality, we take $0 < x < 1$. The conduction electron band and the Kondo resonances will be hybridized, resulting in a count of $1 + x$ electrons per site. The Fermi surface of the conduction electrons alone would therefore have to expand to a size that encloses these $1 + x$ electrons. This is the large Fermi surface.

To see how this might happen, consider the extreme limit of $J_K \gg W \gg I$, where W is the width of conduction electron band, $\varepsilon_{\mathbf{k}}$, and I is the typical exchange interaction among the local moments. This limit is illustrated in Fig. 8.3. At each of the xN_{site} sites, where N_{site} is the number of unit cells in the system, a local moment and a conduction electron form a tightly bound singlet,

$$|s\rangle_i = (1/\sqrt{2})(|\uparrow\rangle_f |\downarrow\rangle_c - |\downarrow\rangle_f |\uparrow\rangle_c), \quad (8.11)$$

with a large binding energy of order J_K . Each of the remaining $(1 - x)N_{\text{site}}$ sites hosts a lone local moment which, when projected onto the low energy subspace, is written as

$$|\text{lone local moment } \sigma\rangle_i = (-\sqrt{2}\sigma)c_{i,\bar{\sigma}}|s\rangle_i. \quad (8.12)$$

We can take $|s\rangle_i$ as the vacuum state at site i , in which case a lone local moment behaves as a hole with infinite repulsion⁴ but with a kinetic energy of order W [10]. In the paramagnetic phase, we can invoke Luttinger's theorem to conclude that the Fermi surface encloses $(1 - x)$ holes or, equivalently, $(1 + x)$ electrons per unit cell. This is the heavy fermion state in which local moments, through an entanglement with conduction electrons, participate in the electron fluid [10]. The Fermi surface is large in this sense. By continuity, the above considerations apply to the paramagnetic part of the phase diagram with more realistic parameters. We label this phase as P_L , with the subscript denoting a large Fermi surface.

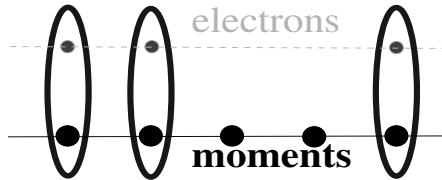
The continuity argument is supported by explicit microscopic calculations. In the regime $I \ll J_K \ll W$, various approaches, in particular the slave-boson mean-field theory, give rise to the following picture. Consider the conduction electron Green's function,

$$G_c(\mathbf{k}, \omega) \equiv F.T.[-\langle T_\tau c_{\mathbf{k},\sigma}(\tau) c_{\mathbf{k},\sigma}^\dagger(0) \rangle], \quad (8.13)$$

where the Fourier transform $F.T.$ is taken with respect to τ . This Green's function is related to a self-energy, $\Sigma(\mathbf{k}, \omega)$, via the standard Dyson equation,

$$G_c(\mathbf{k}, \omega) = \frac{1}{\omega - \varepsilon_{\mathbf{k}} - \Sigma(\mathbf{k}, \omega)}. \quad (8.14)$$

⁴There is only one conduction electron in the singlet.

**FIGURE 8.3**

Kondo singlets in the large Kondo-interaction limit.

In the heavy Fermi liquid state, $\Sigma(\mathbf{k}, \omega)$ is non-analytic and contains a pole in the energy space,

$$\Sigma(\mathbf{k}, \omega) = \frac{(b^*)^2}{\omega - \varepsilon_f^*}. \quad (8.15)$$

Inserting Eq. (8.15) into Eq. (8.14), we end up with two poles in the conduction electron Green's function,

$$G_c(\mathbf{k}, \omega) = \frac{u_{\mathbf{k}}^2}{\omega - E_{1,\mathbf{k}}} + \frac{v_{\mathbf{k}}^2}{\omega - E_{2,\mathbf{k}}}, \quad (8.16)$$

where

$$\begin{aligned} E_{1,\mathbf{k}} &= (1/2)[\varepsilon_{\mathbf{k}} + \varepsilon_f^* - \sqrt{(\varepsilon_{\mathbf{k}} - \varepsilon_f^*)^2 + 4(b^*)^2}], \\ E_{2,\mathbf{k}} &= (1/2)[\varepsilon_{\mathbf{k}} + \varepsilon_f^* + \sqrt{(\varepsilon_{\mathbf{k}} - \varepsilon_f^*)^2 + 4(b^*)^2}]. \end{aligned} \quad (8.17)$$

These two poles describe the dispersion of the two heavy-fermion bands. These bands must accommodate $1+x$ electrons, so the new Fermi energy must lie in a relatively flat portion of the dispersion, leading to a small Fermi velocity and a large quasi-particle mass m^* .

It is important to note that we have used a \mathbf{k} -independent self-energy to describe a large reconstruction of the quasi-particle dispersion ($\varepsilon_{\mathbf{k}} \rightarrow E_{1,\mathbf{k}}, E_{2,\mathbf{k}}$) and a corresponding large reconstruction of the Fermi surface. In fact, the self-energy of Eq. (8.15) contains only two parameters, the strength, i.e., the residue of the pole, $(b^*)^2$, and the location of the pole, ε_f^* . Equation (8.15) does not contain the incoherent features beyond the well-defined pole. Such incoherent components can be introduced, through, e.g., dynamical mean-field theory [20], and they will add damping terms to Eq. (8.16). But the fact remains that a \mathbf{k} -independent self-energy is adequate to capture the Kondo effect and the resulting heavy quasi-particles. We will return to this feature in the discussion of the Kondo breakdown effect.

8.3 Quantum Criticality in the Kondo Lattice

8.3.1 General Considerations

The Kondo interaction drives the formation of Kondo singlets between the local moments and conduction electrons. At high temperatures, the system is in a fully incoherent regime with the local moments weakly coupled to conduction electrons. Going below some scale T_0 , the initial screening of the local moments starts to set in. Eventually, at temperatures below some Fermi-liquid scale, T_{FL} , the heavy quasi-particles are fully developed.

When the AF RKKY interaction among the local moments becomes larger than the Kondo interaction, the system is expected to develop an AF order. An AF QCP is then to be expected when the control parameter, $\delta = T_K^0/I$, reaches some critical value δ_c . At $\delta < \delta_c$, the AF order will develop as the temperature is lowered through the AF-ordering line, $T_N(\delta)$.

In addition, RKKY interactions will eventually lead to the suppression of the Kondo singlets. Qualitatively, RKKY interactions promote singlet formation among the local moments, thereby reducing the tendency of singlet formation between the local moments and conduction electrons. This will define an energy (E_{loc}^*) or temperature (T_{loc}^*) scale, describing the breakdown of the Kondo effect. On very general grounds, the T_{loc}^* line is expected to be a crossover at non-zero temperatures, but turns into a sharp transition at zero temperature. The notion of Kondo breakdown in quantum critical heavy fermions was introduced in the theory of local quantum criticality [7] and a related approach based on fractionalization [8]. It also appeared in subsequent work [21, 22] using a gauge-theory formulation. The Kondo breakdown effect is alternatively referred to as a Mott localization of the f -electrons.

To study these issues theoretically, one key question is how to capture not only the magnetic order and Kondo-screening, but also the dynamical competition between the Kondo and RKKY interactions. The microscopic approach that is capable of doing this is the extended dynamical mean-field theory (EDMFT) [23–25]. The two solutions [7, 26–32] that have been derived through EDMFT are illustrated in Fig. 8.4, and are summarized below.

Large- N approaches based on slave-particle representations of the spin operator are also commonly used to study Kondo-like systems. One type of approach is based on a fermionic representation of the spin [21]. This representation naturally incorporates the physics of singlet formation, so it captures the Kondo singlets, as well as the singlets among the local moments, but it does not include magnetism in the large- N limit. One may allow a magnetic order in a static mean-field theory for a finite- N [21]. However, the magnetic transition and breakdown of Kondo screening are always separated in the phase diagram and the zero-temperature magnetic transition is still of the SDW type. This, we believe, is a manifestation of the static nature of the mean-field theory.

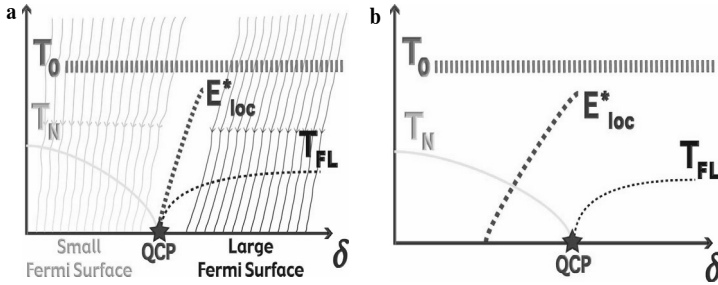


FIGURE 8.4

Two types of QCPs in Kondo lattice models [7] (from Ref. [14]). (a) Locally-critical QPT. A Kondo breakdown, signified by the vanishing of the energy scale E^* , occurs at the continuous onset of AF order. T_N is the AF transition temperature, and T_{FL} is the temperature scale below which Fermi liquid behavior sets in. T_0 is a crossover temperature scale at which Kondo screening initially sets in, and is also the upper bound of the temperature range for quantum-critical scaling; (b) SDW QCP, where the Kondo breakdown does not occur until inside the region of AF order.

A Schwinger-boson-based large- N formulation is another microscopic approach that is being considered in this context [33]. This approach naturally incorporates magnetism. While it is traditionally believed that bosonic representations of spin in general have difficulty in capturing the Kondo screening physics at its large- N limit, there is indication [33] that the dynamical nature of the formulation here allows an access to at least aspects of the Kondo effect. It will be interesting to see what type of QPTs this approach will lead to for the Kondo lattice problem.

Another approach [34] to the Kondo lattice Hamiltonian is based on a quantum non-linear sigma model (QNL σ M) representation of the local moments. This approach is most readily applied to the limit of $J_K \ll I \ll W$, the limit of large δ . To access the Kondo regime requires the incorporation of Berry-phase terms in the representation, and such a study remains to be carried out.

8.3.2 Microscopic Approach Based on the Extended Dynamical Mean-Field Theory

The EDMFT method [23–25] incorporates inter-site collective fluctuations into the dynamical mean-field theory framework [20]. The systematic method is constructed within a cavity, diagrammatic, or functional formalism [23–25]. It is conserving, satisfying the various Ward identities. Diagrammatically, EDMFT incorporates an infinite series associated with inter-site interactions,

in addition to the local processes already taken into account in the dynamical mean-field theory.

Within EDMFT, the dynamical spin susceptibility and the conduction-electron Green's function respectively have the forms $\chi(\mathbf{q}, \omega) = [M(\omega) + I_{\mathbf{q}}]^{-1}$, and $G(\mathbf{k}, \varepsilon) = [\varepsilon + \mu - \varepsilon_{\mathbf{k}} - \Sigma(\varepsilon)]^{-1}$. The correlation functions, $\chi(\mathbf{q}, \omega)$ and $G(\mathbf{k}, \varepsilon)$, are momentum-dependent. At the same time, the irreducible quantities, $M(\omega)$ and $\Sigma(\varepsilon)$, are momentum-independent. They are determined in terms of a Bose-Fermi Kondo model,

$$\begin{aligned} \mathcal{H}_{\text{imp}} = & J_K \mathbf{S} \cdot \mathbf{s}_c + \sum_{p,\sigma} E_p c_{p\sigma}^\dagger c_{p\sigma} \\ & + g \sum_p \mathbf{S} \cdot (\Phi_p + \Phi_{-p}^\dagger) + \sum_p w_p \Phi_p^\dagger \cdot \Phi_p . \end{aligned} \quad (8.18)$$

The fermionic ($c_{p\sigma}$) and bosonic (Φ_p) baths are determined by self-consistency conditions, which manifest the translational invariance, $\chi_{\text{loc}}(\omega) = \sum_{\mathbf{q}} \chi(\mathbf{q}, \omega)$, and $G_{\text{loc}}(\omega) = \sum_{\mathbf{k}} G(\mathbf{k}, \omega)$. The $(0 + 1)$ -dimensional quantum impurity problem, Eq. (8.18), has the following Dyson equations: $M(\omega) = \chi_0^{-1}(\omega) + 1/\chi_{\text{loc}}(\omega)$ and $\Sigma(\omega) = G_0^{-1}(\omega) - 1/G_{\text{loc}}(\omega)$, where $\chi_0^{-1}(\omega) = -g^2 \sum_p 2w_p/(\omega^2 - w_p^2)$ and $G_0(\omega) = \sum_p 1/(\omega - E_p)$ are the Weiss fields. The EDMFT formulation allows us to study different degrees of quantum fluctuations as manifested in the spatial dimensionality of these fluctuations. The case of two-dimensional magnetic fluctuations is represented in terms of the RKKY density of states that has a non-zero value at the lower edge, e.g.,

$$\rho_I(x) \equiv \sum_{\mathbf{q}} \delta(x - I_{\mathbf{q}}) = (1/2I)\Theta(I - |x|) , \quad (8.19)$$

where Θ is the Heaviside step function. Likewise, three-dimensional magnetic fluctuations are described in terms of a $\rho_I(x)$ which vanishes at the lower edge in a square-root fashion, e.g.,

$$\rho_I(x) = (2/\pi I^2) \sqrt{I^2 - x^2} \Theta(I - |x|) . \quad (8.20)$$

The bosonic bath captures the effect of the dynamical magnetic correlations, primarily among the local moments, on the local Kondo effect. As a magnetic QCP is approached, the spectrum of the magnetic fluctuations softens, and so does that of the bosonic bath. Consequently, its ability to suppress the Kondo effect increases. This effect has been explicitly seen in a number of specific studies [7, 26–32]. Moreover, the zero-temperature transition is second-order whenever the same form of the effective RKKY interaction appears in the formalism on both sides of the transition [35, 36].

8.3.3 Spin-Density-Wave Quantum Critical Point

The reduction of the Kondo-singlet amplitude by the dynamical effects of RKKY interactions among the local moments has been considered in some

detail in a number of studies based on EDMFT [7, 26–32]. Irrespective of the spatial dimensionality, this weakening of the Kondo effect is seen through the reduction of the E_{loc}^* scale.

Two classes of solutions emerge depending on whether this Kondo breakdown scale vanishes at the AF QCP. In the case of Eq. (8.20), E_{loc}^* has not yet been completely suppressed to zero when the AF QCP, δ_c , is reached from the paramagnetic side.⁵ This is illustrated in Fig. 8.4(b). The quantum critical behavior, at energies below E_{loc}^* , falls within the spin-density-wave type [2, 5, 6]. The zero-temperature dynamical spin susceptibility has the following form:

$$\chi(\mathbf{q}, \omega) = \frac{1}{f(\mathbf{q}) - i\omega} . \quad (8.21)$$

Here $f(\mathbf{q}) = I_{\mathbf{q}} - I_{\mathbf{Q}}$, and is generically $\propto (\mathbf{q} - \mathbf{Q})^2$ as the wavevector \mathbf{q} approaches the AF ordering wavevector \mathbf{Q} . The QCP is described by a Gaussian fixed point. At non-zero temperatures, a dangerously irrelevant operator invalidates the ω/T scaling [5, 6].

8.3.4 Local Quantum Critical Point

Another class of solutions corresponds to $E_{\text{loc}}^* = 0$ already at δ_c , as shown in Fig. 8.4(a). It arises in the case of Eq. (8.19), where the quantum critical magnetic fluctuations are strong enough to suppress the Kondo effect. The solution to the local spin susceptibility has the form

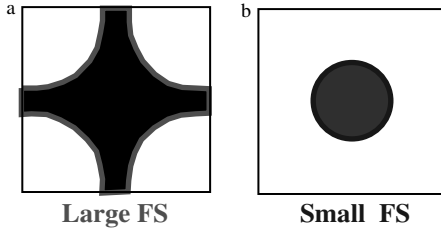
$$\chi(\mathbf{q}, \omega) = \frac{1}{f(\mathbf{q}) + A(-i\omega)^\alpha W(\omega/T)} . \quad (8.22)$$

This expression was derived [7, 26] within EDMFT studies, through the aid of an ϵ -expansion approach to the Bose-Fermi Kondo model. At the AF QCP, the Kondo effect itself is critically destroyed. The calculation of the critical exponent α is beyond the reach of the ϵ -expansion. In the Ising-anisotropic case, numerical calculations have found $\alpha \sim 0.7$ [27, 30–32].

The breakdown of the Kondo effect not only affects magnetic dynamics, but also influences the single-electron excitations. As the QCP is approached from the paramagnetic side, the quasi-particle residue $z_L \propto (b^*)^2$, where b^* is the strength of the pole of $\Sigma(\mathbf{k}, \omega)$ [cf. Eq. (8.15)], goes to zero. The large Fermi surface turns critical.

The breakdown of the large Fermi surface implies that the Fermi surface will be small on the antiferromagnetically ordered side. To consider this property further, we turn to the Kondo effect inside the AF phase.

⁵However, it can go to zero inside the AF region, as further discussed in Sec. 8.4.

**FIGURE 8.5**

Fermi surface evolution across a local quantum critical point. As the system goes across the QCP from the paramagnetic P_L phase to the magnetically ordered AF_S phase, a large Fermi surface [panel (a)] collapses and a small Fermi surface [panel (b)] emerges.

8.4 Antiferromagnetism and Fermi Surfaces in Kondo Lattices

To consider the Kondo effect in the antiferromagnetically ordered phase, we focus on the parameter regime of the Kondo lattice model, Eq. (8.10), in the limit $J_K \ll I \ll W$.

In this parameter regime, we can use as our reference point the $J_K = 0$ limit [34]. Then the local moments with AF exchange interactions are decoupled from the conduction electrons. We will focus on the case that the local-moment system itself is in a collinear AF state. Here, for low-energy physics, we can express the local-moment spin density as

$$\mathbf{S}_x/s = \eta_x \mathbf{n}_x \sqrt{1 - \mathbf{l}_x^2} + \mathbf{l}_x, \quad (8.23)$$

where $s = \frac{1}{2}$ is the size of the local-moment spin, \mathbf{n}_x and \mathbf{l}_x are the staggered and uniform components, respectively, and $\eta_x = \pm 1$ at even/odd sites; consider, for definiteness, a cubic or square lattice with Néel order. The low-energy theory for the local-moment Hamiltonian, the first term of Eq. (8.10), is the QNL σ M [4,37]:

$$\mathcal{S}_{\text{QNL}\sigma\text{M}} = (c/2g) \int d^d x d\tau \left[(\nabla \mathbf{n})^2 + (\partial \mathbf{n}/c \partial \tau)^2 \right]. \quad (8.24)$$

Here c is the spin-wave velocity, and g specifies the quantum fluctuations. There are gapless excitations in two regions of the wavevector space: the staggered magnetization (\mathbf{q} near \mathbf{Q}) specified by the \mathbf{n} field and the uniform magnetization (\mathbf{q} near $\mathbf{0}$) described by $\mathbf{n} \times \partial \mathbf{n} / \partial \tau$.

When the Fermi surface of the conduction electrons does not intersect the

AF zone boundary, only the uniform component of the local moments can be coupled to the spins of the conduction-electron states near the Fermi surface. The effective Kondo coupling takes the following form,

$$S_K = \lambda \int d^d \mathbf{x} d\tau \mathbf{s}_c \cdot \mathbf{n} \times \partial \mathbf{n} / \partial \tau. \quad (8.25)$$

A momentum-shell RG treatment requires a procedure that mixes bosons, which scale along all directions in momentum space, and fermions, which scale along the radial direction perpendicular to the Fermi surface [38]. Using the procedure specified in Ref. [39], we found λ to be marginal at the leading order [34], just like in the paramagnetic case. The difference from the latter appears at the loop level: λ is exactly marginal to infinite loops [34].

The fact that λ does not run towards infinity implies a breakdown of the Kondo effect. This is supplemented by a large- N calculation [34], which showed that the effective Kondo coupling, Eq. (8.25), leads to the following self-energy for the conduction electrons:

$$\Sigma(\mathbf{k}, \omega) \propto \omega^d. \quad (8.26)$$

The absence of a pole in $\Sigma(\mathbf{k}, \omega)$, in contrast to Eq. (8.15), implies the absence of any Kondo resonance. Correspondingly, the Fermi surface is small.

8.5 Towards a Global Phase Diagram

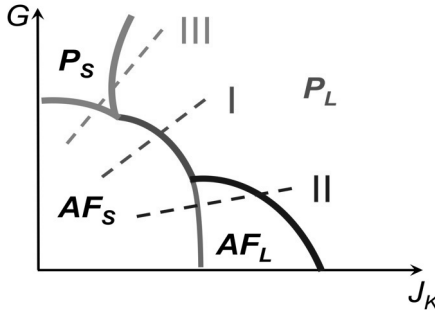
8.5.1 How to Melt a Kondo-Destroyed Antiferromagnet

Given the understanding that the AF state with a small Fermi surface is a stable phase, it would be illuminating to approach the quantum transition from this ordered state.

To do this, we must incorporate the Berry-phase term of the QNL σ M representation:

$$\begin{aligned} S_{\text{Berry}} &= i s \sum_{\mathbf{x}} \eta_{\mathbf{x}} A_{\mathbf{x}}, \\ A_{\mathbf{x}} &= \int_0^\beta d\tau \int_0^1 du \left[\mathbf{n} \cdot \left(\frac{\partial \mathbf{n}}{\partial u} \times \frac{\partial \mathbf{n}}{\partial \tau} \right) \right]. \end{aligned} \quad (8.27)$$

Here, A_x is the area on the unit sphere spanned by $\mathbf{n}(\mathbf{x}, \tau)$ with $\tau \in (0, \beta)$. The Berry-phase term can be neglected deep inside the AF phase. For smooth configurations of \mathbf{n} in the (\mathbf{x}, τ) space, the Berry-phase term vanishes. Topologically non-trivial configurations of \mathbf{n} in (\mathbf{x}, τ) yield a finite Berry phase. However, they cost a non-zero energy inside the AF phase and can be neglected for small J_K and, correspondingly, small λ . On the other hand, as

**FIGURE 8.6**

The $T = 0$ global phase diagram of the AF Kondo lattice. G describes the quantum fluctuations of the magnetic Hamiltonian of the local moments, and j_K is the normalized Kondo coupling. P_L and P_S respectively describe paramagnetic phases with Fermi surfaces that are large and small, in the sense specified in the main text; AF_L and AF_S denote the corresponding phases in the presence of an AF order. (From Ref. [19], and based on Ref. [40].)

J_K is increased these gapped configurations come into play. Indeed, they are expected to be crucial for capturing the Kondo effect. Certainly, the Kondo singlet formation requires the knowledge of the size of the microscopic spins, and the Berry-phase term is what encodes the size of the spin in the QNL σ M representation.

8.5.2 Global Phase Diagram

We can address these effects at a qualitative level, in terms of a global phase diagram [19, 40]. We consider a two-dimensional parameter space, as shown in Fig. 8.6. The vertical axis describes the local-moment magnetism. It is parametrized by G , which characterizes the degree of quantum fluctuations of the local-moment magnetism; increasing G reduces the Néel order. This parameter can be a measure of magnetic frustration, e.g., $G = I_{\text{nnn}}/I_{\text{nn}}$, the ratio of the next-nearest-neighbor exchange interaction to the nearest-neighbor one, or it can be the degree of spatial anisotropy. The horizontal axis is $j_K \equiv J_K/W$, the Kondo coupling normalized by the conduction-electron bandwidth. We are considering a fixed value of I/W , which is typically much less than 1, and a fixed number of conduction electrons per site, which is taken to be $0 < x < 1$ without a loss of generality.

The AF_S phase describes the small-Fermi-surface AF state, whose existence has been established asymptotically exactly using the RG method as described in the previous section. The P_L phase is the standard heavy Fermi liquid with heavy quasi-particles and a large Fermi surface [10]. The AF_L phase corresponds to an AF state in the presence of Kondo screening. It can

either be considered as resulting from the AF_S phase once the Kondo screening sets in, or from the P_L phase via an SDW instability. As alluded to in Ref. [40] and explicitly discussed in Ref. [19], a Ps phase should naturally arise, describing a paramagnetic phase with a Kondo breakdown (and, hence, a small Fermi surface) which either breaks or preserves translational invariance. Related considerations are also being pursued in Ref. [41].

This global phase diagram contains three routes for a system to go from the AF_S phase to the P_L phase.

- *Trajectory I* is a direct transition between the two. This AF_S – P_L transition gives rise to a local QCP. A critical Kondo breakdown occurs at the AF QCP. The Fermi surface undergoes a sudden small-to-large jump of the Fermi surface and the Kondo-breakdown scale E_{loc}^* vanishes at the QCP [7,8]. The quasi-particle residues associated with both the small and large Fermi surfaces must vanish as the QCP is approached from either side.
- *Trajectory II* goes through the AFL phase. The QCP at the AFL – P_L boundary falls in the spin-density-wave type [2,5,6]. A Kondo breakdown transition can still take place at the AFL – AF_S boundary [34,40].
- *Trajectory III* goes through the Ps phase. The Ps – P_L transition could describe either a spin-liquid [21,43] to heavy-Fermi-liquid QCP, or a spin-Peierls to heavy-Fermi-liquid QCP [42].

8.6 Experiments

There has been considerable experimental work on quantum critical heavy fermions. Here, we summarize a few points that are particularly pertinent to the theoretical considerations discussed in this chapter. Readers are referred to Chap. 18 for more details.

8.6.1 Quantum Criticality

The most direct evidence for the local quantum criticality occurs in YbRh₂Si₂ and CeCu_{6-x}Au_x. For YbRh₂Si₂, the Fermi-liquid behavior is observed both inside the AF-ordered phase and the field-induced non-magnetic phase [44]. In addition, Hall-coefficient measurements [45,46] have provided fairly direct evidence for the breakdown of the Kondo effect precisely at the AF QCP. The existence of the Kondo-breakdown scale, T_{loc}^* , has also been seen in both the Hall [45,46] and thermodynamic [47] experiments.

For CeCu_{6-x}Au_x, the unusual magnetic dynamics [16] observed near the

$x = x_c \approx 0.1$ by early neutron scattering measurements is understood in terms of such a critical Kondo breakdown in the form of local quantum criticality. A divergent effective mass expected in this picture is consistent with the thermodynamic measurement in both the doping and pressure-induced QCP in this system [15]. This picture necessarily implies a Fermi-surface jump across the QCP, as well as a Kondo-breakdown energy scale E_{loc}^* going to zero at the QCP, but such characteristics are yet to be probed in $\text{CeCu}_{6-x}\text{Au}_x$.

CeRhIn_5 is a member of the Ce-115 heavy fermions [48]. It contains both antiferromagnetism and superconductivity in its pressure-field phase diagram. When a large-enough magnetic field is applied and superconductivity is removed ($H > H_{c2}$), there is evidence for a single QCP between antiferromagnetic and non-magnetic phases [49]. At this QCP, the de Haas-van Alphen (dHvA) results [50] suggest a jump in the Fermi surface and a divergence in the effective mass. CeRhIn_5 , together with $\beta\text{-YbAlB}_4$ [51], illustrates the possibility that local quantum criticality induces superconductivity.

One of the earliest systems in which anomalous magnetic dynamics was observed is $\text{UCu}_{5-x}\text{Pd}_x$ [52]. It is tempting to speculate [40] that a Kondo-destroying spin-glass QCP underlies this observation.

There are also several heavy fermion systems in which spin-density-wave type QCPs have been implicated. Examples are $\text{Ce}(\text{Ru}_{1-x}\text{Rh}_x)_2\text{Si}_2$ [53] and $\text{Ce}_{1-x}\text{La}_x\text{Ru}_2\text{Si}_2$ [54].

8.6.2 Global Phase Diagram

A number of heavy fermion materials might be classified according to our global phase diagram, Fig. 8.6.

Perhaps the most complete information exists in the pure and doped YbRh_2Si_2 systems. In pure YbRh_2Si_2 , strong evidence exists that the field-induced transition goes along the trajectory I (see below). A surprising recent development came from experiments in the doped YbRh_2Si_2 . In Co-doped YbRh_2Si_2 , the field-induced transition seems to travel along trajectory II [55]. In the Ir-doped [55] and Ge-doped [56] YbRh_2Si_2 , on the other hand, the field-induced transition appears to go along trajectory III.

In $\text{CeCu}_{6-x}\text{Au}_x$, both the pressure- and doping-induced QCPs show the characteristics of local quantum criticality, accessed through trajectory I. However, the field-induced QCP [57] has the properties of an SDW QCP. We interpret the field-tuning as taking the trajectory II. It will be interesting to explore whether an AF_S-AF_L boundary can be located as a function of magnetic field.

CeIn_3 is one of the earliest heavy fermion metals in which an AF QCP was implicated [58]. This system is cubic, and we would expect it to lie in the small G region of the global phase diagram. Indeed, there is indication that this cubic material displays an AF_S-AF_L Lifshitz transition as a function of magnetic field [59].

It is to be expected that magnetic frustration will help reach the P_S phase. The heavy fermion system YbAgGe has a hexagonal lattice, and, indeed, there

is some indication that the P_S phase exists in this system [60]; however, lower-temperature measurements over an extended field range will be needed to help establish the detailed phase diagram.

8.7 Summary and Outlook

We close this chapter with some general observations and a few remarks on open issues.

8.7.1 Kondo Lattice

Kondo lattice systems provide a concrete context in which to study quantum magnetism in a metallic setting. Even though the ground states at generic band fillings are metallic, local moments are well-defined degrees of freedom.

We have emphasized two complementary views of a Kondo lattice system. On the one hand, we can consider it as a lattice of local moments. This view is advantageous for understanding the Kondo-screening effect in the Kondo lattice system. It allows us to build on the insights that have been gained in the extensive studies of the single-impurity Kondo problem.

On the other hand, we can also represent a Kondo lattice in terms of a spin-1/2 Heisenberg model of the local moments, which are magnetically coupled to a conduction electron band. This view allows us to take advantage of the understanding of the inherent quantum fluctuations of an underlying insulating quantum magnet. The coupling to conduction electrons introduces an additional source of quantum fluctuations.

8.7.2 Quantum Criticality

In the transverse-field Ising model we considered at the beginning, the quantum-disordered state at $T = 0$ and $\delta > \delta_c$ has spins polarized along the transverse direction. This polarization is not spontaneously generated, but is instead induced by the externally applied transverse field.

In a Kondo lattice system, the quantum-disordered state has a different character. Here, the quantum coherence is established through the Kondo effect. Kondo-singlet formation, while not breaking any symmetry of the Hamiltonian, shares an important characteristic of the usual symmetry breaking: it is spontaneously generated. This makes it natural for a critical destruction of such a Kondo singlet to create its own critical singularity. The interplay of this type of singularity with that associated with a continuous onset of AF order is at the heart of the local quantum critical and related theoretical approaches to the Kondo breakdown effect.

8.7.3 Global Phase Diagram

Theoretical considerations of the global phase diagram are only at the beginning stage. There is much room for concrete studies. As mentioned earlier, one type of quantum fluctuations in a Kondo lattice system is that associated with the local-moment component alone. These fluctuations can be tuned in various ways, such as varying the degree of magnetic frustration, or tuning the spatial dimensionality [7, 61]. Another type of quantum fluctuations is induced by the coupling of these local moments to the conduction electrons. Whether these two types of quantum fluctuations act in a similar fashion, or lead to different types of ground states, provides a way of thinking about the global phase diagram of the Kondo lattice system. It will be instructive to start from the antiferromagnetically ordered state, and reach the various types of quantum disordered states.

8.7.4 Superconductivity

Unconventional superconductivity is prevalent in the heavy fermion systems. As we mentioned in the beginning, historical studies of such unconventional superconductivity are based on Cooper pairing mediated by antiferromagnetic paramagnons. It will be important to see how Kondo destruction physics influences superconductivity. In local quantum criticality, for instance, there is a strong fluctuation of the Fermi surface, between large and small. The excitations underlying such fluctuations and the associated non-Fermi liquid behavior may very well be a key ingredient for the superconducting pairing.

Acknowledgments – I am grateful to my collaborators for their insights and discussions; more recent work has been done in collaboration with P. Goswami, K. Ingersent, S. Kirchner, J. Pixley, J. Wu, S. Yamamoto, J.-X. Zhu, and L. Zhu. I would like to thank F. Steglich and P. Gegenwart for discussions during the preparation of this chapter. The work has been in part supported by the NSF Grant No. DMR-0706625 and the Robert A. Welch Foundation Grant No. C-1411.

Bibliography

- [1] P. Pfeuty, Ann. Phys. NY **57**, 79 (1970).
- [2] J. A. Hertz, Phys. Rev. B **14**, 1165 (1976).
- [3] S. Sachdev, *Quantum Phase Transitions* (Cambridge University Press, Cambridge, 1999).

- [4] S. Chakravarty, B. I. Halperin, and D. R. Nelson, Phys. Rev. B **39**, 2344 (1989).
- [5] A. J. Millis, Phys. Rev. B **48**, 7183 (1993).
- [6] T. Moriya, *Spin Fluctuations in Itinerant Electron Magnetism* (Springer, Berlin, 1985).
- [7] Q. Si, S. Rabello, K. Ingersent, and J. L. Smith, Nature **413**, 804 (2001).
- [8] P. Coleman, C. Pépin, Q. Si, and R. Ramazashvili, J. Phys. Cond. Matt. **13**, R723 (2001).
- [9] T. Senthil, A. Vishwanath, L. Balents, S. Sachdev, and M. P. A. Fisher, Science **303**, 1490 (2004).
- [10] A. C. Hewson, *The Kondo Problem to Heavy Fermions* (Cambridge University Press, Cambridge, 1993).
- [11] S. Doniach, Physica B **91**, 231 (1977).
- [12] C. M. Varma, Rev. Mod. Phys. **48**, 219 (1976).
- [13] M. B. Maple, C. L. Seaman, D. A. Gajewski, Y. Dalichaouch, V. B. Barbutta, M. C. de Andrade, H. A. Mook, H. G. Lukefahr, O. O. Bernal, and D. E. MacLaughlin, J. Low Temp. Phys. **95**, 225 (2004).
- [14] P. Gegenwart, Q. Si, and F. Steglich, Nat. Phys. **4**, 186 (2008).
- [15] H. v. Löhneysen, A. Rosch, M. Vojta, and P. Wölfle, Rev. Mod. Phys. **79**, 1015 (2007).
- [16] A. Schröder, G. Aeppli, R. Coldea, M. Adams, O. Stockert, H. v. Löhneysen, E. Bucher, R. Ramazashvili, and P. Coleman, Nature **407**, 351 (2000).
- [17] A. Abanov and A. Chubukov, Phys. Rev. Lett. **93**, 255702 (2004).
- [18] D. Belitz, T. R. Kirkpatrick, and T. Vojta, Rev. Mod. Phys. **77**, 579 (2005).
- [19] Q. Si, Phys. Status Solidi B **247**, 476 (2010).
- [20] A. Georges, G. Kotliar, W. Krauth, and M. Rozenberg, Rev. Mod. Phys. **68**, 13 (1996).
- [21] T. Senthil, M. Vojta, and S. Sachdev, Phys. Rev. B **69**, 035111 (2004).
- [22] I. Paul, C. Pépin, and M. R. Norman, Phys. Rev. Lett. **98**, 026402 (2007).
- [23] Q. Si and J. L. Smith, Phys. Rev. Lett. **77**, 3391 (1996).

- [24] J. L. Smith and Q. Si, Phys. Rev. B **61**, 5184 (2000).
- [25] R. Chitra and G. Kotliar, Phys. Rev. Lett. **84**, 3678 (2000).
- [26] Q. Si, S. Rabello, K. Ingersent, and J. Smith, Phys. Rev. B **68**, 115103 (2003).
- [27] D. R. Grempel and Q. Si, Phys. Rev. Lett. **91**, 026401 (2003).
- [28] J. Zhu, D. R. Grempel, and Q. Si, Phys. Rev. Lett. **91**, 156404 (2003).
- [29] P. Sun and G. Kotliar, Phys. Rev. Lett. **91**, 037209 (2003).
- [30] M. Glossop and K. Ingersent, Phys. Rev. Lett. **99**, 227203 (2007).
- [31] J.-X. Zhu, S. Kirchner, R. Bulla, and Q. Si, Phys. Rev. Lett. **99**, 227204 (2007).
- [32] M. Glossop, J.-X. Zhu, S. Kirchner, K. Ingersent, Q. Si, and R. Bulla, to be published (2010).
- [33] J. Rech, P. Coleman, G. Zarand, and O. Parcollet, Phys. Rev. Lett. **96**, 016601 (2006).
- [34] S. J. Yamamoto and Q. Si, Phys. Rev. Lett. **99**, 016401 (2007).
- [35] Q. Si, J.-X. Zhu, and D. R. Grempel, J. Phys.: Condens. Matter **17**, R1025 (2005).
- [36] P. Sun and G. Kotliar, Phys. Rev. B **71**, 245104 (2005).
- [37] F. D. M. Haldane, Phys. Rev. Lett. **50**, 1153 (1983).
- [38] R. Shankar, Rev. Mod. Phys. **66**, 129 (1994).
- [39] S. Yamamoto and Q. Si, Phys. Rev. B **81**, 205106 (2010).
- [40] Q. Si, Physica B **378**, 23 (2006).
- [41] P. Coleman, Phys. Status Solidi B **247**, 506 (2010).
- [42] E. Pivovarov and Q. Si, Phys. Rev. B **69**, 115104 (2004).
- [43] P. W. Anderson, Phys. Rev. Lett. **104**, 176403 (2010).
- [44] J. Custers, P. Gegenwart, H. Wilhelm, K. Neumaier, Y. Tokiwa, O. Trovarelli, C. Geibel, F. Steglich, C. Pèpin, and P. Coleman, Nature **424**, 524 (2003).
- [45] S. Paschen, T. Lühmann, S. Wirth, P. Gegenwart, O. Trovarelli, C. Geibel, F. Steglich, P. Coleman, and Q. Si, Nature **432**, 881 (2004).

- [46] S. Friedemann, N. Oeschler, S. Wirth, C. Krellner, C. Geibel, F. Steglich, S. Paschen, S. Kirchner, and Q. Si, PNAS, in press (2010).
- [47] P. Gegenwart, T. Westerkamp, C. Krellner, Y. Tokiwa, S. Paschen, C. Geibel, F. Steglich, E. Abrahams, and Q. Si, Science **315**, 969 (2007).
- [48] H. Hegger, C. Petrovic, E. G. Moshopoulou, M. F. Hundley, J. L. Sarrao, and Z. Fisk, Phys. Rev. Lett. **84**, 4986 (2000).
- [49] T. Park, F. Ronning, H. Q. Yuan, M. B. Salamon, R. Movshovich, J. L. Sarrao, and J. D. Thompson, Nature **440**, 65 (2006).
- [50] H. Shishido, R. Settai, H. Harima, and Y. Ōnuki, J. Phys. Soc. Jpn. **74**, 1103 (2005).
- [51] S. Nakatsuji, K. Kuga, Y. Machida, T. Tayama, T. Sakakibara, Y. Karaki, H. Ishimoto, S. Yonezawa, Y. Maeno, E. Pearson, G. G. Lonzarich, L. Balicas, H. Lee, and Z. Fisk, Nature Phys. **4**, 603 (2009).
- [52] M. C. Aronson, R. Osborn, R. A. Robinson, J. W. Lynn R. Chau, C. L. Seaman, and M. B. Maple, Phys. Rev. Lett. **75**, 725 (1995).
- [53] H. Kadowaki, Y. Tabata, M. Sato, N. Aso, S. Raymond, and S. Kawarazaki, Phys. Rev. Lett. **96**, 016401 (2006).
- [54] W. Knafo, S. Raymond, P. Lejay, and J. Flouquet, Nat. Phys. **5**, 753 (2009).
- [55] S. Friedemann, T. Westerkamp, M. Brando, N. Oeschler, S. Wirth, P. Gegenwart, C. Krellner, C. Geibel, and F. Steglich, Nat. Phys. **5**, 465 (2009).
- [56] J. Custers, P. Gegenwart, C. Geibel, F. Steglich, P. Coleman, and S. Paschen, Phys. Rev. Lett. **104**, 186402 (2010).
- [57] O. Stockert, M. Enderle, and H. v. Löhneysen, Phys. Rev. Lett. **99**, 237203 (2007).
- [58] N. D. Mathur, F. M. Grosche, S. R. Julian, I. R. Walker, D. M. Freye, R. K. W. Haselwimmer, and G. G. Lonzarich, Nature **394**, 39 (1998).
- [59] S. E. Sebastian, N. Harrison, C. D. Batista, S. A. Trugman, V. Fanelli, M. Jaime, T. P. Murphy, E. C. Palm, H. Harima, and T. Ebihara, Proc. Natl. Acad. Sci. USA **106**, 7741 (2009).
- [60] S. L. Bud'ko, E. Morosan, and P. C. Canfield, Phys. Rev. B **71**, 054408 (2005).
- [61] H. Shishido, T. Shibauchi, K. Yasu, T. Kato, H. Kontani, T. Terashima, and Y. Matsuda, Science **327**, 980 (2010).

9

Quantum Phase Transitions in Spin-Boson Systems: Dissipation and Light Phenomena

Karyn Le Hur

Departments of Physics and Applied Physics, Yale University, New Haven, Connecticut, 06520, U.S.A.

Spin-boson models are useful in the understanding of quantum optics, nuclear physics, quantum dissipation, and quantum computation. We discuss quantum phase transitions (QPTs) in various spin-boson Hamiltonians, and compare and contrast them. We summarize theoretical concepts and results; open questions and implementations of these ideas in cold atomic and QED cavity systems will also be addressed. The chapter is organized as follows.

First, a large collection of harmonic oscillators (bosons) can simulate *dissipation* in quantum mechanics. Through a two-level system coupled to a bath of bosons, we investigate in detail the concept of *dissipation-driven QPTs*. Another section will be devoted to the effect of dissipation on the critical exponents associated with well known phase transitions such as the disordered-ordered transition in the Ising model. Second, a spin-boson model can also describe *light-atom* interactions. In particular, the Dicke model describing an ensemble of two-state atoms interacting with a single quantized mode of the electromagnetic field is well-known to exhibit a zero-temperature phase transition at a critical value of the dipole coupling strength. Finally, we theoretically study the superfluid-Mott transition of polaritons in the Jaynes-Cummings lattice system which consists of an array of coupled optical cavities, each containing a two-level atom.

9.1 Dissipative Transitions for the Two-State System

A dissipative two-state system generally refers to a two-level system coupled to a bath of harmonic oscillators, i.e., a large collection of bosons [1, 2]:

$$H = -\frac{\Delta}{2}\sigma_x + \frac{h}{2}\sigma_z + \frac{1}{2}\sigma_z \sum_i c_i x_i + H_{\text{osc}}, \quad (9.1)$$

$$H_{\text{osc}} \equiv \sum_i \left(\frac{p_i^2}{2m_i} + \frac{1}{2} m_i \omega_i^2 x_i^2 \right). \quad (9.2)$$

Here, σ_x and σ_z are Pauli matrices, Δ is the tunneling amplitude between the states with $\sigma_z = \pm 1$, and h the bias (detuning).¹ Moreover, x_i , p_i , m_i , and ω_i are the coordinate, momentum, mass, and frequency of the i th harmonic oscillator. Here, c_i denotes the strength of the coupling with the i th oscillator. Information about the bath is encapsulated in the spectral function [1, 2] $J(\omega) = \frac{\pi}{2} \sum_i \frac{c_i^2}{m_i \omega_i} \delta(\omega - \omega_i)$. This spin-boson model is a variant of the Caldeira-Leggett model [3] where the quantum system is a spin [1, 4].

9.1.1 Ohmic Case

In the case of Ohmic dissipation, $J(\omega) = \eta \omega e^{-\omega/\omega_c}$. It is then convenient to introduce the dimensionless dissipation (friction) coefficient α such that $\eta = 2\pi\alpha$. In fact, the emergence of a QPT can be understood from a perturbation theory in Δ/h where $h > 0$. More precisely, the order parameter obeys $\langle \sigma_z \rangle + 1 \sim \mathcal{O}(\mathcal{A})$ where $\mathcal{A} = \frac{\Delta^2}{h^2} (h/\omega_c)^{2\alpha}$ [5]. For $\alpha > 1$, one observes that the spin tends to be trapped, meaning that $\langle \sigma_z \rangle \sim -1$ for $h \ll \omega_c$. In contrast, for $\alpha < 1$, \mathcal{A} increases for smaller h and eventually reaches its maximum value $\mathcal{A} \sim 1$. This indeed suggests the existence of a QPT at $\alpha_c \sim 1$. These impurity systems generally display both a classical (trapped) and quantum (untrapped) phase for the spin [6].

To better understand the nature of the dissipation-induced transition, one can integrate out the dissipative bath. This leads to an effective action which is reminiscent of classical spin chains with long-range correlations [7]:

$$\mathcal{S}_{\text{int}} = - \int_0^\beta d\tau \int_0^\tau d\tau' \sigma_z(\tau) \mathcal{G}(\tau - \tau') \sigma_z(\tau'), \quad (9.3)$$

with $\mathcal{G}(\tau) \propto 1/\tau^2$ at long imaginary times $\omega_c^{-1} \ll \tau \ll \beta = 1/k_B T$. It is relevant to observe that Anderson, Yuval, and Hamman [8] found an equivalent Ising model when studying the Kondo problem:²

$$\begin{aligned} H_K &= H_{\text{kin}} + \frac{J_\perp}{2} \sum_{k,k'} \left(c_{k\uparrow}^\dagger c_{k'\downarrow} S^- + c_{k\downarrow}^\dagger c_{k'\uparrow} S^+ \right) \\ &\quad + \frac{J_z}{2} \sum_{k,k'} \left(c_{k\uparrow}^\dagger c_{k'\uparrow} - c_{k\downarrow}^\dagger c_{k'\downarrow} \right) S_z + h S_z, \end{aligned} \quad (9.4)$$

where H_{kin} represents the kinetic energy of the electrons. This is perhaps not so surprising: conduction electrons represent a dissipative bath and as

¹Hereafter, the Planck constant will be set to $\hbar = 1$ to avoid confusion with the bias h .

²We obtain the identity $\langle S_z \rangle = \langle \sigma_z \rangle / 2$. However, a similar relationship does not hold between $\langle S_x \rangle$ and $\langle \sigma_x \rangle$. The electron operator $c_{k\uparrow}$ must not be confused with the coupling constant c_i (or c_k) in the spin-boson model which will prominently appear in the following.

a result tunneling (spin flip) events are not independent. Instead, they feature long-range interactions in time and the equivalent Ising chain acquires long-range interactions. The trapped-untrapped transition in the spin-boson model is in fact equivalent to the ferromagnetic-antiferromagnetic transition in the anisotropic Kondo model [9, 10]. The equivalence between the anisotropic Kondo model and the spin-boson model with Ohmic damping can be formulated rigorously through bosonization [11]. The untrapped region (for the spin) corresponds to the antiferromagnetic Kondo model $J_z > 0$, while the trapped region corresponds to the ferromagnetic Kondo model $J_z < 0$ where the spin is fatally frozen in time. One obtains the precise correspondence $(\rho J_\perp) \rightarrow \Delta/\omega_c$ and $(1 + 2\delta/\pi)^2 \rightarrow \alpha$, where ρ is the conduction electron density of states. The parameter δ is related to the phase shift caused by the J_z Kondo term and is given by $\delta = \tan^{-1}(-\pi\rho J_z/4)$ [11]. Additionally, in the untrapped phase, the effective Kondo energy scale obeys [12]³

$$T_K = \Delta(\Delta/D)^{\alpha/(1-\alpha)}, \quad (9.5)$$

for values of α not too close to the transition. Close to the transition T_K assumes the exponential form of the isotropic, antiferromagnetic Kondo model, $\ln T_K \propto 1/(\alpha_c - \alpha)$. The critical line separating the trapped and untrapped phase in the spin-boson model corresponds to $\alpha_c = 1 + \mathcal{O}(\Delta/\omega_c)$.

Next, we discuss recent developments in spin observables and dynamics.

9.1.2 Exact Results

As shown by Thouless, for the $1/\tau^2$ Ising chain the magnetization $\langle \sigma_z \rangle$ is not continuous at the transition [15]. This is also consistent with the fact that in the Ohmic case, the phase transition is described by Renormalization Group equations similar to those in the XY model in two dimensions. Following Anderson and Yuval, the order parameter $\langle \sigma_z \rangle$ jumps by a non-universal amount $\sqrt{1/\alpha_c}$ along the quantum critical line, $\alpha_c = 1 + \mathcal{O}(\Delta/\omega_c)$ [16].

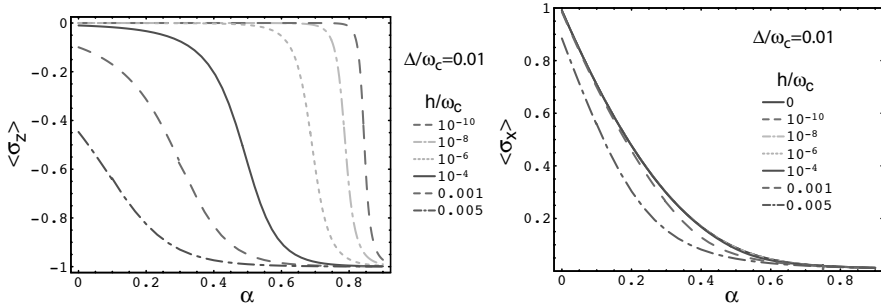
In the untrapped phase ($\alpha < \alpha_c$), one can apply the Bethe ansatz approach to compute observables exactly [5, 13, 14, 17]. For $h \ll T_K$, we obtain [5, 17]

$$\lim_{h \ll T_K} \langle \sigma_z \rangle = -\frac{2e^{b/[2(1-\alpha)]}}{\sqrt{\pi}} \frac{\Gamma[1 + 1/(2 - 2\alpha)]}{\Gamma[1 + \alpha/(2 - 2\alpha)]} \frac{h}{T_K}, \quad (9.6)$$

where $b = \alpha \ln \alpha + (1 - \alpha) \ln(1 - \alpha)$. Note that $\langle \sigma_z \rangle \propto h/T_K$ at small h , in keeping with the Kondo Fermi liquid ground state [1, 2]. The local susceptibility of the spin converges⁴ to $1/\Delta$ for $\alpha \rightarrow 0$ in accordance with the two-level description and diverges in the vicinity of the phase transition due to the exponential suppression of T_K . Note that the longitudinal spin magnetization, the spin order parameter $\langle \sigma_z \rangle$, only depends on the fixed point properties, i.e.,

³We have introduced a high-energy cutoff D for the conduction electrons which is of the order of the Fermi energy; the relation between ω_c and D is given, e.g., in Refs. [5, 13, 14].

⁴For $\alpha \rightarrow 0$, $\Gamma[1] = 1$, $\Gamma[3/2] = \sqrt{\pi}/2$, $\exp(b/[2(1 - \alpha)]) = 1$, and $T_K = \Delta$.

**FIGURE 9.1**

Longitudinal and Transverse spin magnetizations versus α from Bethe ansatz.

this is a universal function of h/T_K in the untrapped phase. Finally, in the trapped phase, one predicts $\langle \sigma_z \rangle \approx -1 + \mathcal{O}((\Delta/\omega_c)^2)$ [18].

The leading behavior of $\langle \sigma_x \rangle$ in the untrapped phase is [5, 13, 14, 17]:

$$\lim_{h \ll T_K} \langle \sigma_x \rangle = \frac{1}{2\alpha - 1} \frac{\Delta}{\omega_c} + M(\alpha) \frac{T_K}{\Delta}, \quad (9.7)$$

$$M(\alpha) \equiv \frac{e^{-b/(2-2\alpha)}}{\sqrt{\pi(1-\alpha)}} \frac{\Gamma[1-1/(2-2\alpha)]}{\Gamma[1-\alpha/(2-2\alpha)]}. \quad (9.8)$$

As $\alpha \rightarrow 0$, $T_K \rightarrow \Delta$ and $M(0) = 1$, so we check that $\langle \sigma_x \rangle \rightarrow 1$. As we turn on the coupling to the environment, we introduce some uncertainty in the spin direction and $\langle \sigma_x \rangle$ decreases. Note that $\langle \sigma_x \rangle$ does not only depend on the fixed point properties; more precisely, in the untrapped and highly non-perturbative regime, $\langle \sigma_x \rangle$ still contains a perturbative part in Δ/ω_c stemming from the trapped region! For $\alpha < 1/2$, the monotonic decrease of T_K/Δ dominates. In contrast, for $\alpha > 1/2$, the first term in Eq. (9.7) dominates:

$$\langle \sigma_x \rangle_{\alpha > 1/2, h \rightarrow 0} = \frac{1}{2\alpha - 1} \frac{\Delta}{\omega_c}. \quad (9.9)$$

This result can also be recovered using perturbation theory in Δ/ω_c [5]. This emphasizes that the observable $\langle \sigma_x \rangle$ is continuous and small at the QPT. This is also consistent with the work by Anderson and Yuval which predicts $\langle \sigma_x \rangle \sim \Delta/\omega_c$ exactly at the QPT [16].

Finally, we can also check that the spin component $\langle \sigma_x \rangle$ evolves continuously close to $\alpha = 1/2$. In the limit $\alpha \rightarrow 1/2$, one can take $M(\alpha) = (4/\pi)\Gamma(1-2\alpha) \rightarrow 4/[\pi(1-2\alpha)]$ and use the identity $D(\alpha = 1/2) = 4\omega_c/\pi$ [5, 13, 14] to find

$$\langle \sigma_x \rangle \rightarrow -(4/\pi)\sqrt{T_K/D} \ln(T_K/D), \quad (9.10)$$

in agreement with the “non-interacting” resonant level description valid at the specific point $\alpha = 1/2$ [5]. Exact results for the spin observables obtained using

the Bethe ansatz are summarized in Fig. 9.1. Usually, a strong reduction of the off-diagonal elements of the spin reduced density matrix leads to quantum decoherence. Using the results above, we observe that quantum decoherence is prominent for $\alpha \geq 1/2$, where $\langle \sigma_x \rangle$ becomes tiny and the entanglement between the spin and the bath becomes almost maximal [5, 17].

9.1.3 Spin Dynamics and Entanglement

Another useful quantity in the context of macroscopic quantum coherence is the occupation probability $P(t) = \langle \sigma_z(t) \rangle$, where the system is subject to the non-equilibrium initial preparation $\sigma_z(t=0) = +1$ and the initial density matrix is in a factorized form [1, 2]. At time $t=0$, the dynamics commences.

To study the spin dynamics it is convenient to perform a polaronic transformation $U = \exp(-i\sigma_z\Omega/2)$ where $\Omega = \sum_i(c_i/m_i\omega_i^2)p_i$, such that the transformed Hamiltonian $H' = U^{-1}HU$ takes the precise form [1, 2]

$$H' = -\frac{1}{2}\Delta(\sigma_+e^{-i\Omega} + \sigma_-e^{i\Omega}) + \sum_i \left(\frac{p_i^2}{2m_i} + \frac{1}{2}m_i\omega_i^2x_i^2 \right). \quad (9.11)$$

In the Heisenberg picture, the equations of motion for $\sigma_{\pm}(t)$ are easily obtained. Integrating and substituting them into the equation of motion for the transverse polarization $\sigma_x(t)$, one obtains the exact formula:

$$\dot{\sigma}_z(t) = -\frac{1}{2}\Delta^2 \int_{-\infty}^t \left(e^{-i\Omega(t)}e^{i\Omega(t')} \sigma_z(t') + \sigma_z(t')e^{-i\Omega(t')}e^{i\Omega(t)} \right) dt'. \quad (9.12)$$

On the other hand, to solve Eq. (9.12), one usually uses approximations [19]. The first approximation generally consists of inserting the free bath dynamics when computing the commutator:

$$[\Omega(t), \Omega(t')] = i \sum_j \left(\frac{c_j^2}{m_j\omega_j^3} \right) \sin(\omega_j(t-t')). \quad (9.13)$$

The next step is to average (9.12) with respect to the bath and to decouple the environmental exponentials from the spin. Then

$$\langle \Omega(t)\Omega(t') + \Omega(t')\Omega(t) \rangle = \sum_j \frac{c_j^2}{m_j\omega_j^3} \coth\left(\frac{1}{2}\beta\omega_j\right) \cos(\omega_j(t-t')). \quad (9.14)$$

This leads to the evolution equation [19]:

$$\dot{P}(t) + \int_{-\infty}^t \mathcal{F}(t-t')P(t')dt' = 0, \quad (9.15)$$

where the function \mathcal{F} obeys $\mathcal{F}(t) = \Delta^2 \cos(A_1(t)) \exp - (A_2(t))$, and

$$\begin{aligned} A_1(t) &= \frac{1}{\pi} \int_0^{+\infty} \sin(\omega t) \frac{J(\omega)}{\omega^2} d\omega, \\ A_2(t) &= \frac{1}{\pi} \int_0^{+\infty} (1 - \cos(\omega t)) \coth\left(\frac{\beta\omega}{2}\right) \frac{J(\omega)}{\omega^2} d\omega. \end{aligned} \quad (9.16)$$

Through the Laplace transform one obtains (C denotes a Bromwich contour):

$$P(t) = \frac{1}{2\pi i} \int_C d\lambda e^{\lambda t} \frac{1}{\lambda + \mathcal{F}(\lambda)}. \quad (9.17)$$

At zero temperature and in the scaling limit $\Delta/\omega_c \ll 1$, one finds [1, 2]

$$\mathcal{F}(\lambda) = \Delta_e \left(\frac{\Delta_e}{\lambda} \right)^{1-2\alpha}, \quad (9.18)$$

where $\Delta_e = \Delta_r [\cos(\pi\alpha)\Gamma(1-2\alpha)]^{1/[2(1-\alpha)]}$; we have introduced the renormalized transverse field $\Delta_r = \Delta(\Delta/\omega_c)^{\alpha/(1-\alpha)}$ which is proportional to the Kondo energy scale T_K . This expression of $P(t)$ coincides with the formula of $P(t)$ obtained via the Non-Interacting Blip Approximation (NIBA) [1, 2].

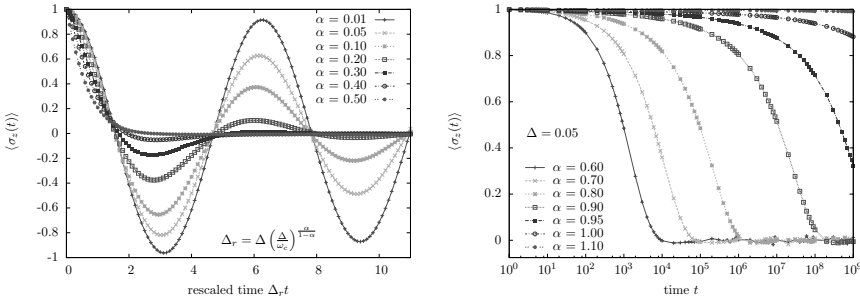
For $\alpha \rightarrow 0$, one recovers perfect Rabi oscillations $P(t) = \cos(\Delta t)$, whereas for $\alpha = 1/2$ one obtains a pure *relaxation* $P(t) = \exp\{-[\pi\Delta^2 t/(2\omega_c)]\}$, which is in accordance with the non-interacting resonant level model [1, 2]. For $0 < \alpha < 1/2$, the spin displays coherent oscillations, due to a pair of simple poles, leading to $P_{coh}(t) = a \cos(\zeta t + \phi) \exp(-\gamma t)$ with the quality factor [1, 2]

$$\frac{\zeta}{\gamma} = \cot\left(\frac{\pi\alpha}{2(1-\alpha)}\right). \quad (9.19)$$

This quality factor has also been found using conformal field theory [20].

Recently, we have developed a time-dependent Numerical Renormalization Group theory (NRG) which allows us to confirm these results [21]; see Fig. 9.2. In particular, we have checked the expression given in (9.19) for the quality factor. In fact, the NRG represents a powerful theoretical tool to study these spin-boson systems [22–25]. Additionally, we have obtained the same quality factor using an exact analytical extension of the NIBA [26].

It is relevant to note that the coherent-incoherent crossover, corresponding either to the strong suppression of the off-diagonal elements of the spin reduced density matrix $\langle s_x \rangle \sim \Delta/\omega_c \rightarrow 0$ or to the complete vanishing of the Rabi quantum oscillations, can be identified with the Toulouse limit $\alpha = 1/2$ and not with the QPT. It is also interesting to emphasize the correspondence between the prominence of spin-bath entanglement and the emergence of quantum decoherence [5, 17]. The entanglement entropy S between the spin and the environment displays a plateau at maximal entanglement for $1/2 < \alpha < 1$. Using the time-dependent NRG [21], we have also studied the strong coupling

**FIGURE 9.2**

Spin dynamics $P(t) = \langle \sigma_z(t) \rangle$ obtained from time-dependent NRG.

regime and in particular the crossover from incoherent decay to localization at the QPT (Fig. 9.2). In particular, for $1/2 < \alpha < 1$, the spin dynamics remains purely incoherent. The authors of Ref. [27] report a multi-exponential form $P(t) = \sum_{n=1}^{+\infty} a_n e^{-2b_n t}$. In contrast with the results of conformal field theory [20], the rate constants appearing in the multi-exponential fit are not integer multiples of a single rate. Our NRG results rather support the form $P(t) = \exp[-(tT_K/2)^{a_\alpha}]$ with the prerequisite that $a_{1/2} = 1$. The exponent a_α evolves linearly with α .

9.1.4 Sub-ohmic Case

Now, we focus on the sub-ohmic situation $J(\omega) = 2\pi\alpha\omega_c^{1-s}\omega^s$ with $0 < s < 1$, which exhibits a second-order QPT [6] by analogy to classical spin chains [7, 28]: in this case $\mathcal{G}(\tau) \propto 1/\tau^{1+s}$ in Eq. (9.3). The second-order QPT separates a localized (trapped) phase for the spin at small Δ from a delocalized (untrapped) phase at large Δ .

For a second-order impurity QPT we can apply the following scaling ansatz for the impurity part of the free energy [6]:

$$F_{\text{imp}} = T F(|\Delta - \Delta_c|/T^{1/\nu}, h T^{-b}), \quad (9.20)$$

where we have re-introduced the detuning h and Δ_c is the value of the transverse field at the quantum critical point. The critical exponent b should not be confused with the parameter b of Sec. 1.1.2. There is no independent dynamical critical exponent for $(0+1)$ -dimensional models, formally $z = 1$. At zero temperature, the crossover from the quantum critical regime to one or the other of the stable regimes defines an energy scale h^* which vanishes at Δ_c , $h^* \propto |\Delta_c - \Delta|^{b\nu}$. In a similar way, at finite temperature, we define the energy scale $T^* = |\Delta_c - \Delta|^\nu$. It should be noted that the ansatz (9.20) is usually well justified when the fixed point is interacting [6]; for a Gaussian fixed point the scaling function would also depend upon dangerously irrelevant variables.

Both analytical arguments, based on the equivalence to an $\mathcal{O}(1) \phi^4$ theory

and numerical simulations for the 1D long-range Ising model, show that the upper-critical dimension is $d_u = 2s$ [29, 30]. In other words, the transition obeys non-trivial critical behavior for $1/2 < s < 1$ and the fixed point is interacting. More precisely, hyperscaling relations imply that there are only two independent exponents, i.e., ν and b . A Ward identity for the spin-boson model ensures that $b = (1+s)/2$ [5, 31, 32]. Defining the exponent δ via $\langle \sigma_z \rangle(h, \Delta_c) \propto |h|^{1/\delta}$, where $\langle \sigma_z \rangle(h, \Delta_c)$ means the average as a function of (h, Δ_c) , one also finds $\delta = (1+s)/(1-s)$. This implies that the local susceptibility $\partial \langle \sigma_z \rangle / \partial h$ at the quantum critical point diverges as T^{-s} . Hyperscaling also guarantees an ω/T scaling, $\chi''_{\text{loc}}(\Delta_c, T=0, \omega) \propto |\omega|^{-s} \text{sgn}(\omega)$. Notably, this was found to be the exact decay exponent of the critical spin correlations in the long-range Ising model for all s [29]. Additionally, the exponent ν diverges as $1/\sqrt{2(1-s)}$ near the Ohmic point $s = 1$ [6]. For $0 < s < 1/2$, the transition is mean-field like and critical exponents obey $\delta = 3$ and $\nu = 1/s$ [29, 30]. Hyperscaling is violated. Very recently, using a powerful continuous time cluster Monte Carlo algorithm, Winter *et al.* have shown that the quantum-to-classical mapping is valid in the case of the sub-ohmic spin-boson model [33]. On the other hand, note that the presence of a dangerously irrelevant variable for $s < 1/2$ impedes the correct extraction of the critical exponents with current versions of the NRG method.

In Refs. [5, 31], we have studied in detail the entanglement properties in the sub-ohmic spin-boson model. In particular, for these second-order QPTs, the entanglement entropy exhibits a visible cusp at the quantum critical point and quantum decoherence becomes maximized.

9.1.5 Realizations

The spin-boson model can be realized in noisy charge qubits built of mesoscopic quantum dots or Cooper pair boxes [34, 35]. The gate voltage controls the detuning h and Δ corresponds to the tunneling amplitude between the dot and the lead(s) or the Josephson coupling energy of the junction. If the gate voltage source is placed in series with an external resistor, which can be modelled by a long LC transmission line, this can describe the spin-boson model with Ohmic dissipation [13, 14]. A 1D Luttinger reservoir could also be used [36, 37]. The spin-boson model can also be derived when coupling a quantum dot to a boson and a fermion bath [38]. These nano-systems may allow one to address new and important issues such as the non-equilibrium transport properties at a given QPT [39]. The sub-ohmic case $s = 1/2$ can be engineered through an RLC transmission line. Charge measurements could provide the quantity $\langle \sigma_z \rangle$, which represents the occupation of the dot or island. In a ring geometry, the application of a magnetic flux generates a persistent current which is proportional to $\langle \sigma_x \rangle$ [13, 14]. Solid-state two-level systems usually feature a coupling strength much below $\alpha = 1/2$. A very promising candidate is the ultracold-atomic quantum dot coupled to a Bose-Einstein Condensate (BEC) [40], which allows an unprecedented control of the coupling(s) between

the qubit and the reservoir. The spin-boson model can also be engineered in trapped ions arranged in Coulomb crystals [41].

9.2 Dissipative Spin Array

We proceed to investigate the ground state of a spin array coupled to a large common collection of harmonic oscillators. We intend to show that when the coupling is longitudinal the system can be mapped onto a dissipative quantum Ising model. To simplify the discussion, we consider a 1D channel model for the bath and allow bosons (phonons, sound waves in a BEC, or photons) to propagate along a single direction with wavevector k and dispersion $\omega_k = v k$. More general results are shown in Ref. [42]. Similar to the single spin case, the interaction between the spins and the boson bath reads

$$H_{\text{int}} = \sum_i \sum_k \frac{c_k}{2} e^{ikx_i} (a_k + a_{-k}^\dagger) \sigma_{iz}, \quad (9.21)$$

whereas the boson bath Hamiltonian reads $H_B = \sum_k \omega_k a_k^\dagger a_k$ ($\hbar = 1$). In this equation, x_i corresponds to the position of the spin impurity at site i .

9.2.1 Boson-Mediated Magnetic Interaction

First, we show that an exchange interaction between the spins is induced by the bosonic environment; this is analogous to the Ruderman-Kittel-Kasuya-Yosida interaction induced by a fermionic bath. For this purpose, we set the transverse field $\Delta = 0$. In fact, the spin-boson interaction can be exactly eliminated through a polaronic (unitary) transformation along the lines of the single spin case [1,2]. More precisely, we perform a unitary transformation $V = \exp A = \exp \left(\sum_i \sum_k \frac{1}{2} A_k e^{ikx_i} (a_k - a_{-k}^\dagger) \sigma_{iz} \right)$. The transformed Hamiltonian then takes the general form (where $H = H_{\text{int}} + H_B + \sum_i \frac{\hbar}{2} \sigma_{iz}$):

$$e^{-A} H e^A = H + [H, A] + \frac{1}{2} [[H, A], A] + \dots . \quad (9.22)$$

Then we choose the coefficients $A_k = c_k / w_k$ such that the induced term $[H_B, A]$ exactly cancels H_{int} . On the other hand, the transformed Hamiltonian also produces an effective interaction between spins:

$$\delta H = -\frac{1}{4} \sum_{i,j} \sum_k \frac{c_k^2}{\omega_k} e^{ik(x_i - x_j)} \sigma_{iz} \sigma_{jz}. \quad (9.23)$$

If one envisions a cold atomic spin array coupled to a BEC reservoir, one can check that the factor c_k^2/ω_k is k-independent [42]. Furthermore, we identify

$$\sum_k e^{ik(x_i - x_j)} = \frac{L}{\pi \xi_h} \text{sinc}((x_i - x_j)/\xi_h), \quad (9.24)$$

where $\text{sinc}(x) = \sin(x)/x$, $\xi_h = v/\omega_c$, ω_c represents the ultraviolet cutoff for the sound modes in the BEC, and L denotes the length of the BEC. Notice that the induced interaction decays very rapidly for separations larger than the healing length ξ_h . In a realistic cold atom experiment, the distance between (atomic) quantum dots is of a size comparable to the healing length. Therefore, we can restrict ourselves to nearest-neighbor spin interactions. It should also be noted that the effective interaction $-K < 0$ is ferromagnetic and independent of the length L since $c_k^2/\omega_k \propto 1/L$ [42].

9.2.2 Solvable Dissipative Model

On the other hand, the boson bath is also expected to give rise to long-range correlations in time similar to the single spin case. In fact, to find these long-range correlations in time, it is judicious to integrate out the phonon (sound wave) modes using coherent state functional integrals. At a general level, this produces the following extra term in the action of the spin array [42]:⁵

$$\delta S = -\frac{c_k^2}{4\beta\omega_k} \sum_{k;n=-\infty}^{\infty} \int_0^{\beta} d\tau d\tau' \left(\frac{\omega_k^2 - i\omega_k\Omega_n}{\omega_k^2 + \Omega_n^2} \right) e^{i\Omega_n(\tau-\tau')} \sigma_k(\tau) \sigma_k^*(\tau'), \quad (9.25)$$

where $\beta = (k_B T)^{-1}$, $\sigma_k(\tau) = \sum_j \sigma_{jz}(\tau) e^{ikx_j}$, and $\Omega_n = 2\pi n/\beta$ are Matsubara frequencies. Interestingly, the coupling to the boson bath provides two distinct contributions, which can be identified using the decomposition, $\sigma_k(\tau) \sigma_k^*(\tau') = \frac{1}{2}(\sigma_k(\tau) \sigma_k^*(\tau) + \sigma_k(\tau') \sigma_k^*(\tau')) - \frac{1}{2}(\sigma_k(\tau) - \sigma_k(\tau'))(\sigma_k^*(\tau) - \sigma_k^*(\tau'))$ [1, 2].

The first term which is local in time is dominated by the Matsubara frequency term $n = 0$. This allows us to recover the ferromagnetic Ising contribution δH found above by applying the unitary transformation V .

Now, similar to the case of a single two-level system coupled to a bosonic bath [1, 2], the second (dissipative) contribution stems from the pole at $\omega_k = \mp i\Omega_n$. One can check that the main dissipative contribution is for $i = j$. This term produces an on-site long-range correlation in time $\propto 1/\tau^2$. Note that correlations in space are short-range, as a result of Eq. (9.24), whereas the correlations in time are long-range due to dissipation.

Re-introducing the transverse field Δ , then we find that the spin dynamics

⁵We use the convention σ_k instead of σ_{kz} to save space.

is dictated by the following action [42]:

$$S_{\text{spin}} = - \sum_i \int_0^\beta d\tau \left[\frac{\Delta}{2} \sigma_{ix}(\tau) + \frac{h}{2} \sigma_{iz}(\tau) \right] \quad (9.26)$$

$$\begin{aligned} & - \frac{1}{8} \sum_i \int_0^\beta d\tau d\tau' \alpha(\tau - \tau') \sigma_{iz}(\tau) \sigma_{iz}(\tau') \\ & - K \sum_{i,j} \int_0^\beta d\tau \sigma_{iz}(\tau) \sigma_{jz}(\tau), \\ \alpha(\tau - \tau') & \equiv \frac{1}{\pi} \int_0^\infty d\omega J(\omega) e^{-\omega|\tau - \tau'|}, \end{aligned} \quad (9.27)$$

and the spectral function reads $J(\omega) = \pi \sum_k c_k^2 \delta(\omega - \omega_k)$. In fact, one can establish that $J(\omega) = 2\pi\alpha\omega^d$, where d denotes the dimensionality of the BEC.

Assuming we consider two-state systems close to the degeneracy point $h = 0$, then one recognizes the action of a *dissipative quantum Ising model* [43].

9.2.3 Dissipative ϕ^4 Theory

For $\Delta = 0$ the system is in a ferromagnetic (ordered) phase whereas for large $\Delta \gg K$ the system will be in a paramagnetic (disordered) phase. The non-dissipative quantum Ising model ($\alpha = 0$) exhibits a second order phase transition around $K \sim \Delta$, separating the paramagnetic and ferromagnetic phase, and can be mapped exactly onto the classical Ising model in $d_{\text{eff}} = d+z = d+1$ dimensions; $z = 1$ is the dynamic critical exponent that describes the relative dimensions of (imaginary) time and space. The classical model itself can be described by a ϕ^4 theory. In particular, the quantum Ising chain lies in the universality class of the two-dimensional classical model [44].

When $\alpha > 0$, the critical behaviour is most profoundly changed in the Ohmic case ($d = 1$). First, as a reminiscence of the single two-state system, the bath will renormalize the transverse field as $\Delta_r = \Delta (\Delta/\omega_c)^{\alpha/(1-\alpha)}$ [1, 2], such that the transition occurs at a smaller $K \sim \Delta_r$. Second, for $d = 1$, the dissipation will generate a term $|\omega|(\phi(q, i\omega))^2$ in the effective ϕ^4 theory which will affect the critical exponents and change the universality class of the phase transition.

9.2.4 Critical Exponents

Here, we summarize the main results for the critical exponents. In fact, the latter have been shown to be independent of the value of the parameter α [43, 45] and have been thoroughly derived through a dissipative ϕ^4 theory in $d = (2 - \varepsilon)$ dimensions for $\varepsilon = 1$ [45, 46] and in Monte Carlo simulations [43].

For $d = 1$, due to the dissipative term $|\omega|\phi(q, i\omega)^2$ in the effective O(1) ϕ^4 theory, the dynamic critical exponent is equal to $z \approx 2$, whereas $z = 1$ for

TABLE 9.1 Critical exponents of dissipative quantum Ising models.

Critical Exponents	β	γ	δ	ν	z
Dissipative Quantum Chain	0.319	1.276	~ 5	0.638	1.98
$d = 2$ Quantum Ising model	0.325	1.241	4.82	0.630	1
Non-dissipative Quantum Chain	1/8	7/4	15	1	1

$d = (2, 3)$. Therefore, the 1D dissipative and two-dimensional quantum Ising models should behave similarly, since they have the same dimension $d_{\text{eff}} = d + z \approx 3$. For $d = 1$, the ϕ^4 theory (up to second order in ε) predicts $z \approx 1.98$ [46] which is in accordance with the Monte Carlo simulations [43, 45]. A summary of some critical exponents for the 1D dissipative (quantum) case and the two-dimensional quantum Ising model is presented in Table 9.1. The exponent δ is defined in Sec. 9.1.4. Additionally, $\sigma_{iz} \propto |\Delta - \Delta_c|^\beta$ and $\chi = d\sigma_{iz}/dh \propto |\Delta - \Delta_c|^{-\gamma}$. The correlation length exponent obeys $\nu \approx 0.638$ [43, 45]. In addition, from scaling laws, $\gamma = z\nu \approx 1.276$ [43, 45, 46] and $\beta = \nu/2 \approx 0.319$. One must also satisfy $z = (\delta - 1)/2$.

9.2.5 Realizations

In Ref. [42], we have shown that a spin-boson mixture of cold atoms can be used to engineer the quantum Ising model in a dissipative bath. We emphasize that this setup embodies the first tunable realization of the quantum Ising model in a dissipative bath, and that several critical exponents can be measured using standard imaging techniques. On the other hand, the effect of a (nuclear spin) bath on the QPT of an Ising ferromagnet in a transverse field has been recently addressed experimentally in Ref. [47].

Regarding our spin-boson mixture [42], the first species lies in a deep optical lattice with tightly confining wells and forms a spin array; spin-up (down) corresponds to occupation by one (zero) atom(s) at each site. The second species forms a superfluid reservoir. Different species are coupled coherently via laser transitions and collisions. Whereas the laser coupling mimics a transverse field for the spins, the coupling to the reservoir sound modes induces the ferromagnetic (Ising) coupling as well as dissipation. By measuring the critical exponents, one may confirm that the dissipative phase transition is still of second-order type where they are related by $\beta(\delta - 1) = \gamma$. The order parameter $\langle \sigma_{iz} \rangle$ now must go continuously to zero at a second-order phase transition, in striking contrast to the case of a single two-level system coupled to an Ohmic bath. Finally, for the dissipative spin chain, the value of the dynamic critical exponent can be directly obtained from the equality $z = (\delta - 1)/2 \sim 2$.

Open issues in the field include the entanglement properties as well as the spin dynamics of the dissipative quantum Ising chain. Concerning the last point, progress in this direction has been recently achieved in Ref. [48]. However, the authors have neglected the long-range spin correlations in time induced by the bath, assuming that the bosons have a non-zero inverse lifetime.

9.3 One-Mode Superradiance Model

An ensemble of N two-level atoms interacting with a radiation field has been studied by many authors [49–51]. In the celebrated Dicke model, the atoms are assumed to be at fixed positions within a linear cavity of volume V and the separations between the atoms are large enough so that the interaction among them can be ignored. However, given the fact that the atoms interact with the same radiation field, they cannot be treated as independent. The importance of treating the radiating atoms as a single quantum system was recognized by Dicke [49]. An exact solution for the Hamiltonian of N identical two-level atoms interacting with a single-mode quantized radiation field at resonance was given by Tavis and Cummings [50]. The thermodynamic properties of the system in the limit $N, V \rightarrow +\infty, N/V = \text{const.}$, have been first obtained by Hepp and Lieb [52]. They reveal a second-order classical phase transition. The single-mode Dicke model also admits a second-order QPT [53, 54]. Below, we analyze this second-order QPT.

9.3.1 Hamiltonian

We study the quantum regime of the one-mode superradiance (Dicke) model [49] where collective and coherent behavior of the pseudospins (atoms) is induced by coupling, with interaction λ , to a physically distinct single-boson subsystem. In the following, when we refer to the Dicke model we shall mean the single-mode Hamiltonian unless otherwise stated. With omission of the A^2 term for the electromagnetic field, the Hamiltonian reads [54]

$$H = \omega_s J_z + \omega a^\dagger a + \frac{\lambda}{\sqrt{2j}} (a + a^\dagger) (J_+ + J_-), \quad (9.28)$$

where this form follows from the introduction of a collective spin operator of length $j = N/2$. The resonance condition is $\omega = \omega_s$. The thermodynamic limit of $N \rightarrow +\infty$ is thus equivalent to making $j \rightarrow \infty$. Here, ω_s is the frequency splitting between the atomic levels, ω is the frequency of the field mode, and κ is the dipole coupling strength. In addition, the collective atomic operators satisfy angular momentum commutation relations $[J_+, J_-] = 2J_z$ and $[J_\pm, J_z] = \mp J_\pm$.

The Dicke model is usually considered in the quantum optics approach of the rotating-wave approximation, which is valid for small values of λ , and consists of neglecting the counter-rotating terms $a^\dagger J_+$ and $a J_-$. This makes the model integrable and simplifies the analysis. Below, we follow Emery and Brandes, and derive exact results without the rotating-wave approximation [54]. In the thermodynamic limit $(N, j) \rightarrow \infty$, the system exhibits a QPT at a critical coupling $\lambda_c = \sqrt{\omega\omega_s}/2$, and the system changes from a normal phase to a superradiant one. Superradiance means the decay of an excited population of atoms via spontaneous emission of photons.

In fact, it is instructive to note that the problem reduces to a two-mode problem by using the Holstein-Primakoff transformation [55] of the angular momentum operators $J_z = (b^\dagger b - j)$, $J_+ = b^\dagger \sqrt{2j - b^\dagger b}$, and $J_- = J_+^\dagger$; here, b and b^\dagger represent Bose operators $[b, b^\dagger] = 1$. The Hamiltonian becomes [54]:

$$H = \omega_s(b^\dagger b - j) + \omega a^\dagger a + \lambda(a + a^\dagger) \left(b^\dagger \sqrt{1 - \frac{b^\dagger b}{2j}} + \sqrt{1 - \frac{b^\dagger b}{2j}} b \right). \quad (9.29)$$

9.3.2 Normal Phase

In the normal phase ($\lambda < \lambda_c$), one can expand the square roots and this gives:

$$H_n = \omega_s b^\dagger b - j\omega_s + \omega a^\dagger a + \lambda(a + a^\dagger)(b + b^\dagger). \quad (9.30)$$

This problem of two-coupled harmonic oscillators is exactly solvable. After diagonalizing the problem, one gets two independent effective oscillators:

$$H_n = E_-^{(n)} c_1^\dagger c_1 + E_+^{(n)} c_2^\dagger c_2 + \frac{1}{2} \left(E_+^{(n)} + E_-^{(n)} - \omega - \omega_s \right) - j\omega_s. \quad (9.31)$$

The bosonic operators $(c_1, c_1^\dagger, c_2, c_2^\dagger)$ are linear combinations of the original operators and describe collective atom-field excitations. The energies $E_\pm^{(n)}$ of the two independent oscillator modes take the form [54]:

$$\left(E_\pm^{(n)} \right)^2 = \frac{1}{2} \left(\omega^2 + \omega_s^2 \pm \sqrt{(\omega_s^2 - \omega^2)^2 + 16\lambda^2\omega\omega_s} \right). \quad (9.32)$$

It should be noted that the excitation energy $E_-^{(n)}$ is real only if $\omega^2 + \omega_s^2 \geq \sqrt{(\omega_s^2 - \omega^2)^2 + 16\lambda^2\omega\omega_s}$ implying $\lambda \leq \sqrt{\omega\omega_s}/2 = \lambda_c$. This underlines the fact that H_n is valid only for $\lambda \leq \lambda_c$, i.e., in the normal phase. For large j , the ground state energy is $-j\omega_s$ whereas the excitation energies $E_\pm^{(n)}$ are $\mathcal{O}(1)$.

In the normal phase there is a conserved quantity, parity, which is given by $\Pi = \exp(i\pi N_e)$. Here, $N_e = a^\dagger a + J_z + j$ is the excitation number which counts the total number of excitation quanta in the system and possesses two eigenvalues, ± 1 . After the Holstein-Primakoff transformation, the parity operator becomes $\Pi = \exp(i\pi(a^\dagger a + b^\dagger b))$. In this formulation, there is an apparent analogy with the parity operator of a 2D harmonic operator. The ground state has a positive parity with an even excitation number: this is obvious at $\lambda = 0$ since the excitation number is zero. In addition, as the energy levels in this phase are non-degenerate the continuity of the ground state with increasing λ ensures that it always has positive parity.

9.3.3 Superradiant Phase

In the superradiant phase ($\lambda > \lambda_c$) the field and the atomic ensemble acquire macroscopic occupations; thus one has to redefine the operators via [54]

$$a^\dagger \rightarrow c^\dagger + \sqrt{m}, \quad b^\dagger \rightarrow d^\dagger - \sqrt{n}, \quad (9.33)$$

where m and n are $\mathcal{O}(j)$. The problem can be still diagonalized, and again one obtains a theory of two decoupled oscillators:

$$\begin{aligned} H_s &= E_-^{(s)} e_1^\dagger e_1 + E_+^{(s)} e_2^\dagger e_2 - j \left(\frac{2\lambda^2}{\omega} + \frac{\omega_s^2 \omega}{8\lambda^2} \right) \\ &+ \frac{1}{2} \left[E_+^{(s)} + E_-^{(2)} - \frac{\omega_s \lambda^2}{2\lambda_c^2} \left(1 + \frac{\lambda_c^2}{\lambda^2} \right) - \omega - \frac{2\lambda^2}{\omega} \left(1 - \frac{\lambda_c^2}{\lambda^2} \right) \right]. \end{aligned} \quad (9.34)$$

The expressions for the bosonic creation and annihilation operators ($e_1, e_1^\dagger, e_2, e_2^\dagger$) can be found in Appendix A of Ref. [54] and the oscillator energies obey the relation

$$2 \left(E_\pm^{(s)} \right)^2 = \frac{\omega_s^2}{\mu^2} + \omega^2 \pm \sqrt{\left(\frac{\omega_s^2}{\mu^2} - \omega^2 \right)^2 + 4\omega^2 \omega_s^2}, \quad (9.35)$$

where the parameter μ is given by $\mu = \omega \omega_s / 4\lambda^2 = \lambda_c^2 / \lambda^2$. Again, one can check that the excitation $E_-^{(s)}$ remains real as long as $\lambda > \lambda_c$, and the ground state energy is given by $-j[(2\lambda^2/\omega) + (\omega_s^2 \omega / 8\lambda^2)]$. It is relevant to observe that every level of the total spectrum is doubly degenerate above the phase transition. In particular, one might also define $a^\dagger \rightarrow c^\dagger - \sqrt{m}$, $b^\dagger \rightarrow d^\dagger + \sqrt{n}$, leading to the same energy spectrum. It implies that the symmetry of the ground state defined by the parity operator Π is spontaneously broken at λ_c . Nevertheless, although the global symmetry Π is broken at the phase transition one can define a new operator $\Pi^{(s)} = \exp(i\pi(c^\dagger c + d^\dagger d))$ which commutes with the superradiant Hamiltonian H_s .

The normal phase allows a ferromagnetic ordering for the pseudospins, $\langle J_z \rangle \rightarrow -j$, whereas in the superradiant phase $\langle J_z \rangle$ decreases continuously.

9.3.4 Second-Order Quantum Phase Transition

The excitations of the system are given by the energies E_\pm , which describe collective modes or polaritons in solid-state physics. As the coupling λ approaches λ_c one can observe that $E_-^{(n)} = E_-^{(s)} = 0$, signaling the occurrence of the QPT. In contrast, E_+ tends to the value $\sqrt{\omega_s^2 + \omega^2}$ as $\lambda \rightarrow \lambda_c$ from either direction. In fact, one may identify E_- with the excitation energy of a photon branch and E_+ with the excitation energy of an atomic branch [54]. In addition, for $\lambda \rightarrow \lambda_c$, from either direction one finds $E_- \propto |\lambda_c - \lambda|^{z\nu}$ as $\lambda \rightarrow \lambda_c$, where the dynamic critical exponent reads $z = 2$ and $\nu = 1/4$ is the critical exponent describing the divergence of the characteristic length $\xi = E_-^{-1/2}$. The fact that E_- vanishes at λ_c implies that the Dicke model exhibits a second-order QPT. The entanglement between the atoms and field diverges with the same critical exponent as the characteristic length [56]. Emery and Brandes have also shown that at the QPT the system changes from being quasi-integrable to quantum chaotic [54]. The finite-size scaling exponents of

the Dicke model have been discussed in Ref. [57]. The QPT for the multi-mode (and continuum) case has been discussed in Ref. [58].⁶

9.3.5 Realizations

In familiar quantum-optical systems, the frequencies ω and ω_s exceed the dipole coupling strength by many orders of magnitude. Therefore, the quantum dissipation due to atomic spontaneous emission and cavity loss is usually unavoidable, and the QPT remains unobserved experimentally. On the other hand, the Dicke model in the QPT regime ($\omega_s \approx \omega \approx \lambda$) may be realized based on the collective interaction of an ensemble of atoms with laser fields and field modes of a high-finesse optical resonator. In particular, cavity quantum electrodynamics (QED) [59] might realize the Dicke model with parameters $\omega_s \approx \omega \approx \lambda$ that are adjustable and can in principle exceed all dissipation rates [60]. More precisely, Dimer *et al.* have proposed a well-defined scheme based on multilevel atoms and cavity-mediated Raman transitions to realize a Dicke model in open system dynamics, with omission of the A^2 term [60]. The ensemble of atoms is simultaneously coupled to the quantized field of the optical cavity mode and the classical field of a pair of lasers. In principle, optical light from the cavity carries signatures of the critical behavior. Another scheme based on a superconducting quantum interference device (SQUID) coupled to a high-quality cavity supporting a single-mode photon has also been proposed in Ref. [61].

9.4 Jaynes-Cummings Lattice

Finally, we consider a two-dimensional array of coupled optical cavities, which may be realized in circuit QED for example, each containing a single two-level atom (spin) in the photon-blockade regime. The coupling between the atom and the photons leads to an effective photon-photon repulsion; this photonic repulsion (blockade) has been shown recently by Birnbaum *et al.* using a single trapped atom [62]. Below, we study the resulting Jaynes-Cummings [63] lattice-type model. Following a mean-field theory, first we show that the system at zero temperature can undergo a characteristic Mott insulator (excitations localized on each site) to superfluid (polaritons delocalized across the lattice) QPT [64]. Then, we make a rigorous comparison between the Jaynes-Cummings lattice and the Bose-Hubbard model [65].

⁶Tolkunov and Solenov argue that by adding the A^2 term in the Hamiltonian, one would observe the same transition with a corrected position of the critical point [58].

9.4.1 Hamiltonian

We consider a system composed of a regular array of identical cavities. For a sufficiently large quality factor, we may restrict our treatment to a single photon mode, similar to the Dicke model above. We assume that the finite quality factor only stems from photon leakage κ among nearest-neighbor cavities. The Jaynes-Cummings lattice model then takes the following form [64]:

$$H = \sum_i H_i^{\text{JC}} - \kappa \sum_{\langle i;j \rangle} \left(a_i^\dagger a_j + a_j^\dagger a_i \right) - \mu \sum_i \left(a_i^\dagger a_i + \sigma_i^+ \sigma_i^- \right), \quad (9.36)$$

where we have introduced the Jaynes-Cummings Hamiltonian:⁷

$$H_i^{\text{JC}} = \omega a_i^\dagger a_i + \omega_s \sigma_i^+ \sigma_i^- + \beta (a_i^\dagger \sigma_i^- + \sigma_i^+ a_i). \quad (9.37)$$

The operator a_i (a_i^\dagger) annihilates (creates) one photon in a given cavity at lattice site i . Similarly, σ_i^\pm denotes the Pauli raising and lowering operators for each two-level atom. The bracket notation $\langle i,j \rangle$ denotes summation over nearest neighbor pairs. The phase boundary between a Mott insulator and a superfluid phase can be determined in a grand canonical approach. To this end, a chemical potential μ is introduced. The grand canonical approach considers a situation in which particle exchange with the surrounding is permitted and is used because of its convenience for determining the phase diagram. The boundary between Mott insulator and superfluid phases is determined by the value of μ for which adding or removing a particle does not require energy. In addition, here we work in the limit of the rotating-wave approximation.

9.4.2 Mott Insulator-Superfluid Transition

In the limit $\kappa \rightarrow 0$, called the atomic limit, the Hamiltonian decouples in the site index and reduces to a Jaynes-Cummings Hamiltonian $H_{\kappa=0} = H^{\text{JC}} - \mu n$, where the total excitation number on each site now obeys $n = a^\dagger a + \sigma^+ \sigma^-$. Since H^{JC} and n commute we can write the eigen-energies of $H_{\kappa=0}$ as $\mathcal{E}_{|n\pm\rangle} = E_{|n\pm\rangle} - \mu n$, where the usual eigenenergies of the Jaynes-Cummings Hamiltonian are given by $E_{|n\pm\rangle} = n\omega - \Delta/2 \pm \sqrt{n\beta^2 + \Delta^2/4}$ for $n \geq 1$ and $E_{|0\rangle} = 0$ for the ground state. Here, $\Delta = \omega - \omega_s$ is the detuning between the two-level atom and the resonator frequency. The polariton states $|n\pm\rangle = (|n, \downarrow\rangle \pm |(n-1), \uparrow\rangle)/\sqrt{2}$ are simultaneous eigenstates of the Jaynes-Cummings Hamiltonian and of the polariton number $n = a^\dagger a + \sigma^+ \sigma^-$. For a given n , since the state $|n+\rangle$ is always higher in energy compared to $|n-\rangle$, we can ignore it completely when focusing on ground state properties. The transition from the boundary $|n-\rangle$ to $|(n+1)-\rangle$ occurs when $\mathcal{E}_{|n-\rangle} = \mathcal{E}_{|(n+1)-\rangle}$ ($n = 0, 1, \dots$). Therefore, this implies $(\mu - \omega)/\beta = \sqrt{n + (\Delta/2\beta)^2} - \sqrt{n + 1 + (\Delta/2\beta)^2}$. This reduces to $(\mu - \omega)/\beta = \sqrt{n} - \sqrt{n+1}$ in the resonant case $\omega = \omega_s$. These boundaries separate the different Mott phases for the polaritons (excitations); see

⁷The light-atom coupling β should not be confused with $1/k_B T$.

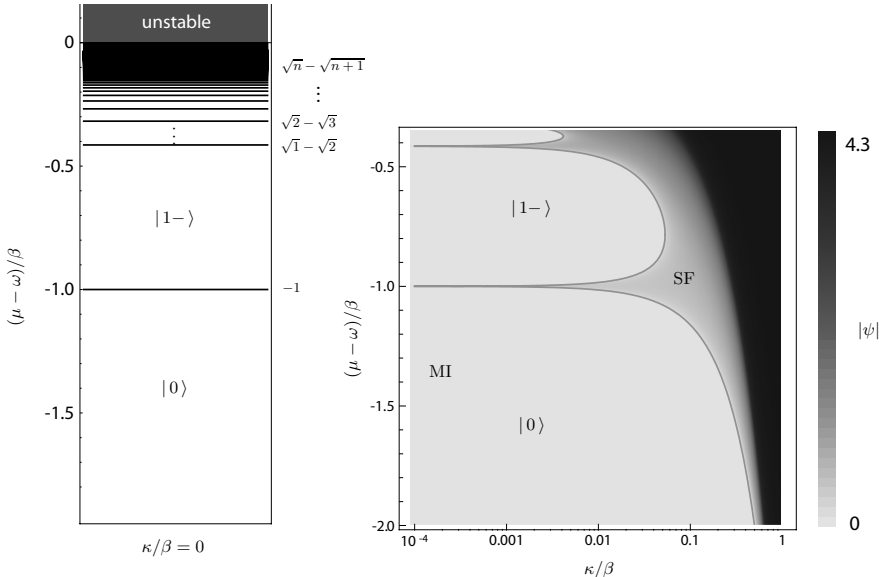
**FIGURE 9.3**(left) Ground state for $\kappa = 0$ and $\Delta = 0$. (right) Mean-field phase diagram.

Fig. 9.3 (left). These results for the atomic limit are consistent with the results of Ref. [64]. By increasing the hopping κ , one expects a second-order QPT from a Mott-insulating (MI) phase to a superfluid phase (SF) of polaritons which can be first described using a mean-field theory.

Introducing the order parameter $\psi = z_c \kappa \langle a_i \rangle$ where z_c is the coordination number of the lattice, the phase boundary between the MI and SF phases can be determined in a way similar to the procedure for the Bose-Hubbard model [66]. In the critical region the ground state energy can be expanded as [65]

$$E_G(\psi) = E_G^{mf} + r|\psi|^2 + \frac{1}{2}u|\psi|^4 + \mathcal{O}(|\psi|^6). \quad (9.38)$$

This represents the standard situation of a quadratic plus quartic potential, ubiquitous in the study of mean-field phase transitions. At the mean-field level, the phase boundary is specified by the condition $r = 0$. In fact, the coefficient r can be expressed as $r = R_n + (z_c \kappa)^{-1}$ where R_n can be obtained from second-order perturbation theory in the photon hopping [64, 65] leading to Fig. 9.3 (right). Recently, a strong-coupling theory for the phase diagram has been developed in Ref. [67], which allows one to include the leading correction due to quantum fluctuations for the phase boundary. The phase boundary is in agreement with Quantum Monte Carlo calculations in two dimensions [68].

9.4.3 Spin-1/2 Mapping for the Polaritons

To make a more concrete analogy with the Bose-Hubbard model, one can build a spin-1/2 mapping for the polaritons between two adjacent Mott lobes. More precisely, the polariton operators are defined [69] as $P_{i,n\alpha}^\dagger = |n\alpha\rangle_i \langle 0-|_i$, where $\alpha = \pm$ and i denotes the site index. Note that these operators do not satisfy the canonical commutation relations of creation and annihilation operators. Now, close to a degeneracy point between two Mott-insulating lobes of polariton occupation numbers $n - 1$ and n , and in the atomic limit $\kappa/\beta \ll 1$, one can build an effective model for low-energy states in this regime from the two relevant product states $|-(n-1)-\rangle^{\otimes j}$ and $|n-\rangle^{\otimes j}$. Within this truncated Hilbert space, the Hamiltonian H_n^{eff} can be rewritten as a spin-lattice XX model. For this purpose, one can introduce spin-1/2 operators $\sigma_i^+ = P_{i,n-}^\dagger P_{i,(n-1)-}$ [69]. Within this definition, one can check that σ_i^+ and its Hermitian conjugate σ_i^- obey standard commutation and anticommutation rules for the Pauli lowering and raising operators [65]. The XX model describing the physics close to the degeneracy points of the Jaynes-Cummings lattice model is given by [65, 69]:

$$H_n^{XX} = \frac{1}{2} (\mathcal{E}_{|n-\rangle} - \mathcal{E}_{|(n-1)-\rangle}) \sum_i \sigma_i^z - \frac{1}{2} \kappa t_n^2 \sum_{\langle i;i' \rangle} (\sigma_i^x \sigma_{i'}^x + \sigma_i^y \sigma_{i'}^y). \quad (9.39)$$

The conversion amplitudes t_n are given in Ref. [65]. This effective description is reminiscent of the Bose-Hubbard model between two Mott lobes.

9.4.4 Field Theory Approach to the Transition

In fact, a field-theory formulation can also be built by analogy to the Bose-Hubbard model [65]. After performing a Hubbard-Stratonovich transformation to decouple the hopping term, one obtains the following effective Lagrangian for the auxiliary fields $\psi^*(x, \tau)$ and $\psi(x, \tau)$, which are proportional to the order parameter $\langle a_i \rangle$ and hence are small in the critical region:

$$\mathcal{L}_{\text{eff}} = K_0 + K_1 \psi^* \frac{\partial \psi}{\partial \tau} + K_2 \left| \frac{\partial \psi}{\partial \tau} \right|^2 + K_3 |\nabla \psi|^2 + \tilde{r} |\psi|^2 + \frac{\tilde{u}}{2} |\psi|^4 \dots . \quad (9.40)$$

As in the case of the Bose-Hubbard model [70, 71], the coefficients \tilde{r} and \tilde{u} can be related to the mean-field coefficients: $\tilde{r} = v^{-1} r$ and $\tilde{u} = v^{-1} u$ where v is the volume per lattice site [65]. To obtain the coefficients K_1 and K_2 one can use the fact that the theory must be invariant under a (time-dependent) $U(1)$ symmetry. Using the gauge symmetry of the action $S_{\text{eff}} = \int_0^\beta d\tau \int d^d x \mathcal{L}_{\text{eff}}$, one then obtains the exact equalities [65]:

$$K_1 = \frac{\partial \tilde{r}}{\partial(\omega - \mu)} \quad \text{and} \quad K_2 = -\frac{1}{2} \frac{\partial^2 \tilde{r}}{\partial(\omega - \mu)^2}. \quad (9.41)$$

Whenever the coefficient K_1 vanishes, the phase transition changes its universality class since the dynamical critical exponent $z = 1$. The physics of these

multicritical points is in complete analogy to the corresponding physics of the Bose-Hubbard model [66, 70, 71]. In contrast, for $K_1 \neq 0$, we have a rather different field theory and the dynamical critical exponent associated with the QPT is $z = 2$.

On the other hand, the Jaynes-Cummings lattice has one additional parameter, the energy scale for the atoms, ω_s . Thus, the phase boundary is a 2D surface in the space spanned by the parameters ω , ω_s , and κ , and the condition $K_1 = 0$ defines curves on the phase boundary, whose position is completely determined by $\partial R_n / \partial \omega|_{\omega_s} = 0$ [65]. For each Mott lobe, there is one such multicritical curve, along which the universality class changes in a similar way to the Bose-Hubbard model. It is interesting to observe that the evidence for these multicritical curves is currently controversial. Schmidt and Blatter [67] have presented evidence for the presence of such multicritical points which is consistent with the results from field theory shown above [65]. However, Zhao *et al.* [68] argue for the absence of such multicritical points based on quantum Monte Carlo simulations. On the other hand, Zhao *et al.* have defined the dynamic critical exponent z from the superfluid stiffness of the photons only, and not of the polaritons; in particular, the photon number cannot be conserved at the lobe-tips.

9.4.5 Realizations

Several candidates have been proposed for an actual realization of the Jaynes-Cummings lattice, ranging from arrays of photonic band-gap cavities to circuit QED systems [72, 73]. A natural candidate system is the microwave strip line resonator for circuit QED [74]. We consider that the realization in circuit QED is especially interesting [65]. Mostly, the basic buildings blocks are well established and show the required Jaynes-Cummings physics [75]. In particular, medium-size arrays (with a number of sites between 10 and 100) should not pose fundamental difficulties, and ideas to prepare the system have been envisioned [69]. First, the system would be prepared in the Mott insulating regime by using a global external microwave signal. Then, the system could cross the phase boundary by varying the detuning Δ , whereas the hopping strength κ is fixed by the fabrication parameters. The realization of this Jaynes-Cummings lattice would share many of the fascinating aspects of ultracold atoms. Finally, a relevant question to address in the future is whether the effect of an additional external drive combined with the presence of dissipation may lead to a change of the universality class of the QPT.

9.5 Conclusion

In this chapter, we have provided a comprehensive and modern investigation of QPTs emerging in spin-boson Hamiltonians. The thermodynamic limit here can be achieved via a large number of bosonic modes resulting in a dissipative environment and/or through a large ensemble of spins (spin array). In the case of a single two-level system coupled to a bosonic dissipative environment, we have summarized recent developments on the computation of observables and spin dynamics for the Ohmic case and we have discussed the QPT in the sub-ohmic case by analogy to Ising spin chains with long-range interactions. Additionally, we have shown that a spin array coupled to the same dissipative bosonic bath via a longitudinal coupling gives rise to a dissipative quantum Ising model which may be engineered in cold atomic systems. On the other hand, the light-atom interaction also results in fascinating QPTs such as the zero-temperature superradiant transition taking place in the Dicke model when tuning the dipole coupling strength λ . The Jaynes-Cummings lattice system comprising an array of optical cavities each containing a single atom also allows one to realize a superfluid-Mott insulator transition for polaritons. The Dicke model and the Jaynes-Cummings lattice may be implemented in QED cavity systems. In this sense, setups of electromagnetic resonators could embody a novel class of quantum simulators of condensed-matter Hamiltonians.

Acknowledgments – We acknowledge C.-H. Chung, Ph. Doucet-Beaupré, W. Hofstetter, A. Imambekov, J. Koch, A. Kopp, M.-R. Li, P. P. Orth, D. Roosen, I. Stanic, M. Vojta, and P. Wölfle for fruitful collaborations. We also thank M. Büttiker, S. Girvin, L. Glazman, D. Goldhaber-Gordon, and G. Zarand for stimulating discussions. The research on entanglement in many-body systems, such as spin-boson systems, is supported by NSF under grant DMR-0803200. We also acknowledge support from NSF through the Center for Quantum Information Physics at Yale (DMR-0653377) and from DOE under grant DE-FG02-08ER46541.

Bibliography

- [1] A. J. Leggett *et al.*, Rev. Mod. Phys. **59**, 1 (1987).
- [2] U. Weiss, *Quantum Dissipative Systems* (World Scientific, Singapore, 2008).
- [3] A. O. Caldeira and A. J. Leggett, Phys. Rev. Lett. **46**, 211 (1981).
- [4] M. Blume, V. J. Emery, and A. Luther, Phys. Rev. Lett. **25**, 450 (1970).

- [5] K. Le Hur, Ann. Phys. (NY) **323**, 2208 (2008).
- [6] M. Vojta, Phil. Mag. **86**, 1807 (2006).
- [7] H. Spohn and R. Dümcke, J. Stat. Phys. **41**, 389 (1985).
- [8] P. W. Anderson, G. Yuval, and D. R. Hamann, Phys. Rev. B **1**, 4464 (1970).
- [9] S. Chakravarty, Phys. Rev. Lett. **49**, 681 (1982).
- [10] A. J. Bray and M. A. Moore, Phys. Rev. Lett. **49**, 1545 (1982).
- [11] F. Guinea, V. Hakim, and A. Muramatsu, Phys. Rev. B **32**, 4410 (1985).
- [12] A. P. Young and T. Bohr, J. Phys. C **14**, 2713 (1981).
- [13] P. Cedraschi, V. V. Ponomarenko, and M. Büttiker, Phys. Rev. Lett. **84**, 346 (2000).
- [14] P. Cedraschi and M. Büttiker, Ann. Phys. (NY) **289**, 1 (2001).
- [15] D. J. Thouless, Phys. Rev. **187**, 732 (1969).
- [16] P. W. Anderson and G. Yuval, J. Phys. C **4**, 607 (1971).
- [17] A. Kopp and K. Le Hur, Phys. Rev. Lett. **98**, 220401 (2007).
- [18] A. Kopp, X. Jia, and S. Chakravarty, Ann. Phys. (NY) **322**, 1466 (2007).
- [19] H. Dekker, Phys. Rev. A **35**, 1436 (1987).
- [20] F. Lesage and H. Saleur, Phys. Rev. Lett. **80**, 4370 (1998).
- [21] D. Roosen, K. Le Hur, and W. Hofstetter, in preparation (unpublished).
- [22] R. Bulla, N.-H. Tong, and M. Vojta, Phys. Rev. Lett. **91**, 170601 (2003).
- [23] R. Bulla, H.-J. Lee, N.-H. Tong, and M. Vojta, Phys. Rev. B **71**, 045122 (2005).
- [24] M.-R. Li, K. Le Hur, and W. Hofstetter, Phys. Rev. Lett. **95**, 086406 (2005).
- [25] F. B. Anders and A. Schiller, Phys. Rev. Lett. **95**, 196801 (2005).
- [26] P. P. Orth, A. Imambekov, and K. Le Hur, in preparation (unpublished).
- [27] H. Wang and M. Thoss, New J. Phys. **10**, 115005 (2008).
- [28] F. J. Dyson, Commun. Math. Phys. **12**, 91 (1969).
- [29] M. E. Fisher, S.-k. Ma, and B. G. Nickel, Phys. Rev. Lett. **29**, 917 (1972).

- [30] E. Luijten and H. W. J. Blöte, Phys. Rev. B **56**, 8945 (1997).
- [31] K. Le Hur, P. Doucet-Beaupré, and W. Hofstetter, Phys. Rev. Lett. **99**, 126801 (2007).
- [32] G. Zaránd and E. Demler, Phys. Rev. B **66**, 024427 (2002).
- [33] A. Winter, H. Rieger, M. Vojta, and R. Bulla, Phys. Rev. Lett. **102**, 030601 (2009).
- [34] Y. Makhlin, G. Schön, and A. Shnirman, Rev. Mod. Phys. **73**, 357 (2001).
- [35] R. J. Schoelkopf *et al.*, arXiv:0210247 (2002).
- [36] K. Le Hur and M.-R. Li, Phys. Rev. B **72**, 073305 (2005).
- [37] A. Furusaki and K. A. Matveev, Phys. Rev. Lett. **88**, 226404 (2002).
- [38] K. Le Hur, Phys. Rev. Lett. **92**, 196804 (2004).
- [39] C.-H. Chung, K. Le Hur, M. Vojta, and P. Wölflé, Phys. Rev. Lett. **102**, 216803 (2009).
- [40] A. Recati *et al.*, Phys. Rev. Lett. **94**, 040404 (2005).
- [41] D. Porras, F. Marquardt, J. von Delft, and J. I. Cirac, Phys. Rev. A **78**, 010101 (2008).
- [42] P. P. Orth, I. Stanic, and K. Le Hur, Phys. Rev. A **77**, 051601(R) (2008).
- [43] P. Werner, K. Völker, M. Troyer, and S. Chakravarty, Phys. Rev. Lett. **94**, 047201 (2005).
- [44] L. Onsager, Phys. Rev. **65**, 117 (1944).
- [45] P. Werner, M. Troyer, and S. Sachdev, J. Phys. Soc. Jpn. **74S**, 67 (2005).
- [46] S. Pankov *et al.*, Phys. Rev. B **69**, 054426 (2004).
- [47] H. M. Ronnow *et al.*, Science **308**, 389 (2005).
- [48] D. Patanè *et al.*, Phys. Rev. Lett. **101**, 175701 (2008).
- [49] R. H. Dicke, Phys. Rev. **93**, 99 (1954).
- [50] M. Tavis and F. W. Cummings, Phys. Rev. **170**, 379 (1968).
- [51] M. O. Scully and W. E. Lamb, Phys. Rev. **159**, 208 (1967).
- [52] K. Hepp and E. H. Lieb, Ann. Phys. (NY) **76**, 360 (1973).
- [53] Y. K. Wang and F. T. Hioe, Phys. Rev. A **7**, 831 (1973).
- [54] C. Emary and T. Brandes, Phys. Rev. Lett. **90**, 044101 (2003).

- [55] T. Holstein and H. Primakoff, Phys. Rev. **58**, 1098 (1940).
- [56] N. Lambert, C. Emery, and T. Brandes, Phys. Rev. Lett. **92**, 073602 (2004).
- [57] J. Vidal and S. Dusuel, Europhys. Lett. **74**, 817 (2006).
- [58] D. Tolkunov and D. Solenov, Phys. Rev. B **75**, 024402 (2007).
- [59] R. Miller *et al.*, J. Phys. B **38**, S551 (2005).
- [60] F. Dimer, B. Estienne, A. S. Parkins, and H. J. Carmichael, Phys. Rev. A **75**, 013804 (2007).
- [61] G. Chen, Z. Chen, and J. Liang, Phys. Rev. A **76**, 055803 (2007).
- [62] K. M. Birnbaum *et al.*, Nature (London) **436**, 87 (2005).
- [63] E. Jaynes and F. W. Cummings, Proc. IEEE **51**, 89 (1963).
- [64] A. D. Greentree, C. Tahan, J. H. Cole, and L. C. L. Hollenberg, Nat. Phys. **2**, 856 (2006).
- [65] J. Koch and K. Le Hur, Phys. Rev. A **80**, 023811 (2009).
- [66] M. P. A. Fisher, P. B. Weichman, G. Grinstein, and D. S. Fisher, Phys. Rev. B **40**, 546 (1989).
- [67] S. Schmidt and G. Blatter, Phys. Rev. Lett. **103**, 086403 (2009).
- [68] J. Zhao, A. W. Sandvik, and K. Ueda, arXiv:0806.3603 (2008).
- [69] D. G. Angelakis, M. F. Santos, and S. Bose, Phys. Rev. A **76**, 031805 (2007).
- [70] S. Sachdev, *Quantum Phase Transitions* (Cambridge University Press, Cambridge, U.K., 1999).
- [71] I. Herbut, *Modern Approach to Critical Phenomena* (Cambridge University Press, Cambridge, U.K., 2007).
- [72] M. Hartmann, G. Brandao, and M. Plenio, Laser & Photon. Rev. **2**, 527 (2008).
- [73] N. Na, S. Utsunomiya, L. Tian, and Y. Yamamoto, Phys. Rev. A **77**, 031803 (2008).
- [74] A. Walraff *et al.*, Nature (London) **431**, 162 (2004).
- [75] R. J. Schoelkopf and S. M. Girvin, Nature (London) **451**, 664 (2008).

10

Topological Excitations in Superfluids with Internal Degrees of Freedom

Yuki Kawaguchi

Department of Physics, University of Tokyo, 7-3-1 Hongo, Bunkyo-ku, Tokyo 113-0033, Japan

Masahito Ueda

Department of Physics, University of Tokyo, 7-3-1 Hongo, Bunkyo-ku, Tokyo 113-0033, Japan

Macroscopic Quantum Control Project, ERATO, JST, Bunkyo-ku, Tokyo 113-8656, Japan

The defining character of a topological object is that it can move and deform freely in space and time, yet retains its identity, characterized by a set of discrete numbers called topological charges. This ability to deform without changing its fundamental character lends a particular importance to the notion of topological excitations that is independent of specific material properties. Such topological excitations are spontaneously generated under classical and quantum phase transitions. This chapter is devoted to an overview of topological excitations with an emphasis on spinor Bose-Einstein condensates (BECs).

Under zero magnetic field, the ground state of a spin-1 BEC has two quantum phases, while that of a spin-2 BEC has three. Indeed, more quantum phases have been predicted for a spin-3 BEC. The classification of these ground-state quantum phases can be made in a coherent manner by a group-theoretic method discussed in [Sec. 10.1](#).

In general, a spinor order parameter varies over space and time, and a question arises as to how to characterize such a complicated spin texture. It turns out that as long as the order parameter belongs to a given manifold, one can classify states such that the states belonging to the same conjugacy class can transform into one another in a continuous manner, whereas those belonging to different classes cannot. This classification can be made using homotopy theory, as shown in [Sec. 10.2](#).

The remaining sections of this chapter are devoted to applications of the general theory to specific examples. [Section 10.3](#) presents a brief overview of typical topological excitations such as vortices, monopoles, and skyrmions. [Section 10.4](#) discusses some of the more recent topics on spinor BECs such

as the Kibble-Zurek mechanism of defect nucleation under a quantum phase transition, and knot solitons. [Section 10.5](#) summarizes the main results of this chapter and discusses some future issues.

10.1 Quantum Phases and Symmetries

10.1.1 Group-Theoretic Characterization of the Order Parameter

A symmetry-breaking phase transition can be understood as the transition in which the symmetry group G of the system at high temperatures is reduced to a subgroup H of G below a *critical* temperature T_c . Here G is a Lie group of transformations that keep the free-energy functional invariant. Below T_c , the full symmetry is broken, but some symmetries remain in general. Let $\psi \in \mathbb{C}^n$ be the n -component order parameter that describes the phase below T_c . Group H , called an isotropy group, is a subgroup of G whose elements constitute symmetry transformations such that

$$H = \{h \in G \mid h\psi = \psi\}. \quad (10.1)$$

In superfluid helium-4, *s*-wave superconductors, and spin-polarized gaseous BECs, the symmetry of the system is the *unitary group* of degree 1, $G = \mathrm{U}(1)$, above T_c and $H = \{\mathbf{1}\}$ below T_c , that is, the symmetry is completely broken below T_c . In systems such as superfluid helium-3 [1], *p*-wave [2, 3] and *d*-wave [4] superconductors, and spinor BECs [5–8], the systems accommodate various continuous and discrete subgroups below T_c , exhibiting a rich variety of phases. In such systems, ground-state quantum phases can be obtained by the following symmetry considerations [9, 10]: (1) list all subgroups H of G ; (2) find an order parameter that is invariant under all $h \in H$ for each H ; and (3) compare energies for the obtained states.

The order parameter for a spin- S system can be described using $2S + 1$ complex functions corresponding to the same number of the internal states. The largest possible symmetry is $GL(2S + 1, \mathbb{C})$; however, the actual symmetry of the system G is reduced due to interactions.

The energy functional has a gauge symmetry as a consequence of the conservation of the total number of particles. When the magnetic dipole-dipole interaction can be ignored, the two-body interaction conserves the total spin, and the interaction has rotational symmetry in spin space. Hence the full symmetry group of the Hamiltonian for a spinor BEC is given by the direct product of $\mathrm{U}(1)$ for the gauge symmetry and the special orthogonal group $\mathrm{SO}(3)$ for the spin-rotational symmetry, i.e.,

$$G = \mathrm{U}(1)_\phi \times \mathrm{SO}(3)_S, \quad (10.2)$$

where subscripts ϕ and \mathbf{S} stand for the gauge and spin, respectively. If an external magnetic field is applied in the z direction, G is reduced to

$$G_B = \mathrm{U}(1)_\phi \times \mathrm{U}(1)_{S_z}. \quad (10.3)$$

The subgroups of G are classified into continuous and discrete groups as follows.

Continuous symmetries. The only continuous subgroup of $\mathrm{SO}(3)$ is $\mathrm{SO}(2)$. When the symmetry axis is the z axis, an infinitesimal transformation $h \in H$ can be expressed as

$$h = e^{-iS_z\delta_z}e^{i\delta_\phi} \simeq 1 - iS_z\delta_z + i\delta_\phi, \quad (10.4)$$

where δ_z and δ_ϕ are real infinitesimals, and S_z is the z -component of the spin operator. The eigenstate of S_z with eigenvalue m is invariant under spin rotation $e^{-iS_z\phi}$ followed by gauge transformation $e^{im\phi}$. This combined symmetry is known as *continuous spin-gauge symmetry*, and denoted as $\mathrm{U}(1)_{S_z+m\phi}$. As will be discussed in Sec. 10.2, the spin-gauge symmetry relates spin textures to a supercurrent.

Discrete symmetries. Let the operator $C_{n\Omega}$ denote a $2\pi/n$ rotation about the direction Ω . It can be expressed in terms of spin operator \mathbf{S} as

$$C_{n\Omega} \equiv \exp \left[-i \frac{2\pi}{n} \mathbf{S} \cdot \frac{\Omega}{|\Omega|} \right]. \quad (10.5)$$

The elements of the point groups of $\mathrm{SO}(3)$ can be expressed as a combination of the following operations:

- *Cyclic group C_n* : the group of rotations about the z axis through $2\pi k/n$, where $k = 1, 2, \dots, n-1$. There is only one generator for this group, $\{C_{nz}\}$.
- *Dihedral group D_n* : the group consisting of C_{nz} and an additional rotation through π about an axis, say the x axis, orthogonal to the z axis. The generators are given by $\{C_{nz}, C_{2x}\}$.
- *Tetrahedral group T* : the point group of the tetrahedron with generators given by $\{C_{2z}, C_{3,x+y+z}\}$.
- *Octahedral group O* : the point group of the octahedron (cube) with generators given by $\{C_{4z}, C_{3,x+y+z}, C_{2,x+y}\}$.
- *Icosahedral group Y* : the point group of the icosahedron. There are six axes of the fifth order, ten of the third, and fifteen of the second.

The state that is invariant under transformation $h = C_{n\Omega}e^{i\phi}$ can be obtained by solving the following eigenvalue equation:

$$C_{n\Omega}\psi = \lambda\psi, \quad \lambda = e^{-i\phi}. \quad (10.6)$$

If the eigenvalue λ is 1, the gauge symmetry is completely broken and the eigenstate is invariant under a spin rotation only. On the other hand, eigenstates with $\lambda \neq 1$ are invariant under simultaneous discrete transformations in spin and gauge. Such symmetry is called *discrete spin-gauge symmetry*. The order parameter with a discrete symmetry is given as a simultaneous eigenstate of a set of generators of the corresponding discrete group. For example, if there is a simultaneous eigenstate of C_{2z} and $C_{3,x+y+z}$, then the state has tetrahedral symmetry. This is the case for the cyclic phase of a spin-2 spinor BEC.

10.1.2 Symmetries and Order Parameters of Spinor BECs

Following the above procedure, we investigate possible states in spin-1 and 2 spinor BECs in the absence of an external magnetic field. The phase diagrams of these systems were obtained by minimizing the mean-field energy [5–8], and all the quantum phases can be obtained by the symmetry considerations. The results in the presence of an external magnetic field are discussed in Ref. [11].

10.1.2.1 Spin-1

A spin-1 BEC can be described by a three-component spinor $\psi = (\psi_1, \psi_0, \psi_{-1})^T$, where T denotes the transpose and subscripts 1, 0, -1 refer to the magnetic sublevels. The spin matrices in this basis are given by

$$S_x = \frac{1}{\sqrt{2}} \begin{pmatrix} 0 & 1 & 0 \\ 1 & 0 & 1 \\ 0 & 1 & 0 \end{pmatrix}, \quad S_y = \frac{i}{\sqrt{2}} \begin{pmatrix} 0 & -1 & 0 \\ 1 & 0 & -1 \\ 0 & 1 & 0 \end{pmatrix}, \quad S_z = \begin{pmatrix} 1 & 0 & 0 \\ 0 & 0 & 0 \\ 0 & 0 & -1 \end{pmatrix}. \quad (10.7)$$

The spin-1 BEC has two quantum phases: ferromagnetic (F) and polar (P) phases. Both phases have continuous symmetries [5, 6]:

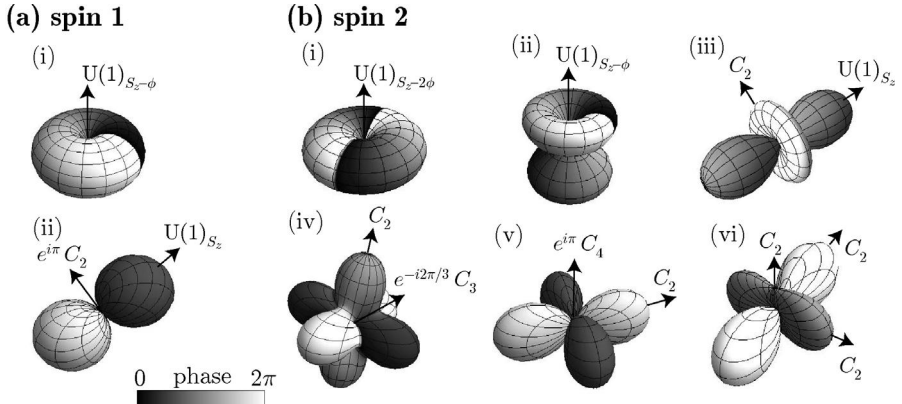
$$\psi_F = \sqrt{\rho} (1, 0, 0)^T \quad (\text{ferromagnetic phase}) \quad (10.8)$$

$$\psi_P = \sqrt{\rho} (0, 1, 0)^T \quad (\text{polar phase}) \quad (10.9)$$

where ρ is the number density of atoms. While ψ_F has a continuous spin-gauge symmetry, i.e., $H_F = U(1)_{S_z+\phi}$, ψ_P has discrete symmetry $C_{2x}e^{i\pi}$ as well as the continuous symmetry $U(1)_{S_z}$. Therefore its isotropy group is $H_P = (\mathcal{D}_\infty)_{S_z, \phi}$.

Another candidate for the ground-state order parameter obtained from symmetry considerations is $\psi = \sqrt{\rho} (\cos \chi, 0, \sin \chi)^T$, where χ is a real number. This state has the combined spin-gauge two-fold symmetry about the z axis. However, by requiring that the free energy be minimal, we find that χ must be either 0 (ferromagnetic phase) or $\pi/2$ (polar phase).¹ Quantum phases which

¹The order parameter $(1, 0, 1)^T/\sqrt{2}$ describes a polar BEC since it is obtained by the $\pi/2$ -rotation of ψ_P about the x axis. See also Eq. (10.13).

**FIGURE 10.1**

Order parameters for (a) $S = 1$ and (b) $S = 2$ spinor BECs. Shown are the surface plots of the amplitude of the order parameter $\Psi \equiv \sum_m \psi_m Y_{Sm}(\hat{s})$, where $Y_{Sm}(\hat{s})$ are rank- S spherical harmonics in spin space. The gray scale on the surface represents $\arg \Psi$. The continuous and discrete symmetry axes are indicated together with the gauge transformation factor. The state (ii) of the spin-2 case is stationary but cannot be the ground state.

TABLE 10.1

Isotropy groups H , generators, and order parameters for spin-1 BECs.

H	generators	ψ	phase
(i) $U(1)_{S_z+\phi}$	$\{e^{i\phi} e^{-iS_z\phi}\}$	$(1, 0, 0)$	ferromagnetic
(ii) $(D_\infty)_{S_z,\phi}$	$\{e^{-iS_z\phi}, e^{i\pi} C_{2x}\}$	$(0, 1, 0)$	polar

have two-fold symmetry arise in the presence of the magnetic field for both ferromagnetic and polar interactions [11–13].

The results for spin-1 BEC are summarized in Table 10.1, and the profile of each order parameter is shown in Fig. 10.1 (a).

10.1.2.2 Spin-2

The results for spin-2 BECs are summarized in Table 10.2 and the profile of each order parameter is shown in Fig. 10.1 (b). Quantum phases (i)–(iii) in Table 10.2 have continuous symmetries, while quantum phases (iv)–(vi) have discrete symmetries. The ferromagnetic (i), uniaxial nematic (iii), cyclic (iv), and biaxial nematic (v, vi) states can be the ground state in certain parameter regimes, where the uniaxial nematic and biaxial nematic I and II states are all degenerate and they are regarded as belonging to the same phase

TABLE 10.2

Isotropy groups, generators, and order parameters for spin-2 BECs, where UN and BN stand for uniaxial nematic and biaxial nematic, respectively.

H	generators	ψ	phase
(i) $U(1)_{S_z+2\phi}$	$\{e^{i2\phi}e^{-iS_z\phi}\}$	$(1, 0, 0, 0, 0)$	ferromagnetic
(ii) $U(1)_{S_z+\phi}$	$\{e^{i\phi}e^{-iS_z\phi}\}$	$(0, 1, 0, 0, 0)$	(unstable)
(iii) $(D_\infty)_{S_z}$	$\{e^{-iS_z\phi}, e^{i\pi}C_{2x}\}$	$(0, 0, 1, 0, 0)$	UN
(iv) $T_{S,\phi}$	$\{C_{2z}, e^{i\frac{2\pi}{3}}C_{3,x+y+z}\}$	$(i, 0, \sqrt{2}, 0, i)$	cyclic
(v) $(D_4)_{S_z,\phi}$	$\{e^{i\pi}C_{4z}, C_{2x}\}$	$(1, 0, 0, 0, 1)$	BN I
(vi) $(D_2)_S$	$\{C_{2z}, C_{2x}\}$	$(\frac{a}{\sqrt{2}}, 0, b, 0, \frac{a}{\sqrt{2}})$	BN II

at the mean field level.² State (ii) cannot be a global minimum for any set of parameters. The symmetries of the ground-state quantum phases of spin-2 BECs are exactly the same as those in d -wave superconductors [4, 9]. The quantum phases with lower symmetries appear in the presence of an external field [11].

10.1.3 Order-Parameter Manifold

We have thus far described the order parameter by fixing the symmetry axis. However, all states which are operated by $g \in G$ are also degenerate. Such a degenerate space is called the *order-parameter manifold* and is expressed as the following coset space:

$$R = G/H. \quad (10.10)$$

The isotropy group H describes the remaining symmetries; thus the coset space R characterizes the broken symmetries.

A general form of $g \in G$ is composed of gauge transformation $e^{i\phi}$ and spin rotation $U(\alpha, \beta, \gamma) \equiv e^{-iS_z\alpha}e^{-iS_y\beta}e^{-iS_z\gamma}$, where α, β , and γ are Euler angles. For a spin-1 system, $U(\alpha, \beta, \gamma)$ is given by

$$U(\alpha, \beta, \gamma) = \begin{pmatrix} e^{-i(\alpha+\gamma)} \cos^2 \frac{\beta}{2} & -\frac{e^{-i\alpha}}{\sqrt{2}} \sin \beta & e^{-i(\alpha-\gamma)} \sin^2 \frac{\beta}{2} \\ \frac{e^{-i\gamma}}{\sqrt{2}} \sin \beta & \cos \beta & -\frac{e^{i\gamma}}{\sqrt{2}} \sin \beta \\ e^{i(\alpha-\gamma)} \sin^2 \frac{\beta}{2} & \frac{e^{i\alpha}}{\sqrt{2}} \sin \beta & e^{i(\alpha+\gamma)} \cos^2 \frac{\beta}{2} \end{pmatrix}. \quad (10.11)$$

²The parameters a and b in the biaxial nematic II state are arbitrary real numbers satisfying $a^2 + b^2 = 1$, since the energy for this state is independent of them. For the same reason, the energies for the uniaxial nematic and biaxial nematic I and II states are all degenerate.

TABLE 10.3

Coset space for various quantum phases of spin-1 and spin-2 spinor BECs.

spin-1	R	spin-2	R
ferromagnetic	$\text{SO}(3)_{S,\phi}$	ferromagnetic	$\frac{\text{SO}(3)_{S,\phi}}{(\mathbb{Z}_2)_{S,\phi}}$
polar	$\frac{\text{U}(1)_\phi \times S_S^2}{(\mathbb{Z}_2)_{S,\phi}}$	uniaxial nematic	$\frac{\text{U}(1)_\phi \times S_S^2}{(\mathbb{Z}_2)_S}$
		biaxial nematic I	$\frac{\text{U}(1)_\phi \times \text{SO}(3)_S}{(D_4)_{S,\phi}}$
		cyclic	$\frac{\text{U}(1)_\phi \times \text{SO}(3)_S}{T_{S,\phi}}$

The general order parameter of a spin-1 ferromagnetic state is given by

$$\psi_F = e^{i\phi} U(\alpha, \beta, \gamma) \sqrt{\rho} \begin{pmatrix} 1 \\ 0 \\ 0 \end{pmatrix} = \sqrt{\rho} e^{i(\phi-\gamma)} \begin{pmatrix} e^{-i\alpha} \cos^2 \frac{\beta}{2} \\ \frac{1}{\sqrt{2}} \sin \beta \\ e^{i\alpha} \sin^2 \frac{\beta}{2} \end{pmatrix}. \quad (10.12)$$

The linear combination $\phi - \gamma$ in Eq. (10.12) reflects the continuous spin-gauge symmetry, i.e., the equivalence between phase change and spin rotation. The physically different configurations of ψ_F are given by the full range of the parameter set $(\alpha, \beta, \gamma - \phi)$. Consequently, the order-parameter manifold is $R_F = \text{SO}(3)_{S,\phi}$.

The general order parameter of a spin-1 polar state is given by

$$\psi_P = e^{i\phi} U(\alpha, \beta, \gamma) \sqrt{\rho} \begin{pmatrix} 0 \\ 1 \\ 0 \end{pmatrix} = \sqrt{\rho} e^{i\phi} \begin{pmatrix} -\frac{e^{-i\alpha}}{\sqrt{2}} \sin \beta \\ \cos \beta \\ \frac{e^{i\alpha}}{\sqrt{2}} \sin \beta \end{pmatrix}. \quad (10.13)$$

Here, ψ_P is independent of γ , which reflects the $\text{U}(1)_{S_z}$ symmetry. The order parameter is expressed with ϕ and the direction of the spin quantization axis is given by $\mathbf{d} = (\cos \alpha \sin \beta, \sin \alpha \sin \beta, \cos \beta)$. The manifold for \mathbf{d} constitutes a unit sphere called 2-sphere S^2 . Since ψ_P is invariant under the simultaneous transformations of ϕ and \mathbf{d} as $(\phi, \mathbf{d}) \rightarrow (\phi + \pi, -\mathbf{d})$, a direct product of S^2 for \mathbf{d} and $\text{U}(1)$ for ϕ covers the order-parameter manifold twice. Therefore, $R_P = (S_S^2 \times \text{U}(1)_\phi)/(\mathbb{Z}_2)_{S,\phi}$. The order-parameter manifolds for various quantum phases of spin-2 BECs are summarized in Table. 10.3.

10.2 Homotopy Classification of Defects

Homotopy theory classifies topological objects according to whether two objects can be transformed into each other in a continuous manner. If they can,

they belong to the same homotopy class; if they cannot, they belong to different homotopy classes. This section provides a brief introduction to homotopy theory for understanding topological excitations in superfluid systems. Most of the materials treated here can be found in standard references [1, 14, 15].

Let us consider a situation in which the system is described by a scalar order parameter $\psi(\mathbf{r}) = |\psi(\mathbf{r})|e^{i\phi(\mathbf{r})}$ and has a vortex. We map phase $\phi(\mathbf{r})$ of the order parameter at each point \mathbf{r} on a real-space loop such as A or B in Fig. 10.2 onto point P on a unit circle called 1-sphere S^1 (right circle in Fig. 10.2). If the loop does not encircle the vortex, the phase of the order parameter may change as we circumnavigate the loop, but eventually returns to the original value without covering the entire circle. If the loop encircles a vortex, point P traces the entire circle n times, where n is the winding number of the vortex. Thus the number of times P covers S^1 as we make a full circuit of the loop defines the topological charge n . For loop A, $n = 0$, while for loop B, n is equal to the winding number of the vortex. If two topological excitations have the same topological charge, they can transform into each other in a continuous manner. If they have different charges, they cannot. We may use this fact to classify the topological excitations.

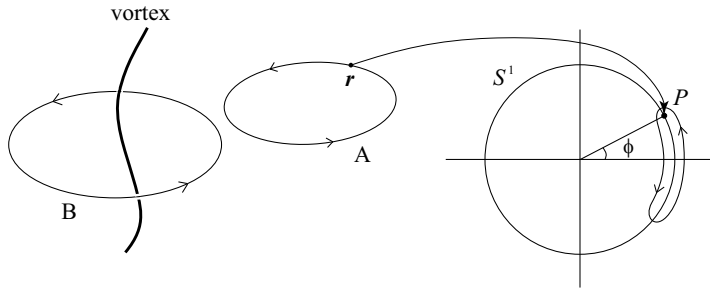


FIGURE 10.2

Mapping from a loop in real space onto the order-parameter manifold S^1 according to the correspondence $\phi(\mathbf{r}) : \mathbf{r} \rightarrow \phi(\mathbf{r}) = \arg \psi(\mathbf{r})$. This mapping defines the first homotopy group $\pi_1(S^1)$.

The above example illustrates how the order parameter $\psi(\mathbf{r})$ defines the mapping from real space \mathbf{r} onto the order-parameter manifold $R = G/H$. In the above case, $G = U(1) \cong S^1$ and $H = 1$; therefore $R = S^1$. If we consider a loop in real space, the mapping defines the first homotopy group $\pi_1(R)$, also known as the fundamental group. When the order-parameter space is S^1 as in the above example, we have

$$\pi_1(S^1) = \mathbb{Z}, \quad (10.14)$$

where \mathbb{Z} denotes the additive group of integers. The first homotopy group

classifies line defects such as quantized vortices in superconductors and superfluids, dislocation in crystals, disclination in liquid crystals, and dysgyration of the orbital angular momentum field in superfluid helium-3. The identity element $0 \in \mathbb{Z}$ stands for nonsingular configurations of the order-parameter field, while the addition law of elements of $\pi_1(R)$ describes the coalescence or disintegration of linear defects.

When we enclose an object with a two-dimensional sphere Σ and consider a mapping from a point r on the sphere onto the order-parameter manifold R , we obtain the second homotopy group $\pi_2(R)$. For example, if the order parameter is the direction of the Heisenberg spin, R constitutes a unit sphere called 2-sphere S^2 (Fig. 10.3), and $\pi_2(S^2)$ is equal to the additive group of integers:

$$\pi_2(S^2) = \mathbb{Z}. \quad (10.15)$$

The second homotopy group of this type classifies point defects such as monopoles.

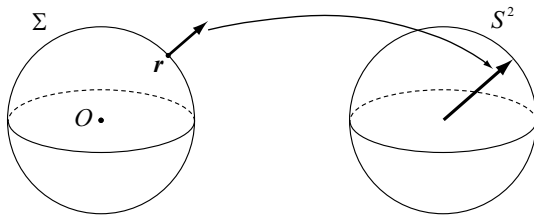


FIGURE 10.3

Mapping from a two-dimensional sphere Σ in real space onto a 2-sphere S^2 in the order-parameter manifold. This mapping defines the second homotopy group $\pi_2(S^2)$.

The third homotopy group $\pi_3(R)$ classifies the mapping from the entire three-dimensional real space onto R under the condition that the order parameter at spatial infinity is uniform, i.e., takes on the same value in every direction at spatial infinity. This assumption allows us to identify all infinite points and regard the entire space as a three-dimensional sphere, just as we can obtain a two-dimensional sphere by identifying infinite points on a plane. The third homotopy group describes particle-like solitons such as skyrmions and knots. In the same way, the first and second homotopy group also describe planar and linear solitons, respectively. The correspondence of the topological objects and homotopy groups are summarized in [Table 10.4](#).

TABLE 10.4

Homotopy classification of defects and solitons.

π_n	defects	solitons
π_0	domain walls	
π_1	vortices	nonsingular domain walls
π_2	monopoles	2D skyrmions
π_3		skyrmions, knots

Here we list some useful formulae for homotopy groups:

$$\pi_n(S^m) = \begin{cases} \mathbb{Z} & \text{if } m = n \geq 1; \\ I & \text{if } m > n \geq 1; \\ I & \text{if } m = 1 \text{ and } n \geq 2; \\ \mathbb{Z} & \text{if } m = 2 \text{ and } n = 3 \text{ (Hopf charge);} \\ \mathbb{Z}_2 & \text{if } n = m + 1 \geq 4 \text{ or } n = m + 2 \geq 4. \end{cases} \quad (10.16)$$

Let G be a Lie group and H be its subgroup. Provided that G is both connected (i.e., $\pi_0(G) = 0$) and simply connected (i.e., $\pi_1(G) = 0$), the following useful isomorphisms hold:

$$\pi_2(G/H) = \pi_1(H), \quad (10.17)$$

$$\pi_1(G/H) = \pi_0(H). \quad (10.18)$$

As a corollary, when $G = \mathrm{SU}(2)$ and $H = \mathrm{U}(1)$, we obtain

$$\pi_2(\mathrm{SU}(2)/\mathrm{U}(1)) = \pi_1(\mathrm{U}(1)) = \mathbb{Z}. \quad (10.19)$$

Some order-parameter spaces R and their first, second, and third homotopy groups are summarized in [Table 10.5](#). For example, for spin-1 ferromagnetic BECs, $\pi_1(\mathrm{SO}(3)) \cong \mathbb{Z}_2$ implies two types of linear defects, which are singular and nonsingular; $\pi_2(\mathrm{SO}(3)) \cong 0$ implies the absence of point defects; and $\pi_3(\mathrm{SO}(3)) \cong \mathbb{Z}$ implies the presence of a nonsingular soliton-like object such as a Shankar monopole, which is, in fact, a skyrmion [16, 17].

10.3 Topological Excitations

Topological excitations belonging to π_1 , π_2 , and π_3 are referred to as line defects and planar solitons, point defects and linear solitons, and particle-like solitons, respectively. The most familiar topological defect is an integer vortex that arises when the order-parameter manifold is $\mathrm{U}(1)$. This order parameter is realized for superfluid helium-4 or spin-polarized atomic BECs. The first homotopy group is $\pi_1(\mathrm{U}(1)) = \mathbb{Z}$ and the system, in principle, can possess integer vortices whose circulation is quantized in units of the quantum unit of

TABLE 10.5

List of homotopy groups, where $\mathbb{R}P^n$ is the n -dimensional projective space, Q and T are the quaternion group and the tetrahedral group, respectively, and T^* is the binary tetrahedral group which is a subgroup of $SU(2)$ [18].

	R	π_1	π_2	π_3
planar spin, scalar BEC	$U(1) \cong S^1$	\mathbb{Z}	0	0
Heisenberg spin	S^2	0	\mathbb{Z}	\mathbb{Z}
nematics	$\mathbb{R}P^2 \cong \frac{S^2}{\mathbb{Z}_2}$	\mathbb{Z}_2	\mathbb{Z}	\mathbb{Z}
biaxial nematics	$\frac{SU(2)}{Q}$	Q	0	\mathbb{Z}
spin-1 ferromagnetic BEC	$SO(3)_{S,\phi} \cong \mathbb{R}P^3_{S,\phi}$	\mathbb{Z}_2	0	\mathbb{Z}
spin-1 polar BEC	$\frac{S^2_S \times U(1)_\phi}{(\mathbb{Z}_2)_{S,\phi}}$	\mathbb{Z}	\mathbb{Z}	\mathbb{Z}
spin-2 cyclic BEC	$\frac{SO(3)_S \times U(1)_\phi}{T_{S,\phi}}$	$\mathbb{Z} \times T^*$	0	\mathbb{Z}

circulation $\kappa = h/M$, where M is an atomic mass. All higher homotopies for this system are zero and the system cannot possess other nontrivial topological excitations. In contrast, spinor BECs can host various types of topological excitation. In this section, we will present some typical examples of spinor BECs for each homotopy group.

10.3.1 Line Defects

10.3.1.1 Nonquantized Circulation

The circulation of the superfluid velocity is not quantized in ferromagnetic BECs due to the continuous spin-gauge symmetry. The general superfluid current density \mathbf{j} for a spinor BEC described by the order parameter ψ_m is given by

$$\mathbf{j} = \frac{\hbar}{2Mi} \sum_m [\psi_m^* \nabla \psi_m - (\nabla \psi_m^*) \psi_m]. \quad (10.20)$$

Substituting Eq. (10.12) into Eq. (10.20) yields

$$\mathbf{j}_F = \frac{\hbar\rho}{M} [\nabla(\phi - \gamma) - \cos\beta \nabla\alpha] \equiv \rho \mathbf{v}_s^F. \quad (10.21)$$

A crucial observation here is that the mass current depends on the spatial derivative of the direction of the expectation value of spin $\mathbf{F} = \sum_{mn} \psi_m^* \mathbf{S}_{mn} \psi_n = \rho(\cos\alpha \sin\beta, \sin\alpha \sin\beta, \cos\beta)$, where \mathbf{S} is a vector of spin-1 matrices (10.7). Therefore, if the direction of the spin varies over space, a supercurrent will be induced.

In the case of a scalar BEC, the superfluid velocity \mathbf{v}_s is proportional to

the phase gradient of the order parameter, and is irrotational, i.e., $\nabla \times \mathbf{v}_s = 0$. However, this is not the case with the ferromagnetic BEC. In fact, it can be shown from Eq. (10.21) that

$$\nabla \times \mathbf{v}_s^F = \frac{\hbar}{M} \sin \beta (\nabla \beta \times \nabla \alpha). \quad (10.22)$$

What makes $\nabla \times \mathbf{v}_s^F$ nonvanishing is the contribution from the Berry phase. To see this, we rewrite Eq. (10.21) as

$$\mathbf{v}_s^F - \frac{\hbar}{M} (1 - \cos \beta) \nabla \alpha = \frac{\hbar}{M} \nabla (\phi - \gamma - \alpha)$$

and integrate both sides along a closed contour C . Due to the single-valuedness of the order parameter, the integral of $\nabla(\phi - \gamma - \alpha)$ should be an integer multiple of 2π . Hence, we obtain

$$\oint_C \mathbf{v}_s^F \cdot d\ell - \frac{\hbar}{M} \oint_C (1 - \cos \beta) \nabla \alpha \cdot d\ell = \frac{\hbar}{M} n \quad (n : \text{integer}). \quad (10.23)$$

The term $\oint_C (1 - \cos \beta) \nabla \alpha \cdot d\ell$ gives the Berry phase enclosed by contour C . Thus, in the ferromagnetic BEC, the circulation alone is not quantized, but the difference between the circulation and the Berry phase is quantized.

The first homotopy group of the ferromagnetic phase of a spin-1 BEC is \mathbb{Z}_2 (see Table 10.5) which implies the existence of only two types of vortices: a vortex with a removable singularity and one with an irremovable singularity. An example of the order parameter for the former case is obtained by taking $\phi - \gamma \rightarrow -\varphi$ and $\alpha \rightarrow \varphi$ with φ being the azimuthal angle around a vortex in Eq. (10.12):

$$\psi_F = \sqrt{\rho} \begin{pmatrix} e^{-2i\varphi} \cos^2 \frac{\beta}{2} \\ \frac{e^{-i\varphi}}{\sqrt{2}} \sin \beta \\ \sin^2 \frac{\beta}{2} \end{pmatrix}. \quad (10.24)$$

While the circulation for $\beta = 0$ is 2κ , it vanishes as we change β from 0 to π . That is, a doubly quantized vortex in the $m = 1$ component can deform continuously to a nonsingular spin texture via a spin rotation. The other type of vortex is a stable *polar-core vortex*. The order parameter outside the vortex core can be obtained by taking $\phi - \gamma \rightarrow 0$ and $\alpha \rightarrow \varphi$ in Eq. (10.12) as

$$\psi_F^{\text{polar-core}} = \sqrt{\rho} \begin{pmatrix} e^{-i\varphi} \cos^2 \frac{\beta}{2} \\ \frac{1}{\sqrt{2}} \sin \beta \\ e^{i\varphi} \sin^2 \frac{\beta}{2} \end{pmatrix}. \quad (10.25)$$

At the vortex core, the $m = \pm 1$ components have to vanish and all atoms are condensed in the $m = 0$ state, i.e., the vortex core is filled with the polar state. In this case, it is impossible to continuously remove the singularity, because the coefficients of the $m = \pm 1$ components cannot simultaneously be zero while keeping the form of Eq. (10.25).

10.3.1.2 Fractional Vortices

Fractional vortices can appear when the order parameter has multiple components with spin-gauge coupled discrete symmetry. Let us illustrate this by considering the polar phase of a spin-1 BEC. Following the definition of the supercurrents in Eq. (10.20), the superfluid velocity for the polar phase is given by the gradient of the overall phase ϕ as $\mathbf{v}_s^P = (\hbar/M)\nabla\phi$, and therefore its circulation is quantized. Note here that the polar order parameter has a two-fold symmetry and changes sign upon spin inversion, as explained below Eq. (10.13). Figure 10.4 shows a situation in which the order parameter undergoes spin inversion as one circumnavigates the vortex. With such a spin configuration, the single-valuedness of the order parameter is satisfied if the gauge angle ϕ changes by π as one makes a complete circuit. Since this phase change is one half of the usual phase change of 2π , the circulation is one half of κ . Therefore, this vortex is called a *half-quantum vortex*, which is also referred to as an *Alice vortex* from the context of cosmology. Since the vortex line is the singularity in the polar state, the core of the half-quantum vortex is locally magnetized. In general, the circulation of the system can take on an integer multiple of $\kappa/2$, in agreement with the fact that the first homotopy group of the polar phase is \mathbb{Z} (see Table 10.5).

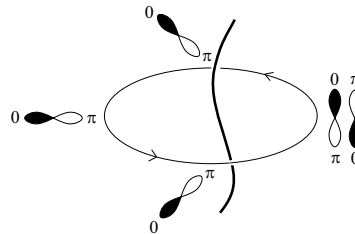


FIGURE 10.4

Half-quantum vortex of the polar phase of a spin-1 BEC. The order parameter rotates through angle π about the horizontal axis as one circumnavigates the vortex. To satisfy the single-valuedness of the order parameter, this rotation must be accompanied by a phase change of π , resulting in a half-quantum vortex.

The cyclic phase of a spin-2 BEC can exhibit a one-third vortex [18, 19]. Figure 10.1(b)(iv) illustrates the profile of the order parameter, where the phase of each lobe is $0, 2\pi/3$, and $4\pi/3$. Consider a situation in which this order parameter is rotated through $2\pi/3$ about the C_3 axis as one makes a circuit of a closed contour. The phase of the order parameter then changes by $-2\pi/3$. The single-valuedness of the order parameter is satisfied if the overall gauge angle changes by $2\pi/3$ during the rotation. Since this phase change is one third of 2π , the system possesses a $1/3$ vortex.

10.3.2 Point Defects

10.3.2.1 't Hooft-Polyakov Monopole (Hedgehog)

The order-parameter manifold R_P of the polar phase of a spin-1 BEC is given in [Table 10.3](#). It has the second homotopy group $\pi_2(R_P) = \mathbb{Z}$ and can possess a point defect. To investigate this, we rewrite the order parameter (10.13) as

$$\psi_P = \sqrt{\frac{\rho}{2}} e^{i\phi} \begin{pmatrix} -d_x + id_y \\ \sqrt{2}d_z \\ d_x + id_y \end{pmatrix}, \quad (10.26)$$

where the unit vector \mathbf{d} is defined below Eq. (10.13). The spherical monopole called a *hedgehog* is obtained by setting $\phi = 0$ and

$$\mathbf{d}(\mathbf{r}) = \frac{\mathbf{r}}{|\mathbf{r}|}. \quad (10.27)$$

In this case, the second homotopy group is isomorphic to $\pi_2(S^2)$ and the topological charge for this hedgehog structure can be expressed in terms of the following surface integral:

$$n_2 = \frac{1}{8\pi} \int \sum_{ijk} \epsilon_{ijk} d_i (\nabla d_j \times \nabla d_k) \cdot dS. \quad (10.28)$$

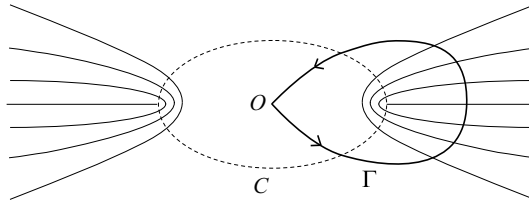
It is straightforward to show that the topological charge for the hedgehog configuration (10.27) is given by $n_2 = 1$.

The 't Hooft-Polyakov monopole is shown to be energetically unstable against deformation into the *Alice ring*, a ring of a half-quantum (Alice) vortex [20]. We consider a situation in which a half-quantum vortex closes upon itself (see dotted loop C in [Fig. 10.5](#)), where the order parameter is singular along C . Although only two disclinations are depicted in Fig. 10.5, the distribution of the actual order-parameter field is such that the pattern of the disclination rotates around the origin O along contour C . Therefore if the system is seen far from the origin, the order-parameter field resembles that of a monopole with $n_2 = 1$. However, if we consider a contour Γ along a closed path starting from the origin, we have the circulation $n_1 = 1$ in units of $\kappa/2$. Therefore, this topological object, known as the Alice ring, cannot be regarded as a simple monopole but rather as a combined object characterized by $n_1 = 1$ along any contour Γ stretching from the origin and $n_2 = 1$ on a sphere that is far away from the origin. The Alice ring was predicted to be realized in an optically trapped spin-1 ^{23}Na BEC [20].

10.3.2.2 Dirac Monopole

The Dirac monopole was originally envisaged as a magnetic analogue of the quantized electric charge:

$$\nabla \cdot \mathbf{B} = 4\pi g\delta(\mathbf{r}), \quad (10.29)$$

**FIGURE 10.5**

Alice ring comprised of continuously distributed half-quantum (Alice) vortices along a contour C . Far from the origin, it resembles a monopole with topological charge $n_2 = 1$.

where g denotes the strength of the magnetic monopole. The solution of this equation is easily found to be $\mathbf{B} = gr/r^3$. The corresponding vector potential is given by

$$\mathbf{A} = -\frac{g}{r(r-z)}(-y, x, 0) = -\frac{g(1 + \cos\theta)}{r \sin\theta} \mathbf{e}_\varphi, \quad (10.30)$$

where (r, θ, φ) are the polar coordinates and \mathbf{e}_φ is the unit vector along the φ direction. The vector potential (10.30) reproduces the magnetic field (10.29), except on the positive z axis (i.e., $\theta = 0$), along which the magnetic field shows a singularity called a Dirac string:

$$\mathbf{B} = \nabla \times \mathbf{A} = g \frac{\mathbf{r}}{r^3} - 4\pi g \delta(x) \delta(y) \theta(z) \mathbf{e}_z, \quad (10.31)$$

where \mathbf{e}_z is the unit vector along the z direction.

A spinor configuration similar to the Dirac monopole can be created in the ferromagnetic phase of a spin-1 BEC [21]. Taking $\phi - \gamma \rightarrow -\varphi$, $\alpha \rightarrow \varphi$, and $\beta \rightarrow \theta$ in Eq. (10.12), we obtain

$$\psi_F = \sqrt{\rho} \begin{pmatrix} e^{-2i\varphi} \cos^2 \frac{\theta}{2} \\ \frac{e^{-i\varphi}}{\sqrt{2}} \sin \theta \\ \sin^2 \frac{\theta}{2} \end{pmatrix}. \quad (10.32)$$

The corresponding superfluid velocity defined by Eq. (10.21) takes the same form as the vector potential (10.30) of the Dirac monopole with the identification $g = \hbar/M$. The second homotopy group corresponding to this order parameter is $\pi_2(\text{SO}(3)) = 0$, which means that monopoles in a ferromagnetic spinor BEC are not stable topological objects, as in the case of Dirac monopoles in gauge theory.

10.3.3 Particle-like Solitons

The third homotopy group classifies topological objects that extend over the entire three-dimensional space. The ferromagnetic BEC supports such

an object because $\pi_3(\mathrm{SO}(3)) = \mathbb{Z}$. The class- n element of $\pi_3(\mathrm{SO}(3)) = \mathbb{Z}$ may be realized in the following manner. We impose the boundary condition that the order parameter takes on the same value at spatial infinity, say $\psi(\infty) = (1, 0, 0)^T$, so that the three-dimensional real space is compactified to S^3 . The order parameter at position \mathbf{r} is obtained by rotating $\psi(\infty)$ about the direction [16, 17, 22]

$$\Omega(\mathbf{r}) = \frac{\mathbf{r}}{r} f(r) n, \quad n \in \mathbb{Z}, \quad (10.33)$$

through angle $f(r)n$, i.e., $\psi(\mathbf{r}) = e^{-i\Omega(\mathbf{r}) \cdot \mathbf{S}} \psi(\infty)$. Here $f(r)$ satisfies $f(\infty) = 0$ to meet the above boundary condition and $f(0) = 2\pi$ to avoid a singularity at the origin.

This object is sometimes called a *Shankar monopole*; however, from a topological point of view, this object should be classified by the third, as opposed to second, homotopy group. Therefore it is, in fact, a skyrmion. The case of $n = 1$ is displayed in Fig. 10.6.

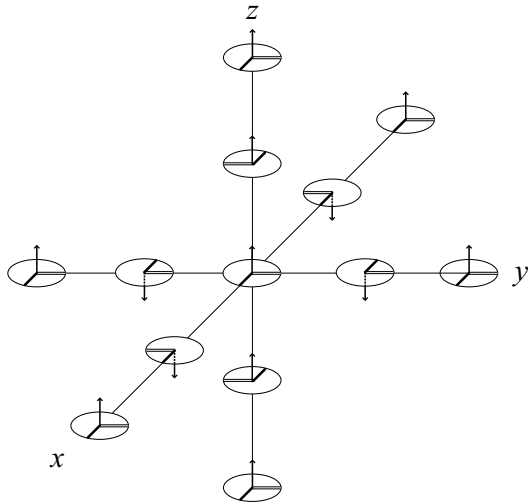


FIGURE 10.6

Shankar monopole with charge 1 in a spin-1 ferromagnetic BEC, where each arrow denotes the direction of the expectation value of the spin, or the $U(1)$ symmetry axis, and the thick solid and double lines on the disk correspond to the direction of $\arg \Psi = 0$ and that of $\pi/2$, respectively, where $\Psi \equiv \sum_m \psi_m(\mathbf{r}) Y_{Sm}(\hat{s})$.

The polar phase of a spin-1 BEC supports a different type of a particle-like soliton. The order-parameter manifold involves a subspace S^2 , whose third homotopy group gives $\pi_3(S^2) = \mathbb{Z}$. The corresponding topological object is called a knot to be described later.

10.4 Special Topics

Spinor BECs have many quantum phases that possess different symmetries depending on atomic spins and interactions, and each of the phases can accommodate various types of topological excitations. In addition, direct observation of topological excitations is possible. For example, a group at Berkeley observed spontaneous formation of spin textures and spin vortices [23]. It is also possible to tune various experimental parameters with high accuracy. Therefore, a spinor BEC is an ideal testing ground for investigating topological excitations. This section discusses recent topics on spinor BECs of ultracold atomic gases: spontaneous defect formation in quenched BEC (Sec. 10.4.1) and new types of topological excitation (Sec. 10.4.2).

10.4.1 The Kibble-Zurek Mechanism

Topological excitations are spontaneously produced in a symmetry-breaking phase transition. The scenario of topological defect formation, known as the Kibble-Zurek (KZ) mechanism [24, 25], is as follows: spontaneous symmetry breaking in phase transitions can produce local domains of an order parameter; if these domains are separated by a great distance such that they are causally disconnected, the local domains initially grow independently and produce topological defects when they overlap.

The ferromagnetic phase transition in a spin-1 ^{87}Rb BEC also exhibits the KZ mechanism, where the quantum phase transition can be triggered by magnetic field quenching [23, 26–28]. The ground state phase is determined by the competition between ferromagnetic energy $E_{\text{ferro}} = \frac{c_1}{2}|\mathbf{F}|^2$ and quadratic Zeeman interaction $E_q = \sum_{m=0,\pm 1} q m^2 |\psi_m|^2$, where $\mathbf{F} = \sum_{mn} \psi_m^* \mathbf{S}_{mn} \psi_n$ is the spin density with \mathbf{S} being a vector of spin-1 matrices (10.7), and $c_1 < 0$ and $q \propto B^2 > 0$ for a spin-1 ^{87}Rb BEC. When q is larger than the critical value $q_c = 2|c_1|\rho$ with ρ being the number density, the ground state is the polar phase $\psi_P = (0, \sqrt{\rho}, 0)^T$. Although ψ_P remains stationary even below q_c , it becomes unstable due to the ferromagnetic interaction. The ground state for $q < q_c$ is the broken-antisymmetry (BA) phase given by [13]

$$\psi_{\text{BA}} = \sqrt{\rho} \begin{pmatrix} e^{-i\alpha} \sqrt{1-Q}/2 \\ \sqrt{(1+Q)/2} \\ e^{i\alpha} \sqrt{1-Q}/2 \end{pmatrix}, \quad (10.34)$$

where $Q = q/q_c$. While the polar phase has no magnetization, the BA phase has transverse magnetization $F_+ \equiv F_x + iF_y = e^{i\alpha} \sqrt{1-Q^2}$. Therefore, starting from a polar phase at $q > q_c$, the $\text{SO}(2)$ symmetry corresponding to the direction of the transverse magnetization spontaneously breaks at $q = q_c$, forming spin vortices.

Bogoliubov analysis provides a quantitative description of this phase tran-

sition. The Bogoliubov spectrum for the spin wave in the polar state is given by³

$$E_{\mathbf{k}} = \sqrt{\left(\frac{\hbar^2 k^2}{2M} + q\right) \left(\frac{\hbar^2 k^2}{2M} + q + 2c_1\rho\right)}. \quad (10.35)$$

When $E_{\mathbf{k}}$ is imaginary, the corresponding modes are dynamically unstable and grow exponentially. Since $c_1 < 0$ and $q > 0$ for spin-1 ^{87}Rb atoms, an exponential growth occurs for $q < q_c$, in agreement with the phase boundary.

[Figure 10.7](#) shows the time evolution of the quench dynamics in a two-dimensional disk where the external field is suddenly decreased to (a) $q = 0$ and (b) $q_c/2$. The final value of q determines the domain size and consequently the number of spin vortices. Here we define spin winding number w as

$$w = \frac{1}{2\pi} \oint_{C(R)} \frac{F_- \nabla F_+ - F_+ \nabla F_-}{2i|F_+|^2} \cdot d\ell = \frac{1}{2\pi} \oint \nabla \alpha \cdot d\ell \quad (10.36)$$

where $C(R)$ is a circle of radius R and w is the number of rotations of the spin vector in the x - y plane along $C(R)$. [Fig. 10.8](#) shows the R dependence of the ensemble average of $w^2(R)$. It should be noted that $\langle w^2(R) \rangle_{\text{avg}}$ is proportional to R for large R as expected from the KZ theory, while it is proportional to R^2 for small R . This R^2 dependence is due to the fact that the probability for a spin vortex to be in the circle is proportional to πR^2 .

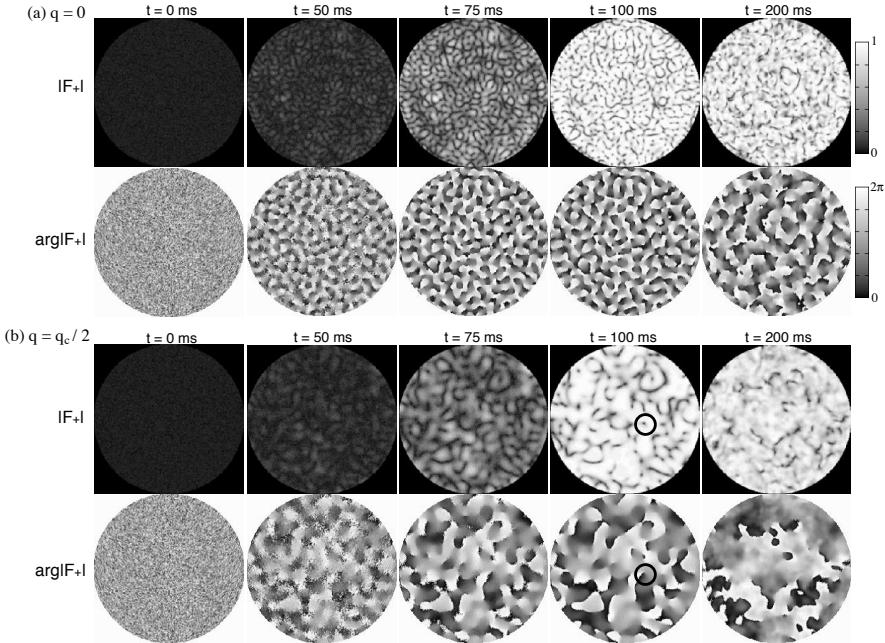
When the final value of q is small enough for the quadratic Zeeman energy to be neglected, spontaneous magnetization grows in such a manner that the total magnetization in the whole system is conserved. One might think that there is a long-range correlation on the scale of the system size and inquire as to how the conservation law is compatible with the KZ postulate of independent growth of magnetization. For small values of q , small magnetic domains are aligned so as to cancel out the local spin when averaged over the correlation length; however, they are independent of each other over a greater length scale.

10.4.2 Knot Soliton

Topological objects are conjectured to play important roles in the formation of the Universe. Among them, knot solitons have aroused the interest of cosmologists since Faddeev and Niemi suggested that knots might exist as stable solitons in a three-dimensional classical field theory [29]. Here we show that knots of spin textures can be created and observed in the polar phase of a spin-1 BEC [30].

Knots are different from such topological excitations, as vortices, monopoles, and skyrmions, in that knots are classified by the linking number,

³The Bogoliubov spectrum can be obtained by linear perturbation of the mean-field theory.

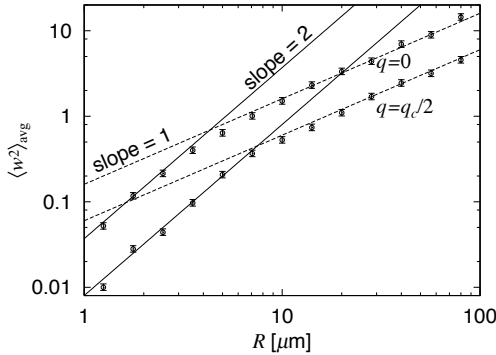
**FIGURE 10.7**

Spontaneous magnetization following the quench from $q > q_c$ to $q < q_c$. Shown is the time development of magnetization $|F_+|$ (upper) and its direction $\arg(F_+)$ (lower) for (a) $q = 0$ and (b) $q = q_c/2$. The black circles indicate the location of a topological defect. Reprinted from Ref. [26].

while the others are classified by the winding number. Knots are characterized by mappings from a three-dimensional sphere S^3 to S^2 . As discussed in Sec. 10.2, the S^3 domain is prepared by imposing a boundary condition that the order parameter takes on the same value in every direction at spatial infinity. Although the order-parameter manifold $R_P = (S^2_S \times U(1)_\phi)/(\mathbb{Z}_2)_{S,\phi}$ for the polar phase is complicated, neither $U(1)$ nor \mathbb{Z}_2 symmetry contributes to homotopy groups in spaces higher than one dimension. Consequently, we have $\pi_3(R_P) \cong \pi_3(S^2) = \mathbb{Z}$. The associated integer topological charge Q is known as the Hopf charge:

$$Q = \frac{1}{4\pi^2} \int d^3x \epsilon_{ijk} \mathcal{F}_{ij} \mathcal{A}_k, \quad (10.37)$$

where $\mathcal{F}_{ij} = \partial_i \mathcal{A}_j - \partial_j \mathcal{A}_i = \mathbf{d} \cdot (\partial_i \mathbf{d} \times \partial_j \mathbf{d})$ [29]. Note that the domain \mathbf{r} is three-dimensional, while the target space \mathbf{d} is two-dimensional. Consequently, the pre-image of a point on target S^2 constitutes a closed loop in S^3 . Furthermore, the Hopf charge is interpreted as the linking number of these loops. If the \mathbf{d}

**FIGURE 10.8**

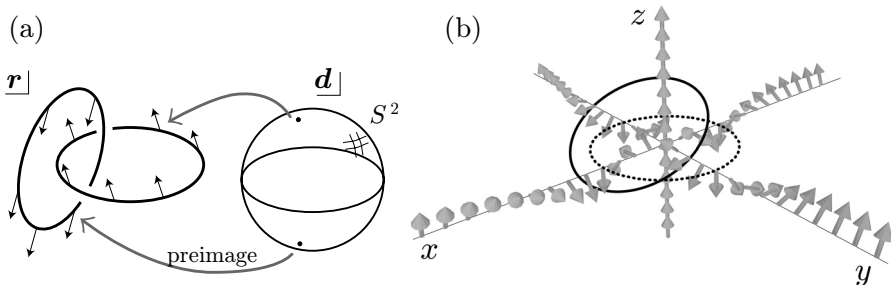
The system size R dependence of the variance of the spin winding number $w(R)$ for instantaneous quench of the magnetic field to $q = 0$ and to $q = q_c/2$. The dashed and dotted lines are, respectively, proportional to R and R^2 . Reprinted from Ref. [26].

field has Hopf charge Q , two loops corresponding to the pre-images of any two distinct points on the target S^2 will be linked Q times [see Fig. 10.9 (a)]. Figure 10.9 (b) shows an example of the \mathbf{d} field of a polar BEC with Hopf charge 1.⁴

Next, we show that knots can be created by manipulating an external magnetic field. In the presence of such a field, the linear Zeeman effect causes the Larmor precession of \mathbf{d} , while \mathbf{d} tends to become parallel to the field because of the quadratic Zeeman effect. Suppose that we prepare an optically trapped BEC in the $m = 0$ state, i.e., $\mathbf{d} = (0, 0, 1)^T$, by applying a uniform magnetic field in the z direction. Then, we suddenly turn off the uniform field and switch on a quadrupole field. The linear Zeeman effect causes \mathbf{d} to rotate around the local magnetic field resulting in the dynamic formation of knots.

Figure 10.10 shows the dynamics of creation of knots in an optical trap subject to the quadrupole field, where the upper panels show the snapshots of the pre-images of $\mathbf{d} = -\hat{z}$ and $\mathbf{d} = \hat{x}$ and the bottom panels show cross sections of the density for the $m = -1$ component on the x - y plane. The density pattern in the $m = -1$ component is the signature of the knots; a double-ring pattern appears that corresponds to one knot. As the \mathbf{d} field winds in the dynamics, the number of rings increases. This prediction can be tested by a Stern-Gerlach-type experiment after slicing the BEC.

⁴Strictly speaking, the configuration in Fig. 10.9 is an *unknot*, since the pre-image of one point on S^2 forms a simple ring and unknotted.

**FIGURE 10.9**

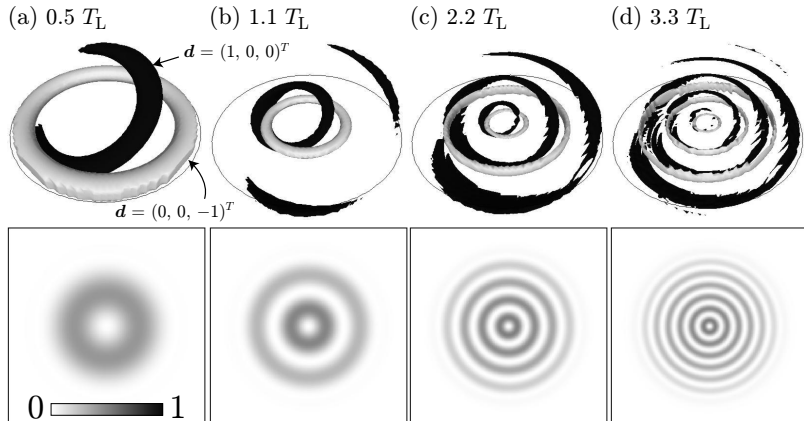
(a) Pre-images of two distinct points on S^2 forming a link. (b) Spin configuration of a knot with the linking number 1 in a polar BEC, where the arrows show the \mathbf{d} field of the polar phase. The solid and dashed lines trace the point where \mathbf{d} points to x and $-z$, respectively, forming a link. Reprinted from Ref. [30].

10.5 Conclusion and Discussion

In this chapter, we have discussed the general properties of ordered states and topological excitations, introducing several examples and recent topics relating to spinor BECs. We applied homotopy theory to describe topological objects in a system of superfluid helium-3 and liquid crystals [14, 15]. Superfluid helium-3 is often referred to as a testing ground to simulate our Universe, because it can accommodate various topological excitations similar to those known in gauge-field theory. The variety of topological excitations in spinor BECs is as rich as that in superfluid helium-3. The great advantage of spinor BECs is that direct observation and manipulation of the topological excitations are possible, while complicated analysis is required when using superfluid helium-3 if one is to identify a topological excitation from nuclear magnetic resonance (NMR) signals. The controllability of spinor BECs would stimulate our imagination, thereby promoting further developments in the study of topological excitations in superfluid systems.

The Kibble-Zurek (KZ) mechanism explains defect-formation dynamics in symmetry-breaking phase transition. The conventional KZ scenario treats only one kind of vortex. A straightforward extension is the case in which the condensate can accommodate various kinds of elementary vortices. Moreover, in a three-dimensional system, topological excitations belonging to different homotopy classes are expected to be generated simultaneously in the phase transition. The interactions among these excitations are highly nontrivial and may affect subsequent dynamics.

When non-Abelian vortices are spontaneously created in a quantum phase

**FIGURE 10.10**

Dynamics of the creation of knots in a spherical optical trap under a quadrupole magnetic field. Snapshots of the pre-images of $\mathbf{d} = (0, 0, -1)^T$ and $\mathbf{d} = (1, 0, 0)^T$ (top), as well as cross sections of the density for the $m = -1$ component on the x - y plane (bottom). Reprinted from Ref. [30].

transition, the scaling law of the KZ mechanism is expected to change qualitatively since spontaneously created vortices forms a new vortex when they collide [31], called a *rung*. The turbulence of non-Abelian vortices also raises several interesting questions. The cascade process, based on reconnection of vortices, is topologically prohibited for non-Abelian vortices. A dramatic change such as the network of the rung is expected to occur for quantum turbulence in non-Abelian vortices.

Another interesting topic is the core structure of vortices and monopoles in spinor BECs. In superfluid helium-4, the superfluid density must vanish at a vortex core. However, in the case of superfluids with internal degrees of freedom there are some alternate possibilities; for example, the vortex core in the spin-1 ferromagnetic BEC can be filled with a polar state and vice versa. In general, the core structure of vortices and monopoles is nontrivial, but is expected to have remaining symmetry [32]. It is in such cases where the relative homotopy theory is expected to play a major role.

Acknowledgments – We acknowledge Hiroki Saito and Michikazu Kobayashi for useful discussions. MU acknowledges the Aspen Center of Physics where part of this work was done.

Bibliography

- [1] D. Vollhardt and P. Wölfle, *The Superfluid Phases of Helium 3* (Taylor & Francis, 1990).
- [2] G. E. Volovik and L. P. Gorkov, Zh. Eksp. Teor. Fiz. **88**, 1412 (1985) [Sov. Phys. JETP **61**, 843 (1985)].
- [3] M. Ozaki, K. Machida, and T. Ohmi, Prog. of Theor. Phys. **74**, 221 (1985).
- [4] N. D. Mermin, Phys. Rev. A **9**, 868 (1974).
- [5] T.-L. Ho, Phys. Rev. Lett. **81**, 742 (1998).
- [6] T. Ohmi and K. Machida, J. Phys. Soc. Jpn. **67**, 1822 (1998).
- [7] C. V. Ciobanu, S.-K. Yip, and T.-L. Ho, Phys. Rev. A **61**, 033607 (2000).
- [8] M. Ueda and M. Koashi, Phys. Rev. A **65**, 063602 (2002).
- [9] C. Bruder and D. Vollhardt, Phys. Rev. B **34**, 131 (1986).
- [10] S.-K. Yip, Phys. Rev. A **75**, 023625 (2007).
- [11] M. Ueda and Y. Kawaguchi, arXiv:1001.2072.
- [12] J. Stenger, S. Inouye, D. M. Stamper-Kurn, H.-J. Miesner, A. P. Chikkatur, and W. Ketterle, Nature **396** 345 (1998).
- [13] K. Murata, H. Saito, and M. Ueda, Phys. Rev. A **75**, 013607 (2007).
- [14] N. D. Mermin, Rev. Mod. Phys. **51**, 591 (1979).
- [15] V. P. Mineev, *Topologically Stable Defects and Solitons in Ordered Media* (Harwood Academic Publishers, Australia, 1998, 1998).
- [16] R. Shankar, J. Phys. **38**, 1405 (1977).
- [17] G. E. Volovik and V. P. Mineev, Zh. Eksp. Teor. Fiz. **73**, 767 (1977) [Sov. Phys. JETP **46**, 401 (1977)].
- [18] G. W. Semenoff and F. Zhou, Phys. Rev. Lett. **98**, 100401 (2007).
- [19] H. Mäkelä, Y. Zhang, and K.-A. Suominen, J. Phys. A **36**, 8555 (2003); H. Mäkelä, J. Phys. A **39**, 7423 (2006).
- [20] J. Ruostekoski and J. R. Anglin, Phys. Rev. Lett. **91**, 190402 (2003).
- [21] C. M. Savage and J. Ruostekoski, Phys. Rev. A **68**, 043604 (2003).

- [22] U. A. Khawaja and H. Stoof, *Nature* **411**, 918 (2001).
- [23] L. E. Sadler, J. M. Higbie, S. R. Leslie, M. Vengalattore, and D. M. Stamper-Kurn, *Nature* **443**, 312 (2006).
- [24] T. W. B. Kibble, *J. Phys. A* **9**, 1387 (1976).
- [25] W. H. Zurek, *Nature* **317**, 505 (1985).
- [26] H. Saito, Y. Kawaguchi, and M. Ueda, *Phys. Rev. A* **76**, 043613 (2007).
- [27] A. Lamacraft, *Phys. Rev. Lett.* **98**, 160404 (2007).
- [28] M. Uhlmann, R. Schützhold, and U. R. Fischer, *Phys. Rev. Lett.* **99**, 120407 (2007).
- [29] L. Faddeev and A. J. Niemi, *Nature* **387**, 58 (1997).
- [30] Y. Kawaguchi, M. Nitta, and M. Ueda, *Phys. Rev. Lett.* **100**, 180403 (2008).
- [31] M. Kobayashi, Y. Kawaguchi, M. Nitta, and M. Ueda, *Phys. Rev. Lett.* **103**, 115301 (2009).
- [32] M. Kobayashi, Y. Kawaguchi, and M. Ueda, arXiv:0907.3716.

11

Quantum Monte Carlo Studies of the Attractive Hubbard Hamiltonian

Richard T. Scalettar

Physics Department, University of California, Davis, California 95616, U.S.A.

George G. Batrouni

INLN, Université de Nice - Sophia Antipolis, CNRS; 1361 route des Lucioles, 06560 Valbonne, France

Originally introduced almost fifty years ago, the Hubbard Hamiltonian,

$$H = -t \sum_{\langle ij \rangle} (c_{i\sigma}^\dagger c_{j\sigma} + c_{j\sigma}^\dagger c_{i\sigma}) + U \sum_i (n_{i\uparrow} - \frac{1}{2})(n_{i\downarrow} - \frac{1}{2}) - \mu \sum_i (n_{i\uparrow} + n_{i\downarrow}), \quad (11.1)$$

has been widely, and very successfully, used to model many-body effects and quantum phase transitions (QPTs) in condensed matter, despite the simplifications it embodies [1–4]; see also Chap. 1. The Hamiltonian, given by Eq. (11.1), contains a kinetic energy term t which describes the hopping of two sets of fermionic particles, labeled by σ , on near-neighbor sites $\langle ij \rangle$ of the lattice.¹ These fermions feel an interaction energy U if they occupy the same site, a term written here in a symmetric form which makes chemical potential $\mu = 0$ correspond to half-filling $\rho = \langle \sum_\sigma n_{i\sigma} \rangle = 1$ at any value of t, U or temperature T , as long as the lattice is bipartite. Many different geometries have been studied, including 1D chains, 2D square, triangular, and honeycomb structures, and 3D cubic lattices.

The Hubbard Hamiltonian neglects the full richness of solid state systems: multiple orbitals and Coulomb coupling between them, defects, lattice vibrations (phonons), and so on. It is remarkable that it seems nevertheless potentially to embody many of the qualitative features of complex materials. Unfortunately, except in 1D, the Hubbard Hamiltonian is not exactly soluble;

¹It is conventional to select $t = 1$ so that energies and temperatures are measured in units of t . Contact can be made with specific physical systems as follows: suppose one were considering a solid, like the cuprate superconductors, which has 2D square-lattice layers of electronic bandwidth $W \sim 1$ eV. Then using the $U = 0$ bandwidth $W = 8t$ one infers $t = 1/8$ eV $\sim 1500^\circ\text{K}$, so that $T/t = 0.1$ ($\beta t = 10$) corresponds to $T = 150^\circ\text{K}$.

so these tantalizing hints that it might provide correct insight into correlation effects in solids cannot be rigorously proven. Recently, ultracold atoms on optical lattices have offered the prospect of systems which are more accurate representations of the Hubbard Hamiltonian, and hence the possibility of doing experiments and theoretical work on precisely the same system.

In the repulsive case, $U > 0$, the interaction term of the Hubbard Hamiltonian suppresses double occupancy, leading to local moment formation (occupation of sites \mathbf{i} by a single species). At half-filling, $\rho = 1$, each site is occupied and the fermions are unable to move without paying the energy cost U . A Mott insulator results. Generically, insulating behavior occurs only when U is sufficiently large, but in some cases, like the square lattice, even for small U a spin density wave instability leads to long range order and opens a gap. Much of the interest in the repulsive Hubbard model arises from the belief that it may exhibit charge inhomogeneities (stripes) and d -wave superconducting order when doped away from half-filling. If true, this confluence of magnetic, charge, and off-diagonal order would encapsulate in a single, remarkably simple model, much of the physics of the cuprate superconductors [1–4].

This chapter concerns the attractive ($U < 0$) Hubbard Hamiltonian which, as we shall see, offers a similar possibility of explaining experimental results in both condensed matter and cold atom contexts. We organize our discussion as follows. In the remainder of this introduction we will summarize some of the qualitative physics of the attractive model, including its connection to the repulsive case. After a discussion of certain features of our numerical methods, we will describe how the attractive model contains spin-gap phenomena in the cuprates, often interpreted as arising from the formation of bosonic pairs, yet still has fermionic signatures in the chemical potential associated with a sharp Fermi surface. This combination of fermionic and bosonic attributes is one of the curious, nontrivial features of the cuprate superconductors. We will then turn to the effect of disorder on the pairing correlations and, in particular, describe the destruction of superconductivity by sufficiently large random chemical potentials. This phenomenon goes beyond Anderson’s theorem, that pairing is robust with respect to disorder which does not break time reversal symmetry. Here, again, we will suggest that both bosonic and fermionic regimes can be accessed, depending on the size of U . Recent cold atom experiments with randomness induced via laser speckle are beginning to probe the physics of the disordered Hubbard model.

Finally, we will discuss the consequences of a σ -dependent chemical potential, $\mu \rightarrow \mu_\sigma$, allowing for different densities of the two fermionic species, physics first discussed in the solid state context by Fulde and Farrell, and by Larkin and Ovchinnikov (FFLO). The resulting *spin-imbalanced* density profiles and pairing correlations are under scrutiny in the cold-atom community. In 1D the QPT to an FFLO phase seems to appear as soon as the polarization is nonzero. However, for the case of unequal mass (a situation realized experimentally in K-Rb mixtures) a QPT to an inhomogeneous collapsed phase occurs only when the mass difference becomes sufficiently large [5].

The key ordering tendency of the attractive Hubbard model is to superconductivity. Just as a repulsive U promotes moment formation, an attractive U leads to pair formation in which the sites \mathbf{i} tend to be doubly occupied. It is natural to suppose that these pairs might ultimately condense into a superconducting phase at low temperatures. The antiferromagnetic alternation of a site occupied by the two different species in the positive (or repulsive) U model at half filling has a counterpart in the half-filled negative (or attractive) U model: empty and doubly occupied sites alternate in a charge density wave (CDW) pattern.

Indeed, this correspondence has a formal basis. For $\rho = 1$ there is a particle-hole mapping between the attractive and repulsive models in which antiferromagnetic order in the xy spin direction is associated with s -wave pairing, and in the z spin direction with CDW order. An interesting consequence is that, because of the rotational invariance of the repulsive model in which the xy and z spin directions are degenerate, CDW and s -wave pairing occur simultaneously in the attractive model at half-filling. This is one special realization of a super-solid. This transformation has further implications away from half-filling, including the fact that the doped 2D attractive model has a finite temperature Kosterlitz-Thouless superconducting transition. Interestingly, this particle-hole symmetry might connect FFLO physics in the attractive model and stripe formation in the repulsive model, as we shall mention in Sec. 11.4.

11.1 Quantum Monte Carlo Methods

Here we will present a brief description of our numerical algorithms, focusing on features which are especially relevant to the physics we will discuss. The majority of our results were obtained with the determinant quantum Monte Carlo (DQMC) method [6, 7]. In this approach, the partition function Z is written as a path integral by discretizing the imaginary time $\beta = L\Delta\tau$, and then separating the incremental time evolution operator into the exponential of one- and two-body terms, the kinetic energy/chemical potential \hat{K} and interaction energies \hat{V} , respectively:

$$Z = \text{Tr}[e^{-\beta\hat{H}}] = \text{Tr}[e^{-\Delta\tau\hat{H}}]^L \approx \text{Tr}[e^{-\Delta\tau\hat{K}}e^{-\Delta\tau\hat{V}}]^L. \quad (11.2)$$

The *Trotter approximation* [8–10] embodied in the last approximate equality results from the noncommutativity of \hat{K} and \hat{V} .

The interaction energy is rewritten using the discrete Hubbard-Stratonovich transformation, which takes a slightly different form depending

on whether $U > 0$ (top) or $U = -|U| < 0$ (bottom),

$$\begin{aligned} e^{-\Delta\tau U(n_{i\uparrow}-\frac{1}{2})(n_{i\downarrow}-\frac{1}{2})} &= \frac{1}{2}e^{-\Delta\tau U/4} \sum_{S_{il}} e^{S_{il}(n_{i\uparrow}-n_{i\downarrow})}, \\ e^{+\Delta\tau|U|(n_{i\uparrow}-\frac{1}{2})(n_{i\downarrow}-\frac{1}{2})} &= \frac{1}{2}e^{-\Delta\tau U/4} \sum_{S_{il}} e^{S_{il}(n_{i\uparrow}+n_{i\downarrow}-1)}. \end{aligned} \quad (11.3)$$

In both cases, the parameter λ is defined by $\cosh \lambda = e^{\Delta\tau U/2}$. In the form of the transformation chosen in 11.3, the Hubbard-Stratonovich variables S_{il} take on the two possible values ± 1 . The index i on S_{il} labels each spatial site at which the transformation must be performed, and similarly the imaginary time index $l = 1, 2, \dots, L$ labels the different incremental time evolution operators in the path integral, which arises when the L terms in Eq. (11.2) are written out explicitly and the potential energy is decoupled in each term through the use of 11.3.

This sequence of operations reduces Z to a trace of exponentials of quadratic forms of the fermion operators, an expression which can be evaluated analytically. The result is a form for Z in which no operators appear. Instead there is a sum over the classical Hubbard-Stratonovich variables S_{il} of a “weight” which takes the form of a product of two determinants, one for each fermionic species. The only inexactness in the procedure is the Trotter approximation. However, this error can be systematically eliminated by extrapolation, a process which is computationally straightforward. Thus DQMC provides a well-converged numerical solution to the many-body problem on lattices of finite size.

Looking at Eq. (11.3) one sees the transformations for positive and negative U are remarkably similar. However, the innocent change in relative sign in the way S_{il} couples to the densities has profound implications. In the case $U < 0$ the coupling is the same for both choices of σ . As a consequence, the two determinants which arise from the fermionic trace are identical. The weight that must be sampled stochastically is a perfect square and hence there is no sign problem.² DQMC simulations of the attractive Hubbard model can be performed for any desired interaction strength, chemical potential (particle density), and temperature. They are limited only by the N^3 scaling of the CPU time with lattice size N .

On the other hand, there is no such symmetry of the determinants in the repulsive model, and DQMC simulations can be performed only for temperatures above $T \approx t/4$. The precise limit on accessible T depends on U and ρ . Below this value, the sign problem causes an exponential scaling with β . At

²The ‘sign problem’ refers to the fact that when one writes down an expression for the quantum partition function $e^{-\beta\hat{H}}$ as a sum over classical degrees of freedom like the Hubbard-Stratonovich variables of Eq. (11.3) the summand in general is not positive. This poses a serious difficulty since the summand then cannot be used as a probability in the generation of configurations of the degrees of freedom.

exactly half-filling, the sign problem is absent and the repulsive model, like the attractive one, can be simulated to arbitrarily low T .

The spin up and down determinants are identical, and the sign problem is absent in simulations of the attractive model, only if $\mu_\uparrow = \mu_\downarrow$. In the spin imbalanced case $\mu_\uparrow \neq \mu_\downarrow$, and this is not true. There is a sign problem even for $U < 0$. Thus we have used a different numerical approach for our studies of FFLO physics. This second method, the continuous time canonical worm algorithm, involves a world-line representation of the fermionic paths in which broken world lines are present both to speed up the equilibration and to allow measurement of pairing correlations at large separations. The approach is more completely described in Ref. [11].

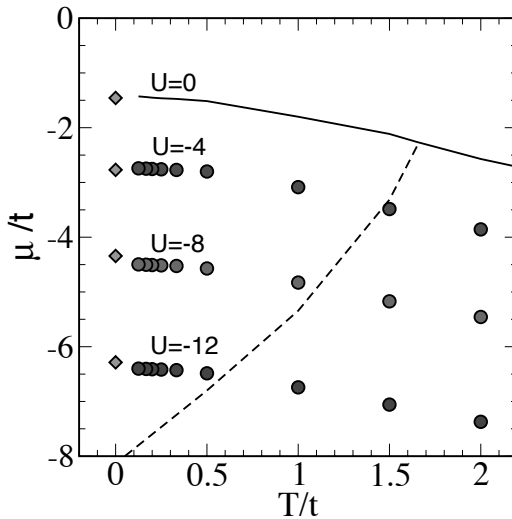
11.2 Pseudogap Phenomena

The phase diagram of cuprate superconductors consists of an antiferromagnetically ordered region, where there is one hole on each copper atom, corresponding to the half-filled $\rho = 1$ sector of the Hubbard Hamiltonian, and a superconducting dome which arises with a small amount of doping. In between these two ordered regions, the metallic phase of the cuprates exhibits an unusual property in its transport, a resistivity which varies linearly with temperature. It also exhibits an unusual magnetic response, a strongly temperature dependent suppression of the uniform susceptibility χ . This pseudo-gap is signaled by χ breaking away below the metallic Pauli form at low T . A natural explanation for this lowering of χ is that tightly bound Cooper pairs preform at a temperature scale T_{pair} which lies well above the ultimate condensation temperature T_c of superconductivity. For intermediate temperatures $T_c < T < T_{\text{pair}}$, the combination of spin up and down degrees of freedom into spin zero bosons results in a reduction of the magnetic response to an applied field. However, at odds with this explanation are photoemission experiments on the cuprates which exhibit a sharp Fermi surface.

It is natural to wonder to what extent these disparate signals of fermionic and bosonic character might likewise coexist in simple models. Answering this question motivates a study of the attractive Hubbard Hamiltonian using DQMC. Indeed, this model allows the general issues involving the crossover between large, weakly bound, BCS pairs at low U and small, tightly bound, BEC pairs at big U to be addressed [13–15].

11.2.1 Chemical Potential and Magnetic Susceptibility

One simple way to look at the degree of fermionic character in the Hubbard Hamiltonian is to examine the temperature and interaction strength dependence of the chemical potential μ . If $\mu(U, T)$ lies well above the bottom of

**FIGURE 11.1**

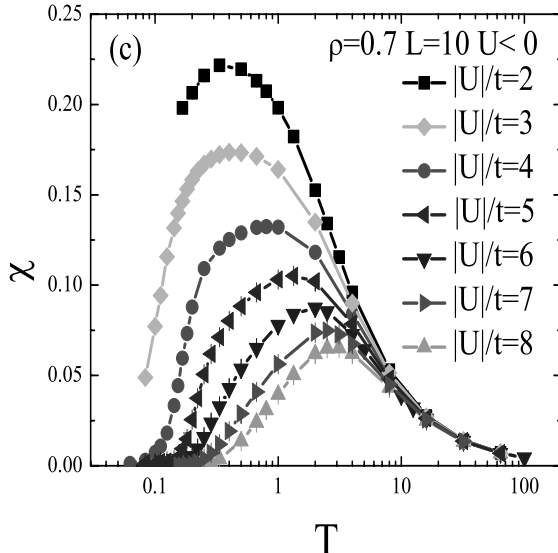
DQMC data for the chemical potential μ on 8×8 lattices ($U/t = -4, -8$) and 4×4 lattices ($U/t = -12$). The dashed curve is Eq. (11.4), which indicates the lower boundary of the degenerate fermionic regime. The solid curve is the result for noninteracting fermions. The diamonds at $T = 0$ are mean field results from Ref. [16]

the band, $-4t$, then the system can be well characterized as a degenerate fermionic gas. More precisely, if

$$\mu(U, T) + 4t + \langle n \rangle U/2 > T, \quad (11.4)$$

where the last term is the Hartree shift, then the system is fermionic. Figure 11.1 shows the result of DQMC calculations for the quarter filled attractive Hubbard model, $\langle n \rangle = 0.5$, for different values of U and T . It is seen that at low temperatures ($T < t/2$) the chemical potential satisfies the criterion Eq. (11.4) for U values as large as $|U| = 12t$. Nevertheless, as U and T increase, the fermionic degeneracy condition is less and less satisfied.

What of the magnetic susceptibility? The noninteracting susceptibility χ_0 of the 2D Hubbard model is roughly constant at low T , the Pauli-like behavior expected of a fermionic system. In Fig. 11.2, $\chi(T)$ for the interacting case is seen to display a strongly T dependent form, $d\chi/dT > 0$, for temperatures T below a local pairing scale T_{pair} [18, 19]. Since the superconducting transition

**FIGURE 11.2**

A local attraction $-|U|$ induces a suppression of the magnetic susceptibility $\chi(T)$ at a preformed pairing scale T_{pair} which is well in excess of the superconducting transition $T_c \approx 0.1t$. T_{pair} is an increasing function of $|U|$. The linear lattice size $L = 10$. Data are from Ref. [19].

temperature T_c is known to be less than $\approx 0.1t$, the behavior of χ is a clear indication of preformed pairs.

The interesting conclusion from Figs. 11.1, 11.2 is that the attractive Hubbard Hamiltonian can simultaneously exhibit fermionic and bosonic character, like the cuprate superconductors.

11.2.2 Scaling of NMR Relaxation Rate

We now argue that, in addition to the coexistence of the bosonic and the fermionic nature of the quasiparticles of the attractive Hubbard Hamiltonian, more detailed cuprate phenomenology can also be reproduced, in particular, the low temperature suppression of the nuclear magnetic resonance (NMR) inverse relaxation time. That this phenomenon might have a common origin in the behavior of the susceptibility is suggested by the experimental observation that the NMR relaxation rate $1/(T_1 T)$ scales as $\chi(T)$ [20].

Before showing this cuprate behavior is present in the attractive Hubbard Hamiltonian, it is worth emphasizing that measuring dynamical properties in QMC simulations is considerably more difficult than measuring equilibrium

thermodynamical ones. One strategy is to do an analytic continuation to the frequency domain of the imaginary time correlation functions which are directly measured in the simulations. This can be done with the maximum entropy method [21]. A somewhat less rigorous approach, which nevertheless has been shown to yield accurate results in many contexts, involves making use of correlation functions at large imaginary time separations [17]. In the case of the NMR relaxation rate, $1/(T_1 T)$, it can be shown [18] that

$$\frac{1}{T_1 T} = \frac{1}{\pi^2 T^2} \sum_{\mathbf{q}} S(\mathbf{q}, \tau = \beta/2), \quad (11.5)$$

where the spin structure factor $S(\mathbf{q}, \tau)$ is the Fourier transform of the real space spin-spin correlation $c(\mathbf{j}, \tau) = \langle (n_{j+i\uparrow} - n_{j+i\downarrow})(\tau)(n_{i\uparrow} - n_{i\downarrow})(0) \rangle$.

[Figure 11.3](#) shows DQMC results for the NMR relaxation rate on 8x8 lattices at quarter filling, $\rho = 0.5$. In the left panel, the steep decline in $1/(T_1 T)$ for $U = 4$ appears qualitatively similar to that of χ in [Fig. 11.2](#), as does the weaker evolution at $U = 8$. This similarity is made manifest in the parametric plot of the right panel in which χ and $1/(T_1 T)$ track each other. This behavior is dramatically different from that of a Fermi liquid, where since χ and $1/(T_1 T)$ are largely temperature independent, all the data would coincide at a single point.

11.3 The Effect of Disorder

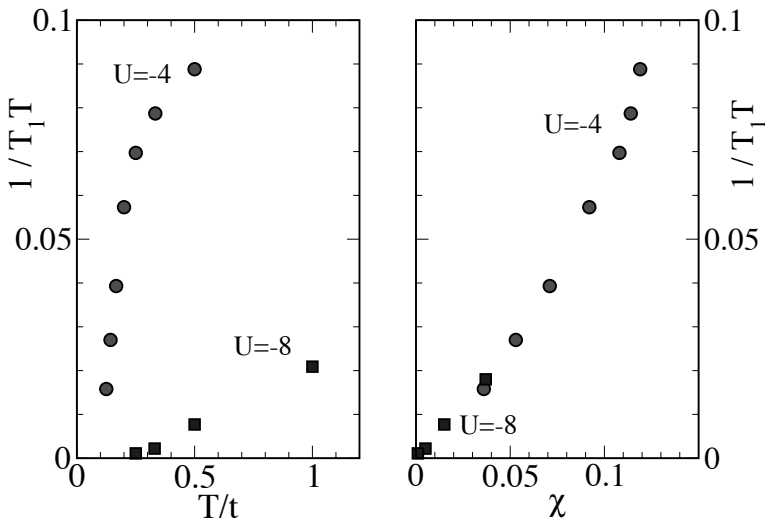
One of the fundamental issues in the physics of solids is the interplay of randomness and interactions. Although most typically this question is studied in the case of repulsive interaction, where the existence of a metallic phase in 2D has been much debated, similar questions apply for attractive interactions. In this section, we examine the effect of disorder on the pairing correlations and superconducting gap in the $-|U|$ Hubbard Hamiltonian by introducing a site dependent chemical potential in Eq. (11.1),

$$H \rightarrow H + \sum_i \mu_i n_i. \quad (11.6)$$

The random chemical potentials will be chosen uniformly with width V and zero mean: $-V/2 < \mu_i < +V/2$.

Anderson's theorem [22] suggests that for weak randomness superconductivity should survive. Indeed, instead of pairing momenta $\pm \mathbf{k}$ into Cooper pairs, as is the case with the translationally invariant system, one simply diagonalizes the one-body part of H including the disorder and forms pairs from the resulting eigenstates.

In the limit of large attractive U , where tightly bound bosonic pairs form in

**FIGURE 11.3**

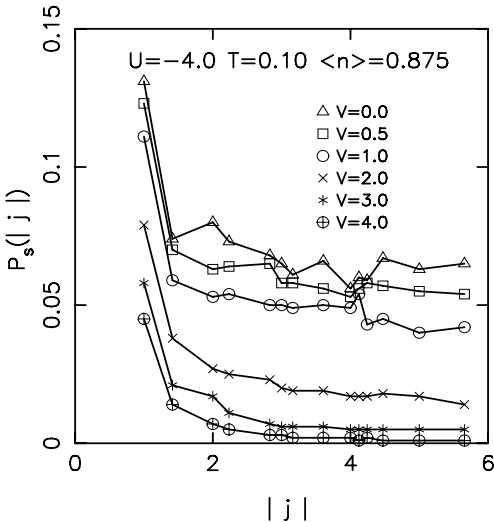
At left the NMR relaxation rate is seen to show a rapid suppression as temperature T is decreased. The right panel shows that this T dependence follows that of the uniform susceptibility.

the attractive Hubbard Hamiltonian, the problem considered here maps onto that of the bosonic Hubbard model with randomness [23–30]. This problem has been the subject of much study and debate over the last decade. Here we will study the model for different values of U and suggest that there is a nontrivial approach to the bosonic limit. In particular, we will argue that at small U disorder destroys pairing and at the same time fills in the gap in the density of states $N(\omega)$, while at large U the pairing can be destroyed while a gap in $N(\omega)$ survives.

11.3.1 Real Space Pair Correlation Function

In Sec. 11.2 we focused on the anomalous properties in the pseudogap phase above the superconducting condensation temperature T_c . Here we will concentrate on $T < T_c$ and see the effect of disorder on pairing. The s -wave pair correlations,

$$p_s(\mathbf{j}) = \langle \Delta_{\mathbf{j}+\mathbf{i}} \Delta_{\mathbf{i}}^\dagger \rangle, \quad (11.7)$$

**FIGURE 11.4**

Pairing correlations as a function of the separation $|j|$ of the points of injection and removal of the Cooper pair. A disorder strength $V = 4t$ has completely suppressed the superconductivity.

where $\Delta_j = c_{j\uparrow}c_{j\downarrow}$ destroys a pair at site j . Equation 11.7 describes the propagation of a pair of fermions injected at site i to site $j+i$. At high temperatures $p_s(j)$ falls off exponentially. Below T_c long range order develops in $p_s(j)$. In the case of 2D, the superconducting transition is Kosterlitz-Thouless in character and in the low temperature phase $p_s(j)$ has a power law dependence.

Fig. 11.4 shows $p_s(j)$ as a function of separation j for an attractive interaction strength $U = -4t$ (one half the band-width) and density $\rho = 0.875$. The temperature $T = 0.10t$. We observe a systematic reduction in the pairing correlations with increase in disorder strength V .

A careful finite size scaling study of $p_s(j)$ and the superconducting structure factor $S = \sum_j p_s(j)$ can be used to determine the critical transition temperature T_c of the clean system [33] and also the critical value of disorder required for the QPT resulting in the destruction of pairing in the ground state at $T = 0$ [17, 31, 32, 34, 35]. The basic conclusion is that Anderson's the-

orem applies only in the weak scattering (Born approximation) regime, and that large amounts of disorder can, and do, destroy superconductivity.

11.3.2 Superfluid Stiffness

The effect of randomness on pairing can be studied by a variety of diagnostics. The preceding discussion focused on the real space Cooper pair correlation function. However, the current-current correlation function $\Lambda_{xx}(\mathbf{l}, \tau)$ can also give information about the charge and superfluid stiffness and gauge invariance, and be used to distinguish insulators, metals, and superconductors [36, 37]:

$$\begin{aligned}\Lambda_{xx}(\mathbf{l}, \tau) &= \langle j_x(\mathbf{l}, \tau)j_x(0, 0) \rangle, \\ j_x(\mathbf{l}, \tau) &= e^{H\tau} \left[it \sum_{\sigma} (c_{\mathbf{l}+\hat{x}, \sigma}^{\dagger} c_{\mathbf{l}, \sigma} - c_{\mathbf{l}, \sigma}^{\dagger} c_{\mathbf{l}+\hat{x}, \sigma}) \right] e^{-H\tau}.\end{aligned}\quad (11.8)$$

We shall frame our discussion in terms of the Fourier transform in space and imaginary time,

$$\Lambda_{xx}(\mathbf{q}, \omega_n) = \sum_{\mathbf{l}} \int_0^{\beta} d\tau e^{i\mathbf{q} \cdot \mathbf{l}} e^{-i\omega_n \tau} \Lambda_{xx}(\mathbf{l}, \tau). \quad (11.9)$$

Here, $\omega_n = 2n\pi/\beta$.

The longitudinal part of Λ_{xx} defined in Eq. (11.8) obeys the f-sum rule,

$$\begin{aligned}\Lambda^L &\equiv \lim_{q_x \rightarrow 0} \Lambda_{xx}(q_x, q_y = 0, \omega_n = 0), \\ \Lambda^L &= K_x,\end{aligned}\quad (11.10)$$

as a consequence of gauge invariance [36, 37]. Here,

$$K_x = \langle t \sum_{\sigma} (c_{\mathbf{l}+\hat{x}, \sigma}^{\dagger} c_{\mathbf{l}, \sigma} + c_{\mathbf{l}, \sigma}^{\dagger} c_{\mathbf{l}+\hat{x}, \sigma}) \rangle \quad (11.11)$$

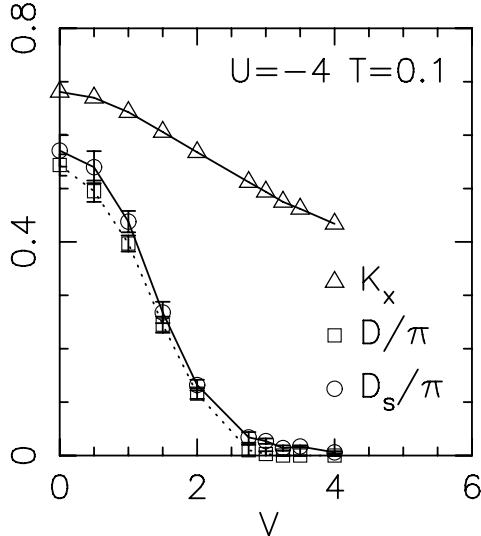
is the magnitude of the kinetic energy in the x direction. The transverse response is

$$\Lambda^T \equiv \lim_{q_y \rightarrow 0} \Lambda_{xx}(q_x = 0, q_y, \omega_n = 0). \quad (11.12)$$

The longitudinal and transverse responses are no longer equal when gauge symmetry is broken. Indeed, their difference is precisely the superfluid stiffness D_s or, equivalently, the superfluid density ρ_s , given by

$$\begin{aligned}\rho_s = D_s/\pi &= [\Lambda^L - \Lambda^T] \\ &= [K_x - \Lambda^T].\end{aligned}\quad (11.13)$$

[Figure 11.5](#) shows the results of DQMC calculations of these quantities. As expected, the magnitude of the kinetic energy declines with increasing randomness, but the suppression is less than a factor of two. In contrast, the

**FIGURE 11.5**

The superfluid density D_s , Drude weight D , and kinetic energy K_x are shown as functions of disorder for $U = -4t$, $\langle n \rangle = 0.875$, and $T = 0.1$. As seen already in Fig. 11.4, $V = 4t$ is large enough to destroy pairing completely.

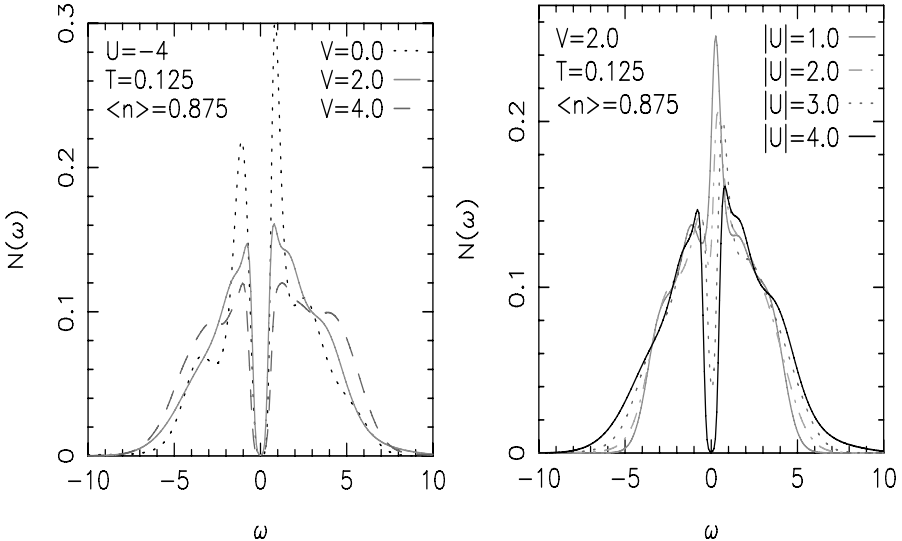
Drude weight and superfluid density decline essentially to zero. These data support the conclusion of the behavior of the real space pair correlations that superconductivity is destroyed.

Eq. (11.13) implies that on a lattice the superfluid density at $T = 0$ is bounded by the kinetic energy. It is natural to suppose that the spatial disorder might suppress superconductivity in an inhomogeneous way. As a consequence, the reduction in the pairing stiffness might be dominated by ‘weak links’ where superconductivity is most tenuous. This possibility has been explored in [38] where an improved upper bound on D_s in a disordered system has been obtained in terms of the local kinetic energy.

11.3.3 Density of States

The density of states $N(\omega)$ is a further quantity which lends insight into superconducting phases. In order to evaluate $N(\omega)$ we use DQMC data to compute the imaginary time dependent Green’s function $G(\tau)$ and invert the integral relation,

$$G(\tau) = \frac{1}{N} \sum_{\mathbf{p}} \langle c_{\mathbf{p}}(\tau) c_{\mathbf{p}}^\dagger(0) \rangle = \int_{-\infty}^{+\infty} d\omega \frac{e^{-\omega\tau} N(\omega)}{1 + e^{-\beta\omega}}. \quad (11.14)$$

**FIGURE 11.6**

Left Panel: Density of states $N(\omega)$ for different disorder strengths V . Despite the fact that the pair correlations and superfluid stiffness have both been driven to zero by the time $V = 4$, a gap remains clearly visible in $N(\omega)$. *Right Panel:* Density of states $N(\omega)$ for different interaction energies U for fixed disorder strength $V = 2t$. Data from [39].

As pointed out earlier in the discussion of dynamics and the NMR relaxation rate, this is a delicate procedure. We have employed the maximum entropy method [21] to accomplish the inversion.

The left panel of Fig. 11.6 shows the result. The striking feature is that the gap in $N(\omega)$ is rather insensitive to the magnitude of V . In particular, there seems to be little signature here in $N(\omega)$ of the dramatic suppression of $p_s(\mathbf{j})$ and D_s seen in Figs. 11.4,11.5 as V increases.

Keeping in mind our description of the two temperature scales $T_{\text{pair}} \approx U$ at which fermions bind, and $T_c \approx t^2/U$ at which they condense in a phase-coherent superconducting state, it is natural to wonder whether a similar separation might be reflected in $N(\omega)$. The right panel of Fig. 11.6 shows $N(\omega)$ for different values of attraction and suggests that there is a distinction between weak and strong coupling. For the smallest degrees of correlation, $U = -t, -2t$, the Fermi surface density of states $N(\omega = 0)$ does not vanish. However, as U increases further to $U = -4t$, a pairing gap is opened. Figure 11.6(left) indicates that this gap is robust to further increases in V .

We have examined here the density of states of the entire system. A very interesting issue concerns the possibility that $N(\omega)$ exhibits significant spatial variation. This possibility has been carefully explored with inhomogeneous

Bogoliubov-de Gennes theory [40]. In this point of view, a distinction between two normal regimes, one of which has a gap in $N(\omega)$ above T_c and the other of which does not, is believed to be absent.

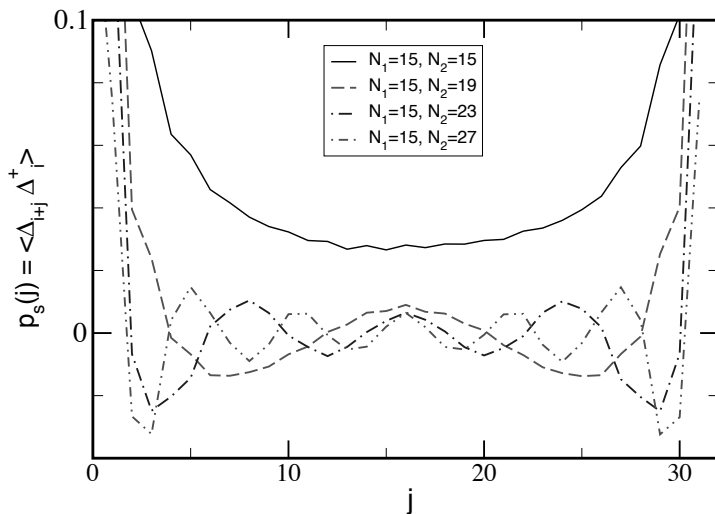
11.4 Imbalanced Populations

Superconductivity arises from an instability of the Fermi surface caused by even weak attractive interactions between the two fermionic species. The resulting Cooper pairs combine an up fermion of momentum \mathbf{k} and a down electron of momentum $-\mathbf{k}$, or, more generally, time-reversed eigenstates, if, for example, disorder is present. It is natural to ask what would be the consequence to superconductivity of a situation in which the numbers of the two fermion species were not equal. Would pairs form nevertheless and flow freely in a superconducting region of the sample, leaving an inhomogeneous system in which the excess fermionic species concentrate in another region? Would pairs still form through combination of fermions at the two different Fermi surfaces, resulting in nonzero total momentum? If the imbalance is sufficiently great, might not superconductivity be destroyed altogether?

These questions have long been asked in the solid state community, beginning with the discussions of Fulde and Ferrell [41] and of Larkin and Ovchinnikov [42], both of whom championed the idea of nonzero momentum FFLO pairs, and continuing with the work of Sarma [43], who favored pairing at zero momentum. Clogston [44] explored the consequences to superconductivity of the Zeeman energy cost exceeding the energy gain from pairing.

These theoretical ideas have proven very difficult to achieve experimentally. It was four decades after the theoretical discussions that Radovan [45] succeeded in demonstrating the FFLO phase in samples of very pure and strongly anisotropic samples of the heavy superconductor CeCoIn₅, by demonstrating the existence of two separate thermodynamic specific heat signals in the low temperature paired regime. More recently, superconductivity in pair-imbalanced systems has been explored in ultracold atomic systems [46, 47]. A large amount of theoretical work has ensued through mean field theory [48–57], bosonization [59], and the Bethe ansatz [60], with both zero momentum and nonzero momentum pairs being discussed.

Before turning to our quantum Monte Carlo work, we comment that particle-hole symmetry makes possible an interesting analogy between the FFLO state in the attractive Hubbard Hamiltonian and charge inhomogeneities in the repulsive model [61]. Inhomogeneous Hartree-Fock calculations and other techniques, including DMRG, have suggested that when the $U > 0$ Hubbard Hamiltonian is doped by choosing chemical potential $\mu < 0$ the resulting holes do not spread uniformly throughout the system but instead organize themselves in ‘striped’ patterns in which linearly ordered hole-rich

**FIGURE 11.7**

The pair Green's function p_s is given in real space on an $L = 32$ site lattice. Population imbalance is seen to induce oscillations into the strictly positive form at equal density. The interaction strength $U = -8$ and the population differences indicated in the legend give polarizations $P = 0.000, 0.118, 0.211$, and 0.286 .

regions alternate with half-filled regions which retain considerable magnetic order. This segregation could have interesting interplay with the superconductivity by allowing the retention of the magnetic pairing ‘glue’ in some spatial regions while the charge carriers are free to move in others, and is, of course, a central experimental feature of the cuprates.

In the particle-hole transformation $\mu(n_{i\uparrow} + n_{i\downarrow})$ maps onto a magnetic field term $B(n_{i\uparrow} - n_{i\downarrow})$. Thus the doped repulsive model corresponds to the spin-imbalanced attractive case. As discussed earlier, xy magnetic correlations become s -wave pairing correlations. Thus the phenomenon of spatially inhomogeneous magnetic correlations in the repulsive model is analogous to the breaking of translational symmetry in the superconducting order in the attractive model. In other words, there is a connection between charge stripes and the FFLO physics we discuss here.

11.4.1 FFLO Pairing in 1D

We have used QMC simulations to distinguish these different scenarios for pairing in population imbalanced situations. [Figure 11.7](#) presents our key conclusion. We show the correlation function $p_s(j)$ as a function of the spatial distance between the points of insertion and removal of the Cooper pair. $p_s(j)$ exhibits a clear spatial modulation which is a feature of binding at nonzero momentum.

This conclusion is made even more apparent in [Fig. 11.8](#), which shows the Fourier transform, $n_{\text{pair}}(k)$, of $p_s(j)$. The latter exhibits a peak at the precise momentum k predicted by FFLO: $k = |k_{F1} - k_{F2}|$. Figure 11.8 also shows the single Fermi functions $n_\sigma(k)$ in momentum space. Besides their different Fermi wave vectors, the majority population $n_2(k)$ exhibits an interesting nonmonotonicity. This is best understood as the enhanced scattering of majority species fermions, and hence reduction of $n_2(k)$, which occurs within the minority Fermi surface.

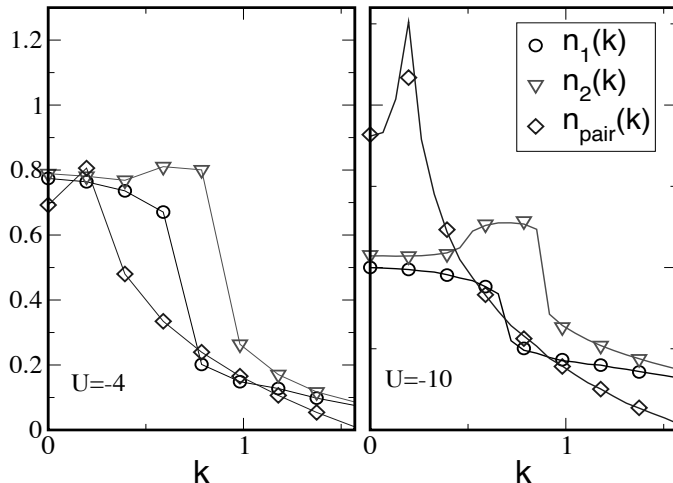
The optical lattice experiments are performed in the presence of a harmonic confining potential. As mentioned earlier, a fundamental issue in imbalanced population systems is the possibility of the formation of spatially segregated domains of the excess species. It is natural therefore to ask whether the non-trivial density profile induced by the external potential might affect the FFLO physics observed in our simulations. We have conducted preliminary studies of this issue. Figure 11.8 shows that the peak in $n_{\text{pair}}(k)$ still occurs at nonzero momentum even when a confining potential is present.

We have recently begun to extend these results to 2D. Initial results are encouraging and appear to show that, contrary to current mean field predictions, the FFLO pairing mechanism is robust in 2D systems with imbalanced populations [62]. Representative results are shown in [Fig. 11.9](#). $n_{\text{pair}}(k)$ is peaked at a symmetry-related set of nonzero momenta about the Γ point.

11.5 Outlook

The attractive Hubbard model, like its repulsive counterpart, provides a remarkably useful qualitative description of quantum many-body effects and QPTs, not only the intuitively obvious phenomena of charge ordering and s -wave pairing, but more subtle features such as the coexistence of bosonic (pseudogap) and fermionic (Fermi surface, degenerate chemical potential) effects as well.

With the introduction of laser speckle allowing for disorder to be incorporated into cold atom systems, it will be interesting to study the disordered attractive Hubbard model with QMC in much more detail than has previously been done, especially with the more powerful capabilities that are

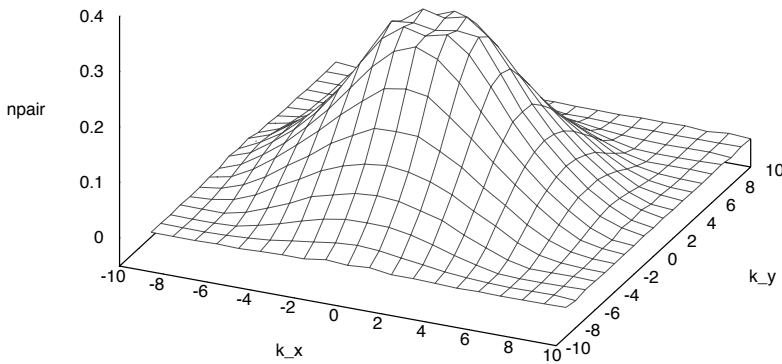
**FIGURE 11.8**

Fourier transform $n_{\text{pair}}(k)$ of the pair Green's function $p_s(j)$ and single particle Fermi functions $n_1(k), n_2(k)$ in momentum space. The symbols correspond to simulations with $N_1 = 7, N_2 = 9, L = 32$, and $\beta = 64$, with $U = -4, -10$ in the left and right panels respectively. The solid lines are for lattices $L = 96$, i.e., three times as large, and at a correspondingly reduced temperature $\beta = 196$. The qualitative physics is the same for the two size, which differ mainly by a sharper quasi-condensate peak on the larger lattice.

developing for these simulations. A particularly intriguing set of questions revolves around the evolution between disordered weakly bound fermions and disordered bosons as $|U|$ increases, that is, extending studies of the Bardeen-Cooper-Schrieffer to Bose-Einstein condensate (BCS to BEC) cross-over to include the effects of randomness.³ Much is known theoretically about the disordered Bose-Hubbard model. What happens when the bosonic degrees of freedom are less tightly bound?

Exploring pairing in spin-imbalanced systems is similarly an area of many new horizons. To date, exact quantum Monte Carlo work has focused on the simplest situation: 1D and, for the most part, in the absence of a confining

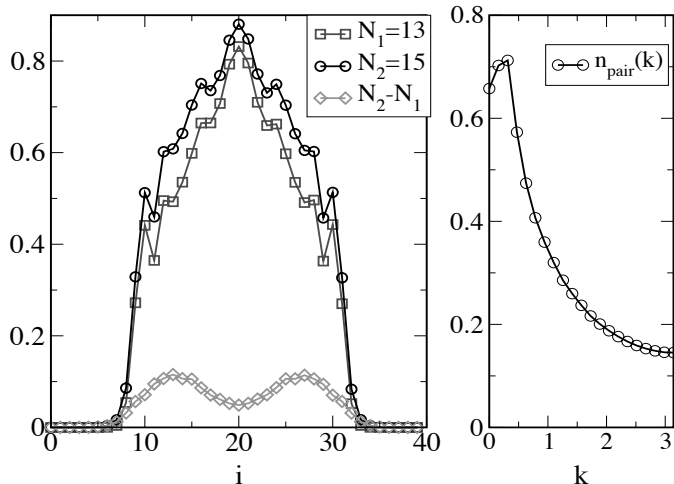
³While many ‘conventional’ superconductors have Cooper pairs whose coherence length ξ is hundreds or thousands of lattice spacings times a_0 , and hence are firmly in the BCS limit, other families such as the cuprates have much smaller values $\xi/a_0 < 10$. The superconducting transition in such systems is sometimes regarded as a BEC of these relatively small pairs. Optical lattice emulators offer a powerful new means to study this phenomenon since the BCS/BEC crossover can be smoothly tuned by changing U/t through a Feshbach resonance.

**FIGURE 11.9**

Fourier transform $n_{\text{pair}}(k_x, k_y)$ of the pair Green's function $p_s(j_x, j_y)$ for a 2D system (20x20 lattice). The on-site attraction $U = -4$, inverse temperature $\beta = 8$, and up and down spin chemical potentials are $\mu_\uparrow = 0.2$, $\mu_\downarrow = 2.1$. The peaks occur for nonzero momentum, indicating FFLO pairing.

potential. These studies appear correctly to discriminate between the different possible types of superconducting order which can occur, e.g. predicting an FFLO phase in agreement with cold-atom experiments. An intriguing area for future work is the question of phase separation, a phenomenon predicted by several calculations but so far not reproduced in quantum Monte Carlo. In addition, little is known about what happens in 2D or in the presence of a trap. Is FFLO still robust in 2D? To what temperatures is it stable? Finally, while we have described here the situation of population imbalance, an equally interesting case is that of mass imbalance, in which hopping t is different for the two species. Experimentally, this is realized in $K - Li$ mixtures. Some of the new possible physics includes selective localization of the heavy species. When mass and population imbalance both are present, which species, light or heavy, is in the majority is likely to prove crucial to the physics! Ongoing QMC work will provide interesting insight into these QPTs.

We believe, however, that one of the most exciting frontiers will be in a careful exploration of the role of trap-induced spatial inhomogeneity. To begin

**FIGURE 11.10**

Left: The density profiles for a system of population imbalanced fermions are shown. The trap curvature is incorporated as an additional term $V_{\text{trap}} \sum_i n_i$ in the Hamiltonian with $V_{\text{trap}} = 0.005$. The local density difference has a minimum at the trap center, reflecting the desire of the fermions to pair. Right: The Fourier transform of the pair correlation function is peaked at nonzero k . The superfluid is of the FFLO variety.

with, on an algorithmic level, what does this portend for the sign problem? We know that the sign problem is completely absent for a translationally invariant half-filled system. How much ‘protection’ from the sign problem do the locally half-filled Mott regions in a trap afford us? Is it enough to be able to say more about d -wave pairing than in a homogeneous system?

Even more importantly, the density variance opens the door to a variety of new phenomena, and indeed might be crucial to many aspects of the experimental behavior. In the solid state community, for example, much speculation has surrounded the possibility that superconductivity in the cuprates is linked to the existence of locally half-filled regions with a high degree of antiferromagnetism (providing the ‘pairing glue’) alongside doped regions which contain the carriers. Other forms of inhomogeneity have been suggested as well, for example ‘plaquette’ Hubbard models where 2×2 clusters with large hopping t form local pairing centers which are then linked to each other by weaker t' [63, 64]. To what extent do similar possibilities occur in systems of trapped fermions? Can the Mott plateau regions provide pairing glue to the superconducting rings which surround them? What pairing symmetry is favored

by this geometrical arrangement of regions? How do the pair-pair correlations decay as one goes around such a ring as compared to a 1D system? QMC simulations that are now possible on lattices of a thousand or more sites will be able to begin to look at these issues.

Acknowledgments – The authors gratefully acknowledge collaborations with Miriam Huntley, Carey Huscroft, Thereza Paiva, Mohit Randeria, Val Rousseau, and Nandini Trivedi, with whom the work described here was done. This work was supported under ARO Award W911NF0710576 with funds from the DARPA OLE Program. GGB is partially supported by the CNRS (France) PICS 3659. RTS thanks the Aspen Center for Physics for its hospitality during the writing of this manuscript. T. Yardbirds also provided very useful input.

Bibliography

- [1] M. Rasetti, *The Hubbard Model - Recent Results*, World Scientific, 1991.
- [2] Arianna Montorsi (ed), *The Hubbard Model*, World Scientific, 1992.
- [3] D.J. Scalapino, Proceedings of the International School of Physics, Enrico Fermi, Course CXXI, edited by R.A. Broglia and J.R. Schrieffer, North-Holland, Amsterdam, 1994.
- [4] Patrik Fazekas, *Lecture Notes on Electron Correlation and Magnetism*, World Scientific (1999).
- [5] G.G. Batrouni, M.J. Wolak, F. Hebert, and V.G. Rousseau, Europhys. Lett. **86**, 47006 (2009).
- [6] R. Blankenbecler, R.L. Sugar, and D.J. Scalapino, Phys. Rev. **D24**, 2278 (1981).
- [7] S.R. White, D.J. Scalapino, R.L. Sugar, N.E. Bickers, and R.T. Scalettar, Phys. Rev. **B39**, 839 (1989).
- [8] M. Suzuki, Phys. Lett. **113A**, 299 (1985).
- [9] R.M. Fye, Phys. Rev. **B33**, 6271 (1986).
- [10] R.M. Fye and R.T. Scalettar, Phys. Rev. **B36**, 3833 (1987).
- [11] G.G. Batrouni, M.H. Huntley, V.G. Rousseau, and R.T. Scalettar, Phys. Rev. Lett. **100**, 116405 (2008).
- [12] C.N. Varney, C.-R. Lee, Z.J. Bai, S. Chiesa, M. Jarrell, and R.T. Scalettar, Phys. Rev. B **80**, 075116 (2009).

- [13] A.J. Leggett in *Modern Trends in the Theory of Condensed Matter*, edited by A. Pekalski and R. Przystawa, Springer, Berlin, 1980.
- [14] P. Noziéres and S. Schmitt-Rink, J. Low Temp. Phys. **59**, 195 (1985).
- [15] M. Randeria, J. Duan, and L. Shieh, Phys. Rev. Lett. **62**, 981 (1989); Phys. Rev. **B41**, 327 (1990).
- [16] L. Belkhir and M. Randeria, Phys. Rev. **B45**, 5087 (1992).
- [17] N. Trivedi, R.T. Scalettar, and M. Randeria, Phys. Rev. **B54**, R3756 (1996).
- [18] M. Randeria, N. Trivedi, A. Moreo, and R.T. Scalettar, Phys. Rev. Lett. **69**, 2001 (1992).
- [19] T. Paiva, R.T. Scalettar, M. Randeria, and N. Trivedi, Phys. Rev. Lett. **104**, 066406 (2009).
- [20] W.W. Warren, Phys. Rev. Lett. **62**, 1193 (1989); R.E. Walstedt, Phys. Rev. **B41**, 9574 (1990); and R.E. Walstedt, R.F. Bell, ad D.B. Mitzi, Phys. Rev. **B44**, 7760 (1991).
- [21] J.E. Gubernatis, M. Jarrell, R.N. Silver, and D.S. Sivia, Phys. Rev. **B44**, 6011 (1991).
- [22] P.W. Anderson, J. Phys. Chem. Solids **11**, 26 (1959); and A.A. Abrikosov and L.P. Gorkov, Sov. Phys. JETP **8**, 1090 (1959).
- [23] M.P.A. Fisher, P.B. Weichman, G. Grinstein and D.S. Fisher, Phys. Rev. **B40**, 546 (1989).
- [24] R.T. Scalettar, G.G. Batrouni, and G.T. Zimanyi, Phys. Rev. Lett. **66**, 3144 (1991).
- [25] K.J. Runge, Phys. Rev. **B45**, 13136 (1992).
- [26] K.G. Singh and D.S. Rokhsar, Phys. Rev. **B46**, 3002 (1992).
- [27] E.S. Sorensen, M. Wallin, S.M. Girvin, and A.P. Young, Phys. Rev. Lett. **69**, 828 (1992).
- [28] B.V. Svistunov, Phys. Rev. **B54**, 16131 (1996).
- [29] J. Kisker and H. Rieger, Phys. Rev. **B55**, 11981 (1997).
- [30] L. Pollet, N.V. Prokofév, B. V. Svistunov, and M. Troyer, Phys. Rev. Lett. **103**, 140402 (2009).
- [31] C. Huscroft and R.T. Scalettar, Phys. Rev. **B55**, 1185 (1997).
- [32] R.T. Scalettar, N. Trivedi, and C. Huscroft, Phys. Rev. **B59**, 4364 (1999).

- [33] T. Paiva, R.R. Dos Santos, P.J.H. Denteneer, and R.T. Scalettar, Phys. Rev. **B69**, 184501 (2004).
- [34] Daniel Hurt, Evan Odabashian, Warren Pickett, Richard Scalettar, Felipe Mondaini, Thereza Paiva, and Raimundo dos Santos, Phys. Rev **B72**, 144513 (2005).
- [35] R. Moradian, J.F. Annett, B.L. Györffy and G. Litak, Phys. Rev. **B** 6302 (2001).
- [36] G. Baym, in *Mathematical Methods in Solid State and Superfluid Theory* (Scottish Universities Summer School, 1967), edited by R. C. Clark and G. H. Derrick (Plenum, New York, 1969).
- [37] D.J. Scalapino, S.R. White, and S.C. Zhang, Phys. Rev. **B47**, 7995 (1993).
- [38] A. Paramekanti, N. Trivedi, and M. Randeria, Phys. Rev. **B57**, 11639 (1998).
- [39] C. Huscroft and R.T. Scalettar, Phys. Rev. Lett. **81**, 2775 (1998).
- [40] A. Ghosal, M. Randeria, and N. Trivedi, Phys. Rev. Lett. **81**, 3940 (1998).
- [41] P. Fulde and A. Ferrell, Phys. Rev. **135**, A550 (1964).
- [42] A. Larkin and Y.N. Ovchinnokov, Zh. Eksp. Teor. Fiz. **47**, 1136 (1964) [Sov. Phys. JETP **20**, 762 (1965)].
- [43] G. Sarma, Phys. Chem. Solids **24**, 1029 (1963); S. Takada and T. Izuyama, Prog. Theor. Phys. **41**, 635 (1969).
- [44] A.M. Clogston, Phys. Rev. Lett. **9**, 266 (1962); and B.S. Chandrasekhar, Appl. Phys. Lett. **1**, 7 (1962).
- [45] H.A. Radovan N.A. Fortune, T.P. Murphy, S.T. Hannahs, E.C. Palm, S.W. Tozer, and D. Hall, Nature **425**, 51 (2003).
- [46] M.W. Zwierlein, A. Schirotzek, C.H. Schunck, and W. Ketterle, Science **311**, 492 (2006); M.W. Zwierlein, C.H. Schunck, A. Schirotzek, and W. Ketterle, Nature **422**, 54 (2006); Y. Shin, M. W. Zwierlein, C. H. Schunck, A. Schirotzek, and W. Ketterle, Phys. Rev. Lett. **97**, 030401 (2006).
- [47] G.B. Partridge, W. Li, R.I. Kamar, Y. Liao, and R.G. Hulet, Science **311**, 503 (2006); G.B. Partridge, Wenhui Li, Y.A. Liao, R.G. Hulet, M. Haque and H.T.C. Stoof, Phys. Rev. Lett. **97**, 190407 (2006).
- [48] P. Castorina M. Grasso, M. Oertel, M. Urban, and Dario Zappalá, Phys. Rev. **A72**, 025601 (2005).
- [49] D.E. Sheehy and L. Radzhovsky, Phys. Rev. Lett. **96**, 060401 (2006).

- [50] J. Kinnunen, L.M. Jensen, and P. Törmä, Phys. Rev. Lett. **96**, 110403 (2006).
- [51] K. Machida, T. Mizushima, and M. Ichioka, Phys. Rev. Lett. **97**, 120407 (2006).
- [52] K.B. Gubbels, M.W.J. Romans, and H.T.C. Stoof, Phys. Rev. Lett. **97**, 210402 (2006).
- [53] M.M. Parish, F.M. Marchetti, A. Lamacraft and B.D. Simons, Nature Phys. **3**, 124 (2007).
- [54] H. Hu, X.J. Liu, and P.D. Drummond, Phys. Rev. Lett. **98**, 070403 (2007).
- [55] Y. He, C.C. Chien, and K. Levin, Phys. Rev. **A75**, 021602(R) (2007).
- [56] E. Gubankova, E. G. Mishchenko, and F. Wilczek, Phys. Rev. Lett. **94**, 110402 (2005).
- [57] J. Kinnunen, J.-P. Martikainen, L.M. Jensen, and P. Törmä, New J. Phys. **8**, 179 (2006).
- [58] D.T. Son and M.A. Stephanov, Phys. Rev. **A74**, 013614 (2006).
- [59] K. Yang, Phys. Rev. **B63**, 140511 (2001).
- [60] G. Orso, Phys. Rev. Lett. **98**, 070402 (2007); and X. W. Guan, M.T. Batchelor, C. Lee, and M. Bortz, Phys. Rev. **B76** 085120 (2007).
- [61] Adriana Moreo and D. J. Scalapino Phys. Rev. Lett. **98**, 216402 (2007).
- [62] M. Wolak, G.G. Batrouni, and R.T. Scalettar, work in progress.
- [63] H. Yao, W.-F. Tsai, and S.A. Kivelson, Phys. Rev. **B76** 161104(R) (2007).
- [64] D.G.S.P. Doluweera, A. Macridin, T.A. Maier, M. Jarrell, and Th. Pruschke, Phys. Rev. **B78** 020504 (2008).

12

Quantum Phase Transitions in Quasi-One-Dimensional Systems

Thierry Giamarchi

University of Geneva, DPMC-MaNEP, Quai Ernest-Ansermet CH-1211 Geneva 4, Switzerland

Among the various systems, one-dimensional (1D) and quasi-one-dimensional (quasi-1D) systems are a fantastic playground for quantum phase transitions (QPTs), with rather unique properties. There are various reasons for that special behavior.

First, purely 1D systems are rather unique. Contrary to their higher-dimensional counterparts [1], interactions play a major role since in 1D particles cannot avoid the effects of interactions. This transforms any individual motion of the particles into a collective one. In addition to these very strong interaction effects, in 1D the quantum and thermal fluctuations are pushed to a maximum, and prevent the breaking of continuous symmetries, making simple mean-field physics inapplicable. The combination of these two effects leads to a very special universality class for interacting quantum systems, known as Luttinger liquids (LLs) [2].

I will not review here all the aspects of LL physics since many such reviews exist, but refer the reader in particular to [3] for a complete description of this area of physics, with the same notations as the ones used in the present chapter. For what concerns us, the important point is that we take the LL to be in a critical phase, in which correlations decrease, at zero temperature, as power laws of space and time. This makes the system extremely fragile to external perturbations and leads to a host of QPTs. Examples of such perturbations are the effects of a lattice, which leads to a Mott transition, and disorder that leads to localized phases such as Anderson localization or the Bose glass. Each of these transitions is characterized by a quantum critical point (QCP) that can be computed from LL theory. The 1D nature of LLs has other consequences: the excitations can fractionalize. In particular, an excitation such as adding an electron can split into several collective excitations, such as one carrying spin but no charge, called a *spinon*, and one carrying charge but no spin, called a *holon*. I will not dwell on this physics of purely 1D systems that

is now well characterized and refer the reader to [3] for this aspect of QCPs in purely 1D systems.

Although purely 1D physics and QPTs are by now rather well under control from the theoretical point of view, there is a category of perturbations that is still at the frontier of our theoretical knowledge. These are the perturbations that are produced by the coupling of several 1D systems. Then, when one parameter, for example the temperature or the inter-chain coupling, is varied, the system crosses over from a 1D situation with exotic LL physics, to the more conventional high dimensional one. How one can reconcile such different physical limits, for example recombining the spinons and holons to re-form an electron, to perform such a dimensional crossover is a very challenging and still open question. Such questions are not only important on the theoretical side but have direct applications to experimental systems such as organic [4] or inorganic [5] superconductors, spin chains and ladders [6–8] and cold atomic systems [9] (see also Chap. 19) which provide realizations of such coupled 1D systems.

Quasi-1D systems thus lead to their own interesting sets of QCPs, and these are the ones on which I will focus in the present chapter. I will start by examining the simple case of coupled spin chains and ladders, then move to the case of bosons, and finally deal with the more complicated and still largely open case of fermions.

12.1 Spins: From Luttinger Liquids to Bose-Einstein Condensates

The simplest example of a coupled 1D system is provided by coupled spin systems (see, e.g., [6, 7] for experimental systems). In addition to their own intrinsic interest and their direct experimental realization, they will also serve to illustrate several important concepts that will be directly transposed with increasing complexity to the case of bosons and fermions.

Coupling chains starting from 1D is a highly nontrivial process. Going from one spin chain to two, called the *spin ladder problem*, already leads to non-trivial physics. Indeed, although spin-1/2 systems are gapless the coupling of two spin-1/2 chains leads to the formation of a spin gap, similar to the Haldane gap that occurs for integer spins [10]. I will not discuss this physics in details since it is by now well established and covered in several textbooks and refer the reader to the literature on the subject [3, 8].

Here, I consider the case when an infinite number of low dimensional units are coupled. As can be readily understood the physics will depend crucially on the fact that the systems that got coupled are already in a critical state (such as spin-1/2 chains) or whether they have a gap (such as spin dimers,

spin 1 chains or two legs ladders). These two cases are the prototypes of QCP in coupled 1D systems and we will examine them separately.

12.1.1 Coupled Spin-1/2 Chains

An isolated spin-1/2 chain is described by a LL. As can be expected in 1D, no long range order can exist. However, the spin-spin correlation functions decay as a power law, at zero temperature, indicating the presence of quasi-long range order. Focusing on the case of the antiferromagnetic exchange, which is the natural realization in condensed matter systems, spin-spin correlations decay as [3]

$$\langle S^+(x)S^-(0) \rangle \propto (-1)^x \left(\frac{1}{x}\right)^{1/(2K)}, \quad \langle S^z(x)S^z(0) \rangle \propto (-1)^x \left(\frac{1}{x}\right)^{2K}, \quad (12.1)$$

where K is the LL parameter and depends only on the spin exchange anisotropy between the XY and Z plane, J_Z/J_{XY} . For an isotropic Heisenberg interaction $K = 1/2$, both correlations decrease as $1/r$, up to logarithmic corrections. Temperature cuts this power-law decrease and transforms it into an exponential decay of the correlation beyond a scale of order $u\beta$, where β is the inverse temperature and u the velocity of spin excitations.

The inter-chain coupling introduces a term of the form

$$H_\perp = J_\perp \sum_{\langle\mu\nu\rangle} \int dx S_\mu(x) \cdot S_\nu(x), \quad (12.2)$$

where $\langle\mu,\nu\rangle$ denotes two neighboring chains μ and ν . Because the spin is an object that admits a good classical limit, one can analyze the physics of such a term in a mean-field approximation by assuming that the spin on each chain acquires an average value, for example in the Z direction. This allows one to decouple (12.2) and transform it to an effective Hamiltonian corresponding to a self-consistent staggered magnetic field applied on a single chain $H_\perp \simeq J_\perp \sum_\nu h_{\text{eff}} \int dx (-1)^\nu S_{\nu,Z}(x)$. Using the standard bosonization representation of the spins, the Hamiltonian then becomes a sine-Gordon Hamiltonian whose sine term represents the effects of the effective staggered field [11]. The physics of such a Hamiltonian is well known, and there are two phases. First, there is a critical phase, where one recovers the massless excitations. This corresponds to the high temperature phase where the chains are essentially decoupled. Second, there is a massive phase where the cosine is relevant¹ and acquires an average value. This means that $\langle(-1)^\nu S_{\nu,Z}(x)\rangle$ is now non-zero, which signals true long range order in the system. The system thus exhibits a genuine phase transition as a function of the temperature towards

¹In the standard language of renormalization theory, terms are defined as *relevant* when they do not tend to zero under a renormalization transformation, and *irrelevant* otherwise.

an ordered state that would correspond to anisotropic antiferromagnetic three-dimensional (3D) behavior. The critical temperature can be analyzed by using scaling analysis of the inter-chain coupling. Using (12.1) leads to the renormalization flow of the inter-chain exchange:

$$\frac{dJ_{XY}}{dl} = J_{XY}(2 - \frac{1}{2K}), \quad (12.3)$$

$$\frac{dJ_Z}{dl} = J_Z(2 - 2K), \quad (12.4)$$

where l describes the renormalization of the bandwidth of the systems $\Lambda(l) = \Lambda_0 e^{-l}$ and Λ_0 is the bare bandwidth. One sees that one of the couplings is always relevant regardless of the value of K and that one has always an ordered state (for a non-frustrated inter-ladder coupling) at low enough temperature.

However, the critical nature of the 1D systems leads to a strong renormalization of the critical temperature with respect to a naive mean-field approximation; the latter would result in $T_c \sim J_\perp$. Instead, strong 1D fluctuations lead to

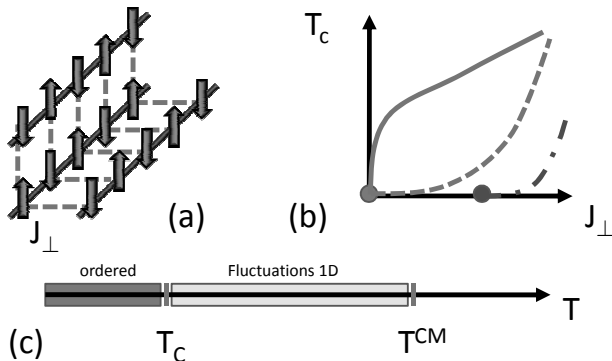
$$T_c^{XY} = J_\parallel \left(\frac{J_\perp}{J_\parallel} \right)^{1/(2-1/2K)}, \quad T_c^Z = J_\parallel \left(\frac{J_\perp}{J_\parallel} \right)^{1/(2-2K)}, \quad (12.5)$$

as can be deduced directly from (12.3), since the critical temperature follows from $l^* = \log(\Lambda_0/T_c)$ for which the running coupling is $J_\perp(l^*) \sim J_\parallel$. The strong 1D fluctuations thus have a large effect on the critical temperature and create a wide regime where the system is dominated by 1D fluctuations, as indicated on Fig. 12.1. Although the temperature scale is strongly affected, the critical behavior still corresponds to that of the higher-dimensional case. However, the quasi-1D nature of the problem has strong consequences for the existence of extra modes of excitations in comparison to what happens for a more isotropic system [11]. We will come back to this point when discussing bosons, where these modes can be more simply understood.

12.1.2 Dimer or Ladder Coupling

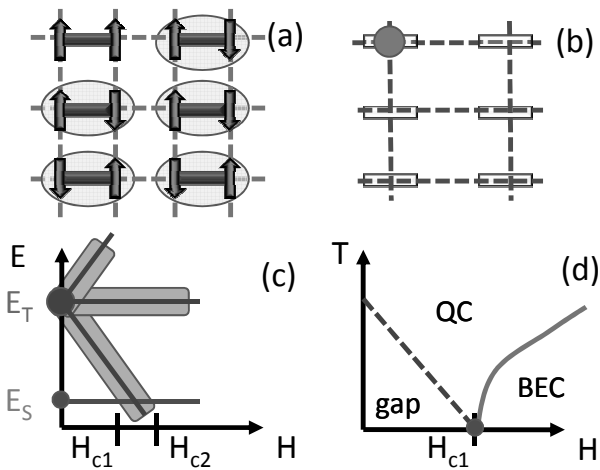
A much more complex behavior occurs when the objects that become coupled have a gap in their spectrum, a gap that is in competition with the presence of the inter-chain coupling (12.2). In this case one can expect a real QPT to occur in which the system goes from a low-dimensional gapped situation, to a higher-dimensional ungapped one. This transition is called generically a *deconfinement transition*, since the system changes both its effective dimensionality and the nature of its spectrum at the same time. This particular type of QCP manifests itself in several types of systems and we will examine it for spins, bosons and fermions.

The case of spin is the simplest. To illustrate the nature of this QCP let us consider first the case of a system made of dimers, weakly coupled by

**FIGURE 12.1**

(a) Coupled 1D chains. The inter-chain coupling J_{\perp} (dashed line) is much weaker than the intra-chain one J_{\parallel} (full line). This leads to properties linked to the Luttinger liquid ones of the 1D chains. (b) Depending on the Luttinger liquid parameter K , the critical temperature is a power law of the inter-chain coupling J_{\perp} , since the coupling is strongly renormalized by 1D fluctuations. The exponent is either smaller than one (full line), or when the fluctuations increase, larger than one (dashed line). If K is below (or above depending on the correlations, see text) a certain value, fluctuations are small enough and lead to an ordered state as soon as some inter-chain coupling is introduced. However, if the fluctuations are large enough, ordering is suppressed unless the inter-chain coupling reaches a critical value (dashed-dotted line). Note that in this case usually another correlation orders since several instabilities are in competition. (c) Because of the strong 1D fluctuations, the mean-field temperature can be quite different from the actual critical temperature to an ordered state.

(12.2). In this case each dimer has a gap between a singlet state and the three triplet states. The gap is of order J_d , the dimer spin exchange. Since there is a gap in the spin excitation spectrum, the dimer is robust to the inter-dimer exchange coupling and the ground state in the case $J_{\perp} \ll J_d$ is made of essentially uncoupled dimers. In this case we are considering a cluster of zero-dimensional objects coupled by the inter-dimer coupling. If we now place the system in a magnetic field the dimer gap reduces and ultimately the lowest triplet state reaches the level of the singlet one as depicted in Fig. 12.2. In this case the inter-dimer coupling is able to delocalize the triplets and lead to a transition where the system will go from a set of essentially uncoupled zero-dimensional objects to an essentially 3D antiferromagnet. Quite remarkably, this deconfinement transition can be analyzed by mapping the singlet-lowest triplet onto a hard-core boson. The system is thus equivalent to a set of

**FIGURE 12.2**

(a) If one of the exchanges J_d (thick line) is larger than the others J (dashed line) then one has a system made of coupled dimers. Because a dimer goes into a singlet state (oval shape), the ground state of such a system is made of decoupled singlets. (b) One can map such a system onto a system of hard-core bosons, the presence of a boson denoting a triplet state on the dimer, and its absence a singlet. Because of spin exchange one has an equivalent system of bosons hopping on a lattice with a kinetic energy given by the inter-dimer magnetic exchange J . In addition to the hard-core constraints bosons have nearest-neighbor interactions. (c) Application of a magnetic field lowers the energy of one of the triplet states (thick dot) compared to the singlet one (small dot). Because the triplet disperses, there is a band of triplet excitations (triplons). Changing the magnetic field allows one to fill this band of triplons which are the hard-core bosons of (b). The field H_{c1} corresponds to the first triplon entering the system, while the field H_{c2} is a filled band of triplons. Such a system thus provides an excellent venue in which to study interacting bosons on a lattice, since the density of bosons can be controlled directly by the magnetic field, and measured by the magnetization along the field direction. (d) This system has a quantum phase transition at H_{c1} ; a similar transition exists at H_{c2} , not shown here. The triplons exhibit Bose-Einstein condensation (BEC), which corresponds in spin language to antiferromagnetic order in the direction perpendicular to the magnetic field. “Gap” and “QC” denote the gapped state in which there are no triplons and the quantum critical state, respectively.

hard-core bosons, the density of which is controlled by the magnetic field.² When the first triplets enter the system at a critical field h_{c1} the bosons are extremely dilute; thus their hard-core interaction is not felt very strongly. The phase transition is thus Bose-Einstein condensation [12]. The QCP at $T = 0$ corresponds to the point where the chemical potential is such that a finite density of bosons starts to appear. This has several interesting consequences for the nature of the phase diagram and in particular allows one to predict features such as the critical temperature which behaves as

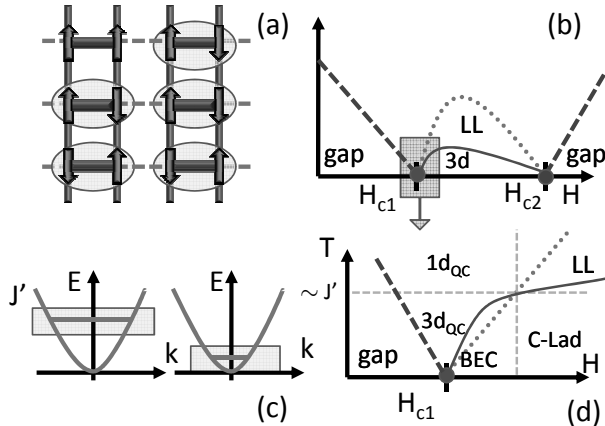
$$T_c \propto (h - h_{c1})^{2/d}, \quad (12.6)$$

as well as non-monotonous temperature dependence of the magnetization of the system. Since its original prediction, these behaviors have been studied and observed in several compounds with both 3D [13–15] and bi-dimensional structure [16]. For a review on these aspects I refer the reader to [17].

A similar class of deconfinement transitions occurs when the objects that are coupled have a 1D structure. For example, when one deals with a spin one chain [18] or a two leg spin ladder [12]. Both these structures are characterized by a gap. Application of a magnetic field allows one to break the gap and to study the transition to the 3D behavior. In this case one gets a very interesting behavior which is depicted in Fig. 12.3. If one is far from the critical field H_{c1} the chemical potential of the excitations in the 1D chain is high and in particular larger than the inter-chain coupling. One is thus dealing essentially with the situation depicted in the previous section, of weakly coupled 1D LL, and one can study the transition to the ordered state. Dimers present several advantages to study this phase transition since the singlet is extremely robust to external perturbations, such as dipolar interactions. Such interactions would break the spin rotation symmetry in the XY plane and thus in the boson mapping break the phase $U(1)$ symmetry. Recently, very nice experimental realizations of ladder systems have been analyzed [19–22]. These analyses have allowed for a quantitative test of the predictions of the LL and of the generic scenarios described above for the transition to the ordered state.

When getting closer to the field H_{c1} one cannot consider that the system is made of coupled LLs since the temperature is getting larger than the distance to the bottom of the band, and one has to consider the 1D quantum critical behavior. Such a situation, although more complex, can still be analyzed by various techniques [23]. In a similar way, when lowering the temperature one has to consider an additional crossover where the temperature becomes smaller than the inter-ladder coupling J_\perp . This corresponds to going from a 1D quantum critical regime of weakly coupled ladders to the 3D one of coupled dimers, as described in Sec. 12.1.1. The resulting physical behavior is thus quite complex and largely not understood, despite the analysis of

²Zero boson density means that all dimers are in the singlet state, while one boson per site means that each dimer is fully polarized.

**FIGURE 12.3**

(a) Coupled ladders correspond to a hierarchy of coupling where the leg coupling J_{\parallel} (solid line) is smaller than the rung coupling J_d (thick line), but larger than the inter-ladder coupling J' (dashed line). In the same way as in Fig. 12.1 this leaves room for 1D fluctuations and Luttinger liquid physics to modify the behavior as compared to the more isotropic case of Fig. 12.2. (b) As a result, a LL regime exists between H_{c1} and H_{c2} . In this regime a good physical description of the triplons is to consider that they behave as spinless fermions. The regime 3d where the spins order antiferromagnetically is the equivalent of the BEC regime of Fig. 12.2. (c) As long as the coupling J' is larger than the chemical potential $H - H_{c1}$ one can consider the system as made of coupled 1D systems and 1D fluctuations play a major role. On the contrary, when $J' > (H - H_{c1})$ one must consider a 3D system from the start since there is no room for 1D fluctuations to take place. One thus returns to the case of Fig. 12.2. (d) As a result there is a more complex crossover regime when the field H gets close to H_{c1} . C-Lad denotes coupled ladders and BEC is the Bose-Einstein condensation of Fig. 12.2.

several quantities, such as the NMR response. Other ways to control such a phase transition include applying pressure instead of the magnetic field; this changes the ratio J_{\perp}/J_{\parallel} and thus makes the system more 3D, as described in Chap. 1. We proceed to consider this type of transition in more detail for the related but different case of itinerant bosons and fermions.

12.2 Bosons: From Mott Insulators to Superfluids

Consider first the case of coupled bosonic chains. In principle, such a system is very close to the problem of coupled spin chains, since a spin 1/2 can be represented by a hard-core boson. However, the absence of the hard-core constraint, and of the nearest neighbor interaction that corresponds to the $J_Z \sum_i S_i^Z S_{i+1}^Z$, leads in practice to quite different regimes than for coupled spin chains. Nevertheless, most of the techniques and concepts that we used for spin chains will be directly useful for coupled bosonic chains.

Although in principle one can realize coupled bosonic systems in condensed matter, e.g., using Josephson junction arrays [24], it is relatively difficult to obtain a good realization. Recently, cold atomic systems in optical lattices have provided a remarkable and very controlled realization on which many of the aspects discussed below can be tested in experiments, as discussed in Chap. 19.

For the case of bosons the coupling between the chains comes mostly from the single-particle hopping from one chain μ to the neighboring one ν . This term in the Hamiltonian takes the form

$$H_\perp = -t_\perp \sum_{\langle \nu, \mu \rangle} \int dx \psi_\mu^\dagger(x) \psi_\nu(x). \quad (12.7)$$

Along the chains, interacting bosons can be represented either by a continuum theory or directly on a lattice by a Bose-Hubbard model. In 1D both these cases can be mapped to a LL description for the low energy properties [3, 25, 26]. The corresponding Hamiltonian is

$$H^0 = \frac{1}{2\pi} \int dx \left\{ \frac{u}{K} [\pi\Pi(x)]^2 + uK(\nabla\theta)^2 \right\}, \quad (12.8)$$

where θ is the superfluid phase determined by $\psi(x) = \rho(x)^{1/2} e^{i\theta(x)}$. The field $\Pi(x)$ is canonically conjugate to θ and is associated with density fluctuations. The long-wavelength density fluctuations can indeed be represented as $\rho(x) = \rho_0 - \pi^{-1} \nabla\phi(x)$ and $\pi\Pi(x) = \nabla\phi(x)$. Also, u is the velocity of the sound waves in the 1D systems, while K is the LL exponent which depends on the microscopic interactions. For bosons with a contact interaction, $K = \infty$ for non-interacting bosons, while $K \rightarrow 1^+$ when the contact interaction becomes infinite. The latter is the *Tonks-Girardeau limit*.

As for spins, the properties will be crucially dependent on whether the 1D bosonic system is gapless or not. In the continuum, the full description of the system is indeed given by (12.8). In the presence of a lattice or a periodic potential one should take into account oscillations of the density with periodicity $2\pi\rho_0$, of the form $\delta\rho(x) \propto \cos(2\pi\rho_0 x - 2\phi(x))$. These oscillations, when commensurate with the period of the lattice, e.g., with one boson per

site, can lead to a Mott-insulating phase for the bosons [3, 26–28]. In this case the full 1D Hamiltonian becomes

$$H = H^0 - g \int dx \cos(2\phi(x)), \quad (12.9)$$

where g is a constant proportional to the lattice strength for small lattices or the interaction for large ones [3]. Such a term becomes relevant for $K < 2$ and leads to an ordered phase $\phi(x)$. Since ϕ is locked by the cosine term, this corresponds to frozen density fluctuations, and thus a Mott-insulating phase with an integer number of bosons per site. Since ϕ and θ are conjugate variables this implies that superfluid correlations decrease exponentially and that the quasi-long-range superfluid order is destroyed. Let us examine both these cases, with and without the commensurate term.

12.2.1 Coupled Superfluid: Dimensional Crossover

The case in the absence of the lattice, or when the lattice is irrelevant, is very similar to the coupled spin chains examined in Sec. 12.2. Each 1D chain is critical with a quasi-long-range superfluid order, since with (12.8) the superfluid correlations decay as a power-law:

$$\langle \psi(x)\psi^\dagger(0) \rangle \propto x^{-1/2K}. \quad (12.10)$$

One can treat the inter-chain coupling in the mean-field approximation, since boson single-particle operators can have a mean-field value:

$$H_\perp = -t_\perp \sum_{\langle\mu\nu\rangle} \int dx [\langle\psi_\mu^\dagger(x)\rangle\psi_\nu(x) + h.c.] \rightarrow -\Delta \int dx \cos(\theta(x)), \quad (12.11)$$

where $\Delta = 2z\rho_0^{1/2}t_\perp\langle\psi^\dagger(x)\rangle$, and z is the coordination of the lattice. Thus one finds a sine-Gordon Hamiltonian in the superfluid phase that can freeze the phase θ and lead to *long range* superfluid order [29,30]. Note that without the mean-field approximation the interaction term in phase language becomes

$$H_\perp = -2t_\perp\rho_0 \sum_{\langle\nu,\mu\rangle} \int dx \cos(\theta_\nu(x) - \theta_\mu(x)). \quad (12.12)$$

Given the quadratic form of (12.8), and taking time as an extra classical dimension, one can immediately map this problem onto coupled XY planes. For a 3D system one would thus be in the universality class of the five-dimensional XY model, justifying the use of the mean-field approximation.³ As for the problem of spins, 1D fluctuations strongly renormalize the critical temperature as compared to the naive mean-field value $T_c \sim t_\perp$. The scaling is very similar to that of Sec. 12.2 [30].

³The mean-field approximation is exact in the limit that the number of nearest neighbors approaches infinity.

An interesting effect can be seen when looking at fluctuations around the ground state in the low temperature superfluid phase. As can be readily seen by performing a random-phase-approximation (RPA) treatment [30] of the Hamiltonian $H^{1D} + H_{\perp}$, two eigenmodes exist. One is the standard phase mode, where the amplitude of the order parameter is essentially fixed but $\theta_{\nu}(x)$ slowly varies in space and from chain to chain. The energy of this mode goes to zero, since this is the standard Goldstone mode of the superfluid. However, another eigenmode exists, corresponding to a change in amplitude of the order parameter, and thus also $\rho(x) = \rho_0 + \delta\rho(x)$. Not surprisingly, this mode is dispersing above a finite energy E_0 but exists as a sharply defined mode, in a way very similar to plasmons in charged systems. Such a mode would not appear in a more isotropic superfluid, as can be readily seen by solving the Gross-Pitaevskii equation [31]. This is one clear-cut case where the higher-dimensional system still shows some traces of its 1D origin and displays qualitative differences as compared to an isotropic system. Such modes have also been observed close to Mott transitions in isotropic systems [30, 32].

12.2.2 Coupled Mott Chains: Deconfinement Transition

As for spins, the situation is much more interesting and complex when the 1D chains are in the Mott-insulating phase. In this case it is clear that there is a competition between the Mott term (12.9), caused by the periodic potential along the chains that prefers order in the phase ϕ controlling the density, and the inter-chain Josephson term (12.12) that prefers to order the superfluid phase θ . This is the bosonic equivalent of the competition between the spin gap and the transverse magnetic order that existed for the spin chains, and was discussed in Sec. 12.2.1. This competition leads to a deconfinement QPT.

In contrast to the case of spins, where the 1D gap was closed by changing the magnetization, in the case of bosons one stays at a commensurate density and the critical point is reached by changing the strength of the inter-chain hopping. This is very similar to the question of the application of pressure in the case of the spins. A similar transition to the one studied in Sec. 12.2.1 could also occur in the case of bosons. It corresponds to the application of a chemical potential taking the system away from the commensurate point. In this case the 1D system is described by a commensurate-incommensurate phase transition [3] and the universality class of the deconfinement transition is different. We confine our present discussion to the commensurate case; see [30] for the incommensurate one.

In the commensurate case there are several ways to analyze the deconfinement transition. In the mean-field approximation the system is described by a *double sine-Gordon Hamiltonian*. This Hamiltonian has a set of remarkable properties that have been looked at in various contexts [33]. The critical point can be crudely obtained via renormalization of the two relevant operators and fixing the phase of the operator that first reaches strong coupling. A more sophisticated analysis can be found in Ref. [30]. In particular, the universality

class of the transition can be shown to be that of the $(d + 1)$ -dimensional XY model [28]. Indeed the operator $\cos(2\phi)$ is nothing but the vortex creation operator for excitations of the phase θ [3]. Each chain can thus be mapped onto a discrete XY Hamiltonian of the form $H = J \sum_{ij} \cos(\theta_i - \theta_j)$ and the inter-chain coupling has a similar form but with a different coefficient. A schematic representation of the phase diagram is shown in Fig. 12.4. As for the spins, there is a deconfinement transition between an essentially 1D insulating phase, where the bosons are in a Mott state, and an anisotropic 3D superfluid phase. In the Mott phase, there is a gap towards excitations, and the density is well ordered, i.e., one particle per site. The anisotropic superfluid phase is gapless and is similar to the one that was discussed in the absence of a lattice in the previous section. Such physics can be probed in cold atomic systems in systems made of coupled bosonic tubes such as [34].

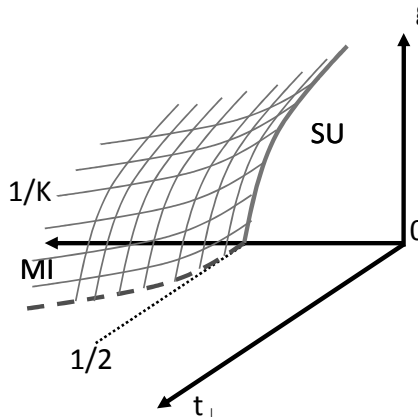
12.3 Fermions: Dimensional Crossover and Deconfinement

Let us finally move to the very challenging problem of coupled 1D fermionic chains. As for bosons, the system is described by a Hamiltonian

$$H = \sum_{\alpha} H_{\alpha}^{1D} - t_{\perp} \sum_{\langle \alpha, \beta \rangle} \int dx \psi_{\alpha}^{\dagger}(x) \psi_{\beta}(x). \quad (12.13)$$

However, there is a very important difference between the fermionic case and the two previous sections. Indeed, for fermions the single-particle operator cannot have an average value: $\langle \psi_{\alpha} \rangle = 0$. We cannot treat the inter-chain coupling by treating the single-particle operator in a mean-field approximation as we did before. It is thus difficult to find theoretical tools to tackle this problem on the analytical side. Similarly, on the numerical side one cannot use the efficient methods of the 1D world, such as the density matrix renormalization group of Chap. 22. One has to use the arsenal of higher-dimensional Monte Carlo methods, which can suffer from the sign problem, as described in several chapters of Part IV.

Analytically, one can use a renormalization technique similar to the one introduced in Secs. 12.2.1-12.2.2 to study the relevance of the inter-chain hopping, as we will discuss in more detail below. Unfortunately, it will only yield information about whether the inter-chain coupling is relevant, not what the strong-coupling fixed point actually is. To understand this physics, and replace the mean-field treatment used in the two previous cases, two approximate methods have proven useful for fermions, as summarized in Fig. 12.5. The first and simplest one is to treat the inter-chain coupling in RPA [35].

**FIGURE 12.4**

Phase diagram for quasi-1D bosons on a lattice (at $T = 0$): g is the intra-chain periodic potential responsible for the Mott transition for commensurate filling; t_{\perp} is the inter-chain kinetic energy or Josephson coupling; and K is the Luttinger parameter that depends on the intra-chain interactions ($K = \infty$ corresponds to free bosons). The thick solid line is the boundary between a 1D Mott insulator and a quasi-ordered 1D superfluid. For very small g the Mott phase occurs for $K < 2$. The thick dashed line indicates how the extra kinetic energy provided by the inter-chain coupling weakens the Mott state. The thin (green) lines are the deconfinement transition between a Mott insulator and an anisotropic 3D superfluid.

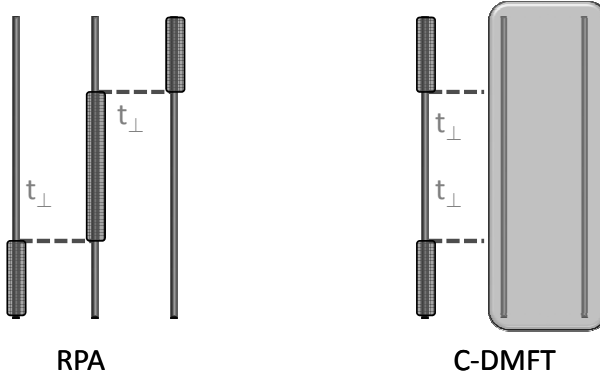
This leads to

$$G(k, k_{\perp}, \omega) = (G_{1D}^{-1}(k, \omega) - t_{\perp} \cos(k_{\perp}))^{-1}. \quad (12.14)$$

RPA has the advantage of being very simple. However, it neglects all feedback of the inter-chain hopping on the 1D properties themselves, which is clearly a very brutal approximation. A better approximation is provided by an extension of dynamical mean-field theory (DMFT) [36], where one treats all the chains but one as an external self-consistent bath into which the particles can jump [37, 38]. This is detailed in Fig. 12.5. From a more formal point of view one could view it naively as performing a mean-field approximation on the second-order term in the hopping in the action

$$\begin{aligned} S'_{\perp} &= t_{\perp}^2 \sum_{\mu, \nu} \int dr dr' \psi_{\mu}^{\dagger}(r) \psi_{\nu}(r) \psi_{\nu}^{\dagger}(r') \psi_{\mu}(r') \\ &\rightarrow t_{\perp}^2 \sum_{\mu, \nu} \int dr dr' \psi_{\mu}^{\dagger}(r) \langle \psi_{\nu}(r) \psi_{\nu}^{\dagger}(r') \rangle \psi_{\mu}(r'), \end{aligned} \quad (12.15)$$

where $r = (x, \tau)$ are the space-time coordinates. One thus has an effective

**FIGURE 12.5**

The two main approximations used to tackle the inter-chain coupling for fermions. RPA: the fermions hop but essentially never come back to the original chain. The properties of a single chain are thus not affected at all by the inter-chain hopping. In particular, the Mott gap is strictly independent of t_{\perp} . Ch-DMFT: all the chains but one are treated as a self-consistent bath. The 1D Green's function thus depends approximately on the inter-chain hopping. This corresponds to the approximation of taking the 1D self-energy independent of the transverse momentum k_{\perp} but potentially dependent on the frequency and momentum along the chains.

intra-chain kinetic energy, nonlocal in space and time, whose amplitude is controlled by the single-particle Green's function on another chain $G_{\nu}(r, r')$. Such a Green's function must thus be determined self-consistently, and one has to solve an effective 1D Hamiltonian with a modified kinetic energy. Because the energy now depends self-consistently on the results of the inter-chain tunneling, there is a direct feedback of the inter-chain tunneling on the 1D features, contrary to the case of the RPA. Although still imperfect this is an improvement which should allow one to obtain several of the features more accurately.

As for bosons, let us examine the two cases depending on whether the 1D system is critical (LL) or gapped (typically a Mott insulator). In the first case the inter-chain hopping leads simply to a dimensional crossover between 1D and higher-dimensional behavior, while in the second case a deconfinement transition occurs.

12.3.1 Dimensional Crossover

If the 1D system is in a critical LL state, the inter-chain hopping has in general a strong influence on it. In a similar way as for the bosons, one can estimate the relevance of the single-particle hopping by a simple scaling analysis. If the

single-particle Green's function decreases as

$$G^{1D}(r) \propto r^{-[K_\rho + K_\rho^{-1} + 2]/4}, \quad (12.16)$$

where K_ρ is the charge LL parameter [3], then the perpendicular hopping obeys the renormalization equation coming from the second order expansion in the inter-chain hopping [39, 40]:

$$\frac{\partial t_\perp}{\partial l} = t_\perp \left[2 - \frac{1}{4} (K_\rho + K_\rho^{-1} + 2) \right]. \quad (12.17)$$

Thus when $K_\rho + K_\rho^{-1} > 6$ the inter-chain hopping is irrelevant. The intra-chain interactions are enough to prevent the coherent hopping since a single-particle excitation must be reconstructed for the electron to be able to hop from one chain to the next. Note that this implies rather strong, as well as finite, range interactions [3]. Indeed, for a purely local interaction such as the one coming from a Hubbard model, $1/2 < K_\rho < 2$ and thus the inter-chain hopping would always be relevant. The fact that the inter-chain hopping is irrelevant does not mean that there is no coupling at all between the chains; it just means that single-particle excitations cannot propagate coherently between them. One must then go to second order in the inter-chain hopping. To second order, the inter-chain hopping generates both particle-hole coupling, i.e., either density-density or spin-spin, or particle-particle coupling, i.e., Josephson. One of these couplings can become relevant and lead to an ordered state. The couplings can be treated by mean-field theory, as explained in the previous sections and in more detail in Ref. [3].

If $K_\rho + K_\rho^{-1} < 6$, called *moderate interactions*, the inter-chain hopping is a relevant perturbation. There will thus exist an energy scale⁴ below which the system will crossover from 1D to higher-dimensional behavior. Note that this is a simple crossover and that no phase transition occurs here. The 1D nature of the system strongly affects the *scale* at which the inter-chain hopping acts. This scale is roughly determined by the condition $t_\perp(l^*) = 1$. Thus one finds the crossover at

$$E_{\text{cross}} \propto E_F \left(\frac{t_\perp}{E_F} \right)^{1/(2-\zeta)}, \quad (12.18)$$

where $\zeta = [K_\rho + K_\rho^{-1} + 2]/4$ is the single-particle correlation exponent. As we saw for spins, interactions considerably lower the crossover scale and reinforce the range of validity of the 1D regime. The properties of the resulting low-temperature phase are still a largely open question. In particular, how much this phase remembers the effects of strong correlations coming from the high energy 1D physics is important to determine. Some elements of response can be obtained via the various mean-field approximations mentioned above. Quantities strongly depending on the transverse directions are very interesting but

⁴For example, temperature, frequency determined via probes such as optical conductivity, energy determined via probes such as STM, etc. For more details on how to probe this crossover see [41, 42].

also very difficult to compute. This includes the Hall effect and the transverse conductivity. In particular, the latter can be an indication of the dimensional crossover transition temperature since the absence in the 1D regime or the presence in the higher-dimensional regime of well formed single-particle excitations will lead to very different temperature dependence. This is the case, e.g., for organics superconductors [43] and for inorganic compounds [5].

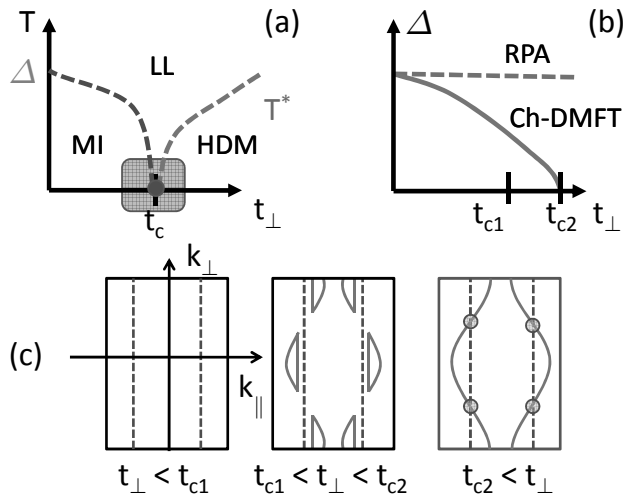
12.3.2 Deconfinement Transition

The situation is particularly difficult for fermions when the 1D phase is gapped. The expected phase diagram is schematically indicated in Fig. 12.6. Let us examine in more detail the features of such a transition. Although the generic shape of the $T - t_{\perp}$ diagram reminds us of what is to be expected for a generic QPT, the order and even the number of transitions are not known with certainty. In some cases, both from the RPA and from Ch-DMFT, two different transitions are expected to occur.

The physics of the massive (Mott) phase is relatively clear. The effective gap is reduced by the additional kinetic energy provided by the inter-chain hopping. Such an effect is well described by the Ch-DMFT approximation, which shows a reduction of the 1D gap as t_{\perp} increases. In principle, one needs the transverse directions to be on a non-bipartite lattice. Otherwise, the Fermi surface remains nested despite the inter-chain hopping and the gap does not vanish. This is specially important for the organic compounds. At a certain critical value of the inter-chain hopping, one expects to break the Mott-insulating phase and recover a higher-dimensional metal. How this transition occurs is still unclear. Within RPA and Ch-DMFT approximations, one goes through an intermediate phase where pockets appear as depicted in Fig. 12.6. At larger values of the inter-chain hopping the pockets merge and one expects to recover an open Fermi surface. This scenario is established for spinless particles [44]. Whether it survives for fermions with spins is still an open question.

Another important open question is to get an accurate description of the properties of the higher-dimensional metal, and in particular whether one gets back a Fermi liquid or whether there is a serious influence of the strong correlations that existed in the 1D part of the phase diagram. Even if one recovers a Fermi liquid, as is the case with the Ch-DMFT method for example, there is clearly a strong variation of the lifetime and quasiparticle weight along the Fermi surface (hot spots). How to reliably compute such effects is a considerable challenge.

Finally, let us point out that such transitions are important for a host of quasi-1D systems. Deconfinement transitions are investigated in organics [42, 45] but the inter-chain hopping also clearly plays a crucial role in systems such as purple bronze [5]. Both these systems still have a poorly understood superconducting phase in the higher-dimensional regime. How much such a phase is influenced by the 1D nature of the material still remains to

**FIGURE 12.6**

(a) Phase diagram for the deconfinement transition of quasi-1D coupled fermionic chains. There is a quantum critical point (dot) that separates a Mott insulator from a higher-dimensional metal (HDM). For small inter-chain hopping $t_{\perp} < t_c$ there is a crossover scale, the renormalized Mott gap Δ . For temperatures $T > \Delta$ the system behaves as a LL, while it acts as a Mott insulator for smaller temperatures. On the metallic side there is a coherence scale T^* scaling with the inter-chain hopping that separates the LL regime from the higher-dimensional metal in which coherent hopping between the chains occurs. The nature of the deconfinement transition and whether there is a unique transition or a more complex scenario such as two consecutive transitions are still largely open questions. (b) The effective Mott gap Δ as predicted both by the RPA and the Ch-DMFT approximation. (c) With the current approximations there would be three different phases, leading to different Fermi surfaces. (i) At small gap one has a Mott insulator with only zeros of the Green's function. (ii) At intermediate gaps the inter-chain hopping induces an indirect doping, leading to pockets on the Fermi surface. (iii) For larger hopping the gap closes and the pockets join to give back the open Fermi surface of a quasi-1D metal. Note that the Fermi parameter varies strongly on such a Fermi surface, reminiscent of the 1D character. In particular, there would be hot spots (dots). The scenario with two transitions can be established for spinless fermions with the Ch-DMFT approximation. Whether such a scenario survives with fermions with spins is still an open question. In the RPA the gap is not destroyed by the inter-chain hopping, leading to a rigid-band scenario. As a consequence, the pockets depicted in (c) never close in such an approximation.

be determined. Cold atomic systems are now allowing us to realize quasi-1D structures of fermions as well, and will undoubtedly provide an excellent experimental realization in which to study these problems.

12.4 Conclusions and Perspectives

1D and quasi-1D systems are a paradise for QPTs. Due to the intrinsic critical nature of interacting quantum systems, a pure 1D system can present a set of instabilities, the simplest one being associated with the occurrence of one or several gaps in the systems. This occurs in the case of the Mott transition in 1D, among many other examples.

Another important class of QPTs is driven by the inter-chain coupling between 1D systems. This is an especially important case given the direct experimental relevance for several realizations, ranging from naturally occurring materials to cold atoms in optical lattices. In this case two main classes exist. If the 1D chain is gapless, one usually finds a dimensional crossover between a high temperature or high energy 1D regime and a low temperature one dominated by the inter-chain coupling. For spins or bosons, the low-temperature state is usually ordered. Although this state is mostly an anisotropic version of the 3D one, it can still retain some special features coming from the quasi-1D character. The case of fermions is more complex and the low-temperature phase is a higher-dimensional metal. If the 1D chains are gapped one finds a deconfinement transition where the system goes at zero temperature from a 1D gapped state to a high dimensional ordered or gapless one, the latter occurring in particular for fermions. The nature of this transition in fermionic systems is largely not understood and constitutes a very challenging research field.

Although we have some of the tools and some understanding of such transitions many crucial questions remain. First, in contrast to the case of a purely 1D system for which we have a whole arsenal of analytical and numerical tools to tackle the questions of such transitions, the quasi-1D case is much more difficult. Most of the numerical techniques are becoming very inefficient, either due to their intrinsic limitations, such as the sign problem for the fermions, or simply the large anisotropy of the system that makes even well-controlled methods difficult to apply. Clearly some new techniques are needed. On the analytical side it is difficult to go beyond mean-field theory, and thus to compute some of the correlation functions, especially those involving directly the transverse degrees of freedom. Going through the critical regime is also quite challenging, even if we have a good idea of the various phases. Of special importance are the transverse transport, the Hall or Nernst effect, and the propagation of some transverse modes.

Some other topics are directly related to these issues and present very

challenging topics in themselves. The self-consistent dynamical mean-field approximation of coupled LL replaces this problem by that of a LL in equilibrium with an external bath. The bath has drastic consequences on the critical properties of the LL. This type of problem also occurs directly, either due to the presence of external electrons or noise. How to tackle such questions is certainly one of the frontiers of our knowledge of 1D systems. Finally, all the examples of QCPs examined in this chapter were based on a LL or a gapped phase as the description of the 1D system. However, there are now several identified 1D cases in which one has to go beyond the LL paradigm to describe the physics of the systems. Understanding the physics of such non-Luttinger liquids is a challenge in itself, much as the understanding of non-Fermi liquids is. How to go from the standard LL behavior to a non-LL one, or what happens when non-LLs are coupled in a 3D lattice is a totally uncharted territory.

Acknowledgments – This work was supported in part by the Swiss NSF under MaNEP and Division II.

Bibliography

- [1] G. D. Mahan, *Many Particle Physics* (Plenum, New York, 1981).
- [2] F. D. M. Haldane, J. Phys. C **12**, 4791 (1979); F. D. M. Haldane, J. Phys. C **14**, 2585 (1981); F. D. M. Haldane, Phys. Rev. Lett. **45**, 1358 (1980).
- [3] T. Giamarchi, *Quantum Physics in One Dimension* (Oxford University Press, Oxford, 2004).
- [4] Chem. Rev. **104**, (2004), special issue on Molecular Conductors.
- [5] F. Wang *et al.*, Physical Review Letters **103**, 136401 (2009); J. Hager *et al.*, Phys. Rev. Lett. **95**, 186402 (2005); X. Xu *et al.*, Phys. Rev. Lett. **102**, 206602 (2009), and refs. therein.
- [6] D. A. Tennant, R. A. Cowley, S. E. Nagler, and A. M. Tsvelik, Phys. Rev. B **52**, 13368 (1995).
- [7] B. Lake, D. A. Tennant, and S. E. Nagler, Phys. Rev. Lett. **85**, 832 (2000).
- [8] E. Dagotto and T. M. Rice, Science **271**, 5249 (1996); E. Dagotto, Rep. Prog. Phys. **62**, 1525 (1999).
- [9] I. Bloch, J. Dalibard, and W. Zwerger, Rev. Mod. Phys. **80**, 885 (2008).
- [10] F. D. M. Haldane, Phys. Rev. Lett. **50**, 1153 (1983); J. P. Renard *et al.*, Europhys. Lett. **3**, 945 (1987).

- [11] H. J. Schulz, Phys. Rev. Lett. **77**, 2790 (1996); M. Bocquet, F. H. L. Essler, A. M. Tsvelik, and A. O. Gogolin, Phys. Rev. B **64**, 094425 (2001).
- [12] T. Giamarchi and A. M. Tsvelik, Phys. Rev. B **59**, 11398 (1999).
- [13] T. Nikuni, M. Oshikawa, A. Oosawa, and H. Tanaka, Phys. Rev. Lett. **84**, 5868 (2000).
- [14] C. Ruegg *et al.*, Nature (London) **423**, 62 (2003).
- [15] M. Matsumoto, B. Normand, T. M. Rice, and M. Sigrist, Phys. Rev. B **69**, 54423 (2004).
- [16] S. E. Sebastian *et al.*, Nature **441**, 617 (2006).
- [17] T. Giamarchi, C. Ruegg, and O. Tchernyshyov, Nature Physics **4**, 198 (2008).
- [18] I. Affleck, Phys. Rev. B **41**, 6697 (1990).
- [19] B. C. Watson *et al.*, Phys. Rev. Lett. **86**, 5168 (2001).
- [20] M. Klanjsek *et al.*, Phys. Rev. Lett. **101**, 137207 (2008).
- [21] C. Rüegg *et al.*, Phys. Rev. Lett. **101**, 247202 (2008).
- [22] B. Thielemann *et al.*, Phys. Rev. B **79**, 020408(R) (2009).
- [23] E. Orignac, R. Citro, and T. Giamarchi, Phys. Rev. B **75**, 140403(R) (2007).
- [24] R. Fazio and H. van der Zant, Phys. Rep. **355**, 235 (2001).
- [25] M. A. Cazalilla, J. Phys. B **37**, S1 (2003).
- [26] T. Giamarchi, in *Lectures on the Physics of Highly Correlated Electron Systems X* (AIP conference proceedings, 2006), p. 94, arXiv:cond-mat/0605472.
- [27] F. D. M. Haldane, Phys. Rev. Lett. **47**, 1840 (1981).
- [28] M. P. A. Fisher, P. B. Weichman, G. Grinstein, and D. S. Fisher, Phys. Rev. B **40**, 546 (1989).
- [29] K. B. Efetov and A. I. Larkin, Sov. Phys. JETP **42**, 390 (1975).
- [30] A. F. Ho, M. A. Cazalilla, and T. Giamarchi, Phys. Rev. Lett. **92**, 130405 (2004); M. A. Cazalilla, A. F. Ho, and T. Giamarchi, New. J. of Phys. **8**, 158 (2006).
- [31] L. Pitaevskii and S. Stringari, *Bose-Einstein Condensation* (Clarendon Press, Oxford, 2003).

- [32] S. D. Huber, B. Theiler, E. Altman, and G. Blatter, Phys. Rev. Lett. **100**, 050404 (2008).
- [33] J. V. José, L. P. Kadanoff, S. Kirkpatrick, and D. R. Nelson, Phys. Rev. B **16**, 1217 (1977); L. P. Kadanoff, J. Phys. A **11**, 1399 (1978); T. Giamarchi and H. J. Schulz, J. Phys. (Paris) **5**, 819 (1988).
- [34] T. Stöferle *et al.*, Phys. Rev. Lett. **92**, 130403 (2004).
- [35] F. H. L. Essler and A. M. Tsvelik, Phys. Rev. B **65**, 115117 (2002).
- [36] A. Georges, G. Kotliar, W. Krauth, and M. J. Rozenberg, Rev. Mod. Phys. **68**, (1996).
- [37] E. Arrigoni, Phys. Rev. Lett. **83**, 128 (1999); A. Georges, T. Giamarchi, and N. Sandler, Phys. Rev. B **61**, 16393 (2000); E. Arrigoni, Phys. Rev. B **61**, 7909 (2000); S. Biermann, A. Georges, A. Lichtenstein, and T. Giamarchi, Phys. Rev. Lett. **87**, 276405 (2001).
- [38] S. Biermann, A. Georges, T. Giamarchi, and A. Lichtenstein, in *Strongly Correlated Fermions and Bosons in Low Dimensional Disordered Systems*, edited by I. V. Lerner *et al.* (Kluwer Academic Publishers, Dordrecht, 2002), p. 81, cond-mat/0201542.
- [39] S. Brazovskii and V. Yakovenko, J. de Phys. (Paris) Lett. **46**, L111 (1985); C. Bourbonnais and L. G. Caron, Physica (Utrecht) **143B**, 450 (1986); X. G. Wen, Phys. Rev. B **42**, 6623 (1990); C. Bourbonnais and L. G. Caron, Int. J. Mod. Phys. B **5**, 1033 (1991); V. M. Yakovenko, JETP Lett. **56**, 510 (1992); D. Boies, C. Bourbonnais, and A.-M. S. Tremblay, Phys. Rev. Lett. **74**, 968 (1995).
- [40] H. J. Schulz, in *Correlated Fermions and Transport in Mesoscopic Systems*, edited by T. Martin, G. Montambaux, and J. Tran Thanh Van (Editions frontières, Gif sur Yvette, France, 1996), p. 81.
- [41] T. Giamarchi, Chem. Rev. **104**, 5037 (2004).
- [42] C. Bourbonnais and D. Jerome, in *Physics of Organic Superconductors and Conductors*, edited by A. G. Lebed (Springer, Heidelberg, 2008), p. 357, T. Giamarchi, ibid, p. 719.
- [43] J. Moser *et al.*, Eur. Phys. J. B **1**, 39 (1998); M. Dressel *et al.*, Phys. Rev. B **71**, 75104 (2005); W. Henderson *et al.*, Eur. Phys. J. B **11**, 365 (1999).
- [44] C. Berthod, T. Giamarchi, S. Biermann, and A. Georges, Phys. Rev. Lett. **97**, 136401 (2006).
- [45] A. Pashkin, M. Dressel, M. Hanfland, and C. A. Kuntscher, Phys. Rev. B **81**, 125109 (2010).

13

Metastable Quantum Phase Transitions in a One-Dimensional Bose Gas

Lincoln D. Carr

Department of Physics, Colorado School of Mines, Golden, CO 80401, U.S.A.

Rina Kanamoto

Division of Advanced Sciences, Ochadai Academic Production, Ochanomizu University, Bunkyo-ku, Tokyo 112-8610 Japan

Masahito Ueda

Department of Physics, University of Tokyo, Bunkyo-ku, Tokyo 113-0033 Japan

Ultracold quantum gases offer a wonderful playground for quantum many-body physics [1], as experimental systems are widely controllable, both statically and dynamically. One such system is the one-dimensional (1D) Bose gas on a ring. In this system binary contact interactions between the constituent bosonic atoms, usually alkali metals, can be controlled in both sign and magnitude; a recent experiment has tuned interactions over seven orders of magnitude [2], using an atom-molecule resonance called a Feshbach resonance. Thus one can directly realize the Lieb-Liniger Hamiltonian (LLH) [3,4], from the weakly- to the strongly-interacting regime. At the same time there are a number of experiments utilizing ring traps [5]. The ring geometry affords us the opportunity to study topological properties of this system as well; one of the main properties of a superfluid is the quantized circulation in which the average angular momentum per particle, L/N , is quantized under rotation [6]. Thus we focus on a tunable 1D Bose system for which the main control parameters are interaction and rotation. We will show that there is a critical boundary in the interaction-rotation control-parameter plane over which the topological properties of the system change. This is the basis of our concept of *metastable quantum phase transitions* (QPTs). Moreover, we will show that the finite domain of the ring is necessary for the QPT to occur at all because the zero-point kinetic pressure can induce QPTs, i.e., the system must be finite; we thus seek to generalize the concept of QPTs to inherently finite, mesoscopic or nanoscopic systems.¹

Specifically, we will show that past the critical boundary the phase of a

¹See also Chap. 27 for a discussion of finite-size effects on QPTs in the context of nuclei.

Bose-Einstein condensate (BEC) can wind and unwind continuously and can therefore no longer be considered a superfluid in the usual sense, despite a single mode still being macroscopically occupied [7]. Since the interaction and rotation will be in units related to the ring size, another way to look at this critical boundary is that the superfluidity in this example is a mesoscopic effect and might vanish in the thermodynamic limit. Using mean-field theory in the form of the celebrated Gross-Pitaevskii or nonlinear Schrödinger equation (NLSE), the presence of the critical boundary can be tied to the appearance of new stationary solutions, *dark solitons*, which bifurcate from a *uniform superflow* or plane-wave branch. Dark solitons, which take the form of a density notch in BECs, can have zero density, in which case they are called *black* and have a node, or a region of decreased density without a node, in which case they are called *gray*. Gray solitons have a characteristic phase structure which allows for the topological winding and unwinding, as we will show. As the density contrast of a gray soliton tends to zero, i.e., as it becomes shallower, its phase structure, density, and energy approach those of uniform superflow. Arrays of regularly spaced dark solitons are called *dark-soliton trains*. Dark solitons, black and gray, singly and in trains, have been observed in BEC experiments, beginning with [8,9] and, more recently, in [10,11]. Although dark-soliton trains are robustly stable in quasi-1D mean-field theory,² in practice they are found to decay in experiments. This has been attributed first to use of 3D geometries, in which dark soliton nodal planes decay via the snake instability into vortex–anti-vortex pairs; in this case mean-field theory provides an excellent description of the ensuing dynamics. However, even in quasi-1D experiments dark solitons are found to decay; the main cause is thought to be thermal [13] and/or quantum fluctuations [14,15].

The study of quantum fluctuations, and the use of dark-soliton decay as a smoking-gun signal for fluctuations, has a long track record. It turns out that dark solitons can also be observed in optical fibers with anomalous dispersion and a Kerr nonlinearity [16]. The governing equation is again the NLSE, and dark solitons decay due to periodically spaced fiber amplifiers. This effect is called Gordon-Haus jitter [17], and can be formulated as a 1D random walk with the accompanying diffusion equation. In BECs, thermal effects can play a similar role [13,18]. However, at very low temperatures and for a quasi-1D mean-field one is left with only quantum fluctuations as the cause of dark soliton decay. Thus a thorough investigation of such fluctuations was undertaken by Dziarmaga *et al.*, starting with [14]. Using the Bogoliubov-de Gennes equations (BdGE) and modified version thereof, they found that although dark solitons delocalized, due to the anomalous or Goldstone mode, they did not in fact decay. That is to say that averaging over many measurements one finds the soliton fills in, but for a single measurement a dark soliton is found somewhere in the condensate. However, the BdGE are limited to weak

²Quasi-1D means that the mean field is confined but the underlying binary scattering problem remains 3D. See [12] for details.

interactions. Recently one of us studied this problem in the more strongly interacting regime, placing the soliton in an optical lattice to enhance quantum fluctuations and using matrix-product-state (MPS) algorithms to follow the dynamics.³ We found that a dark soliton does indeed decay at zero temperature, based on three main pieces of evidence: density-density correlations, inelasticity in soliton-soliton collisions, and a close comparison to Bogoliubov theory via an analysis of modes of the single-particle density matrix. It has recently been demonstrated that it is possible in the weakly interacting regime for the filling-in of density-density correlations to be consistent with delocalization rather than decay [19, 20]; however, the strongly-interacting regime remains an open question. Thermal fluctuations in dark solitons have also been used to study the dynamics of phase transitions in the Kibble-Zurek mechanism [21]; see Chap. 3.

We will show that dark-soliton trains on a ring are in fact the weakly-interacting limit of *yrast states* [22, 23], and that it is really the yrast states that play the key role in our finite-size metastable QPT when analyzed in the full many-body problem beyond mean-field theory. Yrast, a Swedish term originally used in nuclear physics which can be translated as ‘dizziest,’ refers to the lowest energy state for a given angular momentum. We will identify Lieb’s *Type II* or hole excitations with the yrast states, solving the long-standing question of the physical interpretation of this solution branch of the LLH [24]. The uniform superflow states which the soliton trains bifurcate from will be replaced with the more general *center-of-mass rotation* (CMR) states, a special class of yrast states for which L/N is an integer. In the NLS mean-field theory, the phase winding number comes out of a calculation of the circulation; out of the mean-field regime, such terminology becomes questionable if not meaningless. Thus the whole concept of uniform superflow and of superfluidity breaks down; yet our QPT persists as an accurate picture of an abrupt transition in even the strongly-interacting system’s properties. In fact, we can take this description all the way to the *Tonks-Girardeau* (TG) limit in which one obtains an exact solution to the problem via the TG Bose-Fermi mapping [25]. At the end of our chapter, we will come back to the connection between yrast states and quantum fluctuations of dark solitons.

Finally, we wish to make a brief comment on dimensionality. Although there is formally no superfluid phase transition in 1D, nevertheless for an interacting finite system there is in practice still a sharp crossover to a macroscopically occupied mode at a critical temperature. One should keep in mind that bounded and/or finite domain reduced-dimensional systems often have distinctly different properties from their infinite counterparts, for instance graphene, which is unstable on the infinite domain due to thermal fluctuations, but, as we know now, not only stable on finite domain but has many important technical applications [26]. Likewise, this is an exciting time for the study of 1D systems, not so much for the possibility of revolutionizing

³Specifically, we used time-evolving block decimation(TEBD); see Chap. 23.

computing as with graphene, but for revolutionizing our understanding of quantum many-body physics. 1D systems have some special advantages for that purpose. First, there are established exact solution methods such as the Bethe ansatz for special but nevertheless important systems, including the focus of the present study, the LLH. We will take advantage of the plethora of 1D theoretical techniques in our study in order to bring to bear multiple lines of evidence on our problem. Second, experiments in ultracold quantum gases [27] are allowing for the thorough investigation and testing of fundamental 1D questions, including Kolmogorov-Moser-Arnold (KAM) theory for integrable quantum systems, quantum quenches, and a host of other zero and finite-temperature effects. Third, there are exciting new developments in MPS numerical methods that allow one to follow entangled quantum many-body dynamics of 1D systems, integrable or nonintegrable, as discussed in Chaps. 23 and 22.

This chapter draws strongly from three papers [28–30], the foundations for which were laid by [31]; however, our previous work on dark solitons [15,32–34] also plays an important role in our discussion and our thinking. Our set of theoretical techniques for this study included the NLSE, the BdGE, exact diagonalization in a truncated angular momentum basis, the finite-size Bethe ansatz equations, and the TG equations.⁴ We will sketch the results of these techniques, referring the reader to [29, 30] for details.

Unlike the excited state QPTs in nuclear physics described in Chap. 27, our QPT occurs in an inherently finite system. The QPT here disappears in the thermodynamic limit and cannot be extrapolated from finite size scaling or other such arguments. Thus there is no concept of nonanalyticity (see, e.g., Chap. 1) and it is formally a crossover. Given the prevalence of nano-devices and other inherently finite systems, we think the term *finite-system* QPT is a useful one, as we hope to convince the reader in the course of this chapter.

13.1 Fundamental Considerations

We begin with a clear statement of the Hamiltonian. In position representation the LLH is [4]

$$\hat{H}_0 = - \sum_{j=1}^N \partial_{\theta_j}^2 + g_{1D} \sum_{j < k} \delta(\theta_j - \theta_k), \quad (13.1)$$

where θ_j is the azimuthal angle that satisfies $0 \leq \theta_j < 2\pi$ and g_{1D} is the binary contact interaction strength renormalized for our 1D problem. We take the experimental context of the LLH as N bosons in a thin torus, or ring trap.

⁴An MPS approach is also possible, but requires spatial discretization, an aspect we wish to avoid. A continuum limit of MPS is possible in principle but tricky, requiring typically thousands of lattice sites; see [35].

The torus has radius R ; we take the length, angular momentum, and energy to be measured in units of R , \hbar , and $\hbar^2/(2mR^2)$, respectively, throughout our treatment.

In a rotating frame of reference with an angular frequency 2Ω the LLH becomes

$$\hat{H}(\Omega) = \hat{H}_0 - 2\Omega\hat{L} + \Omega^2 N, \quad (13.2)$$

where

$$\hat{L} \equiv -i \sum_{j=1} \partial_{\theta_j} \quad (13.3)$$

is the angular-momentum operator; we refer to Eq. (13.2) as the *rotating LLH* (rLLH). From the single-valuedness boundary condition of the many-body wave function [39], one can show that solving the eigenproblem in the rest frame $\hat{H}_0\Psi_0 = E(0)\Psi_0$ suffices in order to obtain solutions to the eigenproblem $\hat{H}(\Omega)\Psi = E(\Omega)\Psi$ [29]. The eigenvalue is then obtained from $E(\Omega) = E(0) - 2\Omega\langle\hat{L}\rangle + \Omega^2 N$, which is periodic with respect to Ω .

The subclass of solutions to the rLLH we focus on are the yrast states. This approach is useful for our ring system, because all the information about physical properties in the rotating frame are embedded within the spectrum in the rest frame. Thus the physical meanings of yrast states can be extracted by the simple transformation of yrast spectra. Since the LLH commutes with the angular-momentum operator, $[\hat{H}_0, \hat{L}] = 0$, the yrast problem is well defined irrespective of the sign and strength of interaction,⁵ and all the yrast states are eigenstates of both the LLH \hat{H}_0 and the rLLH $\hat{H}(\Omega)$.

We can identify the yrast states by dividing the solution space of \hat{H}_0 and \hat{H} into subspaces according to the two conserved quantities in the problem: the number of bosons N , and the total angular momentum $L \equiv \langle\hat{L}\rangle$. In each such subspace we can index excited states by $q \in \{1, 2, \dots\}$ in ascending order in energy; thus the state-ket is written $|N, L; q\rangle$. Then the yrast states are denoted as $|N, L; q=1\rangle$. The essential properties of the ground and low-lying excited states can be described within the yrast states, as we have verified explicitly with exact diagonalization studies.⁶ Thus we henceforth omit the quantum number q from the notations for eigensolutions. With the abbreviation of the quantum number $q = 1$ and for fixed coupling constant g_{1D} , the eigenvalues that correspond to the yrast states are written as $E_{N,L}(\Omega)$, where we explicitly write the parameter Ω in the notation in order to clarify in which frame the system is. With this notation, the eigenvalues in the nonrotating frame are written as $E_{N,L}(0)$.

Most of the yrast states will turn out to be dark solitons for weak interactions, but in this limit a special subclass corresponds to uniform superflow. Due to the translational invariance of the LLH with respect to θ and Ω , properties of a particular set of yrast states can be analyzed without solving the

⁵Throughout this chapter we focus on repulsive interactions $g_{1D} > 0$, for which QPTs only occur in excited states. However, for attractive interactions, $g_{1D} < 0$, QPTs occur also in the ground state [31].

⁶Such studies necessarily used a truncated single-particle angular-momentum basis, as the Hilbert space is otherwise too large.

problem. These are the CMR states. In particular, they are the states for which the total angular momentum is equal to an integer multiple of the total number of atoms N . The energy of the CMR state takes the form

$$E_{N,L=JN}(0) = J^2 N + V_{\text{int}}, \quad (13.4)$$

where V_{int} is the interaction energy and $J \in \mathbb{Z}$ is an integer. We call J the *center-of-mass quantum number*, because it physically expresses the amount of uniform translation of the center-of-mass momentum. In the NLS mean-field theory, J is conventionally called the phase winding number, but this is a valid concept only in the weakly interacting limit, and we retain the more general notion for our purpose of identifying the QPT through all interaction regimes. In the rotating frame, the energy of the CMR state is given by

$$E_{N,JN}(\Omega) = (J - \Omega)^2 N + V_{\text{int}}, \quad (13.5)$$

where the change in energy associated with the frame change is involved only in the kinetic energy term, and the interaction energy is completely separated from the parameter Ω .

The ground state in the absence of the rotating drive is the state with zero angular momentum, $E_{N,L=0}(0)$. The excitation energy of the CMR states with a finite angular momentum $L = JN$ is thus given by

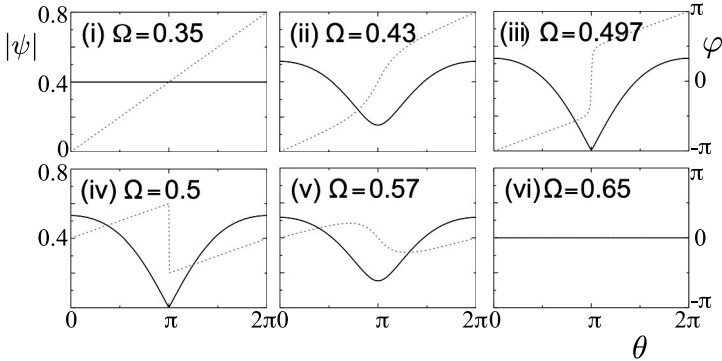
$$E_{N,JN}(0) - E_{N,0}(0) = J^2 N, \quad (13.6)$$

which is independent of the strength of interaction g_{1D} . This is natural because changing the total angular momentum by the amount JN leads to a Galilean transformation without changing the boundary condition for the order parameter. The ground state in the presence of the rotating drive is characterized by the CMR quantum number⁷

$$J_0 = \lfloor \Omega + 1/2 \rfloor. \quad (13.7)$$

Because of the periodicity in the eigensolutions, an eigenstate $|N, L\rangle$ with the energy $E_{N,L}(\Omega)$ has a denumerably infinite number of counterparts $|N, L+JN\rangle$ and $|N, L+JN\rangle$, corresponding to arbitrary values of $J \in \mathbb{Z}$. Solving the yrast problem for a limited range of fixed angular-momentum states, e.g., $-N/2 \leq L < N/2$, therefore suffices to obtain all the eigensolutions. Moreover, the spectra are degenerate for the same magnitude of angular momentum, $E_{N,L} = E_{N,-L}$ in the absence of rotating drive, while this degeneracy is resolved in the presence of rotation due to the Sagnac effect [40]. All other yrast states for L out of this limited range can be obtained by shifting the total angular momentum by N while keeping the internal structure of the eigenstates. This is similar to a band theory concept [29], with $-N/2 \leq L < N/2$ playing the role of the first Brillouin zone.

⁷ $\lfloor x \rfloor$ is the floor function, meaning the largest integer that does not exceed x .

**FIGURE 13.1**

Topological winding and unwinding of a BEC via formation of a dark soliton. Shown are the mean-field amplitude (solid curves with the left reference) and phase (dotted curves with the right reference). Uniform solutions with different values of the phase winding (i) $J = 1$ and (vi) $J = 0$ are smoothly connected through the broken-symmetry dark soliton (ii)–(v) with a self-induced phase slip at (iv) $\Omega = 0.5$. Reproduced from [28].

13.2 Topological Winding and Unwinding: Mean-Field Theory

We first introduce the basic concept of the finite-size metastable QPT in the simplest context, namely mean-field theory. We restrict ourselves to a fairly qualitative discussion; a complete quantitative theory, including full analytical solutions and perturbative stability analysis, can be found in [28, 29].

The NLSE, which can be derived directly from the rLLH [1],⁸ is

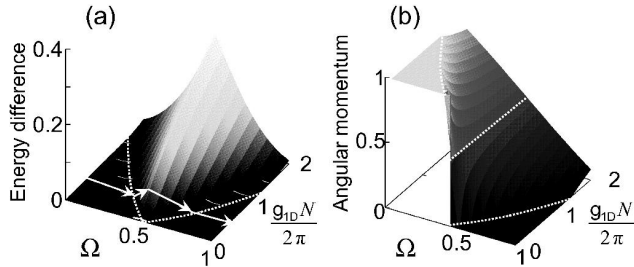
$$[(-i\partial_\theta - \Omega)^2 + g_{1D}N|\psi(\theta)|^2]\psi(\theta) = \mu\psi(\theta), \quad (13.8)$$

where all bosons are taken to be in the same macroscopic mode which is described by the order parameter ψ ; this order parameter can be interpreted physically in terms of a density, $|\psi|^2$, and a phase, $\varphi \equiv \text{Arg}(\psi)$. The single-valuedness of the wave function requires $\varphi(\theta + 2\pi) = \varphi(\theta) + 2\pi J$, where J is an integer and can, in this weakly-interacting limit, be understood as a topological winding number.

The uniform superflow solutions of the NLSE are just plane waves, $\psi(\theta) = \psi_0 \exp(iJ\theta)$, while the dark-soliton train solutions are expressed in terms of Jacobi elliptic functions.⁹ We take the number of density notches in the dark-

⁸The key assumption is to take a macroscopically occupied mode in the single particle density matrix and neglect small fluctuations around that mode; subsequently one replaces averages over products of operators with the product over averages.

⁹In the infinite-system limit a single dark soliton is written in terms of a tanh function.

**FIGURE 13.2**

(a) The bifurcation between uniform-superflow and dark-soliton states are illustrated in terms of (a) energy difference and (b) average angular momentum per particle L/N . The soliton solutions only exist in the area surrounded by two critical boundaries (white dotted curves). The white arrow in (a) indicates the path taken during the unwinding of the phase shown in Fig. 13.1. In (b) one clearly sees two topologically distinct regions: in between the critical boundaries the characteristic quantization of \bar{L} in the BEC breaks down, even though there is still macroscopic occupation of a single mode. Reproduced from [28].

soliton train to be j . For the rest of this section, we consider the single soliton $j = 1$ for simplicity, but our discussion holds for arbitrary soliton trains $j > 1$.

Figure 13.1 illustrates how an initial uniform-superflow solution with $J = 1$ can be continuously unwound to $J = 0$. As Ω increases starting from (i) the uniform superflow with $J = 1$, (ii) solitons start to form past a critical point $\Omega_{\text{crit}}^{(1)}$. (iii) The density notch deepens for $\Omega_{\text{crit}}^{(1)} \leq \Omega \leq 0.5$. (iv) At $\Omega = 0.5$ it forms a node, the phase of the soliton jumps by π , and the energies of the solitons with phase winding number 1 and 0 are degenerate. (v) The soliton with phase winding $J = 0$ deforms continuously as Ω increases. (vi) Finally, the state goes back to the uniform-superflow state with phase winding $J = 0$. For the purposes of illustration we have taken a fixed interaction strength $g_{1D}N = 0.6$; in fact, interaction and/or rotation can be used to wind or unwind the order parameter; likewise, one can characterize the whole process in terms of system size, while holding other parameters fixed.

In Fig 13.1 we observe the characteristic phase structure of dark solitons: inside the density notch, the phase changes more rapidly, and the total difference across the notch yields the soliton's velocity; outside the density-notch region, the phase has a uniform slope, indicating the velocity of the uniform superflow. Since a dark soliton moves with a velocity which is opposite to the direction of increase in phase (to the left in Fig. 13.1), one can understand such stationary solutions as a cancellation between dark-soliton motion to the left, clockwise looking down on the ring from above, and uniform superflow to the right, or counter-clockwise.

Figure 13.2(a) shows the energy difference between a dark soliton and

uniform superflow, as can be calculated analytically. This kind of bifurcation does not occur from the ground-state energy. However, for metastable states a bifurcation can occur between the uniform-superflow state and the soliton state with the same winding number J . After bifurcation, the soliton energy becomes larger than the uniform-superflow energy. For convenience, Fig. 13.2(a) displays a white arrow indicating the higher-energy, soliton path taken in Fig. 13.1. Exact diagonalization studies were used to show that an arbitrary potential which breaks the symmetry of the ring automatically sets the system on this path. Shown in Fig. 13.2(b) is the key physical observable for our QPT, the average angular momentum per particle, expressed as $L/N = \int d\theta \psi^*(-i\partial_\theta)\psi$, in the mean-field theory. Thus a continuous change of angular momentum is possible for 1D Bose systems by taking the metastable states with energy slightly higher than that of the ground state. Both panels of Fig. 13.2 display a lower and an upper critical angular frequency, which we call $\Omega_{\text{crit}}^{(1)}$ and $\Omega_{\text{crit}}^{(2)}$, as a function of g_{1D} .

Bifurcation of the soliton train from the uniform superflow constitutes a second-order QPT with respect to g_{1D} and/or Ω . The derivatives of the soliton and uniform-superflow energies with respect to Ω have a kink at the boundary as can be verified analytically. This identifies the QPT, at least at the mean-field level, which occurs along a curve in the Ω - g_{1D} plane. We also found that the Hessian for the energy is discontinuous along this curve, while the Hessian for the chemical potential diverges.

13.3 Finding the Critical Boundary: Bogoliubov Analysis

We can better understand the QPT through the BdGE. The BdGE can be derived formally as the lowest order quantum fluctuations from the LLH; it can also be simply thought of as linear perturbation theory on the NLSE, and is taken as such in optics. In either case, without Bogoliubov analysis in terms of the BdGE we cannot be certain that our dark-soliton train solutions are stable even in the mean-field limit. Moreover, the BdGE allow us to explicitly identify the critical boundaries shown in Fig. 13.2.

A stationary solution $\psi(\theta)$ of the NLSE under a small perturbation δ evolves in time as

$$\tilde{\psi}(\theta, t) = e^{-i\mu t} \{ \psi(\theta) + \sum_n [\delta u_n(\theta) e^{-i\lambda_n t} + \delta v_n^*(\theta) e^{i\lambda_n^* t}] \}, \quad (13.9)$$

where (u_n, v_n) , and λ_n are the eigenstates and eigenvalues of the BdGE, respectively, and $n \in \mathbb{Z}$ denotes the energy-index of excitations. Recalling the structure of solutions in the Bogoliubov formalism [37], for each eigenvalue λ_n

with positive norm,

$$\int_0^{2\pi} d\theta \left[|u_n(\theta)|^2 - |v_n(\theta)|^2 \right] = 1, \quad (13.10)$$

there is also an eigenvalue $\bar{\lambda}_n \equiv -\lambda_n$ with negative norm. The BdGE predict an infinite set of such solutions. One exception to this rule can exist. This exception corresponds to *Nambu-Goldstone modes*, sometimes called anomalous modes. For instance, consider a black soliton is at rest on the ring with respect to any background superflow in the rotating frame. The Goldstone mode of the soliton corresponds to the soliton moving at a small constant velocity in this frame. We need consider only the Goldstone mode and eigenstates that satisfy (13.10), since the eigenvalues with negative norm do not have physical meaning. For the Goldstone mode the corresponding eigenvalue is zero, and the latter eigenstates that have positive norms can be real (i.e., positive or negative) or complex depending on the stability of the condensate mode. In general, $\lambda_n \in \mathbb{C}$.

The excitations of a uniform superflow with phase-winding J are straightforward to calculate [37]. Fluctuations from that condensate mode are given by the eigensolutions of the BdGE with positive norm,

$$\lambda_l^{(J,\text{us})} = \sqrt{l^2(l^2 + 2\gamma)} - 2l(\Omega - J), \quad u_l \propto e^{i(J+l)\theta}, \quad v_l \propto e^{-i(J-l)\theta}, \quad (13.11)$$

where the ‘us’ subscript stands for uniform superfluid, $\gamma \equiv g_{1D}N/2\pi$, and $l \in \mathbb{Z}$ denotes the single-particle angular momenta of the excitation, a good quantum number since $[\hat{H}(\Omega), \hat{L}] = 0$.

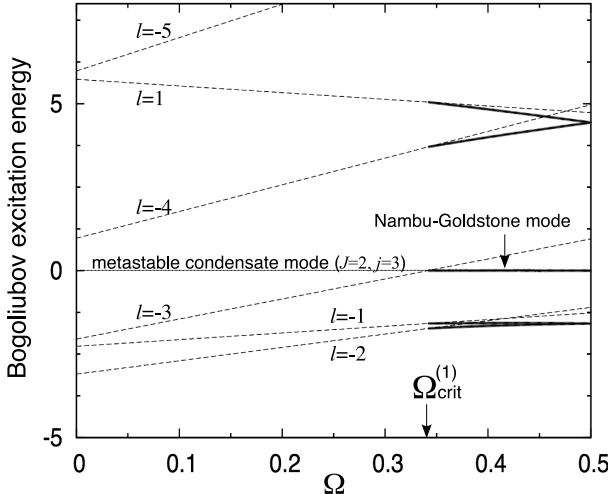
For $\gamma > 0$, all the eigenvalues $\lambda_l^{(J,\text{us})}$ are real, as apparent from Eq. (13.11). From Eq. (13.11) we also find that several negative eigenvalues, associated with eigenstates of positive norm, appear when we take a metastable *excited* state as a condensate mode. These negative eigenvalues correspond to other plane-wave branches located in lower energy regimes than the input condensate mode itself. For the case of repulsive interactions, the number of negative eigenvalues thus coincides with the number of stationary states that are located in a lower energy regime than the metastable state under consideration. Solutions of the BdGE for dark-soliton trains require a numerical calculation.

We can identify the critical boundary $(\gamma_{\text{crit}}, \Omega_{\text{crit}})$ for the QPT by finding where a particular negative eigenvalue changes its sign. One equates l to be $\pm j$ in Eq. (13.11) and imposes the condition on the eigenvalue, $\lambda_{l=\pm j}^{(J,\text{us})} = 0$. Then the critical boundaries are given implicitly by

$$\Omega_{\text{crit}} - J = \pm \sqrt{(j/2)^2 + \gamma_{\text{crit}}/2}, \quad (13.12)$$

where the \pm sign gives the lower and upper boundary, respectively, which we called $\Omega_{\text{crit}}^{(1)}$ and $\Omega_{\text{crit}}^{(2)}$. The region $\gamma \leq \gamma_{\text{crit}}$ is identical to requiring that the critical-boundary condition has a real solution.

In Fig. 13.3 we illustrate the QPT from uniform-superflow to dark-soliton solutions; we illustrate only $0 \leq \Omega \leq 0.5$ since the eigenvalues are symmetric

**FIGURE 13.3**

Bogoliubov analysis of uniform superflow (thin dashed curves) and dark-soliton trains (thick solid curves). The initial uniform-superflow state (zero excitation energy shown as the thin solid curve and labeled with text) with phase winding $J = 2$ becomes the Nambu-Goldstone mode of the three-notch ($j = 3$) dark-soliton train, past the critical frequency $\Omega_{\text{crit}}^{(1)}$. Other curves show excitation energies from the uniform and soliton train states, respectively, with various angular momenta labels l . We take fixed interaction $g_{1D}N/2\pi = 1$ for this illustration. Reproduced from [29].

for the other half of the Brillouin zone. The soliton-train solutions occurring for $\Omega > \Omega_{\text{crit}}^{(1)}$ are therefore linearly stable.¹⁰ The excitation energies from the soliton branch are found to be close to those from the plane-wave branch. The notable feature in the soliton regime is that there appears a Nambu-Goldstone mode, which is continuously connected with one of the negative eigenstates with $l = Sj$ from the plane wave. This mode reflects the *spontaneous symmetry breaking* of the soliton-train state. At the point $\Omega_{\text{nodes}} = 0.5$, a degenerate pair of excitation branches emerges, where the phase jumps up or down by π at each soliton in the soliton train. This degeneracy is similar to that seen for a single soliton in Fig. 13.1, but slightly complicated by the multiple solitons and higher phase winding. For $\Omega > \Omega_{\text{nodes}}$ the excitation branches from the soliton train are also symmetric with respect to Ω_{nodes} .

For expediency we skip more details of BdGE solutions and summarize the overall results. We found that excitations from the uniform superflow in the j^{th} excited-state have j thermodynamically unstable modes within the

¹⁰They are also nonlinearly stable [33].

critical region in the (γ, Ω) -plane. In $\Omega_{\text{crit}}^{(1)} < \Omega \leq 0.5$ in the dark-soliton train states become stable. At the critical boundary, all energies of the stationary solutions and the eigenvalues of the BdG equations continuously connect to the excitations in the soliton regime without any energy discontinuity. In particular, when one of the excitation energies from a plane-wave metastable state changes sign from negative to positive, a soliton branch with the same phase-winding number appears, and the Nambu-Goldstone mode manifests as a result.

Thus, upon consideration of general phase winding J and soliton-number j , one realizes that there are a denumerably infinite set of paths to connect uniform-superflow states via soliton trains in a metastable system of scalar bosons on a ring. Associated with this transition, the energy of the solitons bifurcates, and a continuous change in the angular momentum becomes possible in the mean-field theory past a critical boundary in the interaction-rotation plane. In general, bifurcations can indicate symmetry breaking associated with a QPT, as in the elementary example of the quadratic-quartic potential, where a single potential well bifurcates into two as the relative strengths of quadratic and quartic terms are tuned.

13.4 Weakly-Interacting Many-Body Theory: Exact Diagonalization

We now show how in general to distill the uniform-superflow and soliton-train mean-field branches from a sea of many-body eigenvalues. We show how the mean-field soliton branch, for which average angular momentum is not quantized as an integer, emerges from the yrast spectra. The meaning of spectra related to symmetry breaking and the Nambu-Goldstone mode associated with the existence of the soliton branch is also discussed.

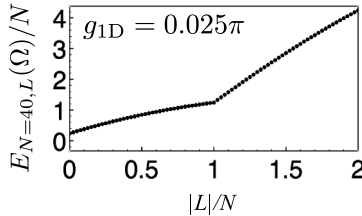
In order to take the next step towards a microscopic many-body solution of the LLH, it is convenient to rewrite it in second-quantized form. One expands the bosonic field operator in terms of a plane-wave basis with the single-particle angular momentum l ,

$$\hat{\psi}(\theta) = (2\pi)^{-1/2} \sum_{l=-\infty}^{+\infty} \hat{b}_l e^{il\theta}, \quad (13.13)$$

where the pre-factor of $(2\pi)^{-1/2}$ comes from the normalization of the plane wave, and \hat{b}_l and \hat{b}_l^\dagger are annihilation and creation operators which obey the usual commutation relations for bosons. Equation (13.13) satisfies the periodic boundary condition $\hat{\psi}(\theta) = \hat{\psi}(\theta + 2\pi)$. Then one finds

$$\hat{H}_0 = \sum_{l=-\infty}^{+\infty} l^2 \hat{b}_l^\dagger \hat{b}_l + g_{1D} \sum_{k,l,m,n=-\infty}^{+\infty} \hat{b}_k^\dagger \hat{b}_l^\dagger \hat{b}_m \hat{b}_n \delta_{k+l,m+n}. \quad (13.14)$$

The eigenstates can be expanded in terms of a Fock-state basis $|\{n_l\}\rangle$ that

**FIGURE 13.4**

Yrast energy eigenstates for $N = 40$ bosons on the ring, obtained by exact diagonalization of the rLLH with the cutoff angular momentum $|l_c| = 2$. The spectrum has a kink where L is an integer multiple of N . Everything is symmetric for $L < 0$, and in the large N limit, the number of points increases and the discrete yrast energies approach a continuous curve while the curvature and kink points remain unchanged. Reproduced from [30].

represents the occupation number of each single-particle angular-momentum state,

$$|\{n_l\}\rangle = |\dots, n_{-1}, n_0, n_1, \dots\rangle. \quad (13.15)$$

These states satisfy the conservation laws

$$\sum_l n_l = N, \quad \sum_l l n_l = L. \quad (13.16)$$

For numerical calculations we use a cutoff angular momentum $l_c \geq 0$; thus $L \in [-l_c N, l_c N]$. In the weakly interacting regime $g_{1D} N \lesssim \mathcal{O}(1)$, a cutoff of $l_c = 2$ provides a quantitative agreement in energy eigenvalues¹¹ with those obtained by the Bethe ansatz shown in Sec. 13.6.

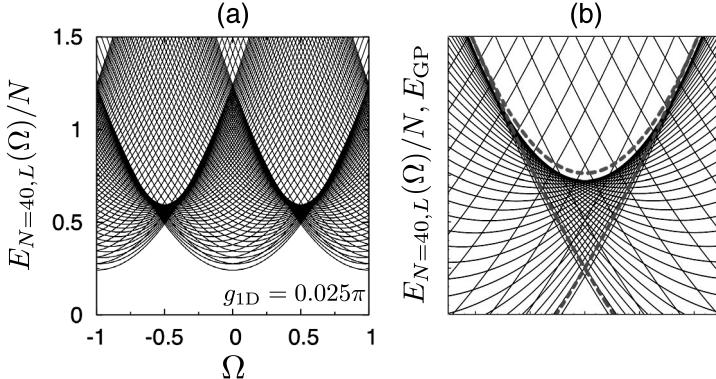
Figure 13.4 shows the yrast energies for the nonrotating LLH, $E_{N,L}(\Omega = 0) = \langle N, L | \hat{H}_0 | N, L \rangle$, for interaction strength $g_{1D} = 2.5 \times 10^{-2}\pi$ and number of bosons $N = 40$. The ratio of the mean-field interaction energy to the kinetic energy corresponding to these values of g_{1D} and N is $g_{1D} N / (2\pi) = 0.5$. The kink observed in the figure is exactly the CMR state $L = JN$, here $L = N$. In the mean field, this would be the uniform-superflow solution. The other non-CMR yrast states contribute to the dark-soliton solutions, as we will show.

To generalize Fig. 13.4 to the rotating rLLH, all we have to do is follow the procedure laid out in Sec. 13.1. We perform a Legendre transform on the LLH yrast spectrum,

$$E_{N,L}(0) \rightarrow E_{N,L}(\Omega) = E_{N,L}(0) - 2\Omega L + \Omega^2 N. \quad (13.17)$$

Figure 13.5 plots transformed yrast energies $E_{N,L}(\Omega)$, where the finite number

¹¹The convergence is better for (i) a larger number of atoms, (ii) lower eigenvalues, and (iii) smaller strength of interaction. Figure 13.9 indicates that for $N = 10$ and up to the yrast states $|L| = 2N$, the deviation of the exact diagonalization results from the Bethe ansatz results starts to emerge for $g_{1D} \gtrsim 1$. The results for $N = 40$ in this section has, in general, better agreement with the rigorous results.

**FIGURE 13.5**

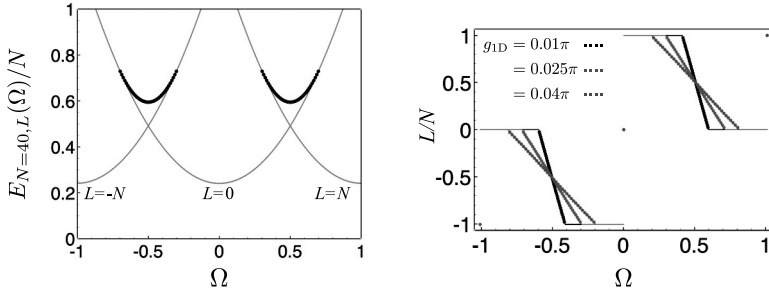
(a) Performing a Legendre transform on the yrast states in Fig. 13.4, we obtain the full yrast spectrum of the rLLH as a function of Ω . Each curve is distinguished by a different total angular momentum L . (b) A zoom of (a) in the important region where solitons appear in the mean-field theory. The dashed curves show a comparison to the NLSE superflow (blue) and soliton (red) branches. The enclosed region is called a swallowtail. Reproduced from [30].

of points from Fig. 13.4, each of which was characterized by a different angular momentum L , become convex downward curves in Fig. 13.5. Each curve is thus characterized by a different total angular momentum and has a minimum at a certain value of Ω .

The energy $E_{N,L=J_0N}(\Omega)$, shown in Fig. 13.5, corresponds to the ground state where J_0 is the ground-state CMR quantum number given by Eq. (13.7). The angular-momentum states with $L = JN$ correspond to the CMR states, and the center of the parabola is located at $\Omega \in \{\mathbb{Z}\}$ at which the CMR state becomes the ground state.

In Fig. 13.5(a) we observe an extremely high density of states around $\Omega \in \{\pm 0.5, \pm 1.5, \dots\}$ due to the crossing of many eigenvalues, as shown more clearly in the zoom in panel (b). The region of high density takes the shape of a *swallowtail*; the same shape was found to occur purely within mean-field theory, past the critical boundary for the QPT [29]. This swallowtail region is almost filled by various energy eigenvalues of various angular-momentum states crossing each other. The domain with the high-density swallowtail shape looks as if it is enclosed by the two kinds of stationary branches predicted by the mean-field theory.

How can we understand this spectrum? It is an interesting fact that mean-field theories tend to break the symmetries of many-body theories. In our case, if the NLSE has a soliton solution, the solution must be localized on the ring; the NLSE is nonlinear and cannot work with superpositions of solitons. In

**FIGURE 13.6**

The mean-field solutions can be extracted from our microscopic many-body analysis by using an extremization condition. (a) Energy. The thin curves have integer average angular momenta and agree with the energy of the mean-field uniform-superflow states; the thick points signify noninteger angular momentum and have an energy close to that of the mean-field dark-soliton states. (b) Angular momentum. Note that we use the same parameter set as Figs. 13.4 and 13.5. Reproduced from [30].

contrast, the quantum theory finds a superposition of all possible positions.¹² This is the main reason why Dziamarga *et al.* found that an initial mean-field soliton delocalizes at a higher level of quantum theory [14].

We can also see this effect in vortex formation in a scalar condensate under rotation. Solving the yrast problem in 2D results in all the angular-momentum states, including the at-rest condensate ($L = 0$), off-axis vortex ($0 < L < N$), a centered vortex ($L = N$), and vortex lattices ($L > N$). However, in experiments one drives the system with a specific angular frequency. In such a situation, there exists a small distortion in the trap, which selects a metastable angular-momentum state with respect to the variation in the angular momentum of the condensate. As a result, in reality one does not observe a stationary off-centered vortex except as a transient state.

The same argument applies to our case. In the presence of any kind of noise, such as an infinitesimal distortion of the trapping potential, quantum measurement of the matter wave, or whatever else breaks the translation symmetry of the ring trap, the realizable stationary state or metastable stationary state is determined by extremization with respect to variations in angular momentum. In order to find the metastable states we impose the condition

$$\partial_L E_{N,L}(\Omega) = 0, \quad (13.18)$$

with Ω and g_{1D} held fixed. Figure 13.6(a) plots energy eigenvalues that satisfy this condition as a function of Ω ; and Fig. 13.6(b) shows the corresponding angular momentum. These figures are quite similar to those given by mean-

¹²There is a quantum entropy associated with this degeneracy [32].

field theory, i.e., by imposing the stationary condition (13.18) for the manifold of eigenvalues we identify the mean-field stationary branches.

Referring to Fig. 13.6(a), we cannot call the thick curve a soliton branch in a rigorous sense, because each point is an eigenvalue of the rLLH and thus the associated eigenstate still possesses translational symmetry, unlike mean-field dark solitons. Instead, we call all the angular-momentum states inside the swallowtail in Fig. 13.5 the *soliton components*, because in the presence of infinitesimal noise these states do form a broken-symmetry state, which we denote $|\chi\rangle$. Soliton solutions of the NLSE can be interpreted in terms of the eigensolutions of the rLLH as a state where the several eigenvalues in the swallowtail region are collectively superimposed.

The energy associated with this superposition does not change significantly because the energy required to make it is on the order of $1/N$. As a result, the energy of the broken-symmetry soliton state $|\chi\rangle$ is also well approximated by the thick curve in Fig. 13.6(a). In the presence of an infinitesimal symmetry-breaking potential, the angular momentum is no longer a good quantum number. However, the expectation value of the angular momentum $\langle\chi|\hat{L}|\chi\rangle$ agrees well with that of the dark solitons obtained by mean-field theory, and thus behaves like that shown in Fig. 13.6(b) [28].

With all these caveats in mind, we briefly state that the branch drawn by the thick curve in Fig. 13.6(a) is the *quantum soliton* branch in the weakly interacting regime.

We also calculated the second derivative $d^2E_{N,L}(\Omega)/dL^2$ with respect to Ω in order to check whether the metastable angular-momentum state is a local maximum or minimum. The superflow state with a CM quantum number $J_0 = \lfloor \Omega + 1/2 \rfloor$ is indeed the ground state because the second derivative is positive at that point, while the thick points are local maxima with respect to L , since the second derivative is negative.

Let us summarize our first foray into the many-body theory. In this section we obtained the yrast states $|N, L\rangle$ of the rLLH by exact diagonalization. We used an extremization condition to extract the mean-field results, among them the characteristic swallowtail shape in the spectrum. We again found two kinds of metastable branches, uniform superflow and quantum soliton, consistent with mean-field theory. The region of a high density of states, where the different angular-momentum states in the quantum theory densely cross, indeed agrees with the soliton regime predicted by the mean-field and Bogoliubov theories. The phrase “quantum flesh sewn onto classical bones” has been used elsewhere [41] as a visual metaphor, perhaps inspired by x-ray images, to describe this accord.

13.5 Strongly-Interacting Many-Body Theory: Tonks-Girardeau Limit

Let us now move to the other extreme from the mean field. Taking the interactions to be very large, the bosons become impenetrable and thus can be mapped to spinless fermions. This is the TG regime. We again solve the yrast eigenproblem and study the consequences. In particular, we introduce the particle and hole excitations, which are well defined in the fermionized gas, and show that these excitations are related to the mean-field stationary states in the opposite weakly interacting limit.

To be precise, the TG Bose-Fermi mapping theorem [38] is

$$\Psi_B(\{\theta\}) = \prod_{i>j} \text{sgn}(\theta_i - \theta_j) \Psi_F(\{\theta\}), \quad (13.19)$$

where $\Psi_B(\{\theta\})$ is the bosonic many-body wavefunction, expressed in first quantization, and $\Psi_F(\{\theta\})$ is the equivalent spinless fermionic many-body wavefunction. This theorem holds for all the eigensolutions [42], and hence significantly simplifies our eigenproblem.¹³

The ground state of N (odd) free fermions is obtained by the occupation of the angular-momentum states from $l = -l_F$ to $l = l_F$ [see $L = 0$ in Fig. 13.7], where $l_F \equiv (N - 1)/2$ is the Fermi momentum. The ground-state energy is thus

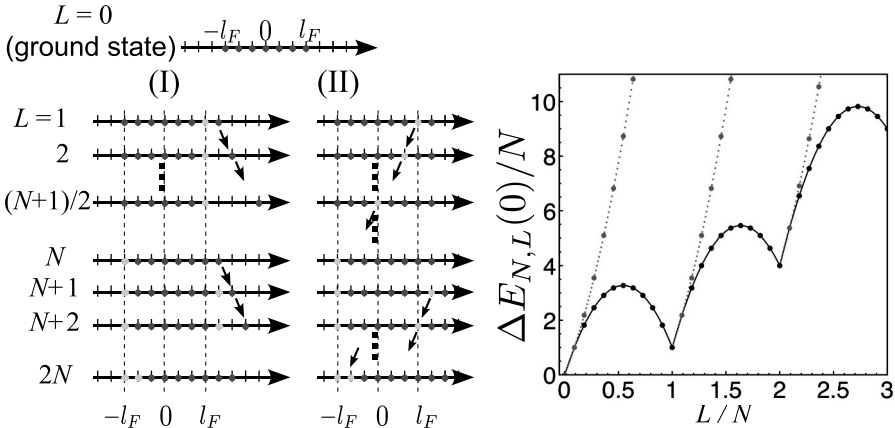
$$E_{N,L=0}(\Omega = 0) = \sum_{l=-l_F}^{l_F} l^2 = N(N^2 - 1)/12. \quad (13.20)$$

Beyond the ground state, Lieb has shown [3] that excitation of the repulsively interacting Bose gas in the thermodynamic limit has two branches. The first branch is called *type I* and was shown to be in agreement with the Bogoliubov spectrum of plane waves in the weakly-interacting regime. The second branch is called *type II*, and this was supposed to be absent in the Bogoliubov spectrum. For the fermionic formulation of the TG gas we observe that the type I and II branches correspond to particle and hole excitations, respectively.

Let us reconsider these branches in the context of yrast states. For the excited state $E_{N,L}(0)$ we can find the particle and hole excitations. The procedure is slightly technical, but we provide a sketch in Fig. 13.7(a), and a brief description below.

Type I: Remove a particle at the Fermi momentum l_F and place it at the momentum $l_F + L$. For free fermions, there is no energy-level reconstruction in an $(N \pm 1)$ -particle system associated with removal or addition of a particle. The energy of the type I excited state $E_{N,L}^{(I)}(0)$ is thus obtained as $E_{N,L}^{(I)}(0) =$

¹³For simplicity of notation we will show the analytic expression only for an odd total number of particles. For an even number of particles the periodic boundary condition must be taken as antisymmetric.

**FIGURE 13.7**

(Left) A sketch of how to construct TG yrast states. (I) Particle excitations where the angular momentum of a particle increases while a hole is positioned at $l_F + J$. (II) Hole excitations where a particle is placed at the lowest unoccupied state and the angular momentum of a hole decreases. When L is an integer multiple of N , only the center-of-mass angular momentum is shifted from the ground-state configuration. (Right) Type I and type II excitation energies as a function of L/N for $N = 11$ free fermions. Reproduced from [30].

$E_{N,0}(0) - l_F^2 + (l_F + L)^2$, or, relative to the ground state,

$$\Delta E_{N,L}^{(I)}(0) \equiv E_{N,L}^{(I)}(0) - E_{N,0}(0) = L(N + L - 1). \quad (13.21)$$

There is no limitation on the single-particle angular momentum for Type I excitations. Such excitations are doubly degenerate for $\Omega = 0$, for $l \rightarrow -l$. The excitations from the CMR states are similarly obtained: to get the excitations from the $J = JN$ state, remove a particle at $l_F + J$ and replace it at $l = l_F + J + L - JN$. The resulting excitation energy is given by $\Delta E_{N,L}^{(I)}(0) = J^2 N + (l_F + J + L - JN)^2 - (l_F + J)^2$, $L \geq JN$.

Type II: Starting from the ground state, remove a particle (create a hole) at the momentum $l_F - L + 1$ and place the particle at $l_F + 1$, where $0 \leq L \leq N$. It is clear from Fig. 13.7 that the hole with this kind of low-lying excitation energy be created only within the range $-l_F \leq l \leq l_F$. The energy of this excited state is given by $E_{N,L}^{(II)}(0) = E_{N,0}(0) - (l_F - L + 1)^2 + (l_F + 1)^2$, or, relative to the ground state, $\Delta E_{N,L}^{(II)}(0) = L(N - L + 1)$, $0 < L \leq N$. Starting from the CMR state $L = JN$, we can extend this procedure to $L > N$, producing the series of humps shown in Fig. 13.7. From the fact that the excitation energy of the CMR state $L = JN$ is $\Delta E_{N,L=JN}(0) = J^2 N$, we can

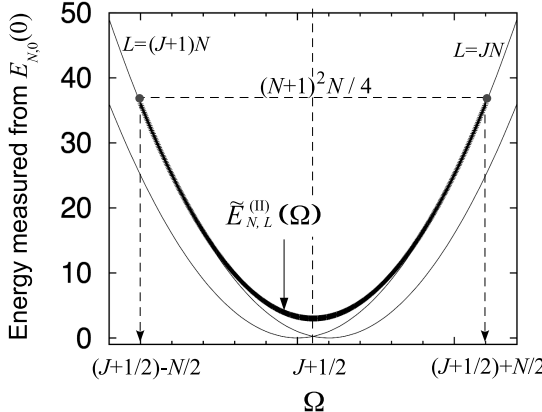


FIGURE 13.8

We can again use an extremization condition to get the realizable yrast eigenstates in the strongly-interacting TG limit. Shown is the result obtained from the TG Bose-Fermi mapping for $N = 11$ bosons. All energies are plotted relative to the nonrotated ground-state energy. The thin curves show the neighboring CMR states with angular momentum $L = JN$ and $L = (J + 1)N$. The bold curve shows the intervening type II states with angular momenta between these values. The angular momentum decreases from $(J + 1)N$ to JN according to Eq. (13.24) along the bold curve. The arrows show the critical frequencies for the QPT. Reproduced from [30].

obtain the type II hole excitation energy for the general case as

$$\Delta E_{N,L}^{(II)}(0) = J^2 N + (l_F + J + 1)^2 - (l_F - L + JN + J + 1)^2, \quad (13.22)$$

where $JN < L \leq (J + 1)N$ and $\Delta E_{N,L}^{(II)}(0) \equiv E_{N,L}^{(II)}(0) - E_{N,0}(0)$ is again the energy relative to the ground state. We note that Lieb's original study focused on the region $0 \leq L/N \leq 0.5$ [3].

Next we rotate these states to the TG yrast states for the rLLH, again using our Legendre transform. The energy of the type II excited state for $JN < L \leq (J + 1)N$ measured relative to $E_{N,L=0}(0)$ is given by

$$\tilde{E}_{N,L}^{(II)}(\Omega) = \Delta E_{N,L}^{(II)}(0) - 2\Omega L + \Omega^2 N. \quad (13.23)$$

We can again get the key solutions from the extremization condition (13.18), where now we take the energy to be that of type II excitations. By inspection, CMR states $L = JN$ are metastable states, either ground or excited. Condition (13.18) gives another metastable angular momentum,

$$\bar{L} = (N + 1)(J + 1/2) - \Omega, \quad (13.24)$$

and the corresponding energy,

$$\tilde{E}_{N,\bar{L}}^{(II)}(\Omega) = (N + 1)[\Omega - (J + 1/2)]^2 + N(N + 1)/4. \quad (13.25)$$

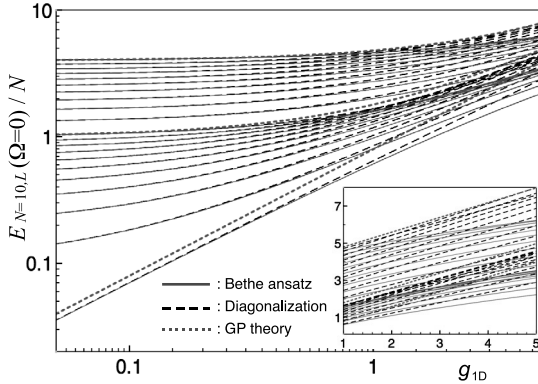


FIGURE 13.9

Evaluation of three many-body solution methods, Bethe equations, exact diagonalization, and mean-field NLSE (labeled GP Theory), in the weakly- to medium-interacting regime in terms of yrast eigenenergies (note log scale). We take $N = 10$ particles and CMR quantum number $J \in \{0, 1, 2\}$ only for the purposes of illustration. The inset enlarges the medium-interacting regime on a linear scale. Reproduced from [30].

As a function of Ω this is a parabolic curve, shown in Fig. 13.8.

We again find certain critical angular frequencies where the metastable type II branch disappears and merges into the CMR branch:

$$\Omega_{\text{cr}}^{\mp} = (J + 1/2) \mp N/2. \quad (13.26)$$

The stable angular momentum approaches $\bar{L} = (J+1)N$ at Ω_{cr}^- and $\bar{L} = JN$ at Ω_{cr}^+ , respectively, and the corresponding energy coincides with the energy of CMR states. Equation (13.26) determines the critical boundary for our QPT in the strongly interacting limit.

This whole picture closely matches that of the uniform-superflow to dark-soliton transition in the weakly interacting limit, where there exists a critical angular frequency at which the soliton branch bifurcates from the superflow branch: here type II yrast states branch off of the type I CMR states. We therefore interpret the hole excitations in the TG limit with the soliton branch in the weakly interacting limit. It remains to fill in the picture between, as we proceed to do in the following section via the Bethe equations.

13.6 Bridging All Regimes: Finite-Size Bethe Ansatz

In this section we will show that our QPT stretches over the whole interaction range, and also validate our physical interpretation of Lieb Type II excitations.

We note that, complementary to our work, the spectrum of the LLH has been obtained [43] by treating the inverse of the TG parameter, which is infinite at the TG regime, as the expansion parameter, and its analytical interpolation was given recently [44].

Using the Bethe ansatz, we obtain the N simultaneous *Bethe equations* for our system,

$$(-1)^{N-1} e^{-2\pi i \ell_n} = \prod_{m=1}^N \frac{\ell_n - \ell_m + ig_{1D}/2}{\ell_n - \ell_m - ig_{1D}/2}, \quad (13.27)$$

which determine the set of values $\{\ell_n\}$, called *quasi-angular momenta* for each atom $n \in \{1, \dots, N\}$.¹⁴ The quasi-angular momenta fully characterize the angular momentum and energy, given by $L = \sum_{n=1}^N \ell_n$ and $E_{N,L}(\Omega = 0) = \sum_{n=1}^N \ell_n^2$, respectively.

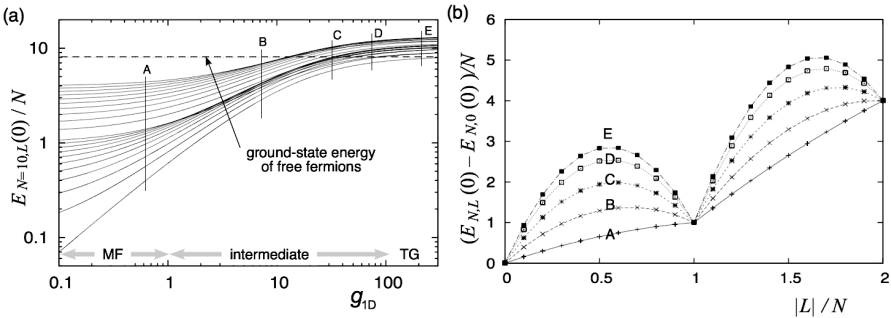
We numerically solve the real part of the Bethe equations (13.27) for each set of energy levels characterized by the different total angular momenta. The numerical solution of Eqs. (13.27) is highly sensitive to the initial set of trial values of $\{\ell_n\}$. If this initial set is sufficiently close to a solution for a target angular-momentum state, the set of solutions $\{\ell_n\}$ can be correctly obtained. In contrast, if the initial set is closer to another angular-momentum state, the total angular momentum reveals undesired jumps, deviating from the target angular momentum. In such a case we again start from another initial set of trial values of quasi-momenta. Our algorithm is outlined in [30].

In Fig 13.9, we first perform a comparative study for mean-field, TG, and Bethe solution methods in the weakly- to medium-interacting regime.¹⁵ As can be seen, for $g_{1D} \lesssim \mathcal{O}(1)$, the three methods agree to a few percent.

In Fig. 13.10(a) we show the spectra over the entire interaction range, for the system in the nonrotating frame: specifically, $E_{N,L}(\Omega = 0)$ for $|L| \in \{0, \pm 1, \dots, \pm 2N\}$. All ground- and excited-state energies monotonically increase with respect to $g_{1D} > 0$. However, the energy does not monotonically increase with respect to the total angular momentum for a fixed strength of interaction. This is illustrated in Fig. 13.10(b). The labels A, B, C, D, and E correspond to the cross-cuts labeled in panel (a). While in the very weakly-interacting limit (curve A) the spectrum still looks almost linear, as the interaction increases, the kinks in the yrast spectra at the location of CMR state, $L = JN$, become more pronounced due to the large increase in the energy of the yrast states with L in between neighboring CMR states at JN and $(J+1)N$. For strong interactions (curve E), the system is in the TG regime; compare to the TG calculation for Type II excitations from Fig. 13.7(b). We observe numerically that the excitation energy of the CMR state $L = JN$ is independent of g_{1D} , and is given by Eq. (13.6), namely

¹⁴It is sufficient to solve for only the real part of these equations [30].

¹⁵We note that the concept of yrast state for the angular momenta $JN < L < (J+1)N$ does not exist in the mean-field theory: this theory is concerned only with the single-particle angular momentum, which coincides with the average angular momentum in this theory. We thus plot the mean-field energy for the integral single-particle angular momenta.

**FIGURE 13.10**

(a) Solutions of the Bethe equations in the nonrotating frame for a range of angular momenta $|L| \leq 2N$ and $N = 10$ particles. The horizontal dashed line corresponds to the energy of free fermions (13.20) with the same number of atoms. (b) Excitation energies of yrast states as a function of average angular momentum $|L|/N$ for fixed strengths of interaction. A, B, C, D, and E are marked in (a). The kinks are again the CMR states. Reproduced from [30].

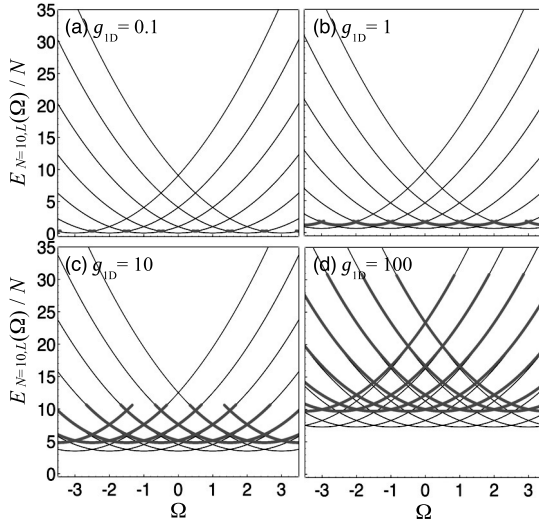
$(E_{N,L} - E_{N,0})/N = (L/N)^2$. This follows from the nature of the CMR state $L = JN$, which is just a Galilean boost of the nonrotating state; under this transformation interactions are unchanged.

We proceed to the rotating frame, as before, via our Legendre transform, which can be framed in terms of quasi-angular momenta as

$$E_{N,L}(\Omega) = \sum_{j=1}^N (\ell_j - \Omega)^2 = E_{N,L}(0) - 2\Omega L + \Omega^2 N. \quad (13.28)$$

The results are shown in Fig. 13.11 for various strengths of interaction. The thin curves are parabolas $(\Omega - J)^2 + V_{\text{int}}$ for various values of center-of-mass quantum numbers J . The lowest possible energy of the CMR state is thus given by V_{int} at $\Omega = J \in \{\mathbb{Z}\}$. The thick curves plot other stable yrast states of noninteger L/N from the condition (13.18). The weakly-interacting mean-field regime is shown in Fig. 13.11(a), where the type II branch that satisfies the metastable condition just starts to appear. Thus these are the energies of the quantum solitons [see also Fig. 13.6(a)]. As the interaction increases [Figs. 13.11(b) and 13.11(c)] the domain with the swallowtail shape enclosed by the two CMR branches, as well as the size of the type II branch, increases. In the TG limit [13.11(d)], the area of the swallowtail region saturates the spectra.

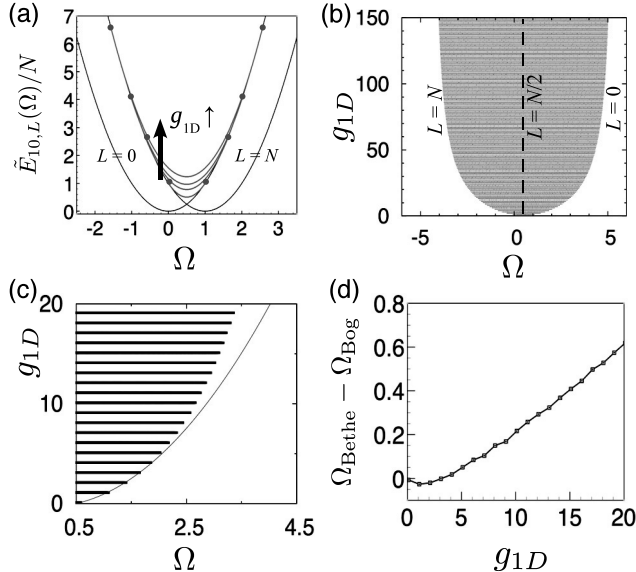
These behaviors are quantitatively summarized in Fig. 13.12(a), which shows the energy $E_{N,L}(\Omega)/N$ of metastable states relative to the interaction energy V_{int} at each strength of interaction. The CMR branches drawn by the thin curves no longer have a g_{1D} -dependence because of the subtraction of V_{int} , while the thick curve gradually increases the domain over which it extends as the interaction increases. For simplicity we plot only two CMR branches with

**FIGURE 13.11**

Spectra of the rLLH obtained via the Bethe equations and satisfying the extremization condition for (a) weakly-interacting regime, (b) and (c) medium-interacting regime, and (d) strong-interacting regime. The thin curves show CMR states, while the thick curves show yrast states with L/N noninteger, and come from the type II excitation branch. Reproduced from [30].

angular momenta $L = 0, N$, and a metastable state associated with the type II branch that smoothly connects these two CMR states.

As Ω increases, the thick curve bifurcates from the CMR branch with angular momentum $L = N$ at a certain critical $\Omega < 0.5$, and at $\Omega = 0.5$ the energy is minimal. As Ω increases further, this branch smoothly merges into the CMR branch with angular momentum $L = 0$ and eventually disappears at a certain critical $\Omega > 0.5$. We therefore find that the same kind of energy bifurcation which was found in the mean-field theory persists over the full range of repulsive interactions. Figure 13.12(b) illustrates this idea by plotting the existence range of the metastable-state type II excitation branch. The shaded area indicates the existence of such a branch. The angular momentum on the lower critical boundary is given by $L = N$, and the angular momentum linearly decreases as Ω increases, just like in Fig. 13.6(b). At $\Omega = 0.5$ (vertical dashed line), the value of the angular momentum is given by $L = N/2$ irrespective of the strength of interaction. At a certain value of $\Omega (> 0.5)$ the angular momentum eventually goes to zero, causing the metastable hole excitation branch to disappear. This behavior corresponds to the fact that in the mean-field theory the type II branch bifurcates from the uniform-superflow regime, developing nodes, and it again merges into the uniform-superflow regime with the in-

**FIGURE 13.12**

(a) Two CMR states with $L = 0, N$ (thin curves) and the type II branch (thick curve) that connects them. The energy is defined relative to the interaction energy V_{int} . (b) The quantum phase diagram over all interaction strengths; in the gray region yrast states corresponding to Lieb's type II excitations allow for a continuous change in angular momentum, while in the white region only CMR states with quantized L/N are allowed. (c) Enlargement of (b) in the weakly-interacting regime. The solid curve is the critical boundary given by the Bogoliubov theory. (d) Difference between the phase boundaries given by the Bethe ansatz and the Bogoliubov theory. The Bogoliubov critical boundary overestimates the correct Bethe result. Reproduced from [30].

crease of Ω [28, 29]. The critical boundary approaches $\Omega = (J + 1/2) \pm N/2$ in the strongly-interacting regime.

Finally, we explicitly evaluate the BdGE analytical predictions for the critical boundary. In Fig. 13.12(c)-(d) the Bethe-equation prediction for the critical boundary is compared with that obtained from the BdGE in the weakly-interacting regime. We observe that Bogoliubov theory predicts the quantitatively correct critical boundary to the 5% level up to $g_{1D} \lesssim 5$ (for $N = 10$), but it significantly overestimates the boundary as the interaction increases.

Thus we find a critical boundary for all values of interaction strength.

13.7 Conclusions and Outlook

We have tied together a number of outstanding issues in ultracold quantum gases. The first is the understanding of quantum effects on characteristic mean-field solutions, namely dark solitons. The second is the concept of a phase transition in a mesoscopic system which is strongly isolated from its environment. Other issues we addressed included the physical interpretation of Lieb's Type-II excitations and the correspondence of various 1D techniques, ranging from the NLSE to the Bethe equations to the TG mapping.

The first issue has occupied many people over the last decade. Work in this area includes quantum delocalization of dark solitons in the weakly interacting regime [14, 19], decay of dark solitons in the more strongly interacting regime [15], the search for dark solitons in the extreme limit of the TG gas via the TG Bose-Fermi mapping [46], and most recently the role of thermal fluctuations in defect formation by the Kibble-Zurek mechanism [21]. Our results indicate that while the mean-field dark soliton bears some meaning in the weakly-interacting regime, where one can make a close correspondence between the underlying many-body quantum soliton branch and the symmetry-broken mean-field soliton, in the medium- to strongly-interacting regime no such correspondence is likely. Thus for stronger interactions we do not expect to observe a density notch with a characteristic phase structure. Given recent experiments tuning the interactions over seven orders of magnitude and the increasing commonness of ring traps, we hope to see tests of these ideas in the near future. A new dynamical study by Brand and Kolovsky [45] indicates that in various regimes stretching from the NLSE to the TG gas our ideas have some merit; after all, if our predicted many-body generalization of dark solitons took the lifetime of the universe to nucleate, our ideas would remain restricted to the realm of theory; this appears not to be the case. A complementary study to Brand and Kolovsky's might use MPS methods to address this question.

The second issue is trickier. We all have a thermodynamic view of phase transitions and states of matter drummed into us, and new contexts such as graphene are showing that some of these ideas have to be generalized. In our case we find a QPT, technically a crossover, that nevertheless displays characteristics of phase transitions: topological properties of the system change and the energy reveals a cusp at some level of derivative. Moreover, our QPT is inherently finite size and has no meaning in the thermodynamic limit. For isolated systems such as ultracold quantum gases or nuclei (see Chap. 27) a QPT in excited states is a useful concept, in contrast to QPTs in solid-state materials. The mean-field theory is expressed in a nonlinear partial differential equation, the NLSE; it is useful to note that bifurcations appearing in the solution space of such effective nonlinear theories often point to a QPT in the underlying linear many-body theory.

As a very brief summary of other issues addressed in this chapter, we showed that the soliton-train uniform-superflow picture falls naturally out of consideration of center-of-mass-rotation states and quantum soliton states, the latter being yrast states contained within a swallowtail. These considerations provided a complete description of the finite-system metastable QPT from the weakly- to strongly-interacting regimes. In the process we cleared up the long-standing problem of the physical interpretation of Lieb's type-II or hole excitation branch: type-II excitations are exactly the yrast states, which in the weakly-interacting limit can be expressed as dark-soliton trains, appearing in broken-symmetry form in mean-field theory.

Our static study can be extended to many different contexts in ultracold quantum gases, for example, spinor Bose systems, where the hyperfine structure of the constituent atoms in the BEC plays the role of a spin, and one finds spin-one or even spin-two and higher models, as described in Chap. 10. A number of metastable and/or finite-size QPTs are possible in these systems. Ultracold fermions also provide a fine candidate, and we expect a metastable QPT occurs in the Bardeen-Cooper-Schrieffer (BCS) superconducting phase. One could trace this QPT through the BCS-to-BEC transition. This problem is particularly interesting halfway through the crossover in the unitary regime,¹⁶ a many-body system under intensive investigation in ultracold quantum gases, in the quark gluon plasma (see Chap. 25), and in the AdS/CFT (anti-de Sitter / conformal field theory) mapping (see Chap. 28).

More generally, we can ask if the concept of QPTs in finite systems is useful beyond ultracold quantum gases. What happens to critical exponents? Can they be defined without the use of finite-size scaling? Is the concept of a universality class useful? Can backing off from the thermodynamic limit but retaining the QPT concept in some fashion help us better understand the fundamental physics of mesoscopic systems and help us invent better nanodevices?

Acknowledgments – This work was supported by the National Science Foundation under Grant PHY-0547845 as part of the NSF CAREER program (L.D.C.), a Grant-in-Aid for Scientific Research under Grant Numbers 17071005 (M.U.) and 21710098 (R.K.), and by the Aspen Center for Physics.

Bibliography

- [1] A. J. Leggett, Rev. Mod. Phys. **73**, 307 (2001).
- [2] S. E. Pollack *et al.*, Phys. Rev. Lett. **102**, 090402 (2009).

¹⁶The unitary regime is where the scattering length for binary contact interactions, a_s , diverges: $k_F a_s \rightarrow \infty$, with k_F the Fermi momentum.

- [3] E. H. Lieb, Phys. Rev. **130**, 1616 (1963).
- [4] E. H. Lieb and W. Liniger, Phys. Rev. **130**, 1605 (1963).
- [5] S. O. Demokritov *et al.*, Nature **426**, 159 (2003); S. Gupta *et al.*, Phys. Rev. Lett. **95**, 143201 (2005); A. S. Arnold, C. S. Garvie, and E. Riis, Phys. Rev. A **73**, 041606(R) (2006); S. R. Muniz *et al.*, Opt. Express **14**, 8947 (2006); C. Ryu *et al.*, Phys. Rev. Lett. **99**, 260401 (2007); B. P. Anderson, K. Dholakia, and E. M. Wright, Phys. Rev. A **67**, 033601 (2003).
- [6] A. J. Leggett, Rev. Mod. Phys. **71**, S318 (1999).
- [7] O. Penrose and L. Onsager, Phys. Rev. **104**, 576 (1956).
- [8] S. Burger *et al.*, Phys. Rev. Lett. **83**, 5198 (1999).
- [9] J. Denschlag *et al.*, Science **287**, 97 (2000).
- [10] A. Weller *et al.*, Phys. Rev. Lett. **101**, 130401 (2008).
- [11] S. Stellmer *et al.*, Phys. Rev. Lett. **101**, 120406 (2008).
- [12] V. Dunjko, V. Lorent, and M. Olshanii, Phys. Rev. Lett. **86**, 5413 (2001).
- [13] B. Jackson, C. F. Barenghi and N. P. Proukakis, J. Low Temp. Phys. **148**, 387 (2006).
- [14] J. Dziarmaga, Z. P. Karkuszewski, and K. Sacha, J. Phys. B: At. Mol. Opt. Phys. **36**, 1217 (2003).
- [15] R. V. Mishmash and L. D. Carr, Phys. Rev. Lett. **103**, 140403 (2009); R. V. Mishmash, I. Danshita, C. W. Clark, and L. D. Carr, Phys. Rev. A **80**, 053612 (2009).
- [16] Y. S. Kivshar, Phys. Rep. **298**, 81 (1998).
- [17] J. P. Gordon and H. A. Haus, Opt. Lett. **11**, 665 (1986).
- [18] P. O. Fedichev, A. E. Muryshev, and G. V. Shlyapnikov, Phys. Rev. A **60**, 3220 (1999).
- [19] A. D. Martin and J. Ruostekoski, Phys. Rev. Lett. **104**, 194102 (2010).
- [20] P. Deuar, J. Dziamarga, and K. Sacha, Phys. Rev. Lett. **105**, 018903 (2010); R. V. Mishmash and L. D. Carr, Phys. Rev. Lett. **105**, 018904 (2010).
- [21] B. Damski and W. H. Zurek, Phys. Rev. Lett. **104**, 160404 (2010).
- [22] D. A. Butts and D. S. Rokhsar, Nature **397**, 327 (1999).

- [23] G. F. Bertsch, T. Papenbrock, Phys. Rev. Lett. **83**, 5412 (1999).
- [24] M. Ishikawa and H. Takayama, J. Phys. Soc. Jpn. **49**, 1242 (1980).
- [25] V. I. Yukalov and M. Girardeau, Laser Phys. Lett. **2**, 375 (2005).
- [26] A. K. Geim and K. S. Novoselov, Nature Materials **6**, 183 (2007).
- [27] T. Kinoshita, T. Wenger, and D. Weiss, Science **305**, 1125 (2004).
- [28] R. Kanamoto, L. D. Carr, and M. Ueda, Phys. Rev. Lett. **100**, 060401 (2008).
- [29] R. Kanamoto, L. D. Carr, and M. Ueda, Phys. Rev. A **79**, 063616 (2009).
- [30] R. Kanamoto, L. D. Carr, and M. Ueda, Phys. Rev. A **81**, 023625 (2010).
- [31] R. Kanamoto, H. Saito, and M. Ueda, Phys. Rev. Lett. **94**, 090404 (2005).
- [32] L. D. Carr, C. W. Clark, and W. P. Reinhardt, Phys. Rev. A **62**, 063610 (2000).
- [33] L. D. Carr, M. A. Leung, and W. P. Reinhardt, J. Phys. B: At. Mol. Opt. Phys. **33**, 3983 (2000).
- [34] L. D. Carr, J. Brand, S. Burger, and A. Sanpera, Phys. Rev. A **63**, 051601(R) (2001).
- [35] D. Muth, B. Schmidt, and M. Fleischhauer, e-print arXiv:0910.1749 (2009).
- [36] M. Olshanii, Phys. Rev. Lett. **81**, 938 (1998).
- [37] A. L. Fetter and A. A. Svidzinsky, J. Phys.: Condens. Matter **13**, R135 (2001); L. J. Garay *et al.*, Phys. Rev. Lett. **85**, 4643 (2000).
- [38] M. Girardeau, J. Math. Phys. (N.Y.) **1**, 516 (1960).
- [39] A. J. Leggett, Phys. Fenn. **8**, 125 (1973).
- [40] G. Sagnac, C.R. Acad. Sci. **157**, 708 (1913); **157**, 1410 (1913); J. Phys. **4**, 177 (1914).
- [41] E. D. Davis, Phys. Rev. A **70** 032101 (2004); Alisa Bokulich, *Reexamining the Quantum-Classical Relation: Beyond Reductionism and Pluralism* (Cambridge University Press, New York, 2008).
- [42] M. D. Girardeau and E. M. Wright, Laser Phys. **12**, 8 (2002).
- [43] A. Y. Cherny and J. Brand, Phys. Rev. A **73**, 023612 (2006).
- [44] A. Y. Cherny and J. Brand, Phys. Rev. A **79**, 043607 (2009).
- [45] J. Brand and A. Kolovsky, to be submitted (2010).
- [46] M. D. Girardeau and E. M. Wright, Phys. Rev. Lett. **84**, 5691 (2000).

Part III

Experimental Realizations of Quantum Phases and Quantum Phase Transitions

Quantum Phase Transitions in Quantum Dots

Ileana G. Rau

Department of Applied Physics, Stanford University, Stanford, California 94305, U.S.A.

Sami Amasha

Department of Physics, Stanford University, Stanford, California 94305, U.S.A.

Yuval Oreg

Department of Condensed Matter Physics, Weizmann Institute of Science, Rehovot 96100, Israel

David Goldhaber-Gordon

Department of Physics, Stanford University, Stanford, California 94305, U.S.A.

Over the past 25 years, developments in nano-fabrication and low temperature cooling techniques, as well as the development of new calculational tools, have given rise to a new field of research: the design of artificial nanostructures that imitate conventional materials. Initially these nanostructures could only mirror the behavior of some basic building blocks of matter: for example, a quantum dot acts as an artificial atom and can be used to model a localized magnetic moment [1–3]. More recent technological advances have made it possible to build increasingly complex artificial structures: multi-dot systems coupled to distinct electron reservoirs now offer a way to study the interplay between single spins and conduction electrons, the transport of heat through low dimensional structures, and charge as well as spin transport through atoms and molecules [4–6].

The advantage offered by these artificial structures is the fact that their individual properties such as energy spectrum, magnetic moment, coupling to the environment, and the spatial distribution of the wavefunction are tunable *in situ* by “knobs” such as gate voltage, magnetic field, or voltage bias. In real materials these microscopic properties can be changed only by altering a material’s structure or chemical composition, or by changing an external parameter such as the applied pressure or magnetic field. As a consequence, it is difficult to tune a single microscopic parameter without changing other

parameters or even the effective Hamiltonian of the system, and therefore the two phases of a quantum phase transition often belong to two different though related materials. In contrast, quantum dot parameters can be tuned continuously and nearly independently of one another, allowing the exploration of the complete phase diagram, including the quantum critical point (QCP). These artificial structures have advantages and disadvantages that make them complementary to bulk materials: it is difficult to measure thermodynamic quantities such as specific heat or magnetic susceptibility but one can investigate transport properties of impurity quantum phase transitions which will be described in the next paragraphs.

Quantum phase transitions (QPTs) are a class of phase transitions that occur at absolute zero temperature as one varies a parameter other than temperature. Second order (continuous) QPTs are driven by quantum fluctuations of the order parameter, which have properties completely different from those of the familiar thermal fluctuations. The inherent zero-temperature nature of the QPT makes it impossible to observe directly. However, in the low-temperature limit, correlation lengths and times diverge near the transition between two ground states. These long-range correlations influence the behavior of the system at finite temperature: near the QCP, a distinctive set of excitations can be accessed experimentally. These excitations are collective, so that Fermi-liquid theory fails to describe the physics in the quantum critical region. The behavior of the system as a function of external parameters obeys scaling laws with non-trivial exponents that are determined only by the universality class of the transition and not by the microscopic details.

We generally think of second-order phase transitions (classical or quantum) as requiring the thermodynamic limit of system size. However, for a special kind of QPT involving a boundary (e.g., an interface or impurity) embedded in a bulk system, only the degrees of freedom belonging to the boundary become critical, while the thermodynamic limit is only required for the bulk part of the system. Boundary phase transitions show the same fascinating quantum critical behavior as bulk transitions. However, while the entropy at a bulk QCP vanishes at zero temperature, an impurity QCP can have residual entropy: fluctuations are strong enough to preserve some of the local degrees of freedom.

Impurity QPTs have been predicted to occur in various materials, but at first glance one might expect their experimental observation to be impeded by effects present in real materials: the crystalline field anisotropy or exchange or dipolar interaction between spins should break the symmetry of the low-lying states at the QCP. While this generally happens, there are some exceptions where the required symmetries occur naturally, as is the case for f-electron heavy fermion materials based on Uranium or Cerium [7,8], Copper or Titanium nano-constrictions [9,10], and glassy metal junctions or single crystals [11]. Non-Fermi liquid behavior, as evidenced by non-trivial power laws in thermodynamic and transport quantities, has been measured, but it

has proved difficult to connect directly to theory, and alternative explanations have been suggested [12].

Two decades ago it was noticed that a quantum dot with a net spin-1/2, coupled by tunneling to an electron reservoir, has the same Hamiltonian as a magnetic site interacting with electrons in a host metal [2, 3]. This quantum impurity problem is the basis for the Kondo effect, in which the local magnetic moment is fully screened by the spins of the conduction electrons, and the conduction electrons can be described as a Fermi liquid, even near the local site. This chapter will focus on variations of this system, involving one or more quantum dots, generally each with spin-1/2, interacting with one or more electron reservoirs. For example, adding an additional reservoir of conduction electrons (screening channel) leads to a “2-channel Kondo” (2CK) system with the Hamiltonian

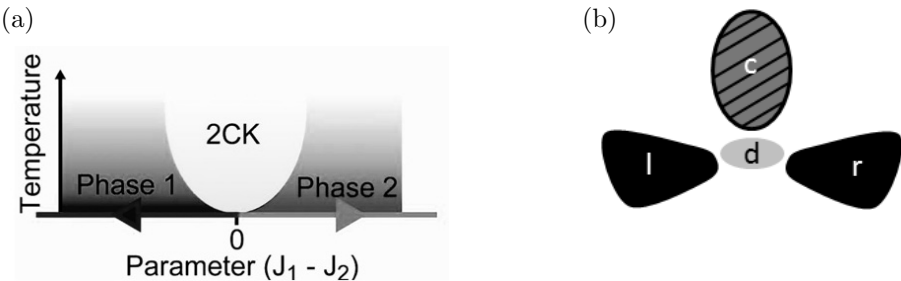
$$H_{\text{2CK}} = J_1 \vec{s}_1 \cdot \vec{S} + J_2 \vec{s}_2 \cdot \vec{S}, \quad (14.1)$$

where $J_1, J_2 > 0$ are the antiferromagnetic interaction between the spins of the reservoir electrons \vec{s}_1 and \vec{s}_2 and the local spin \vec{S} . When the two reservoirs are symmetrically coupled to the impurity ($J_1 = J_2$) the local magnetic moment is overscreened, the system shows local non-Fermi liquid (nFL) behavior, and there is a residual entropy at zero temperature. This model has been used to explain the experimentally observed specific heat anomalies in certain heavy fermion materials [7,8] as well as transport signatures in metallic nano-constrictions [9, 13].

The two-channel Kondo state also corresponds to the QCP in a boundary QPT between two distinct single-channel Kondo states. This transition takes place as a function of the relative couplings of the two channels to the impurity. For equal coupling, the system is in the 2CK state described above, but when one channel is more strongly coupled the traditional Kondo-screening behavior is recovered. Thus the two ground states on either side of the transition are both the standard Kondo singlet state (left and right regions in the phase diagram in Fig. 14.1(a)), with a different set of electrons participating in the screening of the local moment in each phase. In the quantum critical region (center region in Fig. 14.1(a)) temperature fluctuations mask the channel anisotropy and the long range correlations of the 2CK ground state dominate the behavior of the system, resulting in nFL scaling laws (see Sec. 14.1.3).

Another interesting model system is that of two spins coupled to a bath of conduction electrons and to each other. This two-impurity Kondo (2IK) system undergoes a QPT from a ground state with total spin 0 (the two impurities antiferromagnetically coupled, forming a spin singlet) to another ground state where the impurities are individually screened by the electrons in the reservoirs. The physics of a 2IK system can also be studied using a singlet-triplet transition in a quantum dot. In this case magnetic field can induce a transition from two spins on the quantum dot in a singlet state to a state where an electron reservoir attempts to screen part or all of the triplet state in the dot.

After briefly reviewing the theoretical predictions for the 2CK model, we

**FIGURE 14.1**

(a) Schematic phase diagram of the 2CK system, including the quantum critical point and the associated parabolic-shaped critical region. The vertical axis is labeled temperature, but any energy (frequency, bias voltage) will play a similar role. The tuning parameter shown is the difference in exchange coupling to two reservoirs, but a similar phase diagram is expected if the exchange couplings are kept equal and the tuning parameter is instead magnetic field. (b) Schematic of a quantum system that realizes the 2CK model. A spin on the small dot d can influence transport from the left l to the right r lead. c is a finite electron reservoir formed by a large quantum dot which will act as another screening channel for the small dot.

will describe the quantum dot system that implements this model, and the observation of the nFL state. We will also discuss other experimental observations of the 2CK model, and the related 2IK model. We conclude with forward-looking theoretical predictions and promising experimental designs.

14.1 The Kondo Effect and Quantum Dots: Theory

14.1.1 Brief History of the Kondo Effect

In 1964, motivated by a set of striking experiments [14], Kondo calculated the effect on a metal's resistivity of magnetic impurities which can scatter electrons. Using perturbation theory on the s-d model

$$H_{s-d} = \sum_k \epsilon_{ks} \psi_{ks}^\dagger \psi_{ks} + J \sum_i \vec{\sigma}_i \cdot \vec{S}_i, \quad (14.2)$$

he was able to explain the observed upturn in resistivity at low temperatures. Here \vec{S}_i is the i^{th} impurity spin, $\vec{\sigma}_i$ is the spin of the conduction electrons at the location of the i^{th} impurity, and ψ and ψ^\dagger represent the annihilation and creation operators for the conduction electrons with given momentum and

spin. However, Kondo's perturbative results break down below the Kondo temperature

$$T_K = De^{1/(J\nu)} \quad (14.3)$$

where D is the conduction electron bandwidth, J the antiferromagnetic coupling of the local spin to the conduction electrons, and ν the thermodynamic density of states of the conduction electrons. At first glance, this local spin coupled to a non-interacting Fermi sea is a simple system, but below the Kondo temperature the repeated impurity spin-flips and the corresponding response of the Fermi sea lead to complex many-body dynamics. This became known as the Kondo problem and the attempts to find a solution led to the development of a series of useful mathematical and physical concepts such as the Abrikosov-Suhl resonance [15], bosonization [16], and renormalization group [17] as applied to the alternating Coulomb gas [18].

Only a few years later Schrieffer and Wolff [19] showed that the s-d model is equivalent to the Anderson model

$$H_A = \sum_k \epsilon_{ks} \psi_{ks}^\dagger \psi_{ks} + Un_\downarrow n_\uparrow + \sum_s [\epsilon_{ds} d_s^\dagger d_s + (V\psi_s^\dagger(0)d_s + h.c.)], \quad (14.4)$$

in the limit in which local charge fluctuations can be neglected. Here U is the interaction parameter on the impurity site, V the hybridization between the conduction electrons and the impurity, and the d 's are the creation and annihilation operators of the impurity with $n_s = d_s^\dagger d_s$.

The generalization of the s-d model to multiple screening channels was introduced in 1980 by Nozieres and Blandin [20]

$$H_{MCK} = \sum_k \epsilon_{ks\alpha} \psi_{ks\alpha}^\dagger \psi_{ks\alpha} + J \sum_\alpha \vec{\sigma}_\alpha \cdot \vec{S}. \quad (14.5)$$

In the multichannel Kondo system they identified a non-trivial fixed point associated with a novel metallic phase, unlike in the single channel case, where at energies well below T_K the conduction electrons around the spin- $\frac{1}{2}$ impurity behave as a Fermi liquid. This new phase joined Fermi liquids, Luttinger liquids, fractional quantum Hall systems, and disordered systems with Coulomb interaction as the only known classes of metals. In parallel, Zawadowski studied two-level systems [21] that display similar behavior.

In the early '90s [22, 23] Affleck and Ludwig applied boundary conformal field theory (BCFT) to calculate the properties of the multichannel Kondo system at low temperature [24]. However, it is difficult to use conformal field theory to identify physical situations in which the interesting boundary state is realized. Instead, one can use numerical renormalization group methods, which are very reliable in giving the whole (equilibrium) crossover behavior of quantum impurity problems, including the single-channel Kondo effect and the two-channel and the two-impurity Kondo effects with their special points of nFL behavior. However, it demands special expertise and many computational tricks that help to accelerate the calculations. Therefore other methods

were developed to approximate simple solutions such as slave bosons [25], the non-crossing approximation (NCA) [26], the Equation of Motion (EOM) method [27], functional renormalization group (FRG) [28], and density matrix renormalization group (DMRG) [29] and its novel time dependent version [30]; the latter is described in Chap 22.

14.1.2 Theory of Conductance through Quantum Dots

In this section we briefly review theoretical expressions for the conductance through a quantum dot. The possibility of observing the Kondo effect in a quantum dot was established once Anderson-type models were used to describe dots. A convenient way of probing the state of the dot is by measuring its conductance. Using the Anderson Hamiltonian, one can derive scaling relations for this conductance in different regimes (i.e., 1CK and 2CK). In the study of bulk materials, scaling relations for thermodynamic quantities are a powerful tool for probing QPTs and low energy fixed points, and in a similar way the conductance scaling relations presented below will play a crucial role in identifying the 2CK QPT in a system of quantum dots.

We consider the conductance from the left to the right lead of the system in Fig. 14.1(b) [31]. As explained below, with the proper tuning of the system parameters this system exhibits 2CK physics.

The modified Anderson Hamiltonian that describes the system is given by

$$\begin{aligned} H = & \sum_{k\sigma} \varepsilon_{lk\sigma} l_{k\sigma}^\dagger l_{k\sigma} + \sum_{k\sigma} \varepsilon_{rk\sigma} r_{k\sigma}^\dagger r_{k\sigma} + \sum_{k\sigma} \varepsilon_{ck\sigma} c_{k\sigma}^\dagger c_{k\sigma} \\ & + E_c(n - \mathcal{N})^2 + \varepsilon_{d\sigma} d_\sigma^\dagger d_\sigma + U n_{d\uparrow} n_{d\downarrow} \\ & + \sum_{k\sigma} \left(t_{kl} l_{k\sigma}^\dagger d_\sigma + t_{kr} r_{k\sigma}^\dagger d_\sigma + t_{kc} c_{k\sigma}^\dagger d_\sigma + \text{h.c.} \right). \end{aligned} \quad (14.6)$$

Here the operators $l_{\sigma k}(l_{\sigma k}^\dagger)$, $r_{\sigma k}(r_{\sigma k}^\dagger)$, and $c_{\sigma k}(c_{\sigma k}^\dagger)$ are the annihilation (creation) operators of a free electron in state k with spin σ , for the left and right leads and the finite dot, respectively. The fourth term describes the interaction energy E_c of the large dot, where $n = \sum_{k\sigma} c_{k\sigma}^\dagger c_{k\sigma}$ is the number operator of the electrons in the large dot, while $\mathcal{N} \propto V_g$ gives the effective interaction with an external gate voltage V_g . The fifth term describes the level spacing of the small dot, with $d_\sigma(d_\sigma^\dagger)$ the annihilation (creation) operator of an electron with spin σ on the small dot. The sixth term describes the charging energy U of the small dot, with $n_{d\sigma} = d_\sigma^\dagger d_\sigma$. The last term describes the hopping matrix elements $t_{k\alpha}$ between the small dot and the two leads or the large dot (here $\alpha = l, r, c$). We assume that the hopping matrix elements are independent of k , and define $t_\alpha \equiv t_{k\alpha}$. In this Hamiltonian, we assume there is only one level in the small dot. This assumption is valid at an energy scale smaller than the level spacing of the small dot, which is the ultraviolet cutoff of the theory. For simplicity we have also ignored the inter-dot electrostatic coupling, which does not qualitatively change the picture.

Typically, in an experiment a bias voltage V is applied between the left and the right leads of the small dot, and the resulting current I is measured. From this measurement, one can extract the differential conductance,

$$G(V, T) = \frac{dI}{dV}. \quad (14.7)$$

Using 14.6, one can derive theoretical expressions for dI/dV as a function of V , T , and the parameters of the Hamiltonian. We briefly outline a calculation here; more details of these calculations are discussed in references [32] and [33]. I is related to the local spectral density of the small dot by [34]:¹

$$I = \frac{e}{h} \sum_{s=\uparrow,\downarrow} \int d\varepsilon [f_l(\varepsilon) - f_r(\varepsilon)] \left[\frac{2\Gamma_l\Gamma_r}{\Gamma_l + \Gamma_r} A_s(\varepsilon) \right]. \quad (14.8)$$

Here $f_{l(r)}$ is the Fermi function in the left (right) lead, $\Gamma_{l(r)} = \pi\nu |t_{l(r)}|^2$, we assume that $\Gamma_{l(r)}$ does not depend on spin, and we assume that the density of states ν is identical for the two leads. In this equation, $A_s(\varepsilon)$ is the spectral density of spin s and it is related to the retarded Green's function of the dot $G_{ds}^{\text{ret}}(\varepsilon)$ through

$$A_s(\varepsilon) = -2 \text{ Im} [G_{ds}^{\text{ret}}(\varepsilon)]. \quad (14.9)$$

In general, $A_s(\varepsilon)$ may depend upon the chemical potential of the left and right leads. However, in the limit where the bias V is small or the tunneling matrix element to one of the leads is much smaller than to the other lead, it is possible to write

$$G(V, T) = \nu \tilde{G}_0 \sum_{s=\uparrow,\downarrow} \int d\varepsilon f'(\varepsilon - eV) \text{ Im} \mathcal{T}^\sigma(\varepsilon), \quad (14.10)$$

where $\mathcal{T}^\sigma(\varepsilon)$ is the scattering \mathcal{T} -matrix and \tilde{G}_0 is a proportionality constant depending on $\Gamma_{l,r}$ [33]. As a part of this calculation one sees that because electrons can move from the left to the right lead, these leads do not form independent screening channels, but rather form one effective screening channel. This channel then competes with the second screening channel formed by the large dot. This is also discussed in Sec. 14.2.1.

14.1.3 Examples of Conductance Scaling Curves

Using Eq. (14.10) together with the specific expressions for the scattering matrix \mathcal{T} of Ref. [23] we can calculate the scaling curves for the 2CK and the 1CK Kondo models.² These curves will be essential for identifying the QPT in the data in Sec. 14.2.1.

¹Eq. (14.8) is valid only if the coupling matrices to the left and right leads are proportional to one another. When there is only one state in the dot [34], as we have assumed in Eq. (14.6), this condition is satisfied.

²Note that the 1CK model is in fact just the 2CK model with strongly asymmetric channel coupling.

14.1.3.1 $G(V, T)$ in the Two-Channel Kondo Case

Using the results for the scattering matrix from Ref. [23] we can write

$$G(V, T) = G_0 \frac{1}{2} \left[1 - \sqrt{\frac{\pi T}{T_{K2}}} F_{2CK} \left(\frac{eV}{\pi T} \right) \right], \quad (14.11)$$

where the function F_{2CK} is given in Ref. [33]. Its asymptotes are

$$F_{2CK}(x) \approx \begin{cases} c \frac{x^2 + 1}{\sqrt{x}} & \text{for } x \ll 1 \\ \frac{3}{\sqrt{\pi}} \sqrt{x} & \text{for } x \gg 1 \end{cases} \quad (14.12)$$

where it was numerically determined that $c = 0.748336$. Setting $V = 0$ we find

$$G(0, T) = \frac{1}{2} G_0 \left(1 - \sqrt{\frac{\pi T}{T_{K2}}} \right). \quad (14.13)$$

Examining Eqs. (14.11) and (14.13), we find that the scaling relation for the conductance of a quantum dot in the 2CK regime is

$$\frac{2}{G_0} \frac{G(0, T) - G(V, T)}{\sqrt{\pi T / T_{K2}}} = Y \left(\frac{|eV|}{\pi T} \right), \quad (14.14)$$

with the scaling function $Y(x) = F_{2CK}(x) - 1$. One of the remarkable features of the 2CK model is that one obtains the full scaling function rather than just a power law approximation valid only at low energies. The scaling curve $Y(x)$ was used in Ref. [4].

14.1.3.2 $G(V, T)$ in the Single-Channel Kondo Case

The 1CK case can be viewed as a limit of the 2CK case when one of the channels, either the large dot or the leads, is more strongly coupled to the small dot than the other channel. In this case, at temperatures smaller than the crossover temperature T_Δ [35] we should have regular single-channel behavior: the small dot should be Kondo-screened by the more strongly coupled channel. Here ΔJ is the asymmetry parameter and is taken to be positive when the leads are more strongly coupled to the small dot.

For $T, eV \ll T_\Delta$ we can use the scattering matrix given by [23] and obtain, in the limit $|t_l| \ll |t_r|$ or vice versa,

$$G(V, T) = G_0 \left\{ \theta(\Delta J) - \text{sign}(\Delta J) \left(\frac{\pi T}{T_\Delta} \right)^2 \left[1 + \frac{3}{2} \left(\frac{eV}{\pi T} \right)^2 \right] \right\}. \quad (14.15)$$

At zero bias, the conductance is given by:

$$G(0, T) = G_0 \left\{ \theta(\Delta J) - \text{sign}(\Delta J) \left(\frac{\pi T}{T_\Delta} \right)^2 \right\}. \quad (14.16)$$

Examining Eq. (14.15) we note that the scaling relation for the conductance of a quantum dot in the 1CK regime is:

$$\frac{1}{G_0} \frac{G(0, T) - G(V, T)}{(\pi T/T_\Delta)^2} = \text{sign}(\Delta J) \frac{3}{2} \left(\frac{eV}{\pi T} \right)^2. \quad (14.17)$$

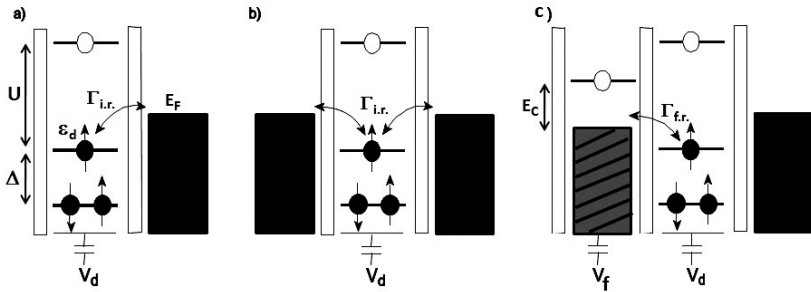
This scaling curve is different from the 2CK curve and was used to analyze the data in Ref. [4].

14.2 Kondo and Quantum Dots: Experiments

14.2.1 The Two-Channel Kondo Effect in a Double Quantum Dot

The first experimental observation of the 2CK state in a quantum dot system occurred in the double dot geometry (Fig. 14.2(c)) proposed by Oreg and Goldhaber-Gordon [31], though there were earlier related proposals (see Sec. 14.2.2). The Hamiltonian that describes this system is that of Eq. (14.6). The localized magnetic impurity is represented by a small quantum dot containing an odd number of electrons. The conduction electrons that screen this local moment belong to two reservoirs, as illustrated in Fig. 14.2. One of the reservoirs corresponds to the source and drain leads (“left” and “right” electrons), which, although physically separated, form a single effective reservoir [2], denoted by *i.r.* for infinite reservoir. The second reservoir, denoted by *f.r.*, is a finite electron bath, i.e., a much larger quantum dot with fixed electron occupancy. It constitutes a second independent screening channel (striped in Fig. 14.2(c)) at low temperature, where a Coulomb blockade forbids it from exchanging electrons with the infinite reservoir (black in Fig. 14.2(c)).

The QPT of Fig. 14.2 occurs as a function of the relative coupling of the two channels to the localized impurity. The antiferromagnetic coupling between the impurity and each reservoir depends on the tunneling rate to that reservoir and the depth of the impurity level with respect to that reservoir’s Fermi level; this coupling determines the reservoirs’ respective ability to Kondo-screen the local moment. Two processes, one involving electrons and one involving holes, contribute to Kondo screening. In energies E_l^n to follow, the subscript refers to the number of electrons on the dot and the superscript refers to the change in the number of electrons in the finite reservoir. To first order, the virtual exchange of electrons with the local moment requires an energy $\Delta E_{e,i.r.} = E_2^0 - E_1^0$ for spin-flip events with the infinite reservoir, and an energy $\Delta E_{e,f.r.} = E_2^{-1} - E_1^0$ for spin-flips with the finite reservoir. The equivalent hole process between the dot and the infinite reservoir requires an energy difference $\Delta E_{h,i.r.} = E_0^0 - E_1^0$ or alternatively, an energy $\Delta E_{h,f.r.} = E_0^1 - E_1^0$ for spin-flip events between the dot and the finite reservoir. Therefore, the two exchange

**FIGURE 14.2**

(a) Tunneling $\Gamma_{i.r.}$ between a quantum dot and a nearby reservoir gives rise to antiferromagnetic exchange coupling between the local spin and the spins in the reservoirs. (b) Physically separated reservoirs are not necessarily independent: if a localized electron can hop off the site to the right reservoir and a new electron can hop onto the site from the left, the two reservoirs will cooperate in screening the localized spin. (c) Adding a second reservoir that also antiferromagnetically couples to the local spin: Coulomb charging on the second (finite) reservoir causes the two reservoirs, labeled *i.r.* (infinite) and *f.r.* (finite), to screen the local spin independently. If the couplings of the two reservoirs are equal, this results in the overscreening characteristic of the two-channel Kondo effect.

couplings are given by [31]

$$J_{i.r.} = \Gamma_{i.r.} \left(\frac{1}{E_2^0 - E_1^0} + \frac{1}{E_0^0 - E_1^0} \right), \quad (14.18)$$

$$J_{f.r.} = \Gamma_{f.r.} \left(\frac{1}{E_2^{-1} - E_1^0} + \frac{1}{E_0^1 - E_1^0} \right). \quad (14.19)$$

At zero temperature the system is in one of the three distinct ground states: a Fermi liquid (Kondo singlet state with the finite reservoir) when $J_{f.r.} > J_{i.r.}$, another Fermi liquid (Kondo singlet state with the infinite reservoir) when $J_{i.r.} > J_{f.r.}$, and the nFL 2CK state at the QCP ($J_{i.r.} = J_{f.r.}$).

At finite temperature, the presence of the QCP manifests itself in the scaling behavior of the system. For temperatures below the Kondo temperature but above the energy scale T_Δ associated with the channel anisotropy $\Delta J = J_{i.r.} - J_{f.r.}$ (see Sec. 14.3.1) the system will obey the 2CK scaling form of Eq. (14.14). This is the quantum critical region. On the two sides of the quantum critical region, where $T < T_\Delta$, the scaling law for single channel Kondo given by Eq. (14.17) is expected. When the infinite reservoir is better coupled, the Kondo effect manifests as an enhancement around zero bias and zero temperature, compared to the conductance at higher bias and

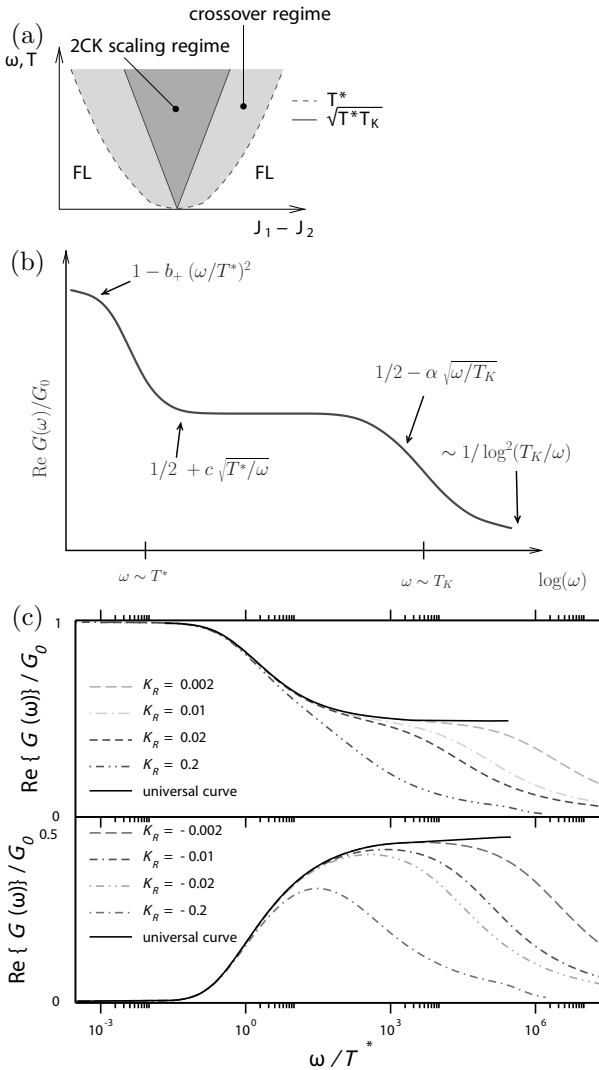
temperature. Conversely, when the finite channel is better coupled to the impurity, it effectively steals the Kondo state away from the leads. This results in a suppression rather than enhancement of the conductance through the small quantum dot at low bias and temperature. Recent work suggests that a crossover region divides the 1CK Fermi liquid from the 2CK nFL regime [36]. This is the lightly shaded region in Fig. 14.3 and is discussed in more detail in Sec. 14.3.1.

This 2CK system was realized in a lateral GaAs quantum dot geometry (Fig. 14.4(a)). The metal gates patterned on the surface of the GaAs/AlGaAs heterostructure define the small quantum dot and the finite reservoir, and allow precise tuning of both the electrostatic potential of each quantum dot and the tunneling rates to the two reservoirs.

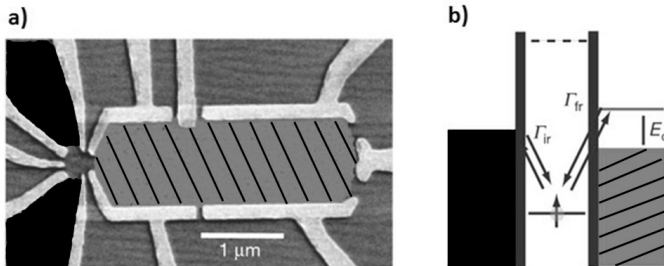
The small quantum dot contains ≈ 25 electrons and acts as the Kondo impurity. Its bare charging energy is ≈ 1 meV (corresponding to ≈ 10 K) and the single-particle energy level spacing is $100 \mu\text{eV}$. It is coupled to a set of leads (black regions in Fig. 14.4(a) and (b)) that form a bound singlet state with the dot, with $kT_K \approx 13 \mu\text{eV}$. The second independent channel consists of electrons in the $3 \mu\text{m}^2$ dot (striped region in Fig. 14.4(a) and (b)) which corresponds to a charging energy E_c of $100 \mu\text{eV}$. This prevents the exchange of electrons with the other reservoir when the large dot is tuned to a Coulomb blockade valley which corresponds to a well-defined charge state, since the lowest electron temperature is $T_{\text{base}} = 12 \text{ mK}$. Yet the large dot effectively has a continuum of single-particle states: its single-particle energy level spacing of $\approx 2 \mu\text{eV}$ cannot be resolved at base temperature since $kT_{\text{base}} \approx 1 \mu\text{eV}$. Thus the finite reservoir acts as a second, independent Kondo-screening channel, as required for observing the 2CK effect.

The measurement of the conductance through the quantum dot for three different couplings to the two channels reveals the different scaling regions of the phase diagram in Fig. 14.1(a). Voltages on the different gates in Fig. 14.4(a) are used to control the small and large dot energy levels relative to the Fermi levels in the leads as well as the overall tunnel coupling; together these determine the exchange coupling to the finite and infinite reservoirs (Eq. (14.18) and (14.19)). When the infinite reservoir is much more strongly coupled to the dot than is the finite reservoir, the zero bias conductance enhancement characteristic of 1CK is observed (Fig. 14.5(a)). Conversely, for increased interdot tunneling ($J_{i.r.} < J_{f.r.}$), the 1CK state is formed with the finite reservoir and causes the suppression of the conductance in Fig. 14.5(c). In both cases, the differential conductance at different temperatures and biases scales according to Eq. (14.17) as shown in Fig. 14.5(a) and (c). The exponent α from the scaled conductance $(G(0, T) - G(V_{ds}, T))/T^\alpha$ is numerically determined to be 1.72 ± 0.40 , which is consistent with the value $\alpha = 2$ characteristic of the 1CK Fermi liquid ground state and the exponent in Eq. (14.17).

The evolution of the differential conductance with tuning from the 1CK state with the infinite reservoir to the 1CK state with the finite reservoir doesn't show clear $\sqrt{V_{ds}}$ behavior as one would expect when crossing through

**FIGURE 14.3**

(a) A more detailed look at the phase transition: a cross-over region separates the 2CK scaling region from the 1CK scaling region. (b) Sketch of the AC conductance as a function of frequency for $\Delta J > 0$. The stated dependences in the different regions are based on conformal field theory [36]. (c) Numerical renormalization group calculations of the real part of the conductance in the universal cross-over regime. Reprinted figures with permission from [Tóth *et al.*, Phys. Rev. B 76, 155318 (2007)]. Copyright (2007) by the American Physical Society.

**FIGURE 14.4**

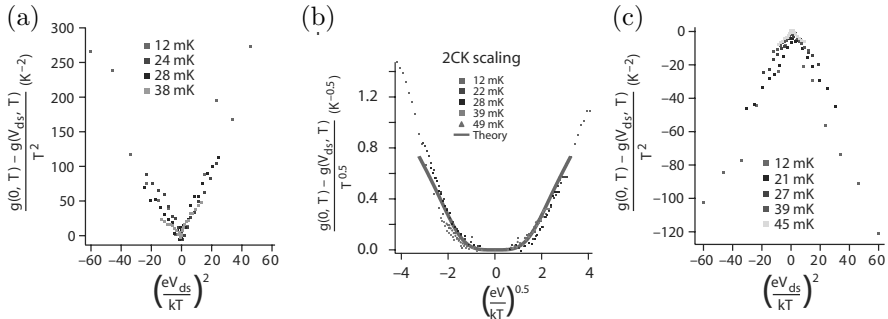
(a) Annotated SEM image of the two-channel Kondo nanostructure: an additional finite reservoir (striped) is coupled to an artificial magnetic impurity already connected to an infinite reservoir composed of two conventional leads (black). (b) Coulomb blockade suppresses exchange of electrons between the finite reservoir and the normal leads at low temperature. The two reservoirs hence act as two independent screening channels. Figure adapted from Potok *et al.* [4].

the 2CK point. However, Fig. 14.5(b) shows that the scaled conductances $(G(0, T) - G(V_{ds}, T))/T^\alpha$ at different temperatures collapse onto the same line when $\alpha = 0.5$, as expected for the 2CK nFL state and in agreement with Eq. (14.14). Single-channel Kondo scaling of the same data fails [4]. A two dimensional nonlinear fit to the data in Fig. 14.5(b) produced the value $\alpha = 0.62 \pm 0.21$, consistent with 2CK behavior.

14.2.2 The Two-Channel Kondo Effect in Other Quantum Dot Geometries

For the three distinct Kondo states involved in the QPT described above, the degeneracy is provided by the unpaired spin- $\frac{1}{2}$ in the small quantum dot. There are several theoretical proposals for the realization of the 2CK effect where the local degeneracy is based on the charge degree of freedom. In fact, the earliest proposal for observing the 2CK effect in semiconductor nanostructures [37] involved a large semiconductor quantum dot coupled via single-mode point contacts to a reservoir. Here, at the charge degeneracy points of the dot, strong charge fluctuations are expected to give rise to a 2CK effect [38]: two successive charge states play the role of the local two-fold degeneracy, while the two independent screening channels are the spin-up and spin-down electrons of the reservoir. Due to conflicting constraints on the size of the dot this specific proposal may not be experimentally realizable [39].

This difficulty can be overcome by introducing a single resonant level between the large quantum dot and the reservoir. At the charge degeneracy

**FIGURE 14.5**

(a) Measurements showing single-channel Kondo scaling of the data for $J_{i.r.} > J_{f.r.}$ (b) Measurements showing 2CK scaling of the data when $J_{i.r.} = J_{f.r.}$ (c) Measurements showing 1CK scaling in the $J_{i.r.} < J_{f.r.}$ case. Figure adapted from Potok *et al.* [4].

point of the large dot, and in the mixed-valence regime of the small dot, a 2CK effect with a nFL fixed point is expected to occur [40]. This modified geometry is in fact identical to the double dot geometry described above, where spin-2CK is observed away from the charge degeneracy points of both dots. In fact, further analysis of the different parameter regimes of this double dot system predicts several exotic effects such as a line of two-channel fixed points, a continuous transition from the spin-2CK to the charge-2CK effect [41], and an SU(4) Kondo effect with a stable fixed point [42].

14.2.3 The Two-Channel Kondo Effect in Graphene Sheets

In pristine graphene, there are always two angular momentum channels that couple to a local moment; so when the exchange coupling is the same for the two channels 2CK behavior is expected. Recently, researchers studying tunneling into Cobalt adatoms on graphene observed a conductance scaling law consistent with that expected for 2CK physics [43]. In this system the Fermi level was far from the Dirac point (in Sec 14.3.3.1 we will discuss the effects of suppressing the density of states near the Fermi energy).

Low-temperature scanning tunneling spectroscopy measurements on epitaxial graphene monolayers exhibiting a linear Dirac dispersion, dosed with a low coverage of Cobalt atoms, revealed two kinds of Kondo resonances. The difference between them is associated with whether the Co atom occupies the middle of a hexagon in the graphene lattice or is located on top of a carbon atom. The spin of the Cobalt atom is calculated [44] to be 1/2. The degenerate K and K' valleys in graphene result in two screening channels for the localized magnetic impurity. When the adatom is in the center of a hexagon, it

should be equally coupled to the K and K' valleys, resulting in 2CK behavior. In this case, scaling of differential conductance with tip bias at constant low temperature (4 K) over a bias range from $V = kT$ to $V = kT_K$ was observed to be consistent with the exponent 0.5 expected for 2CK. In contrast, when the Co atom is located on top of a carbon atom it should locally break the valley symmetry and thus show single channel Kondo physics. The exponent extracted from the voltage scaling in this case is close to the Fermi liquid value of 2. This also agrees with measurements of Cobalt atoms on Copper which show single channel Kondo physics [43].

14.2.4 The Two-Impurity Kondo Effect in a Double Quantum Dot Geometry

The single-channel and two-channel Kondo effects describe the behavior of a single magnetic impurity interacting with conduction electrons. In bulk materials with magnetic impurities, this corresponds to the dilute limit, where the density of magnetic impurities is sufficiently low that the local spins do not interact with each other. At the opposite extreme there are materials, such as Kondo lattice materials based on Cerium and Uranium, where local moments are closely spaced [45]. In these materials, interactions between the impurities are mediated by the conduction electrons via the Ruderman-Kittel-Kasuya-Yosida (RKKY) mechanism. The unique properties of these materials arise from the competition between the Kondo screening of individual impurities and the inter-impurity interactions, and studying this competition is important to gaining a more complete understanding of these materials.

As a first step toward tackling this complex problem, consider a simpler system which can be realized in a nanostructure: just two magnetic impurities coupled to conduction electrons and to one another, known as the 2-impurity Kondo system (2IK) [46]. The model Hamiltonian for this system is

$$H_{2\text{IK}} = J_1 \vec{s}_1 \cdot \vec{S}_1 + J_2 \vec{s}_2 \cdot \vec{S}_2 + K \vec{S}_1 \cdot \vec{S}_2 \quad (14.20)$$

where \vec{S}_1 and \vec{S}_2 are the spins of the two magnetic impurities, \vec{s}_1 and \vec{s}_2 are the spins of the conduction electrons at the impurity sites, and $J_1, J_2 > 0$ are the antiferromagnetic (AFM) interaction between the conduction electrons and the impurities that cause the Kondo screening of the impurities. K is the inter-impurity interaction, from the RKKY mechanism. We consider the case where $T_{K,1} \sim T_{K,2} \sim T_K$, where T_K is a single effective Kondo temperature for the full system. For $-T_K < K < K_c$ (where $K_c \approx 2.5T_K$) the Kondo effect dominates and each impurity is individually screened by the conduction electrons. However, for $K > K_c$ the inter-impurity interaction dominates and the two impurities pair to form a spin singlet that does not interact with the conduction electrons [46]. At the critical coupling $K = K_c$ between the Kondo-screened and singlet ground states the system is predicted to go through a QPT associated with a novel non-Fermi liquid fixed point [47].

Nanostructures offer a natural means of realizing the 2IK Hamiltonian (see [48] and references therein). The 2IK Hamiltonian has been modeled experimentally with gated semiconductor quantum dots: Craig *et al.* [5] have studied two quantum dots coupled by an intermediate reservoir of electrons, while Jeong *et al.* [49] and Chen *et al.* [50] have studied a double quantum dot system with no intervening reservoir, where the AFM coupling is provided by the exchange interaction between the two dots. These authors found a suppression of the Kondo conductance of a dot as they increased the strength of the AFM inter-dot coupling, evidence that the formation of an inter-impurity spin singlet was disrupting the Kondo coupling to the leads and hence conduction through the dots. Heersche *et al.* [51] studied transport through a gold grain quantum dot in the presence of cobalt impurities which could couple to a spin on the grain. They observed a similar suppression of the Kondo conductance in the presence of the cobalt impurities and found that the Kondo peak could be restored by application of a magnetic field. These observations show that one can tune a 2IK system to either side of the QPT. However, the nFL behavior at the QCP has yet to be observed.

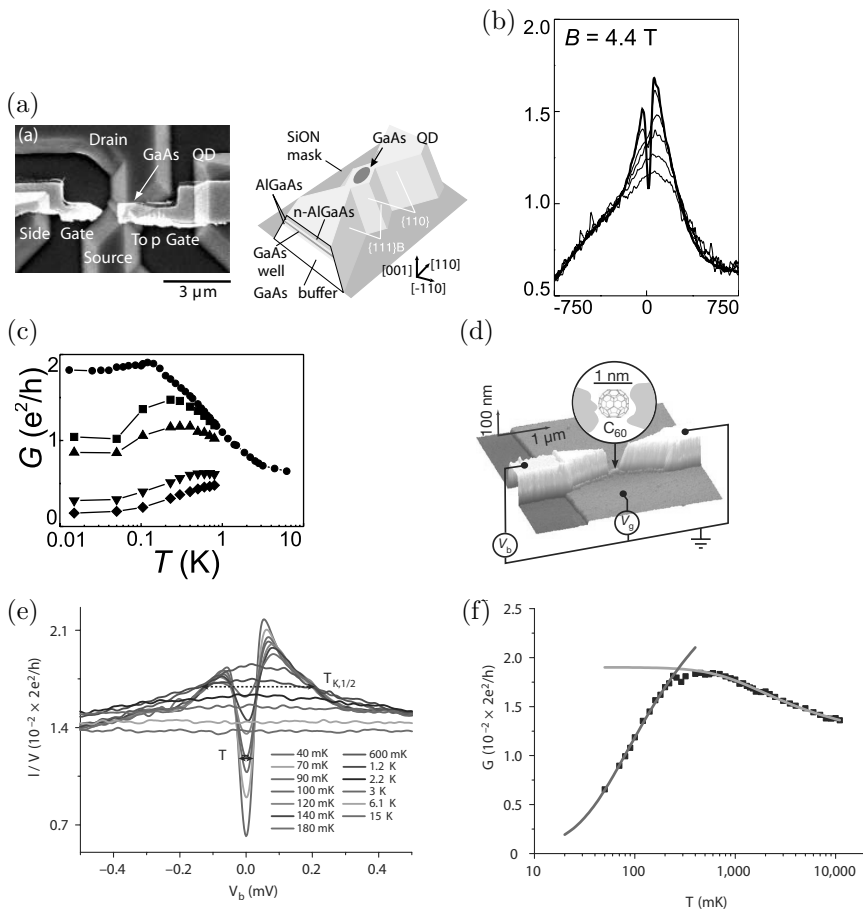
14.2.5 The Two-Impurity Kondo Effect in a Quantum Dot at the Singlet-triplet Transition

The 2IK Hamiltonian can be also used to describe a quantum dot at the singlet-triplet degeneracy point [52]. Therefore, a QPT of the Kosterlitz-Thouless type should also take place in a single dot geometry, where the quantum dot has an even number of electrons and is coupled to one electron reservoir.

The ground state of a two-electron system is a spin singlet ($S = 0$), with both electrons occupying the same orbital. The triplet state ($S = 1$) will have lower energy if the exchange energy gained for parallel spin filling exceeds the level separation between adjacent orbitals [53]. Instead of the fully screened or overscreened scenarios of the 1CK or 2CK cases, for a single reservoir mode coupled to the S=1 quantum dot, Kondo correlations only partially screen the local impurity and a residual spin- $\frac{1}{2}$ is left over. Therefore, an underscreened Kondo effect takes place on the triplet side.

The energy difference between the singlet and the triplet states can be controlled by applying a magnetic field or by tuning the gate voltage. A singlet-triplet Kondo effect has been observed in transport measurements through vertical quantum dots, lateral quantum dots, carbon nanotubes, and single molecule transistors (see [54], [55], [56] and references therein).

A system near a singlet-triplet transition can exhibit a two-stage Kondo effect [57, 58] which is characterized by a logarithmic and non-monotonic dependence of the conductance on temperature and bias. When two reservoir channels couple to the spin-1 impurity, two Kondo-screening channels with two different Kondo temperatures T_{K1} and T_{K2} form [59]. With decreasing temperatures, the conductance is enhanced when $T_{K2} < T < T_{K1}$ as half of

**FIGURE 14.6**

(a) SEM and schematic of a lateral quantum dot device. (b) Conductance on one side of the degeneracy point as a function of bias for different temperatures. The zero-bias anomaly develops a dip with decreasing temperatures. (c) The logarithmic dependence of the conductance on temperature as the device is tuned away from the singlet-triplet transition point. Reprinted figures with permission from [W. G. van der Wiel *et al.*, Phys. Rev. Lett. 88, 126803 (2002)]. Copyright (2002) by the American Physical Society. (d) Sketch of C₆₀ single molecule transistor. On the singlet side, the characteristic dip in the zero-bias conductance enhancement (e) as well as the logarithmic enhancement and suppression of the conductance as a function of temperature (f) is observed. Adapted by permission from Macmillan Publishers Ltd: Roch *et al.*, Nature 453, 633 (2008).

the spin 1 is screened by one channel. Once $T < T_{K2} < T_{K1}$ the residual spin- $\frac{1}{2}$ is screened by the second channel, and the conductance is reduced by the interference of the two modes. On the singlet side of the degeneracy a similar two stage Kondo effect is predicted to occur if only one channel is coupled to the quantum dot [57].

The transition from the singlet to the triplet state of a quantum dot is very different, depending on which Kondo state is present on each side. When one reservoir is coupled, the transition happens from a two-stage Kondo state on the singlet side to an underscreened Kondo state on the triplet side via a QCP of the same type as that of the 2IK model [57]. When two reservoirs couple to the quantum dot, the transition from a spin zero system on the singlet side to a two-stage Kondo system on the triplet side is a crossover, and the ground state has Fermi liquid properties throughout [58, 60].

This effect has been observed in lateral quantum dots [61, 62] and single molecule transistors [54]. In the experiment by van der Wiel *et al.* [61] a lateral quantum dot is tuned near a singlet-triplet degeneracy point using magnetic field. Conductance measurements show a dip in the zero-bias anomaly at low temperatures, which disappears with increasing temperature (Fig. 14.6(b)), as well as the predicted logarithmic increase and decrease of the conductance with temperature and or bias (Fig. 14.6(c)). However, in this system it is not possible to unambiguously distinguish whether a singlet or triplet ground state is responsible for the observed effect. This makes it impossible to determine which of the two proposed mechanisms is responsible.

Roch *et al.* [54] have measured transport through a C-60 single electron transistor shown in Fig. 14.6(d), and used a gate voltage to tune through the singlet-triplet transition. Using bias spectroscopy as a function of both gate voltage and magnetic field, they are able to clearly identify the singlet and triplet sides of the transition. In Fig 14.6(e) they observe a zero-bias dip in the conductance on the singlet side of the transition, whose width narrows as the gate voltage is tuned toward the transition. The zero-bias conductance of the dip increases logarithmically with increasing temperature (Fig. 14.6(f)), and conductance dips at different distances from the transition can be scaled to lie on a single curve. On the triplet side, they observe a zero-bias peak in conductance, which also has a logarithmic temperature dependence. This behavior, as well as the scaling of the conductance with temperature and bias, is consistent with predictions for a QPT between the singlet and the triplet regions.

14.3 Looking Forward

Having reviewed the progress in observing QPTs in nanostructures, we now look forward and examine some of the most promising proposals for charac-

terizing existing QPTs and finding new QPTs in novel and as yet unrealized nanostructures.

14.3.1 Influence of Channel Asymmetry and Magnetic Field on the Two-Channel Kondo Effect

The experiments in Sec. 14.2.1 demonstrated that one can tune to the region where the asymmetry parameter $\Delta J = J_{i.r.} - J_{f.r.}$ is large and 1CK behavior dominates, and to the point where $\Delta J \approx 0$ and one observes 2CK behavior. The next important step is to map out the full phase diagram sketched in Fig. 14.3(a). Of especial interest is the region around $\Delta J = 0$ where the asymmetry is small but finite: here theory predicts that the proximity of the QCP influences the behavior of the system at both low and high energy [36]. Specifically, a new energy scale $T_\Delta \propto (\Delta J)^2$ emerges. In the region $T > (T_\Delta T_K)^{1/2}$ (dark gray in Fig. 14.3(a)) the 2CK scaling law should hold. However, for $T_\Delta < T < (T_\Delta T_K)^{1/2}$ it is predicted that one should enter a cross-over region (light gray in Fig. 14.3(a)) where conductance is described by a new universal function that has been calculated numerically (Fig. 14.3(c)). Finally, for $T < T_\Delta$ it is predicted that one should observe a modified 1CK scaling law, where the relevant scaling parameter is T/T_Δ , not T/T_K . The full evolution is sketched in Fig. 14.3(b). This phase diagram can also be accessed with bias replacing temperature, and together these experimental knobs should allow a complete mapping of the phase diagram.

The QCP can also be accessed at $\Delta J = 0$ as a function of magnetic field: unlike for 1CK, Zeeman splitting is a relevant perturbation and any non-zero magnetic field will move the system away from the QCP. The phase diagram is similar to the one shown in Fig. 14.1(a) for a transition driven by channel anisotropy, but here Fermi liquid behavior should appear below an energy scale given by $E_B = (g\mu B)^2/(kT_K)$, and the functional form of the conductance curves will be different from the anisotropy-driven case. The contrast between 1CK and 2CK behavior is manifested in the effect of the field on the Kondo peak in the spin-averaged density of states (differential conductance) as a function of bias. For 1CK, there is a threshold magnetic field B_{thresh} above which the Kondo peak will split [56], but for $B < B_{\text{thresh}}$ no splitting is observed. In contrast, for 2CK it is predicted [36] that the Kondo peak remains split even down to infinitesimal fields. This measurement is experimentally challenging because the magnetic field needs to be applied parallel to the two-dimensional electron gas at the GaAs/AlGaAs interface. If there is a sizable component of the field perpendicular to the interface, then this component will couple to the orbital motion of the electrons and modify the wavefunction overlap of the dot and its leads. The result of this will be to disrupt the delicate tuning necessary to maintain $\Delta J = 0$, making it impossible to measure the desired splitting. Such field alignment is well established but non-trivial.

14.3.2 Multiple Sites

A natural extension beyond two neighboring local sites is three sites arranged as vertices of an equilateral triangle. Such a system can be built either by using STM to position atoms or molecules on a surface (e.g., Cr₃ on Au(111) [63], Co₃ on Cu(111) [64], or a linear Mn chain on CuN on Cu(111) [65] or using laterally-coupled quantum dots; see, e.g., [66]. But even after defining the geometry there are many options for the Hamiltonian and its parameters: occupancy and spin of each site, strength of antiferromagnetic coupling between pairs of sites and between a site and mobile conduction electrons, symmetry of local site energies and couplings, etc.

This has given rise to a wide range of theoretical proposals, many of which are reviewed in [67]. Without trying to survey all the theoretical contributions, we point out a few that are particularly intriguing to us. In 2005, Ingersent *et al.* and Lazarovits *et al.* considered three antiferromagnetically-coupled half-integer spins arranged in a triangle, and coupled to conduction electrons by a standard Kondo coupling [68]. They found that the frustration of the antiferromagnetic coupling led to a net local spin of 1/2 and a novel non-Fermi-liquid phase when the Kondo coupling is included. Ingersent *et al.* found that this phase should be stable to asymmetries that would likely occur in a realistic quantum dot-based realization of this system, even with careful tuning, whereas Lazarovits *et al.* found that the phase would not be stable to spin-orbit coupling. Further decreasing the symmetry of couplings between sites and to leads, Mitchell *et al.* [69] found a QPT between an antiferromagnetically Kondo-coupled ground state and a ferromagnetically-coupled (local moment) Kondo ground state, as a function of the coupling between two particular dots. Restoring the symmetry of the trimer but increasing the tunnel couplings to a “molecular regime,” Vernek *et al.* found a Fermi liquid S=1 Kondo ground state [70]. Going beyond three impurities, and beyond transport spectroscopy (the main probe envisioned in the works noted above), Karzig *et al.* recently investigated full counting statistics of transport through a chain of quantum dots, finding a type of phase transition as a function of tunnel coupling between dots [71].

Experimentally, all these systems are at an early stage. An equilaterally arranged Cr₃ on Au(111) shows no Kondo effect at 7K, whereas a similar trimer Co₃ on Cu(111) shows a Kondo resonance with an unusual ring-shaped spatial arrangement. The Cr trimer may have a lower Kondo temperature due to nFL physics, but this has yet to be verified. With respect to quantum dot trimers, researchers have mainly determined and tuned the occupancy and coupling of the three sites, through transport and charge-sensing measurements. The situation would seem to be ripe for testing the predicted exotic physics, though this would involve a tour de force measurement: the number of tunable parameters remains daunting.

14.3.3 Different Types of Reservoirs

14.3.3.1 Superconducting Leads and Graphene at the Dirac Point

The ability of the fermions in the reservoir to screen the local moment depends on the density of states of the reservoir around the Fermi energy. In the most generic cases, the effective density of states is smooth and finite around the Fermi energy, and at sufficiently low temperature the conduction electrons will be able to form the spin-singlet state with the impurity spin no matter how small the exchange coupling constant is.

In materials with a non-trivial density of states in the reservoir around the Fermi energy, the Kondo effect can be suppressed: the lack of low energy states prevents screening when the exchange coupling is below some critical coupling. If the density of states is zero over some energy interval around the Fermi energy, as is the case in *s*-wave superconductors, a first order QPT between a Kondo-screened phase and a local moment phase occurs. If the density of states is zero only at the Fermi energy, as is the case for *d*-wave superconductors or single layer graphene at the Dirac point, a second order QPT between the two regimes can take place; however, whether this transition takes place is contingent on the exact power-law dependence of the density of states on the energy relative to the Fermi level [72].

In particular, when the density of states of the reservoir vanishes linearly with energy, Castanello *et al.* [73] predict a QPT between the Kondo-screened phase and the local moment phase, driven by the exchange coupling between the local spin and the conduction electrons. They also predict logarithmic corrections to the Kondo scaling in the Kondo-screened region of the phase diagram. An alternative approach suggests a suppression of this phase transition for certain combination of local degeneracy number and number of channels [74]. A physical system that might exhibit such a transition, but which has not yet been realized, is a quantum dot with *d*-wave superconducting leads. This system is of interest because it can help one to understand the effect of impurities in the cuprates, where even non-magnetic atoms such as Zn may induce magnetic effects [75].

A quantum dot with *s*-wave superconducting leads has been realized using a nanotube quantum dot contacted with Al leads [76], a self-assembled InAs dot with Al leads [77], and more recently in a C-60 molecule coupled to Al leads [78]. In these dots T_K could be varied, and the authors observed the expected suppression of the Kondo conductance when $kT_K < \Delta$, where Δ is the superconducting gap. Surprisingly, for $T_K > \Delta$, it was observed that the Kondo conductance was larger than the normal state conductance [76], an effect attributed to the interplay of the Kondo effect and multiple Andreev reflections [79]. The competition between Kondo screening and Cooper pair binding studied in these mesoscopic systems is now being found in real bulk materials: recent work by Sun *et al.* [80] suggests that by applying pressure to CeFeAsO_{1-x}F_x they could drive a phase transition from a superconducting state where the itinerant Fe 3d electrons are in Cooper pairs to a state where

these conduction electrons Kondo-screen the local moments of the Ce atoms, thus breaking the superconducting state. Although $\text{CeFeAsO}_{1-x}\text{F}_x$ is not a conventional *s*-wave superconductor, investigating the competition between the Kondo effect and superconductivity in mesoscopic systems offers insight into the fascinating behavior of electrons in real materials.

14.3.3.2 The Bose-Fermi Kondo Model in Quantum Dots

In the previous sections, the bath that coupled to the local moment consisted of fermions. There are other systems where the bath consists of bosons, or where a bosonic and a fermionic bath are coupled to the local spin, and the system can undergo a QPT. The case where a spin-1 boson bath and a spin-1/2 fermion bath are coupled to a spin-1/2 local moment is described by the Bose-Fermi Kondo model. When the coupling to the fermionic bath is large, the system undergoes the usual Kondo screening of the local moment by the fermions; when the coupling to the bosonic bath dominates, Kondo processes are suppressed and the systems exhibit universal local moment fluctuations [81]. Between the two regimes, as a function of the coupling anisotropy to the bosonic/fermionic bath, a continuous phase transition takes place. This model has been proposed to describe some high T_c cuprates where the Kondo temperature might be suppressed by the coupling to a bosonic mode, magnetic nanostructures coupled to a metallic bath, or systems near a magnetic QCP [82].

In mesoscopic systems, this model can be implemented in a quantum dot coupled to ferromagnetic leads [83]. Here, a quantum dot with an odd number of electrons plays the usual role of a localized spin-1/2. It is coupled to a bath of conduction electrons, where, due to the nature of the ferromagnetic leads, collective excitations in the form of spin waves exist. The spin of the conduction electrons to which the magnetic impurity couples is determined not only by the spin of the particle-hole excitations in the leads, but also by the spin-waves. Therefore, the local moment is coupled to the fermionic bath of quasiparticles as well as the bosonic bath of spin-waves. For anti-aligned magnetization in the source and drain leads, the QPT of the Bose-Fermi Kondo model is predicted to take place as a function of gate voltage [83]. The gate voltage controls ϵ , the energy of the localized state relative to the Fermi level, which determines the strength of the coupling to the fermionic and the bosonic bath. For ϵ comparable to the level broadening, the usual Kondo effect will take place. As this energy (ϵ) is increased, interactions with the spin-waves destroy the Kondo effect and drive the system to a universal local moment fluctuation phase. A QCP with non-Fermi liquid behavior is expected where the Kondo resonance is replaced by a fluctuating moment due to the coupling to the spin waves. Recent work has demonstrated the Kondo effect in a C-60 quantum dot with ferromagnetic leads [84], as well as in a ferromagnetic atomic contact [85]. These developments are a promising step toward realizing nanostructures that can model the Bose-Fermi Kondo effect.

Acknowledgments – Work at Stanford was supported by NSF contract DMR-0906062, and by a Fellowship from the David and Lucile Packard Foundation. Work at Weizmann was supported by a DIP H.2.1 grant. Both were supported by the US-Israel Binational Science Foundation, grant number 2008149.

Bibliography

- [1] L. P. Kouwenhoven *et al.*, *Science* **278**, 1788 (1997).
- [2] L. I. Glazman and M. E. Raikh, *JETP Letters* **47**, 452 (1988).
- [3] T. K. Ng and P. A. Lee, *Phys. Rev. Lett.* **61**, 1768 (1988).
- [4] R. M. Potok *et al.*, *Nature* **446**, 167 (2007).
- [5] N. J. Craig *et al.*, *Science* **304**, 565 (2004).
- [6] J. P. Pekola, F. Giazotto, and O.-P. Saira, *Phys. Rev. Lett.* **98**, 037201 (2007); G. D. Scott *et al.*, *Phys. Rev. B* **79**, 165413 (2009).
- [7] C. L. Seaman *et al.*, *Phys. Rev. Lett.* **67**, 2882 (1991); M. J. Besnus *et al.*, *Journal of Magnetism And Magnetic Materials* **76-7**, 471 (1988).
- [8] M. Maple *et al.*, *Journal of Low Temperature Physics* **99**, 223 (1995).
- [9] D. C. Ralph and R. A. Buhrman, *Phys. Rev. Lett.* **69**, 2118 (1992).
- [10] S. K. Upadhyay, R. N. Louie, and R. A. Buhrman, *Phys. Rev. B* **56**, 12033 (1997).
- [11] R. J. P. Keijsers, O. I. Shklyarevskii, and H. van Kempen, *Phys. Rev. Lett.* **77**, 3411 (1996); T. Cichorek *et al.*, *Phys. Rev. Lett.* **94**, 236603 (2005).
- [12] N. S. Wingreen, B. L. Altshuler, and Y. Meir, *Phys. Rev. Lett.* **75**, 769 (1995).
- [13] D. C. Ralph, A. W. W. Ludwig, J. Vondelft, and R. A. Buhrman, *Phys. Rev. Lett.* **72**, 1064 (1994).
- [14] W. J. de Haas, J. H. de Boer, and G. J. van den Berg, *Physica* **1**, 1115 (1934); M. P. Sarachik, E. Corenzwit, and L. D. Longinotti, *Phys. Rev.* **135**, A1041 (1964).
- [15] A. A. Abrikosov, *Physics* **2**, 5 (1965); H. Suhl, *Phys. Rev.* **138**, A515 (1965).

- [16] K. D. Schotte and U. Schotte, Phys. Rev. **185**, 509 (1969).
- [17] K. G. Wilson, Rev. Mod. Phys. **47**, 773 (1975).
- [18] G. Yuval and P. W. Anderson, Phys. Rev. B **1**, 1522 (1970); P. W. Anderson, J. Phys. C: Solid State **3**, 2436 (1970).
- [19] J. R. Schrieffer and P. A. Wolff, Phys. Rev. **149**, 491 (1966).
- [20] P. Nozieres and A. Blandin, J. Phys. (Paris) **41**, 193 (1980).
- [21] A. Zawadowski, Phys. Rev. Lett. **45**, 211 (1980).
- [22] I. Affleck, Nucl. Phys. B **336**, 517 (1990); I. Affleck and A.W.W. Ludwig, Nucl. Phys. B **352**, 849 (1991); I. Affleck and A.W.W. Ludwig, Nucl. Phys. B **360**, 641 (1991); I. Affleck and A.W.W. Ludwig, Phys. Rev. Lett. **67**, 161 (1991); A.W.W. Ludwig and I. Affleck, Phys. Rev. Lett. **67**, 3160 (1991).
- [23] I. Affleck and A. W. W. Ludwig, Phys. Rev. B **48**, 7297 (1993).
- [24] I. Affleck, Acta Phys. Polon. B **26**, 1869 (1995).
- [25] G. Kotliar and A. E. Ruckenstein, Phys. Rev. Lett. **57**, 1362 (1986).
- [26] D. L. Cox and A. E. Ruckenstein, Phys. Rev. Lett. **71**, 1613 (1993).
- [27] M. Krawiec, Journal of Physics: Condensed Matter **19**, 346234 (2007).
- [28] S. Andergassen, T. Enss, C. Karrasch, and V. Meden, Chapter 1 in *Quantum Magnetism*, NATO Science for Peace and Security Series B: Physics and Biophysics, (Springer Netherlands, Amsterdam, 2006).
- [29] S. R. White, Phys. Rev. Lett. **69**, 2863 (1992).
- [30] G. De Chiara, M. Rizzi, D. Rossini, and S. Montangero, Journal of Computational and Theoretical Nanoscience **5**, 1277 (2008); U. Schollwöck, Rev. Mod. Phys. **77**, 259 (2005).
- [31] Y. Oreg and D. Goldhaber-Gordon, Phys. Rev. Lett. **90**, 136602 (2003).
- [32] L. I. Glazman and M. Pustilnik, arXiv:cond-mat/0302159 (2003).
- [33] Y. Oreg and D. Goldhaber-Gordon, in *Physics of Zero- and One-Dimensional Nanoscopic Systems.*, Vol. 156 of *Springer Series in Solid-State Sciences*, edited by S. N. Karmakar, S. K. Maiti, and J. Chowdhury (Springer, Berlin, 2007), pp. 27 – 44.
- [34] Y. Meir and N. S. Wingreen, Phys. Rev. Lett. **68**, 2512 (1992).
- [35] M. Pustilnik, L. Borda, L. I. Glazman, and J. von Delft, Phys. Rev. B **69**, 115316 (2004).

- [36] A. I. Toth, L. Borda, J. von Delft, and G. Zarand, Phys. Rev. B **76**, 155318 (2007).
- [37] K. A. Matveev, Soviet Physics, JETP **72**, 892.
- [38] K. A. Matveev, Phys. Rev. B **51**, 1743. E. Lebanon, A. Schiller, and F. Anders, Phys. Rev. B **68**, (2003).
- [39] G. Zarand, G. T. Zimanyi, and F. Wilhelm, Phys. Rev. B **62**, 8137 (2000).
- [40] E. Lebanon, A. Schiller, and F. B. Anders, Phys. Rev. B **68**, 155301 (2003).
- [41] F. Anders, E. Lebanon, and A. Schiller, Phys. Rev. B **70**, 20 (2004).
- [42] K. Le Hur, P. Simon, and L. Borda, Phys. Rev. B **69**, 045326 (2004).
- [43] L. Mattos, *et al.* in preparation (unpublished).
- [44] T. O. Wehling *et al.*, arXiv:0911.2103 (2009); Y. Yagi *et al.*, Phys. Rev. B **69**, 075414 (2004).
- [45] A. C. Hewson, *The Kondo Problem to Heavy Fermions, Cambridge Studies in Magnetism* (Cambridge University Press, Cambridge, 1993).
- [46] B. A. Jones and C. M. Varma, Phys. Rev. Lett. **58**, 843 (1987).
- [47] B. A. Jones, B. G. Kotliar, and A. J. Millis, Phys. Rev. B **39**, 3415 (1989); B. A. Jones and C. M. Varma, Phys. Rev. B **40**, 324 (1989); I. Affleck and A. W. W. Ludwig, Phys. Rev. Lett. **68**, 1046 (1992).
- [48] A. M. Chang and J. C. Chen, Reports on Progress in Physics **72**, 096501 (25pp) (2009).
- [49] H. Jeong, A. M. Chang, and M. R. Melloch, Science **293**, 2221 (2001).
- [50] J. C. Chen, A. M. Chang, and M. R. Melloch, Phys. Rev. Lett. **92**, 176801 (2004).
- [51] H. B. Heersche *et al.*, Phys. Rev. Lett. **96**, 17205 (2006).
- [52] K. Kikoin and Y. Avishai, Phys. Rev. Lett. **86**, 2090 (2001).
- [53] S. Tarucha *et al.*, Phys. Rev. Lett. **84**, 2485 (2000).
- [54] N. Roch *et al.*, Nature **453**, 633 (2008).
- [55] C. H. L. Quay *et al.*, Phys. Rev. B **76**, 245311 (2007).
- [56] M. Grobis, I. G. Rau, R. M. Potok, and D. Goldhaber-Gordon, *Handbook of Magnetism and Advanced Magnetic Materials* (Wiley, 2006), Vol. 5.

- [57] W. Hofstetter and H. Schoeller, Phys. Rev. Lett. **88**, 016803 (2002).
- [58] M. Pustilnik, L. I. Glazman, and W. Hofstetter, Phys. Rev. B **68**, 161303 (2003).
- [59] M. Pustilnik and L. I. Glazman, Phys. Rev. Lett. **87**, 216601 (2001).
- [60] M. Pustilnik and L. Glazman, Phys. Rev. Lett. **85**, 2993 (2000).
- [61] W. G. van der Wiel *et al.*, Phys. Rev. Lett. **88**, 126803 (2002).
- [62] G. Granger *et al.*, Phys. Rev. B **72**, 165309 (2005).
- [63] T. Jamneala, V. Madhavan, and M. F. Crommie, Phys. Rev. Lett. **87**, 256804 (2001).
- [64] H. Manoharan, C. Lutz, and D. Eigler, Private Communication, 2010.
- [65] C. F. Hirjibehedin, C. P. Lutz, and A. J. Heinrich, Science **312**, 1021 (2006).
- [66] A. Vidan *et al.*, Applied Physics Letters **85**, 3602 (2004); L. Gaudreau *et al.*, Phys. Rev. Lett. **97**, 036807 (2006); M. C. Rogge and R. J. Haug, New Journal of Physics **11**, 113037 (10pp) (2009); S. Amaha *et al.*, Applied Physics Letters **94**, 092103 (2009); D. Schröer *et al.*, Phys. Rev. B **76**, 075306 (2007).
- [67] K. Kikoin, Low Temperature Physics **33**, 105 (2007).
- [68] K. Ingersent, A. W. W. Ludwig, and I. Affleck, Phys. Rev. Lett. **95**, 257204 (2005); B. Lazarovits, P. Simon, G. Zaránd, and L. Szunyogh, Phys. Rev. Lett. **95**, 077202 (2005).
- [69] A. K. Mitchell, T. F. Jarrold, and D. E. Logan, Phys. Rev. B **79**, 085124 (2009).
- [70] E. Vernek *et al.*, Phys. Rev. B **80**, 035119 (2009).
- [71] T. Karzig and F. von Oppen, Phys. Rev. B **81**, 045317 (2010).
- [72] D. Withoff and E. Fradkin, Phys. Rev. Lett. **64**, 1835 (1990); M. Vojta, Philosophical Magazine **86**, 1807 (2006).
- [73] C. R. Cassanello and E. Fradkin, Phys. Rev. B **53**, 15079 (1996).
- [74] C. Gonzalez-Buxton and K. Ingersent, Phys. Rev. B **54**, R15614 (1996).
- [75] M. Vojta, R. Zitzler, R. Bulla, and T. Pruschke, Phys. Rev. B **66**, 134527 (2002); S. H. Pan *et al.*, Nature **403**, 746 (2003).
- [76] M. R. Buitelaar, T. Nussbaumer, and C. Schönenberger, Phys. Rev. Lett. **89**, 256801 (2002).

- [77] C. Buizert *et al.*, Phys. Rev. Lett. **99**, 136806 (2007).
- [78] C. Winkelmann *et al.*, Nature Physics **5**, 876 (2009).
- [79] Y. Avishai, A. Golub, and A. D. Zaikin, Phys. Rev. B **67**, 041301 (2003).
- [80] L. Sun *et al.*, arXiv:0907.4212 (2009).
- [81] J. L. Smith and Q. Si, Europhys. Lett. **45**, 228 (1999); A. M. Sengupta, Phys. Rev. B **61**, 4041 (2000); L. Zhu and Q. Si, Phys. Rev. B **66**, 024426 (2002); G. Zaránd and E. Demler, Phys. Rev. B **66**, 024427 (2002).
- [82] J. Bobroff *et al.*, Phys. Rev. Lett. **83**, 4381 (1999); J. Bobroff *et al.*, Phys. Rev. Lett. **86**, 4116 (2001); M. Vojta and M. Kirćan, Phys. Rev. Lett. **90**, 157203 (2003); A. J. Millis, D. K. Morr, and J. Schmalian, Phys. Rev. Lett. **87**, 167202 (2001); A. J. Millis, D. K. Morr, and J. Schmalian, Phys. Rev. B **66**, 174433 (2002).
- [83] S. Kirchner, L. Zhu, Q. Si, and D. Natelson, PNAS **102**, 18824 (2005).
- [84] A. N. Pasupathy *et al.*, Science **306**, 86 (2004).
- [85] M. R. Calvo *et al.*, Nature **458**, 1150 (2009).

Quantum Phase Transitions in Two-Dimensional Electron Systems

Alexander Shashkin

Institute of Solid State Physics, Chernogolovka, Moscow District 142432, Russia

Sergey Kravchenko

*Physics Department, Northeastern University, Boston, Massachusetts 02115,
U.S.A.*

15.1 Strongly and Weakly Interacting 2D Electron Systems

Two-dimensional (2D) electron systems are realized when the electrons are free to move in a plane but their motion perpendicular to the plane is quantized in a confining potential well. Quantum phase transitions realized experimentally in such systems so far include metal-insulator transitions in perpendicular magnetic fields, metal-insulator transition in zero magnetic field, and a possible transition to a Wigner crystal. The first transition is governed by the externally controlled electron density or magnetic field, while the other two are governed by the electron density. At low electron densities in 2D systems, the strongly-interacting limit is reached because the kinetic energy is overwhelmed by the energy of electron-electron interactions. The interaction strength is characterized by the ratio between the Coulomb energy and the Fermi energy, $r_s^* = E_{ee}/E_F$. Assuming that the effective electron mass is equal to the band mass, the interaction parameter r_s^* in the single-valley case reduces to the Wigner-Seitz radius, $r_s = 1/(\pi n_s)^{1/2} a_B$, and therefore increases as the electron density, n_s , decreases (here a_B is the Bohr radius in the semiconductor). Possible candidates for the ground state of the system include a Wigner crystal characterized by spatial and spin ordering [1], a ferromagnetic Fermi liquid with spontaneous spin ordering [2], a paramagnetic Fermi liquid [3], etc. In the strongly-interacting limit ($r_s \gg 1$), no analytical theory has been developed to date. According to numerical simulations [4], Wigner

crystallization is expected in a very dilute regime, when r_s reaches approximately 35. Refined numerical simulations [5] have predicted that prior to the crystallization, in the range of the interaction parameter $25 \leq r_s \leq 35$, the ground state of the system is a strongly correlated ferromagnetic Fermi liquid. At higher electron densities, $r_s \sim 1$, the electron liquid is expected to be paramagnetic, with the effective mass, m , and Landé g factor renormalized by interactions. Apart from the ferromagnetic Fermi liquid, other intermediate phases between the Wigner crystal and the paramagnetic Fermi liquid may also exist.

In real 2D electron systems, the inherent disorder leads to a drastic change of the above picture, which significantly complicates the problem. According to the scaling theory of localization [6], all electrons in a disordered infinite noninteracting 2D system become localized at zero temperature and zero magnetic field. At finite temperatures, regimes of strong and weak localizations are distinguished: (i) if the conductivity of the 2D electron layer is activated, the resistivity diverges exponentially as $T \rightarrow 0$; and (ii) in the opposite limit of weak localization the resistivity increases logarithmically with decreasing temperature, an effect originating from the increased probability of electron backscattering from impurities to the starting point. Interestingly, the incorporation of weak interactions ($r_s < 1$) between the electrons promotes the localization [7]. However, for weak disorder and $r_s \geq 1$ a possible metallic ground state was predicted [8].

In view of the competition between the interactions and disorder, high- and low-disorder limits can be considered. In highly disordered electron systems, the range of low densities is not accessible as the strong (Anderson) localization sets in. This corresponds to the weakly-interacting limit in which an insulating ground state is expected. The case of low-disordered electron systems is much more interesting because low electron densities corresponding to the strongly-interacting limit become accessible. According to the renormalization group analysis for multi-valley 2D systems [9], strong electron-electron interactions can stabilize the metallic ground state, leading to the existence of a metal-insulator transition in zero magnetic field.

In quantizing magnetic fields, the interaction strength is characterized by the ratio between the Coulomb energy and the cyclotron splitting. In the ultra-quantum limit, it is similar to the interaction parameter r_s^* . Within the concept of single-parameter scaling for noninteracting 2D electrons [10], there is only one extended state in the Landau level, and the localization length diverges at the center of the Landau level [11]. For consistency with the scaling theory of localization in zero magnetic field, it was predicted that extended states in the Landau levels cannot disappear discontinuously with decreasing magnetic field but must “float up” (move up in energy) indefinitely in the limit [12] of $B \rightarrow 0$. The corresponding phase diagram plotted in disorder versus inverse filling factor ($1/\nu = eB/hcn_s$) plane is known as the global phase diagram for the quantum Hall effect (QHE) [13]. As long as no merging of the extended states was considered to occur, their piercing of the Fermi level was predicted

to cause quantization of the Hall conductivity in weak magnetic fields [14]. The case of strongly interacting 2D electrons in the quantum Hall regime has not been considered theoretically. In the very dilute regime, there are theoretical predictions that Wigner crystallization is promoted in the presence of a magnetic field (see, e.g., Ref. [15]).

In this chapter, attention is focused on experimental results obtained in low-disordered strongly interacting 2D electron systems, in particular, (100)-silicon metal-oxide-semiconductor field-effect transistors (MOSFETs). Due to the relatively large effective mass, relatively small dielectric constant, and the presence of two valleys in the spectrum, the interaction parameter in silicon MOSFETs is an order of magnitude bigger at the same electron density than in the 2D electron system in GaAs/AlGaAs heterostructures. Except at very low electron densities, the latter electron system can be considered weakly interacting. It is worth noting that the observed effects of strong electron-electron interactions are more pronounced in silicon MOSFETs compared to GaAs/AlGaAs heterostructures, although the fractional QHE, which is usually attributed to electron-electron interactions, has not been reliably established in silicon MOSFETs.

15.2 Proof of the Existence of Extended States in the Landau Levels

In a magnetically quantized 2D electron system, the Landau levels bend up at the sample edges due to the confining potential, and edge channels are formed where these intersect the Fermi energy (see, e.g., Ref. [16]). There arises a natural question as to whether the current in the quantum Hall state¹ flows in the bulk or at the edges of the sample. Although the Hall conductivity σ_{xy} was not directly measured in early experiments on the QHE, it seemed obvious that this value corresponds to the Hall resistivity ρ_{xy} , in agreement with the concept of currents that flow in the bulk [18]; it stands to reason that finite σ_{xy} would give evidence for the existence of extended states in the Landau levels [16, 19]. This concept was challenged by the edge current model [20]. In the latter approach extended states in the bulk are not crucial and the problem of current distributions in the QHE is reduced to a one-dimensional task in terms of transmission and reflection coefficients as defined by the backscattering current at the Fermi level between the edges. Importantly, if the edge current contributes significantly to the net current, conductivity/resistivity tensor inversion is not justified, because the conductivities σ_{xx} and σ_{xy} are related to the bulk of the 2D electron system. That is to say, a possible shunt-

¹In this state the Hall resistivity, $\rho_{xy} = h/\nu e^2$, is quantized at integer filling factor ν , accompanied by vanishing longitudinal resistivity, ρ_{xx} [17].

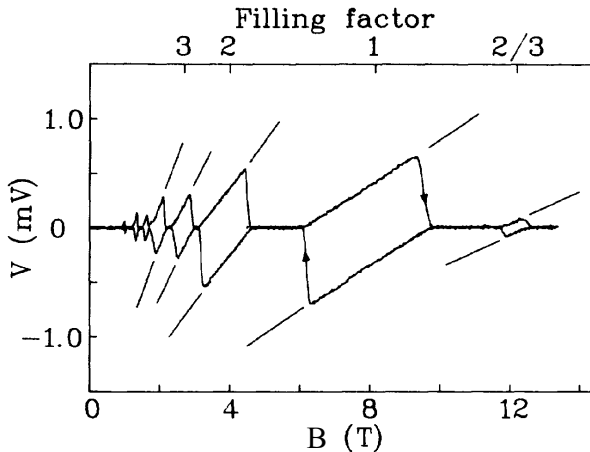


FIGURE 15.1

The induced voltage in a Corbino sample of a GaAs/AlGaAs heterostructure in up- and down-sweeps of the magnetic field. Also shown by straight lines are the expected slopes for $\nu = 2/3, 1, 2, 3$, and 4 . From Ref. [22].

ing effect of the edge currents in the Hall bar (rectangular) geometry makes it impossible to extract the value σ_{xy} from the magnetotransport data for ρ_{xx} and ρ_{xy} .

To verify whether or not the Hall conductivity is quantized, direct measurements of σ_{xy} are necessary, excluding the shunting effect of the edge currents. Being equivalent to Laughlin's *gedanken* experiment [21], such measurements were realized using the Corbino (ring) geometry which allows separation of the bulk contribution to the net current (see, e.g., Ref. [22]). A Hall charge transfer below the Fermi level between the borders of a Corbino sample is induced by a magnetic field sweep through the generated azimuthal electric field. If the dissipative conductivity $\sigma_{xx} \rightarrow 0$, no discharge occurs, allowing determination of the transferred charge, $Q = \sigma_{xy}\pi r_{\text{eff}}^2 c^{-1} \delta B$, where r_{eff} is the effective radius. The induced voltage, $V = Q/C$, which is restricted due to a large shunting capacitance, C , changes linearly with magnetic field with a slope determined by σ_{xy} in the quantum Hall states until the dissipationless quantum Hall state breaks down (Fig. 15.1). The fact that the quantization accuracy of σ_{xy} (about 1%) is worse compared to that of ρ_{xy} may be attributed to nonconstancy of the effective area in not very homogeneous samples. Thus, the Hall current in the QHE flows not only at the edges but also in the bulk of the 2D electron system through the extended states in the filled Landau levels.

The finite Hall conductivity measured in the Corbino geometry in the arrangement of Laughlin's *gedanken* experiment establishes the existence of

extended states in the Landau levels for both strongly and weakly interacting 2D electron systems. Note that the insignificance of edge-channel effects in transport experiments is verified in the usual way by coincidence of the results obtained in Hall bar and Corbino geometries.

15.3 Metal-Insulator Transitions in Perpendicular Magnetic Fields

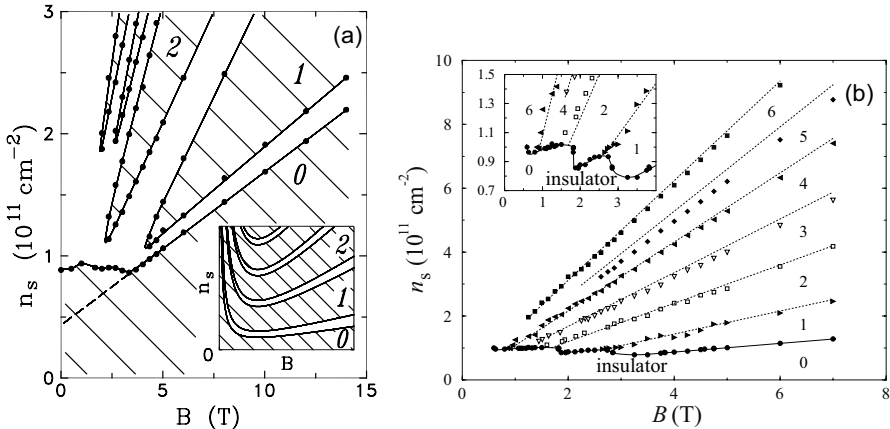
Metal-insulator transitions were studied for the quantum Hall phases and the insulating phase at low electron densities. The insulating phase was attributed to possible formation of a pinned Wigner crystal [23–25]. However, floating-up of the extended states relative to the Landau level centers and a close similarity of all insulating phases have been found experimentally [26–28]. Thus, the experimental results excluded the formation of a pinned Wigner crystal in available samples, but supported the existence of a metallic state in zero field. It was also found that the bandwidth of the extended states in the Landau levels is finite, which is in contradiction to scaling arguments. Strangely, the latter experimental result has not attracted much of theorists' attention.

15.3.1 Floating-Up of Extended States

The first experimental results on the metal-insulator phase diagram at low temperatures in low-disordered silicon MOSFETs [26] already revealed discrepancies with the theory (Fig. 15.2(a)). In that paper, a somewhat arbitrary criterion for the longitudinal conductivity, $\sigma_{xx} = e^2/20h$, was used to map out the phase boundary that corresponds to the Anderson transition to the regime of strong localization. However, first, the phase boundary was shown to be insensitive to the choice of the cutoff value (see, e.g., Ref. [29]). Second, that particular cutoff value is consistent with the results obtained for quantum Hall states by a vanishing activation energy combined with a vanishing nonlinearity of current-voltage characteristics when extrapolated from the insulating phase [27].² The metallic phase surrounds each insulating phase as characterized by the dimensionless Hall conductivity, $\sigma_{xy}h/e^2$, that counts the number of quantum levels below the Fermi level.³ This indicates that the extended states indeed do not disappear discontinuously. Instead, with decreasing magnetic field they float up in energy relative to the Landau level centers and merge forming a metallic state in the limit of $B = 0$ (for more

²Note that for the lowest-density phase boundary, a lower value $\sigma_{xx}^{-1} \approx 100$ kOhm at a temperature ≈ 25 mK follows from the latter method.

³In bivalley (100)-silicon MOSFETs, spin and valley degeneracies of the Landau level should be taken into account.

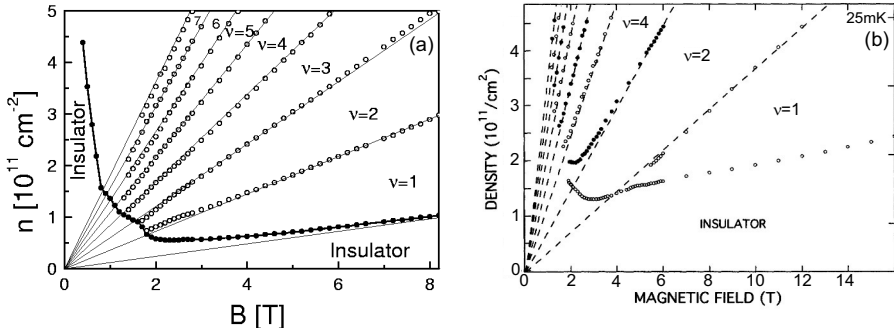
**FIGURE 15.2**

(a) Metal-insulator phase diagram in a low-disordered 2D electron system in silicon MOSFETs obtained using a cutoff criterion, $\sigma_{xx} = e^2/20h$, at a temperature ≈ 25 mK. The dimensionless $\sigma_{xy}h/e^2$ in different insulating phases is indicated. The slope of the dashed line is close to $e/2hc$. A sketch of the expected phase diagram is displayed in the inset. From Ref. [26]. (b) The map of extended states determined by maxima in σ_{xx} in a low-disordered silicon MOSFET. Numbers show σ_{xy} in units of e^2/h . From Ref. [30].

on this, see Sec. 15.4). This contradicts the theoretical scenario that in the limit of zero magnetic field the extended states should float up indefinitely in energy [12] leading to an insulating ground state. Besides, the experimental phase boundary at low electron densities oscillates as a function of B with minima corresponding to integer filling factors. The phase boundary oscillations manifest themselves in that the magnetoresistance at electron densities near the $B = 0$ metal-insulator transition oscillates with an amplitude that diverges as $T \rightarrow 0$ [24]. The regions in which the magnetoresistance diverges are referred to as the reentrant insulating phase.

The topology of the observed metal-insulator phase diagram⁴ is robust, being insensitive to the method for spotting the phase boundary [27, 30] and to the choice of 2D carrier system [31]. This robustness was verified using a criterion of vanishing activation energy and vanishing nonlinearity of current-voltage characteristics as extrapolated from the insulating phase, allowing more accurate determination of the Anderson transition [27]. A method that had been suggested in Ref. [32] was also applied for similar silicon MOSFETs [30]. The extended states were studied by tracing maxima in the longi-

⁴We refer here to merging of the extended states and, hence, the presence of direct transitions between the insulating phase with $\sigma_{xy} = 0$ and quantum Hall phases with $\sigma_{xy}h/e^2 > 1$.

**FIGURE 15.3**

(a) A map of the extended states for a highly disordered 2D hole system in a Ge/SiGe quantum well. The open circles represent maxima in ρ_{xx} and/or $d\rho_{xy}/dB$. The solid circles correspond to crossing points of ρ_{xx} at different temperatures. Numbers show the value of $\sigma_{xy}h/e^2$. Adapted from Ref. [31]. (b) Behavior of the extended states determined by maxima in σ_{xx} in a strongly disordered 2D electron system in GaAs/AlGaAs heterostructures. Numbers show σ_{xy} in units of e^2/h . Adapted from Ref. [32].

tudinal conductivity in the (B, n_s) plane (Fig. 15.2(b)) and good agreement with the aforementioned results was found. A similar merging of at least the two lowest extended states was observed in a more strongly disordered 2D hole system in a Ge/SiGe quantum well [31] (Fig. 15.3(a)). The extended states were associated either with maxima in ρ_{xx} and/or $d\rho_{xy}/dB$, or with crossing points of ρ_{xx} at different temperatures. It is noteworthy that a bad combination of the criterion for determining the phase boundary and the 2D carrier system under study may lead to a failure in mapping out the phase diagram down to relatively weak magnetic fields. In Ref. [32], extended states were studied by measuring maxima in the longitudinal conductivity in the (B, n_s) plane for the strongly disordered 2D electron system in GaAs/AlGaAs heterostructures (Fig. 15.3(b)). Because of strong damping of the Shubnikov-de Haas oscillations in low magnetic fields, the desired region on the phase diagram below 2 T was not accessible in that experiment. This invalidates the claim of Glozman *et al.* [32] that the extended states do not merge. The behavior of the lowest extended state in Fig. 15.3(b), which Glozman *et al.* [32] claim to float up above the Fermi level as $B \rightarrow 0$, simply reflects the occurrence of a phase boundary oscillation minimum at filling factor $\nu = 2$, similar to both the minimum at $\nu = 1$ in Fig. 15.3(a) and to the case of silicon MOSFETs (Fig. 15.2). Such a minimum manifests itself in that there exists a minimum in ρ_{xx} at integer $\nu \geq 1$ that is straddled by the insulating phase.

To this end, all available data for the metal-insulator phase diagrams agree well with each other, except those in the vicinity of $B = 0$. In weak magnetic fields, experimental results obtained in 2D electron systems with high disorder

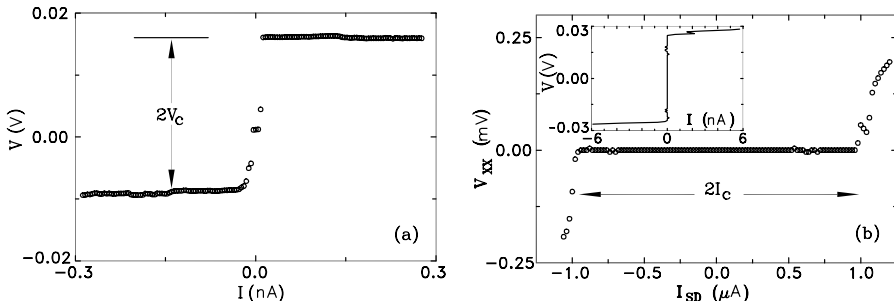
are not method-independent. Glazman *et al.* [32] found that the cutoff criterion yields basically a flat phase boundary towards $B = 0$, which is in agreement with the data for silicon MOSFETs ([Fig. 15.2\(a\)](#)). On the contrary, Hilke *et al.* [31] employed the method based on temperature dependencies of ρ_{xx} and obtained a turn up on the phase boundary in [Fig. 15.3\(a\)](#). Note that the validity of the data for the lowest extended state at magnetic fields ≤ 1.5 T in [Fig. 15.3\(a\)](#) is questionable because the weak temperature dependencies of ρ_{xx} as analyzed by Hilke *et al.* [31] cannot be related to either an insulator or a metal.

As a matter of fact, the weak-field problem, whether or not there is an indefinite rise of the phase boundary as $B \rightarrow 0$, is a problem of the existence of a metal-insulator transition at $B = 0$ and $T = 0$. In dilute 2D electron systems with low enough disorder, the resistivity, ρ , strongly drops with decreasing temperature [33, 34], providing an independent way of facing the issue. Given strong temperature dependencies of ρ , those with $d\rho/dT > 0$ ($d\rho/dT < 0$) can be associated with a metallic (insulating) phase [33, 34]. If extrapolation of the temperature dependencies of ρ to $T = 0$ is valid, the curve with $d\rho/dT = 0$ should correspond to the metal-insulator transition (see [Sec. 15.4](#)). As long as in more-disordered 2D carrier systems the metallic ($d\rho/dT > 0$) behavior is suppressed (see, e.g., Refs. [35, 36]) or disappears entirely, it is definitely incorrect to extrapolate those weak temperature dependencies of ρ to $T = 0$ with the aim to distinguish between insulator and metal.

Another point at which one can compare experiment and theory is the oscillating behavior of the phase boundary that restricts the insulating phase with $\sigma_{xy} = 0$ (see, e.g., [Fig. 15.2](#)). Note that the oscillations persist down to the magnetic fields corresponding to the fillings of more than one Landau level. The oscillation period includes the following stages. With decreasing magnetic field the lowest extended states follow the Landau level, float up in energy relative to its center, and merge with extended states in the next quantum level. No merging was present in the original theoretical considerations [12–14], leading to discrepancies between experiment and theory. Recently, theoretical efforts have been concentrated on modifications of the global phase diagram for the QHE to reach topological compatibility with the observed metal-insulator phase diagram. Although floating and/or merging of the extended states can be obtained in the calculations, the oscillations of the phase boundary at low electron densities have not yet been described theoretically.

15.3.2 Similarity of the Insulating Phase and Quantum Hall Phases

The insulating phase at low electron densities was considered to be a possible candidate for a pinned Wigner crystal. It was argued that its aforementioned reentrant behavior is a consequence of the competition between the QHE and the pinned Wigner crystal [24]. Another supporting argument was strongly nonlinear current-voltage characteristics in the insulating phase which were

**FIGURE 15.4**

Current-voltage characteristics in a low-disordered silicon MOSFET in $B = 12$ T at $T \approx 25$ mK for the low-density insulating phase at $n_s = 1.74 \times 10^{11}$ cm $^{-2}$ (a) and the insulating phase with $\sigma_{xy}h/e^2 = 1$ at $n_s = 2.83 \times 10^{11}$ cm $^{-2}$ (b). In (b) the measured breakdown dependence $V_{xx}(I_{sd})$ is converted into current-voltage characteristics (inset). From Ref. [27].

attributed to depinning of the Wigner crystal. Similar features of the insulating phase in a 2D electron (near $\nu = 1/5$) [23] and 2D hole (near $\nu = 1/3$) [25] systems in GaAs/AlGaAs heterostructures with relatively low disorder were also attributed to a pinned Wigner crystal which is interrupted by the fractional quantum Hall state. An alternative scenario was discussed in terms of percolation metal-insulator transition [29, 37, 38]. To distinguish between the two scenarios, the behavior of activation energy and current-voltage characteristics in the insulating phase was studied and compared to that in quantum Hall phases [27, 28].

In contrast to the low-density insulating phase, the way of determining the current-voltage characteristics of the quantum Hall phases is different for Corbino and Hall bar geometries. In the former the dissipationless Hall current does not contribute to the dissipative current that is proportional to σ_{xx} , allowing straightforward measurements of current-voltage curves for all insulating phases. In the latter the two current channels are connected through edge channels (see Sec. 15.2), and current-voltage characteristics correspond to quantum-Hall-effect breakdown curves. The dissipative backscattering current, I , that flows between opposite edge channels is balanced by the Hall current in the filled Landau levels associated with the longitudinal voltage, V_{xx} . As long as $\sigma_{xx} \ll \sigma_{xy}$, the quantized value of σ_{xy} is a factor that allows determination of $I = \sigma_{xy}V_{xx}$ and the Hall voltage, $V = I_{sd}/\sigma_{xy}$, from the experimental breakdown dependence of V_{xx} on source-drain current, I_{sd} . The dependence $V(I)$ is a current-voltage characteristic, which is equivalent to the case of Corbino geometry [27] (Fig. 15.4). Not only are the current-voltage curves similar for all insulating phases, but they also behave identically near the metal-insulator phase boundaries (Fig. 15.5(a)). The dependence of the critical voltage, V_c , on the distance from the phase boundary is close to a

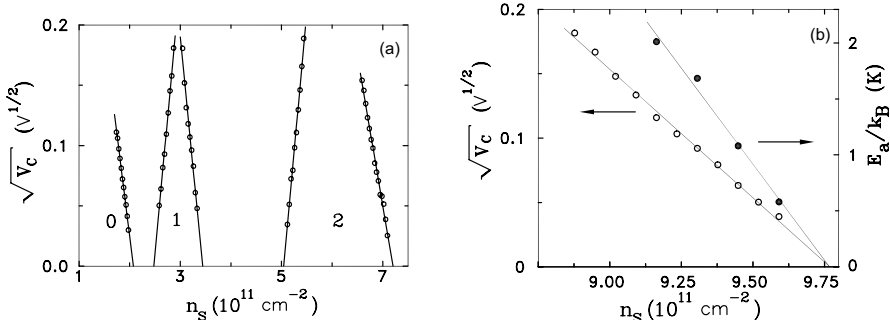
parabolic law [29]. The phase boundary position determined by a vanishing V_c is practically coincident with that determined by a vanishing activation energy, E_a , of electrons from the Fermi level E_F to the mobility edge, E_c ([Fig. 15.5\(b\)](#)). The value E_a is determined from the temperature dependence of the conduction in the linear interval of current-voltage curves, which is activated at not too low temperatures [39]; note that it transforms into variable range hopping as $T \rightarrow 0$ (see below). The activation energy changes linearly with the distance from the phase boundary, reflecting constancy of the thermodynamic density of states near the transition point (see also [Sec. 15.4](#)). The threshold behavior of the current-voltage characteristics is caused by the breakdown in the insulating phases. The breakdown occurs when the localized electrons at the Fermi level gain enough energy to reach the mobility edge in an electric field, V_c/d , over a distance given by the localization length, L [27, 40]:

$$eV_cL/d = |E_c - E_F|, \quad (15.1)$$

where d is the corresponding sample dimension. The values E_a and V_c are related through the localization length which is temperature independent and diverges near the transition as $L(E_F) \propto |E_c - E_F|^{-s}$ with exponent s close to unity, in agreement with the theoretical value $s = 4/3$ in the classical percolation problem [41]. The value of the localization length is practically the same near all metal-insulator phase boundaries, which indicates that even quantitatively, all insulating phases are very similar. Note that since the localization length in Eq. (15.1) is small compared to the sample sizes, the phase boundary position determined by the diverging localization length refers to an infinite 2D system. As inferred from the vanishing of both E_a and V_c at the same point (see [Fig. 15.5\(b\)](#)), possible shifts of the mobility threshold due to finite sample dimensions are small, which justifies extrapolations to the limit of $L \rightarrow \infty$.

The consequences of the method include the following. (i) As long as no dramatic changes occur in transport properties, this excludes the pinned Wigner solid as the origin for the insulating phase at low electron densities in available samples of low-disordered silicon MOSFETs. (ii) The metal-insulator phase diagram of [Fig. 15.2\(a\)](#) is verified and substantiated. (iii) The existence of a metal-insulator transition in zero magnetic field is supported (see [Sec. 15.4](#)). (iv) The bandwidth of the extended states in the Landau levels is finite. All of these are also valid for relatively low-disordered 2D carrier systems in GaAs/AlGaAs heterostructures with the distinction that fractional quantum Hall phases are involved. Yet, the topology of the phase diagram remains unchanged, including the oscillating behavior of the phase boundary that restricts the low-density insulating phase. Additional confirmation of the percolation transition to the low-density insulating phase in GaAs/AlGaAs heterostructures was obtained by studies of the high-frequency conductivity [42] and time-resolved photoluminescence of 2D electrons [43], as discussed in Ref. [28].

The insulating phase at low electron densities is special in what follows.

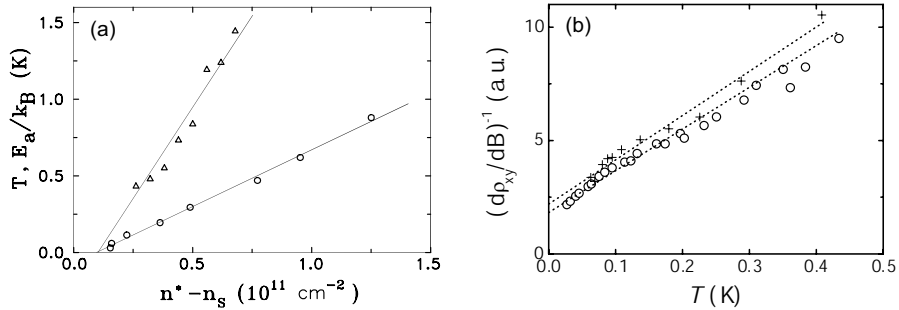
**FIGURE 15.5**

(a) Square root of the critical voltage as a function of electron density at the phase boundaries corresponding to $\sigma_{xy}h/e^2 = 0, 1$, and 2 in $B = 12$ T for a low-disordered 2D electron system in silicon MOSFETs. (b) Behavior of the critical voltage and the activation energy near the phase boundary in $B = 16$ T. From Ref. [27].

Deep in the insulating state and at low temperatures the variable-range-hopping regime occurs in which the conductivity σ_{xx} is small compared to its peak value [41]. In this regime it was predicted that the deviation, $\Delta\sigma_{xy}$, of σ_{xy} from its quantized value in strong magnetic fields is much smaller than $\sigma_{xx} \propto \exp(-(T_0/T)^{1/2})$ [44]: $\Delta\sigma_{xy} \propto \sigma_{xx}^\gamma$ with exponent $\gamma \approx 1.5$. A finite ρ_{xy} contrasted by diverging ρ_{xx} was found in calculations of the $T = 0$ magneto-transport coefficients in the insulating phase with vanishing σ_{xx} and σ_{xy} [45]. Such a behavior of ρ_{xx} and ρ_{xy} indicates a special quadratic relation between conductivities: $\sigma_{xy} \propto \sigma_{xx}^2$. Moreover, it was shown that ρ_{xy} is close to the classical value ($B/n_s e c$) [46], providing arguments for the existence of a Hall insulator phase [13]. Indeed, values ρ_{xy} close to $B/n_s e c$ were experimentally found in the low-density insulating phase. Thus, the distinction of the Hall insulator phase from the quantum Hall phases, i.e., the absence of extended states below the Fermi level, becomes evident when expressed in terms of ρ_{xx} and ρ_{xy} .

15.3.3 Scaling and Thermal Broadening

It was predicted that the localization length diverges as a power law at a single energy, E^* , which is the center of the Landau level [11]: $L(E) \propto |E - E^*|^{-s}$. An idea to check this prediction based on low-temperature measurements of σ_{xx} [47] was quickly developed to a concept of single-parameter scaling [10]. It was suggested that the magnetoresistance tensor components are functions of a single variable that is determined by the ratio of the dephasing length, $L_d(T) \propto T^{-p/2}$ (where p is the inelastic-scattering-time exponent), and the localization length. The concept was claimed to be confirmed by measure-

**FIGURE 15.6**

(a) Temperature dependence of the ρ_{xx} peak width ($n^* - n_s$) at half of the peak height counted from n^* corresponding to $\nu^* = 2.5$ (circles) and the behavior of the activation energy (triangles) in a low-disordered silicon MOSFET in $B = 14$ T. From Ref. [27]. (b) Temperature dependence of the ρ_{xx} peak width as determined by the maximum $d\rho_{xy}/dB$ at $\nu^* = 1.5$ in a highly disordered 2D electron system in GaAs/AlGaAs heterostructures. Different symbols correspond to different runs. The dashed lines are linear fits to the data. Adapted from Ref. [52].

ments of temperature dependencies of the peak width, ΔB , in ρ_{xx} (or σ_{xx}) and the maximum of $d\rho_{xy}/dB$ in a highly disordered 2D electron system in InGaAs/InP heterostructures, yielding $\Delta B \propto T^\kappa$, where $\kappa = p/2s \approx 0.4$ [48]. Later, both deviations in the power law and different exponents in the range between $\kappa = 0.15$ and $\kappa = 1$ were observed for other 2D carrier systems, different Landau levels, and different disorder strengths (see, e.g., Refs. [49–52]). Importantly, the scaling analysis of experimental data in question is based on two unverified assumptions: (i) zero bandwidth of the extended states in the Landau levels; and (ii) constancy of the thermodynamic density of states in the scaling range. If either assumption is not valid, this may lead, at least, to underestimating the experimental value of exponent κ .

The method of vanishing activation energy and vanishing nonlinearity of current-voltage characteristics as extrapolated from the insulating phase shows that the former assumption is not justified. Also, measurements of the peak width in ρ_{xx} as a function of temperature in low-disordered silicon MOSFETs yield a linear dependence which extrapolates to a finite peak width [27] as $T \rightarrow 0$ (Fig. 15.6(a)). Very similar temperature and frequency dependencies were observed in highly disordered 2D carrier systems in GaAs/AlGaAs heterostructures [53] and Ge/SiGe heterostructures [54]. It is noteworthy that a similar behavior is revealed if the data from the publications, which claim the observation of scaling, are plotted on a linear rather than logarithmic scale (see, e.g., Fig. 15.6(b)); finite values of the peak width as $T \rightarrow 0$ are even more conspicuous for the data of Refs. [49, 50, 55]. The reason for the ambiguity is quite simple: within experimental uncertainty, it is difficult, es-

pecially on a logarithmic scale, to distinguish between sublinear/superlinear fits to the data and linear fits which do not have to run through the origin. Note that attempts were made to relate the finite peak width as $T \rightarrow 0$ to the dephasing length reaching the sample size [50, 55]. However, the suggested finite-size effect is not supported by experimental data, because in different samples with different sizes, the disorder is also different. It is the disorder, rather than the sample size, that may be responsible for the behavior of the values measured in different samples.

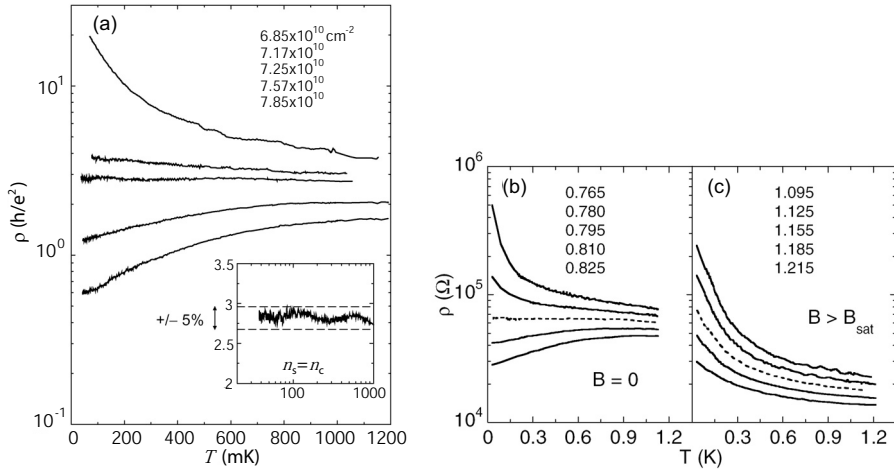
Although lack of data in most of the above experimental papers does not allow one to verify the validity of both assumptions, it is very likely that there is no qualitative difference between all of the discussed results. As a matter of fact, they can be described by a linear, or weakly sub-linear temperature dependence with a finite offset at $T = 0$. This is concurrent with the results obtained by vanishing activation energy and vanishing nonlinearity of current-voltage characteristics as extrapolated from the insulating phase. So, the single-parameter scaling is not confirmed by the experimental data which establish the finite bandwidth of the extended states in the Landau levels.

There is an alternative and simple explanation of the temperature dependence of the peak width in ρ_{xx} in terms of thermal broadening. Within a percolation picture, if the activation energy $E_a \sim k_B T$, the conduction is of the order of the maximum σ_{xx} so that the value of $\sim k_B T$ gives a thermal shift of the effective mobility edge corresponding to the σ_{xx} peak width [27]. Although the concept of thermal broadening has been basically ignored in the literature in the search for less trivial data interpretations, it looks as if no experimental results go beyond this, favoring the concept of single-parameter scaling. Once the behavior of the localization length is not reflected by the temperature-dependent peak width in ρ_{xx} , no experimental support is provided for numerical calculations of the localization length which give a somewhat larger exponent $s \approx 2$ compared to $s = 4/3$ in classical percolation problem (see, e.g., Ref. [56]).

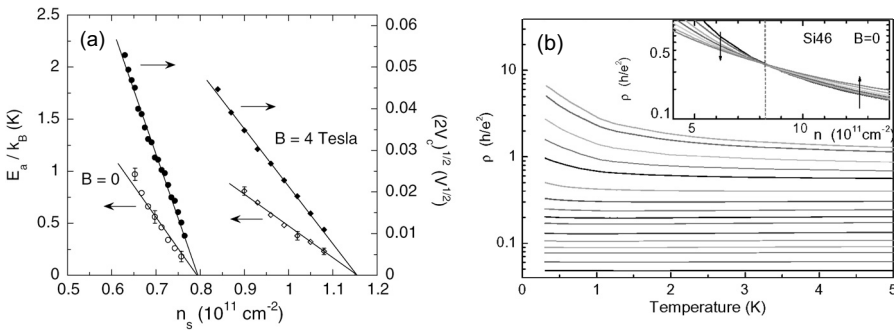
15.4 Zero-Field Metal-Insulator Transition

In contrast to the case of quantizing magnetic fields, no extended states are expected in zero magnetic field, at least for weakly-interacting 2D electron systems. The criterion of vanishing activation energy and vanishing nonlinearity of current-voltage characteristics as extrapolated from the insulating phase, however, results in an opposite conclusion. To sort out this inconsistency, further support by independent experimental verifications is needed.

Another criterion is based on the analysis of the temperature dependences of the resistivity at $B = 0$. Provided these are strong, those with positive (negative) derivative $d\rho/dT$ are indicative of a metal (insulator) [33, 34]; note

**FIGURE 15.7**

(a) Resistivity as a function of temperature at different electron densities in a low-disordered silicon MOSFET. The inset shows the middle curve on an expanded scale. From Ref. [57]. (b, c) Temperature dependence of the resistivity of a low-disordered silicon MOSFET at different electron densities near the metal-insulator transition, (b) in zero magnetic field and (c) in a parallel magnetic field of 4 T. The electron densities are indicated in units of 10^{11} cm^{-2} . From Ref. [58].

**FIGURE 15.8**

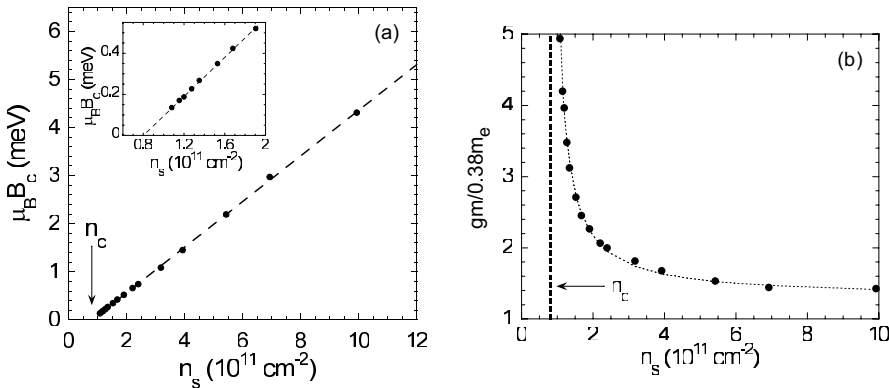
(a) Activation energy and square root of the threshold voltage as a function of electron density in zero magnetic field (circles) and in a parallel magnetic field of 4 T (diamonds) for the same silicon MOSFET as in Fig. 15.7(b, c). The critical densities correspond to the dashed lines in Fig. 15.7(b,c). From Ref. [58]. (b) Resistivity versus temperature in a strongly disordered silicon MOSFET at the following electron densities: $3.85, 4.13, 4.83, 5.53, 6.23, 7.63, 9.03, 10.4, 11.8, 13.2, 16.0, 18.8, 21.6, 24.4, 30.0$, and $37.0 \times 10^{11} \text{ cm}^{-2}$. The $\rho(n_s)$ isotherms are shown in the inset. Adapted from Ref. [36].

that in the vicinity of the transition, $\rho(T)$ dependencies obey the scaling law with exponent $\kappa \approx 1$, which is consistent with the concept of thermal broadening/shift by the value $\sim k_B T$ of the effective mobility edge in the insulating phase (see Sec. 15.3.3). If extrapolation of $\rho(T)$ to $T = 0$ is valid, the critical point for the metal-insulator transition is given by $d\rho/dT = 0$. In a low-disordered 2D electron system in silicon MOSFETs, the resistivity at a certain electron density shows virtually no temperature dependence over a wide range of temperatures [33,57] (Fig. 15.7(a)). This curve separates those with positive and negative $d\rho/dT$ nearly symmetrically at temperatures above 0.2 K [34]. Assuming that it remains flat down to $T = 0$, one obtains the critical point which corresponds to a resistivity $\rho \approx 3h/e^2$.

Recently, these two criteria have been applied simultaneously to the 2D metal-insulator transition in low-disordered silicon MOSFETs [58,59]. In zero magnetic field, both methods yield the same critical density n_c (Figs. 15.7(b) and 15.8(a)). Since one of the methods is temperature independent, this equivalence strongly supports the existence of a metal-insulator transition at $T = 0$ in $B = 0$. This also adds confidence that the curve with zero derivative $d\rho/dT$ will remain flat (or at least will retain finite resistivity value) down to zero temperature. Additional confirmation in favor of zero-temperature zero-field metal-insulator transition is provided by magnetic measurements [60], as described in the next section. It is argued that the metal-insulator transition in silicon samples with very low disorder potential is driven by interactions. This is qualitatively different from a localization-driven transition in more-disordered samples that occurs at appreciably higher densities.

For 2D electron systems both with high disorder in zero magnetic field (see Sec. 15.3.1) and in parallel magnetic fields, the metallic ($d\rho/dT > 0$) behavior is suppressed [35,36,58,61] or disappears entirely, and extrapolation of the weak $\rho(T)$ dependence to $T = 0$ is not justified, invalidating the derivative criterion for the critical point for the metal-insulator transition (Figs. 15.7(c) and 15.8(b)). Once one of the two methods fails, it remains to be seen how to verify the conclusion as inferred from the other method. This makes uncertain the existence of a zero-temperature metal-insulator transition in 2D electron systems both with high disorder in zero magnetic field and in parallel magnetic fields.

Owing to its simplicity, the derivative method is widely used for describing metallic ($d\rho/dT > 0$) and insulating ($d\rho/dT < 0$) temperature dependencies of resistance in a restricted temperature range. However, to avoid confusion with metallic and insulating phases, one should employ alternative methods for determining the metal-insulator transition point. Such methods, including a vanishing activation energy and noise measurements, have been applied to highly disordered 2D carrier systems [59,62]. Being similar, they yield lower critical densities n_c for the metal-insulator transition compared to those obtained using formally the derivative criterion. This simply reflects the fact that the metallic ($d\rho/dT > 0$) behavior is suppressed. The critical density n_c , at which the exponential divergence of the resistivity as $T \rightarrow 0$ ends,

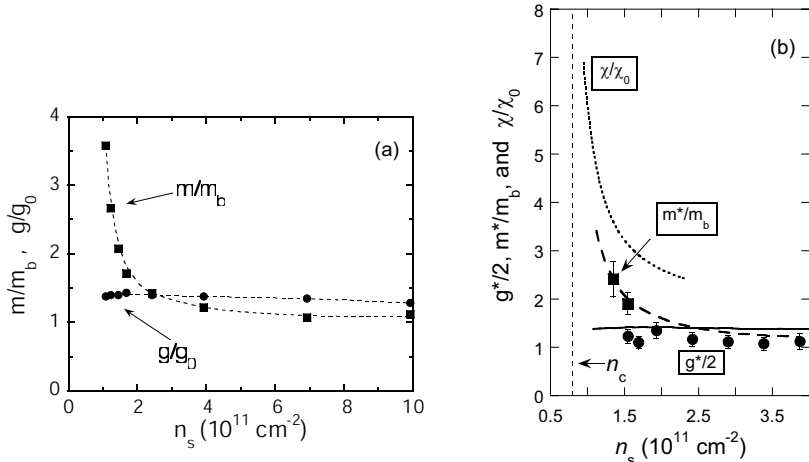
**FIGURE 15.9**

(a) Dependence of the polarization field on electron density, obtained by scaling the parallel-field magnetoresistance, in a low-disordered silicon MOSFET. The dashed line is a linear fit. The critical density n_c is indicated. (b) The product gm versus electron density obtained from the data for B_c . From Ref. [64].

increases naturally with disorder strength. It also increases somewhat with parallel magnetic field, saturating above a certain field, as was found in dilute silicon MOSFETs [38, 58].

15.5 Possible Ferromagnetic Transition

After a strongly enhanced ratio gm of the spin and the cyclotron splittings was found at low electron densities in silicon MOSFETs [63], it became clear that the system behavior was well beyond the weakly interacting Fermi liquid. It was reported that the parallel magnetic field required to produce complete spin polarization, $B_c \propto n_s/gm$, tends to vanish at a finite electron density $n_\chi \approx 8 \times 10^{10} \text{ cm}^{-2}$, which is close to the critical density n_c for the metal-insulator transition in this electron system [64] (Fig. 15.9). These findings point to a sharp increase of the spin susceptibility, $\chi \propto gm$, and possible ferromagnetic instability in dilute silicon MOSFETs. The fact that n_χ is close to the critical density n_c indicates that the metal-insulator transition in silicon samples with very low disorder potential is a property of a clean 2D system and is driven by interactions [64]. A similar although less pronounced behavior was observed in other 2D carrier systems [65]. The experimental results indicated that in silicon MOSFETs it is the effective mass, rather than the g factor, that sharply increases at low electron densities [66] (Fig. 15.10(a)). They also indicated

**FIGURE 15.10**

(a) The effective mass and g factor versus electron density determined from an analysis of the temperature-dependent conductivity and parallel-field magnetoresistance. The dashed lines are guides to the eye. From Ref. [66]. (b) The effective mass (squares) and g factor (circles), determined by magnetization measurements in perpendicular magnetic fields, as a function of the electron density. The solid and long-dashed lines represent, respectively, the g factor and effective mass, previously obtained from transport measurements [66], and the dotted line is the Pauli spin susceptibility obtained by magnetization measurements in parallel magnetic fields [70]. The critical density n_c for the metal-insulator transition is indicated. From Ref. [71].

that the anomalous rise of the resistivity with temperature is related to the increased mass. The magnitude of the mass does not depend on the degree of spin polarization, which points to a spin-independent origin of the effective mass enhancement [67]. It was found that the relative mass enhancement is system- and disorder-independent and is determined by electron-electron interactions only [68].

In addition to transport measurements, thermodynamic measurements of the magnetocapacitance and magnetization of a 2D electron system in low-disordered silicon MOSFETs were performed, and very similar results for the spin susceptibility, effective mass, and g factor were obtained [69–71] (Fig. 15.10(b)). The Pauli spin susceptibility behaves critically close to the critical density n_c for the $B = 0$ metal-insulator transition: $\chi \propto n_s/(n_s - n_c)$. This is in favor of the occurrence of a spontaneous spin polarization (either Wigner crystal or ferromagnetic liquid) at low n_s , although in currently available samples, the residual disorder conceals the origin of the low-density phase. The effective mass increases sharply with decreasing density while the enhancement of the g factor is weak and practically independent of n_s . Unlike

in the Stoner scenario, it is the effective mass that is responsible for the dramatically enhanced spin susceptibility at low electron densities.

Thus, the experimental results obtained in low-disordered silicon MOS-FETs indicate that on the metallic side the metal-insulator transition is driven by interactions, while on the insulating side this is still a classical percolation transition with no dramatic effects from interactions. One can consider the metal-insulator transition in the cleanest of currently available samples as a quantum phase transition, even though the problem of the competition between metal-insulator and ferromagnetic transitions is not yet resolved. It is not yet clear whether or not electron crystallization expected in the low-density limit is preceded by an intermediate phase like ferromagnetic liquid.

15.6 Outlook

Critical analysis of the available experimental data for 2D electron systems both in zero and in quantizing magnetic fields shows that consequences of the scaling theory of localization for noninteracting 2D electrons are not confirmed. The main points to be addressed by theory are the problem of finite bandwidth of the extended states in the Landau levels and that of a quantum phase transition in low-disordered 2D electron systems in zero magnetic field, including the competition between metal-insulator and ferromagnetic transitions. Recently, some progress has been made in describing the behavior of low-disordered strongly interacting 2D electron systems in zero magnetic field: it has been shown that the metallic ground state can be stabilized by electron-electron interactions [9]. It is possible that it may also be necessary to take into account electron-electron interactions to describe the quantum phase transitions that are characterized by the finite bandwidth of the extended states in the Landau levels.

The finding that in dilute 2D electron systems the spin susceptibility tends to diverge due to strong increase in the effective mass remains basically unexplained, and the particular mechanism leading to the effect remains to be seen. It is worth discussing the latest theoretical developments which are claimed to be valid for the strongly-interacting limit. According to the renormalization group analysis for multi-valley 2D systems, the effective mass dramatically increases at disorder-dependent density for the metal-insulator transition while the g factor remains nearly intact [9]. However, the prediction of disorder-dependent effective mass is in contradiction to the experiment. Besides, the results of Ref. [9] are valid only in the near vicinity of the metal-insulator transition, while the tendency of the spin susceptibility to diverge can be traced up to the densities exceeding n_c by a factor on the order of a few times unity. In the Fermi liquid-based model of Ref. [72], a flattening at the Fermi energy in the spectrum has been predicted that leads to a diverging effective mass.

Still, the expected dependence of the effective mass on temperature is not confirmed by the experimental data. The strong increase of the effective mass has been obtained, in the absence of the disorder, by solving an extended Hubbard model using dynamical mean-field theory [73]. This is consistent with the experiment, especially taking into account that the relative mass enhancement has been experimentally found to be independent of the level of the disorder. The dominant increase of m near the onset of Wigner crystallization follows also from an alternative description of the strongly-interacting electron system beyond the Fermi liquid approach (see, *e.g.*, Ref. [74]).

On the experimental side, progress in the fabrication of increasingly high mobility Si, Si/SiGe, and GaAs-based devices will open up the possibility of probing the intrinsic properties of clean 2D electron systems at still lower densities, where electron-electron interactions are yet stronger and, presumably, the previously observed behaviors will be yet more pronounced. Moreover, as high-mobility devices made with other semiconductors become available, further tests of the universality of the observed phenomena will add to our knowledge of 2D quantum phase transitions.

Bibliography

- [1] E. Wigner, Phys. Rev. **46**, 1002 (1934).
- [2] E. C. Stoner, Rep. Prog. Phys. **11**, 43 (1946).
- [3] L. D. Landau, Sov. Phys. JETP **3**, 920 (1957).
- [4] B. Tanatar and D. M. Ceperley, Phys. Rev. B **39**, 5005 (1989).
- [5] C. Attaccalite, S. Moroni, P. Gori-Giorgi, and G. B. Bachelet, Phys. Rev. Lett. **88**, 256601 (2002).
- [6] E. Abrahams, P. W. Anderson, D. C. Licciardello, and T. V. Ramakrishnan, Phys. Rev. Lett. **42**, 673 (1979).
- [7] B. L. Altshuler, A. G. Aronov, and P. A. Lee, Phys. Rev. Lett. **44**, 1288 (1980).
- [8] A. M. Finkelstein, Sov. Phys. JETP **57**, 97 (1983); Z. Phys. B **56**, 189 (1984); C. Castellani, C. Di Castro, P. A. Lee, and M. Ma, Phys. Rev. B **30**, 527 (1984).
- [9] A. Punnoose and A. M. Finkelstein, Science **310**, 289 (2005).
- [10] A. M. M. Pruisken, Phys. Rev. Lett. **61**, 1297 (1988).

- [11] S. V. Iordansky, Solid State Commun. **43**, 1 (1982); T. Ando, J. Phys. Soc. Jpn. **52**, 1740 (1983); H. Aoki, J. Phys. C **16**, 1893 (1983).
- [12] D. E. Khmelnitskii, Phys. Lett. A **106**, 182 (1984); R. B. Laughlin, Phys. Rev. Lett. **52**, 2304 (1984).
- [13] S. A. Kivelson, D. H. Lee, and S. C. Zhang, Phys. Rev. B **46**, 2223 (1992).
- [14] D. E. Khmelnitskii, Helv. Phys. Acta **65**, 164 (1992).
- [15] Y. E. Lozovik and V. I. Yudson, JETP Lett. **22**, 11 (1975).
- [16] B. I. Halperin, Phys. Rev. B **25**, 2185 (1982).
- [17] K. von Klitzing, G. Dorda, and M. Pepper, Phys. Rev. Lett. **45**, 494 (1980).
- [18] *The Quantum Hall Effect*, ed. by R. E. Prange and S. M. Girvin (Springer-Verlag, 1987).
- [19] H. Levine, S. B. Libby, and A. M. M. Pruisken, Phys. Rev. Lett. **51**, 1915 (1983).
- [20] M. Büttiker, Phys. Rev. B **38**, 9375 (1988).
- [21] R. B. Laughlin, Phys. Rev. B **23**, 5632 (1981); A. Widom and T. D. Clark, J. Phys. D **15**, L181 (1982).
- [22] V. T. Dolgopolov, A. A. Shashkin, N. B. Zhitenev, S. I. Dorozhkin, and K. von Klitzing, Phys. Rev. B **46**, 12560 (1992).
- [23] E. Y. Andrei, G. Deville, D. C. Glattli, F. I. B. Williams, E. Paris, and B. Etienne, Phys. Rev. Lett. **60**, 2765 (1988).
- [24] M. D'Iorio, V. M. Pudalov, and S. G. Semenchinsky, Phys. Lett. A **150**, 422 (1990).
- [25] M. B. Santos, Y. W. Suen, M. Shayegan, Y. P. Li, L. W. Engel, and D. C. Tsui, Phys. Rev. Lett. **68**, 1188 (1992).
- [26] A. A. Shashkin, G. V. Kravchenko, and V. T. Dolgopolov, JETP Lett. **58**, 220 (1993).
- [27] A. A. Shashkin, V. T. Dolgopolov, and G. V. Kravchenko, Phys. Rev. B **49**, 14486 (1994).
- [28] A. A. Shashkin, V. T. Dolgopolov, G. V. Kravchenko, M. Wendel, R. Schuster, J. P. Kotthaus, R. J. Haug, K. von Klitzing, K. Ploog, H. Nickel, and W. Schlapp, Phys. Rev. Lett. **73**, 3141 (1994).

- [29] V. T. Dolgopolov, G. V. Kravchenko, A. A. Shashkin, and S. V. Kravchenko, Phys. Rev. B **46**, 13303 (1992).
- [30] S. V. Kravchenko, W. Mason, J. E. Furneaux, and V. M. Pudalov, Phys. Rev. Lett. **75**, 910 (1995).
- [31] M. Hilke, D. Shahar, S. H. Song, D. C. Tsui, and Y. H. Xie, Phys. Rev. B **62**, 6940 (2000).
- [32] I. Glozman, C. E. Johnson, and H. W. Jiang, Phys. Rev. Lett. **74**, 594 (1995).
- [33] M. P. Sarachik and S. V. Kravchenko, Proc. Natl. Acad. Sci. USA **96**, 5900 (1999).
- [34] E. Abrahams, S. V. Kravchenko, and M. P. Sarachik, Rev. Mod. Phys. **73**, 251 (2001); S. V. Kravchenko and M. P. Sarachik, Rep. Prog. Phys. **67**, 1 (2004).
- [35] Y. Hanein, U. Meirav, D. Shahar, C. C. Li, D. C. Tsui, and H. Shtrikman, Phys. Rev. Lett. **80**, 1288 (1998); M. Y. Simmons, A. R. Hamilton, M. Pepper, E. H. Linfield, P. D. Rose, D. A. Ritchie, A. K. Savchenko, and T. G. Griffiths, Phys. Rev. Lett. **80**, 1292 (1998).
- [36] V. M. Pudalov, G. Brunthaler, A. Prinz, and G. Bauer, cond-mat/0103087.
- [37] V. T. Dolgopolov, G. V. Kravchenko, and A. A. Shashkin, JETP Lett. **55**, 140 (1992).
- [38] V. T. Dolgopolov, G. V. Kravchenko, A. A. Shashkin, and S. V. Kravchenko, JETP Lett. **55**, 733 (1992).
- [39] C. J. Adkins, S. Pollitt, and M. Pepper, J. Phys. C **37**, 343 (1976).
- [40] D. G. Polyakov and B. I. Shklovskii, Phys. Rev. B **48**, 11167 (1993).
- [41] B. I. Shklovskii and A. L. Efros, *Electronic Properties of Doped Semiconductors* (Springer, New York, 1984).
- [42] Y. P. Li, PhD thesis, Princeton University, 1994.
- [43] I. V. Kukushkin and V. B. Timofeev, Sov. Phys. Usp. **36**, 549 (1993).
- [44] K. I. Wysokinski and W. Brenig, Z. Phys. B **54**, 11 (1983).
- [45] O. Viehweger and K. B. Efetov, J. Phys. Condens. Matter **2**, 7049 (1990).

- [46] S. C. Zhang, S. Kivelson, and D. H. Lee, Phys. Rev. Lett. **69**, 1252 (1992).
- [47] H. Aoki and T. Ando, Phys. Rev. Lett. **54**, 831 (1985).
- [48] H. P. Wei, D. C. Tsui, M. A. Paalanen, and A. M. M. Pruisken, Phys. Rev. Lett. **61**, 1294 (1988).
- [49] V. T. Dolgopolov, A. A. Shashkin, B. K. Medvedev, and V. G. Mokerov, Sov. Phys. JETP **72**, 113 (1991).
- [50] S. Koch, R. J. Haug, K. von Klitzing, and K. Ploog, Phys. Rev. Lett. **67**, 883 (1991).
- [51] J. Wakabayashi, M. Yamane, and S. Kawaji, J. Phys. Soc. Jpn. **58**, 1903 (1989); T. Wang, K. P. Clark, G. F. Spencer, A. M. Mack, and W. P. Kirk, Phys. Rev. Lett. **72**, 709 (1994).
- [52] H. P. Wei, S. Y. Lin, D. C. Tsui, and A. M. M. Pruisken, Phys. Rev. B **45**, 3926 (1992).
- [53] N. Q. Balaban, U. Meirav, and I. Bar-Joseph, Phys. Rev. Lett. **81**, 4967 (1998); D. Shahar, M. Hillke, C. C. Li, D. C. Tsui, S. L. Sondhi, J. E. Cunningham, and M. Razeghi, Solid State Commun. **107**, 19 (1998).
- [54] M. Hillke, D. Shahar, S. H. Song, D. C. Tsui, Y. H. Xie, and D. Monroe, Phys. Rev. B **56**, R15545 (1997).
- [55] W. Li, C. L. Vicente, J. S. Xia, W. Pan, D. C. Tsui, L. N. Pfeiffer, and K. W. West, Phys. Rev. Lett. **102**, 216801 (2009).
- [56] B. Huckestein, Rev. Mod. Phys. **67**, 357 (1995).
- [57] S. V. Kravchenko and T. M. Klapwijk, Phys. Rev. Lett. **84**, 2909 (2000).
- [58] A. A. Shashkin, S. V. Kravchenko, and T. M. Klapwijk, Phys. Rev. Lett. **87**, 266402 (2001).
- [59] J. Jaroszyński, D. Popović, and T. M. Klapwijk, Phys. Rev. Lett. **89**, 276401 (2002).
- [60] A. A. Shashkin, Phys. Usp. **48**, 129 (2005).
- [61] A. A. Shashkin, E. V. Deviatov, V. T. Dolgopolov, A. A. Kapustin, S. Anissimova, A. Venkatesan, S. V. Kravchenko, and T. M. Klapwijk, Phys. Rev. B **73**, 115420 (2006).
- [62] S. Bogdanovich and D. Popović, Phys. Rev. Lett. **88**, 236401 (2002); R. Leturcq, D. L'Hote, R. Tourbot, C. J. Mellor, and M. Henini, Phys. Rev. Lett. **90**, 076402 (2003).

- [63] S. V. Kravchenko, A. A. Shashkin, D. A. Bloore, and T. M. Klapwijk, Solid State Commun. **116**, 495 (2000).
- [64] A. A. Shashkin, S. V. Kravchenko, V. T. Dolgopolov, and T. M. Klapwijk, Phys. Rev. Lett. **87**, 086801 (2001).
- [65] X. P. A. Gao, A. P. Mills Jr., A. P. Ramirez, L. N. Pfeiffer, and K. W. West, Phys. Rev. Lett. **89**, 016801 (2002); J. Zhu, H. L. Stormer, L. N. Pfeiffer, K. W. Baldwin, and K. W. West, Phys. Rev. Lett. **90**, 056805 (2003); T. Okamoto, M. Ooya, K. Hosoya, and S. Kawaji, Phys. Rev. B **69**, 041202 (2004).
- [66] A. A. Shashkin, S. V. Kravchenko, V. T. Dolgopolov, and T. M. Klapwijk, Phys. Rev. B **66**, 073303 (2002).
- [67] A. A. Shashkin, M. Rahimi, S. Anissimova, S. V. Kravchenko, V. T. Dolgopolov, and T. M. Klapwijk, Phys. Rev. Lett. **91**, 046403 (2003).
- [68] A. A. Shashkin, A. A. Kapustin, E. V. Deviatov, V. T. Dolgopolov, and Z. D. Kvon, Phys. Rev. B **76**, 241302(R) (2007).
- [69] V. S. Khrapai, A. A. Shashkin, and V. T. Dolgopolov, Phys. Rev. Lett. **91**, 126404 (2003).
- [70] A. A. Shashkin, S. Anissimova, M. R. Sakr, S. V. Kravchenko, V. T. Dolgopolov, and T. M. Klapwijk, Phys. Rev. Lett. **96**, 036403 (2006).
- [71] S. Anissimova, A. Venkatesan, A. A. Shashkin, M. R. Sakr, S. V. Kravchenko, and T. M. Klapwijk, Phys. Rev. Lett. **96**, 046409 (2006).
- [72] V. A. Khodel, J. W. Clark, and M. V. Zverev, Europhys. Lett. **72**, 256 (2005).
- [73] S. Pankov and V. Dobrosavljević, Phys. Rev. B **77**, 085104 (2008).
- [74] B. Spivak and S. A. Kivelson, Phys. Rev. B **70**, 155114 (2004).

16

Local Observables for Quantum Phase Transitions in Strongly Correlated Systems

Eun-Ah Kim

Department of Physics, Cornell University, Ithaca, NY 14853, U.S.A.

Michael J. Lawler

Department of Physics, Applied Physics and Astronomy, The State University of New York at Binghamton, Binghamton, NY 13902, U.S.A.

Department of Physics, Cornell University, Ithaca, NY 14853, U.S.A.

J.C. Davis

Department of Physics, Cornell University, Ithaca, NY 14853, U.S.A.

Condensed Matter Physics and Materials Science Department, Brookhaven National Laboratory, Upton, NY 11973, U.S.A.

School of Physics and Astronomy, University of St. Andrews, North Haugh, St. Andrews, Fife KY16 9SS, Scotland

This chapter is a progress report on the challenging yet promising frontier of quantum phase transitions (QPTs) in strongly correlated systems from the perspective of modern local probes and recent theoretical developments. The focus will be on our latest developments at this frontier. An outlook based on opportunities and questions emerging from these latest developments concludes the discussion.

Let us first state what we mean by strongly correlated systems: systems in the intermediate regime. A natural consequence of being in the intermediate regime is the close competition between multiple instabilities. Hence it is natural to anticipate QPTs in strongly correlated systems; the study of strongly correlated systems cannot be disentangled from the study of QPTs.

Since the seminal study of two-dimensional quantum antiferromagnets by Chakravarty, Halperin and Nelson [1], theorists have been anticipating various quantum critical points (QCPs) and experimentalists have been gleaning hints in favor of, or against QCPs in strongly correlated systems. However, to date, a successful marriage between experiment and theory is rare except for the cases of insulating frustrated spin systems. Experimentally, the challenge is in identifying both smoking-gun evidence of a change of symmetry near $T = 0$

as a function of a tuning parameter, and evidence for a continuous phase transition. Theoretically, the challenge is in identifying the relevant degrees of freedom involved, and trying to adapt the traditional theoretical tools and concepts to heterogeneous systems without a clean separation of scales. These challenges have resulted in a multitude of proposals that have revealed the richness in the phase space of possibilities.

Our strategy is to make progress by studying strongly correlated systems with putative QPTs in a manner that integrates theory and experiment from the outset. On the one hand, we will build on existing experiments to restrict the phase space of possibilities; on the other hand, we will also take advantage of the frontier technology of local probe spectroscopy. This approach requires developing new theoretical concepts and measures that can extract the relevant information. The resulting information should lead to concrete progress, when properly translated into the language of the established framework of quantum criticality theory.

16.1 Why Use Local Probes?

Conventional wisdom on QPTs evolved around thermodynamic quantities such as magnetic susceptibility and specific heat or transport coefficients. Scaling in such bulk properties allows one to discuss quantum criticality as an extension of classical finite temperature criticality. However, we argue for the need of a new perspective on QPTs in strongly correlated systems which incorporates insights local probes can offer in the following aspects.

16.1.1 Nanoscale Heterogeneity

By now it has been well established that heterogeneity at the nano-scale is common among strongly correlated systems. Clearly quenched disorder plays an important role in this observation. However, analytic studies and numerical simulations of models of ideal strongly correlated systems in the absence of quenched disorder have been discovering an interaction-driven tendency towards heterogeneity through electronic phase separation. This has been especially evident in models of underdoped Mott insulators. Hence, it is most likely the observed nano-scale heterogeneity is a consequence of the complex interplay between quenched disorder and correlation effects. Whether nano-scale inhomogeneities are nucleated by quenched disorder or driven by phase separation, they will hinder long range order.

When facing this nano-scale heterogeneity, detection of even a local remnant of ordering can offer critical insight into the physics of strongly correlated systems. Clearly the absence of long range order presents a challenge in the experimental identification of the dominant local ordering tendencies among

competing possibilities. For such a task, local probes are invaluable. Indeed, nuclear magnetic resonance (NMR) or muon spin resonance (μ SR) have offered indispensable insights into the local tendency of magnetism and its interplay with superconductivity in systems such as the cuprates and ruthenates. Scanning probes can further correlate local remnants of order to the local environment and map out spatial distribution of local ordering tendencies. Scanning probes are particularly ideal when special symmetry breaking is suspected.

16.1.2 Quenched Impurity as a Tool

Modern developments in material science have enabled a great deal of control over the location and type of quenched impurities in some strongly correlated systems. Even when the location is not controllable as for the case of oxygen dopant impurities in $\text{Bi}_2\text{Sr}_2\text{CaCu}_2\text{O}_{8+\delta}$ (BSCCO) [2] much understanding regarding their location and distribution is now available. Such overall progress in dealing with quenched disorder puts us in a position to take an active role against quenched disorder, i.e., to use quenched disorder as a tool.

Local probes are ideal for turning dilute impurities into tools. This approach can be especially useful for exploring the interplay between the interaction-energy-driven locality and the kinetic-energy- or quantum-fluctuation-driven itineracy. A good example of using intentionally placed impurities is the Zn and Ni impurity bound-state studies, which provided key insights into the superconducting gap symmetry of cuprates. Another example of using impurities as a tool is quasi-particle-interference (QPI) studies of the Fourier transform of spectroscopic imaging scanning tunneling microscopy (SI-STM) images taken in the presence of dilute impurities. QPI offers a valuable connection between the real space information ideal for the local limit and the momentum space information ideal for the itinerant limit; increasing applicability of this tool has been demonstrated [3].

16.1.3 Interplay between Inhomogeneity and Dynamics

Dynamical information is crucial for constructing a theory of quantum criticality. In homogeneous systems, we expect low-energy dynamics in the vicinity of a QCP for a continuous QPT to be non-local in space as there is no scale to set apart short-distance from long-distance in the the critical regime. Furthermore, we expect no energy scale other than critical temperature or an energy gap, which are proportional to a specific power of the distance away from the QCP in the tuning-parameter axis.

Heterogeneity introduces two key questions to a system proximate to a putative QCP. One question is the impact of quenched disorder or heterogeneity on the QCP: whether or not the QCP would be washed out all together. For instance, in the language of classical Ising criticality, a random field would wash out a QCP by locally introducing an external field. On the other hand, randomness in local T_c may or may not wash out a QCP depending on the

spatial dimension of the system and the order parameter exponent. Another question is the impact of heterogeneity on the phase. Spatial heterogeneity can introduce a new characteristic energy scale. In this case, the heterogeneity may be invisible in the dynamical information at energies below this characteristic energy scale.

If a scanning local probe can couple to the order parameter associated with a putative QPT we may gain clues about the interplay between heterogeneity and dynamics. In fact, SI-STM experiments on superconducting BSCCO and other strongly correlated systems have already demonstrated differing degrees of heterogeneity as a function of probing energy and hole density. However, relevant local order parameters suited to local observables in such experiments have not been fully established. We discuss recent progress on this front in Sec. 16.4.

16.1.4 Guidance for Suitable Microscopic Models

A key theoretical challenge in studying QPTs in strongly correlated systems lies in defining a minimalistic microscopic model suitable for the ordering associated with the QPT. An ideal microscopic model will represent an optimal balance between the details at the level of quantum chemistry and universal aspects of low-energy physics. In practice, such negotiation between complexity and simplicity is a challenging task, especially for systems in the intermediate regime. At the same time, we can only anticipate progress when the community effort is directed towards a suitable minimal microscopic model.

Local probes can guide the negotiation between complexity and simplicity by revealing local degrees of freedom that are active at different energy scales and different regimes of the phase diagram. For instance, recent STM studies [4] indicate the importance of oxygen in the CuO₂ plane, possibly challenging whether the Hubbard model has a sufficient degree of complexity.

16.2 What are the Challenges?

Quantifying broken symmetry associated with any phase transition is most straightforward when a bulk probe couples directly to the order parameter. Even when ordering involves a modulation with a finite wave vector as in an anti-ferromagnet and various density wave states, such broken symmetry is evident from additional elastic peaks in diffraction experiments. However, in order to use local probes to study QPTs in inhomogeneous strongly correlated systems, we need relevant local measures for local forms of broken symmetry. This is both an experimental and a theoretical challenge.

Since the establishment of the concept of spontaneous symmetry breaking, we have perfected bulk measurements using probes that couple directly to the

order parameter. At the same time we have developed theoretical formalisms best suited to aid the connection between bulk measurements and the physics of symmetry breaking and phase transitions. However, such conventional theoretical formalisms of QPTs assume homogeneity.

We now need local measures that can connect insights from local probes to the theory of QPTs. This is a particular challenge for scanning local probes. Space-averaging local probes such as μ SR and NMR report statistical information about spatially varying local environments whose interpretation can be aided by tools of statistical analysis. However, atomic precision scanning probes provide extensive information at each position of the sample, allowing for a more direct study of spatial variations of local measurements.

In order to define local forms of ordering, we need observables that can coarse-grain atomic scale information into intermediate length scale information defining the spatial extent of ordered regions. One should not underestimate the value of high resolution. High resolution could be necessary to reveal patterns of broken symmetry. However, a proper coarse-graining scheme will allow us to define a region with a particular broken symmetry.

It would be ideal if local measures used for identifying broken symmetry from scanning local probes offered a natural connection with bulk measures, especially diffraction, measurements. Until now, attempts at connecting bulk, especially diffraction measurements and scanning-local-probe measurements have been infrequent. This is mostly due to experimental constraints: systems that have good cleaving properties tend to not yield large single crystals. However, with experimental developments in understanding surfaces and preparing samples, we are getting closer to overcoming the technical challenges of this connection. What is needed are proposals of observables that can do the job. In the next section we discuss recent progress in such proposals.

16.3 Searching for Quantum Phase Transitions Using STM

The SI-STM can be an effective tool for tracking local forms of broken symmetry as a function of a tuning parameter such as chemical doping or magnetic field at low temperatures. This is especially the case for cuprates, where all energy scales are typically much higher than typical operational temperatures of atomic precision STM ($\sim 4K$); we hope to effectively produce zero temperature phase diagrams, and, in doing so, reveal the position of QCPs themselves. Moreover, millikelvin scanned probe systems are now coming online.

In the remainder of this chapter we discuss BSCCO, as a concrete example where STM can contribute to the study of QPTs in strongly correlated systems. Much discussion of quantum criticality in the context of cuprate physics had been motivated by various normal state observations near the doping

range where the superconducting T_c is maximal (optimal doping). The linear temperature dependence of the normal state resistivity [5, 6] in this *strange metal regime* was attributed to quantum criticality early on. While this and other normal-state observations invite the notion of a QCP inside the superconductor near optimal doping, signatures of quantum criticality inside the superconducting phase have not been conclusively identified. This is because a suitable probe of a broken symmetry and criticality inside the superconducting phase is rare. Recent developments indicate [7] that local broken-symmetry patterns observed via SI-STM [4] are consistent with electronic nematic ordering. This development offers a concrete measure to study the possibility of an associated QPT.

In the remainder of this section we will discuss recent progress regarding establishing the existence of an electronic nematic phase in the cuprates, a translationally invariant phase that breaks discrete rotational symmetry.

16.3.1 STM Hints towards Quantum Phase Transitions

The accomplishment of atomic scale resolution has led to observations of local patterns that break spatial symmetry in underdoped-cuprate high T_c superconductors.¹ While early observations of a locally broken symmetry in slightly overdoped $\text{Bi}_2\text{Sr}_2\text{CaCu}_2\text{O}_{8+\delta}$ (Bi-2212) near the halo of vortices at energies of the order of, or greater than, the local gap (see Fig. 16.3.1(a-b)) indicated these glassy patterns could be related to the nature of the mysterious normal state from which superconductivity develops upon cooling, at the same time they raised several key questions. (1) Are the effects an intrinsic element of hole-doped CuO_2 electronic structure? (2) What are the microscopic implications of this local tendency towards broken symmetry? (3) How do these tendencies evolve as a function of tuning parameters such as doping, magnetic field, and temperature? (4) Is there a way to quantify an observed local tendency of broken symmetry? This last question is particularly important from the perspective of using scanning local probes such as STM to study QPTs in strongly correlated systems. Ultimately, in order to build an experimentally grounded theoretical understanding of possible QPTs associated with these local ordering tendencies, we need to be able to objectively quantify them.

A hint towards an answer to question (1) was provided by a systematic comparative study of two radically different cuprates: strongly underdoped Na-CCOC ($\text{Ca}_{1.88}\text{Na}_{0.12}\text{CuO}_2\text{Cl}_2$; critical temperature $T_c = 21$ K) and Dy-Bi2212 ($\text{Bi}_2\text{Sr}_2\text{Dy}_{0.2}\text{Ca}_{0.8}\text{Cu}_2\text{O}_{8+d}$; $T_c = 45$ K) [4] (see Fig. 16.3.1(c-d)). Despite their distinct crystallographic structures in all respects except for the existence of CuO_2 planes, both showed the same intense spatial variations in the tunneling asymmetry of spectra at higher energies, strongly suggesting that the locally broken spatial symmetries are intrinsic elements of hole-doped CuO_2 . The loss of both translational and 90°-rotational (C_4) symmetry in the

¹The electronic structure locally breaks a point group symmetry of the underlying lattice.

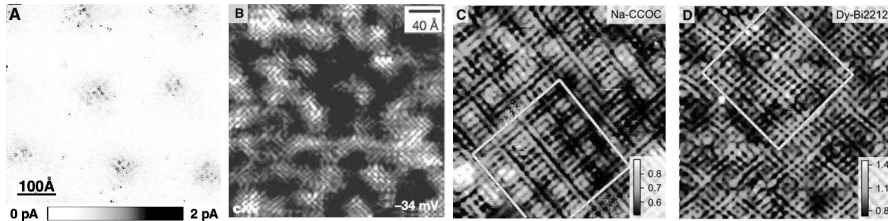


FIGURE 16.1

Patterns of locally broken spatial symmetry observed in atomic scale STS over time (a) in halos of vortices [8] and (b-d) in the high energy regime [4, 9]. (a) Integrated LDOS; (b) LDOS in hole-doped BSCCO; (c)-(d) tunneling asymmetry in Na-CCOC and in Dy-Bi2212.

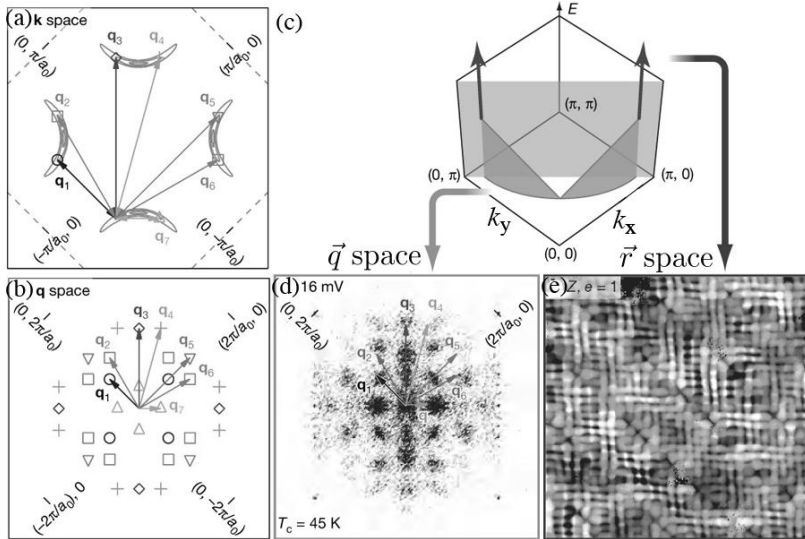
spatial arrangements of electronic structure at the $4a$ scale, where a is the Cu-Cu distance, is virtually indistinguishable in Na-CCOC and Dy-Bi2212. Both systems exhibited $4a$ -wide unidirectional domains extending along one or the other Cu-O direction. Thus, at the nm scale, the electronic structure of these lightly hole-doped cuprates breaks both C_4 symmetry and translational symmetry of the ideal square crystal lattice.

Ref. [4] further revealed important clues to question (2) by demonstrating that spatial variations in tunneling asymmetry occur primarily at the planar oxygen sites at high energies. The spatial arrangement of tunneling asymmetry turned out to form a Cu-O-Cu bond-centered electronic pattern. Within a given domain, O sites in two Cu-O-Cu bonds related to each other by a 90° rotation are electronically inequivalent even though they are crystallographically equivalent. These observations highlighted the role of oxygen atoms as a key ingredient in the observed local symmetry-breaking tendencies.

Questions (3) and (4) are ultimate challenges for establishing $T - g$ phase diagrams based on scanning-local-probe experiments, where g stands for a generic tuning parameter controlling the degree of quantum fluctuations and therefore the QPT. Clearly, traversing the phase space in a controlled manner will require tremendous experimental effort. However, even with such an effort, it will not be possible to establish a phase diagram that can guide a search for and understanding of QPTs without a quantitative measure to base the phase boundary upon.

Below we review experimental progress in traversing the phase diagram. There has been progress in STM studies in tracking qualitative systematic trends in local electronic structure as a function of doping and temperature. One study [10] found a systematic dependence of the quasi-particle dispersion upon doping, extracted from quasi-particle interference.

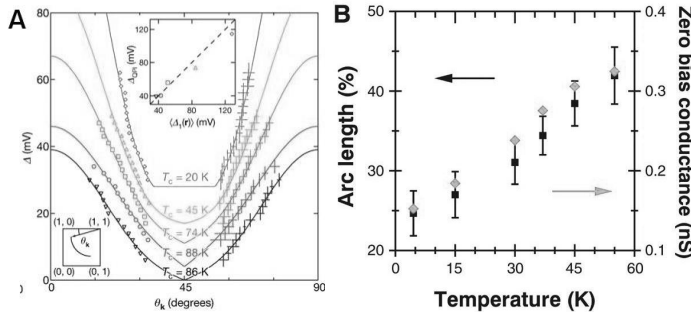
Another study found a crossover in the simultaneous position \vec{r} -space and momentum \vec{k} -space features as a function of excitation energy [4]. In this study, a qualitative change was observed in the electronic structure of under-

**FIGURE 16.2**

Crossover between extended and local excitations. Figures reproduced with permission [10].

doped Bi-2212 ($T_c = 45$ K) at a particular energy scale Δ_0 . For $\omega < \Delta_0$ the SI-STM yields images which are homogeneous and featureless in \vec{r} -space while it shows peaks that disperse with energy in the Fourier (\vec{q}) space (Fig. 16.2(d)). The manner in which \vec{q} -space peaks disperse in this regime of energy E is consistent with the existence of well-defined Bogoliubov quasi-particles at the tips of the equal-energy contour in momentum space [9, 11], i.e., quasi-particle momenta \vec{k} with $E_{\vec{k}} = E$. Figures 16.2a and 16.2b illustrate the connection between \vec{q} -space peaks and the inferred distribution of Bogoliubov quasi-particles with momentum \vec{k} . The distribution of quasi-particle momenta obtained from this QPI is largely that of a d -wave superconductor, except that \vec{k} points are missing over an arc-shaped region centered at nodal points [10] (See Fig. 16.3(a)).

On the other hand, for $\omega > \Delta_0$ SI-STM measurements develop patterns in \vec{r} -space that locally break the point-group symmetry of the underlying crystal (see Fig. 16.2(e)). At the same time, most Fourier peaks diminish and two remaining sets of broad peak locations become energy independent at $q_1^* \lesssim \frac{1}{4}(2\pi/a)$ and $q_5^* \gtrsim \frac{3}{4}(2\pi/a)$, where again a is the Cu-Cu distance. These two sets of vectors are not equivalent once the O sites within unit cells are taken into account. Hence the energy scale Δ_0 marks a crossover from the regime with spatially extended excitations with well-defined \vec{k} -space excitations to a regime where local excitations break spatial symmetries.

**FIGURE 16.3**

Systematic doping and temperature dependence. (a) Gap function extracted from STM data on samples at different doping levels [10]. (b) Temperature dependence of the arc length [12].

A systematic investigation of five different samples with different doping demonstrated a qualitative trend in the crossover energy scale Δ_0 , the gap scale inferred from spatially averaged spectra Δ_1 , and the angular extent of the arc-shaped region in \vec{k} -space where the Bogoliubov quasi-particle excitation energy is below the energy resolution of SI-STM [10]. While Δ_1 rises rapidly with a reduced hole concentration (underdoping), Δ_0 (the upper bound of the data points in Fig. 16.3(a)) and the angular extent of the arc (distance between lower bounds of the data points in Fig. 16.3(a)) appeared largely insensitive to doping in the range of study. Reference [10] noted that weakly doping-dependent Δ_0 is consistent with the energy of a Bogoliubov quasi-particle whose momentum \vec{k} -value is at crossing points between the normal state Fermi surface, as determined by angle resolved photoemission spectroscopy, and the diagonal lines connecting $(0, \pm\pi/a)$ and $(\pm\pi/a, 0)$ (see Fig. 16.2(c)). Interestingly, strongly doping-dependent Δ_1 indicates an increasing degree of the flattening of the quasi-particle dispersion upon underdoping, i.e., the slope of the fitted curve near $\theta_{\vec{k}} = 45^\circ$ in Fig. 16.3(a).

In a third study [12], crucial insights towards a full understanding of the $T-g$ phase diagram were reported through a temperature-dependence study of strongly underdoped Bi-2212. Three observations reported were of particular importance in the context of QPTs: (i) the absence of pronounced changes in the general phenomenology of either the low-energy QPI phenomena or high-energy local spatial symmetry-breaking patterns, as a function of temperature up to temperatures as high as $1.5T_c$ (see Fig. 16.4); (ii) approximately linear temperature dependence of the ungapped arc length (Fig. 16.3(b)) [13]; and (iii) a rough trend of high-temperature behavior at lower energies, resembling that of higher energies at lower temperatures (Fig. 16.4). With a concrete measure to quantitatively track these trends in the context of a suitable pu-

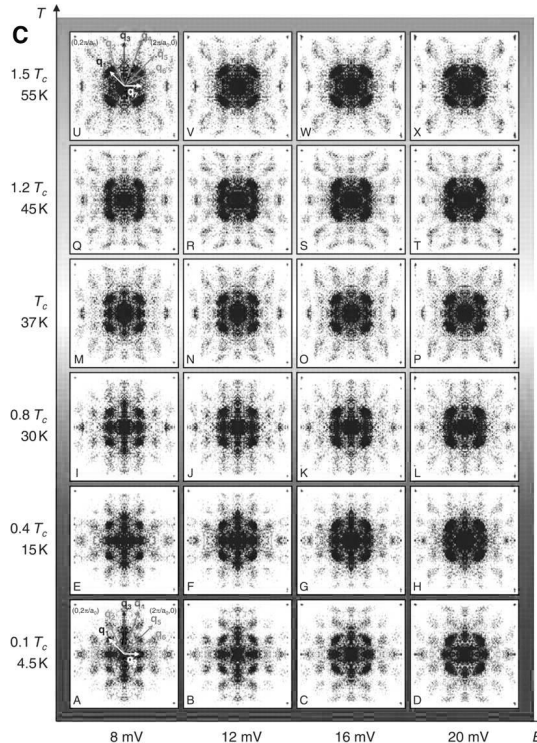


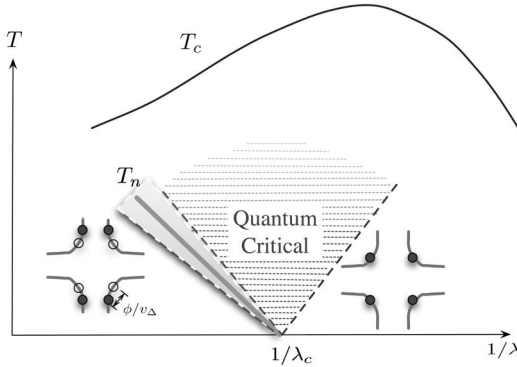
FIGURE 16.4
Systematic temperature dependence.

tative QPT, these observations may help us investigate the full $T - g$ phase diagram.

The aforementioned insights from recent experimental developments can serve as stepping stones for answering questions (3) and (4) at a quantitative level and investigating QPTs through joint efforts between theory and experiments. The first step would be to identify ordering possibilities that are consistent with existing observations and can lead to a QPT. We turn now to discuss a theory of a nematic QPT which promises definitive observations/predictions ideally suited for STM studies of cuprates.

16.3.2 Theory of the Nodal Nematic Quantum Critical Point in Homogeneous d -wave Superconductors

There have been many proposals for broken-symmetry patterns and associated QPTs in the context of cuprate superconductors. Examples include the staggered flux phases [14], d -density waves [15], current loops [16], and various electronic liquid crystalline phases [17]. A number of these proposals involve

**FIGURE 16.5**

QCP at $\lambda = \lambda_c$, separating the nodal nematic phase for $\lambda^{-1} < \lambda_c^{-1}$ from the symmetric phase, and its quantum critical fan. T_c and T_n are the superconducting and nematic critical temperatures and the shaded wedge corresponds to the thermal critical regime.

spatial arrangements or space-group symmetry breaking, as opposed to magnetic ordering.

Here we will limit our discussion to QPTs within the d -wave superconducting phase of a quasi-two-dimensional tetragonal crystal. There are two reasons for this focus. Firstly, there is now considerable experimental evidence that a nodal nematic phase, which is a specific type of additional ordering in a d -wave superconductor, occurs in at least some under-doped cuprate superconductors [18–20]. Moreover, local patterns observed in Bi-2212 and NaCCOC break the C_{4v} point group symmetry of the underlying lattice in much the same way as we anticipate in a nematic phase: $C_{4v} \rightarrow C_{2v}$. Secondly, by assuming a superconducting ground state we can restrict the phase space for gapless fermions to four nodal points. The combination of this restriction and momentum conservation limits the allowed scattering mechanisms and permits a controlled theoretical analysis.

Since scattering mechanisms for low-energy fermionic excitations inside d -wave superconductors are limited, the number of conventional QCPs are strongly restricted. Assuming that the properties of the cuprates deep inside the superconducting phase can be understood in the framework of Bardeen-Cooper-Schrieffer (BCS) theory, we start with Bogoliubov quasi-particles near the node as the only low lying fermionic excitations in the superconducting phase. There are two constraints for QCPs as effective scattering mechanisms for nodal quantum phases. (a) Due to momentum conservation, an order parameter with a non-zero net momentum \mathbf{Q} is unlikely because it would couple

via derivative couplings that are less relevant compared to direct coupling.² While a \mathbf{Q} that connects nodal points would be an exception, this requires fine tuning. We shall therefore assume $\mathbf{Q} = 0$; (b) Experimental observations limit the possibilities significantly. In particular, the additional ordering should leave the nodal quantum phases gapless. Starting from these two constraints, Vojita, Zhang and Sachdev [21, 22] constructed the following exhaustive catalog for additional ordering possibilities based on symmetry considerations: *ig*-pairing, *s*-pairing, *d*_{xy}-excitons, *d*_{xy}-pairing, and *p* excitons. All of these except the *ig*-pairing correspond to a shift of nodal positions breaking C_{4v} symmetry of the tetragonal lattice. In particular, *s*-pairing and *d*_{xy}-excitons both reduce C_{4v} symmetry down to an *Ising nematic* with the easy and hard axes along the *a* or *b* direction for *s*-pairing and along one of the diagonal directions for *d*_{xy}-excitons.

Here we will focus on the *ab*-axis nematic, an additional *s*-pairing, based on experimental support from BSCCO and YBaCuO; the diagonal nematic possibility will be relevant for La_{2-x}Sr_xCuO₄. There is evidence for such an ordered phase in YBCO [18, 20, 23]. Glassy patterns in under-doped BSCCO revealed by STM appear to break *ab*-symmetry locally.

Once the symmetry breaking of interest has been established, the first theoretical question to ask involves the order of the transition. A QCP associated with a single continuous transition would be a saddle point with only one unstable direction, the tuning parameter, in the renormalization group sense. Such a QCP would involve critical fluctuations which could scatter nodal quasi-particles severely. In contrast, discontinuous transitions occur with little precursor or associated fluctuations. Unlike QCPs of continuous transitions which affect a region of phase space called the critical region, discontinuous QCPs are isolated points or lines in phase space. Discontinuous transitions are also far more common in nature.

Vojta, Zhang and Sachdev [21, 22] first investigated the order of transition for the case of nodal nematic ordering. They employed an ϵ expansion ($\epsilon = 3 - d$) to derive perturbative RG flows near the free fixed point (pure *d*-wave), $\lambda = 0$.³ They found runaway flows for the nematic case, which they tentatively interpreted as a fluctuation-induced first order transition. Of course, a runaway flow can also imply a breakdown of perturbation theory.

Below we review an alternative large- N theory in the physical dimension of $d = 2$ to access a non-trivial QCP at finite coupling λ_c . This is achieved by generalizing the problem to one in which there are N *flavors* of nodal quantum phases; the physical $N = 2$ case corresponds to two spin polarizations. In the large- N limit, we present a theory of the nodal nematic QPT, whose critical behavior should be smoothly and systematically corrected by

²In the standard language of renormalization group (RG) analysis, couplings are defined as *relevant* when their strength increases under RG transformation to long distance limit, and *irrelevant* otherwise.

³In accordance with standard notation, d is used in two senses here: first for the spatial dimensionality in $\epsilon = 3 - d$, and second as a partial-wave symmetry of the order parameter.

the $1/N$ expansion. We find the following. (a) The QPT is continuous, with non-trivial critical exponents that we compute in the limit $N \rightarrow \infty$. (b) The transition occurs at a finite critical coupling between the nodal quasi-particles and the nematic order parameter, so it is inaccessible by perturbation theory. (c) The anisotropy of the nodal quasi-particle dispersion strongly influences the interplay between the critical fluctuations and the quasi-particles. We also speculate on the implications of this theory to the phenomenology of nodal quasi-particles in cuprates.

The effective Lagrangian which describes the coupling of the nodal quasi-particles to the nematic order parameter is $\mathcal{L} = \mathcal{L}_\Psi + \mathcal{L}_{\text{int}} + \mathcal{L}_\phi$, where \mathcal{L}_Ψ is the linearized nodal-quasi-particle Lagrangian in a pure $d_{x^2-y^2}$ SC and is given by

$$\mathcal{L}_\Psi = \sum_{n,\alpha} \bar{\Psi}_{n,\alpha} \left(\partial_\tau - i\tau_3 \vec{v}_F^n \cdot \vec{\nabla} - i\tau_1 \vec{v}_\Delta^n \cdot \vec{\nabla} \right) \Psi_{n,\alpha}. \quad (16.1)$$

Here $\Psi_{n,\alpha}(\vec{p}) \equiv (c_{\vec{K}_n+\vec{p},\alpha}, \epsilon_{\alpha\beta} c_{-(\vec{K}_n+\vec{p}),\beta}^\dagger)$ are two-component Nambu spinors representing the nodal quasi-particles for node index $n = 1, 2$, and $\alpha, \beta = 1, \dots, N$ are $Sp(N/2)$ flavor indices which, for $N = 2$, correspond to the quasi-particle spin polarizations ($Sp(1) \simeq SU(2)$). $\Psi_{n,\alpha}(\vec{p})$ represents nodal quasi-particles at momentum positions \vec{p} relative to each pair of nodes at $\vec{K}_1 = (K, K)$ and $\vec{K}_2 = (-K, K)$ ($K = 0.39\pi$ at optimal doping) for $n = 1, 2$, respectively; and $\vec{v}_F^n = \vec{\nabla}_k \epsilon_k|_{\vec{k}=\vec{K}_n}$, $\vec{v}_\Delta^n = \vec{\nabla}_k \Delta_k|_{\vec{k}=\vec{K}_n}$ are velocities normal and tangential to the Fermi surface. We use τ_1 and τ_3 to denote 2×2 Pauli matrices acting on the Nambu spinors. Note that we investigate our model for general values of v_F and v_Δ . We will return to this point later.

The Lagrangian density of Eq. (16.1) corresponds to the low-energy limit of the Bogoliubov-de Gennes effective Hamiltonian for quasi-particles for a singlet superconductor with spatially uniform order given by Δ_k :

$$\hat{H}^{\text{BdG}} = \sum'_{\vec{k},\alpha} \Upsilon_\alpha^\dagger(\vec{k})(\epsilon_{\vec{k}} \tau_3 + \Delta_{\vec{k}} \tau_1) \Upsilon_\alpha(\vec{k}). \quad (16.2)$$

In Eq. (16.2) the sum Σ' is over the upper half plane of the Brillouin zone $k_y > 0$ and the four-component Nambu spinor Υ is defined as $\Upsilon_\alpha(\vec{k}) \equiv (c_{\vec{k},\alpha}, \epsilon_{\alpha\beta} c_{-\vec{k},\beta}^\dagger)$ for each spin component $\alpha = \uparrow, \downarrow$. The low-energy effective theory for a d -wave superconductor is obtained by separating out the contribution from \vec{k} -points where the dispersion deviates from a linear approximation near the nodes:

$$\begin{aligned} \hat{H}^{\text{BdG}} &= \sum_{\vec{p},m,\alpha}^\Lambda \Upsilon_\alpha^\dagger(\vec{K}_m + \vec{p})(\tau_3 \vec{v}_F^m \cdot \vec{p} + \tau_1 \vec{v}_\Delta^m \cdot \vec{p}) \Upsilon_\alpha(\vec{K}_m + \vec{p}) + \hat{H}_> \\ &= \int d\vec{x} \sum_{m,\alpha} \Psi_{m,\alpha}^\dagger(\vec{x})(-i\tau_3 \vec{v}_F^m \cdot \vec{\nabla} - i\tau_1 \vec{v}_\Delta^m \cdot \nabla) \Psi_{m,\alpha}(\vec{x}) + \hat{H}_>, \end{aligned} \quad (16.3)$$

where $\Upsilon_\alpha(\vec{x}) = \sum_m \Psi_{m,\alpha}(\vec{x}) e^{i\vec{K}_m \cdot \vec{x}} + \Upsilon_\alpha^>$, Λ is an ultra-violet cutoff for linear dispersion, i.e., the dispersion deviates from linear form for $|\vec{p}| > \Lambda$, and $\hat{H}_> = \dots$ denotes the contribution to the Hamiltonian from quasi-particles with momentum \vec{p} such that $|\vec{p}| > \Lambda$. Upon integrating out the high energy contributions the effective Euclidean Lagrangian density \mathcal{L}_Ψ for the nodal quasi-particles is given by Eq. (16.1).

Since there are two discrete possibilities for C_{2v} -symmetric states resulting from a nematic ordering of a C_{4v} -symmetric system, the nematic order parameter of interest has Ising symmetry; hence the name *Ising nematic*. Therefore the appropriate Lagrangian for the order parameter ϕ is

$$\mathcal{L}_\phi = \frac{m^2}{2} \phi^2 + \frac{1}{2} [(\partial_\tau \phi)^2 + c^2 (\nabla \phi)^2] + \frac{u}{8N} \phi^4 + \dots, \quad (16.4)$$

where the ellipses represent higher order terms in powers of the nematic order parameter field ϕ . We assume that $u > 0$ and that $m^2 > 0$, i.e., in the absence of coupling to the nodal quasi-particles, the nematic mode is gapped and the system is in its isotropic C_{4v} -symmetric phase with $\langle \phi \rangle = 0$. Here, the physical meaning of the order parameter $\langle \phi \rangle$ is an s -wave component of the superconducting gap.

The leading interaction term that couples the nematic order parameter to nodal quasi-particles is

$$\mathcal{L}_{\text{int}} = \frac{\lambda}{\sqrt{2N}} \sum_{n,\alpha} \phi \bar{\Psi}_{n,\alpha} \tau_1 \Psi_{n,\alpha}, \quad (16.5)$$

where the coupling constant λ can be held fixed in the large- N limit.

This model, $\mathcal{L}_\Psi + \mathcal{L}_{\text{int}} + \mathcal{L}_\phi$, is symmetric under combined discrete transformations of $(\phi \rightarrow -\phi, \vec{p} \rightarrow -\vec{p}, \Psi \rightarrow \tau_2 \Psi)$. The combination of these discrete transformations, the implicit symmetry of the Nambu notation, and the symmetry associated with $(\Psi_1 \rightarrow \Psi_2, k_x \rightarrow k_y)$ amounts to C_{4v} symmetry. Should $\langle \phi \rangle \neq 0$, the position of the nodes shift in the \vec{v}_Δ^n direction and the C_{4v} symmetry is broken down to C_{2v} associated with $(\Psi_1 \leftrightarrow \Psi_2, k_x \leftrightarrow k_y)$ (see Fig. 16.5).

The strong-coupling fixed point for the nodal nematic QCP inaccessible by perturbative renormalization group methods [21, 22] was first found and studied with a large- N procedure [24]. As a first step, the effective action for the nematic order parameter field $S_{\text{eff}}[\phi]$ was obtained by formally integrating out the fermions:

$$\mathcal{Z} = \int \mathcal{D}\tilde{\phi} \mathcal{D}\Psi \mathcal{D}\bar{\Psi} e^{-\int d\vec{x} d\tau \mathcal{L}} \propto \int \mathcal{D}\phi e^{-S_{\text{eff}}[\phi]}. \quad (16.6)$$

The large- N limit provides a small parameter while we tune the coupling constant λ through the phase transition. The path integral is dominated by the saddle point and the effects of fluctuations can be studied via a controlled

$1/N$ expansion. The effective action has the standard form

$$S_{\text{eff}}[\phi] = \int d^3x \left\{ \frac{m^2}{2} \phi^2 + \frac{1}{2} [(\partial_\tau \phi)^2 + c^2 (\nabla \phi)^2] + \frac{u}{8N} \phi^4 \right\} - N \sum_n \ln \text{Det} \left(\partial_\tau - i\tau_3 \vec{v}_F^n \cdot \vec{\nabla} - i\tau_1 \vec{v}_\Delta^n \cdot \vec{\nabla} + \frac{\lambda}{\sqrt{2N}} \tau_1 \phi \right). \quad (16.7)$$

The fermionic determinant in Eq. (16.8) represents the sum of fermionic bubble Feynman diagrams. Since the action of the nodal fermions has the structure of an anisotropic Dirac theory with a coupling to the nematic order parameter ϕ , each bubble diagram involves a trace over a product of Dirac fermion propagators with appropriate insertions of the matrices τ_1 dictated by the form of the coupling. Upon rescaling the order parameter $\phi \rightarrow \sqrt{2N}\phi$, it is apparent that the effective action for the rescaled field ϕ has the form $2NS_{\text{eff}}[\phi]$. Hence, in the large- N limit the path integral is dominated by paths that solve the saddle point equations.

The spontaneous symmetry breaking in this model can be studied through the effective potential $V[\tilde{\phi}_0] \equiv -S_{\text{eff}}[\tilde{\phi}_0]/\Omega$ for a uniform rescaled field $\tilde{\phi}$ where Ω is the space-time volume:

$$V[\tilde{\phi}] = 2N \left\{ \frac{m^2}{2} \tilde{\phi}^2 + \frac{1}{4} u \tilde{\phi}^4 - \frac{1}{2N} \sum_{n,\alpha} \int \frac{d\vec{q}}{(2\pi)^2} \frac{d\omega}{2\pi} \ln [\bar{\omega}^2 + (\vec{v}_F^n \cdot \vec{q})^2 + (\vec{v}_\Delta^n \cdot \vec{q} + \lambda \tilde{\phi})^2] \right\} = 2N \left[\frac{1}{2} \left(m^2 - \frac{\Lambda \ln 2}{2\pi v_F v_\Delta} \lambda^2 \right) \tilde{\phi}^2 + \frac{1}{4} u \tilde{\phi}^4 + \frac{1}{288\pi^2} \frac{1}{v_\Delta v_F} \frac{\lambda^6}{\Lambda^3} \tilde{\phi}^6 + \dots \right], \quad (16.8)$$

where Λ is an ultraviolet cutoff. From Eq. (16.8) we can define the critical coupling λ_c such that $\langle \phi \rangle \neq 0$ for $\lambda^2 > \lambda_c^2 \equiv 2\pi v_F v_\Delta m^2 / (\Lambda \ln 2)$. The value of $\langle \phi \rangle$ is determined by the saddle point equation,

$$m^2 \langle \phi \rangle = -\frac{\lambda}{\sqrt{2N}} \sum_{n,\alpha} \langle \bar{\Psi}_{n,\alpha} \tau_1 \Psi_{n,\alpha} \rangle. \quad (16.9)$$

For $\lambda \gtrsim \lambda_c$, the solution of Eq. (16.9) satisfies

$$\langle \phi \rangle \propto (\lambda - \lambda_c)^{1/2}. \quad (16.10)$$

Hence, there is a continuous QPT between the weak-coupling C_4 -symmetric phase and a strong-coupling nematic phase in the large- N limit.

For the stability of the QCP and the critical properties, the effect of fluctuations should be considered. In general this can be challenging. However, in the present case the theory of fluctuations is Gaussian to leading order in $1/N$ and higher order terms are irrelevant. This is due to a large anomalous

dimension η according to the Gaussian action:

$$\begin{aligned} S^{(2)}[\varphi] = & \int \frac{d^2 p d\omega}{(2\pi)^3} \frac{1}{2} \left[(\lambda_c^2 - \lambda^2) + \kappa(\omega^2 + c^2 \vec{p}^2) \right. \\ & \left. + \gamma \sqrt{\omega^2 + E_1(\vec{p})} \left(1 - \frac{v_\Delta^2 p_y^2}{\omega^2 + E_1(\vec{p})} \right) + [p_x \leftrightarrow p_y] \right] |\varphi(p)|^2, \end{aligned} \quad (16.11)$$

where $\kappa \equiv \lambda_c/m^2$, $\gamma \equiv \lambda_c^2/(32v_F v_\Delta)$, the fluctuations of the nematic mode $\varphi(x) \equiv (m/\lambda_c)(\phi(x) - \langle \phi \rangle)$. There are two separate energy scales associated with any given momentum \vec{p} : $E_1(\vec{p}) \equiv \sqrt{v_F^2 p_x^2 + v_\Delta^2 p_y^2}$ and $E_2(\vec{p}) \equiv \sqrt{v_F^2 p_y^2 + v_\Delta^2 p_x^2}$ which are related to each other upon $[p_x \leftrightarrow p_y]$, due to broken Lorentz invariance, i.e., velocity anisotropy. The non-local term generated by integrating out the nodal fermions has a lower dimension than the bare dynamical terms in Eq. (16.12) and sets the scaling dimension $\text{dim}[\varphi] = 1$ at the QCP. This implies all higher order terms are irrelevant and the non-local Gaussian fixed point is stable. Further, given $z = 1$ inherited from the spectrum of the fermions and $\text{dim}[\varphi] = (d+z-2+\eta)/2$ with the space dimension d , Eq. (16.12) indicates $\eta = 1$.

Away from criticality, the correlation length scales as $\xi \sim |\lambda_c - \lambda|^{-\nu}$ with $\nu = 1$. To the extent that scaling holds, the general shape of the phase diagram is therefore known. In particular, scaling predicts $T_c(\lambda) \sim (\lambda - \lambda_c)$ for $\lambda > \lambda_c$ ($\nu z = 1$). The resulting phase diagram based on these arguments, with a v-shaped quantum critical fan, is sketched in Fig. 16.5.

To conclude this section, we briefly describe what is known beyond the large- N limit. $1/N$ corrections to the critical properties of both the order parameter fluctuations and the angle-resolved photo-emission spectroscopy (ARPES) spectral function were considered by Kim *et al.* [24]. A long-lived nematic mode that is separated from a particle-antiparticle continuum emerges in this limit, much like a zero-sound mode in Helium 3. This mode survives for arbitrary $v_\Delta/v_F > 0$.

The full ARPES spectral function was also obtained at $1/N$ for arbitrary v_Δ/v_F . Unlike gauge fluctuations which wipe out all long-lived Bogoliubov quasi-particles [25–27], nematic fluctuations leave untouched those excitations found near the tip of the arc formed by finite-energy excitations. In other words, excitations with velocity $\partial\varepsilon/\partial\vec{p} = \vec{v}_\Delta$ are long-lived while those with $\partial\varepsilon/\partial\vec{p} = \vec{v}_F$ are short-lived due to scattering off of the nematic mode.

One may worry about the correctness of the above observations since they are drawn from a large- N expansion. Quite remarkably, it turns out that $\alpha \equiv v_\Delta/v_F \sim 1/20$ is a small parameter [28] through which controlled calculations can be made. As a result, the large- N analysis, in which $1/N$ is essentially invented as a small parameter, is unnecessary. However, a small α analysis demonstrates that corrections to the large- N limit are sub-logarithmic. This suggests that, for small α , the leading behavior at large N can be trusted even

at $N = 1$. Given that the experimentally determined degree of anisotropy is extreme,⁴ the above calculations are controlled and falsifiable. However, to test the relevance of this theory a key missing ingredient may be the role of disorder, as it can potentially wash out the QCP should it act as a random symmetry-breaking field.

16.4 Looking Ahead

We now return to the key questions posed at the beginning of Sec. 16.3 and discuss recent developments and future outlook. The theory of nodal nematic QPTs reviewed in Sec. 16.3.2 gives a number of interesting phenomena, including the marginal Fermi liquid self-energy and an enhancement of quasi-particle interference due to momentum-dependent critical fluctuations, in addition to the possibility of continuous QPT inside a d -wave superconductor. However, there has not been a direct experimental test of this theory yet. As we discussed in the Sec. 16.2, further progress in making a concrete connection between theory and local probe experiments requires first establishing relevant local measures of the observed tendency of broken symmetry. We need to extract simple quantities which robustly characterize local information allowing direct comparison with both theory and other probes. There has been some effort to address this need, including characterizing checkerboard and stripe ordering patterns [31–34] and probing the degree of “Mott-ness” using particle-hole asymmetry [35–37]. Accumulating evidence for glassy patterns of clusters breaking various spatial symmetries at the pseudo-gap energy scale in BSCCO(BSCCO), as we discussed in Sec. 16.3 specifically calls for a new measure that can quantitatively assess such inhomogeneous patterns. Classification of electronic liquid crystal phases [17] based on various spatial symmetry-breaking patterns can be a guide.

In the classification of electronic liquid crystal phases, the nematic phase and the smectic phase play paradigmatic roles. An electronic nematic arises when charge degrees of freedom collectively break point-group symmetry of space while preserving lattice translation. An electronic smectic is a lower symmetry phase which additionally breaks translational symmetry in one direction via modulation.

The challenges for detecting different electronic liquid crystals are twofold: (a) a scarcity of probes that couple directly to the quadrupole moment which is the nematic order parameter [34]; and (b) the heterogeneity driven by the interplay between quenched disorder and correlation effects hindering long range order. Due to these challenges, successful detection of electronic liquid

⁴ $v_F/v_\Delta \sim 19$ for BSCCO from thermal conductivity [29] and ARPES [30], and $v_F/v_\Delta \sim 14$ for YBCO from thermal conductivity [29].

crystals has been only achieved thus far in high-purity systems supporting long-range order. Nematic phases have been mostly detected through transport anisotropy ratios in high-purity systems [20, 23, 38, 39]. The transport anisotropy ratio has the correct symmetry to serve as a nematic order parameter. However, as transport necessarily averages over the entire sample it glosses over inhomogeneous nematic domains and works best in the presence of long range order. Smectic phases have been mostly established through additional peaks in the elastic diffraction measurements, for instance in La-based cuprates [40]. Hence, development of successful measures for local electronic liquid crystallinity using nano-scale domains in under-doped BSCCO as a test case may have a broader impact in the search for local electronic liquid crystalline behaviors [38, 41] and open doors to new discoveries.

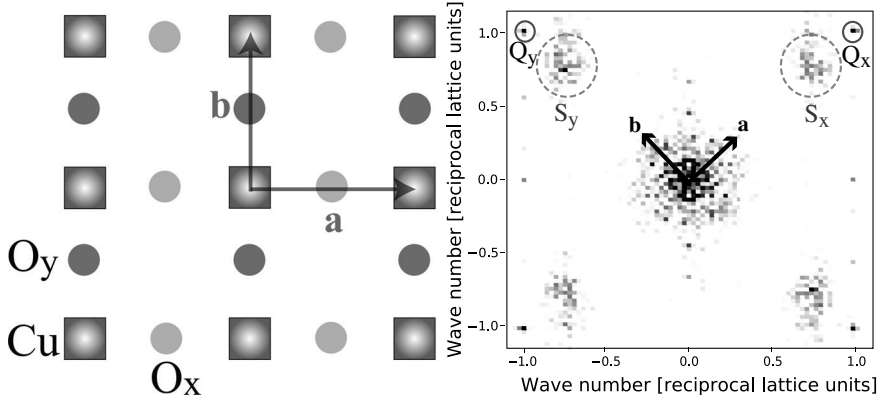
Here we propose to use the sensitivity of STM to intra-unit-cell electronic structure to characterize local nematic orientational ordering. We lay out a general method for characterizing different local spatial symmetry-breaking patterns, taking advantage of information surrounding Fourier peaks, including Bragg peaks. This idea can also be readily adapted and tested with diffraction probes. Moreover, the connection between the unit cell internal structure and nematicity offers a new observable for other local probes such as nuclear quadrupole resonance. In the context of STM data on under-doped BSCCO discussed in Sec. 16.3, regimes with non-dispersive peaks may give clear-cut signatures of electronic liquid crystalline ordering. Typical Fourier transforms of these published data at high energies show broad peaks associated with $4a/3$ wavelength modulations observed in Figs 16.3.1 and 16.2 and extremely sharp atomic Bragg peaks at $\pm\vec{Q}_x = \pm\frac{2\pi}{a}(1, 0)$ and $\pm\vec{Q}_y = \pm\frac{2\pi}{a}(0, 1)$, where a is Cu-Cu distance (see Fig. 16.6(b)).

We propose a nematic order parameter consisting of Bragg peaks $\pm\vec{Q}_x$, $\pm\vec{Q}_y$. This could allow us to separate the signatures of nematic ordering, or orientational order, from translational symmetry breaking encoded in other Fourier peaks, such as the broad peaks centered at \vec{S}_x and \vec{S}_y associated with $4a/3$ wavelength modulations in Fig. 16.6(b). For any local map of scalar quantity $Z(\vec{x})$ we define a measure of long range nematic order \mathcal{O}_N and of the lattice order $\mathcal{O}_{\vec{R}}$ as

$$\begin{aligned}\mathcal{O}_N &\equiv \tilde{Z}(\vec{Q}_x) - \tilde{Z}(\vec{Q}_y) + \tilde{Z}(-\vec{Q}_x) - \tilde{Z}(-\vec{Q}_y), \\ \mathcal{O}_{\vec{R}} &\equiv \tilde{Z}(\vec{Q}_x) + \tilde{Z}(\vec{Q}_y) + \tilde{Z}(-\vec{Q}_x) + \tilde{Z}(-\vec{Q}_y),\end{aligned}\quad (16.12)$$

where $\vec{Q}_x = \frac{2\pi}{a}(1, 0)$ and $\vec{Q}_y = \frac{2\pi}{a}(0, 1)$, with a the size of the unit cell and $\tilde{Z}(\pm\vec{Q}_x)$ and $\tilde{Z}(\pm\vec{Q}_y)$ the Fourier components of Z at four Bragg peaks.⁵ Clearly, \mathcal{O}_N will vanish if only the copper lattice sites $\vec{R} = (ma, na)$ (with m, n integer) contribute to $Z(\vec{x})$ since $\tilde{Z}(\vec{Q})$ would be independent of the choice of

⁵Here we are considering a square CuO₂ plane, but the following discussion can be generalized to other lattices.

**FIGURE 16.6**

(a) A pattern in a CuO₂ lattice consistent with $\mathcal{O}_N \neq 0$. This pattern breaks the C_4 symmetry but retains the translational symmetry of the Cu lattice. (b) The Fourier transform of a Z-map from Ref. [4]. The Bragg peaks \vec{Q}_x , \vec{Q}_y and the broad weight around peaks S_x and S_y are marked with the respective ultraviolet cutoff's, Λ_N and Λ_S .

the Bragg peak \vec{Q} . Hence $\mathcal{O}_N \neq 0$ requires an internal structure within the unit cell.

That \mathcal{O}_N would be sensitive to the intra-unit-cell structure has significant implications for the choice of a minimal microscopic model for cuprate superconductors between a one-band Hubbard model and a three-band Emery model [16, 42]. The importance of the role of oxygen for non-zero \mathcal{O}_N is evident from the Fourier transforms of a simple ideal pattern of $Z(\vec{x})$, drawing contributions from the three sites within the unit cell of the CuO₂ plane:

$$\tilde{Z}(\vec{Q}_x) = \bar{Z}_{\text{Cu}} - \bar{Z}_{\text{O}_x} + \bar{Z}_{\text{O}_y}, \quad \tilde{Z}(\vec{Q}_y) = \bar{Z}_{\text{Cu}} + \bar{Z}_{\text{O}_x} - \bar{Z}_{\text{O}_y}, \quad (16.13)$$

where \bar{Z}_{Cu} , \bar{Z}_{O_x} , and \bar{Z}_{O_y} are averages of $Z(\vec{x})$ at Cu, O_x and O_y sites respectively. For such a simple model of the $Z(\vec{x})$ distribution, a non-zero value of \mathcal{O}_N will imply an imbalance of Z-intensity between two oxygen sites O_x and O_y within each unit cell. A cartoon representation of this is shown in Fig. 16.6. Clearly, a one-band Hubbard model cannot realize such a pattern without introducing intensity at bonds. In data analysis, it should be possible to assess contributions from O sites compared to the rest of Cu-Cu bond region. However, for meaningful studies using Eq. 16.12, two conditions must be met: (i) the map $Z(\vec{x})$ should have sub-unit-cell resolution; and (ii) due to the extreme sensitivity of \mathcal{O}_N to the phase of Fourier transform, highly accurate registry of the location of Cu sites is crucial.

Given the various indications of heterogeneity from STM measurements of BSCCO (see Sec. 16.1) a local version of the order parameter $\mathcal{O}_N(\vec{x})$ can

offer valuable information. In order to capture variations of the ordering at scales longer than the lattice scale and the 4/3 period modulations, we can define a coarse-grained field with a coarsening length scale $1/\Lambda_N$, which acts as an effective ultraviolet cutoff (see dashed circles around the Bragg peaks in Fig. 16.6(b)). The necessary precise registry of Cu sites can be achieved by using the simultaneous topographic map to correct for the piezo drift using a *displacement field* $\vec{u}(\vec{r})$. For the generic cutoff Λ , a coarse-grained field associated with Fourier peak \vec{Q} can be defined as

$$\begin{aligned}\hat{Z}(\vec{Q}; \vec{x})_\Lambda &\equiv \sum_{\vec{x}'} Z(\vec{x}') e^{i\vec{Q}\cdot(\vec{x}' - \vec{u}(\vec{x}'))} f_\Lambda(\vec{x}' - \vec{x}), \\ &\approx \sum_k \tilde{Z}(\vec{Q} - \vec{k}) \frac{1}{\sqrt{N}} e^{i\vec{k}\cdot(\vec{x} - \vec{u}(\vec{x}))} e^{-k^2/2\Lambda^2},\end{aligned}\quad (16.14)$$

where $f_\Lambda(\vec{x}) \equiv \frac{\Lambda^2}{2\pi} \exp(-\Lambda^2|\vec{x}|^2/2)$ coarse-grains over the length scale of $1/\Lambda$. A local version of \mathcal{O}_N can be defined as:

$$\mathcal{O}_N(\vec{x})_{\Lambda_N} \propto [\hat{Z}(\vec{Q}_x; \vec{x})_{\Lambda_N} - \hat{Z}(\vec{Q}_y; \vec{x})_{\Lambda_N} + \hat{Z}(-\vec{Q}_x; \vec{x})_{\Lambda_N} - \hat{Z}(-\vec{Q}_y; \vec{x})_{\Lambda_N}], \quad (16.15)$$

with the normalization requiring the field-of-view average to equal \mathcal{O}_N , i.e., $\sum_{\vec{x}} \mathcal{O}_N(\vec{x}) = N \mathcal{O}_N$, for the number of lattice sites N .⁶ Once a local order parameter $\mathcal{O}_N(\vec{x})_{\Lambda_N}$ is extracted, spatial fluctuations can be quantified through the correlation length ξ_N .

An analogous analysis for other Fourier peaks would measure broken rotational symmetry in the modulation tendencies. For instance, the order parameter \mathcal{O}_S for the C_4 symmetry breaking of $4a/3$ modulation, i.e., unidirectional striping tendency or smectic ordering, can be defined in the same manner as \mathcal{O}_N by replacing the wave vectors \vec{Q}_1 and \vec{Q}_2 by $\vec{S}_1 = \frac{2\pi}{a}(3/4, 0)$ and $\vec{S}_2 = \frac{2\pi}{a}(0, 3/4)$ in Eq. (16.12). We can also define a local measure of smectic tendency $\mathcal{O}_S(\vec{x})$ and the associated correlation length ξ_S .

Finally, in lieu of a summary, we briefly describe new doors the above suggested measures can open, and how they might bring together the experimental and theoretical study of QPTs using local probes.

First, a comparative study of energy and temperature dependence of $\xi_N(\omega, T)$ and $\xi_S(\omega, T)$ would allow us to track the spatial fluctuation of orientational ordering and translational symmetry breaking separately. The possibility of longer-ranged orientational ordering in the presence of disordered translational symmetry breaking was suggested for a charge-density-wave system $\text{Nb}_x\text{Ta}_{1-x}\text{S}_2$ in Ref. [43]. Comparative correlation length studies will allow us to test the tantalizing possibility in under-doped BSCCO.

Second, the above local measures can be used for dynamical scaling analysis on STM data. In the study of classical statistical models, scaling analysis

⁶The second line of Eq. (16.15) is obtained assuming $\vec{u}(\vec{x})$ does not vary within the length scale of $1/\Lambda_N$, consistent with the definition of $\vec{u}(\vec{x})$ for $1/\Lambda_N \ll 1/\Lambda_u$, where Λ_u is the very small effective Bragg peak cutoff of the topograph.

provided the foundation for the renormalization-group-based theory of critical phenomena. The search for dynamical scaling directly from data using the above measure may open new doors for the study of highly correlated systems at the verge of instability. For instance, it could allow us to extrapolate the degree of nematicity up to temperatures far beyond the reach of STM. Such a scaling study will be particularly valuable inside the superconducting phase. Much discussion of quantum criticality in cuprates is motivated by various normal state observations near the doping range where T_c is maximum. The linear temperature dependence of normal state resistivity [5,6] in this strange metal regime was attributed to quantum criticality early on. While this and other normal-state observations invite the notion of a QCP inside the superconductor near optimal doping, signatures of quantum criticality inside the superconducting phase have not been conclusively identified. Partially, the lack of observation of scaling inside the superconducting phase is due to the inaccessibility of the DC charge transport in that phase. However, recent observations of doping-dependent anisotropy in the Nernst effect [20] bring the question of the QCP location inside the superconducting dome to the forefront again. The proposed scaling study of correlation length might give a clue regarding this question.

Third, the above measures will enable study of topological defects. In the well known theory of classical melting in two dimensions, topological defects play a key role in sequential restoration of various spatial symmetries leading to intermediate liquid crystalline phases. The new scheme for analyzing local tendencies for electronic liquid crystal ordering would allow one to study topological defects in a concrete setting. For instance, one might be able to disentangle the role of fluctuations and pinning sites on the population and configuration of topological defects and explain the observed glassy patterns.

Furthermore, as the spatial average of nematic ordering defined in Eq. (16.12) is defined in terms of Bragg peaks, it can be used to compare the STM measurements against bulk probe measurement as long as the nematic domain is larger than the beam size. For instance, it might be possible to study systems that are known to develop smectic, or stripe ordering upon cooling from bulk measurements such as nickelates, at temperatures higher than their stripe-ordering temperature. If the system first enters a nematic phase above the smectic transition, the rotational symmetry breaking can be measured from the Bragg peaks using Eq. (16.12) in the absence of stripe peaks.

Finally, the above local measures combined with the knowledge of impurity locations [2] will enable identification and simulation of impurity effects near an electronic nematic QPT. Nematic QPTs inside superconducting phases have been proposed both in the context of cuprates [24] and Fe-based superconductors [44,45]. How quenched disorder will affect such a putative QPT is an important issue regarding nematic quantum criticality on actual systems. Chemical dopants, which are unavoidable in taking cuprates and Fe-based su-

perconductors from the parent anti-ferromagnet to the superconducting phase, naturally introduce quenched disorder to these systems.

For ordering involving an Ising order parameter such as Ising nematic, whether disorder induces *random mass*, or equivalently random local T_c for ordering, or *random field* makes a crucial difference in the role of disorder. For instance, a random field breaks the order parameter symmetry and rounds the transition in $d \leq 2$ [46]. However, hysteresis and noise are expected to carry non-trivial insight, as the study of classical effects in the context of YBCO nano-wires have shown [47]. A quantum analog of these effects could be of interest in the context of quantum Griffith phases [48, 49]. The main effect of random mass is to potentially change the nature of the transition, i.e., if $\nu d < 2$, where ν is the correlation length exponent [50]. By extracting the main effect of disorder on Ising nematicity, which may be different for different family of systems, one may be able to assess the actual role of disorder and study relevant effects [51].

Acknowledgements – We thank P. Abbamonte, D. Bonn, J.C. Campuzano, A. Chubukov, E. Fradkin, T. Hanaguri, W. Hardy, S. Kivelson, Y. Kohsaka, A.P. Mackenzie, M. Norman, B. Ramshaw, S. Sachdev, G. Sawatzky, J. Sethna, K. Shen, K. Sun, H. Takagi, J. Tranquada, O. Vafek, T. Vojta, and J. Zaanen for useful discussions. This work was supported in part by NSF DMR-0520404 to the Cornell Center for Materials Research. We thank the KITP for its hospitality.

Bibliography

- [1] S. Chakravarty *et al.*, Phys. Rev. Lett. **60**, 1057 (1988).
- [2] K. McElroy *et al.*, Science **309**, 1048 (2005).
- [3] J. Lee *et al.*, Nat Phys **5**, 800 (2009).
- [4] Y. Kohsaka *et al.*, Science **315**, 1380 (2007).
- [5] M. Gurvitch and A. T. Fiory, Phys. Rev. Lett **59**, 1337 (1987).
- [6] H. Takagi *et al.*, Phys. Rev. Lett **69**, 2975 (1992).
- [7] M. Lawler *et al.*, unpublished (2010).
- [8] J. E. Hoffman *et al.*, Science **295**, 466 (2002).
- [9] K. McElroy *et al.*, Nature **422**, 592 (2003).
- [10] Y. Kohsaka *et al.*, Nature **454**, 1072 (2008).
- [11] Q.-H. Wang *et al.*, Phys. Rev. Lett **87**, 167004 (2001).

- [12] J. Lee *et al.*, Science **325**, 1099 (2009).
- [13] A. Kanigel *et al.*, Nat Phys **2**, 447 (2006).
- [14] D. A. Ivanov *et al.*, Phys. Rev. Lett **84**, 3958 (2000).
- [15] S. Chakravarty *et al.*, Phys. Rev. B **63**, 094503 (2001).
- [16] C. M. Varma, Phys. Rev. Lett. **83**, 3538 (1999).
- [17] S. A. Kivelson *et al.*, Nature **393**, 550 (1998).
- [18] V. Hinko *et al.*, Science **319**, 597 (2008).
- [19] M. Matsuda *et al.*, Phys. Rev. Lett **101**, 197001 (2008).
- [20] R. Daou *et al.*, Nature **463**, 519 (2010).
- [21] M. Vojta *et al.*, Phys. Rev. Lett **85**, 4940 (2000).
- [22] M. Vojta *et al.*, IJMP B **14**, 3719 (2000).
- [23] Y. Ando *et al.*, Phys. Rev. Lett **88**, 137005 (2002).
- [24] E.-A. Kim *et al.*, Phys. Rev. B **77**, 184514 (2008).
- [25] L. Balents *et al.*, IJMPB **12**, 1033 (1998).
- [26] O. Vafek *et al.*, Phys. Rev. Lett. **89**, 157003 (2002).
- [27] M. Hermele *et al.*, Phys. Rev. B **72**, 104404 (2005).
- [28] J. Ye and S. Sachdev, Phys. Rev. B **44**, 10173 (1991).
- [29] M. Chiao *et al.*, Phys. Rev. B **62**, 3554 (2000).
- [30] M. R. Norman *et al.*, Phys. Rev. B **52**, 615 (1995).
- [31] C. Howald *et al.*, PNAS **100**.9705 (2003).
- [32] J. A. Robertson *et al.*, Phys. Rev. B **74**, 134507 (2006).
- [33] A. D. Maestro *et al.*, Phys. Rev. B **74**, 024520 (2006).
- [34] S. A. Kivelson *et al.*, Rev. Mod. Phys. **75**, 1201 (2003).
- [35] M. B. J. Meinders *et al.*, Phys. Rev. B **48**, 3916 (1993).
- [36] P. Anderson and N. Ong, JPCS **67**, 1 (2006).
- [37] M. Randeria *et al.*, Phys. Rev. Lett **95**, 137001 (2005).
- [38] R. A. Borzi *et al.*, Science **315**, 214 (2007).
- [39] M. P. Lilly *et al.*, Phys. Rev. Lett **82**, 394 (1999).

- [40] J. M. Tranquada, *Handbook of High-Temperature Superconductivity* edited by J.R. Schrieffer, Springer (2007).
- [41] T.-M. Chuang *et al.*, Science **327**, 181 (2010).
- [42] V. J. Emery, Phys. Rev. Lett **58**, 2794 (1987).
- [43] H. Dai *et al.*, Phys. Rev. Lett. **66**, 3183 (1991).
- [44] C. Fang *et al.*, Phys. Rev. B **77**, 224509 (2008).
- [45] C. Xu *et al.*, Phys. Rev. B **78**, 20501 (2008).
- [46] Y. Imry and S.-K. Ma, Phys. Rev. Lett **35**, 1399 (1975).
- [47] E. W. Carlson *et al.*, Phys. Rev. Lett **96**, 097003 (2006).
- [48] H. Rieger and A.P. Young, Phys. Rev. B **54**, 3328 (1996).
- [49] A.H. Castro Neto *et al.* Phys. Rev. Lett. **81**, 3531 (1998).
- [50] A. Harris, Journal of Physics C **7**, 1671 (1974).
- [51] T. Vojta, Journal of Physics A **39**, 143 (2006).

Molecular Quasi-Triangular Lattice Antiferromagnets

Reizo Kato

Condensed Molecular Materials Laboratory, RIKEN, Wako-shi, Saitama 351-0198, Japan

Tetsuaki Itou

Graduate School of Human and Environmental Studies, Kyoto University, Kyoto 606-8501, Japan

We demonstrate here the possibility of a quantum spin-liquid state and related phenomena in a 2D molecular Mott system based on the Pd(dmit)₂ (dmit = 1,3-dithiole-2-thione-4,5-dithiolate) molecule. The quantum spin liquid is a spin state in which quantum fluctuations prevent order, leading to liquid-like properties among the spins, even at absolute zero temperature. It was proposed early on that this state can be realized in quantum spin systems on frustrated lattices [1]. In frustrated lattices, there exist a huge number of different classical spin configurations with nearly the same energy. Quantum mechanics causes resonance between these degenerate configurations and consequently leads to a liquid-like wavefunction. In this state, all the spins form spin-singlet pairs, i.e., valence bonds, and they fluctuate between many different configurations. The quantum spin liquid is a long-sought state of matter that has attracted much theoretical attention. However, one of the difficulties in the search for the quantum spin liquid is that there are few candidates in real materials: only “two” are known in molecular systems, one being found in the Pd(dmit)₂ compounds.

We also show that the Pd(dmit)₂ compounds undergo several kinds of ordering by small chemical modifications. The ordered ground state varies between several phases, including an antiferromagnetic ordered phase, a valence-bond-solid phase, and a charge ordered phase. This result implies that the Pd(dmit)₂ compounds have high potential in the future study of quantum phase transitions (QPTs). We also note that the quantum-spin-liquid state in the present system is realized in close vicinity to these ordered phases, and it is thus possible that it is situated around a quantum critical point between these ordered phases.

In general, the molecular system has the following characteristics: (1) weak spin-orbit coupling; (2) an isotropic spin-1/2 Heisenberg model is available; (3) a simple and clear band structure which can be well described by the tight-binding method based on the extended Hückel molecular orbital calculation [2]; (4) low dimensionality (1D or 2D); (5) stoichiometrically clean samples; and (6) rich chemical modification.

The Pd(dmit)₂ system in an insulating state can be modeled as a spin-1/2 Heisenberg antiferromagnet with a quasi-triangular lattice exhibiting frustration, and we can control the anisotropy of the electronic structure by chemical and physical methods. As described in the following, chemical modifications of a component molecule provide fine tuning of the intermolecular interactions, which mainly affects the anisotropy and strength of the magnetic interactions in the insulating state. An application of hydrostatic or uniaxial pressure enhances the intermolecular interactions and thus the bandwidth. This leads the system from the Mott insulating state to the metallic, frequently superconducting state. In particular, the uniaxial strain yields selective enhancement of the intermolecular interaction, and we can observe an effect of the frustration in this Mott transition. This quantum spin system has several tuning parameters which can induce a QPT in the ground state.

17.1 Anion Radical Salts of Pd(dmit)₂

The Pd(dmit)₂ molecule provides many conducting anion radical salts with closed-shell monovalent cations, Et_xMe_{4-x}Z⁺ (Et = C₂H₅-, Me = CH₃-, Z = N, P, As, Sb; x=0, 1, 2) [3]. The molar ratio is 1:2 (Et_xMe_{4-x}Z[Pd(dmit)₂]₂), and thus the formal charge of the Pd(dmit)₂ molecule is -1/2. All of them have a common structural feature, a quasi-triangular lattice of dimerized Pd(dmit)₂ molecules. However, their physical properties, including the ground state of the spin system, depend strongly on the choice of the cation and they are full of variety. We will especially focus on the competition between frustration, antiferromagnetic order, and valence bond formation in this quantum spin system.

17.2 Crystal Structure

There are three main structural types: (1) the *solid-crossing column* structure, most frequently observed in the Pd(dmit)₂ salts; (2) the *parallel column* structure, observed in two forms of the EtMe₃P salt, monoclinic and triclinic; and (3) the *single column* structure, observed in the Et₂Me₂N salt. All of them

have 2D conduction anion layers separated from each other by the insulating and non-magnetic cation layer. It should be emphasized that the molecular arrangement in the anion layer is essentially the same.

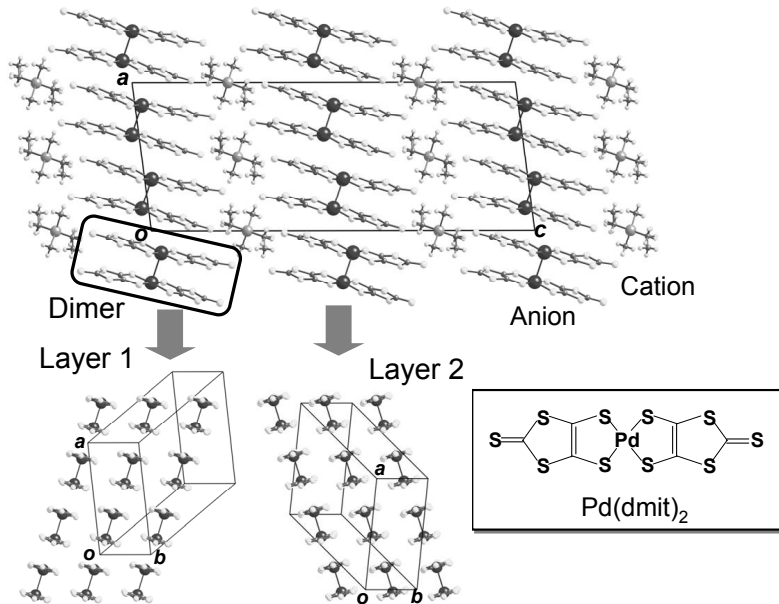


FIGURE 17.1
Crystal structure of $\text{EtMe}_3\text{Sb}[\text{Pd}(\text{dmit})_2]_2$.

The EtMe_3Sb salt has the solid-crossing column structure (Fig. 17.1). The crystal system is monoclinic with the space group of $C2/c$. The unit cell contains two crystallographically equivalent conduction layers (1 and 2) interrelated by the glide plane. The cations are located on the two-fold axis. Because the cation does not have two-fold symmetry, it has two possible orientations with an occupancy of 50 % for each one. The $\text{Pd}(\text{dmit})_2$ molecules stack along the $a + b$ direction in layer 1 and along the $a - b$ direction in layer 2, which is the nature of the solid-crossing column structure. An important point is that the $\text{Pd}(\text{dmit})_2$ molecules are strongly dimerized with a short $\text{Pd}\cdots\text{Pd}$ distance. Within the dimer, two $\text{Pd}(\text{dmit})_2$ molecules overlap in an eclipsed mode.

17.3 Electronic Structure: Molecule, Dimer, and Crystal

We now describe the unique nature of the electronic structure of the $\text{Pd}(\text{dmit})_2$ molecule and an effect of the strong dimerization. In general, the conduction band of the molecular conductor is formed by a single frontier molecular orbital, the HOMO (highest occupied molecular orbital) or LUMO (lowest unoccupied molecular orbital). In this sense, the electronic structure of the molecular conductor is very clear and simple. An important aspect of metal-dithiolene complexes, including $\text{Pd}(\text{dmit})_2$, is a small HOMO-LUMO energy difference (Fig. 17.2). The metal d orbital can mix into the LUMO, but the HOMO has no contribution from the metal d orbital due to its symmetry. Therefore, there is no metal-ligand interaction which stabilizes the HOMO. This results in the small energy difference between the HOMO and LUMO.

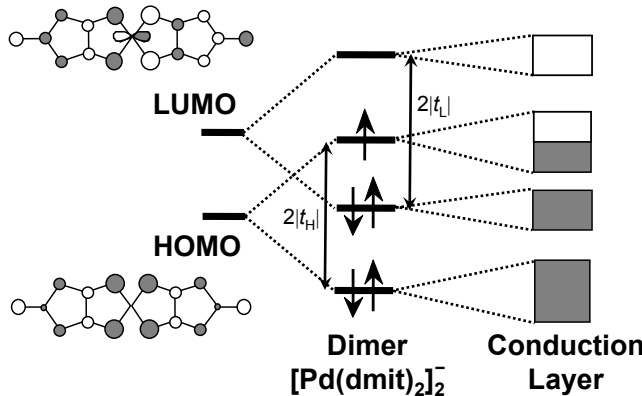


FIGURE 17.2

Energy scheme of the $\text{Pd}(\text{dmit})_2$ system.

Since the $\text{Pd}(\text{dmit})_2$ molecules are strongly dimerized, each HOMO and LUMO in the monomer forms bonding and anti-bonding combinations separated by $2|t_H|$ and $2|t_L|$, where t_H and t_L are intermonomer HOMO \cdots HOMO and LUMO \cdots LUMO transfer integrals within the dimer, respectively (Fig. 17.2). The stronger dimerization provides the larger dimerization gaps, $2|t_H|$ and $2|t_L|$. In the $\text{Pd}(\text{dmit})_2$ salt, the dimerization gaps are large enough and the bonding LUMO combination can be lower than the anti-bonding HOMO combination [4, 5]. Due to this HOMO-LUMO level crossing, the orbital degree of freedom plays an important role. Since this dimer unit has one negative charge, the anti-bonding HOMO combination has one unpaired electron. When each energy level forms an energy band in the crystal,

the conduction band originates from the HOMO in the monomer. This conduction band is 2D, half-filled, and narrow [6,7]. Therefore, most of Pd(dmit)₂ salts are Mott insulators at ambient pressure.

In the crystal, the dimer-based tight-binding picture, where electrons move from dimer to dimer, is available, because the dimerization is very strong. Interdimer transfer integrals indicate that these dimers form a quasi-triangular lattice and give a very simple expression for the conduction band (Fig. 17.3),

$$E(\mathbf{k}) = 2.0[t_r \cos \mathbf{k}y + t_B \cos (\mathbf{y} - \mathbf{x}) + t_s \cos \mathbf{kx}].$$

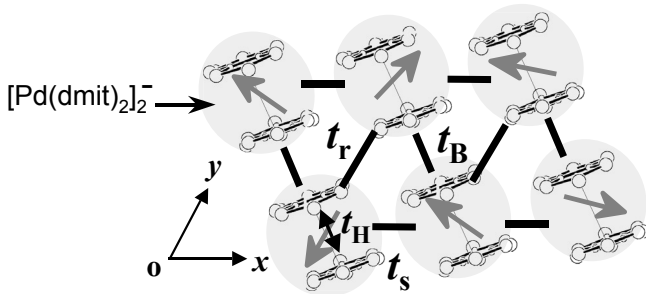


FIGURE 17.3

Quasi-triangular lattice of $[\text{Pd}(\text{dmit})_2]_2^-$ dimers.

At ambient pressure, the Pd(dmit)₂ salts behave as Mott insulators where one spin is localized on each dimer and the spin frustration plays an important role. The electronic structure is characterized by the intradimer and interdimer HOMO \cdots HOMO transfer integrals, t_H , t_B , t_s , and t_r , which exhibit the relation $|t_H| \gg |t_B| \sim |t_s| \geq |t_r|$ and can be tuned by the choice of the cation. The intradimer transfer integral t_H is approximately correlated with the effective on-site Coulomb energy on the dimer [8]. The larger interdimer transfer integrals, t_B and t_s , determine the band width, W . Although the dimers are connected by three unequal transfer integrals to form a scalene-triangular lattice, we tentatively treat a dimer lattice as an isosceles-triangular lattice for convenience, because t_B is nearly equal to t_s in most salts. The ratio t'/t , where $t = t_B \sim t_s$ and $t' = t_r$, indicates deviation from the regular triangular lattice and the degree of frustration. Using the ratio $|t_H|/W$, we can roughly estimate the relative strength of electron-electron correlation effects. Hereafter, we focus mainly on EtMe₃Sb ($t'/t = 0.92$), EtMe₃P ($t'/t = 1.05$), and Et₂Me₂Sb ($t'/t = 1.01$) salts with a nearly regular triangular lattice. It should be noted that crystals of molecular conductors are soft and the t'/t value depends on temperature and pressure. For example, the t'/t value in the EtMe₃Sb salt changes from 0.92 (at room temperature) to 0.79 (at 4.5 K).

17.4 Long-Range Antiferromagnetic Order vs. Frustration

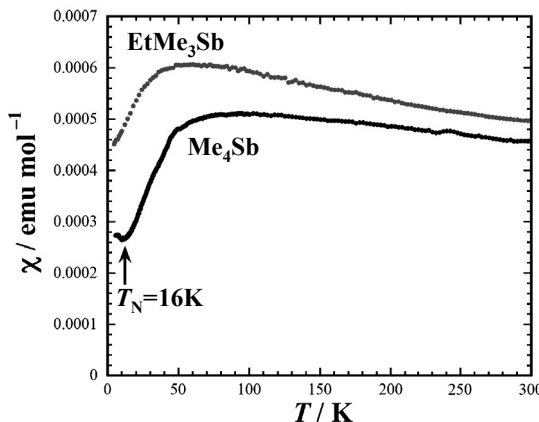


FIGURE 17.4

Temperature dependence of the magnetic susceptibility for the Me_4Sb and EtMe_3Sb salts.

For most $\text{Pd}(\text{dmit})_2$ salts in the Mott-insulating state, the magnetic susceptibility χ shows frustrated paramagnetism which can be modeled by a spin-1/2 Heisenberg antiferromagnet on the triangular lattice (Fig. 17.4) [9]. However, with decreasing temperature the anisotropic system, where the deviation from the regular triangular lattice is large, undergoes a transition toward long-range antiferromagnetic order and removes the spin frustration, as observed in the Me_4Sb salt ($t'/t = 0.87$, Fig. 17.4). Figure 17.5 shows a relation between the Néel temperature and the frustration parameter (t'/t) at room temperature. The Néel temperature increases with increasing deviation from the regular triangular lattice. In other words, the frustration suppresses long-range antiferromagnetic order. Indeed, the magnetic susceptibility of the EtMe_3Sb salt with a nearly regular triangular lattice does not show any transition down to 4.5 K [10]. The $\chi - T$ curve can be described by the [7/7] Padé approximants¹ for the high temperature expansion of χ (in $J/4k_{\text{B}}T$) of the regular-triangular spin-1/2 system with Heisenberg antiferromagnetic interactions [11], $J = 220\text{--}250$ K. It should be added that there is no change of the

¹The notation $[L/M]$ means that the series is represented by an L th order polynomial in the numerator and an M th order polynomial in the denominator.

space group and the cation disorder remains down to 4.5 K in the EtMe₃Sb salt.

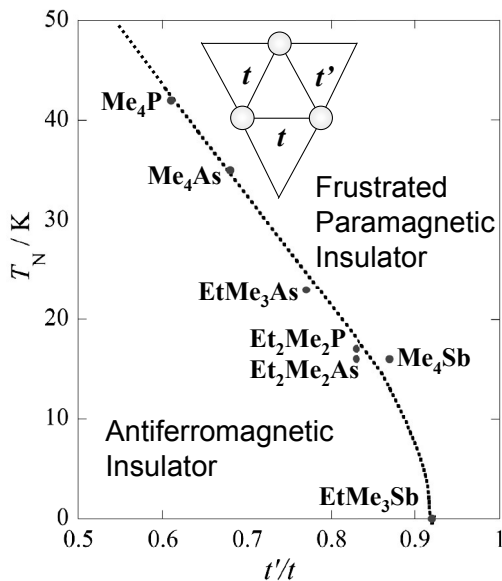


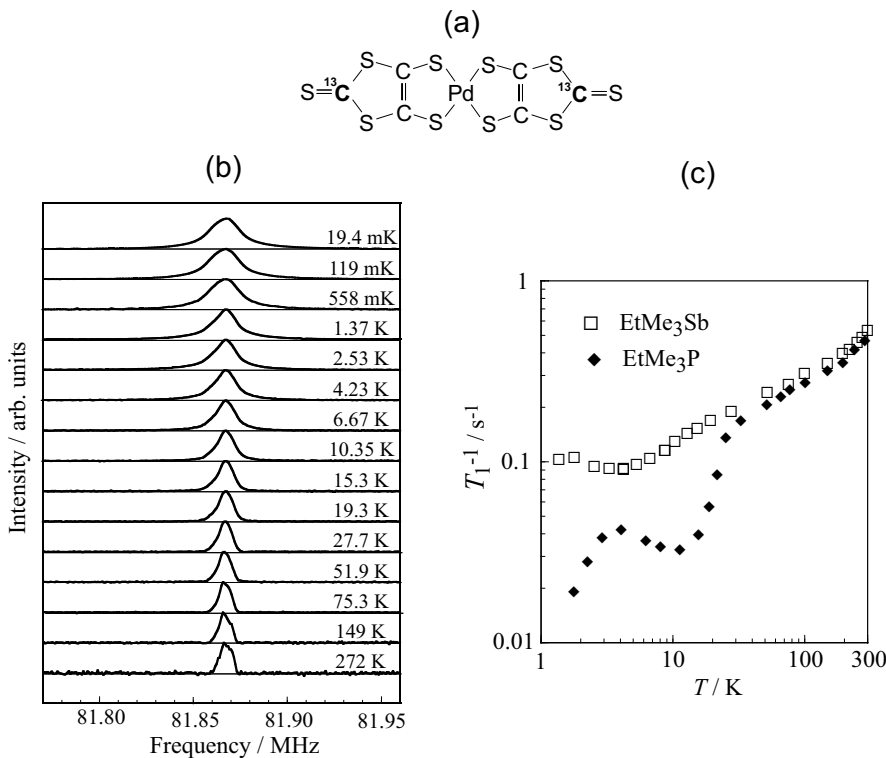
FIGURE 17.5

Relation between Néel temperature T_N and degree of frustration t'/t .

17.5 Quantum Spin-Liquid State in the EtMe₃Sb Salt

In this section, we focus on the EtMe₃Sb salt, which is a candidate material for a quantum spin liquid because the susceptibility does not show any sign of long-range magnetic order, as mentioned in the previous section.

To confirm the absence of spin ordering/freezing and to investigate the nature of spin excitations, ¹³C-NMR measurements were performed. For the ¹³C-NMR measurements, the thiolketone carbon sites were enriched with ¹³C atoms as shown in Fig. 17.6 (a). Figure 17.6 (b) shows the ¹³C-NMR spectra under 7.65 T down to 19.4 mK for a large number of single crystals with no particular orientation. The spectra do not show large broadening, although very slight gradual broadening is observed at low temperatures. The spectral tails are at most within ± 50 kHz. This width is much smaller than the scale of the hyperfine coupling constant of the ¹³C sites, which is about 9×10^2

**FIGURE 17.6**

(a) $\text{Pd}(\text{dmit})_2$ molecule with selective substitution of ^{13}C isotope. (b) ^{13}C -NMR spectra for randomly oriented samples of $\text{EtMe}_3\text{Sb}[\text{Pd}(\text{dmit})_2]_2$. (c) Temperature dependence of ^{13}C nuclear spin-lattice relaxation rate of the EtMe_3Sb salt. For comparison, we also display that of the EtMe_3P salt, which shows rapid decrease below 25 K owing to a spin-gap transition accompanied by lattice dimerization (see Sec. 17.6.2).

$\text{kHz}/\mu\text{B}$ [12, 13]. This clearly demonstrates that the EtMe_3Sb salt does not undergo spin ordering/freezing down to 19.4 mK. Since this temperature is smaller than 0.01% of J , thermal fluctuations are completely negligible in this temperature regime. Thus, the absence of spin ordering/freezing is unambiguously attributed to quantum fluctuations.

Figure 17.6 (c) displays the spin-lattice relaxation rate T_1^{-1} of the EtMe_3Sb salt down to 1.37 K. The critical divergence of T_1^{-1} , which indicates the critical slowing down of the spin dynamics, is not observed. In addition to the spectral analysis mentioned above, this result also demonstrates the absence of spin ordering/freezing. For comparison, we also present T_1^{-1} of the EtMe_3P salt, which has a spin-gapped ground state and will be discussed in Sec. 17.6.2. Both

salts show similar temperature dependence of T_1^{-1} above 25 K, where T_1^{-1} gradually decreases upon cooling. The EtMe₃P salt shows a rapid decrease of T_1^{-1} below 25 K owing to a spin-gap transition accompanied by lattice dimerization.² In contrast, T_1^{-1} of the EtMe₃Sb salt stops decreasing and retains a finite value below around 5 K. In the present measurement region down to 1.37 K, it does not show any sign of decreasing that is associated with a spin gap. This suggests that the spin excitation of the EtMe₃Sb salt is gapless at least down to 1.37 K, in contrast to the EtMe₃P salt.

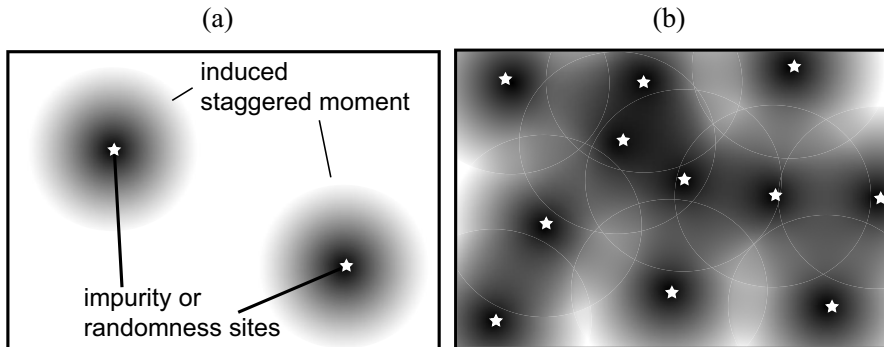


FIGURE 17.7

Sketch of the staggered magnetization nucleated around impurity or randomness sites in the gapless spin-liquid state. The stars signify impurity or randomness sites. The black areas around them indicate the regions where the staggered magnetization is nucleated. The shade of gray corresponds to the amplitude of the magnetization. (a) A clean system in which only a very slight amount of impurity or randomness exists. The outstanding feature of the gapless spin-liquid state is a quasi-long-range spatial spin correlation, which causes a large region of nucleated magnetization around an impurity or randomness site. (b) A somewhat higher concentration of impurities or randomness. Even though the concentration is not very heavy, the quasi-long-range spatial spin correlation will easily cause a spin-glass-like state.

As just described, the EtMe₃Sb salt is considered to show a quantum spin-liquid state which has a gapless excitation at least down to 1.37 K. One may wonder why a slight broadening of the spectrum is observed at low temperatures in such a spin-liquid state, as shown in Fig. 17.6 (b). We shall now discuss this issue.

Despite the broadening, the spin-spin relaxation rate T_2^{-1} remains almost constant over the entire temperature region and is approximately 1×10^3 s⁻¹, which is much smaller than the spectral width. Thus, this broadening is an

²Although a shoulder structure is observed around 3–5 K, this extrinsic relaxation is likely due to remaining unpaired free spins at sites that fail to dimerize [14].

inhomogeneous broadening due to small static field. In addition, the spectral tail is composed of the minor fraction of the spectrum, while the dominant fraction stays at the center with little shift. This means that the small local moment exists only on a minority of the $[\text{Pd}(\text{dmit})_2]_2$ dimers. We should note that the ^{13}C -NMR spectra of another organic spin-liquid candidate with a triangular lattice, $\kappa\text{-}(\text{BEDT-TTF})_2\text{Cu}_2(\text{CN})_3$ ($\text{BEDT-TTF} = \text{bis(ethylenedithio)tetrathiafulvalene}$), also shows a similar inhomogeneous broadening at low temperatures [15]. Thus, such inhomogeneous broadening is considered to be a universal nature of the spin liquid with no appreciable spin gap. We speculate that this is because the gapless spin-liquid state is extremely sensitive to a slight amount of impurity or randomness owing to the quasi-long-range spatial spin correlation. In general, the staggered magnetization nucleated around locally symmetry-broken sites extends for a distance characterized by a spatial spin correlation length. In the ground state, the correlation length is roughly estimated to be J/Δ , where Δ is the spin gap of the system. In the case of the gapless spin liquid with $\Delta \rightarrow 0$, the correlation length diverges and, as a result, a power-law decay of the spatial correlation function is expected. In such a case, even though the amount of impurity or randomness is very slight, we think that it has an appreciable effect on the NMR spectrum because it affects a large area of the system on account of the quasi-long-range spin correlation, as shown in Fig. 17.7 (a). This is likely the reason why the organic spin-liquid materials, which are stoichiometrically clean systems, show inhomogeneous broadening of the NMR spectra. If the concentration of impurity or randomness becomes high to some degree and the distance between these sites becomes short compared to the quasi-long-range spin-correlation decay as shown in Fig. 17.7 (b), the nucleated-magnetization regions overlap and interact with each other, and consequently a spin-glass-like state³ is naturally expected to be realized. We speculate that this is the reason why attempts to seek spin liquids in inorganic materials with frustrated lattices have often resulted in failure. The inorganic materials, more or less, exhibit ion deficiencies/excesses and are not perfectly stoichiometric. Therefore, spin-liquid states with quasi-long-range spin correlation, which was possibly realized in stoichiometrically clean conditions, are easily replaced by the spin-glass-like states. In fact, several inorganic magnetic materials with frustrated lattices are found to have the spin-glass-like ground states [16–18].

Next, we will discuss in detail why the spin-liquid state is realized in EtMe_3Sb salts with a nearly regular-triangular lattice. The orbital wave function on which the spin exists is composed of the HOMO, whose density lies only on the dmit ligands with no contribution of Pd 4d orbitals as mentioned in Sec. 17.3 (Fig. 17.2). Because the wave function spreads only on light elements, the spin-orbit interaction is sufficiently weak and, as a result, the spin-spin exchange interactions of this system are expected to be spherically symmet-

³A spin-glass-like state means a highly disordered state where the expected value of the spin moment at each site, $\langle \mathbf{S}_i \rangle$, is nonzero but varies randomly with the site i .

ric Heisenberg ones. However, it should be noted that a number of theoretical studies suggest that the regular-triangular Heisenberg spin-1/2 system has the 120° spiral ordered ground state [11, 19–21], in contrast to our experimental result. We conceive that the realization of the spin liquid in the EtMe₃Sb salt is explained by the following two scenarios.

One possible reason is slight deviation from the regular triangle. Several theoretical studies on isosceles-triangular Heisenberg systems have suggested that slight deviation from the regular triangle can destroy the spiral-ordered state and realize the spin-liquid state [22–28]. Our result may be rationalized from this standpoint. It is desirable to study whether or not the deviation from the regular-triangle lattice leads to a spin-liquid state even on a scalene-triangular lattice, because our system has a scalene-triangular structure rather than an isosceles one.

Another possible mechanism of the observed spin liquid is explained in light of the proximity of the Mott transition. Although the EtMe₃Sb salt is a Mott insulator, its insulating nature is easily destroyed by a pressure of a few kilobars, as will be discussed in Sec. 17.7.1. This means that its transfer integrals, whose perturbing effect yields exchange interactions, are not much smaller than the electron correlation energy. Therefore, not only the second-order Heisenberg terms, but also the higher order ones are expected to emerge as ring exchange⁴ and long-range Heisenberg interactions. While the nearest-neighbor Heisenberg interactions seem to be predominant, as the temperature dependence of the susceptibility shows, it is possible that such extra higher-order interactions are not negligible and play a significant role in the realization of the present spin liquid. In fact, some theories based on the spin Hamiltonian including ring exchange [29], and the Hubbard Hamiltonian with moderate on-site Coulomb repulsion [30, 31], successfully predict the gapless quantum spin-liquid state.

Lastly, we mention future interest in the present spin-liquid state. We clarified the gapless spin-liquid nature at least down to 1.37 K, as already stated. In general, gapless quantum liquids have instabilities which are not well described by classical crystallization, but rather by quantum mechanics. The best known example is the superconducting or superfluid instability in the Fermi liquid composed of electrons or ³He. In this context, of great interest is whether or not exotic symmetry breaking other than classical magnetic ordering occurs also in the present spin liquid. Actually, theorists have proposed several possible exotic forms of symmetry breaking, such as spinon pairing [32, 33] and chiral order, i.e., a chiral spin liquid [34, 35]. However, it should be noted that the temperature dependence of T_1^{-1} in Fig. 17.6 (c) has no anomaly. This suggests the absence of a phase transition, that is, absence of

⁴The second order perturbation of the transfer integral yields the Heisenberg exchange interaction between two spins, $J\mathbf{S}_1 \cdot \mathbf{S}_2$. In general, the n th order perturbation causes the multiple-spin interaction between n spins, which is called the *ring exchange interaction* for $n \geq 3$. For example, the fourth order perturbation yields ring exchange terms such as $J(\mathbf{S}_1 \cdot \mathbf{S}_2)(\mathbf{S}_3 \cdot \mathbf{S}_4)$.

such exotic forms of symmetry breaking, at least in our experimental systems, in the present measurement region down to 1.37 K. We are now examining whether such forms of symmetry breaking occurs in the EtMe₃Sb salt in a region below 1.37 K. We note that it is difficult to judge from NMR spectra the existence of symmetry breaking other than magnetic ordering, because the spectra mainly reflect the expected value of the spin moment at each site, $\langle \mathbf{S}_i \rangle$, which strongly varies only in the case of magnetic ordering. The spin-lattice relaxation rate and thermal properties will likely be good quantities by which to judge the existence of exotic symmetry breaking, which will appear as second-order quantum phase transitions.

17.6 Other Ground States: Charge Order and Valence Bond Solid

When the deviation from the regular-triangular lattice is large, antiferromagnetic long range order is dominant and the frustration is removed [36, 37]. On the other hand, in the system with a nearly regular-triangular lattice, the spin-liquid state appears to compete with static valence bond formation.

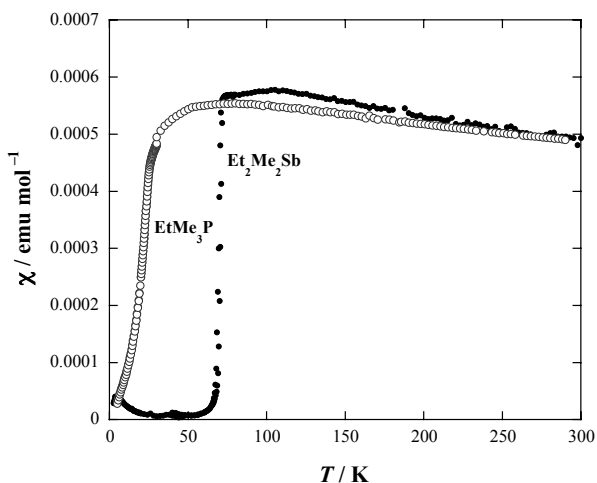
17.6.1 Charge Order Transition in the Et₂Me₂Sb Salt

The Et₂Me₂Sb salt is isostructural with the EtMe₃Sb salt, with no disorder at the cation sites, and has a nearly regular-triangular lattice ($t'/t = 1.01$). However, the magnetic behavior of the Et₂Me₂Sb salt is quite different from that of the EtMe₃Sb salt [38].

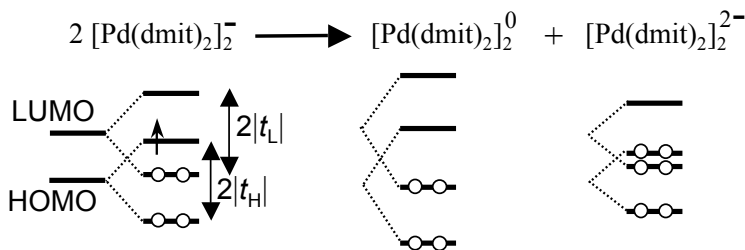
The magnetic susceptibility shows a very sharp first-order transition from the frustrated paramagnetic state to the non-magnetic state at about 70 K (Fig. 17.8) [36]. The low-temperature X-ray crystal structure analysis below the transition temperature revealed a doubling of the *b*-axis and a drastic change in the interplanar distance within the dimer [39]. At room temperature, every dimer has the same interplanar distance (3.233 Å). At 10 K, there exist two crystallographically different dimers; one is expanded (3.362 Å), while the other is constricted (3.047 Å), which is accompanied by decrease and increase of the intradimer transfer integral t_H . The alternating arrangement of stronger (constricted) and weaker (expanded) dimers is observed along the *b* axis.

This phase transition is characterized by charge order (charge separation), $2\text{dimer}^- \rightarrow \text{dimer}^0 + \text{dimer}^{2-}$, where the neutral and divalent dimers correspond to the stronger and weaker ones, respectively. This charge-order transition is associated with the HOMO-LUMO level crossing in the dimer [40].

Because the dimerization gaps ($2|t_H|$ and $2|t_L|$, $|t_H| \sim |t_L|$) are enhanced in the neutral dimer with stronger dimerization, the neutral dimer gains considerable stability due to the HOMO-LUMO double bond; the bonding levels

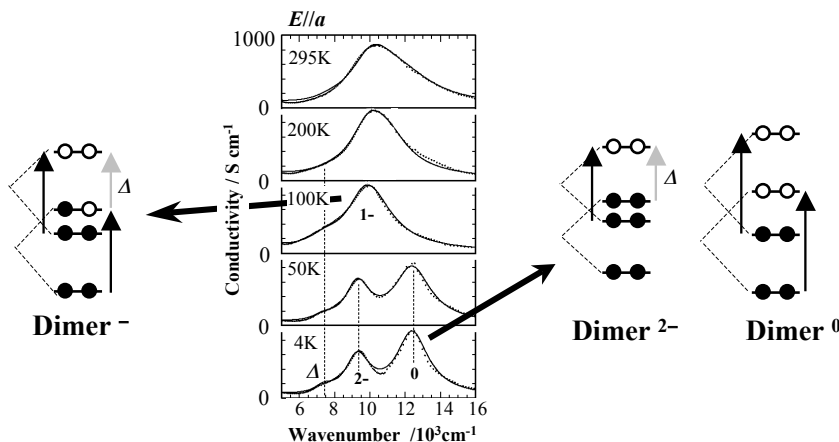
**FIGURE 17.8**

Temperature dependence of magnetic susceptibility for the $\text{Et}_2\text{Me}_2\text{Sb}$ and $\text{Et}\text{Me}_3\text{P}$ salts.

**FIGURE 17.9**

Energy scheme for the charge order transition in the $\text{Et}_2\text{Me}_2\text{Sb}$ salt.

of the HOMO and LUMO are fully occupied, and the antibonding levels are vacant (Fig. 17.9). On the other hand, the divalent dimer is at a disadvantage in the bonding energy. But, the weaker dimerization absorbs this energy cost. Reflectivity spectra were used to probe the charge order directly [41]. The conductivity spectra show a splitting for the bonding-antibonding excitation of the dimer with an intensity ratio of 1:2 below the transition temperature (Fig. 17.10). The splitting in the low temperature phase is consistently ex-

**FIGURE 17.10**

Temperature dependence of conductivity spectra corresponding to the reflectivity spectra in the near-infrared-visible region for the $\text{Et}_2\text{Me}_2\text{Sb}$ salt.

plained by the charge order. This is a new type of charge order transition. It should be noted that this mechanism is possible only for a system with the HOMO-LUMO level crossing.

17.6.2 Valence-Bond Solid State in the EtMe_3P Salt

The spin frustration can be removed by spin singlet formation coupled with lattice distortion. The monoclinic EtMe_3P salt has the parallel column structure with the space group of $P2_1/m$ [42].⁵ The unit cell also contains two crystallographically equivalent conduction layers. There is no disorder at the cation site. In contrast to the solid crossing structure, all anion columns are parallel to each other. However, the anion arrangement within the conduction layer is essentially the same, including the quasi-triangular lattice of the $[\text{Pd}(\text{dmit})_2]^-$ dimer. This EtMe_3P salt also has a nearly regular-triangular lattice ($t'/t = 1.05$). The temperature dependence of the static magnetic susceptibility is well modeled by a spin-1/2 Heisenberg antiferromagnet on a triangular lattice with $J = 250$ K and exhibits a second-order transition to a non-magnetic spin-gapped state at 25 K (Fig. 17.8) [43]. The spin gap is estimated at about 40 K from magnetic susceptibility and multi-frequency-ESR [44].

In the 10 K structure, the stacking period of the dimers is doubled and alternation of the inter-dimer distances and overlap integrals indicate pairing

⁵See *International Tables for Crystallography* for details of this notation.

of the dimers and thus pairing of the spins [42]. Such a singlet state formation coupled with the lattice distortion is similar to the *spin Peierls transition*⁶ in a 1D spin-chain system. But, it should be noted that the present system is 2D. The stability of the 2D singlet-pair order is not trivial. In 2D cases, there is a trade-off between the pairing energy gain and the antiferromagnetic exchange energy, which operates on more than two paths per spin. The elastic energy cost is a key issue for the 2D singlet-pair order. This transition is associated with the parallel column structure. The lattice distortion occurs mainly along the stacking direction. In the solid-crossing column structure where the columns are running along two different directions, such a lattice distortion would cost more elastic energy. In contrast, the parallel column structure has a unique direction of distortion, which minimizes the elastic energy cost.

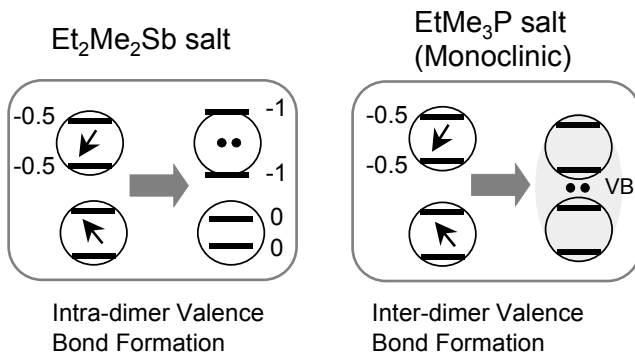
17.6.3 Intra- and Inter-Dimer Valence Bond Formations

The above-mentioned two phase transitions where the spin frustration is removed in the Et₂Me₂Sb and EtMe₃P salts share a common concept, i.e., valence bond formation (Fig. 17.11). Lattice and orbital degrees of freedom play an important role as well as charge degree of freedom. In the Et₂Me₂Sb salt, the transition generates neutral and divalent dimers. The mechanism is possible only for systems with a HOMO-LUMO level crossing, and this transition is classified as intradimer valence bond formation. The EtMe₃P salt also shows a transition towards a spin-singlet state. However, in this case all the dimers are equivalent, even after the transition. The lattice is distorted to form a singlet pair of [Pd(dmit)₂]⁻ dimers and the singlet pairs are ordered in the crystal. This valence bond solid (VBS) state results from inter-dimer valence bond formation. In this strongly correlated 2D system, valence bond formation appears to compete with the spin-liquid state.

17.7 Pressure-Induced Mott Transition

The Mott-insulating state in the Pd(dmit)₂ salts can be removed by application of pressure. The pressure effect depends on the choice of the counter cation.

⁶In a spin-1/2 1D Heisenberg spin chain, the energy gain of valence bond (singlet pair) formation prevails over antiferromagnetic exchange energy removed by the valence bond formation. When the decrease in magnetic free energy due to the valence bond formation outweighs the increase in lattice free energy, a periodic lattice distortion occurs spontaneously at a finite temperature to form a regular array of singlet pairs along the chain. This magneto-elastic transition accompanied by lattice-symmetry breaking is called a spin Peierls transition. In the spin Peierls phase, there is a finite energy gap between the ground state and the excited states.

**FIGURE 17.11**

Intra- and inter-dimer valence bond formations in the Et₂Me₂Sb and EtMe₃P salts.

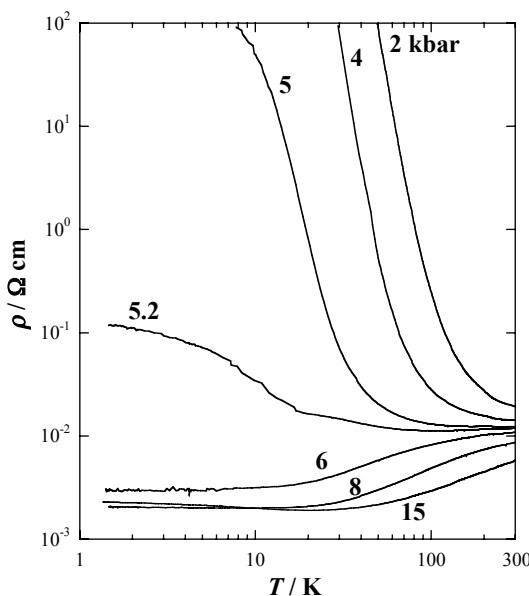
17.7.1 Pressure-Induced Metallic State in the Solid-Crossing Column System

As for the system with the solid-crossing column structure, the Me₄Sb salt with the antiferromagnetic ground state turns metallic and shows superconductivity under hydrostatic pressure ($T_c = 3$ K at 10.1 kbar) [45]. The Mott-insulating state of the system with a higher Néel temperature, or larger anisotropy, cannot be suppressed under the hydrostatic pressure. Even in such a case, uniaxial strain suppresses the non-metallic behavior and induces superconductivity [46, 47]. This indicates that uniaxial strain can effectively reduce electron-electron correlations. The EtMe₃Sb salt with the spin-liquid state also shows metallic behavior under hydrostatic pressure, but no superconductivity is observed up to the highest pressure (Fig. 17.12) [10].

The charge ordering transition in the Et₂Me₂Sb salt is accompanied by a sharp increase of the resistivity under ambient pressure. The application of hydrostatic pressure turns this resistivity anomaly to a metal-insulator transition. This metal-insulator transition is suppressed with increasing pressure.

17.7.2 Phase Diagram for the EtMe₃P Salt: Superconductivity and Valence-Bond Solid

The pressure-temperature phase diagram of the monoclinic EtMe₃P salt with the VBS state is of special interest. Figure 17.13 shows temperature dependence of the resistivity under hydrostatic pressure for the EtMe₃P salt [48]. At 4.0 kbar, an abrupt resistivity drop of more than 3 orders of magnitude occurs in a narrow temperature range, $17 \text{ K} < T < 20 \text{ K}$, showing a first-order insulator-metal (I-M) Mott transition. Below 13 K, a resistivity jump

**FIGURE 17.12**

Temperature dependence of resistivity for the EtMe_3Sb salt under several hydrostatic pressures.

accompanied by thermal hysteresis is observed, which indicates a first-order metal-insulator (M-I) transition. However, the system is still conducting, because there remain metallic domains due to the phase separation associated with the first-order character of the transition. This reentrant Mott transition is followed by the reduction of resistivity below 5.3 K. This is attributed to the formation of percolated superconducting domains which arise from the remaining metallic domains in the predominant insulating phase. With increasing pressure, the reentrant M-I transition is rapidly suppressed and disappears at 4.1 kbar. At the same time, the resistivity drop at 5.3 K becomes much sharper, indicating a superconducting transition in the bulk. The bulk superconductivity in the EtMe_3P salt was confirmed by the magnetic susceptibility measurement under pressure [49,50]. In the pressure (P)-temperature (T) phase diagram (Fig. 17.14), the negative dT/dP slope of the first-order reentrant M-I transition line is consistent with the presence of a VBS state in the low-temperature insulator phase, because the Clapeyron-Clausius relation $dT/dP = \Delta V/\Delta S (< 0)$ requires that the insulator phase has smaller entropy than the metal phase ($\Delta S = S_{\text{ins}} - S_{\text{metal}} < 0$), when the metal phase appears at the high pressure region ($\Delta V = V_{\text{ins}} - V_{\text{metal}} > 0$). The reentrant M-I transition shifts to lower temperature with increasing magnetic field, and

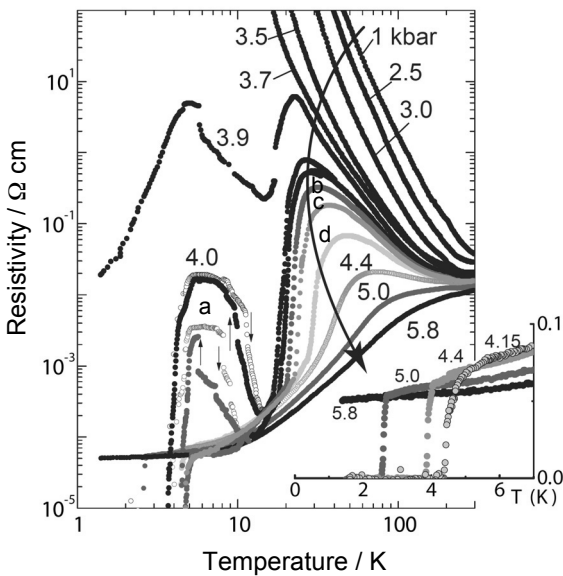


FIGURE 17.13

Temperature dependence of resistivity for the EtMe₃P salt under several hydrostatic pressures ($a = 4.08$, $b = 4.10$, $c = 4.12$, and $d = 4.15$ kbar).

disappears above 10 T. In the magnetic-field-temperature (H - T) phase diagram, the dT/dH slope of the reentrant M-I transition line is negative. This means that the magnetization of the low-temperature insulator phase must be smaller than that of the metal phase ($\Delta M = M_{\text{ins}} - M_{\text{metal}} < 0$), from the thermodynamic relation $dH/dT = -\Delta S/\Delta M$, when ΔS is negative as mentioned above. The result $\Delta M < 0$ strongly indicates that the insulator phase adjacent to the metal and superconductor phases is non-magnetic.

To obtain direct microscopic proof that the insulating phase is non-magnetic in the whole pressure region, and to obtain insight into the nature of the metallic phase, ^{13}C -NMR measurements were also performed under pressure, using enriched molecules shown in Fig. 17.6 (a). The applied magnetic field is 7.65 Tesla, where the superconducting phase is destroyed and replaced by the metallic phase. Figures 17.15 and 17.16 show the NMR spectra and spin-lattice relaxation rates under several pressures, respectively.

In order to determine whether the system was in an insulating or metallic phase, a detailed analysis of the NMR intensity and relaxation curves was carried out [14], and the ground state was found to be insulating for $P < 4.3$ kbar and metallic for $P > 4.3$ kbar. Both these two phases coexist at $P = 4.3$

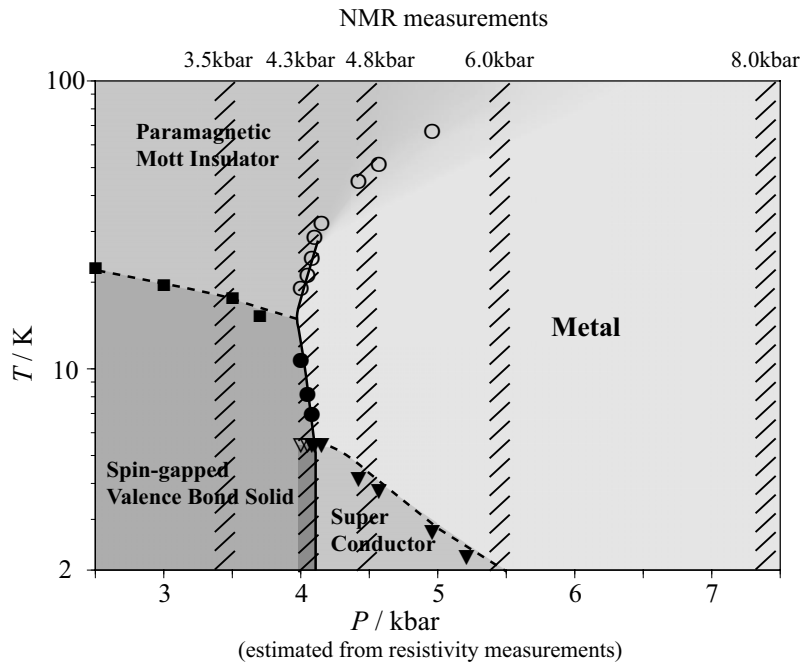


FIGURE 17.14

Pressure-temperature phase diagram of the EtMe₃P salt. The hatched lines indicate pressures where NMR measurements were performed.

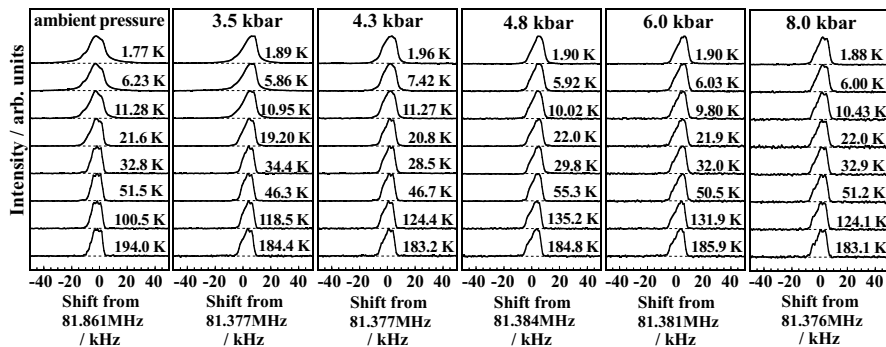


FIGURE 17.15

¹³C-NMR spectra for randomly oriented samples of the EtMe₃P salt at several pressures. All the spectra are sharp and within ± 20 kHz, indicating the absence of magnetic ordering in the whole pressure region.

kbar, which means that the system at 4.3 kbar lies just on the first-order Mott transition line as shown in Fig. 17.14.⁷

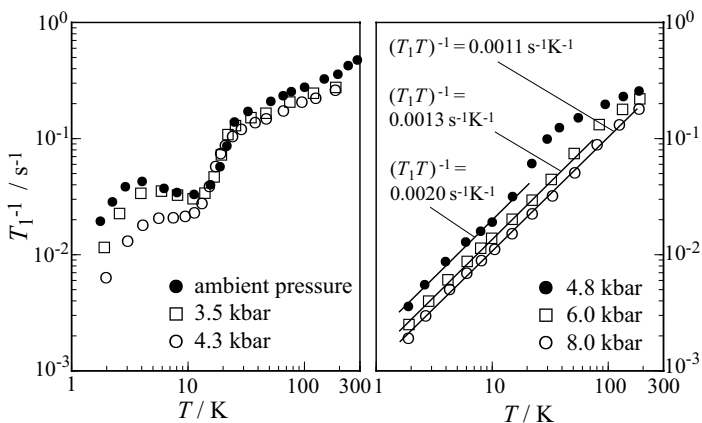


FIGURE 17.16

Temperature dependence of ¹³C nuclear spin-lattice relaxation rate of the EtMe₃P salt at several pressures. The solid lines in the right figure are fits to the Korringa relation $(T_1 T)^{-1} = \text{const}$.

In the metallic phase for $P > 4.3$ kbar, the Korringa relation $T_1^{-1} \propto T$ is observed, as shown in the right of Fig. 17.16. This means that the metallic phase has a Fermi-liquid-like low-energy excitation. Although the present metallic phase borders the spin-gapped insulating phase as will be explained in the next paragraph, the legacy of the spin gap, or the pseudo-spin gap, does not exist in the metallic phase.

In the insulating phase ($P \leq 4.3$ kbar), neither large broadening of the spectra nor critical divergence of T_1^{-1} is observed. Instead, T_1^{-1} shows a rapid decrease below 20–25 K, indicating spin-gap formation.⁸ This clearly proves that, in the insulating phase, the spin-gapped ground state survives over the whole pressure region, and is not replaced by a magnetically ordered state. Therefore, one can definitely conclude that the superconducting phase of the present system borders the spin-gapped VBS insulating phase, as shown in Fig. 17.14. This stands in stark contrast to the phase diagram of the large majority of other correlated-electron superconductors in which the superconducting phase borders a magnetically ordered phase, and therefore suggests the possibility that the present superconductivity has an exotic origin and nature. This remains an open question for future investigation.

⁷A small disagreement on pressures estimated from the resistivity and NMR measurements is caused by difference in pressure estimation methods.

⁸A positive deviation from a gap-type decrease below about 10 K is an extrinsic effect that is likely caused by a slight quantity of remaining unpaired free spins at sites that fail to dimerize [14].

17.8 Conclusion

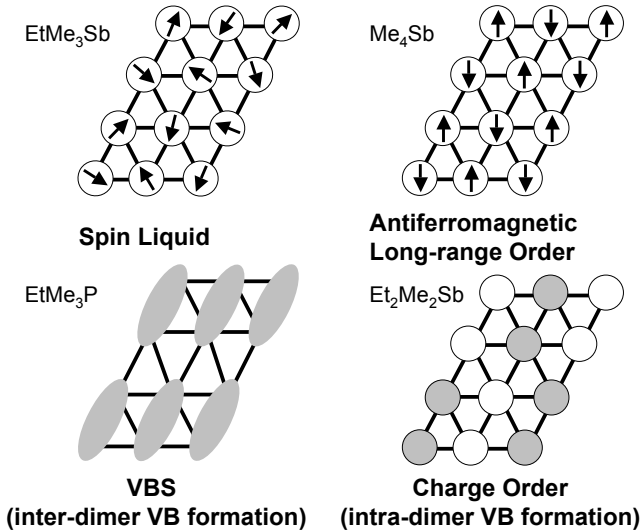


FIGURE 17.17

Schematic ground states for the Mott-insulating $\text{Pd}(\text{dmit})_2$ salts.

The anion radical salts of $\text{Pd}(\text{dmit})_2$ form the dimer Mott system with a quasi-triangular lattice. Anisotropy of the quasi-triangular lattice is controlled by chemical and physical methods, which leads the system to exotic electronic states associated with the interplay between various degrees of freedom, including charge, spin, lattice, and orbital [51].

The EtMe_3Sb salt with a nearly regular-triangular lattice is a quantum spin liquid without trivial symmetry breaking down to 1.37 K. The possibility of nontrivial hidden symmetry breaking and/or topological ordering in the lower temperature region is a quite interesting open issue. Replacement of one methyl group with an ethyl group at the cation site ($\text{Et}_2\text{Me}_2\text{Sb}$) results in a charge ordered state, and replacement of the central atom (EtMe_3P) leads to a valence-bond-solid state which borders the superconducting state. Both salts also have a nearly regular-triangular lattice. Parameters which induce a difference in the ground state between the EtMe_3Sb , $\text{Et}_2\text{Me}_2\text{Sb}$, and EtMe_3P salts, as well as roles of charge and lattice fluctuations in the quantum critical phenomena, are unanswered outstanding questions for the comprehensive understanding of the $\text{Pd}(\text{dmit})_2$ system. Finally, replacement of one ethyl group (Me_4Sb) leads to an antiferromagnetic long-range order

(Fig. 17.17). In this system, one should consider an effect of frustration on the spin dynamics in a thermal transition toward an antiferromagnetic long-range order. An important aspect which was not treated in this manuscript is that we can easily obtain mixed crystals (alloys) in an isostructural series (for example, $(\text{Me}_4\text{Sb})_x(\text{EtMe}_3\text{Sb})_{1-x}[\text{Pd}(\text{dmit})_2]_2$). This provides a powerful experimental tuning knob for the quantum fluctuations.

The Pd(dmit)₂ system is an excellent playground for strongly correlated 2D electrons on a quasi-triangular lattice with tunable parameters. The ground state of the Pd(dmit)₂ system varies drastically with slight modifications of the counter cation. This system will be, therefore, a treasury of QPT physics, if future studies directly observe the change between these states by hyper-fine tuning such as uniaxial strain/extension [52] and cation mixing.

Bibliography

- [1] P.W. Anderson, Mater. Res. Bull. **8**, 153 (1973).
- [2] S. Kagoshima, R. Kato, H. Fukuyama, H. Seo, and H. Kino, in *Advances in Synthetic Metals - Twenty Years of Progress in Science and Technology*, edited by P. Bernier, S. Lefrant, and G. Bidan (Elsevier, Amsterdam, 1999), p. 262.
- [3] R. Kato, Chem. Rev. **104**, 5319 (2004).
- [4] E. Canadell, S. Ravy, J.-P. Pouget, and L. Brossard, Solid State Commun. **75**, 633 (1990).
- [5] H. Tajima, T. Naito, M. Tamura, A. Kobayashi, H. Kuroda, R. Kato, H. Kobayashi, R.A. Clark, and A.E. Underhill, Solid State Commun. **79**, 337 (1991).
- [6] R. Kato, Y.-L. Liu, H. Sawa, S. Aonuma, A. Ichikawa, H. Takahashi, and N. Mori, Solid State Commun. **94**, 973 (1995).
- [7] T. Miyazaki and T. Ohno, Phys. Rev. B **59**, R5269 (1999).
- [8] M. Tamura and R. Kato, J. Phys. Soc. Jpn. **73**, 3108 (2004).
- [9] M. Tamura and R. Kato, J. Phys.: Condens. Matter **14**, L729 (2002).
- [10] R. Kato, A. Tajima, A. Nakao, N. Tajima, and M. Tamura, in *Multi-functional Conducting Molecular Materials*, edited by G. Saito, F. Wudl, R.C. Haddon, K. Tanigaki, T. Enoki, H.E. Katz, and M. Maesato (RSC Publishing, Cambridge, 2007), p. 32. [Erratum] Caption of Figure 4 in page 35 should be corrected to “right; Cation = EtMe₃Sb, left; Cation = EtMe₃As.”

- [11] N. Elstner, R.R.P. Singh, and A.P. Young, Phys. Rev. Lett. **71**, 1629 (1993).
- [12] T. Itou, A. Oyamada, S. Maegawa, M. Tamura, and R. Kato, J. Phys.: Condens. Matter **19**, 145247 (2007).
- [13] T. Itou, A. Oyamada, S. Maegawa, M. Tamura, and R. Kato, Phys. Rev. B **77**, 104413 (2008).
- [14] T. Itou, A. Oyamada, S. Maegawa, K. Kubo, H.M. Yamamoto, and R. Kato, Phys. Rev. B **79**, 174517 (2009).
- [15] Y. Shimizu, K. Miyagawa, K. Kanoda, M. Maesato, and G. Saito, Phys. Rev. B **73**, 140407(R) (2006).
- [16] A.P. Ramirez, G.P. Espinosa, and A.S. Cooper, Phys. Rev. Lett. **64**, 2070 (1990).
- [17] M.J.P. Gingras, C.V. Stager, N.P. Raju, B.D. Gaulin, and J.E. Greedan. Phys. Rev. Lett. **78**, 947 (1997).
- [18] H. Takeya, K. Ishida, K. Kitagawa, Y. Ihara, K. Onuma, Y. Maeno, Y. Nambu, S. Nakatsuji, D.E. MacLaughlin, A. Koda, and R. Kadono, Phys. Rev. B **77**, 054429 (2008).
- [19] D.A. Huse and V. Elser, Phys. Rev. Lett. **60**, 2531 (1988).
- [20] B. Bernu, P. Lecheminant, C. Lhuillier, and L. Pierre, Phys. Rev. B **50**, 10048 (1994).
- [21] L. Capriotti, A.E. Trumper, and S. Sorella, Phys. Rev. Lett. **82**, 3899 (1999).
- [22] W. Zheng, R.H. McKenzie, and R.R.P. Singh, Phys. Rev. B **59**, 14367 (1999).
- [23] J. Merino, R.H. McKenzie, J.B. Marston, and C.H. Chung, J. Phys.: Condens. Matter **11**, 2965 (1999).
- [24] A.E. Trumper, Phys. Rev. B **60**, 2987 (1999).
- [25] L.O. Manuel and H.A. Ceccatto, Phys. Rev. B **60**, 9489 (1999).
- [26] C.H. Chung, J.B. Marston, and R.H. McKenzie, J. Phys.: Condens. Matter **13**, 5159 (2001).
- [27] J. Alicea, O.I. Motrunich, and M.P.A. Fisher, Phys. Rev. B **73**, 174430 (2006).
- [28] S. Yunoki and S. Sorella, Phys. Rev. B **74**, 014408 (2006).
- [29] O.I. Motrunich, Phys. Rev. B **72**, 045105 (2006).

- [30] S.-S. Lee and P.A. Lee, Phys. Rev. Lett. **95**, 036403 (2005).
- [31] T. Mizusaki and M. Imada, Phys. Rev. B **74**, 014421 (2006).
- [32] S.-S. Lee, P.A. Lee, and T. Senthil, Phys. Rev. Lett. **98**, 067006 (2007).
- [33] V. Galitski and Y.B. Kim, Phys. Rev. Lett. **99**, 266403 (2007).
- [34] V. Kalmeyer and R.B. Laughlin, Phys. Rev. Lett. **59**, 2095 (1987).
- [35] G. Baskaran, Phys. Rev. Lett. **63**, 2524 (1989).
- [36] M. Tamura and R. Kato, Polyhedron **24**, 2817 (2005).
- [37] S. Ohira, M. Tamura, R. Kato, I. Watanabe, and M. Iwasaki, Phys. Rev. B **70**, 220404(R) (2004).
- [38] M. Tamura, A. Tajima, and R. Kato, Synth. Met. **152**, 397 (2005).
- [39] A. Nakao and R. Kato, J. Phys. Soc. Jpn. **74**, 2754 (2005).
- [40] M. Tamura and R. Kato, Chem. Phys. Lett. **387**, 448 (2004).
- [41] M. Tamura, K. Takenaka, H. Takagi, S. Sugai, A. Tajima, and R. Kato. Chem. Phys. Lett. **411**, 133 (2005).
- [42] R. Kato, A. Tajima, A. Nakao, and M. Tamura, J. Am. Chem. Soc. **128**, 10016 (2006).
- [43] M. Tamura, A. Nakao, and R. Kato, J. Phys. Soc. Jpn. **75**, 093701 (2006).
- [44] H. Ohta, S. Okubo, N. Souda, M. Tomoo, T. Sakurai, T. Yoshida, E. Ohmichi, M. Fujisawa, H. Tanaka, and R. Kato, Appl. Magn. Reson. **35**, 399 (2009).
- [45] Y. Kashimura, Doctoral Thesis, The University of Tokyo, 1998.
- [46] R. Kato, N. Tajima, M. Tamura, and J.-I. Yamaura, Phys. Rev. B **66**, 020508(R) (2002).
- [47] A. Tajima, A. Nakao, and R. Kato, J. Phys. Soc. Jpn. **74**, 412 (2005).
- [48] Y. Shimizu, H. Akimoto, H. Tsujii, A. Tajima, and R. Kato, Phys. Rev. Lett. **99**, 256403 (2007).
- [49] Y. Ishii, M. Tamura, and R. Kato, J. Phys. Soc. Jpn. **76**, 033704 (2007).
- [50] M. Tamura, Y. Ishii, and R. Kato, J. Phys.: Condens. Matter **19**, 145239 (2007).
- [51] M. Tamura and R. Kato, Sci. Technol. Adv. Mater. **10**, 024304 (2009).
- [52] T. Yamamoto, R. Kato, H.M. Yamamoto, A. Fukaya, K. Yamasawa, I. Takahashi, H. Akutsu, A. Akutsu-Sato, and P. Day, Rev. Sci. Instrum., **78**, 083906 (2007).

18

Probing Quantum Criticality and its Relationship with Superconductivity in Heavy Fermions

Philipp Gegenwart

First Physics Institute, University of Göttingen, Germany

Frank Steglich

Max Planck Institute for Chemical Physics of Solids, Dresden, Germany

Quantum many-body systems may undergo a quantum phase transition (QPT), i.e., a transformation between different types of order at zero temperature. A QPT is driven by a non-thermal control parameter like pressure; if continuous, it takes place at a quantum critical point (QCP). During the past years, the investigation of QCPs has become a fascinating area of condensed-matter research on a variety of material classes, ranging from insulating quantum magnets to conducting transition-metal oxides and heavy-fermion (HF) metals [1]. Antiferromagnetic (AF) HF metals have emerged as model systems to explore quantum criticality and its potential to give way to novel phases, notably superconductivity. Moreover, recent studies concerning the interrelationship between the Kondo effect and magnetic correlations in these systems revealed two qualitatively different types of QCPs.

In this chapter, we present a short review of the physics of HFs, before addressing HF quantum criticality and its interplay with unconventional superconductivity. The chapter is concluded by summarizing a number of unsettled questions.

18.1 Heavy Fermions

Within the last three decades, an increasing number of rare-earth (RE) and actinide-based intermetallic compounds have been found to exhibit anomalous

physical properties: whereas at high temperatures they normally show clear indications of f -electron-derived local magnetic moments, the low-temperature properties can be best explained by the existence of itinerant, albeit very heavy, fermions. There are numerous manifestations of these HF phenomena to derive from the local Kondo interaction [2] which, at high temperatures, implies a tiny energetic preference of the conduction electrons to align their spins antiparallel to the local f spins. Upon cooling to well below the characteristic Kondo temperature T_K , typically between a few K and about 100 K, this AF coupling becomes very strong such that, eventually, the local moment is fully screened by the conduction electrons: the ground state of this *Kondo singlet* is an entangled state between the local $4f$ spin and the conduction electrons, $\sqrt{1/2}(|\uparrow\rangle_f|\downarrow\rangle_c - |\downarrow\rangle_f|\uparrow\rangle_c)$.¹ In a periodic lattice of Kondo ions, the *Kondo lattice*, Bloch's theorem causes the Kondo singlets to couple coherently and act as *composite* charge carriers with internal quantum numbers which are identical to those of the bare electron, i.e., spin $\hbar/2$ and charge e. The mobility of these carriers is vastly reduced by the local Coulomb repulsion which prevents double occupancy of the f sites. Therefore, the composite charge carriers exhibit a very small Fermi velocity v_F^* or, correspondingly, a large effective mass, $m^* \approx 100 - 1000 m_{el}$, m_{el} being the mass of the bare electron [3].

HF phenomena were first observed in the low-temperature thermodynamic and transport properties of the hexagonal intermetallic CeAl₃ [4], which resemble those of the charge-neutral heavy Landau Fermi liquid (LFL) system ³He [5]. Therefore, the obvious question arose whether an HF metal like CeAl₃ could possibly show a superconducting state, phenomenologically related to the superfluidity of ³He [5]. No surprise, the subsequent discovery of superconductivity (SC) in the HF metal CeCu₂Si₂ [6] initiated worldwide research activities in HF physics. Because of their small Fermi velocity, the heavy charge carriers in CeCu₂Si₂ cannot escape their own polarization cloud. Therefore, electron-phonon coupling had to be discarded as the major Cooper-pairing mechanism [6]. It was proposed instead that, similar to superfluidity in ³He, SC in CeCu₂Si₂ as well as in its U-based counterparts UBe₁₃ [7], UPt₃ [8] and URu₂Si₂ [9] is driven magnetically [10, 11]. This implied highly anisotropic non-s-wave superconducting order parameters, which had indeed been inferred from the measured non-exponential temperature dependences of the electronic specific heat, $C_{el}(T)$, and related properties [3]. As far as the spin state of the Cooper pairs is concerned, early measurements of the upper critical field, $H_{c2}(T)$, in CeCu₂Si₂ had highlighted even-parity spin-singlet $S = 0$ SC [12], in contrast to the spin-triplet pair state in superfluid ³He [5].

¹Recall that a state of this form is called a *spin singlet* and is maximally entangled: a partial trace over one spin yields a completely mixed density matrix for the other.

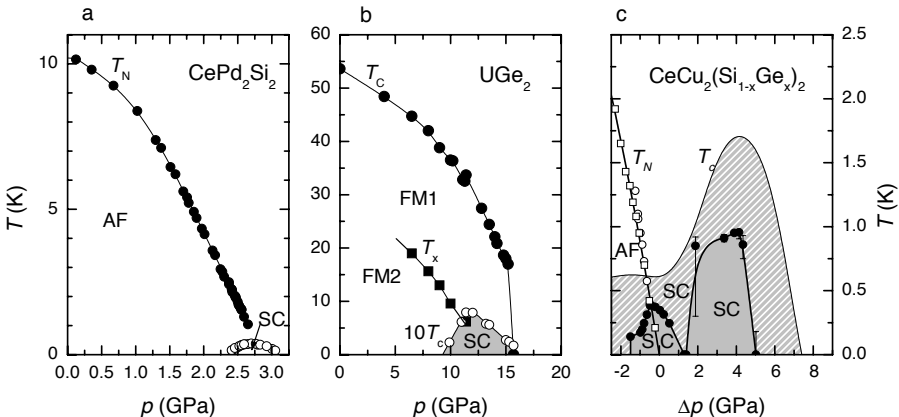
18.2 Heavy Fermi Liquids and Antiferromagnets

HF metals have been considered prototypes of heavy LFLs. Here, the composite quasiparticles are adiabatically connected to the bare conduction electrons, dressed by the local spin entropy and giving rise to a huge *Kondo resonance* at the Fermi energy. Due to the entanglement in the Kondo singlets, the local moments have to be counted in the Fermi volume, resulting in a large Fermi surface [13]. Common properties of the heavy LFLs are a T^2 -dependence of the electrical resistivity, $\rho(T) = \rho_0 + AT^2$ (ρ_0 is the residual resistivity), a linear T -dependence of $C_{\text{el}} = \gamma T$ and a temperature-independent Pauli spin susceptibility, $\chi = \chi_0$. Because of the huge effective mass, A, γ and χ_0 adopt correspondingly huge values. The quasiparticles experience some residual interactions, described by Landau parameters. Most frequently, AF order, mediated by the indirect exchange Ruderman-Kittel-Kasuya-Yosida (RKKY) interaction [14–16], and SC are observed.

The large number of HF antiferromagnets may be divided [3] into those systems whose magnetic ordering temperature T_N is of comparable magnitude to the Kondo temperature T_K , like CeAl₂ [17,18], and those with $T_N \ll T_K$; the former, for which $T_N \sim T_K$, are called *local-moment* magnets, while the latter are called *itinerant HF* antiferromagnets. The transition from local-moment to itinerant HF antiferromagnetism was studied, e.g., in Ce(Cu_{1-x}Ni_x)₂Ge₂ as a function of increasing Ni concentration [19]. More recently, itinerant HF magnetism, i.e., spin-density-wave (SDW) order, could be verified via neutron-diffraction in CeCu₂Si₂ [20]. AF inter-site correlations have been found to exist in the heavy LFL phase and to compete with local on-site Kondo fluctuations: in a thorough study of the inelastic neutron scattering (INS) on CeCu₆ and CeRu₂Si₂, Rossat-Mignod *et al.* [21] revealed quite different weights of the inter-site correlations relative to on-site ones. While meta-magnetic CeRu₂Si₂ exhibits 40 % of the former, in the case of CeCu₆ they amount to only 10% [21]. No surprise, single-ion Kondo behavior dominates at low T up to large values of x in (La_{1-x}Ce_x)Cu₆ [22]. Also, no magnetic order is found in these alloy systems, despite the La-induced volume expansion, which generally weakens the Kondo interaction relative to the RKKY interaction in Ce-based HF systems. On the other hand, in (La_{1-x}Ce_x)Ru₂Si₂ long-range AF order develops above $x_c \approx 0.075$ [23].

18.3 Heavy-Fermion Superconductors

Heavy-fermion superconductivity (HFSC), which has by now been observed in more than 35 compounds, frequently exists in the vicinity of some kind of instability, cf. Fig. 18.1. The compound CePd₂Si₂ [24], the prototype of sev-

**FIGURE 18.1**

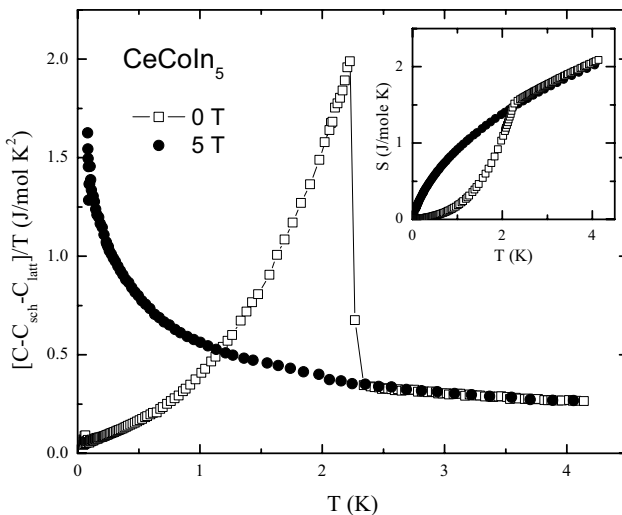
Superconductivity (SC) near magnetic and valence instabilities in temperature-pressure phase diagrams. (a) Antiferromagnetism below T_N and SC for CePd_2Si_2 [24]. (b) Curie temperature T_C , transition temperature T_x between two ferromagnetic states and superconducting transition temperature T_c versus pressure for UGe_2 [25]. (c) T_N and T_c for $\text{CeCu}_2(\text{Si}_{1-x}\text{Ge}_x)_2$ versus pressure increment $\Delta p = p - p_{c1}(x)$ with $p_{c1}(0) \approx 0$ and $p_{c1}(0.1) = 1.5$ GPa. Superconducting regions for $x = 0$ and $x = 0.1$ are indicated as shaded and filled regions, respectively [28].

eral Ce-based pressure (p)-induced superconductors, exhibits a narrow dome of SC around the critical pressure $p_c \approx 2.8$ GPa, necessary to destroy AF order (Fig. 18.1(a)). A few U-based compounds, like UGe_2 [25], become superconducting within a ferromagnetically ordered state (Fig. 18.1(b)). Undoped CeCu_2Si_2 [26], like CeCu_2Ge_2 [27], shows SC in a wide pressure range. However, upon doping the former compound with 10 at% Ge,² two distinct superconducting domes emerge [28] (Fig. 18.1(c)) with substantially reduced T_c . The low- p dome occurs around an AF instability near $p = 0$, resembling the case of CePd_2Si_2 . The second dome is centered around the critical pressure $p_c \approx 5.5$ GPa at which, presumably, a weak valence transition of Ce takes place [28].

U-based and related compounds. While most of the HF superconductors exhibit a highly anisotropic, even-parity $S = 0$ order parameter, presumably of d -wave type, a few U-based compounds are considered prime candidates for odd-parity ($S = 1$) pairing. In all of them, SC coexists with long-range magnetic order, either of AF (UPt_3 [29], UNi_2Al_3 [30]) or ferromagnetic (FM) nature (UGe_2 [25], URhGe [31], UCoGe [32]).

The weak antiferromagnet UPt_3 ($T_N \approx 5$ K [33]) has attracted much attention in the past, because it shows different superconducting phases, similar

²In $\text{CeCu}_2(\text{Si}_{0.9}\text{Ge}_{0.1})_2$ 10% of the Si atoms have been substituted by Ge.

**FIGURE 18.2**

Temperature dependence of the Sommerfeld coefficient, $C_{\text{el}}(T)/T$, of CeCoIn₅ at zero magnetic field and $H = 5$ T, with H parallel to the c-axis. Inset shows the entropy recovered as a function of temperature in the superconducting (open squares) and field-induced normal (solid circles) state, respectively [44].

to the different superfluid phases of ³He [5]. Multi-phase diagrams were also established for thorianated UBe₁₃ [34] as well as for PrOs₄Sb₁₂ [35], a unique HF superconductor in which quadrupolar rather than dipolar fluctuations are believed to mediate the formation of the Cooper pairs.

Neutron-diffraction experiments on UPt₃ revealed the first experimental evidence for magnetically-driven SC, i.e., by a drop in the magnetic scattering intensity observed upon cooling through $T_c \approx 0.5$ K [33]. A combined analysis of inelastic neutron-scattering (INS) [36] and quasiparticle-tunneling results [37] on UPd₂Al₃ ($T_c = 2$ K [38]) suggested that in this local-moment antiferromagnet ($T_N = 14.3$ K [38], $\mu_{\text{ord}} \approx 0.85\mu_B/U$ [39]),³ with unconventional superconducting order parameter [40], it is the acoustic magnon at the AF ordering wave vector which provides the glue for SC [36].

Ce-based and related compounds. Motivated by the theoretical prediction of AF spin-fluctuation-mediated HFSC [10, 11], *p*-induced SC in a substantial number of clean, stoichiometric Ce-based HF antiferromagnets was detected during the last two decades. Early examples were CeCu₂Ge₂ [27] and CeRh₂Si₂ [41], which both lose their AF order *discontinuously* at a critical pressure p_c . In either case, heavy LFL phenomena are observed in the low-temperature normal state at $p \geq p_c$ [42, 43]. By contrast, strong deviations

³ μ_{ord} denotes the 5f-derived magnetic moment of U in the $T \rightarrow 0$ limit of the antiferromagnetically ordered state, as determined by neutron diffractometry.

from LFL behavior are observed in the normal state of many *p*-induced HF superconductors. Such non-Fermi-liquid (NFL) effects are ascribed to the critical fluctuations associated with a QCP ($p = p_c$) at which AF order disappears *continuously*.

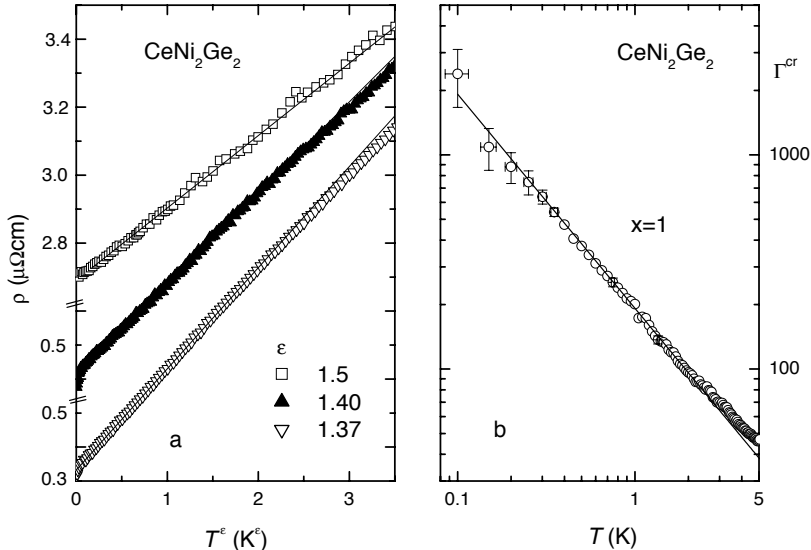
It is interesting to note that the majority of recently discovered *NFL superconductors* belong to two distinct families of intermetallics, namely (i) the $\text{Ce}_n\text{T}_m\text{In}_{3n+2m}$ systems,⁴ like CeCoIn_5 [44], Ce_2RhIn_8 [45] and, more recently, Ce_2PdIn_8 [46] and (ii) the non-centrosymmetric HF superconductors whose crystal structure is lacking a center of inversion symmetry, CePt_3Si being the prototypical example [47]. The former compounds can be regarded as quasi-two-dimensional (2D) variants of cubic CeIn_3 , a *p*-induced superconductor with very low T_c (≈ 0.2 K) [24]. They were synthesized by stacking alternating layers of CeIn_3 and TIn_2 sequentially along the *c*-axis. The observation that CeCoIn_5 exhibits SC at T_c as high as 2.3 K nicely confirmed the theoretical prediction [48] of substantially enhanced T_c values in quasi-2D, AF spin-fluctuation-mediated superconductors relative to their 3D counterparts. Fig. 18.2 demonstrates that for this compound a large molar spin entropy, almost 30% of $R\ln 2$,⁵ is released just below T_c , which is recovered in the normal state at low temperatures. These data suggest that low-lying spin fluctuations are involved in the Cooper-pair formation on the one hand and cause the pronounced increase of the Sommerfeld coefficient $\gamma(T) = C_{\text{el}}(T)/T$ upon cooling within the normal state on the other. These spin fluctuations have to be associated with an AF QCP which in CeCoIn_5 is, however, masked by SC [49].

A further drastic increase of T_c could be achieved in the 115 systems when Ce, with well localized *4f* shell, was replaced by Pu, whose *5f* shell is spatially more extended. This way, $T_c = 8.7$ K for PuRhGa_5 [50] and even 18.5 K for PuCoGa_5 [51], the world record in HFSC, were observed. The compound NpPd_5Al_2 , with a different crystal symmetry, is another actinide-based HF superconductor showing an enhanced T_c of 4.9 K [52].

In the non-centrosymmetric system CePt_3Si , HFSC coexists below $T_c = 0.75$ K with AF order ($T_N = 2.2$ K) [47]. The antiferromagnet CeIrSi_3 , which is lacking inversion symmetry as well, exhibits a wide superconducting dome at elevated pressure [53]. The putative QCP ($T_N \rightarrow 0$) is extrapolated to be close to $p \approx 2.6$ GPa, where T_c assumes its maximum value (1.7 K). This is typical for Ce-based *p*-induced HF superconductors, cf. Figs. 18.1(a) and (c). Interestingly, for the related U-based system UIr , SC (below $T_c = 0.15$ K) is found to coexist with FM order [54]. The group of non-centrosymmetric superconductors has attracted much theoretical interest, because the lack of inversion symmetry allows for a mixing of even-parity and odd-parity pair states, the degree of this mixing depending on the strength of the antisymmetric spin-orbit coupling [55, 56]. This was clearly demonstrated by comparing $\text{Li}_2\text{Pt}_3\text{B}$

⁴We use T to indicate certain transition metals.

⁵ $R = k_B N_A$ is the Gas constant; k_B and N_A are the Boltzmann constant and Avogadro's number, respectively.

**FIGURE 18.3**

SDW-type quantum criticality in the HF metal CeNi_2Ge_2 . (a) Electrical resistivity as a function of temperature for three high-quality samples with increasing residual resistivity (from bottom to top). Lines display power-law temperature dependences $\Delta\rho = (\rho - \rho_0) \sim T^\varepsilon$ [66]. (b) Temperature dependence of the critical Grüneisen ratio for single crystalline CeNi_2Ge_2 in a log-log plot. Line represents $\Gamma^{\text{cr}} \propto T^{-x}$ with $x = 1$ [68].

with its Pd homologue, two non-centrosymmetric superconductors lacking any magnetic and HF properties [57].

As discussed before, many of the HF superconductors exhibit a NFL normal state, hinting at a nearby AF QCP. In the following sections, we describe the two different QCP scenarios relevant for HF metals, before addressing the interplay between quantum criticality and unconventional SC.

18.4 Spin-Density-Wave-Type Quantum Criticality

The magnetic QPT in HF metals arises from the competition of the Kondo effect with the RKKY interaction, which both depend on the coupling $g = N_F|J|$, where N_F is the conduction-band density of states at the Fermi energy, E_F , and $J < 0$ is the local f -conduction electron exchange integral [58]. For sufficiently strong coupling the Kondo effect dominates, leading to a para-

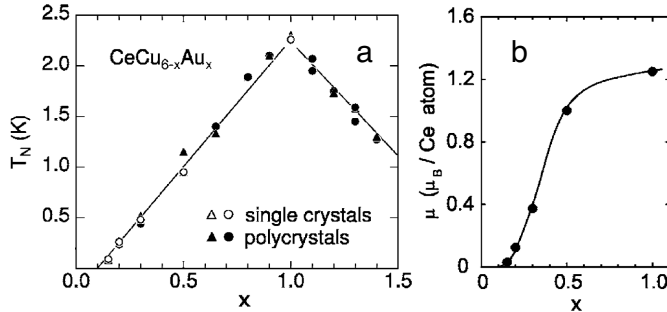
magnetic heavy LFL ground state, in which the f -electrons are completely delocalized and contribute to a large Fermi-surface volume. Upon reducing the coupling constant g below a critical value g_c , e.g., by volume expansion in Ce-based HF metals, a magnetically ordered ground state may emerge either (i) as SDW instability of the heavy LFL state or (ii) as local-moment type of ordering. The main distinction between these two magnetically ordered states is the size of the Fermi-surface volume, which remains large upon entering the former state, but is small in the latter case, in which the f -electrons are localized due to a breakdown of Kondo-singlet formation. In the SDW scenario, the heavy fermions stay intact at the magnetic instability. Their scattering off the critical SDW fluctuations gives rise to NFL behavior, which has been treated by the renormalization-group analysis [59–61] and by the self-consistently renormalized (SCR) formalism [62], respectively.

Since singular scattering is restricted to certain *hot lines* at the Fermi surface, connected by the critical \mathbf{Q} -vector of the nearby SDW order, large parts of the Fermi surface remain normal for 3D critical fluctuations in this scenario. Therefore, the quasiparticle mass saturates upon approaching the QCP.⁶ In the temperature-dependent part of the low- T electrical resistivity, $\Delta\rho(T)$, an anomalous $T^{3/2}$ contribution arises from the scattering near the hot lines. However, as first realized by Hlubina and Rice [63], the ordinary quasiparticle-quasiparticle scattering events of all other states on the Fermi surface result in the usual T^2 law, which should short-circuit the anomalous $T^{3/2}$ term, at sufficiently low temperatures. Nevertheless, a T^2 dependence appears to be almost unobservable in real systems, since small amounts of disorder always lead to a crossover behavior with exponents ranging between 1.5 in the dirty case to 1.0 in the very clean case [64]. Indications for such SDW-type quantum criticality in the electrical resistivity have been found in the stoichiometric HF metal CePd₂Si₂ near the critical pressure [65] as well as for CeNi₂Ge₂, which already at ambient pressure is located very close to an AF QCP [66]. As shown in Fig. 18.3(a), the low- T electrical resistivity of three CeNi₂Ge₂ samples with decreasing residual resistivity displays a clear variation of the low- T exponent between 1.5 and 1.37 over more than one decade in temperature.

It has been pointed out that the volume thermal expansion, β , and the Grüneisen ratio, $\Gamma \propto \beta/C_{\text{el}}$, are powerful tools to investigate the nature of quantum criticality in HF metals [67] and, specifically, to distinguish between the two scenarios mentioned above. Due to the entropy accumulation close to the QCP, divergent behavior in the Grüneisen ratio is expected. For a CeNi₂Ge₂ single crystal [68], $\beta(T) = aT + b\sqrt{T}$ and $C_{\text{el}}(T)/T = \gamma_0 - c\sqrt{T}$ over nearly two decades in temperature have been observed, resulting in a *critical* Grüneisen ratio⁷ which diverges like T^{-1} , as shown in Fig. 18.3(b). This temperature dependence is in full agreement with the prediction of the

⁶For 2D critical fluctuations, theory predicts a logarithmic mass divergence.

⁷After subtraction of constant LFL contributions to β/T and C_{el}/T .

**FIGURE 18.4**

Quantum critical point in $\text{CeCu}_{6-x}\text{Au}_x$. (a) Néel temperature T_N versus Au concentration x [73, 74]. (b) Staggered moment per Ce^{3+} -ion extracted from neutron diffractometry [77].

SDW scenario for an AF QCP [67]. Similar behavior was observed in the vicinity of other HF QCPs, too [69, 70].

Evidence for a 3D SDW QCP has also been found in INS experiments on $\text{Ce}_{1-x}\text{La}_x\text{Ru}_2\text{Si}_2$ near the critical concentration $x_c \approx 0.075$ [71]. Furthermore, quantum criticality in the archetypical HF superconductor CeCu_2Si_2 [6], which is related to the suppression of SDW ordering [20], is also consistent with the predictions of the itinerant theory [72] (see Sec. 18.6).

18.5 Quantum Criticality Beyond the Conventional Scenario

Strong indications for quantum criticality incompatible with the predictions of SDW theory have been found in the two prototypical systems $\text{CeCu}_{6-x}\text{Au}_x$ [73, 74] and YbRh_2Si_2 [75, 76]. The $T - x$ phase diagram (Fig. 18.4(a)) of the former system, together with the *continuous* evolution of the ordered moment (Fig. 18.4(b)), proves the existence of an AF QCP.

For quantum critical $\text{CeCu}_{5.9}\text{Au}_{0.1}$ the Sommerfeld coefficient displays a logarithmic divergence between 0.06 K and ~ 2.5 K [73]. Very similar specific-heat data have also been obtained for $x = 0.2$ and $x = 0.3$ at hydrostatic pressures of 0.41 GPa and 0.82 GPa, respectively [78], demonstrating the universality of this NFL behavior. INS results on $\text{CeCu}_{5.9}\text{Au}_{0.1}$ [79] show that the critical magnetic fluctuations are strongly anisotropic and extend on four rods, related to the orthorhombic symmetry, in \mathbf{q} -space. The origin of this strong magnetic anisotropy is not clear up to now. While 2D SDW quantum critical fluctuations can explain the observed logarithmic divergence of the

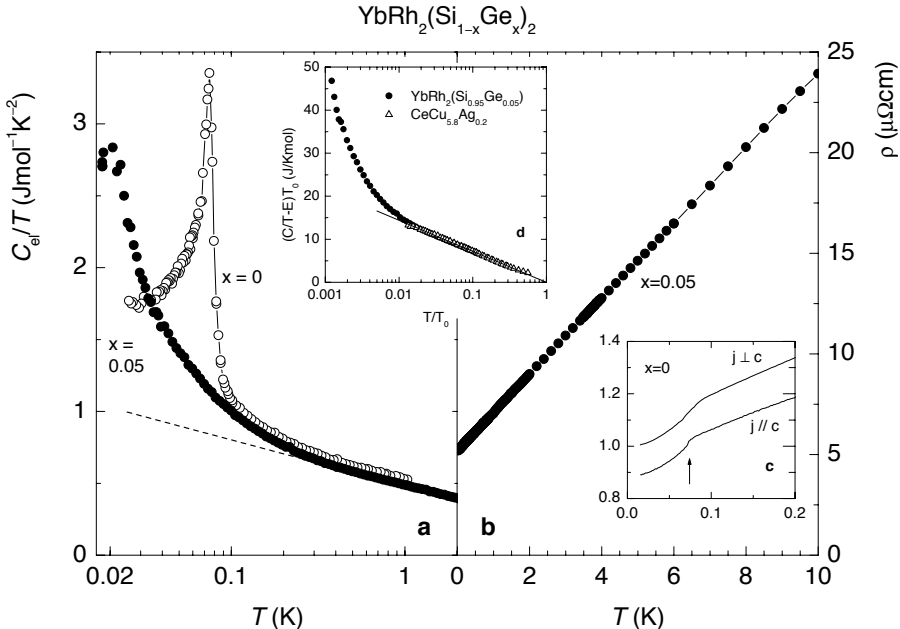


FIGURE 18.5

Comparison of the low-temperature electronic specific heat as C_{el}/T vs. T on a logarithmic scale (a) and the electrical resistivity ρ (b and c) of high-quality $\text{YbRh}_2(\text{Si}_{1-x}\text{Ge}_x)_2$ single crystals with nominal Ge contents $x = 0$ and $x = 0.05$ [85]. Arrow in (c) denotes T_N as obtained from the maximum in $d\rho(T)/dT$ [76]. (d) Scaling of the low- T specific heat of $\text{CeCu}_{5.8}\text{Ag}_{0.2}$ and $\text{YbRh}_2(\text{Si}_{0.95}\text{Ge}_{0.05})_2$ as $(C/T - E)T_0$ vs. $\log(T/T_0)$ using $T_0 = 4.6$ K and $E = 0.105$ J/K²mole for the former system as well as $T_0 = 23.3$ K and $E = 0.066$ J/K²mole for the latter one, respectively [86]; see text. The solid line represents the scaling function $7.2 \log(T_0/T)$ observed in several HF systems [87].

Sommerfeld coefficient as well as the linear T dependence of $\Delta\rho(T)$ [73], the energy over temperature scaling of the dynamical susceptibility with fractional exponent, found to be wave-vector independent, is incompatible with this scenario [80]. This has led to the idea of a Kondo-breakdown, *locally-critical* QCP [81] and related scenarios [82, 83].

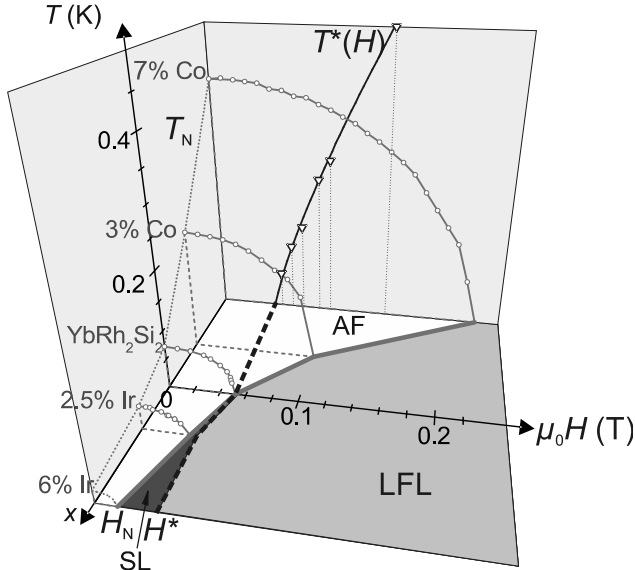
The tetragonal compound YbRh_2Si_2 is one of the few clean and stoichiometric HF metals known up to now, which are located at ambient pressure and zero magnetic field extremely close to a QCP [75]. It shows very weak AF ordering at $T_N = 70$ mK and a tiny magnetic field $H_N(\perp c)$ of 0.06 T which suffices to suppress the AF order and tune its ground state across the QCP into the paramagnetic LFL regime [76]. Hydrostatic pressure increases T_N [84], as expected for Yb systems, whereas a partial substitution of Si by the

isoelectronic but larger Ge reduces T_N to 20 mK in $\text{YbRh}_2(\text{Si}_{0.95}\text{Ge}_{0.05})_2$ [85]. According to Fig. 18.5(a), the low-temperature Sommerfeld coefficient displays a stronger-than-logarithmic divergence below 0.3 K, which is in sharp contrast to the predictions of SDW theory. The corresponding electrical resistivity (cf. Fig. 18.5(b)) follows a linear temperature dependence from 10 K down to almost 10 mK [85]. Here, in contrast to the specific heat, no change is found around 0.3 K. This observed disparity between transport and thermodynamic properties has been ascribed to a breakup of the heavy quasiparticles in the approach to the QCP [85]. As shown in the inset d of Fig. 18.5, the electronic-specific-heat coefficients of $\text{CeCu}_{5.8}\text{Ag}_{0.2}$ (which is almost identical to that of $\text{CeCu}_{5.9}\text{Au}_{0.1}$) and $\text{YbRh}_2(\text{Si}_{0.95}\text{Ge}_{0.05})_2$ are very similar on a reduced temperature scale $t = T/T_0$ for $t \geq 0.01$ [86]. Remarkably, the *spin-fluctuation temperature* T_0 is close to the Kondo temperature T_K in either case. In fact, a substantial number of quantum critical HF systems located near a QCP display a similar specific-heat behavior. At $t < 0.01$, not yet reached in $\text{CeCu}_{6-x}\text{M}_x$ ($\text{M}=\text{Au}, \text{Ag}$), a weak power-law upturn is found in $\text{YbRh}_2(\text{Si}_{0.95}\text{Ge}_{0.05})_2$. The latter system has been tuned towards the LFL regime using magnetic fields. Temperature over magnetic field scaling in both the electronic specific heat and the electrical resistivity indicates that the characteristic energy of the heavy quasiparticles is governed only by the ratio of the thermal energy to the distance from the QCP, $h = H - H_N$, and vanishes at $h \rightarrow 0$ [85]. The quasiparticle mass, derived from the Sommerfeld coefficient within the LFL regime, diverges as $\gamma_0 \propto h^{-1/3}$ [85].

The critical Grüneisen ratio of YbRh_2Si_2 displays a fractional exponent $\Gamma^{\text{cr}} \propto T^{-2/3}$ [68], in contrast to the T^{-1} divergence predicted by the SDW theory [67]. Within the LFL regime at $H > H_N$, the *magnetic* Grüneisen ratio $\Gamma_{\text{mag}} = -(dM/dT)/C$, where M is the magnetization, follows $\Gamma_{\text{mag}} = -G_r(H - H_N)^{-1}$ with $G_r = -0.3 \pm 0.01$ [88]. Assuming scaling [67],⁸ $G_r = \nu(d - z)$, the Sommerfeld coefficient within the LFL regime is expected to follow $\gamma_0 \propto r^{-G_r}$, where $r = H - H_N$ is the control parameter; this power law has indeed been found in $\text{YbRh}_2(\text{Si}_{0.95}\text{Ge}_{0.05})_2$ [85].

In order to investigate a possible Fermi-surface reconstruction at the QCP in YbRh_2Si_2 , the evolution of the Hall coefficient upon tuning through the QCP has been studied at low temperatures [89]. Most remarkably, suppression of the weak magnetic ordering by a tiny magnetic field leads to a substantial change of the Hall coefficient. A new line $T^*(H)$ in the temperature-field phase diagram has been discovered across which the isothermal Hall coefficient as a function of the applied magnetic field exhibits a temperature-broadened crossover. Upon decreasing the temperature this feature sharpens, suggesting for the zero-temperature extrapolation a sudden change of the Fermi volume at the magnetic critical field $H_N(T_N \rightarrow 0)$ [89]. Subsequent thermodynamic and transport investigations confirmed $T^*(H)$ to be an additional energy scale

⁸Here ν , d and z are the correlation-length exponent, dimensionality and dynamical exponent, respectively, in keeping with standard notation; critical exponents define the universality class.

**FIGURE 18.6**

Evolution of temperature-magnetic field phase diagram of YbRh_2Si_2 under negative and positive chemical pressure [91]. Open circles in $T-H$ planes show AF phase boundaries $T_{\text{N}}(H)$, while open triangles for $\text{Yb}(\text{Rh}_{0.93}\text{Co}_{0.07})_2\text{Si}_2$ show a Kondo-breakdown crossover $T^*(H)$ as determined from the maxima of the AC susceptibility, $\chi'(T)$. For $\text{Yb}(\text{Rh}_{0.94}\text{Ir}_{0.06})_2\text{Si}_2$, $T_{\text{N}}(H)$ has been extrapolated from hydrostatic pressure experiments on undoped YbRh_2Si_2 . The dotted line in $H = 0$ plane represents T_{N} as a function of chemical pressure. Kondo-breakdown (H^*) and AF (H_{N}) critical fields as well as antiferromagnetically ordered (AF), Landau Fermi liquid (LFL) and putative spin liquid (SL) phases are displayed in $T = 0$ plane.

which vanishes at the QCP [90]. Because of the crossover in the Hall coefficient, $T^*(H)$ may be associated with the finite-temperature signature of an abrupt change from a small to a large Fermi-surface volume at zero temperature.

The evolution of the AF phase boundary, $T_{\text{N}}(H)$, of the LFL-NFL crossover, $T_{\text{LFL}}(H)$, as well as of the additional energy scale $T^*(H)$ have recently been studied under variation of positive and negative chemical pressure [91]. It was observed that the AF state is stabilized/weakened by volume compression/expansion (cf. Fig. 18.6). Unexpectedly, however, the $T^*(H)$ line is almost independent of chemical pressure, as indicated by the doping-independent " H^* " value, at which $T^* \rightarrow 0$. Under volume compression (Co-doping) the AF QCP occurs at a field substantially higher than H^* . In this situation, the SDW theory is expected to be applicable to the AF QCP which could indeed be confirmed [91]. Under volume expansion (Ir-doping), H_{N} be-

comes substantially smaller than H^* , and the NFL-LFL crossover appears to be linked to $T^* \rightarrow 0$. Most remarkably, for $\text{Yb}(\text{Rh}_{0.94}\text{Ir}_{0.06})_2\text{Si}_2$, AF order and the LFL ground state are not connected by a single QCP but are separated by an extended, metallic *spin-liquid* (SL)-type phase, in which the $4f$ moments are neither Kondo screened nor magnetically ordered (see also Sec. 18.7). Hydrostatic pressure experiments on undoped YbRh_2Si_2 have recently confirmed [92] the phase diagram found in chemically pressurized $\text{Yb}(\text{Rh}_{1-x}\text{Co}_x)_2\text{Si}_2$, proving that the intersection of $T_N(H)$ and $T^*(H)$ (cf. Fig. 18.6) has to be ascribed to the alloying-induced volume compression rather than disorder.

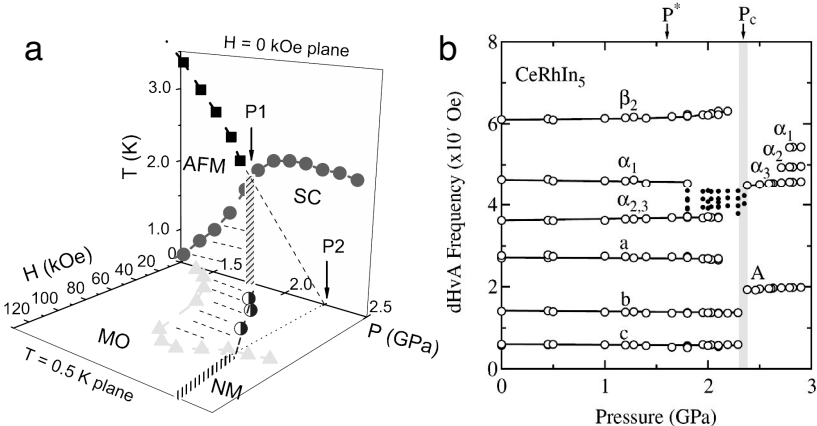
18.6 Interplay between Quantum Criticality and Unconventional Superconductivity

As early as 1986, phase diagrams similar to the one observed for the prototypical NFL metal CePd_2Si_2 [24] (Fig. 18.1(a)) were already discussed for HF superconductors near an SDW instability [93]. Unfortunately, since the QCP in CePd_2Si_2 arises at a relatively high pressure, neither the nature of the ordered state nor its magnetic excitation spectrum in the vicinity of the AF instability could yet be probed. CeCu_2Si_2 is ideally suited for such an investigation because here HFSC already occurs in the vicinity of an AF QCP at ambient pressure (left part of Fig. 18.1(c)). Its weak AF order, with $\mu_{\text{ord}} \approx 0.1\mu_B/\text{Ce}$, turned out to be an incommensurate SDW, determined by the nesting of the renormalized Fermi surface [20]. Earlier resistivity and specific-heat measurements in the field-induced normal state had already led to the suggestion of 3D quantum critical SDW fluctuations [72]. Recent INS studies on *paramagnetic* CeCu_2Si_2 clearly revealed spin excitations associated with a nearby 3D SDW QCP [94]. These dispersive and overdamped SDW fluctuations have a velocity much smaller than the already quite small Fermi velocity of the heavy charge carriers, indicating a retarded coupling between the HFs and the spin excitations [94]. This mechanism for driving the formation of massive Cooper pairs in CeCu_2Si_2 has, in fact, been concluded from a large gain in exchange energy between the superconducting and the normal state; this gain exceeds the superconducting condensation energy by a factor of order 20 [94].

Phase diagrams like those in Figs. 18.1(a) and (c)⁹ were observed in other Ce-based NFL superconductors as well and in several of the recently discovered iron pnictides [95]. While these new *high-T_c* superconductors seem to exhibit a QCP of SDW type, its existence in the former materials has yet to be verified with the aid of neutron diffractometry.

Interestingly, for the unconventional quantum critical material YbRh_2Si_2

⁹At low pressures.

**FIGURE 18.7**

(a) Temperature-pressure-magnetic field phase diagram for CeRhIn₅ [101]. Vertical $T - P$ plane shows the evolution of antiferromagnetic order (solid squares) and superconductivity (solid circles) in the absence of an applied field. Horizontal $H - P$ plane is constructed from measurements at a fixed temperature of 0.5 K. In this plane, solid triangles correspond to the upper critical field H_{c2} and half-filled circles give the field at which magnetic order (MO) is induced inside the superconducting state. Hatching indicates region in which magnetic order is suppressed by applying pressure above H_{c2} . (b) Measured de Haas-van Alphen frequencies as a function of pressure for CeRhIn₅ [104].

no SC could be detected down to $T = 10$ mK, the lowest temperature accessible in the resistivity experiments so far. In future work it will have to be clarified if SC in this compound (i) occurs at even lower temperatures, (ii) does not form because of the competition between AF and strong FM quantum critical correlations in wide parts of the phase diagram [96] or (iii) is inhibited due to the unconventional nature of its quantum criticality, i.e., the coincidence of an AF and a Kondo-breakdown QCP (or 4f-selective Mott transition).

In the following, some HF superconductors will be addressed for which the nature of quantum criticality could not be definitively determined up to now. Some evidence has been provided for a magnetic-field-induced 3D SDW QCP, in the range $H = 4 - 5$ Tesla, either to exist in the superconducting state (in UBe₁₃ [97]) or being masked by SC (in CeCoIn₅, $H \parallel c$ [49, 98]). For the recently discovered HF superconductor β -YbAlB₄ [99], a possible AF QCP at finite pressure has yet to be resolved. While for this system the low- T ($\geq T_c = 80$ mK) resistivity shows a $T^{1.5}$ -dependence [99], consistent with an *itinerant* 3D SDW QCP scenario, recent low-temperature ESR results sug-

gest a *localized* $4f$ state [100]. The compound CeRhIn₅ exhibits a very rich temperature-magnetic field-pressure phase diagram (Fig.18.7(a)) [101]: in the ($H = 0$) $T - p$ plane, SC and AF order coexist in a wide pressure range below $p_1 \approx 1.7$ GPa, where the magnetic ($T_N(p)$) and superconducting ($T_c(p)$) phase boundaries intersect. Extrapolating $T_N(p)$ to $T_N \rightarrow 0$ yields a critical pressure $p_2 \approx 2.3$ GPa. As displayed in the $H - p$ plane at $T = 0.5$ K, assumed to be identical to the $T = 0$ plane, this coexistence of SC and antiferromagnetism is thought to terminate at a quantum critical *line* between $(p_1, H = 0)$ and $(p_2, H = H_{c2}(0))$, while only bulk superconductivity was observed at higher pressures. In the $T - H$ planes at fixed values of pressure between 1.51 and 1.71 GPa, the upper critical field H_{c2} at which $T_c \rightarrow 0$ surprisingly agrees with the field at which incommensurate AF order, coexisting with SC, is replaced by commensurate order [102]. Furthermore, for $p \leq p_1$ neutron diffractometry revealed a seemingly abrupt change in the incommensurate ordering wave vector upon cooling to below $T = T_c(p)$, which indicates that antiferromagnetism is indeed affected by SC [103]. Whether or not AF spin fluctuations are driving SC in this material has to be found out by future studies. The compound CeRhIn₅ shows very interesting normal-state properties at high magnetic fields, near the critical pressure p_2 : de Haas van Alphen measurements, done between 10 and 17 T [104], indicate a pronounced increase in the Fermi-surface volume upon increasing the pressure through $p_2 = 2.3$ GPa, cf. Fig.18.7(b). This and the observation of a seemingly diverging m^* are commonly considered evidence for a Kondo-breakdown QCP [105], but have also been ascribed to a valence transition [106].

In summary we state that, except for CeCu₂Si₂, in none of the HF superconductors discussed above can the occurrence of SC be unambiguously related to a specific type of quantum criticality. Very recently it was predicted [107] that SC may form at low temperatures on the LFL side of a $4f$ -selective Mott transition, which separates the LFL from an SL state. Future activities will, therefore, have to be devoted to searching for a non-magnetic, clean and stoichiometric counterpart of 6 at% Ir-doped YbRh₂Si₂ for which no SC could be detected down to $T \approx 20$ mK [91].

18.7 Conclusions and Open Questions

As discussed above, the existence of QCPs has well been established for HF metals over the last decade. They arise from the suppression of long-range AF ordering by tuning pressure, chemical composition or magnetic field [74, 108, 109]. As a thermodynamic consequence of the accumulation of entropy above the QCP, the Grüneisen ratio of thermal expansion to electronic specific heat diverges [67]. This has meanwhile been observed for different materials. Also, the existence of profound deviations from LFL theory,

i.e., NFL behavior, is well established [74, 108, 109]. While HF antiferromagnets in the vicinity of a QCP are commonly considered to be of the *itinerant* type ($T_K \gg T_N$, cf. Sec. 18.2), and for several HF systems quantum criticality appears indeed to be in accordance with the predictions of the itinerant theory, strong disparities with these predictions have been found for $\text{CeCu}_{6-x}\text{Au}_x$ [73] and YbRh_2Si_2 [75]. In the case of these two systems, the potential breakdown of the Kondo effect at the AF QCP may result in an ordering of *local* 4f-derived magnetic moments [81–83]. In the former system, INS experiments have revealed strongly anisotropic, quasi-2D quantum critical fluctuations [79], whereas for YbRh_2Si_2 , a two-component spectrum with strong FM and AF contributions has been deduced [90]. This raises the question of the importance of low-dimensional fluctuations or, more generally, on the relevance of magnetic frustration: for example, what is the origin of the quasi-2D AF spin fluctuations in the 3D orthorhombic material $\text{CeCu}_{6-x}\text{Au}_x$ observed by INS [79] and previously inferred from the linear T -dependence of the electrical resistivity as well as from the logarithmic T -divergence of the Sommerfeld coefficient [73]?

In the absence of any published INS data probing the spin-fluctuation spectrum of YbRh_2Si_2 , we note that the resistivity and specific-heat data obtained for this compound above $T \approx 0.3$ K [85] agree well with those for $\text{CeCu}_{5.9}\text{Au}_{0.1}$ [73], cf. Fig. 18.5(d). It is natural to assume the presence of quasi-2D AF spin fluctuations in YbRh_2Si_2 , too, because of the tetragonal 122 crystal structure [75, 76]: a likely explanation for the magnetic top and bottom layers of the tetragonal unit-cell being substantially decoupled involves effective frustration of the Yb^{3+} ion residing on the body-centered position [24].

When Rh in YbRh_2Si_2 is partially substituted by the isoelectronic, smaller Co, the AF spin fluctuations become essentially 3D as inferred from both the field dependence of the Néel temperature, $T_N \sim (H - H_N)^{-0.65}$, and the T -dependence of the resistivity, $\Delta\rho \sim T^{1.5}$ [91]. Thus, the 4f-selective Mott transition occurs at H^* *inside* the AF phase of $\text{Yb}(\text{Rh}_{1-x}\text{Co}_x)_2\text{Si}_2$, i.e., well below H_N where $T_N \rightarrow 0$ at a conventional, 3D SDW, QCP. A selective Mott transition has been found to take place prior to an AF instability also in another correlated material, i.e., CeIn_3 under increasing magnetic field [110]. Most interestingly, recent quantum oscillation studies on $\text{YBa}_2\text{Cu}_3\text{O}_{6+x}$ reveal the metal-insulator (Mott) transition to be followed, under increasing carrier concentration, by a partial Mott transition from a small to a large Fermi volume. Furthermore, the $T - x$ phase diagram of $\text{YBa}_2\text{Cu}_3\text{O}_{6+x}$ is thought to display two intersecting superconducting domes, centered around these two different QPTs, both of which appear to be of continuous nature [111].

Although the magnetization results on Co-doped YbRh_2Si_2 [91] agree very well with recent ones obtained on the pure compound under hydrostatic pressure [92], the role of disorder has still to be explored by future experiments. This is particularly necessary for Ir-doped YbRh_2Si_2 , in which the average unit-cell volume is expanded compared to the undoped compound and, thus,

AF order becomes substantially weakened. As seen in Fig. 18.6, the Mott critical field H^* appears to coincide with the magnetic critical field H_N at low Ir concentration, at least below 2.5 at% ($H_N \approx H^* \approx 40$ mT). At higher Ir doping, however, H_N and H^* become detached. For 6 at% Ir, $H_N \leq 15$ mT, both critical fields are separated by a metallic SL-type phase [91]. It is interesting to note that the $T = 0$ plane of the 3D global phase diagram of Fig. 18.6 shows some resemblance to the generic $T = 0$ phase diagram near HF QCPs as recently proposed; see Chap. 8.

In closing this chapter, we summarize a number of outstanding unsolved questions concerning quantum criticality in HF metals.

- Why is the Kondo-breakdown critical field H^* in YbRh_2Si_2 rather insensitive to a change of the unit-cell volume, although the Kondo temperature is strongly pressure dependent [112]?
- Do H_N and H^* also coincide within a finite range of low (positive) pressure (cf. Fig. 18.6)?
- Which mechanism is causing the detachment of H_N and H^* when, in this compound, the Ir concentration exceeds a critical value (≥ 2.5 at%)?
- What are the genuine low-temperature properties of the presumed new metallic SL-type phase?
- Can a 4f-selective Mott transition at zero magnetic field, apart from AF order, be identified in YbRh_2Si_2 when sufficiently doped with Ir, or in YbIr_2Si_2 [113] under sufficiently high pressure? If so, will SC be found at the LFL side of this partial Mott transition, as theoretically predicted [107]?
- Can a Kondo-breakdown-crossover (T^*) line be established for $\text{CeCu}_{6-x}\text{Au}_x$, too?
- Is it feasible for CeRhIn_5 to perform sufficiently sensitive measurements of the volume as a function of pressure near $p_2 = 2.3$ GPa in order to distinguish between a *valence crossover* and a *Kondo-breakdown QCP*?
- What is the driving mechanism for SC in pressurized CeRhIn_5 ?
- How can, in the latter as well as in other HF metals [17, 18], the ordering of *local*, 4f-derived magnetic moments in an *incommensurate* AF structure be interpreted?
- Is there any clean, stoichiometric HF metal which exhibits a FM QCP?

We expect that future efforts in the field of HF physics towards answering these and related questions will also advance the current understanding of other strongly correlated materials, ranging from cuprate and transition-metal pnictide/chalcogenide high- T_c superconductors to organic charge transfer salts.

Acknowledgments – We would like to thank Q. Si for many stimulating discussions and helpful suggestions while drafting this chapter as well as S. Wirth for his critical comments and thorough reading of the manuscript. Valuable conversations with M. Brando, A. Chubukov, P. Coleman, S. Friedemann, C. Geibel, S. Kirchner, C. Krellner, C. Pépin and O. Stockert are gratefully acknowledged. This work was partially supported by the DFG Research Unit 960 “Quantum Phase Transitions.”

Bibliography

- [1] Special Issue: Quantum Criticality and Novel Phases (QCNP 2009), *Phys. Status Solidi B* **247**, 457 (2010).
- [2] J. Kondo, *Progr. Theor. Phys.* **32**, 37 (1964).
- [3] For reviews, see, e.g.: G.R. Stewart, *Rev. Mod. Phys.* **56**, 755 (1984); H.R. Ott, *Characteristic features in heavy electron materials*, *Prog. Low Temp. Phys.*, Vol. XI, D.F. Brewer, ed. (Elsevier, Amsterdam, 1987) p. 215; N. Grewe and F. Steglich, Heavy fermions, in *Handbook on the Physics and Chemistry of Rare Earths*, Vol. 14, K.A. Gschneidner Jr and L. Eyring L, eds. (Elsevier, Amsterdam, 1991) p. 343; Y. Kuramoto and Y. Kitaoka, *Dynamics of Heavy Electrons* (Oxford Science Publications, Oxford, 2000).
- [4] K. Andres, J.E. Graebner, and H.R. Ott, *Phys. Rev. Lett.* **35**, 1779 (1975).
- [5] See, e.g., D. Vollhardt and P. Wölfle, *The Superfluid Phases of ^3He* (Taylor and Francis, London, 1990).
- [6] F. Steglich *et al.*, *Phys. Rev. Lett.* **43**, 1892 (1979).
- [7] H.R. Ott *et al.*, *Phys. Rev. Lett.* **50**, 1595 (1983).
- [8] G.R. Stewart *et al.*, *Phys. Rev. Lett.* **52**, 679 (1984).
- [9] W. Schlabitz *et al.*, Poster contribution to ICVF, Cologne, 1984 (unpublished); *Z. Phys. B* **62**, 171 (1986).
- [10] K. Miyake, S. Schmitt-Rink, and C.M. Varma, *Phys. Rev. B* **34**, 6554 (1986).
- [11] D.J. Scalapino, E. Loh, and J.E. Hirsch, *Phys. Rev. B* **34**, 8190 (1986).
- [12] U. Rauchschwalbe *et al.*, *Phys. Rev. Lett.* **49**, 1448 (1982); *ibid.* **49**, 1960(E) (1982).

- [13] A.C. Hewson, *The Kondo Problem to Heavy Fermions* (Cambridge University Press, Cambridge, 1993).
- [14] M.A. Ruderman and C. Kittel, Phys. Rev. **96**, 99 (1954).
- [15] T. Kasuya, Prog. Theor. Phys. **16**, 45 (1956).
- [16] K. Yosida, Phys. Rev. **106**, 893 (1957).
- [17] B. Barbara *et al.*, Sol. State Commun. **24**, 481 (1977).
- [18] C.D. Bredl, F. Steglich, and K.D. Schotte, Z. Phys. B **29**, 327 (1978).
- [19] A. Loidl *et al.*, Ann. Phys. **504**, 78 (1992).
- [20] O. Stockert *et al.*, Phys. Rev. Lett. **92**, 136401 (2004).
- [21] J. Rossat-Mignod *et al.*, J. Magn. Magn. Mat. **76&77**, 376 (1988).
- [22] Y. Ōnuki and T. Komatsubara, J. Magn. Magn. Mat. **63&64**, 281 (1987).
- [23] M.J. Besnus, P. Lehmann, and A. Meyer, J. Magn. Magn. Mat. **76&77**, 323 (1988).
- [24] N.D. Mathur *et al.*, Nature **394**, 39 (1998).
- [25] S.S. Saxena *et al.*, Nature **406**, 587 (2000).
- [26] F. Thomas *et al.*, Physica B **186–188**, 303 (1993).
- [27] D. Jaccard, K. Behnia, and J. Sierras, Phys. Lett. A **163**, 475 (1992).
- [28] H.Q. Yuan *et al.*, Science **302**, 2104 (2003).
- [29] H. Tou *et al.*, Phys. Rev. Lett. **80**, 3129 (1998).
- [30] K. Ishida *et al.*, Phys. Rev. Lett. **89**, 37002 (2002).
- [31] F. Lévy *et al.*, Science **309**, 1343 (2005).
- [32] N.T. Huy *et al.*, Phys. Rev. Lett. **99**, 067006 (2007).
- [33] G. Aeppli *et al.*, Phys. Rev. Lett. **63**, 676 (1989).
- [34] H.R. Ott *et al.*, Phys. Rev. B **31**, 1651 (1985).
- [35] M.B. Maple *et al.*, J. Phys. Soc. Jpn. **71** (Supplement): 23 (2002).
- [36] N.K. Sato *et al.*, Nature **410**, 340 (2001).
- [37] M. Jourdan, M. Huth, and H. Adrian, Nature **398**, 47 (1999).
- [38] C. Geibel *et al.*, Z. Phys. B **84**, 1 (1991).

- [39] A. Krimmel *et al.*, Z. Phys. B **86**, 161 (1992).
- [40] Y. He *et al.*, Nature **357**, 227 (1992).
- [41] R. Movshovich *et al.*, Phys. Rev. B **35**, 8241 (1996).
- [42] D. Jaccard *et al.*, Physica B **259–261**, 1 (1999).
- [43] S. Nischigori *et al.*, Physica B **359–361**, 172 (2005).
- [44] C. Petrovic *et al.*, J. Phys.: Condens. Matter **13**, L337 (2001).
- [45] M. Nicklas *et al.*, Phys. Rev. B **67**, 020506 (2003).
- [46] D. Kaczorowski *et al.*, Phys. Rev. Lett. **103**, 027003 (2009).
- [47] E. Bauer *et al.*, Phys. Rev. Lett. **92**, 027003 (2004).
- [48] P. Monthoux and G.G. Lonzarich, Phys. Rev. B **59**, 14598 (1999).
- [49] See, e.g., S. Singh *et al.*, Phys. Rev. Lett. **98**, 057001 (2007).
- [50] F. Wastin *et al.*, J. Phys.: Condens. Matter **15**, S2279 (2003).
- [51] J.L. Sarrao *et al.*, Nature **420**, 297 (2002).
- [52] D. Aoki *et al.*, J. Phys. Soc. Jpn. **76**, 063701 (2007).
- [53] I. Sugitani *et al.*, J. Phys. Soc. Jpn. **95**, 043703 (2006).
- [54] T. Akazawa *et al.*, J. Phys. Soc. Jpn. **73**, 3129 (2004).
- [55] L.P. Gor'kov and E.I. Rashba, Phys. Rev. Lett. **87**, 037004 (2001).
- [56] D.F. Agterberg *et al.*, Physica B **378–380**, 351 (2006).
- [57] H.Q. Yuan *et al.*, Phys. Rev. Lett. **97**, 017006 (2006).
- [58] S. Doniach, Physica B+C **91**, 231 (1977).
- [59] J.A. Hertz, Phys. Rev. B **14**, 1165 (1976).
- [60] A.J. Millis, Phys. Rev. B **48**, 7183 (1993).
- [61] M.A. Continentino, G.M. Japiassu, and A. Troper, Phys. Rev. B **39**, 9734 (1993).
- [62] T. Moriya and T. Takimoto, J. Phys. Soc. Jpn. **64**, 960 (1995).
- [63] R. Hlubina and T.M. Rice, Phys. Rev. B **51**, 9253 (1995).
- [64] A. Rosch, Phys. Rev. Lett. **82**, 4280 (1999).
- [65] S.R. Julian *et al.*, J. Phys.: Condens. Matter **8**, 9675 (1996).

- [66] P. Gegenwart *et al.*, Phys. Rev. Lett. **82**, 1293 (1999).
- [67] L. Zhu *et al.*, Phys. Rev. Lett. **91**, 066404 (2003).
- [68] R. Küchler *et al.*, Phys. Rev. Lett. **91**, 066405 (2003).
- [69] R. Küchler *et al.*, Phys. Rev. Lett. **96**, 256403 (2006).
- [70] J.G. Donath *et al.*, Europhys. Lett. **87**, 57011 (2009).
- [71] W. Knafo *et al.*, Nature Phys. **5**, 753 (2009).
- [72] P. Gegenwart *et al.*, Phys. Rev. Lett. **81**, 1501 (1998).
- [73] H. von Löhneysen *et al.*, Phys. Rev. Lett. **72**, 3262 (1994).
- [74] H. von Löhneysen *et al.*, Rev. Mod. Phys. **79**, 1015 (2007).
- [75] O. Trovarelli \diamond et al., Phys. Rev. Lett. **85**, 626 (2000).
- [76] P. Gegenwart \diamond et al., Phys. Rev. Lett. **89**, 056402 (2002).
- [77] H. von Löhneysen \diamond et al., J. Alloys Comp. **408–412**, 9 (2006).
- [78] B. Bogenberger and H. von Löhneysen, Phys. Rev. Lett. **64**, 1016 (1995).
- [79] O. Stockert *et al.*, Phys. Rev. Lett. **80**, 5627 (1998).
- [80] A. Schröder *et al.*, Nature **407**, 351 (2000).
- [81] Q. Si *et al.*, Nature **413**, 804 (2001).
- [82] P. Coleman *et al.*, J. Phys.: Condens. Matter **13**, R723 (2001).
- [83] T. Senthil, M. Vojta, and S. Sachdev, Phys. Rev. B **69**, 035111 (2004).
- [84] S. Mederle *et al.*, J. Phys.: Condens. Matter **14**, 10731 (2002).
- [85] J. Custers *et al.*, Nature **424**, 524 (2003).
- [86] R. Küchler *et al.*, Phys. Rev. Lett. **93**, 096402 (2004).
- [87] J. Sereni, Physica B **230–232**, 580 (1997).
- [88] Y. Tokiwa *et al.*, Phys. Rev. Lett. **102**, 066401 (2009).
- [89] S. Paschen *et al.*, Nature **432**, 881 (2004).
- [90] P. Gegenwart *et al.*, Science **315**, 969 (2007).
- [91] S. Friedemann *et al.*, Nature Phys. **5**, 465 (2009).
- [92] Y. Tokiwa *et al.*, J. Phys. Soc. Jpn. **78**, 123708 (2009).
- [93] D.J. Scalapino (private communication, 2007).

- [94] O. Stockert *et al.* (to be published).
- [95] See, e.g., J.-H. Chu *et al.*, Phys. Rev. B **79**, 014506 (2009).
- [96] P. Gegenwart *et al.*, Phys. Rev. Lett. **94**, 076402 (2005).
- [97] P. Gegenwart *et al.*, Physica C **408–410**, 157 (2004).
- [98] J.G. Donath *et al.*, Phys. Rev. Lett. **100**, 136401 (2008).
- [99] S. Nakatsuji *et al.*, Nature Phys. **4**, 603 (2008).
- [100] L.M. Holanda *et al.*, ArXiv 0908.0044vl.
- [101] J.L. Sarrao and J.D. Thompson, J. Phys. Soc. Jpn. **76**, 051013 (2007).
- [102] T. Park *et al.*, Proc. Ntl. Acad. Sciences **105**, 6825 (2008).
- [103] N. Aso *et al.*, J. Phys. Soc. Jpn. **78**, 073703 (2009).
- [104] H. Shishido *et al.*, J. Phys. Soc. Jpn. **74**, 1103 (2005).
- [105] T. Park *et al.*, Nature, **440**, 65 (2006).
- [106] S. Watanabe *et al.*, J. Phys. Soc. Jpn. **79**, 104706 (2009).
- [107] C. Pépin (to be published).
- [108] G.R. Stewart, Rev. Mod. Phys. **73**, 797 (2001); *ibid* **78**, 743 (2006).
- [109] P. Gegenwart P, Q. Si, and F. Steglich, Nature Phys. **4**, 186 (2008).
- [110] S.E. Sebastian *et al.*, Proc. Ntl. Acad. Sciences **106**, 7741 (2009).
- [111] S.E. Sebastian *et al.*, ArXiv 0910.2359vl.
- [112] Y. Tokiwa *et al.*, Phys. Rev. Lett. **94**, 226402 (2005).
- [113] Z. Hossain *et al.*, Physica B **378–380**, 74 (2006).

19

Strong Correlation Effects with Ultracold Bosonic Atoms in Optical Lattices

Immanuel Bloch

Ludwig-Maximilians-Universität, 80799 München, Germany

Ultracold atoms in optical lattices have proven to be a versatile model system in which strong correlation effects in a many-body quantum system can be studied [1]. The tunability and control over almost all underlying system parameters makes them rather unique and allows one to switch between different ground states of the underlying many-body quantum system. One of the most prominent effects in this respect is the quantum phase transition (QPT) from a superfluid (SF) to a Mott insulator (MI) that started the field of strong-correlation physics with ultracold gases. First theoretically proposed by Fisher *et al.* [2], the Bose-Hubbard model (BHM) was introduced into the field of ultracold atoms by Jaksch *et al.* [3], eventually being realized in subsequent experiments [4–7]. This article focuses on giving a brief summary of the main results achieved in the SF-MI transition with ultracold bosons in optical lattices. A brief introduction into the setup of optical lattices is followed by a discussion of key results such as the coherence properties, the density profiles, transport properties and SF characteristics across the QPT.

19.1 Optical Lattices

In the following, we will discuss how to confine cold atoms by laser light into configurations of a reduced dimensionality or in periodic lattices, thus generating situations in which the effects of interactions are strongly enhanced.

19.1.1 Optical Potentials

The physical origin of the confinement of cold atoms with laser light is the dipole force

$$\mathbf{F} = \frac{1}{2}\alpha(\omega_L)\nabla(|\mathbf{E}(\mathbf{r})|^2), \quad (19.1)$$

due to a spatially varying AC-Stark shift which atoms experience in an off-resonant light field [8]. Since the time scale for the center-of-mass motion of the atoms is much slower than the inverse laser frequency ω_L , only the time-averaged intensity $|\mathbf{E}(\mathbf{r})|^2$ matters. The direction of the force depends on the sign of the polarizability $\alpha(\omega_L)$. In the vicinity of an atomic resonance from the ground state $|g\rangle$ to an excited state $|e\rangle$ at frequency ω_0 , the polarizability has the standard form $\alpha(\omega_L) \approx |\langle e | \hat{d}_{\mathbf{E}} | g \rangle|^2 / \hbar(\omega_0 - \omega_L)$, with $\hat{d}_{\mathbf{E}}$ the dipole operator in the direction of the field. Atoms are thus attracted to the nodes or to the anti-nodes of the laser intensity for blue detuned ($\omega_L > \omega_0$) or red detuned ($\omega_L < \omega_0$) laser light, respectively. A spatially-dependent intensity profile $I(\mathbf{r})$ therefore creates a trapping potential for neutral atoms. Within a two-level model, an explicit form of the dipole potential may be derived by using the rotating wave approximation, which is a reasonable approximation provided that the detuning $\Delta = \omega_L - \omega_0$ of the laser field is small compared to the transition frequency itself, $|\Delta| \ll \omega_0$. With Γ as the decay rate of the excited state, one obtains for $|\Delta| \gg \Gamma$ [8]

$$V_{\text{dip}}(\mathbf{r}) = \frac{3\pi c^2}{2\omega_0^3} \frac{\Gamma}{\Delta} I(\mathbf{r}), \quad (19.2)$$

which is attractive or repulsive for red ($\Delta < 0$) or blue ($\Delta > 0$) detuning, respectively. Atoms are thus attracted or repelled from an intensity maximum in space.

It is important to note that, in contrast to the form suggested in Eq. (19.1), the light force is not fully conservative. Indeed, spontaneous emission gives rise to an imaginary part of the polarizability. Within a two-level approximation, the related scattering rate $\Gamma_{\text{sc}}(\mathbf{r})$ leads to an absorptive contribution $\hbar\Gamma_{\text{sc}}(\mathbf{r})$ to the conservative dipole potential (19.2), which can be estimated as [8]

$$\Gamma_{\text{sc}}(\mathbf{r}) = \frac{3\pi c^2}{2\hbar\omega_0^3} \left(\frac{\Gamma}{\Delta} \right)^2 I(\mathbf{r}). \quad (19.3)$$

As Eqs. (19.2)-(19.3) show, the ratio of two-level scattering rate to the optical potential depth vanishes in the limit $|\Delta| \gg \Gamma$. A strictly conservative potential can thus be reached in principle by increasing the detuning of the laser field. However, in practice such an approach is limited by the maximum available laser power. For experiments with ultracold quantum gases of alkali atoms, the detuning is typically chosen to be large compared to the excited state hyperfine structure splitting and in most cases even large compared to the fine structure splitting in order to sufficiently suppress spontaneous scattering events.

The intensity profile $I(r, z)$ of a Gaussian laser beam propagating along the z -direction has the form

$$I(r, z) = [2P/(\pi w^2(z))] \exp(-2r^2/w^2(z)). \quad (19.4)$$

Here P is the total power of the laser beam, r is the distance from the center

and $w(z) = w_0 \sqrt{1 + z^2/z_R^2}$ is the $1/e^2$ radius. This radius is characterized by a beam waist w_0 which is typically around $100\text{ }\mu\text{m}$. Due to the finite beam divergence, the beam width increases linearly with z on a scale $z_R = \pi w_0^2/\lambda$, called the Rayleigh length. Typical values for z_R are in the mm range. Around the intensity maximum a potential depth minimum occurs for a red detuned laser beam, leading to an approximately harmonic potential

$$V_{\text{dip}}(r, z) \approx -V_{\text{trap}} \left\{ 1 - 2 \left(\frac{r}{w_0} \right)^2 - \left(\frac{z}{z_R} \right)^2 \right\}. \quad (19.5)$$

The trap depth V_{trap} is linearly proportional to the laser power and typically ranges from a few kHz up to a MHz, i.e., from the nanokelvin to the microkelvin regime. The harmonic confinement is characterized by radial and axial trapping frequencies $\omega_r = (4V_{\text{trap}}/Mw_0^2)^{1/2}$ and $\omega_z = (2V_{\text{trap}}/Mz_R^2)^{1/2}$, respectively. Optical traps for neutral atoms have a wide range of applications [8]. In particular, they are inevitable in situations where magnetic trapping does not work for the atomic states under consideration. This is often the case when the interactions are manipulated via Feshbach resonances, involving high-magnetic-field-seeking atomic states.

19.1.2 Optical Lattices

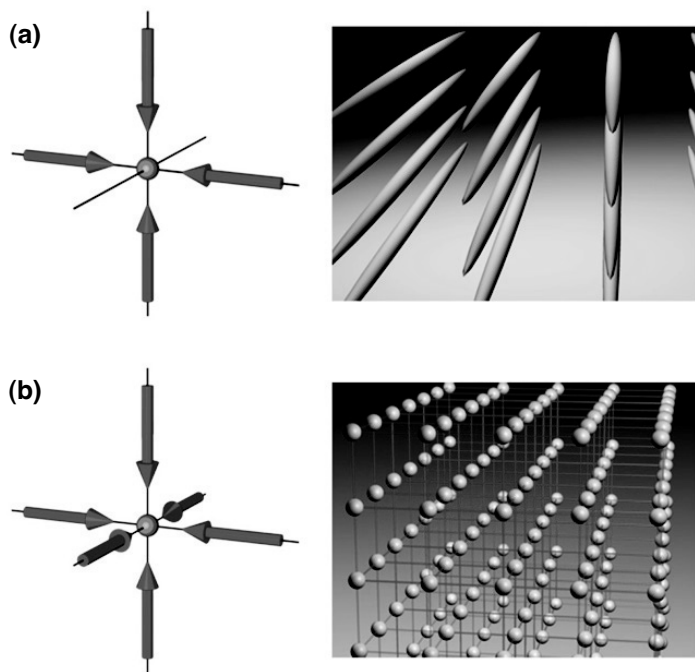
A periodic potential is generated by overlapping two counter-propagating laser beams. Due to the interference between the two laser beams an optical standing wave with period $\lambda/2$ is formed, in which the atoms can be trapped. More generally, by choosing the two laser beams to interfere under an angle less than 180° , one can also realize periodic potentials with a larger period [9, 10]. The simplest possible periodic optical potential is formed by overlapping two counter-propagating beams. For a Gaussian profile, this results in a trapping potential of the form

$$V(r, z) = -V_0 \exp(-2r^2/w^2(z)) \sin^2(kz) \quad (19.6)$$

where $k = 2\pi/\lambda$ is the wave vector of the laser light and V_0 the maximum depth of the lattice potential. Note that due to the interference of the two laser beams V_0 is four times larger than V_{trap} if the laser power and beam parameters of the two interfering lasers are equal.

Periodic potentials in two dimensions can be formed by overlapping two optical standing waves along different, usually orthogonal, directions. For orthogonal polarization vectors of the two laser fields no interference terms appear. The resulting optical potential in the center of the trap is then a simple sum of a purely sinusoidal potential in both directions.

In such a two-dimensional (2D) optical lattice potential, the atoms are confined to arrays of tightly confining 1D tubes ([Fig. 19.1\(a\)](#)). For typical experimental parameters the harmonic trapping frequencies along the tube are very weak and on the order of 10-200 Hz, while in the radial direction the

**FIGURE 19.1**

(a) Two-dimensional and (b) three-dimensional optical lattice potentials formed by superimposing two or three orthogonal standing waves. For a 2D optical lattice, the atoms are confined to an array of tightly confining 1D potential tubes, whereas in the 3D case the optical lattice can be approximated by a 3D simple cubic array of tightly confining harmonic oscillator potentials at each lattice site.

trapping frequencies can become as high as up to 100 kHz. For sufficiently deep lattice depths, atoms can thus move only axially along the tube. In this manner, it is possible to realize quantum wires with neutral atoms, which allow one to study strongly correlated gases in 1D. Arrays of such quantum wires have been realized by several groups [11, 12].

For the creation of a 3D lattice potential, three orthogonal optical standing waves have to be overlapped. For different frequencies forming each standing wave, the resulting optical potential is given by the sum of three standing waves. In the center of the trap, for distances much smaller than the beam waist, the trapping potential can be approximated as the sum of a homogeneous periodic lattice potential

$$V_p(x, y, z) = V_0 (\sin^2 kx + \sin^2 ky + \sin^2 kz) \quad (19.7)$$

and an additional external harmonic confinement due to the Gaussian laser beam profiles. In addition to this harmonic confinement, a confinement due to the magnetic trapping is often used, which has to be taken into account as well for the total harmonic confinement of the atom cloud.

For deep optical lattice potentials, the confinement on a single lattice site is approximately harmonic. The atoms are then tightly confined at a single lattice site, with trapping frequencies ω_0 of up to 100 kHz. The energy $\hbar\omega_0 = 2E_r(V_0/E_r)^{1/2}$ of local oscillations in the well is on the order of several recoil energies $E_r = \hbar^2 k^2 / 2m$, which is a natural measure of energy scales in optical lattice potentials. Typical values of E_r are in the range of several kHz for ^{87}Rb .

19.1.2.1 Band Structure

We consider in this section the single particle eigenstates in an infinite periodic potential. Any additional potential that could originate from the intensity profile of the laser beams or from some magnetic confinement is neglected.¹ In a simple cubic lattice, the potential is given by Eq. (19.7), with a tunable amplitude V_0 and lattice constant $d = \pi/k$. In the limit $V_0 \gg E_r$, each well supports a number of vibrational levels, separated by an energy $\hbar\omega_0 \gg E_r$. At low temperatures, the atoms are restricted to the lowest vibrational level at each site. Their kinetic energy is then frozen, except for the small tunneling amplitude to neighboring sites. The associated single-particle eigenstates in the lowest band are Bloch waves with quasi-momentum \mathbf{q} and energy

$$\varepsilon_0(\mathbf{q}) = \frac{3}{2}\hbar\omega_0 - 2J(\cos q_x d + \cos q_y d + \cos q_z d) + \dots \quad (19.8)$$

The parameter $J > 0$ is the gain in kinetic energy due to nearest-neighbor tunneling. In the limit $V_0 \gg E_r$, J can be obtained from the width $W \rightarrow 4J$ of the lowest band in the 1D Mathieu equation,

$$J = \frac{4}{\sqrt{\pi}} E_r \left(\frac{V_0}{E_r} \right)^{3/4} \exp[-2(V_0/E_r)^{1/2}]. \quad (19.9)$$

For lattice depths larger than $V_0 > 15E_r$ this approximation yields J to better than 10% accuracy. More generally, for any periodic potential $V_p(\mathbf{r} + \mathbf{R}) = V_p(\mathbf{r})$ which is not necessarily deep and separable, the exact eigenstates are Bloch functions $\psi_{n,\mathbf{q}}(\mathbf{r})$. They are characterized by a discrete band index n and a quasi-momentum \mathbf{q} within the first Brillouin zone of the reciprocal lattice [14]. Since Bloch functions are multiplied by a pure phase factor $\exp(i\mathbf{q} \cdot \mathbf{R})$ upon translation by one of the lattice vectors \mathbf{R} , they are extended over the whole lattice.

An alternative single-particle basis, which is more useful for describing the hopping of particles among the discrete lattice sites \mathbf{R} , are the Wannier

¹For the single particle spectrum in the presence of an additional harmonic confinement see [13].

functions $w_{n,\mathbf{R}}(\mathbf{r})$. They are connected with the Bloch functions by a Fourier transform

$$\psi_{n,\mathbf{q}}(\mathbf{r}) = \sum_{\mathbf{R}} w_{n,\mathbf{R}}(\mathbf{r}) e^{i\mathbf{q} \cdot \mathbf{R}} \quad (19.10)$$

on the lattice. The Wannier functions depend only on the relative distance $\mathbf{r} - \mathbf{R}$ and, at least for the lowest bands, they are centered around the lattice sites \mathbf{R} . By choosing a convenient normalization, they obey the orthonormality relation

$$\int d^3 r w_n^*(\mathbf{r} - \mathbf{R}) w_{n'}(\mathbf{r} - \mathbf{R}') = \delta_{n,n'} \delta_{\mathbf{R},\mathbf{R}'} \quad (19.11)$$

for different bands n and sites \mathbf{R} . Since the Wannier functions for all bands n and sites \mathbf{R} form a complete basis, the operator $\hat{\psi}(\mathbf{r})$ which destroys a particle at an arbitrary point \mathbf{r} can be expanded in the form

$$\hat{\psi}(\mathbf{r}) = \sum_{\mathbf{R},n} w_n(\mathbf{r} - \mathbf{R}) \hat{a}_{\mathbf{R},n}. \quad (19.12)$$

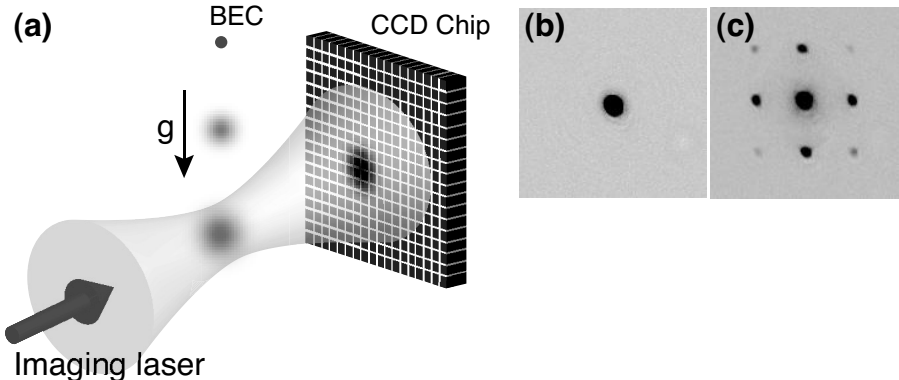
Here, $\hat{a}_{\mathbf{R},n}$ is the annihilation operator for particles in the corresponding Wannier states, which are not necessarily well localized at site \mathbf{R} . The Hamiltonian for free motion on a periodic lattice then has the form

$$\hat{H}_0 = \sum_{\mathbf{R},\mathbf{R}',n} J_n(\mathbf{R} - \mathbf{R}') \hat{a}_{\mathbf{R},n}^\dagger \hat{a}_{\mathbf{R}',n}. \quad (19.13)$$

It describes the hopping in a given band n with matrix elements $J_n(\mathbf{R})$, which in general connect lattice sites at arbitrary distance \mathbf{R} . The diagonalization of this Hamiltonian by Bloch states (19.10) shows that the hopping matrix elements $J_n(\mathbf{R})$ are uniquely determined by the Bloch band energies $\varepsilon_n(\mathbf{q})$ via

$$\sum_{\mathbf{R}} J_n(\mathbf{R}) \exp i\mathbf{q} \cdot \mathbf{R} = \varepsilon_n(\mathbf{q}). \quad (19.14)$$

In the case of separable periodic potentials $V_p(\mathbf{r}) = V(x) + V(y) + V(z)$, generated by three orthogonal optical lattices, the single-particle problem is 1D, and a complete analysis of Wannier functions has been given by [15]. Choosing appropriate phases for the Bloch functions, there is a unique Wannier function for each band, which is real and exponentially localized. The decay $\sim \exp(-h_n|x|)$ is characterized by a decay constant h_n , which is a decreasing function of the band index n . For the lowest band $n = 0$, where the Bloch function at $q = 0$ is finite at the origin, the Wannier function $w(x)$ can be chosen to be symmetric around $x = 0$; correspondingly, it is antisymmetric for the first excited band. More precisely, the asymptotic behavior of the 1D Wannier functions and the hopping matrix elements is $|w_n(x)| \sim |x|^{-3/4} \exp -h_n|x|$ and $J_n(R) \sim |R|^{-3/2} \exp -h_n|R|$, respectively [16]. In the particular case of a purely sinusoidal potential $V_0 \sin^2(kx)$ with lattice constant $d = \lambda/2$, the decay constant h_0 increases monotonically with V_0/E_r . In the deep lattice limit $V_0 \gg E_r$, it approaches $h_0 d = \pi \sqrt{V_0/E_r}/2$. It is important to realize that, even in this limit, the Wannier function does not uniformly converge to the local harmonic oscillator ground state ϕ of each well: the $w_n(x)$ decay exponentially rather than in a Gaussian manner and they always have nodes in order to guarantee the orthogonality relation (19.11). Yet, the overlap is near unity even for shallow optical lattices.

**FIGURE 19.2**

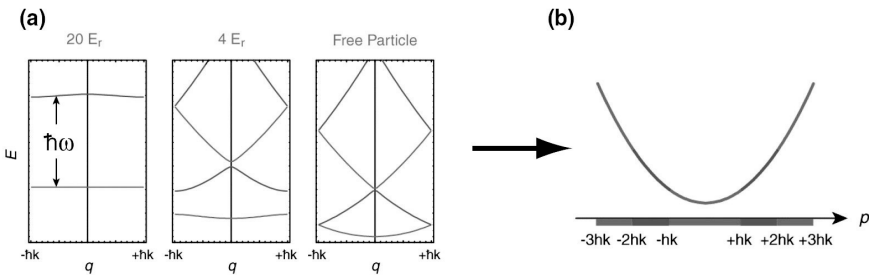
(a) Schematic setup for absorption imaging after a time-of-flight period. (b) Absorption image for a BEC released from a harmonic trap. (c) Absorption image for a BEC released from a shallow optical lattice ($V_0 = 6 E_r$). Note the clearly visible interference peaks in the image.

19.1.3 Time-of-Flight Imaging and Adiabatic Mapping

19.1.3.1 Sudden Release

When releasing ultracold quantum gases from an optical lattice, two possible release methods can be chosen. If the lattice potential is turned off abruptly and interaction effects can be neglected, a given Bloch state with quasi-momentum q will expand according to its momentum distribution as a superposition of plane waves with momenta $p_n = \hbar q \pm (2\hbar k)n$, where n is an integer. This is a direct consequence of the fact that Bloch waves can be expressed as a superposition of plane wave states $\exp[i(\mathbf{q} + \mathbf{G}) \cdot \mathbf{r}]$ with momenta $\mathbf{q} + \mathbf{G}$, which include arbitrary reciprocal lattice vectors \mathbf{G} . In a simple cubic lattice with lattice spacing $d = \pi/k$, the vectors \mathbf{G} are integer multiples of the fundamental reciprocal lattice vector $2k$. After a certain time-of-flight time, this momentum distribution can be imaged using standard absorption imaging methods. If only a single Bloch state is populated, as is the case for a Bose-Einstein condensate (BEC) with quasi-momentum $\mathbf{q} = \mathbf{0}$, this results in a series of interference maxima that can be observed after a time-of-flight period t (Fig. 19.2). The density distribution observed after a fixed time-of-flight at position \mathbf{x} is nothing but the momentum distribution of the particles trapped in the lattice,

$$n(\mathbf{x}) = \left(\frac{M}{\hbar t} \right)^3 |\tilde{w}(\mathbf{k})|^2 \mathcal{G}(\mathbf{k}). \quad (19.15)$$

**FIGURE 19.3**

(a) Bloch bands for different potential depths. During an adiabatic ramp down the quasi-momentum is conserved and (b) a Bloch wave with quasi-momentum q in the n th energy band is mapped onto a free particle with momentum p in the n th Brillouin zone of the lattice. From [11].

Here $\mathbf{k} = M\mathbf{x}/\hbar t$ due to the assumption of ballistic expansion while $\tilde{w}(\mathbf{k})$ is the Fourier transform of the Wannier function. The coherence properties of the many-body state are characterized by the Fourier transform

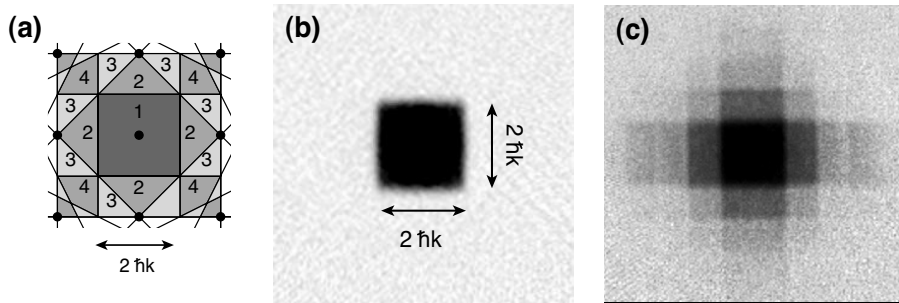
$$\mathcal{G}(\mathbf{k}) = \sum_{\mathbf{R}, \mathbf{R}'} e^{i\mathbf{k}\cdot(\mathbf{R}-\mathbf{R}')} G^{(1)}(\mathbf{R}, \mathbf{R}') \quad (19.16)$$

of the one-particle density matrix $G^{(1)}(\mathbf{R}, \mathbf{R}') = \langle \hat{a}_{\mathbf{R}}^\dagger \hat{a}_{\mathbf{R}'} \rangle$.

In a BEC, the long range order in the amplitudes leads to a constant value of the first order coherence function $G^{(1)}(\mathbf{R}, \mathbf{R}')$ at large separations $|\mathbf{R} - \mathbf{R}'|$. The resulting momentum distribution coincides with the standard multiple wave interference pattern obtained from light diffracting off a material grating ([Fig. 19.2\(c\)](#)). The atomic density distribution observed after a fixed time-of-flight thus yields information on the coherence properties of the many-body system. However, the observed density distribution after time-of-flight can deviate from the in-trap momentum distribution, if interaction effects during the expansion occur, or the expansion time is not so long that the initial size of the atom cloud can be neglected (far-field approximation) [17].

19.1.3.2 Adiabatic Mapping

One of the advantages of using optical lattice potentials is that the lattice depth can be dynamically controlled by tuning the laser power. This opens another possibility for releasing the atoms from the lattice potential, i.e., by adiabatically converting a deep optical lattice into a shallow one and eventually completely turning off the lattice potential. Under adiabatic transformation of the lattice depth, the quasi-momentum \mathbf{q} is preserved and during the turn-off process a Bloch wave in the n th energy band is mapped onto a corresponding free particle momentum \mathbf{p} in the n th Brillouin zone ([Fig. 19.3](#)) [11, 18, 19].

**FIGURE 19.4**

(a) Brillouin zones of a 2D simple cubic optical lattice. (b) For a homogeneously filled lowest Brillouin band, an adiabatic shut off of the lattice potential leads to a homogeneously populated first Brillouin zone, which can be observed through absorption imaging after a time-of-flight expansion. (c) If in addition higher Bloch bands were populated, higher Brillouin zones become populated as well. From [11].

The adiabatic mapping technique has been used with both bosonic [11] and fermionic [19] atoms. For the situation of a homogeneous filled lowest energy band, an adiabatic ramp down of the lattice potential leaves the central Brillouin zone, a square of width $2\hbar k$, fully occupied (Fig. 19.4(b)). On the other hand, if higher-energy bands are populated, one also observes populations in higher Brillouin zones (Fig. 19.4(c)). As in this method each Bloch wave is mapped onto a specific free-particle momentum state, it can be used to efficiently probe the distribution of the particles over Bloch states in different energy bands.

19.2 Many-Body Effects in Optical Lattices

To illustrate how cold atoms in optical lattices can be used to study genuine many-body phenomena in dilute gases, we discuss the Mott-Hubbard transition for bosonic atoms. Following the original idea by [3], this transition was first observed experimentally by [4]. The theory of the underlying QPT is based on the BHM, originally introduced by [2] to describe the destruction of superfluidity due to strong interactions and disorder.

19.2.1 Bose-Hubbard Model

A conceptually simple model to describe cold atoms in an optical lattice at finite density is obtained by combining the kinetic energy (19.13) in the lowest band with the on-site repulsion arising in the limit of a sufficiently deep optical lattice. More precisely, the BHM is obtained from a general many-body Hamiltonian with a pseudo-potential interaction under the following assumptions: (i) both the thermal and the mean interaction energies at a single site are much smaller than the separation $\hbar\omega_0$ to the first excited band; and (ii) the Wannier functions decay essentially within a single lattice constant.

Then only the lowest band needs to be taken into account in Eq. (19.12). Moreover, the hopping matrix elements $J(\mathbf{R})$ are nonnegligible only for $\mathbf{R} = \mathbf{0}$ or to nearest neighbors in Eq. (19.13), and the interaction constants are dominated by the on-site contribution (19.18). This leads to the BHM

$$\hat{H} = -J \sum_{\langle \mathbf{R}, \mathbf{R}' \rangle} \hat{a}_{\mathbf{R}}^\dagger \hat{a}_{\mathbf{R}'} + \frac{U}{2} \sum_{\mathbf{R}} \hat{n}_{\mathbf{R}} (\hat{n}_{\mathbf{R}} - 1) + \sum_{\mathbf{R}} \epsilon_{\mathbf{R}} \hat{n}_{\mathbf{R}}, \quad (19.17)$$

where $\langle \mathbf{R}, \mathbf{R}' \rangle$ denotes a sum over all lattice sites \mathbf{R} and its nearest neighbors at $\mathbf{R}' = \mathbf{R} + \mathbf{d}$, and \mathbf{d} runs through the possible nearest-neighbor vectors. The hopping matrix element to nearest neighbors, $J(\mathbf{d}) = -J < 0$, is always negative in the lowest band, because the ground state must have zero momentum $\mathbf{q} = \mathbf{0}$ in a time-reversal-invariant situation. For a separable lattice and in the limit $V_0 \gg E_r$, it is given by Eq. (19.9). More generally, the hopping matrix elements are determined by the exact band energy using Eq. (19.14). An alternative but more indirect expression is $J(\mathbf{R}) = \langle w(\mathbf{R}) | \hat{H}_0 | w(\mathbf{0}) \rangle$ [3]. At the two-particle level, the interaction between atoms in Wannier states localized around \mathbf{R} and \mathbf{R}' is reduced to a local form $U \delta_{\mathbf{R}, \mathbf{R}'}$ with

$$U = g \int d^3r |w(\mathbf{r})|^4 = \sqrt{\frac{8}{\pi}} ka E_r \left(\frac{V_0}{E_r} \right)^{3/4}, \quad (19.18)$$

where a denotes the s -wave scattering length between the particles.

Since the standard BHM includes nearest-neighbor hopping only, a convenient approximation for J in Eq. (19.17) is obtained by adjusting it to the given bandwidth. Concerning the on-site repulsion U , which disfavors configurations with more than one boson at a given site, its precise value as determined by Eq. (19.18) requires the exact Wannier function. In the low filling regime, $\bar{n} \lesssim 1$, it follows from the single-particle Bloch states via Eq. (19.10). For higher fillings, the mean-field repulsion on each lattice site leads to an admixture of excited states in each well and eventually to a description in which for $\bar{n} \gg 1$ one has a lattice of coupled Josephson junctions with a Josephson coupling $E_J = 2\bar{n}J$ and an effective ‘charging energy’ U [2, 20]. For intermediate fillings, the Wannier functions entering both the effective hopping matrix element J and on-site repulsion U have to be adjusted to account for the mean-field interaction [21]. The change in the on-site interaction energy with filling has been observed experimentally by [6]. In a more detailed description, the effects of interactions at higher filling can be accounted for by a

multi-orbital generalization of the Gross-Pitaevskii *ansatz* [22]. This leads to effective *dressed* Wannier states which include higher bands and coupling between different sites. The last term with a variable on-site energy $\epsilon_{\mathbf{R}} = \tilde{V}(\mathbf{R})$ describes the effect of the smooth trapping potential $\tilde{V}(\mathbf{r})$. It includes the constant band center energy, arising from the $J(\mathbf{R}=\mathbf{0})$ term of the hopping contribution (19.13) and acts like a spatially varying chemical potential.

The BHM describes the competition between the kinetic energy J , which is gained by delocalizing particles over the lattice sites in an extended Bloch state, and the repulsive on-site interaction U , which disfavors having more than one particle at any given site. In an optical lattice loaded with cold atoms, the ratio U/J between these two energies can be changed easily by varying the dimensionless depth V_0/E_r of the optical lattice. Indeed, from Eqs. (19.9) and (19.18), the ratio $U/J \sim (a/d) \exp(2\sqrt{V_0/E_r})$ increases exponentially with the lattice depth. To see strong interaction effects, the average site occupation $\langle \hat{n}_{\mathbf{R}} \rangle$ needs to be on the order of one; otherwise the atoms never see each other.

19.2.2 Superfluid-Mott-Insulator Transition

The BHM Eq. (19.17) is not an exactly solvable model, not even in 1D, despite the fact that the corresponding continuum model in 1D, the Lieb-Liniger model, is exactly solvable. Nevertheless, the essential physics of the model and, in particular, the existence and properties of the QPT which the BHM exhibits as a function of U/J are rather well understood [2]. In fact, for the 3D case and effectively unit filling, the existence of a QPT from a homogeneous BEC to a MI with a nonzero gap has been proven rigorously in a model of hard core bosons in the presence of a staggered field by [23]. Let us first discuss the limiting cases, which describe the two possible phases within the BHM.

19.2.2.1 Superfluid Phase

In the trivial limit $U = 0$, the many-body ground state is an ideal BEC where all N atoms are in the $\mathbf{q} = 0$ Bloch-state of the lowest band. Including the normalization factor in a lattice with N_L sites, this state can be written in the form

$$|\Psi_N\rangle(U=0) = \frac{1}{\sqrt{N!}} \left(\frac{1}{\sqrt{N_L}} \sum_{\mathbf{R}} \hat{a}_{\mathbf{R}}^\dagger \right)^N |0\rangle. \quad (19.19)$$

Therefore, in the limit $U/J \rightarrow 0$ the ground state of the BHM is a Gross-Pitaevskii-type state with a condensate fraction which is trivially equal to one. The critical temperature of the ideal Bose gas in an optical lattice at filling $\bar{n} = 1$ can be obtained from the condition $\int d\varepsilon g(\varepsilon)n_B(\beta_c\varepsilon) = 1$, where $g(\varepsilon)$ is the density of states in the lowest band and $n_B(x) = (\exp(x) - 1)^{-1}$ the Bose-Einstein distribution. This gives $k_B T_c = 5.59 J$. Therefore, in the presence of an optical lattice the critical temperature for BEC is significantly reduced compared with the free space situation, essentially due to the in-

creased effective mass M^* of the particles in the lattice. However, the relevant parameter is not the temperature but the entropy. Indeed, by starting with a deeply degenerate gas and adiabatically switching on the optical lattice, the degeneracy parameter stays constant and the temperature is essentially reduced by a factor M/M^* [24–26].

For a sufficiently large system² $N, N_L \rightarrow \infty$ at fixed density N/N_L , the perfect condensate Eq. (19.19) becomes indistinguishable in practice from a coherent state

$$\exp\left(\sqrt{N}\hat{a}_{q=0}^\dagger\right)|0\rangle = \prod_{\mathbf{R}} \left(\exp\left[\sqrt{N/N_L}\hat{a}_{\mathbf{R}}^\dagger\right] |0\rangle_{\mathbf{R}} \right). \quad (19.20)$$

It factorizes into a product of *local* coherent states at every lattice site \mathbf{R} with average $\bar{n} = \langle \hat{n} \rangle = N/N_L$ because bosonic operators at different sites commute. The probability distribution for the number of atoms at any given site for a perfect BEC in an optical lattice is therefore Poissonian with a standard deviation given by $\sigma(\bar{n}) = \sqrt{\bar{n}}$. Taking $N = N_L$, i.e., an average density such that there is one atom for each lattice site, there is a $1 - 2/e = 0.27$ probability that any given site is occupied with more than one atom. The kinetic-energy-minimization requirement that each atom be at all lattice sites with equal amplitude thus necessarily leads to a substantial probability of finding more than one atom on a given site. At finite repulsion $U > 0$ such configurations are disfavored.

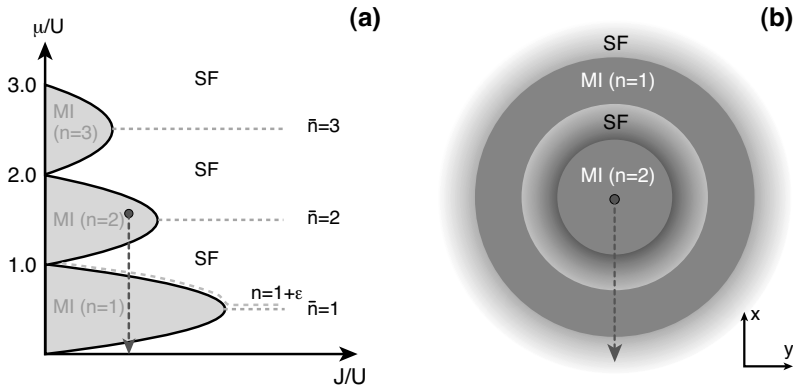
19.2.2.2 Mott-Insulating Phase

To understand the behavior in the opposite limit $U \gg J$, it is useful to consider the case of unit filling, i.e., the number N of atoms is precisely equal to the number N_L of lattice sites. In the limit $U \gg J$, hopping of the atoms is negligible and the obvious ground state

$$|\Psi_{N=N_L}\rangle(J=0) = \left(\prod_{\mathbf{R}} \hat{a}_{\mathbf{R}}^\dagger \right) |0\rangle \quad (19.21)$$

is a simple product of local Fock-states with precisely one atom per site. With increasing J , the atoms start to hop around, which necessarily involves double occupancy, increasing the energy by U . Now as long as the gain J in kinetic energy due to hopping is smaller than U , the atoms remain localized. However, for any $J \neq 0$ the ground state is no longer a simple product state as in Eq. (19.21). Once J becomes of order or larger than U , the gain in kinetic energy outweighs the repulsion due to double occupancies. The atoms then undergo a transition to a SF, in which they are delocalized over the whole lattice. This is a sharp QPT in the thermodynamic limit, because the state (19.19), in contrast to (19.21), exhibits off-diagonal long range order, which cannot disappear in a continuous manner. By contrast, the evolution between these two states is completely smooth for, e.g., two particles in two

²In the experiment [4], the total number of occupied lattice sites was about 10^5 .

**FIGURE 19.5**

Schematic zero temperature phase diagram of the Bose-Hubbard model. The dashed lines of constant integer density $\langle \hat{n} \rangle = 1, 2, 3$ in the SF hit the corresponding MI phases at the tips of the lobes at a critical value of J/U , which decreases with density \bar{n} . For $\langle \hat{n} \rangle = 1 + \varepsilon$ the line of constant density stays outside the $\bar{n} = 1$ MI because a fraction ε of the particles remains superfluid down to the lowest values of J . In an external trap with an $\bar{n} = 2$ MI phase in the center, a series of MI and SF regions appear by going towards the edge of the cloud, where the local chemical potential has dropped to zero.

wells, where a simple crossover occurs from a state with a well-defined relative phase at $J \gg U$ to one with a well-defined particle number in each well at $J \ll U$.

19.2.2.3 Phase Diagram

The zero temperature phase diagram of the homogeneous BHM is shown schematically in Fig. 19.5(a) as a function of J/U , with the density controlled by a chemical potential μ . At $U/J \rightarrow 0$, the kinetic energy dominates and the ground state is a delocalized SF, described by Eq. (19.20) to lowest order. At large values of U/J , interactions dominate and one obtains a series of MI phases with fixed integer filling $\bar{n} = 1, 2, \dots$. These states are *incompressible*, meaning that their density remains unchanged upon varying the chemical potential. In fact, it is the fact that the compressibility $\kappa \equiv \partial n / \partial \mu = 0$ which is the defining property of a MI, and not a description via local Fock pure states; the latter only exist at $J = 0$. The transition between the SF and MI phases is associated with the loss of long range order in the one-particle density matrix $g^{(1)}(\mathbf{x})$. In the 3D case, the order parameter of the SF-MI transition is therefore the condensate fraction n_0/n , which drops continuously from unity at $U/J \ll 1$ to zero at $(U/J)_c$. The continuous nature of the SF-MI QPT in any number of dimensions follows from the fact that the effective field

theory for the complex order parameter ψ is of that of a $d + 1$ -dimensional XY-model [2, 27]. More precisely, this is valid only for the special transition at integer density, which is driven by phase fluctuations only. By contrast, crossing the SF-MI phase boundary at any other point, by a change in chemical potential, the associated change in the density gives rise to a different critical behavior [2].³ For instance, the excitation gap in the MI phase vanishes linearly with the distance from the boundary of the Mott lobe in this more generic case.

Within a mean-field approximation, the critical value for the transition from a MI to a SF in a 3D optical lattice is given by $(U/J)_c = 5.8z$ for $\bar{n} = 1$ and $(U/J)_c = 4\bar{n}z$ for $\bar{n} \gg 1$ [2, 28, 29]. Here z is the number of nearest neighbors and thus $2zJ$ is the total bandwidth of the lowest Bloch band, which is the relevant parameter which has to be compared with U . Recently, precise quantum Monte Carlo simulations by [30] have determined the critical value for the $\bar{n} = 1$ transition in a simple cubic lattice to be at $(U/J)_c = 29.36$ with an accuracy of about 0.1%. In 1D and for the special case of integer filling, the SF-MI transition is of the Berzinski-Kosterlitz-Thouless type, with a finite jump of the SF density at the transition; see Chap. 12 for details. Precise values for the critical coupling are available from density matrix renormalization group (DMRG) calculations, giving $(U_1/J)_c = 3.37$ [31, 32] for the $\bar{n} = 1$ transition. For $\bar{n} \gg 1$, the BHM is equivalent to a chain of Josephson junctions with coupling energy $E_J = 2\bar{n}J$. The SF-MI transition is then described by the $(1 + 1)$ -dimensional $O(2)$ quantum-rotor model, which gives $(U_1/J)_c = 2.2\bar{n}$ [33].

From Eqs. (19.9) and (19.18), the critical value of the dimensionless lattice depth V_0/E_r for rather deep lattices is obtained from

$$(V_0/E_r)_c = \frac{1}{4} \ln^2 \left(\frac{\sqrt{2}d}{\pi a} (U/J)_c \right). \quad (19.22)$$

Using the experimental parameters $d = 426$ nm and $a = 5.7$ nm [4], the precise result for $(U/J)_c$ in a simple cubic lattice gives a critical value $(V_0/E_r)_c = 11.89$ for the SF-MI transition with $\bar{n} = 1$. Given that Eq. (19.9), on which the above estimate for the critical lattice depth is based, is not very precise in this regime, this result is in reasonable agreement with the lattice depth of $V_0 = 12 - 13E_r$, where the transition is observed experimentally [4, 34].

Consider now a filling with $\langle \hat{n} \rangle = 1 + \varepsilon$, $\varepsilon \ll 1$. For large J/U the ground state has all the atoms delocalized over the whole lattice and the situation is hardly different from the case of unit filling. However, upon lowering J/U the line of constant density remains slightly above the $\bar{n} = 1$ Mott lobe, and stays in the SF regime down to the lowest J/U (Fig. 19.5). For any noninteger filling, therefore, the ground state remains SF as long as the atoms can hop at all. This is a consequence of the fact, that even for $J \ll U$ there is a small

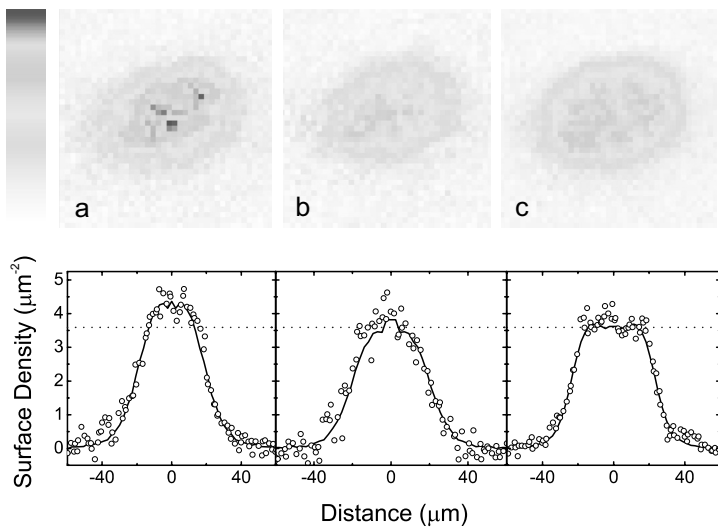
³This is true in two and higher dimensions. There are formally no QPTs in 1D. However, due to the mesoscopic nature of dilute gas BECs a sharp crossover occurs in 1D [35]; see Chaps. 13 and 27 for a discussion of QPTs in various finite systems.

fraction ε of atoms which remain SF on top of a frozen MI-phase with $\bar{n} = 1$. Indeed, this fraction can still gain kinetic energy by delocalizing over the whole lattice without being blocked by the repulsive interaction U because two of those particles will never be at the same place. The same argument applies to holes when ε is negative. As a result, in the homogeneous system the QPT from a SF to a MI only appears if the density is equal to a commensurate, integer value.

19.2.2.4 In-Trap Density Distribution

Fortunately, the situation is much less restrictive in the presence of a harmonic trap. Indeed, within a local density approximation, the inhomogeneous situation in a harmonic trap is described by a spatially varying chemical potential $\mu_{\mathbf{R}} = \mu_0 - \epsilon_{\mathbf{R}}$ with $\epsilon_{\mathbf{R}} = 0$ at the trap center. Assuming, e.g., that the chemical potential μ_0 at trap center falls into the $\bar{n} = 2$ Mott lobe, one obtains a series of MI domains separated by a SF by moving to the boundary of the trap where $\mu_{\mathbf{R}}$ vanishes ([Fig. 19.5\(b\)](#)). In this manner, all the different phases which exist for given J/U below μ_0 are present simultaneously! The SF phase has a finite compressibility κ and a gapless excitation spectrum of the form $\omega(q) = cq$ because there is a finite SF density n_s . By contrast, in the MI-phase both n_s and κ vanish. As predicted by [3], the incompressibility of the MI phase allows one to distinguish it from the SF by observing the local density distribution in a trap. Since $\kappa = 0$ in the MI, the density stays constant in the Mott phases, even though the external trapping potential rises. In the limit as $J \rightarrow 0$ the SF regions vanish and one obtains a *wedding-cake-type* density profile, with radii R_n of the different MI regions, given by $R_n = \sqrt{[2(\mu_0 - nU)/M\omega^2]}$ [36].

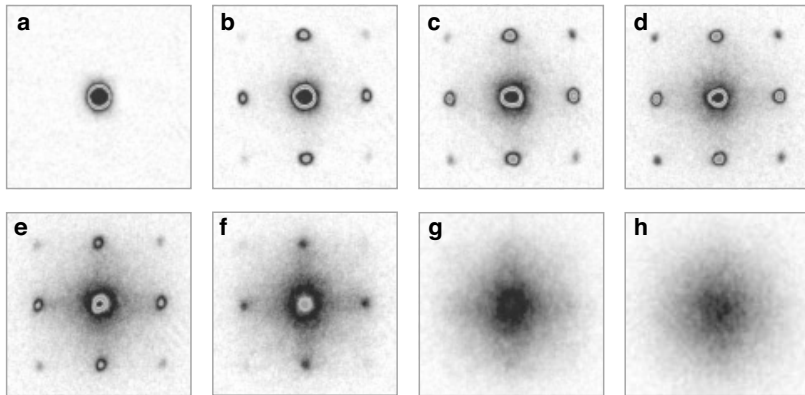
The existence of such wedding-cake-like density profiles of a MI has been supported by Monte Carlo [38–40] and DMRG [32] calculations in 1D, 2D, and 3D. Very recently number-state resolved, in-trap density profiles have been detected experimentally by [6] and [37, 41]. In the two latter cases it has been possible to directly observe the wedding-cake density profiles and thus confirm the incompressibility of the MI regions of the atomic gas in the trapping potential. In the work of Gemelke *et al.* [37] a single lattice plane could be prepared and therefore averaging effects in absorption imaging avoided. The in-trap density change could therefore be well resolved in the experiment ([Fig. 19.6](#)). It should be noted that the in-trap density profiles can be used as a sensitive thermometer for the strongly-interacting quantum gas. For typical experimental parameters, one finds that for temperatures around $T^* \gtrsim 0.2U/k_B$, the wedding cake profiles become completely washed out [42]. Within the strongly-interacting regime, the SF shells accommodate most of the entropy of the system and can turn already into a normal thermal gas at a lower temperature $T_c \sim zJ$ with the MI shells still intact [30, 42, 43]. In order to reach the lowest temperatures in this regime, it is advantageous to keep the external harmonic confinement as low as possible, or even decrease it during an increase of the lattice depth [42, 43].

**FIGURE 19.6**

Absorption images and line cuts along major axis of density profiles for $N = 7,500$ ultracold cesium atoms at scattering length $a = 310a_B$ in 2D optical lattices. (a) Superfluid regime, (b) phase transition regime, and (c) Mott-insulator regime. Images are averaged over three experimental repetitions. Line cuts are taken along the major axis, and compared to two-level radial average of two-level density (solid line) over the entire image. The horizontal dotted line indicates the density of one atom per site. Reprinted by permission from Macmillan Publishers Ltd: Nature **460**, 995 (2009), copyright (2009).

19.2.2.5 Phase Coherence Across the SF-MI Transition

The disappearance of superfluidity at the SF-MI transition was initially observed experimentally by a time-of-flight method [4]. The corresponding series of images is shown in Fig. 19.7 for different values of V_0 , ranging between (a) $V_0 = 0$ and (h) $V_0 = 20E_r$. One observes a series of interference peaks around the characteristic zero-momentum peak of a condensate in the absence of an optical lattice. With increasing V_0 these peaks become more pronounced. Beyond a critical lattice depth around (e) $V_0 \approx 12 - 13E_r$, which agrees very well with the above estimate for the SF-MI transition for one Boson per site, this trend is suddenly reversed, however, and the interference peaks eventually disappear completely. In order to understand why these pictures indeed provide a direct evidence for a SF to MI transition predicted by the BHM, it is useful to consider the idealized situation of a perfect periodic lattice in the absence of any trapping potential. From Eq. (19.15) the observed density at position \mathbf{x} reflects the momentum distribution at $\mathbf{k} = M\mathbf{x}/\hbar t$. Factoring out

**FIGURE 19.7**

Absorption images of multiple matter wave interference patterns after releasing the atoms from an optical lattice potential with a potential depth of (a) $0 E_r$, (b) $3 E_r$, (c) $7 E_r$, (d) $10 E_r$, (e) $13 E_r$, (f) $14 E_r$, (g) $16 E_r$, and (h) $20 E_r$. The ballistic expansion time was 15 ms. Reprinted by permission from Macmillan Publishers Ltd: Nature **415**, 39 (2002), copyright (2002).

the number of lattice sites, it is proportional to the lattice Fourier transform

$$n(\mathbf{k}) \sim |\tilde{w}(\mathbf{k})|^2 \sum_{\mathbf{R}} e^{i\mathbf{k} \cdot \mathbf{R}} G^{(1)}(\mathbf{R}) \quad (19.23)$$

of the one-particle density matrix $G^{(1)}(\mathbf{R})$ at separation \mathbf{R} . For optical lattice depths below the critical value, the ground state in a 3D situation is a true BEC, where $G^{(1)}(|\mathbf{R}| \rightarrow \infty) = n_0$ approaches a finite value at large separation. For the MI phase, in turn, $G^{(1)}(\mathbf{R})$ decays to zero exponentially. The SF phase of cold atoms in a homogeneous optical lattice is thus characterized by a momentum distribution which exhibits sharp peaks at the reciprocal lattice vectors⁴ $\mathbf{k} = \mathbf{G}$, plus a smooth background from the short-range correlations. The fact that the peaks in the momentum distribution at $\mathbf{k} = \mathbf{G}$ initially grow with increasing depth of the lattice potential is a result of the strong decrease in spatial extent of the Wannier function $w(\mathbf{r})$, which entails a corresponding increase in its Fourier transform $\tilde{w}(\mathbf{k})$ at higher momenta. In the MI regime, where $G^{(1)}(\mathbf{R})$ decays to zero, remnants of the interference peaks still remain (e.g., Fig. 19.7(f)) as long as $G^{(1)}(\mathbf{R})$ extends over several lattice spacings, because the series in Eq. (19.23) adds up constructively at $\mathbf{k} = \mathbf{G}$.

A more detailed picture for the residual short-range coherence features beyond the SF-MI transition is obtained by considering perturbations deep in the MI regime at $J = 0$. There, $G^{(1)}(\mathbf{R})$ vanishes beyond $\mathbf{R} = \mathbf{0}$ and the momentum distribution is a structureless Gaussian, reflecting the Fourier

⁴Defined by $\mathbf{G} \cdot \mathbf{R} = 2\pi$ times an integer, see, e.g., [14].

transform of the Wannier wave function ([Fig. 19.7\(h\)](#)). With increasing tunneling J , the Mott state as $J/U \rightarrow 0$ is modified by a coherent admixture of particle-hole pairs. However due to the presence of a gapped excitation spectrum, such particle-hole pairs cannot spread out and are rather tightly bound to close distances. However, they do give rise to a significant degree of short range coherence. Using first-order perturbation theory with the tunneling operator as a perturbation on the dominating interaction term, one finds that the amplitude of the coherent particle-hole admixtures in a MI state is proportional to J/U :

$$|\Psi\rangle_{U/J} \approx |\Psi\rangle_{U/J \rightarrow \infty} + \frac{J}{U} \sum_{\langle \mathbf{R}, \mathbf{R}' \rangle} \hat{a}_{\mathbf{R}}^\dagger \hat{a}_{\mathbf{R}'} |\Psi\rangle_{U/J \rightarrow \infty}. \quad (19.24)$$

Close to the transition point, higher order perturbation theory or a Green's function analysis can account for coherence beyond nearest neighbors and the complete liberation of the particle-hole pairs, which eventually leads to the formation of long range coherence in the SF regime. The coherent particle-hole admixture and its consequence on the short-range coherence of the system have been investigated theoretically and experimentally in [34, 44, 45].

The SF-MI QPT therefore shows up directly in the interference pattern. For the homogeneous system it reveals the existence or lack thereof of off-diagonal long range order in the one-particle density matrix. The relevant order parameter is the condensate fraction. The actual system is not homogeneous and a numerical computation of the interference pattern is necessary for a quantitative comparison with experiment. This has been done, e.g., for the 3D case in [38] and for 1D case in [32, 39]. Due to the finite size and the fact that different MI phases are involved, the pattern evolves continuously from the SF to the MI regime. While the critical values for J/U are different for the MI phases with $\bar{n} = 1$ and $\bar{n} = 2$ which are present in the experiment [4], the transition seen in the time-of-flight images occurs rather rapidly with increasing lattice depth. Indeed, from Eq. (19.22), the experimental control parameter V_0/E_r depends only logarithmically on the relevant parameter U/J of the BHM. The small change from $V_0 = 13E_r$ in (e) to $V_0 = 14E_r$ in (f) thus covers a range in J/U wider than that, which would be required to distinguish the $\bar{n} = 1$ from the $\bar{n} = 2$ transition.

When approaching the SF-MI transition from the SF regime, the increasing interactions tend to increase the depletion of the condensate and thereby reduce the long range phase coherent component with increasing U/J [10, 46, 47]. For increasing lattice depth, the condensate density, as a measure of the long range coherent fraction, then decreases continuously and vanishes at the transition point. However, the visibility of the interference pattern in general evolves smoothly across the SF-MI transition, due to the presence of a strong short range coherent fraction in the MI just across the transition point (see discussion above). Above the transition point the visibility of the momentum distribution can also show kinks as the lattice depth is increased, which have been attributed to the onset of shell structures in the MI state [34, 44, 45].

19.2.2.6 Excitation Spectrum

A second signature of the SF-MI transition is the appearance of a finite excitation gap $\Delta \neq 0$ in the MI. Deep in the MI phase, this gap has size U , which is just the increase in energy if an atom tunnels to an already occupied adjacent site.⁵ The existence of a gap has been observed experimentally by applying a potential gradient in the MI [4] or by using a modulation spectroscopy method [5] and measuring the resulting excitations. Recent calculations indicate that such measurements simultaneously probe global [48, 49] and local properties of the system. In particular, a peaked excitation spectrum can also appear in a strongly-interacting SF regime, where $U > J$ [50]. A way to probe global features of the many-body excitation spectrum, also close to the transition point, might be achieved by employing Bragg spectroscopy techniques as proposed in [51].

In the SF regime, there is no excitation gap. Instead, the homogeneous system exhibits a sound-like mode with frequency $\omega(q) = cq$. The associated sound velocity c is determined by $Mc^2 = n_s/\kappa$ and thus gives information about the SF density n_s . The existence of a sound-like excitation even in the presence of an underlying lattice which explicitly breaks translation invariance is a consequence of long range phase coherence in the SF. Its observation would therefore directly probe superfluidity, in contrast to the peaks in the interference pattern, which measure BEC.

19.2.2.7 Number Statistics

Associated with the transition from a SF to a MI state is a profound change in the atom number statistics per lattice site. As noted above, in the homogeneous system the ground state in the extreme MI limit ($J/U \rightarrow 0$) is a product of Fock states with an integer number \bar{n} of particles at each site. At finite hopping $J \neq 0$, this simple picture breaks down because the atoms have a finite amplitude to be at different sites. The many-body ground state can then no longer be written as a simple product state. In the opposite limit $U \rightarrow 0$, the ground state is a condensate of zero quasi-momentum Bloch states. In the limit $N, N_L \rightarrow \infty$ at fixed density $\bar{n} = N/N_L$, the associated perfect condensate is a product of coherent states on each lattice site,

$$|\alpha\rangle = e^{-|\alpha|^2/2} \sum_n \frac{\alpha^n}{\sqrt{n!}} |n\rangle, \quad (19.25)$$

with α describing the amplitude and phase of the coherent matter wave field. This corresponds to a Poissonian atom number distribution on each lattice site with average $|\alpha|^2 = \bar{n}$.

A remarkable consequence of the representation (19.20) is that, at least for integer densities $\bar{n} = 1, 2, \dots$, the many-body ground state may be factorized

⁵Note that U is much smaller than the gap $\hbar\omega_0$ for the excitation of the next vibrational state.

into a product over single sites

$$|\Psi_{GW}\rangle = \prod_{\mathbf{R}} (\sum_{n=0}^{\infty} c_n |n\rangle_{\mathbf{R}}) \quad (19.26)$$

in both limits $J \rightarrow 0$ and $U \rightarrow 0$. The associated atom number probability distribution $p_n = |c_n|^2$ is either a pure Fock or a full Poissonian distribution. It is now very plausible to use the factorized form in Eq. (19.26) as an *approximation* for arbitrary J/U , taking the coefficients c_n as variational parameters which are determined by minimizing the ground state energy [28, 52]. As pointed out by [52], this is effectively a Gutzwiller *ansatz* for bosons. Beyond being very simple computationally, this *ansatz* describes the SF to MI transition in a mean-field sense, becoming exact in infinite dimensions. In addition, it provides one with a very intuitive picture of the transition to a MI state, which occurs precisely at the point, where the local number distribution becomes a pure Fock distribution. Indeed, within the Gutzwiller approximation, the expectation value

$$\langle \Psi_{GW} | \hat{n}_{\mathbf{R}} | \Psi_{GW} \rangle = \sum_{n=1}^{\infty} \sqrt{n} c_{n-1}^* c_n \quad (19.27)$$

of the local matter wave field vanishes if and only if the probability for finding different particle numbers at any given site is equal to zero. However, it is important to emphasize that the Gutzwiller *ansatz* fails to account for the nontrivial correlations between different sites present at any finite J . These correlations imply that the single-particle density matrix $G^{(1)}(\mathbf{R})$ is different from zero at finite distance $|\mathbf{R}| \neq 0$, becoming long-ranged at the transition to a SF. By contrast, in the Gutzwiller approximation, the single-particle density matrix has no spatial dependence at all: it is zero at any $|\mathbf{R}| \neq 0$ in the MI and is completely independent of \mathbf{R} in the SF. Moreover, in the Gutzwiller approximation, the QPT is directly reflected in the local number fluctuations, with the variance of $n_{\mathbf{R}}$ vanishing throughout the MI phase. However, in reality local variables like the on-site number distribution will change in a smooth manner near the transition and the variance of the local particle number will only vanish in the limit $J \rightarrow 0$.

Therefore, in crossing the SF-MI transition the number statistics evolves rather smoothly from a Poissonian distribution to Fock states on each lattice site. Recent experimental progress has allowed measurements of the number distribution in the optical lattice via microwave spectroscopy exploiting collisional frequency shifts [6], spin changing collisions [53] or interaction blockade effects [54]. Another possibility to observe the number squeezing of the initially Poissonian atom number distribution in the weakly-interacting regime due to increasing interatomic interactions has been to use a matter-wave beam splitter and observe the timescale of the collapse in the ensuing phase diffusion dynamics [55–57], which is discussed in the following section.

19.2.2.8 Dynamics near Quantum Phase Transitions

One of the major advantages of cold atoms in studying many-body phenomena is the possibility to change the parameters characterizing the relative strength

of the kinetic and interaction energy dynamically. This opens the possibility to study the real-time dynamics of strongly correlated systems in a controlled manner. As a simple example, we discuss the quantum quench of the system from the SF into the MI regime. This issue has been investigated in an experiment, observing collapses and revivals of the matter wave due to the coherent superposition of states with different atom numbers in the SF [55]. In the weakly-interacting regime of a BEC in an optical lattice potential, the ground state (19.20) is a product of coherent states on each lattice site with a Poissonian atom number distribution. If the lattice depth is now suddenly increased to a parameter regime where the ground state of the system is a MI state, the initial atom number fluctuations of the coherent state will be frozen out, as the system is not given enough time to redistribute towards the novel many-body ground state. The evolution with time of such a coherent state can be evaluated by taking into account the time evolution of the different Fock states forming the coherent state:

$$|\alpha\rangle(t) = e^{-|\alpha|^2/2} \sum_n \frac{\alpha^n}{\sqrt{n!}} e^{-i\frac{1}{2}U(n-1)t/\hbar} |n\rangle. \quad (19.28)$$

The coherent matter wave field ψ on each lattice site can then be evaluated through $\psi = \langle \alpha(t) | \hat{a} | \alpha(t) \rangle$, which exhibits an intriguing dynamical evolution [58, 59]. At first, the different phase evolutions of the atom number states lead to a collapse of ψ . However, at integer multiples in time of \hbar/U all phase factors in the above equation re-phase modulo 2π and thus lead to a revival of the initial coherent state. In fact, precise revivals appear as long as the initial state can be written in the factorized form of Eq. (19.26). Since the time-evolution operator $\exp(-i\hat{H}t/\hbar)$ factorizes into a product of on-site terms $\exp[-in(n-1)Ut/2\hbar]$, the time dependence is perfectly periodic with period $t_{\text{rev}} = \hbar/U_f$, where U_f is the value of the on-site repulsion after the quench. Clearly the period is independent of the precise form of the initial number distribution $|c_n|^2$. The collapse time $t_c \approx t_{\text{rev}}/\sigma_n$ in turn depends on the variance $\sigma_n^2 = \langle n^2 \rangle - \langle n \rangle^2$ of the local number distribution. Its measurement thus provides information about how the coherent superposition of different particle numbers in the SF state is eventually destroyed by approaching the MI regime [55].

The collapse and revival of the coherent matter wave field of a BEC is reminiscent to the collapse and revival of the Rabi oscillations in the interaction of a single atom with a single mode electromagnetic field in cavity quantum electrodynamics [60]. There, the nonlinear atom-field interaction induces the collapse and revival of the Rabi oscillations whereas here the nonlinearity due to the interactions between the atoms themselves leads to the series of collapse and revivals of the matter wave field. It should be pointed out that such a behavior has also been theoretically predicted to occur for a coherent light field propagating in a nonlinear medium [58] but to our knowledge has never been observed experimentally. Such a dynamical evolution of the atomic quantum state due to the nonlinear interactions between the particles is also known as quantum phase diffusion and has been detected in [55] for low atom

numbers on each site. For larger atom numbers, the initial time evolution of the quantum phase diffusion could be recently observed by [57] in a double well scenario.

The simple single site description is valid only in the limits $U_i \ll J$ of a nearly perfect SF in the initial state and $U_f \gg J$ of negligible tunneling in the final state. To determine the dynamics in a more general situation is a complicated nonequilibrium many-body problem. Numerical results for arbitrary values of U_i and U_f have been obtained for the 1D BHM by [61], using the time-dependent density matrix renormalization group [62].

In a related scenario it has been proposed that when jumping from an initial MI state into the SF regime, one should observe oscillations of the SF order parameter [63]. For large filling factors, oscillating coherence has been observed after a quench from a deep to a shallow lattice by [64]. The formation of a SF from an initial MI phase poses a general problem of interest in the context of the dynamics of strongly correlated quantum systems. Both experiment [4] and theory [65] have confirmed that the emergence of coherence in the system can occur rather rapidly on timescales of a few tunneling times \hbar/J . However, it is an open question whether off-diagonal long range order in the one-particle density matrix indeed sets in within such a short time and what length scales are relevant; answers to these questions must be established in order to observe coherence in a time-of-flight picture.

19.2.2.9 Bose-Hubbard Model with Finite Current

The SF-MI transition discussed in 19.2.2 above is a continuous QPT in the ground state of a many-body Hamiltonian. The observation from the time-of-flight images that long range phase coherence is lost beyond a critical value of U/J provides a signature for the disappearance of BEC. The expected simultaneous loss of *superfluidity* across this transition may be studied by considering the phase boundary, where stationary states with a finite current lose their stability. Such stationary out-of-equilibrium states may be created experimentally by boosting the condensate to a finite-momentum state [66], or by inducing a center-of-mass oscillation in the trap [67]. The question of what happens to the equilibrium SF-MI transition in a situation with a finite current has been addressed by [68]. For a given number \bar{n} of bosons per site, the kinetic energy term in the BHM (19.17) gives rise to a Josephson coupling energy $E_J = 2\bar{n}J$ due to next neighbor-tunneling which favors a vanishing relative phase between adjacent lattice sites. In the limit $E_J \gg U$, there is a nonvanishing matter wave field $\psi_{\mathbf{R}} = \langle \hat{a}_{\mathbf{R}} \rangle$. In the ground state, all bosons have zero momentum and $\psi_{\mathbf{R}}$ is uniform. States with a finite current, in turn, are BECs in which single particle states with nonzero momentum \mathbf{q} are macroscopically occupied. To zeroth order in U/E_J , their energy is the Bloch band energy Eq. (19.8). The associated current per particle $\mathcal{J} = (2J/\hbar) \sin q_x d$ for motion along the x -direction has a maximum at $p = q_x d = \pi/2$. States with a larger momentum are unstable in a linear stability analysis [68]. This

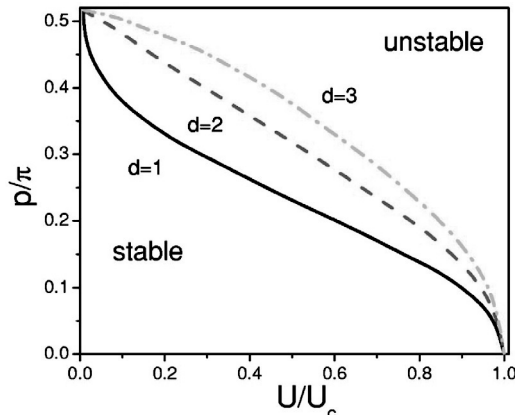
instability was observed experimentally by [66]. A moving optical lattice is created by two counter-propagating beams at frequencies which differ by a small detuning $\delta\nu$. Averaged over the optical frequencies, this gives rise to an interference pattern which is a standing wave moving at velocity $v = \lambda\delta\nu/2$. Adiabatically switching on such a lattice in an existing BEC then leads to a condensate in a state with quasi-momentum $q = Mv/\hbar$. Its lifetime shows a very rapid decrease for momenta near the critical value q_c .

In the strongly-interacting regime near the SF-MI transition, such a single particle picture is no longer valid. At the mean-field level, the problem may be solved by using the field theoretical description of the SF-MI transition. The SF phase is then characterized by a nonzero complex order parameter ψ , whose equilibrium value $|\psi| \sim \xi^{-1}$ vanishes like the inverse of the correlation length ξ .⁶ The stationary solutions of the dimensionless order-parameter equation $\nabla^2\psi + \xi^{-2}\psi = |\psi|^2\psi$ with *finite* momentum are of the form $\psi(x) = \sqrt{\xi^{-2} - p^2} \exp(ipx)$. Evidently, such solutions exist only if $|p| < 1/\xi$. The critical value of the dimensionless momentum p , where current-carrying states become unstable, thus approaches zero continuously at the SF-MI transition [68]. In fact, the same argument can be used to discuss the vanishing of the critical current in superconducting wires near T_c [69]. The complete mean-field phase diagram, shown in Fig. 19.8, interpolates smoothly between the classical instability at $p_c = \pi/2$ and $p_c \rightarrow 0$ in the limits $U \rightarrow 0$ and $U \rightarrow U_c$, respectively. In contrast to the equilibrium transition at $p = 0$ which is continuous, the dynamical transition is of *first order*. Crossing the phase boundary at any nonzero current is therefore connected with an irreversible decay of the current to zero. Experimentally, the decrease of the critical momentum near the SF-MI transition has been observed by [70]. Their results are in good agreement with the phase diagram shown in Fig. 19.8.

In the mean-field picture, states of a SF with nonzero momentum have an infinite lifetime. However, more precisely, such states can only be *metastable*, because the ground state of any time-reversal invariant Hamiltonian necessarily has zero current. Therefore, the crucial requirement for a SF in practice is that current-carrying states have lifetimes which far exceed experimentally relevant scales. This requires these states to be separated from the state with vanishing current by energy barriers, which are much larger than the thermal or relevant zero point energy.⁷ The rate for phase slip formation near the critical line in Fig. 19.8 has been calculated by [68]. It turns out that the mean-field transition survives fluctuations in 3D; so in principle it is possible to locate the equilibrium SF-MI transition by extrapolating the dynamical transition line to zero momentum. In the experiments of [67], the system still showed sharp interference peaks even in the over-damped regime where the

⁶This relation holds in the mean-field approximation, which is appropriate for the transition at integer densities in 3D.

⁷This is different from the well-known Landau criterion of SF flow below a finite critical velocity [71]. Indeed, the existence of phase slips implies that the critical velocity is always zero in a strict sense.

**FIGURE 19.8**

Mean-field phase diagram separating stable and unstable motion of condensate regions. The vertical axis denotes the condensate momentum in inverse lattice units and the horizontal axes denotes the normalized interaction. Reprinted figure with permission from A. Polkovnikov *et al.*, Phys. Rev. A, 71, 063613 (2005). Copyright (2005) by the American Physical Society.

condensate motion was locked by the optical lattice. This may be due to localized atoms at the sample edges, which block the dipole oscillation even though the atoms in the center of the trap are still in the SF regime. A theoretical study of the damped oscillations of 1D bosons has been performed by [72].

19.3 Outlook

In addition to bosonic MIs, recently MIs in two-component fermionic spin mixtures have been realized [73]. This constitutes an important milestone on the way to map out the low temperature phase diagram of the Hubbard model, including magnetically ordered phases and possibly a d -wave superconducting phase [25, 74]. One of the next major challenges in this direction will be to cool strongly-interacting bosonic or fermionic spin mixtures below the super-exchange energy scale, in order to observe such magnetically ordered quantum phases in the system. At present, experiments still seem to be a factor of two to three too high in entropy, in order to reach this regime. However, novel cooling schemes have been proposed that make use of the inhomogeneous entropy distribution in the trap, allowing one to access and eventually remove highly entropic regions to achieve further cooling. The recently developed capabilities

to address atoms on single lattice sites could be helpful in achieving this goal [75]. By adding frustration effects through, e.g., ring-exchange couplings, one might be then able to induce QPTs in magnetically ordered phases that are of current interest, as described in Chap. 1.

Bibliography

- [1] D. Jaksch and P. Zoller, Ann. Phys. (N.Y.) **315**, 52 (2005); M. Lewenstein *et al.*, Adv. Phys. **56**, 243 (2007); I. Bloch, J. Dalibard, and W. Zwerger, Rev. Mod. Phys. **80**, 885 (2008).
- [2] M. P. A. Fisher, P. B. Weichman, G. Grinstein, and D. S. Fisher, Phys. Rev. B **40**, 546 (1989).
- [3] D. Jaksch *et al.*, Phys. Rev. Lett. **81**, 3108 (1998).
- [4] M. Greiner *et al.*, Nature **415**, 39 (2002).
- [5] T. Stöferle *et al.*, Phys. Phys. Lett. **92**, 130403 (2004).
- [6] G. Campbell *et al.*, Science **313**, 5787 (2006).
- [7] I. B. Spielman, W. D. Phillips, and J. V. Porto, Phys. Rev. Lett. **98**, 080404 (2007).
- [8] R. Grimm, M. Weidemüller, and Y. B. Ovchinnikov, Adv. At. Mol. Opt. Phys. **42**, 95 (2000).
- [9] S. Peil *et al.*, Phys. Rev. A **67**, 051603 (2003).
- [10] Z. Hadzibabic *et al.*, Phys. Rev. Lett. **93**, 180403 (2004).
- [11] M. Greiner *et al.*, Phys. Rev. Lett. **87**, 160405 (2001).
- [12] H. Moritz, T. Stöferle, M. Köhl, and T. Esslinger, Phys. Rev. Lett. **91**, 250402 (2003); B. L. Tolra *et al.*, Phys. Rev. Lett. **92**, 190401 (2004); B. Paredes *et al.*, Nature **429**, 277 (2004); T. Kinoshita, T. Wenger, and D. S. Weiss, Science **305**, 1125 (2004).
- [13] C. Hooley and J. Quintanilla, Phys. Rev. Lett. **93**, 080404 (2004).
- [14] N. W. Ashcroft and N. D. Mermin, *Solid State Physics* (Holt, Rinehardt and Winston, New York, 1976).
- [15] W. Kohn, Phys. Rev. **115**, 809 (1959).
- [16] L. He and D. Vanderbilt, Phys. Rev. Lett. **86**, 5341 (2001).

- [17] P. Pedri *et al.*, Phys. Rev. Lett. **87**, 220401 (2001); F. Gerbier, S. Fölling, A. Widera, and I. Bloch, cond-mat/0701420 (2007).
- [18] A. Kastberg *et al.*, Phys. Rev. Lett. **74**, 1542 (1995).
- [19] M. Köhl *et al.*, Phys. Rev. Lett. **94**, 080403 (2005).
- [20] F. S. Cataliotti *et al.*, Science **293**, 843 (2001).
- [21] J. Li, Y. Yu, A. Dudarev, and Q. Niu, New J. Phys. **8**, 154 (2006).
- [22] O. E. Alon, A. I. Streltsov, and L. S. Cederbaum, Phys. Rev. Lett. **95**, 030405 (2005).
- [23] M. Aizenman *et al.*, Phys. Rev. A **70**, 023612 (2004).
- [24] M. Olshanii and D. Weiss, Phys. Rev. Lett. **89**, 090404 (2002).
- [25] W. Hofstetter *et al.*, Phys. Rev. Lett. **89**, 220407 (2002).
- [26] P. Blakie and J. Porto, Phys. Rev. A **69**, 013603 (2004).
- [27] S. Sachdev, *Quantum Phase Transitions* (Cambridge University Press, Cambridge, 1999).
- [28] K. Sheshadri, H. R. Krishnamurty, R. Pandit, and T. V. Ramakrishnan, Europhys. Lett. **22**, 257 (1993).
- [29] D. van Oosten, P. van der Straten, and H. T. C. Stoof, Phys. Rev. A **63**, 053601 (2001).
- [30] B. Capogrosso-Sansone, N. V. Prokof'ev, and B. V. Svistunov, Phys. Rev. B **75**, 134302 (2007).
- [31] T. D. Kühner, S. R. White, and H. Monien, Phys. Rev. B **61**, 12474 (2000).
- [32] C. Kollath, U. Schollwöck, J. von Delft, and W. Zwerger, Phys. Rev. A **69**, 031601(R) (2004).
- [33] C. J. Hamer and J. B. Kogut, Phys. Rev. B **20**, 3859 (1979); H. H. Roothaan and H. W. Wyld, Phys. Rev. D **21**, 3341 (1980).
- [34] F. Gerbier *et al.*, Phys. Rev. Lett. **95**, 050404 (2005).
- [35] L. D. Carr *et al.*, Phys. Rev. A **81**, 013613 (2010).
- [36] B. DeMarco, C. Lannert, S. Vishveshwara, and T.-C. Wei, Phys. Rev. A **71**, 063601 (2005).
- [37] N. Gemelke, X. Zhang, C.-L. Hung, and C. Chin, Nature **460**, 995 (2009).

- [38] V. A. Kashurnikov, N. V. Prokof'ev, and B. V. Svistunov, Phys. Rev. A **66**, 031601 (2002).
- [39] G. G. Batrouni *et al.*, Phys. Rev. Lett. **89**, 117203 (2002).
- [40] S. Wessel, F. Alet, M. Troyer, and G. G. Batrouni, Phys. Rev. A **70**, 053615 (2004); M. Rigol, R. T. Scalettar, P. Sengupta, and G. G. Batrouni, Phys. Rev. B **73**, 121103 (2006).
- [41] S. Fölling *et al.*, Phys. Rev. Lett. **97**, 060403 (2006).
- [42] F. Gerbier, Phys. Rev. Lett. **99**, 120405 (2007).
- [43] T.-L. Ho and Q. Zhou, cond-mat/0703169 (2007).
- [44] F. Gerbier *et al.*, Phys. Rev. A **72**, 053606 (2005).
- [45] P. Sengupta *et al.*, Phys. Rev. Lett. **95**, 220402 (2005).
- [46] C. Orzel *et al.*, Science **291**, 2386 (2001).
- [47] C. Schori *et al.*, Phys. Rev. Lett. **93**, 240402 (2004); K. Xu *et al.*, Phys. Rev. Lett. **96**, 180405 (2006).
- [48] A. Iucci, M. A. Cazalilla, A. F. Ho, and T. Giamarchi, Phys. Rev. A **73**, 041608 (2006).
- [49] S. D. Huber, E. Altman, H. P. Buchler, and G. Blatter, Phys. Rev. B **75**, 085106 (2007).
- [50] C. Kollath *et al.*, Phys. Rev. Lett. **97**, 050402 (2006).
- [51] D. van Oosten *et al.*, Phys. Rev. A **71**, 021601 (2005); A. M. Rey *et al.*, Phys. Rev. A **72**, (2005); G. Pupillo, A. Rey, and G. Batrouni, Phys. Rev. A **74**, 013601 (2006).
- [52] D. S. Rokhsar and B. G. Kotliar, Phys. Rev. B **44**, 10328 (1991).
- [53] F. Gerbier *et al.*, Phys. Rev. Lett **96**, 090401 (2006).
- [54] P. Cheinet *et al.*, Phys. Rev. Lett. **101**, 090404 (2008).
- [55] M. Greiner, M. O. Mandel, T. Hänsch, and I. Bloch, Nature **419**, 51 (2002).
- [56] J. Sebby-Strabley *et al.*, Phys. Rev. Lett. **98**, 200405 (2007).
- [57] G.-B. Jo *et al.*, Phys. Rev. Lett. **98**, 030407 (2007).
- [58] B. Yurke and D. Stoler, Phys. Rev. Lett. **57**, 13 (1986).

- [59] F. Sols, Physica B **194-196**, 1389 (1994); E. M. Wright, D. F. Walls, and J. C. Garrison, Phys. Rev. Lett. **77**, 2158 (1996); A. Imamoglu, M. Lewenstein, and L. You, Phys. Rev. Lett. **78**, 2511 (1997); Y. Castin and J. Dalibard, Phys. Rev. A **55**, 4330 (1997); J. A. Dunningham, M. J. Collett, and D. F. Walls, Phys. Lett. A **245**, 49 (1998).
- [60] G. Rempe, H. Walther, and N. Klein, Phys. Rev. Lett. **58**, 353 (1987); M. Brune *et al.*, Phys. Rev. Lett. **76**, 1800 (1996).
- [61] C. Kollath, A. Läuchli, and E. Altman, Phys. Rev. Lett. **98**, 180601 (2007).
- [62] U. Schollwöck, Reviews of Modern Physics **77**, 259 (2005).
- [63] E. Altman and A. Auerbach, Phys. Rev. Lett. **89**, 250404 (2002); A. Polkovnikov, S. Sachdev, and S. M. Girvin, Phys. Rev. A **66**, 053607 (2002).
- [64] A. Tuchman, C. Orzel, A. Polkovnikov, and M. A. Kasevich, Phys. Rev. A **74**, 051601 (2006).
- [65] S. R. Clark and D. Jaksch, Phys. Rev. A **70**, 043612 (2004).
- [66] L. Fallani *et al.*, Phys. Rev. Lett. **93**, 140406 (2004).
- [67] C. D. Fertig *et al.*, Phys. Rev. Lett. **94**, 120403 (2005).
- [68] A. Polkovnikov *et al.*, Phys. Rev. A **71**, 063613 (2005).
- [69] M. Tinkham, *Introduction to Superconductivity* (McGraw-Hill, New York, 1996).
- [70] J. Mun *et al.*, arXiv:0706.3946 (2007).
- [71] L. Pitaevskii and S. Stringari, *Bose-Einstein Condensation* (Oxford University Press, Oxford, 2003).
- [72] J. Gea-Banacloche *et al.*, Phys. Rev. A **73**, 013605 (2006).
- [73] R. Jördens *et al.*, Nature **455**, 204 (2008); U. Schneider *et al.*, Science **322**, 1520 (2008).
- [74] P. Lee, N. Nagaosa, and X.-G. Wen, Rev. Mod. Phys. **78**, 17 (2006).
- [75] T. Gericke *et al.*, Nat. Phys. **4**, 949 (2008); W. S. Bakr *et al.*, Nature **462**, 74 (2009).

Part IV

Numerical Solution Methods for Quantum Phase Transitions

20

Worm Algorithm for Problems of Quantum and Classical Statistics

Nikolay Prokof'ev

Department of Physics, University of Massachusetts, Amherst, MA, U.S.A.

Boris Svistunov

Department of Physics, University of Massachusetts, Amherst, MA, U.S.A.

Theoretical studies often involve mappings of the original system onto an equivalent description in terms of abstract mathematical/graphical objects, where ‘equivalent’ means one obtains the same final answer for some particular property. Path integrals, high-temperature expansions, and Feynman diagrams are the well-known examples considered in this chapter. Under such mappings, one has to deal with the infinite-dimensional configuration space having complex topology and non-local constraints which severely reduce efficiency of Monte Carlo simulations based on standard local updates. This sometimes leads to ergodicity problems in large systems when the entire configuration space can not be sampled in a reasonable computation time. A somewhat related difficulty facing conventional Monte Carlo schemes is the computation of off-diagonal correlation functions since they have no direct relation to the configuration space of the partition function. In what follows we consider path integrals for lattice and continuous systems, high-temperature expansions, and Feynman diagrams, explain the general idea of how Worm Algorithms (WAs) deal with the topological constraints by going to the enlarged configuration space, and present illustrative results for several physics problems.

20.1 Path-Integrals in Discrete and Continuous Space

For clarity, we start by introducing the Hamiltonian describing lattice bosons¹ making hopping transitions between the nearest-neighbor sites $\langle ij \rangle$, interacting by the pairwise potential U_{ik} , and subject to the external potential

¹A straightforward generalization to fermions will be mentioned later.

μ_i :

$$H = H^{(0)} + H' = \frac{1}{2} \sum_{i,k} U_{ik} n_i n_k - \sum_i \mu_i n_i - t \sum_{\langle ij \rangle} b_j^\dagger b_i . \quad (20.1)$$

Here b_i is the bosonic annihilation operator and $n_i = b_i^\dagger b_i$. In the Fock basis of site occupation numbers, $|\alpha\rangle = |\{n_i\}\rangle$, the first two terms, representing $H^{(0)}$, are diagonal, while the last term, representing H' , is not. We write the statistical operator as

$$e^{-\beta H} = e^{-\beta H^{(0)}} \exp \left\{ - \int_0^\beta d\tau H'(\tau) \right\} , \quad (20.2)$$

where $H'(\tau) = e^{\tau H^{(0)}} H' e^{-\tau H^{(0)}}$, and the exponential is understood as the time-ordered expansion

$$1 - \int_0^\beta d\tau H'(\tau) + \int_0^\beta d\tau_1 \int_{\tau_1}^\beta d\tau_2 H'(\tau_1) H'(\tau_2) + \dots . \quad (20.3)$$

Lattice path integrals immediately follow from the graphical representation of the expansion (20.3). Consider the partition function Z given by the trace of $e^{-\beta H}$ and write explicitly the m th term, before integration over time, as

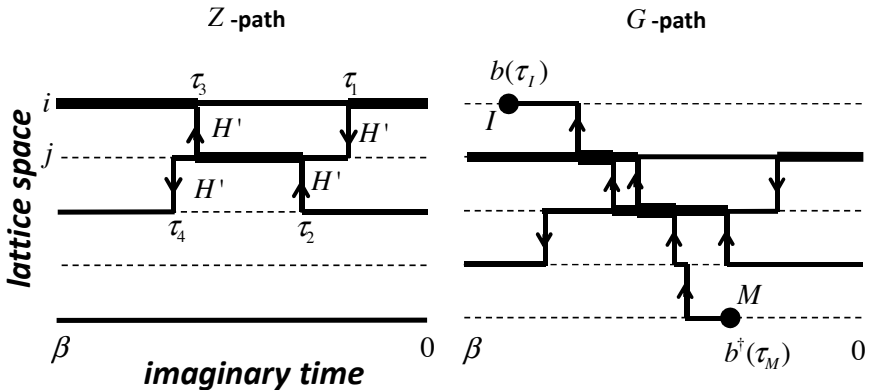
$$(-1)^m d^m \tau e^{-(\beta-\tau_1) H_{\alpha_0}^{(0)}} (H'_{\alpha_0, \alpha_1}) e^{-(\tau_1 - \tau_2) H_{\alpha_1}^{(0)}} \dots (H'_{\alpha_{m-1}, \alpha_m}) e^{-\tau_m H_{\alpha_m}^{(0)}} , \quad (20.4)$$

with $\alpha_m \equiv \alpha_0$ to reflect the trace condition, i.e., a periodic boundary condition in imaginary time, and $d^m \tau \equiv d\tau_1 \dots d\tau_m$. Since hopping terms in H' change the state by shifting only one particle to a nearest-neighbor site, the sequence of matrix elements is completely determined by specifying the *evolution* or *imaginary time trajectory* of occupation numbers $\{n_i(\tau)\}$. In the left panel of Fig. 20.1 we show the trajectory describing one of the 4th order terms which contributes $t^4 d^4 \tau 1 \cdot 2 \cdot \sqrt{2} \cdot \sqrt{2} \exp\{-\int_0^\beta d\tau H^{(0)}(\tau)\}$ to Z , where for brevity we use $H^{(0)}(\tau)$ for the energy of the state $|\{n_i(\tau)\}\rangle$ and give explicit expressions for the hopping matrix elements $\langle n_i - 1, n_j + 1 | -t b_j^\dagger b_i | n_i, n_j \rangle = -t \sqrt{n_i(n_j + 1)}$. Thus, the partition function can be written as a sum over all possible paths $\{n_i(\tau)\}$ such that $n_i(\beta) = n_i(0)$,

$$Z = \sum_{\{n_i(\tau)\}} W[\{n_i(\tau)\}] , \quad (20.5)$$

with strict rules relating the trajectory shape to its contribution to Z . The trajectory weight is sign-positive if t is positive or the lattice is bi-partite.

The path-integral language at this point is nothing but a convenient way of visualizing each term in the perturbative expansion (20.3). Due to the particle number conservation, the many body trajectory can be decomposed into

**FIGURE 20.1**

Lattice path-integral representations for the partition function and the Green's function. Line thickness is proportional to n_i

the set of closed (in the time direction) single-particle trajectories, or world-lines. Worldlines can *wind* around the β -circle several times before closing on themselves. In a system with periodic boundary conditions in space, the trajectories can also wind in the space direction. Worldlines with non-zero β - and space-winding numbers are said to form exchange cycles and winding numbers, respectively; they are directly responsible for superfluid properties of the system [1] and are the origin of non-local topological constraints mentioned in the introductory paragraph.

The Green's function of the system,

$$G(\tau_M - \tau_I, i_M - i_I) = T_\tau \langle b_{i_M}^\dagger(\tau_M) b_{i_I}(\tau_I) \rangle , \quad (20.6)$$

has a similar path-integral representation, as shown in the right panel in Fig. 20.1, with one notable difference: due to operators b^\dagger at point (i_M, τ_M) and b at point (i_I, τ_I) there is one more particle present in the system on the time interval (τ_I, τ_M) , i.e., when the $\{n_i(\tau)\}$ evolution is decomposed into worldlines there will be one *open* worldline originating at point τ_M and terminating at point τ_I . These special points will be labeled as \mathcal{I} ("Ira") and \mathcal{M} ("Masha") throughout the text. We will use short-hand notations, Z -path and G -path, to distinguish configuration spaces of Z and G .

We skip here the standard derivation of Feynman's path-integral representation for an interacting N -particle Hamiltonian in continuous space [2]:

$$H = K + V = -\frac{1}{2m} \sum_{i=1}^N \nabla_i^2 + \frac{1}{2} \sum_{i \neq j=1}^N U(r_i - r_j) - \sum_{i=1}^N \mu(r_i) , \quad (20.7)$$

leading to

$$Z = \oint \mathcal{D}\mathbf{R}_\tau \exp \left\{ - \int_0^\beta \left[\frac{m\dot{\mathbf{R}}^2}{2} + U(\mathbf{R}) - \mu(\mathbf{R}) \right] d\tau \right\}. \quad (20.8)$$

where $R_\tau = \{r_i(\tau)\}$ represents positions of all particles at time τ , $U(R)$ and $-\mu(R)$ stand for internal and external potential energy, respectively, and $R_\beta \equiv R_0$ to satisfy the trace condition. In practice, the imaginary time axis is sliced into a sufficiently large number of intervals and the trajectory is defined by specifying particle positions at a discrete set of time points. Apart from time slicing, there is no fundamental difference between the lattice and continuous path integrals. The Z -path consists of closed worldlines,² and the G -path contains one *open* worldline originating at (r_M, τ_M) and terminating at (r_I, τ_I) .

The only difference between fermionic and bosonic systems is in the sign rule: for fermions the trajectory weight W involves an additional factor $(-1)^p$, where p is the parity of the permutation between the particle coordinates in R_β relative to R_0 .

20.2 Loop Representations for Classical High-Temperature Expansions

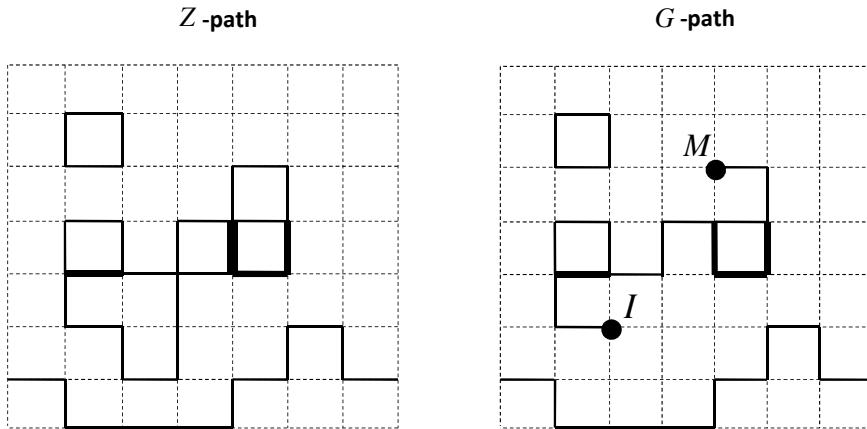
Classical statistical models can also be mapped to the configuration space of closed loops. Important examples include Ising, XY, and $|\psi|^4$ models, as well as their multi-component generalizations with or without the gauge coupling, e.g., the CP^1 model. We illustrate the general idea of the mapping by considering the simplest case of the Ising model when $-H/T = K \sum_{<ij>} \sigma_i \sigma_j$ for N Ising spin variables $\sigma_i = \pm 1$. One starts with the partition function and expands bond Gibbs factors into Taylor series,

$$Z = \sum_{\{\sigma_i = \pm 1\}} \prod_{b=<ij>} e^{K \sigma_i \sigma_j} = \sum_{\{\sigma_i = \pm 1\}} \prod_{b=<ij>} \sum_{N_b=0}^{\infty} \frac{K^{N_b}}{N_b!} (\sigma_i \sigma_j)^{N_b}, \quad (20.9)$$

where to simplify notations we have used subscript b for lattice bonds. By exchanging summation over $\{N_b\}$ and $\{\sigma_i = \pm 1\}$ we obtain

$$Z = 2^N \sum_{\{N_b\}}^{\text{loops}} \prod_{b=<ij>} \frac{K^{N_b}}{N_b!} \equiv 2^N \sum_{\{N_b\}}^{\text{loops}} W[\{N_b\}]. \quad (20.10)$$

²The decomposition of the many-body path into individual worldlines is unique in continuous space.

**FIGURE 20.2**

Loop representations for the partition function and the correlation function for the Ising model. Line thickness is proportional to N_b .

The *loops* label on the sum represents the constraint that the sum of all bond numbers incident on every lattice site, $L_i = \sum_{b=\langle ij \rangle} N_b$, has to be even; otherwise $\sum_{\sigma_i \pm 1} \sigma^{L_i}$ is zero. In the graphical representation where N_b is substituted with N_b lines drawn on the corresponding bond, this is equivalent to demanding that the allowed configuration of lines is that of closed un-oriented loops, since loops always contribute an even number to $L_i = \sum_{b=\langle ij \rangle} N_b$, as shown in the left panel in Fig. 20.2.³ In close analogy with the Green's function, the configuration space of the spin-spin correlation function $G_{IM} = \langle \sigma_I \sigma_M \rangle$ is that of closed loops with one open line originating at site I and terminating at M , as shown in the right panel in Fig. 20.2. The difference between the XY and Ising models is that loops are oriented in the XY-case, i.e., $N_b \in (-\infty, \infty)$.

20.3 Worm Algorithm: The Concept and Realizations

The WA strategy for updating loop configuration spaces involves two major ideas:

³Using the identity $e^{K\sigma_i \sigma_j} = \cosh(K) \sum_{N_b=0,1} [\tanh(K)\sigma_i \sigma_j]^{N_b}$ we get a more compact formulation since only one line can be drawn on the bond.

- (i) The configuration space is enlarged to include one open line, as if someone started drawing a new loop but is not finished yet. In all examples mentioned above this is not merely an algorithmic trick but also an important tool to have direct access to off-diagonal correlation functions, such as the Green's function [3, 4]; with two worms one may calculate multi-particle off-diagonal correlations as well [5, 6]. From time to time the two ends of the open line come close and get connected, thus making a loop and transforming the G -path to the Z -path. In Monte Carlo, drawing and erasing processes are balanced and are complementary to each other.
- (ii) All updates on G -paths are performed exclusively through the endpoints of the open line; no global updates or local updates transforming one Z -path to another Z -path are necessary.

More generally, the WA idea is to consider an enlarged configuration space which includes structures violating constraints present in the Z -sector of the space. Often, this can be achieved automatically by considering the relevant correlation functions. Green's function and, for paired states, higher-order off-diagonal correlators are the appropriate choice for the path-integral space. However, one should feel free to introduce un-physical configurations which bear no meaning at all and are used solely for employing local updates to produce non-trivial global changes of physical configurations. An example with the momentum conservation law in Feynman diagrams discussed below illustrates the point.

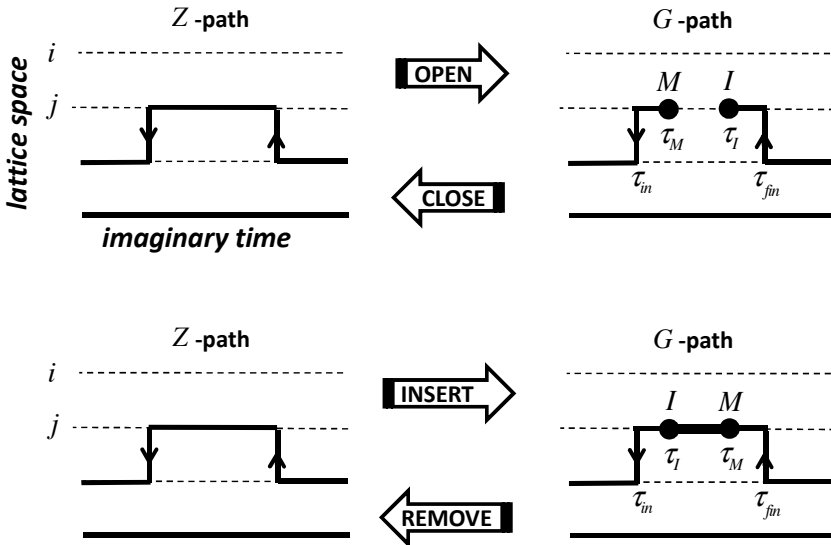
The WA is a local Metropolis scheme, but, remarkably, its efficiency is similar to or better than the best cluster methods at the critical point, i.e., it does not suffer from the critical slowing down problem. It has no problem producing loops winding around the system, allows efficient simulations of off-diagonal correlations, grand canonical ensembles, disordered systems, etc. Below we provide more specific details of how it works.

20.3.1 Discrete Configuration Space: Classical High-Temperature Expansions

We start with the simplest case of the classical Ising model. The entire algorithm consists of just one update: if $\mathcal{I} = \mathcal{M}$, select at random a new lattice site j and assign $\mathcal{I} = \mathcal{M} = j$; otherwise skip this step.⁴ Select at random the direction (bond) to shift *Masha* to a nearest-neighbor site, let it be k , and propose to change the bond number from N_b to $N'_b = \text{mod}_2(N_b + 1)$. Accept the move with probability $R = \max[1, \tanh^{N'_b - N_b}(K)]$. This is a complete description of the algorithm!

Every configuration contributes unity to the statistics of $G_{I,M}$. For the Ising model $Z = G_{I=M}$. Generalizations to other classical statistical models

⁴In other words, put your pencil/eraser anywhere.

**FIGURE 20.3**

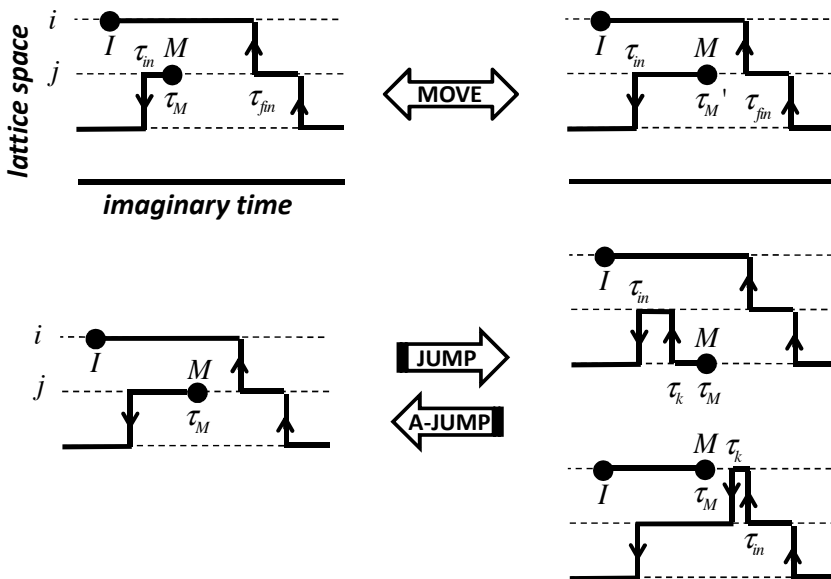
The upper and lower panels illustrate transformations performed by the *open/close* and *insert/remove* pairs of updates on the lattice path-integral configurations, respectively.

are straightforward [3]. Ergodicity is guaranteed because a finite number of steps is required to erase any initial trajectory and then to draw a new one, line after line. The efficiency is ultimately linked to the fact that the WA works directly with the correlation function of the order parameter field.

20.3.2 Continuous Time: Quantum Lattice Systems

We now illustrate the WA updating strategy for the system of lattice bosons described by Eqs. (20.1), (20.5) with the configuration space shown in Fig. 20.1. The set of updates presented below forms an ergodic set. It is sufficient to describe updates performed with the *Masha-end* of the open worldline; updates involving the *Ira-end* follow immediately from the time reversal symmetry.

Open/Close – This pair of updates takes us back and forth between the Z - and G -paths by selecting an existing worldline and erasing a small part of it (*open*) or drawing a small piece of worldline between the end-points of the open line to complete the loop (*close*). These updates are illustrated in the upper panel of Fig. 20.3. In the *open* update the path interval characterized by time-independent occupation numbers on a given site is selected at random

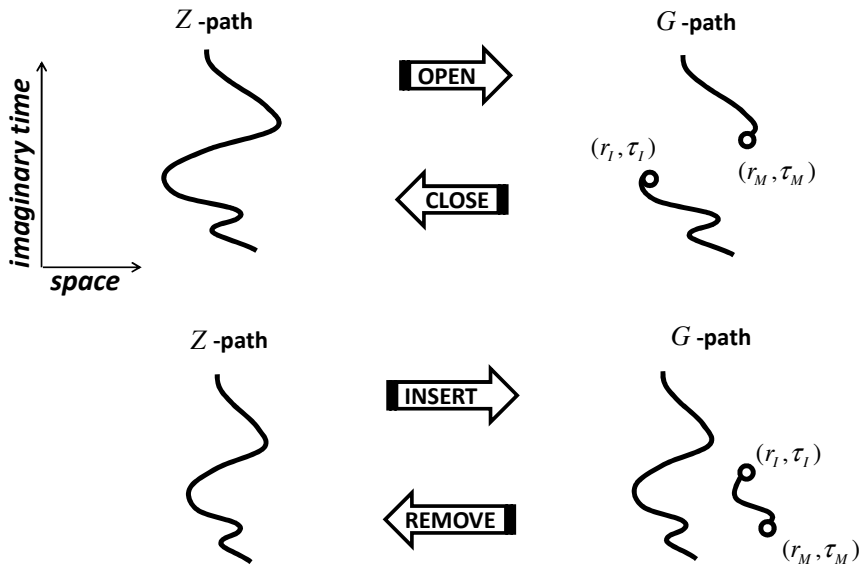
**FIGURE 20.4**

The upper and lower panels illustrate transformations performed by the *move* and *jump/anti-jump* updates on the lattice path-integral configurations, respectively.

from the list of such intervals, and the imaginary times $\tau_I < \tau_M$ are seeded from the normalized probability distribution $p(\tau_I, \tau_M)$ with $\tau_I, \tau_M \in (\tau_{in}, \tau_{fin})$. Formally, the distribution function is arbitrary, and this freedom should be used to optimize the acceptance ratio $R \propto W_{\text{new}}/[W_{\text{old}} p(\tau_I, \tau_M)]$. In the *close* update one checks whether *Ira* and *Masha* are connected by a single path interval with time-independent occupation numbers on a given site, and if true, proposes to eliminate them by connecting the dots. We skip here further minimal technical details, as well as explicit expressions for acceptance ratios, which can be found elsewhere [4].

Insert/Remove – This pair of updates also switches back and forth between the *Z*- and *G*-paths by drawing a small piece of a new worldline (*insert*) or erasing a small piece of worldline between the end points (*remove*). The two updates are illustrated in Fig. 20.3 and in all respects are similar to the *open/close* pair except that the time ordering of τ_I and τ_M is reversed; see the lower panel in Fig. 20.3.

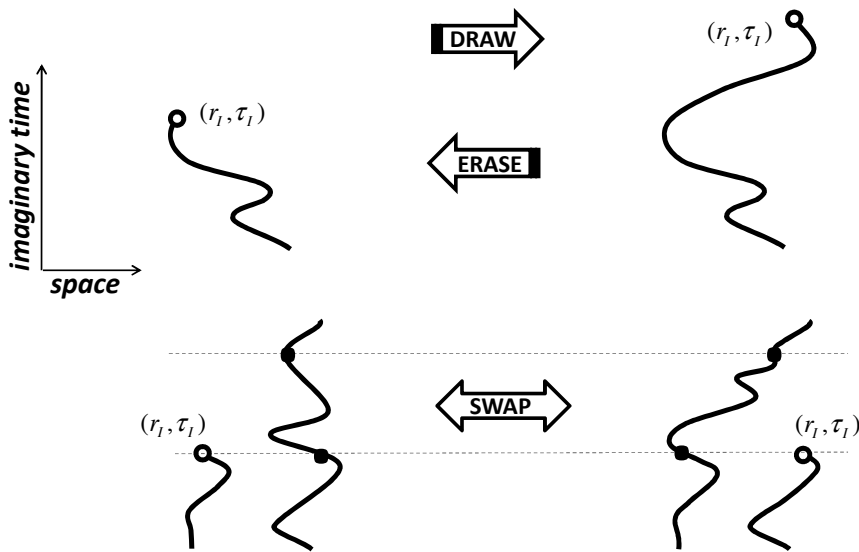
Move – Once in the *G*-path space the algorithm proposes to move *Masha* along the time axis, $\tau_M \rightarrow \tau'_M$ within the bounds determined by the change of the occupation numbers on a given site. This motion is equivalent to drawing/erasing the worldline; see the upper panel in Fig. 20.4.

**FIGURE 20.5**

The upper and lower panels illustrate transformations performed by the *open/close* and *insert/remove* pairs of updates on the continuous-space path-integral configurations, respectively.

Jump/anti-jump – This is the only complementary pair of updates which is different from continuous transformations of lines since it involves the motion of end-points in space. Without changing the time position of *Masha*, we place it on the neighboring site and connect worldlines of the two sites involved in the update in such a way that the rest of the path remains intact. This requires adding/removing a kink immediately before or after τ_M . We illustrate the *jump/anti-jump* updates in the lower panel of Fig. 20.4. Note the difference between the two cases. When the kink is inserted to the left of *Masha*, the transformation can still be interpreted as proceeding with drawing the same worldline. When the kink is inserted to the right of *Masha*, we reconnect existing worldlines and ultimately effectively sample all allowed topologies of the path.

This concludes the description of the algorithm. Such properties as density, energy, density-density correlations, etc. are computed using standard rules when the configuration is in the *Z*-path sector. Every *G*-configuration makes a direct contribution to the statistics of $G(\tau_M - \tau_I, i_M - i_I)$.

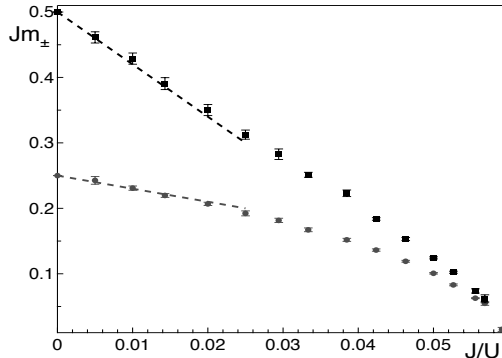
**FIGURE 20.6**

The upper and lower panels illustrate transformations performed by the *draw/erase* and *swap* updates on the continuous-space path-integral configurations, respectively.

20.3.3 Bosons in Continuous Space

WAs for continuous and lattice systems are essentially identical at the conceptual level. Most differences are technical and originate from having discrete instead of continuous time and continuous instead of discrete space. Specific protocols of how one proposes new variables and performs measurements can be found in Ref. [7]. The only difference worth mentioning is that in continuous space the decomposition of the path into individual worldlines is unique, which actually simplifies things. Here we simply illustrate the updates. Since in all cases we know how to compute the path contribution to the statistics of Z or G , graphical representations can always be converted to precise mathematical expressions for the acceptance ratios which account for the ratio of the configuration weights and probabilities/probability densities of applying a particular type of update.

Figures 20.5 and 20.6 show an ergodic set of updates which allow one to efficiently simulate continuous space systems. The *open/close* and *insert/remove* pairs of updates are reminiscent of those in lattice systems. The *draw/erase* pair naturally combines in one update both space and time motion of the endpoint and is a literal implementation of the draw-and-erase algorithm. The *swap* update is equivalent to the version of the *jump* update which involves

**FIGURE 20.7**

Effective mass for particle (circles) and hole (squares) excitations in the 2D Bose-Hubbard model at unity filling as a function of the hopping-to-interaction ratio J/U . The exact results at $J/U = 0$ are $m_+ = 0.25/J$ and $m_- = 0.5/J$. The dashed lines show the lowest-order corrections in J/U to the effective masses. Close to the critical point the two curves overlap, revealing the emergence of the particle-hole symmetry implied by criticality-induced emergent Lorentz invariance. The sound velocity of the relativistic spectrum in the Lorentz-invariant regime is found to be $c/J = 4.8 \pm 0.2$. (Reproduced from Ref. [11].)

reconnection of the particle worldlines. In the *swap* update all modifications of the path are restricted to occur between the two dashed lines; see Fig. 20.6.

The rules for collecting statistics of the diagonal and off-diagonal properties are similar to lattice models.

20.3.4 Momentum Conservation in Feynman Diagrams

Diagrammatic Monte Carlo (see, e.g., Ref. [8] and references therein) is a technique of sampling entities expressed in terms of Feynman's diagrammatic series by a Markov process. The configurational space of the process consists of Feynman's diagrams with fixed internal variables. It is the sampling process itself that accounts for the integration over these variables, on equal footing with summation over the order and topology of the diagrams. In the process of producing the Markov chain of diagrams, generating the $(n + 1)$ st diagram is performed by applying one of a few elementary updates to the n th diagram. The elementary updates are supposed to change the structure of a diagram by adding/removing/reconnecting a small number of propagators and the values of a small number of internal variables. In the space-time representation, updating internal variables causes no problem since these are nothing but the space-time points corresponding to the ends of propagators, their values being naturally generated with the appearance of new propagators and

abandoned when the corresponding propagators are removed. In momentum and/or frequency representation, the situation is quite different. For brevity, we restrict ourselves to momentum in the ensuing discussion. The momentum of a given propagator is not independent of the momenta of other propagators in view of the momentum-conservation constraint taking place at each vertex. Adding/removing a propagator to/from a diagram would thus involve a change of momenta of other propagators, rendering the updating routine complicated and less efficient.

A simple and efficient way out is provided by the *worm* idea of working in an extended configurational space. The additional class of diagrams that we need consists of diagrams featuring worms, by which here we mean vertices with non-conserving momenta. Clearly, the minimal non-trivial number of worms is two. Normally, working with no more than two worms proves sufficient. Note that if the algebraic sum of all the momenta at one of the two worms is $\vec{\delta}$, then its counterpart at the other worm is $-\vec{\delta}$, so that $\vec{\delta}$ is the only continuous parameter associated with the pair of worms.

A crucial observation is that if all the structural updates of diagrams are performed in the subspace of diagrams with worms and the ends of the propagator(s) to be added/removed/reconnected are linked to the two worms, then the worms will readily absorb the residual momentum, \vec{k}_{res} , associated with the update, the only consequence for the worms being $\vec{\delta} \rightarrow \vec{\delta} + \vec{k}_{\text{res}}$. Details on implementing this idea can be found in Ref. [8]. The overall updating scenario is as follows. Switching between physical and worm sectors of the configurational space is achieved by a pair of complementary updates creating/deleting a pair of worms at the ends of a propagator, while simultaneously changing the momentum of this propagator. The rest of the updates are performed in the worm sector. The efficiency of the scheme is achieved by introducing an update that translates worms along one of the propagators attached to the worm vertex. In the updated diagram, the conservation of momentum at the worm's original position is ensured by appropriately changing the momentum of the propagator along which the translation is being performed. Translating worms along propagators allows one to efficiently sample all their positions and thus apply the updates changing the structure of the diagram, associated with the worms, as discussed above, in a generic way.

20.4 Illustrative Applications

20.4.1 Optical-Lattice Bosonic Systems

Bosons in optical lattices, being accurately described by the Hubbard Hamiltonian (20.1) [9], are perfectly suitable for simulations by WAs. With a standard desktop computer, one can simulate equilibrium properties of 3D systems with

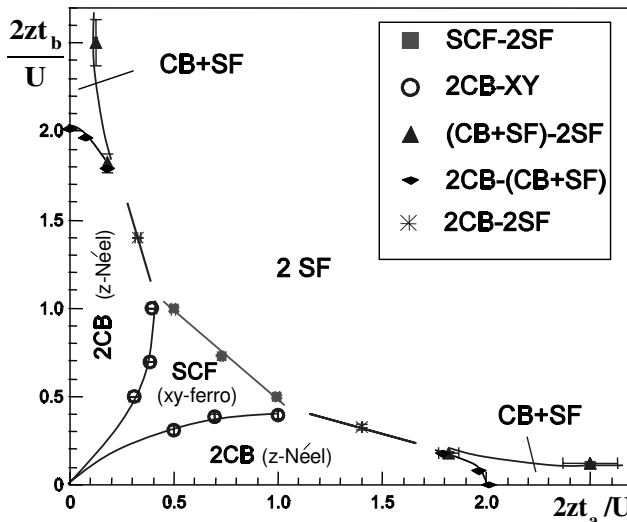
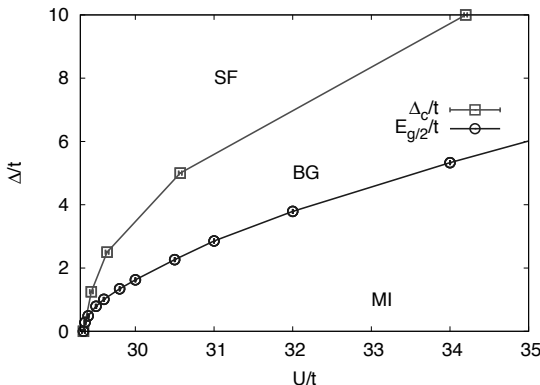


FIGURE 20.8

Ground-state phase diagram of 2D two-component bosonic Hubbard model at half-integer filling factor for each component. The on-site interactions within each component are infinitely strong (hard-core limit), while the inter-component interaction, U , is finite. The hopping elements of the two components are t_a and t_b , and the parameter $z = 4$ is the coordination number. The revealed phases are as follows: (i) checkerboard solid in both components, a.k.a. z -Néel phase (2CB); (ii) checkerboard solid in one component and superfluid in its counterpart (CB+SF); (iii) superfluid in both components (2SF); (iv) super-counter-fluid, a.k.a. XY -ferromagnet (SCF). The observed transition lines are 2CB-SCF (first-order), SCF-2SF (second-order), 2CB-2SF (first-order), 2CB-CB+SF (second-order), and CB+SF-2SF (first-order). Lines are used to guide an eye. (Reproduced from Ref. [6].)

200³ lattice sites. In Refs. [10, 11] it has been demonstrated that this approach allows one to obtain precise results for equations of state and produce an accurate phase diagram of the system. It is also possible to trace the evolution of the particle/hole spectrum of elementary excitations with decreasing interaction strength, from the strong coupling limit down to the critical point of the Mott-insulator to superfluid quantum phase transition. Especially interesting is the vicinity of the quantum critical point, where the emergent Lorentz invariance brings about particle-hole symmetry; see Fig. 20.7. Along with the pure single-component bosonic Hubbard model, one can simulate multi-component and disordered systems; see Figs. 20.8-20.9.

The lattice bosonic systems are in the focus of the Optical Lattice Emulator project supported by DARPA and aimed at the development, within the next few years, of experimental tools of accurately mapping phase diagrams of

**FIGURE 20.9**

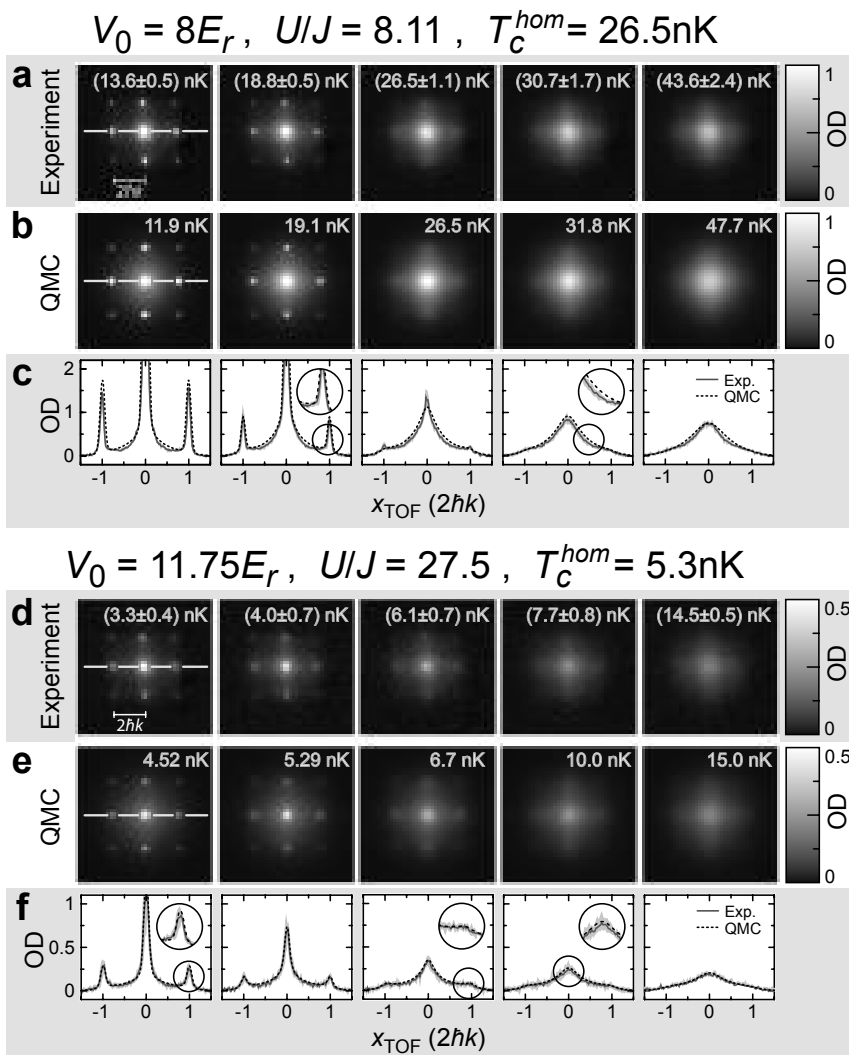
Ground-state phase diagram of the disordered 3D Bose-Hubbard model at unity filling in the vicinity of the point of the superfluid to Mott-insulator (SF to MI) quantum phase transition. The $E_{g/2}(U)$ curve marks the Bose-glass to Mott-insulator (BG to MI) transition boundary according to the conjecture that the transition occurs when the bound of disorder reaches the half-gap, $E_{g/2}$, of the pure Mott insulator. Error bars are shown, but are smaller than point sizes. (Reproduced from Ref. [12].)

lattice systems by emulating them with ultracold atoms in optical lattices. The numerically exact solutions for real experimental systems will be used for validating the emulators. The first successful validation of the emulator of the Bose-Hubbard model was reported in Ref. [13]. At the heart of the protocol is the direct comparison of the experimental time-of-flight images with the theoretical ones. The latter are produced by time-evolving the single-particle density matrix obtained in a direct simulation of a given number of atoms in a trap; see Fig. 20.10.

20.4.2 Supersolidity of Helium-4

A supersolid is a quantum solid that can support a dissipationless flow of its own atoms. Here the term ‘solid’ is understood in the most general context of any state with broken translation symmetry, including regular or amorphous, and continuous-space or lattice states.

The modern age of supersolidity of bosonic crystals in continuous space began with the discovery by Kim and Chan of non-classical rotational inertia (NCRI) in solid ${}^4\text{He}$ [14, 15]; for reviews of further developments in the field, including direct observation of a superflow, as well as preceding work, see Refs. [16–18] and references therein. In the combined experimental and theoretical effort aimed at understanding the microscopic picture behind the effect, the first-principles simulations of regular and disordered solid ${}^4\text{He}$ play

**FIGURE 20.10**

Comparison of experimental and simulated time-of-flight distributions: shown are the integrated column density $n_{\perp}(x, y)$ represented by the optical density as obtained from the experiment and the QMC simulations for different temperatures and two lattice depths. (Reproduced from Ref. [13]; see this reference for more detail.)

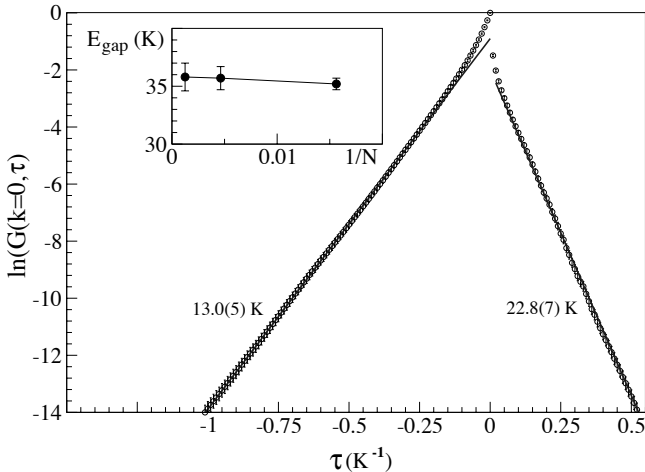


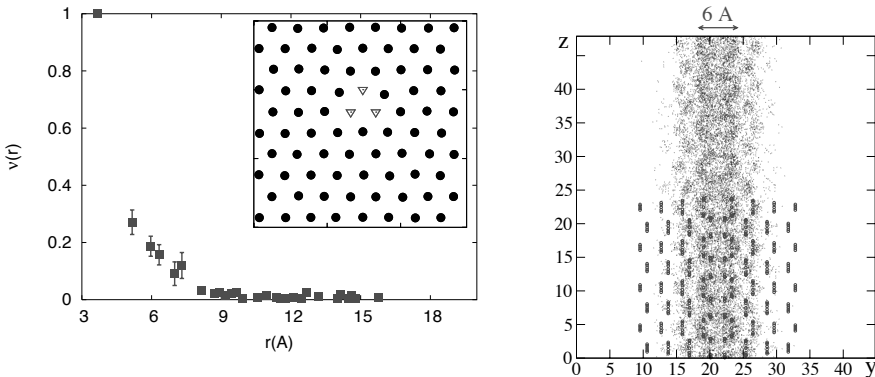
FIGURE 20.11

Single-particle Green's function $G(\mathbf{k} = 0, \tau)$ computed by WA for HCP ${}^4\text{He}$ at the melting density $n_o = 0.0287 \text{ \AA}^{-3}$ and $T = 0.2 \text{ K}$. Symbols refer to numerical data; solid lines are fits to the long-time exponential decay. The given numerical values are the interstitial ($\Delta_I = 22.8 \pm 0.7 \text{ K}$) and the vacancy ($\Delta_V = 13.0 \pm 0.5 \text{ K}$) activation energies, inferred from the slopes of G . The straight-line asymptotic behavior indicates that finite-temperature corrections are negligible. The inset shows the vacancy-interstitial gap $E_{\text{gap}} = \Delta_I + \Delta_V$ for different system sizes, proving that the results have reached their macroscopic limit. (Reproduced from Ref. [21].)

a very important part. Here we present some numerical results shedding a direct light on microscopic mechanisms of supersolidity in ${}^4\text{He}$.

To introduce a general theoretical background for interpreting numeric results, we start with a number of rigorous statements. From the field-theoretical perspective, a superfluid/supersolid ground state, as opposed to an insulating one, is almost trivial, since the topological constant of motion responsible for the superfluidity is naturally introduced in terms of the phase of the classical matter field, so that phenomenon of superfluidity in a quantum field is simply inherited from the classical counterpart of the latter. An insulating ground state is possible only in a quantum field. It is an essentially non-perturbative and thus non-trivial phenomenon.

A proof of the existence of insulating ground states in bosonic crystals immediately follows from the theorem stating that a necessary condition for supersolidity is the presence of either vacancies, or interstitials, or both [19]. With this theorem, one just needs to make sure that there are ground states in which creating a vacancy and an interstitial cost finite energy. The latter is known to be the fact at least since Andreev and Lifshitz' analysis [20]:

**FIGURE 20.12**

(left) The vacancy-vacancy correlation function $\nu(r)$ as a function of the distance r between the vacancies shows that three vacancies easily cluster and form a tight bound state. The inset shows a typical snapshot of a layer of atomic positions averaged over the time interval $[0, \beta]$ (filled black circles). It is seen that the three vacancies (triangles) have a tendency to cluster in layers. (right) Luttinger liquid in the core of the screw dislocation in solid ${}^4\text{He}$ revealed by columnar winding-cycle map. Simulations correspond to the temperature 0.25 K and density 0.0287 \AA^{-3} . View is along the x -axis in the basal plane, perpendicular to the core. Shown with large dots (in the lower half of the plot only) are the atomic positions in initial configuration. The unit of length is 1 Å. (Reproduced from Refs. [21] and [22], respectively.)

the energy for creating a vacancy/interstitial is positive, and arbitrarily close to the classical-crystal value, in the limit of strong interaction/large particle mass.

The theorem of Ref. [19] offers a reliable protocol of numerical proof that the ground state of the perfect ${}^4\text{He}$ hexagonal-close-packed (HCP) crystal is an insulator. It is sufficient to demonstrate the following: (i) creating a vacancy/interstitial in the simulation box costs a finite energy, the value of which does not vanish with increasing system size and decreasing temperature; and (ii) a state with finite concentration of vacancies/interstitials, that could potentially differ from the single-vacancy/interstitial situation due to collective effects, is unstable in the thermodynamical limit with respect to aggregation, i.e., a crystal at $T = 0$ purges itself from the vacancies and interstitials. Both facts are demonstrated in Fig. 20.11 and the left panel of Fig. 20.12.⁵

Having established that the perfect HCP ${}^4\text{He}$ crystal is not supersolid, one has to explore *disordered* scenarios, when the superflow in a crystal is

⁵The aggregation of interstitials has not been studied since these cost much more energy than the vacancy, rendering the scenario of interstitial-induced supersolidity not realistic.

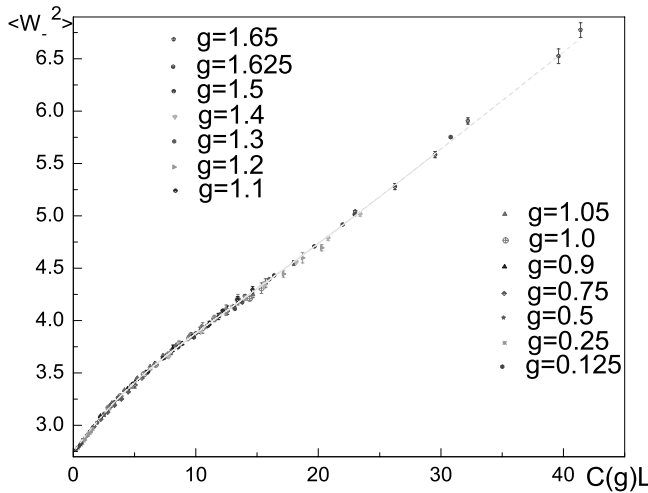
supported by defects. First-principles simulations, briefly reviewed in Ref. [18], have revealed a number of disorder-induced mechanisms of supersolidity in ^4He : superfluid dislocations, grain boundaries, ridges, and also a metastable amorphous supersolid, the *superglass*. Here we confine ourselves to presenting the results for the superfluidity in the core of a screw dislocation, arguably the cleanest Luttinger liquid system in nature.

To visualize spatially inhomogeneous superfluidity in a WA simulation, one can employ two similar approaches. One approach is to plot the condensate density map. The other and more general approach, that also works for lower-dimensional systems with genuine long-range order destroyed by fluctuations of phase, is to visualize the macroscopic worldline loops responsible for non-zero winding numbers, and thus for the superfluid response. Identifying these loops in a given worldline configuration, projecting them from the $(d + 1)$ dimensions onto a plane in the real space, and performing the average over a representative set of configurations, one obtains the *winding-circle map* of the superfluid region. The Luttinger liquid core of a screw dislocation visualized with this technique is shown in the right panel of Fig. 20.12.

20.4.3 The Problem of Deconfined Criticality and the Flowgram Method

The standard Ginzburg-Landau-Wilson (GLW) scenario of critical phenomena excludes generic continuous transitions between states which break different symmetries, thus implying that the transition, if it exists, is first order. An intriguing possibility of breaking the GLW paradigm was proposed in Refs. [23–25] for *deconfined critical points* (DCP) in two spatial dimensions. Nowadays the problem of DCP is one of the most exciting and yet controversial topics in the theory of phase transitions. Remarkably, the field-theoretical model for deconfined criticality, to be referred to below as the *DCP action*, is given by two identical complex-valued classical fields coupled to a gauge vector field, in three dimensions. Despite its simplicity and apparent closeness to the single-component counterpart, known to be in the inverted XY universality class of continuous phase transitions, the DCP action is not amenable to reliable analytic treatments because of its runaway renormalization flow to strong coupling at large scales. To establish the order of the phase transition in this model one has to resort to numerics.

In Refs. [26, 27], the order of the phase transition in the DCP action was studied by the WA, for the $\text{U}(1) \times \text{U}(1)$ - and $\text{SU}(2)$ -symmetric actions, respectively. Within the given universality class, the optimal choice of microscopic model is the high-temperature expansion (cf. Sec. 20.3.1) of a cubic-lattice theory, resulting in the bond-current model with the following partition func-

**FIGURE 20.13**

Data collapse for the flows of the SU(2) symmetric DCP action. The line is a fit representing the master curve. The horizontal axis is the scale reduced variable $C(g)L$. (Reproduced from Ref. [27].)

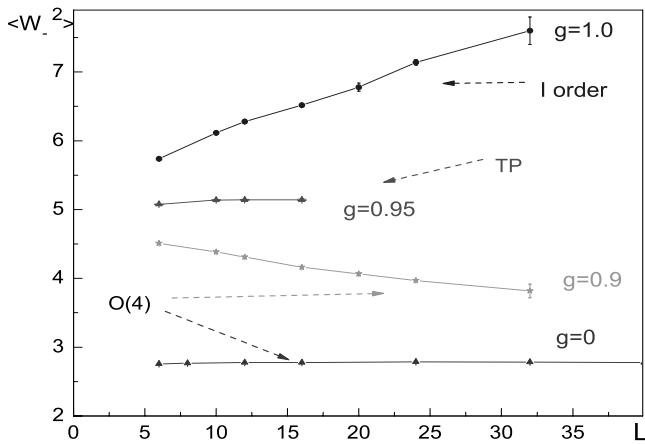
tion:⁶

$$Z = \sum_{\{J\}} \mathcal{Q}_{\text{site}} \mathcal{Q}_{\text{bond}} \exp(-H_J), \quad H_J = (g/2) \sum_{i,j; a,b; \mu=1,2,3} I_{i,\mu}^{(a)} V_{ij} I_{j,\mu}^{(b)}, \quad (20.11)$$

$$\mathcal{Q}_{\text{site}} = \prod_i \frac{\mathcal{N}_i^{(1)}! \mathcal{N}_i^{(2)}!}{(1 + \mathcal{N}_i^{(1)} + \mathcal{N}_i^{(2)})!}, \quad \mathcal{N}_i^{(a)} = \frac{1}{2} \sum_{\mu} J_{i,\mu}^{(a)}, \quad \mathcal{Q}_{\text{bond}} = \prod_{i,a,\mu} \frac{t^{J_{i,\mu}^{(a)}}}{J_{i,\mu}^{(a)}!}.$$

Here $J_{i,\mu}^{(a)}$ is an integer non-negative bond current of the component $a = 1, 2$, living on the bond (i, μ) . The bond subscript of a current is represented by the site, i , and direction $\mu = \pm 1, \pm 2, \pm 3$ from this site. The direction-dependent subscript reflects the fact that for a given geometric bond there are *two* different bond currents of the same component a , and $I_{i,\mu}^{(a)} = J_{i,\mu}^{(a)} - J_{i+\hat{\mu},-\mu}^{(a)}$ is their algebraic sum, where $\hat{\mu}$ is a unit translation vector in the direction μ . The bond currents are subject to the conservation constraint on each site: $\sum_{\mu} I_{i,\mu}^{(a)} = 0$. The parameter t controls the strength of the lattice gradient term for the complex fields in the DCP action, and g is the coupling constant for the interaction between the complex and gauge fields. The integration over the gauge field results in the long-range interaction, V_{ij} , between the currents.

⁶For the sake of definiteness, we present the answer for the SU(2)-symmetric case.

**FIGURE 20.14**

Flowgrams for the short-range model $V_{ij} = g\delta_{ij}$. The lower horizontal line features the $O(4)$ universality scaling behavior; for $g < g_c \approx 0.95$ all flows are attracted to this line. The upper horizontal line is the tricritical separatrix (marked as TP). Above it, flows diverge due to the first-order transition detected by the bi-modal distribution of energy. (Reproduced from Ref. [27].)

The lattice Fourier transform of V_{ij} is given by $V_{\mathbf{q}} = 1/[\sum_{\mu=1,2,3} \sin^2(q_{\mu}/2)]$ and implies an asymptotic behavior $V_{ij} \sim 1/r_{ij}$ at large distances. It is this Coulomb asymptotic tail of the current-current interaction that leads to a qualitative difference of the DCP action from its short-range counterparts.

With its closed-loop structure enforced by the current conservation constraint and the positive-definiteness of the weighting factors, the model (20.11) is in the domain of applicability of the WA, each of the two components being updated by its individual pair of worms. The results of simulations of both $U(1) \times U(1)$ - and $SU(2)$ -symmetric actions lead to conclusion that the phase transition is first order, unfortunately for the DCP theory. The definitive conclusion is based on the *flowgram method* [26] of finite-size analysis. The key idea is to demonstrate that the universal large-scale behavior as $g \rightarrow 0$ is identical to that at some finite coupling $g = g_{\text{coll}}$ where the nature of the transition can be easily revealed. The procedure is as follows:

- (i) Introduce a definition of the critical point for a finite-size system of linear size L consistent with the thermodynamic limit and insensitive to the order of the transition. Specifically, for any given g and L the critical value of t is defined by the requirement that the ratio of statistical weights of configurations with and without windings be equal to a fixed constant.

- (ii) At the critical point, calculate a quantity $R(L, g)$ that is supposed to be scale-invariant for the continuous phase transition in question, vanishes in one of the phases, and diverges in the other. Specifically, one can take $R(L, g)$ to be the variance of the winding number in the counter-flow channel: $R(L, g) \equiv \langle W_-^2 \rangle \equiv \sum_\mu \langle (W_{1,\mu} - W_{2,\mu})^2 \rangle$, where $W_{a,\mu}$ is the winding number of the component a in the direction μ .⁷
- (iii) Perform a data collapse for flowgrams of $R(L, g)$, by rescaling the linear system size, $L \rightarrow C(g)L$, where $C(g)$ is a smooth and monotonically increasing function of the coupling constant g .⁸

A collapse of the rescaled flows within an interval $g \in [0, g_{\text{coll}}]$ implies that the type of the transition within the interval remains the same, and thus can be inferred by dealing with the $g = g_{\text{coll}}$ point only. Since the $g \rightarrow 0$ limit implies large spatial scales, and, therefore, a model-independent runaway renormalization flow pattern, the conclusions are universal.

As is seen in Fig. 20.13, the flows for the DCP action collapse perfectly in the region $0.125 \leq g < g_{\text{coll}} = 1.65$. The rescaling function $C(g)$ exhibits the expected linear behavior $C(g) \propto g$ at small g .

In accordance with the above-outlined logic of flowgram method, the flow collapse within the interval $g \in [0, g_{\text{coll}}]$ proves that the order of the transition within this interval does not change. The mere fact of the data collapse on a master curve with a finite slope is not sufficient to conclude that the transition is of the first order. What appears in Fig. 20.13 to be divergent behavior characteristic of a first-order transition might be just a reconstruction of the flow from the O(4)-universality at $g = 0$ to a novel DCP-universality at strong coupling. To complete the proof, one has to determine the nature of the transition for $g = g_{\text{coll}}$. In this parameter range, the standard technique of detecting discontinuous transitions by the bi-modal energy distribution becomes feasible. At $g = 1.65$ it becomes possible to clearly see a bi-modal energy distribution that gets more and more pronounced with increasing system size. This leads to a conclusion that the whole phase transition line for small g features a generic weak first-order transition. Driven by long-range interactions, this behavior develops on length scales $\propto 1/g \rightarrow \infty$ for small g and thus is universal.

Finally, it is very instructive to contrast the flowgram for the DCP action (20.11) with the flowgram for the short-range counterpart of (20.11), where $V_{ij} = g\delta_{ij}$. The flows for the short-range model are presented in Fig. 20.14. As opposed to the DCP action case, it is impossible to collapse the data on a single master curve by re-scaling L . Now the flows clearly reveal a tri-critical point separating the second-order part of the phase transition line from the first-order part.

⁷See Ref. [26] for the motivation of this choice.

⁸In the present case, it is *a priori* known that $C(g \rightarrow 0) \propto g$.

20.5 Conclusions and Outlook

Worm Algorithm is a technique for performing efficient updates of configurations that have the form of closed paths/loops. The closed-loop structure imposes topological constraints and thus creates ergodicity problems for local updates in large system sizes. Worm Algorithm works in an extended configuration space containing all the original configurations as well as configurations with open loops. All updates are local and are performed exclusively at the open loop ends, referred to as worms. In most cases, the open-loop configurations themselves are of prime physical interest being associated with correlation functions, such as the single-particle Green function. It was demonstrated for a variety of systems and universality classes that WA eliminates problems with ergodicity and critical slowing down, successfully competing even with model-specific cluster algorithms [28]. At the same time, it is a flexible approach with a broad range of applications in many-particle bosonic and spin systems. It readily produces loops winding around the system, allows efficient simulations of off-diagonal correlations, grand canonical ensembles, disordered systems, etc. At the moment WA has no competitors among unbiased first-principles approaches for bosons with strong interactions between the particles, as well as with strong external—both regular and disordered—potential. It is easy to predict that in the nearest future WA will remain the method of choice for detailed studies of non-trivial strongly correlated bosonic systems (multicomponent, disordered, with long-range interactions, solid and supersolid ^4He , etc.). Recently, WA has proved indispensable for guiding experimental efforts in creating optical lattice emulators; it will continue playing this important role.

In its most general form, the idea of WA is to work in an enlarged configuration space which includes configurations violating constraints characteristic of the physical configurations. Nowadays worm-type updates and/or worm-type estimators for the Green function are an integral part of many other state-of-the-art lattice Monte Carlo algorithms [29–32]. It is only upon the implementation of the worm-type updates it became possible to overcome the critical slowing down in the Stochastic Series Expansion scheme [31]. Important improvements have been made to achieve maximal efficiency of the worm-type updates by suppressing bouncing: the so-called directed (guided) loop and geometrical WA [31,33] appear to be an optimal combination in terms of universality and performance. Successful applications of WA in high-energy physics [34–36], with the exciting most recent developments [37–39], render the approach interdisciplinary. Whenever a new representation for Quantum Monte Carlo appears, the generalized WA idea may prove useful for developing an efficient updating strategy.

Acknowledgments – We acknowledge support from the NSF (Grant No. PHY-0653183) and from the Army Research Office with funding from the

DARPA OLE program, and the hospitality of the Aspen Center for Physics where this chapter was written.

Bibliography

- [1] E.L. Pollock and D.M. Ceperley, Phys. Rev. B **36**, 8343-8352 (1987); P. Sindzingre, M.L. Klein, and D.M. Ceperley, Phys. Rev. Lett. **63**, 1601-1604 (1989).
- [2] R. Feynman, Rev. Mod. Phys. **20**, 367-387 (1948).
- [3] N. Prokof'ev and B. Svistunov, Phys. Rev. Lett. **87**, 160601 (2001).
- [4] N.V. Prokof'ev, B.V. Svistunov, and I.S. Tupitsyn, JETP **87**, 310-321 (1998).
- [5] A. Kuklov, N. Prokof'ev, and B. Svistunov, Phys. Rev. Lett. **92**, 030403 (2004).
- [6] S.G. Söyler, B. Capogrosso-Sansone, N.V. Prokof'ev, and B.V. Svistunov, New J. Phys. **11**, 073036 (2009).
- [7] M. Boninsegni, N. V. Prokof'ev, and B. V. Svistunov, Phys. Rev. E **74**, 036701 (2006).
- [8] K. Van Houcke, E. Kozik, N. Prokof'ev, and B. Svistunov, in *Computer Simulation Studies in Condensed Matter Physics XXI*, Eds. D.P. Landau, S.P. Lewis, and H.B. Schuttler (Springer-Verlag, Heidelberg, Berlin 2008).
- [9] D. Jaksch *et al.*, Phys. Rev. Lett. **81**, 3108 (1998).
- [10] B. Capogrosso-Sansone, N. V. Prokof'ev, and B. V. Svistunov, Phys. Rev. B **75**, 134302 (2007).
- [11] B. Capogrosso-Sansone, G. Söyler, N.V. Prokof'ev, and B.V. Svistunov, Phys. Rev. A **77**, 015602 (2008).
- [12] L. Pollet, N.V. Prokof'ev, B. V. Svistunov, and M. Troyer, Phys. Rev. Lett. **103**, 140402 (2009).
- [13] S. Trotzky *et al.*, arXiv:0905.4882.
- [14] E. Kim and M.H.W. Chan, Nature, **427**, 225-227 (2004).
- [15] E. Kim and M.H.W. Chan, Science, **305**, 1941-1944 (2004).
- [16] N. Prokof'ev, Advances in Physics, **56**, 381-402 (2007).

- [17] S. Balibar and F. Caupin, J. Phys.: Cond. Matter, **20**, 173201 (2008).
- [18] B. Svistunov, Physica B **404**, 521-523 (2009).
- [19] N. Prokof'ev and B. Svistunov, Phys. Rev. Lett. **94**, 155302 (2005).
- [20] A.F. Andreev and I.M. Lifshitz, Sov. Phys. – JETP, **29**, 1107 (1969).
- [21] M. Boninsegni *et al.*, Phys. Rev. Lett. **97**, 080401 (2006).
- [22] M. Boninsegni *et al.*, Phys. Rev. Lett. **99**, 035301 (2007).
- [23] O.I. Motrunich and A. Vishwanath, Phys. Rev. B, **70**, 075104 (2004).
- [24] T. Senthil *et al.*, Science, **303**, 1490-1494 (2004).
- [25] T. Senthil *et al.*, Phys. Rev. B, **70**, 144407 (2004).
- [26] A. Kuklov, N. Prokof'ev, B. Svistunov, and M. Troyer, Ann. of Phys. **321**, 1602-1621 (2006).
- [27] A.B. Kuklov *et al.*, Phys. Rev. Lett. **101**, 050405 (2008).
- [28] Y. Deng, T.M. Garoni, and A.D. Sokal, Phys. Rev. Lett. **99**, 110601 (2007).
- [29] R. Brower, S. Chandrasekharan, and U.-J. Wiese, Physica **A261**, 520-533 (1998).
- [30] A. Dorneich and M. Troyer, Phys. Rev. E **64**, 066701 (2001).
- [31] O.F. Syljuasen and A.W. Sandvik, Phys. Rev. E **66**, 046701 (2002); A.W. Sandvik, Prog. Theor. Phys. Suppl. **145**, 332-338 (2002).
- [32] N. Kawashima and K. Harada, Phys. Soc. Jpn. **73**, 1379 (2004).
- [33] F. Alet and E.S. Sorensen, Phys. Rev. E **68**, 026702 (2003).
- [34] D.H. Adams and S. Chandrasekharan, Nucl. Phys. B **662**, 220-246 (2003).
- [35] S. Chandrasekharan and F.J. Jiang, Phys. Rev. D **68**, 091501 (2003).
- [36] M. Fromm, Nucl. Phys. A, **820**, 179c-182c (2003).
- [37] U. Wenger, Phys. Rev. D **80**, 071503 (2009).
- [38] U. Wolff, Nucl. Phys. B **810**, 491-502 (2009); Nucl. Phys. B **814**, 549-572 (2009); Nucl. Phys. B **824**, 254-272 (2010).
- [39] Ph. de Forcrand and M. Fromm, Phys. Rev. Lett. **104**, 112005 (2010).

21

Cluster Monte Carlo Algorithms for Dissipative Quantum Phase Transitions

Philipp Werner

Theoretische Physik, ETH Zurich, Switzerland

Matthias Troyer

Theoretische Physik, ETH Zurich, Switzerland

Dissipation and decoherence in quantum systems have important practical implications, from stabilizing superconductivity in granular materials, to the loss of information stored in qubits. In the models we consider in this chapter, energy dissipation is introduced by coupling a quantum mechanical degree of freedom to a bath of suitably chosen harmonic oscillators. The degrees of freedom of this bath can be integrated out analytically, which leads to an effective action with long-range interactions in imaginary time. We will review and present a number of recently developed efficient cluster Monte Carlo algorithms for various dissipative quantum systems. This chapter is based in large part on Refs. [1, 2] but has been updated with more recent developments, especially in the applications section.

These algorithms have been used to study spin chains with dissipation coupling to site variables and resistively shunted Josephson junctions [1, 3–12]. We will also present relevant theoretical background for these models and mention questions which have been addressed in the numerical investigations, and issues that still remain open.

21.1 Dissipative Quantum Models

21.1.1 The Caldeira-Leggett Model

While the concept of coupling a quantum mechanical degree of freedom to an environment goes back to the early days of quantum mechanics, it was the work of Caldeira and Leggett [13, 14] which pointed out the important consequences of dissipation at a time when experimental results on macroscopic quantum tunneling became available. To introduce their model we consider a classical system whose dissipative dynamics in terms of some coordinate q is

described in the absence of external forces by the phenomenological equation of motion

$$M\ddot{q}(t) + \eta\dot{q}(t) + [V'(q)](t) = 0, \quad (21.1)$$

where η denotes the friction coefficient. Because the frictional force is proportional to \dot{q} , one calls the dissipation *Ohmic*.

The equation of motion (21.1) can be obtained from a microscopic model by coupling the system linearly in the coordinates to an appropriately chosen set of harmonic oscillators, that is, from the Lagrangian

$$L = \frac{M}{2}\dot{q}^2 - V(q) + \frac{1}{2} \sum_{\alpha} \left\{ m_{\alpha} \dot{x}_{\alpha}^2 - m_{\alpha} \omega_{\alpha}^2 \left(x_{\alpha} - \frac{c_{\alpha}}{m_{\alpha} \omega_{\alpha}^2} q \right)^2 \right\}, \quad (21.2)$$

where x_{α} , m_{α} , ω_{α} and c_{α} denote the oscillator positions, masses, frequencies and coupling strengths, respectively. Defining the spectral density

$$J(\omega) = \frac{\pi}{2} \sum_{\alpha} \frac{c_{\alpha}^2}{m_{\alpha} \omega_{\alpha}} \delta(\omega - \omega_{\alpha}), \quad (21.3)$$

we can reproduce the phenomenological equation (21.1) by setting

$$J(\omega) = \eta\omega, \quad (21.4)$$

for $\omega \geq 0$ [1,14,15]. In any real physical system, the harmonic oscillators representing the environment will have finite frequencies; so the linear relationship (21.4) must be cut off at some value ω_c .

The partition function of the quantum mechanical system can be obtained from the classical Euclidean Lagrangian

$$L^E = \frac{M}{2}\dot{q}^2 + V(q) + \frac{1}{2} \sum_{\alpha} \left\{ m_{\alpha} \dot{x}_{\alpha}^2 + m_{\alpha} \omega_{\alpha}^2 \left(x_{\alpha} - \frac{c_{\alpha}}{m_{\alpha} \omega_{\alpha}^2} q \right)^2 \right\}, \quad (21.5)$$

by the path integral formalism [1,14,15]. Integrating out the harmonic oscillator degrees of freedom leads to an effective action

$$\begin{aligned} S_{\text{eff}}[q] &= \int_0^{\beta} d\tau \left[\frac{M}{2} \dot{q}^2(\tau) + V(q(\tau)) \right] \\ &\quad + \frac{\eta}{4\pi} \int_0^{\beta} \int_0^{\beta} d\tau d\tau' \left(\frac{\pi}{\beta} \right)^2 \frac{(q(\tau) - q(\tau'))^2}{(\sin(\frac{\pi}{\beta}|\tau - \tau'|))^2}. \end{aligned} \quad (21.6)$$

In analytical calculations, but also for certain algorithms discussed in Sec. 21.5, it is useful to express the damping term (proportional to η) in Fourier space. In the limit $\beta \rightarrow \infty$ and for asymmetric Fourier transforms one obtains

$$S_{\text{damp}} = \frac{\eta}{4\pi} \int_{-\infty}^{\infty} d\omega |\omega| |q(\omega)|^2, \quad (21.7)$$

which is local in the frequency ω , in contrast to the imaginary-time integral (21.6).

21.1.2 Dissipative Quantum Spin Chains

An effective action for a single $O(n)$ spin with on-site dissipation is obtained from Eq. (21.6) by choosing an n -component vector \vec{q} as the coordinate which couples to the environment and a double-well potential

$$V(q) = \frac{s}{2}q^2 + \frac{u}{24}q^4 \quad (21.8)$$

with minima at $|\vec{q}| = 1$. Coupling the spins spatially through nearest neighbor bonds of the form $-K\vec{q}_j \cdot \vec{q}_{j+1}$ then yields the action for the spin chain

$$\begin{aligned} S = & \sum_{j=1}^{N_x} \int_0^\beta d\tau \left[\frac{M}{2}(\partial_\tau \vec{q}_j)^2 - K\vec{q}_j \cdot \vec{q}_{j+1} + \frac{s}{2}q_j^2 + \frac{u}{24}q_j^4 \right] \\ & + \frac{\eta}{4\pi} \sum_{j=1}^{N_x} \int_0^\beta \int_0^\beta d\tau d\tau' \left(\frac{\pi}{\beta} \right)^2 \frac{(\vec{q}_j(\tau) - \vec{q}_j(\tau'))^2}{(\sin(\frac{\pi}{\beta}|\tau - \tau'|))^2}. \end{aligned} \quad (21.9)$$

The special cases $n = 1$ (Ising spin chain) and $n = 2$ (XY-spin chain) will be discussed in Sec. 21.6.

To simplify the calculations, we will discretize the action (21.9) in imaginary time, noting that the cutoff of the linear spectral density $J(\omega)$ at ω_c would anyhow lead to modifications in S_{damp} at small $\tau - \tau'$. The Trotter number N_τ corresponds to a discretization step $\Delta\tau = \beta/N_\tau$. Furthermore, we employ a “hard spin” approximation and choose the potential (21.8) such that the spin states at any time can be described as $O(n)$ vectors $\vec{\sigma}$ of norm $|\vec{\sigma}| = 1$. Introducing the coefficients $\Gamma = M/\Delta\tau$ and $\alpha = \eta/\pi$, the discretized action becomes

$$\begin{aligned} S = & - \sum_{j=1}^{N_x} \sum_{k=1}^{N_\tau} [K\vec{\sigma}_{j,k} \cdot \vec{\sigma}_{j+1,k} + \Gamma\vec{\sigma}_{j,k} \cdot \vec{\sigma}_{j,k+1}] \\ & - \alpha \sum_{j=1}^{N_x} \sum_{k < k'} \left(\frac{\pi}{N_\tau} \right)^2 \frac{\vec{\sigma}_{j,k} \cdot \vec{\sigma}_{j,k'}}{(\sin(\frac{\pi}{N_\tau}|k - k'|))^2}, \end{aligned} \quad (21.10)$$

which can be simulated as a two-dimensional system of classical $O(n)$ -spins with short-range interactions in the “space” direction and long-range interactions in the “imaginary time” direction.

21.1.3 Resistively Shunted Josephson Junction

Another example of a dissipation-coupled quantum system is a Josephson junction with Josephson coupling energy E_J and capacitance C , which is shunted by an Ohmic resistor R_s , as illustrated in Fig. 21.1. While Cooper pairs can tunnel through the junction, which consists of a thin layer of insulating material or a constriction in the superconductor, electrons can flow

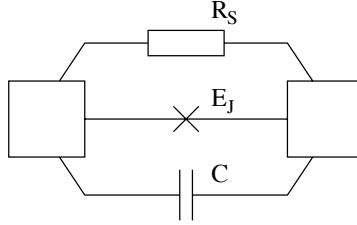
**FIGURE 21.1**

Illustration of a resistively shunted Josephson junction. It consists of two superconducting islands connected by a Josephson junction of coupling energy E_J and capacitance C and a parallel resistor R_s through which electrons can flow.

through the resistor and dissipate energy. Let ϕ_l and ϕ_r denote the phases of the superconducting order parameter on the left and right island, respectively, and $\phi = \phi_l - \phi_r$ the phase difference across the junction. This phase difference is related to the voltage drop V across the junction and the super-current I_s by the Josephson relations ($h/2e$ is the flux quantum) [16]

$$V = \frac{\hbar}{2e} \dot{\phi}, \quad (21.11)$$

$$I_s = I_c \sin \phi, \quad (21.12)$$

where I_c denotes the critical current, which is related to the coupling energy by

$$E_J = \frac{\hbar I_c}{2e}. \quad (21.13)$$

The dynamics of such a device can be determined from a balance of currents, which for zero external current reads

$$\begin{aligned} 0 &= I_{\text{displacement}} + I_{\text{shunt}} + I_{\text{super}} = C \dot{V} + \frac{V}{R_s} + I_c \sin \phi \\ &= C \frac{\hbar \ddot{\phi}}{2e} + \frac{1}{R_s} \frac{\hbar \dot{\phi}}{2e} + \frac{2e E_J}{\hbar} \sin \phi. \end{aligned} \quad (21.14)$$

If we identify $\frac{\hbar \phi}{2e}$ with a coordinate q and introduce the potential

$$U(q) = -E_J \cos(\phi(q)) = -E_J \cos((2e/\hbar)q), \quad (21.15)$$

then (21.14) becomes

$$C \ddot{q} + \frac{1}{R_s} \dot{q} + U'(q) = 0, \quad (21.16)$$

which is just equation (21.1) with the substitutions $M \rightarrow C$ and $\eta \rightarrow \frac{1}{R_s}$. According to the recipe of Caldeira and Leggett outlined above, the dissipation

in the shunt resistor can be reproduced by coupling q to an Ohmic heat bath, which is integrated out and leads to the effective action (21.6). Expressing q , M and η again in terms of the original variables ϕ , C and R_s , one finds the action for the resistively shunted Josephson junction. Furthermore, introducing the effective charging energy of the junction $E_C = \frac{e^2}{2C}$ (which sets the energy scale), the quantum of resistance $R_Q = \frac{\hbar}{4e^2}$, and $\alpha = R_Q/R_s$ the action becomes (setting $\hbar = 1$)

$$\begin{aligned} S[\phi] = & \int_0^\beta d\tau \left[\frac{1}{16E_C} \left(\frac{d\phi}{d\tau} \right)^2 - E_J \cos(\phi) \right] \\ & + \frac{1}{8\pi^2 \alpha} \int_0^\beta \int_0^\beta d\tau d\tau' \frac{(\pi/\beta)^2 (\phi(\tau) - \phi(\tau'))^2}{\sin((\pi/\beta)(\tau - \tau'))^2}. \end{aligned} \quad (21.17)$$

Resistively shunted Josephson junctions at zero temperature undergo a superconductor-to-metal transition if the shunt resistance R_s is increased beyond the critical value R_Q . This dissipative phase transition was first predicted by Schmid [17] and Bulgadaev [18] and subsequently studied by several authors [19–22].

21.1.4 Single Electron Box

The *single-electron* box, which consists of a low-capacitance metallic island connected to an outside lead by a tunnel junction, is described by the action of a dissipative quantum rotor. Due to the large charging energy of the island, the presence of excess charges influences single electron tunneling and such a device thus exhibits Coulomb blockade phenomena.

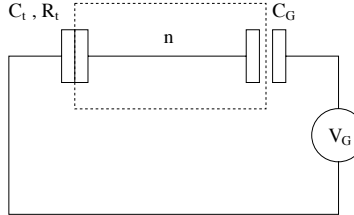
A circuit diagram of a single electron box is shown in Fig. 21.2. The box with excess charge n is controlled by an external voltage source V_G , to which it is connected through a capacitor C_G and a tunnel junction with resistance R_t and capacitance C_t . The bare charging energy $E_C = \frac{e^2}{2(C_t + C_G)}$ sets the energy scale. An applied gate voltage V_G induces a continuous polarization charge $n_G = C_G V_G / e$.

The effective action of the single electron box with zero gate charge can be derived from a microscopic theory, as detailed in Refs. [1, 21, 23–25]:

$$S[\theta] = \frac{1}{4E_C} \int_0^\beta d\tau \dot{\theta}(\tau)^2 - \frac{1}{2\pi e^2 R_t} \int_0^\beta d\tau d\tau' \frac{(\pi/\beta)^2 \cos(\theta(\tau') - \theta(\tau))}{(\sin((\pi/\beta)(\tau - \tau')))^2}. \quad (21.18)$$

The compact angular variable θ is conjugate to the number of excess charges on the island and the partition function can be written as the sum over all paths with winding number $\omega = \pm n$, $n = 0, 1, 2, \dots$

At low temperatures, $k_B T \ll E_C$, and for high tunneling resistance, $R_t \gg R_K = h/e^2 \approx 25.8 k\Omega$, the number of excess charges on the island is a staircase function with unit jumps at $n_G = 1/2$. Thermal fluctuations will round off the corners of the step structure. But even at zero temperature, electron-tunneling

**FIGURE 21.2**

Circuit diagram of the single electron box. The box with excess charge n is indicated by the dashed rectangle. It is connected to a voltage source through a capacitor C_G and a tunnel junction with resistance R_t and capacitance C_t .

processes can smear out the staircase, which for large tunneling approaches a straight line. These quantum fluctuations renormalize the ground state energy and lead to an effective charging energy E_C^* , which can be computed from the expectation value of the winding number ω squared [26],

$$\frac{E_C^*}{E_C} = \frac{2\pi^2}{\beta E_C} \langle \omega^2 \rangle = \frac{2\pi^2}{\beta E_C} \frac{1}{Z} \int_0^{2\pi} d\theta_0 \sum_{n=0}^{\infty} n^2 \int_{\theta_0}^{\theta_0 \pm 2\pi n} \mathcal{D}\theta e^{-S[\theta]}. \quad (21.19)$$

In Sec. 21.6 we will address the behavior of E_C^*/E_C in the limit of large tunneling conductance.

21.2 Importance Sampling and the Metropolis Algorithm

In a Monte Carlo simulation we would like to compute the expectation value of some observable O ,

$$\langle O \rangle = \sum_{\Omega} P(x)O(x), \quad (21.20)$$

where P denotes a probability distribution defined on the configuration space Ω . Since it is usually not possible to sum over all configurations, the strategy is to sample random configurations x_1, \dots, x_N , according to their importance $P(x_i)$ and approximate Eq. (21.20) by

$$\overline{O} \approx \frac{1}{N} \sum_{i=1}^N O(x_i). \quad (21.21)$$

For statistically independent $O(x_i)$ and large enough N it follows from the central limit theorem that \overline{O} follows a Gaussian distribution centered at $\langle O \rangle$

and standard deviation

$$\sigma \equiv \Delta \bar{O} = \sqrt{\frac{\text{Var}(O)}{N}} \approx \sqrt{\frac{\bar{O}^2 - \bar{O}^2}{N-1}}. \quad (21.22)$$

As a consequence, the accuracy of a Monte Carlo simulation scales as $1/\sqrt{N}$ with computation time N .

The challenge is to generate a chain of configurations x_1, \dots, x_N such that the x_i are sampled according to their weight $P(x_i)$. For this purpose we introduce a Markov process which defines a probability distribution P_{t+1} at time (Monte Carlo step) $t + 1$ from the distribution P_t at time t by means of a transition matrix T ,

$$P_{t+1}(y) = \sum_x T_{y|x} P_t(x). \quad (21.23)$$

The elements $T_{y|x}$ of T correspond to the transition probabilities from state x to state y and therefore

$$T_{y|x} \geq 0, \quad \sum_y T_{y|x} = 1. \quad (21.24)$$

As a consequence P_{t+1} is a probability distribution if P_t is one. An additional requirement for T is ergodicity: it must be possible to reach every configuration y from any configuration x in a finite number of Markov steps. This assures that in the limit of infinitely many steps, the whole configuration space is sampled. Finally, T must be such that the probability distribution P is *stationary*,

$$P(y) = \sum_x T_{y|x} P(x). \quad (21.25)$$

This condition is satisfied, if

$$T_{y|x} P(x) = T_{x|y} P(y), \quad (21.26)$$

as is obvious by summing over x . The relation (21.26) is referred to as *detailed balance*.

Given the above, any probability distribution $P_0(x) = \delta_{x,x_i}$ will converge to $P(x)$ as $t \rightarrow \infty$ [27]. Hence, an infinitely long Markov chain starting with x_i and defined by the transition matrix T generates configurations according to their weight $P(x)$.

We would now like to explicitly construct the transition matrix T . To this end we decompose the transition probability to move from a configuration x to a configuration y , $T_{y|x}$, into an *a priori* probability $p_{y|x}^{\text{prop}}$ to propose the move from x to y and $p_{y|x}^{\text{acc}}$ to accept the move. Assuming that $p_{x|x}^{\text{prop}} = 0$ and $p_{y|x}^{\text{prop}}$ satisfies conditions (21.24), the transition matrix defined as

$$T_{y|x} = \begin{cases} p_{y|x}^{\text{prop}} p_{y|x}^{\text{acc}} & y \neq x \\ 1 - \sum_{y \neq x} p_{y|x}^{\text{prop}} p_{y|x}^{\text{acc}} & y = x \end{cases} \quad (21.27)$$

satisfies Eq. (21.24) as well. The detailed balance condition (21.26) now reads

$$p_{y|x}^{\text{prop}} p_{y|x}^{\text{acc}} P(x) = p_{x|y}^{\text{prop}} p_{x|y}^{\text{acc}} P(y), \quad (21.28)$$

and can be satisfied in several ways. The Metropolis algorithm [28] is based on the choice

$$p_{y|x}^{\text{acc}} = \min \left(1, \frac{p_{x|y}^{\text{prop}} P(y)}{p_{y|x}^{\text{prop}} P(x)} \right). \quad (21.29)$$

21.3 Cluster Algorithms for Classical Spins

21.3.1 The Swendsen-Wang and Wolff Cluster Algorithms

The Monte Carlo simulation of spin systems near criticality requires the use of efficient algorithms, which we will first discuss for the Ising model with nearest neighbor interactions ($K > 0$, $\langle i, j \rangle$ denotes a pair of nearest neighbor sites):

$$S = -K \sum_{\langle i, j \rangle} \sigma_i \sigma_j. \quad (21.30)$$

Since the correlation length diverges in the vicinity of a phase transition, large domains of aligned spins appear. Thus, local update schemes become very inefficient in changing the overall configuration, which leads to large autocorrelation times. In order to overcome this problem it is necessary to flip entire clusters of spins in each Monte Carlo update. The Swendsen-Wang algorithm [29] chooses these clusters in a way in which detailed balance is automatically satisfied and no cluster move is rejected.

This algorithm is an example of a dual Monte Carlo algorithm [30], which switches back and forth between two configuration spaces, as illustrated in Fig. 21.3. One representation is in terms of Ising *spin variables* $\sigma_i \in \{-1, 1\}$, while the other one is the random cluster representation of Fortuin and Kasteleyn [31], which is expressed in terms of *bond variables* $b_{ij} \in \{0, 1\}$. The transition probabilities between configurations in both spaces follow directly from the joint Edwards-Sokal representation in terms of spin and bond variables [32, 33].

The partition function of the Ising model (21.30) in these three representations reads

- spin representation

$$Z = \sum_{\{\sigma\}} e^{K \sum_{\langle i, j \rangle} \sigma_i \sigma_j} = \sum_{\{\sigma\}} \prod_{\langle i, j \rangle} e^{K \sigma_i \sigma_j}, \quad (21.31)$$

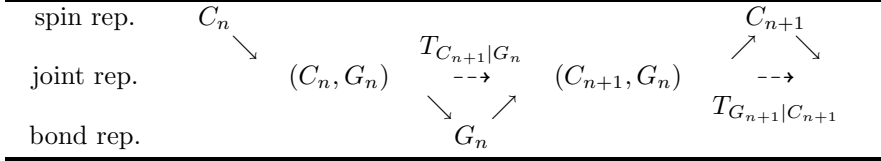
**FIGURE 21.3**

Illustration of the Markov process in the Swendsen-Wang cluster algorithm, which switches back and forth between spin configurations (C_n) and bond configurations (G_n). The transition probabilities $T_{C_{n+1}|G_n}$ and $T_{G_{n+1}|C_{n+1}}$ can be found from the joint representation in terms of spin and bond variables.

- joint representation

$$Z = \sum_{\{b\}} \sum_{\{\sigma\}} \prod_{\langle i,j \rangle} e^K \left[\delta_{b_{ij},0} e^{-2K} + \delta_{b_{ij},1} \delta_{\sigma_i,\sigma_j} (1 - e^{-2K}) \right], \quad (21.32)$$

- bond representation

$$Z = e^{-KN_b^{\text{tot}}} \sum_{\{b\}} (e^{2K} - 1)^{n_b} 2^{n_c}, \quad (21.33)$$

where N_b^{tot} denotes the total number of bonds, n_b the number of bond variables with value $b_{ij} = 1$ and n_c the number of clusters.

The joint representation in Eq. (21.32) is obtained from Eq. (21.31) by introducing bond variables $b_{ij} \in \{0, 1\}$ using the identity

$$e^{-K} e^{K\sigma_i\sigma_j} = \sum_{b_{ij}} \left[\delta_{b_{ij},0} e^{-2K} + \delta_{b_{ij},1} \delta_{\sigma_i,\sigma_j} (1 - e^{-2K}) \right]. \quad (21.34)$$

Summing over the spin variables in Eq. (21.32) then yields the Fortuin-Kasteleyn random cluster representation, Eq. (21.33).

The Swendsen-Wang algorithm follows directly from the joint representation [32]. Given a spin configuration $\{\sigma_i\}$, the conditional probability for freezing a bond ($b_{ij} = 1$) is found from Eq. (21.32) to be

$$T_{b_{ij}=1|\sigma_i=\sigma_j} = \frac{1 - e^{-2K}}{e^{-2K} + (1 - e^{-2K})} = 1 - e^{-2K}, \quad (21.35)$$

$$T_{b_{ij}=1|\sigma_i \neq \sigma_j} = 0. \quad (21.36)$$

In the more general case, where spins interact over arbitrary distances with different strengths, the probability of a bond between the sites i and j becomes

$$T_{b_{ij}=1} = \max(0, 1 - \exp[-\Delta S(i, j)]), \quad (21.37)$$

where $\Delta S(i, j) = S_{\text{updated}}(i, j) - S_{\text{original}}(i, j)$ denotes the cost in action of flipping a spin associated with the pair (i, j) .

The Swendsen-Wang algorithm proceeds in the following three steps, which for the case of the dissipative quantum Ising chain (21.10) are illustrated in Fig. 21.4. First, bonds are inserted between the sites of interacting spins with probability (21.37). Second, clusters of connected spins are identified. Third, the spins of each cluster are flipped with probability $\frac{1}{2}$.

Wolff [34] extended the ideas of Swendsen and Wang to $O(n)$ spin models. First of all he noted that it is more efficient to build a single cluster from a randomly chosen site and update all the spins in this cluster. This has the advantage that most updates take place in the largest regions of aligned spins. By choosing a random direction \vec{e} on the n -sphere and projecting the spins onto this direction, one ends up with an Ising-like system. Updating a spin then means flipping this projected component, or in other words mirroring the spin on the plane perpendicular to \vec{e} ,

$$\vec{\sigma} \rightarrow \vec{\sigma} - 2(\vec{\sigma} \cdot \vec{e})\vec{e}. \quad (21.38)$$

The probability (21.37) for inserting a bond between two spins at sites i and j remains valid. A Wolff cluster update therefore proceeds in the following three steps. First, choose a random site and a direction \vec{e} . Second, find all spins connected to this site using the bond probability (21.37), where $\Delta S(i, j) = S(\sigma_i - 2(\vec{\sigma}_i \cdot \vec{e})\vec{e}, \vec{\sigma}_j) - S(\vec{\sigma}_i, \vec{\sigma}_j)$. Third, mirror all the spins in the cluster on the plane perpendicular to \vec{e} .

21.3.2 Efficient Treatment of Long-Range Interactions

In the presence of long-range forces, every site interacts with every other site and an algorithm which iterates over all bonds would be of order $O(N^2)$, where N is the number of sites. This is prohibitively slow and thus we present here a more sophisticated algorithm, proposed by Luijten and Blöte [35], which is of order $N \log N$. The idea of Luijten and Blöte is essential for the simulation of dissipative quantum systems at low temperature, since we have seen in Sec. 21.1 that dissipation introduces long-range interactions in the imaginary time direction.

We consider first a chain of classical Ising spins with long-range interactions,

$$S = - \sum_{i,j} g(i-j) \sigma_i \sigma_j. \quad (21.39)$$

The kernel g of interest in our applications is of the form ($j \neq 0$)

$$g(j) = \alpha \frac{(\frac{\pi}{N})^2}{(\sin(\frac{\pi}{N}j))^2}, \quad (21.40)$$

but this is of no importance for the following discussion. From Eq. (21.37) it

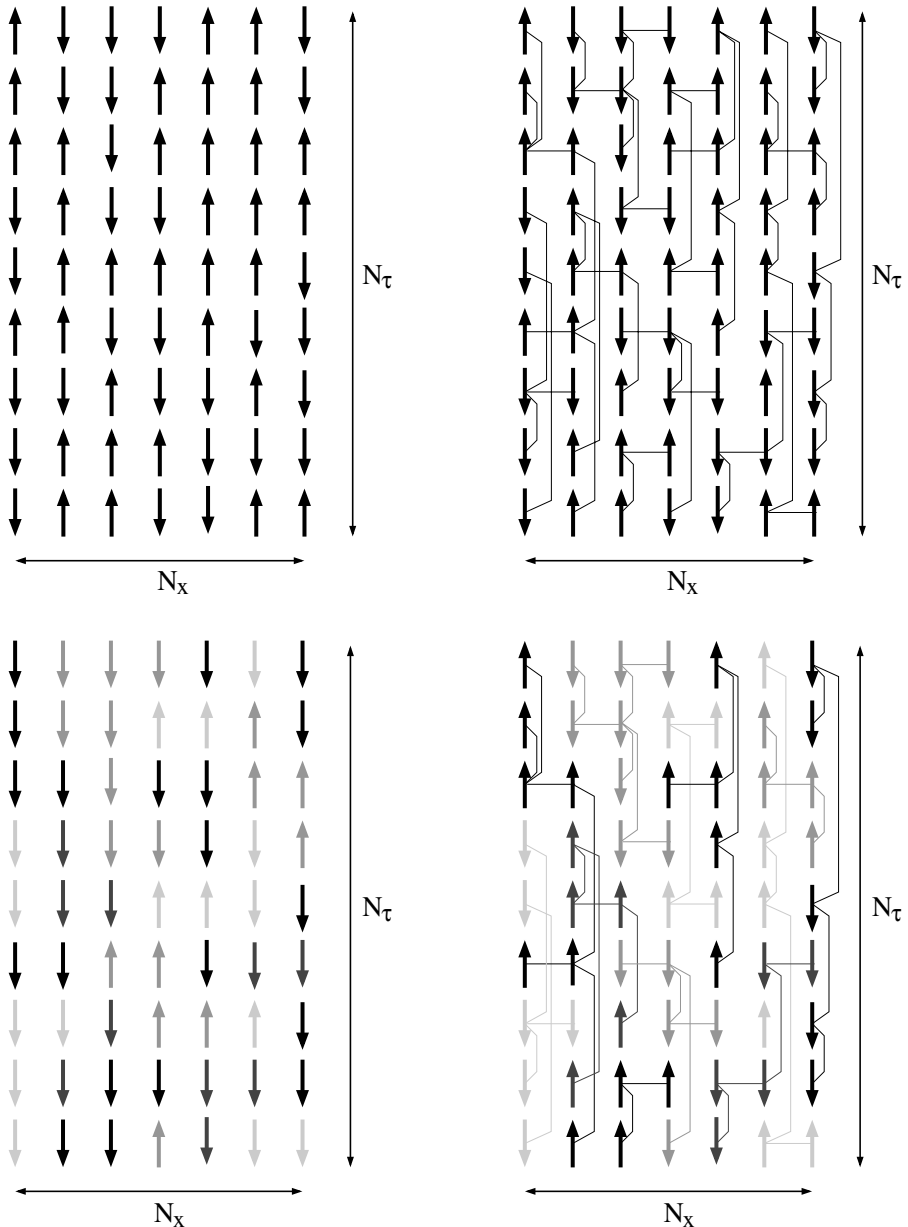
**FIGURE 21.4**

Illustration of the Swendsen-Wang cluster algorithm. The figures show clockwise from the top left: (i) original spin configuration, (ii) insertion of bonds, (iii) clusters of connected spins, (iv) new spin configuration obtained by flipping the spins of each cluster with probability $\frac{1}{2}$. Illustration taken from Refs. [1, 2].

follows that the probability of a long-range bond between two parallel spins at sites 0 and j is

$$P_{\text{bond}}(0; j) = 1 - e^{-2g(j)}. \quad (21.41)$$

Hence, the probability that no bond is formed between spin 0 and spins $j + 1, \dots, n - 1$ (all assumed parallel) becomes

$$P_{\text{no bond}}(0; j + 1, \dots, n - 1) = \prod_{i=j+1}^{n-1} e^{-2g(i)} = \exp \left[-2 \sum_{i=j+1}^{n-1} g(i) \right]. \quad (21.42)$$

If we define an array (lookup table) A of length N with elements $A[0] = 1$, and $A[n] = \prod_{i=1}^n e^{-2g(i)}$ for $n = 1, \dots, N - 1$, then Eq. (21.42) can be written as

$$P_{\text{no bond}}(0; j + 1, \dots, n - 1) = \frac{A[n - 1]}{A[j]}. \quad (21.43)$$

The spins connected to site 0 are then calculated as follows: a random number r_1 is chosen in the interval $[0, 1)$ and the array A is searched for the first index, say n_1 , such that $A[n_1] \leq r_1$. For the calculation of the next bond, the values of A must be divided by $A[n_1]$, or equivalently, the random number r_2 multiplied by $A[n_1]$. The site number n_2 of the second connected spin is the first index, such that $A[n_2] \leq A[n_1]r_2$. This process is continued until $A[n_{k-1}]r_k < A[N - 1]$.

The outlined procedure assumes that all spins are aligned. Before actually inserting a proposed bond, we have to check whether the two spins are parallel. If the bisection method is used to search for the lowest index such that $A[n] \leq r$, the calculation time is of order $\log N$ per site. An update of the whole lattice with lookup-table is therefore of order $N \log N$.

In the case of $O(n)$ -spins, where the bond strength depends on the spin components projected on some random direction \vec{e} ,

$$\sigma^{\text{proj}} = \vec{\sigma} \cdot \vec{e}, \quad (21.44)$$

one proposes bonds as explained for the Ising case. To account for the fact that the interaction is weaker than assumed in the look-up table, a random number $r \in [0, 1)$ is chosen and a proposed bond between sites i and j is only inserted if

$$r(1 - e^{-2g(i-j)}) < 1 - e^{-2g(i-j)\sigma_i^{\text{proj}}\sigma_j^{\text{proj}}}. \quad (21.45)$$

21.4 Cluster Algorithm for Resistively Shunted Josephson Junctions

For the resistively shunted Josephson junction, introduced in Sec. 21.1.3, one cannot directly employ the cluster algorithms available for spin systems because of the Josephson coupling energy and the non-compact nature of the

phase variable in this action. In order to simulate resistively shunted junctions efficiently, we developed a new algorithm [8], consisting of two kinds of updates: (i) local updates in Fourier space compatible with the Gaussian terms in Eq. (21.17) and (ii) rejection-free cluster updates. The first type of move assures ergodicity of the algorithm and the second type produces global cluster updates compatible with the energetic constraints from the Josephson potential.

21.4.1 Local Updates in Fourier Space

For the Monte Carlo simulation, we discretize imaginary time into N time steps, assumed odd. The action (21.17) can then be expressed in the simple form

$$S[\phi] = \sum_{k=0}^{N-1} a_k |\tilde{\phi}_k|^2 - E_J \Delta\tau \sum_{j=0}^{N-1} \cos(\phi_j), \quad (21.46)$$

where $\tilde{\phi}_k = \sum_{j=0}^{N-1} e^{i\frac{2\pi}{N}jk} \phi_j$ denotes the Fourier transform of ϕ . The positive coefficients a_k are defined as $a_k = \frac{2}{N}(\tilde{g}_0 - \tilde{g}_k)$, with \tilde{g}_k the Fourier transform of the kernel ($j \neq 0$)

$$g(j) = \frac{1}{32E_C \Delta\tau} (\delta_{j,1} + \delta_{j,N-1}) + \frac{\alpha}{8\pi^2} \frac{(\pi/N)^2}{\sin((\pi/N)j)^2}. \quad (21.47)$$

Since $\tilde{\phi}_k^* = \tilde{\phi}_{N-k}$, only $\{\tilde{\phi}_k | k = 0, \dots, (N-1)/2\}$ need to be considered.

In a local update of the frequency components $\tilde{\phi}_k$ and $\tilde{\phi}_{N-k}$, we choose a new value according to the probability distribution of the Gaussian term in Eq. (21.46),

$$p(\phi_k) \sim e^{-2a_k |\tilde{\phi}_k|^2}, \quad (21.48)$$

by fixing the phase at a random value in the interval $[0, 2\pi]$ and $|\tilde{\phi}_k|^2$ using exponentially distributed random numbers with mean $1/(2a_k)$. This move is accepted with probability

$$p(\phi_{\text{old}} \rightarrow \phi_{\text{new}}) = \min \left(1, e^{-\{S_J[\phi_{\text{new}}] - S_J[\phi_{\text{old}}]\}} \right), \quad (21.49)$$

where $S_J[\phi] = -E_J \Delta\tau \sum_{j=0}^{N-1} \cos(\phi_j)$ and $\phi_{\text{old}}, \phi_{\text{new}}$ denote the backward Fourier transform of the old and new k -space configuration, respectively. Such local updates can be performed in a time $O(N)$ and have recently been used in the simulation of 2D Josephson junction arrays [36].

21.4.2 Cluster Updates

For reasonably large values of E_J , local k -space updates which introduce phase changes on the order of 2π will be strongly suppressed, because their sinusoidal shape does not resemble an optimal phase-slip path. Algorithms based on local

updates alone will therefore be ineffective near the phase transition, where phase slips start to proliferate. A typical path will stay most of the time near one or the other of the minima in the cosine-potential, as shown in Fig. 21.5. A simple idea for a global update compatible with this overall structure would be step-updates which shift the phases ϕ_j by $\pm 2\pi$ in some random interval $[j_{\min}, j_{\max}]$. However, it would be better to let the algorithm choose itself the phase variables ϕ_j , which can be shifted to a different potential minimum.

The observation which leads to such a cluster algorithm is that a shift by multiples of $\pm 2\pi$ is not the only operation which leaves S_J invariant. The same is true for reflections on $\{n\pi\}_{n \in \mathbb{Z}}$, that is, the positions of the maxima and minima of the cosine potential. We exploit the latter symmetry to design a rejection-free cluster update consisting of the following three steps, which are illustrated in Fig. 21.5:

1. An axis $\phi = n^{\text{axis}}\pi$ with integral n^{axis} is randomly chosen as the axis closest to the phase variable of a randomly chosen site. Another random site j_{root} is picked as the root site of the cluster. We introduce relative coordinates

$$\phi_j^{\text{axis}} = \phi_j - n^{\text{axis}}\pi, \quad (21.50)$$

which are updated in a cluster move as $\phi_j^{\text{axis}} \rightarrow -\phi_j^{\text{axis}}$, in complete analogy to the projected spin components (21.44) in the Wolff algorithm. Such updates do not change the value of S_J .

2. A cluster of sites connected to j_{root} is constructed in a way analogous to the case of $O(n)$ -spins which was explained in Sec. 21.3. Two sites at positions i and j are connected with probability

$$p(i, j) = \max \left(0, 1 - e^{-\{S[\phi_i^{\text{axis}}, -\phi_j^{\text{axis}}] - S[\phi_i^{\text{axis}}, \phi_j^{\text{axis}}]\}} \right), \quad (21.51)$$

where

$$S[\phi_i^{\text{axis}}, -\phi_j^{\text{axis}}] - S[\phi_i^{\text{axis}}, \phi_j^{\text{axis}}] = 8g(i-j)\phi_i^{\text{axis}}\phi_j^{\text{axis}}. \quad (21.52)$$

This expression is identical to the spin case, up to a factor of two, because the quadratic contributions cancel.

3. The phases of the sites j belonging to the cluster are updated according to

$$\phi_j^{\text{axis}} \rightarrow -\phi_j^{\text{axis}}. \quad (21.53)$$

Using the ideas of Luijten and Blöte [35] discussed in Sec. 21.3.2, the cluster move can be performed in a time $O(N \log N)$ despite long-range interactions, which allows us to compute precise data for large systems, up to $N \approx 10^4$ if $\Delta\tau E_C = 0.25$. Figure 21.6 plots the integrated autocorrelation time τ for $\langle(\phi - \bar{\phi})^2\rangle$ as a function of system size N . Even though the CPU time for a cluster update is $O(N \log N)$ as compared to $O(N)$ for a local update, the gain in sampling efficiency is considerable.

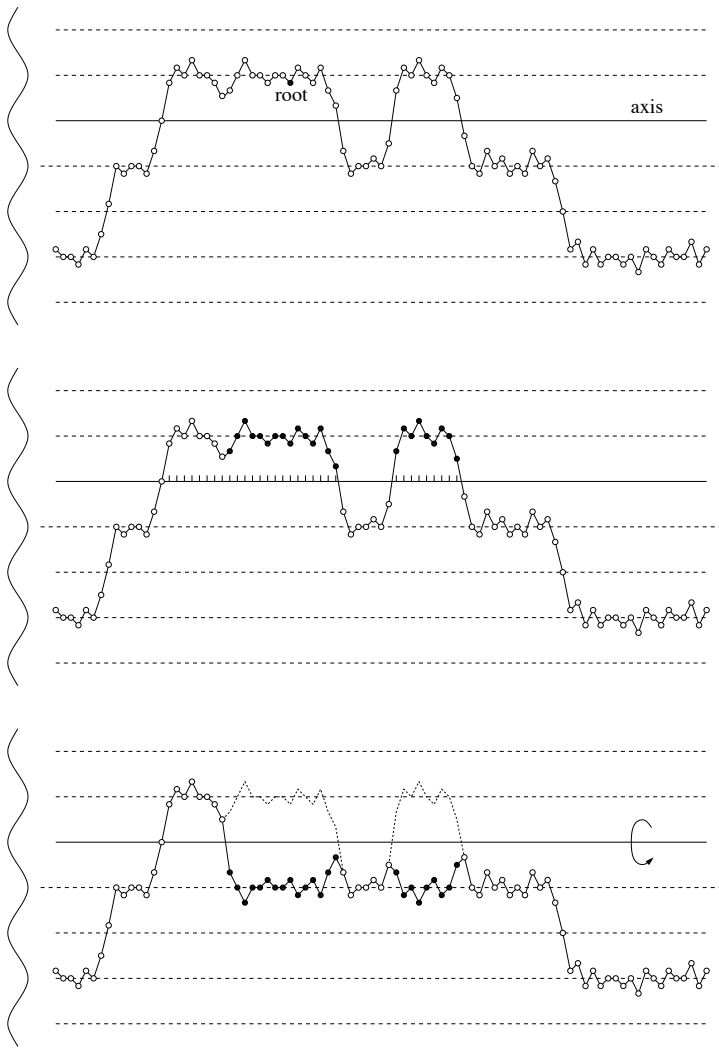
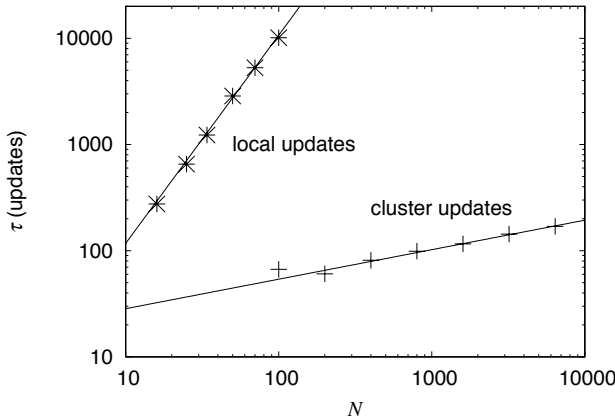
**FIGURE 21.5**

Illustration of the cluster algorithm for non-compact phase variables. The figures show from top to bottom: (i) Original phase configuration. Possible axis positions are indicated with dashed lines, located at the maxima and minima of the cosine potential. The randomly chosen axis and root site of the cluster are marked with the black solid line and black dot respectively. (ii) Cluster of connected sites. The sites which could potentially connect to the root site are indicated with tick marks. (iii) New phase configuration obtained by flipping the cluster around the axis. Illustration taken from Ref. [8].

**FIGURE 21.6**

Integrated autocorrelation times τ for $\langle (\phi - \bar{\phi})^2 \rangle$ versus system size N . The data were obtained at the critical point $\alpha = 1$ using $E_J/E_C = 1$. Illustration taken from Ref. [8].

21.5 Winding Number Sampling

In Sec. 21.1.4 it was shown that the effective charging energy of the single electron box can be computed from the winding number distribution of the phase configurations. If we discretize imaginary time into N time steps $\Delta\tau = \beta/N$, the action (21.18) becomes

$$S[\phi] = -\frac{1}{2E_C\Delta\tau} \sum_{j=1}^N \cos(\phi_{j+1} - \phi_j) - \alpha \sum_{j < j'} \frac{(\frac{\pi}{N})^2 \cos(\phi_j - \phi_{j'})}{\sin^2(\frac{\pi}{N}(j - j'))}, \quad (21.54)$$

where we have introduced the dimensionless tunneling conductance $\alpha = (1/2\pi^2)(R_K/R_t)$, with $R_K = h/e^2$ ($\alpha = 1/(\pi e^2 R_t)$ for $\hbar = 1$). Periodic boundary conditions $\phi_{N+1} = \phi_1$ are employed. Since only 2π -periodic functions appear in Eq. (21.54), $\phi_j \in [0, 2\pi]$ can be interpreted as the angle which defines the orientation of an XY-spin. Comparing Eqs. (21.10) and (21.54) we see that the action of the single electron box is equivalent to that of a single dissipative quantum rotor.

In Fourier space, Eq. (21.54) becomes local,

$$S[\phi] = \frac{1}{N} \sum_{k=0}^{N-1} g_k |\psi_k|^2, \quad (21.55)$$

where $\psi_k = \sum_{j=0}^{N-1} e^{i\frac{2\pi}{N}jk} e^{i\phi_j}$ denotes the Fourier transform of $e^{i\phi}$ and g_k the

Fourier transform of the kernel ($j \neq 0$)

$$g(j) = -\frac{1}{4E_C\Delta\tau}(\delta_{j,1} + \delta_{j,N-1}) - \frac{\alpha}{2} \frac{(\pi/N)^2}{\sin((\pi/N)j)^2}. \quad (21.56)$$

Using fast Fourier transforms it is therefore possible to compute the action of a configuration in a time $O(N \log N)$ despite the long-range interactions. This is important for the transition matrix Monte Carlo algorithm presented below.

21.5.1 Path-Integral Monte Carlo

The expectation value $\langle \omega^2 \rangle$, and hence the effective charging energy (21.19), can be computed using path-integral Monte Carlo with cluster updates, as explained in Sec. 21.3. This approach works well for small and intermediate values of the tunneling conductance α . Configurations with winding number $w = \pm n$ are generated according to their weight w_n in the partition sum,

$$w_n = \frac{\int_0^{2\pi} d\phi_0 \int_{\phi_0}^{\phi_0 \pm 2\pi n} \mathcal{D}\phi e^{-S[\phi]}}{\int_0^{2\pi} d\phi_0 \sum_{n=0}^{\infty} \int_{\phi_0}^{\phi_0 \pm 2\pi n} \mathcal{D}\phi e^{-S[\phi]}}. \quad (21.57)$$

However, for large α , the effective charging energy, and therefore also the fraction of paths with winding number different from zero, decreases as $\exp(-\pi^2\alpha)$ according to theoretical predictions. A huge number of configurations with winding number zero will be generated for each configuration with non-zero winding number. Due to this rapidly deteriorating efficiency, the cluster algorithm can only be used in the range of tunneling conductances for which $E_C^* > 10^{-8}E_C$.

21.5.2 Transition Matrix Monte Carlo

In order to compute the effective charging energy at even larger values of the tunneling conductance, we developed a new Monte Carlo approach [7], which attempts to insert or remove phase slips (kinks) and in doing so measures the relative weights of the different winding number sectors. As only paths of winding number 0 and 1 contribute in the limit of large α , we restrict the discussion to the calculation of the relative weight of these two winding number sectors. However, the algorithm can also be used to study additional winding number sectors.

The effective charging energy (21.19) can be expressed for large α as

$$\frac{E_C^*}{E_C} = \frac{2\pi^2}{\beta E_C} \frac{\sum_{n=0}^{\infty} n^2 w_n}{\sum_{n=0}^{\infty} w_n} \approx \frac{2\pi^2}{\beta E_C} \frac{w_1}{w_0}. \quad (21.58)$$

The weights w_0 and w_1 are proportional to the time which a Metropolis-Monte Carlo simulation would spend in winding sectors 0 and 1, respectively. A

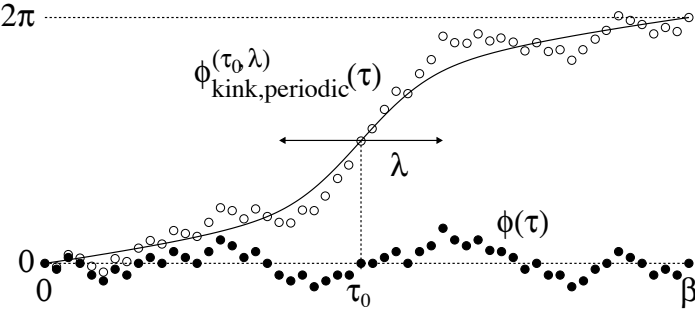
**FIGURE 21.7**

Illustration of a kink (phase-slip) insertion. The filled dots show the original phase configuration $\{\phi_n = \phi(\tau_n) | n = 1, \dots, N\}$ with winding number $\omega = 0$, and the line a phase-slip path $\phi_{\text{kink,periodic}}^{(\tau_0, \lambda)}$. Both the position τ_0 and the width λ of this phase slip path are randomly chosen. The open dots show the new configuration with winding number $\omega = 1$, which would be obtained by adding $\phi_{\text{kink,periodic}}^{(\tau_0, \lambda)}$ to $\phi(\tau)$. Illustration taken from Ref. [1, 2].

“flat histogram,” which means equal occupation probabilities for both winding sectors, could be obtained by adding an additional “inverse-weight” factor to the usual Boltzmann term. The acceptance probability for a proposed kink update from a configuration with winding number n and action S to winding number n' and action S' then becomes

$$P_{(n,S) \rightarrow (n',S')} = \min \left(1, \frac{w_n}{w_{n'}} e^{-(S' - S)} \right), \quad (21.59)$$

whereas a cluster update from n to n' , which takes the change in action into account, would be accepted with probability

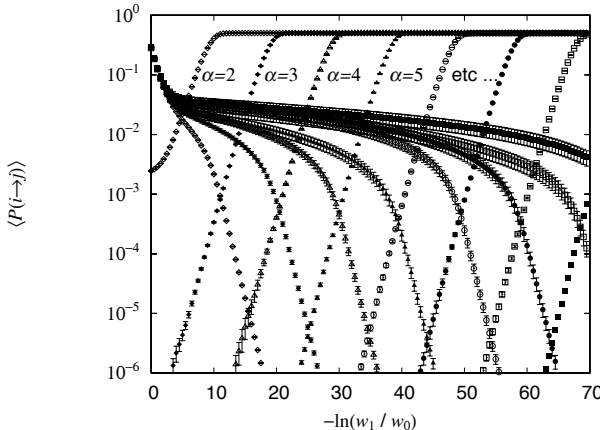
$$P_{n \rightarrow n'} = \min \left(1, \frac{w_n}{w_{n'}} \right). \quad (21.60)$$

The “flat histogram,” or detailed balance condition for the *a priori* unknown relative occupation probability w_1/w_0 , can then be expressed for $n, n' \in \{0, 1\}$ as

$$\langle P_{0 \rightarrow 1}(w_1/w_0) \rangle = \langle P_{1 \rightarrow 0}(w_1/w_0) \rangle, \quad (21.61)$$

where the averages are taken over a random sequence of kink and cluster updates.

Our strategy is to determine the transition probabilities $\langle P_{0 \rightarrow 1} \rangle$ and $\langle P_{1 \rightarrow 0} \rangle$ for different values of w_1/w_0 in order to find the solution of Eq. (21.61), rather than trying to adjust the relative occupation of the winding sectors by a Wang-Landau type iterative procedure [38]. This is an approach in the spirit of the transition Matrix Monte Carlo method [39].

**FIGURE 21.8**

Transition probabilities $\langle P_{0 \rightarrow 1} \rangle$ (with positive slope) and $\langle P_{1 \rightarrow 0} \rangle$ (with negative slope) plotted as a function of $-\ln(w_1/w_0)$. The intersection points of these curves determine w_1/w_0 . From left to right, the data correspond to $\alpha = 2, 3, \dots, 9$. Illustration taken from Ref. [1, 2].

Each winding number sector is treated separately and the cluster updates serve essentially to randomize the configurations within that sector, although their contribution to the probabilities $\langle P_{i \rightarrow j} \rangle$ becomes important for smaller α . In a kink update, illustrated in Fig. 21.7, we insert a phase slip $\phi_{\text{kink}}^{(\tau_0, \lambda)} = \pm 2 \arctan((\tau - \tau_0)/\lambda)$ of random width λ at some random position τ_0 , or rather

$$\phi_{\text{kink, periodic}}^{(\tau_0, \lambda)} = \pm \pi \frac{\arctan((\tau - \tau_0)/\lambda)}{\arctan(\beta/2\lambda)}, \quad (21.62)$$

periodically continued outside the interval $-\frac{\beta}{2} \leq \tau - \tau_0 \leq \frac{\beta}{2}$, which is a slightly modified version compatible with the finite size of the system. These are stationary paths of the long-range part of the action (21.18) in the limit $\beta \rightarrow \infty$.

Inserting $\phi_{\text{kink}}^{(\tau_0, \lambda)}$ changes the original configuration ϕ with winding number n to ϕ' with winding number $n \pm 1$. The corresponding Boltzmann weights $\exp(S[\phi] - S[\phi'])$ are computed using Eq. (21.55) and stored during the simulation. Updates which produce a configuration with winding number $|n| > 1$ as well as cluster updates which leave the winding number unchanged get a weight of 0. A cluster update which connects to the other winding number sector gets a weight of 1. From these data, one can calculate the average transition probabilities $\langle P(i \rightarrow j) \rangle$ as a function of w_1/w_0 using Eqs. (21.59) and (21.60). Finally, the relative weight of winding sector 1 is determined by solving Eq. (21.61).

To illustrate this procedure, Fig. 21.8 shows the probabilities $\langle P(0 \rightarrow 1) \rangle$

(with positive slope) and $\langle P(1 \rightarrow 0) \rangle$ (with negative slope) as a function of $-\ln(w_1/w_0)$ for several values of α . The intersection points of these curves determine w_1/w_0 . The effective charging energies obtained by this new method are consistent with the results from cluster Monte Carlo simulations for the values of α which can be treated by the latter method. However, the new approach allows us to simulate the system at much higher tunneling conductance. It increases the range of accessible effective charging energies by 30 orders of magnitude [7].

21.6 Applications and Open Questions

In this section we summarize results of QMC simulations of environmentally coupled quantum systems, such as dissipative spin chains or resistively shunted Josephson junctions and address some of the open issues.

21.6.1 Single Spins Coupled to a Dissipative Bath

The first simulations for an Ising spin coupled to a dissipative bath were done by Luijten and Messingfeld [3] using a cluster-algorithm optimized for long-range interactions. The validity of the mapping from a dissipative d -dimensional quantum model to a $(d+1)$ -dimensional classical model with long range interactions was recently doubted in the sub-Ohmic case [40] but subsequent detailed simulations using a continuous-time variant of the cluster algorithms confirmed the validity of this mapping [12, 41].

21.6.2 Dissipative Spin Chains

Extensions to chains of Ising spins were done in Ref. [4] using the cluster algorithm of Sec. 21.3. Since the two spin states could represent, for example, the two flux states in a SQUID, such a chain can be thought of as a model of a qubit-register. The simulations showed that no locally critical phase exists even for large dissipation strength, and that the second order phase transition from the disordered to the ordered state is controlled by a single fixed point. In particular, the dynamical critical exponent takes the value $z \approx 2$. This finding, as well as the values of the critical exponents η and ν , was in remarkably good agreement with the predictions from a dissipative ϕ^4 -field theory [5, 42].

A similar agreement with analytical results was found for the chain of dissipative XY-spins. This chain was studied in Ref. [5] as a model for a nanowire formed out of superconducting grains. Besides the bulk phase transition, the properties of finite open chains have been studied. If normal leads are attached, the (infinite) wire becomes insulating, while superconducting leads turn the whole device superconducting. For mixed leads (normal and super-

conducting), the wire is metallic and its zero-bias conductance *universal*, in the sense that it does not matter how strongly the superconducting lead fixes the phase of the neighboring grain.

Since simulations are efficient for dissipation coupled to the spin variables, and the two-dimensional case is at the upper critical dimension, there are no open questions for the types of spin chains studied here. The biggest open question are chains and higher-dimensional models with dissipation coupling to the bonds (i.e., phase differences) instead of the sites. Dissipation then introduces couplings between four sites, and no efficient simulation algorithms exist for this interesting problem.

21.6.3 The Single Electron Box

Refs. [7, 9] have used the algorithm described in Sec. 21.5 to calculate the effective charging energy E_C^* up to large values of the tunneling conductance α . The leading exponential suppression, $E_C^*/E_C \sim \exp(-\pi^2\alpha)$, can be traced over more than 34 orders of magnitude, as compared to 2 (8) orders of magnitude for path-integral Monte Carlo simulations with local (cluster) updates.

In the zero-temperature regime, a pre-exponential factor α^k was predicted with widely varying values [26, 43–46] and inconclusive numerics [7, 26, 47–49] for the exponent k ranging from 1 to 6.5. Only a detailed analysis of sub-leading corrections combined with extensive simulations has managed to resolve this issue [9].

21.6.4 Resistively Shunted Josephson Junctions

With the cluster algorithm described in Sec. 21.4 and Ref. [8], one is able to verify that the superconductor-to-metal transition in a single resistively shunted Josephson junction occurs for $R_s = R_Q$, independent of the Josephson coupling E_J . Furthermore, the temperature dependence of the resistance in the $T = 0$ superconducting phase is proportional to $T^{2(R_Q/R_s - 1)}$, as predicted in Ref. [50]. Remarkably, on the phase transition line, continuously varying correlation exponents were found, and later explained theoretically and verified numerically using the same algorithm [11].

In the two-junction model discussed in Ref. [51], such a line of fixed points was predicted to control the superconductor-to-metal transition. Our numerical calculations in Ref. [10], which utilized adapted versions of the cluster moves discussed in Sec. 21.4, showed that the critical properties in this interacting system are, within error-bars, the same as in the single junction and a mean field theory, which assumes non-interacting junctions, was even capable of accurately predicting the phase boundary for intermediate Josephson coupling. These examples illustrate how the ability to simulate single junctions and extended systems with high precision has led to new insights and will be important in future investigations.

Acknowledgments – We thank the Aspen Center for Physics, where part of

this work was done. This work was supported by the Swiss National Science Foundation.

Bibliography

- [1] P. Werner, PhD thesis No. 16134, ETH Zürich (2005).
- [2] P. Werner and M. Troyer, Prog. Theor. Phys. Suppl. **160**, 395 (2005).
- [3] E. Luijten and H. Messingfeld, Phys. Rev. Lett. **86**, 5305 (2001).
- [4] P. Werner, K. Völker, M. Troyer, and S. Chakravarty, Phys. Rev. Lett. **94**, 047201 (2005).
- [5] S. Sachdev, P. Werner and M. Troyer, Phys. Rev. Lett. **92**, 237003 (2004).
- [6] P. Werner, M. Troyer and S. Sachdev, J. Phys. Soc. Jpn. Suppl. **74**, 67 (2005).
- [7] P. Werner and M. Troyer, J. Stat. Mech. P01003 (2005).
- [8] P. Werner and M. Troyer, Phys. Rev. Lett. **95**, 060201 (2005).
- [9] S.L. Lukyanov and P. Werner, J. Stat. Mech. P11012 (2006).
- [10] P. Werner, G. Refael and M. Troyer, J. Stat. Mech. P12003 (2005).
- [11] S.L. Lukyanov and P. Werner, J. Stat. Mech. P06002 (2007).
- [12] A. Winter, H. Rieger, M. Vojta, and R. Bulla, Phys. Rev. Lett. **102**, 030601 (2009).
- [13] A. O. Caldeira and A. J. Leggett, Phys. Rev. Lett. **46**, 211 (1981).
- [14] A. O. Caldeira and A. J. Leggett, Ann. Phys. **149**, 374 (1983)
- [15] U. Weiss, *Quantum Dissipative Systems*, World Scientific (Singapore, 1993).
- [16] D. B. Josephson, Phys. Lett. **1**, 251 (1962).
- [17] A. Schmid, Phys. Rev. Lett. **51**, 1506 (1983).
- [18] S. A. Bulgadaev, Sov. Phys. JETP Lett. **39**, 315 (1984).
- [19] F. Guinea *et al.*, Phys. Rev. Lett. **54**, 263 (1985).
- [20] M. P. A. Fisher and W. Zwerger, Phys. Rev. B **32**, 6190 (1985).

- [21] G. Schön and A. D. Zaikin, Phys. Rep. **198**, 237 (1990).
- [22] J. Fröhlich and B. Zegarlinksyi, J. Stat. Phys. **63**, 455 (1991).
- [23] W. Hofstetter, Diploma thesis, Ludwig-Maximilians-Universität München, (1997).
- [24] E. Ben-Jacob, E. Mottola and G. Schön, Phys. Rev. Lett. **51**, 2064 (1983).
- [25] U. Eckern, G. Schön and V. Ambegaokar, Phys. Rev. B **30**, 6419 (1984).
- [26] W. Hofstetter and W. Zwerger, Phys. Rev. Lett. **78**, 3737 (1997).
- [27] G. J. Kemeny and J. Snell, *Finite Markov Chains*, The University Series in Undergraduate Mathematics, (Van Nostrand, New York, 1960).
- [28] N. Metropolis *et al.*, J. Chem. Phys. **21**, 1087 (1953).
- [29] R. H. Swendsen and J.-S. Wang, Phys. Rev. Lett. **58**, 86 (1987).
- [30] D. Kandel and E. Domany, Phys. Rev. B **43**, 8539 (1991).
- [31] C. M. Fortuin and P. W. Kasteleyn, Physica **57**, 536 (1972).
- [32] R. G. Edwards and A. D. Sokal, Phys. Rev. D **38**, 2009 (1988).
- [33] H. G. Evertz, H. M. Erkinger and W. von der Linden, in *Computer Simulation Studies in Condensed Matter Physics XIV*, eds. D. P. Landau, S. P. Lewis and H. B. Schüttler (Springer, 2001).
- [34] U. Wolff, Phys. Rev. Lett. **62**, 361 (1989).
- [35] E. Luijten and H. W. J. Blöte, Int. J. Mod. Phys. C **6**, 359 (1995).
- [36] L. Capriotti *et al.*, Phys. Rev. Lett. **91** (2003), 247004; Phys. Rev. Lett. **94**, 157001 (2005).
- [37] H. G. Evertz *et al.*, Phys. Rev. Lett. **70**, 875 (1993); H. G. Evertz *et al.*, Phys. Lett. **254B**, 185 (1991); M. Hasenbusch *et al.*, Physica **A211**, 255 (1994).
- [38] F. Wang and D. P. Landau, Phys. Rev. Lett. **86**, 2050 (2001).
- [39] J.-S. Wang and R. H. Swendsen, J. Stat. Phys. **106**, 245 (2002).
- [40] M. Vojta, N. Tong, and R. Bulla, Phys. Rev. Lett. **94**, 070604 (2005).
- [41] M. Vojta, N. Tong, and R. Bulla, Phys. Rev. Lett. **94**, 249904 (2009).
- [42] S. Pankov *et al.*, Phys. Rev B **69**, 054426 (2004).
- [43] S. V. Panyukov and A. D. Zaikin, Phys. Rev. Lett. **67**, 3168 (1991).

- [44] X. Wang and H. Grabert, Phys. Rev. B **53**, 12621 (1996).
- [45] I.S. Beloborodov, A.V. Andreev and A.I. Larkin, Phys. Rev. B **68**, 024204 (2003).
- [46] S. Lukyanov and A. B. Zamolodchikov, J. Stat. Mech. **P05003** (2004)
- [47] X. Wang, R. Egger and H. Grabert, Europhys. Lett. **38**, 545 (1997).
- [48] J. König and H. Schoeller, Phys. Rev. Lett. **81**, 3511 (1998).
- [49] C. P. Herrero, G. Schön and A.D. Zaikin, Phys. Rev. B **59**, 5728 (1999).
- [50] S. E. Korshunov, Zh. Eksp. Teor. Fiz. **93**, 1526 (1987); Sov. Phys. JETP **66**, 872 (1987).
- [51] G. Refael *et al.*, Phys. Rev. B **68**, 214515 (2003).

Current Trends in Density Matrix Renormalization Group Methods

Ulrich Schollwöck

*Arnold Sommerfeld Center for Theoretical Physics, University of Munich,
Germany*

22.1 The Density Matrix Renormalization Group

22.1.1 Introduction

Since its invention in 1992 by White [1, 2], the density matrix renormalization group (DMRG) has firmly established itself as the currently most powerful method to calculate static and more recently also dynamic [3–5] properties of low-lying eigenstates of strongly correlated Hamiltonians defined on one-dimensional quantum lattices. At the same time, its extension to the analysis of two-dimensional classical [6] and one-dimensional quantum [7, 8] transfer matrices has given access to highly precise thermodynamics in classical two-dimensional and quantum one-dimensional systems. It has even been extended to the numerically much more demanding study of non-Hermitian (pseudo-)Hamiltonians emerging in the analysis of classical steady states in one-dimensional systems [9–11]. However, it also turned out quite quickly that extending DMRG to the study of two-dimensional systems did not lead to similarly huge successes.

The analytical understanding of the successes of the DMRG family of methods quickly led to the study of *matrix product states* (MPSs). In fact, MPSs have such a simple but powerful structure that it is no surprise that they have been introduced and used under a huge variety of names over the last fifty or more years – for an extensive account of current developments, see also Chap. 23. In the present context, the most relevant prehistory is perhaps given by the exact expression of the seminal one-dimensional quantum Affleck-Kennedy-Lieb-Tasaki (AKLT) state in this form [12–14], which gave rise to extensive studies of their translationally-invariant subclass known as finitely-correlated states [15]. This form was then subsequently used in a variety of contexts for analytical variational calculations, e.g., for spin-1 Heisenberg antiferromagnets [16–19] and ferrimagnets [20, 21].

The connection to DMRG was made in two steps. First, Ostlund and Rommer [22] realized that the block growth step of the *infinite-system* DMRG could be expressed as a matrix in the same form it takes in an MPS. As in homogeneous systems this block growth step leads in the infinite-size limit to a fixed point; they took the fixed-point matrix as a building block for a translationally-invariant MPS. In a further step, it was recognized that the more important finite-system DMRG leads to quantum states in MPS form, over which it variationally optimizes [23]. It was also recognized that in traditional DMRG the state class over which is optimized changes as the algorithm progresses, such that if one demands perfect variational character, a small change to the algorithm is needed [24, 25].

It remains a curious historical fact that only a few of the DMRG practitioners up to 2004 took this development very seriously. While it was considered useful for some conceptual purposes, little thought was given to rethinking and reexpressing real-life DMRG implementations purely in the MPS language; arguably, this was because the overwhelming majority of conventional DMRG applications, i.e., ground states for quantum chains with open boundary conditions, hardly profits. What was overlooked is that it easily opens up the way to extensions to DMRG hard to see and express in conventional DMRG language. A non-exhaustive list of such extensions would include real-time evolutions [26–30] at zero and finite temperature [30], periodic boundary conditions [31], numerical renormalization group (NRG) applications [32], and higher dimensions [33], where in the latter case the MPS class has to be generalized [34].

The relationship between the DMRG method and the MPS class of quantum states can be explored completely in the framework of elementary quantum mechanics. Yet another light has been shed in the last five or so years on DMRG by the use of entanglement, which has emerged as a very powerful tool to understand the successes and failures of the method, starting with the analysis of the ground state entanglement in one-dimensional systems [35, 36]. While entanglement theory predicts that DMRG should work very well for gapped phases, it also indicates that numerical resources would have to diverge to reach the thermodynamic limit at criticality. However, resource growth with system size happens only at a very weak power law, such that reachable system sizes are so large, up to thousands of sites, that quantitative observation of power laws for correlators and finite-size extrapolations are very easy. Therefore, DMRG is an ideal tool to study quantum phase transitions in one-dimensional systems.

The goal of this work is to cover some aspects of these ongoing new developments, where I take “new” to be developments either just started at or occurring after the date of my DMRG review [37], i.e., late in 2004. In order to establish common ground between various readerships, I will briefly discuss the conventional DMRG formulation. I will then move on to its connection to entanglement theory, and above all its connection to MPSs. As one obvious way of going beyond conventional DMRG in the MPS language, I will consider

the use of matrix product operators (MPOs) [30, 38, 39], the usage of which should in my view be much more widespread.

Of the many new developments, only a few can be covered here. As two-dimensional algorithms are discussed at length in Chap. 23, I will focus on time-evolution in 1D, and one proposal made pointing a way to overcome current limits of time-dependent DMRG without much effort. Also, I will discuss the connection between DMRG and Wilson's NRG [40–42], because it unravels a conceptually interesting connection between the two methods and shows how NRG can be expressed in a very concise fashion as well as be improved upon [32]. This closes an interesting historical loop, as the failure of NRG for one-dimensional quantum lattices was at the starting point of White's invention of DMRG. Both axes of development are definitely open to speculation about their future, and lots of work remains to be done!

22.1.2 Infinite-System and Finite-System Algorithms

As a toy model, let us consider an anisotropic Heisenberg antiferromagnetic ($J = 1$) spin chain of length L in one spatial dimension with external magnetic field h ,

$$\hat{H} = \sum_{i=1}^{L-1} \frac{J}{2} (S_i^+ S_{i+1}^- + S_i^- S_{i+1}^+) + J^z S_i^z S_{i+1}^z + \sum_{i=1}^L h S_i^z, \quad (22.1)$$

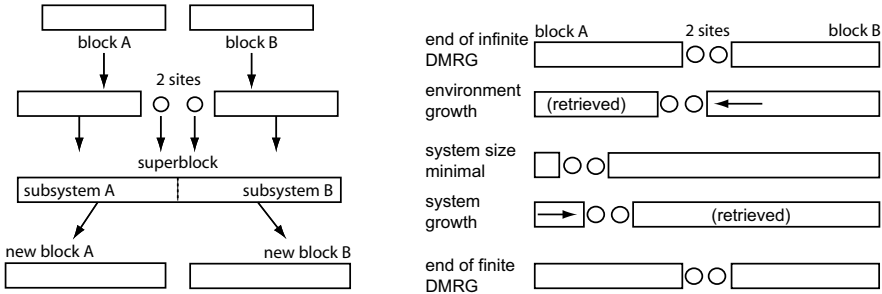
where $S_i^\pm \equiv S_i^x \pm i S_i^y$ and S_i^z are the usual spin operators on site i . However, it should be clear from the outset that, as DMRG is a variational method in a certain state class, it does not suffer from anything like the fermionic sign problem, and can be applied to bosonic and fermionic systems alike.

The starting point of DMRG is to ask for the ground state and ground state energy of \hat{H} . The answer is provided for by a two-step procedure: (i) the infinite-system DMRG and (ii) the finite-system DMRG.

In the infinite-system DMRG (Fig. 22.1), a system is built iteratively from the left and right end, from left and right blocks of spins described in effective Hilbert spaces. Starting from empty blocks, the key step of the iterative procedure is building blocks of length $\ell + 1$ from those of length ℓ by adding the neighboring sites. This is done as follows. Assume we have an effective description of a block A in a D -dimensional Hilbert space with orthonormal basis $|a_\ell\rangle_A$, where D is some small number, and also the matrix elements of all operators living on the block we might need. For very small blocks at the beginning, D may not even be exhausted; for larger blocks some truncation must have occurred, which we assume as granted for the moment.

To find the D -dimensional basis for the next larger block, we consider the system or superblock $A \bullet\bullet B$, described by

$$|\psi\rangle = \sum_{a_A \sigma_A \sigma_B a_B} \psi_{a_A \sigma_A \sigma_B m_B} |a\rangle_A |\sigma\rangle_A |\sigma\rangle_B |a\rangle_B \equiv \sum_{i_A j_B} \psi_{i_A j_B} |i\rangle_A |j\rangle_B. \quad (22.2)$$

**FIGURE 22.1**

The left and right half of the figure present the iteration taken in the infinite-system and finite-system DMRG procedures, respectively. In both cases, new blocks are formed from integrating a site into a block, with a state space truncation according to the density matrix prescription of DMRG. Whereas in the infinite-system version this growth happens on both sides of the chain, leading to chain growth, in the finite system it happens only for one side at the expense of the other, leading to constant chain length.

By numerical diagonalization (some sparse matrix eigensolver such as Lanczos or Jacobi-Davidson) we find the $|\psi\rangle$ that minimizes the energy with respect to the effective Hamiltonian of the superblock, which can be built from the explicit operators on the explicit spins and the effective operators on the blocks.

If we take the $|i\rangle_A$ as the basis states of the next larger block, the basis grows to dD , where d is the local Hilbert space dimension. To avoid exponential growth, we truncate this basis back to D states – but which ones? The DMRG procedure is to consider the reduced density operator for $A\bullet$, namely

$$\hat{\rho}^{A\bullet} = \text{Tr}_{\bullet B} |\psi\rangle\langle\psi|, \quad \rho_{ii'}^{A\bullet} = \sum_j \psi_{ij} \psi_{i'j}^*. \quad (22.3)$$

The eigensystem of $\hat{\rho}^{A\bullet}$ is determined by exact diagonalization; the choice is to take those D orthonormal eigenstates that have the largest eigenvalues. After an approximate transformation of all desired operators on $A\bullet$ into the new basis, system size can be increased again, until the final desired size is reached. B is grown at the same time; for reflection-symmetric systems this is accomplished by simple mirroring.

The motivation of the truncation procedure is twofold. The first one, which is on a weaker basis, is that we are interested in the states of $A\bullet$ contributing most to the ground state for $A\bullet$ embedded in the final system. This final system ground state, which we don't know yet, we approximate to the best of our knowledge by that of $A\bullet\bullet B$, the largest superblock we can efficiently form. In that sense, we are bootstrapping, and the finite-system DMRG will take care of the large approximations this possibly incurs. The second one, namely

which states then to retain, is on much firmer foundation: both from statistical physics arguments and from minimizing the 2-norm distance $\| |\psi\rangle - |\psi\rangle_{\text{trunc}} \|_2$ to the state in the truncated basis the above prescription follows. The overall success of DMRG rests on the observation that even for moderate D , often only a few 100, the total weight of the truncated eigenvalues is extremely close to 0, say 10^{-10} or less.

Once the desired final system size is reached, it is important in all but the most trivial applications to follow up by the *finite-system* DMRG procedure. This will not merely lead to some slight quantitative improvements of our results, but may even change them completely: consider [43] for an example where the central physical statement changes!

What the finite-system algorithm does is the following ([Fig. 22.1](#)): it continues the growth process of, say, block B following the same prescription as before: finding the ground state of the superblock system, determining the reduced density operator, finding the eigensystem, and retaining the D highest weight eigenstates for the next larger block. But it does so at the expense of block A, which shrinks, i.e., old shorter blocks A are reused. This is continued until A is so small as to have a complete Hilbert space. Then the growth direction is reversed: A grows at the expense of B, until B is small enough to have a complete Hilbert space, which leads to yet another reversal of growth direction.

This *sweeping* through the system is continued until energy, or, more precisely, the wave function, converges. The intuitive motivation for this highly successful procedure is that after each sweep, blocks A or B are determined in the presence of an improved embedding.

In practice, this algorithm involves a lot of bookkeeping, as all needed operators have to be maintained in the current effective bases which will change from step to step. This means that the truncated basis transformations determined at each step have to be carried out after each step. Another important feature is that for finding the ground state $|\psi\rangle$ at each step in the current $A \bullet B$ configuration one employs some iterative large sparse matrix eigensolver.¹ To speed up this time-consuming part of the algorithm, it is highly desirable to have a good prediction for a starting vector, i.e., as close as possible to the final solution. This can be achieved by approximately transforming the result of the last step into the shifted $A \bullet B$ configuration [44] by applying two basis transformations, e.g., $A \bullet \rightarrow A$ and $B \rightarrow \bullet B$ for a right shift.

An important observation is that both the infinite-system and finite-system algorithm can also be carried out by inserting only a single explicit spin \bullet ; hence one would study superblocks of the form $A \bullet B$, with slightly adapted growth procedures. In the infinite-system algorithm an obvious disadvantage would be that superblock lengths oscillate between odd and even; in the finite-system algorithm the question is much more interesting, as discussed below.

¹In practice, D will be too big to allow for exact diagonalization in the $d^2 D^2$ dimensional state space.

This short description obviously misses out on many aspects of DMRG which turn it into a highly successful algorithm, such as the use of quantum symmetries, reflection properties, optimized ways of multiplying effective Hamiltonians to a DMRG state; for these, I refer to [37].

22.2 DMRG and Entanglement

The DMRG algorithm quite naturally leads to the consideration of bipartite quantum systems, where the parts are $A\bullet$ and $\bullet B$. For an arbitrary bipartition, $|\psi\rangle = \sum_{ij} \psi_{ij} |i\rangle_A |j\rangle_B$, where the states $|i\rangle_A$ and $|j\rangle_B$ form orthonormal bases, respectively. Thinking of the ψ_{ij} as entries of a rectangular matrix Ψ of dimension $N_A \times N_B$, one can apply a singular value decomposition (SVD) to $\Psi = U\Sigma V^\dagger$: assuming $N_A \geq N_B$ for definiteness, U is an $(N_A \times N_B)$ -dimensional matrix of orthonormal columns, Σ is a diagonal $(N_B \times N_B)$ -matrix with non-negative entries (singular values) $\sqrt{w_\alpha}$ on the diagonal, and V is a unitary $(N_B \times N_B)$ -matrix. Upon insertion of the SVD in the representation of $|\psi\rangle$, the matrices U and V^\dagger act as basis transformations in A and B, respectively, and

$$|\psi\rangle = \sum_{\alpha=1}^{N_B} \sqrt{w_\alpha} |\alpha\rangle_A |\alpha\rangle_B \quad (22.4)$$

is the *Schmidt decomposition* of $|\psi\rangle$. The sum over the *Schmidt coefficients* $\sqrt{w_\alpha}$ is in general limited by $\min(N_A, N_B)$; if more than one Schmidt coefficient is non-vanishing, entanglement between A and B is present in $|\psi\rangle$. The states $|\alpha\rangle_A$ and $|\alpha\rangle_B$ are orthonormal within A and B, respectively, and can be extended to orthonormal bases of A and B. From the Schmidt decomposition, we can immediately read off the reduced density operators for A and B that share the spectrum $\{w_\alpha\}$.

Assuming a decomposition of an exact quantum state, a DMRG approximation to it that can sustain at most D block states is provided by retaining the D largest eigenvalue (singular value) contributions, and the quality of DMRG depends on how quickly the w_α decrease. In cases where sufficient information about the eigenspectrum is not available, entanglement entropies can serve as proxy quantities, namely the von Neumann entanglement $S_{A|B} = -\hat{\rho}_A \log_2 \hat{\rho}_A = -\sum w_\alpha \log_2 w_\alpha$. In a mathematically non-rigorous way one can now make contact to the area laws of quantum entanglement: between D -dimensional state spaces, the maximal entanglement is $\log_2 D$; thus one needs at least a state of dimension 2^S to encode that entanglement properly. The area law for ground states of gapped systems [45–48] implies $S \sim \text{const.}$ in one dimension and $S \sim L$ in two dimensions. This means that in one dimension system size will not lead to a strong increase in D ; in two dimensions, $D \sim 2^L$, such that DMRG will fail even for relatively small system sizes.

22.3 Density Matrix Renormalization Group and Matrix Product States

22.3.1 Matrix Product States

For making the connection between DMRG and MPSs we reconsider the truncated basis transformation when going from $\mathbf{A} \bullet \rightarrow \mathbf{A}$. Calling the effective basis sets $|a_{\ell-1}\rangle$ and $|a_\ell\rangle$ for the shorter and longer block, and the local spin states $|\sigma_\ell\rangle$, we must have $|a_\ell\rangle = \sum_{a_{\ell-1}\sigma_\ell} \langle a_{\ell-1}\sigma_\ell|a_\ell\rangle |a_{\ell-1}\rangle|\sigma_\ell\rangle$. Introducing d matrices A^{σ_ℓ} of dimension $(D \times D)$ each, we can rewrite as

$$|a_\ell\rangle = \sum_{a_{\ell-1}\sigma_\ell} A_{a_{\ell-1}a_\ell}^{\sigma_\ell} |a_{\ell-1}\rangle|\sigma_\ell\rangle \quad (22.5)$$

where $A_{a_{\ell-1}a_\ell}^{\sigma_\ell} \equiv \langle a_{\ell-1}\sigma_\ell|a_\ell\rangle$. From basis orthonormality $\langle a_\ell|a'_\ell\rangle = \delta_{aa'}$ we can immediately deduce that

$$\sum_{\sigma_\ell} A^{\sigma_\ell\dagger} A^{\sigma_\ell} = I. \quad (22.6)$$

Such matrices we call *left-normalized*. Similarly, we can introduce matrices \tilde{A}^σ for the growth $\bullet \mathbf{B} \rightarrow \mathbf{B}$ from the right. Here, the right-normalization identity

$$\sum_{\sigma_\ell} \tilde{A}^{\sigma_\ell} \tilde{A}^{\sigma_\ell\dagger} = I \quad (22.7)$$

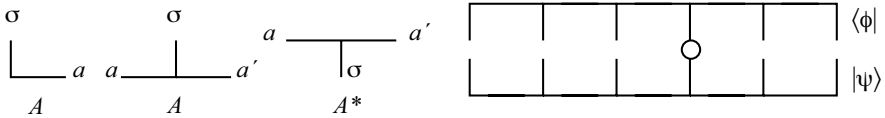
holds. Obviously, for small blocks, state space and matrix dimensions will be less than $(D \times D)$; in particular, the first and last matrices will be row and column vectors. It should also be emphasized that we do not make reference to the specific truncation procedure of DMRG.

The advantage of the matrix notation is that it allows for a simple recursion from a block of length ℓ to the smallest, i.e., vanishing block:

$$\begin{aligned} |a_\ell\rangle &= \sum_{a_{\ell-1}} \sum_{\sigma_\ell} A_{a_{\ell-1}a_\ell}^{\sigma_\ell} |a_{\ell-1}\rangle|\sigma_\ell\rangle \\ &= \sum_{a_{\ell-2}} \sum_{\sigma_{\ell-1}, \sigma_\ell} A_{a_{\ell-2}a_{\ell-1}}^{\sigma_{\ell-1}} A_{a_{\ell-1}a_\ell}^{\sigma_\ell} |a_{\ell-2}\rangle|\sigma_{\ell-1}\rangle|\sigma_\ell\rangle = \dots \\ &= \sum_{a_1, a_2, \dots, a_{\ell-1}} \sum_{\sigma_1, \sigma_2, \dots, \sigma_\ell} A_{1,a_1}^{\sigma_1} A_{a_1,a_2}^{\sigma_2} \dots A_{a_{\ell-1},a_\ell}^{\sigma_\ell} |\sigma_1\rangle|\sigma_2\rangle \dots |\sigma_\ell\rangle \\ &= \sum_{\sigma_i} (A^{\sigma_1} A^{\sigma_2} \dots A^{\sigma_\ell})_{1,a_\ell} |\sigma_1\rangle|\sigma_2\rangle \dots |\sigma_\ell\rangle, \end{aligned} \quad (22.8)$$

and similarly from the right. At the first and last site, we introduce a dummy index 1. The DMRG state then takes the form

$$|\psi\rangle = \sum_{\sigma} A^{\sigma_1} A^{\sigma_2} \dots A^{\sigma_{\ell-1}} \Psi^{\sigma_\ell, \sigma_{\ell+1}} \tilde{A}^{\sigma_{\ell+2}} \dots \tilde{A}^{\sigma_{L-1}} \tilde{A}^{\sigma_L} |\sigma\rangle, \quad (22.9)$$

**FIGURE 22.2**

Elements of matrix product states, from left to right as follows. (i) A corner matrix $A_{1,a}^\sigma$. (ii) A normal matrix $A_{a,a'}^\sigma$: the physical index points up, and the matrix indices are horizontal. (iii) A conjugated matrix $A_{a,a'}^{\sigma*}$: the physical index points downwards. (iv) Overlaps and matrix elements of operators: for overlaps, the physical indices of a bra and a ket are contracted (vertical lines), with operators inserted, if they occur. Note that the actual order of contraction follows a zipping procedure along the state; see text.

where $\Psi_{a_{\ell-1},a_{\ell+1}}^{\sigma_\ell,\sigma_{\ell+1}}$ is nothing but $\psi_{m^A\sigma^A\sigma^Bm^B}$ of Eq. (22.2). If we choose to use only one \bullet in DMRG, the superscript of Ψ changes accordingly.

If we grow block A all the way to the right, we then obtain a left-normalized MPS,

$$|\psi\rangle = \sum_{\sigma} A^{\sigma_1} A^{\sigma_2} \dots A^{\sigma_{L-1}} A^{\sigma_L} |\sigma\rangle, \quad (22.10)$$

similarly a right-normalized one from \tilde{A}^{σ_i} .

A particularly attractive feature of MPSs is that all typical quantum mechanical state manipulations can be carried out at a cost of at most $\mathcal{O}(LD^3)$, i.e., very moderate polynomial expense. As the most important example, let us briefly consider the calculation of an overlap $\langle \phi | \psi \rangle$ or a matrix element $\langle \phi | \hat{O}^i | \psi \rangle$. In this context, it is useful to introduce a graphical notation (Fig. 22.2), where horizontal lines to the left and right carry the row and column indices m, n of the matrix $A_{aa'}^\sigma$, whereas the vertical line carries the physical index σ . With the vertical line sticking out below we encode $A_{aa'}^{\sigma*}$.

The overlap calculation reads with matrices A for $|\psi\rangle$ and B for $|\phi\rangle$

$$\begin{aligned} \langle \phi | \psi \rangle &= \sum_{\sigma} B^{\sigma_1*} \dots B^{\sigma_{L*}} A^{\sigma_1} \dots A^{\sigma_L} = \sum_{\sigma} B^{\sigma_L\dagger} \dots B^{\sigma_1\dagger} A^{\sigma_1} \dots A^{\sigma_L} \\ &= \sum_{\sigma_L} B^{\sigma_L\dagger} \left(\sum_{\sigma_{L-1}} B^{\sigma_{L-1}\dagger} \dots \left(\sum_{\sigma_1} B^{\sigma_1\dagger} A^{\sigma_1} \right) \dots A^{\sigma_{L-1}} \right) A^{\sigma_L}. \end{aligned} \quad (22.11)$$

The decisive step is the reordering of the implicit matrix summations and the explicit physical index summations: without the ordering, there would be $\mathcal{O}(d^L)$ operations; now there are $\mathcal{O}(2Ld)$ matrix multiplications, each of complexity $\mathcal{O}(D^3)$. In the pictorial representation, one sees that one simply has to contract the open bonds in the right order, like for a zipper, in order to arrive at the optimal operation count. Evaluating a matrix element becomes similarly easy: one simply inserts the operator O^{σ_i, σ'_i} into the picture, leading to a double sum at site i .

22.3.2 Density Matrix Renormalization in Matrix Product State Language

A representation of the DMRG procedure in the MPS instead of the old block picture would now look as follows: we want to minimize the energy of an MPS, which we suppose to be in a representation $A^{\sigma_1} A^{\sigma_2} \dots A^{\sigma_{\ell-1}} \Psi^{\sigma_\ell \sigma_{\ell+1}} \tilde{A}^{\sigma_{\ell+2}} \tilde{A}^{\sigma_{\ell+3}} \dots \tilde{A}^{\sigma_L}$. Left- and right-normalization ensure translation to orthonormal block bases. We minimize energy with respect to Ψ , assuming we have an expression for the Hamiltonian, yielding some set of matrices $\Psi_{a_{\ell-1}, a_{\ell+1}}^{\sigma_\ell \sigma_{\ell+1}}$. In DMRG, a density matrix analysis is carried out now on Ψ taken as the $d^2 D^2$ coefficients of the wave function. In the MPS language, we reshape the d^2 matrices of size $(D \times D)$ into a single matrix of size $(dD \times dD)$, namely $\Psi_{a_{\ell-1} \sigma_\ell, \sigma_{\ell+1} a_{\ell+1}}$. Then we carry out a singular value decomposition on Ψ , yielding up to dD singular values, the square roots of the density matrix eigenvalues of DMRG. As in DMRG, we only keep the largest D , and truncate matrices $U \Sigma V^\dagger$ accordingly. But as U and V^\dagger maintain their orthogonality properties, they can be interpreted as basis transformations. In particular, we can use them to shift by one site, say to the right, in the finite-system DMRG procedure: this means just putting U as A on site ℓ , after reshaping indices, and lumping together ΣV^\dagger and $\tilde{A}^{\sigma_{\ell+2}}$ to a new $\Psi^{\sigma_{\ell+1} \sigma_{\ell+2}}$, continuing our procedure, sweeping forth and back. Effectively, the right block has been shortened.

Incidentally, the new Ψ can serve as an often very good approximation to the next minimization step: in the MPS language, the finite-system DMRG prediction invented by White [44] appears without further thought. One also sees that if one does single-site DMRG and considers Ψ^σ , the limit on Schmidt coefficients shows that no truncation occurs at all. This is mathematically even better, although it helps metastability to happen.²

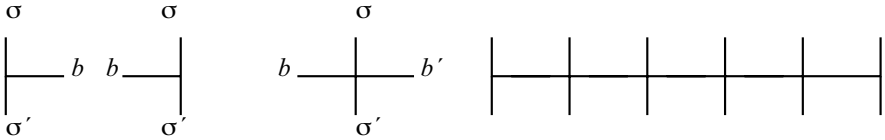
Overall, a much clearer view is obtained in the MPS language, although DMRG with a single site and variational minimization over an MPS are exactly the same!

A question I have not discussed is how the effective Hamiltonians are constructed: in effect, in each block, one keeps track of all necessary operators, subjecting them to basis transformations as the blocks grow; they are initialized at the moment when their site is added into the block. But there is a much neater way of doing this, which is more transparent, using MPOs [38].

22.3.3 Matrix Product Operators

If we consider a single coefficient $\langle \sigma | \psi \rangle$ of an MPS, $\langle \sigma | \psi \rangle = A^{\sigma_1} A^{\sigma_2} \dots A^{\sigma_{L-1}} A^{\sigma_L}$, it is a natural generalization to try to write coefficients $\langle \sigma | \hat{O} | \sigma' \rangle$

²The downside of a variationally optimal approach is that it might be metastable, i.e., get trapped in minimum other than the global one; the deviations from optimality introduced by truncation strongly help one to get out of such traps.

**FIGURE 22.3**

Elements of matrix product operators, from left to right as follows. (i) A corner matrix operator $B_{1,a}^{\sigma\sigma'}$. (ii) A corner operator at the right end. (iii) A normal matrix operator $B_{a,a'}^{\sigma\sigma'}$: the physical indices point up and down, and the matrix indices are horizontal. (iv) A matrix operator as it would represent a Hamiltonian exactly.

of operators as

$$\langle \sigma | \hat{O} | \sigma' \rangle = B^{\sigma_1 \sigma'_1} B^{\sigma_2 \sigma'_2} \dots B^{\sigma_{L-1} \sigma'_{L-1}} B^{\sigma_L \sigma'_L} \quad (22.12)$$

where the $B^{\sigma\sigma'}$ are matrices just like the A^σ , with the only difference that as representations of operators they need both outgoing and ingoing physical states:

$$\hat{O} = \sum_{\sigma, \sigma'} B^{\sigma_1 \sigma'_1} B^{\sigma_2 \sigma'_2} \dots B^{\sigma_{L-1} \sigma'_{L-1}} B^{\sigma_L \sigma'_L} |\sigma\rangle \langle \sigma'|. \quad (22.13)$$

The pictorial representation introduced for MPSs can be extended in a straightforward fashion: instead of one vertical line for the physical state in the representation of A , we now have two vertical lines, one up, one down, for the ingoing and outgoing physical state in B (Fig. 22.3):

The application of an MPO to an MPS can be worked out as follows:

$$\begin{aligned} \hat{O}|\psi\rangle &= \sum_{\sigma, \sigma'} (B^{\sigma_1, \sigma'_1} B^{\sigma_2, \sigma'_2} \dots) (A^{\sigma'_1} A^{\sigma'_2} \dots) |\sigma\rangle \\ &= \sum_{\sigma, \sigma'} \sum_{\mathbf{a}, \mathbf{b}} (B_{1, b_1}^{\sigma_1, \sigma'_1} B_{b_1, b_2}^{\sigma_2, \sigma'_2} \dots) (A_{1, a_1}^{\sigma'_1} A_{a_1, a_2}^{\sigma'_2} \dots) |\sigma\rangle \\ &= \sum_{\sigma, \sigma'} \sum_{\mathbf{a}, \mathbf{b}} (B_{1, b_1}^{\sigma_1, \sigma'_1} A_{1, a_1}^{\sigma'_1}) (B_{b_1, b_2}^{\sigma_2, \sigma'_2} A_{a_1, a_2}^{\sigma'_2}) \dots |\sigma\rangle \\ &= \sum_{\sigma} \sum_{\mathbf{a}, \mathbf{b}} C_{(1,1), (b_1, a_1)}^{\sigma_1} C_{(b_1, a_1), (b_2, a_2)}^{\sigma_2} \dots |\sigma\rangle = \sum_{\sigma} C^{\sigma_1} C^{\sigma_2} \dots |\sigma\rangle. \end{aligned}$$

An MPS reappears, but with multiplied dimensions.

What would be the MPO representation for Eq. (22.1) [38]? It is of course an abbreviation for sums of tensor products of operators:

$$\begin{aligned} H &= JS_1^z \otimes S_2^z \otimes 1 \otimes 1 \otimes 1 \dots + \\ &\quad 1 \otimes JS_2^z \otimes S_3^z \otimes 1 \otimes 1 \dots + \dots \end{aligned}$$

Reconsider the building block $B_{bb'}^{\sigma\sigma'}$ combined with its associated projector $|\sigma\rangle\langle\sigma'|$ to become an operator-valued matrix $\hat{B}_{bb'} = \sum_{\sigma\sigma'} B_{bb'}^{\sigma\sigma'} |\sigma\rangle\langle\sigma'|$ such that the MPO takes the simple form

$$\hat{O} = \hat{B}^{[1]}\hat{B}^{[2]}\dots\hat{B}^{[L]}. \quad (22.14)$$

Each $\hat{B}^{[i]}$ acts on a different local Hilbert space at site i . Multiplying such operator-valued matrices yields sums of tensor products of operators such that expressing \hat{H} in a compact form seems feasible.

To understand the construction, we move through an arbitrary operator string: starting from the right end, the string contains unit operators, until at one point we encounter a non-trivial operator. For the field operator, the string part further to the left may only contain unit operators; for the interaction operators, the complementary operator must follow immediately to complete the interaction term, to be continued by unit operators further to the left. For bookkeeping, we introduce 5 corresponding states of the string at some given bond: state 0, only units to the right; states 1,2,3, one $(J/2)S^+$, $(J/2)S^-$, J^zS^z just to the right; state 4, completed interaction or field term to the right. Comparing the state of a string left and right of one site, only a few transitions are allowed: $0 \rightarrow 0$ by the unit operator 1, $0 \rightarrow 1$ by $(J/2)S^+$, $0 \rightarrow 2$ by $(J/2)S^-$, $0 \rightarrow 3$ by J^zS^z , and $0 \rightarrow 4$ by hS^z . Furthermore $1 \rightarrow 4$ by S^- , $2 \rightarrow 4$ by S^+ and $3 \rightarrow 4$ by S^z , to complete the interaction term, and $4 \rightarrow 4$ for a completed interaction. All string states must start at 0 to the right of the last site and end at 4 to the left of the first site. This can now be encoded by the following operator-valued matrices:

$$\hat{B}^{[i]} = \begin{bmatrix} 1 & 0 & 0 & 0 & 0 \\ (J/2)S^+ & 0 & 0 & 0 & 0 \\ (J/2)S^- & 0 & 0 & 0 & 0 \\ J^zS^z & 0 & 0 & 0 & 0 \\ hS^z & S^- & S^+ & S^z & 1 \end{bmatrix}, \quad (22.15)$$

and on the first and last sites,

$$\begin{aligned} \hat{B}^{[1]} &= [hS^z \quad S^- \quad S^+ \quad S^z \quad 1], \\ \hat{B}^{[L]} &= [1 \quad \frac{J}{2}S^+ \quad \frac{J}{2}S^- \quad J^zS^z \quad hS^z]^T. \end{aligned} \quad (22.16)$$

Indeed, a simple multiplication shows how the Hamiltonian emerges. Inserting the explicit operator representations gives the desired B -matrices for the MPO. The advantage of the exact MPO representation becomes apparent if powers of \hat{H} are needed, as in some time-evolution approaches or for precision control by variance calculations.

22.4 Time-Dependent Simulation: Extending the Range

22.4.1 Basic Algorithms

Current DMRG or MPS time-evolution methods [26–30] are either based on a Trotter decomposition of the Hamiltonian or use a kind of look-ahead procedure pioneered in [49], best combined with Krylov exponentiation [50]. In the following, I will only consider the former.

The standard decomposition of the HAFM Hamiltonian reads $\hat{H} = \sum_i h_i$, where each h_i is a bond Hamiltonian connecting sites $i, i+1$. We may regroup $\hat{H} = \hat{H}_{\text{odd}} + \hat{H}_{\text{even}}$, where all terms in each part commute, but not between parts. If we do a lowest order Trotter decomposition, we obtain

$$e^{-i\hat{H}\Delta t} \approx e^{-i\hat{H}_{\text{odd}}\Delta t} e^{-i\hat{H}_{\text{even}}\Delta t} \quad (22.17)$$

with an $\mathcal{O}(\Delta t^2)$ error due to non-commutativity.

In fact, using MPOs allows also other Trotter decompositions, e.g., decomposing the Heisenberg Hamiltonian in its x , y , and z -dependent parts, useful for longer-ranged interactions [39]. Essentially, all forms of applying, e.g., $e^{-i\hat{H}_{\text{odd}}\Delta t}$, lead to the need to truncate the MPS representation of the state back to dimension D .

Time-dependent DMRG has been used extensively in the meantime and found to open completely new perspectives on the non-equilibrium behaviour of strongly correlated one-dimensional systems, including [29, 49, 51–56].

However, it turns out that the time spans over which the algorithm works are often quite limited. Early on [51], it was realized that apart from purely numerical effects, there are two error sources in the method, one from the Trotter decomposition, the other from the truncations at each timestep. Whereas the former grow only linearly in time, as there are $t/\Delta t$ timesteps, and can be made very small by advanced higher-order Trotter expansions, the latter may increase at worst exponentially. It was soon realized that this is an inherent feature of quantum states under time evolution, as out-of-equilibrium states show lots of excitations propagating entanglement through the system [57]. Increasing entanglement leads to, in the worst case, exponentially higher D , eventually limiting the applicability of the algorithm. In the following I want to show, for the case of finite- T time evolutions, one simple way of circumventing this issue at very little cost.

22.4.1.1 Time Evolution at Finite Temperatures

It was quickly demonstrated [30] that time evolution can be easily extended to the simulation of the static and dynamic behavior at $T > 0$ by using the *purification* [59, 60] of the mixed state density operator: any density operator $\hat{\rho}$ of some physical system \mathcal{H} can be encoded by a pure state of a combined

physical and ancillary system, $|\rho\rangle \in \mathcal{H} \otimes \mathcal{A}$, such that the density matrix is retained by tracing out \mathcal{A} , $\hat{\rho} = \text{tr}_{\mathcal{A}}|\rho\rangle\langle\rho|$.

The ancillary system \mathcal{A} can be taken as a copy of the physical state space \mathcal{H} . For unnormalized thermal density operators $\hat{\rho}_\beta = e^{-\beta\hat{H}}$, the purification can be constructed by an imaginary-time evolution starting from the purification of the trivial infinite- T ($\beta = 0$) density operator $\hat{\rho}_0 = I$. A possible purification for this $\beta = 0$ ensemble is

$$|\rho_0\rangle = \otimes_{\ell=1}^L |\rho_{0,\ell}\rangle \quad \text{with} \quad |\rho_{0,\ell}\rangle = \sum_{\sigma_\ell} |\sigma_\ell\rangle_{\mathcal{H}} \otimes |\sigma_\ell\rangle'_{\mathcal{A}}, \quad (22.18)$$

where $\{|\sigma_\ell\rangle_{\mathcal{H}}\}$ and $\{|\sigma_\ell\rangle'_{\mathcal{A}}\}$ denote the bases of the physical state space of site ℓ and its associated ancillary state space. With this, we have $\hat{\rho}_0 = \text{Tr}_{\mathcal{A}}|\rho_0\rangle\langle\rho_0|$. Then

$$\hat{\rho}_\beta = e^{-\beta\hat{H}} = \text{Tr}_{\mathcal{A}}|\rho_\beta\rangle\langle\rho_\beta| \quad \text{with} \quad |\rho_\beta\rangle = e^{-\beta\hat{H}/2}|\rho_0\rangle.$$

Proper normalization is restored by imposing $\langle\rho_\beta|\rho_\beta\rangle = 1$. The mixed state $\hat{\rho}_\beta$ can then be evolved in time as $|\rho_\beta(t)\rangle = e^{-i\hat{H}t}|\rho_\beta(0)\rangle$ and $\hat{\rho}_\beta(t) = \text{Tr}_{\mathcal{A}}|\rho_\beta(t)\rangle\langle\rho_\beta(t)|$.

As a product state, the initial $\beta = 0$ purification $|\rho_0\rangle$ is uncorrelated and hence can be expressed exactly with block Hilbert spaces of dimension $D = 1$. Imaginary-time evolution will introduce correlations, requiring one to increase D . For the evaluation of expectation values, both physical and ancillary degrees of freedom are traced over:

$$\begin{aligned} \text{Tr}_{\mathcal{H}}(S_i^z(t)S_j^z(0)\hat{\rho}_\beta) &= \text{Tr}_{\mathcal{H} \otimes \mathcal{A}}(S_i^z(t)S_j^z(0)|\rho_\beta\rangle\langle\rho_\beta|) \\ &= \langle\rho_\beta|e^{i\hat{H}t}S_i^z e^{-i\hat{H}t}S_j^z|\rho_\beta\rangle. \end{aligned} \quad (22.19)$$

Unfortunately, for going to frequency space for structure functions, the time scales that can be reached are too limited, introducing low frequency resolution or artifacts. In order to circumvent this limitation at very low numerical cost, we adapt a linear prediction technique [58] already successfully employed at $T = 0$ in Ref. [61, 62], extending t and refining the frequency domain.

22.4.2 Linear Prediction and Spectral Functions

For a time series of complex data x_0, x_1, \dots, x_N at equidistant points in time $t_n = n\Delta t$ (and $t_{\text{obs}} := N\Delta t$) obtained by DMRG one makes a prediction of x_{N+1}, x_{N+2}, \dots . For the data points beyond $t = t_{\text{obs}}$, linear prediction makes the ansatz

$$\tilde{x}_n = - \sum_{i=1}^p a_i x_{n-i}. \quad (22.20)$$

The (predicted) value \tilde{x}_n at time step n is assumed to be a linear combination of p previous values $\{x_{n-1}, \dots, x_{n-p}\}$. Once the a_i are determined from known data, they are used to calculate an approximation of all x_n with $n > N$.

The coefficients a_i are determined by minimizing the least square error in the predictions over a subinterval $t_n \in (t_{\text{obs}} - t_{\text{fit}}, t_{\text{obs}}]$ of the known data, i.e., we minimize in the simplest approach $E \equiv \sum_{t_n} |\tilde{x}_n - x_n|^2$. We found $t_{\text{fit}} = t_{\text{obs}}/2$ to be a robust choice with little short-time influence and enough data points. Minimization of E with respect to a_i yields the linear system

$$R\vec{a} = -\vec{r}, \quad (22.21)$$

where R and \vec{r} are the autocorrelations $R_{ji} = \sum_{t_n} x_{n-j}^* x_{n-i}$ and $r_j = \sum_{t_n} x_{n-j}^* x_n$. Eq. (22.21) is solved by $\vec{a} = -R^{-1}\vec{r}$; R is a positive definite matrix.

One may wonder why the extrapolation to infinite time is possible in this fashion. As demonstrated below, linear prediction generates a superposition of oscillating and exponentially decaying or growing terms, a type of time dependence that emerges naturally in many-body physics: Green's functions of the typical form $G(k, \omega) = (\omega - \epsilon_k - \Sigma(k, \omega))^{-1}$ are in time-momentum representation dominated by the poles; e.g., for a single simple pole at $\omega = \omega_1 - i\eta_1$ with residue c_1 , it will read $G(k, t) = c_1 e^{-i\omega_1 t - \eta_1 t}$, and similarly it will be a superposition of such terms for more complicated pole structures. So the ansatz of the linear prediction is well suited for the typical properties of the response quantities we are interested in. Where such an ansatz does not hold, the method is probably inadequate.

To see the special form of time-series generated by the prediction, we introduce vectors $\vec{x}_n := [x_{n-1}, \dots, x_{n-p}]^T$ such that (22.20) takes the form

$$\tilde{\vec{x}}_{n+1} = A\vec{x}_n, \quad (22.22)$$

with

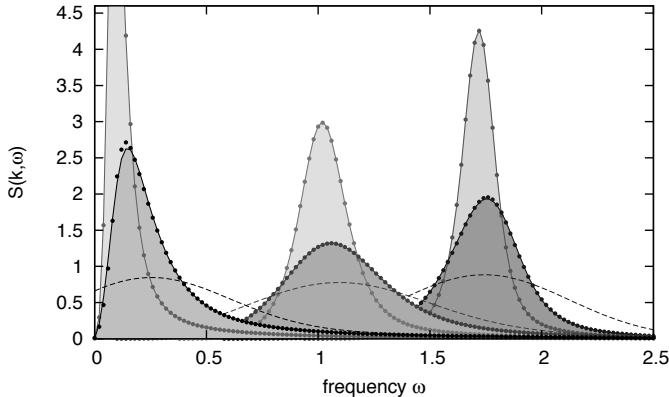
$$A \equiv \begin{bmatrix} -a_1 & -a_2 & -a_3 & \cdots & -a_p \\ 1 & 0 & 0 & \cdots & 0 \\ 0 & 1 & 0 & \cdots & 0 \\ \vdots & \ddots & \ddots & \ddots & \vdots \\ 0 & \cdots & 0 & 1 & 0 \end{bmatrix}. \quad (22.23)$$

Prediction therefore corresponds to applying powers of A to the initial vector \vec{x}_N . A right eigenvector decomposition of A with eigenvalues α_i leads to

$$\tilde{\vec{x}}_{N+m} = [A^m \vec{x}_N]_1 = \sum_{i=1}^p c_i \alpha_i^m, \quad (22.24)$$

where coefficients c_i are determined from \vec{x}_N and the eigenvectors of A . The eigenvalues α_i encode the physical resonance frequencies and dampings. The connection is given as $\alpha_i = e^{i\omega_i \Delta t - \eta_i \Delta t}$. Spurious $|\alpha_i| \geq 1$ may appear, but can be dealt with [58].

At $T = 0$, critical one-dimensional systems exhibit power-law decays in their time-dependent correlators. The superposition of exponential decays

**FIGURE 22.4**

Curves and points represent exact analytical and numerical solutions for the lineshape of the spectral function $S^{+-}(k, \omega)$ of an XY -chain at temperatures $\beta = 10$ and $\beta = 50$ (thick and thin curves) for $k = \pi/8$, $k = \pi/3$, $k = 3\pi/4$ (left to right). The dashed curves are the shapes that would optimally be extracted from the $\beta = 10$ simulation without prediction. Adapted from [58].

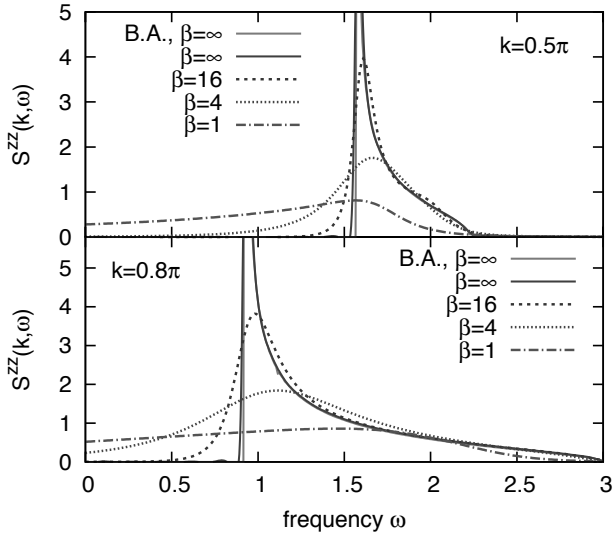
is then taken to mimic these power-laws [61]. At finite temperatures, time-dependent correlators $S(k, t)$ decay typically exponentially for large times, due to thermal broadening, making linear prediction especially well-suited for this situation.

As an example, let us consider a field-free Heisenberg antiferromagnet with $J^z = 0$ (XY -chain) and $J^z = 1$. The former case allows for an exact analytical solution. It turns out that prediction allows one to extend the time series $S(k, t)$ over an order of magnitude without appreciable loss of precision. In frequency space, this corresponds to extremely high-precision spectral lineshapes (Fig. 22.4).

As the dispersion relation of the XY -chain is just a simple magnon line, its self-energy structure is very simple; hence the prediction method is easily applicable. As a more demanding example, we studied the spinon continuum of an isotropic $S = 1/2$ chain. In the zero-temperature limit, results agree extremely well with Bethe-ansatz results.³ At finite temperatures, simulations at different precision indicate that results are fully converged and essentially exact. This makes us expect that this method will be a powerful tool in, e.g., simulating the results of neutron scattering experiments.

Let me conclude this section by mentioning that recently two very exciting complementary approaches for extending the time range have emerged, which might also be combined with the prediction scheme, but demand more effort at

³Where remaining differences are hard to attribute: the Bethe ansatz here can only be evaluated in approximation [63].

**FIGURE 22.5**

Spectral function of the isotropic Heisenberg chain at two momenta and four different temperatures. At $T = 0$, Bethe ansatz and numerics agree extremely well. Adapted from [58].

implementation. At finite temperature, White's minimally entangled typical thermal states [64] seem to provide an extremely efficient sampling of the statistics of states at finite temperature and make optimal use of numerical use of resources as entanglement stays low [65]. At the same time, the so-called transverse folding approach [66], which evaluates time evolution along the spatial direction in a transfer matrix approach and groups together the time evolution of bra and ket states by a folding technique, quite generally seems to make much larger time scales accessible.

22.5 Density Matrix and Numerical Renormalization Groups

22.5.1 Wilson's Numerical Renormalization Group and Matrix Product States

Wilson's Numerical Renormalization Group (NRG) [40–42] originates in attempts to explain why metals with a small concentration of magnetic impurities exhibit a non-monotonic behavior of resistivity. It was found that an

adequate minimal model is provided by

$$\hat{H}_A = \sum_{k\sigma} \epsilon_k \hat{c}_{k\sigma}^\dagger \hat{c}_{k\sigma} + \sum_{k\sigma} V_k (\hat{f}_\sigma^\dagger \hat{c}_{k\sigma} + \text{h.c.}) + U(n_{f\uparrow} - 1/2)(n_{f\downarrow} - 1/2). \quad (22.25)$$

This single-impurity Anderson model contains an impurity site that can be occupied by up to two electrons, operators \hat{f}_σ^\dagger , with on-site repulsion U and which couples to a conduction band, operators $\hat{c}_{k\sigma}^\dagger$, with energy dispersion ϵ_k through some hybridization function V_k .

In order to make it tractable, one changes from momentum to energy representation, assuming that only low-energy isotropic s -wave scattering matters, and introduces logarithmic discretization: the band is represented by band segments of an energy width that decreases exponentially close to the Fermi energy ϵ_F . This accounts for the observation that the decisive feature of quantum impurity physics, namely the appearance of a very narrow resonance peak at the Fermi energy in the local impurity spectral function, is linked exponentially strongly to the states close to the Fermi energy. However, logarithmic discretization is also required to make NRG work at all on a technical level!

After further manipulations, the Anderson Hamiltonian is finally mapped to a semi-infinite chain of non-interacting sites with the exception of the first one:

$$\hat{H} = U(n_{f\uparrow} - 1/2)(n_{f\downarrow} - 1/2) + t_{-1} \sum_{\sigma} (f_\sigma^\dagger d_{0\sigma} + \text{h.c.}) + \sum_{n=0}^{\infty} t_n (d_{n\sigma}^\dagger d_{n+1,\sigma} + \text{h.c.}), \quad (22.26)$$

where the d_σ are fermionic operators. The crucial point is that the t_n decay exponentially, $t_n \sim \Lambda^{-n}$, where Λ is the shrinkage factor of the energy bands in the logarithmic discretization. This leads to a separation of energy scales: assuming we know the spectrum of the partial chain up to some length, all remaining sites will only make exponentially small corrections to it because of the exponentially small energy scales further down the chain. Finding the ground state, and more generally the low lying spectrum, is now achieved by iterative exact diagonalization: assume that we have an effective D -dimensional eigenspace for some left-end part of the chain. Then the next-larger chain has state space dimension $dD = 4D$; in order to avoid exponential growth, we have to truncate down to D states. The NRG prescription is to diagonalize that system and to retain the D lowest-lying eigenstates. Starting out from very short chains that can still be done exactly, this procedure resolves the lowest-lying states exponentially well and is justified by the separation of energy scales: the decision of which states to retain at some step would not be drastically changed with hindsight, as all further sites in the chain interact at much lower energies. The obtained eigenspectra at different energy scales (chain lengths) can then be used to extract RG flow information or calculate thermodynamic or dynamic quantities for the impurity problem.

Given that the building block A^σ of an MPS can be interpreted as encoding a decimation step upon growing a block by one site, irrespective of the

decimation prescription, it is immediately obvious that NRG, like DMRG, can be seen as operating on MPSs. This is to me exciting as failures of NRG gave rise to the development of DMRG. An NRG state would look like

$$|a_\ell\rangle = \sum_{\sigma_1, \dots, \sigma_\ell} (A^{\sigma_1} \dots A^{\sigma_\ell})_{a_\ell} |\sigma_1 \dots \sigma_\ell\rangle. \quad (22.27)$$

Given that DMRG is variational over the MPS ansatz space, it is reasonable to expect that at least some improvement must be possible over the NRG method. In fact this is the case; in the next section, I am going to discuss some improvements which are already firmly established and others which are more speculative, i.e., where benchmarking on relevant complex problems is still lacking.

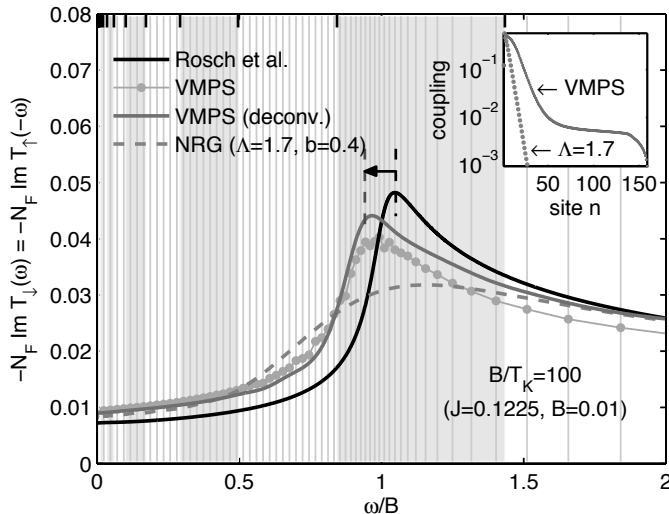
22.5.2 Going Beyond the Numerical Renormalization Group

In fact, considering an MPS formulation of NRG helps even without resorting to the connection to variational methods like DMRG, as exemplified by the strict enforcement of certain sum rules [69]. However, what we can further accomplish is to subject the final MPS construction generated by NRG to DMRG-like sweeping. This will somewhat improve the quality of the ground state, but above all, the truncation procedure for high energies (short chains) will enable one to learn about truncation at low energies, and vice versa. As opposed to NRG, there is now a feedback between energy scales. In that sense, NRG for an impurity problem is a similar conceptual step as the warm-up procedure infinite-system DMRG provides for variational finite-system DMRG.

For logarithmic discretization, energy-scale separation is big enough that this effect is minor and for a simple single impurity problem with a focus on the Abrikosov-Kondo-Suhl resonance the ultimate improvement is limited, as NRG is geared to describe this feature optimally. The essential point is that energy-scale separation can now be abandoned altogether due to feedback, hence also logarithmic discretization, and we may choose a more fine-grained resolution of the energy band wherever it is physically suitable. This could find a variety of applications.

In one application, variational calculus over MPSs was applied to an impurity problem in an external field. The external field leads to a splitting of the peak into two spin-dependent ones, shifted above and below the Fermi energy. In Fig. 22.6 we consider one of these peaks, in three techniques: in NRG, in an analytical approach [68], and in variational MPS calculus. NRG due to logarithmic discretization focuses on ϵ_F and does not see the field-dependent peak at all. Relaxing logarithmic discretization and providing sufficiently fine energy intervals around the expected peak positions away from ϵ_F , the shifted resonance can be resolved clearly and is even in very good agreement with analytics.

A second interesting application could be to replace NRG as an impurity solver in the context of dynamical mean-field theory (DMFT). In that case,

**FIGURE 22.6**

Impurity spectral function for a Kondo model in an external field. Thin vertical lines indicate the energy intervals: below a certain energy, logarithmic discretization is turned linear. Variational MPS calculations (with and without deconvolution) reveal a peak missed by NRG, where the peak position is in very good agreement with a calculation by Rosch *et al.* [68] combined with a perturbatively found peak shift. Taken from [32].

information beyond the metallic resonance at the Fermi energy is required such that improving spectral resolution on other energy scales would be highly desirable.

As the semi-infinite chain is non-interacting but on the first site, one can think about unfolding it into an infinite chain of spin-1/2, with the impurity at the center and the presence or absence of spin-up or spin-down fermions corresponding to the two spin states, the left half of the chain corresponding to the spin-up fermions and the right half to the spin-down fermions [70]. Similar energies are no longer grouped together, but in a DMRG-like approach this does not matter anymore! The intuition that spins interacting only through the central impurity might be essentially unentangled is corroborated by actual calculations. This is important as it means we will not pay a strong price by increased matrix dimensions. On the contrary, if in the NRG approach we are essentially looking at two uncoupled spin chains parallel to each other, this means that the corresponding MPS has dimension $\mathcal{O}(D^2)$ if the spin chain has dimension D . We can therefore expect that an NRG calculation with state number D can be replaced by a faster DMRG calculation with a state number $\mathcal{O}(\sqrt{D})$.

Beyond this speed up, unfolding can of course also be applied if the im-

rity couples to multiple bands, where NRG becomes exponentially complex. The central site, of course, remains the same, and its numerical treatment can become extremely costly, such that new strategies have to be designed for that site. The only thing that is safe to say is that there is still lots of room for innovation and excitement here!

Acknowledgments – I would like to thank the Aspen Center for Physics and the International Center for Theoretical Physics in Trieste, Italy, where major parts of this work were carried out, for their hospitality. Their combination of stimulating discussions and room for withdrawal to pursue intensive work sets a great example.

Bibliography

- [1] S. R. White, Phys. Rev. Lett. **69**, 2863 (1992).
- [2] S. R. White, Phys. Rev. B **48**, 10345 (1993).
- [3] K. Hallberg, Phys. Rev. B **52**, 9827 (1995).
- [4] T. D. Kühner and S. R. White, Phys. Rev. B **60**, 335 (1999).
- [5] E. Jeckelmann, Phys. Rev. B **66**, 045114 (2002).
- [6] T. Nishino, J. Phys. Soc. Jpn. **64**, 3598 (1995).
- [7] X. Q. Wang and T. Xiang, Phys. Rev. B **56**, 5061 (1997).
- [8] N. Shibata, J. Phys. Soc. Jpn. **66**, 2221 (1997).
- [9] E. Carlon, M. Henkel, and U. Schollwöck, Eur. J. Phys. B **12**, 99 (1999).
- [10] E. Carlon, M. Henkel, and U. Schollwöck, Phys. Rev. E **63**, 036101 (2001).
- [11] M. Henkel and U. Schollwöck, J. Phys. A **34**, 3333 (2001).
- [12] I. Affleck, T. Kennedy, E. H. Lieb, and H. Tasaki, Phys. Rev. Lett. **59**, 799 (1987).
- [13] I. Affleck, T. Kennedy, E. H. Lieb, and H. Tasaki, Comm. Math. Phys. **115**, 477 (1988).
- [14] M. Fannes, B. Nachtergael, and R. F. Werner, Europhys. Lett. **10**, 633 (1989).
- [15] M. Fannes, B. Nachtergael, and R. F. Werner, Comm. Math. Phys. **144**, 443 (1992).

- [16] A. Klümper, A. Schadschneider, and J. Zittartz, *Europhys. Lett.* **24**, 293 (1993).
- [17] A. K. Kolezhuk, R. Roth, and U. Schollwöck, *Phys. Rev. Lett.* **77**, 5142 (1996).
- [18] A. K. Kolezhuk, R. Roth, and U. Schollwöck, *Phys. Rev. B* **55**, 8928 (1997).
- [19] A. K. Kolezhuk and H. J. Mikeska, *Phys. Rev. Lett.* **80**, 2709 (1998).
- [20] A. K. Kolezhuk, H. J. Mikeska, and S. Yamamoto, *Phys. Rev. B* **55**, R3336 (1997).
- [21] A. K. Kolezhuk, H. J. Mikeska, K. Maisinger, and U. Schollwöck, *Phys. Rev. B* **59**, 13565 (1997).
- [22] S. Ostlund and S. Rommer, *Phys. Rev. Lett.* **75**, 3537 (1995).
- [23] J. Dukelsky, M.A. Martín-Delgado, T. Nishino, and G. Sierra, *Europhys. Lett.* **43**, 457 (1998).
- [24] H. Takasaki, T. Hikihara, and T. Nishino, *J. Phys. Soc. Jpn.* **68**, 1537 (1999).
- [25] S. R. White, *Phys. Rev. B* **72**, 180403 (2005).
- [26] G. Vidal, *Phys. Rev. Lett.* **93**, 076401 (2004).
- [27] G. Vidal, *Phys. Rev. Lett.* **93**, 040502 (2004).
- [28] A. J. Daley, C. Kollath, U. Schollwöck, and G. Vidal, *J. Stat. Mech.: Theor. Exp.*, P04005 (2004).
- [29] S. R. White and A. E. Feiguin, *Phys. Rev. Lett.* **93**, 076401 (2004).
- [30] F. Verstraete, J. J. García-Ripoll, and J. I. Cirac, *Phys. Rev. Lett.* **93**, 207204 (2004).
- [31] F. Verstraete, D. Porras, and J. I. Cirac, *Phys. Rev. Lett.* **93**, 227205 (2004).
- [32] A. Weichselbaum, F. Verstraete, U. Schollwöck, J.I. Cirac, and J. von Delft, *Phys. Rev. B* **80**, 165117 (2009).
- [33] F. Verstraete and J. I. Cirac, arXiv:cond-mat/0407066 (2004).
- [34] T. Nishino and K. Okunishi, *J. Phys. Soc. Jpn.* **67**, 3066 (1998).
- [35] G. Vidal, J. I. Latorre, E. Rico, and A. Kitaev, *Phys. Rev. Lett.* **90**, 227902 (2003).

- [36] J. I. Latorre, E. Rico, and G. Vidal, Quant. Inf. Comp. **4**, 48 (2004).
- [37] U. Schollwöck, Rev. Mod. Phys. **77**, 259 (2005).
- [38] I.P. McCulloch, J. Stat. Mech.: Theor. Exp. P10014 (2007).
- [39] V. Murg, J.I. Cirac, B. Pirvu, and F. Verstraete, New J. Phys. **12**, 025012 (2010).
- [40] K. G. Wilson, Rev. Mod. Phys. **47**, 773 (1975).
- [41] R. Bulla, T. A. Costi, and T. Pruschke, Rev. Mod. Phys. **80**, 395 (2008).
- [42] H. R. Krishna-murthy, J. W. Wilkins, and K. G. Wilson, Phys. Rev. B **21**, 1003 (1980).
- [43] U. Schollwöck, S. Chakravarty, J. O. Fjaerestad, J. Marston, and M. Troyer, Phys. Rev. Lett. **90**, 186401 (2003).
- [44] S. R. White, Phys. Rev. Lett. **77**, 3633 (1996).
- [45] J. D. Bekenstein, Phys. Rev. D **7**, 2333 (1973).
- [46] M. B. Plenio, J. Eisert, J. Dreissig, and M. Cramer, Phys. Rev. Lett. **94**, 060503 (2005).
- [47] M. Srednicki, Phys. Rev. Lett. **71**, 666 (1993).
- [48] C. G. Callan and F. Wilczek, Phys. Lett. B **333**, 55 (1994).
- [49] A. E. Feiguin and S. R. White, Phys. Rev. B **72**, 020404 (2005).
- [50] P. Schmitteckert, Phys. Rev. B **70**, 121302 (2004).
- [51] D. Gobert, C. Kollath, U. Schollwöck, and G. Schütz, Phys. Rev. E **71**, 036102 (2005).
- [52] C. Kollath, U. Schollwöck, and W. Zwerger, Phys. Rev. Lett. **95**, 176401 (2005).
- [53] S. Trebst, U. Schollwöck, M. Troyer, and P. Zoller, Phys. Rev. Lett. **96**, 250402 (2006).
- [54] M. Cramer, A. Flesch, I. McCulloch, U. Schollwöck and J. Eisert, Phys. Rev. Lett. **101**, 063001 (2008).
- [55] T. Barthel, C. Kasztelan, I.P. McCulloch and U. Schollwöck, Phys. Rev. A **79**, 053627 (2009).
- [56] A. Feiguin and S. White, Phys. Rev. B **72**, 220401 (2005).
- [57] P. Calabrese and J. Cardy, J. Stat. Mech.: Theor. Exp. P04010 (2006).

- [58] T. Barthel, U. Schollwöck and S. R. White, Phys. Rev. A **79**, 245101 (2009).
- [59] A. Uhlmann, Rep. Math. Phys. **9**, 273 (1976).
- [60] A. Uhlmann, Rep. Math. Phys. **24**, 229 (1986).
- [61] R. G. Pereira, S. R. White and I. Affleck, Phys. Rev. Lett. **100**, 027206 (2008).
- [62] S. R. White and I. Affleck, Phys. Rev. B **77**, 134437 (2008).
- [63] J.-S. Caux and R. Hagemans, J. Stat. Mech.: Theor. Exp. P12013 (2006).
- [64] S. R. White, Phys. Rev. Lett. **102**, 190601 (2009).
- [65] U. Schollwöck, Physics **2**, 39 (2009).
- [66] M. C. Banuls, M. B. Hastings, F. Verstraete and J. I. Cirac, Phys. Rev. Lett. **102**, 240603 (2009).
- [67] F. Verstraete and J. I. Cirac, Phys. Rev. B **73**, 094423 (2006).
- [68] A. Rosch, T.A. Costi, J. Paaske and P. Wölfle, Phys. Rev. B **68**, 014430 (2003); M. Garst, P. Wölfle, L. Borda, J. von Delft and L. Glazman, Phys. Rev. B **72**, 205125 (2005).
- [69] A. Weichselbaum and J. von Delft, Phys. Rev. Lett. **99**, 076402 (2007).
- [70] C. Raas, G. S. Uhrig and F. B. Anders, Phys. Rev. B **69**, 041102(R) (2004); C. Raas and G. S. Uhrig, Eur. Phys. J. B **45**, 293 (2005).

23

Simulations Based on Matrix Product States and Projected Entangled Pair States

Valentin Murg

Max-Planck-Institut für Quantenoptik, Hans-Kopfermann-Str. 1, D-85748 Garching, Germany

Ignacio Cirac

Max-Planck-Institut für Quantenoptik, Hans-Kopfermann-Str. 1, D-85748 Garching, Germany

Frank Verstraete

Fakultät für Physik, Universität Wien, Boltzmanngasse 5, A-1090 Wien, Austria

The formulation of renormalization group methods in terms of matrix product states (MPS) has the big advantage that it allows one to describe time evolution. This opens up the possibility of simulating the non-equilibrium properties of spin chains, a topic that is currently very relevant given the recent breakthroughs in creating strongly-correlated quantum spin systems, for example in optical lattices [1].

Another advantage is that the generalization of the MPS picture to higher dimensions is rather straightforward: the main reason for the success of the MPS approach is that it allows one to represent very well local properties that are compatible with, e.g., the translational symmetry in the system. These strong local correlations are obtained by sharing maximally entangled states between neighbors, and longer range correlations are basically mediated by intermediate particles. This is a very physical picture, as the Hamiltonian does not force any long-range correlations to exist *a priori*, and they only come into existence because of frustration effects. The generalization to higher dimensions can therefore be obtained by distributing virtual maximally entangled states between all neighboring sites [2], and as such corresponds to a generalization of the Affleck-Kennedy-Lieb-Tasaki (AKLT) picture.

23.1 Time Evolution using Matrix Product States

Since the development of DMRG, several methods for the simulation of time evolution have been proposed [3–8]. In the following, we review the variational approach, the time-evolving block-decimation (TEBD) method, and applications thereof to imaginary-time evolution and infinite spin chains. For a deeper discussion we refer the reader to Ref. [13]. We refer to Chap. 22 and Ref. [9] for density-matrix renormalization group (DMRG) and related approaches.

23.1.1 Variational Formulation of Time Evolution with MPS

Mathematically, the problem is to evolve an initial MPS in real time by updating the tensors in the MPS description under Hamiltonian evolution. In practice, this can be used to investigate, for example, how excitations travel through the spin chain or to get spectral information about a Hamiltonian of interest. In a similar spirit as in DMRG, we would like to do this in a variational way: given a Hamiltonian and an initial MPS, evolve that state within the manifold of MPS in such a way that the error in approximating the exact evolution is minimized at every infinitesimal step [6].

We are particularly interested in the case where the Hamiltonian, which can be time-dependent, is a sum of local terms of the form

$$\mathcal{H}(t) = \sum_{\langle ij \rangle} f_{ij}(t) \hat{O}_i \otimes \hat{O}_j,$$

where $\langle ij \rangle$ means that the sum has to be taken over all pairs of nearest neighbors.¹ There are several tools to discretize the corresponding evolution. This is not completely trivial because generically the different terms in the Hamiltonian don't commute. A standard tool is to use the Trotter decomposition [10]

$$e^{A+B} = \lim_{n \rightarrow \infty} \left(e^{\frac{A}{n}} e^{\frac{B}{n}} \right)^n.$$

Suppose, e.g., that the Hamiltonian can be split into two parts A and B such that all terms within A and within B are commuting: $\mathcal{H} = A + B$; $A = \sum_i A_i$; $B = \sum_i B_i$; $[A_i, A_j]_- = 0 = [B_i, B_j]_-$. This ensures that one can efficiently represent e^{iA} as a product of terms. The evolution can then be approximated by evolving first under the operator $e^{i\delta t A}$, then under $e^{i\delta t B}$, again under $e^{i\delta t A}$, and so forth. The time step can be chosen so as to ensure that the error made due to this discretization is smaller than a pre-specified error; there is an extensive literature on how to improve this by using, e.g., higher order Trotter decompositions [11]. In the case of nearest-neighbor Hamiltonians, a convenient choice for A is to take all terms that couple the even sites with the odd ones to the right of it and for B the ones to the left of it. In that

¹The situation with long-range interactions can be treated in a very similar way.

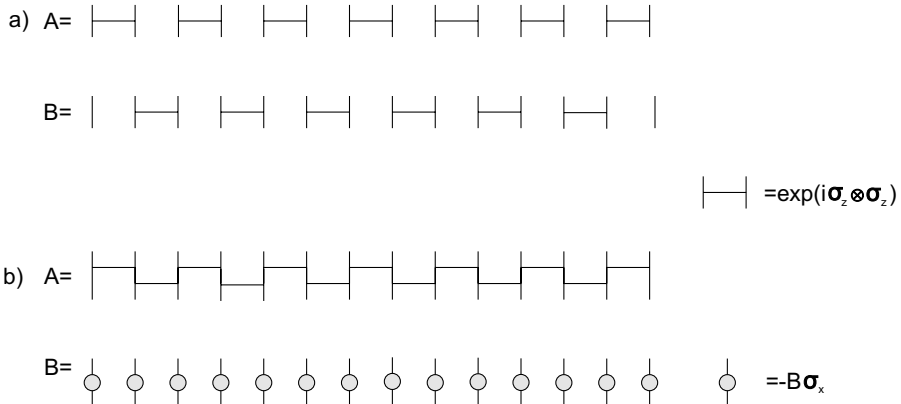


FIGURE 23.1

Spin-network representation of the different operators obtained in the case of a Trotter expansion of the Ising Hamiltonian in transverse field with (a) nearest-neighbor decomposition and (b) Ising vs. magnetic-field decomposition.

case, e^{iA} and e^{iB} are tensor products of nearest-neighbor 2-body operators; see Fig. 23.1(a) for a pictorial representation of this in terms of spin networks. However, it is important to note that different choices of A and B might work better practice. Consider, e.g., the Ising Hamiltonian in a transversal field and its decomposition into two different terms A and B (see also Fig. 23.1(b)):

$$\mathcal{H}_{\text{Ising}} = \underbrace{\sum_k \sigma_z^k \otimes \sigma_z^{k+1}}_A + \underbrace{H \sum_k \sigma_x^k}_B. \quad (23.1)$$

Obviously, a similar kind of decomposition is possible in the case of the Heisenberg model, but there three terms are needed instead. The advantage of evolution with such a decomposition is that it does not break translational invariance as in the even-odd case.

Let us next investigate how to treat this time evolution in a variational way within the class of MPS. A sensible cost function to minimize is given by

$$\|V|\psi(k)\rangle - |\psi(k+1)\rangle\|^2 \quad (23.2)$$

where $|\psi(k)\rangle$ is the initial MPS, $|\psi(k+1)\rangle$ is the one to be found, and V is the operator arising out of the Trotter expansion.² First of all, it is important to note that this cost function can indeed be evaluated efficiently when $|\psi(k)\rangle$ and $|\psi(k+1)\rangle$ are MPS and V is of the form discussed above. In principle, this

²Note that as alternative cost-function we could have chosen $\frac{|\langle \psi(k+1) | V | \psi(k) \rangle|^2}{\langle \psi(k+1) | \psi(k+1) \rangle}$ which has the aim of finding the normalized MPS $|\psi(k+1)\rangle$ that has maximal overlap with the evolved version of the original one. However, it is an easy exercise to find out that this optimization problem leads exactly to the same optimal MPS, up to a normalization factor.

cost function can be made equal to zero by increasing the bond dimension D by a factor of at most d^2 ; this is indeed the largest possible Schmidt number of an operator acting on two sites. However, the whole point of using MPS is that MPS with low bond dimension are able to capture the physics needed to describe the low-energy sector of the Hilbert space. So if we stay within that sector, the hope is that the bond dimension will not have to be multiplied by a constant factor at each step, which would lead to an exponential computational cost as a function of time, but will instead saturate. This is certainly the case if we evolve using, e.g., imaginary-time evolution of a constant local Hamiltonian, as we know that in this case the ground state is indeed well represented with an MPS with a bond dimension which is not too large. However, it is important to keep in mind that an exponential explosion is in principle possible for other kinds of evolution: the worst-case computational complexity for time evolution using MPS is exponential as a function of time.

Taking this into account, a justified way of dealing with time evolution is to pre-specify an error ϵ that can be tolerated, and then look for the minimal D for which there exists an MPS $|\psi(k+1)\rangle$ that yields an error smaller than ϵ . Looking back at the cost function (23.2), one can see how to minimize it: the cost function has only quadratic and linear terms, and we will hence be able to minimize it by a method very similar to the alternating least squares method discussed in the previous section. More specifically, the cost function has only multi-quadratic and multi-linear terms in the variables of the MPS, and we will solve this in a recursive way where at each recursion step an optimization of the form

$$x^\dagger V_{\text{eff}} x - 2x^\dagger y_{\text{eff}}$$

has to be solved. The solution to this problem is the simple solution of the linear set of equations

$$V_{\text{eff}} x = y_{\text{eff}},$$

and this hence leads to a very efficient way of minimizing the cost function for time evolution in a recursive way: sweeping back and forth,³ we solve the above optimization subproblem at each step, and we are guaranteed that the total cost function goes down at every step and hence will converge. After convergence, we can check how big the error has been for the particular value of D that we choose, and if this error is too big, we can increase D and repeat the optimization. Note that the only requirement for the complete Trotter step evolution to be successful is that the tensor network when sandwiching the operator V between two MPS can be contracted efficiently. It is clear that this method works in both real- and imaginary-time evolution, and for both time-independent and time-dependent Hamiltonians. We mention that this will be crucial in applications of variational time evolution of MPS to higher-dimensional spin systems; we also want to point out that nowhere did we use the fact that the operator V was close to the identity; i.e., this method

³See also the description in Chap. 22.

is applicable in a more general way than only for small Trotter steps. Note also that this method is applicable to systems with both open and periodic boundary conditions, and also with long-range interactions.

23.1.2 Time-Evolving Block-Decimation

There has recently been a lot of attention paid to studying time evolution using MPS, but instead of using the optimal variational way described above, the vast majority of the work has been using the TEBD procedure introduced by Vidal [5]. The reason for this is that this method can readily be implemented with existing DMRG code [4]. It explicitly uses the Schmidt normal form described in [12, 13], and is hence more suitable for MPS with open boundary conditions. Also, one has to use the Trotter expansion with even-odd sites decomposition. It can also be understood as a variational method, but in the more restricted sense in which we consider the following set-up: given an MPS and one, possibly non-unitary gate acting on two nearest-neighbors, find the new MPS with given dimension D that approximates this optimally. This can be done using the singular value decomposition (SVD): using the normal form for MPS with open boundary conditions, we know that the original MPS is of the form

$$|\psi\rangle = \sum_{n=1}^D |\psi_n^L\rangle |\psi_n^R\rangle$$

with $\{|\psi_n^L\rangle\}$ and $\{|\psi_n^R\rangle\}$ orthogonal sets. The gate which acts on the nearest neighbors locally increases the dimension of the bond with a factor of at most d^2 , and we would like to reduce the dimension of that bond to D again. One can orthonormalize everything again and obtain the Schmidt decomposition over that particular bond, and then the reduction can trivially be done by discarding, i.e., projecting out, the smallest Schmidt coefficients.⁴ In the next step, evolution between the next-nearest neighbors is considered, and so on. Note that the variational method discussed above could deal with all these gates at once; nevertheless, the computational cost of both methods is very similar, and in practice both methods seem to achieve a similar accuracy if the time steps are small. However, the first one can be improved by choosing longer time steps and higher Trotter orders [8].

It is also possible to devise more sophisticated methods that make use of the fact that superpositions of MPS can still be dealt with in an efficient way. For a nice review that compares all such methods and the ones described before, see [8]. For nice examples of the power of real-time evolution, we refer to the review article [9].

⁴This is indeed the virtue of SVD: if we want to approximate a given matrix with one of lower rank in an optimal way, in the sense of minimizing the Frobenius norm of the difference, then the solution is given by taking the SVD and setting the smallest singular values equal to zero.

23.1.3 Finding Ground States by Imaginary-Time Evolution

The tools discussed in the previous section apply both to real- and imaginary-time evolution. This provides a completely different way of finding ground states of local quantum spin Hamiltonians: if we start with an arbitrary state $|\psi_0\rangle$, evolution in imaginary time leads to

$$|\psi(t)\rangle = e^{-Ht}|\psi_0\rangle = \sum_{k=1}^n e^{-\lambda_k t} |\chi_k\rangle \langle \chi_k | \psi_0 \rangle,$$

with $H = \sum_{k=1}^n \lambda_k |\chi_k\rangle \langle \chi_k|$ the eigenvalue decomposition of H . Hence, as long as the ground state is not degenerate and the time is longer than the inverse gap, the state $|\psi(t)\rangle$ will converge exponentially fast to the ground state, and the speed of convergence is exactly quantified by the gap. This is indeed something that is a recurring theme: the smaller the gap, the slower all variational methods seem to converge. This is expected because it is difficult to discriminate excited states with small energy from the ground state. However, it is interesting to note that the closer a system is to criticality, i.e., as the gap goes to zero, the bigger D has to be for an MPS to approximate the ground state for a fixed error.⁵ A very interesting question would be to relate the density of states above the gap to the decay of the Schmidt coefficients that one gets by dividing the ground state into two pieces.

In practice, finding a ground state using imaginary-time evolution is pretty reliable. The time steps have to be adjusted such that they become smaller and smaller, but one of the great features of imaginary-time evolution is its inherent robustness: it does not really matter if one makes mistakes in the beginning, as there is anyway an exponential convergence to the ground state afterwards. This is in contrast to evolution in real time.

23.1.4 Infinite Spin Chains

Another advantage of the imaginary-time evolution approach is that one can easily treat systems with periodic boundary conditions and/or in the thermodynamic limit by making use of the inherent translational invariance of MPS with all tensors A^i equal to each other.

To illustrate how this can be done, let us consider the specific case treated in [14] and assume that we want to model the ground state of the Ising Hamiltonian in a transverse field defined on a spin chain. As discussed in Sec. 23.1 following Eq. 23.1, one can choose the decomposition in the Trotter step in such a way that both the operators A and B ,

$$\begin{aligned} A &= \sum_k \sigma_z^k \otimes \sigma_z^{k+1}, \\ B &= h \sum_k \sigma_x^k, \end{aligned}$$

are completely translational invariant, and hence we can stay within the manifold of translationally-invariant states to describe its evolution. The next step

⁵In critical systems, this scaling is polynomial in the number of spins in the worst case scenario

is to see what $\exp(\delta tA)$ and $\exp(\delta tB)$ look like. The latter is simple, as it is just equal to

$$\exp(\delta tB) = \otimes_k \exp(\delta t h \sigma_x).$$

The former expression is obviously a product of commuting operators, and a simple exercise allows one to see that there is a simple matrix product description for it:

$$\exp(\delta tA) = \sum_{i_1 i_2 \dots} \text{Tr}(C_{i_1} C_{i_2} \dots) X_{i_1} \otimes X_{i_2} \otimes \dots, \quad (23.3)$$

where $C_0 = \frac{1}{2}[\alpha(I + \sigma_z) + \beta(I - \sigma_z)]$, $C_1 = \sqrt{\sinh(\delta t)} \cosh(\delta t) \sigma_x$, $X_0 = I$, $X_1 = \sigma_z$, and I is the 2×2 identity matrix. This can justifiably be called a matrix product operator (MPO), as described in the next section. The associated bond dimension is 2, and this means that when acting on an MPS of dimension D with this MPO, the exact representation of the new MPS will at most be $2D$. In this particular example of the Ising Hamiltonian, imaginary-time evolution would now amount to acting subsequently with $\exp(\delta tA)$ and $\exp(\delta tB)$ on an initial state. Combined together, it happens that their product $Q = \exp(\delta tB/2) \exp(\delta tA) \exp(\delta tB/2)$ is again exactly of the form (23.3) with unchanged tensor C_i and X_i but where we have to replace $X_0 = I$ with $X_0 = \exp(\delta t \sigma_x)$. So Q is a very simple MPO with bond dimension 2, and the goal is to evolve a translationally-invariant MPS using this MPO. This can be done in a very simple way: given an MPS with tensor A_i of dimension D , the action of Q is such that we have to replace

$$A_i \rightarrow \sum_{k,l} A_k \otimes C_l \langle i | X_l | k \rangle.$$

The new MPS corresponding to this A_i has bond dimension $2D$, and this has to be reduced as otherwise its size would increase exponentially. The optimal choice is again simple if we consider a system with open boundary conditions: we consider its normal form [12, 13], and cut it in the appropriate way without losing translational invariance.⁶ That last step is not so easy to justify rigorously, but seems to work very well in practice: we calculate the Schmidt normal form with respect to the $2D$ dimensional bonds, and then cut all bonds together. The tricky thing is that cutting the bond somewhere changes the Schmidt coefficients somewhere else, but the point is that these changes are only of the order of the Schmidt coefficients that are cut, and the latter are very small. Amazingly, this procedure works very well, and

⁶More specifically, a possible procedure is as follows [14]: calculate the leading left $|v_l\rangle$ and right eigenvector $|v_r\rangle$ of $\sum_k C_k \otimes \bar{C}_k$; this can be done in a sparse way. Reshape these eigenvectors in the square matrices X_l and X_r , and as these matrices are the fixed points of the CP-maps $\sum_k C_k \cdot C_k^\dagger$ and $\sum_k C_k^\dagger \cdot C_k$, X_l and X_r are guaranteed to be positive. Next take the singular value decomposition of $\sqrt{X_r} \sqrt{X_l} = U \Sigma V^\dagger$, and reduce the number of columns of U and V to D and discard the D lowest singular values in Σ ; U and V hence become $2D \times D$ matrices and Σ a $D \times D$ matrix. Define $G_r = \sqrt{X_r^{-1}} U \sqrt{\Sigma}$ and $G_l = \sqrt{\Sigma} V^\dagger \sqrt{X_l^{-1}}$, and make the transformation $A_i \rightarrow G_l A_i G_r$ such that it corresponds to an MPS with D -dimensional bonds instead of $2D$.

even a small bond dimension of $D = 32$ already reproduces the ground state energy-density E of the critical Ising model ($h = 1$) up to a precision better than $E - 4/\pi < 10^{-7}$. Much better conditioning can also be obtained [14] by working with Hermitian matrices $\{A^i\}$.

Clearly, this procedure can be repeated for any translationally-invariant Hamiltonian like the Heisenberg model,⁷ and the big advantage is that it allows one to treat infinite systems. The finite system with periodic boundary conditions can be dealt with in a similar way, although the cutting procedure is more involved.

A variant of this procedure can be obtained by using the even-odd Trotter decomposition. In that case, exact translational invariance is broken, but it is still perfectly translationally-invariant with period 2:

$$|\psi\rangle = \sum_{i_1 i_2 \dots} A_{i_1} B_{i_2} A_{i_3} B_{i_4} \dots |i_1\rangle |i_2\rangle |i_3\rangle |i_4\rangle.$$

This type of imaginary-time evolution has been studied in detail by G. Vidal [15], and convergence seems to be fast. The updating and cutting works in a very similar way as discussed in the example above. Note that from the point of view of variational states, it could be advantageous to work with such an $ABAB\dots$ scheme when an antiferromagnetic ordering is expected.

23.2 PEPS and Ground States of 2D Quantum Spin Systems

In this section, we present a natural generalization of 1D MPS to two and higher dimensions and build simulation techniques based on those states which effectively extend DMRG to higher dimensions. We call these states *projected entangled-pair states* (PEPS) [16,17], since they can be understood in terms of pairs of maximally entangled states of some auxiliary systems that are locally projected in some low-dimensional subspaces. This class of states includes the generalizations of the 2D AKLT-states known as tensor product states [2,18] which have been used for 2D problems but is much broader since every state can be represented as a PEPS, as long as the dimension of the entangled pairs is large enough. We also develop an efficient algorithm to calculate correlation functions of these PEPS, which allows us to extend the 1D algorithms to higher dimensions. This leads to many interesting applications, such as scalable variational methods for finding ground or thermal states of spin systems in higher dimensions as well as to simulate their time evolution. For the sake of simplicity, we will restrict to a square lattice in 2D. The generalization to higher dimensions and other geometries is straightforward.

However, we want to emphasize that the PEPS method is not yet as well

⁷Note that the bond dimension will be bigger in this case.

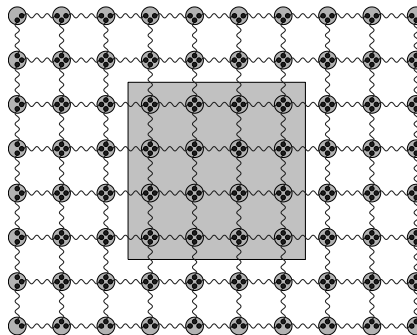


FIGURE 23.2

Representation of a quantum spin system in 2 dimensions using the PEPS representation. If we calculate the entropy of a block of spins, then this quantity will obey an area law and scale as the length of the boundary between the block and the rest. PEPS-states are constructed such as to have this property built in.

established as the 1D MPS or DMRG methods; this is mainly due to its bigger complexity, but also to a big extent due to the fact that these PEPS methods are relatively unexplored which means that there are a lot of ways for improvement and exciting research.

23.2.1 Construction and Calculus of PEPS

There have been various attempts at using the ideas developed in the context of the numerical renormalization group and DMRG to simulate 2D quantum spin systems. However, in hindsight it is clear why those methods were never very successful: they can be reformulated as variational methods within the class of 1D matrix product states, and the structure of these MPS is certainly not well suited to describing ground states of 2D quantum spin systems. This can immediately be understood when reconsidering the area law discussed (see Fig. 23.2): if we look at the number of degrees of freedom needed to describe the relevant modes in a block of spins, this has to scale as the boundary of the block, and hence this increases exponentially with the size of that boundary. This means that it is impossible to use a numerical renormalization group (NRG) or DMRG approach,⁸ where the number of degrees of freedom is bounded to D .

The generalization of MPS to two dimensions is straightforward: each physical system at site i is represented by four auxiliary systems, a_i , b_i , c_i , and d_i , of dimension D , except at the borders of the lattices. Each of those systems

⁸Clearly, the VMPS/DMRG methods can reveal very valuable information in the case of quasi-2D systems such as ladders with a few rungs; see, e.g., [30] for a nice illustration.

is in a maximally entangled state

$$|I\rangle = \sum_{i=1}^D |ii\rangle$$

with one of its neighbors, as shown in the figure. The PEPS $|\Psi\rangle$ is then obtained by applying to each site one operator Q_i that maps the four auxiliary systems onto one physical system of dimension d . This leads to a state with coefficients that are contractions of tensors according to a certain scheme. Each of the tensors is related to one operator Q_i according to

$$[A_i]_{lrud}^k = \langle k|Q_i|l, r, u, d\rangle,$$

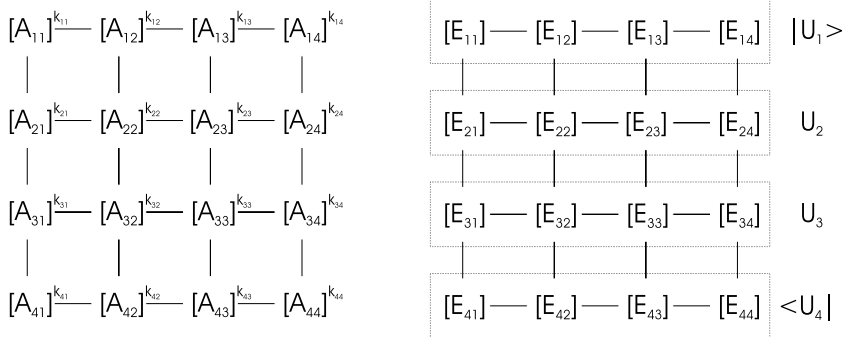
and thus associated with one lattice site i . All tensors possess one physical index k of dimension d and four virtual indices l, r, u , and d of dimension D . The scheme according to which these tensors are contracted mimics the underlying lattice structure: the four virtual indices of the tensors are related to the left, right, upper, and lower bond emanating from the corresponding lattice site. The coefficients of the PEPS are then formed by joining the tensors in such a way that all virtual indices related to the same bonds are contracted. This is illustrated in Fig. 23.3 (left) for the special case of a 4×4 square lattice. Assuming this contraction of tensors is performed by the function $\mathcal{F}(\cdot)$, the resulting PEPS can be written as

$$|\Psi\rangle = \sum_{k_1, \dots, k_M=1}^d \mathcal{F}([A_1]^{k_1}, \dots, [A_M]^{k_M}) |k_1, \dots, k_M\rangle.$$

This construction can be generalized to any lattice shape and dimension and one can show that any state can be written as a PEPS if we allow the bond dimension to become very large. In this way, we also resolve the problem of the entropy of blocks mentioned above, since now this entropy is proportional to the bonds that connect a block with the rest, and therefore to the area of the block. Note also that, in analogy to the MPS [19], the PEPS are guaranteed to be ground states of local Hamiltonians.

There has recently been a lot of progress in justifying this PEPS picture; Hastings has shown [20] that indeed every ground state of a local quantum spin Hamiltonian has an efficient representation in terms of a PEPS, i.e., one whose bond dimension D scales sub-exponentially with the number of spins under interest. Also, he has shown that all thermal states have an efficient representation in terms of MPOs. Thus we have identified the relevant manifold describing the low-energy physics of quantum spin systems. This can lead to many applications in theoretical condensed matter physics, as the questions about the possibility of some exotic phase of matter can now be answered by looking at the set of PEPS, hence skipping the bottleneck of simulation of ground states.

The family of PEPS also seems to be very relevant in the field of quantum information theory. For example, all quantum error-correcting codes such as Kitaev's toric code [21] exhibiting topological quantum order have a very

**FIGURE 23.3**

Left: Structure of the coefficients related to the state $|k_{11}, \dots, k_{44}\rangle$ in the PEPS $|\Psi_A\rangle$. The bonds represent the indices of the tensors $[A_i]^k$ that are contracted. Right: Structure of the contractions in $\langle\Psi_A|\Psi_A\rangle$. In this scheme, the first and last rows can be interpreted as MPS $|U_1\rangle$ and $\langle U_4|$ and the rows in between as MPOs U_2 and U_3 . The contraction of all tensors is then equal to $\langle U_4|U_3U_2|U_1\rangle$.

simple and exact description in terms of PEPS [22]. Furthermore, the PEPS-picture has been used to show the equivalence between different models of quantum computation [2]; more specifically, cluster states [23] have a simple interpretation in terms of PEPS, and this picture demystifies the inner workings of the one-way quantum computer.

23.2.2 Calculus of PEPS

We now show how to determine expectation values of operators in the state $|\Psi\rangle$. We consider a general operator $O = \prod_i O_i$ and define the $D^2 \times D^2 \times D^2 \times D^2$ tensors

$$[E_j^{O_j}]_{(ll')(rr')}^{(uu')(dd')} = \sum_{k,k'=1}^d \langle k | O_j | k' \rangle [A_j^*]_{lrud}^{k'} [A_j]_{l'r'u'd'}^k.$$

In this definition, the symbols (ll') , (rr') , (uu') , and (dd') indicate composite indices. We may interpret the 4 indices of this tensor as being related to the 4 bonds emanating from site j in the lattice. Then, $\langle\Psi|O|\Psi\rangle$ is formed by joining all tensors $E_j^{O_j}$ in such a way that all indices related to the same bonds are contracted, as in the case of the coefficients of PEPS. These contractions have a rectangular structure, as depicted in Fig. 23.3 (right). In terms of the function $\mathcal{F}(\cdot)$, the expectation value reads

$$\langle\Psi|O|\Psi\rangle = \mathcal{F}(E_1^{O_1}, \dots, E_N^{O_N}).$$

The contraction of all tensors $E_j^{O_j}$ according to this scheme requires a number of steps that scales exponentially with N , and makes calculations intractable

as the system grows larger. Because of this, an approximate method has to be used to calculate expectation values.

The approximate method suggested in [16] is based on MPS and MPOs. The main idea is to interpret the first and last row in the contraction scheme as MPS and the rows in between as MPOs. The horizontal indices thereby form the virtual indices, and the vertical indices are the physical indices. Thus, the MPS and MPOs have both virtual dimension and physical dimension equal to D^2 . Explicitly written, the MPS read

$$\begin{aligned} |U_1\rangle &= \sum_{\tilde{d}_1, \dots, \tilde{d}_L=1}^{D^2} \text{Tr} \left([E_{11}^{O_{11}}]^{1\tilde{d}_1} \cdots [E_{1L}^{O_{1L}}]^{1\tilde{d}_L} \right) |\tilde{d}_1, \dots, \tilde{d}_L\rangle, \\ \langle U_L| &= \sum_{\tilde{u}_1, \dots, \tilde{u}_L=1}^{D^2} \text{Tr} \left([E_{L1}^{O_{L1}}]^{\tilde{u}_1 1} \cdots [E_{LL}^{O_{LL}}]^{\tilde{u}_L 1} \right) \langle \tilde{u}_1, \dots, \tilde{u}_L|, \end{aligned}$$

and the MPO at row r is

$$U_r = \sum_{\substack{\tilde{u}_1, \dots, \tilde{u}_L=1 \\ \tilde{d}_1, \dots, \tilde{d}_L=1}}^{D^2} \text{Tr} \left([E_{r1}^{O_{r1}}]^{\tilde{u}_1 \tilde{d}_1} \cdots [E_{rL}^{O_{rL}}]^{\tilde{u}_L \tilde{d}_L} \right) |\tilde{u}_1, \dots, \tilde{u}_L\rangle \langle \tilde{d}_1, \dots, \tilde{d}_L|.$$

In terms of these MPS and MPOs, the expectation value is a product of an MPO and MPS:

$$\langle \Psi | O | \Psi \rangle = \langle U_L | U_{L-1} \cdots U_2 | U_1 \rangle.$$

The evaluation of this expression is intractable. With each multiplication of an MPO with an MPS, the virtual dimension increases by a factor of D^2 . Thus, after L multiplications, the virtual dimension is D^{2L} , which is exponential in the number of rows. However, the expression is reminiscent of the time evolution of an MPS. There, each multiplication with an MPO corresponds to one evolution step. The problem of the exponential increase of the virtual dimension is circumvented by restricting the evolution to the subspace of MPS with a certain virtual dimension \tilde{D} . This means that after each evolution step the resulting MPS is approximated by the “nearest” MPS with virtual dimension \tilde{D} . This approximation can be done efficiently, as described in Sec. 23.1.1. In this way, also $\langle \Psi | O | \Psi \rangle$ can be calculated efficiently: first, the MPS $|U_2\rangle$ is formed by multiplying the MPS $|U_1\rangle$ with MPO U_2 . The MPS $|U_2\rangle$ is then approximated by $|\tilde{U}_2\rangle$ with virtual dimension \tilde{D} . In this fashion the procedure is continued until $|U_{L-1}\rangle$ is obtained. The expectation value $\langle \Psi | O | \Psi \rangle$ is then

$$\langle \Psi | O | \Psi \rangle = \langle U_L | \tilde{U}_{L-1} \rangle.$$

Interestingly enough, this method to calculate expectation values can be adapted to develop very efficient algorithms to determine the ground states of 2D Hamiltonians and the time evolution of PEPS by extending DMRG and time-evolution schemes to 2D.

23.2.3 Variational Method with PEPS

Let us begin with an algorithm to determine the ground state of a Hamiltonian with short range interactions on a square $L \times L$ lattice. The goal is to determine

the PEPS $|\Psi\rangle$ with a given dimension D which minimizes the energy:

$$\langle H \rangle = \frac{\langle \Psi | H | \Psi \rangle}{\langle \Psi | \Psi \rangle}. \quad (23.4)$$

Following [12], the idea is to iteratively optimize the tensors A_i one by one while fixing all the other ones until convergence is reached. The crucial observation is the fact that the exact energy of $|\Psi\rangle$, and also its normalization, is a quadratic function of the components of the tensor A_i associated with a single lattice site i . Because of this, the optimal parameters A_i can be found by solving a generalized eigenvalue problem.

The challenge that remains is to calculate the matrix pair for which the generalized eigenvalues and eigenvectors shall be obtained. In principle, this is done by contracting all indices in the expressions $\langle \Psi | H | \Psi \rangle$ and $\langle \Psi | \Psi \rangle$ except those connecting to A_i . By interpreting the tensor A_i as a dD^4 -dimensional vector \mathbf{A}_i , these expressions can be written as

$$\langle \Psi | H | \Psi \rangle = \mathbf{A}_i^\dagger \mathcal{H}_i \mathbf{A}_i, \quad (23.5)$$

$$\langle \Psi | \Psi \rangle = \mathbf{A}_i^\dagger \mathcal{N}_i \mathbf{A}_i. \quad (23.6)$$

Thus, the minimum of the energy is attained by the generalized eigenvector \mathbf{A}_i of the matrix pair $(\mathcal{H}_i, \mathcal{N}_i)$ to the minimal eigenvalue μ :

$$\mathcal{H}_i \mathbf{A}_i = \mu \mathcal{N}_i \mathbf{A}_i.$$

It turns out that the matrix pair $(\mathcal{H}_i, \mathcal{N}_i)$ can be efficiently evaluated by the method developed for the calculation of expectation values: \mathcal{N}_i relies on the contraction of all but one tensor E_j^I , where I denotes the identity, according to the same rectangular scheme as before. The one tensor that has to be omitted is E_i^I , the tensor related to site i . Assuming this contraction is performed by the function $\mathcal{G}_i(\cdot)$, \mathcal{N}_i can be written as

$$[\mathcal{N}_i]_{lrud}^{k' l' r' u' d'} = \mathcal{G}_i(E_1^I, \dots, E_N^I)_{lrud}^{l' r' u' d'} \delta_{k'}^k.$$

If we join the indices $(klrud)$ and $(k'l'r'u'd')$, we obtain the $dD^4 \times dD^4$ matrix that fulfills Eq. (23.6). To evaluate $\mathcal{G}_i(\cdot)$ efficiently, we proceed in the same way as before by interpreting the rows in the contraction structure as MPS and MPOs. First, we join all rows that lie above site i by multiplying the topmost MPS $|U_1\rangle$ with subjacent MPO and reducing the dimension after each multiplication to \tilde{D} . Then, we join all rows lying below i by multiplying $\langle U_L|$ with the adjacent MPO and reducing the dimension as well. We end up with two MPS of virtual dimension \tilde{D} , which we can contract efficiently with all but one of the tensors E_j^I lying in the row of site i .

The effective Hamiltonian \mathcal{H}_i can be determined in an analogous way, but here the procedure has to be repeated for every term in the Hamiltonian, i.e., on the order of $2N$ times in the case of nearest-neighbor interactions. Assuming

a single term in the Hamiltonian has the tensor-product structure $H^s \equiv \prod_i h_i^s$, the effective Hamiltonian \mathcal{H}_i^s corresponding to this term is obtained as

$$[\mathcal{H}_i^s]_{lrud}^{k' l' r' u' d'} = \mathcal{G}_i(E_1^{h_1^s}, \dots, E_N^{h_N^s})_{lrud}^{l' r' u' d'} [h_i^s]_{k'}^k.$$

The complete effective Hamiltonian \mathcal{H}_i that fulfills Eq. (23.5) is then

$$\mathcal{H}_i = \sum_s \mathcal{H}_i^s.$$

Thus, both the matrices \mathcal{N}_i and \mathcal{H}_i are directly related to the expressions $\mathcal{G}_i(E_1^I, \dots, E_N^I)$ and $\mathcal{G}_i(E_1^{h_1^s}, \dots, E_N^{h_N^s})$. However, these expressions can be evaluated efficiently using the approximate method introduced before for the calculation of expectation values. Therefore, the optimal A_i can be determined, and one can proceed with the following site, iterating the procedure until convergence.

23.2.4 Time Evolution with PEPS

We now describe how time evolution can be simulated on a PEPS. We will assume that the Hamiltonian only couples nearest neighbors, although more general settings can be considered. The principle of simulating a time evolution step is as follows: first, a PEPS $|\Psi_A^0\rangle$ with physical dimension $d = 2$ and virtual dimension D is chosen as a starting state. This state is evolved by the time evolution operator $U = e^{-iH\delta t}$ (we assume $\hbar = 1$) to yield another PEPS $|\Psi_B\rangle$ with a virtual dimension D_B increased by a factor η :

$$|\Psi_B\rangle = U|\Psi_A^0\rangle.$$

The virtual dimension of this state is then reduced to D by calculating a new PEPS $|\Psi_A\rangle$ with virtual dimension D that has minimal distance to $|\Psi_B\rangle$. This new PEPS is the starting state for the next time evolution step. The crucial point in simulating time evolution with PEPS is thus the development of an efficient algorithm for reducing the virtual dimension of a PEPS.

Before formulating this algorithm, let us recite how to express the product $U|\Psi_A^0\rangle$ in terms of a PEPS. This is done by means of a Trotter approximation: first, the interaction terms in H are classified as *horizontal* and *vertical* according to their orientation and as *even* and *odd* depending on whether the interaction is between even-odd or odd-even rows, or columns. The Hamiltonian can then be decomposed into a *horizontal-even*, a *horizontal-odd*, a *vertical-even*, and a *vertical-odd* part:

$$H = H_{he} + H_{ho} + H_{ve} + H_{vo}.$$

The single-particle operators of the Hamiltonian can be incorporated in one of the four parts.⁹ Using the Trotter approximation, the time evolution oper-

⁹Note that different Trotter decompositions are again possible, e.g., grouping all Pauli operators of the same kind in 3 different groups as we discussed earlier; in some cases this leads to a clear computational advantage.

ator U can be written as a product of four evolution operators:

$$U = e^{-iH\delta t} \approx e^{-iH_{\text{he}}\delta t} e^{-iH_{\text{ho}}\delta t} e^{-iH_{\text{ve}}\delta t} e^{-iH_{\text{vo}}\delta t}. \quad (23.7)$$

Since each of the four parts of the Hamiltonian consists of a sum of commuting terms, each evolution operator equals a product of two-particle operators w_{ij} acting on neighboring sites i and j . These two-particle operators have a Schmidt decomposition consisting of, say, η terms:

$$w_{ij} = \sum_{\rho=1}^{\eta} u_i^{\rho} \otimes v_j^{\rho}.$$

One such two-particle operator w_{ij} applied to the PEPS $|\Psi_A^0\rangle$ modifies the tensors A_i^0 and A_j^0 associated with sites i and j as follows: assuming the sites i and j are horizontal neighbors, A_i^0 has to be replaced by

$$[B_i]_{l(r\rho)ud}^k = \sum_{k'=1}^d [u_i^{\rho}]_{k'}^k [A_i^0]_{lrud}^{k'},$$

and A_j^0 becomes

$$[B_j]_{(l\rho)rud}^k = \sum_{k'=1}^d [v_j^{\rho}]_{k'}^k [A_j^0]_{lrud}^{k'}.$$

These new tensors have a joint index related to the bond between sites i and j . This joint index is composed of the original index of dimension D and the index ρ of dimension η that enumerates the terms in the Schmidt decomposition. Thus, the effect of the two-particle operator w_{ij} is to increase the virtual dimension of the bond between sites i and j by a factor of η . Consequently, $e^{-iH_{\text{he}}\delta t}$ and $e^{-iH_{\text{ho}}\delta t}$ increase the dimension of every second horizontal bond by a factor of η ; $e^{-iH_{\text{ve}}\delta t}$ and $e^{-iH_{\text{vo}}\delta t}$ do the same for every second vertical bond. By applying all four evolution operators consecutively, we have found an approximate form of the time evolution operator U that, when applied to a PEPS $|\Psi_A^0\rangle$, yields another PEPS $|\Psi_B\rangle$ with a virtual dimension multiplied by a constant factor η .

The aim of the approximate algorithm is now to optimize the tensors A_i related to a PEPS $|\Psi_A\rangle$ with virtual dimension D , such that the distance between $|\Psi_A\rangle$ and $|\Psi_B\rangle$ tends to a minimum. The function to be minimized is thus

$$K(A_1, \dots, A_M) = \|\langle \Psi_A | - |\Psi_B \rangle\|^2.$$

This function is non-convex with respect to all parameters $\{A_1, \dots, A_M\}$. However, due to the special structure of PEPS, it is quadratic in the parameters A_i associated with *one* lattice site i . Because of this, the optimal parameters A_i can be found by solving a system of linear equations. The concept of the algorithm is to do this one-site optimization site-by-site until convergence is reached.

The coefficient matrix and the inhomogeneity of the system of linear equations can be calculated efficiently using the method developed for the calculation of expectation values. In principle, they are obtained by contracting all indices in the expressions for the scalar products $\langle \Psi_A | \Psi_A \rangle$ and $\langle \Psi_A | \Psi_B \rangle$ except

those connecting to A_i . By interpreting the tensor A_i as a dD^4 -dimensional vector \mathbf{A}_i , these scalar products can be written as

$$\langle \Psi_A | \Psi_A \rangle = \mathbf{A}_i^\dagger \mathcal{N}_i \mathbf{A}_i, \quad (23.8)$$

$$\langle \Psi_A | \Psi_B \rangle = \mathbf{A}_i^\dagger \mathcal{W}_i. \quad (23.9)$$

Since

$$K = \langle \Psi_B | \Psi_B \rangle + \langle \Psi_A | \Psi_A \rangle - 2\text{Re}\langle \Psi_A | \Psi_B \rangle,$$

the minimum is attained as

$$\mathcal{N}_i \mathbf{A}_i = \mathcal{W}_i.$$

The efficient calculation of \mathcal{N}_i was described in Sec. 23.2.3. The scalar product $\langle \Psi_A | \Psi_B \rangle$ and the inhomogeneity \mathcal{W}_i are calculated in an efficient way following the same ideas. First, the $DD_B \times DD_B \times DD_B \times DD_B$ tensors

$$[F_j]_{(ll')(rr')}^{(uu')(dd')} = \sum_{k=1}^d [A_j^*]_{lrud}^k [B_j]_{l'r'u'd'}^k$$

are defined. The scalar product $\langle \Psi_A | \Psi_B \rangle$ is then obtained by contracting all tensors F_j according to the previous scheme, which is performed by the function $\mathcal{F}(\cdot)$:

$$\langle \Psi_A | \Psi_B \rangle = \mathcal{F}(F_1, \dots, F_M).$$

The inhomogeneity \mathcal{W}_i relies on the contraction of all but one of the tensors F_j , namely the function $\mathcal{G}_i(\cdot)$, in the sense that

$$[\mathcal{W}_i]_{lrud}^k = \sum_{l'r'u'd'=1}^D \mathcal{G}_i(F_1, \dots, F_M)_{lrud}^{l'r'u'd'} [B_i]_{l'r'u'd'}^k.$$

Joining all indices ($klrud$) in the resulting tensor leads to the vector of length dD^4 that fulfills Eq. (23.9). Thus, both the scalar product $\langle \Psi_A | \Psi_B \rangle$ and the inhomogeneity \mathcal{W}_i are directly related to the expressions $\mathcal{F}(F_1, \dots, F_M)$ and $\mathcal{G}_i(F_1, \dots, F_M)$. However, these expressions can be evaluated efficiently using the approximate method from Sec. 23.2.3.

Even though the principle of simulating a time evolution step has now been laid out, the implementation in this form is numerically expensive. Thus we append some notes about how to make the simulation more efficient.

1. Partitioning of the evolution: The number of required numerical operations decreases significantly as one time evolution step is partitioned into 4 sub-steps: first the state $|\Psi_A^0\rangle$ is evolved by $e^{-iH_{\text{vo}}\delta t}$ only and the dimension of the increased bonds is reduced back to D . Next, evolutions according to $e^{-iH_{\text{ve}}\delta t}$, $e^{-iH_{\text{ho}}\delta t}$, and $e^{-iH_{\text{he}}\delta t}$ follow. Even though the partitioning increases the number of evolution steps by a factor of 4, the number of multiplications in one evolution step decreases by a factor of η^3 .

2. Optimization of the contraction order: Most critical for the efficiency of the numerical simulation is the order in which the contractions are performed. We have optimized the order in such a way that the scaling of the number of multiplications with the virtual dimension D is minimal. For this, we assume

that the dimension \tilde{D} that tunes the accuracy of the approximate calculation of \mathcal{N}_i and \mathcal{W}_i is proportional to D^2 , i.e., $\tilde{D} = \kappa D^2$. The number of required multiplications is then of order¹⁰ $\kappa^2 D^{10} L^2$ and the required memory scales as $d\eta\kappa^2 D^8$.

3. Optimization of the starting state: The number of sweeps required to reach convergence depends on the choice of the starting state for the optimization. The idea for finding a good starting state is to reduce the bonds with increased virtual dimension ηD by means of a Schmidt decomposition. This is done as follows: assuming the bond is between the horizontal neighboring sites i and j , the contraction of the tensors associated with these sites, B_i and B_j , along the bond $i-j$ forms the tensor

$$[\mathcal{M}_{ij}]_{lud}^{k'} = \sum_{\rho=1}^{D\eta} [B_i]_{l\rho ud}^k [B_j]_{\rho r' u' d'}^{k'}.$$

By joining the indices $(klud)$ and $(k'r'u'd')$, this tensor can be interpreted as a $dD^3 \times dD^3$ matrix. The Schmidt decomposition of this matrix is

$$\mathcal{M}_{ij} = \sum_{\rho=1}^{dD^3} c_{\rho} \mathcal{A}_i^{\rho} \otimes \mathcal{A}_j^{\rho},$$

with Schmidt coefficients $c_{\rho} \geq 0$ and corresponding matrices \mathcal{A}_i^{ρ} and \mathcal{A}_j^{ρ} . We can relate these matrices to a new pair of tensors A_i^0 and A_j^0 associated with sites i and j :

$$\begin{aligned} [A_i^0]_{l\rho ud}^k &= \sqrt{c_{\rho}} [\mathcal{A}_i^{\rho}]_{lud}^k, \\ [A_j^0]_{\rho r' u' d'}^{k'} &= \sqrt{c_{\rho}} [\mathcal{A}_j^{\rho}]_{rud}^{k'}. \end{aligned}$$

The virtual dimension of these new tensors related to the bond between sites i and j is equal to the number of terms in the Schmidt decomposition. Since these terms are weighted with the Schmidt coefficients c_{ρ} , it is justified to keep only the D terms with coefficients of largest magnitude. Then, the contraction of the tensors A_i^0 and A_j^0 along the bond $i-j$ with dimension D yields a good approximation to the true value \mathcal{M}_{ij} :

$$[\mathcal{M}_{ij}]_{lud}^{k'} \approx \sum_{\rho=1}^D [A_i^0]_{l\rho ud}^k [A_j^0]_{\rho r' u' d'}^{k'}.$$

This method applies to all bonds with increased dimension and provides us with the starting state for the optimization.

23.2.5 Examples

Let us now illustrate the variational methods with some examples. Models to which the PEPS algorithms have already been applied include the Heisenberg

¹⁰The scaling D^{10} is obtained when at all steps in the algorithm, a sparse matrix algorithm is used. In particular, we have to use an iterative sparse method for solving the linear set of equations in the approximation step.

antiferromagnet [16], the Shastry-Sutherland model [24] and the system of hard-core bosons in a 2D optical lattice [17]. In the following, we describe the results for the latter system, which include calculations of ground state properties and studies of time evolution after sudden changes in the parameters.

The system of bosons in a 2D optical lattice is characterized by the Bose-Hubbard Hamiltonian

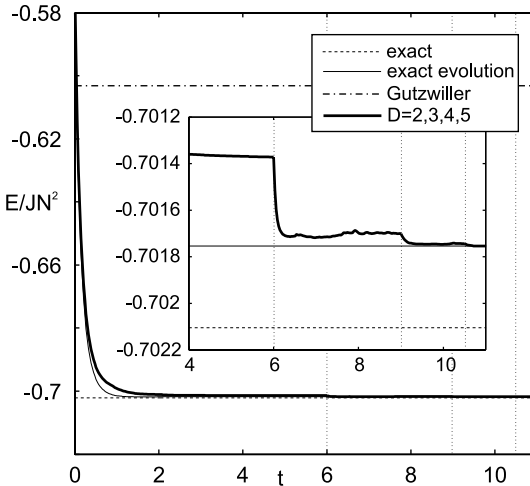
$$H = -J \sum_{\langle i,j \rangle} (a_i^\dagger a_j + h.c.) + \frac{U}{2} \sum_i \hat{n}_i (\hat{n}_i - 1) + \sum_i V_i \hat{n}_i,$$

where a_i^\dagger and a_i are the creation and annihilation operators on site i and $\hat{n}_i = a_i^\dagger a_i$ is the number operator. This Hamiltonian describes the interplay between the kinetic energy due to the next-neighbor hopping with amplitude J and the repulsive on-site interaction U of the particles. The last term in the Hamiltonian models the harmonic confinement of magnitude $V_i = V_0(i - i_0)^2$. The experimental context of H is described in Chap. 19. Since the total number of particles $\hat{N} = \sum_i \hat{n}_i$ is a symmetry of H , the ground state will have a fixed number of particles. This number can be chosen by appending the term $-\mu \hat{N}$ to the Hamiltonian and tuning the chemical potential μ . In the limit of hard-core interaction, $U/J \rightarrow \infty$, two particles are prevented from occupying a single site. This limit is especially interesting in 1D where the particles form the *Tonks-Girardeau gas* [25, 26]. The particles in this gas are strongly correlated, which leads to algebraically decaying correlation functions. In 2D and without the harmonic potential, the model was studied in detail in [27]. In the hard-core limit, the Bose-Hubbard model is equivalent to a spin system with XX interactions described by the Hamiltonian

$$H = -\frac{J}{2} \sum_{\langle i,j \rangle} (\sigma_x^{(i)} \sigma_x^{(j)} + \sigma_y^{(i)} \sigma_y^{(j)}) + \frac{1}{2} \sum_i (V_i - \mu) \sigma_z^{(i)}.$$

Here, $\sigma_x^{(i)}$, $\sigma_y^{(i)}$, and $\sigma_z^{(i)}$ denote the Pauli-operators acting on site i . This Hamiltonian has a structure that can be simulated with the PEPS algorithm: it describes L^2 physical systems of dimension $d = 2$ on an $L \times L$ square lattice.

In Fig. 23.4, the energy in the case of a 4×4 lattice is plotted as the system undergoes imaginary-time evolution. A time step $\delta t = -0.03 i$ is assumed and the magnitude of the harmonic confinement, in units of the tunneling constant, is chosen as $V_0/J = 36$. In addition, the chemical potential is tuned to $\mu/J = 3.4$ so that the ground state has particle number $\langle \hat{N} \rangle = 4$. With this configuration, the imaginary-time evolution is performed both exactly and variationally with PEPS. As a starting state a product state is used that represents a Mott-like distribution with 4 particles arranged in the center of the trap and none elsewhere. The variational calculation is performed with $D = 2$ first until convergence is reached; then, evolutions with $D = 3, 4$, and 5 follow. At the end, a state is obtained that is very close to the one found by exact evolution. The difference in energy is $|E_{D=5} - E_{\text{exact}}| \simeq 6.4614 \cdot 10^{-5} J$. For comparison, the exact ground-state energy obtained by an eigenvalue calcu-

**FIGURE 23.4**

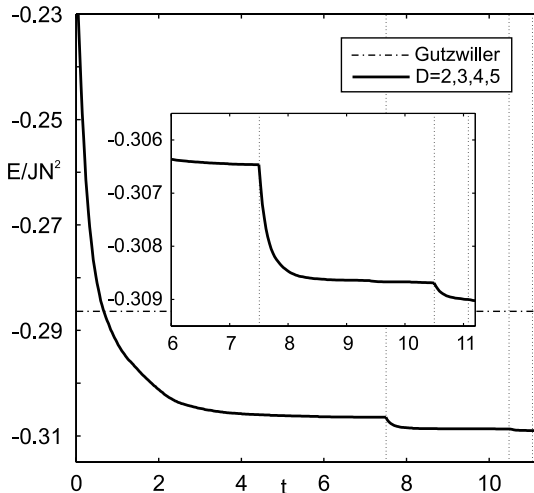
Energy as a function of time for the imaginary-time evolution of the system of hard-core bosons on a 4×4 lattice. The evolutions are performed sequentially with PEPS of virtual dimension $D = 2, 3, 4, 5$. The times at which D is increased are indicated by vertical lines. For comparison, the exact ground-state energy, the exact imaginary-time evolution and the energy of the optimal Gutzwiller ansatz are included. Taken from [17].

lation and the energy of the optimal Gutzwiller ansatz¹¹ are also included in Fig. 23.4. The difference between the exact result and the results of the imaginary-time evolution is due to the Trotter error and is of order $O(\delta t^2)$. The energy of the optimal Gutzwiller ansatz is well separated from the exact ground-state energy and the results of the imaginary-time evolution.

In Fig. 23.5, the energy as a function of time is plotted for the imaginary-time evolution on an 11×11 lattice. Again, a time step $\delta t = -0.03 i$ is assumed for the evolution. The other parameters are set as follows: the ratio between harmonic confinement and the tunneling constant is chosen to be $V_0/J = 100$ and the chemical potential is tuned to $\mu/J = 3.8$ such that the total number of particles $\langle \hat{N} \rangle = 14$. The starting state for the imaginary-time evolution is, similar to before, a Mott-like distribution with 14 particles arranged in the center of the trap. This state is evolved within the subset of PEPS with $D = 2, 3, 4, 5$. As can be gathered from the plot, this evolution shows a definite convergence. In addition, the energy of the final PEPS lies well below the energy of the optimal Gutzwiller ansatz.

An application of the time evolution algorithm with PEPS is found in the study of dynamic properties of hard-core bosons on a lattice of size 11×11 .

¹¹The Gutzwiller ansatz assumes a product state between sites, and so has zero spatial entanglement.

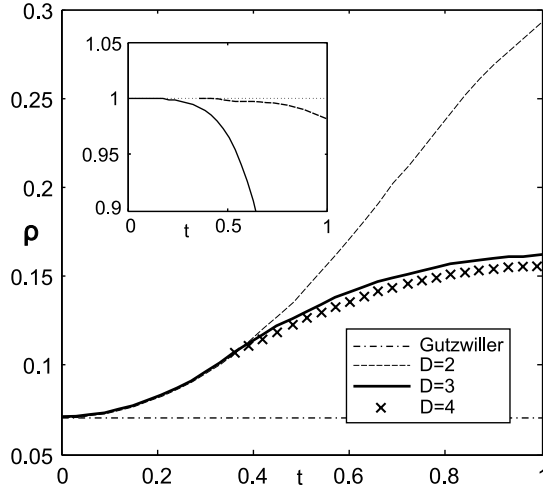
**FIGURE 23.5**

Energy as a function of time for the imaginary-time evolution of the system of hard-core bosons on an 11×11 lattice. The evolutions are performed sequentially with PEPS of virtual dimension $D = 2, 3, 4, 5$. The times at which D is increased are indicated by vertical lines. For comparison, the energy of the optimal Gutzwiller ansatz is included. Taken from [17].

Here, the response of this system to sudden changes in the parameters is investigated and the numerical results are compared to those obtained by a Gutzwiller ansatz. An interesting property that is observed is the fraction of particles that are condensed. For interacting and finite systems, this property is best measured by the condensate density ρ , which is defined as largest eigenvalue of the correlation matrix $\langle a_i^\dagger a_j \rangle$.

In Fig. 23.6, the evolution of a Mott distribution with 14 particles arranged in the center of the trap is studied. It is assumed that $V_0/J = 100$, $\mu/J = 3.8$ and $\delta t = 0.03$. To assure that the results are accurate, the following procedure was used for simulating time evolution: first, the simulation has been performed using PEPS with $D = 2$ and $D = 3$ until the overlap between these two states fell below a certain value. Then, the simulation has been continued using PEPS with $D = 3$ and $D = 4$ as long as the overlap between these two states was close to 1. The results of this calculation are illustrated in Fig. 23.6. We observe a definite increase in the condensate fraction. The Gutzwiller ansatz is in contrast to this result since it predicts that the condensate density remains constant. The inset in Fig. 23.6 shows the overlap of the $D = 2$ with the $D = 3$ PEPS and the $D = 3$ with the $D = 4$ PEPS.

Finally, we make a few comments about the accuracy of the algorithm. One indicator for the accuracy is the distance between the time-evolved state and the state with reduced virtual dimension. For the time evolution of the Mott

**FIGURE 23.6**

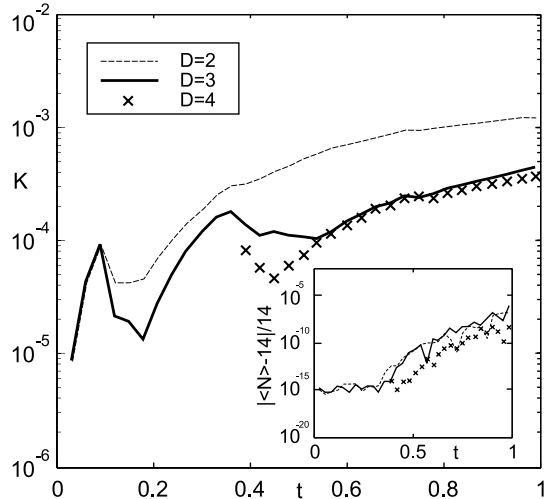
Time evolution of the condensate density starting from a Mott distribution with 14 particles arranged in the center of the trap. The magnitude of the trapping potential is $V_0/J = 100$. For the evolution, the Gutzwiller ansatz and PEPS with $D = 2, 3, 4$ are used. The inset shows the overlap between the $D = 2$ and $D = 3$ PEPS (solid curve) and the $D = 3$ and $D = 4$ PEPS (dashed curve). Taken from [17].

distribution that was discussed before, this quantity is plotted in Fig. 23.7. We find values of order 10^{-3} for $D = 2$ and 10^{-4} for $D = 3$ and $D = 4$. Another quantity that is monitored is the total number of particles $\langle \hat{N} \rangle$. Since $\langle \hat{N} \rangle$ is supposed to be conserved during the whole evolution, its fluctuations indicate the reliability of the algorithm. This is shown in Fig. 23.7; fluctuations are at most of order 10^{-5} .

23.2.6 PEPS and Fermions

The critical reader should by now have complained that we are only talking about spin systems but not about fermionic systems. Indeed, one of the long-term goals of the numerical approaches discussed here is to be able to simulate, e.g., the Fermi-Hubbard model in the relevant parameter regime.

The methods that we discussed in 1D are perfectly applicable to fermionic systems, as the amazing Jordan-Wigner transformation allows one to map a local Hamiltonian of fermions to a local Hamiltonian of spins, and we know that the MPS techniques work provably well on the latter. However, the big problem is that the Jordan-Wigner transformation only works in 1D: if we use it on a 2D lattice, a local Hamiltonian of fermions is mapped to a highly nonlocal Hamiltonian of spins. On the other hand, PEPS are designed to have

**FIGURE 23.7**

Distance K between the time-evolved state and the state with reduced virtual dimension. The virtual dimensions $D = 2$, $D = 3$, and $D = 4$ are included. The distance is plotted for the evolution of a Mott distribution with $N = 14$, as explained in Fig. 23.6. (Inset) Deviation of the particle number from the value 14. Taken from [17].

extremal local properties; if the Hamiltonian contains a lot of strong nonlocal terms, we can not expect PEPS to exhibit the corresponding extremal long-range correlations. Therefore, the natural question to ask is whether there exists a generalization of the Jordan-Wigner transformation to higher dimensions. This was indeed shown to be possible in [28]: given any local Hamiltonian in terms of fermionic operators such as the Hubbard model in 2D or 3D, then there exists a local spin 3/2 Hamiltonian whose low-energy sector corresponds exactly to the original fermionic Hamiltonian. The conclusion is that the PEPS methods are equally applicable to quantum spin systems as to fermionic systems.

Another and more efficient approach is to make use of quantum numbers. In general, it is difficult to keep track of quantum numbers on a 2D lattice. However, an exception is given by the parity of the occupation number between two sites: by blocking the PEPS tensors in a specific way, one can invoke the even or odd occupation number between any sites and as such eliminate the fact that spurious effective long-range interactions arise in fermionic lattice systems [14]. This is very relevant as it leads to a huge speed-up of the algorithms for these systems.

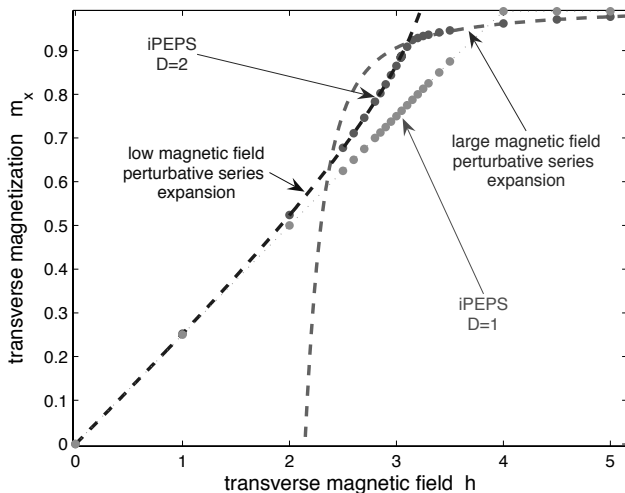
23.2.7 PEPS on Infinite Lattices

In parallel with 1D MPS, we can also explicitly make use of the translational symmetry in the class of PEPS to simulate low-energy properties of infinite lattices. A naive procedure is to impose complete translational symmetry and do a line-search, such as conjugate gradient, within the parameter space of the tensor; this can be done as expectation values of the corresponding PEPS can be calculated using the appropriate 1D infinite algorithms discussed above. However, the cost function is highly nonlinear and the number of parameters grows very fast with D , such that these brute-force methods will typically lead to local minima. A smarter approach is to use imaginary-time evolution, but keep the translational invariance. It was already shown how to do this in the 1D case, where a particular kind of Trotter expansion leads to a translationally invariant MPO, and we can repeat this in 2D, leading to a translationally invariant PEPS operator. The only nontrivial part is the question of how to reduce the bond dimension after one time evolution step; but here we can again take inspiration from the 1D case, and ask the question which projectors we can put on the bonds such as to maximize the overlap of the projected one with the evolved one.

A more straightforward approach is to assume an $\dots ABAB\dots$ symmetry where each tensor A has all its neighboring tensors B and vice versa.¹² Again, imaginary-time evolution can be used to find the ground state; this was first studied in the paper [29] where the term iPEPS (infinite PEPS) was coined. The idea is as follows: take the even-odd-horizontal-vertical Trotter decomposition as discussed previously, and next evolve with just one operator acting on two nearest-neighbor sites. Effectively, this increases the bond dimension between these two sites (A and B). The environment of these spins can be readily calculated using the infinite 1D translationally invariant methods discussed above, and then the variational problem becomes the problem of finding new A' and B' that approximate the one with higher bond optimally. Again, this can be done using the alternating least squares method. Subsequently, we replace all tensors A and B with A' and B' , and continue until convergence. The last step, replacing all tensors with the optimal local ones, is only justified if the time step in the imaginary-time evolution is very small, but in practice this seems to work very well, as illustrated in Fig. 23.8.¹³

¹²This is only possible for bipartite lattices; a different choice can be made for different types of lattices.

¹³ $D = 3$ leads to results that could hardly be distinguished from those for $D = 2$ in this figure.

**FIGURE 23.8**

Magnetization $m_x(h)$ in the ground state $|\Psi_h\rangle$ of the two-dimensional quantum Ising model with transverse magnetic field. A trivial iPEPS (inner dimension $D = 1$) produces a magnetization that grows essentially linearly with the magnetic field until it saturates. Instead, the simplest non-trivial iPEPS (inner dimension $D = 2$) produces a magnetization curve that overlaps with the results of series expansions for both small and large magnetic fields. Notice that around $h \approx 3.1$ the derivative of the magnetization $m_x(h)$ changes suddenly. Taken from [29].

23.3 Conclusions

Recent progress in quantum information theory has provided scientists with new mathematical tools to describe and analyze many-body quantum systems. These new tools have given rise to novel descriptions of the quantum states that appear in nature, which are very efficient both in terms of the number of variables used to parameterize states and the number of operations to determine expectation values of typical observables. In a sense, they allow us to describe the corner of Hilbert space where relevant states are located, with an effort that only scales polynomially with the number of particles, as opposed to the exponential scaling resulting from other descriptions. These results have automatically led to a diverse set of new powerful algorithms to simulate quantum systems. These algorithms allow us to describe ground states, thermal equilibrium, low excitations, dynamics, random systems, etc., of many-body quantum systems, and thus to attack new kinds of problems

obtaining very precise results. Moreover, the methods work in one or more spatial dimensions. In the first case, the success of some of those methods is directly related to the extraordinary performance of DMRG. In higher dimensions, they also give rise to a better understanding of several many-body systems for which a description has not been possible with existing techniques.

These algorithms bear the potential to attack many standing problems in condensed matter physics, like solving the Fermi-Hubbard model, and to shed light on mysteries like high-temperature superconductivity. In addition, they present a new point of view for looking at problems in more distant fields like quantum field theory or quantum chemistry, and could lead to exciting new insights in these fields.

Bibliography

- [1] J. I. Cirac and P. Zoller, Physics Today **57**, 38 (2004).
- [2] F. Verstraete and I. J. Cirac, Phys. Rev. A **70**, 060302 (2004).
- [3] M. A. Cazalilla and J. B. Marston, Phys. Rev. Lett. **88**, 256403 (2002); H. G. Luo, T. Xiang, and X. Q. Wang, Phys. Rev. Lett. **91**, 049701 (2003); M. A. Cazalilla and J. B. Marston, Phys. Rev. Lett. **91**, 049702 (2003).
- [4] S. R. White and A. E. Feiguin, Phys. Rev. Lett **93**, 076401 (2004); A. J. Daley, C. Kollath, U. Schollwöck, and G. Vidal, J. Stat. Mech.: Theor. Exp., P04005 (2004).
- [5] G. Vidal, Phys. Rev. Lett **93**, 040502 (2004).
- [6] F. Verstraete, J. J. García-Ripoll, and J. I. Cirac, Phys. Rev. Lett **93**, 207204 (2004).
- [7] A. Feiguin and S. White, Phys. Rev. B **72**, 220401 (2005); D. Gobert, C. Kollath, U. Schollwöck, and G. Schütz, Phys. Rev. E **71**, 036102 (2005).
- [8] J. J. García-Ripoll, New J. Phys. **8**, 305 (2006).
- [9] U. Schollwöck and S. R. White, in G. G. Batrouni and D. Poilblanc (eds.): Effective models for low-dimensional strongly correlated systems, p. 155, AIP, Melville, New York (2006).
- [10] M. Suzuki, Phys. Lett. A **146**, 319 (1990); M. Suzuki, J. Math. Phys. **32**, 400 (1991).
- [11] A. T. Sornborger and E. D. Stewart, Phys. Rev. A **60**, 156 (1999); I. P. Omelyan, I. M. Mryglod, and R. Folk, Comp. Phys. Comm. **146**, 188 (2002).

- [12] F. Verstraete, D. Porras, and J. I. Cirac, Phys. Rev. Lett. **93**, 227205 (2004).
- [13] F. Verstraete, J. I. Cirac, and V. Murg, Adv. Phys. **57** (2), 143 (2008).
- [14] B. Pirvu, F. Verstraete, V. Murg and J. I. Cirac, New J. Phys. **12**, 025012 (2010).
- [15] G. Vidal, Phys. Rev. Lett. **98**, 070201 (2007).
- [16] F. Verstraete and J. I. Cirac, arXiv:cond-mat/0407066v1 (2004).
- [17] V. Murg, F. Verstraete, and J. I. Cirac, Phys. Rev. A **75**, 033605 (2007).
- [18] Y. Hieida, K. Okunishi, and Y. Akutsu, New J. Phys. **1**, 7 (1999); K. Okunishi and T. Nishino, Prog. Theor. Phys. **103**, 541 (2000); T. Nishino, K. Okunishi, Y. Hieida, N. Maeshima, and Y. Akutsu, Nucl. Phys. B **575**, 504 (2004); Y. Nishio, N. Maeshima, A. Gendiar, and T. Nishino, arXiv:cond-mat/0401115v1 (2004); H. Niggeman, A. Klümper, and J. Zittartz, Z. Phys. B **104**, 103 (1997); M. A. Martin-Delgado, M. Roncaglia, and G. Sierra, Phys. Rev. B **64**, 075117 (2001).
- [19] M. Fannes, B. Nachtergaele, and R. F. Werner, Comm. Math. Phys. **144**, 443 (1992).
- [20] M. B. Hastings, Phys. Rev. B **76**, 035114 (2007).
- [21] A. Kitaev, Annals of Phys. **303**, 2 (2003).
- [22] F. Verstraete, M. M. Wolf, D. Perez-Garcia, and J. I. Cirac, Phys. Rev. Lett. **96**, 220601 (2006).
- [23] R. Raussendorf and H. J. Briegel, Phys. Rev. Lett **86**, 5188 (2001).
- [24] A. Isacsson and O. F. Syljuasen, Phys. Rev. E **74**, 026701 (2006).
- [25] M. Girardeau, J. Math. Phys. **1**, 516 (1960).
- [26] B. Paredes, A. Widera, V. Murg, O. Mandel, S. Fölling, I. Cirac, G. V. Shlyapnikov, T. W. Hänsch, and I. Bloch, Nature **429**, 277 (2004).
- [27] T. Kennedy, E. H. Lieb, and B. S. Shastry, Phys. Rev. Lett. **61**, 2582 (1988).
- [28] F. Verstraete and J. Cirac, J. Stat. Mech. **0509**, P012 (2005).
- [29] J. Jordan, R. Orus, G. Vidal, F. Verstraete, and J. I. Cirac, Phys. Rev. Lett. **101**, 250602 (2008).
- [30] S. R. White and A. Chernyshev, Phys. Rev. Lett. **99**, 127004 (2007).

24

Continuous-Time Monte Carlo Methods for Quantum Impurity Problems and Dynamical Mean Field Calculations

Philipp Werner

Theoretische Physik, ETH Zurich, 8093 Zürich, Switzerland

Andrew J. Millis

Department of Physics, Columbia University, 538 West, 120th Street, New York, NY 10027, U.S.A.

An atom or molecule embedded in an infinite host material defines a quantum impurity model (QIM). Exchange with the host causes the impurity to make transitions between different quantum states, leading to a nontrivial dynamics which may be described as a quantum field theory in zero space and one time dimension. QIMs exhibit many phenomena of intrinsic theoretical interest including quantum phase transitions (QPTs). The development over the past 15 years of dynamical mean field theory (DMFT) shows that they also serve as an auxiliary problem from whose solution important information relating to the physics of interacting lattice models can be obtained. Numerical simulation of these models remains a challenging task but the development of diagrammatic Monte Carlo techniques over the last few years has led to significant improvements in efficiency and flexibility. Highly precise results on few-orbital models can be computed and large Hilbert-space multi-orbital models are now within reach. This chapter provides an overview of recent developments in quantum Monte Carlo methods and their application to multi-orbital systems. It presents both the weak-coupling approach, which scales favorably with system size and allows the efficient simulation of large impurity clusters, and the strong-coupling approach, which can handle QIMs with strong interactions.

24.1 Quantum Impurity Models

A QIM consists of three parts: a finite degree-of-freedom system called the *impurity*; one or more infinite reservoirs, called the *baths*, which are typically

characterized by independent particle correlations; and an impurity-bath coupling. The QIM concept has broad applicability across the sciences, from the paradigmatic Kondo problem of condensed matter physics to the Redfield theory of chemical reaction dynamics. They are important in modeling issues as diverse as the effects of dissipative environments on qubits for quantum computers and the conductance of prospective molecular devices. QIMs have assumed an additional importance in condensed matter physics as auxiliary problems whose solution, in combination with an appropriate self-consistency condition, provides important information on the physics of bulk correlated electron materials [1]. Most recently developments in nanoscience have focused attention on the non-equilibrium properties of QIMs, and on potentially new classes of non-equilibrium QPTs [2].

QIMs were historically important to the subject of QPTs. The change in behavior between the ferromagnetic and antiferromagnetic Kondo problems and the closely related localization/delocalization transitions in the macroscopic quantum tunneling problems were among the first examples of non-mean-field QPTs to be understood, and these results were later generalized to higher spin, more channels, and multiple impurities.

From a fundamental theoretical point of view, QIMs are quantum field theories in 0 space and 1 time dimension, and their universal properties are believed to be solvable using the methods of boundary conformal field theory. However, numerical studies remain important. Many questions of interest involve non-universal, or at least sub-leading behavior for which theoretical methods are absent or very difficult to implement. Furthermore, work aimed at explicating correlated electron physics and at understanding the properties of nanostructures has motivated research into more complicated QIMs, which seem to exhibit new, or at least as yet unclassified, quantum critical points (QCPs).

The Hamiltonian of a QIM may be written

$$H = H_{\text{loc}} + H_{\text{bath}} + H_{\text{mix}}. \quad (24.1)$$

In this chapter we focus on those QIMs in which the impurity H_{loc} can be expressed in terms of a finite set of fermion fields labeled by a finite set of discrete quantum numbers a , representing, e.g., spin and orbital indices, the reservoirs may be modeled as free electron metals labeled by a continuous quantum number p and a set of discrete quantum numbers ν , representing, e.g., spin and channel degrees of freedom, and the impurity-bath coupling involves exchange of electrons between the impurity and the bath. Thus explicitly

$$H_{\text{loc}} = \sum_{ab} E^{ab} d_a^\dagger d_b + \sum_{abcd} U^{abcd} d_a^\dagger d_b^\dagger d_c d_d, \quad (24.2)$$

$$H_{\text{bath}} = \sum_{p,\nu} \epsilon_p^b a_{p,\nu}^\dagger a_{p,\nu}, \quad (24.3)$$

$$H_{\text{mix}} = \sum_{p,ab} (V_p^{a\nu} d_a^\dagger a_{p,\nu} + h.c.), \quad (24.4)$$

with the bath operators having free fermion correlation functions.

A familiar model of this sort is the *one-orbital Anderson model*, a simplified representation of a magnetic impurity in a metallic host, where the only quantum number labeling the impurity or bath state is the spin σ ; so $H_{\text{loc}} = H_0 + H_U$ with

$$H_0 = -(\mu - U/2)(n_\uparrow + n_\downarrow), \quad (24.5)$$

$$H_U = U[n_\uparrow n_\downarrow - (n_\uparrow + n_\downarrow)/2], \quad (24.6)$$

$$H_{\text{bath}} = \sum_{p,\sigma} \epsilon_p a_{p,\sigma}^\dagger a_{p,\sigma}, \quad (24.7)$$

$$H_{\text{mix}} = \sum_{p,\sigma} (V_p^\sigma d_\sigma^\dagger a_{p,\sigma} + h.c.). \quad (24.8)$$

Generalizations to different forms of coupling are also of interest. For example, in the spin 1/2 Kondo model H_{imp} is a constraint that the number of electrons on the impurity is 1 and the impurity-bath coupling becomes $J\vec{S} \cdot \vec{\sigma}$, with $\vec{\sigma}$ the local spin density of the conduction band on the impurity site and \vec{S} the spin density of the impurity. The methods we describe here can be generalized to those models [3, 4]. However, for the purposes of this chapter we specialize on models of the general form specified in Eqs. (24.2)-(24.4). For Monte Carlo calculations it is furthermore convenient to formally integrate out the bath electrons, which has the effect of replacing the Hamiltonian by an action involving a frequency-dependent hybridization function.

24.2 Dynamical Mean Field Theory

Impurity solvers are a key ingredient of DMFT [5, 6], which is currently one of the most promising tools to study strongly correlated lattice models. For a comprehensive description of DMFT we refer the reader to one of the several excellent review articles on this topic [1]. Here we note that DMFT is in essence an approximation to the physics of a lattice model in which the momentum dependence of the electron self-energy Σ is expressed in terms of a finite sum of pre-specified basis functions ϕ_μ as

$$\Sigma(k, \omega) = \sum_\mu \phi_\mu(k) \Sigma_\mu(\omega). \quad (24.9)$$

Different implementations of DMFT correspond to different choices of ϕ_μ . For example, in the single-site DMFT approximation [6] $\phi \rightarrow 1$ and there is no sum over μ , whereas in the dynamical-cluster-approximation (DCA)

implementation [7] the Brillouin zone is divided into N non-overlapping, equal sized momentum tiles $\mu = 1, \dots, N$ such that $\phi_\mu(k) = 1$ if k is in tile μ and $\phi_\mu(k) = 0$ otherwise.

The Σ_μ may be computed from the solution of a QIM of the form of Eqs. (24.2)-(24.4). The interaction terms in Eq. (24.2) are obtained by appropriate projections of the physical lattice interactions onto the multi-orbital/multi-site impurity, and the hybridization function F is specified by a self-consistency condition which may be written as

$$F(-\omega) = \omega + \mu - \Sigma - \left(\sum_k G_{\text{lattice}}(k, \omega) \right)^{-1} \quad (24.10)$$

with $G_{\text{lattice}}(k, \omega) = [\omega + \mu - \epsilon_k - \Sigma(k, \omega)]^{-1}$. Note that Σ , G , and F are matrices in spin/orbital space. Numerical solution of the QIM is necessary because one needs the self-energy at all frequencies.

The DMFT equations are normally solved using a self-consistency loop in which one begins with an arbitrary F , solves the QIM to compute the impurity G and thus Σ , which is then inserted into Eqs. (24.9) and (24.10) to generate a new F . This process is iterated until convergence is reached. Once the calculation has converged, the hybridization carries the information about the underlying lattice. The computationally expensive step in the iterative procedure is the solution of the impurity problem.

DMFT is an important tool which allows one to compute phase diagrams and excited state properties of strongly correlated materials. However, as parameters are varied QCPs may be encountered, which can be different from QIM QCPs because of the self-consistent coupling to the bath states. There are several possibilities, whose interplay has not yet been clarified. As parameters are varied the local Hamiltonian Eq. (24.2) will have level crossings. Coupling to the continuous degrees of freedom of the bath may promote these to QPTs, or may cause level mixing, leading to an avoided criticality. Additionally, the coupling to the bath may induce QPTs not present in the impurity-only model.

24.3 Continuous-Time Impurity Solvers

In this section we discuss the recently developed diagrammatic Monte Carlo methods for QIMs, focusing for simplicity on the one-orbital Anderson QIM (Eqs. (24.5)-(24.8)). The QIM partition function Z is

$$Z = \text{Tr} e^{-\beta H}, \quad (24.11)$$

with β the inverse temperature, and $\text{Tr} = \text{Tr}_d \text{Tr}_a$ the trace over the impurity and bath states. By “solving the QIM” we mean computing the impurity Green’s function.

Diagrammatic Monte Carlo simulation relies on an expansion of the partition function into a series of diagrams and the stochastic sampling of collections of these diagrams. We represent the partition function as a sum, or, more precisely, an integral of configurations c with weight w_c ,

$$Z = \sum_c w_c, \quad (24.12)$$

and implement a random walk $c_1 \rightarrow c_2 \rightarrow c_3 \rightarrow \dots$ in configuration space in such a way that each configuration can be reached from any other in a finite number of steps (*ergodicity*) and that *detailed balance* is satisfied,

$$|w_{c_1}| p(c_1 \rightarrow c_2) = |w_{c_2}| p(c_2 \rightarrow c_1). \quad (24.13)$$

This assures one that each configuration is visited with a probability proportional to $|w_c|$ and one can thus obtain an estimate for the Green's function from a finite number N of measurements:

$$g = \frac{\sum_c w_c g_c}{\sum_c w_c} = \frac{\sum_c |w_c| \text{sign}_c g_c}{\sum_c |w_c| \text{sign}_c} \approx \frac{\sum_{i=1}^N \text{sign}_{c_i} g_{c_i}}{\sum_{i=1}^N \text{sign}_{c_i}} = \frac{\langle \text{sign} \cdot g \rangle_{MC}}{\langle \text{sign} \rangle_{MC}}. \quad (24.14)$$

The error on this estimate decreases as $1/\sqrt{N}$. If the average sign of the configurations is small and decreases exponentially with decreasing temperature, the algorithm suffers from a *sign problem*.

24.3.1 General Recipe for Diagrammatic Quantum Monte Carlo

The first step in the diagrammatic expansion is to rewrite the partition function as a time-ordered exponential using some *interaction representation*. We split the Hamiltonian into two parts, $H = H_1 + H_2$, and define the time-dependent operators in the interaction picture as $O(\tau) = e^{\tau H_1} O e^{-\tau H_1}$. In a second step, the time-ordered exponential is expanded into a power series,

$$\begin{aligned} Z &= \text{Tr} \left[e^{-\beta H_1} T e^{-\int_0^\beta d\tau H_2(\tau)} \right] = \sum_{n=0}^{\infty} \int_0^\beta d\tau_1 \dots \int_{\tau_{n-1}}^\beta d\tau_n \\ &\quad \times \text{Tr} \left[e^{-(\beta-\tau_n)H_1} (-H_2) \dots e^{-(\tau_2-\tau_1)H_1} (-H_2) e^{-\tau_1 H_1} \right], \end{aligned} \quad (24.15)$$

which is a representation of the partition function of the form (24.12), namely the sum of all configurations $c = \{\tau_1, \dots, \tau_n\}$, $n = 0, 1, \dots$, $\tau_i \in [0, \beta]$ with weight

$$w_c = \text{Tr} \left[e^{-(\beta-\tau_n)H_1} (-H_2) \dots e^{-(\tau_2-\tau_1)H_1} (-H_2) e^{-\tau_1 H_1} \right] d\tau^n. \quad (24.16)$$

In the following we will discuss in detail two complementary diagrammatic Monte Carlo algorithms, namely

1. a *weak-coupling* approach, based on an expansion of Z in powers of the interaction U , and on an interaction representation in which the time evolution is determined by the *quadratic* part $H_0 + H_{\text{bath}} + H_{\text{mix}}$ of the Hamiltonian,
2. a *strong-coupling* approach, based on an expansion of Z in powers of the impurity-bath hybridization V , and an interaction representation in which the time evolution is determined by the *local* part $H_0 + H_U + H_{\text{bath}}$ of the Hamiltonian.

24.3.2 Weak-Coupling Approach

The first diagrammatic impurity solver, proposed by Rubtsov *et al.* [8], is based on an expansion in $H_2 = H_U$. Here, we will consider a variant of the weak-coupling approach, worked out by Gull and collaborators [9], which combines the weak-coupling expansion with an auxiliary field decomposition. This *continuous-time auxiliary field method* is an adaptation of an algorithm by Rombouts *et al.* [10] for lattice models, the first diagrammatic Monte Carlo algorithm for fermions. For models with density-density interactions it is equivalent to Rubtsov's method [11] and in some respects resembles the well-known Hirsch-Fye algorithm [12].

24.3.2.1 Monte Carlo Configurations

Following Rombouts and collaborators, we define $H_2 = H_U - K/\beta$ and $H_1 = H - H_2 = H_0 + H_{\text{bath}} + H_{\text{mix}} + K/\beta$, with K some non-zero constant. Equation (24.15) then gives the expression for the partition function after expansion in H_2 , and (24.16) the weight of a configuration of n *interaction vertices*. At this stage, we expand our configuration space by decoupling each interaction vertex using the decoupling formula [10]

$$-H_2 = K/\beta - U[n_\uparrow n_\downarrow - (n_\uparrow + n_\downarrow)/2] = \frac{K}{2\beta} \sum_{s=-1,1} e^{\gamma s(n_\uparrow - n_\downarrow)}, \quad (24.17)$$

$$\cosh(\gamma) = 1 + (\beta U)/(2K). \quad (24.18)$$

The configuration space then becomes the collection of all possible *Ising spin configurations* on the imaginary time interval $[0, \beta]$: $c = \{\{\tau_1, s_1\}, \dots, \{\tau_n, s_n\}\}$, $n = 0, 1, \dots$, $\tau_i \in [0, \beta]$, $s_i = \pm 1$. These configurations have weight

$$w_c = \text{Tr} \left[e^{-(\beta - \tau_n)H_1} e^{\gamma s_n(n_\uparrow - n_\downarrow)} \dots e^{-(\tau_2 - \tau_1)H_1} e^{\gamma s_1(n_\uparrow - n_\downarrow)} e^{-\tau_1 H_1} \right] \left(\frac{K d\tau}{2\beta} \right)^n. \quad (24.19)$$

All the operators in the trace are quadratic in c and a ; so we can first separate the spin components and then proceed to the analytical calculation of the

trace. Introducing $H_1^\sigma = -(\mu - U/2)n_\sigma + \sum_p \epsilon_p a_{p,\sigma}^\dagger a_{p,\sigma} + \sum_p (V_{\sigma,p} d_\sigma^\dagger a_{p,\sigma} + h.c.)$, which is the σ -component of the non-interacting QIM, the trace in Eq. (24.19) becomes

$$\text{Tr}[\dots] = e^{-K} \prod_\sigma \text{Tr}\left[e^{-(\beta-\tau_n)H_1^\sigma} e^{\gamma s_n \sigma n_\sigma} \dots e^{-(\tau_2-\tau_1)H_1^\sigma} e^{\gamma s_1 \sigma n_\sigma} e^{-\tau_1 H_1^\sigma}\right]. \quad (24.20)$$

Using the identity $e^{\gamma s \sigma n_\sigma} = e^{\gamma s \sigma} c_\sigma^\dagger c_\sigma + c_\sigma c_\sigma^\dagger = e^{\gamma s \sigma} - (e^{\gamma s \sigma} - 1)c_\sigma c_\sigma^\dagger$, the trace factors can be expressed in terms of non-interacting impurity Green's functions g_0 ($Z_{0,\sigma} = \text{Tr}[e^{-\beta H_1^\sigma}]$):

$$\text{Tr}\left[e^{-(\beta-\tau_n)H_1^\sigma} e^{\gamma s_n \sigma n_\sigma} \dots e^{-(\tau_2-\tau_1)H_1^\sigma} e^{\gamma s_1 \sigma n_\sigma} e^{-\tau_1 H_1^\sigma}\right] = Z_{0,\sigma} \det N_\sigma^{-1}(\{s_i, \tau_i\}). \quad (24.21)$$

Here, N_σ is an $(n \times n)$ matrix defined by the location of the decoupled interaction vertices, the spin orientations, and the non-interacting Green's functions:

$$N_\sigma^{-1}(\{s_i, \tau_i\}) \equiv e^{\Gamma_\sigma} - G_{0\sigma}(e^{\Gamma_\sigma} - I). \quad (24.22)$$

The notation is $e^{\Gamma_\sigma} \equiv \text{diag}(e^{\gamma \sigma s_1}, \dots, e^{\gamma \sigma s_n})$, $(G_{0\sigma})_{i,j} = g_{0\sigma}(\tau_i - \tau_j)$ for $i \neq j$, $(G_{0\sigma})_{i,i} = g_{0\sigma}(0_+) > 0$. Combining Eqs. (24.19)-(24.22) we thus obtain the weight for configuration $c = \{\{\tau_1, s_1\}, \dots, \{\tau_n, s_n\}\}$:

$$w_c = e^{-K} \left(\frac{K d\tau}{2\beta}\right)^n \prod_\sigma Z_{0\sigma} \det N_\sigma^{-1}(\{s_i, \tau_i\}). \quad (24.23)$$

24.3.2.2 Sampling Procedure and Detailed Balance

For ergodicity it is sufficient to insert/remove spins with random orientation at random times, because this allows one in principle to generate all possible configurations. Furthermore, the random walk in configuration space must satisfy the detailed balance condition (24.13). Splitting the probability to move from configuration c_i to configuration c_j into a probability to *propose* the move and a probability to *accept* it,

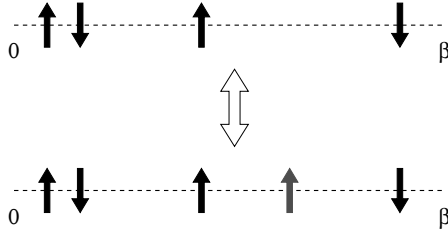
$$p(c_i \rightarrow c_j) = p^{\text{prop}}(c_i \rightarrow c_j)p^{\text{acc}}(c_i \rightarrow c_j), \quad (24.24)$$

we arrive at the condition

$$\frac{p^{\text{acc}}(c_i \rightarrow c_j)}{p^{\text{acc}}(c_j \rightarrow c_i)} = \frac{p^{\text{prop}}(c_j \rightarrow c_i)}{p^{\text{prop}}(c_i \rightarrow c_j)} \frac{|w_{c_j}|}{|w_{c_i}|}. \quad (24.25)$$

There is some flexibility in choosing the proposal probabilities. A reasonable choice for the insertion/removal of a spin is the following, illustrated in Fig. 24.1:

- *Insertion:* Pick a random time in $[0, \beta)$ and a random direction for the new spin; $p^{\text{prop}}(n \rightarrow n+1) = (1/2)(d\tau/\beta)$.

**FIGURE 24.1**

Local update in the continuous-time auxiliary field method. The dashed line represents the imaginary time interval $[0, \beta]$. We increase the perturbation order by adding a spin with random orientation at a random time. The perturbation order is decreased by removing a randomly chosen spin.

- *Removal:* Pick a random spin; $p^{\text{prop}}(n+1 \rightarrow n) = 1/(n+1)$.

For this choice, the ratio of acceptance probabilities becomes

$$\frac{p^{\text{acc}}(n \rightarrow n+1)}{p^{\text{acc}}(n+1 \rightarrow n)} = \frac{K}{n+1} \prod_{\sigma=\uparrow,\downarrow} \frac{|\det(N_\sigma^{(n+1)})^{-1}|}{|\det(N_\sigma^{(n)})^{-1}|}, \quad (24.26)$$

and the random walk can thus be implemented for example on the basis of the Metropolis algorithm, i.e., the proposed move from n to $n \pm 1$ is accepted with probability $\min[1, p^{\text{acc}}(n \rightarrow n \pm 1)/p^{\text{acc}}(n \pm 1 \rightarrow n)]$.

24.3.2.3 Determinant Ratios and Fast Matrix Updates

From Eq. (24.26) it follows that each update requires the calculation of a ratio of two determinants. Computing the determinant of a matrix of size $(n \times n)$ is an $O(n^3)$ operation. However, each insertion or removal of a spin merely changes one row and one column of the matrix N_σ^{-1} . We will now show that it is therefore possible to evaluate the ratio in Eq. (24.26) in a time $O(n^2)$ (insertion) or $O(1)$ (removal) [8].

The objects which are stored and manipulated during the simulation are, besides the lists of the times $\{\tau_i\}$ and spins $\{s_i\}$, the matrices $N_\sigma = [e^{\Gamma_\sigma} - G_{0\sigma}(e^{\Gamma_\sigma} - I)]^{-1}$. Inserting a spin adds a new row and column to N_σ^{-1} . We define the blocks, omitting the σ index, as

$$(N^{(n+1)})^{-1} = \begin{pmatrix} (N^{(n)})^{-1} & Q \\ R & S \end{pmatrix}, \quad N^{(n+1)} = \begin{pmatrix} \tilde{P} & \tilde{Q} \\ \tilde{R} & \tilde{S} \end{pmatrix}, \quad (24.27)$$

where Q, R, S denote $(n \times 1)$, $(1 \times n)$, and (1×1) matrices, respectively, which contain the contribution of the added spin. The determinant ratio needed for the acceptance/rejection probability is then given by

$$\frac{\det(N^{(n+1)})^{-1}}{\det(N^{(n)})^{-1}} = \frac{1}{\det \tilde{S}} = S - [R][N^{(n)}Q]. \quad (24.28)$$

As we store $N^{(n)}$, computing the acceptance/rejection probability of an insertion move is an $O(n^2)$ operation. If the move is accepted, the new matrix $N^{(n+1)}$ is computed out of $N^{(n)}$, Q , R , and S , also in a time $O(n^2)$ [9]:

$$\tilde{S} = (S - [R][N^{(n)}Q])^{-1}, \quad (24.29)$$

$$\tilde{Q} = -[N^{(n)}Q]\tilde{S}, \quad (24.30)$$

$$\tilde{R} = -\tilde{S}[RN^{(n)}], \quad (24.31)$$

$$\tilde{P} = N^{(n)} + [N^{(n)}Q]\tilde{S}[RN^{(n)}]. \quad (24.32)$$

It follows from Eq. (24.28) that the calculation of the determinant ratio for removing a spin is $O(1)$, since it is just element \tilde{S} , and from the above formulas we also immediately find the elements of the reduced matrix:

$$N^{(n)} = \tilde{P} - \frac{[\tilde{Q}][\tilde{R}]}{\tilde{S}}. \quad (24.33)$$

24.3.2.4 Measurement of the Green's Function

To compute the contribution of a configuration c to the Green's function, $g_\sigma^c(\tau)$, we insert in Eq. (24.19) a creation operator d^\dagger at time 0 and an annihilation operator d at time τ and divide by w_c . Wick's theorem then leads to the expression

$$g_\sigma^c(\tau) = g_{0\sigma}(\tau) + [g_{0\sigma}(\tau - \tau_j)(e^{\Gamma_{\sigma j}} - 1)]N_\sigma^{(n)}[g_{0\sigma}(\tau_i)]. \quad (24.34)$$

Square brackets denote vectors of length n . To avoid unnecessary and time consuming summations during the Monte Carlo simulations, we only accumulate the quantity [9]

$$S_\sigma(\tilde{\tau}) \equiv \sum_{k=1}^n \delta(\tilde{\tau} - \tau_k) \sum_{l=1}^n [(e^{\Gamma_\sigma} - I)N_\sigma^{(n)}]_{kl} g_{0\sigma}(\tau_l), \quad (24.35)$$

binning the time points $\tilde{\tau}$ on a fine grid. After the simulation is completed, the Green's function is computed as

$$g_\sigma(\tau) = g_{0\sigma}(\tau) + \int_0^\beta d\tilde{\tau} g_{0\sigma}(\tau - \tilde{\tau}) \langle S_\sigma(\tilde{\tau}) \rangle_{MC}. \quad (24.36)$$

24.3.2.5 Expansion Order and Role of the Parameter K

It follows from Eq. (24.15) that $\langle -H_2 \rangle = \frac{1}{\beta} \int_0^\beta d\tau \langle -H(\tau) \rangle = \frac{1}{\beta} \langle n \rangle$ and because $\langle -H_2 \rangle = K/\beta - U \langle n_\uparrow n_\downarrow - (n_\uparrow + n_\downarrow)/2 \rangle$ the average perturbation order $\langle n \rangle$ is related to the parameter K and the potential energy by

$$\langle n \rangle = K - \beta U \langle n_\uparrow n_\downarrow - (n_\uparrow + n_\downarrow)/2 \rangle. \quad (24.37)$$

Increasing K leads to a higher perturbation order, and thus slower matrix updates, but through Eq. (24.18) also to a smaller value of γ and thus to less polarization of the auxiliary spins. We also learn from Eq. (24.37) that the average perturbation order grows essentially proportional to U , as expected for a weak-coupling method, and proportional to inverse temperature.

Note that $K = -\beta U/4$ corresponds to a Rubtsov expansion in powers of $H_2 = U(n_\uparrow - \frac{1}{2})(n_\downarrow - \frac{1}{2})$. This choice is optimal in the particle-hole symmetric case, since only even perturbation orders must be sampled.

24.3.3 Strong-Coupling Approach: Expansion in the Impurity-Bath Hybridization

The second diagrammatic method, which is in many ways complementary to the weak-coupling approach, is based on an expansion of the partition function in powers of the impurity-bath hybridization V . This method was first developed for the Anderson QIM [13] and soon thereafter extended to a matrix formulation which allows one to treat general classes of QIMs [3, 14]. We will first discuss the implementation for the Anderson QIM.

24.3.3.1 Monte Carlo Configurations

In the strong-coupling formulation, we decompose the Hamiltonian as $H_2 = H_{\text{mix}}$ and $H_1 = H - H_2 = H_0 + H_U + H_{\text{bath}}$. Since $H_2 \equiv H_2^{d^\dagger} + H_2^d = \sum_{\sigma,p} V_p^\sigma d_\sigma^\dagger a_{p,\sigma} + \sum_{\sigma,p'} V_{p'}^{\sigma*} d_\sigma a_{p,\sigma}^\dagger$ has two terms, corresponding to electrons hopping from the bath to the impurity and from the impurity back to the bath, only even perturbation orders contribute to Eq. (24.15). Furthermore, at perturbation order $2n$ only the $(2n)!/(n!)^2$ terms corresponding to n creation operators d^\dagger and n annihilation operators d will contribute. We can therefore write the partition function as a sum over configurations $c = \{\tau_1, \dots, \tau_n; \tau'_1, \dots, \tau'_n\}$:

$$\begin{aligned} Z &= \sum_{n=0}^{\infty} \int_0^\beta d\tau_1 \dots \int_{\tau_{n-1}}^\beta d\tau_n \int_0^\beta d\tau'_1 \dots \int_{\tau'_{n-1}}^\beta d\tau'_n \\ &\quad \times \text{Tr} \left[e^{-\beta H_1} T H_2^d(\tau_n) H_2^{d^\dagger}(\tau'_n) \dots H_2^d(\tau_1) H_2^{d^\dagger}(\tau'_1) \right]. \end{aligned} \quad (24.38)$$

Since the time evolution of the Anderson model given by H_1 does not rotate the spin, there is an additional constraint, namely that both for spin up and spin down, there is an equal number of creation and annihilation operators. Taking this into account and writing out the expressions for H_2^d and

$H_2^{d^\dagger}$ explicitly, we find

$$\begin{aligned}
Z &= Z_{\text{bath}} \sum_{\{\eta_\sigma\}} \prod_\sigma \int_0^\beta d\tau_1^\sigma \dots \int_{\tau_{n_\sigma-1}^\sigma}^\beta d\tau_{n_\sigma}^\sigma \int_0^\beta d\tau_1'^\sigma \dots \int_{\tau_{n_\sigma-1}'}^\beta d\tau_{n_\sigma}'^\sigma \\
&\times \text{Tr}_d \left[e^{-\beta H_{\text{loc}}} T \prod_\sigma d_\sigma(\tau_{n_\sigma}^\sigma) d_\sigma^\dagger(\tau_{n_\sigma}'^\sigma) \dots d_\sigma(\tau_1^\sigma) d_\sigma^\dagger(\tau_1'^\sigma) \right] \\
&\times \frac{1}{Z_{\text{bath}}} \text{Tr}_a \left[e^{-\beta H_{\text{bath}}} T \prod_\sigma \sum_{p_1, \dots, p_{n_\sigma}} \sum_{p'_1, \dots, p'_{n_\sigma}} V_{p_1}^\sigma V_{p'_1}^{\sigma*} \dots V_{p_{n_\sigma}}^\sigma V_{p'_{n_\sigma}}^{\sigma*} \right. \\
&\quad \left. a_{\sigma, p_{n_\sigma}}^\dagger(\tau_{n_\sigma}^\sigma) a_{\sigma, p'_{n_\sigma}}(\tau_{n_\sigma}'^\sigma) \dots a_{\sigma, p_1}^\dagger(\tau_1^\sigma) a_{\sigma, p'_1}(\tau_1'^\sigma) \right], \quad (24.39)
\end{aligned}$$

where we have used the fact that H_1 does not mix the impurity and the bath to separate the d and a operators. $Z_{\text{bath}} = \text{Tr}_a e^{-\beta H_{\text{bath}}}$, and $H_{\text{loc}} = H_0 + H_U$. Introducing the β -antiperiodic hybridization function

$$F_\sigma(\tau) = \sum_p \frac{|V_p|^2}{e^{-\epsilon_p \beta} + 1} \begin{cases} e^{-\epsilon_p(\beta-\tau)} & \tau > 0 \\ -e^{-\epsilon_p(-\tau)} & \tau < 0 \end{cases}, \quad F_\sigma(-i\omega_n) = \sum_p \frac{|V_p^\sigma|^2}{i\omega_n - \epsilon_p}, \quad (24.40)$$

which is related to the non-interacting Green's function $G_{0\sigma}$ of Section 24.3.2 by $F_\sigma(-i\omega_n) = i\omega_n + \mu - U/2 - G_{0\sigma}(i\omega_n)^{-1}$, the trace over the bath states can be expressed as

$$\frac{1}{Z_{\text{bath}}} \text{Tr}_a \left[e^{-\beta H_{\text{bath}}} T \prod_\sigma \sum_{p_1, \dots, p_{n_\sigma}} \sum_{p'_1, \dots, p'_{n_\sigma}} V_{p_1}^\sigma V_{p'_1}^{\sigma*} \dots V_{p_{n_\sigma}}^\sigma V_{p'_{n_\sigma}}^{\sigma*} \right. \\
\left. a_{\sigma, p_{n_\sigma}}^\dagger(\tau_{n_\sigma}^\sigma) a_{\sigma, p'_{n_\sigma}}(\tau_{n_\sigma}'^\sigma) \dots a_{\sigma, p_1}^\dagger(\tau_1^\sigma) a_{\sigma, p'_1}(\tau_1'^\sigma) \right] = \prod_\sigma \det M_\sigma^{-1}, \quad (24.41)$$

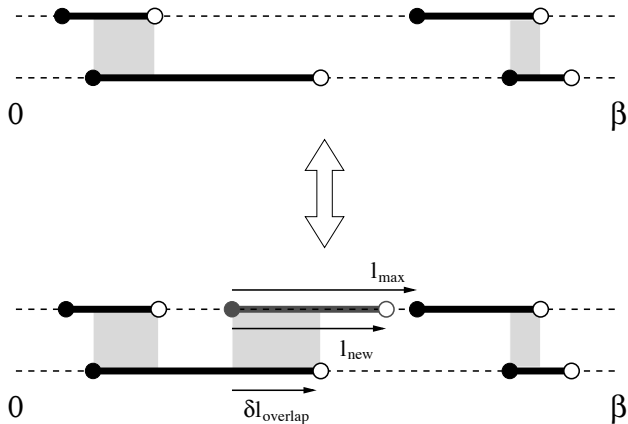
where M_σ^{-1} is the $(n_\sigma \times n_\sigma)$ matrix with elements

$$M_\sigma^{-1}(i, j) = F_\sigma(\tau_i^\sigma - \tau_j'^\sigma). \quad (24.42)$$

In the hybridization expansion method, the configuration space consists of all sequences $c = \{\tau_1^\uparrow, \dots, \tau_{n_\uparrow}^\uparrow; \tau_1'^\uparrow, \dots, \tau_{n_\uparrow}'^\uparrow | \tau_1^\downarrow, \dots, \tau_{n_\downarrow}^\downarrow; \tau_1'^\downarrow, \dots, \tau_{n_\downarrow}'^\downarrow\}$, of n_\uparrow creation and annihilation operators for spin up ($n_\uparrow = 0, 1, \dots$), and n_\downarrow creation and annihilation operators for spin down ($n_\downarrow = 0, 1, \dots$). The weight of this configuration is

$$\begin{aligned}
w_c &= Z_{\text{bath}} \text{Tr}_d \left[e^{-\beta H_{\text{loc}}} T \prod_\sigma d_\sigma(\tau_{n_\sigma}^\sigma) d_\sigma^\dagger(\tau_{n_\sigma}'^\sigma) \dots d_\sigma(\tau_1^\sigma) d_\sigma^\dagger(\tau_1'^\sigma) \right] \\
&\times \prod_\sigma \det M_\sigma^{-1}(\tau_1^\sigma, \dots, \tau_{n_\sigma}^\sigma; \tau_1'^\sigma, \dots, \tau_{n_\sigma}'^\sigma) (d\tau)^{2n_\sigma}. \quad (24.43)
\end{aligned}$$

The trace factor represents the contribution of the impurity, which fluctuates between different quantum states, as electrons hop in and out. The determinants re-sum all the bath evolutions which are compatible with the given sequence of transitions [3].

**FIGURE 24.2**

Local update in the segment picture. The two segment configurations correspond to spin up and spin down. Each segment depicts a time interval in which an electron of the corresponding spin resides on the impurity; the end points are the locations of the operators d^\dagger and d . We increase the perturbation order by adding a segment or anti-segment of random length for random spin. The perturbation order is decreased by removing a randomly chosen segment.

To evaluate the trace factor, one may use the eigenbasis of H_{loc} . In this basis, the time evolution operator $e^{-\tau H_{\text{loc}}}$ is diagonal while the operators d_σ and d_σ^\dagger will produce transitions between eigenstates with amplitude ± 1 .

Because the time evolution does not flip the spin, the creation and annihilation operators for given spin have to alternate. This allows us to separate the operators for spin up from those for spin down and to depict the time evolution by a *collection of segments*, each segment representing a time interval in which an electron of spin up or down resides on the impurity. At each time, the eigenstate of the impurity follows immediately from the segment representation and we can easily compute the trace factor as

$$\text{Tr}_d \left[e^{-\beta H_{\text{loc}}} T \prod_\sigma d_\sigma(\tau_{n_\sigma}^\sigma) d_\sigma^\dagger(\tau'_{n_\sigma}^\sigma) \dots d_\sigma(\tau_1^\sigma) d_\sigma^\dagger(\tau'_1) \right] = \exp \left[\mu(l_\uparrow + l_\downarrow) - U l_{\text{ol}} \right], \quad (24.44)$$

with l_σ the total length of the segments for spin σ and l_{ol} the total length of the overlap between up and down segments. The lower panel of Fig. 24.2 shows a configuration with 3 segments for spin up and two segments for spin down; the time intervals where segments overlap, indicated by gray rectangles, correspond to a doubly occupied impurity and cost a repulsion energy U .

24.3.3.2 Sampling Procedure and Detailed Balance

For ergodicity, it is sufficient to insert and remove pairs of creation and annihilation operators (segments or anti-segments) for spin up and down. One possible strategy for inserting a segment is the following: we pick a random time in $[0, \beta)$ for the creation operator. If it falls on an existing segment, the impurity is already occupied and the move is rejected. If it falls on an empty space, we compute l_{\max} , the length from this position to the next segment, in the direction of increasing τ . If there are no segments, $l_{\max} = \beta$. The position of the new annihilation operator is then chosen randomly in this interval of length l_{\max} (see Fig. 24.2). If we propose to remove a randomly chosen segment for this spin, then the proposal probabilities are

$$p^{\text{prop}}(n_\sigma \rightarrow n_\sigma + 1) = \frac{d\tau}{\beta} \frac{d\tau}{l_{\max}}, \quad p^{\text{prop}}(n_\sigma + 1 \rightarrow n_\sigma) = \frac{1}{n_\sigma + 1}, \quad (24.45)$$

and the ratio of acceptance probabilities therefore becomes

$$\frac{p^{\text{acc}}(n_\sigma \rightarrow n_\sigma + 1)}{p^{\text{acc}}(n_\sigma + 1 \rightarrow n_\sigma)} = \frac{\beta l_{\max}}{n_\sigma + 1} e^{\mu l_{\text{new}} - U \delta l_{\text{ol}}} \frac{|\det(M_\sigma^{(n_\sigma+1)})^{-1}|}{|\det(M_\sigma^{(n_\sigma)})^{-1}|}. \quad (24.46)$$

Here, l_{new} is the length of the new segment, and δl_{ol} the change in the overlap. Again, we compute the ratio of determinants using the fast update formulas discussed in Section 24.3.2.

24.3.3.3 Measurement of the Green's Function

The strategy here is to create configurations which contribute to the Green's function measurement by decoupling the bath from a given pair of creation and annihilation operators in c . The idea is to write

$$g(\tau) = \frac{1}{Z} \sum_c w_c^{d(\tau)d^\dagger(0)} = \frac{1}{Z} \sum_c w_c^{(\tau,0)} \frac{w_c^{d(\tau)d^\dagger(0)}}{w_c^{(\tau,0)}}, \quad (24.47)$$

where $w_c^{d(\tau)d^\dagger(0)}$ denotes the weight of configuration c with additional operators $d^\dagger(0)$ and $d(\tau)$ in the trace factor, and $w_c^{(\tau,0)}$ the complete weight corresponding to the enlarged operator sequence, including enlarged hybridization determinants. Since the trace factors of both weights are identical,

$$\frac{w_c^{d(\tau)d^\dagger(0)}}{w_c^{(\tau,0)}} = \frac{\det M_c^{-1}}{\det(M_c^{(\tau,0)})^{-1}} = (M_c^{(\tau,0)})_{j,i}, \quad (24.48)$$

with i and j denoting the row and column corresponding to the new operators d^\dagger and d in the enlarged $(M_c^{(\tau,0)})^{-1}$. Hence, the measurement formula for the Green's function becomes

$$g(\tau) = \frac{1}{Z} \sum_{\tilde{c}} w_{\tilde{c}} \sum_{i,j} \frac{1}{\beta} \Delta(\tau, \tau_i - \tau'_j) (M_{\tilde{c}})_{j,i} = \left\langle \sum_{i,j} \frac{1}{\beta} \Delta(\tau, \tau_i - \tau'_j) M_{j,i} \right\rangle_{MC}, \quad (24.49)$$

with $\Delta(\tau, \tau') = \delta(\tau - \tau')$ for $\tau' > 0$, and $\Delta(\tau, \tau') = -\delta(\tau - \tau' - \beta)$ for $\tau' < 0$.

24.3.3.4 Generalization: Matrix Formalism

It is obvious from the derivation in [Section 24.3.3.1](#) that the hybridization expansion formalism is applicable to general classes of QIMs. Because the trace factor in the weight (24.43) is computed exactly, H_{loc} can contain essentially arbitrary interactions, such as spin-exchange terms in multi-orbital models, degrees of freedom, such as spins in Kondo-lattice models, or constraints, such as no double occupancy in the t - J model.

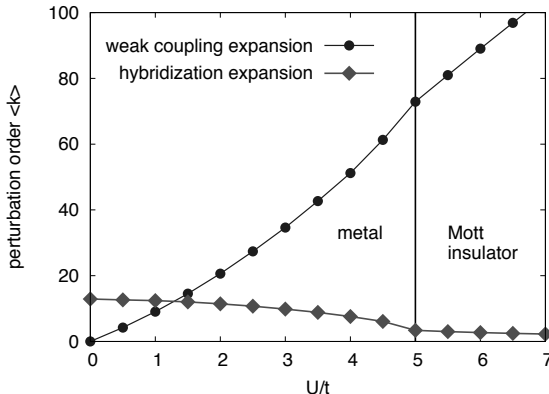
For multi-orbital QIMs with density-density interactions, the segment formalism is still applicable: we have now a collection of segments for each *flavor* α (orbital, spin) and the trace factor can still be computed from the length of the segments (chemical potential contribution) and the overlaps between segments of different flavors (interaction terms).

If H_{loc} is not diagonal in the occupation number basis defined by the d_α^\dagger , the calculation of $\text{Tr}_d[e^{-\beta H_{\text{loc}}} T \prod_\alpha d_\alpha(\tau_{n_\alpha}^\alpha) d_\alpha^\dagger(\tau_{n_\alpha}'^\alpha) \dots d_\sigma(\tau_1^\alpha) d_\sigma^\dagger(\tau_1'^\alpha)]$ becomes more involved. We now have to compute the trace explicitly in some basis of H_{loc} , for example the eigenbasis, in which the time evolution operators $e^{-H_{\text{loc}}\tau}$ become diagonal. The operators d_α and d_α^\dagger are expressed as matrices in this eigenbasis, and the evaluation of the trace factor thus involves the multiplication of matrices whose size is equal to the size of the Hilbert space of H_{loc} . Since the dimension of the Hilbert space grows *exponentially* with the number of flavors, the calculation of the trace factor becomes the computational bottleneck of the simulation, and the matrix formalism is therefore restricted to a relatively small number of flavors, up to about 10.

An important point is the use of *conserved quantum numbers*, typically particle number for spin up and spin down, momentum, etc. [14]. If the eigenstates of H_{loc} are grouped according to these quantum numbers, the operator matrices will acquire a sparse block structure, because for example $d_{\uparrow,q}^\dagger$ will connect the states corresponding to quantum numbers $m = \{n_\uparrow, n_\downarrow, K\}$ to those corresponding to $m' = \{n_\uparrow + 1, n_\downarrow, K + q\}$, if they exist. Checking the compatibility of the operator sequence with a given starting block furthermore allows one to find the potentially contributing quantum-number sectors (denoted “contr. m ” below) without any matrix multiplications. The evaluation of the trace is thus reduced to a block matrix multiplication of the form

$$\sum_{\text{contr. } m} \text{Tr}_m \left[\dots (O)_{m'',m'} (e^{-(\tau' - \tau) H_{\text{loc}}})_{m'} (O)_{m',m} (e^{-\tau H_{\text{loc}}})_m \right]. \quad (24.50)$$

For large multi-orbital problems, the Krylov method [15], based on the occupation number representation, is a more efficient alternative. We will not discuss it here.

**FIGURE 24.3**

Average perturbation order for the weak-coupling and strong-coupling hybridization-expansion algorithm. These results correspond to the DMFT solution of the one-band Hubbard model with semi-circular density of states of bandwidth $4t$, and temperature $\beta t = t/T = 30$. The bath is therefore different for each data point. (Figure adapted from Ref. [16].)

24.3.4 Comparison Between the Two Approaches

The weak- and strong-coupling methods are in many ways complementary and their respective strengths/weaknesses result from the scaling of the computational effort with interaction strength and system size. For the one-orbital Anderson QIM, the U dependence of the average perturbation order is shown in Fig. 24.3. These are the converged DMFT results for a semi-circular density of states of bandwidth $4t$ and temperature $T = t/30$ [16]. In the weak-coupling algorithms, where the average perturbation order is related to the potential energy, one finds a roughly linear increase of the perturbation order with U . In the hybridization-expansion method, the average perturbation order is related to the kinetic energy and decreases as the interaction strength increases. Thus, in single-site models with only density-density interactions, where the evaluation of the trace factor in Eq. (24.43) is cheap, the hybridization-expansion method beats the weak-coupling method in the regime of strong correlations.

For more complicated models, or impurity clusters, which require the matrix formalism discussed in Sec. 24.3.3.4, the hybridization-expansion method scales exponentially with system size and can only be applied to relatively small systems.¹ Here, the weak-coupling approach, if applicable, becomes the method of choice. Table 24.1 gives a summary of the different scalings, as

¹While the calculation of the trace over atomic states is time consuming, it also yields useful information about the system, i.e., the histogram of visited states.

solver	scaling		use for
weak-coupling	β^3	L^3	impurity clusters with d-d int's and hopping
hybridization expansion (segment formulation)	β^3	L	single site m-o models with d-d interaction
hybridization expansion (matrix formulation)	β	$\exp(L)$	single site m-o models with general U_{ijkl}

TABLE 24.1

Scaling of the different impurity solvers with inverse temperature and system size; m-o = multi-orbital; d-d = density-density; int's = interactions.

suming diagonal hybridization, and indicates which solver is appropriate for which type of problem.

Another issue which affects the performance of the algorithm is the sign problem. No comprehensive analysis has yet been performed. The single orbital Anderson model does not suffer from a sign problem in either algorithm, which can be demonstrated along the lines of the proof for the Hirsch-Fye algorithm [17]. Single site multi-orbital models with *diagonal bath*, as those discussed in the following section, can be simulated without a sign problem in the hybridization-expansion approach. However, interorbital correlated hopping terms and/or off-diagonal hybridizations may lead to a sign problem. Four-site cluster approximations to the one-band Hubbard model have been studied with both impurity solvers in Ref. [16]. While the unfrustrated, half-filled model is sign-free, a sign problem appears in doped systems or in the presence of next-nearest neighbor hopping. The sign problem is particularly severe in the weak-coupling approach.

24.4 Application: Phase Transitions in Multi-Orbital Systems with Rotationally Invariant Interactions

The complex physics of materials with strong electronic correlations results from the competition between the repulsive interactions felt by electrons in partially filled transition metal *d*-orbitals or lanthanide/actinide *f*-orbitals and the itineracy arising from hybridization with other orbitals in the material. In some cases, for example the cuprate high temperature superconductors [18], the degeneracy is fully lifted and the low-energy physics may be described by the one-band Hubbard model in which the multiplet structure is trivial [19]. However, for many materials of interest, including for example the (La/Ca)TiO₃ series, the SrVO_x materials, the (Sr/Ca)RuO₃ compounds and

their Ruddlesden-Popper variants, the recently discovered Fe-based superconductors, and the A_nC_{60} series of materials, as well as essentially all interesting lanthanide/actinide compounds, the orbital degeneracy is not fully lifted and nontrivial multiplet effects are expected to be important. These may lead to different types of QPTs. Examples include transitions related to level crossings of the QIM such as the high-spin/low-spin transitions discussed, e.g., in Ref. [20], spin freezing transitions [21], Mott transitions [22, 23], and orbital-selective Mott transitions [20, 24, 25]. While many studies have appeared, a comprehensive picture is only now beginning to emerge and more work remains to be done to classify the quantum phases and QPTs.

24.4.1 Model

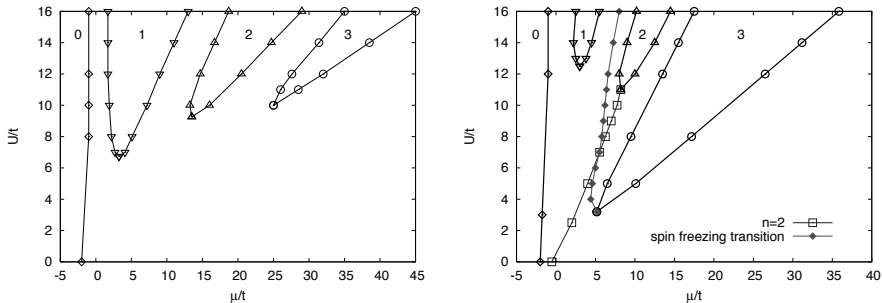
DMFT studies of transition metal oxides proceed from the basic equations (24.2)-(24.4), with the labels in Eq. (24.2) representing two e_g levels in the case of manganites or nickelates, three t_{2g} levels in the case of titanates and vanadates, or the full five orbitals of the d multiplet, as may be needed to describe the iron-arsenide superconductors. In the simplest situation E^{ab} is proportional to the unit matrix, indicating degenerate levels, but additional level splittings Δ_a may be introduced: $H_0 = -\mu \sum_{a,\sigma} (n_{a,\sigma} - \Delta_a)$. The crucial feature of the bath is the density of states $D^{ab}(\omega) = \int dk \delta(\omega - \varepsilon_k^{ab})$. In typical situations the density of states is orbital-diagonal and independent of a ; this assumption holds for pseudo-cubic materials such as the La-titanates and the 113 Sr/Ca ruthenates, as well as for A_nC_{60} . Off-diagonal structure in D may lead to a sign problem in Monte Carlo simulations. The appropriate interaction term is generally believed to be the one specified by Slater and Kanamori,

$$\begin{aligned} H_U &= \sum_a U n_{a,\uparrow} n_{a,\downarrow} + \sum_{a>b,\sigma} \left[U' n_{a,\sigma} n_{b,-\sigma} + (U' - J) n_{a,\sigma} n_{b,\sigma} \right] \\ &\quad - \sum_{a \neq b} J (d_{a,\downarrow}^\dagger d_{b,\uparrow}^\dagger d_{b,\downarrow} d_{a,\uparrow} + d_{b,\uparrow}^\dagger d_{b,\downarrow}^\dagger d_{a,\uparrow} d_{a,\downarrow} + h.c.), \end{aligned} \quad (24.51)$$

and the relation $U' = U - 2J$, which follows from symmetry considerations for d -orbitals in free space, is typically assumed. With this choice of interaction parameters and crystal field splittings $\Delta_a = 0$, H_{loc} is rotationally invariant in orbital space. In the following sections we will present DMFT results for a semi-circular density of states of bandwidth $4t$ and temperature $T = 0.02t$, unless otherwise specified.

24.4.2 Metal-Insulator Phase Diagram of the Three-Orbital Model

[Figure 24.4](#) shows the metal-insulator phase boundaries of the three-orbital model without crystal field splittings, computed for $J = 0$ (left panel) and $J = U/6$ (right panel). We see that J has a very substantial effect on the

**FIGURE 24.4**

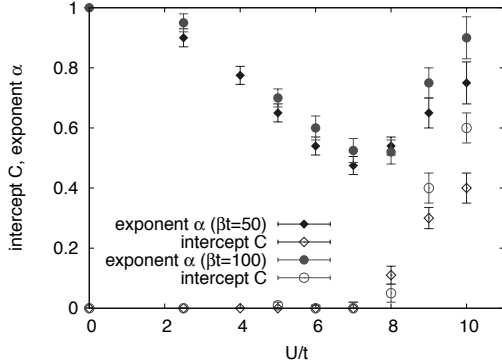
Metal-insulator phase diagram of the three-orbital model presented in the space of chemical potential μ and interaction strength U for $\Delta_a = 0$, $\beta t = 50$ at Hund coupling $J = 0$ (left panel) and $J = U/6$ (right panel). Orbital and spin symmetry were enforced in the calculation. The numerals in the lobes indicate the electron concentration per site in the insulating phases. In the right panel the solid diamonds indicate the boundary of a spin-freezing transition discussed in Ref. [21]. Figures taken from Ref. [25].

phase boundaries. This can be understood by analyzing the eigenstates of the local Hamiltonian and their dependence on μ [25]. The lines separating the metallic and insulating regions are quantum critical lines, but the detailed critical behavior has not yet been studied. It is interesting to note that at $n = 1, 2$ the transition occurs in an intrinsically particle-hole asymmetric situation and involves multiply degenerate states; so the physics may differ from the familiar single-site case.

24.4.3 Spin-Freezing Transition in the Paramagnetic Metallic State

The curve with diamonds in the right panel of Fig. 24.4 indicates the location of an apparent QPT between a paramagnetic Fermi liquid and an incoherent metallic phase characterized by frozen local moments [21], i.e., a spin-spin correlation function which does not decay to zero at long times. The new phase appears for multiple orbitals, a different number of electrons than orbitals, and a rotationally invariant on-site exchange $U/3 > J > 0$. For densities per site $n = 2, 3$ the Mott transition occurs within or at the boundary of the frozen-moment phase.

The transition into the frozen-moment phase produces a non-Fermi liquid self-energy which varies as $\sqrt{\omega}$, and the quantum critical regime of the QPT is sufficiently large that the non-Fermi liquid behavior is observable over a wide range of temperature, interaction strength, spin polarization, and carrier concentration. Interestingly, the QPT seems to be a single-impurity phenomenon:

**FIGURE 24.5**

Results of a fit of the Matsubara axis self-energy to the scaling form $-\text{Im } \Sigma/t = C + A(\omega_n/t)^\alpha$ at temperatures $T = t/50$ (diamonds) and $T = t/100$ (circles), density $n = 2$, and interaction strengths indicated. The plot illustrates the wide quantum critical regime of the spin-freezing transition. Figure taken from Ref. [21].

varying the carrier density while holding the mean-field function fixed leads to a similar critical behavior; so the feedback induced by the self-consistency condition is not important.

The spin-freezing phase boundary in Fig. 24.4 can be defined from the QIM spin-spin correlation function $\langle S_z(\tau)S_z(0) \rangle$ or from the self-energy. In a Fermi liquid at low T the imaginary part of the real axis scattering rate is $\Sigma''(\omega) \sim \max(\omega^2, T^2)$; so the imaginary part of the Matsubara axis self-energy $\Sigma(i\omega_n) \sim i\omega_n$ at small ω_n . Frozen moments may be expected to scatter electrons so that the real axis self-energy is $\Sigma''(\omega) \sim \Gamma$, implying on the Matsubara axis $\text{Im } \Sigma(i\omega_n \rightarrow 0) = i\Gamma \text{sgn}(\omega_n)$. At the QCP we expect a power law behavior $\Sigma''(\omega) \sim \omega^\alpha$; if $\alpha < 1$ then $\Sigma(i\omega_n \rightarrow 0) \sim (i\omega_n)^\alpha$. The imaginary part of the Matsubara axis self-energy is indeed consistent with this behavior [21], vanishing linearly in the Fermi liquid phase, and exhibiting an intercept in the frozen moment phase and an exponent $\alpha \approx 1/2$ near the phase boundary. The behavior of the self-energy in the region not too far from the transition is described by a quantum critical crossover function. In Ref. [21] we have used the fitting function $-\text{Im } \Sigma(\omega_n)/t = C + A(\omega_n/t)^\alpha$, recognizing that the varying value of α represents the different regimes of the crossover function. In Fig. 24.5 we plot the exponent α and intercept C extracted from the fit as the transition line is crossed by varying interaction strength at fixed density $n = 2$.

One might speculate that the $\sqrt{\omega}$ self-energy found here is related to the still-mysterious optical conductivity $\sigma(\Omega)$ of SrRuO₃ and CaRuO₃ [26]. These materials are pseudo-cubic perovskites with two holes in the t_{2g} d shell and

their behavior should be roughly modeled by a 3-orbital calculation at carrier density $n = 2$. In these materials $\sigma(\Omega)$ varies approximately as $1/\sqrt{\Omega}$ at higher frequencies, but rolls over to an approximately constant behavior, in a way which depends on temperature and on the material. In the momentum-independent self-energy approximation, vertex corrections may be neglected; if the self-energy is small compared to the bare electron bandwidth the real part of the optical conductivity may be written

$$\sigma(\Omega) \approx \frac{1}{\Omega} \int \frac{d\omega}{\pi} \frac{f(\omega + \Omega) - f(\omega)}{\Omega - \Sigma(\omega + \Omega) + \Sigma^*(\omega)}, \quad (24.52)$$

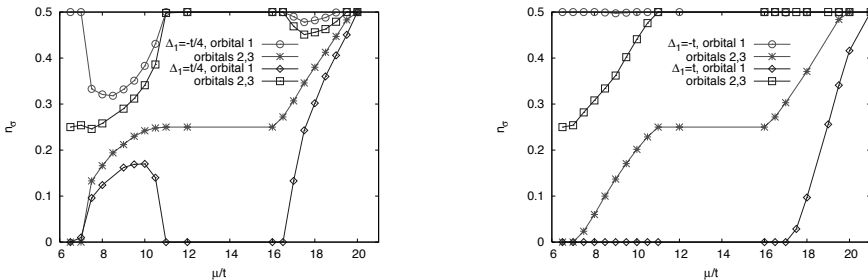
where f is the Fermi function, so that a square-root self-energy implies that the conductivity varies as $1/\sqrt{\Omega}$ for frequencies such that $\Sigma(\Omega) > \Omega$. Our finding, that the phase boundary runs close to $n = 2$ for a range of interaction strengths, suggests that an extreme degree of fine tuning is not necessary to produce a square root self-energy. Further study of this phenomenon is clearly needed.

24.4.4 Crystal Field Splittings and Orbital Selective Mott Transitions

An explicit breaking of the orbital symmetry has been found to lead to a new family of QPTs. We focus here on the three-orbital model with $J > 0$ and dopings between $n = 1$ and $n = 3$. We consider a cubic-tetragonal distortion which splits the 3-fold degeneracy of the t_{2g} state into a singlet and a doublet. The cases $n = 1$ and $n = 3$ are straightforward. At $J > 0$, the $n = 3$ state is a filled shell, stable against orbital splitting for small differences among the orbitals, while for larger crystal field splitting a high-spin/low-spin transition will occur [20], with physics analogous to that discussed in the next section. For $n = 1$, the model becomes either an effective one-orbital model or an effective two-orbital model.

One may parameterize this splitting by moving one orbital, which we take to be orbital 1, by an energy Δ while keeping the other two fixed, so $\Delta_1 = \Delta$ and $\Delta_2 = \Delta_3 = 0$. There are two cases: either the doublet lies lower than the singlet (“1 up, 2 down”, $\Delta > 0$) or the reverse (“1 down, 2 up”, $\Delta < 0$). Other ways of breaking the symmetry, e.g., choosing different bandwidths, will have similar effects.

Representative results are shown in Fig 24.6, which plots orbital occupancies as a function of chemical potential for two different level splittings. A rich family of behaviors is seen, including insulating phases, in which all densities are independent of μ and correspond to integer total filling, orbitally selective phases, in which densities of some orbitals vary while others are pinned to an insulating value, and fully metallic phases. Transitions between these phases can induce a substantial charge transfer between orbitals, as evident in the left hand panel. The precise nature of the orbital-selective transitions remains

**FIGURE 24.6**

μ -dependence of the orbital occupancy per spin $n_{\sigma}(\mu)$ for $U/t = 12$, $J/t = 1$ at $\beta t = 50$ and in the presence of a cubic-tetragonal crystal field $\Delta_1 = \pm 0.25t$ (left) and $\Delta_1 = \pm t$ (right). The crystal field splits the threefold degenerate d level into a singlet (orbital 1) and a doublet (orbitals 2,3). The chemical potential range runs from the $n = 1$ Mott phase ($\mu \sim 6t$) to the $n = 3$ Mott phase ($\mu \sim 20t$). Figures taken from Ref. [25].

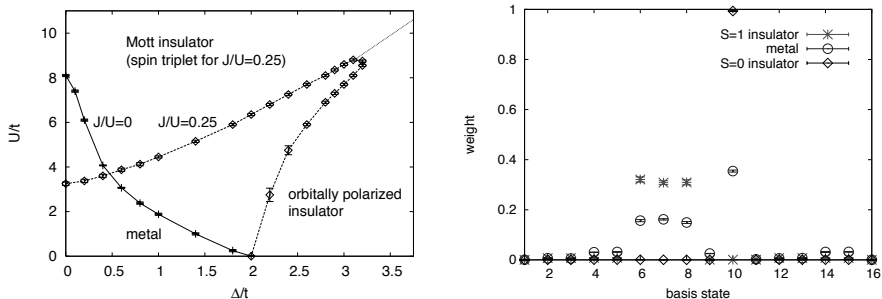
to be clarified, as does the stability of the orbitally selective phases against various perturbations.

24.4.5 High-Spin to Low-Spin Transition in a Two-Orbital Model

In this section, we show that a two-orbital model with Hund coupling and crystal field splitting exhibits two fundamentally different Mott phases, one characterized by a vanishing orbital susceptibility, and one adiabatically connected to the band insulating state [21]. We characterize these phases in terms of the atomic ground states.

The left panel of Fig. 24.7 shows the metal-insulator phase diagram in the space of crystal field splitting and Coulomb repulsion for several values of J/U . In the absence of a crystal field splitting ($\Delta = 0$), one observes a metal-insulator transition at a strongly J -dependent critical U . For $J = 0$, the critical U decreases monotonically with increasing Δ . For $J > 0$, the first effect of a small Δ is to stabilize the metallic phase. Then, at larger Δ , a reentrant insulating phase occurs. This behavior arises from the unusual nature of the insulating state at $J > 0$ and small Δ , which is characterized at $T = 0$ by a strictly vanishing orbital susceptibility. If Δ is increased at large U , this state makes a transition to an orbitally polarized insulator at $\Delta \approx \sqrt{2}J$. We therefore plot in Fig. 24.7 the curve $\Delta = \sqrt{2}J$ as a dotted line, and suggest that it corresponds to the $T = 0$ phase boundary between two distinct insulating states.

Indeed, at $\Delta = \sqrt{2}J$ a level crossing occurs between the spin triplet eigenstates, with energy $U - 3J - 2\mu$ and the lowest energy singlet eigenstate, with

**FIGURE 24.7**

Left panel: Phase diagram in the plane of crystal field splitting Δ and intraorbital Coulomb repulsion U for indicated values of J/U . For $J = 0$ the phase boundary is a monotonic function of Δ , whereas for $J/U > 0$ it peaks near $\Delta = \sqrt{2}J$ (indicated by the dotted lines). The insulating state in the region $\Delta < \sqrt{2}J$ is characterized by a vanishing orbital susceptibility. Right panel: Weight of the different eigenstates of H_{loc} for $U/t = 6$, $J/U = 0.05$, and $\Delta/t = 0.3, 0.5, 0.7$. The smallest crystal field splitting corresponds to a spin 1 insulating state with suppressed orbital susceptibility, the intermediate value to a metallic state, and the largest splitting to a spin 0 orbitally polarized insulator. Figures taken from Ref. [21].

energy $U - \sqrt{J^2 + 4\Delta^2} - 2\mu$, of H_{loc} . The triplet states have one electron in each orbital and gain no energy from orbital polarization, while the energy of the spin singlet states depends on Δ .

It is instructive to look at the contribution to the partition function from the different eigenstates of the local Hamiltonian. The right hand panel of Fig. 24.7 plots the probability of the system to be in one of the 16 eigenstates of H_{loc} at any given time, where $J/U = 0.05$ and $\Delta/t = 0.3, 0.5$, and 0.7. In the small- Δ insulating phase, the triplet states, labeled '6,' '7,' and '8,' are occupied, with small excursions into states with occupancy 1 or 3. In the metallic phase, a large number of states are visited, while in the orbitally polarized insulator, the dominant local state, whose weight increases continuously with Δ , is the lowest energy spin singlet state, labeled '10.' The triplet states are almost completely suppressed in the orbitally polarized phase. The insulator-insulator transition at large U therefore appears to be a phenomenon related to a level crossing in the impurity system, which survives the coupling to the lattice because of the gap in the many-body density of states.

24.5 Conclusion

QIMs provided some of the first clearly understood examples of QPTs and remain to this day a source of new stimulation for the field. They are also important as auxiliary problems in the DMFT of bulk correlated electron systems. The development of powerful new numerical methods has provided access to the low temperature behavior of broad families of QIMs. These improved capabilities and their application to DMFT calculations have led to the discovery of apparently new classes of QPTs, whose properties and consequences have not yet been fully explored.

Acknowledgements – We are grateful to our collaborators A. Comanac, E. Gull, O. Parcollet, M. Troyer, and many others for stimulating discussions and collaborations. AJM was supported by NSF-DMR-0705847 and PW by SNF Grant PP002-118866.

Bibliography

- [1] A. Georges *et al.*, Rev. Mod. Phys. **68**, 13 (1996); T. Maier *et al.*, Rev. Mod. Phys. **77**, 1027 (2005); G. Kotliar *et al.*, Rev. Mod. Phys. **78**, 865 (2006).
- [2] J. K. Freericks *et al.*, Phys. Rev. Lett. **97**, 266408 (2006); M. Eckstein, M. Kollar, and P. Werner, Phys. Rev. Lett. **103**, 056403 (2009); M. Eckstein, M. Kollar, and P. Werner, Phys. Rev. B **81**, 035108 (2010).
- [3] P. Werner and A. J. Millis, Phys. Rev. B **74**, 155107 (2006).
- [4] J. Otsuki, H. Kusunose, P. Werner, and Y. Kuramoto, J. Phys. Soc. Jpn. **76**, 114707 (2007).
- [5] W. Metzner and D. Vollhardt, Phys. Rev. Lett. **62**, 324 (1989).
- [6] A. Georges and G. Kotliar, Phys. Rev. B **45**, 6479 (1992).
- [7] M. H. Hettler *et al.*, Phys. Rev. B **58**, R 7475 (1998).
- [8] A. N. Rubtsov, V. V. Savkin, and A. I. Lichtenstein, Phys. Rev. B **72**, 035122 (2005).
- [9] E. Gull, P. Werner, O. Parcollet, and M. Troyer, Europhys. Lett. **82**, 57003 (2008).
- [10] S. M. Rombouts, K. Heyde, and N. Jachowicz, Phys. Rev. Lett. **82**, 4155 (1999).

- [11] K. Mikelsons, A. Macridin, and M. Jarrell, Phys. Rev. E **79**, 057701 (2009).
- [12] J. E. Hirsch and R. M. Fye, Phys. Rev. Lett. **56**, 2521 (1986).
- [13] P. Werner, A. Comanac, L. de' Medici, M. Troyer, and A. J. Millis, Phys. Rev. Lett. **97**, 076405 (2006).
- [14] K. Haule, Phys. Rev. B **75**, 155113 (2007).
- [15] A. Läuchli and P. Werner, Phys. Rev. B **80**, 235117 (2009).
- [16] E. Gull, P. Werner, A. J. Millis, and M. Troyer, Phys. Rev. B **76**, 235123 (2007).
- [17] Jaebeom Yoo *et al.*, J. Phys. A: Math. Gen. **38** (2005) 10307-10310.
- [18] J. Orenstein and A. J. Millis, Science **288**, 468 (2000).
- [19] P. W. Anderson, Science **235**, 1196 (1987).
- [20] P. Werner and A. J. Millis, Phys. Rev. Lett. **99**, 126405 (2007).
- [21] P. Werner, E. Gull, M. Troyer, and A. J. Millis, Phys. Rev. Lett. **101**, 166405 (2008).
- [22] O. Gunnarsson, E. Koch, and R. M. Martin, Phys. Rev. B **54** 11026 (1996).
- [23] E. Pavarini *et al.*, Phys. Rev. Lett. **92**, 176403 (2004).
- [24] A. Liebsch, Phys. Rev. B **77**, 115115 (2008); L. de' Medici, S. R. Hassan, M. Capone, and X. Dai, Phys. Rev. Lett. **102**, 126401 (2009).
- [25] P. Werner, E. Gull, and A. J. Millis, Phys. Rev. B **79**, 115119 (2009).
- [26] P. Kostic *et al.*, Phys. Rev. Lett. **81**, 2498 (1998); J. S. Dodge *et al.*, Phys. Rev. Lett. **85**, 4932 (2000).

Part V

Quantum Phase Transitions Across Physics

Quantum Phase Transitions in Dense QCD

Tetsuo Hatsuda

Physics Department, The University of Tokyo, Tokyo 113-0033, Japan

Kenji Maeda

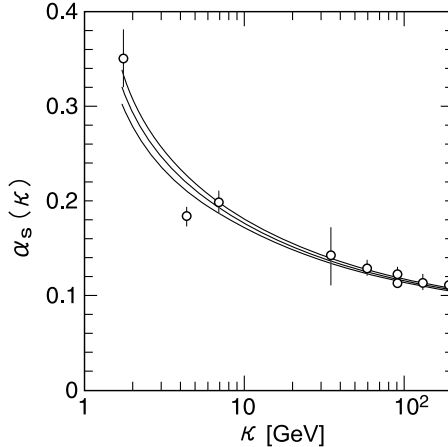
Physics Department, The University of Tokyo, Tokyo 113-0033, Japan

Quantum chromodynamics (QCD) at finite temperature, T , and quark chemical potential, μ , has a rich phase structure: at low T and low μ , the Nambu-Goldstone (NG) phase with nearly massless pions is realized by the dynamical breaking of chiral symmetry through condensation of quark-anti-quark pairs, while, at low T and high μ , a Fermi liquid of deconfined quarks is expected to appear as a consequence of asymptotic freedom. Furthermore, in such cold quark matter, condensation of quark-quark pairs leads to color superconductivity (CSC). At high T for arbitrary μ , all the condensates melt away and a quark-gluon plasma (QGP) is realized. The experimental exploration of thermal phase transitions from the NG phase to QGP is being actively pursued in ultrarelativistic heavy ion collisions at RHIC (Relativistic Heavy Ion Collider), and will be continued at the LHC (Large Hadron Collider). The quantum phase transition (QPT) from the NG phase to the CSC at low T is also relevant to heavy-ion collisions at moderate energies, and is of interest in the interiors of neutron stars and possible quark stars. In this chapter, after a brief introduction to the basic properties of QCD, the current status of the QCD phase structure and associated QPTs will be summarized with particular emphasis on the symmetry realization of each phase. Possible connections between the physics of QCD and that of ultracold atoms are also discussed.

25.1 Introduction to QCD

Quantum chromodynamics (QCD), which is the color $SU(3)_C$ gauge theory of quarks and gluons [1], is now established as the fundamental theory of strong interactions. The Lagrangian density of QCD reads

$$\mathcal{L}_{\text{QCD}} = \bar{q}_{\text{L}} i \not{D} q_{\text{L}} + \bar{q}_{\text{R}} i \not{D} q_{\text{R}} - \frac{1}{4} G_{\mu\nu}^{\alpha} G_{\alpha}^{\mu\nu} + \bar{q}_{\text{L}} m q_{\text{R}} + \bar{q}_{\text{R}} m q_{\text{L}}, \quad (25.1)$$

**FIGURE 25.1**

The QCD fine-structure constant α_s determined from τ decay, Υ decay, deep inelastic scattering, e^+e^- annihilation and the Z -boson resonance shape and width [3].

where $D \equiv \gamma_\mu D^\mu$, the covariant derivative is $D^\mu \equiv \partial^\mu + igt^\alpha A_\alpha^\mu$ with g being the QCD coupling constant, t^α the $SU(3)_C$ group generator and A_α^μ the gluon field belonging to the adjoint representation of $SU(3)_C$. The gluon field-strength tensor is $G_\alpha^{\mu\nu} \equiv \partial^\mu A_\alpha^\nu - \partial^\nu A_\alpha^\mu - gf^{\alpha\beta\gamma} A_\beta^\mu A_\gamma^\nu$ with $f^{\alpha\beta\gamma}$ being the structure constant of the $SU(3)_C$ group.

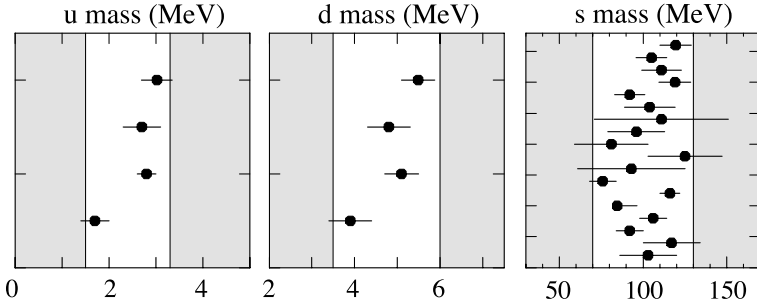
The quark field q belongs to the fundamental representation of $SU(3)_C$. The right- (left-) handed quark $q_R = \frac{1}{2}(1 + \gamma_5)q$ ($q_L = \frac{1}{2}(1 - \gamma_5)q$) is an eigenstate of the chirality operator γ_5 with the eigenvalue +1 (-1). Although quarks have six flavors (u,d,c,s,t,b) in the real world, we focus only on three light quarks (u,d,s) in this chapter, so that the quark mass matrix is $m = \text{diag}(m_u, m_d, m_s)$. As is evident from Eq. (25.1), only the mass term can mix the left-handed quark and the right-handed quark in the QCD Lagrangian.

The running coupling constant $g(\kappa)$ is defined as an effective coupling strength at the energy scale κ . Due to the asymptotic freedom of QCD [2], $g(\kappa)$ becomes small when κ increases as seen explicitly in the two-loop perturbation,

$$\alpha_s(\kappa) = \frac{g^2(\kappa)}{4\pi} \simeq \frac{1}{4\pi\beta_0 \ln(\kappa^2/\Lambda_{\text{QCD}}^2)} \left[1 - \frac{\beta_1}{\beta_0^2} \frac{\ln(\ln(\kappa^2/\Lambda_{\text{QCD}}^2))}{\ln(\kappa^2/\Lambda_{\text{QCD}}^2)} \right], \quad (25.2)$$

where $\beta_0 = (11 - \frac{2}{3}N_f)/(4\pi)^2$ and $\beta_1 = (102 - \frac{38}{3}N_f)/(4\pi)^4$ with N_f being the number of flavors. Here, $\Lambda_{\text{QCD}} \simeq 200$ MeV = 2×10^8 eV is called the QCD scale parameter which is determined from the comparison of Eq. (25.2) with the experimental data in high energy processes satisfying $\kappa \gg \Lambda_{\text{QCD}}$ (see Fig. 25.1).

Equation (25.2) implies that $\alpha_s(\kappa \sim \Lambda_{\text{QCD}}) \sim O(1)$, so that QCD pertur-

**FIGURE 25.2**

The masses of u, d and s quarks at the scale $\kappa = 2$ GeV determined from various observables and methods [3].

bation theory breaks down. This leads to various non-perturbative phenomena such as the confinement of quarks and gluons and the dynamical breaking of chiral symmetry [4, 5] at low energies, $\kappa < \Lambda_{\text{QCD}}$. These are responsible for the formation of hadrons ($q\bar{q}$ mesons and qqq baryons), and also for the origin of their masses. On the other hand, at extremely high temperature and/or high baryon density where $\alpha_s(\kappa \gg \Lambda_{\text{QCD}}) \ll 1$, the system may be treated as weakly-interacting matter made of quarks and gluons. Thus, there must be a phase transition from the hadronic matter composed of confined quarks and gluons at low energies to the deconfined quark-gluon matter at high energies.

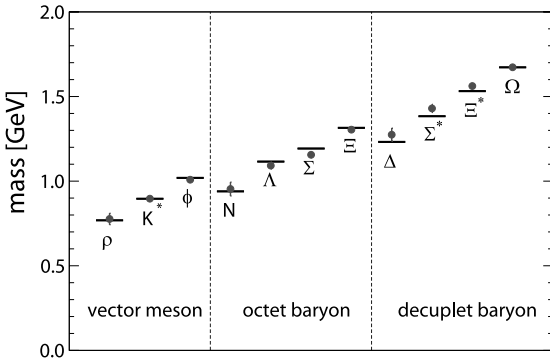
Due to quantum corrections, the quark mass m also becomes κ dependent. As seen from Fig. 25.2, the current determination of the u and d quark masses at $\kappa = 2$ GeV indicates that they are about 50 to 100 times smaller than Λ_{QCD} , while the s quark mass is comparable to Λ_{QCD} . Therefore, it is legitimate to treat m_u/Λ_{QCD} and m_d/Λ_{QCD} as small expansion parameters, while the expansion by m_s/Λ_{QCD} does not necessarily work. Systematic expansion in terms of the quark masses is called chiral perturbation theory and has been successfully applied to a wide variety of QCD phenomena [6].

25.1.1 Symmetries in QCD

Let us consider the following transformations of the quark fields:

$$q_L \rightarrow e^{-i\theta_B} e^{-i\theta_A} V_L V_C q_L, \quad q_R \rightarrow e^{-i\theta_B} e^{+i\theta_A} V_R V_C q_R, \quad (25.3)$$

where the gauge rotation V_C is a local $SU(3)_C$ transformation in the color space, while the chiral rotation $V_{L(R)}$ is a global $SU(3)_{L(R)}$ transformation in the flavor space. The phases θ_B and θ_A are associated with a global $U(1)_B$ transformation, baryon-number rotation, and a global $U(1)_A$ transformation, axial rotation, respectively. For $m_{u,d,s} = 0$, the flavor- $SU(3)$ chiral limit, the QCD Lagrangian Eq. (25.1) is invariant under Eq. (25.3) together with the

**FIGURE 25.3**

Light hadron spectra obtained from lattice QCD Monte Carlo simulations with dynamical u, d, s quarks in the Wilson fermion formalism. The spatial lattice volume V and the lattice spacing a are $(2.9 \text{ fm})^3$ and 0.09 fm , respectively. Horizontal bars denote the experimental values [8].

$SU(3)_C$ gauge transformation of the gluons, so that the full continuous symmetries of QCD become

$$\mathcal{G} \equiv [SU(3)_C]_{\text{local}} \otimes [SU(3)_L \otimes SU(3)_R]_{\text{global}} \otimes [U(1)_B]_{\text{global}}. \quad (25.4)$$

Although the $U(1)_A$ looks like a symmetry of Eq. (25.1), it is explicitly broken by a quantum effect known as the axial anomaly [7] which reduces $U(1)_A$ to its discrete subgroup $Z(2N_f)_A = Z(6)_A$. The masses of light quarks $m_{u,d,s}$ act as small external fields to break the global chiral symmetry $[SU(3)_L \otimes SU(3)_R]_{\text{global}}$.

In the past few years, remarkable progress has occurred in calculating hadron spectra on the basis of lattice QCD Monte Carlo simulations with light dynamical u, d, s quarks. This has been achieved partly due to the growth of supercomputer speed and partly due to new algorithms: simulations with quark masses very close to the physical values are now possible in the Wilson fermion formalism [8, 9]. Shown in Fig. 25.3 is an example of such calculations for meson and baryon masses extrapolated to the physical quark masses using the simulation data taken in the interval, $\frac{1}{2}(m_u + m_d) = 3.5 \text{ MeV} - 67 \text{ MeV}$ at $\kappa = 2 \text{ GeV}$. The experimental values are reproduced to 3% accuracy at present.

25.1.2 Dynamical Breaking of Chiral Symmetry

Although the QCD Lagrangian in the flavor-SU(3) chiral limit has the symmetry \mathcal{G} in Eq. (25.4), the ground state of the system breaks some of the symmetries dynamically. Consider the QCD vacuum $|0\rangle$ at zero temperature and zero baryon density. Taking into account the fact that QCD does not allow dynamical breaking of parity and vector symmetries in the vacuum [10], the following is one of the possible symmetry breaking patterns,

$$\mathcal{G} \rightarrow \text{SU}(3)_C \otimes \text{SU}(3)_{L+R} \otimes \text{U}(1)_B, \quad (25.5)$$

where simultaneous transformation of the left- and right-handed quarks (vector rotation, $V_L = V_R$) as indicated by $\text{SU}(3)_{L+R}$ remains as a symmetry of the vacuum. An order parameter to characterize this *dynamical breaking of chiral symmetry* would be the *chiral condensate*, $\langle\bar{q}q\rangle_0 \equiv \langle 0|\bar{q}q|0\rangle$, which is not invariant under the opposite rotation of the left- and right-handed quarks, $V_L = V_R^\dagger$. Recent lattice QCD simulations using overlap Dirac fermion with dynamical u, d, s quarks indeed show that Eq. (25.5) is realized with the chiral condensate [11]

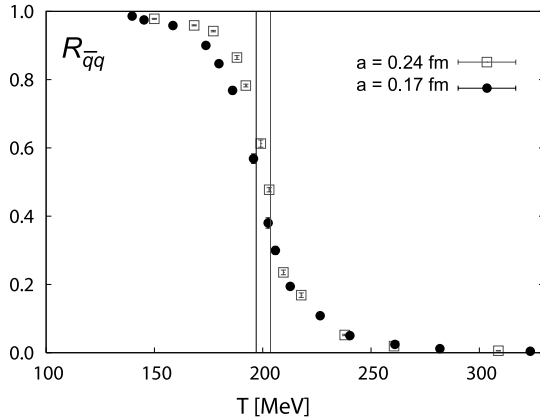
$$\frac{1}{2}\langle\bar{u}u + \bar{d}d\rangle_0 \simeq -(249 \text{ MeV})^3 \text{ at } \kappa = 2 \text{ GeV}. \quad (25.6)$$

The non-vanishing chiral condensate, $\langle\bar{q}q\rangle_0 = \langle\bar{q}_L q_R + \bar{q}_R q_L\rangle_0 \neq 0$, implies that the quark–anti-quark pairs are Bose-Einstein condensed. It also implies that a non-perturbative mixing between the left- and right-handed quarks takes place in the QCD vacuum: in other words, an effective quark mass called the chiral gap is dynamically generated. Indeed, there is phenomenological evidence that the u, d quarks and s quark have effective masses $M_{u,d} \sim 350$ MeV and $M_s \sim 550$ MeV inside hadrons [5].

The NG bosons associated with the dynamical breaking of the flavor-SU(3) chiral symmetry are nothing but the pions, kaons and the η -meson. Moreover, one can derive a spectral sum rule, called the Gell-Mann–Oakes–Renner relation, which relates the pion mass to the chiral condensate as $f_\pi^2 m_{\pi^\pm}^2 = -\hat{m}\langle\bar{u}u + \bar{d}d\rangle_0 + O(\hat{m}^2)$. Here $\hat{m} \equiv (m_u + m_d)/2$, $f_\pi = 92.4$ MeV is the pion decay constant, and $m_{\pi^\pm} \simeq 140$ MeV are the charged pion masses. A similar relation holds also for the neutral pion π^0 . In the limit $m_{u,d} \rightarrow 0$, the pion mass vanishes, in accordance with the NG theorem.

25.2 QCD Matter at High Temperature

As the temperature T of the system increases, the condensed $q\bar{q}$ pairs in the QCD vacuum are melted away by thermal fluctuations. This is analogous to the phase transition in metallic superconductors with the electron pairing $\langle e_\uparrow e_\downarrow \rangle$ as an order parameter.

**FIGURE 25.4**

Normalized chiral condensate $\mathcal{R}_{\bar{q}q} = [\langle \bar{u}u \rangle - (\hat{m}/m_s)\langle \bar{s}s \rangle]/[\langle \bar{u}u \rangle_0 - (\hat{m}/m_s)\langle \bar{s}s \rangle_0]$ as a function of T for two different lattice spacings, $a = 0.24$ fm and $a = 0.17$ fm, calculated by lattice QCD simulations with dynamical u, d, s quarks in the staggered fermion formalism. The vertical band in the middle indicates the pseudo-critical temperature T_{pc} [12].

To see that $\langle \bar{q}q \rangle$ vanishes at extreme high T , let us consider the QCD partition function at zero baryon density, $Z_{QCD} = \text{Tr exp}(-\hat{H}_{QCD}/T) \equiv \exp(P(T)V/T)$, which leads to $\langle \bar{q}q \rangle = -\partial P(T)/\partial m_q$. If we have a situation where $T \gg \Lambda_{QCD}$, the system is approximated by a Stefan-Boltzmann gas of free quarks and gluons because of asymptotic freedom. Since the quark-gluon vertex does not change chirality¹ the expectation value of $\bar{q}q = \bar{q}_L q_R + \bar{q}_R q_L$ vanishes to any finite order of the perturbation as long as $m_q = 0$.

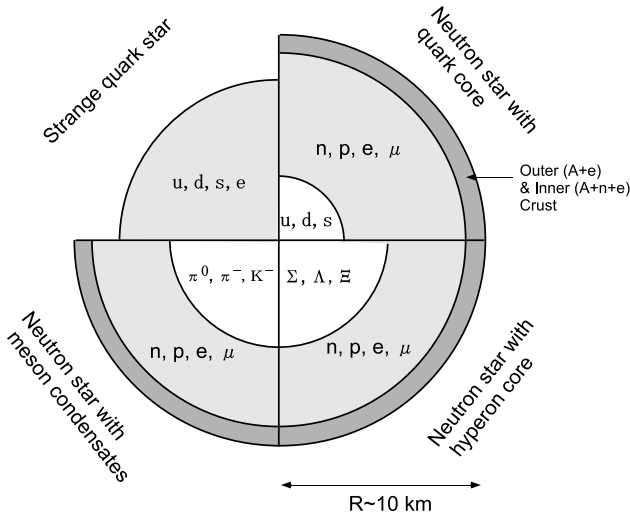
As shown in Fig. 25.4, lattice QCD Monte Carlo simulations at finite T with zero baryon density [12] indeed indicate a sudden drop of the chiral condensate around the pseudo-critical temperature determined from the susceptibility peak,

$$T_{pc} \simeq 200 \text{ MeV} = 2.3 \times 10^{12} \text{ K}. \quad (25.7)$$

Note that the phase transition from the low- T , NG phase to the high T , QGP phase is first order in the flavor-SU(3) chiral limit, $m_{u,d,s} = 0$ and is second order in the flavor-SU(2) chiral limit, $m_{u,d} = 0, m_s = \infty$ [13]. On the other hand, in the presence of finite quark masses $m_{u,d,s}$ acting as external fields, the transition is a crossover, as seen in Fig. 25.4. For more details on the QCD thermodynamics, see [14].

The high temperature QGP is believed to have been present in the early

¹The transition between q_L and q_R is not allowed in perturbation theory.

**FIGURE 25.5**

Possible internal structures and compositions of four different types of compact stars [13].

universe up to 10^{-5} sec after the Big Bang. Attempts to create extremely hot systems in which a QGP occurs have a long history, starting with experiments in the 1980's and 1990's at the SPS (Super Proton Synchrotron) at CERN, continuing from 2000 at RHIC at BNL (Brookhaven National Laboratory), as well as the new LHC at CERN; the latter is slated to begin heavy ion studies in the Fall of 2010. RHIC has already produced plenty of data showing not only evidence of a QGP but also its strongly interacting character [13, 15]. In the following, we will focus more on QCD matter with finite baryon density at low T . Such a system may undergo successive QPTs which are relevant to the physics of neutron stars and of possible quark stars.

25.3 QCD Matter at High Baryon Density

Soon after the discovery of the asymptotic freedom of QCD, a possible transition from hadronic matter to quark matter in the core of neutron stars was pointed out [16]. A strange quark star entirely made of deconfined u, d, s quarks, yet undiscovered, was also proposed [17].

Shown in Fig. 25.5 is a schematic view of various forms of compact stars, from the neutron star to the quark star. The typical radius of a neutron star is about 10 km, while its mass is comparable to the solar mass $M_{\odot} \simeq 2 \times 10^{30}$ kg.

Since neutrons cannot be bound by the strong interaction alone, the presence of the gravitational force is essential to holding the neutron star together. This implies that the radius increases as the mass decreases. The masses of neutron stars in binary systems are centered around $1.35M_{\odot}$. The observed upper limit of the surface temperature of neutron stars is less than 10^9 K after 1 year from their birth. In early stages, cooling occurs through neutrino emissions, while in later stages it is dominated by surface photon emissions.

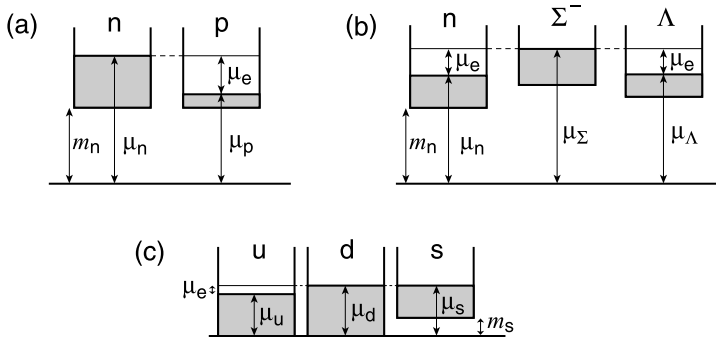
For pulsars, i.e., rotating neutron stars, the measured rotational frequency ranges from milliseconds to several seconds. The surface magnetic field is typically 10^{12} gauss for ordinary pulsars with rotational period $P \sim 1$ s and $dP/dt \sim 10^{-15}$. There are also stars with much larger (smaller) dP/dt and larger (smaller) magnetic field $\sim 10^{15}(10^9)$ gauss. Sudden spin-up of the rotation associated with a subsequent relaxation to the normal rotation has been observed and is called a *glitch*. This phenomena should be related to the internal structure of neutron stars, in particular the superfluidity of the neutron liquid.

The outer crust of neutron stars is a solid composed of heavy nuclei forming a Coulomb lattice in the sea of degenerate electrons. As the pressure and the density increase toward the inner region, electrons tend to be captured by nuclei and at the same time neutrons drip out from the nuclei, so that the system is composed of neutron-rich heavy nuclei in the Fermi sea of the neutrons and electrons. Eventually, the nuclei dissociate into a neutron liquid and the system becomes a degenerate Fermi system composed of superfluid neutrons together with a small fraction of superconducting protons and normal electrons.

When the baryon number density (ρ) of the core of neutron stars exceeds a few times the central density of heavy atomic nuclei, $\rho_0 = 0.16 \text{ fm}^{-3} = 0.16 \times 10^{39} \text{ cm}^{-3}$, one may expect exotic components such as the hyperons (baryons with s quarks), Bose-Einstein condensates of pions and kaons, and deconfined quark matter, which can contribute to the acceleration of the neutron-star cooling. For more details of the physics of high density matter and compact stars, see, e.g., [18].

25.3.1 Neutron-Star Matter and Hyperonic Matter

Although neutron stars are mainly composed of degenerate neutrons, other species are also present as a result of chemical equilibrium conditions. Indeed, matter made of only neutrons is unstable against β -decay, $n \rightarrow p + e^- + \bar{\nu}_e$. After the decay, the electron-neutrino leaves the star without much interaction if the neutron star is cold enough. On the other hand, the protons and the electrons remain in the star and form a degenerate Fermi liquid together with the neutrons. The equilibrium configuration of n, p and e^- , which we call *standard neutron-star matter* (see Fig. 25.6(a)), is determined by three conditions, chemical equilibrium, charge neutrality and the baryon-number

**FIGURE 25.6**

Compositions of matters under chemical equilibrium and charge neutrality conditions in the Fermi gas model. Shaded areas show the occupied states. (a) Neutron-star matter with n, p, and e^- . (b) Hyperon matter with n, Σ^- and Λ . (c) u-d-s quark matter with finite strange quark mass m_s .

conservation: $\mu_n = \mu_p + \mu_e$, $\rho_p = \rho_e$, and $\rho = \rho_n + \rho_p$, where ρ_i denotes the number density of i -species.

If we assume non-interacting degenerate fermions for simplicity, it is easy to find an analytic solution for the above conditions; then the proton fraction in a neutron star for a given baryon number density ρ reads $\rho_p/\rho_n \simeq \frac{1}{8}[1 + (m_n^3/3\pi^2\rho_n)^{2/3}]^{-3/2}$. This is a monotonically increasing function of ρ_n and approaches the asymptotic limit 1/8 from below. As the neutron density further increases and the electron chemical potential exceeds the muon mass, $\mu_e > m_\mu = 105$ MeV, the system composed of n, p, e^- and μ^- is realized.

As the baryon density increases further, hyperons enter into the game. This is because the Fermi energy of the neutron exceeds the threshold for neutron-decay into hyperons; see Fig. 25.6(b). Hyperons such as Σ^- and Λ may appear for $\rho > (2 - 3)\rho_0$. Which hyperon appears first depends on the still uncertain hyperon-nucleon interactions.

25.3.2 Quark Matter

As the baryon number density ρ of the system exceeds $(3 - 5)\rho_0$, the neutrons, protons and hyperons start to strongly overlap; the process of overlap leading to a new state of matter can be described by percolation theory. The quark number density ρ_q for each flavor is related to ρ as $\rho_q = (N_c/N_f)\rho$ with $N_c = 3$ being the number of colors and N_f the active number of flavors so that the critical quark chemical potential, above which the percolation to quark matter

takes place, is estimated as

$$\mu_c = (\pi^2 \rho_q)^{1/3} \simeq (380 - 450) \text{ MeV}. \quad (25.8)$$

Here we have assumed a non-interacting and degenerate quark matter composed of massless u and d quarks.

Let us now consider quark matter composed of only u, d and e^- . The condition of chemical equilibrium ($d \leftrightarrow u + e^-$), charge neutrality, and the baryon number conservation read $\mu_d = \mu_u + \mu_e$, $\frac{2}{3}\rho_u - \frac{1}{3}\rho_d - \rho_e = 0$, and $\frac{1}{3}(\rho_u + \rho_d) = \rho$, respectively. The factors $2/3$ and $-1/3$ originate from the electric charges of the quarks and $1/3$ from the baryon number of a quark. If we assume non-interacting quarks at high density ($\mu_q \gg m_q$), one immediately finds $\mu_u \simeq 0.80 \mu_d$. Thus the Fermi energy of the d quark is slightly higher than that of the u quark. This is different from the situation of neutron matter, where n and p have quite different Fermi energies due to non-relativistic kinematics, as shown in Fig. 25.6(a).

If the quark matter is composed of u, d, s and e^- , chemical equilibration is achieved through the processes $d \leftrightarrow u + e^-$, $s \leftrightarrow u + e^-$, and $d + u \leftrightarrow u + s$. Then the equilibrium conditions read $\mu_d = \mu_u + \mu_e$, $\mu_s = \mu_d$, $-\frac{1}{3}(\rho_d + \rho_s) + \frac{2}{3}\rho_u - \rho_e = 0$, and $\frac{1}{3}(\rho_u + \rho_d + \rho_s) = \rho$. For $\mu_q \gg m_q$, they lead to $\mu_u = \mu_d = \mu_s$ and $\mu_e = 0$. That is, massless u-d-s quark matter is charge-neutral by itself without electrons. If we have finite m_s , then ρ_s is reduced relative to $\rho_{u,d}$ and the electrons become necessary to make the system charge-neutral, as shown in Fig. 25.6(c).

25.4 Superfluidity in Neutron-Star Matter

If there exists an attractive channel between the fermions near the Fermi surface, the system undergoes a transition to superfluidity or superconductivity in three spatial dimensions. This is indeed the case in neutron-star matter where the attraction between the neutrons due to the spin-orbit nuclear force in the $(S, L, J) = (\text{spin}, \text{orbital angular momentum}, \text{total angular momentum}) = (1, 1, 2)$ channel leads to the condensation of $^{2S+1}L_J = ^3P_2$ Cooper pairs, i.e., neutron superfluidity, and the attraction between the protons due to the spin-independent nuclear force in the $(S, L, J) = (0, 0, 0)$ channel leads to the condensation of 1S_0 Cooper pairs, i.e., proton superconductivity [19].

Other than the superfluidity and superconductivity of the nucleons, the condensation of pions (π^0 and π^-) and kaons (K^-) have been studied extensively. For more details on nucleon superfluidity, meson condensation and its implications for the physics of compact stars, see [20, 21].

25.5 Color Superconductivity in Quark Matter

Quark matter exhibits CSC which originates from the formation of Cooper pairs of quarks near the Fermi surface (see [22] and references therein). The dominant attractive interaction responsible for quark-quark pairing at high density is the color-magnetic interaction mediated by the gluon.

There are some characteristic differences between CSC and standard BCS-type superconductivity:

- (i) Quark matter at high density is a relativistic system where the quark chemical potential μ is comparable to or larger than the quark mass m_q . In such a case, the velocities of quarks near the Fermi surface are close to the velocity of light and the magnetic interaction is no longer suppressed in comparison to the electric interaction.
- (ii) The color-magnetic interaction is screened only dynamically by Landau-damping, while the color-electric interaction is Debye-screened as usual. Therefore, collinear quark-quark scattering on the Fermi surface is dominated by the color-magnetic interaction, which leads to an unconventional form of the fermion gap $\Delta \propto \mu e^{-c/\sqrt{\alpha_s}}$ [23]. Because of this non-BCS form where the coupling strength enters as $\sqrt{\alpha_s}$ instead of α_s , Δ/μ becomes sizable even for weak coupling.
- (iii) Due to color and flavor indices of the quarks, the CSC gap acquires color-flavor matrix structure, which leads to various phases depending on μ and T ; these include the 2SC (2-flavor color superconducting) phase, the CFL (color-flavor-locked) phase, the FFLO phase (Fulde-Farrel-Larkin-Ovchinnikov, see Chap. 11), the crystalline phase, and so on [22].

25.5.1 The Gap Equation

Let us illustrate the role of the above color-magnetic interaction by considering a simplified situation where quark matter is composed of only massless u and d quarks with equal Fermi energies [24]. In this case, the u quark with red color and the d quark with green color in flavor-singlet and color anti-triplet combinations are paired, while all the other quarks are unpaired. This is called the 2SC phase.

Using the standard Nambu-Gor'kov representation $\Psi = \begin{pmatrix} q \\ q_c \end{pmatrix}$ with the charge conjugate field $q^c \equiv C\bar{q}^t$ and the charge conjugation matrix $C \equiv i\gamma^0\gamma^2$, the Schwinger-Dyson equation for the quark self-energy Σ in the ladder approximation is written as

$$\Sigma(k) = -i \int \frac{d^4 p}{(2\pi)^4} g^2(p, k) \Gamma_a^\mu S(p) \Gamma_b^\nu D_{\mu\nu}^{ab}(p - k), \quad (25.9)$$

where $g^2(p, k)$ is the momentum-dependent effective coupling, $D_{\mu\nu}^{ab}$ is the in-medium gluon propagator and Γ_μ^a is the bare quark-gluon vertex. The off-diagonal anomalous component of Σ in the Nambu-Gor'kov space is directly related to the gap function $\Delta(k) = \Delta_+(k)\Lambda_+ + \Delta_-(k)\Lambda_-$, where Λ_\pm are the projection operators onto the positive and negative energy states. Therefore, $\Delta_+(k)$ and $\Delta_-(k)$ are interpreted as the quark gap and anti-quark gap, respectively.

As for $g(q, k)$, the Higashijima-Miransky ansatz, a momentum-dependent QCD coupling with phenomenological infrared regulator, may be adopted [25]. As for the gluon propagator, we take the screened propagator in the Landau gauge,

$$D_{\mu\nu}(k) = -\frac{P_{\mu\nu}^L}{k^2 + m_D^2} - \frac{P_{\mu\nu}^T}{k^2 + i\frac{\pi}{4}m_D^2|k_0|/|k|}, \quad (25.10)$$

where $P_{\mu\nu}^{L,T}$ are the longitudinal and transverse projection operators. The longitudinal (electric) part of the propagator has static screening by the Debye mass $m_D^2 = (1/\pi^2)g^2\mu^2$, so that the static interaction between quarks in the coordinate space is the Yukawa-type short range potential. On the other hand, the transverse magnetic part has only dynamical screening due to Landau damping, so that the static interaction between quarks in the coordinate space is the Coulomb-type long range potential.

In the high density limit, or equivalently the weak coupling limit due to asymptotic freedom, only the interactions near the Fermi surface become relevant and the gap equation can be simplified to give [22, 23]

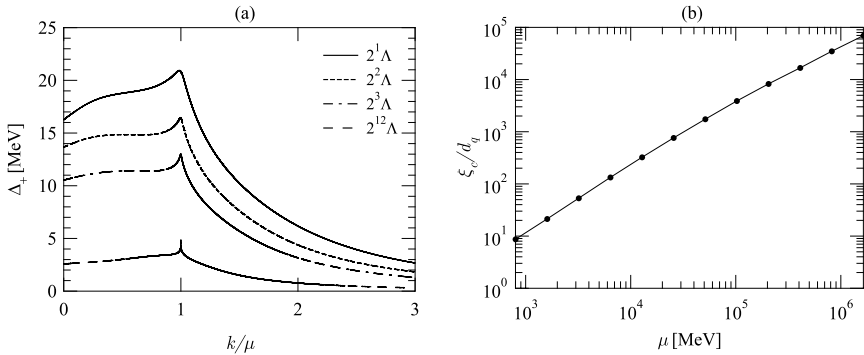
$$\Delta_+ (|\mathbf{k}| = \mu) \cong 2b \mu e^{-(3\pi^2/\sqrt{2})/g(\mu)}, \quad (25.11)$$

with $b = 256\pi^4/g^5(\mu)$ and $g(\mu) = \sqrt{4\pi\alpha_s(\kappa = \mu)}$. The characteristic form of the gap, $e^{-c/g}$, in Eq. (25.11) originates from the long-range color-magnetic interaction in Eq. (25.10) and is different from the BCS form e^{-c/g^2} .

At low densities, sizable diffusion of the Fermi surface occurs and the weak-coupling approximation leading to Eq. (25.11) is not justified. Therefore, we need to solve the gap equation Eq. (25.9) numerically with both magnetic and electric interactions. In Fig. 25.7(a), we show such numerical solution of $\Delta_+(k)$ as a function of $|\mathbf{k}|/\mu$ for a wide range of density. The figure shows that (i) the ratio of the gap and the quark chemical potential Δ_+/μ can be sizable in magnitude, of order 0.03, even for baryon density as high as $\rho \sim 10\rho_0$, and (ii) the gap function $\Delta_+(\mathbf{k})$ has non-trivial momentum dependence with a peak near the Fermi surface.

25.5.2 Tightly Bound Cooper Pairs

The CSC phase is a strongly coupled system partly due to the large value of the coupling constant $\alpha_s(\kappa = \mu)$ and partly due to the long-range nature of the color-magnetic interaction. To clarify this point further, let us consider the

**FIGURE 25.7**

(a) The quark gap $\Delta_+(\mathbf{k})$ as a function of $|\mathbf{k}|/\mu$ for various quark chemical potentials, $\mu = 2^n \times \mu_c$ with $\mu_c = 400$ MeV and $n = 1, 2, 3, 12$, obtained by solving the gap equation Eq. (25.9) numerically [24]. (b) Ratio of the coherence length ξ_c and the average inter-quark distance d_q as a function of μ [24].

coherence length ξ_c defined as a root-mean-square radius of the Cooper-pair wave function, $\varphi_+(\mathbf{r}) \propto \langle q(\mathbf{r})q(\mathbf{0}) \rangle \propto \int \frac{d^3k}{(2\pi)^3} e^{i\mathbf{k} \cdot \mathbf{r}} \frac{\Delta_+(\mathbf{k})}{2\sqrt{(|\mathbf{k}|-\mu)^2 + \Delta_+^2(\mathbf{k})}}$.

Shown in Fig. 25.7(b) is the ratio of the coherence length ξ_c and the average inter-quark distance $d_q = (\pi^2/2)^{1/3} \mu^{-1}$ in u-d quark matter. At high density, this ratio is very large, about 10^5 at $\mu \sim 10^6$ MeV, while at low densities, the ratio becomes small, about 10 at $\mu = 800$ MeV, and may even become less than one at lower densities. This situation is quite similar to the BCS-BEC crossover phenomenon which was recently observed in ultracold atomic systems [26]. The result here suggests that the quark matter possibly realized in the core of neutron stars ($\mu \sim 400$ MeV) may be rather like the BEC of tightly bound Cooper pairs. For further studies of the BCS-BEC crossover in the relativistic system, see, e.g., [27].

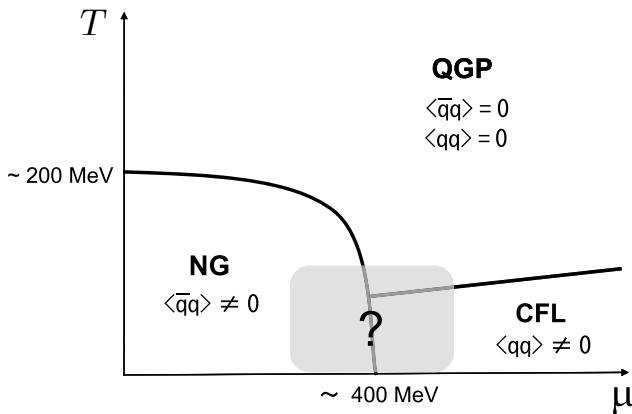
25.6 QCD Phase Structure

The continuous QCD symmetry in the flavor-SU(3) chiral limit ($m_{u,d,s} = 0$), Eq. (25.4), exhibits various symmetry breaking patterns depending on the temperature T and the quark chemical potential μ . In Table 25.1, three examples of the symmetry realizations are shown; the QGP phase, the NG phase and the color-flavor-locked (CFL) phase to be discussed in more detail below. Each phase would appear in the $T - \mu$ phase diagram as illustrated

TABLE 25.1

Symmetry breaking patterns of QCD in the flavor-SU(3) chiral limit ($m_{u,d,s} = 0$). The NG phase, the QGP phase, and the CFL phase denote the Nambu-Goldstone phase, the quark-gluon plasma phase and the color-flavor-locked phase, respectively.

phase	region	unbroken continuous symmetries
QGP phase	$\frac{T}{\Lambda_{\text{QCD}}} \gg 1$	$\text{SU}(3)_C \otimes \text{SU}(3)_L \otimes \text{SU}(3)_R \otimes \text{U}(1)_B$
NG phase	$\frac{T}{\Lambda_{\text{QCD}}} \ll 1, \frac{\mu}{\Lambda_{\text{QCD}}} \ll 1$	$\text{SU}(3)_C \otimes \text{SU}(3)_{L+R} \otimes \text{U}(1)_B$
CFL phase	$\frac{T}{\Lambda_{\text{QCD}}} \ll 1, \frac{\mu}{\Lambda_{\text{QCD}}} \gg 1$	$\text{SU}(3)_{C+L+R}$

**FIGURE 25.8**

The three basic phases of QCD in the T - μ plane in the flavor-SU(3) chiral limit. The phase labels are defined in [Table 25.1](#).

in Fig. 25.8. At intermediate values of $\mu \sim 400$ MeV at low T , a variety of quantum phases have been proposed [20, 22].

As we have discussed in [Sec. 25.1.2](#), the NG phase is characterized by the dynamical breaking of chiral symmetry due to nonvanishing chiral condensate $\langle \bar{q}q \rangle$. On the other hand, in the CSC phase at high chemical potential, the diquark condensate $\langle qq \rangle$ is formed as discussed in [Sec. 25.5](#). In the presence of these condensates, the light quarks and anti-quarks acquire the Dirac-type mass M and the Majorana-type mass Δ_{\pm} , which leads to the relativistic quasi-particle spectrum of a quark near the Fermi surface,

$$\omega(\mathbf{p}) = \sqrt{(\sqrt{\mathbf{p}^2 + M^2} - \mu)^2 + |\Delta_+|^2}. \quad (25.12)$$

25.6.1 Ginzburg-Landau Potential for Hot/Dense QCD

In this subsection, we focus our attention on the QCD phase structure at intermediate values of the chemical potential $\mu \sim 400$ MeV where there would be an interplay between the quark–anti-quark pairing characterized by the chiral condensate $\langle \bar{q}q \rangle$ and the quark–quark pairing characterized by the diquark condensate $\langle qq \rangle$ [28]. Study of this region is not only important to understand the phase transition to quark matter in the deep interior of neutron stars, but also interesting in relation to similar phenomena in other systems such as the interplay between magnetically ordered phases and metallic superconductivity [29] and that between superfluidity and magnetism in ultracold atoms [30].

To analyze such interplay in QCD in a model-independent manner, let us construct a Ginzburg-Landau (GL) potential Ω on the basis of the QCD symmetry Eq. (25.4) as $\Omega(\Phi, d_L, d_R) = \Omega_\chi(\Phi) + \Omega_d(d_L, d_R) + \Omega_{\chi d}(\Phi, d_L, d_R)$. Here the chiral field Φ , which has a 3×3 matrix structure in the flavor space, is defined with the transformation property under Eq. (25.3) as

$$\Phi_{ij} \equiv \langle [\bar{q}_R]^j_a [q_L]^i_a \rangle, \quad \Phi \rightarrow e^{-2i\theta_A} V_L \Phi V_R^\dagger. \quad (25.13)$$

On the other hand, the diquark field d_L , which has a 3×3 matrix structure in the flavor-color space, is defined with the transformation property as

$$[d_L^\dagger]_{ai} \equiv \epsilon_{ijk} \epsilon_{abc} \langle [q_L]^j_b C [q_L]^k_c \rangle, \quad d_L \rightarrow e^{2i\theta_A} e^{2i\theta_B} V_L d_L V_C^t, \quad (25.14)$$

where $C = i\gamma^2\gamma^0$ is the charge conjugation matrix. A similar definition holds for d_R . By definition, the 3×3 matrix $[d_{L(R)}]_{ia}$ belongs to the fundamental representation of $SU(3)_C$ and $SU(3)_{L(R)}$.

The most general form of the GL potential which is invariant under \mathcal{G} in Eq. (25.4), written in terms of the chiral field up to $\mathcal{O}(\Phi^4)$, reads [31],

$$\Omega_\chi = \frac{a_0}{2} \text{Tr } \Phi^\dagger \Phi + \frac{b_1}{4!} (\text{Tr } \Phi^\dagger \Phi)^2 + \frac{b_2}{4!} \text{Tr } (\Phi^\dagger \Phi)^2 - \frac{c_0}{2} (\det \Phi + \det \Phi^\dagger), \quad (25.15)$$

where Tr and det are taken over the flavor indices, i and j . The first three terms on the right hand side are invariant under $\mathcal{G} \otimes U(1)_A$, while the last term represents the axial anomaly which breaks $U(1)_A$ down to $Z(6)_A$. The potential Ω_χ is bounded from below for $b_1 + b_2/3 > 0$ and $b_2 > 0$. If these conditions are not satisfied, we need to introduce terms to $\mathcal{O}(\Phi^6)$ to stabilize the potential, a situation we will indeed encounter. We assume c_0 to be positive so that the chiral condensate at low temperature is positive. Also, we assume that a_0 changes its sign at a certain temperature to drive the chiral phase transition.

The most general form of the GL potential which is invariant under \mathcal{G} , written in terms of the d -field up to $\mathcal{O}(d^4)$, reads [32],

$$\begin{aligned} \Omega_d = & \alpha_0 \text{Tr}[d_L d_L^\dagger + d_R d_R^\dagger] \\ & + \beta_1 \{[\text{Tr}(d_L d_L^\dagger)]^2 + [\text{Tr}(d_R d_R^\dagger)]^2\} + \beta_2 (\text{Tr}[(d_L d_L^\dagger)^2] + \text{Tr}[(d_R d_R^\dagger)^2]) \\ & + \beta_3 \text{Tr}[(d_R d_L^\dagger)(d_L d_R^\dagger)] + \beta_4 \text{Tr}(d_L d_L^\dagger) \text{Tr}(d_R d_R^\dagger). \end{aligned} \quad (25.16)$$

The transition from the normal state to CSC is driven by α_0 changing sign. Unlike $\det \Phi$ in Ω_χ , terms such as $\det d_{L(R)}$ are not allowed in Ω_d , since $\det d_{L(R)}$ carries baryon number and is not invariant under $U(1)_B$.

Finally, the interaction potential which is invariant under \mathcal{G} , written in terms of both chiral and diquark fields to fourth order, reads [28,33],

$$\begin{aligned} \Omega_{\chi d} = & \gamma_1 \text{Tr}[(d_R d_L^\dagger) \Phi + (d_L d_R^\dagger) \Phi^\dagger] \\ & + \lambda_1 \text{Tr}[(d_L d_L^\dagger) \Phi \Phi^\dagger + (d_R d_R^\dagger) \Phi^\dagger \Phi] + \lambda_2 \text{Tr}[d_L d_L^\dagger + d_R d_R^\dagger] \cdot \text{Tr}[\Phi^\dagger \Phi] \\ & + \lambda_3 \{\det \Phi \cdot \text{Tr}[(d_L d_R^\dagger) \Phi^{-1}] + h.c.\}. \end{aligned} \quad (25.17)$$

The term with the coefficient γ_1 originates from the axial anomaly, which imposes that the sign of γ_1 in Eq. (25.17) and of c_0 in Eq. (25.15) be the same.

Equations (25.15)-(25.17) constitute the most general form of the GL potential under the conditions that the phase transition is not strongly first order, i.e., the magnitudes of $\Phi, d_{L(R)}$ are sufficiently smaller than those at zero temperature, and that the condensed phases are spatially homogeneous. To proceed analytically for the flavor-SU(3) chiral limit, we restrict ourselves to maximally symmetric condensates of the form

$$\Phi = \text{diag}(\sigma, \sigma, \sigma), \quad d_L = -d_R = \text{diag}(d, d, d), \quad (25.18)$$

where σ and d are assumed to be real and spatially uniform. We have chosen the relative sign between d_L and d_R in Eq. (25.18) so that the ground state has positive parity, as is indeed favored by the axial anomaly together with finite quark masses. The above ansatz for the diquark condensate has residual symmetry $SU(3)_{C+L+R} \otimes Z(2)$ and is called color-flavor-locking (CFL) because of its symmetry realization [34].²

The reduced GL potential with Eq. (25.18) is

$$\Omega_{3F} = \left(\frac{a}{2} \sigma^2 - \frac{c}{3} \sigma^3 + \frac{b}{4} \sigma^4 + \frac{f}{6} \sigma^6 \right) + \left(\frac{\alpha}{2} d^2 + \frac{\beta}{4} d^4 \right) - \gamma d^2 \sigma + \lambda d^2 \sigma^2. \quad (25.19)$$

Here the axial anomaly leads to $c > 0$ and $\gamma > 0$, while microscopic calculation based on the Nambu–Jona-Lasinio model as well as weak-coupling QCD suggests that λ is positive and plays a minor role in comparison to γ [33]. Note that we have introduced the f -term with $f > 0$ in case b becomes negative. This system can have four phases with dynamical breaking of continuous symmetries;

$$\begin{aligned} \text{QGP phase} & : \sigma = 0, d = 0 \\ \text{NG phase} & : \sigma \neq 0, d = 0 : \mathcal{G} \rightarrow SU(3)_C \otimes SU(3)_{L+R} \otimes U(1)_B \\ \text{CFL phase} & : \sigma = 0, d \neq 0 : \mathcal{G} \rightarrow SU(3)_{C+L+R} \\ \text{COE phase} & : \sigma \neq 0, d \neq 0 : \mathcal{G} \rightarrow SU(3)_{C+L+R}. \end{aligned} \quad (25.20)$$

²Note that $Z(2)$ corresponds to the reflection $q_{L(R)} \rightarrow -q_{L(R)}$.

The COE (coexistence) phase is favored by the axial anomaly, since the simultaneous presence of d and positive σ makes the GL potential lower because of the γ -term with $\gamma > 0$. Note that even the unbroken discrete symmetry $Z(2)$ is common between CFL and COE phases, so that they cannot be distinguished from the symmetry point of view.

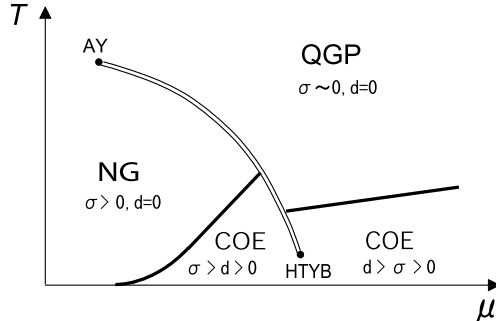
For the flavor-SU(2) chiral limit with $m_{u,d} = 0$ and $m_s = \infty$, the condensates with the s quark disappear, so that we have $\Phi = \text{diag}(\sigma, \sigma, 0)$ and $d_L = -d_R = \text{diag}(0, 0, d)$. Then the reduced GL potential becomes $\Omega_{2F} = \left(\frac{a}{2}\sigma^2 + \frac{b}{4}\sigma^4 + \frac{f}{6}\sigma^6\right) + \left(\frac{\alpha}{2}d^2 + \frac{\beta}{4}d^4\right) + \lambda d^2\sigma^2$. Thus, the coexistence of d and σ is disfavored in this case, because of the λ -term with $\lambda > 0$.

25.6.2 Possible Phase Structure for Realistic Quark Masses

The mapping of the phase diagrams obtained from the GL potentials, Ω_{3F} and Ω_{2F} , in the $a - \alpha$ plane to the $T - \mu$ plane is a dynamical question which cannot be addressed within the phenomenological GL theory. Nevertheless, we can draw a *speculative* phase structure of QCD for $m_s \sim \Lambda_{\text{QCD}} \gg m_{u,d} \neq 0$ by interpolating the phase structures obtained from Ω_{3F} and Ω_{2F} as shown in Fig. 25.9 [28]. In this figure, the double (single) curve indicates the first (second) order phase transition driven by the negative b in Eq. (25.19). The single curves indicate the second order phase transitions, within the analysis of the GL potential without fluctuations, which separate the $d \neq 0$ and $d = 0$ phases. We draw two critical points at which the first order phase transition turns into a crossover; the one near the vertical axis indicated as ‘AY’ (Asakawa-Yazaki critical point [35]) and the other one near the horizontal axis indicated as ‘HTYB’ [28]. The latter is driven by the axial anomaly with positive γ in Eq. (25.19).

The existence of the AY critical point implies that the transition from the NG phase to the QGP phase on the $\mu = 0$ axis is a crossover. Indeed, the lattice QCD Monte Carlo simulations at finite T with finite-size scaling analyses indicate that the thermal phase transition at $\mu = 0$ is likely to be a crossover [36]. We note here that the AY critical point has special importance to the fluctuation observables in relativistic heavy-ion collisions [37] and the determination of its location is highly called for both theoretically and experimentally.

On the other hand, the existence of the HTBY critical point implies that the hadronic matter characterized by $\sigma > d > 0$ and the quark matter characterized by $d > \sigma > 0$ are continuously connected with each other and both are classified into the COE phase. This is intimately related to the idea of hadron-quark continuity, i.e., a smooth transition from superfluid/superconducting hadronic matter to superconducting quark matter [38–40]. Indeed, there is evidence of the continuity not only for the ground state but also for the excitation spectra: a typical example is the continuity of the flavor-octet vector mesons in hadronic matter at low μ and the color-octet gluons in quark matter

**FIGURE 25.9**

Schematic phase structure with two light (up and down) quarks and a medium heavy (strange) quark [28]. The double curve indicates the first order transition. AY and HTYB are the second-order critical points at which the first-order line terminates.

at high μ [38, 41]. Unfortunately, lattice QCD simulations have difficulty in treating matter with $\mu/T \gg 1$ because of the severe sign problem originating from the complex fermion determinant in the presence of μ [42]. Therefore, the quantitative study of this region is still an open issue.

25.7 Simulating Dense QCD with Ultracold Atoms

Ultracold atomic systems and high density QCD matter, although differing by some twenty orders of magnitude in energy scales, share certain analogous physical aspects, e.g., BEC-BCS crossovers [43]. Motivated by phenomenological studies of QCD that indicate a strong spin-singlet diquark correlation inside the nucleon [44], we focus here on modeling the transition from 2-flavor quark matter at high density to nuclear matter at low density in terms of a boson-fermion system, in which small-size diquarks are the bosons, unpaired quarks the fermions, and the extended nucleons are regarded as composite Bose-Fermi particles [45]. This would be a starting point to understand the QPT at $\mu \sim \mu_c$ between the hadronic superfluid discussed in Sec. 25.4 and the CSC discussed in Sec. 25.5.

Recent advances in atomic physics have made it possible indeed to realize a boson-fermion mixture in the laboratory. In particular, tuning the atomic interaction via a Feshbach resonance allows formation of heteronuclear molecules, as recently observed in a mixture of ^{87}Rb and ^{40}K atomic vapors in an optical dipole trap [46].

Let us start from a non-relativistic boson-fermion mixture with Hamilton-

nian density,

$$\begin{aligned}\mathcal{H} = & \frac{1}{2m_b} |\nabla \phi(x)|^2 - \mu_b |\phi(x)|^2 + \frac{1}{2} \bar{g}_{bb} |\phi(x)|^4 \\ & + \sum_{\sigma} \left(\frac{1}{2m_f} |\nabla \psi_{\sigma}(x)|^2 - \mu_f |\psi_{\sigma}(x)|^2 \right) + \bar{g}_{ff} |\psi_{\uparrow}(x)|^2 |\psi_{\downarrow}(x)|^2 \\ & + \sum_{\sigma} \bar{g}_{bf} |\phi(x)|^2 |\psi_{\sigma}(x)|^2,\end{aligned}\quad (25.21)$$

where ϕ (ψ) is the bosonic (fermionic) field. The two internal states of the fermions are labeled by spin indices $\sigma = \{\uparrow, \downarrow\}$. For simplicity, we consider an equally populated mixture of n bosons and n fermions with $n_{\uparrow} = n_{\downarrow} = n/2$.

The bare boson-fermion coupling \bar{g}_{bf} is related to the renormalized coupling g_{bf} and to the s-wave scattering length a_{bf} by

$$\frac{m_R}{2\pi a_{bf}} = \frac{1}{\bar{g}_{bf}} + \int_{|\mathbf{k}| \leq \Lambda} \frac{d^3 k}{(2\pi)^3} \frac{1}{\varepsilon_b(k) + \varepsilon_f(k)}, \quad (25.22)$$

where $\varepsilon_i(k) = k^2/2m_i$ ($i = b, f$) is the single-particle kinetic energy, m_R is the boson-fermion reduced mass, and $\Lambda = \pi/(2r_0)$ is a high momentum cutoff with r_0 being a typical atomic scale. We assume an attractive bare b-f interaction $\bar{g}_{bf} < 0$, tunable in magnitude, with Λ fixed, so that the scattering length a_{bf} can change sign: $a_{bf} \rightarrow \bar{g}_{bf} m_R / (2\pi)$ for small negative \bar{g}_{bf} , while $a_{bf} \rightarrow r_0$ for large negative \bar{g}_{bf} . We keep the bare boson-boson and fermion-fermion interactions fixed and repulsive ($\bar{g}_{bb} > 0, \bar{g}_{ff} > 0$) for the stability of this system.

In the regime of weak bare b-f coupling where the dimensionless parameter $\eta \equiv -1/(n^{1/3} a_{bf})$ is large and positive, the system at low temperature is a weakly-interacting mixture of BEC of the b-bosons (b-BEC) and degenerate f-fermions. The induced interaction through the density fluctuation of b-BEC may also lead to the pairing of fermions (f-BCS).

On the other hand, in the regime of strong bare b-f coupling where η is large and negative, bound molecules of b-bosons and f-fermions called *composite fermions*, $N = (bf)$, are formed with a kinetic mass $m_N = m_b + m_f$. The s-wave scattering length of two N's of opposite spins can be estimated by the exchange of constituent b or f [45],

$$a_{NN} \simeq -\frac{m_N}{2m_R} a_{bf}. \quad (25.23)$$

This is the same in magnitude but is opposite in sign from the scattering length between di-fermion molecules due to different statistics. It can be shown that this result is the leading order term in an extension of the present model to large internal degrees of freedom.

Equation (25.23) implies that the low energy effective interaction between composite fermions in the spin-singlet channel is weakly attractive; the

TABLE 25.2

Correspondence between the boson-fermion mixture in ultracold atoms and the diquark-quark mixture in high density QCD.

cold atoms	dense QCD
b (bosonic atom)	d (diquark),
$f_{\uparrow,\downarrow}$ (fermionic atom)	$q_{\uparrow,\downarrow}$ (unpaired quark)
$N_{\uparrow,\downarrow}$ (boson-fermion molecule)	$\mathcal{N}_{\uparrow,\downarrow}$ (nucleon)
b-f attraction	gluonic attraction
b-BEC	2-flavor color superconductivity
N-BCS	nucleon superfluidity

stronger the bare b-f attraction the weaker the N-N attraction. Such an effective interaction causes composite fermions to become BCS-paired (N-BCS) below a transition temperature,

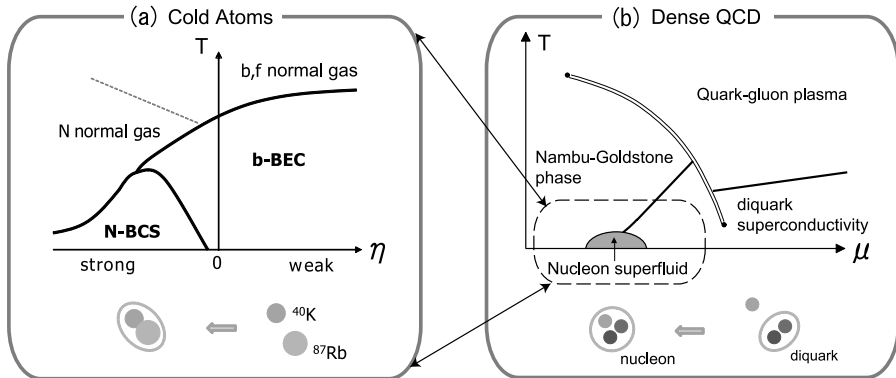
$$T_c(\text{N-BCS}) = \frac{e^\gamma}{\pi} \left(\frac{2}{e} \right)^{7/3} \varepsilon_N e^{\pi/(2k_F a_{NN})}, \quad (25.24)$$

where $\varepsilon_N = k_F^2/2m_N$ is the Fermi energy of the N.

The above analyses for large $|\eta|$ suggest a possible phase structure of boson-fermion mixtures in the $T - \eta$ plane as shown in Fig. 25.10(a). At intermediate bare b-f coupling ($\eta \sim 0$) where a transition from the b-BEC phase to N-BCS takes place, the phase diagram would have complex structure depending on the relative magnitudes of \bar{g}_{bb} , \bar{g}_{ff} , and \bar{g}_{bf} . The f-BCS phase possibly occurs for $\eta > 0$ is not shown in this figure. For more detailed analyses of the phase diagram of the present model, see [45].

Phases in the region $\eta \sim 0$ may be classified by the realization of internal symmetry. If we focus only on the continuous symmetries, the Hamiltonian density, Eq. (25.21), has $U(1)_b \otimes U(1)_{f_\uparrow} \otimes U(1)_{f_\downarrow}$ symmetry corresponding to independent phase rotations of ϕ , ψ_\uparrow and ψ_\downarrow . On the other hand, b-BEC and N-BCS break $U(1)_b$ and $U(1)_{b+(f_\uparrow+f_\downarrow)}$ symmetries, respectively. The difference in such symmetry breaking patterns implies the existence of a well-defined phase boundary between b-BEC and N-BCS as indicated in Fig. 25.10(a). This is in contrast to the continuous BEC-BCS crossover in two-component Fermi systems.

The phase structure we find for a boson-fermion mixture of ultracold atoms displays features of that in QCD with equal numbers of u and d quarks. The ground state of such a system at high density is the 2SC phase discussed in Sec. 25.5.1. The order parameter for color-symmetry breaking is the diquark condensate $\langle d_3 \rangle$ with the diquark operator $d_c = \epsilon_{ijk} \epsilon_{abc} [q]_a^i C \gamma_5 [q]_b^j$. The gap is of order a few tens of MeV; the remaining quarks are unpaired and form degenerate Fermi seas. On the other hand, the ground state of QCD at low density is nuclear matter with equal numbers of protons and neutrons denoted by $\mathcal{N}_{\uparrow,\downarrow}^i$, a superfluid state with a pairing gap of a few MeV [21]; the order

**FIGURE 25.10**

(a) A possible phase structure of the boson-fermion mixture (such as ^{87}Rb and ^{40}K) in ultracold atoms with attractive b-f interaction and repulsive b-b and f-f interactions. Large and positive (large and negative) η corresponds to weak (strong) b-f attraction. (b) A possible phase structure of QCD. Large (small) chemical potential μ corresponds to weak (strong) coupling due to asymptotic freedom.

parameter for the spontaneous breaking of baryon-number symmetry $U(1)_B$ is the six-quark condensate $\langle \mathcal{N}_\uparrow^i \mathcal{N}_\downarrow^j \rangle = \langle (d_a[q_\uparrow]^i_a)(d_b[q_\downarrow]^j_b) \rangle$. If we model the nucleon, of radius $r_N \sim 0.86$ fm, as a bound molecule of a diquark, of radius $r_d \sim 0.5$ fm, and an unpaired quark, we can make a correspondence between a boson-fermion mixture of cold atoms and the diquark-quark mixture in QCD as shown in Table 25.2.

Such a correspondence can also be found between the phase diagram of ultracold atoms in Fig. 25.10(a) and that of dense QCD in Fig. 25.10(b). In particular, the BCS-like superfluidity of composite fermion (N) with a small gap is a natural consequence of the strong b-f attraction as shown in Eq. (25.23), which may explain why the fermion gap in nucleon superfluidity is an order of magnitude smaller than the gap in BEC-like CSC. It is thus quite interesting to carry out experiments on boson-fermion mixtures in ultracold atoms for a wide range of the boson-fermion attraction.

However, note that tuning the coupling strength at fixed density is not possible in dense QCD matter because of the running coupling $\alpha_s(\kappa = \mu)$; furthermore, dynamical breaking of chiral symmetry and its interplay with the CSC have an important role in the QPT in QCD as discussed in Sec. 25.6.1. With these reservations in mind, we suggest that fuller understanding, both theoretical and experimental, of the boson-fermion mixture [45] as well as a mixture of three species of atomic fermions [30, 47] can reveal properties of high-density QCD not readily observable in high energy physics experiments.

25.8 Conclusions

In this chapter, we have discussed thermal and quantum phase transitions in QCD. The former is relevant to the physics of hot matter in the early universe right after the Big Bang, while the latter is relevant to the physics of dense matter in the interiors of neutron stars and quark stars. There are three fundamental QCD phases in the $T - \mu$ plane: the NG phase, the QGP phase and the CSC such as the CFL phase (Fig. 25.8).

We have shown an interesting possibility of hadron-quark continuity in which the superfluid hadronic phase and the CSC phase are continuously connected with each other at low temperature due to the QCD axial anomaly (Fig. 25.9). We have also discussed that the existence of nucleon superfluidity may be a logical consequence of tightly bound diquarks interacting with unpaired quarks in the CSC phase. Although such a system with $\mu/T \gg 1$ is difficult to treat in lattice QCD Monte Carlo simulations at present, a mixture of ultracold atoms with different masses, different statistics, and different internal degrees of freedom would provide us with an exciting new tool to study the essential features of QPTs in dense QCD (Fig. 25.10).

Acknowledgments – The authors thank H. Abuki, G. Baym, K. Iida, Y. Nishida, M. Tachibana and N. Yamamoto for useful discussions and collaborations on various subjects covered in this article. This research was supported in part by the Grant-in-Aid for Scientific Research on Innovative Areas (No. 2004: 20105003) and by JSPS Research Fellowship for young scientists.

Bibliography

- [1] Y. Nambu, in *Preludes in Theoretical Physics, in honor of V. F. Weisskopf* (North-Holland, Amsterdam), 133 (1966).
- [2] F. Wilczek, Proc. Nat. Acad. Sci. **102**, 8403 (2005).
- [3] C. Amsler *et al.*, Phys. Lett. **B667**, 1 (2008).
- [4] Y. Nambu and G. Jona-Lasinio, Phys. Rev. **122** (1961); *ibid.* **124**, 246 (1961).
- [5] T. Hatsuda and T. Kunihiro, Phys. Rept. **247**, 221 (1994).
- [6] S. Weinberg, PoS **CD09**, 001 (2009) [arXiv:0908.1964 [hep-th]].
- [7] S. Treiman, R. Jackiw, B. Zumino and E. Witten, *Current Algebra and Anomalies* (Princeton Univ. Press, New Jersey, 1985).

- [8] S. Aoki *et al.* (PACS-CS Collaboration), Phys. Rev. **D79**, 034503 (2009).
- [9] S. Dürr *et al.* (BMW Collaboration), Science **322**, 1224 (2008).
- [10] C. Vafa and E. Witten, Nucl. Phys. **B234**, 173 (1984).
- [11] T. W. Chiu *et al.* (JLQCD and TWQCD Collaborations), PoS **LATTICE2008**, 072 (2008) [arXiv:0810.0085 [hep-lat]].
- [12] M. Cheng *et al.*, Phys. Rev. **D77**, 014511 (2008).
- [13] K. Yagi, T. Hatsuda and Y. Miake, *Quark-Gluon Plasma: From Big Bang to Little Bang* (Cambridge Univ. Press, London, 2005).
- [14] C. E. DeTar and U. M. Heller, Eur. Phys. J. **A41**, 405 (2009).
- [15] E. Shuryak, Prog. Part. Nucl. Phys. **62**, 48 (2009).
- [16] J. C. Collins and M. J. Perry, Phys. Rev. Lett. **34**, 1353 (1975).
- [17] E. Witten, Phys. Rev. **D30**, 272 (1984).
- [18] J. M. Lattimer and M. Prakash, Phys. Rept. **442**, 109 (2007).
- [19] T. Takatsuka and R. Tamagaki, Prog. Theor. Phys. **46**, 114 (1971).
- [20] T. Kunihiro, T. Muto, T. Takatsuka, R. Tamagaki and T. Tatsumi, Prog. Theor. Phys. Suppl. **112**, 1 (1993).
- [21] D. J. Dean and M. Hjorth-Jensen, Rev. Mod. Phys. **75**, 607 (2003).
- [22] M. G. Alford, A. Schmitt, K. Rajagopal and T. Schäfer, Rev. Mod. Phys. **80**, 1455 (2008).
- [23] D. T. Son, Phys. Rev. **D59**, 094019 (1999).
- [24] H. Abuki, T. Hatsuda and K. Itakura, Phys. Rev. **D65**, 074014 (2002).
- [25] K. Higashijima, Prog. Theor. Phys. Suppl. **104**, 1 (1991).
- [26] C. A. Regal, M. Greiner and D. S. Jin, Phys. Rev. Lett. **92**, 040403 (2004).
- [27] Y. Nishida and H. Abuki, Phys. Rev. **D72**, 096004 (2005).
- [28] T. Hatsuda, M. Tachibana, N. Yamamoto and G. Baym, Phys. Rev. Lett. **97**, 122001 (2006).
- [29] M. Sigrist and K. Ueda, Rev. Mod. Phys. **63**, 239 (1991).
- [30] R. W. Cherng, G. Refael and E. Demler, Phys. Rev. Lett. **99**, 130406 (2007).

- [31] R. D. Pisarski and F. Wilczek, Phys. Rev. **D29**, 338 (1984).
- [32] K. Iida and G. Baym, Phys. Rev. **D63**, 074018 (2001); *ibid.* **D66**, 059903(E) (2002).
- [33] N. Yamamoto, M. Tachibana, T. Hatsuda and G. Baym, Phys. Rev. **D76**, 074001 (2007).
- [34] M. G. Alford, K. Rajagopal and F. Wilczek, Nucl. Phys. **B537**, 443 (1999).
- [35] M. Asakawa and K. Yazaki, Nucl. Phys. **A504**, 668 (1989).
- [36] Y. Aoki, G. Endrodi, Z. Fodor, S. D. Katz and K. K. Szabó, Nature **443**, 675 (2006).
- [37] M. Stephanov, K. Rajagopal and E. Shuryak, Phys. Rev. **D60**, 114028 (1999).
- [38] T. Schäfer and F. Wilczek, Phys. Rev. Lett. **82**, 3956 (1999).
- [39] K. Fukushima, Phys. Rev. **D70**, 094014 (2004).
- [40] N. Yamamoto, JHEP **0812**, 060 (2008).
- [41] T. Hatsuda, M. Tachibana and N. Yamamoto, Phys. Rev. **D78**, 011501 (2008).
- [42] S. Ejiri, PoS **LATTICE2008**, 002 (2008) [arXiv:0812.1534 [hep-lat]].
- [43] G. Baym, T. Hatsuda, M. Tachibana and N. Yamamoto, J. Phys. **G35**, 104021 (2008).
- [44] A. Selem and F. Wilczek, in *Ringberg 2005, New trends in HERA physics*, [hep-ph/0602128].
- [45] K. Maeda, G. Baym and T. Hatsuda, Phys. Rev. Lett. **103**, 085301 (2009).
- [46] J. J. Zirbel *et al.*, Phys. Rev. A **78**, 013416 (2008).
- [47] A. Rapp, G. Zaránd, C. Honerkamp and W. Hofstetter, Phys. Rev. Lett. **98**, 160405 (2007).

Quantum Phase Transitions in Coupled Atom-Cavity Systems

Andrew D. Greentree

School of Physics, University of Melbourne, VIC 3010, Australia

Lloyd C. L. Hollenberg

Centre for Quantum Computer Technology, School of Physics, University of Melbourne, VIC 3010, Australia

Condensed matter physics studies complex systems of interacting particles to understand macroscopic and emergent phenomena of those systems. In general, sample perfection and homogeneity are critical to the observation of most many-body effects. Conversely, quantum optics has conventionally looked at interactions between some of the most perfect and isolated systems available, for example monochromatic optical fields and single atoms. The perfection and control of large ensembles of strongly interacting particles is extending to levels of uniformity never before reached, although often with only global control and readout, while quantum optical techniques are now increasingly allowing the treatment of systems of increasing complexity, but with the added advantage of local control and readout. Coupled cavity systems are ideally placed to straddle this gap of scales, i.e., local control of small systems vs global control of large systems, to give insight into both fields. Systems of interacting photons in coupled cavities have been predicted to show quantum phase transitions (QPTs), and may be important as quantum simulators of complex dynamics. But the nature of the interactions is subtly different from more conventional condensed matter models. Here we describe the emergence of Hubbard-like dynamics in coupled cavity systems spanning finite to infinite structures, the nature of the excitations involved, how these coupled cavity systems can be understood as the optical analog of a solid-state system, and prospects for structures that can be fabricated to demonstrate the required interactions.

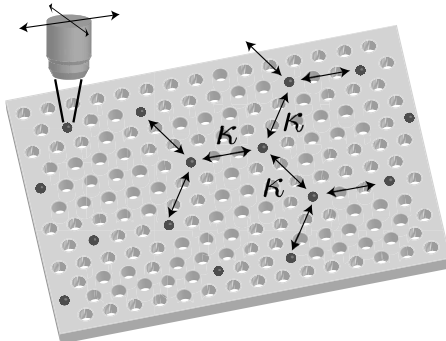
26.1 Introduction

In 1981, Feynman discussed the computational intractability of certain quantum mechanical problems [1]. The state space of a system of interacting particles, and hence the resources required to solve it, grows exponentially with the number of particles. This means that if each particle had only two levels, adding a single extra particle would double the size of the problem. This exponential growth in problem size has been converted into a virtue, and it is from here that the promise of quantum computing arises. However, quantum computers demand extreme levels of control and perfection to work. Feynman's original goal was to design quantum systems that were easily controlled and measured that could be made equivalent to the original problem. One could then simulate the difficult quantum problem on an essentially analog machine. The problems that could be attacked include important problems in quantum chemistry and QPTs. Cold atom lattices provide one feasible platform to realize Feynman's vision. Here we will explore an alternative: a coupled cavity lattice where atom-mediated photon-photon interactions give rise to nontrivial quantum many-body physics [2–4].

That photons do not interact with each other in free space is an essential feature of our natural world. It means that you can read this text in bright or dim light and that laser pointers can be used to highlight features, without distorting them. It is also a fundamental point of departure between the physics of conventional optical systems (lenses, mirrors, light sources) and condensed matter systems dominated by matter that can be either fermionic, or, in the case of superconductors and cold-atoms, interacting bosons.

However, photon-photon interactions can be achieved, and this leads to the very important branches of physics and technology of nonlinear optics and photonics [5]. Conventionally, such interactions are achieved by optical fields modifying the medium that they are traveling through, and thereby causing a change in the very optical properties that they sense. Typical examples are Kerr media which have intensity-dependent refractive indices and photo-bleaching where the absorption of a material is modified by the intensity of the light. However, usually such effects are very weak, requiring intense optical fields, and typically are associated with large optical losses. Until recently, this has essentially limited the study of most deterministic nonlinear optical effects to the classical rather than the quantum domain, and kept the realms of nonlinear optics and condensed matter physics well separated. All that appears set to change.

Here we describe some of the first steps towards connecting quantum optics and condensed matter physics by the design of networks of strongly interacting photons. This conjunction is made possible by the observation of photon-photon interactions at the single photon level (photon blockade) [6–8] and breakthroughs in nano-fabrication which mean that large-scale integrated

**FIGURE 26.1**

Concept for a lattice of interacting atom-cavity systems to realize a Jaynes-Cummings-Hubbard model. Photonic crystal cavities, each containing a single two-level atom, provide the required nonlinear interactions and hopping is via evanescent coupling of the cavities with intercavity hopping rate κ . Local readout can be performed with nano-positioned microscope objectives of near-field probes, while local control of the atom-cavity systems can be via electrostatic and radio-frequency gates, or locally applied lasers (not shown).

photonic structures can be considered [9, 10]. A concept diagram is shown in Fig. 26.1 which shows a lattice of coupled photonic crystal cavities, each containing a single two-level atom. Local readout can be via microscope objectives or near-field probes, and individual gates (not shown) can provide local perturbations and control. We will describe the physics of the Jaynes-Cummings-Hubbard model (JCHM) [3, 4, 11], which is one of the simplest nontrivial models that might be realized in such a network of interacting atom-cavity systems and demonstrates an analog of the Mott-insulator (MI) to superfluid (SF) QPT seen in the Bose-Hubbard model (BHM). Then we discuss some of the work that will need to be performed in few-cavity systems en route to developing full blown photonic emulators of condensed matter systems [2, 4]. Finally we will discuss some potential platforms for the JCHM which include implementations in the optical and radio frequency domains.

26.2 Photon-Photon Interactions in a Single Cavity

Before one can consider networks of interacting photons, the fundamental means by which a photon-photon interaction can be induced must be explained. There are several different means that have been considered in the literature. Here we focus on cavity-mediated interactions as being one of the most practical approaches, although there is also interest in traveling-wave

configurations under conditions of small mode volume and sometimes slow light propagation [12,13]. By confining photons to cavities containing individual atoms, the Jaynes-Cummings model (JCM) is retrieved [14], and evanescent tunneling of photons realizes a tight-binding hopping model for transport.

In this section we will review the two main methods for generating photon-photon interactions, namely the JCM, which is achieved for a single two-state system in a cavity, and the giant Kerr effect which is realized for a four-state system in a cavity. We will also discuss the effect of increasing the number of atoms in the cavities, which can have surprising implications, and highlights the importance of using individual atoms, rather than ensembles, for most applications.

26.2.1 Jaynes-Cummings Model

The JCM deals with the interactions between a single two-state system and a quasi-resonant electromagnetic field confined in a cavity [14], and this is illustrated in Fig. 26.2. The strength of the interaction between the atom and photon is determined by the dipole moment of the coupled transition and the electric field strength of the cavity mode, which in turn is set by the geometry of the cavity. We may write down the Hamiltonian, in the rotating wave approximation, for the interaction of a transition with a single cavity mode as

$$\mathcal{H}^{\text{JC}} = \hbar\epsilon\sigma^+\sigma^- + \hbar\omega a^\dagger a + \hbar\beta(\sigma^+a + \sigma^-a^\dagger), \quad (26.1)$$

where \hbar is the usual reduced Planck's constant, ϵ the atomic transition frequency, ω the field frequency, β the atom-cavity coupling constant, a and a^\dagger the usual bosonic lowering and raising operators, and σ^- and σ^+ the atomic lowering and raising operators on the $|g\rangle - |e\rangle$ transition. Under the dipole approximation the atom-cavity coupling constant can be expressed as

$$\beta = d\sqrt{\omega/(2\hbar\epsilon_0 V)}, \quad (26.2)$$

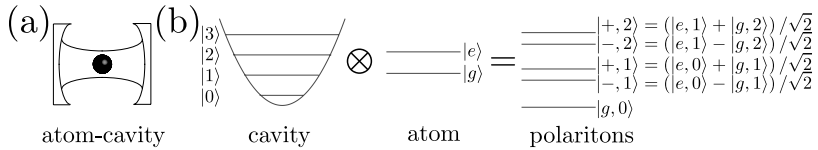
where d is the dipole moment, assumed to be optimally aligned, ϵ_0 is the permittivity of free-space, and V is the effective mode volume.

It is relatively straightforward to diagonalize \mathcal{H}^{JC} to obtain the eigenstates, which are conventionally termed as either *dressed states* or *polaritons*. These are superpositions of atom and field states that can be written

$$|\pm, n\rangle = \frac{\beta\sqrt{n}|g, n\rangle + [-\frac{\Delta}{2} \pm \chi(n)]|e, n-1\rangle}{\sqrt{2\chi^2(n) \mp \chi(n)\Delta}} \quad \forall n \geq 1, \quad \text{and } |g, 0\rangle, \quad (26.3)$$

where g (e) labels the atomic ground (excited) state, n is equivalently the number of excitations (atomic+photonic) for the dressed states (left-hand side), or the number of photons for the bare states (right-hand side), $\Delta = \omega - \epsilon$ is the cavity-atom detuning, and the n -photon generalized Rabi frequency is

$$\chi(n) = \sqrt{n\beta^2 + \Delta^2/4}. \quad (26.4)$$

**FIGURE 26.2**

(a) Schematic showing an atomic transition (a two-level atom in this case) coupled to a mode of an optical cavity. (b) The cavity mode is described by a simple harmonic oscillator, and the transition by a two-state system. The interaction between the transition and the field gives rise to dressed states or polaritons which are superpositions of the atomic and field states. Here we show the case for a resonant interaction.

Note that the ground state, $|g, 0\rangle$, can be thought of equivalently as being both a bare and a dressed state.

The eigenenergies of Eq. (26.1) are

$$E_{|g,0\rangle} = 0, \quad \text{and} \quad E_{|\pm,n\rangle} = n\hbar\omega \pm \hbar\chi(n) - \hbar\Delta/2. \quad (26.5)$$

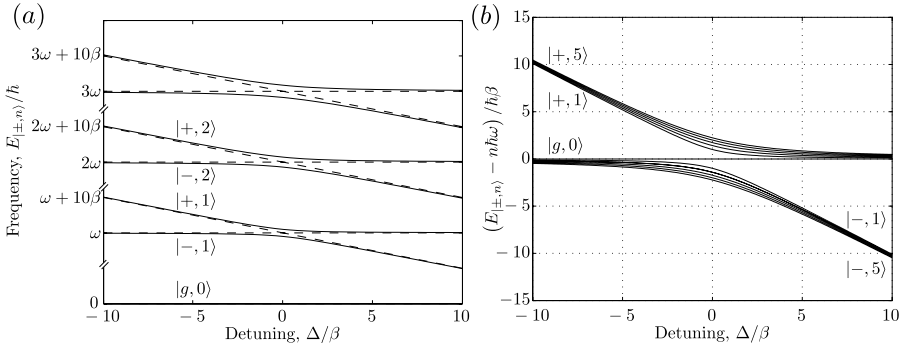
These eigenstates are shown in Fig. 26.3 (a) which shows the ladder of states obtained for increasing photon number as a function of detuning for some arbitrary photon energy. These data can be more meaningfully seen with the photon energy subtracted, and this is shown in Fig. 26.3 (b). The nonlinear nature of the JCM can be seen immediately from the shift of the energy levels with increasing number of excitations, i.e., the extra energy contributed by the atom-photon interaction. Also clear is the separation of the eigenstates into two branches depending on the parity of the dressed state, $|+\rangle$ or $|-\rangle$. The exception is the ground state, which can be thought of as belonging to both branches.

The nonlinear interaction can also be viewed in another fashion, by considering the frequency shift between states $|\pm, n\rangle$ and $|\pm, n-1\rangle$; this is

$$\delta_\omega(\pm, n) = (E_{|\pm,n\rangle} - E_{|\pm,n-1\rangle})/\hbar - \omega. \quad (26.6)$$

This shift is plotted in Fig. 26.4 as a function of detuning, which also shows the stable domains that the system will be found in between these boundaries. This figure allows us to explore the origin of photon blockade in the JCM [6, 8, 15] which is important as this is the effect that enables the JCHM.

Photon blockade can be understood quite simply. As the energy levels of the JCM depend on the number of excitations, for a perfect enough cavity with small enough mode volume, the interaction-induced shift in the resonance frequency of the atom-cavity system can be sufficient to detune the system from the external pump laser that is exciting it. Because of this, the cavity is constrained to never have more than one excitation; hence a single

**FIGURE 26.3**

(a) Eigenspectrum of the JCM showing both the interacting (solid curves) and noninteracting (dashed curves) cases as a function of detuning, Δ . (b) Condensed eigenspectra from $|g, 0\rangle$ to $|\pm, 5\rangle$, where the photon energies in each manifold have been subtracted to allow easy comparison. The nonlinearity at the heart of the JCM can be identified by the shift in the energy states with increasing excitations, i.e., the extra energy due to the interaction. Note that these differences are greatest for fewer excitations and at resonance.

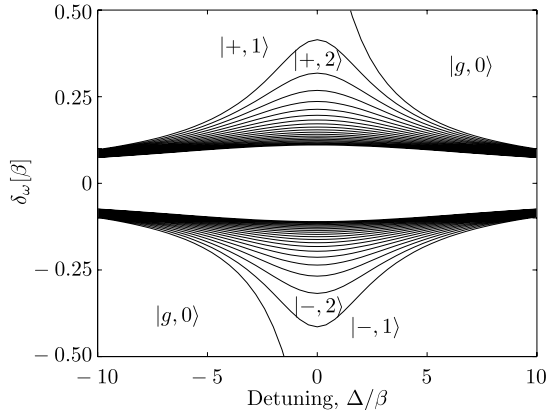
photon stops further absorption of photons. This is termed photon blockade by analogy with the similar effect, Coulomb blockade, which is observed in nano-scale electrical circuits [16].

Despite the qualitative similarity between photon and Coulomb blockade, the photon-blockade effect is also quite different from Coulomb blockade in terms of the *scaling* of the nonlinear interaction. Coulomb blockade is more akin to a conventional Kerr-type nonlinearity, where the frequency shifts would be expected to be a constant irrespective of the number of particles. Instead, for photon blockade on resonance ($\Delta = 0$), the frequency shift goes like $\sqrt{n} - \sqrt{n - 1}$. This means that the effect decreases with increasing excitation number. This is to be expected as in the limit of large excitation the classical result must be obtained, which will not show any effects at the single photon level, i.e., $\sqrt{n} - \sqrt{n - 1} \rightarrow 0$ as $n \rightarrow \infty$. This \sqrt{n} form of the interaction also leads to serious problems in determining if the symmetry of the polaritons at resonance is bosonic or fermionic, and we will discuss this below.

One limit which is particularly easy to examine is the large detuning limit and this has certain analytical advantages over other cases. In the limit of large detuning, one may adiabatically eliminate the atomic states, and rewrite the Hamiltonian of Eq. (26.1) as

$$\mathcal{H} = \hbar\omega a^\dagger a + (\hbar\beta^2/\Delta)a^\dagger a^\dagger aa, \quad (26.7)$$

i.e., an ideal Kerr nonlinear interaction where the coefficient of nonlinearity goes as β^2/Δ . This is nothing other than the well-known light shift. In this

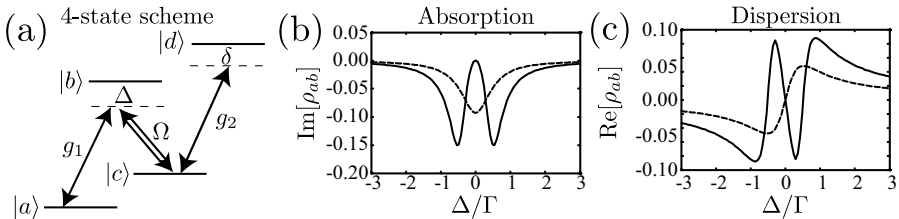
**FIGURE 26.4**

Frequency shifts between states in the same polaritonic branch as a function of detuning. The domains between the lines correspond to the stable ground state, where these are labeled. The shifts are greatest for fewer excitations and at resonance, which is to be expected from the form of the Jaynes-Cummings interaction. Note that the shifts tend to zero in the limit of very large excitations (not shown on this plot) which explains the blank zone between the positive and negative branches. This figure also shows what the ground state of the system should be for given excitation frequency, and these states are indicated. These curves can also be interpreted as the critical chemical potential (see below).

limit the excitations are purely bosonic. The problem with this is that in many practical implementations the reduction in the strength of the nonlinearity by the detuning is likely to hamper efforts at detecting the effects. One clear exception is the recent demonstrations of superconducting stripline cavities (circuit QED [17], see Sec. 26.5.3), which seem to be ideally suited to exploring this important regime.

26.2.2 The Giant Kerr Nonlinearity in Four-State Systems

The original proposal for photon blockade [7] invoked an extremely interesting mechanism to enhance the nonlinear interaction called the giant Kerr effect. The required level scheme is a four-level atom in the N configuration, depicted in Fig. 26.5 (a). In essence, the effect combines the dispersive interaction with the sensitivity of electromagnetically induced transparency (EIT) [18]. One particularly elegant feature of the giant Kerr effect is that there is a qualitative difference between the role of the first photon in the atomic scheme, from the second photon, and hence the origin of the nonlinearity is manifest. Perhaps remarkably, however, there appears to be little gain in terms of the magnitude of the nonlinear interaction compared with the JC case [15].

**FIGURE 26.5**

The giant Kerr effect is based around perturbing the electromagnetically induced transparency (EIT) feature in a three level Λ atom with an extra transition. (a) Level scheme. A classical pump field (double line) couples the $|b\rangle - |c\rangle$ transition and prepares the system in $|a\rangle$. The first photon interacts with the $|a\rangle - |b\rangle$ transition, and with the classical pump effects EIT, with coupling strength g_1 . The second photon is then able to perturb the EIT transition via the light shift. Because the slope of the EIT profile is so steep, the non-linearity can be very large. (b) Absorption under EIT (solid line) exhibits a narrow transparency window with a linewidth set by the two-photon Rabi frequency and limited by the ground state dephasing, which can be much less than the natural linewidth. The detuning axis has been scaled by Γ , the excited-state spontaneous emission rate. A comparable two-state absorption feature is shown for comparison (dashed line). (c) Accompanying the narrow absorption feature is a very steep region of anomalous dispersion which can be used, e.g., for slow light. Perturbing this feature with another field, as is done for the giant Kerr effect, gives rise to a very large change in refractive index. The solid line gives the EIT-related feature while the dashed line is again a two-state calculation for comparison.

The optical Kerr effect describes an intensity-dependent refractive index, i.e., we may express the refractive index as $\eta = \eta_0 + \eta_2 I$ where I is the intensity of the field, η the total refractive index, and η_0 and η_2 are the linear and Kerr-type refractive indices. In most media, η_2 is very small and so one is restricted to classical photon fields. The giant Kerr effect uses atomic coherence to effect a single photon, lossless Kerr effect that is in principle many orders of magnitude greater than conventionally attainable Kerr effects.

To realize the giant Kerr effect, we require a four-state scheme with two metastable ground states [Fig. 26.5 (a)], which we label $|a\rangle$ and $|c\rangle$, and two excited states, labeled $|b\rangle$ and $|d\rangle$. The principle is relatively straightforward although some of the details need to be carefully considered before evaluating whether the scheme offers any practical advantage over the JCM scheme. The four-state system is placed in a cavity, which is resonant with the quantum field. This cavity is detuned from the $|a\rangle - |b\rangle$ transition by an amount Δ , and from the $|b\rangle - |d\rangle$ transition by δ . The single-photon Rabi frequency on these transitions is g_1 and g_2 , respectively, which could differ, for example,

by different relative dipole moments for the two transitions. In addition we have a classical pump field with Rabi frequency Ω , which is detuned from the $|b\rangle - |c\rangle$ transition by Δ so that the $|a\rangle - |c\rangle$ transition is two-photon resonantly coupled via the quantum and classical fields. The classical field is always on; so before the protocol starts, the atom is optically pumped into $|a\rangle$. This field could, for example, be applied perpendicularly to the cavity mode, and is therefore free from many of the constraints of mode matching. In general, the mean number of photons in the classical field is very large, warranting the semiclassical description that we employ here.

The giant Kerr effect manifests when the quantum field is incident on the cavity. When the quantum field is turned on, the EIT condition between the two fields will give rise to a narrow coherent spectral hole, which is the EIT feature. In general, the width of this feature is set by the two-photon Rabi frequency of the driving fields, and can be much narrower than the natural linewidth of the original transition. Ultimately, the width of the EIT feature is limited only by the ground-state decoherence. As an example, for alkali atoms in a vapor cell or cold-atom conditions, the ground-state decoherence times might be typically longer than milliseconds, while the excited state spontaneous emission rate might be tens of nanoseconds. Associated with this narrow absorption feature is a rapid change in refractive index with frequency, via the Kramers-Kronig relation. This narrow feature is the target for the nonlinearity. As the feature is so sharp, a small detuning leads to a large change in refractive index. This small detuning can be obtained, for example, by the light shift that we discussed in the context of two-state systems above.

Although this image of the giant Kerr effect is appealing, some of the complexities and limitations of the effect are masked by the simplistic treatment. First of all, one needs to be aware of the state formed under conditions of EIT. EIT has the effect of coherently pumping the atom into a state called the *dark state*. This important eigenstate is decoupled from the two fields, and has the form, for one photon driving the $|a\rangle - |b\rangle$ transition,

$$|\mathcal{D}\rangle = \frac{\Omega}{\sqrt{g_1^2 + \Omega^2}}|a\rangle - \frac{g_1}{\sqrt{g_1^2 + \Omega^2}}|c\rangle. \quad (26.8)$$

Now unless $g_1 \sim \Omega$, there will be minimal population in $|c\rangle$ to sense the light shift caused by the $|b\rangle - |d\rangle$ transition. This has the effect of reducing the effective light shift by the population in $|c\rangle$. For practical reasons, Ω cannot be made arbitrarily small, due to the limitation imposed by the ground-state decoherence. Hence large, single photon Rabi frequencies are still required, which is the same requirement as the JCM. Similarly, the role of the light shift induced by the second photon needs to be explored. The off-resonant light shift is g_2^2/δ ; so in general one wants the smallest detuning. However, one cannot naively reduce the detuning to zero, as the off-resonant assumption breaks down. In practice the absorption of the two-state system goes like $(g_2/\delta)^2$. The full case, without restrictions on detunings, is treated experimentally and theoretically in Refs. [19], and the absorptive nonlinearity

can also be used to generate nonlinear gates at the single photon level, albeit lossy ones [20]. Hence, to avoid any appreciable absorption, $g^2 \ll \delta$ with at least an order of magnitude overhead is desirable for high-fidelity gates. These competing factors, combined with the increased complexity of maintaining the four-state over the two-state scheme, would seem to diminish the importance of the four-state scheme for QPT work. Despite this, there remains keen interest in the four-state scheme for QPTs [2] and other quantum applications [21] where the advantages that the scheme affords compensate the increased complexity. Finally, we note that relaxing the condition of the two-photon resonance condition has been shown to increase the strength of the interaction significantly [22]. This latter analysis moves into a different regime from the canonical regime studied above and it remains to be seen how this will work experimentally.

26.2.3 Many-Atom Schemes

In the initial proposal for photon blockade [7], the scheme employed an ensemble of atoms in a moderately good cavity, i.e., not one with as high Q and low mode volume as required for single atom work. In this case the effect of the photon blockade should be enhanced by increasing the number of atoms. At first glance this sounds reasonable and amplification of effects of this kind are certainly observed in classical laser systems and traveling-wave geometries. However, it was quickly pointed out that the adiabatic elimination process used in [7] was not valid in the many-atom, good cavity regime [23]. Subsequent analyses highlighted how the effects degrade with increasing atomic number and the importance of single atom configurations [24]. Nevertheless, there are certain advantages to using many-atom schemes for QPT physics, most notably that purely bosonic interactions can be achieved [2, 25, 26], at least in the limit that the number of atoms exceeds the maximum number of photons.

26.2.4 Other Atomic Schemes

There is not the scope here to perform more than just a cursory survey of some of the other schemes that have been considered for observing lossless nonlinear photonic interactions at the single photon level. Whether these schemes will ultimately prove useful for the purpose of investigating QPTs is still unclear and further investigations are required.

One lesson from the four-state work is that the extra transitions affords opportunities for new kinds of nonlinear interactions. This was explored in the context of nonlinear group velocities in chain Λ systems [27], and enhanced nonlinearities in the chain- N system [28], both for ensembles. Other work showed that in particular the five-state N scheme can be used to realize single-photon gates without many of the conflicting requirements of the N scheme [29]. The tripod scheme (one excited state, three ground states) is another very

interesting nonlinear medium [30]. Because the equivalent of the $|d\rangle$ state from the N scheme is a ground state, the robustness of this state is perhaps better than for the N scheme. Brandão *et al.* have also discussed a novel three-state configuration which exhibits a very large nonlinearity [31].

26.3 The Jaynes-Cummings-Hubbard Model

In Sec. 26.2 we explored some of the means proposed to realize strong, lossless photon-photon interactions at the single photon level. Now we look at networks of cavities and the requirements to realize analogs of Hubbard-type models which exhibit controlled QPTs. We will focus on the JCHM, using the JC interaction of Sec. 26.2.1 as this is conceptually the simplest and may well turn out to be the first to be experimentally verified. In this section we will briefly review the essential features of the BHM for our purposes, and then describe the means by which the JC interaction can be used to effect a JCHM that demonstrates a polaritonic equivalent of the MI to SF transition via a mean-field description.

26.3.1 The Bose-Hubbard Model

The BHM is one of the simplest condensed matter models with nontrivial dynamics that can be explored. The seminal paper by Fisher and co-workers [32] showed the existence of an insulator-SF transition in systems of interacting bosons. Much of the recent explosion of interest in this model derives from the recent prediction [33], and demonstration [34], that this model can be directly realized in cold-atom lattices, thereby setting the groundwork for the quantum emulation being performed with cold gases at present.

The BHM over an arbitrary lattice is described by the Hamiltonian

$$\mathcal{H}^{\text{BH}} = -t \sum_{\langle i,j \rangle} (a_j^\dagger a_i + h.c.) + U_i \sum_i a_i^\dagger a_i^\dagger a_i a_i - \sum_i \mu_i a_i^\dagger a_i, \quad (26.9)$$

where a_i , a_i^\dagger are bosonic annihilation/creation operators satisfying the usual commutation relations, $\langle i,j \rangle$ indicates a sum over nearest neighbors, t is the hopping or tunneling energy, interactions U_i are taken as on-site only, and μ_i is the chemical potential for site i . We assume a perfectly ordered system, $\mu_i = \mu$ for all i . We can normalize μ and t to U : this gives rise to two control parameters for QPTs, μ/U and t/U . The interplay between them gives rise to QPTs in two universality classes [35].

The essence of the QPT for the BHM is set by whether the hopping dynamics or the on-site repulsion dominate the Hamiltonian. If the hopping dominates, $t > nU$ where n is the number of particles per site, then one can expect the particles to not significantly interact. In this case the system should

be in a SF phase, and the particle statistics should be coherent-state like. On the other hand, if the on-site interaction dominates, then the particles will repel each other. In this case an insulator phase will be realized, and the excitations will divide equally with more definite number-state like dynamics on each site.

To quantify the QPT, we review mean-field analysis of the BHM [35]. To do this we approximate the full many-body physics by focusing on a single site, while the rest of the system is described by mean-field interactions. Clearly this approach hides much of the physics, especially that describing extended spatial dynamics; however, it does afford a relatively easy and computationally tractable method to gain significant insight into the ground state. To perform our mean-field analysis, we introduce a SF order parameter, $\psi = \langle a_i \rangle$, which is assumed to be real [36] and identical for all sites, and invoke the dynamic decoupling approximation, i.e.,

$$a_i^\dagger a_j = \langle a_i^\dagger \rangle a_j + \langle a_j \rangle a_i^\dagger - \langle a_i^\dagger \rangle \langle a_j \rangle. \quad (26.10)$$

So the mean-field BHM as a sum of single-site Hamiltonians is

$$\mathcal{H}_{\text{MF}}^{\text{BH}} = \sum_i U a_i^\dagger a_i^\dagger a_i a_i - zt\psi \left(a_i^\dagger + a_i \right) + zt|\psi|^2 - \mu a_i^\dagger a_i, \quad (26.11)$$

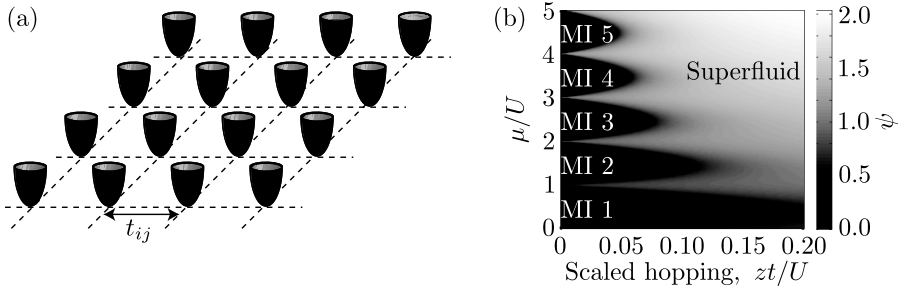
where the number of nearest neighbors, z , has been introduced. This equation must be solved self-consistently for the ψ which minimizes the ground state energy of $\mathcal{H}_{\text{MF}}^{\text{BH}}$. This phase diagram is displayed in Fig. 26.6 (b). The phase diagram shows a sequence of plateaus or lobes with SF order parameter of zero, and then regions with increasing SF order parameter. The plateaus are termed *MI lobes* and in these lobes, each site is occupied by a definite number of particles. When the SF order parameter changes from 0 in the MI lobes, to nonzero, the system undergoes a QPT to the SF state.

The change in the correlation function of the particles on the sites has measurable consequences, and indeed was the signature of the phase change as reported in the demonstration due to Greiner *et al.* [34]. However, for our purposes this textbook example serves as a point of reference for the exploration of the photonic QPT in the JCHM, treated below.

26.3.2 Mean-Field Analysis of the JCH Model

The mean-field treatment of the JCHM is generated by extension of the BHM case treated above [3, 11], although the presence of a nontrivial detuning parameter, and the change in the form of U between the two cases, introduces qualitative differences between the models. Indeed, Zhao and co-workers have suggested that the JCHM belongs in a different universality class from the BHM [37] which is an important detail when trying to show equivalence between the JCHM and other, more standard, condensed matter models.

We have already seen in Sec. 26.2.1 how the JCM can provide an effective nonlinear interaction for polaritons. We must now motivate the equivalent of

**FIGURE 26.6**

(a) Schematic of array of trapping potentials with inter-site hopping t . (b) Mean-field phase diagram showing the Mott-insulator–superfluid QPT represented by the SF order parameter (gray scale) as a function of scaled hopping, $\hbar zt/U$ and chemical potential, μ/U . Only the first five MI lobes are shown, labeled MI 1 to MI 5, indicating integer filling $n = 1, 2, \dots, 5$. When hopping dominates, the system is in a SF phase; when on-site repulsion dominates, the system is in an insulator phase. Note that the MI lobes are equally spaced, and reduce in size with increasing particle number, their length scaling approximately as $1/n$.

the hopping term from more standard Hubbard models. To achieve the strong atom-photon coupling that is necessary for our purposes requires the formation of large Q-factor, small volume cavities. The Q-factor is a figure of merit for the storage of energy inside a system and for a given resonance is defined as $Q = \Delta_\omega/\omega$ where ω is the resonance frequency and Δ_ω the width of the resonance. The hopping term can come from a variety of sources, but physically one of the most straightforward to consider is via the evanescent tails of the photon distributions within the cavities for coupled photonic bandgap cavities, or via the finite reflectivity of the confining mirrors for directly coupled cavities. A concept for a photonic crystal implementation is given in Fig. 26.1. These points will be elaborated on in Sec. 26.5; for the time being we will assume that a tight-binding model for the photonic excitations is valid, and that the inter-cavity hopping rate is κ . Furthermore we will assume that the cavity Q is dominated by κ and not other loss mechanisms.

The JCHM is¹

$$\begin{aligned} \mathcal{H}^{\text{JCH}} = & \sum_i \left[\hbar\epsilon_i \sigma_i^+ \sigma_i^- + \hbar\omega_i a_i^\dagger a_i + \hbar\beta_i (\sigma_i^+ a_i + \sigma_i^- a_i^\dagger) \right] \\ & - \hbar\kappa \sum_{\langle i,j \rangle} (a_i^\dagger a_j + h.c.) - \sum_i \mu_i (\sigma_i^+ \sigma_i^- + a_i^\dagger a_i) \end{aligned} . \quad (26.12)$$

It is important to explore the role of the chemical potential term in the JCHM,

¹In the context of cavity physics it is useful to speak of rates, rather than energies: thus $\hbar\kappa$ plays the role of hopping energy t from the BHM, etc. Only chemical potential is retained as an energy.

μ . Although this is a conventional parameter in many-body physics, in quantum optics it can be problematic. Indeed, for photons it is usual that $\mu = 0$, indicating that it costs no energy to add a photon. However, in general in the JCHM with appreciable nonlinear interactions, one should realize that it is possible, in fact necessary, to define a nonzero μ . This is because the conserved excitations in this problem are not photons: they are polaritons. This point is well explored in Refs. [38, 39]. For the present discussion we will simply treat μ as a valid parameter and note when difficulties with this parameter arise, in the SF regime.

The mean-field Hamiltonian, by close analogy with the BHM mean-field Hamiltonian of Eq. (26.11), under the rotating wave and dynamic decoupling approximations is

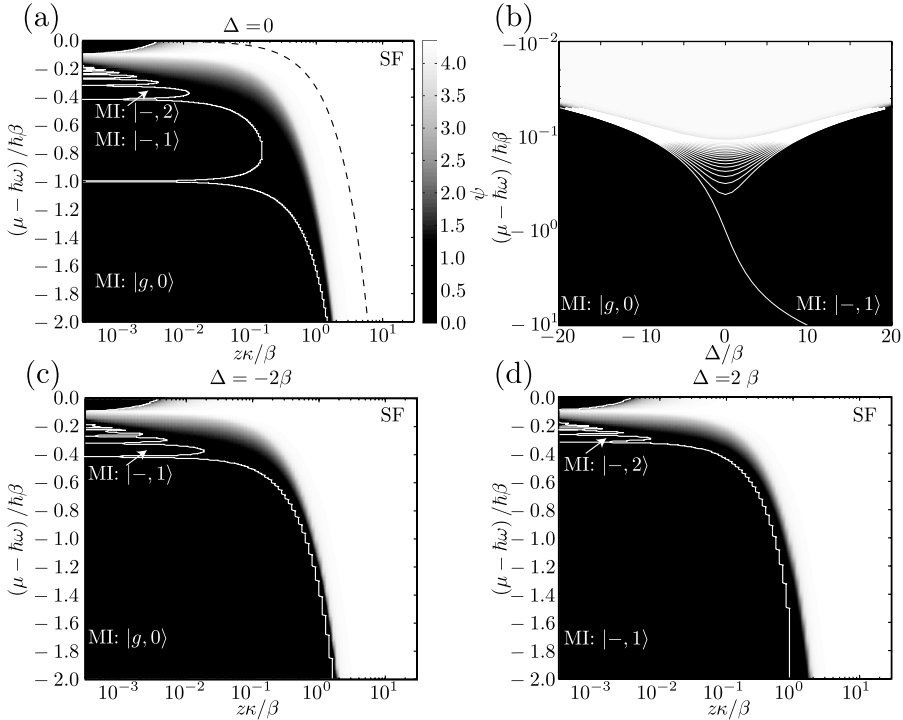
$$\mathcal{H}_{\text{MF}}^{\text{JCH}} = \sum_i \left[\hbar\epsilon_i \sigma_i^+ \sigma_i^- + \hbar\omega_i a_i^\dagger a_i + \hbar\beta_i (\sigma_i^+ a_i + \sigma_i^- a_i^\dagger) - z\hbar\kappa\psi (a_i^\dagger + a_i) + z\hbar\kappa|\psi|^2 - \mu_i (\sigma_i^+ \sigma_i^- + a_i^\dagger a_i) \right], \quad (26.13)$$

where the first line corresponds to the JCM, which plays a role analogous to the U_i in the conventional Hubbard model, and the second line corresponds to the mean-field extensions. From now on we will only treat the case where all parameters are the same from site to site.

To solve Eq. (26.13) we perform the same strategy used for Eq. (26.11), i.e., we determine the value for the SF order parameter that minimizes the ground state energy. The phase space for the JCHM is perforce richer than for the BH due to the presence of an additional energy scale: detuning, as compared with just interaction and hopping in the BHM.

The JCHM phase diagram calculated using the mean-field approach is presented in Fig. 26.7 (a) for the case of zero detuning, and shares some features in common with the BHM. When $\kappa/\beta \ll 1$, on-site interactions dominate and the system shows plateaus where the ground state is an integer number of excitations per site. With increasing chemical potential, the lobes correspond to each atom-cavity system being in the ground state $|g, 0\rangle$, $|-, 1\rangle$, $|-, 2\rangle$, etc. Such lobes correspond to the MI lobes identified in the BHM. Unlike the BHM, these lobes are not of equal extent along the μ axis. This is a consequence of the reduction in the effective polariton-polariton interaction with increasing excitation number in the JCM, which can be likened to an effective U that is excitation-number dependent.

With increasing κ/β we observe a QPT evidenced by the SF order parameter being nonzero. This QPT has also been confirmed using other methods, density matrix renormalization group [40], variational cluster [41], linked-cluster expansion [42], Quantum Monte-Carlo [43], and the one-polariton approximation [44]. Across this boundary, the ground state is found to be a coherent superposition of states of different excitation number, which is identified with a SF fraction. In the limit $\kappa/\beta \gg 1$ we find a rapid increase in SF order parameter which indicates that there are no restrictions on the excitation number, or equivalently the number of polaritons, that can be found in

**FIGURE 26.7**

Mean field phase diagrams for atom-cavity detunings of (a) $\Delta = 0$, (c) $\Delta = -2\beta$ and (d) $\Delta = 2\beta$, and (b) as a function of Δ for $\kappa = 0$. (a), (c), and (d) Diagrams show the superfluid order parameter, ψ , as a function of the scaled chemical potential, $(\mu - \hbar\omega) / \hbar\beta$ and scaled photon hopping $z\kappa / \beta$. Also shown are the extents of the MI lobes as guides to the eye (white solid curves) and the boundary $\mu - \hbar\omega = z\hbar\kappa$. (b) Phase diagram for zero hopping, where the color indicates different MI lobes as a function of detuning, Δ / β and scaled chemical potential, $(\mu - \hbar\omega) / \hbar\beta$. The color axis was determined using a mean-field calculation, while the overlayed lines correspond to the frequency shifts reported in Fig. 26.4. For this reason the spectral JCM frequency shifts can also be identified with critical chemical potentials, i.e., the chemical potential where the system moves from one phase to the next.

each cavity [11]. This is entirely to be expected and in keeping with our understanding of conventional linear cavities. In this regime one would not expect the chemical potential to be a useful axis, as the chemical potential should be zero in the SF regime, and the grand canonical ensemble will provide an infinite number of particles. This accords with our intuition developed through Bose-Einstein condensation and conventional JCMs. Alternatively, Koch and

Le Hur identify this region with instability [11] and identify the boundary between the zones occurring when $\mu - \hbar\omega = z\hbar\kappa$; although we disagree with their interpretation of the system state in this regime, we have added this useful line of demarcation to Fig. 26.7 (a), but also identify the SF regime to the right of this boundary in contrast to the identification made in [11].

As stated above, the JCHM provides additional richness over the BHM due to the presence of a detuning parameter, which is an extra energy scale that introduces dynamics not present in the BHM. To explore the effect of detuning, we present in Figs. 26.7 (c)-(d) mean-field phase diagrams where the detuning is (c) $\Delta = -2\beta$ and (d) $\Delta = 2\beta$. Note that there are some similarities in all cases, namely the presence of the MI and SF phases. Also observe that for both positive and negative large detunings, the MI lobes become more evenly spaced, but smaller, as is to be expected as the effective polaritonic interaction has been reduced by the detuning, but the interaction becomes closer to the ideal Kerr-type interaction.

An alternative means for exploring the effect of detuning is shown in Fig. 26.7 (b) which shows the phase diagram as a function of Δ/β and $(\mu - \hbar\omega)/\hbar\beta$ when the hopping parameter is zero. In this case the extent of the lobes exactly matches with the frequency shift plots from Fig. 26.4. For this reason we can identify the quantity $\hbar\delta_\omega(\pm, n) = \mu_c$, i.e., the critical chemical potential which is the chemical potential, in the limit of zero hopping, which gives rise to a phase change from one MI lobe to the next [3].

26.4 Few-Cavity Systems

The QPT that is predicted for the JCHM can of course formally only be realized in the limit of an infinite number of cavities.² It is therefore instructive to explore how the phase diagram develops as the number of cavities is increased from the well-known one-cavity result to the thermodynamic limit. This was the subject of Ref. [38] and we review some of the pertinent results here.

The Hamiltonian for the finite cavity limit is Eq. (26.12) summed over a finite, rather than infinite, network. To proceed, observe that Eq. (26.12) with finite cavities can be expressed in block diagonal form with each block describing the system with a definite number of excitations, i.e., we may write

$$\mathcal{H}^{\text{JCH}} = \begin{bmatrix} \mathcal{H}^{(0)} & 0 & 0 & \cdots & 0 \\ 0 & \mathcal{H}^{(1)} & 0 & \cdots & 0 \\ 0 & 0 & \mathcal{H}^{(2)} & \cdots & 0 \\ \vdots & \vdots & \vdots & \ddots & \vdots \\ 0 & 0 & 0 & \cdots & \mathcal{H}^{(n)} \end{bmatrix}, \quad (26.14)$$

²QPTs in finite systems are discussed in Chaps. 13 and 27.

where $\mathcal{H}^{(i)}$ is the $(i+1)^{\text{th}}$ block of the Hamiltonian for i total number of excitations for a given lattice. These blocks grow rapidly with increasing number of excitations, and as an example we show the form of the first three blocks for the two-cavity case, labeled $\mathcal{H}^{(0)}$, $\mathcal{H}^{(1)}$, and $\mathcal{H}^{(2)}$, under the assumption of identical cavities and β and κ real. For comparison we also give the basis ordering in the braces beside the matrices. $\mathcal{H}^{(0)}$ is always trivial and is

$$\mathcal{H}^{(0)} = [0], \quad \{|g, 0\rangle_1|g, 0\rangle_2\}, \quad (26.15)$$

the subscripts denote each atom-cavity system, and for the general case with N JCMs the ground state is $|g, 0\rangle^{\otimes N}$. $\mathcal{H}^{(1)}$ and $\mathcal{H}^{(2)}$ are

$$\mathcal{H}^{(1)} = \hbar \begin{bmatrix} \epsilon & \beta & 0 & 0 \\ \beta & \omega & 0 & \kappa \\ 0 & 0 & \epsilon & \beta \\ 0 & \kappa & \beta & \omega \end{bmatrix}, \quad \left\{ \begin{array}{l} |e, 0\rangle_1|g, 0\rangle_2 \\ |g, 1\rangle_1|g, 0\rangle_2 \\ |g, 0\rangle_1|e, 0\rangle_2 \\ |g, 0\rangle_1|g, 1\rangle_2 \end{array} \right\}, \quad (26.16)$$

$$\mathcal{H}^{(2)} = \hbar \begin{bmatrix} H_a^{(2)} & H_b^{(2)} \\ (H_b^{(2)})^T & H_c^{(2)} \end{bmatrix}, \quad (26.17)$$

$$H_a^{(2)} = \begin{bmatrix} \epsilon + \omega & \sqrt{2}\beta & 0 & \kappa \\ \sqrt{2}\beta & 2\omega & 0 & 0 \\ 0 & 0 & 2\epsilon & \beta \\ \kappa & 0 & \beta & \epsilon + \omega \end{bmatrix}, \quad \left\{ \begin{array}{l} |e, 1\rangle_1|g, 0\rangle_2 \\ |g, 2\rangle_1|g, 0\rangle_2 \\ |e, 0\rangle_1|e, 0\rangle_2 \\ |e, 0\rangle_1|g, 1\rangle_2 \end{array} \right\}, \quad (26.18)$$

$$H_b^{(2)} = \begin{bmatrix} 0 & 0 & 0 & 0 \\ 0 & \sqrt{2}\kappa & 0 & 0 \\ \beta & 0 & 0 & 0 \\ 0 & \beta & 0 & 0 \end{bmatrix}, \quad \left\{ \begin{array}{l} |e, 1\rangle_1|g, 0\rangle_2 \\ |g, 2\rangle_1|g, 0\rangle_2 \\ |e, 0\rangle_1|e, 0\rangle_2 \\ |e, 0\rangle_1|g, 1\rangle_2 \end{array} \right\}, \quad (26.19)$$

$$H_c^{(2)} = \begin{bmatrix} \epsilon + \omega & \beta & \kappa & 0 \\ \beta & 2\omega & 0 & \sqrt{2}\kappa \\ \kappa & 0 & \epsilon + \omega & \sqrt{2}\beta \\ 0 & \sqrt{2}\kappa & \sqrt{2}\beta & 2\omega \end{bmatrix}, \quad \left\{ \begin{array}{l} |g, 1\rangle_1|e, 0\rangle_2 \\ |g, 1\rangle_1|g, 1\rangle_2 \\ |g, 0\rangle_1|e, 1\rangle_2 \\ |g, 0\rangle_1|g, 2\rangle_2 \end{array} \right\}. \quad (26.20)$$

Due to the complexity of the blocks, analytical insight is difficult for the many excitation manifolds, but perhaps surprisingly the boundary between the zero and one-excitation manifolds can be analytically determined, and is [38]

$$\mu - \hbar\omega = -\frac{\hbar}{2} \left[\Delta + z\kappa + \sqrt{(\Delta - z\kappa)^2 + 4\beta^2} \right]. \quad (26.21)$$

Although Eq. (26.12) is not analytically tractable beyond the one-excitation manifold, it is relatively straightforward to solve numerically in the limit of few cavities and few excitations. To compare with the mean-field, Fig. 26.8 shows the domains for each ground state of the Hamiltonian as a function of chemical potential and scaled hopping for periodic boundary conditions in a ring topology. We also superimpose the mean-field-determined

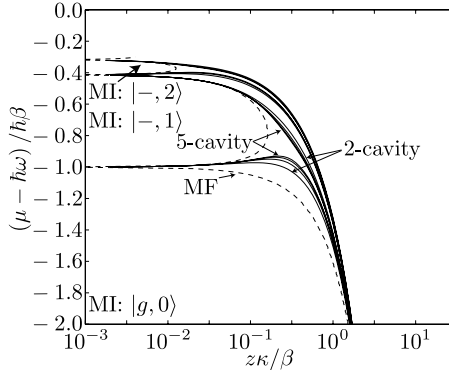


FIGURE 26.8

Ground state domains as a function of chemical potential and hopping rate for systems of increasing number of cavities in a ring geometry (nearest-neighbor coupling with periodic boundary conditions). For comparison is a mean-field determination of the QPT (dashed line). Note the connections between the MI lobes determined via mean-field, with the large domains determined using finite calculations. The finite system domains converge to the mean-field domains with increasing number of cavities, and we have performed calculations up to 5 cavities about the first MI lobes, and 4 cavities around the second. When the mean-field calculated ground state is $|\alpha, n\rangle$, where $\alpha = g, \pm$ and n is an integer, then the corresponding finite system ground state is $|\alpha, n\rangle^{\otimes N}$ where N is the number of cavities.

QPTs. Note the qualitative similarity between the regions. The MI lobes are mirrored in the finite cavity calculations, with the ground state corresponding well with the predicted mean-field ground state. The finite calculations cannot capture the SF physics; however, it is clear that in the region with nonzero SF order parameter, there is a rapid decrease in the size of the domains for the ground states, indicating that fluctuations could easily shift the state, which is suggestive of agreement. Finally, note the slight difference in the form of the maximum extent along the κ axis of the MI lobes as predicted with the finite cavity case compared with the mean-field case. This ‘pinch-off’ is also seen in other treatments, e.g., the variational cluster approach of Aichhorn *et al.* [41] and the one-polariton expansion of Ref. [44]. This suggests that these methods are able to capture physics missed by the mean-field treatment, namely the importance of inter-cavity correlations.

The strong connection between the finite cavity treatment and the mean-field phase diagram is highly suggestive that significant progress can be made on experimental investigations of the JCHM, without going to the expense of constructing massive systems of identical cavities. This is important as although the QPT will not be definitively shown except in the limit of a thermodynamic number of cavities, its signature can be observed in quite modest

setups of fewer than ten coupled JCMs, and by studying ring topologies with periodic boundary conditions (i.e., $z = 2$) the effect of the hopping will be relatively diminished compared with β so that structures in the higher MI lobes will be easier to identify.

26.5 Potential Physical Implementations

Although the physics of the JCHM must apply to any lattice of coupled cavities, at present there are certain platforms which appear most promising, although all require further development before even the few cavity limits in Sec. 26.4 can be achieved. We cannot discuss all possible implementations, nor capture the whole spectrum of developments in each potential implementation. Instead we consider three main platforms: rubidium in microtraps, photonic crystals in diamond, and circuit QED. Other important platforms include Rydberg states in supercavities [45], excitons in photonic crystal lattices, which is the basis of the proposal of Na *et al.* [25], and photon-enhanced phononic QPTs in ion trap arrays [46].

26.5.1 Rubidium Microtrap Arrays

Alkali metal vapors have long been one of the main stays for experimentation in light-matter interactions. This derives mainly from its convenient level structure with transitions accessible to cheap, stable laser diodes. Because of this, some of the most dramatic experiments in quantum optics and cavity quantum electrodynamics (QED) have been performed using cesium and rubidium. Particularly relevant to our work are the demonstrations of strong atom-cavity coupling for the purposes of single atom trapping, and cavity-assisted single-photon generation [47], leading to photon blockade [8].

However, one problem with most alkali-metal vapor systems is the overhead in generating the trapping fields, and the relatively large physical size of the Fabry-Perot cavities. These problems hamper efforts to generate networks of coupled cavities. Promising steps to overcoming such limitations have been made through the use of microtrap arrays that have been developed by the Hinds group [48]. By using advanced microfabrication techniques, arrays of curved mirrors can be fabricated on a single chip, and then coupled directly to fibers or free-space optics. These cavities have already shown strong-coupling dynamics, and the possibility of arbitrary coupling between cavities could pave the way for the realization of lattice connectivity not accessible to more conventional lattice structures, e.g., hopping terms well beyond nearest neighbor.

26.5.2 Diamond Photonic Crystal Structures

Diamond is a remarkable medium and for many properties constitutes an extreme material. For example, it has the highest thermal conductivity, the highest Young's modulus, and the widest bandgap for any naturally occurring material. However, for the purposes of JCHM physics there is one feature that distinguishes diamond above most others, namely the presence of over 500 photo-stable color centers [49]. One color center in particular, the negatively charged nitrogen-vacancy (NV), is particularly appealing due to demonstrations of single photon emission [50], quantum key distribution [51], coherent single spin dynamics and readout [52], and magnetometry [53], all at room temperature. At cryogenic temperatures the control necessary to tune NVs via Stark shifting has also been demonstrated [54]. As such, NV diamond is rapidly becoming one of the most promising solid-state platforms for optically coupled quantum-information-processing devices [55].

There are major impediments to constructing JCHMs and scalable quantum computers from diamond, including the difficulties of (i) fabricating integrated photonic circuits that are either compatible with diamond, or from monolithic diamond, and (ii) the relatively large inhomogeneous broadening of the color centers. There has been considerable progress on both fronts.

Amongst diamond's properties are that it is extremely chemically inert and the hardest of all naturally occurring substances. This presents extreme challenges to fabricating high-quality monolithic microstructures. In addition, the lack of convenient sacrificial layers precludes many conventional silicon and gallium-arsenide processing techniques. However, focused-ion-beam milling has been shown to be an effective tool to sculpt structures in diamond, having been employed in the first photonic crystal design in diamond [56], and electron-beam combined with reactive-ion etching has also been used [57]. Both of these demonstrations were with nano-crystal diamond films; however, the techniques also apply to single-crystal diamond, where liftoff, achieved by graphitizing a subsurface layer via ion irradiation, is used to set the membrane thickness [58]. Although single-crystal diamond provides superior optical properties, and superior center stability compared with nano-crystalline films, the quality of single-crystal diamond membranes has been disappointing to date and further understanding of the properties of the resulting diamond is required before the promise of monolithic diamond can be realized.

Despite these limitations, there has been considerable effort in translating the advances of silicon integrated optical structures to diamond, especially high-Q, low mode volume cavities [9] and coupled cavity networks [10]. In addition to the fabrication challenges, the lower refractive index and optical transitions³ means that some care is required in such translation. Some of the most promising work has been in the study of heterostructure cavities which can be realized entirely by geometry [59] or a combination of geometry and post-processing refractive-index modification using ion irradiation [60]. These

³The zero-phonon line transition for NV is 637 nm.

designs promise Q-factors in the vicinity of 10^6 to 10^7 , with mode volumes around 2 cubic wavelengths.

In addition to photonic-crystal cavities, other cavity designs have been explored, e.g., microtoroidal cavities [61]. Alternative cavity designs can have mode volumes less than one cubic wavelength; for example, slot cavity structures [62] can also be designed to work with diamond [13], offering potential vacuum Rabi frequencies nearly two orders of magnitude greater than more conventional cavity designs. Because of the difficulties in sculpting diamond nano-structures, much effort has been directed towards hybrid platforms where more mature photonic platforms are combined with nano-positioned diamond nano-crystals. An example using a SiN heterostructure cavity and a diamond nano-particle that would appear suited for integrated cavity applications can be found in Ref. [63]. Finally, although NV is the most well-understood center in diamond, and is so far the front runner for quantum applications, other centers may well be more promising for JCMs. These centers, many of which have larger or comparable dipole moments, and narrow zero phonon lines, include the NE8 center [64], silicon-vacancy center [65], and a chromium-related center [66].

The combination of high dipole moment centers, obvious applications to quantum information processing tasks, room temperature operation, and the prospects for integrated quantum circuitry in or with diamond, have led to an explosion of activity in diamond in recent years. Given the large number of groups, rapid progress, and new ideas, diamond seems set to play a central role in coming quantum technology, and also in the study of JCHM QPTs.

26.5.3 Superconducting stripline Cavities: Circuit QED

Probably the most exciting developments in cavity QED have been the demonstrations of single-photon manipulation in superconducting stripline circuits: circuit QED [17]. Given that the transition frequencies of these circuits are in the gigahertz regime, and individual photon energies very small, it is perhaps surprising that strong atom-photon coupling should be attainable, let alone that these systems now provide the strongest single photon coupling, relative to linewidth, of any cavity QED system to date. There are two major innovations that underpin the breakthrough of circuit QED, combined with the exquisite control of electronic fabrication that is now achievable.

The first major innovation is in the effective cavity mode volume. As shown in Eq. (26.2), the single photon Rabi frequency has a $1/\sqrt{V}$ dependence, where V is the mode volume. Conventional optical cavities have volumes of order $V \sim \lambda^3$. The strip-line cavities presented in [17] had a length of 24 mm, but a width of only a few microns, with total volume of only $\sim 10^{-6} \lambda^3$. The second major innovation is in terms of the electric dipole of the transition. The first iteration used a Cooper-pair box which has a dipole moment many orders of magnitude greater than atomic systems. These facts combined to give rise to a single photon Rabi frequency of ~ 10 MHz, which should be compared

with the characteristic linewidths of the transitions of around ~ 1 MHz. In addition, the Q-factor of the circuit was measured to be $\sim 10^4$.

Further work has greatly extended these results. Quantum non-demolition measurements of the number of photons inside the cavity have been performed [67] which show the necessary resolution to resolve the JCHM ladder exists. Further developments in the stability and dipole moment of the qubit have also been made, with the *transmon qubit* allowing unprecedented atom-photon couplings of 154 MHz compared with the width of the transitions of 2.6 MHz [68]. It would appear that the only remaining issues to be solved before superconducting realizations of JCHMs can be achieved are to design effective and scalable two-cavity coupling mechanisms, with sufficient control over the fabrication lines to ensure high degrees of qubit uniformity.

26.6 Outlook

With advances in nano-fabrication and integration of quantum photonic circuitry, a nexus between photonics and condensed matter has opened. The first example of this is the prediction of polaritonic quantum phase transitions, analogous to the Mott insulator to superfluid transition observed in the Bose-Hubbard Model. This gives rise to the Jaynes-Cummings-Hubbard model, and experimental prospects for verification appear good with existing and near-term technology. However, the main significance of the JCHM is probably not in the realization of a well-known QPT - the significance is far greater.

The statistics of the polaritons in the Jaynes-Cummings model are in general unknown and problematic [69], and only in certain limits can the bosonic commutation relations be achieved. This, combined with the extra energy scales in the JCHM compared with the BHM, means that the JCHM should offer a richness not present in the BHM. Two examples of this richness include the identification of novel spin-chain phenomena in a one-dimensional coupled JCHM array [70], and novel modes and bandgaps when the detuning in the JCHM is varied in an analogy to periodic doping of semiconductors [44].

Although the differences between the JCHM and other models are important, so too are the similarities. For example, Angelakis, Santos and Bose [4] showed the equivalence of the JCHM to the XY model in certain limits, and with minimal extension provide many more spin models that can be replicated [71]. With such equivalencies, the true power of the coupled atom-cavity systems becomes evident, in that there is potentially substantial freedom to tailor the form of the inter-cavity and intra-cavity couplings, and possibly also to design nontrivial lattice connectivity, i.e., long range coupling or hopping terms, e.g., via fiber coupling. When combined with local readout and initialization, the JCHM and related coupled-cavity models become highly flexible

quantum emulators. It is certain that the JCHM is already a rich condensed matter playground, ripe for exploration and almost within experimental reach.

Acknowledgments – The authors would like to thank M. I. Makin and A. M. Martin for useful discussions and careful proofreading, and further thank M. I. Makin for assistance with Fig. 26.8. ADG and LCLH acknowledge the Australian Research Council for financial support (project nos. DP0880466 and DP0770715).

Bibliography

- [1] R. Feynman, Int. J. Theor. Phys., **21**, 467 (1982).
- [2] M. J. Hartmann, F. G. S. L. Brandão, and M. B. Plenio, Nat. Phys. **2**, 856 (2006).
- [3] A. D. Greentree, C. Tahan, J. H. Cole, and L. C. L. Hollenberg, Nat. Phys. **2**, 856 (2006).
- [4] D. G. Angelakis, M. F. Santos, and S. Bose, Phys. Rev. A **76**, 031805(R) (2007).
- [5] L. Mandel and E. Wolf, *Optical Coherence and Quantum Optics* (Cambridge University Press, Cambridge, UK, 1995).
- [6] L. Tian and H. J. Carmichael, Phys. Rev. A **46**, R6801 (1992).
- [7] A. Imamoğlu, H. Schmidt, G. Woods, and M. Deutsch, Phys. Rev. Lett. **79**, 1467 (1997),
- [8] K. M. Birnbaum *et al.*, Nature (London) **436**, 87 (2005).
- [9] B. -S. Song, S. Noda, T. Asano, and Y. Akahane, Nat. Mater. **4**, 207 (2005).
- [10] M. Notomi, E. Kuramochi, and T. Tanabe, Nat. Photonics **2**, 741 (2008).
- [11] J. Koch and K. Le Hur, Phys. Rev. A **80**, 023811 (2009).
- [12] D. E. Chang *et al.*, Nat. Phys. **4**, 884 (2008); Q. Quan, I. Bulu, and M. Lončar, Phys. Rev. A **80**, 011810 (2009).
- [13] M. P. Hiscock *et al.*, Opt. Express **17**, 7295 (2009).
- [14] E. T. Jaynes and F. W. Cummings, Proc. IEEE **51**, 89 (1963).
- [15] S. Rebić, A. S. Parkins, and S. M. Tan, Phys. Rev. A **65** 063804 (2002).

- [16] H. Grabert, and M. H. Devoret (eds) Single charge tunneling: coulomb blockade phenomena in nanostructures. NATO Adv. Stud. Inst. **B294**, (1992).
- [17] A. Wallraff *et al.*, Nature (London) **431**, 162 (2004).
- [18] M. Fleischhauer, A. Imamoğlu, and J. P. Marangos, Rev. Mod. Phys. **77**, 633 (2005).
- [19] M. Yan, E. G. Rickey and Y. Zhu, Phys. Rev. A **64**, 013412 (2001); S. R. de Echaniz *et al.*, Phys. Rev. A **64**, 013812 (2001).
- [20] S. E. Harris and Y. Yamamoto, Phys. Rev. Lett. **81**, 3611 (1998).
- [21] A. M. Stephens *et al.*, Phys. Rev. A **78**, 032318 (2008); A. D. Greentree *et al.*, New J. Phys. **11**, 093005 (2009).
- [22] M. J. Hartmann and M. B . Plenio, Phys. Rev. Lett. **99**, 103601 (2007).
- [23] P. Grangier, D. F. Walls, and K. M. Gheri, Phys. Rev. Lett. **81**, 2833 (1998).
- [24] S. Rebic, S. M. Tan, A. S. Parkins, and D. F. Walls, J. Opt. B: Quantum Semiclass. Opt. **1**, 490 (1999); A. D. Greentree *et al.*, J. Opt. B: Quantum Semiclass. Opt. **2**, 252 (2000).
- [25] N. Na, S. Utsunomiya, L. Tian, and Y. Yamamoto, Phys. Rev. A **77**, 031803(R) (2008).
- [26] S. C. Lei and R. K. Lee, Phys. Rev. A **77**, 033827 (2008).
- [27] A. D. Greentree *et al.*, Phys. Rev. A **67**, 023818 (2003).
- [28] M. S. Zubairy, A. B. Matsko, and M. O. Scully, Phys. Rev. A **65**, 043804 (2002).
- [29] C. Ottaviani, S. Rebić, D. Vitali, P. Tombesi, Phys. Rev. A **73**, 010301 (2006).
- [30] S. Rebić *et al.*, Phys. Rev. A **70**, 032317 (2004).
- [31] F. G. S. L. Brandão, M. J. Hartmann, and M. B. Plenio, New J. Phys. **10**, 043010 (2008).
- [32] M. P. A. Fisher, P. B. Weichman, G. Grinstein, and D. S. Fisher, Phys. Rev. B **40**, 546 (1989).
- [33] D. Jaksch *et al.*, Phys. Rev. Lett. **81**, 3108 (1998).
- [34] M. Greiner *et al.*, Nature **415**, 39 (2002).

- [35] S. Sachdev, *Quantum Phase Transitions* (Cambridge University Press, Cambridge, UK, 1999).
- [36] D. van Oosten, P. van der Straten, and H. T. C. Stoof, Phys. Rev. A **63**, 053601 (2001).
- [37] J. Zhao, A. Sandvik, and K. Ueda (2008), arXiv:0806.3603.
- [38] M. I. Makin *et al.*, Phys. Rev. A **77**, 053819 (2008).
- [39] M. Grochol, Phys. Rev. B **79**, 205306 (2009).
- [40] D. Rossini and R. Fazio, Phys. Rev. Lett. **99**, 186401 (2007).
- [41] M. Aichhorn, M. Hohenadler, C. Tahan, and P. B. Littlewood, Phys. Rev. Lett. **100**, 216401 (2008).
- [42] S. Schmidt and G. Blatter, Phys. Rev. Lett. **103**, 086403 (2009).
- [43] P. Pippan, H. G. Evertz, and M. Hohenadler, Phys. Rev. A **80**, 033612 (2009).
- [44] J. Quach *et al.*, Phys. Rev. A **80**, 063838 (2009).
- [45] M. Weidinger, B. T. Varcoe, R. Heerlein, and H. Walther, Phys. Rev. Lett. **82**, 3795 (1999).
- [46] P. A. Ivanov *et al.*, Phys. Rev. A **80**, 060301 (2009).
- [47] C. J. Hood, M. S. Chapman, T. W. Lynn, and H. J. Kimble, Phys. Rev. Lett. **80**, 4157 (1998); P. Münstermann *et al.*, Phys. Rev. Lett. **82**, 3791 (1999); A. D. Boozer *et al.*, Phys. Rev. Lett. **98**, 193601 (2007).
- [48] M. Trupke *et al.*, Appl. Phys. Lett. **87**, 211106 (2005); M. Trupke *et al.*, Phys. Rev. Lett. **99**, 063601 (2007).
- [49] A.M. Zaitsev, *Optical Properties of Diamond* (Springer-Verlag, Berlin Heidelberg, Germany, 2001).
- [50] C. Kurtseifer, S. Mayer, P. Zarda, and H. Weinfurter, Phys. Rev. Lett. **85**, 290 (2000).
- [51] A. Beveratos *et al.*, Phys. Rev. Lett. **89**, 187901 (2002).
- [52] F. Jelezko *et al.*, Phys. Rev. Lett. **92**, 076401 (2001).
- [53] J. R. Maze *et al.*, Nature **455**, 644 (2008); G. Balasubramanian *et al.*, Nature **455**, 648 (2008).
- [54] Ph. Tamarat *et al.*, Phys. Rev. Lett. **97**, 083002 (2006).
- [55] A. D. Greentree, B. A. Fairchild, F. M. Hossain, and S. Prawer, Mater. Today **11**, 22 (2008).

- [56] J. W. Baldwin *et al.*, *J. Vac. Sci. Technol. B* **24**, 50 (2006).
- [57] C. F. Wang *et al.*, *Appl. Phys. Lett.* **91**, 201112 (2007).
- [58] P. Olivero *et al.*, *Adv. Materials* **17**, 2427 (2005); B. A. Fairchild *et al.*, *Adv. Materials* **20**, 4793 (2008).
- [59] I. Bayn, and J. Salzman, *Opt. Express* **16**, 4972 (2008).
- [60] S. Tomljenovic-Hanic, A. D. Greentree, C. Martijn de Sterke, and S. Prawer, *Opt. Express* **17**, 6465, (2009).
- [61] C. F. Wang *et al.*, *Appl. Phys. Lett.* **90**, 081110 (2007).
- [62] V. R. Almeida, Q. Xu, C. A. Barrios, and M. Lipson, *Opt. Lett.* **29**, 1209 (2004).
- [63] M. Barth, N. Nüsse, B. Löchel, and O. Benson, *Opt. Lett.* **34**, 1108 (2009).
- [64] V. A. Nadolinnny *et al.*, *J. Phys.: Condens. Matter* **11**, 7357 (1999).
- [65] C. D. Clark, H. Kanda, I. Kiflawi, and G. Sittas, *Phys. Rev. B* **51**, 16681 (1995).
- [66] I. Aharonovich *et al.*, *Nano Lett.* **9** 3191 (2009).
- [67] D. I. Schuster *et al.*, *Nature (London)* **445**, 515 (2007).
- [68] J. M. Fink *et al.*, *Nature (London)* **454**, 315 (2008).
- [69] V. Hussin and L. M. Nieto, *J. Math. Phys.* **46**, 122102 (2005).
- [70] M.I. Makin *et al.*, *Phys. Rev. A* **80**, 043842 (2009).
- [71] A. Kay and D. G. Angelakis, *EPL* **84**, 20001 (2008).

Quantum Phase Transitions in Nuclei

Francesco Iachello

*Center for Theoretical Physics, Sloane Physics Laboratory, Yale University,
New Haven, Connecticut 06520-8120, U.S.A.*

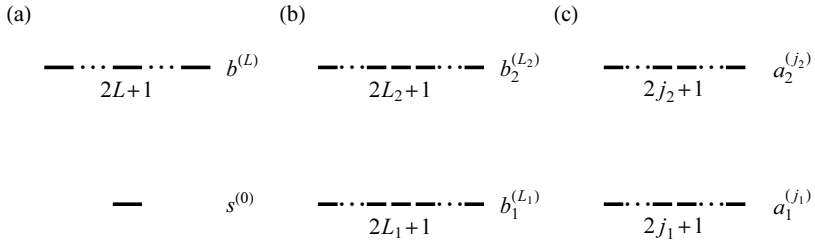
Mark A. Caprio

*Department of Physics, University of Notre Dame, Notre Dame, Indiana
46556-5670, U.S.A.*

Quantum phase transitions (QPTs) are qualitative changes in the ground-state properties of a physical system that occur as a function of one or more parameters ξ_1, ξ_2, \dots , called control parameters, which appear in the quantum Hamiltonian describing the system, $H(\xi_1, \xi_2, \dots) = \varepsilon(H_1 + \xi_1 H_2 + \dots)$. Originally introduced within the context of nuclear physics and called ground-state phase transitions [1,2], they have had in recent years many application to various areas of physics ranging from condensed matter systems [3] to atomic condensates, from atomic nuclei to elementary particles. The concept of QPTs has also been extended to that of *excited-state* QPTs (ESQPTs) [4–6], that is, qualitative changes in the properties of a physical system that occur as a function of excitation energy for fixed values of the control parameter(s). In this chapter, QPTs and ESQPTs arising in the study of atomic nuclei will be presented.

For atomic nuclei, one has specific theoretical models that can be studied in depth, namely, the algebraic models [7] wherein the Hamiltonian is written in terms of elements of a Lie algebra, usually the unitary algebra $U(n)$ in n dimensions. These algebraic models can be solved exactly, i.e., in explicit analytic form in terms of quantum numbers, for certain values of the control parameters, giving exact solutions known as dynamical symmetry limits. The predictions of these models can be and have been tested with experiments. The algebraic structure of these models may be used to good advantage, both computationally and in providing benchmarks, i.e., dynamical symmetry solutions, for the various phases of the system. Therefore, algebraic models can be used to study complex situations, such as coupled two-fluid bosonic systems and bosonic systems with fermionic impurities, i.e., Bose-Fermi systems.

Atomic nuclei are finite systems, with a relatively small number of particles $\lesssim 250$. Therefore, an important aspect of QPTs in nuclei and for algebraic models, in general, is the study of finite size scaling, i.e., scaling of such quantities as the order parameter (OP) with the number N of constituent particles.

**FIGURE 27.1**

Single-particle level degeneracies for the various classes of two-level models considered: (a) the *s-b* boson models, (b) the more general two-level bosonic pairing models, and (c) the two-level fermionic pairing models. Figure from Ref. [6].

TABLE 27.1

The *s-b* models and some of their applications.

l	n	Application
0	2	Lipkin model: a schematic many-body system [8] 1D vibron model: stretching vibrations of molecules [9]
$\frac{1}{2}$	3	2D vibron model: bending vibrations in polyatomic molecules [10, 11]; cuprate superconductors [12, 13]
1	4	3D vibron model: rotations/vibrations of diatomic molecules [9]
2	6	interacting boson model: rotations/vibrations of nuclei [14]
3	8	octupole vibrations in nuclei [14]
4	10	hexadecapole vibrations in nuclei [14]

It has been found that, even with a relatively small number of particles, the system exhibits quantum critical behavior. More precisely, although the singular behaviors associated with QPTs in the large- N limit are smoothed out, precursors are found at finite N which approach the singular limit according to definite power-law scalings.

27.1 QPTs and Excited-State QPTs in *s-b* Boson Models

QPTs have been studied extensively in a class of algebraic models, the two-level boson models, or *s-b* models, defined in terms of a singlet boson $s^{(0)}$ and a $(2l+1)$ -fold degenerate boson $b^{(l)}$, Fig. 27.1(a). These models have had many applications in physics, some of which are shown in Table 27.1. The *s-b* models are special cases of a broader family of two-level and multi-level models [Fig. 27.1(b,c)], discussed further in Sec. 27.3. One of the most important applications of *s-b* boson models is to the study of rotations and vibrations of

atomic nuclei, for which case $l = 2$ (Sec. 27.4). In this section, we consider a generic s - b boson model with $l = 0, \frac{1}{2}, 1, \frac{3}{2}, 2, \dots$. In many applications the integer or half-integer number l represents the physical angular momentum, but in others it is just a number that labels the degeneracy $2l + 1$ of the b -boson level.

27.1.1 Algebraic Structure of s - b Boson Models

Introducing boson creation and annihilation operators, s^\dagger and s for $s^{(0)}$ bosons and b_m^\dagger and b_m for b -bosons ($m = -l, \dots, +l$), one can generate the Lie algebra $U(n)$, which is spanned by the bilinear products:

$$U(n) : s^\dagger s, s^\dagger b_m, b_m^\dagger s, b_m^\dagger b_{m'} \quad (m, m' = -l, \dots, +l). \quad (27.1)$$

The Hamiltonian is written in terms of elements of $g \equiv U(n)$. From the construction 27.1, it is clear that $n = 2l + 2$. Denoting generically by G_α the elements of the algebra g , the Hamiltonian is written as an expansion in the elements

$$H = E_0 + \sum_\alpha \varepsilon_\alpha G_\alpha + \sum_{\alpha, \beta} \frac{1}{2} u_{\alpha\beta} G_\alpha G_\beta + \dots \quad (27.2)$$

The algebra g upon which the Hamiltonian is expanded is called the *spectrum generating algebra* (SGA). In most applications the expansion is truncated at quadratic terms, i.e., two-body interactions. The generic quantum s - b boson Hamiltonian can therefore also be written, in normal-ordered form, as

$$\begin{aligned} H = E_0 + e_s s^\dagger s + \sum_{m, m'} e_{mm'} b_m^\dagger b_{m'} + e'_s s^\dagger s^\dagger ss + \sum_{m, m'} u_{mm'} b_m^\dagger s^\dagger b_{m'} s \\ + \sum_{m, m'} u'_{mm'} \left(b_m^\dagger b_{m'}^\dagger ss + \text{h.c.} \right) + \sum_{m_1, m_2, m'_1, m'_2} w_{m_1 m_2 m'_1 m'_2} b_{m_1}^\dagger b_{m_2}^\dagger b_{m'_1} b_{m'_2}, \end{aligned} \quad (27.3)$$

in terms of various interaction constants E_0 , e_s , e'_s , etc.

In algebraic models, the possible phases of the system are obtained by considering all possible breakings of the algebra g into its subalgebras,

$$g \supset g_1 \supset g'_1 \supset \dots, g \supset g_2 \supset g'_2 \supset \dots, \dots, g \supset g_\nu \supset g'_\nu \supset \dots, \quad (27.4)$$

in the sense that each subalgebra chain leads to a distinct dynamical symmetry solution and therefore distinct structural phase for the system. Whether or not there is a QPT between these structures then is determined by further analysis. For applications to nuclear and molecular physics, it is convenient to impose three-dimensional (3D) rotational invariance for problems with $2l + 1$ odd (l integer) and two-dimensional (2D) rotational invariance for problems with $2l + 1$ even (l half-integer). The subalgebras g_1, g_2, \dots, g_ν define *dynamical symmetries* (DS) of the model. These are situations in which the Hamiltonian

of (27.2) is specialized to contain only the invariant Casimir operators of the algebras in one of the chains in (27.4), e.g., for $g \supset g_1 \supset g'_1 \supset \dots$,

$$H = aC(g) + a_1C(g_1) + a'_1C(g'_1) + \dots \quad (27.5)$$

In this case, the energy eigenvalues can be written in explicit analytic form in terms of quantum numbers $\lambda_1, \lambda_2, \dots$ uniquely characterizing the states,

$$E(\lambda_1, \lambda_2, \dots) = a \langle C(g) \rangle + a_1 \langle C(g_1) \rangle + a_2 \langle C(g'_1) \rangle + \dots \quad (27.6)$$

The dynamical symmetries of H then represent qualitatively different structures of the system, characterized by qualitatively different energy spectra.

The angular-momentum algebra plays an important role in systems with rotational invariance, such as nuclei and molecules. The decomposition of the algebra of $U(n)$ for the case n even ($n = 2, 4, 6, \dots$), i.e., l integer, with the constraint that the physical angular-momentum algebra $SO(3)$ be contained in the chain, has been carried out explicitly. The case of $n = 2$ ($l = 0$) is special, since there is no rotational algebra, and only a parity ± 1 is kept as a good quantum number. There are two chains, $U(2) \supset U(1)$ and $U(2) \supset SO(2)$. For $n = 4$, there are two chains containing the angular-momentum algebra $SO(3)$, namely, $U(4) \supset U(3) \supset SO(3) \supset SO(2)$ and $U(4) \supset SO(4) \supset SO(3) \supset SO(2)$. The case of $n = 6$ is richer, in that there are three chains containing the angular-momentum algebra, as described in Sec. 27.4. For $n = 8, 10, \dots$, it can be shown that at least two chains containing $SO(3)$ always exist,

$$U(n) \supset \left\{ \begin{array}{c} SO(n) \\ U(n-1) \end{array} \right\} \supset SO(n-1) \supset \dots \supset SO(3). \quad (27.7)$$

These chains have in common $SO(n-1)$, which has a consequence that transitional Hamiltonians between $U(n-1)$ and $SO(n)$ dynamical symmetries are integrable. The decomposition of $U(n)$ with n odd (l half-integer), subject to the constraint that the 2D angular momentum $SO(2)$ be contained in the chain, has also been considered, for low values of n [15].

27.1.2 Geometric Structure of s - b Boson Models

Geometry can be associated to s - b boson models with $U(n)$ algebraic structure by the introduction of coherent states and coset spaces $U(n)/[U_b(n-1) \otimes U_s(1)]$ [14, 16]. There are $n - 1$ variables in this space, α_m ($m = -l, \dots, +l$). The α_m have the same transformation properties under $SO(3)$ or $SO(2)$ as the operators b_m . Properties of the ground state of the system can be obtained by introducing coherent states expressed in terms of the variables α_m . There are several forms of coherent states [17], but for a finite system with a conserved number of particles it is most natural to use *number-projected* coherent states. The ground state of the system is written as a condensate of N bosons,

$$|N, \alpha\rangle = (N!)^{-1/2} (s^\dagger + \sum_m \alpha_m b_m^\dagger)^N |0\rangle. \quad (27.8)$$

Note that $\langle N, \alpha | N, \alpha \rangle = (1 + \sum_m |\alpha_m|^2)^N$. The energy expectation value in states (27.8) is

$$\frac{\langle N, \alpha | H | N, \alpha \rangle}{\langle N, \alpha | N, \alpha \rangle} \equiv E(\alpha). \quad (27.9)$$

Minimization of $E(\alpha)$ in parameters α_m yields a variational ground state. The nature of QPTs in s - b boson models can be studied by taking the $N \rightarrow \infty$ limit, in which the variational ground state becomes exact and may exhibit nonanalytic changes with external parameters.

Since in the class of models discussed here, with a finite single-particle space, the contribution of one-body terms to the ground-state energy grows as N , while that of two-body terms grows as N^2 , it is convenient in these systems to consider the energy per particle and scale two-body terms with an extra factor N relative to one-body terms [2, 18]. Then, $E(\alpha)$ does not depend on N and represents, in the limit $N \rightarrow \infty$, the classical Hamiltonian of the system. This is so because of the scaling with N , which implies that the quantum fluctuations of the energy per particle,

$$\frac{\langle N, \alpha | H^2 | N, \alpha \rangle}{\langle N, \alpha | N, \alpha \rangle} - \left(\frac{\langle N, \alpha | H | N, \alpha \rangle}{\langle N, \alpha | N, \alpha \rangle} \right)^2, \quad (27.10)$$

die out as $O(N^{-1})$. In fact the value of N^{-1} plays the role of the Planck constant here.¹

The variables α_m are complex variables in the coset space. It is possible to introduce canonical coordinates, q_m , and momenta, p_m , by

$$q_m = [(-1)^m \alpha_{-m} + \alpha_m^*]/\sqrt{2}, \quad p_m = i[(-1)^m \alpha_{-m}^* - \alpha_m]/\sqrt{2}, \quad (27.11)$$

which have the property $q_m^* = (-1)^m q_{-m}$ and $p_m^* = (-1)^m p_{-m}$. The new variables are still complex, but due to their $m \rightarrow -m$ symmetry, one can separate $(2l+1)$ real coordinates (e.g., real and imaginary parts of q_m with $m \geq 0$) and $(2l+1)$ associated real momenta. In this $(n-1)$ -dimensional space one can choose any set of coordinate systems. A convenient set is the hyperspherical set in terms of a hyperradius r and $n-2$ angles $\Theta \equiv (\theta_1 \theta_2 \dots)$.

Associated with the quantum Hamiltonian (27.2) there is a classical Hamiltonian written in terms of coordinates and momenta

$$H_{\text{cl}} = T(p_r, p_\Theta, r, \Theta) + V(r, \Theta). \quad (27.12)$$

Note that in this classical Hamiltonian the kinetic energy T may also depend on the coordinates. The potential function $V(r, \Theta)$ is obtained by setting all momenta equal to zero in the Hamiltonian ($p_m = 0$).

¹This is an important distinction of the present class of models, with a finite-dimensional Hilbert space, from infinite models, e.g., lattice models, for which quantum fluctuations disappear only at the critical value of the interaction strengths indicating QPTs. In the discussion in this subsection, “quantum” phase transitions result solely from the classical properties of the system; this is analogous to the semiclassical analysis frequently used in mean-field models in condensed matter physics; see preceding chapters.

27.1.3 Phase Diagram and Phase Structure of *s-b* Boson Models

A convenient way to study QPTs in algebraic models is by writing the Hamiltonian of the system in Casimir form (27.5) as

$$H = \varepsilon (H_1 + \xi_1 H_2 + \xi_2 H_3 + \cdots + \xi_{\nu-1} H_\nu). \quad (27.13)$$

The number of control parameters is $\nu - 1$, since the structure of the system is unchanged by an overall redefinition of the energy scale ε , and the phase diagram is therefore $(\nu - 1)$ -dimensional. In principle, all Casimir operators of chain 1, $g \supset g_1 \supset g'_1 \supset \dots$, may be included in H_1 , and similarly for the other chains, and these operators may indeed be needed for physically realistic spectroscopic studies. However, to study the essential features of the QPT, it suffices to consider only one Casimir operator for each chain and write

$$H = \varepsilon [C(g_1) + \xi_1 C(g_2) + \xi_2 C(g_3) + \cdots + \xi_{\nu-1} C(g_\nu)]. \quad (27.14)$$

For situations with only two phases, one may take

$$H = \varepsilon [(1 - \xi) H_1 + \xi H_2], \quad (27.15)$$

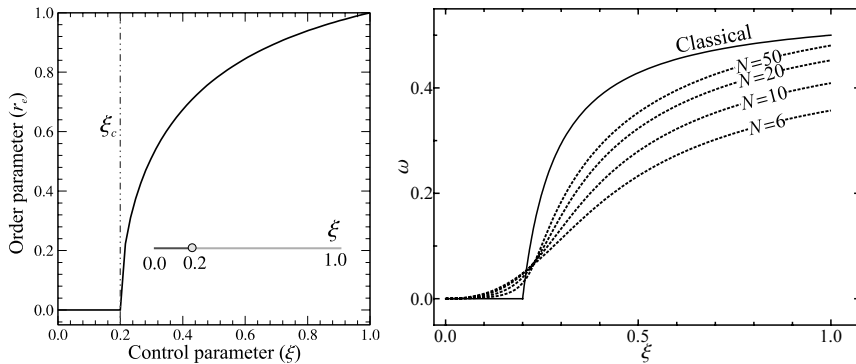
so that the QPT occurs as the control parameter traverses the finite interval $[0, 1]$. When $\xi = 0$, the eigenstates of H are those of H_1 , and, when $\xi = 1$, the eigenstates of H are those of H_2 .

The phase structure of *s-b* boson systems can be simply obtained with the usual classical analysis in terms of the potential function V which is now a function not only of the coordinates but also of the control parameters $V(\Xi; r, \Theta)$ where $\Xi \equiv (\xi_1, \dots, \xi_{\nu-1})$. Minimizing the potential function V with respect to the coordinates (r, Θ) , one obtains the equilibrium coordinate values (r_e, Θ_e) , which may be taken as the *classical OPs*, and also the classical ground-state energy $V_e(\Xi; r_e, \Theta_e)$. The study of V_e and its derivatives determines the order of the QPT. A common terminology is provided by the Ehrenfest classification [19], originally introduced for thermodynamic phase transitions, where the control parameter is the temperature, but also applicable here: the QPT is called of zeroth order if V_e is discontinuous, first-order if $\partial V_e / \partial \Xi$ is discontinuous, second-order if $\partial^2 V_e / \partial \Xi^2$ is discontinuous, etc. If no discontinuity is present, there is no QPT, and the transition between dynamical symmetries is instead called a *crossover*.

The phase structure of *s-b* boson models can also be studied in a “quantum” approach by introducing *quantum OPs*. In the classical limit, these reduce to the classical OPs.² The most basic quantum OP is the expectation value of the number of *b* bosons in the ground state,

$$\omega = \langle N_b \rangle / N. \quad (27.16)$$

²For a system with multiple phases, multiple OPs may be needed to fully characterize these phases.

**FIGURE 27.2**

Classical and quantum OPs for the $U(n-1)$ - $SO(n)$ QPT. (Left) Evolution of classical equilibrium coordinate r_e . (Right) Quantum calculations of OP ω at finite N , for the $U(5)$ - $SO(6)$ QPT of the interacting boson model, and the classical limit ($N \rightarrow \infty$). Left panel adapted from Ref. [11].

The quantum OP ω is related to the classical OP r_e by

$$\omega = r_e^2 / (1 + r_e^2). \quad (27.17)$$

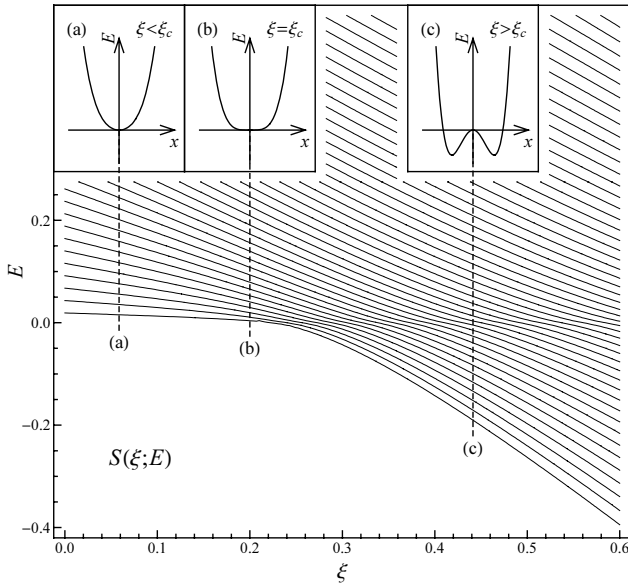
The quantum Hamiltonian is diagonalized numerically, and the OPs, ground-state energy, and its derivatives are calculated. From their behavior one infers the order of the QPT. QPTs in this sense are closely related to QPTs studied in infinite lattice and many-body systems.

The results obtained in this way depend on the number of particles N . The behavior of the OPs and other quantities as $N \rightarrow \infty$, called *finite size scaling behavior* [20, 21] is then studied as well as the divergence of correlations [22] at the critical point.

27.2 *s-b* Models with Pairing Interaction

A subclass of the *s-b* boson models consists of models with *pairing interactions*. These are special cases of the general class of *s-b* models of Sec. 27.1 in which only two phases $SO(n)$ and $U(n-1)$ remain, described by the algebraic structure (27.7). This subclass has been extensively investigated in recent years. Models with pairing interactions occupy a special place in physics due to the successes of BCS theory in the description of superconductivity and the dominance of pairing interactions in nuclei.

The QPT between the two phases $SO(n)$ and $U(n-1)$ can be studied by

**FIGURE 27.3**

Contour plot of the classical action $S(\xi; E)$ for the classical Hamiltonian (27.20), through the different regimes determined by the shape of the quadratic-quartic potential energy function (27.21), which is shown for (a) $\xi < \xi_c$, (b) $\xi = \xi_c$, and (c) $\xi > \xi_c$. The individual contours are related semi-classically to the evolution of the level eigenvalues. Figure from Ref. [6].

considering a Hamiltonian which is a linear combination of Casimir operators

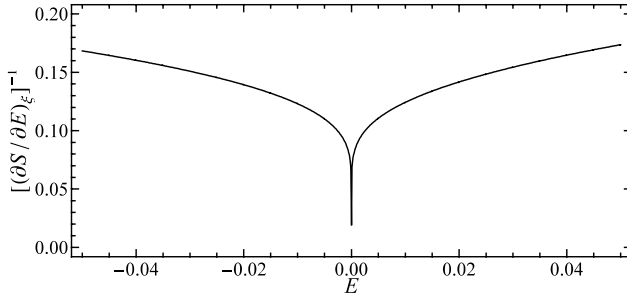
$$H = \varepsilon [(1 - \xi) C_1[\mathrm{U}(n - 1)] + \xi C_2[\mathrm{SO}(n)]], \quad (27.18)$$

where $C_p(g)$ denotes a Casimir operator of order p of the algebra g . This Hamiltonian yields $\mathrm{U}(n - 1)$ symmetry for $\xi = 0$ and $\mathrm{SO}(n)$ symmetry for $\xi = 1$. Rewriting H in terms of creation and annihilation operators gives

$$H = [(1 - \xi)/N] \hat{N}_b - (\xi/N^2) (s^\dagger \tilde{b} + b^\dagger \tilde{s}) \cdot (s^\dagger \tilde{b} + b^\dagger \tilde{s}), \quad (27.19)$$

where $\hat{N}_b \equiv (-1)^l b^\dagger \cdot b$ is the b boson occupancy. Standard spherical tensor notation has been used, with $\tilde{T}_\mu^{(\lambda)} \equiv (-1)^{\lambda-\mu} T_{-\mu}^{(\lambda)}$ and $U^{(\lambda)} \cdot V^{(\lambda)} \equiv (-1)^\lambda (2\lambda + 1)^{1/2} (U \times V)^{(0)}$, and some constant terms have been dropped in going from (27.18) to (27.19). This Hamiltonian is invariant under the common $\mathrm{SO}(n - 1)$ algebra in (27.7) and therefore conserves a $(2l + 1)$ -dimensional angular-momentum quantum number v .

As ξ is increased from $\xi = 0$, the increasing strength of the interaction between s and b bosons changes the structure of the ground state from a pure s -boson condensate to a condensate involving both types of bosons. There is

**FIGURE 27.4**

Singularity in the derivative of the classical action for Hamiltonian (27.20), specifically, the inverse of the partial derivative $(\partial S / \partial E)_\xi$, proportional to the semi-classical estimate for the gap. Figure from Ref. [6].

in this case only one control parameter and thus the phase diagram is a line [Fig. 27.2 (left)]. The two symmetries (phases) are put at the two end points. For asymptotically large values of the total particle number $N = N_s + N_b$, the change in condensate structure is abrupt and a ground-state QPT occurs.

The classical Hamiltonian corresponding to the pairing Hamiltonian (27.19) is [18, 23]

$$H = \frac{1-\xi}{2N^2} [p_r^2 + r^{-2}T_\Theta(v)] + \frac{\xi}{N^2} [r^2 p_r^2 + T_\Theta(v)] + V(\xi; r), \quad (27.20)$$

where $T_\Theta(v)$ has eigenvalue $v(v+n-2)$ [and the coordinate r is defined in the domain $0 \leq r \leq \sqrt{2}$]. The potential function is

$$V(\xi; r) = [(1-5\xi)/2]r^2 + \xi r^4. \quad (27.21)$$

This potential gives rise to a second-order QPT at a critical value $\xi_c = \frac{1}{5}$ of the control parameter. The OP is

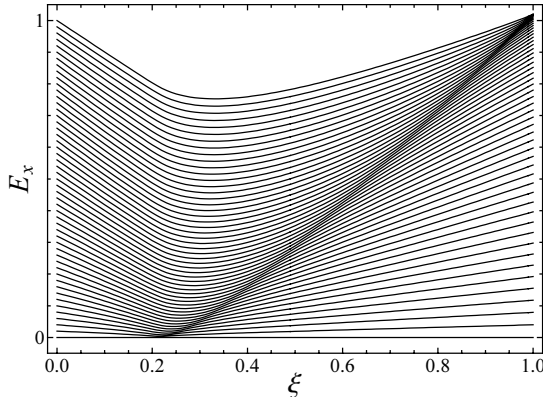
$$r_e = \begin{cases} 0 & \xi < \xi_c, \\ \sqrt{(5\xi-1)/(4\xi)} & \xi \geq \xi_c. \end{cases} \quad (27.22)$$

Its behavior is shown in Fig. 27.2 (left). The classical OP behaves in the neighborhood of the critical point as a power law

$$r_e \propto (\xi - \xi_c)^\mu. \quad (27.23)$$

Its critical exponent is $\mu = 1/2$, as one can see directly from (27.22).

In addition to studying the critical behavior, the Hamiltonian (27.20) can also be used to study the semi-classical dynamics of the problem. In Fig. 27.3(a–c), the potential (27.21) is shown as a function of $x \equiv r$. For $\xi < \xi_c$ the potential has a minimum at $r = 0$. At $\xi = \xi_c$, the potential is

**FIGURE 27.5**

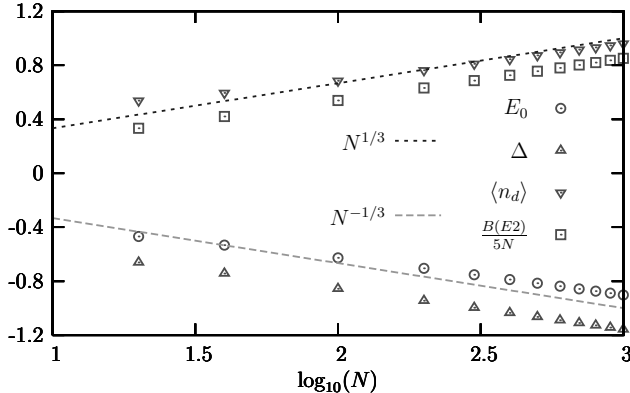
Excitation energies for the two-level fermionic pairing model, illustrating the compression of level density associated with an ESQPT. Figure from Ref. [6].

rather flat (purely quartic), and for $\xi > \xi_c$ it has a minimum at $r \neq 0$, shown as a double-well potential for $l = 0$ or a *sombrero* potential for $l > 0$. For the Hamiltonian (27.20), the zero in energy is such that the top of the barrier is always at $E = 0$, independent of ξ .

At the top of the barrier in Fig. 27.3(c), the classical action undergoes a logarithmic singularity [4, 6], which leads semi-classically to the prediction of an infinite level density. This has been interpreted as the occurrence of a QPT for the excited states, or an ESQPT [5, 6]. Fig. 27.3 shows the classical action $S(\xi; E)$ for the Hamiltonian (27.20). The compression of the contours at $E = 0$ in Fig. 27.3 corresponds to a semi-classical prediction of a compression in level density at $E = 0$, becoming a singularity in the limit $N \rightarrow \infty$. The singularity is clearly visible in Fig. 27.4, where the inverse of the partial derivative $(\partial S / \partial E)_\xi$ is plotted as a function of E . This quantity is the semi-classical estimate of the gap between adjacent levels $\Delta(E) = 2\pi N^{-1} (\partial S / \partial E)^{-1}$. From its semi-classical dynamics, the system thus undergoes a QPT as a function of the excitation energy E_x .

Going beyond semiclassical analysis, one can perform a quantum analysis. The study of QPTs in *s-b* models with pairing interaction can also be done by numerically diagonalizing the quantum Hamiltonian for a finite number of particles N . The resulting eigenvalues can be plotted as a function of the control parameter ξ , yielding a *correlation diagram*, as in Fig. 27.5.

The numerical evaluation of the OP ω as a function of ξ is shown in Fig. 27.2(b) for various values of N [24]. It is seen that even for moderate values of N a QPT behavior is observed. The discontinuity is smoothed out, i.e., it is not a true singularity, but there is still a substantial increase at $\xi = \xi_c$. Moreover, the relationship between this finite- N precursor of the singularity and the true large- N singularity can be established quantitatively,

**FIGURE 27.6**

Log-log plot showing the finite size scaling of several calculated quantities (points) for the interacting boson model and the expected power law behavior (guide lines). For this model, the transition probability is $T \sim B(E2)$. (Only the linearity and slope of the points should be compared with the guide lines. The vertical displacement is irrelevant to the scaling.) Figure from Ref. [20].

TABLE 27.2

Scaling exponents for the $U(n-1)$ - $SO(n)$ QPTs.

Φ	ξ_Φ	n_Φ	$-(n_\Phi + 2\xi_\Phi/3)$
E_0	$1/2$	1	$-4/3$
Δ	$1/2$	0	$-1/3$
$\langle n_b \rangle$	$-1/2$	0	$1/3$
T	$-1/2$	-1	$4/3$

as seen below in our discussion of finite-size scaling. Returning to Fig. 27.5, note that, at the critical point of the QPT $\xi = \xi_c$, the energies of the low-lying excited states collapse towards zero energy, leading to a singularity in the level density at zero energy, specifically, $\rho(E) \sim E^{-1/4}$. This is equivalent to a vanishing of the gap Δ .³

For $\xi > \xi_c$ there is a compression of the quantum levels along a curve, the curve of ESQPT, as was seen in the semi-classical dynamics. This curve separates regions of the spectrum where the eigenstates are structurally distinct, and a singularity in the quantum OP occurs as a function of excitation energy at the ESQPT.

Finite size scaling of the second-order QPT $U(n-1)$ - $SO(n)$ for s - b boson models has been studied in depth both analytically and numerically. The analytic results have been obtained by the method of continuous unitary trans-

³For finite N , the gap does not strictly vanish, but, rather, it approaches zero according to a definite scaling.

formation (CUT) [20, 21]. The behavior of the $1/N$ expansion has been determined for several quantities: the expectation value of \hat{n}_b (the OP), the ground-state energy E_0 , the gap Δ , and the transition rate T between the ground state and the first excited state induced by the operator $\hat{T}_m \propto s^\dagger \tilde{b}_m + b_m^\dagger s$. All these quantities display a singular behavior at the critical point $\xi = \xi_c$. Denoting generically by Φ one of those quantities, it has been proven that at the critical point Φ scales as $\Phi(\xi_c) \sim N^{-(A_\Phi + 2B_\Phi/3)}$. The specific exponents for the $U(n-1)-SO(n)$ QPTs are shown in [Table 27.2](#). For instance, the OP ω defined in (27.16) has scaling exponent $-2/3$. Scaling exponents for this QPT can also be obtained by semi-classical arguments [25], based on the observation that the potential (27.21) at $\xi = \xi_c$ is quartic in the variable r .⁴

The numerical results for the dependence of these various quantities on N are compared with the expected finite size scaling behavior in [Fig. 27.6](#). Note that the power-law behavior is well established already at very small values of $N \sim 10^{1.5}-10^2$.

27.3 Two-Level Bosonic and Fermionic Systems with Pairing Interactions

The $s\text{-}b$ boson systems with pairing interactions, of the type described by (27.19), have an overlaid algebraic structure $SU(1, 1) \otimes SO(n)$. This overlaid algebraic structure, or an analogous $SU(2) \otimes Sp(n)$ structure, is common to a larger class of two-level models whose QPTs and ESQPTs can be easily studied: the two-level bosonic and fermionic systems [[Fig. 27.1\(b,c\)](#)], with pairing interactions [6]. The algebraic structure of these models is either

$$U(n_1+n_2) \supset \left\{ \begin{array}{c} SO(n_1+n_2) \\ U_1(n_1) \otimes U_2(n_2) \end{array} \right\} \supset SO_1(n_1) \otimes SO_2(n_2) \supset SO_{12}(3) \quad (27.24)$$

in the bosonic case, with $n_1 = 2l_1 + 1$ and $n_2 = 2l_2 + 1$, directly generalizing the $U(1+n_2)$ algebraic structure of $s\text{-}b$ boson models, or

$$U(n_1+n_2) \supset \left\{ \begin{array}{c} Sp(n_1+n_2) \\ U_1(n_1) \otimes U_2(n_2) \end{array} \right\} \supset Sp_1(n_1) \otimes Sp_2(n_2) \supset SU_{12}(2) \quad (27.25)$$

in the fermionic case, with $n_1 = 2j_1 + 1$ and $n_2 = 2j_2 + 1$. Introducing operators c_j that represent either bosonic operators $b_1^{(l_1)}$ and $b_2^{(l_2)}$ [[Fig. 27.1\(b\)](#)] or fermionic operators $a_1^{(j_1)}$ and $a_2^{(j_2)}$ [[Fig. 27.1\(c\)](#)], as appropriate, the $U(n_1+n_2)$ generators are of the form $(c_1^\dagger \times \tilde{c}_1)^{(\lambda)}$, $(c_1^\dagger \times \tilde{c}_2)^{(\lambda)}$, $(c_2^\dagger \times \tilde{c}_1)^{(\lambda)}$, and $(c_2^\dagger \times \tilde{c}_2)^{(\lambda)}$. The $SO_1(n_1)$ and $SO_2(n_2)$ [or $Sp_1(n_1)$ and $Sp_2(n_2)$] algebras provide

⁴Likewise, scaling properties of the ESQPT can be deduced by semi-classical arguments [6].

conserved n_1 -dimensional and n_2 -dimensional angular-momentum quantum numbers v_1 and v_2 , as in the s - b boson models described in Sec. 27.2. The ground-state QPT is between the $\text{SO}(n_1 + n_2)$ or $\text{Sp}(n_1 + n_2)$ dynamical symmetry and the $\text{U}_1(n_1) \otimes \text{U}_2(n_2)$ dynamical symmetry.

The generic pairing Hamiltonian is of the form

$$H = \sum_j \varepsilon_j \left(\sum_m c_{jm}^\dagger \tilde{c}_{jm} \right) + \frac{1}{4} \sum_{jj'} G_{jj'} \left(\sum_{m'} c_{j'm'}^\dagger \tilde{c}_{j'm'}^\dagger \right) \left(\sum_m \tilde{c}_{jm} c_{jm} \right). \quad (27.26)$$

The pair creation, pair annihilation, and number operators for each level form an $\text{SU}(1, 1)$ algebra for bosons [26] or an $\text{SU}(2)$ algebra for fermions [27]. That is, the quasi-spin operators

$$\hat{S}_{j+} \equiv \frac{1}{2} \sum_m c_{jm}^\dagger \tilde{c}_{jm}^\dagger, \quad \hat{S}_{j-} \equiv \frac{1}{2} \sum_m \tilde{c}_{jm} c_{jm}, \quad \hat{S}_{jz} \equiv \frac{1}{4} \sum_m \left(c_{jm}^\dagger \tilde{c}_{jm} + \tilde{c}_{jm} c_{jm}^\dagger \right) \quad (27.27)$$

obey commutation relations

$$[\hat{S}_{j+}, \hat{S}_{j-}] = \mp 2\hat{S}_{jz}, \quad [\hat{S}_{jz}, \hat{S}_{j+}] = +\hat{S}_{j+}, \quad [\hat{S}_{jz}, \hat{S}_{j-}] = -\hat{S}_{j-}, \quad (27.28)$$

where the upper and lower signs apply to the bosonic and fermionic cases, respectively. The Hamiltonian (27.26) is rewritten in terms of quasi-spin operators as

$$H = \sum_j \varepsilon_j (2\hat{S}_{jz} \mp \Omega_j) + \sum_{jj'} G_{jj'} \hat{S}_{j'+} \hat{S}_{j-} \quad (27.29)$$

where $\Omega_j \equiv (2j + 1)/2$. For the case of uniform pairing strengths ($G_{jj'} \equiv G$), the algebraic structure reduces to $\text{SU}(1, 1) \otimes \text{SO}(n_1 + n_2)$ or $\text{SU}(2) \otimes \text{Sp}(n_1 + n_2)$, and the Hamiltonian can be reexpressed in the form of Sec. 27.2 as

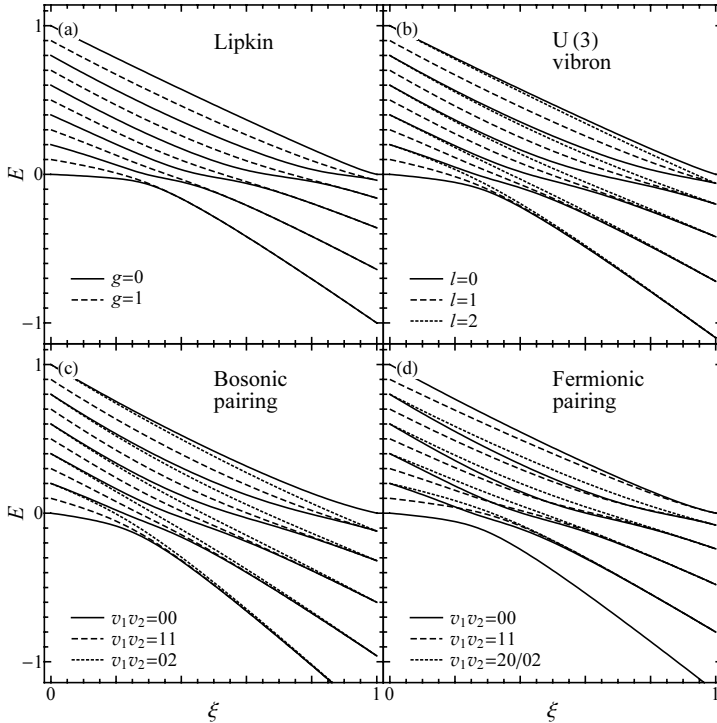
$$H = [(1 - \xi)/N]\hat{N}_2 + (4\xi/N^2)(-1)^\eta (\hat{S}_{1+} + \hat{S}_{2+})(\hat{S}_{1-} + \hat{S}_{2-}), \quad (27.30)$$

where $(-1)^\eta$ is a phase related to the sign of the pairing interaction.⁵ The ground state experiences a second-order QPT at $\xi_c = 1/5$.

Since QPTs occur in the limit of large particle number, an important distinction arises between bosonic and fermionic models. Arbitrarily large particle number can be achieved in the bosonic models, even for fixed level degeneracies, simply by increasing the total occupancy. However, for a fermionic model the total occupancy is limited by Pauli exclusion to the total degeneracy $[(2j_1 + 1) + (2j_2 + 1)]$. Therefore, the limit of large particle number can only be achieved if the number of available sub-states in each level is simultaneously increased.

Numerical analysis of the general two-level pairing models is no more difficult than for the s - b models. In Fig. 27.7, calculations for bosonic pairing [Fig. 27.7(c)] and fermionic pairing [Fig. 27.7(d)] models are shown together

⁵This Hamiltonian is equivalent to (27.19) for the s - b case, to within an additive constant.

**FIGURE 27.7**

Eigenvalues for two-level pairing models, as functions of the coupling parameter ξ . Calculations are shown for (a) the Lipkin model [U(2) bosonic realization], (b) the U(3) vibron model, (c) the bosonic pairing model ($L_1 = L_2 = 1$), and (d) the fermionic pairing model ($j_1 = j_2 = 9/2$), all for total particle number $N = 10$. Figure from Ref. [6].

with those of two s - b boson models [Fig. 27.7(a,b)]. It is seen that the evolution of levels with respect to ξ is similar in many basic aspects, including the presence of the ground-state QPT and a sharp transition in the structure of the spectrum at $E = 0$, related to the ESQPT. Important differences also arise in the detailed spectra, though, especially due to the Pauli principle for the fermionic case.

A full semi-classical analysis of arbitrary pairing models requires the introduction of classical variables and their conjugate momenta. The natural space is the coset space $U(n_1+n_2)/[U(n_1) \otimes U(n_2)]$. Although these spaces have been considered [28], no explicit construction is available, except for the case $n_1 = 1$ discussed in Sec. 27.2. An alternative is to use the overlaid algebraic structure and consider the semi-classical dynamics in the spaces $SU(1, 1)/SO(2)$ and $SU(2)/SO(2)$ [2].

27.4 *s-b* Bosonic Systems with Generic Interactions: The Interacting-Boson Model of Nuclei

An *s-b* boson model which has been extensively investigated is the interacting boson model of nuclei (IBM) [14]. Indeed an original motivation in the late 1970's to study ground-state QPTs was that of investigating the phase structure of the IBM [2]. The IBM is a model of even-even nuclei in terms of correlated pairs of nucleons, treated as bosons, with angular momentum $l = 0$ (*s*-bosons) and angular momentum $l = 2$ (*d*-bosons).

27.4.1 Algebraic Structure

The algebraic structure of the interacting boson model is $U(6)$ [see (27.1)]. If one imposes rotational invariance, the IBM has three dynamical symmetries characterized by the chains

$$U(6) \supset \left\{ \begin{array}{c} U(5) \\ SO(6) \\ SU(3) \end{array} \right\} \supset SO(5) \supset SO(3) \supset SO(2). \quad (27.31)$$

Spectra of systems in one of the three dynamical symmetry limits, with Hamiltonian of the form (27.5), can be written down explicitly in terms of quantum numbers specifying the states. They are given by

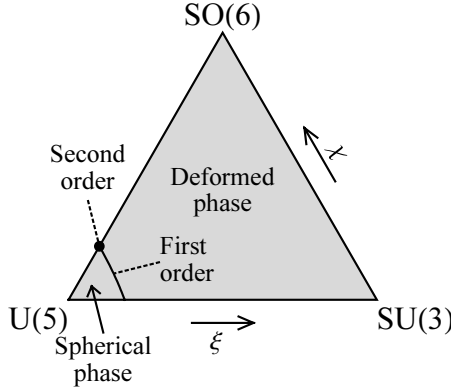
$$\begin{aligned} E(N, n_d, v, n_\Delta, L, M_L) &= E_0 + \varepsilon n_d + \alpha n_d(n_d + 4) + \beta v(v + 3) + \gamma L(L + 1), \\ E(N, \lambda, \mu, K, L, M_L) &= E_0 + \kappa(\lambda^2 + \mu^2 + \lambda\mu + 3\lambda + 3\mu) + \kappa'L(L + 1), \\ E(N, \sigma, \tau, \nu_\Delta, L, M_L) &= E_0 + A\sigma(\sigma + 4) + B\tau(\tau + 3) + CL(L + 1), \end{aligned} \quad (27.32)$$

for the $U(5)$, $SU(3)$, and $SO(6)$ chains, respectively, where $\lambda, \mu, \sigma, \tau, \dots$ are labels for irreducible representations of the algebras. Since this is a bosonic system, all states belong to the totally symmetric irreducible representation of $U(6)$. There are six quantum numbers for each chain which uniquely characterize states in this representation. Among the quantum numbers there are the total number of bosons, $N = N_s + N_d$, the total angular momentum, L , and its projection, M_L .

27.4.2 Phase Structure and Phase Diagram

The general method discussed in Sec. 27.1 can be used to study the phase diagram and phase structure of the IBM. Since there are three dynamical symmetries, and thus three structural phases, the phase diagram is 2D. The essential Hamiltonian is

$$H = \varepsilon [C_1[U(5)] + \xi_1 C_2[SU(3)] + \xi_2 C_2[SO(6)]] \quad (27.33)$$

**FIGURE 27.8**

Phase diagram of the IBM. A curve of first-order QPT $[\xi_c(\chi) = (5 + \frac{2}{7}\chi^2)^{-1}]$ and point of second-order QPT separate spherical and deformed phases.

with two control parameters. For physical reasons, it is convenient to parameterize H in the form

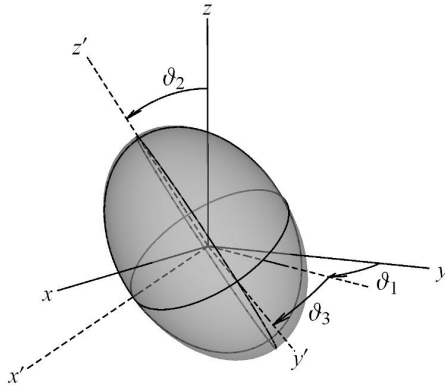
$$H = (\varepsilon/N)[(1 - \xi)\hat{n}_d - (\xi/N)\hat{Q}^\chi \cdot \hat{Q}^\chi], \quad (27.34)$$

with $\hat{n}_d = d^\dagger \cdot \tilde{d}$ and $\hat{Q}^\chi = (d^\dagger \times \tilde{s} + s^\dagger \times \tilde{d})^{(2)} + \chi(d^\dagger \times \tilde{d})^{(2)}$. The operator \hat{Q}^χ then has the physical meaning of the quadrupole-quadrupole interaction among s and d bosons. For $\chi = 0$, the interaction reduces to the form (27.19) and can therefore also be rewritten in terms of a pairing interaction (27.26). If the phase diagram is represented as a triangle with the three dynamic symmetries at its vertices, as in Fig. 27.8, then each set of values for the control parameters is represented by a point in the triangle. The three symmetries correspond to parameter choices (I) $\xi = 0$ (χ arbitrary) for $U(5)$, (II) $\xi = 1$ and $\chi = -\sqrt{7}/2$ for $SU(3)$, or (III) $\xi = 1$ and $\chi = 0$ for $SO(6)$.

We proceed to perform a semi-classical analysis. The coset space is here $U(6)/[U(5) \otimes U(1)]$. It has five complex variables, α_μ ($\mu = -2, \dots, +2$), or five real coordinates and five real momenta, as in (27.11). In order to study the phase structure of the IBM it is sufficient to put all momenta p_μ equal to zero and consider the number-projected coherent state [29]

$$|N; \alpha_\mu\rangle = (s^\dagger + \sum_\mu \alpha_\mu d_\mu^\dagger)^N |0\rangle, \quad (27.35)$$

where the α_μ thus reduce to real variables. Since the system has rotational [$SO(3)$] invariance, it is natural to separate out Euler angles for these rotations, by transformation to the Bohr variables β , γ , and $\Omega \equiv (\vartheta_1, \vartheta_2, \vartheta_3)$. Here β and γ are *intrinsic* variables, and the ϑ_i are Euler angles. The original variables α_μ are related to these by $\alpha_\mu = \sum_\nu a_\nu D_{\mu\nu}^{(2)}(\Omega)$, in terms of the Wigner D -function $D_{\mu\nu}^{(2)}$, with $a_0 = \beta \cos \gamma$, $a_{\pm 2} = \frac{1}{\sqrt{2}}\beta \sin \gamma$, and $a_{\pm 1} = 0$. The choice of these variables is also motivated by the physical interpretation, in which the

**FIGURE 27.9**

Liquid-drop model of the nucleus with ellipsoidal shape. Intrinsic axis orientations are described by Euler angles ϑ_i , and axis lengths are determined by β and γ .

nucleus is a liquid drop with surface radius $R(\theta, \varphi) = R_0[1 + \sum_\mu \alpha_\mu Y_{2\mu}(\theta, \varphi)]$, as shown in Fig. 27.9. By rotational invariance, the ground-state intrinsic state can simply be taken as

$$|N; \beta, \gamma\rangle = \{s^\dagger + \beta[\cos \gamma d_0^\dagger + (\sin \gamma / \sqrt{2})(d_{+2}^\dagger + d_{-2}^\dagger)]\}^N |0\rangle. \quad (27.36)$$

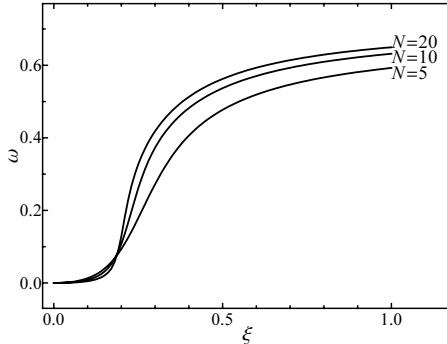
The potential function can then be constructed by taking the expectation value of the Hamiltonian in this state, yielding, for $N \rightarrow \infty$,

$$V(\xi, \chi; \beta, \gamma) = \frac{(1 - \xi)\beta^2}{1 + \beta^2} - \frac{\xi[4\beta^2 - 4\sqrt{2/7}\chi\beta^3 \cos 3\gamma + 2\chi^2\beta^4/7]}{(1 + \beta^2)^2}. \quad (27.37)$$

The *classical* OPs are the equilibrium deformations β_e and γ_e where the potential is at a minimum. A study of $V_e \equiv V(\beta_e, \gamma_e)$ and its derivatives with respect to ξ and χ produces the phase structure of Fig. 27.8. The QPT from U(5) to SU(3) is first-order, from U(5) to SO(6) is second-order, and from SU(3) and SO(6), just a crossover. Within the triangle, there is a curve of first-order QPTs, ending in a point of second-order QPT.

A complete quantum analysis for this model requires a study of the OPs and other quantities as functions of the two control parameters ξ and χ . For purposes of illustration it is convenient to present two cuts of this study, one along the QPT line from U(5) to SO(6) (χ fixed at $\chi = 0$) and one along the line U(5) to SU(3) (χ fixed at $\chi = -\sqrt{7}/2$). The only varying parameter is then ξ .

The OP ω is shown along the U(5)-SO(6) QPT in Fig. 27.2(b) and along the U(5)-SU(3) QPT in Fig. 27.10. Even for relatively small values of the particle number $N \sim 10$, both plots show a sharp increase [24]. However, it

**FIGURE 27.10**

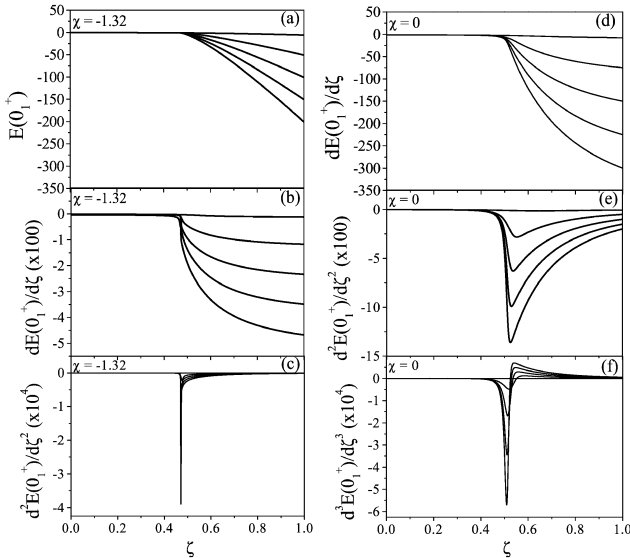
Quantum calculations of the OP ω , for the interacting boson model, across the U(5)–SU(3) QPT. Calculations are shown for various finite N .

is not immediately possible to distinguish between first order QPT (discontinuous OP) and second-order QPTs (discontinuous slope) at finite N . The classical ($N \rightarrow \infty$) expectation [Fig. 27.2(b)] is related to the equilibrium β_e by (27.17).

The behavior of the ground-state energy E and its derivatives is shown in Fig. 27.11 [30] for the two transition lines, which appear qualitatively different. From these plots one can see that there are indications of a first-order QPT along the transition line U(5)–SU(3). First-order QPTs have a discontinuity in $\partial E / \partial \xi$ and thus a singularity in $\partial^2 E / \partial \xi^2$.

The correlation diagrams along these same transition lines, i.e., the evolution of the eigenenergies as a function of ξ , are shown in Fig. 27.12. The correlation diagram for U(5)–SO(6) [Fig. 27.12(a)] is of the type described in Sec. 27.2, and, when carried to higher excitation energies, it similarly exhibits an ESQPT. The nature of the correlation diagram for highly excited states along the U(5)–SU(3) QPT is less straightforward, due to the removal of SO(5) invariance, but it is being investigated at the present time [31].

Finite size scaling for the second-order U(5)–SO(6) QPT in the IBM has been investigated by means of the continuous unitary transformation (CUT) [20]. This investigation is part of the general theory of scaling in two-level boson models (*s-b* models) with pairing interactions discussed in Sec. 27.2. The scaling exponents are thus the same as those of Table 27.2. Finite size scaling for the first-order U(5)–SU(3) QPT has not been investigated.⁶

**FIGURE 27.11**

The ground-state energy $E(0_1^+)$ and its derivatives for the IBM, across first-order U(5)-SU(3) (left) and second-order U(5)-SO(6) (right) QPTs, at finite N . The lines shown are for $N = 10, 100, 200, 300$, and 400 . The control parameter used for these plots is $\zeta \equiv 4\xi/(1 + 3\xi)$. Thus, the critical point is at $\zeta_c \approx 0.47$ at left or $\zeta_c = 1/2$ at right. Figure from Ref. [30].

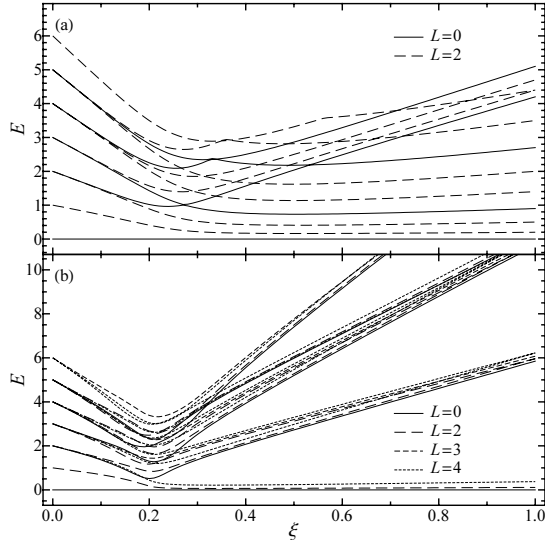
27.4.3 Experimental Evidence

One of the main points of the study of QPTs in nuclei is that the predictions can be tested by experiments. Medium-mass and heavy atomic nuclei can be well described by the interacting boson model with Hamiltonian

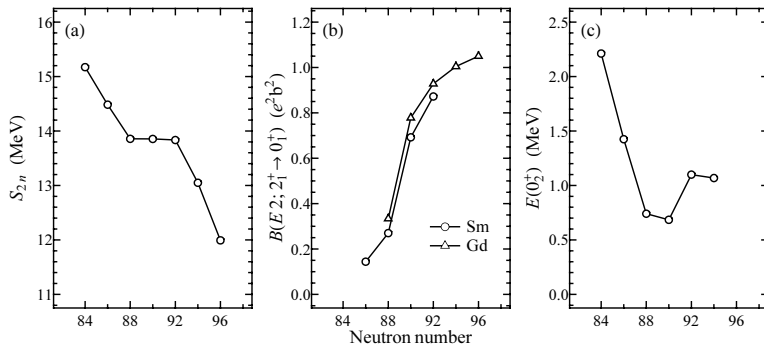
$$H = \varepsilon \hat{n}_d - \kappa \hat{Q}^\chi \cdot \hat{Q}^\chi. \quad (27.38)$$

The interactions in the model are effective interactions, which depend upon the number of nucleons in the system. The control parameters in the Hamiltonian therefore vary with proton and neutron number and can thus effectively be swept by moving from one nuclide to the next. The Hamiltonian can be converted to the form (27.15) with a control parameter ξ which, to first approximation, depends linearly on neutron or proton number. By measuring properties of nuclei with different neutron number and fixed proton number or vice versa, one can therefore study the properties of the eigenvalues and eigenstates of the quantum Hamiltonian H with varying ξ and, in particular, look for QPTs as follows.

⁶A rigorous theory of finite size scaling at first-order QPTs has been proposed in another context [32] but has not been developed for the present models.

**FIGURE 27.12**

Correlation diagrams for the IBM across the (a) U(5)-SO(6) second-order and (b) U(5)-SU(3) first-order QPTs, for $N = 20$.

**FIGURE 27.13**

Experimental data for Sm isotopes (circles) and Gd isotopes (triangles): (a) two-neutron separation energy S_{2n} , (b) electromagnetic transition strength $B(E2; 2_1^+ \rightarrow 0_1^+)$, and (c) energy of the lowest $J = 0$ excitation $E(0_1^+)$. These are surrogates for the first derivative of the ground-state energy, for the OP, and for the gap, respectively.

(a) Ground-state energies E_0 of nuclei can be easily measured. Since the derivative of the ground-state energy is of interest for QPTs, it is more useful to plot the differences

$$S_{2n}(N) = E_0(N+1) - E_0(N) \propto \partial E_0 / \partial \xi. \quad (27.39)$$

[Fig. 27.13\(a\)](#) shows this quantity as measured in the samarium isotopes. These isotopes are along the U(5)–SU(3) transition line in the phase diagram of [Fig. 27.8](#). The discontinuity in $\partial E_0 / \partial \xi$ is clearly apparent here, suggesting a first-order QPT.

(b) The deformation β of a nucleus determines the electric quadrupole moment. Direct measurements are difficult, but instead one can measure a related quantity, the electric quadrupole transition probability between the ground state and the first excited state. The square of this probability, denoted by $B(E2)$, is proportional to the square of the quantum OP

$$B(E2; 2_1 \rightarrow 0_1) \propto \langle n_d \rangle^2. \quad (27.40)$$

Fig. 27.13(b) shows this quantity for the samarium isotopes; the neighboring gadolinium isotopes are also included, to extend the curve. Again there is a sharp increase in the OP at the critical value, neutron number 90 in the figure.

(c) The gap can be measured by measuring the energy of the first excited state with the same angular momentum as the ground state, $J = 0$.

$$E(0_2) - E(0_1) \propto \Delta. \quad (27.41)$$

This is shown in Fig. 27.13(c) for samarium isotopes. A lowering of the 0_2 level at the critical value is observed.

27.5 Two-Fluid Bosonic Systems

In the preceding sections, the phase structure of *one-fluid* bosonic systems was studied. That is, only a single species of conserved particle was involved, distributing itself among the available single-particle levels of the system. For nuclei, which consist of two distinct species of conserved particle, protons and neutrons, clearly the structure of *two-fluid* systems is of interest as well. The Hamiltonian for a one-fluid model is written in terms of a single elementary Lie algebra $U(n)$. Multi-fluid systems are described by a coupling of such Lie algebras, $U_1(n_1) \otimes U_2(n_2) \otimes \dots$. Two-fluid interacting boson systems have applications both in quantum chemistry and in nuclear physics, summarized in [Table 27.3](#).

The analysis of QPTs in these coupled systems proceeds as in the previously discussed case of one-fluid systems: (i) construction of the algebraic structure $U_1(n_1) \otimes U_2(n_2)$, (ii) determination of the dynamical symmetries and thus of the possible phases, (iii) introduction of geometry in the coset spaces, with variables $\alpha_{1,m}$ and $\alpha_{2,m}$, (iv) semi-classical analysis of the Hamiltonian and potential to determine the phase structure of the problem, (v) quantum analysis by numerical diagonalization for finite boson numbers, N_1 and N_2 , and (vi) study of the finite size scaling behavior. This study has been done

TABLE 27.3

Two-fluid or coupled *s-b* models and some of their applications.

<i>l</i>	<i>n</i>	Application
0	2	Coupled stretching vibrations of molecules [9]
$\frac{1}{2}$	3	Coupled bending vibrations of molecules [10]
1	4	Coupled rotations/vibrations of molecules [9]
2	6	Proton-neutron interacting boson model [14]

for two systems, $U(3) \otimes U(3)$ [33] and $U(6) \otimes U(6)$ [34, 35], the latter of which we now discuss.

The *proton-neutron interacting boson model* (IBM-2) is a model of nuclei in terms of correlated pairs of protons and neutrons with angular momentum $l = 0$ and 2, treated as bosons s_π , d_π , s_ν , and d_ν , where π and ν denote protons and neutrons, respectively. The algebraic structure of this model is $U_\pi(6) \otimes U_\nu(6)$ [14]. Since each of the constituent fluids has three possible dynamical symmetries, and the interaction of the fluids introduces yet further possibilities, the number of phases of the systems is large.

A schematic Hamiltonian which retains the essential features of the model is

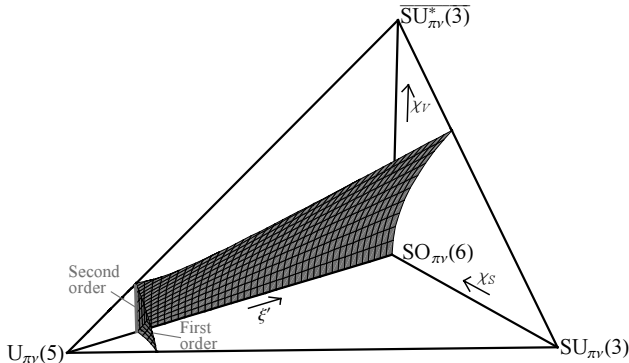
$$H = \varepsilon(\hat{n}_{d\pi} + \hat{n}_{d\nu}) + \kappa(\hat{Q}_\pi^{\chi_\pi} + \hat{Q}_\nu^{\chi_\nu}) \cdot (\hat{Q}_\pi^{\chi_\pi} + \hat{Q}_\nu^{\chi_\nu}), \quad (27.42)$$

where $\hat{n}_{d\rho} \equiv d^\dagger \cdot \tilde{d}$ and $\hat{Q}_\rho^{\chi_\rho} \equiv (s^\dagger \times \tilde{d} + d^\dagger \times \tilde{s})^{(2)} + \chi(d^\dagger \times \tilde{d})^{(2)}$ ($\rho = \pi$ or ν). It is convenient to introduce scalar and vector parameters $\chi_S \equiv (\chi_\pi + \chi_\nu)/2$ and $\chi_V \equiv (\chi_\pi - \chi_\nu)/2$. Three of the IBM-2 symmetries occur for $\chi_V = 0$ and have a direct analog in the one-fluid IBM: $U_{\pi\nu}(5)$ for $\kappa = 0$, $SO_{\pi\nu}(6)$ for $\varepsilon = 0$ and $\chi_\pi = \chi_\nu = 0$, and $SU_{\pi\nu}(3)$ for $\varepsilon = 0$ and $\chi_\pi = \chi_\nu = -\sqrt{7}/2$. However, a symmetry special to the IBM-2, denoted by $SU_{\pi\nu}^*(3)$, is obtained for $\varepsilon = 0$, $\chi_\pi = +\sqrt{7}/2$, and $\chi_\nu = -\sqrt{7}/2$.

There are three control parameters for this Hamiltonian, ξ , χ_π , and χ_ν (or ξ , χ_S , and χ_V). The phase diagram is 3D, and it can be represented as a tetrahedron with the four dynamical symmetries at its vertices and the control parameters plotted as in Fig. 27.14.

The study of the phase structure of the problem is done as in the one-fluid case by minimizing the energy functional $E = \langle H \rangle$ [34, 35]. For the Hamiltonian (27.42), it is found that the minimum occurs only for vanishing relative Euler angles, i.e., for aligned proton and neutron intrinsic frames. This effectively reduces the number of OPs for the system to four: β_π , γ_π , β_ν , and γ_ν . The order of the QPT is described in the same way as before according to the Ehrenfest classification. In the previous case of the *s-b* models with pairing interactions, the minimization could be done analytically. Here it is done numerically.⁷ Fig. 27.14 shows the phase structure of the IBM-2 with Hamiltonian (27.42), involving surfaces of first-order and second-order QPT.

⁷It should be noted that, whenever the order of the QPT is obtained by numerical analysis, application of the Ehrenfest criterion is limited by the ability to numerically resolve

**FIGURE 27.14**

Phase diagram of the proton-neutron interacting boson model (IBM-2), as obtained by numerical minimization of the classical energy surface. Surfaces of first-order and second-order QPT demarcate regions of undeformed, axially symmetric deformed, and triaxially deformed equilibria. Figure from Ref. [34].

The plane with $\chi_V = 0$ displays the same phase structure as the one-fluid interacting boson model, given in Fig. 27.8.

27.6 Bosonic Systems with Fermionic Impurities

Another class of models for which the study of QPTs has begun is that of *s-b* bosonic systems with fermionic impurities. These are systems composed by a number of bosons N_B and a number of fermions N_F with Hamiltonian

$$H = H_B + H_F + V_{BF}. \quad (27.43)$$

These models have had applications in quantum chemistry, e.g., the electron-vibron model [36], and in nuclear physics, e.g., the interacting boson fermion model (IBFM) [37]. The number of fermions is typically small. In fact, in the applications to nuclear physics, $N_F = 1$ or 2, corresponding to a single unpaired proton and/or neutron, and the motion of the single fermion is studied in the presence of the bosons.

Although the models have been extensively used in phenomenological applications, the study of QPTs has only recently begun [38, 39]. The QPTs here are QPTs in which the motion of the single particle is studied in the presence of the bosons when $N_B \rightarrow \infty$.

sufficiently small discontinuities, especially a consideration for points of first-order QPT very close to a point of second-order QPT.

27.6.1 The Interacting Boson-Fermion Model

This is a model of nuclei in terms of correlated pairs of nucleons with angular momentum $l = 0$ and 2 (treated as s and d bosons as in the IBM) and unpaired particles (fermionic impurities) [37]. QPTs in this model have been investigated by means of the Hamiltonian [38]

$$H = \varepsilon \hat{n}_d + \kappa \hat{Q}^\chi \cdot \hat{Q}^\chi + \kappa' \hat{Q}^\chi \cdot \hat{q}, \quad (27.44)$$

where \hat{n}_d and \hat{Q}^χ are the boson occupation number and quadrupole operator, as in (27.34), and $\hat{q} = (a_j^\dagger \times \tilde{a}_j)^{(2)}$ is the quadrupole operator of the fermion.⁸

A complete semi-classical analysis of bosonic systems with a single fermion can be done by introducing coherent states of the type [40]

$$|N_B; \beta, \gamma, \alpha_{j,m}\rangle \propto \left[[b_c^\dagger(\beta, \gamma)]^{N_B} |0_B\rangle \right] \otimes \left[\sum_{j,m} \alpha_{j,m} a_{j,m}^\dagger |0_F\rangle \right], \quad (27.45)$$

where $|0_B\rangle$ and $|0_F\rangle$ denote the vacua of bosons and fermions and $b_c^\dagger(\beta, \gamma)$ is the boson condensate introduced in the previous sections. By taking the expectation value of the Hamiltonian (27.44) in this coherent state, one obtains

$$E^{BF}(N_B; \beta, \gamma, \alpha_{j,m}) = E^B(N_B; \beta, \gamma) + \sum_{m_1, m_2} g_{m_1, m_2}^j(\beta, \gamma) \alpha_{j, m_1} \alpha_{j, m_2}. \quad (27.46)$$

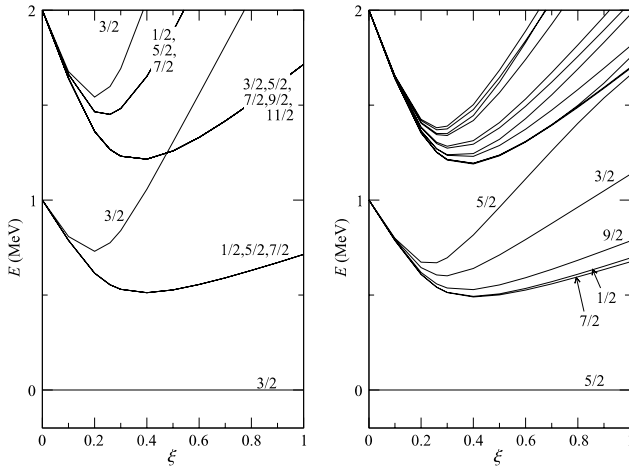
The amplitudes $\alpha_{j,m}$ and the values of β and γ can be taken as variational parameters. The equilibrium deformations β_e , γ_e , and $\alpha_{j,m;e}$ are defined by the global minimum of the combined energy surface. Since the N_B dependence is quadratic for the boson part and linear for the boson-fermion part, terms in V_{BF} can cause a shift in the equilibrium position of the order of $1/N_B$ from the value in the purely bosonic system.

Going beyond semi-classical analysis, the Hamiltonian H can be diagonalized numerically for fixed number of bosons N_B and varying control parameters. Several studies of this type have already been done [38, 39]. Fig. 27.15 shows one of these studies, for the QPT U(5)-SO(6) [38]. Fig. 27.15(a) shows the correlation diagram for $j = 3/2$, while Fig. 27.15(b) shows the diagram for $j = 5/2$. By comparing this diagram with the purely bosonic diagram one can study numerically the quantum $1/N$ corrections induced by the presence of the fermionic impurity in the bosonic system.

Mixed Bose-Fermi systems possess also dynamical symmetries, called Bose-Fermi symmetries. For each of the symmetries of the bosons, U(5), SU(3), and SO(6), one can construct corresponding Bose-Fermi symmetries [37], $U_{BF}(5)$, $SU_{BF}(3)$, and $SO_{BF}(6)$.

Furthermore, if systems differing in the number of particles are considered, e.g., by creation of a boson and destruction of a fermion ($b^\dagger a$), these Bose-Fermi symmetries can be embedded in dynamical supersymmetries. The

⁸For a single fermion with a single value of the angular momentum j , the fermionic part H_F of the Hamiltonian yields a constant term which can be neglected.

**FIGURE 27.15**

Correlation diagram for the IBFM $U(5)$ - $SO(6)$ QPT, for $N = 7$ bosons and either a $j = 3/2$ fermion (left) or a $j = 5/2$ fermion (right). Figure adapted from Ref. [38].

conditions for supersymmetries to occur are: (i) the fermions must sit on the same representation of the superalgebra $U(n|m)$ as the bosons, which can only occur for certain values of the angular momenta of the fermion;⁹ and (ii) the Hamiltonian H must be invariant under Bose-Fermi transformations. For instance, restricting (27.44) to the form

$$H = (\varepsilon/N)[(1 - \xi)(\hat{n}_d + \hat{n}_j) - (\xi/N)(\hat{Q} + \hat{q}) \cdot (\hat{Q} + \hat{q})] \quad (27.47)$$

gives a Hamiltonian which is invariant under Bose-Fermi transformations. Fig. 27.15 shows that the QPT in the Bose-Fermi system with supersymmetric conditions ($j = 3/2$) has properties identical to those of the QPT in the purely bosonic system, while, in the absence of supersymmetry ($j = 5/2$), the QPT is blurred in the mixed system.

27.7 Conclusions and Outlook

Quantum phase transitions (QPTs) have been investigated extensively within the framework of algebraic models, in particular s - b boson models, which have applications in nuclear and molecular physics. An extension of the concept of

⁹In the example of Fig. 27.15, $j = 3/2$ sits on the same representation as the s and d bosons [41], but $j = 5/2$ does not.

QPTs to excited-state QPTs (ESQPTs) has been introduced. The finite-size-scaling behavior for second-order QPTs has been determined. Phase transitional behavior has been experimentally found. The study has been extended to two-fluid systems and is in the course of being extended to *s-b* bosonic systems with an additional single fermion, i.e., a fermionic impurity.

Apart from completing the study of Bose-Fermi systems, some essential areas for further work are: (i) a study of finite size scaling behavior in first-order QPTs; and (ii) a study of ESQPTs and level densities in first-order QPTs. In other words, first-order QPTs need to be put on rigorous ground.

The class of models discussed here is similar to the class of models discussed in condensed matter physics [3], often with qualitatively similar quantum aspects. The quantum Ising model with Hamiltonian

$$H_I = J[-g \sum_i \hat{\sigma}_i^x - \sum_{\langle ij \rangle} \langle \hat{\sigma}_i^z \hat{\sigma}_j^z \rangle] \quad (27.48)$$

has the same structure as an *s-b* model, with algebra SU(2), and $J = \varepsilon$ and $g = \xi$. The difference is that in the Ising model the spins are put on a lattice, while in applications to nuclear and molecular physics the bosons are in free 3D or 2D space. The QPT that occurs in the Ising model is a second order QPT qualitatively similar to the $U(n-1)-SO(n)$ QPT.

An important aspect of algebraic models is the occurrence of dynamical symmetries which allows a rigorous (mathematical) definition of phases. The occurrence of these symmetries also simplifies the study of QPTs in complex systems, e.g., two-fluid and Bose-Fermi.

Another important aspect is the possibility to do semi-classical dynamics. A rigorous definition of the geometry associated with algebraic Hamiltonians can be given. Although the semi-classical dynamics on the coset space is rather complex, static properties, i.e., the location of minima in the potential energy surfaces, are straightforward. Consequently, critical values of the control parameters, critical exponents, etc., can be easily computed.

Because of their solvability at the limits, i.e., dynamical symmetries, and the possibility to introduce a geometric space, algebraic models could also in principle be used for models on an infinite lattice. The use of infinite-dimensional Lie algebras, i.e., *Kac-Moody algebras* [42], could be useful in these cases.

Bibliography

- [1] R. Gilmore and D. H. Feng, Nucl. Phys. A **301**, 189 (1978).
- [2] D. H. Feng, R. Gilmore, and S. R. Deans, Phys. Rev. C **23**, 1254 (1981).
- [3] S. Sachdev, *Quantum Phase Transitions* (Cambridge University Press, Cambridge, 1999); M. Vojta, Rep. Prog. Phys. **66**, 2069 (2003).

- [4] W. D. Heiss and M. Müller, Phys. Rev. E **66**, 016217 (2002).
- [5] P. Cejnar *et al.*, J. Phys. A **39**, L515 (2006).
- [6] M. A. Caprio, P. Cejnar, and F. Iachello, Ann. Phys. (N.Y.) **323**, 1106 (2008).
- [7] F. Iachello, *Lie Algebras and Applications*, Lecture Notes in Physics Vol. 708 (Springer, Berlin, 2006).
- [8] H. J. Lipkin, N. Meshkov, and A. J. Glick, Nucl. Phys. **62**, 188 (1965).
- [9] F. Iachello and R. D. Levine, *Algebraic Theory of Molecules* (Oxford University Press, Oxford, 1995).
- [10] F. Iachello and S. Oss, J. Chem. Phys. **104**, 6956 (1996).
- [11] F. Pérez-Bernal and F. Iachello, Phys. Rev. A **77**, 032115 (2008).
- [12] F. Iachello, Phil. Mag. Lett. **82**, 289 (2002).
- [13] F. Pan *et al.*, Phys. Lett. A **341**, 291 (2005).
- [14] F. Iachello and A. Arima, *The Interacting Boson Model* (Cambridge University Press, Cambridge, 1987).
- [15] P. Cejnar and F. Iachello, J. Phys. A **40**, 581 (2007).
- [16] R. Gilmore, *Lie Groups, Lie Algebras, and Some of Their Applications* (Wiley, New York, 1974).
- [17] W. Zhang, D. H. Feng, and R. Gilmore, Rev. Mod. Phys. **62**, 867 (1990).
- [18] O. S. Van Roosmalen, Ph.D. thesis, Rijksuniversiteit Groningen, 1982.
- [19] P. Ehrenfest, Proc. Amsterdam. Acad. **36**, 153 (1933).
- [20] S. Dusuel *et al.*, Phys. Rev. C **72**, 011301(R) (2005).
- [21] S. Dusuel *et al.*, Phys. Rev. C **72**, 064332 (2005).
- [22] R. Somma *et al.*, Phys. Rev. A **70**, 042311 (2004).
- [23] R. L. Hatch and S. Levit, Phys. Rev. C **25**, 614 (1982).
- [24] F. Iachello and N. V. Zamfir, Phys. Rev. Lett. **92**, 212501 (2004).
- [25] D. J. Rowe, P. S. Turner, and G. Rosensteel, Phys. Rev. Lett. **93**, 232502 (2004).
- [26] H. Ui, Ann. Phys. (N.Y.) **49**, 69 (1968).
- [27] A. K. Kerman, Ann. Phys. (N.Y.) **12**, 300 (1961).

- [28] A. O. Barut and R. Racza, *Theory of Group Representations and Applications* (Polish Scientific Publishers, Warsaw, 1977).
- [29] A. E. L. Dieperink, O. Scholten, and F. Iachello, Phys. Rev. Lett. **44**, 1747 (1980); A. E. L. Dieperink and O. Scholten, Nucl. Phys. A **346**, 125 (1980); J. N. Ginocchio and M. W. Kirson, Phys. Rev. Lett. **44**, 1744 (1980); A. Bohr and B. R. Mottelson, Physica Scripta **22**, 468 (1980).
- [30] E. Williams, Ph.D. thesis, Yale University, 2009.
- [31] P. Cejnar and P. Stránský, Phys. Rev. E **78**, 031130 (2008).
- [32] C. Borgs and R. Kotecký, J. Stat. Phys. **61**, 79 (1990).
- [33] F. Iachello and F. Pérez-Bernal, Mol. Phys. **106**, 223 (2009).
- [34] M. A. Caprio and F. Iachello, Phys. Rev. Lett. **93**, 242502 (2004).
- [35] M. A. Caprio and F. Iachello, Ann. Phys. (N.Y.) **318**, 454 (2005); J. M. Arias, J. Dukelsky, and J. E. García-Ramos, Phys. Rev. Lett. **93**, 212501 (2004).
- [36] A. Frank, R. Lemus, and F. Iachello, J. Chem. Phys. **91**, 29 (1989).
- [37] F. Iachello and P. Van Isacker, *The Interacting Boson-Fermion Model* (Cambridge University Press, Cambridge, 1991).
- [38] C. E. Alonso, J. M. Arias, L. Fortunato, and A. Vitturi, Phys. Rev. C **72**, 061302(R) (2005).
- [39] C. E. Alonso, J. M. Arias, and A. Vitturi, Phys. Rev. C **75**, 064316 (2007); C. E. Alonso, J. M. Arias, L. Fortunato, and A. Vitturi, Phys. Rev. C **79**, 014306 (2009).
- [40] A. Leviatan, Phys. Lett. B **209**, 415 (1988); S. Pittel and A. Frank, Nucl. Phys. A **454**, 226 (1986).
- [41] F. Iachello, Phys. Rev. Lett. **44**, 772 (1980).
- [42] V. G. Kac, *Infinite Dimensional Lie Algebras* (Cambridge University Press, Cambridge, 1990).

Quantum Critical Dynamics from Black Holes

Sean Hartnoll

Harvard University, Department of Physics, Jefferson Laboratory, Cambridge, MA 02138, U.S.A.

Free or weakly-interacting field theories underpin a great deal of our physical intuition. The fact that effective weakly-interacting quasi-particles can emerge even when the fundamental microscopic degrees of freedom are strongly interacting, as illustrated dramatically by Landau's theory of Fermi liquids [1], has allowed great progress in physics without confronting head-on the problem of strong coupling. Even where genuinely strongly-interacting physics is required, for instance at the Wilson-Fisher fixed point in 2+1 dimensions, computational techniques such as the (vector) large- N or $4 - \epsilon$ expansions allow us to move the problem into a weakly-coupled regime. At small ϵ or large N one can compute, using weak-coupling notions such as single-particle propagators, and then extrapolate back to the physical values of $\epsilon = 1$ or $N = 2, 3$. Remarkably, this procedure often gives qualitative and even quantitatively correct answers. However, such expansions are difficult and less accurate for real time correlators at finite temperature, as described in Chap. 1 and [2].

A weak-coupling intuition also informs our expectations of the low-temperature states of matter. Broadly speaking, in the presence of bosonic quasi-particles one expects a condensate, while fermions are expected to build up a Fermi surface.

One might ask whether there may be inherently strongly-coupled physical phenomena and novel states of matter at low temperature that cannot easily be conceptualized from weak coupling. This question has become more pressing following the discovery of a plethora of physical systems exhibiting non-Fermi liquid behavior, most infamously, the strange-metal region of the cuprate superconductors [3].

The holographic correspondence to be reviewed in this chapter presents model quantum field theories in which controlled computations may be performed directly at strong coupling. It is hoped that this approach may at the very least help to cast away some of the conceptual baggage of weak coupling. More ambitiously, by turning on a finite chemical potential in these models, one can hope to discover novel states of matter that could inform our theoretical approach to real world systems. For instance, we will encounter below

cases of gapless charged bosons that do not condense at low temperatures, as well as a strongly-coupled onset of superconductivity without quasi-particles. We will also uncover computationally controlled non-Fermi liquid behavior in fermionic spectral densities, and indications of an underlying strongly-coupled Fermi surface. Throughout, I will emphasize certain notions that arise, such as the importance of *quasi-normal poles*, that may inform general systematic approaches to strongly-interacting matter.

28.1 The Holographic Correspondence as a Tool

It has been argued that theories of quantum gravity obey a holographic principle.¹ This is the statement that the number of local degrees of freedom in gravitational theories should scale like the area enclosing a volume, in Planck units, rather than the volume itself. While this principle remains to be fully understood in general, following the seminal papers [5–7] it has been made precise in a specific framework which we will call the *holographic correspondence*.

There is a large amount of evidence that certain quantum field theories are holographically equivalent to theories of quantum gravity in one higher dimension:²

$$\begin{array}{ccc} \text{Quantum field theory} & \rightsquigarrow & \text{Quantum gravitational theory} \\ d \text{ spacetime dimensions} & & d+1 \text{ spacetime dimensions.} \end{array} \quad (28.1)$$

The most established examples are $\mathcal{N} = 4$ super Yang-Mills theory in 3+1 dimensions and the infrared fixed point of $\mathcal{N} = 8$ super Yang-Mills theory in 2+1 dimensions. These are supersymmetric $SU(N)$ gauge theories. Their field content is a gauge field A together with multiple scalar (Φ) and fermionic (Ψ) fields transforming in the adjoint representation of $SU(N)$. All the fields can therefore be written as $N \times N$ matrices. The Lagrangian is schematically

$$\mathcal{L}_{\text{QFT}} \sim \text{Tr} \left(F^2 + (\partial\Phi)^2 + i\bar{\Psi}\Gamma \cdot \partial\Psi + g^2[\Phi, \Phi]^2 + ig\bar{\Psi}[\Phi, \Psi] \right), \quad (28.2)$$

where $F = dA + gA \wedge A$ is the non-Abelian field strength. There are no mass terms; in the 3+1 dimensional case the Yang-Mills coupling g is exactly marginal, and the theory is conformal at all couplings. In 2+1 dimensions, the coupling runs to a strongly-coupled infrared fixed point.

The right hand side of the correspondence (28.1) has still not been completely defined and is difficult to work with. What makes the correspondence useful is a simplification that occurs in the t’Hooft large- N limit [10, 11] of

¹See, e.g., [4] for a pedagogical exposition of these ideas.

²See [8] and [9] for conceptual overviews with references.

these gauge theories. In this limit the gravitational theory becomes classical:

$$\begin{array}{ccc} \text{large-}N \text{ gauge theory} & \rightsquigarrow & (\text{Semi})\text{classical gravitational theory} \\ d \text{ spacetime dimensions} & & d + 1 \text{ spacetime dimensions.} \end{array} \quad (28.3)$$

The essential feature of the t'Hooft limit that allows a dual classical description is that it induces a *large- N factorization* of single trace operators. Namely, if the operator $\mathcal{O}(x) = \text{Tr}(\dots)$ then the disconnected parts of n -point functions are bigger by powers of N than connected contributions. Thus the single trace operators are classical, or *mean field*, for many purposes. For instance,

$$\langle \mathcal{O}(x)\mathcal{O}(y) \rangle = \langle \mathcal{O}(x) \rangle \langle \mathcal{O}(y) \rangle + \mathcal{O}(N^{-2}). \quad (28.4)$$

However, unlike in the large- N limit of vector models, the theory remains strongly-coupled. For instance, the operators $\mathcal{O}(x)$ generically have large anomalous dimensions and the field theory will not be describable in terms of quasi-particles. The t'Hooft limit of gauge theories retains more features of the strongly-coupled theories of physical interest.

While an extra dimension of spacetime may seem mysterious to the field theorist, it has a clear physical meaning: it is the renormalization group scale. The renormalization group flow equations are differential equations for couplings that are local in the energy scale. The holographic correspondence realizes this locality on an equal footing with spacetime locality of the field theory. Certain components of the gravitational field equations, determining the evolution of the *bulk* spacetime along the extra dimension, will precisely correspond to the renormalization group equations of the *boundary* field theory. The picture that one has in mind is the following Fig. 28.1:

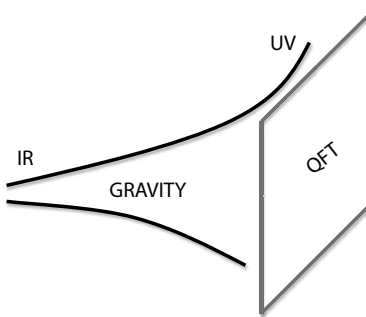


FIGURE 28.1

The extra spatial dimension of the gravitational dual represents the renormalization group flow of the quantum field theory.

The first ingredient needed to make the correspondence more precise is an action for the bulk theory. This will underlie the dual description of the field theory given by (28.2). The classical gravitational action in $d + 1$ dimensions will depend on the dual d -dimensional large- N field theory. The full action

will generically be complicated, with infinitely many fields. However, often it is possible to consistently truncate the full action to a small number of fields that capture the physics of interest. We can start with the most universal sector of the theory, which is the action for the metric g_{ab} . The simplest action we can consider is the Einstein-Hilbert action together with a negative cosmological constant:

$$S[g] = \frac{1}{2\kappa^2} \int d^{d+1}x \sqrt{-g} \left[R + \frac{d(d-1)}{L^2} \right]. \quad (28.5)$$

Here R is the Ricci scalar, L is a length scale whose meaning will become apparent shortly and κ is the gravitational constant.³ The Einstein equations of motion following from this action are

$$R_{ab} = -\frac{d}{L^2} g_{ab}, \quad (28.6)$$

where R_{ab} is the Ricci tensor. The most symmetric solution to these equations is Anti-de Sitter space (AdS) which has the metric

$$ds^2 = L^2 \left(\frac{-dt^2 + dx^i dx^i}{r^2} + \frac{dr^2}{r^2} \right). \quad (28.7)$$

We think of the coordinates $\{t, x^i\}$ as parameterizing the space on which the field theory lives, while r is the extra radial coordinate in Fig. 28.1 running from $r = 0$, called the *boundary*, to $r = \infty$, called the *horizon*. Two aspects of this solution should be discussed: its symmetries and the overall scale L .

The full isometry group of the spacetime (28.7) is $SO(d, 2)$. This is precisely the conformal group in d dimensions. The symmetries of the bulk action act on the boundary quantum field theory (QFT) as conformal transformations [6, 7], indicating that the dual QFT is conformally invariant. In particular, the scaling symmetry of the QFT acts on the spacetime as

$$\{t, x^i, r\} \rightarrow \{\lambda t, \lambda x^i, \lambda r\}, \quad (28.8)$$

which clearly leaves the metric (28.7) invariant. This gives a first indication of why the radial direction r is associated with the energy scale: as we scale to late times, we also scale towards large values of r , consistent with these being the low energy, or *IR* region of Fig. 28.1.

The overall factor of L in (28.7) sets the radius of curvature of the AdS spacetime. In order for classical gravity to be a valid description we need this radius to be large in Planck units. This requires

$$c \sim \frac{L^{d-1}}{\kappa^2} \gg 1. \quad (28.9)$$

This limit ensures that quantum corrections to (28.5) generated by graviton

³A modern introduction to general relativity is [12].

loops will be small, allowing us to focus on classical solutions to the Einstein equations. We denoted the ratio in (28.9) by c because it is the area enclosing a spatial volume of AdS in Planck units. The holographic principle suggests that this quantity should be associated with the number of degrees of freedom of the dual field theory. For more precise arguments see [4, 9, 13]. Indeed, we will see below that c is proportional to the central charge of the QFT defined, for instance, as the coefficient of the free energy when the theory is placed at a high temperature [14]. In most of the established examples of the correspondence for $3+1$ dimensional gauge theories, $c \sim N^2$, where N is the rank of the gauge group of the QFT with action (28.2). We will therefore refer to (28.9) as the *large- N limit*. In general c will scale like some positive power of N . If we were to discretize the QFT to put it on a lattice, c would indicate the number of degrees of freedom per site.

Two further comments are necessary regarding the limit (28.9) of the action (28.5). The first is that it is an unnatural tuning from a Wilsonian point of view, effectively ignoring the cosmological constant problem by imposing that the cosmological constant be small in Planck units. One might worry whether there are any theories of quantum gravity for which this is a consistent limit to impose. Secondly, there could in principle be higher derivative terms, such as curvature-squared terms R^2 , in the classical action. These terms can and have been incorporated into the holographic correspondence, but they increase the difficulty of computations and introduce additional parameters. If the couplings of such terms are natural, then they will be highly suppressed in the limit (28.9). For peace of mind, we would like to know if there are concrete examples of gravitational theories which are described by the Einstein-Hilbert action (28.5) together with the limit (28.9).

The large- N limit of the best studied examples of the holographic correspondence, $\mathcal{N} = 4$ super Yang-Mills theory in $3+1$ dimensions and $\mathcal{N} = 8$ super Yang-Mills theory in $2+1$ dimensions, are dual to *Freund-Rubin* compactifications of string theory which do indeed have sectors described by the Einstein-Hilbert action with a weakly curved AdS vacuum. However, there are many more theories for which this is the case. These are found in the *landscape* of string theory vacua [15]. The string landscape was in fact discovered in attempting to justify fine-tuning the cosmological constant [16]. In the present context the landscape indicates the existence of many conformal field theories with large central charge and a universal sector dually described by the Einstein-Hilbert action [17]. More generally, the existence of a vast landscape of string vacua enables us to fine-tune the cosmological constant and then use effective field reasoning in the bulk gravitational description. While it may be that some effective field theories cannot be completed into a UV-consistent theory of quantum gravity,⁴ the existence of a large number of effective field theories that can be UV-completed, i.e., the string landscape, will allow us to ignore considerations of quantum gravity UV consistency for the remainder.

⁴Such theories are sometimes said to belong to the *swampland* [18].

Granted the existence of many QFTs with classical gravity duals, we still do not have a precise characterization of this set of QFTs. Having a large central charge, as in (28.9), is one necessary feature. Another appears to be that there is a parametrically large gap in the spectrum of anomalous dimensions of operators in the QFT [19]. This means that there are only a handful of relevant operators, with most operators being highly irrelevant. While all of the well-understood examples of theories with holographic duals are supersymmetric, it is not clear at the time of writing whether this is an essential ingredient or a technical crutch. Finally, while I will focus in this chapter on quantum critical theories that are Lorentz invariant, the holographic correspondence has recently been extended to theories with dynamical critical exponent $z \neq 1$ [20–22]. I will furthermore set the speed of light equal to unity throughout.

28.1.1 The Basic Dictionary

The most basic and useful entry in the holographic correspondence dictionary is that for every gauge-invariant operator \mathcal{O} in the QFT, there is a corresponding field ϕ in the bulk gravitational theory:

$$\begin{array}{ccc} \text{operator } \mathcal{O} & \longleftrightarrow & \text{dynamical field } \phi \\ (\text{quantum field theory}) & & (\text{bulk}) \end{array} \quad (28.10)$$

So far the only bulk field we have discussed is the metric g_{ab} . By the above statement, this should be dual to an operator in the QFT, but which one? Given that the metric is universal, present by definition in all classical theories of gravity, we should expect to match the metric to an operator that exists in all QFTs. Furthermore, we can expect the operator to have spin 2, just like the graviton. The natural guess is that the correct operator is the energy-momentum tensor $T^{\mu\nu}$ of the QFT. The indices μ, ν run over the d spacetime dimensions of the QFT while a, b run over the $d + 1$ dimensions of the bulk. In many situations we can work in a gauge in the bulk in which fluctuations of the metric (gravitons) have no components in the radial direction, $\delta g_{ar} = 0$, thus allowing a matching between components of metric fluctuations and components of the QFT energy-momentum tensor.

More generally the bulk action will contain more fields than just the metric. Each field in the bulk will correspond to an additional operator in the QFT. Examples of the field-operator correspondence we will need here are:

$$\begin{array}{ccc} \text{energy-momentum tensor: } T^{\mu\nu} & & \text{graviton: } g_{ab} \\ \text{global current: } J^\mu & \longleftrightarrow & \text{Maxwell field: } A_a \\ \text{scalar operator: } \mathcal{O}_B & & \text{scalar field: } \phi \\ \text{fermionic operator: } \mathcal{O}_F & & \text{fermionic field: } \psi \end{array} \quad (28.11)$$

Given these correspondences we can now state the dynamical relationship between the quantities involved: adding a source J for an operator \mathcal{O} in the

QFT is dual to imposing a boundary condition at infinity for the field ϕ corresponding to \mathcal{O} . The boundary condition is that as $r \rightarrow 0$ in the spacetime (28.7), the field ϕ tends towards the value $\delta\phi_{(0)} = J$, up to an overall power of r . That is,

$$Z_{\text{bulk}}[\phi \rightarrow \delta\phi_{(0)}] = \left\langle \exp \left(i \int d^d x \delta\phi_{(0)} \mathcal{O} \right) \right\rangle_{\text{QFT}}. \quad (28.12)$$

This formula is illustrated in Fig. 28.2. As anticipated in the figure, the usefulness of expression (28.12) is that it will enable us to compute expectation values and n -point functions of the operator \mathcal{O} in the QFT by differentiating the left hand side with respect to $J = \delta\phi_{(0)}$.

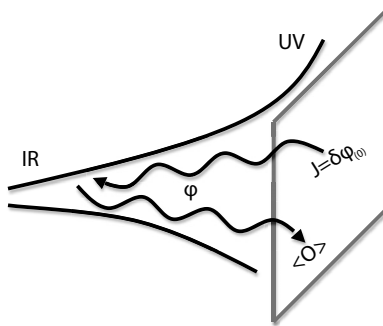


FIGURE 28.2

A source J for an operator \mathcal{O} in the QFT corresponds to a boundary condition $\delta\phi_{(0)}$ for the bulk field ϕ dual to \mathcal{O} . Solving the bulk equations of motion for ϕ allows computation of the expectation value $\langle \mathcal{O} \rangle$ due to the source J .

From the basic relation (28.12), one can quickly obtain the following two important statements. See for instance [9, 23] for a more leisurely exposition of these facts as well as the field-operator correspondence more generally. The first statement is that

$$\text{Global symmetry (QFT)} \quad \rightsquigarrow \quad \text{Gauged symmetry (gravity)}. \quad (28.13)$$

This was implicit in our previous claim in (28.11) that a bulk Maxwell field was dual to a global current operator. It is also closely related to the notion that gauge symmetries include large gauge transformations that can act on the boundary of spacetime as global symmetry operations.

Secondly, suppose that the bulk bosonic or fermionic fields are simply free fields with actions

$$S[\phi] = \int d^{d+1}x \sqrt{-g} \left(|\partial\phi - iqA\phi|^2 + m^2|\phi|^2 \right), \quad (28.14)$$

and

$$S[\psi] = \int d^{d+1}x \sqrt{-g} [i\bar{\psi}\Gamma \cdot (\partial + \frac{1}{4}\omega_{\mu\nu}\Gamma^{\mu\nu} - iqA) \psi + m\bar{\psi}\psi], \quad (28.15)$$

respectively. For future convenience we have allowed the fields to have charge q under some $U(1)$ gauge symmetry. Here the Γ s are Dirac gamma matrices and $\omega_{\mu\nu}$ is the spin connection needed to describe fermions in a curved spacetime background. Given the above two actions, then the bosonic and fermionic operators \mathcal{O}_B and \mathcal{O}_F , dual to ϕ and ψ respectively, will have scaling dimensions

$$\Delta_B(\Delta_B - d) = (mL)^2, \quad \Delta_F = \frac{d}{2} + Lm. \quad (28.16)$$

Recall that in the d dimensional field theory, an operator \mathcal{O} will be relevant if $\Delta_{\mathcal{O}} < d$, marginal if $\Delta_{\mathcal{O}} = d$ and irrelevant otherwise. From (28.16) we can see that very massive bulk fields, in units of the AdS radius L , correspond to highly irrelevant operators. The computations we will outline in this chapter will involve a handful of light fields in the bulk. This is therefore dual to a handful of low-dimensional operators controlling the dynamics of the QFT. Note that masses in the bulk do not correspond to masses in the dual QFT, which is still scale invariant.

We can outline the use of (28.12) to calculate a two-point function in the strongly-coupled CFT. For simplicity we will compute the Euclidean two-point function, in terms of the imaginary time $\tau = it$. We wish to evaluate

$$\langle \mathcal{O}(x)\mathcal{O}(y) \rangle = \frac{\delta^2}{\delta\delta\phi_{(0)}^2} Z_{\text{bulk}}[\phi \rightarrow \delta\phi_{(0)}] = \frac{\delta^2}{\delta\delta\phi_{(0)}^2} e^{-S[\phi \rightarrow \delta\phi_{(0)}]}. \quad (28.17)$$

In the second equality we have used the bulk classical limit (28.9); $S[\phi \rightarrow \delta\phi_{(0)}]$ is the bulk action evaluated on a solution to the equations of motion subject to the boundary condition $\phi \rightarrow \delta\phi_{(0)}$. This is all very much in the spirit of Hamilton-Jacobi theory. We therefore need to solve the bulk equations of motion with general boundary conditions.

Consider an operator \mathcal{O} dual to a neutral scalar field ϕ in the bulk with action (28.14). The solution to the bulk equations of motion that is regular at the *AdS horizon* $r = \infty$ is given by the modified Bessel function

$$\phi \propto \delta\phi_{(0)} r^{d/2} K_{\Delta_+ - \frac{d}{2}}\left(r\sqrt{k^2 + \omega^2}\right) e^{-i\omega\tau + ik \cdot x}. \quad (28.18)$$

We expressed the solution as a Fourier mode. The weight Δ_+ is the larger of the two solutions to (28.16). We now need to evaluate the action (28.14) on the solution (28.18) and use the prescription (28.17). This is complicated by the need to renormalize infinities coming from the infinite volume of AdS space (see [23] and references therein); under the holographic correspondence these divergences are dual to the standard UV divergences encountered in QFT. The upshot is a general result that applies to all types of operators and to Lorentzian as well as Euclidean signatures. Near the boundary, the bulk solution will behave like

$$\phi = \phi_{(0)} r^{d-\Delta} + \cdots + \phi_{(1)} r^\Delta + \cdots, \quad (\text{as } r \rightarrow 0). \quad (28.19)$$

This behavior can be taken to define Δ . The two-point function, retarded in the case of Lorentzian signature, is then found to be

$$\langle \mathcal{O}(x)\mathcal{O}(y) \rangle_R = \frac{2\Delta - d}{L} \frac{\phi_{(1)}}{\phi_{(0)}}. \quad (28.20)$$

The above formula is normalized by assuming that the bulk field ϕ has kinetic term $\frac{1}{2}(\partial\phi)^2$. If this is not the case, the bulk field should be appropriately rescaled to put the kinetic term in this form. The rescaling will result in an extra overall factor in (28.20). Taking the $r \rightarrow 0$ limit of the solution (28.18) one easily obtains

$$\langle \mathcal{O}\mathcal{O} \rangle(k, \omega) \propto (k^2 + \omega^2)^{-\frac{d}{2} + \Delta_+}. \quad (28.21)$$

This is the correct result for the Euclidean two-point function of a scalar operator of scaling dimension $\Delta = \Delta_+$ in a d dimensional CFT.

The result (28.21) is completely fixed by conformal invariance. This would not be the case for higher-point functions. However, the holographic correspondence will come into its own when we place the QFT at a finite temperature.

28.1.2 Finite Temperature

Real-time processes in a QFT at finite temperature can be difficult to compute, even at weak coupling. A powerful feature of the holographic correspondence is that the finite temperature computations are essentially no harder than computations at zero temperature: they still involve only classical fields in a background curved spacetime. The important difference is that the spacetime is no longer AdS space (28.7) but rather an asymptotically AdS black hole, illustrated in Fig. 28.3.

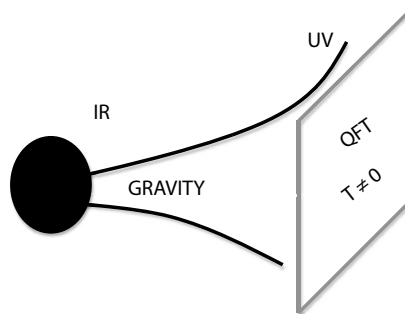


FIGURE 28.3

The strongly-coupled QFT at finite temperature is dual to classical gravity in a black-hole spacetime.

While black holes may seem exotic, their appearance here is both natural

and in fact necessary. Given that all quantum field theories can be placed at a finite temperature, the dual description of heating up the theory should not require any new ingredients to be introduced. Thus we should still be able to use the action (28.5). Temperature introduces an energy scale T which must break the scaling invariance (28.8). If we relax the scaling symmetry and look for solutions to the Einstein equations (28.6) which are still invariant under spatial rotations and spacetime translations, it turns out that there is a unique regular solution: the Schwarzschild-AdS black hole. This has metric

$$ds^2 = \frac{L^2}{r^2} \left(-f(r)dt^2 + \frac{dr^2}{f(r)} + dx^i dx^i \right), \quad (28.22)$$

where

$$f(r) = 1 - \left(\frac{r}{r_+} \right)^d. \quad (28.23)$$

This solution is called a black hole because $f(r_+) = 0$, indicating that light emitted to an asymptotic observer becomes infinitely redshifted at the *event horizon* $r = r_+$.

The length scale r_+ determines the temperature of the dual field theory via

$$T = \frac{d}{4\pi r_+}. \quad (28.24)$$

This is in fact the Hawking temperature of the black hole. However, Hawking radiation is a quantum-mechanical effect in the bulk [24] and therefore suppressed in the large- N limit. A slightly formal argument that leads to (28.24) can be made by considering the analytic continuation of the black hole (28.22) to Euclidean signature $\tau = it$ [25]. At the radius $r = r_+$ the Euclidean time direction shrinks to a point. This is precisely like the origin of polar coordinates: $dR^2 + R^2 d\theta^2$. The only way such shrinking can occur without introducing a conical singularity is if τ is periodic with period

$$\tau \sim \tau + \frac{4\pi}{|f'(r_+)|} = \tau + \frac{4\pi r_+}{d}. \quad (28.25)$$

This period is obtained by changing coordinates so that the $\{r, \tau\}$ part of the black-hole metric, to leading order at $r \rightarrow r_+$, looks like the $\{R, \theta\}$ metric for flat space in polar coordinates. Requiring θ to have period 2π leads to (28.25). The standard interpretation of the period of the Euclidean time circle as the inverse temperature then gives (28.24).

The simplest finite temperature quantity we can calculate is the free energy of the theory. This is given by

$$F = -T \log Z = TS_E[g_{\text{BH}}] = -\frac{(4\pi)^d L^{d-1}}{2\kappa^2 d^d} V_{d-1} T^d, \quad (28.26)$$

where in the second equality we have used the large- N relation $Z = e^{-S_E[g]}$, expressing the partition function as the Wick rotated, Euclidean classical action evaluated on the black-hole saddle point (28.22). The final equality involves performing the evaluation. This again requires renormalizing divergences due to the infinite volume of the spacetime (see [23] and references therein). The dependence of the free energy (28.26) on the spatial volume and temperature is fixed by the scale invariance of the underlying QFT. However, the coefficient gives physical information and is one definition of the central charge of the theory. Thus (28.26) confirms our previous statement that $F \sim c T^d$ with $c \gg 1$ given by (28.9). From the free energy (28.26) we can easily obtain the entropy,

$$S = -\frac{\partial F}{\partial T} = \frac{(4\pi)^d L^{d-1}}{2\kappa^2 d^{d-1}} V_{d-1} T^{d-1}. \quad (28.27)$$

The black-hole solution (28.22) describes the theory in equilibrium at finite temperature, with the free energy (28.26). To perturb the system away from equilibrium we simply need to perturb the black-hole solution and compute response functions in the same way as we did in the previous section at zero temperature. Dissipation due to the finite temperature is described by matter falling through the black-hole horizon.

28.1.3 Spectral Functions and Quasi-normal Modes

Retarded Green's functions at finite temperature are obtained via the holographic correspondence in the same way as at zero temperature: one solves the bulk equations of motion of the field ϕ dual to the operator \mathcal{O} of interest. The equations are linearized about the black-hole background (28.22). Near the asymptotic boundary ($r \rightarrow 0$) the black-hole metric behaves in the same way as pure AdS space, and therefore the asymptotic solution for the field ϕ will again take the form (28.19). The retarded Green's function is given by (28.20).

Generally wave equations in black-hole backgrounds cannot be solved analytically. After a Fourier decomposition

$$\phi = \phi(r) e^{-i\omega t + ik \cdot x}, \quad (28.28)$$

one is left with an ODE for $\phi(r)$. However, it is straightforward to solve the differential equation numerically and extract the coefficients $\phi_{(0)}$ and $\phi_{(1)}$ from (28.19). In solving the differential equation one needs to impose boundary conditions at the horizon $r = r_+$. The correct boundary conditions are *ingoing* boundary conditions, in which bulk matter is falling into the black hole rather than coming out. This amounts to imposing

$$\phi(r) \propto e^{-i(\omega/4\pi T) \log(r-r_+)} + \dots \quad (\text{as } r \rightarrow r_+). \quad (28.29)$$

The key element here is the sign of the exponent. Combining (28.29) and

(28.28) we see that the wave moves towards the horizon $r = r_+$ as time advances. The temperature T is given by (28.24).

The strongly-coupled theories we are studying typically do not have quasi-particle excitations. Therefore, except for specific interesting circumstances to be addressed shortly, we do not expect sharp features in the response functions along the real frequency axis. This raises the question of how best to characterize the spectral functions in such theories.

In all the known retarded Green's functions obtained via the holographic correspondence, the only nonanalyticities found at finite temperature are poles at specific complex frequencies. At zero temperature the poles can degenerate into branch cuts, but at finite temperature the Green's functions appear to be meromorphic in the complex frequency plane.⁵ These poles are called the quasi-normal frequencies of the Green's function, ω_* , and they largely determine the interesting structure of the function

$$\langle \mathcal{O} \mathcal{O} \rangle_R(\omega) \sim \sum_{\omega_*} \frac{c_*}{\omega - \omega_*}, \quad (28.30)$$

up to an overall function of ω that is holomorphic everywhere except possibly at infinity. It is clear from (28.20) that the poles occur whenever

$$\phi_{(0)}(\omega_*) = 0. \quad (28.31)$$

From the bulk point of view a quasi-normal mode is a solution to the linearized equations of motion satisfying ingoing boundary conditions (28.29) at the horizon together with (28.31) at the boundary [26]. The quasi-normal modes can therefore be determined numerically from the linearized bulk equations of motion using numerical shooting techniques. We will see some examples below.

The quasi-normal frequencies have an interesting structure, as we will see in the following sections. For the moment we can note one circumstance in which quasi-normal poles can approach the real frequency axis even at strong coupling. This is in the hydrodynamic regime. Hydrodynamic modes can be associated to conserved quantities or to broken symmetries and describe the long wavelength dynamics of the system [27].

Focus for a moment on the case of $d = 3 + 1$ dimensional field theories. All such theories will have hydrodynamic shear and sound modes, as these follow from conservation of the energy-momentum tensor. The shear mode, for example, is a quasi-normal mode of the form

$$\omega_* = -i \frac{\eta}{\epsilon + P} k^2, \quad (\text{as } k \rightarrow 0), \quad (28.32)$$

where η is the shear viscosity, ϵ the energy density and P the pressure. Via the holographic correspondence the energy and pressure are determined from the

⁵Strictly speaking, we are referring to the analytic continuation of the retarded Green's function from the upper imaginary axis.

free energy (28.26). The pole can be found by computing the retarded Green's function of the xy components of the energy-momentum tensor $\langle T^{xy}T^{xy} \rangle_R$, taking the momentum to be along the z direction.

As stated in (28.11), the operator dual to T^{xy} is a fluctuation of the g_{xy} metric component in the bulk. We can therefore sketch a computation of the Green's function $\langle T^{xy}T^{xy} \rangle_R$. First, we linearize the equations of motion (28.6) about the black-hole spacetime (28.22):

$$ds^2 = ds_{\text{BH}}^2 + 2\delta g_{xy}(r)e^{-i\omega t+ikz}dxdy. \quad (28.33)$$

The resulting equation is

$$rf(rf\delta g'_{xy})' = (8f + k^2r^2f - \omega^2r^2 - 4f^2)\delta g_{xy}. \quad (28.34)$$

To extract the Green's function, one now simply imposes ingoing boundary conditions at the black-hole horizon (28.29), solves the above equation using, e.g., a small frequency and momentum expansion, and then computes the Green's function from (28.19) and (28.20). A shear-mode pole (28.32) is found with a shear viscosity η most famously expressed as [28]

$$\frac{\eta}{s} = \frac{1}{4\pi}, \quad (28.35)$$

where the entropy density $s = S/V_3$ is given by (28.27). A very clear pedagogical exposition of this result can be found in [29]. The result (28.35) appears to be generic in the holographic correspondence to leading order at large N , but can have corrections with either sign.⁶

Other hydrodynamic coefficients, such as sound speeds and electrical conductivities, can similarly be computed by exhibiting poles in Green's functions or by using Kubo formulae [29]. For instance, the electrical conductivity σ over the charge susceptibility χ is given by [31].

$$\frac{\sigma}{\chi} = \frac{1}{4\pi T} \frac{d}{d-2}, \quad (28.36)$$

to leading order at large N .

Upon adding a chemical potential, and hence working with a finite charge density, we will see that there are two additional circumstances in which quasi-normal modes can come close to the real frequency axis. The first is the case of bosonic operators, at the onset of superconducting instabilities, while the second is for fermionic operators, leading to strong-coupling analogs of Fermi surfaces.

Before closing this section, we can note that beyond linear response, holographic techniques have recently started to be applied to the study of far-from-equilibrium dynamics of strongly-interacting theories [32].

⁶See [30] for a summary of the status of the *viscosity bound conjecture* at the time of writing.

28.2 Finite Chemical Potential

We started with the observation that at zero temperature the holographic correspondence gives a geometrical realization of conformal invariance that allows computation of correlators in certain strongly-coupled quantum critical theories. We then discussed the most universal deformation away from scale invariance, by placing the theories at a finite temperature. Another very important deformation away from scale invariance, especially in condensed matter systems, is to place the theory at finite chemical potential and hence induce a charge density.

Finite charge density means an expectation value for the time component of a global current $\langle J^t \rangle$. We claimed in (28.11) that the bulk dual to a global current is a Maxwell field. We therefore need to supplement our existing actions with the term

$$S[A] = -\frac{1}{4g^2} \int d^{d+1}x \sqrt{-g} F^2, \quad (28.37)$$

where $F = dA$ is the field strength. As with the Einstein-Hilbert action (28.5) there can in principle be higher-derivative corrections to this action. Under a naturalness assumption, i.e., in the absence of very large dimensionless numbers, they will be suppressed in the large- N limit. This is known to occur in specific examples.

The gravitational dual description of working with a finite charge density in the field theory is to add an electric charge to the black hole. This is illustrated in Fig. 28.4.

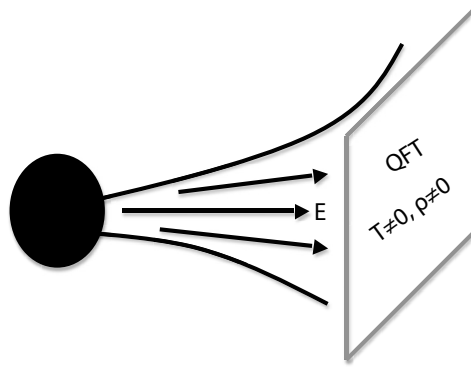


FIGURE 28.4

The strongly-coupled QFT at finite temperature and finite charge density is dual to classical gravity in a charged black-hole spacetime.

There is a unique solution to Einstein-Maxwell theory, i.e., the theory

given by the actions (28.5) plus (28.37), that describes a black hole carrying an electric charge. This is called the *Reissner-Nordstrom-AdS* black hole.⁷ The metric is given by

$$ds^2 = \frac{L^2}{r^2} \left(-f(r)dt^2 + \frac{dr^2}{f(r)} + dx^i dx^i \right), \quad (28.38)$$

where now

$$f(r) = 1 - \left(1 + \frac{r_+^2 \mu^2}{\gamma^2} \right) \left(\frac{r}{r_+} \right)^d + \frac{r_+^2 \mu^2}{\gamma^2} \left(\frac{r}{r_+} \right)^{2(d-1)}. \quad (28.39)$$

In this last expression we defined

$$\gamma^2 = \frac{(d-1)g^2 L^2}{(d-2)\kappa^2}, \quad (28.40)$$

which is a dimensionless measure of the relative strengths of the gravitational and Maxwell forces. The nonzero Maxwell potential is

$$A_t = \mu \left[1 - \left(\frac{r}{r_+} \right)^{d-2} \right]. \quad (28.41)$$

The above solution is parameterized by two scales: the chemical potential of the field theory μ and the horizon radius r_+ . The latter is related to the temperature by

$$T = \frac{1}{4\pi r_+} \left(d - \frac{(d-2)r_+^2 \mu^2}{\gamma^2} \right). \quad (28.42)$$

As in the neutral case above, the temperature is determined by regularity of the Wick-rotated Euclidean spacetime at the horizon $r = r_+$. By evaluating the action on-shell one can obtain the free energy

$$\Omega(T, \mu) = -\frac{L^{d-1}}{2\kappa^2 r_+^d} \left(1 + \frac{r_+^2 \mu^2}{\gamma^2} \right) V_{d-1} = \mathcal{F} \left(\frac{T}{\mu} \right) V_{d-1} T^d, \quad (28.43)$$

where in the second equality r_+ has been eliminated in favor of the temperature by using (28.42). By scale invariance of the underlying quantum critical theory, the only nontrivial dependence on temperature and chemical potential must be in the dimensionless ratio T/μ .

From the free energy (28.43) one can again determine the entropy $S = -\partial_T \Omega$, as well as the charge density $\rho V_d = -\partial_\mu \Omega$ and other functions of state. One exotic feature that is found is that the entropy remains finite at zero temperature. At the time of writing it is not clear whether this constitutes a prediction of the holographic correspondence (*critical spin ice?*), an artifact

⁷For a slower exposition of the following material see [23, 33].

of the large- N limit, or perhaps an indication that the Reissner-Nordstrom black-hole spacetime is not capturing the correct finite-density ground state of the theory.

Taking the above black-hole as the dual of the theory at finite density and temperature, two natural questions arising as the system is cooled down are first, whether it develops superconductivity and second, whether there are indications of a sharp Fermi surface. At weak coupling the answers to these questions would only depend on the existence of charged bosonic and/or fermionic quasi-particles. The strongly-coupled picture that emerges from the holographic correspondence is somewhat more subtle.

28.2.1 Bosonic Response and Superconductivity

At this point we know nothing about what exactly is carrying the charge density. In this section we probe the finite-density state with bosonic operators. The following section will address fermionic probes. Suppose that our strongly-coupled field theory has at least one charged bosonic operator \mathcal{O} . This will be dual to a charged scalar field ϕ in the bulk with an action along the lines of (28.14). We can compute the spectral density $\text{Im}(\langle \mathcal{O}\mathcal{O} \rangle_R(\omega, k))$ using the methods discussed above. As we have suggested, an instructive way to think about the spectral density at strong coupling is to compute the quasi-normal frequencies of the Green's function. Some illustrative results are shown in Fig. 28.5. For details of the computation see [34].

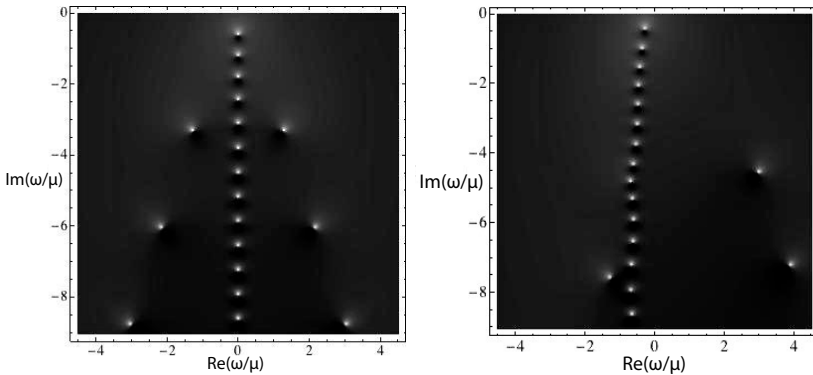


FIGURE 28.5

Zero momentum quasi-normal poles of charged bosons at temperature $T/\mu = 0.075$. The operators \mathcal{O} have scaling dimension $\Delta = 3$ in 2+1 dimensions and charges $q = 0$ (left plot) and $q = 2$ (right plot).

The quasi-normal poles of a neutral operator (left-hand plot in Fig. 28.5), come in two types spaced by either the temperature or the chemical-potential scales. As the charge of the operator is increased (right-hand plot), the

chemical-potential poles move to the right and can merge with the temperature poles. The physics of these mergers has not yet been elucidated.

The other important pole motion in Fig. 28.5 is that as the charge of the operator is increased, the topmost pole moves closer to the real axis. If the charge is increased sufficiently, the pole will move into the upper half frequency plane, indicating an exponentially growing mode and an instability of the vacuum. When this occurs, the operator \mathcal{O} will gain an expectation value, leading to a superconducting state [35–37]. For scalar fields with action (28.14) there is a precise criterion for when an operator \mathcal{O} is unstable against condensing. In $d = 2 + 1$ this occurs at some temperature T_c if [17]

$$q^2 \gamma^2 \geq 3 + 2\Delta_{\mathcal{O}}(\Delta_{\mathcal{O}} - 3). \quad (28.44)$$

Recall that γ was defined in (28.40), effectively setting the units of charge, while q and $\Delta_{\mathcal{O}}$ are respectively the charge and scaling dimension of \mathcal{O} .

There are several important lessons from (28.44), which is a criterion for the onset of superconductivity in a strongly-coupled field theory. There are no quasi-particles or glue or pairing mechanism in sight. Instead the instability is described in terms of the motion of quasi-normal poles and the criterion for instability is phrased in terms of the scaling dimension and charge of operators in a quantum critical theory.

The spacetime picture of the onset of superconductivity is shown in Fig. 28.6. The instability is closely related to *superradiance instabilities* of black holes. Below the instability temperature T_c , the Reissner-Nordstrom black hole (28.38) is no longer the correct ground state. Instead one must solve the coupled Einstein-Maxwell-scalar equations of motion to find new solutions in which the scalar ϕ is nonzero. These are called *hairy* black holes.⁸

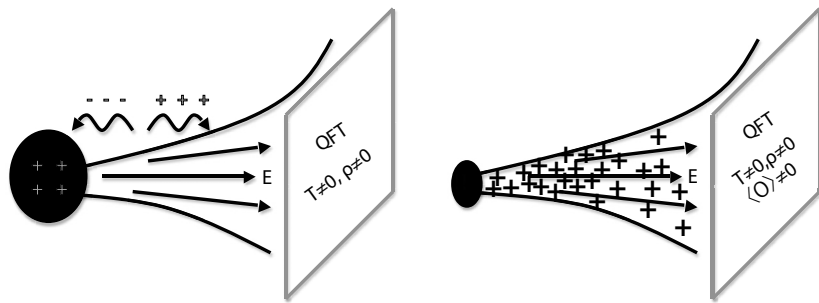


FIGURE 28.6

The superconducting instability of black holes can be thought of as a polarization of the spacetime. Below T_c the charge is largely carried by the condensate rather than the black hole. Such solutions are called hairy black holes.

⁸For more details and references, for instance the computation of T_c , $\langle \mathcal{O} \rangle(T)$ and spectral functions in the superconducting state; see [23, 33].

28.2.2 Fermionic Response and Non-Fermi Liquids

While many theories with holographic duals do indeed develop superconducting instabilities at low temperatures [17], it is not clear that they all do. It is an open question whether there necessarily exist operators in the QFT satisfying (28.44). Interestingly this question is dually related to the *weak gravity conjecture* [17,38]. In cases where the Reissner-Nordstrom black hole (28.38) is stable down to low temperature or, alternatively, one removes the superconducting phase with a large magnetic field, then one can study the low temperature fermionic response, in search for signs of a Fermi surface. This was first attempted in [39] while a comprehensive analytic understanding was achieved in [40]. We shall very briefly outline some of the ideas arising from [40].

Consider a charged fermionic operator Ψ dual to a bulk fermion with action (28.15). The spectral density of this operator at zero temperature and finite charge density is obtained following the prescription described above. It was found in [40] that if the charge of the fermionic operator is sufficiently big compared to its scaling dimension (cf. the criterion for superconductivity in (28.44)) then there is a quasi-normal pole with the dispersion relation

$$\frac{\omega_*}{v_F} + h e^{i\theta} \omega_*^{2\nu} = k - k_F, \quad (28.45)$$

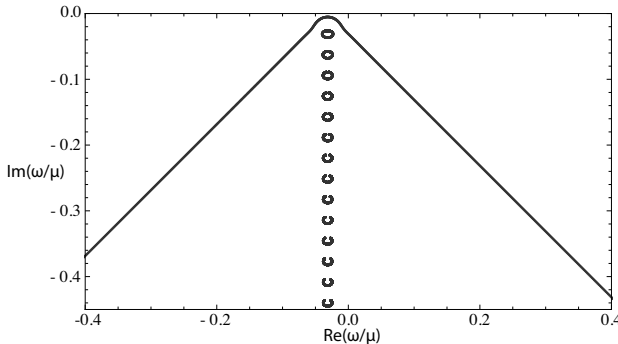
where v_F, k_F, ν, θ and h are positive constants. The pole bounces off the real axis as the momentum k reaches the Fermi momentum k_F . This is characteristic of Fermi liquids. However, the residue of the pole is found to vanish as it hits the real axis, and therefore there is not a well-defined quasi-particle. Furthermore, the dispersion relation (28.45) is not that of a Fermi liquid. In general, the low energy dispersion relation $\omega_*(k)$, following from (28.45), depends on whether ν is greater or less than $\frac{1}{2}$. The case $\nu = \frac{1}{2}$ is an interesting separate case and leads to

$$\frac{\omega_*}{v_F} + h e^{i\theta} \omega_* \log \omega_* = k - k_F, \quad (28.46)$$

which is precisely of the form required for a *marginal Fermi liquid* originally postulated on phenomenological grounds to describe the cuprates [41].

Thus the holographic correspondence at finite density and zero temperature leads to computationally controlled non-Fermi liquid behavior of fermion spectral densities. No assumption about the existence of quasi-particles is made; instead the dispersion relation emerges from a quasi-normal mode of a fermionic operator which has been consistently treated together with all the other quasi-normal modes. An illustrative motion of the quasi-normal modes $\omega_*(k)$ at a finite low temperature is shown in Fig. 28.7 [34,40].

The poles close to the negative imaginary frequency axis in Fig. 28.7 coalesce at zero temperature to form the branch cut visible in Eq. (28.45). The same occurs with the bosonic poles in Fig. 28.5. It is clear in (28.45) that this branch cut is intimately connected with the non-Fermi liquid dispersion of the quasi-normal pole. In Fig. 28.7 one sees that the branch cut poles also

**FIGURE 28.7**

Motion of quasi-normal poles at low temperature as k is varied through k_F .

move significantly (in circles), as the pole of (28.45) moves up to and bounces off the real frequency axis. To correctly compute the effect of *pole dancing* on physical quantities it will generally be important to consider all the poles close to the real axis, not just the pole with dispersion relation (28.45), e.g., [34]. This is a crucial difference in general between quasi-normal modes and quasi-particles. While we have a well-defined non-Fermi liquid, with a dispersion relation (28.45), strong coupling requires us to consider the dynamics of the branch cut as well as the almost-quasi-particle pole. Unlike almost all conventional models of non-Fermi liquids, the holographic correspondence allows this to be done in a controlled way.

28.3 Current and Future Directions

At zeroth order, the holographic correspondence gives a geometrical perspective on quantum criticality that is particularly amenable to the study of finite-temperature real-time processes, such as response functions and also far-from-equilibrium dynamics. In a large- N limit, that nonetheless retains the strongly-coupled nature of the theory, computation of all of these quantities is reduced to solving classical gravitational equations in one higher dimension than the field theory. The calculations are both significantly easier and conceptually more transparent than conventional approaches.

Moreover, current excitement about the possibilities of an applied holographic correspondence has been deepened by recent discoveries concerning the strongly-interacting theories at finite charge density and low temperatures. We have outlined above how charged bosonic operators were found to lead to superconducting phases while charged fermionic operators captured non-Fermi liquid behavior. It is likely that deepening our understanding of

these two phenomena, and the connection between them, will be an important focus of future research.

The onset of superconductivity in holographic models was found to be mediated by the charge and scaling dimension of operators in the quantum critical theory. These are the natural and well-defined quantities to consider at strong coupling, rather than electrons and glue and pairing. It will be important to understand if criteria such as Eq. (28.44) can be applied generally to strongly-interacting systems, without reference to a holographic description.

While field theories that become superconducting according to (28.44) are interesting, equally interesting are those that do not. At weak coupling, a theory with gapless charged bosonic excitations will necessarily develop condensates when placed at a nonzero chemical potential. This statement is not true at strong coupling if there are no operators in the theory satisfying (28.44). It will be interesting to explore if these theories can provide realizations of exotic *Boson metal* phases.

Non-Fermi liquid dispersion such as (28.45) of poles in a fermion propagator that are not weakly-interacting quasi-particles hints at a notion of a strongly-coupled Fermi surface. This concept needs to be developed further. In [34] the magnetic susceptibility in these theories was computed as a function of the magnetic field, in a search for quantum oscillations that are characteristic of Fermi surfaces. At low temperatures, the anticipated periodic nonanalyticities were found, taking the schematic form

$$\chi = - \lim_{T \rightarrow 0} \frac{\partial^2 \Omega}{\partial B^2} \sim \sum_{\ell} \left| \ell B - \frac{A_F}{2\pi q} \right|^{-2+1/2\nu}, \quad (28.47)$$

where $A_F = \pi k_F^2$ is the Fermi surface area and ν is as in (28.45). These divergences are softer than the usual weak-coupling divergences in the susceptibility, which become delta functions at zero temperature. At the time of writing, quantum oscillations are proving to be valuable probes of the cuprate superconductors. It will be important to identify any generic qualitative differences between weak and strong coupling both in order to interpret data correctly and also to have signatures for novel states of matter.

Obtaining the result (28.47) involved developing a formula for the leading correction in $1/N$ to the large- N result. It was shown that the correction to the free energy due to a specific bulk field could be expressed as a sum over the corresponding quasi-normal frequencies

$$\Omega = \Omega_0 + T \sum_{\omega_*} \log \left(\frac{1}{2\pi} \left| \Gamma \left(\frac{i\omega_*}{2\pi T} + \frac{1}{2} \right) \right|^2 \right) + \dots, \quad (28.48)$$

where Ω_0 is the leading order large- N result (28.43) of the Reissner-Nordstrom black hole. The above formula is for fermionic operators. Expressions like (28.48) reinforce the idea that quasi-normal modes may be the correct and required generalization of quasi-particles to describe strongly-interacting sys-

tems. Indeed it seems likely that (28.48) can be generalized beyond the holographic correspondence and to other observables such as response functions.

A possible fly in the ointment is that the non-Fermi liquid dispersion (28.45) is closely tied to the presence of a branch cut in the zero-temperature Green's function. This in turn is directly related to the AdS_2 near-horizon region of the zero-temperature Reissner-Nordstrom black hole [34, 40]. Finally, this AdS_2 region is ultimately responsible for the finite entropy of the system at zero temperature. It remains to be seen whether interesting fermion dispersion relations can be obtained without a finite entropy at zero temperature. The zero temperature limit of superconducting states appears to have a vanishing entropy, e.g., [42, 43]; it will be very interesting to see whether these states show signs of Fermi surfaces or not. More generally the fate of the quasi-normal poles (28.45) across a superconducting transition is an important open question.

A distinct direction of future research will be the study of disorder and impurities in strongly-interacting systems. Disorder plays a crucial role in many systems of technological and theoretical interest. The holographic correspondence will provide a framework in which familiar phenomena such as Anderson localization or the Kondo effect can be studied at strong coupling. A first attempt to include weak disorder can be found in [44].

Bibliography

- [1] P. W. Anderson, *Basic notions of condensed matter physics*, Addison-Wesley, USA (1984).
- [2] S. Sachdev, *Quantum phase transitions*, Cambridge University Press, UK (2001).
- [3] E. W. Carlson, V. J. Emery, S. A. Kivelson and D. Orgad, arXiv:cond-mat/0206217.
- [4] L. Susskind and J. Lindesay, *An Introduction to Black Holes, Information and the String Theory Revolution: The Holographic Universe*, World Scientific, USA (2005).
- [5] J. M. Maldacena, Adv. Theor. Math. Phys. **2**, 231 (1998) [Int. J. Theor. Phys. **38**, 1113 (1999)] [arXiv:hep-th/9711200].
- [6] E. Witten, Adv. Theor. Math. Phys. **2**, 253 (1998) [arXiv:hep-th/9802150].
- [7] S. S. Gubser, I. R. Klebanov and A. M. Polyakov, Phys. Lett. B **428**, 105 (1998) [arXiv:hep-th/9802109].

- [8] G. T. Horowitz and J. Polchinski, arXiv:gr-qc/0602037.
- [9] J. McGreevy, arXiv:0909.0518 [hep-th].
- [10] G. 't Hooft, Nucl. Phys. B **72**, 461 (1974).
- [11] S. R. Coleman, *Aspects of symmetry*, Cambridge University Press, UK (1988).
- [12] S. M. Carroll, *Spacetime and geometry*, Addison-Wesley, USA (2004).
- [13] L. Susskind and E. Witten, arXiv:hep-th/9805114.
- [14] P. Kovtun and A. Ritz, Phys. Rev. Lett. **100**, 171606 (2008) [arXiv:0801.2785 [hep-th]].
- [15] F. Denef, arXiv:0803.1194 [hep-th].
- [16] R. Bousso and J. Polchinski, JHEP **0006**, 006 (2000) [arXiv:hep-th/0004134].
- [17] F. Denef and S. A. Hartnoll, Phys. Rev. D **79**, 126008 (2009) [arXiv:0901.1160 [hep-th]].
- [18] C. Vafa, arXiv:hep-th/0509212.
- [19] I. Heemskerk, J. Penedones, J. Polchinski and J. Sully, JHEP **0910**, 079 (2009).
- [20] D. T. Son, Phys. Rev. D **78**, 046003 (2008) [arXiv:0804.3972 [hep-th]].
- [21] K. Balasubramanian and J. McGreevy, Phys. Rev. Lett. **101**, 061601 (2008) [arXiv:0804.4053 [hep-th]].
- [22] S. Kachru, X. Liu and M. Mulligan, Phys. Rev. D **78**, 106005 (2008) [arXiv:0808.1725 [hep-th]].
- [23] S. A. Hartnoll, Class. Quant. Grav. **26**, 224002 (2009).
- [24] S. W. Hawking, Nature **248**, 30 (1974).
- [25] G. W. Gibbons and S. W. Hawking, Phys. Rev. D **15**, 2752 (1977).
- [26] D. T. Son and A. O. Starinets, JHEP **0209**, 042 (2002) [arXiv:hep-th/0205051].
- [27] D. Forster, *Hydrodynamic fluctuations, broken symmetry and correlation functions*, Perseus books, USA (1975).
- [28] P. Kovtun, D. T. Son and A. O. Starinets, Phys. Rev. Lett. **94**, 111601 (2005) [arXiv:hep-th/0405231].

- [29] D. T. Son and A. O. Starinets, Ann. Rev. Nucl. Part. Sci. **57**, 95 (2007) [arXiv:0704.0240 [hep-th]].
- [30] A. Sinha and R. C. Myers, Nucl. Phys. A **830**, 295C (2009).
- [31] P. Kovtun and A. Ritz, Phys. Rev. D **78**, 066009 (2008) [arXiv:0806.0110 [hep-th]].
- [32] P. M. Chesler and L. G. Yaffe, Phys. Rev. Lett. **102**, 211601 (2009) [arXiv:0812.2053 [hep-th]].
- [33] C. P. Herzog, J. Phys. A **42**, 343001 (2009) [arXiv:0904.1975 [hep-th]].
- [34] F. Denef, S. A. Hartnoll and S. Sachdev, Phys. Rev. D **80**, 126016 (2009).
- [35] S. S. Gubser, Phys. Rev. D **78**, 065034 (2008) [arXiv:0801.2977 [hep-th]].
- [36] S. A. Hartnoll, C. P. Herzog and G. T. Horowitz, Phys. Rev. Lett. **101**, 031601 (2008) [arXiv:0803.3295 [hep-th]].
- [37] S. A. Hartnoll, C. P. Herzog and G. T. Horowitz, JHEP **0812**, 015 (2008) [arXiv:0810.1563 [hep-th]].
- [38] N. Arkani-Hamed, L. Motl, A. Nicolis and C. Vafa, JHEP **0706**, 060 (2007) [arXiv:hep-th/0601001].
- [39] S. S. Lee, Phys. Rev. D **79**, 086006 (2009).
- [40] T. Faulkner, H. Liu, J. McGreevy and D. Vegh, arXiv:0907.2694 [hep-th].
- [41] C. M. Varma, P. B. Littlewood, S. Schmitt-Rink, E. Abrahams and A. E. Ruckenstein, Phys. Rev. Lett. **63**, 1996 (1989).
- [42] S. S. Gubser and A. Nellore, arXiv:0908.1972 [hep-th].
- [43] G. T. Horowitz and M. M. Roberts, arXiv:0908.3677 [hep-th].
- [44] S. A. Hartnoll and C. P. Herzog, Phys. Rev. D **77**, 106009 (2008) [arXiv:0801.1693 [hep-th]].